

Mushabbar A. Syed  
Raad H. Mohiaddin  
*Editors*

# Magnetic Resonance Imaging of Congenital Heart Disease

Second Edition



 Springer

---

# Magnetic Resonance Imaging of Congenital Heart Disease



---

Mushabbar A. Syed • Raad H. Mohiaddin  
Editors

# Magnetic Resonance Imaging of Congenital Heart Disease

Second Edition

 Springer

*Editors*

Mushabbar A. Syed  
Rolf & Merian Gunnar Professor of Medicine-  
Cardiology, Director Cardiovascular Imaging  
& Program Director, Cardiovascular Disease  
Fellowship  
Loyola University Medical Center  
Maywood, IL, USA

Raad H. Mohiaddin  
Professor of Cardiovascular Imaging  
Royal Brompton and Harefield Hospitals, Guy's  
and St Thomas' NHS Foundation Trust  
& National Heart and Lung Institute, Imperial  
College London  
London, UK

ISBN 978-3-031-29234-7      ISBN 978-3-031-29235-4 (eBook)

<https://doi.org/10.1007/978-3-031-29235-4>

© The Editor(s) (if applicable) and The Author(s), under exclusive license to Springer Nature Switzerland AG 2012, 2023, corrected publication 2023

This work is subject to copyright. All rights are solely and exclusively licensed by the Publisher, whether the whole or part of the material is concerned, specifically the rights of translation, reprinting, reuse of illustrations, recitation, broadcasting, reproduction on microfilms or in any other physical way, and transmission or information storage and retrieval, electronic adaptation, computer software, or by similar or dissimilar methodology now known or hereafter developed.

The use of general descriptive names, registered names, trademarks, service marks, etc. in this publication does not imply, even in the absence of a specific statement, that such names are exempt from the relevant protective laws and regulations and therefore free for general use.

The publisher, the authors, and the editors are safe to assume that the advice and information in this book are believed to be true and accurate at the date of publication. Neither the publisher nor the authors or the editors give a warranty, expressed or implied, with respect to the material contained herein or for any errors or omissions that may have been made. The publisher remains neutral with regard to jurisdictional claims in published maps and institutional affiliations.

This Springer imprint is published by the registered company Springer Nature Switzerland AG  
The registered company address is: Gewerbestrasse 11, 6330 Cham, Switzerland

*“To my family, Jennifer, Ameena, Aleena, Daneyal, and Cassie (and Newt—the best golden retriever) for their unwavering love and support and to my trainees (past, present, and future) for making work fun and productive.”*

*—Mushabbar A. Syed*

*“To the memory of my parents for their tremendous sacrifices, may they rest in eternal peace.*

*To my wife, Khalida, and my children, Hasan, Zain, and Reema, for their love, support and understanding”*

*—Raad H. Mohiaddin*

---

## Foreword

### **A CMR team experienced in and dedicated to congenital heart disease is integral to any Congenital Heart Disease Program**

As an Adult Congenital Heart Disease (ACHD) cardiologist who dedicated his career to ACHD, I read with great interest *Magnetic Resonance Imaging in Congenital Heart Disease*, and I feel honored and privileged to write a foreword to this landmark book. I congratulate the editors and the expert contributors to their second edition of their outstanding and comprehensive book.

Cardiovascular Magnetic Resonance Imaging (CMR) provides highly valuable contributions to the diagnostic assessment, decision making, and management of congenital heart disease (CHD) patients. It is essential to accurately describe cardiac anatomy and to investigate (normal and abnormal) blood flow. CMR has become the reference imaging modality because of its highly reliable, reproducible data for the serial assessment which is crucial and more important than a single snapshot. CMR is the noninvasive imaging modality of choice to quantify ventricular volumes and ejection fraction, shunt calculations, and blood flow measurements in patient with complex CHD and multiple resources of pulmonary and/or systemic blood supply. It overcomes the concerning limitations of the Fick method to calculate the complex pulmonary blood supply in such patients and to estimate pulmonary vascular resistance. CMR has also become an integral diagnostic puzzle for risk stratification of sudden death.

It is not appropriate to perform CMR in CHD patients as a “boutique business” in the current century anymore: CMR in CHD must be performed as a core business, with a team of imagers with expertise in CHD, who is embedded in a multidisciplinary team of a CHD program.

This book sets these high-quality standards for how CMR is to be performed in CHD. The first chapter describes the *general principles of cardiac CMR*, including physics and CMR hardware, and makes this complex information understandable for non-radiologists; it also includes novel advanced techniques such as 4D flow analysis. This chapter extensively discusses the standard pediatric/congenital heart disease examination and protocols. It also highlights important tips and tricks to remain motionless in the CMR scanner and to perform a CMR under sedation or general anesthesia, a very challenging, but very important issue in the growing number of patients with syndromes and neurodevelopmental and neurocognitive deficits and disorders.

The second chapter is dedicated to *CMR Safety*, including absolute and relative contradictions for patients with devices, CMR during pregnancy, stress medication for CMR, and many other issues related to this very safe diagnostic modality, but some potential risks. A special chapter then discusses the benefit of Gadolinium-based contrast agents to assess perfusion, characterize the tissue, and identify scar. Adverse reactions rarely occur despite the excellent safety profile.

Chapter 4, *Introduction to Congenital Heart Disease Anatomy*, prepares the readers for the following chapters with detailed presentation of specific congenital heart defects (e.g., septal defects, tetralogy of Fallot, transposition of the great arteries, Ebstein anomaly). This key Chap. 4 describes the segmental approach in CHD that is fundamental and based on the foun-

dition of morphology: we always refer to morphology in CHD, we never refer to the position of a chamber (e.g., the right atrium and right ventricle can be positioned on the left, and they are still called right atrium and right ventricle, respectively).

The editors and authors then present important CMR-related information about inherited cardiomyopathies, coronary artery anomalies, pericardial disease, cardiac tumors, and stress CMR in CHD. *Fetal Cardiovascular Magnetic Resonance* (Chap. 21) is another highlight of the book and addresses “investigation of fetal circulatory physiology in health and disease.” CMR is playing emerging and instrumental roles in the catheter laboratory (*Interventional Cardiovascular Magnetic Resonance*—Chap. 22) and in the electrophysiology suite (*Magnetic Resonance in ACHD Electrophysiology*—Chap. 23) to guide catheter-based interventions, to plan venous and arterial access, “to create 3D volume reconstruction and image integration with 3D electrophysiology mapping systems to facilitate retrograde approach and to avoid puncture of baffles in patients with atrial switch procedures or a Fontan circulation.” And last but not least, the chapter about *3D printing in CHD*, including 3D CMR reconstruction for virtual tours through the heart, highlights the role of these novel, evolving, innovative techniques for teaching of trainees, interventionalists, and congenital heart surgeons for planning of catheter-based interventions and surgical repairs of complex congenital heart defects.

In summary, the very informative book chapters are very well structured and organized. The text is supported by very informative tables, high-quality figures, and movies. The excellent schematic diagrams are very well designed and very illustrative for the readers. This book takes the readers on an exciting CMR journey of the broad spectrum of cardiovascular diseases with a special focus on CHD.

Navigating through the book and the different chapters, I am reinforced in my strong opinion that CHD patients need to be imaged by radiologists with special expertise in CHD and/or CHD cardiologists with special training in CMR: cardiovascular imaging in CHD should not be offered as a “boutique business” anymore; it needs to be a core business in centers with expertise in complex CHD! The ideal organizational world of a CMR suite would combine the talents of the radiologists with CHD expertise and the talents of CHD cardiologists with CMR training to consolidate their experiences and expertise in dedicated teams!

The readers highly appreciate the wonderful work of the editors and contributors who invested a tremendous amount of time to put together such an informative, very well-illustrated book.

Dr. Erwin Oechslin, FESC  
FRCPC Cardiology / DRCPC Adult Congenital Heart Disease  
Professor of Medicine, University of Toronto  
Peter Munk Cardiac Centre, Toronto ACHD Program  
Toronto, ON, USA

---

## Foreword (First Edition)

As a cardiologist with a career interest in congenital heart disease in adults, I was delighted to have the opportunity to read *Magnetic Resonance Imaging of Congenital Heart Disease* and write a foreword for it. Over the past two decades, CMR has come to occupy an ever more important place in the assessment and management of patients with congenital heart defects (CHD) and other cardiovascular disorders. Thus, this new text will be of broad interest to both imagers and clinicians who deal with cardiovascular disease. Cardiovascular MRI offers an ever-expanding amount of information about the heart and circulation. It can provide outstanding images of cardiovascular morphology and function. It is increasingly being used to detect pathologic fibrosis and has an expanding role in the assessment of myocardial viability. Amazing though CMR is, its limitations and weaknesses also need to be clearly understood. As CMR has evolved, it has challenged other imaging modalities to improve and evolve, all of which improve the understanding that we clinicians have of our patients and consequently the care we can offer them. In many ways, cardiovascular CMR has offered important new insights that clinicians and imagers a generation ago would have considered impossible.

The editors and their expert contributors have taken a large step toward making detailed information about CMR accessible to those working in the field and to those who use the information derived from CMR in their clinical practices. The field is ever changing and ever improving. This text offers an excellent foundation for the reader who is not familiar with the field and up to date descriptions of where we stand with imaging a broad range of cardiovascular diseases. The text is well referenced without being overwhelming, and the illustrations are generally outstanding, including many movie images.

The opening chapter reviews the general principles of CMR, including information about the physics of the technique, and the hardware used. It reviews such useful subjects as remaining motionless in the scanner and the use of sedation and anesthesia. It provides important information relating to how to structure a study of various congenital cardiovascular conditions. The second chapter deals with the important issue of MRI safety, culminating (as in many chapters) with a series of “practical pearls.” Chapter 3 provides an introduction to the anatomy of CHD. The next seven chapters cover the subject of CMR in CHD in all its various forms. A particular emphasis is given to the role of CMR of septal defects, tetralogy of Fallot, Ebstein anomaly, transposition of the great arteries, and single ventricle/Fontan circulations. Chapter 12 focuses on aortic abnormalities including aortic coarctation, PDA, aortic aneurysms, and vascular rings. Chapter 13 deals with inherited cardiomyopathies, including hypertrophic cardiomyopathy, dilated cardiomyopathy, left ventricular non-compaction, and arrhythmogenic right ventricular dysplasia. Chapter 14 addresses coronary artery anomalies and discusses the appropriate roles of CMR and CT angiography in assessing such patients. The next two chapters deal with pericardial diseases and cardiac tumors. Chapter 17 discusses CMR in children, and Chap. 18 describes the current status of interventional CMR, an area with exciting potential. The final chapter explores the emerging roles for CMR in ACHD electrophysiology. These last two chapters represent an exciting marriage of differing imaging and therapeutic modalities that move the field forward.

Overall, the text offers the reader an exciting and comprehensive voyage through the place of CMR in a broad range of cardiovascular diseases with a special focus on congenital heart disease. It succeeds in describing the technical details of MRI techniques in sufficient detail to also help the clinician understand the most important elements of CMR in assessing and managing their patients. We readers are indebted to the editors and their contributors for having put together such an excellent and much needed text on this topic.

Gary Webb

---

## Preface

We are pleased to present the second edition of *Magnetic Resonance Imaging of Congenital Heart Disease*. We felt that the expanding role of MRI in congenital heart disease required a comprehensive reference text which led to the original book in 2013, and we were humbled and pleased with the reception it received. Since the first publication, there have been new advances in the field necessitating a revised and expanded new edition. Our publication schedule was significantly delayed due to the COVID pandemic; however, we took great care in assembling an expert panel of international authors to make this book as accurate and useful as possible.

For the second edition, all previous chapters have been extensively reviewed and updated. In addition, we have added five new chapters on Gadolinium-Based Contrast Agents (Chap. 3), Pulmonary Hypertension (Chap. 8), Stress MRI in Congenital Heart Disease (Chap. 19), Fetal CMR Imaging (Chap. 21), and 3D Printing in Congenital Heart Disease (Chap. 24). We believe that this edition provides a contemporary and comprehensive review of the topic of MRI in congenital heart disease that will be useful to a wide variety of readers from trainees to expert professionals.

Foreword to the original edition was written by Professor Gary Webb, a preeminent leader in the field of congenital heart disease who sadly died in 2021. We fondly remember him and his numerous contributions and accomplishments in this field that are an inspiration to us all. We are thankful to Professor Erwin Oechslin for writing the Foreword to the second edition. Professor Oechslin trained under Professor Webb in adult congenital heart disease at Toronto General Hospital/University of Toronto and later succeeded him as the Director of Toronto Adult Congenital Heart Disease Program.

We are indebted to all of our chapter authors who believed in this project and ensured its completion despite their schedules impacted by the pandemic. We are also grateful to the Springer team led by Grant Weston for their patience and support throughout this project.

Lastly, we are thankful to our readers, and hope that they enjoy reading this book as much as we enjoyed editing and authoring it.

Maywood, IL, USA  
London, UK

Mushabbar A. Syed  
Raad H. Mohiaddin

---

This work contains media enhancements, which are displayed with a “play” icon. Material in the print book can be viewed on a mobile device by downloading the Springer Nature “More Media” app available in the major app stores. The media enhancements in the online version of the work can be accessed directly by authorized users.



---

## Contents

<b>1</b>	<b>General Principles of Cardiac Magnetic Resonance Imaging</b> .....	<b>1</b>
	Mark Alan Fogel	
<b>2</b>	<b>MRI Safety</b> .....	<b>39</b>
	Roger Luechinger	
<b>3</b>	<b>Gadolinium-Based Contrast Agents</b> .....	<b>51</b>
	Menhel Kinno and Joanne Sutter	
<b>4</b>	<b>Introduction to Congenital Heart Disease Anatomy</b> .....	<b>59</b>
	Pierangelo Renella and J. Paul Finn	
<b>5</b>	<b>Venoatrial Abnormalities</b> .....	<b>79</b>
	Henryk Kafka and Raad H. Mohiaddin	
<b>6</b>	<b>Septal Defects</b> .....	<b>103</b>
	Inga Voges and Sylvia Krupickova	
<b>7</b>	<b>Right Ventricular Anomalies</b> .....	<b>115</b>
	Frédérique Bailliard	
<b>8</b>	<b>Pulmonary Hypertension</b> .....	<b>137</b>
	Daniel Knight and Vivek Muthurangu	
<b>9</b>	<b>Tetralogy of Fallot</b> .....	<b>147</b>
	Michael A. Quail, Vivek Muthurangu, and Andrew M. Taylor	
<b>10</b>	<b>Ebstein’s Anomaly and Other Tricuspid Valve Anomalies</b> .....	<b>167</b>
	Steve W. Leung and Mushabbar A. Syed	
<b>11</b>	<b>Abnormalities of Left Ventricular Inflow and Outflow</b> .....	<b>179</b>
	Tal Geva and Puja Banka	
<b>12</b>	<b>Single Ventricle and Fontan Procedures</b> .....	<b>199</b>
	Sylvia Krupickova, Inga Voges, and Raad H. Mohiaddin	
<b>13</b>	<b>Transposition of Great Arteries</b> .....	<b>213</b>
	Joel R. Wilson and Mushabbar A. Syed	
<b>14</b>	<b>Aortic Anomalies</b> .....	<b>229</b>
	Sylvia S. M. Chen and Raad H. Mohiaddin	
<b>15</b>	<b>Inherited Cardiomyopathies</b> .....	<b>251</b>
	Theodore Murphy, Rory O’Hanlon, and Raad H. Mohiaddin	
<b>16</b>	<b>Coronary Artery Anomalies</b> .....	<b>273</b>
	Andrew Crean	
<b>17</b>	<b>Pericardial Diseases</b> .....	<b>303</b>
	Edward T. Martin	

---

<b>18 Cardiac Tumors</b> .....	315
Mushabbar A. Syed and Raad H. Mohiaddin	
<b>19 Stress MRI in Congenital Heart Disease</b> .....	331
W. A. Helbing	
<b>20 Paediatric CMR</b> .....	347
Emanuela R. Valsangiacomo Buechel	
<b>21 Fetal Cardiovascular Magnetic Resonance</b> .....	361
Adrienn Szabo, Liqun Sun, and Mike Seed	
<b>22 Interventional Cardiovascular Magnetic Resonance</b> .....	383
Vivek Muthurangu, Oliver Richard Tann, and Andrew M. Taylor	
<b>23 Emerging Roles for Cardiovascular Magnetic Resonance in Adult Congenital Heart Disease Electrophysiology</b> .....	397
Sophie A. Jenkins, Jennifer Keegan, Sabine Ernst, and Sonya V. Babu-Narayan	
<b>24 3D Printing in Congenital Heart Disease</b> .....	415
Michael D. Seckeler, Claudia E. Guerrero, and Andrew W. Hoyer	
<b>Correction to: 3D Printing in Congenital Heart Disease</b> .....	C1
Michael D. Seckeler, Claudia E. Guerrero, and Andrew W. Hoyer	
<b>Index</b> .....	429



# General Principles of Cardiac Magnetic Resonance Imaging

1

Mark Alan Fogel

## 1.1 Introduction

A basic understanding of the underlying principles of cardiovascular magnetic resonance imaging (CMR) and methods used to form images is important if one is to successfully image in clinical practice or research and interpret the data correctly. This section will provide a brief overview of the fundamentals and some techniques in CMR imaging. For more information, the reader is referred to the references in this chapter or the larger textbooks on fundamentals of magnetic resonance imaging as well as other chapters in this book [1].

## 1.2 Physics and CMR Hardware

The crux of CMR is nuclear magnetic resonance where a signal is emitted by a sample of tissue after radiofrequency energy is applied to it. Note that this signal is emitted by tissue molecules in contrast to X-ray imaging where the tissue or contrast agents attenuate externally applied radiation. At the atomic level, it has been well known that spins and charge distributions of protons and neutrons generate magnetic fields. Only certain nuclei can selectively absorb and subsequently release energy since it requires an odd number of protons or neutrons to exhibit a magnetic moment associated with its net spin. The hydrogen atom is the one utilized in CMR imaging since it consists of a single proton with no neutrons (which gives it a net spin of  $\frac{1}{2}$ ), its large magnetic

moment and its abundance in the body (water and fat). Although each magnetic moment of individual hydrogen protons themselves is small, because of the abundance of that atom in the body, the additive effect of the many magnetic moment vectors makes it detectable in CMR.

Generally, the net magnetization of a tissue in the body is zero as there is a random orientation of the individual protons or “spins”; stochastically, the odds greatly favor a zero magnetization. However, when the body is placed in a strong magnetic field (Fig. 1.1) such as 1.5 or 3 T MRI systems (for comparison, the Earth’s magnetic field is approximately 0.05 mT at the surface), the spins align themselves with the applied field either parallel or anti-parallel to the field. In addition, the atoms undergo a phenomenon known as precession (such as the motion of a spinning top as it loses its speed) whose axis is based around the direction of the magnetic field (Fig. 1.1a); this precession, described as cycles per second, is described by the most famous equation in CMR and MRI—the Larmor equation,  $\omega = \gamma B_0$ , where  $\omega$  is the frequency of precession of protons in an external magnetic field,  $\gamma$  is a constant called gyromagnetic ratio, and  $B_0$  is the external magnetic field (the magnetic field generated by the MRI system). There is a different gyromagnetic ratio for each atom; for hydrogen, it is 42.58 MHz/T which generates a frequency of approximately 64 MHz at 1.5 T (Larmor frequency for a 1.5 T magnet is  $1.5 \text{ (T)} \times 42.56 \text{ (MHz/T)} = 63.8 \text{ MHz}$ ). When a radiofrequency pulse is applied which just happens to match the Larmor precessional frequency, some of the protons will flip to a high energy state. For protons at field strengths used for CMR, radiofrequencies in range of “very high frequency” or VHF can be used which is non-ionizing, contributing to the inherent safety of MRI when compared to X-rays.

To get from here to how a signal is generated from tissue, two more concepts must be introduced. As mentioned, the hydrogen spins are either in the low or high energy spin states with only slightly more spins in the low energy state. The number of excess spins is directly proportional to the

---

M. A. Fogel (✉)  
Pediatrics (Cardiology) and Radiology, Perelman School of  
Medicine at The University of Pennsylvania,  
Philadelphia, PA, USA

Director of Cardiac Magnetic Resonance, The Children’s Hospital  
of Philadelphia, Philadelphia, PA, USA  
e-mail: [fogel@chop.edu](mailto:fogel@chop.edu)

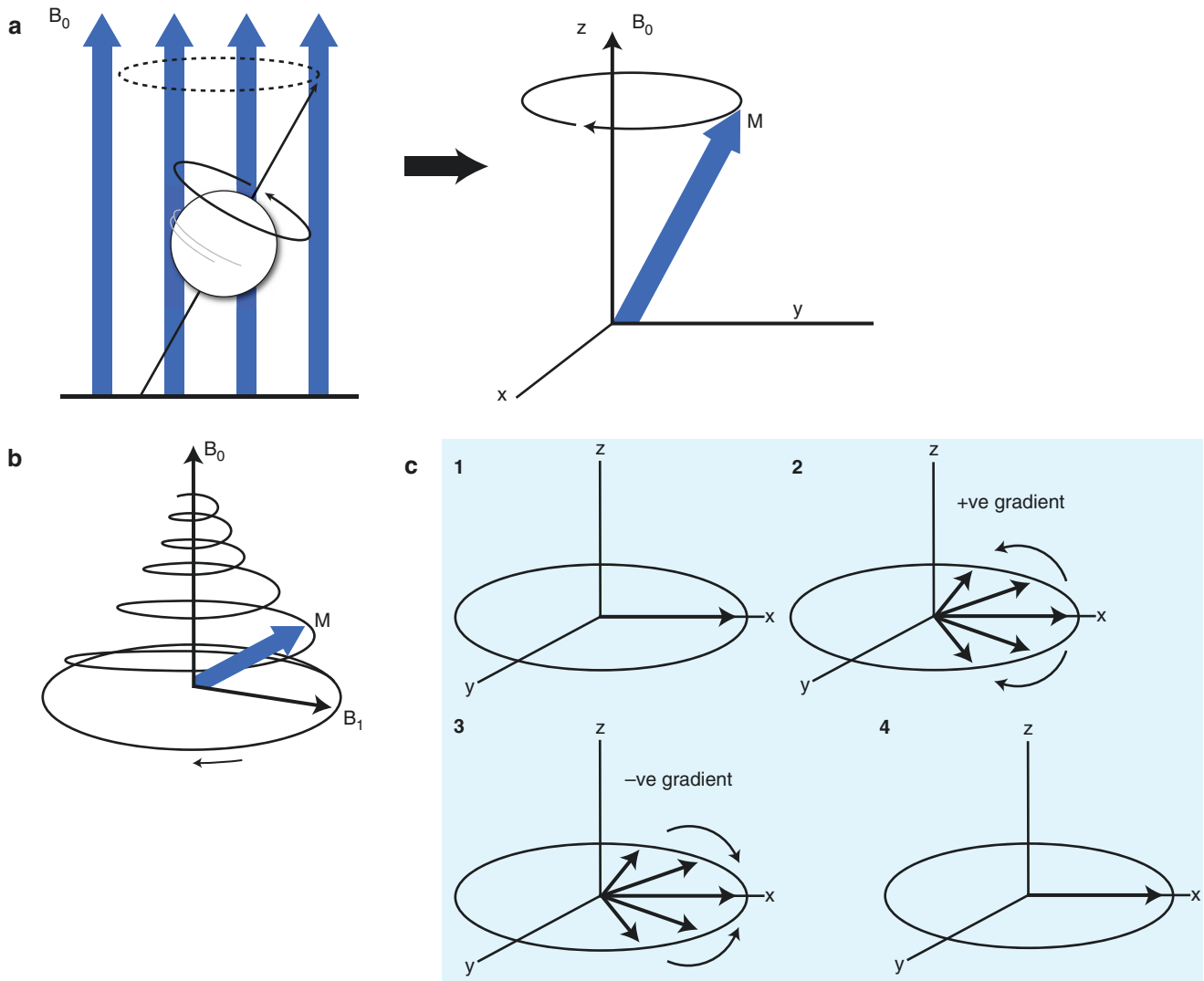


**Fig. 1.1** (a) Protons spin and precess like a top wobbling (left). If the proton is at the  $(0, 0, 0)$  coordinate of an  $x, y, z$  coordinate system (right), its axis is represented by the blue vector  $M$  and wobbles around the  $z$  axis which is in line with  $B_0$  at a frequency  $\omega$ . (b) After energy is inputted into the system, the axis flips (in this particular instance,  $90^\circ$ ) and then slowly returns to its original position. (c) In (1) the protons are

flipped  $90^\circ$  with subsequent “dephasing” of the spins in (2) which can be increased by a gradient (i.e., faster protons and slower protons will separate). In (3), energy can be inputted into the system to flip the protons to an exact mirror image so that the faster spins are not behind the slower spins. Finally, the faster spinning protons catch up to the slower spins to create a large detectable signal (in (4))

total number of spins in the sample and the energy difference between states (Boltzmann equilibrium probability). The formula used to determine this difference is  $N^-/N^+ = e^{-E/kT}$  where  $N^-$  is the number of spins in high energy state,  $N^+$  is number of spins in the lower energy state,  $k$  is Boltzmann’s constant ( $1.3805 \times 10^{-23}$  J/K),  $T$  is the temperature (in Kelvin), and  $E$  is the energy difference between the spin states. The second concept is that the energy of a proton ( $E$ ) is directly proportional to its Larmor frequency  $\nu$  (in Hz), such that  $E = h\nu$ , where  $h$  is Planck’s constant ( $h = 6.626 \times 10^{-34}$  J s). By substituting into the Larmor equation, this yields the relationship between  $E$  and the magnetic field  $B_0$ ,  $E = h\gamma B_0$ . When energy is inputted into the system

and it matches the energy difference between the lower and higher energy spin states, atoms from the lower energy states get flipped up to the higher energy states. As these atoms then return to the lower energy state, they release energy and this signal, the resonance phenomenon, can be detected (Fig. 1.1b). This is how the MRI signal is generated.

It follows that only those excess spins in the low energy state can be excited to the high energy state and generate the MRI signal. It is amazing that there are only approximately nine more spins in the low energy state compared to the high energy state for each two million spins at 1.5 T! However, one must also realize that since each mL of water contains nearly  $10^{23}$  hydrogen atoms, the Boltzmann distribution

discussed above predicts over  $10^{17}$  spins contributing to the MRI signal in each mL of water! It is interesting to note that the higher the magnetic field strength, the greater the number of excess spins in low versus high energy state; it follows that as the field strength increases, so does the magnitude of the MRI signal. Hence, there is a push by manufacturers to create larger and larger magnetic fields from the 1.5 T fields most commonly used today. Indeed, many 3 T systems have been deployed and 7 T systems have been discussed for clinical use. It should also be noted, as well, that there is research in the opposite direction into lower field systems such as 0.55 T. With modern technology such as advanced gradient systems, pulse sequences, computers, and software, high-quality CMR can be performed at that field strength close to the quality of higher field strength systems [2, 3].

When the radiofrequency energy is applied that matches the Larmor frequency, some of the protons in the low energy state jump up to the high energy level as noted above. This radiofrequency pulse (RF) has a magnetic field itself,  $B_1$ , which is perpendicular to the direction of  $B_0$ . It is of mT order of magnitude and tilts the longitudinal magnetization ( $M_z$ ) a certain amount depending upon the duration of the RF pulse and the strength of  $B_1$  field. If an RF pulse is applied to tilt the net magnetization from the longitudinal plane (Z plane) totally to the transverse (XY) plane (called a  $90^\circ$  RF), the transverse component of the net magnetization is the one that will generate an induced voltage in a receiver antenna (the MR signal). The way this occurs is through what is termed “relaxation” where the protons return from their excited state to a low energy state (Fig. 1.1b). The duration of the induced voltage is a function of the time it takes to undergo relaxation and is described by relaxation time constants termed  $T_1$  and  $T_2$  which describe the changes in longitudinal magnetization ( $M_z$ ) and transverse magnetization ( $M_{xy}$ ) respectively.

### 1.2.1 $T_1$ Relaxation

When the protons are flipped to transverse plane, the  $M_z$  component of magnetization decreases to near zero (Fig. 1.1b, c); the time for return of this magnetization  $M_z$  after the RF pulse is turned off is measured by the time constant  $T_1$  which is defined as the time necessary to recover 63% of the equilibrium magnetization  $M_0$  after the  $90^\circ$  RF pulse (Fig. 1.2):  $M_z(t) = M_0(1 - \exp(-t/T_1))$ . Physically, the return of longitudinal magnetization is a function of how fast the spins release their energy to the tissue which is termed the “lattice” hence  $T_1$  being called spin-lattice relaxation. As one might guess, this process depends in part on the physical properties of the tissue where the frequency of precession of the spins needs to overlap the frequencies of the molecules in the lattice. In addition, the process is also dependent on the

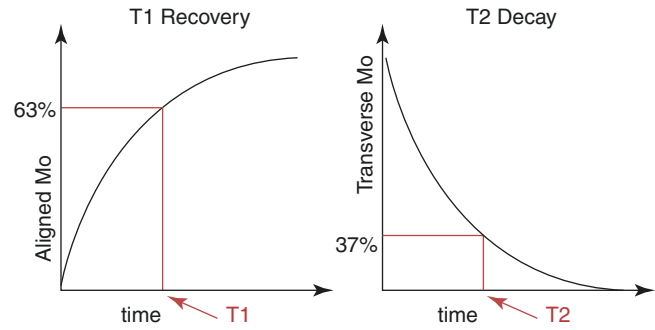


**Fig. 1.2**  $T_1$  relaxation or recovery (left) is the return of magnetization  $M_z$  to the equilibrium magnetization  $M_0$ ; the time constant is defined as recovering to 63%.  $T_2$  relaxation or decay (right) is the decay in the transverse plane

main magnetic field strength; at higher fields, the frequencies of spins precession increase with less overlap of frequencies in the lattice, resulting in a longer  $T_1$ . Water, however, has a frequency range that is large.

### 1.2.2 $T_2$ Relaxation

When the protons are flipped to transverse plane, the  $M_{xy}$  component of magnetization becomes maximized as all the protons precess with the same phase, called phase coherence (Fig. 1.1b, c). The spins of each proton in the general vicinity of each other interact with each other, however, and in time, this coherence is lost resulting in a decrease in the net magnetization (Fig. 1.1c) and induced voltage in the receiver antenna. This is appropriately called spin-spin relaxation or transverse relaxation and is measured by the  $T_2$  time constant. The transverse magnetization ( $M_{xy}$ ) will decay exponentially from  $M_z$  by the following formula (Fig. 1.2):  $M_{xy}(t) = M_z(0)\exp(-t/T_2)$ . The time constant is defined as decaying to 37% of its initial value. This relaxation is highly dependent on the makeup of the tissue; small molecules in a generally unstructured tissue have long  $T_2$  values because fast and rapidly moving spins average out the intrinsic magnetic field inhomogeneities while large molecules in densely packed tissue have shorter  $T_2$  values. Unfortunately, there are other factors responsible for decay of magnetization in the transverse plane; imperfections of the main magnetic field, susceptibility differences between nearby tissues can and do contribute to the loss of phase coherence (Fig. 1.1c). This is measured by the time constant  $T_2^*$ . In general,  $T_1$  is always greater than  $T_2$  which is always greater than  $T_2^*$ .

### 1.2.3 Image Formation

Now that the basic physical properties are defined, the discussion can turn to creating images. To create images, a

magnetic field gradient must be formed. Within the main magnetic field,  $B_0$ , all protons precess at the same frequency (Fig. 1.1a). The Larmor equation tells us that this precession is a function of this field strength; by changing the magnetic field ever so slightly by position and time, the precession of the protons can be changed ever so slightly by position and time. Using this information, localization of the MR signal from the precise part of the body can be accomplished and images can be generated. This precision controlled alteration of the magnetic field is created by gradient coils, which generate linear variations in the main magnetic field strength in three orthogonal planes (Figs. 1.1c and 1.3a). By using these coils simultaneously, a linear magnetic field gradient can be generated in any direction. This gradient changes the precession frequency of the protons at precise locations in a linear fashion.

To select a certain plane (slice) in the body (Fig. 1.3b), an RF pulse is applied and it follows that if the RF pulse center frequency is shifted to match a specific location along the gradient, it will selectively excite the protons at that region. A slice of arbitrary thickness, orientation, and location along the direction of the “slice select gradient” can therefore be selectively excited to generate the signal used to form the MR image and the signal detected by the MRI receiver coil will come from the excited slice only

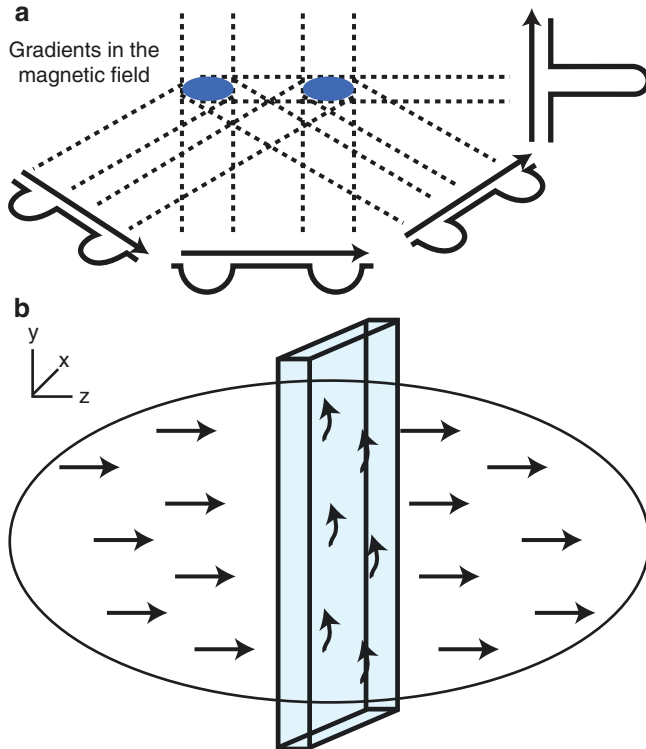


**Fig. 1.3** By altering the magnetic field in three orthogonal planes, gradients can isolate a plane in space (a). This is accomplished by flipping the protons only in the plane desired (b)

(Fig. 1.3b). The amplitude of the signal is directly proportional to its thickness, practically limiting the thickness at approximately 2 mm.

After selecting the slice, the image itself needs to be created in two dimensions in the  $xy$  plane (practically speaking in 2 orthogonal planes of the bore of the magnet—right/left and up/down when looking into the bore). This creates the pixels (2-dimensional picture elements); in 3-dimensional imaging, this is called voxels (3-dimensional volume elements). As with choosing the slice, linear field gradients and the Larmor relationship between field strength and precessional frequency are used to encode spatial location information into the MRI signal. After a slice-selective RF pulse, a linear magnetic field gradient is switched on in one of the in-plane directions of the image, perpendicular to the “slice select gradient”; this gradient changes the precessional frequency in a linear distribution along the gradient direction allowing the identification of every location along the gradient by the frequency of the signal (Fig. 1.3). This is called *frequency encoding*. The MR signal is detected and put through an analog-to-digital converter; remembering that we have encoded the slice and one direction in the plane of the image at this point, the signal is thus the amalgamation of all of these frequencies. Therefore, the signal varies with position, also called its “spatial frequency”; this is called “ $k$ -space.” If one looks at the distribution of the signal, it creates a sinusoidal distribution of phase across the direction of the gradient; this describes a single spatial frequency  $k_x$  (important in phase encoding in the next step). A special mathematical technique called the “Fourier transformation” is used to separate out the individual frequency components in the detected signal, decoding the signal into individual signals coming from locations along the frequency encoding gradient. The Fourier transformation can be used to translate the signal from “ $k$ -space” to the image and vice versa (Fig. 1.3).

Finally, the third spatial dimension (second in-plane dimension) must also be encoded (if frequency encoding is the “ $x$ ,” the “ $y$ ” in the “ $xy$ ” plane must also be created); the technique used is called “phase encoding” (Fig. 1.4) and is also based on the Larmor equation. Phase encoding is accomplished with the application of a number of gradient pulses of differing amplitudes which encode a specific spatial frequency,  $k_y$  (Fig. 1.5). This phase encoded gradient pulse is changed to encode a different spatial frequency component prior to each frequency encoding gradient. In this manner, by successive phase encoding pulses, and “ $y$ ” part of the image is built up and a matrix is formed; this matrix is referred to as  $k$ -space, and the numerous gradient pulses “fill” the  $k$ -space until the image is complete. The 2-dimensional Fourier transform is utilized to convert the spatial frequencies created by the phase encoding steps into an image (Fig. 1.3). Phase encoding can also be used in the slice direction to



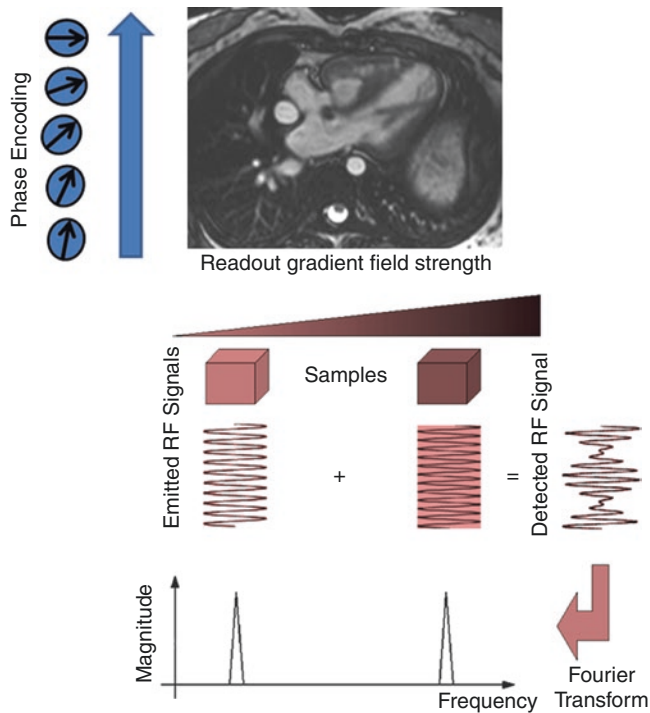


**Fig. 1.4** The image is created by a combination of frequency encoding in one direction (in this case, in the  $x$  plane or the horizontal portion of the image) and phase encoding in the other dimension (in this case, in the  $y$  plane or the vertical portion of the image). For frequency encoding, a gradient is applied to change the magnetic field in that direction (right triangle). Different frequencies correspond to different positions (different colors and waves on the diagram) which produce a detected radiofrequency (RF) signal which is a combination of all the frequencies of the various positions (rightmost signal). When put through the Fourier transform, signals can be separated into their different positions (lower graph). The vertical portion of the image is created by changing the phases of the radiofrequency pulses (phase encoding, see text). The cardiac magnetic resonance image is of a “4-chamber” view of a patient with single ventricle after Fontan

encode thinner slices than possible with the slice selection gradient technique, so-called 3D data acquisition.

### 1.2.4 MRI Hardware

Once all the components of generating an MR signal are known, it is important to review the equipment needed. There is of course the main magnet ( $B_0$  or  $B_z$  field), the RF transmitter coil ( $B_1$  field), the gradient coils ( $G_x$ ,  $G_y$ ,  $G_z$  fields), and receiver coils which “listen” for the signal. In addition, there are second-order shim coils which are often used to achieve a more homogeneous  $B_0$  field. There are a number of computer systems including those which are used to control the MRI magnetic field-generating units and those used to reconstruct the acquired data. There is also a system which provides an interface for the user and the other systems.

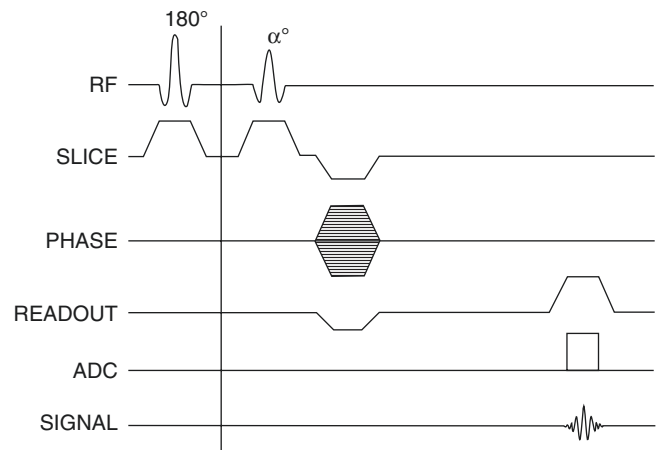


**Fig. 1.5** A typical pulse sequence diagram includes (a) when the radio-frequency (RF) pulse is applied (top line) and at times, how much of a flip angle (in this case,  $180^\circ$ ), (b) when the slice selection gradient ( $G_z$  or slice) is turned on (second line), (c) when the phase encoding gradient ( $G_y$ ) is turned on (third line), when the frequency encoding gradient (readout or  $G_x$ ) is turned on (fourth line), and when the analog to digital converter is turned on (fifth line) and the signal is created (sixth line). This is an example of a magnetization prepared gradient echo pulse sequence

### 1.2.5 Pulse Sequences

This is the sequence of events which control all the various factors involved in the creation of an image. It is important to note that these times are on a microsecond scale and need to be controlled by computer for precise timing. Timing of all the gradients switching on and off, the phase encoding, the RF pulses, the analog to digital converting data sampling, and control of transmitter and receiver operation are all defined by the pulse sequence. As there are a limitless amount of pulse sequences, it is impossible to describe all of them; however, to understand them, a pulse sequence diagram is used which details the timing of each component; a representative pulse sequence diagram is shown in Fig. 1.5. To simplify the concepts, it should be noted that there are five broad concepts with regard to pulse sequences which may be understood to aid in examining many of the pulse sequences in use. They are as follows:

1. *Magnetization preparation* is a technique employed, usually at the beginning of the sequence, which changes the tissue characteristics prior to actually creating the image (Fig. 1.5).  $T_2$  preparation, for example, can be employed to suppress myocardial muscle and is used in visualizing coronary arteries (Fig. 1.6). The inversion recovery technique uses a  $180^\circ$  RF pulse to magnify differences in different tissue characteristics of  $T_1$ ; the saturation recovery technique uses a  $90^\circ$  RF pulse prior to image. The inversion recovery technique is used in

**Fig. 1.6** (a)  $T_2$  prepared steady-state free precession to visualize coronary arteries. The image on the left demonstrates a right coronary artery (RCA) giving rise to a left circumflex coronary artery (LCx). The image on the right demonstrates a coronary artery aneurysm from Kawasaki's disease from the RCA. (b) ECG-gated contrast-enhanced inversion recovery gradient echo imaging of the right (upper left) and left (upper right) coronary arteries with a 3D reconstruction (lower image)

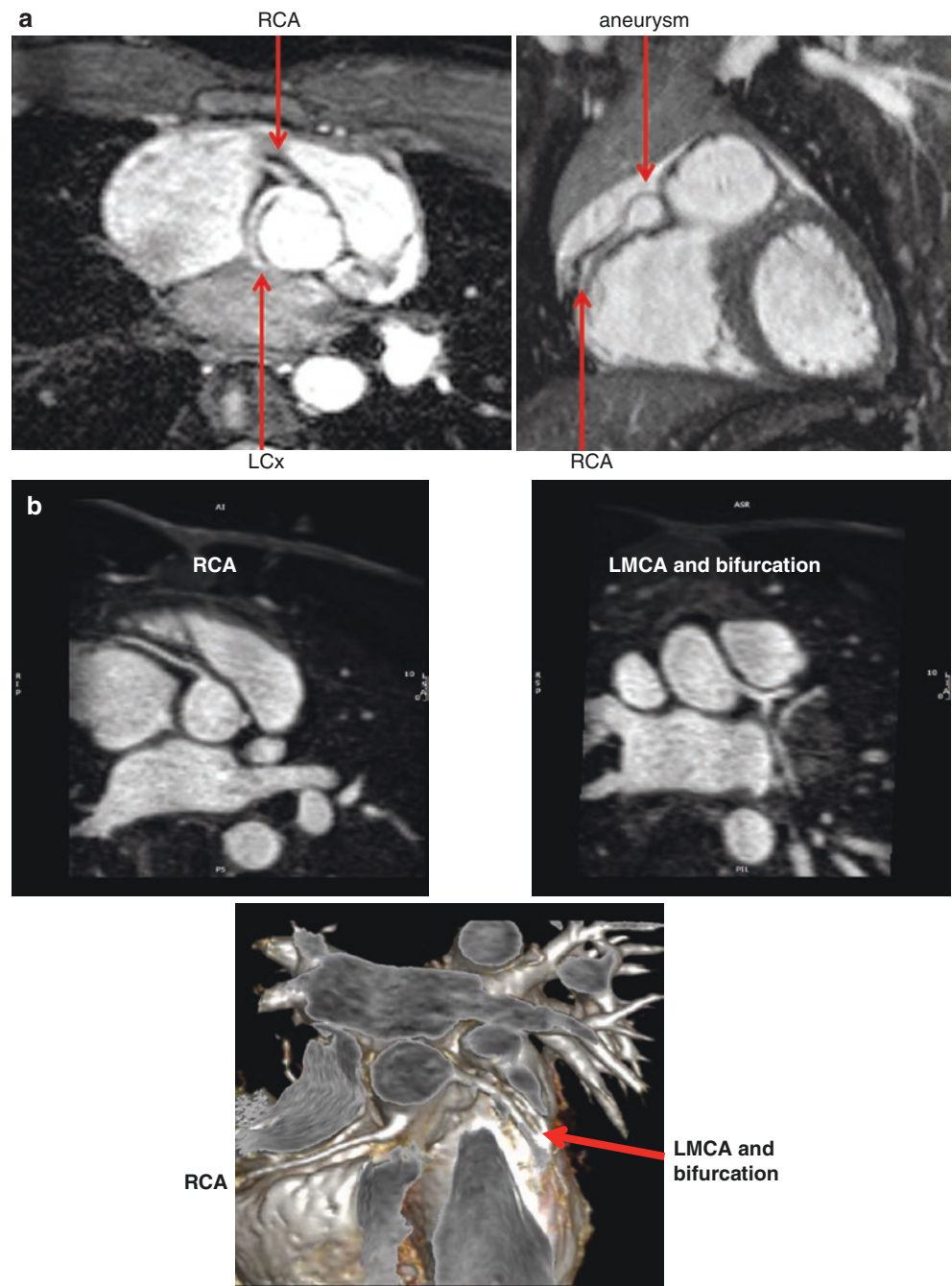
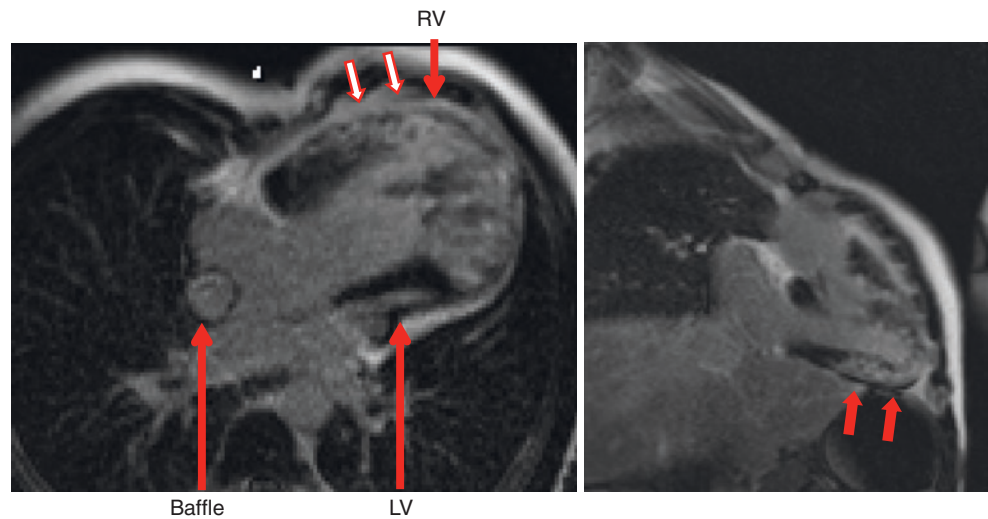




**Fig. 1.7** Delayed enhancement imaging from a “4-chamber” (left) and long axis view (right) of a patient with hypoplastic left heart syndrome after Fontan. White arrows in red outline demonstrate some of the areas of myocardial scarring



delayed-enhancement (Fig. 1.7),  $T_1$  mapping as well as dark blood imaging [4] (Fig. 1.8) while saturation recovery is used in  $T_1$  mapping as well as first-pass perfusion imaging (Fig. 1.9).

2. *Echo Formation:* This is the “echo” referred to above and various types of echo formation is used in CMR. An older technique of echo formation which still has applicability today is called spin-echo, which is used most often in dark blood imaging for morphology and tissue characterization (e.g., myocardial edema) (Fig. 1.8). Another technique of echo formation, gradient-echo imaging (Fig. 1.10), is used in a whole host of applications such as:

- Cine imaging for cardiac function including myocardial tagging (Figs. 1.11 and 1.12)
- Assessing valve morphology (Fig. 1.13), valve regurgitation as well as valve or vessel stenosis
- In delayed-enhancement (Figs. 1.7 and 1.10) and first-pass perfusion (Fig. 1.9) for myocardial scarring and myocardial perfusion respectively
- Phase contrast velocity mapping to determine blood flow (Fig. 1.14)

Gradient echo imaging comes in couple of forms: (a) unbalanced gradient echo imaging and (b) balanced gradient echo imaging also known as steady-state free precession imaging (SSFP) (Figs. 1.15, 1.16, and 1.17). SSFP is more commonly used than the unbalanced gradient echo form due to its high signal to noise, blood to myocardium contrast, and imaging efficiency [5]. Echo-planar imaging is used as a method for perfusion imaging due to its high efficiency.

3. *Filling  $k$ -Space:* As noted above,  $k$ -space is filled with each phase encoding step. Most sequences employ what is known as Cartesian  $k$ -space sampling, where there is a linear filling of  $k$ -space with each phase encoding step. There are, however, other methodologies which have come into existence and are used. A “radial” filling of  $k$ -space has some advantages over Cartesian sampling when it comes to efficiently filling the matrix and has been used in cine imaging [11]. A “spiral” filling of  $k$ -space trajectory has been utilized for coronary artery imaging, because it has some advantages in speed and most importantly, insensitivity to motion; unfortunately, it is highly sensitive to field inhomogeneities and, therefore, has not gained in popularity. A “radial” filling of  $k$ -space can be used as well, collecting  $k$ -space in a series of spokes, with the “golden angle” technique being the most efficient and robust way to do so [12].

4. *Segmentation:* This refers to the number of lines of  $k$ -space filled per cardiac cycle [13]. If one line of  $k$ -space is filled per cardiac cycle, that pulse sequence is said to be “segmented”; if all the lines are filled in one cardiac cycle, that pulse sequence is said to be “single-shot” or “non-segmented.” There are of course gradations of segmentation between the two and the degree of segmentation is referred to by the number of lines of  $k$ -space filled per heartbeat (e.g., 3, 5, 7 segments or views, etc.). Any level of segmentation can be used with any of the methods of magnetization preparation, echo formation, or the ways of filling  $k$ -space. It generally follows that if the more lines of  $k$ -space filled in a heartbeat, the less time it will take to form the image while the reverse is true with

**Fig. 1.8** (a) Multiparametric mapping. Upper right and left images are  $T_1$  maps before and after gadolinium administration respectively where each pixel's intensity represents  $T_1$  relaxation time. Using the hematocrit, an extracellular volume map can be created (lower left) where each pixel's signal intensity represents the extracellular volume percentage. The lower right panel is a  $T_2$  map where each pixel's intensity represents  $T_2$  relaxation time. (b) Dark blood imaging in a patient with a left ventricular hemangioma (tumor). The upper left panel is a dark blood  $T_1$ -weighted image of the tumor demonstrating slight hyperenhancement; note the fat in the chest wall. The upper right panel is the same dark blood  $T_1$ -weighted image with a "fat saturation" pulse applied prior to imaging (prepulse). Note how the fat in the chest wall is not present in this image because the prepulse destroyed all the spins of the fat; however, the tumor is still present, indicating there are no fatty elements in the tumor (it is not a lipoma). The lower left panel demonstrates hyperenhancement on  $T_1$ -weighted imaging after gadolinium administration. The lower right image is a  $T_2$ -weighted image with fat saturation demonstrating hyperenhancement indicating increased water content

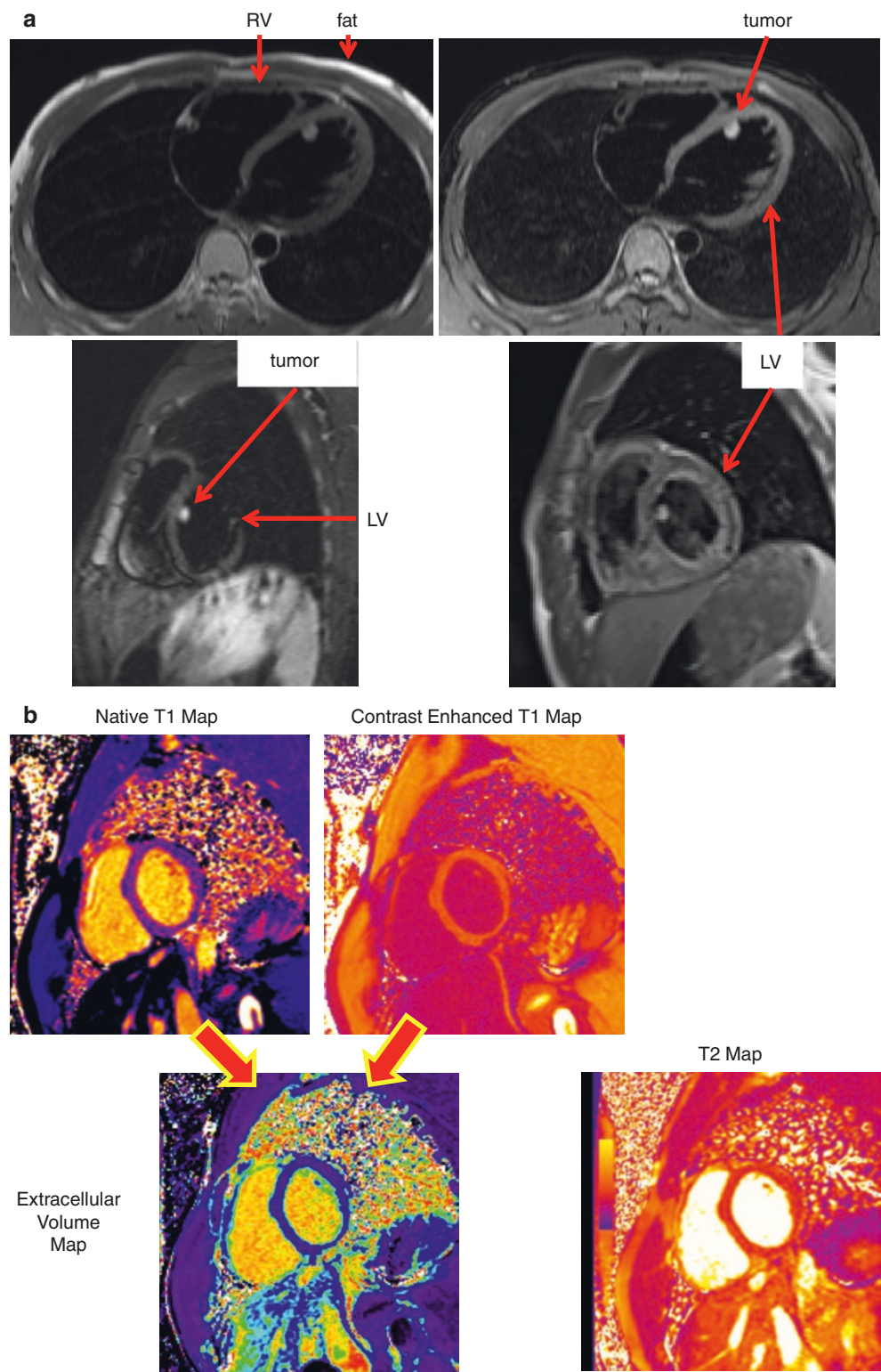


**Fig. 1.9** Perfusion imaging in the patient in Fig. 1.8 with a left ventricular hemangioma (tumor). Four frames during the first pass myocardial perfusion imaging demonstrate contrast in the right ventricular (RV) cavity (I), the left ventricular (LV) cavity (II) where the tumor can be seen, and phases III and IV where the contrast enters the LV myocardium. Note how the tumor becomes signal intense in III and IV; so much so that it is indistinguishable from the cavity (somewhat in III and indistinguishable in IV). The tumor can be visualized in II as the contrast is in the cavity but not in the myocardium where presumably the tumor receives its blood supply from

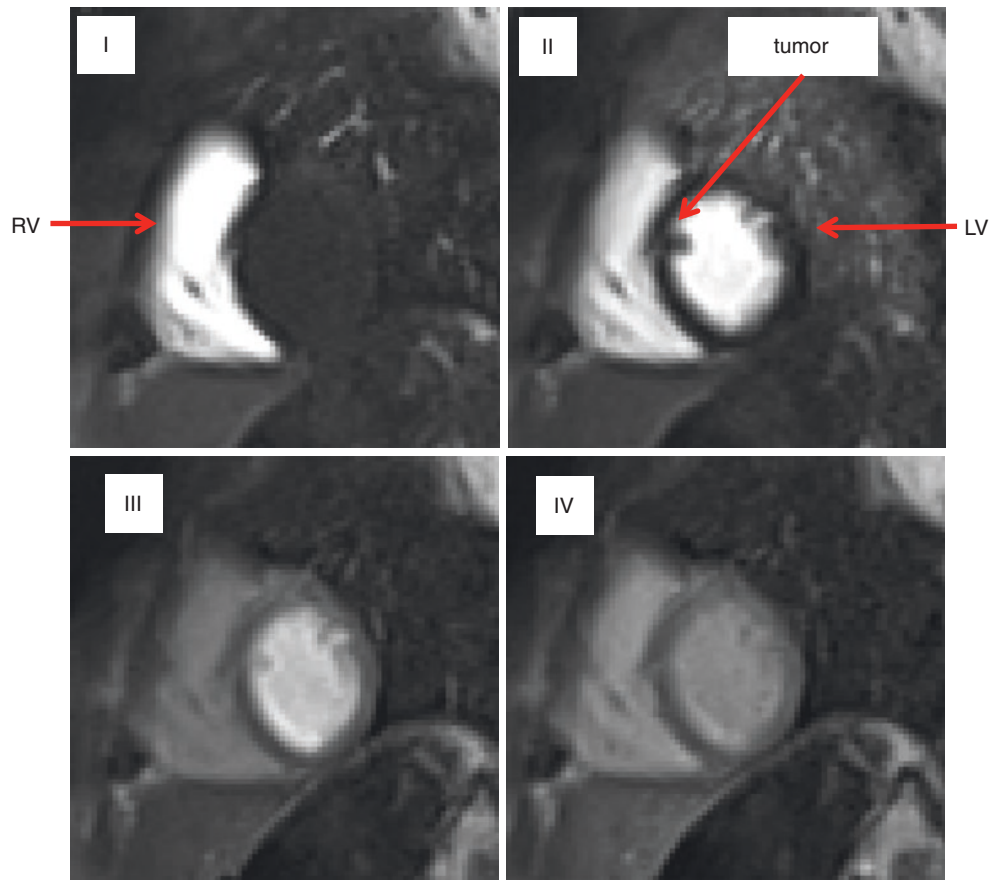


**Fig. 1.10** Tissue characterization in the patient in Figs. 1.8 and 1.9 with a left ventricular hemangioma. The upper left panel is a steady-state free precession image in short axis clearly showing the spherical tumor while the upper right panel is an axial gradient echo sequence also clearly showing the tumor. Note the tumor is isointense with cardiac muscle on steady-state free precession and the hypoenhancement on gradient echo imaging. The lower image is a delayed enhancement image of the tumor demonstrating hyperenhancement

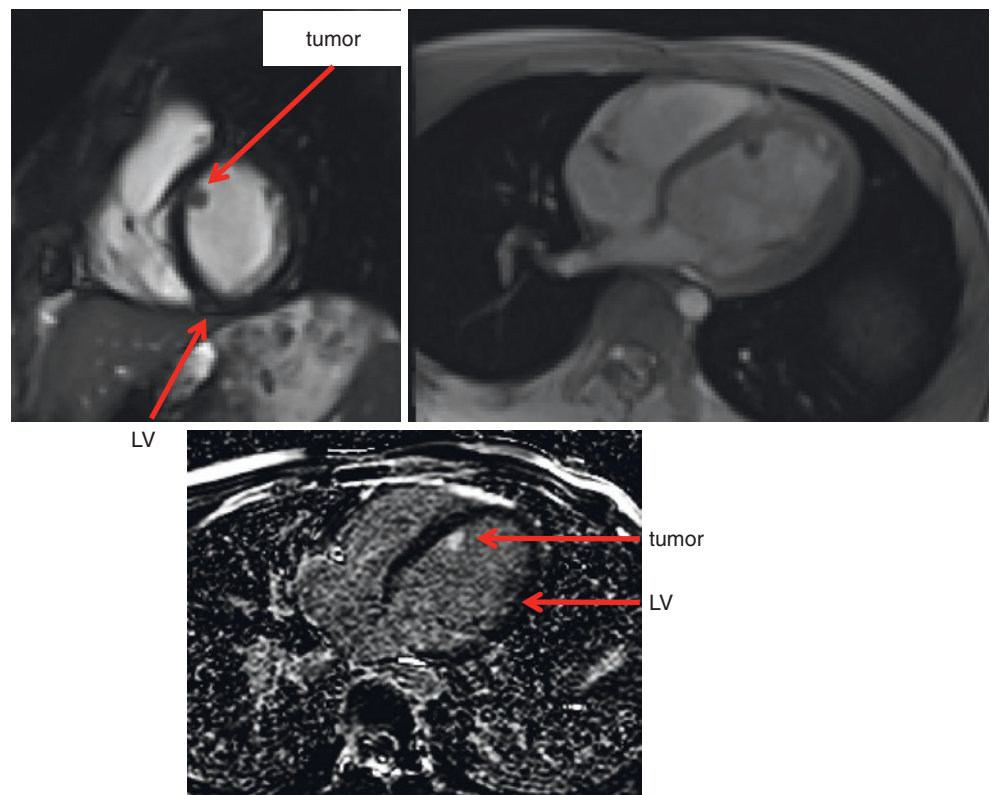




**Fig. 1.11** Myocardial tagging in the “3-chamber” (upper and lower left), short axis (upper right), and long axis views (lower left) of a patient with a single left ventricle after Fontan. This is an example of spatial modulation of magnetization (SPAMM) where a grid is laid down on the myocardium and deformation can be visualized from end-diastole (ED, upper left) to mid-systole (lower left) in the “3-chamber” view. It is the equivalent of speckle tracking in echocardiography except by CMR; the “speckles” are purposefully created in a certain geometry for strain and wall motion assessment

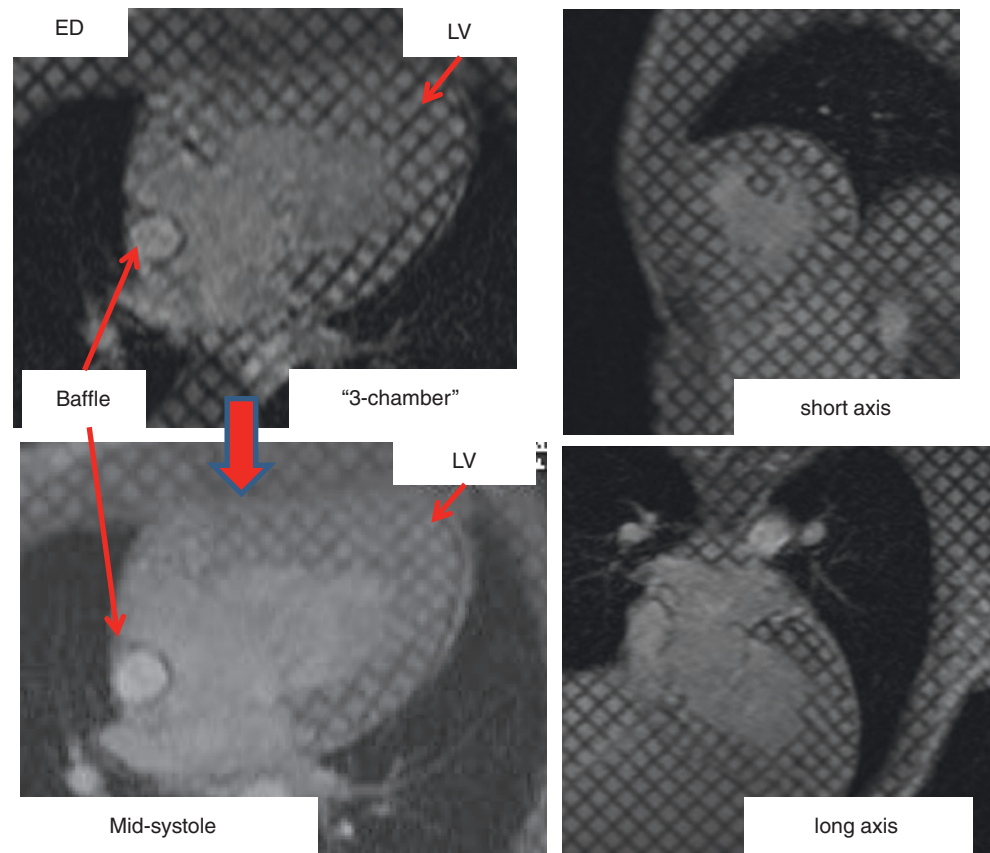


**Fig. 1.12** Myocardial tagging in the “4-chamber” (left) and long axis of the right ventricle (right) in a patient with pulmonic stenosis after balloon dilation. Note how this differs from Fig. 1.11 with one set of parallel lines laid down on the myocardium—the so-called 1-dimensional tagging [10]

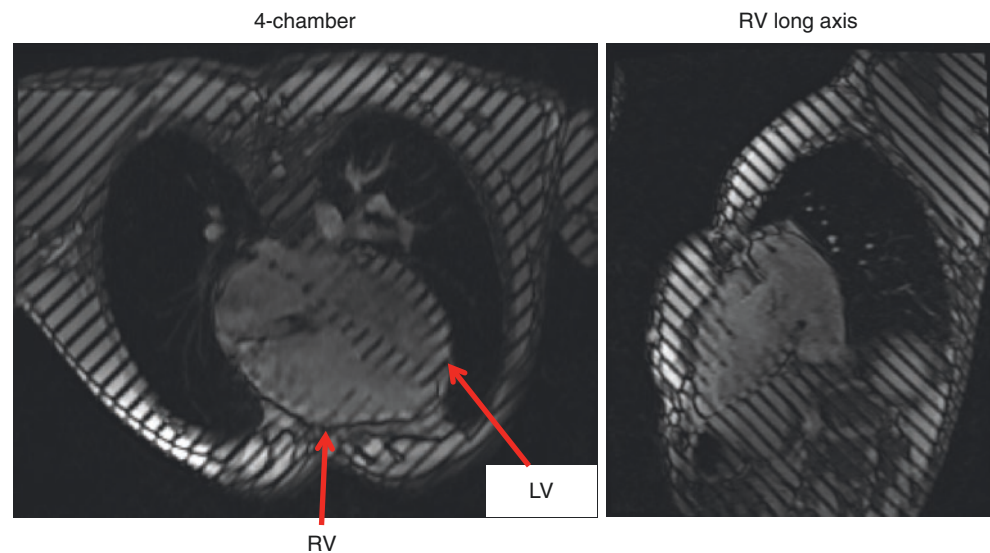
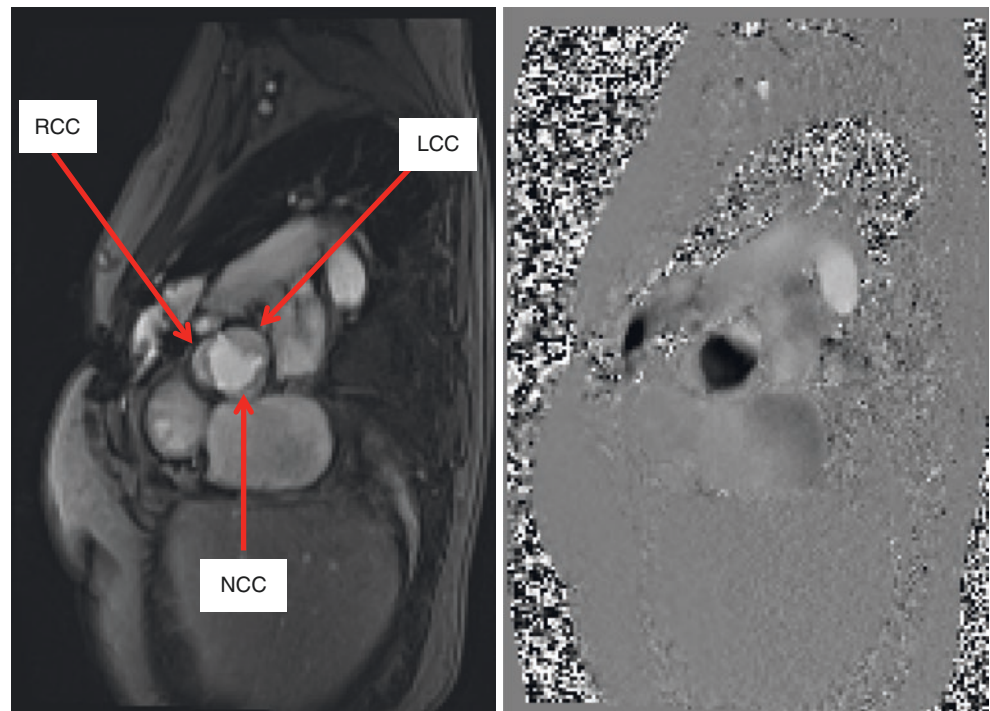


**Fig. 1.13** Gradient echo imaging (left) and through plane phase-encoded velocity mapping (right) of the aortic valve. Note how the right (RCC), left (LCC), and non-coronary commissures are easily visualized on both images, demonstrating the trileaflet valve



the less lines of  $k$ -space per heartbeat (i.e., the number of segments inversely proportional to the time it takes to create the image). It is also true, however, that the more lines of  $k$ -space acquired per heartbeat, the worse the temporal resolution will be (i.e., the number of segments inversely proportional to the number of time points that can be created in the cardiac cycle). Tradeoffs are part of CMR and for most applications such as phase contrast velocity mapping and flow, image creation can be obtained in a breath-hold. It is important to realize that a regular cardiac rhythm is needed to ensure that lines of  $k$ -space from each cardiac cycle is acquired during the same point in time of the cardiac and respiratory cycles. In patients with arrhythmias or an inability to breath-hold, single-shot or real-time methods are commonly used [14] although there are also arrhythmia rejection techniques whereby an R-R interval and target heart rate are set and only beats falling within that range are accepted to build the image. For those patients who cannot hold their breath, using segmented techniques with multiple “averages” or “exci-

tations” can be used to smooth out the respiratory motion at a minor cost to image fidelity (most times).

5. *Image Reconstruction:* As mentioned above, the Fourier transformation is used to create an image from the lines of  $k$ -space which is acquired from the MR signal. A technique called “partial Fourier” or “partial  $k$ -space” has been used for many years which reduces scan time with a lower signal-to-noise than using a “full” Fourier transformation. Parallel imaging with names such as SENSE [15], SMASH, GRAPPA, and TSENSE [16] uses multiple coils and multiple channels and has become ubiquitous in many sequences; they sample only a fraction of the full  $k$ -space but yet allow for a full field-of-view and resolution images with significant time savings at the cost of signal-to-noise. Compressed sensing CMR is another method that undersamples  $k$ -space losing very little fidelity to speed up the image acquisition and to reconstruct images that are nearly indistinguishable from those that do not undersample  $k$ -space [17].

**Fig. 1.14** (a) In-plane phase-encoded velocity mapping in a patient with double outlet right ventricle after a right ventricle to pulmonary artery conduit. On the left is a magnitude image of the right ventricular (RV) outflow tract (RVOT). In the middle is a mid-systole frame of the in-plane phase-encoded velocity map in the exact orientation and position as the image on the left where flow cephalad is signal intense; on the right is a mid-systolic frame where flow caudad is signal poor (dark on the image) indicating severe conduit insufficiency. (b) 4D flow in systole (right) and diastole (left) of a single ventricle patient after Fontan. Note the fenestration flow (arrows) and the vortex formation in the dilated ascending aorta (AAo)

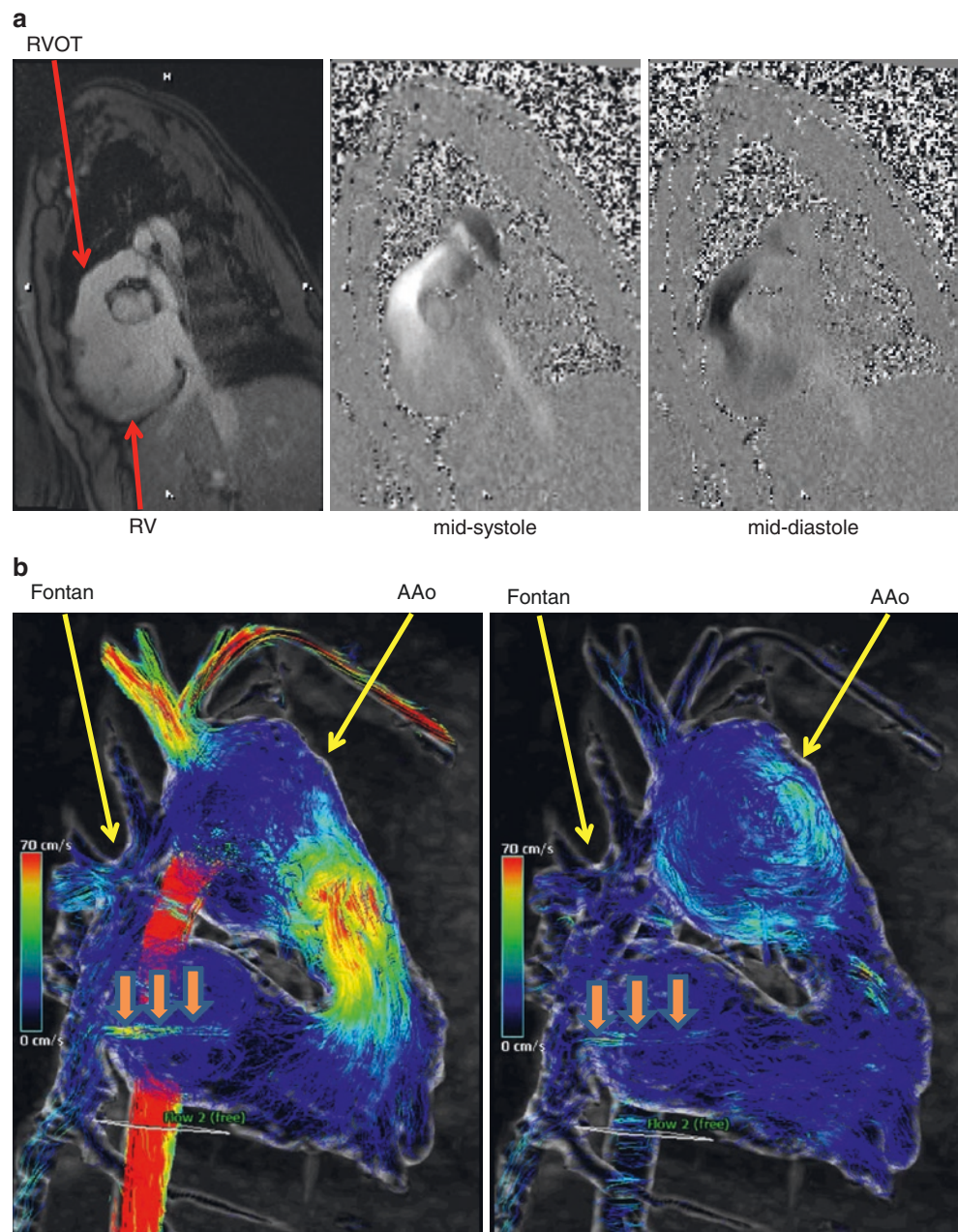




**Fig. 1.15** Steady-state free precession imaging in the 4-chamber view (left) at end-diastole (ED, upper) and end-systole (ES, lower) in a patient with tetralogy of Fallot. The long axis of the right ventricle (RV) is on the right. LV left ventricle

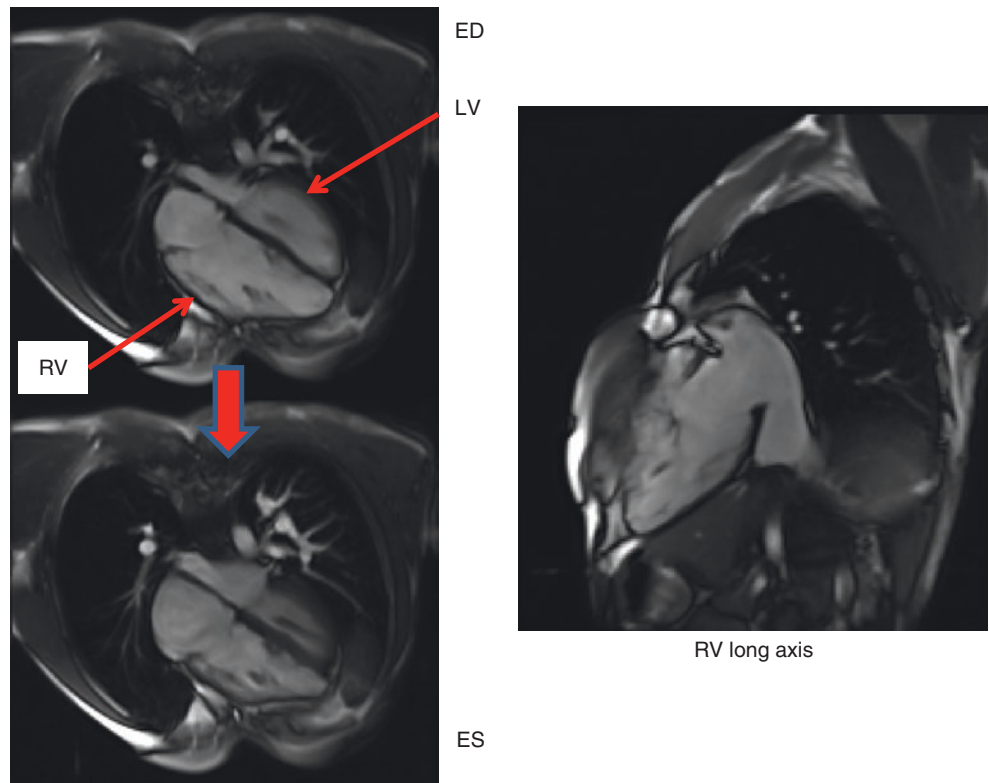


**Fig. 1.16** Steady-state free precession imaging in the short axis view at end-diastole (ED, left) and end-systole (ES, right) in the patient with tetralogy of Fallot in Fig. 1.15

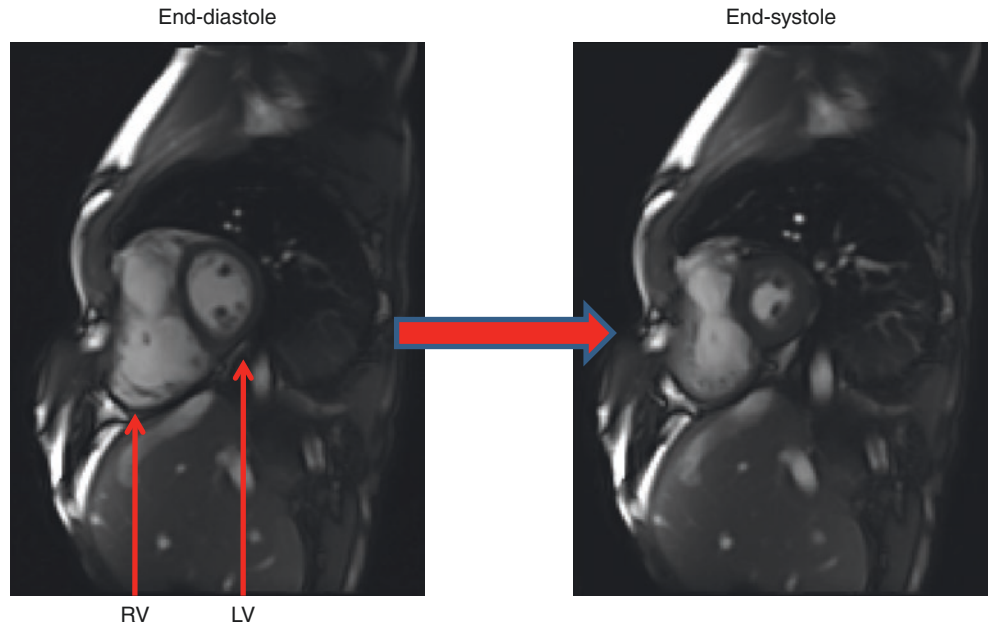
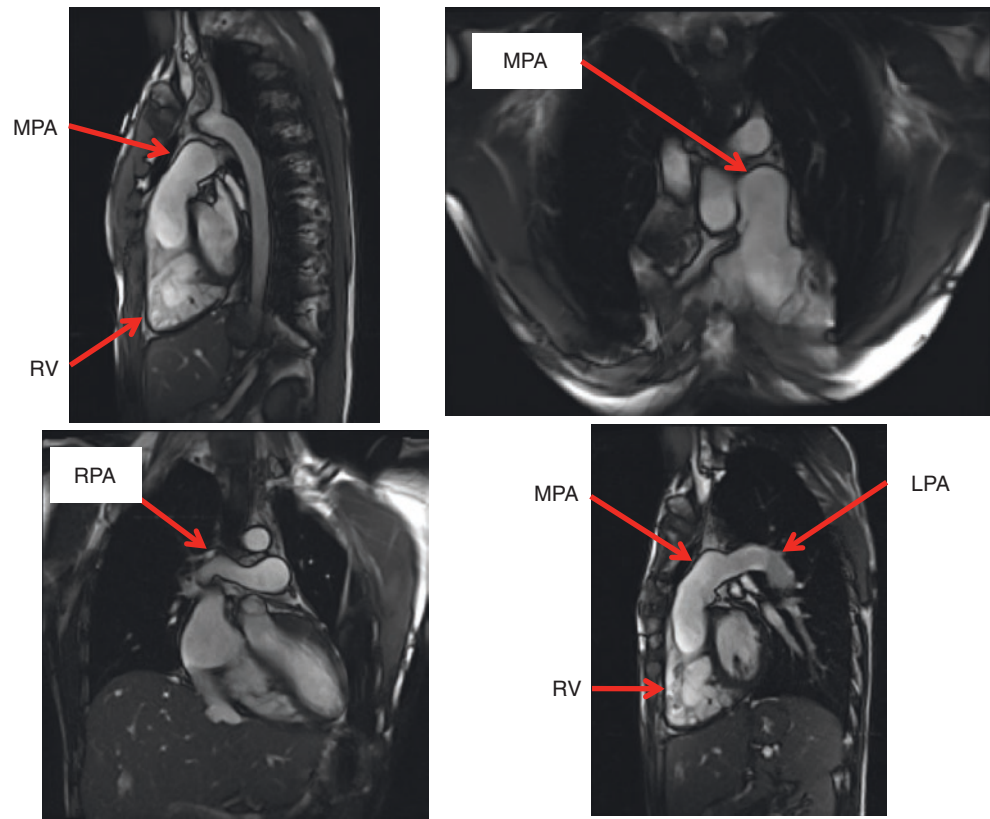


**Fig. 1.17** Various steady-state free precession cines of the patient in Figs. 1.15 and 1.16 with tetralogy of Fallot. The right ventricular outflow tract views are seen in the upper panels in off-axis sagittal (left) and coronal (right) views which are orthogonal to each other. The right (RPA) and left pulmonary arteries (LPA) are seen in long axis in the left lower and right lower panels respectively. *MPA* main pulmonary artery, *RV* right ventricle



### 1.3 Prospective Triggering/Retrospective Gating

Because the heart needs to be at the same phase of the cardiac cycle with any segmented technique, as noted above, a way is needed to determine this phase. This is nearly universally the R-wave of the ECG. A static or non-moving image uses the R wave to signal the beginning of systole as is the touchstone of the cycle; the CMR sequence then begins. This technique is called prospective triggering since the sequence is initiated by the R wave; lines of  $k$ -space are then acquired. Phases of the cardiac cycle are defined by a fixed time after the R-wave, so small perturbations of rhythm will put the heart at a slightly different point in the cardiac cycle; this generally does not affect the image too much. In addition, there is generally some “dead space” prior to the next R wave so very late diastole is usually not imaged or utilized. Cine or moving images are acquired by either this method or the method of retrospective gating. With retrospective gating, lines of  $k$ -space are acquired continuously regardless of the phase of the cardiac cycle while the ECG is simultaneously recorded; after image acquisition, the software “bins” the lines of  $k$ -space relative to the ECG and cardiac cycle. In this way, each cardiac phase is defined as a certain percentage of the cardiac cycle, allowing the actual duration of each phase to vary flexibly with variation in cardiac cycle. In addition,

no “dead space” is left prior to the next phase which can be important in assessing flows or ventricular function.

The above paragraph makes a distinction between static and dynamic techniques. Static ones are generally used for cardiovascular anatomy or characterizing tissue. Dynamic techniques are used to assess function or flow in addition to anatomy. A run of single-shot images, acquired quickly, can be strung together as motion and this is termed “real-time” and is asynchronous with the cardiac cycle; this can be used in cine imaging, phase contrast velocity mapping, or dynamic 3D angiography. First-pass perfusion imaging can be thought of as a hybrid between static and dynamic imaging, where each image depicts a different phase of the cardiac cycle over time.

### 1.4 ECG Signal

For many years, the upstroke of the R wave on the ECG signal was used to trigger the scanner and used as a marker for end-diastole; unfortunately, artifacts occurred because of the high magnetic field strength and radiofrequency pulses which precluded reliable detection of the true R wave. Bizarre T waves and spikes during the ST segment of the ECG would cause the triggering to falsely detect these waves as the R wave. This is especially true in congenital heart dis-



ease where abnormal QRS axes and bundle branch blocks from surgery can make the distinction of the R wave even more problematic in the scanner. On most systems in use today, detection of the R wave as a trigger has been replaced by the use of vectorcardiography (VCG), which is less susceptible to distortion from the magnetic field and of flowing blood in the thoracic aorta which can act as a conductor. Although wired connection between the VCG and the imaging systems has been utilized in the past, this has been nearly universally replaced by wireless transmission which allows for more flexibility in the scanner.

There are alternatives to the direct connection between the “MRI ECG” and the patient. The ECG signal from external monitoring systems such as the anesthesia equipment can be used which can generate a signal contemporaneous with the R-wave to the MR scanner. Alternatively, the ECG signal can be discarded for “peripheral pulse triggering” where a finger or ear pulse may also be used; obviously, this requires good peripheral circulation. If the patient is cold or has a coarctation, this will often be unsuccessful. It also should be noted that because there is a delay in transmission of the pulse to the distal part of the body that is being monitored, the waveform will be delayed by 200–300 ms when compared with the ECG; this needs to be taken into account during the analysis and interpretation phase of the examination. Peripheral pulse gating is especially useful in patients where a good detection of the R wave cannot be obtained otherwise. Another alternative is the use of non-triggered SSFP sequences where lines of  $k$ -space are continually being obtained by the imaging system without regard to the ECG or respiration (see above and below). With the use of parallel imaging in the spatial or time domains, a temporal resolution as high as 30–40 ms can be acquired; even higher temporal resolution can be obtained by combining this with compressed sensing. This type of imaging can be used in patients with arrhythmias to obtain functional information when triggering the ECG is problematic (see below). Finally, recent advances in hardware and software have enabled the use of “self-gating” sequences, where a coil is used to monitor the motion of the ventricle which is used as a signal for ventricular contraction and relaxation. This approach allows the heart itself to be monitored and act as its own signal for the imager; retrospective analysis of the lines of  $k$ -space can then be “binned” to construct moving images. There are now techniques that not only “self-gate” but also compensate for respiration where a 3D cine data set can be acquired at multiple respiratory phases without an ECG or navigator (see below) [18].

A special note is required on patients with arrhythmias. With frequent premature ventricular contractions, runs of supraventricular tachycardia or trigeminy for example, it is unclear what an ejection fraction, cardiac index, or end-diastolic volume would mean given that these ventricular

performance parameters can change from beat-to-beat. A qualitative assessment using real-time steady-state free precession is one way to get a handle on ventricular function. Nevertheless, there may be instances when some quantitative information may be needed; in these particular cases, “arrhythmia rejection” can be used (see above). With this approach, a range of heart rates or R-R intervals can be set, and the imaging system will only allow those lines of  $k$ -space which meet these requirements into the final image; the rest of the lines of  $k$ -space which fall outside these heart rates are ignored. This approach is inefficient, however, in this manner, quantitative ventricular performance information can be obtained for a range of heart rates. For example, if the range is set between an RR of 700 and 800 ms, the resulting cardiac index can be said to be present for heart rates between 75 and 86 beats/min. Finally, some real-time cine sequences have arrhythmia compensation built in [14].

---

## 1.5 Respiration

Besides cardiac phases, respiration must be dealt with as it causes positional variation of the heart from movement of the lungs and diaphragm; if not taken into account, this will lead to motion artifacts. There are a number of ways in which this is dealt with in CMR:

1. Breath-holding, where the patient’s breath is held during image acquisition. For many common applications such as cine and phase contrast velocity mapping, image acquisitions are fast enough to be performed in a reasonably short breath-hold. This can be done in adults or in children under anesthesia who are paralyzed, intubated, and mechanically ventilated. These pulse sequences are widely available and commonly used routinely.
2. Signal averaging, also termed multiple excitations, where the signal from the complete image is “averaged” over many respiratory and cardiac cycles, “averaging out” the respiratory motion and making the image sharper than without this technique but less sharp than breath-holding. This can be used in small children unable to voluntarily breath-hold or adults who cannot cooperate. It has the advantage of being more “physiologic” and representative of the true state of the patient’s physiology as the patient is continually breathing the information is averaged over many respiratory cycles.
3. Respiratory gating, where the motion of the diaphragm or the chest wall is tracked by either a navigator pulse (which tracks diaphragmatic motion, the equivalent of an “M-mode” of the diaphragm on echocardiography), respiratory bellows which are placed around the chest wall, or a signal from the respirator if the patient is under anesthesia. Lines of  $k$ -space are continuously acquired

during the cardiac cycle and only those lines of  $k$ -space which fall within certain positional parameters of the diaphragm or chest wall are incorporated into the image; the others are discarded. Although this is a very inefficient method of imaging, it is very effective and used in imaging coronary arteries, for example, where high resolution is needed. Whole heart angiography is also unsuitable for anything but respiratory gating.

4. Single-shot imaging, where all the lines of  $k$ -space are acquired within a single heartbeat. Advances in hardware and parallel imaging have dramatically improved the speed and quality of these single-shot and real-time techniques and are now often used for scanning patients unable to breath-hold.
5. The newer “self-gated” techniques, referenced above, that also compensate for respiration where a 3D cine data set can be acquired at multiple respiratory phases without an ECG or navigator [18].

## 1.6 Contrast Agents

These agents offer another important source of distinguishing tissues from each other besides the intrinsic properties of  $T_1$ ,  $T_2$ , and  $T_2^*$  for example. The most commonly used imaging agents, the paramagnetic chelates of gadolinium ( $Gd^{3+}$ ), generally work by predominantly shortening  $T_1$  and to a certain extent  $T_2$ ; they generally enhance the signal on  $T_1$ -weighted images. Gadolinium, which has a very large magnetic moment, has unpaired orbital electron spins and shortens  $T_1$  by allowing free protons to become bound creating a hydration layer, which helps energy release from excited spins and accelerates the return to equilibrium magnetization. For other contrast agents which predominantly shorten  $T_2$ , the reverse is true; shortened  $T_2$  leads to decreased signal on  $T_2$ -weighted images. The effects of these agents can be described by the following formulae:

$$\frac{1}{T_1} = \frac{1}{T_{1_0}} + r_1 C$$

$$\frac{1}{T_2} = \frac{1}{T_{2_0}} + r_2 C$$

where  $T_{1_0}$  and  $T_{2_0}$  are the relaxation times prior to and  $T_1$  and  $T_2$  are the relaxation times after contrast agent administration,  $C$  is the concentration of the agent, and  $r_1$  and  $r_2$  are the longitudinal and transverse “relaxivities” of the individual agent (which are field strength dependent). CMR applications which utilize these agents include delayed enhancement, first pass perfusion, coronary angiography in certain sequences, and characterization of tumors and masses.

Another contrast agent that has become increasingly used is ferumoxytol, which is an iron-based contrast agent that is administered slowly over 15 min. This contrast agent has the distinct advantage of having a long half-life in the blood so that high-resolution segmented imaging may occur. This contrast agent is generally used in conjunction with high-resolution static inversion recovery gradient echo imaging to visualize coronary arteries, to perform whole heart 3D imaging, or to enhance 4D flow imaging signal [19] (see below). In addition, ferumoxytol has been used to acquire 4D whole heart cine imaging to obtain a 3D beating heart [20], combining anatomy, cine imaging, and 4D flow [19] and for the self-gated technique mentioned above that acquires cine at multiple respiratory cycles [18] (see above).

The safety profile of these agents is beyond the scope of this chapter. However, it should be noted that there has been a recently published multicenter trial of ferumoxytol demonstrating a safety profile equivalent to other imaging agents and in certain regards, better [21].

## 1.7 Remaining Motionless in the CMR Scanner: Anesthesia and Sedation

The degree of cooperation necessary for successful performance of CMR is generally greater than that of any other type of MRI examination; scans require no significant movement, repeated breath-holds at the same point of the respiratory cycle over a period of 45 min to an hour, and can be lengthy. Couple this with the strange environment of the scanning room and the loud banging noises, it is no wonder that both adults and children alike find this very intimidating. Therefore, the use of medication may be required; either conscious sedation or general anesthesia is generally administered so that children who are too young to cooperate or adults with congenital heart disease who may not want to cooperate for one reason or another (e.g., claustrophobia) can still undergo successful CMR. With conscious sedation, patients continue to breathe throughout the scan and imaging has to be substantially altered because of this whereas in a paralyzed, intubated, and mechanically ventilated patient under general anesthesia, the effect of “breath-holding” can be created by having the anesthesiologist temporarily suspend ventilation. This is not to say that anytime a patient undergoes general anesthesia in the CMR environment that suspending respiration should be performed but rather that this technique is available to the CMR imager. It should be noted that imaging using sedation or general anesthesia with free breathing is much more physiologic than imaging with positive pressure mechanical ventilation and breath-holding (see above) and, therefore, may be more advantageous than the minor increase in image fidelity with breath-holding. For example, a single ventricle patient after Fontan depends

upon both cardiac and respiratory effects to allow for pulmonary blood flow; suspending respiration may alter the physiology artificially and therefore, although accurate for suspended respiration, the physiology is not reflective of the patient's true state. In addition, because systemic venous return changes during the respiratory cycle, imaging during suspended respiration will obtain data only in that state while if the patient is imaged during free breathing, the loading conditions across the respiratory cycle is "averaged" into the image and is more reflective of the patient's true physiologic state.

There is no definitive cut-off age for the age range where medication is needed to remain motionless for a successful CMR study; however, in general, most children greater than or equal to 10–12 years old can cooperate. Of course, this is just a rule of thumb as there can be 7-year-olds who are very mature and can follow directions while there are some 15-year-olds who will simply not cooperate and will require pharmacology. Limited scans with reduced times may be possible with younger patients who would normally require conscious sedation or general anesthesia and this may be considered; it is all in the judgment and purview of the family, physicians, and other healthcare providers caring for the patient. Preparation of the child prior to the scan is important; the involvement of child life experts, a supportive parent or other regular caregiver in the scanner room can reduce anxiety and be the difference between a scan under medication, without medication, or a successful versus an unsuccessful scan.

As the CMR environment can be a challenging one for the anesthesiologist or the pediatrician/nurse sedation specialist, monitoring is extremely important since the patient's body will be mostly within the scanner itself; direct visualization during the study is not possible without removing the patient from the bore of the magnet and removing the coil. Many centers utilize a direct video feed with cameras designed to work within the CMR environment and placed in critical positions. For example, a camera pointed down the bore of the magnet is essential along with cameras in other areas to get a good view of what is occurring in the scan room. In addition, extensive physiological monitoring of subjects using equipment specifically designed to be operated in the MR scan room is essential for the safe conduct of the study. Pulse oximetry, limb-lead ECG, blood pressure monitoring, inspiratory and expiratory gas analysis such as end-tidal carbon dioxide, and temperature monitoring (especially in young children) should all be available and used. The monitoring systems should be available wherever the anesthesiology/sedation teams are positioned; this is generally either in the control room or scan rooms. Many facilities position the anesthetic equipment and gas tanks directly outside the scan room, with the gas lines passing through "wave guides" in the wall of the scanner room installed for just this

purpose. This arrangement has two advantages: (a) there is reduced risk of inadvertently introducing non-CMR compatible equipment into the scan room and (b) communication between the anesthesiology/sedation team and imaging teams is much easier in this setup. It should be noted, however, that this comes at the cost of increased compliance in the anesthetic circuit. If the decision is made to keep monitoring and anesthetic equipment in the scan room, there is usually a minimum distance that this equipment must be kept from the magnet within which it may not operate correctly, may interfere with the images, and might even be attracted into the scanner bore. Careful establishment of this distance from the manufacturer is mandatory before the equipment is first introduced into the scan room. Even the use of physical restraints to prevent incursion of the equipment within such a distance, and thus avoid accidents, should be considered. Direct verbal communication between the anesthesiology/sedation teams and the imaging teams should be on-going at all times with visual contact preferably as well.

Neonates and very small infants less than 6 months of age may undergo CMR successfully while sleeping using a "feed and swaddle" technique [22, 23]. The patient usually is kept awake for a while prior to scanning (3–4 h); when the child enters the preparation area, the intravenous is inserted and the ECG leads are placed. At this point, the baby is very fussy; however, feeding the infant and subsequently swaddling with a warm blanket in a quiet and dimly-lit environment prior to the study will allow the patient to fall asleep; the patient is subsequently transported to the scanner room. Vacuum-shaped support bags can also be utilized to reduce patient motion; placing ear plugs, a hat over the head and ears as well as blankets around the head all aid in keeping the child comfortable and asleep. Imaging sequences that allow for free breathing must be used.

Whether to use deep sedation or anesthesia to perform CMR has been debated for many years. Consideration should be given to how long the CMR scan is likely to take, the patient's age, the flexibility of CMR scanner time, and the availability of anesthesiology staffing and/or the availability of specialized sedation teams which include nurses and pediatricians. The practice is obviously a matter for individual, institutional, and patient preferences. Anesthesia is much more predictable when it comes to onset of action and duration/depth of impaired consciousness; this is advantageous in scheduling CMR examinations and running the schedule smoothly. Deep sedation use has been associated with reduced image quality in some studies [24] but not in others [25], and in some institutions, is far more likely to fail than anesthesia [26], though failure rates can be reduced to close to zero [25] by careful use of expert personnel and strict sedation regimes [25, 27–30]. Imaging performed under anesthesia can be shorter "in theory" because of the

ability to breath-hold; in practice, however, the scanning time difference is marginal at best and breath-holding, as mentioned above, is less physiologic. Anesthesia has been reported to be marginally safer than deep sedation in some studies [24, 31] and equal in others [25], but there is no doubt that it is more costly and invasive. There are numerous pediatric centers with many years of experience at performing CMR under deep sedation with excellent safety records [25, 27, 28, 30]. The end result is that both techniques are likely to remain in practice for the foreseeable future.

## 1.8 The Standard Pediatric/Congenital Heart Disease Examination

There are numerous protocols for a standard CMR examination of the heart, many equally as valid as the other. The one presented in this chapter is meant to be as complete and as efficient as possible; however, it should be recognized that this is not the only one. As each phase of the protocol is delineated, the technique utilized will be expanded upon in detail to give the basics of the different types of CMR.

### 1.8.1 Axial Imaging (Fig. 1.18)

The initial part of the examination begins with a set of static steady-state free precession (bright blood) images in the axial (transverse plane) extending from the thoracic inlet to the diaphragm. Generally, 45–50 contiguous end-diastolic slices are obtained of three (for babies) to 5 mm in thickness; end-diastole is acquired by placing a “delay” after the R wave of the ECG. At this point in the cardiac cycle, the heart is relatively motionless, allowing for high-fidelity imaging. This set of data, which usually takes two and a half to four and a half minutes to acquire (depending upon the patient’s heart rate and size), is utilized as a general survey of the anatomy and may be used as a localizer for subsequent higher fidelity cine imaging, flow measurements, etc. These images are usually acquired with multiple averages (generally 3) during free breathing. In babies, to maintain signal to noise but nevertheless obtain thinner slices, overlapping slices can be used; the cost is prolonged acquisition time.

1. From this survey, a number of features may be gleaned with regard to cardiovascular structure in congenital heart disease [32]: (1) the position of the heart in the chest and

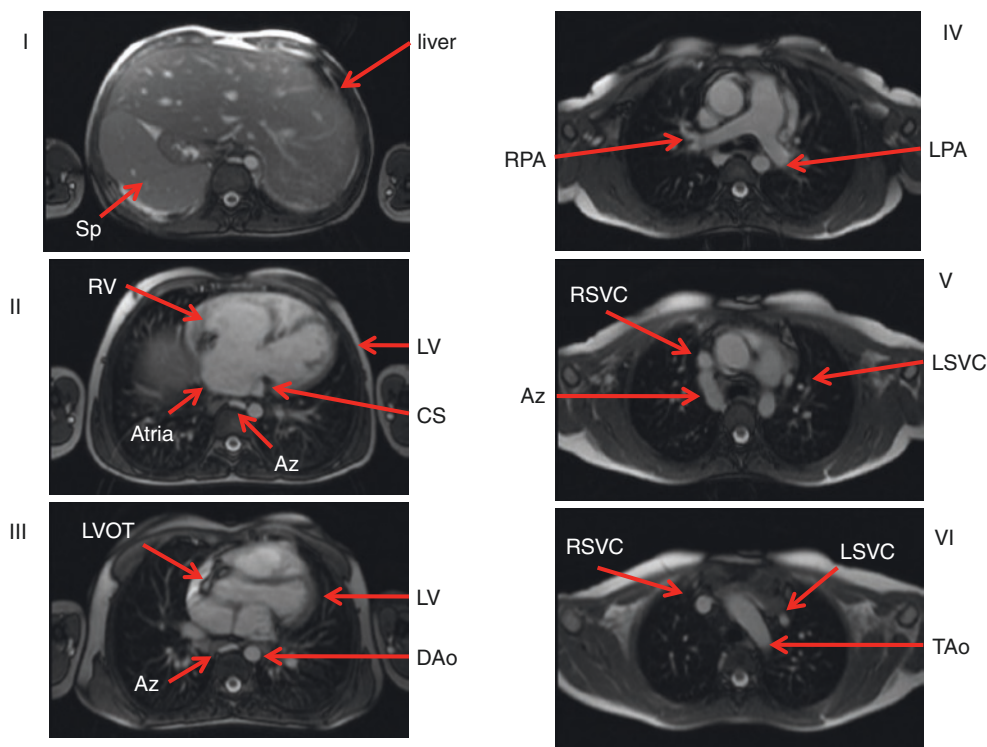


**Fig. 1.18** Selected initial axial images of a patient with heterotaxy and complete common atrioventricular canal. Note how much can be gleaned from the first set of static steady-state free precession images. Images progress from inferior to superior as the roman numerals increase from top to bottom and from left to right. In I, a transverse abdominal view shows a midline liver and spleen (sp). In II, note the complete common atrioventricular canal, the dilated coronary sinus (CS),

and dilated midline azygos (Az). In III, note the widely patent left ventricular outflow tract. IV (top right) demonstrates the main pulmonary artery as well as the right (RPA) and left pulmonary artery (LPA) being confluent. In V, note how the dilated AZ enters the right superior vena cava (RSVC) as well as the presence of a left superior vena cava (LSVC). Finally, in VI, note the left aortic arch along with the RSVC and LSVC without a bridging vein. *TAo* transverse aortic arch



in which direction the apex is pointing, (2) normal cardiac segments (atria/ventricles/great arteries), (3) the intersegmental connections (atrio-ventricular and ventriculo-arterial), (4) veno-atrial connections, (5) aortic arch anatomy such as coarctation of the aorta and sidedness of the aortic arch, (6) pulmonary arterial tree (such as pulmonary stenosis, pulmonary sling), (7) extracardiac anatomy and its relationship with the cardiovascular system such as the trachea and tracheobronchial tree, abdominal situs such as the position of the liver, spleen, and stomach, qualitative assessment of lung size (e.g., important in Scimitar syndrome). For lesions such as main and branch pulmonary artery stenosis and coarctation of the aorta, off-axis imaging planes are necessary to confirm and better display these findings; however, these lesions can often be inferred from the stack of axial images. Qualitative assessment of lung hypoplasia and unbalanced pulmonary blood flow can be roughly estimated by the pulmonary vascular markings. If the study is ordered to determine if the patient has a vascular ring, the diagnosis is nearly always readily obtained using this stack of images using the feed and swaddle technique if an infant mentioned above [23]. Image acquisition time for the three-dimensional dataset can be accomplished in 20–30 s depending on the patient's heart rate.

2. There are drawbacks to using the axial stack when using it for diagnostic purposes; it must be remembered that is solely a survey and to be used as localizers for higher resolution imaging. As examples, smaller anatomic structures such as the pulmonary veins may not be visualized well or seem to appear to be connected anomalously but really be connected normally because of partial volume effects. Follow-up with off-axis imaging is mandatory.
3. In addition to the axial stack of SSFP images, a set of HASTE (Half-Fourier-Acquired Single-Shot Turbo Spin Echo) axial images (Fig. 1.19) can be very useful and are usually obtained while multiplanar reconstruction is being performed on the SSFP images (see below). HASTE is a dark blood, single-shot (image obtained in one heartbeat) technique which is low resolution and acquired during free breathing, generally obtained in 1–2 min. If the RR interval of the patient is under 600 ms, the images are generally acquired every other heartbeat (doubling the acquisition time) to allow the protons to relax further. HASTE images are less susceptible to flow artifacts and metal artifacts. For example, turbulence in the systemic to pulmonary artery shunt (Blalock-Taussig shunt) or Sano shunt in a single ventricle patient after Stage I Norwood reconstruction will demonstrate signal loss in the shunt itself and the pulmonary arteries on SSFP imaging. Turbulent flow occurs in diastole as well as systole in this scenario and recalling that the static SSFP images are acquired in diastole, these structures are

difficult if not impossible to see on the SSFP images. These structures are, however, readily visualized on the HASTE images. Multiple patients can present with braces on their teeth which is common in adolescents as well as stents in their great arteries or other blood vessels; these metallic objects can and generally do produce artifacts which appear on the SSFP imaging, but not on the HASTE images. Note, however, that because of the “cage effect” (see below in the dark blood section 1.8.3), direct measurement of the cavity of the stent is not possible. HASTE imaging can also be useful with visualizing regions of the coronaries and in characterizing masses; however, dedicated subsequent imaging of these structures is mandatory. The HASTE images give the imager a “first pass” at the problem and, similar to the stack of SSFP imaging, is simply a survey.

### 1.8.2 Multiplanar Reconstruction

During the acquisition of the HASTE images, multiplanar reconstruction is performed on the axial SSFP (or HASTE) images. Multiplanar reconstruction is the act of taking the contiguous stack of images and reconstructing these images into other planes (e.g., axial images being resliced as coronal images or in a double oblique angle to obtain the “candy cane” view of the aorta). Nearly all scanners today come with software which allows this to be readily performed. The purpose of this obviously is to obtain orientation and slice positions for dedicated images of the anatomy in question, functional imaging, tissue characterization, and blood flow. Further anatomy can be obtained with cine, the various types of dark blood imaging, or 3-dimensional contrast-enhanced images (see below). For the 3-dimensional contrast-enhanced slab, these axial images act to ensure that the anatomy in question is covered by the slab. Ventricular function and blood flow are obtained using cine and phase contrast magnetic resonance (PCMR) (see below). Off-axis imaging planes can be used, for example, to profile the ventricular outflow tracts, the atrio-ventricular valves, major systemic and pulmonary arteries and veins and all their connections to the heart.

### 1.8.3 Dark Blood Imaging (Figs. 1.8 and 1.20)

High-resolution dark blood imaging (as compared to the low-resolution HASTE images) is static in nature and is used sparingly because it is time consuming; 1–2 images can be obtained in a breath-hold. There are numerous types of dark blood imaging such as  $T_1$  weighting,  $T_2$  weighting, spin echo imaging, turbo spin echo imaging, double or triple inversion recovery, etc. This technique is generally utilized for tissue

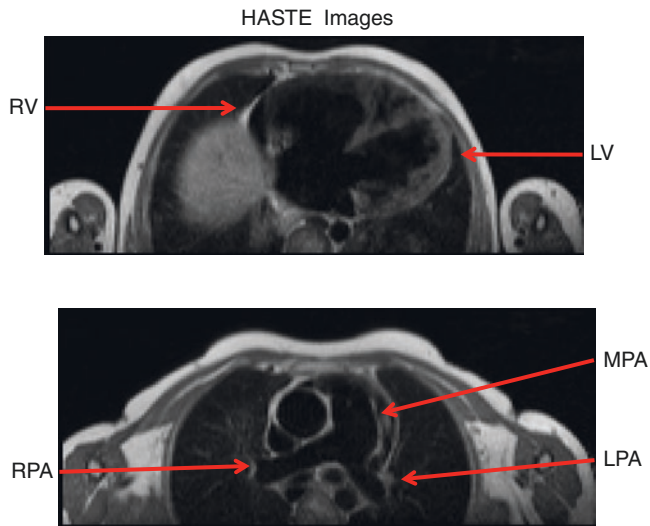


**Fig. 1.19** Two initial axial HASTE images of the patient in Fig. 1.18 with heterotaxy and complete common atrioventricular canal. The upper and lower panels are equivalent to panel II and IV in Fig. 1.18; compare these images with those of Fig. 1.18

characterization and to define anatomy when turbulence or artifacts get in the way of bright blood techniques. The blood from the heart cavities and blood vessels is black while soft tissue is signal intense. Most dark blood imaging in children utilizes either  $T_1$ - or  $T_2$ -weighted imaging with the double inversion approach. The details of how each type of dark blood imaging is created are beyond the scope of this chapter; however, a simple example is instructive. The double inversion  $T_1$ -weighted dark blood technique is utilized to maximally suppress signal from blood and begins with a nonselective inversion pulse which can be thought of as flipping all the protons  $180^\circ$  throughout the body, destroying all the signal from these spins. This is subsequently followed by a selective inversion pulse which flips the protons once again  $180^\circ$  but in a selected region of the body (such as the imaging plane needed); a standard  $T_1$ -weighted spin echo sequence is then run. In this way, all the blood entering the imaging plane is signal poor with the spins destroyed in the nonselective inversion pulse and detailed endocardial or endovascular surfaces can be visualized. Dark blood imaging can be used,

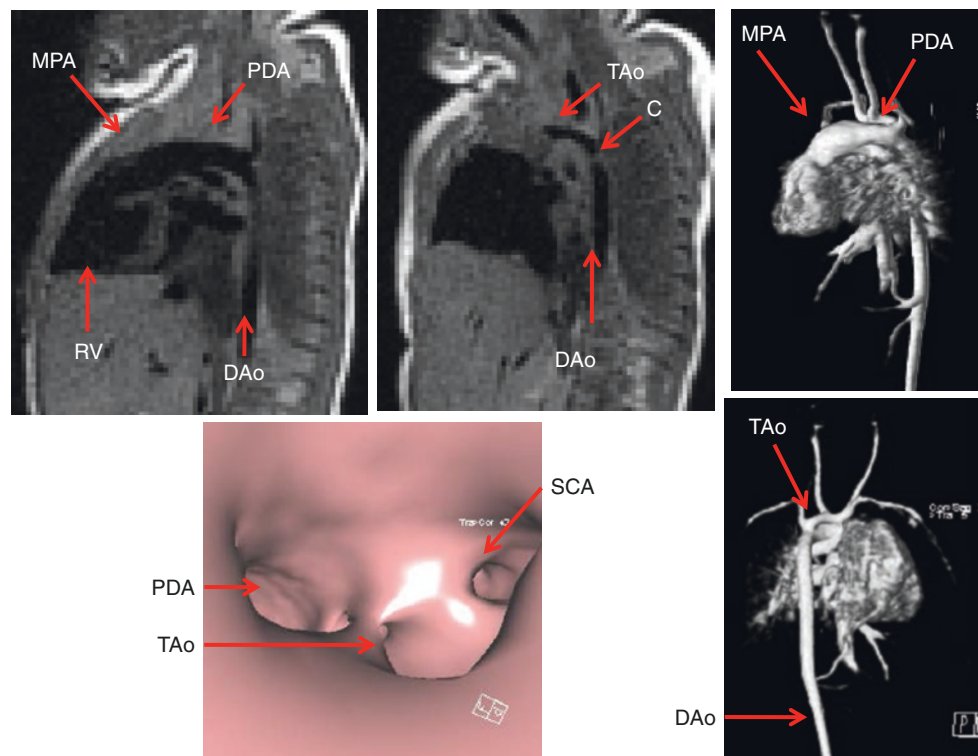


**Fig. 1.20** Dark blood, 3-dimensional gadolinium and “fly-through” imaging of a neonate with hypoplastic left heart syndrome who has not undergone surgery. The left upper image is an off-axis sagittal view demonstrating the right ventricular outflow tract giving rise to the main pulmonary artery (MPA), patent ductus arteriosus (PDA) connecting to the descending aorta (DAo). The upper middle is similar to the upper left except a few millimeters over to the right demonstrating the hypo-

plastic transverse aortic arch (TAo), the coarctation (C), and the DAo. The right upper and right lower images are 3-dimensional reconstructions from a time-resolved gadolinium sequence which demonstrates the MPA, PDA, hypoplastic TAo and DAo from a sagittal (top) and posterior (bottom) view. The lower left is a “fly-through” image of the 3-dimensional reconstruction looking up from the DAo towards the os of the PDA, hypoplastic TAo and subclavian artery (SCA)

as mentioned above, to characterize different types of tissue as these will generate different signals. As an example, fat will be intensely bright on  $T_1$ -weighted imaging while myocardium will be much less so. In addition, special pulses can be used to change the signal intensity and determine if indeed this tissue is what is suggested; taking for example fat as was just mentioned, a “fat saturation” pulse may be coupled with dark blood imaging and will turn the very bright signal of fat without this fat saturation pulse into a very dark signal with the fat saturation pulse, confirming that the bright signal is indeed fat. This may be useful for lipomas—visualizing this mass on  $T_1$ -weighted images with and without a fat saturation can confirm the diagnosis. Triple inversion recovery may be used to delineate edema in the tissue from, for example, a myocardial infarction or myocarditis.

Typically, in our imaging protocols, if needed, this is performed after the SSFP and HASTE imaging but should not be used after gadolinium administration except for specific applications such as myocarditis or tumor characterization. If used after gadolinium administration, the blood pool will demonstrate signal which is counterproductive to the intent of dark blood imaging in the first place. Use for dark blood imaging besides myocarditis is to visualize the pericardium, image the tracheobronchial tree (useful in a vascular ring study), and tumor characterization (with and without gadolinium). As mentioned above, it is useful to image patients when coils, stents, braces, spinal rods, and other foreign material cause artifacts on bright blood imaging. Precise measurements cannot be performed within a stent, however, because of the “cage effect.” The image artifact caused by the stent prevents the physician from seeing the critical area in and around the stent. This is caused by the fact that a metallic stent behaves as a “Faraday Cage” due to its geometry and material, and the stent additionally creates a magnetic susceptibility artifact due to the material of manufacture of the stent.

A more modern approach is the use of a 3D dark blood acquisitions such as SPACE (Sampling Perfection with Application-optimized Contrasts using different flip angle Evolution) which is not only gated to the cardiac cycle but also employs a navigator pulse to obtain high-resolution (1–1.2 mm isotropic) imaging. It is generally performed in systole, aiding to null the signal from blood. It has found utility in patients who have hardware in place such as stents or devices or where turbulence makes SSFP imaging problematic.

#### 1.8.4 Cine (Figs. 1.10, 1.13, 1.15, 1.16, and 1.17)

Myocardial motion and blood flow can be visualized with cine imaging to determine function and physiology. It is one of the two workhorses of CMR in this regard (the other being

phase contrast velocity mapping which will be discussed next). The two major types of cine imaging are unbalanced gradient echo imaging and SSFP as mentioned above. The unbalanced gradient echo technique is older but still has a number of uses in state-of-the-art CMR. For example, unbalanced gradient echo imaging is useful to determine valve morphology using a high flip angle (Fig. 1.13); in this way, flowing blood into the imaging plane is bright and outlines the leaflets of the valve very well. It is also useful when artifacts plague SSFP as a low echo time (TE) and high bandwidth gradient echo image is less susceptible to these artifacts. High TE gradient echo imaging will enhance turbulence (where SSFP is less susceptible to turbulence) and may be useful in identifying these areas of flow disturbances. It is also the cine workhorse when ferumoxytol is administered as the contrast agent, using a high bandwidth.

High-resolution SSFP cine imaging (Figs. 1.15, 1.16, and 1.17) can demonstrate exquisite images of the myocardium, valves, blood pool, and vessels. In assessing myocardial function, it is the technique of choice and the gold standard. These cine images provide excellent spatial and temporal resolution for the assessment of global and regional myocardial wall motion. These cine sequences should be retrospectively gated so that wall motion data is available for the entire cardiac cycle. As mentioned, with prospective triggering, the phases prior to the R wave is generally truncated as noted above in the physics section. With retrospective gating, the number of calculated phases should be figured so that there is only one or less interpolated phase between each measured phase; an interpolated phase is one that shares data between the two measured phases. This is easily performed by doubling the patient’s RR interval and then dividing by the heart-beat “TR” (line TR  $\times$  number of segments) to get the maximum number of phases or dividing by the number of phases desired to obtain the maximum TR needed.

Temporal resolution should be set to provide, in general, 20–30 phases across the cardiac cycle, depending upon the heart rate. Obviously, in a patient with a heart rate of 150 beats/min (R-R of 400 ms), 20 frames/heartbeat is more than adequate (20 ms temporal resolution) while if the heart rate is 50 beats/min (R-R of 1200 ms), 20 frames/heartbeat is not sufficient (60 ms temporal resolution). This is because systole does not vary too much as a function of heart rate; it is diastole that lengthens or shortens. A 60 ms temporal resolution for a heart rate of 50 beats/min will not capture enough frames in systole to adequately assess the ventricle.

When an entire ventricular volume dataset is acquired, ventricular volume and mass at end-diastole and end-systole are measured yielding end-diastolic and end-systolic volumes, stroke volume, ejection fraction, cardiac output, and mass [33–37]. To perform an entire ventricular volume set, generally a 4-chamber view is first obtained by cine (orientation and slice position determined by multiplanar reconstruc-

tion as noted above); the 4-chamber view is defined as the view that intersects the middle of both atrioventricular valves at the atrioventricular valve plane and the apex of the heart. Subsequently, a series of short axis views are obtained which are perpendicular to the 4-chamber view and span from atrioventricular valve to apex. It should be noted that this requires obtaining short axis slices one slice past the atrioventricular valve level and one slice past the apex to ensure the entire volume is obtained; this can be clearly positioned off the 4-chamber view at end-diastole. Measurement of ventricular volumes involves contouring the endocardial border of each slice of a given phase (e.g., end-diastole or end-systole) from base to apex and planimeterizing this area. The product of the sum of the areas on each slice encompassing the ventricle and the slice thickness yields the ventricular volume at that phase. This procedure, if performed at end-diastole and end-systole, will yield two values and the difference between these values is the stroke volume; and the ratio of the stroke volume to the end-diastolic volume multiplied by 100 yields the ejection fraction. The cardiac output is obtained by multiplying the ventricular stroke volume and the average heart rate during the cine acquisition (note that if there is atrioventricular valve insufficiency, a ventricular septal defect or there is double outlet ventricle, this will not equate to aortic outflow). Ventricular mass is similarly measured, generally at end-diastole, by contouring the epicardial border on each slice which contains ventricle and planimeterizing the area which contains both the ventricular volume and mass. This value is subtracted from the ventricular volume measurement at each slice and yields the ventricular mass multiplied by the density of the myocardium. Most scanners come with and numerous independent companies sell software which semiautomates this process; ventricular volumes and mass can generally be obtained in a few minutes of post-processing. More tedious is contouring ventricular volumes through every phase of the cardiac cycle; however, this will yield a ventricular volume–time curve which may be useful in some situations. Because CMR can acquire multiple contiguous, parallel tomographic slices, there is no need for geometric assumptions, making the technique an excellent tool for precise measurement of ventricular volumes and mass in congenital heart disease. Indeed, cine CMR is considered the “gold standard” for ventricular volume and mass in both adult cardiology, pediatric CMR, and congenital heart disease. Ventricular size and shape can vary considerably in various forms of congenital heart disease (e.g., single ventricles, corrected transposition of the great arteries, etc.). Ventricular cine is also utilized not only for global but for regional wall motion abnormalities as well.

Besides ventricular size, mass, and wall motion, cine imaging is excellent for identifying vessel sizes as well as stenosis or hypoplasia including great arteries, along a ventricular outflow tract or in a baffle or conduit. On the flip

side, cine can also be used to qualitatively assess regurgitation of valves of which there should be minimal in the normal heart. All this is determined not only by the shape of the vessel but by loss of signal due to acceleration of flow through a stenotic vessel/valve or a regurgitant valve; a classic example is the flow void through coarctation of the aorta. In addition, shunts can be identified by cine as turbulence visualized across atrial or ventricular septae will indicate interatrial and interventricular communication. A way in which shunting can be accentuated visually is with the use of a presaturation tag. When the protons in a plane of tissue are flipped  $180^\circ$  to destroy their spins prior to imaging (similar to a selective inversion pulse in a plane of tissue intersecting the imaging plane), a presaturation tag is said to be laid down. This presaturation tag labels the tissue it intersects with decreased signal intensity (black on the image). If the presaturation tag is laid down on the left atrium prior to a gradient echo sequence in a patient with an atrial septal defect, blood flowing from left to right will be dark on the bright blood cine and visualized to cross from left to right atria. Similarly, if there is right to left flow, bright signal from the right atrium would be seen to cross to the darkness of the left atrium.

By stringing a series of continuous single-shot images together in one plane (“single plane, multiphase” imaging), motion can be captured and this is termed “real-time cine CMR” (see above). Essentially, the SSFP technique is used to acquire all the lines of *k*-space needed to create an image continuously in the same plane. “Interactive real-time cine CMR” adds the ability to be able to manipulate the real-time imaging plane interactively, similar to echocardiographic (“sweeps”); this provides a fast way to assess cardiovascular anatomy, function, and flow. These images can be used for localization for higher resolution regular cine CMR and have been utilized in the past to actually acquire fetal cardiac motion. It is also used in the event there is too much arrhythmia so that at least a qualitative assessment of the heart can be made. Temporal resolution can be as low as 35 ms using parallel imaging.

CMR techniques in general and cine in particular build the image of multiple heartbeats. If multiple averages (excitations) are used, this can be in the hundreds. The disadvantage to this is the time it takes to acquire the data unlike “real-time” CMR cine imaging just mentioned or echocardiography where the cardiac motion is instantaneously obtained. The distinct advantage to this approach, however, is because the image is built over many heartbeats; it represents the “average” of all those heartbeats over the acquisition time. This truly is an advantage as it would be assumed that this “average,” embedded in the image, is more reflective of the patient’s true physiologic state than the instantaneous images of echocardiography. To perform the equivalent, the echocardiographer would have to view hun-



dreds of heartbeats and “average” it in the imager’s mind with all the subjectivity that entails. Picture measuring hundreds of M-mode dimensions of the ventricle (end-diastolic and end-systolic diameters) and then averaging them all together to get a shortening fraction: that is what is obtained with cine CMR in one image when measuring ventricular function parameters!

### 1.8.5 Phase Contrast (Encoded) Magnetic Resonance (PCMR) (Figs. 1.13, 1.14, 1.21, 1.22, and 1.23) [38–46]

This CMR technique, also known as “velocity mapping,” is used to measure flow and velocity in any blood vessel with few limitations (for example, generally 4–6 pixels must fit across the blood vessel in cross-section for it to be accurate). Broadly speaking, there are two types of PCMR—through plane which encodes velocity into and out of the imaging plane and in plane which encodes velocity in the imaging plane (as in Doppler echocardiography). For example, through plane PCMR can measure cardiac output, the

aortic, and the pulmonary valves by measuring the velocities across the valves in cross-section, multiplying by the pixel size summed across the entire vessel, integrated over the entire cardiac cycle, and multiplied again by the heart rate. In the absence of intracardiac shunts, the flows across the aortic and pulmonary valves should be equal—an internal check to the measurement. In another example, relative flows to each lung may be measured by utilizing through-plane velocity maps across the cross-section of the right and left pulmonary arteries, obviating the need for nuclear medicine scans. By placing a through-plane velocity map across the main pulmonary artery, an internal check on the branch pulmonary artery flows is obtained as the sum of the blood flow to the branch pulmonary arteries must equal the blood flow in the main pulmonary artery. In addition, it is also common to utilize PCMR as a check on cine measurements (e.g., cardiac index of the aorta should be equal to the cardiac index of the left ventricle in the absence of mitral insufficiency or intracardiac shunts). It is clear that this is a strength of CMR—the ability to perform these checks for internal validation of the quantitative data, unlike other imaging modalities.

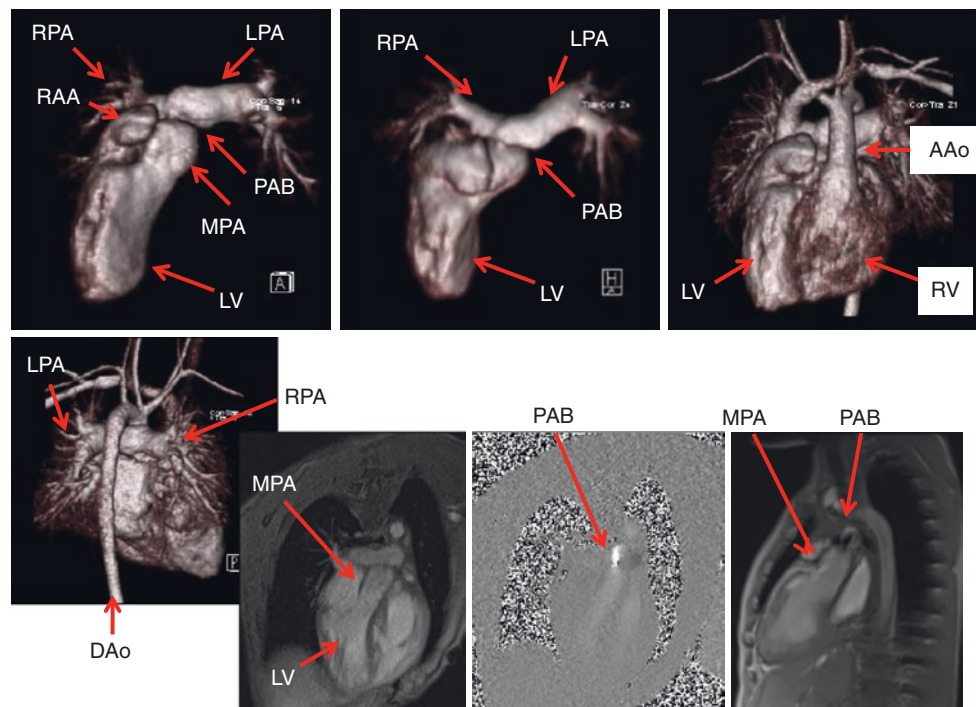


**Fig. 1.21** Various types of imaging in an infant with corrected transposition of the great arteries after a pulmonary artery band (PAB). The upper left and middle panels are two views of a 3-dimensional gadolinium image of the right-sided circulation showing the left ventricle, main pulmonary artery (MPA), PAB, and the right (RPA) and left pulmonary arteries (LPA) from anterior (left) and anterior tipped up to transverse view (middle). Note how the right atrial appendage (RAA) is easily seen. The right upper and left lower images are 3-dimensional gadolinium reconstructions of both circulations demonstrating the ante-

rior aorta and branch pulmonary arteries form the anterior (upper right) and posterior (lower left) views. The lower panel second from the left and second from the right are magnitude and in-plane phase images from phase-encoded velocity mapping demonstrating the left ventricular outflow tract and showing the jet through the PAB (signal intense is caudad) with a VENC of 400 cm/s. The right lower image is an orthogonal view through the left ventricular outflow tract demonstrating the turbulence distal to the PAB

**Fig. 1.22** Data and images from a patient with a bicuspid aortic valve, aortic stenosis, and insufficiency. The graph of flow versus time is on the lower left and on the upper left is the relevant data. Gradient echo images of the left ventricular outflow tract in two orthogonal views demonstrating the aortic insufficiency jet during diastole (arrow). *AAo* ascending aorta, *LV* left ventricle

Aortic Regurgitation

Cardiac output = 3.8 l/min/m<sup>2</sup>  
 Forward flow = 108 cc  
 Reverse flow = 38 cc  
 Regurgitant fraction = 35%  
 Heart rate = 87 BPM  
 Peak velocity = 3.7 m/s

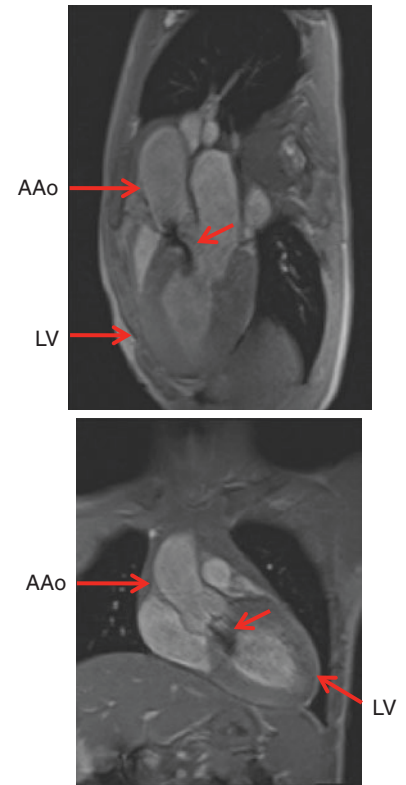
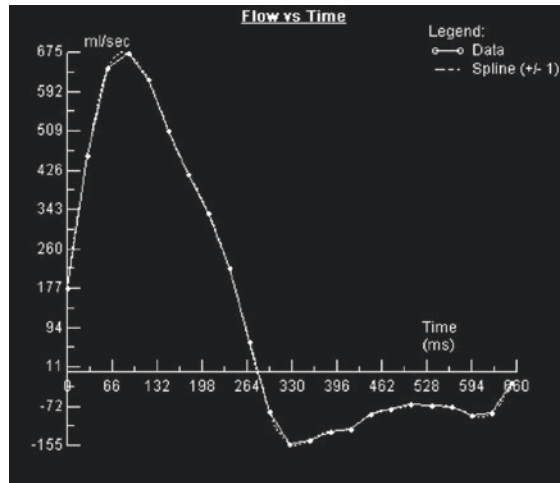


**Fig. 1.23** Data and images from a 2-year-old with an atrial septal defect (ASD) of the inferior vena cava type and anomalous right pulmonary venous connections to the right atrium (RA). The off-axis sagittal magnitude image (upper right) demonstrates the ASD while the in-plane, colored phase-encoded velocity map (lower right) in the same orientation as the magnitude image demonstrates left to right flow by the red color jet as in echocardiography (red is caudad and blue is cephalad flow). The aortic and pulmonary flow are both graphed simultaneously (lower left); data demonstrates as  $Q_p/Q_s$  2.3

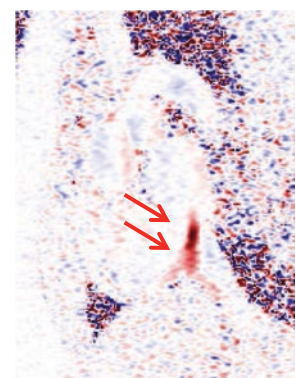
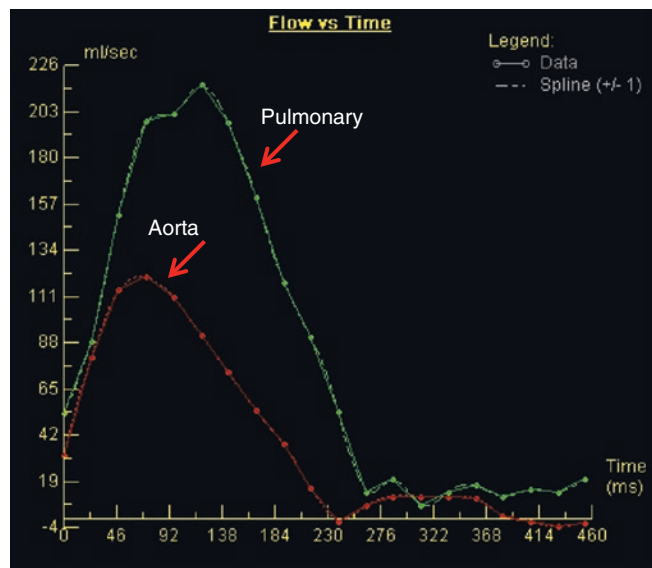
Aortic flow

Cardiac output = 4.6 l/min/m<sup>2</sup>

Pulmonary flow

Cardiac output = 10.7 l/min/m<sup>2</sup>

$Q_p/Q_s = 2.3$



It is key to understand what the “phase” means in the term “phase-encoded velocity mapping” for one to understand how this is used to measure flow. Phase was discussed in the physics section and will be explained in a slightly different way in this section, although it represents the same physical principle. When tissue is excited by radiofrequency energy, the subsequent signal that gets generated when the protons relax (for example, a sine wave) can be described by its frequency (how many cycles per second), its amplitude (the strength of the signal), and its phase (where, in a given time, is the sine wave in its cycle). Two waves can have the same frequency and amplitude but be in different points in their cycle (i.e., they are identical waves but shifted in time); they are out of phase. Think of two identical sine waves placed one atop the other in a signal amplitude-time graph (signal amplitude on the  $Y$  axis and time on the  $X$  axis) and then shift one slightly to the right in time; these sine waves are identical but out of phase with each other. Another way to understand this is that the same part of each of the two identical sine wave occurs at a different point of time (e.g., the peak of sine wave “A” occurs prior to the peak of sine wave “B”).

The principle underlying phase contrast CMR very simply is that moving tissue within a magnetic field that has a gradient applied to it changes phase. Put another way, whenever anything moves along the axis of an applied gradient, the phase of the spinning vectors in that object becomes altered relative to the stationary object. Remember the Larmor equation states the precessional frequency of the protons is directly proportional to the magnetic field; if that magnetic field is altered by position creating a gradient, the precessional frequency will change depending upon position. Any tissue moving across the gradient will change precessional frequency and accumulate phase shift selectively “labeling” itself. Phase contrast velocity mapping utilizes a “bipolar” radiofrequency pulse which is equal in magnitude but opposite in direction (e.g., turns from positive to negative and then from negative to positive); this is done with two back-to-back pulses with a slight delay. The sequence has the following effect: Before any radiofrequency pulse is applied, protons are tilted as a function of where they are positioned in the magnetic gradient. When the first radiofrequency pulse is applied, both stationary and moving tissue protons are further tilted; when the second equal and opposite radiofrequency pulse is applied immediately afterwards, protons of the stationary tissue return the tilt of their protons back to their original position and accumulate a net phase of zero (their tilt goes back to their original position since they experienced an equal and opposite radiofrequency pulse and haven’t moved position—they are experiencing the same magnetic field before and after these pulses). Protons of the moving tissue, however, do not revert to their original tilt since they have moved and are experiencing a different magnetic field because of the magnetic gradient in position.

These protons are said to have accumulated a “phase shift.” To summarize, this will yield a zero phase change for stationary objects when both pulses are applied whereas there will be a net accumulation of phase in moving tissue. By subtracting, pixel by pixel, the phases of one pulse from the other, background phase changes of stationary objects are canceled out and the phase shift of the moving tissue is amplified. Then, usually, the “phase difference” method is used to map the phase shift angles into signal intensities. Flow is calculated by the formula:

$$\Delta \text{phase} = g \times v \times T \times A_g$$

where  $g$  = gyromagnetic ratio,  $v$  = velocity,  $T$  = duration of the gradient pulse and  $A_g$  is the area of each lobe of the gradient pulse.

By tailoring the strength of the radiofrequency pulse to the anticipated velocities, accurate measurement can be obtained; this is called a VENC (velocity encoding) and is the equivalent of the Nyquist limit in echocardiography. Using the VENC and the signal intensity, the velocity of moving tissue in each pixel can then be encoded. This can occur with either blood (hence blood phase-encoded velocity mapping) or with myocardial tissue (also called myocardial velocimetry and is the equivalent to Doppler tissue imaging).

As mentioned, spatially, there are two ways to encode velocity in the image: (a) “through plane” where each pixel encodes velocity into and out of the plane of the image and (b) “in-plane,” where velocities are encoded in the plane of the image and not into and out of the plane similar to Doppler echocardiography. Unlike Doppler echocardiography, however, velocities are encoded in either the  $Y$ - or  $X$ -direction of the image. This is advantageous as each pixel can encode velocity in three orthogonal planes. Motion in one direction is mapped onto the anatomic image as increased signal intensity or bright and motion in the other direction appears signal poor and dark; stationary tissue appears gray. Air, such as in the lungs or around the patient, is encoded in a mosaic black and white. Color can be added to make it similar to Doppler echocardiography.

Flow measurements by this methodology utilize the cross-sectional area of the vessel perpendicular to the transaxial direction of flow. All software can identify the regions of interest simultaneously on the anatomic or “magnitude” images as well as the “phase” images (which can sometimes be difficult to read). The product of the velocity and the area of an individual pixel give flow through that pixel; summing this across the vessel cross-sectional region will yield the flow at a given phase of the cardiac cycle. Integrating this across the entire cardiac cycle (i.e., each phase plotted as a time-flow curve), the flow during one heartbeat is calculated. The product of the heart rate and this flow in one heartbeat will yield the cardiac output.

Through plane phase-encoded velocity mapping can also be used to assess the peak velocity for gradient calculations as might be used for coarctation of the aorta or ventricular pressure estimates as with a tricuspid regurgitant jet. If the plane is perpendicular to flow in the region of maximum velocity, the greatest velocity in any pixel in the region of interest in the cardiac cycle is used in the simplified Bernoulli equation. It should be noted that planes not perpendicular to flow or one at a level where the maximum velocity is not present will underestimate this number; generally, this is used in conjunction with in-plane velocity mapping (see below) to measure maximum velocities. This is similar to Doppler echocardiography where, if the plane is angled obliquely to the jet of interest or the sector is not in the area of maximum velocity, an underestimate of the maximum velocity will occur.

Encoding velocity parallel to flow (“in-plane” velocity encoding) is predominantly used to measure peak velocities which is similar to what Doppler echocardiography measures. The advantage of this type of phase encoding over the through plane technique in measuring maximum velocities is that velocities can be measured along a jet of interest in the direction the jet is pointing (similar to continuous wave Doppler), through plane mapping is placed at a certain level of the jet and the velocity measured which is similar to the range-gating technique of pulse wave Doppler echocardiography. With in-plane velocity mapping, the jet is aligned by rotating the entire field of view to make one side exactly perpendicular to the jet. The peak flow velocities can then be translated into pressure gradients via the simplified Bernoulli equation. The phase maps on present-day scanners can give a temporal resolution of about 15–20 ms with non-breath-hold techniques.

Phase-encoded velocity mapping has limitations. Reliability of both through plane and in-plane velocity mapping is a function of a few factors such as slice thickness (“partial volume” effects may induce inaccuracies in velocity calculations) and the angle of the jet (the jet needs to be aligned perpendicular to the direction of phase encoding, similar in some sense, to Doppler flow measurements). In addition, if the VENC is not chosen close but not below the maximum velocity anticipated, errors may occur. If the VENC chosen is too low, velocities in the vessel will exceed the ability of the CMR scanner to encode them which is akin to aliasing and exceeding the Nyquist limit in Doppler echocardiography. If the VENC chosen is too high, the lower velocities will not be measured as accurately as well as signal to noise decreasing; this is analogous to the difference when measuring a 4 oz of fluid in a 6 oz measuring cup (appropriate setting of the VENC) versus a gallon measuring cup (in appropriate setting of the VENC). Maxwell terms, eddy currents, and whether or not background subtraction is used will also play a role in velocity mapping accuracy.

Finally, by combining through plane and in-plane velocity mapping into the same sequence, CMR can acquire a 3-dimensional slab of velocities termed 4-dimensional or “4D flow” meaning three dimensions of space plus time [47, 48]. Using modern-day gradients and advanced software such as compressed sensing, the entire heart and great vessels can be acquired in anywhere from 3 to 8 min. There are multiple vendors with excellent software that can qualitatively visualize and quantitatively assess these datasets (Fig. 1.14).

There are multiple advantages to 4-D flow including being able to “go back” to any blood vessel in the thorax after the patient exam has ended to measure flow; 2D PCMR is aimed at one vessel at a time and once the patient leaves the scanner, there is no one to measure flow in another vessels. In addition, all vessels are measured at the same average heart rate as opposed to 2D flow where it is generally different, making 4D flow more consistent. Further, flow profiles in blood vessels and the heart and their interactions in 4D are easily visualized by this methodology. There are even implementation of these sequences where cine imaging and flow can be acquired at the same time, obviating the need for cine imaging and anatomic imaging (generally with the addition of a contrast agent however) [49]. Finally, metrics such as pulse wave velocity, pressure drop, and energy loss can be calculated whereas with 2-D PCMR, it may be difficult to impossible to do so (see below).

There are drawbacks to 4D flow as well. For some implementation of these sequences, administering a contrast agent such as gadolinium or ferumoxytol (see MRA section below) is useful for better signal to noise.

PCMR by 2D has many applications in congenital heart disease and in broad categories, they are (a) flow quantification, (b) flow visualization, (c) velocity measurements, and (d) myocardial velocimetry.

### 1.8.5.1 Flow Quantification

1. Cardiac Output (Figs. 1.22 and 1.23): Measuring cardiac output is an essential factor in assessing cardiovascular performance; this is especially true in patients who have undergone surgical procedures or who have undergone catheter intervention. Lesions such as single ventricles, corrected transposition, tetralogy of Fallot, etc. all benefit from measuring an elementary parameter such as cardiac output. This can also be used as an internal check to the ventricular stroke volume measurements.
2. Regurgitant Lesions (Fig. 1.22): As flow can be quantified as forward and reverse flow, the regurgitant volumes and fractions can be measured and calculated; lesions such as tetralogy of Fallot after repair with a transannular patch [50] or in patients with a bicuspid aortic valve and severe aortic insufficiency all require measurement of



leaky semilunar valves. These measurements are readily obtained by placing phase-encoded velocity map at the sinotubular junction (for the aortic valve) and just above the pulmonary valve and measuring the forward and reverse area under the flow-time curve. The regurgitant fraction is simply the area under the reverse flow (regurgitant volume) divided by the area under the forward flow (forward volume) multiplied by 100. An internal check is the measure flow in the cavae which should be the net cardiac output measured by velocity mapping in across the leaky semilunar valve. To obtain how much leakage there is across an atrioventricular valve, a combination of techniques are used; cine CMR is used to measure the stroke volume of the ventricle and phase-encoded velocity mapping to measure the amount of forward flow through the semilunar valve. The difference between the two (with no intracardiac shunts) is the regurgitant volume of the atrioventricular valve. Alternatively, the forward flow across the atrioventricular valve during diastole and the net flow across the semilunar valve in systole can be used (assuming no shunting).

3. Shunts (Fig. 1.23): Many lesions in congenital heart disease have shunting between the circulations present; this shunt flow can be easily calculated by placing velocity maps across the aortic valve and main pulmonary artery and measuring flow (e.g.,  $Q_p/Q_s$ ) [51]; if there is a aortopulmonary window, branch pulmonary artery flow is generally used instead. Measuring flow in both branch pulmonary arteries can add an internal check on the amount of pulmonary blood flow for intracardiac shunts and the sum of the flow in the cavae can be used as a check on the amount of systemic blood flow.
4. Flow Distribution to Each Lung: [52] Altered flow distribution to left and right lungs can be common in many lesions in congenital heart disease such as in single ventricle lesions after Fontan, tetralogy of Fallot, or in transposition of the great arteries after arterial switch procedure; all may have branch pulmonary stenosis. Relative flow to each lung is assessed by placing a phase-encoded velocity map at each branch pulmonary artery although care must be taken to place the map in the branch pulmonary artery proximal to the takeoff of the first branches to ensure this blood flow is included. Flow measured in the main pulmonary artery must equal the sum of the flows to each lung in the absence of collaterals and is used as an internal check.
5. Collateral Flow: [53] Patients with single ventricles after bidirectional Glenn or Fontan operation develop aortopulmonary collaterals presumably in response to decreased pulmonary blood flow and cyanosis [54]. In addition, patients with relatively long-standing coarctation of the aorta can develop aortic collaterals which bypass the obstructed segment. In the former, the amount

of collateral flow can be quantified in two ways: (1) by measuring flow via velocity mapping across the ventricular outflow tract and subtracting measured caval return and (2) measuring flow in the pulmonary veins and subtracting measured flow in the branch pulmonary arteries. In coarctation, the amount of collateral flow can be determined by placing a phase-encoded velocity map across the aorta just distal to the coarctation site and across the aorta at the level of the diaphragm. Normally, flow at each level will be very similar or the flow at the level of the diaphragm slightly lower (because of flow to the intercostal arteries); however, in the presence of coarctation with collaterals, flow just distal to the coarctation site in the aorta will be lower than flow in the aorta at the level of the diaphragm since collateral flow will present in the latter and not in the former.

### 1.8.5.2 Velocity Measurements

1. Pressure Gradients: Stenoses of a blood vessel such as a great artery (e.g., coarctation of the aorta, left pulmonary artery stenosis, or a pulmonary artery band, Fig. 1.21) or of a valve (aortic stenosis in a bicuspid aortic valve) can occur in numerous congenital heart lesions. It is important for many reasons to determine pressure gradients in these lesions; as noted above, the determination of gradients by CMR is similar to Doppler echocardiography, using the simplified Bernoulli equation. A maximum velocity is measured, typically in the vena contracta, and the gradient is simply the product of 4 and the velocity (in meter/second) squared. Measurement of maximum velocities may be performed in two ways: (a) “in-plane” velocity mapping directed parallel to the obstruction to flow and (b) “through plane” velocity mapping perpendicular to flow. Both have their strengths and weaknesses (see above discussion).

### 1.8.5.3 Flow Visualization

1. Septal Defects Using In-Plane Velocity Mapping: Septal defects at both the atrial and ventricular level can be visualized with i2D  $n$ -plane velocity mapping. The imaging plane needs to be oriented in the direction of the flow across the defect to successfully visualize it; blood flowing one way would be dark and flow the other way would be bright. In addition, color can be superimposed on the image to simulate color Doppler echocardiography.
2. Flow Directionality in Blood Vessels Using Through Plane Velocity Mapping: A good example of this is isolation or disruption of the subclavian arteries; this may be caused by surgery (e.g., a subclavian flap angioplasty to

repair coarctation of the aorta) or may be congenital. When this occurs, the subclavian artery usually is supplied with blood in a retrograde fashion via the vertebral artery; sometimes, with some paraspinal plexuses or other collaterals supply the subclavian artery. Clinically, a “subclavian steal” can occur and CMR velocity mapping techniques can be used to identify retrograde flow in the vertebral arteries. Normally, if an axial through plane velocity map is placed in the neck, both carotid and vertebral arteries will be labeled as either bright or black on the images as they are all flowing in the same direction. With isolation of a subclavian artery, flow in the ipsilateral vertebral artery is retrograde while flow in the other three head vessels (carotid and vertebral arteries) will be antegrade. A velocity map in this scenario will encode the vertebral artery ipsilateral to the isolated subclavian artery in one direction (e.g., dark) and the other three head vessels will be encoded in the opposite direction (e.g., bright), proving the physiology.

3. Valve Morphology (Fig. 1.13): Phase contrast velocity mapping is also useful for identifying valve morphology; as through plane phase contrast velocity mapping “tags” flowing blood, this can be used to outline the leaflets tips making a cast of the valve morphology while it opens and closes; the flowing blood is bright or dark and highlights the valve leaflet tips which are gray. Bicuspid, unicuspid, and quadricuspid valves are easily seen. Of particular note, bicuspid aortic valve is very common clinically; it can easily be identified by phase contrast mapping and the degree of valvular stenosis and regurgitation assessed [55, 56].

#### 1.8.5.4 Myocardial Velocimetry

This application of phase contrast velocity mapping is the CMR equivalent to Doppler tissue imaging in echocardiography; velocities of the myocardial tissue can be recorded. The phase contrast velocity mapping sequence is configured such that the VENC is set fairly low (15–30 cm/s); modifications in the sequence must be made to keep the TE as low as possible. Doppler tissue imaging can only record myocardial velocities in one direction; that is parallel to the Doppler beam. Myocardial velocimetry, however, is a much more comprehensive measurement of myocardial velocities in that, similar to other phase contrast velocity mapping applications, each pixel can encode velocities in three orthogonal planes; a 3-dimensional velocity map of the myocardium can be measured. Both myocardial velocimetry in CMR and Doppler tissue imaging in echocardiography suffer from the same drawback in that both techniques do not truly measure the velocity of a specific piece of myocardium; they identify a point in space and the velocity of myocardium moving into and out of that point is mea-

sured. Only CMR myocardial tagging and Doppler spectral tracking truly measure the velocity of a piece of myocardium noninvasively. An excellent review comparing the merits of myocardial velocimetry to myocardial tagging was published in 1996.

4D flow imaging has found utility in multiple applications in congenital heart disease [57]. All the above-mentioned metrics with 2D flow can also be calculated and visualized by 4D flow, especially visualizing shunts or regurgitant fraction. In addition, however, pulse wave velocity, which has a bearing on aortic stiffness and ventricular performance, can be obtained easily by multiple 4D flow methodologies [58]. Pressure flow fields and pressure drops across the entire aorta can also be calculated and can come in very useful in lesions such as coarctation of the aorta [59]. In addition, wall shear stress can be derived from 4D flow images in the aorta in patients, for example, with a bicuspid aortic valve [60]. Finally, as a last example, new metrics such as energy loss can be measured and assessed in congenital heart disease, such as in the single ventricle [61] (Fig. 1.14).

#### 1.8.5.5 Magnetic Resonance Angiography (MRA) (Figs. 1.20, 1.21, 1.24, and 1.25)

Magnetic resonance angiography, most based on intravenous gadolinium diethylenetriamine pentaacetic acid (Gd-DTPA), can determine detailed anatomy such as major pulmonary and systemic arteries and veins and to glean physiology is a key part of the examination. As discussed above, gadolinium is a paramagnetic element which is administered in a chelated form and is an extracellular agent that changes the magnetic property of the tissue or vessel it is in. It markedly decreases  $T_1$  relaxation and which allows its application to distinguish the target structure (e.g., the aorta) from background (e.g., lung, other mediastinal contents). It is considered a highly safe substance with adverse events occurring in one in 200,000–400,000. Usually a “double dose” of contrast is given (for most agents, this is 0.4 cm<sup>3</sup>/kg; please check the labeling of your individual agent).

In the past, much attention has been given to the incidence of nephrogenic systemic fibrosis (NSF) in patients with chronic, severe renal failure, first described in 2000 in 15 patients undergoing hemodialysis who presented with “scleromyxoedema-like” skin lesions. A detailed discussion of this entity is beyond the scope of this chapter; suffice it to say that after modifications of gadolinium use, NSF is nearly eradicated. Very few reports of children developing NSF exist and none under 6 years of age.

In addition, there have also been reports of linear gadolinium contrast agents accumulating in small amounts in the brain of individuals exposed to more than four doses of the agent. The recent FDA communication on this issue states that although more testing is needed, data supports the notion that no adverse effects are noted from this issue.

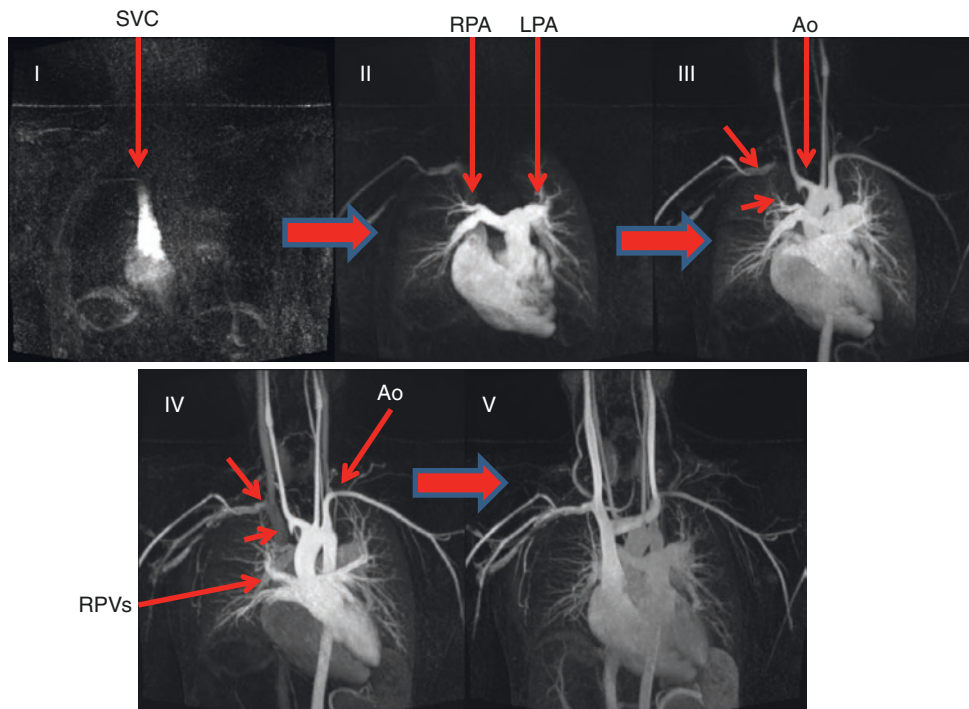
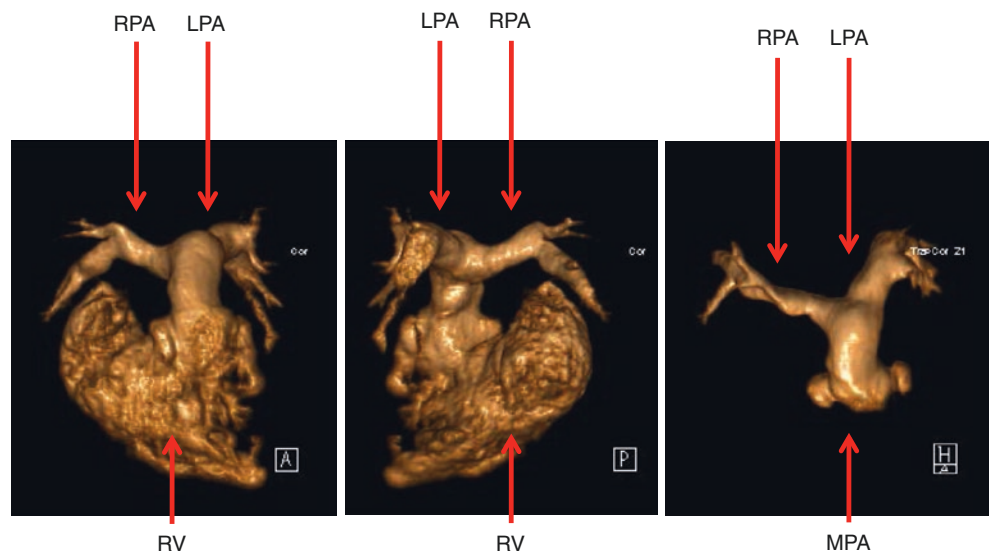


**Fig. 1.24** Three-dimensional time-resolved gadolinium imaging in a coronal view. The images are maximum intensity projections (MIPs) and temporally follow the roman numeral from left to right and from top to bottom. Each phase can be created into a 3-dimensional image. Spatial resolution is an isotropic  $1 \times 1 \times 1$  mm and temporal resolution is 2.2 s. In I, flow into the superior vena cava (SVC) is seen followed by flow into the right side of the heart (II). In III, flow is now seen in the

pulmonary veins and the beginnings of the aorta (Ao). In IV, flow has left the right side of the heart and is now mostly in the pulmonary veins, the left side of the heart, and the aorta. In V, flow is seen returning to the heart from the systemic veins. Note the interrupted right subclavian artery in III and IV (arrows). *LPA* left pulmonary artery, *RPA* right pulmonary artery, *RPVs* right pulmonary veins

**Fig. 1.25** Three-dimensional right heart reconstructions of the patient in Fig. 1.24. The right ventricle (RV), main (MPA), right (RPA), and left pulmonary artery (LPA) are clearly seen from an anterior (left), posterior (middle), and transverse (right) view. The RV was removed from the transverse view (right) to facilitate visualizing the branch pulmonary arteries



This can be performed anytime during the examination; however, it is performed after cine imaging. It can be performed before or after PCMR; however, if performed before PCMR, the contrast agent boosts the signal of the PCMR flow sequence, giving better signal to noise and more robust

data. Since approximately 10 min is needed between gadolinium administration and imaging for delayed enhancement and even more for  $T_1$  mapping (see below), the time after gadolinium administration but before viability imaging is used to perform either phase contrast velocity mapping or

3-dimensional static inversion recovery gradient echo imaging (see below). There are two types of contrast-enhanced techniques commonly used to evaluate 3-dimensional anatomy:

1. Static 3-dimensional imaging can be utilized to create a 3-dimension image of the cardiovascular system which can be rotated and cut in any plane desired. The 3-dimensional slab (see Physics section) can be acquired in any orientation and can be viewed in its raw data format, as a maximum intensity projection, a shaded surface display, or as a volume rendered object. As it is a 3-dimensional acquisition with one frequency encoding and two phase encoding directions, the thickness of the slices can be much thinner than other techniques—on the order of  $\frac{3}{4}$  to 1 mm. As the resolution is higher than other techniques in CMR, this type of imaging is used to visualize smaller vessels (e.g., aortic-pulmonary collaterals in pulmonary atresia/intact ventricular septum, aortic collaterals in coarctation, etc.). Multiple 3-dimensional data sets are generally obtained which (a) can separate out the systemic and pulmonary circulations and (b) increases the chances of successfully imaging what is needed.

Older techniques relied on knowing exactly when the contrast agent reaches the target vessel to begin the 3-dimensional sequence. This was performed in either two ways: (a) Bolus tracking, where the target structure (e.g., the pulmonary arteries in the case of tetralogy of Fallot) is imaged with “real-time” sequence during gadolinium injection—once the contrast agent is seen to arrive at the target structure, the 3-dimensional sequence is then obtained. (b) Timing bolus, where a small amount of contrast agent is injected and timed to determine when it will arrive at the target vessel. Injecting the full dose of gadolinium followed by the 3-dimensional sequence with a delay placed based on the small amount of contrast agent initially given is then performed knowing the gadolinium will arrive at the target vessel based on the initial timing bolus. Modifications need to be made, depending upon the 3-dimensional sequence, if it is “center weighted  $k$ -space” or “front-loaded  $k$ -space.”

The current state of the art is performing a static 3D sequence (inversion recovery gradient echo imaging with ECG gating utilizing the navigator technique and respiratory motion adaptation) either immediately after time-resolved imaging (see below) or with the “slow-drip” of gadolinium technique (which finishes administering gadolinium in the first 1/3 of the sequence) [62]. The navigator technique uses a coil to monitor the diaphragm and allows the algorithm to accept all the data within a certain range of where the diaphragm is (2–4 mm), adjust as

needed, and discard the rest. In this way respiratory motion is compensated for. This 3D technique is generally done isotropic and can be performed with resolutions as low as 0.6 mm using ferumoxytol (see below). Newer techniques under study now allow for creating 3D images without the need for a navigator and the sequence monitors the motion of the heart itself, not rejecting any imaging data at all [63].

2. Time-resolved (dynamic) 3-dimensional gadolinium imaging (Fig. 1.24) is similar to the static version mentioned above; however, multiple 3-dimensional data sets are obtained in an extremely short period of time (subsecond). These 3-dimensional data sets are acquired continuously and the bolus of gadolinium is followed through the cardiovascular system. This can be performed successfully with parallel imaging (multiple coils used), strong gradients and slew rates, and advanced software and sequences. Each phase of the acquisition can be made into a high-resolution (1 mm or less isotropic voxels) 3-dimensional image. This approach can be used to image physiology (view shunt flow or small connections) as well as determining lung perfusion (e.g., regions of lung with higher flows will be much brighter than regions of lung with low flow or no flow such as with pulmonary embolism).

In either technique, it is recommended, as best as possible, to acquire isotropic voxels (voxels with the same dimensions in all three directions). When acquiring the data in this manner, the 3-dimensional image can be manipulated and resliced in any plane and the resulting image would appear as if it was acquired in that orientation. In neonates and infants where smaller spatial resolution is needed, isotropic voxels are also very important but signal to noise takes on a very important role; as long as the voxel sizes are small, the field of view can remain high (i.e., by keeping the matrix high) and signal to noise will be preserved.

The advent of a new iron-based contrast agent, ferumoxytol, had changed the game in pediatrics. It has a long half-life of approximately 14 h which means that high-resolution imaging can be done in a longer period of time without loss of signal (as opposed to a first pass technique like cardiac catheterization angiography or ultrasound contrast agents). In a large-scale multicenter safety trial, it has been found safe in children as well as adults [21]. Using the free breathing 3D inversion recovery gradient echo sequence, resolutions of 0.8 mm can be easily reached in less than 5–7 min in young patients, visualizing coronaries in neonates and creating 4D cine images [20]. With the ability to maintain signal, both respiratory and cardiac phases can be imaged, yielding 4D cine imaging at different phases of the respiratory cycle without the need for a navigator for the diaphragm [18].



### 1.8.5.6 Viability (Delayed Enhancement) (Figs. 1.7 and 1.10) [64]

It is generally believed that infarcted myocardium is less of an issue in congenital heart disease than it is in adults and there is some truth to this—but just some. Many lesions in pediatric cardiology, either in the native state or postoperatively, are at risk for myocardial necrosis. The list of diseases that may manifest discrete myocardial scarring can be divided into three large categories and examples given below.

1. **Native coronary lesions** such as anomalous left coronary artery from the pulmonary artery or from the opposite sinus or coronary fistula or sinusoids in lesions such as pulmonary atresia with intact ventricular septum.
2. **Surgical coronary manipulation/postsurgical lesions** such as transposition of the great arteries after arterial switch operation or after a Ross operation where coronaries are manipulated or patients with single ventricle or repaired tetralogy of Fallot.
3. **Acquired pediatric heart disease** such as Kawasaki's disease, myocarditis, or dilated cardiomyopathy.
4. **Native myocardial lesions** such as hypertrophic cardiomyopathy, Duchenne's muscular dystrophy, and in tumor characterization (e.g., fibroma).

CMR viability imaging, also known as delayed enhancement, has shown to be effective in the detection of myocardial scarring and can be applied to the infant through adult with congenital heart disease [65–67]. With viability imaging, intravenous gadolinium chelate, which can freely distribute in extracellular water but cannot cross intact cellular membranes, is delivered to the myocardium and accumulates in areas of fibrosis due to increased volume of distribution and slower washout kinetics [68]. This imaging technique distinguishes areas of myocardial scarring with high signal intensity in comparison to viable myocardium.

As examples, many studies have used delayed enhancement to correlate myocardial scarring with heart function and clinical outcome in different diseases. Babu-Narayan et al. correlated delayed enhancement in transposition of the great arteries patients after surgical repair with age, length of time after surgery, higher right ventricle end-systolic volume index, and lower RV ejection fraction [69]. Babu-Narayan et al. also showed correlation of scarring with increased QRS duration, QT dispersion, and JT dispersion from ECG exams as well as a significantly higher occurrence of arrhythmia/syncope. Myocardial scarring has also been investigated in tetralogy of Fallot patients after repair [70, 71]. RV delayed enhancement was shown to correlate with decreased exercise tolerance, increased RV indexed end-systolic volume, decreased RV ejection fraction, and more documented clinical arrhythmia. Left ventricular delayed enhancement correlated with more arrhythmia, shorter exercise duration,

increased LV indexed end-diastolic and end-systolic volume, and decreased LV ejection fraction. Regions of myocardial delayed enhancement have also been known to occur in patients with hypertrophic cardiomyopathy [72, 73] and the extent of delayed enhancement has been associated with clinical markers of sudden death risk and progression to heart failure [74].

Regions of irreversible myocardial injury will exhibit high signal intensity on  $T_1$ -weighted images when administered gadolinium which significantly shortens the longitudinal relaxation time. Although the mechanism by which this occurs is open to debate, it is thought that ruptured cell membranes of myocytes allow the gadolinium to be avidly taken up by the scarred myocardium into the intracellular regions; this results in increased tissue concentration of the contrast agent and, hence, an increased signal intensity. In addition, with scar tissue, there is increased interstitial space between collagen fibers, allowing for gadolinium to inculcate itself in these regions and become more concentrated. This is opposed to normally perfused myocardium where the gadolinium is subsequently “washed” out by coronary blood flow. The signal intensity-time curves separate, with the infarcted myocardium gadolinium curve becoming signal intense much before perfused myocardium and remaining highly signal intense after 5–20 min whereas normal myocardium becomes much less so. CMR pulse sequences, first described in the literature in the mid-1980s, have taken advantage of this high concentration and slow washout of contrast agent when attempting to image infarcted myocardium. With segmented inversion recovery fast gradient echo sequences and other techniques such as steady-state free precession, signal intensity differences between normal and infarcted myocardium can be as high as 500%. The technique has been shown to accurately delineate the presence, extent, and location of acute and chronic myocardial infarction.

After preliminary scout images and cine sequences are obtained, 0.1–0.2 mmol/kg of intravenous gadolinium is administered. The myocardium is then imaged approximately 5–20 min after this injection; as neonates and children wash out the contrast agent quicker, they are usually imaged on the “sooner side” or if imaged later, have a longer inversion time (TI) (see below). The sequence makes use of a nonselective  $180^\circ$  inversion pulse which spoils all the spins in the myocardium (black on the image) and gives it  $T_1$  weighting. The magnetization of tissue goes from +1 to –1 by this process. As both the myocardial and scar tissue begin to recover their spins (enabling the myocardial and scar tissue to “give off” signal), because scar tissue shortens the  $T_1$ , it recovers signal much quicker than normal myocardium. A time delay is placed after the  $180^\circ$  inversion pulse (TI) to image the ventricle at just the point where the normal myocardium is about to regain signal again (and because the scar tissue recovers spins much quicker, can give off signal). That

is to say that the TI is chosen between the nonselective 180° pulse and the center of  $k$ -space of the sequence so that the magnetization of normal myocardium is near the zero line (i.e., normal myocardium is dark on the image). This allows for maximizing the difference in signal intensity between scarred and normal myocardium; the ventricle is imaged in mid-late diastole. TI time can be manually changed as the acquisition time continues. Collections of lines of  $k$ -space generally occur every other heartbeat.

There are a number of recent advances that have further refined the ability of CMR delayed enhancement to detect myocardial fibrosis. Some manufacturers have implemented 3-dimensional volumes slabs to allow for thinner slices. Steady-state free precession imaging can be used as opposed to gradient echo imaging to decrease the time needed for image acquisition. In addition, “single-shot” techniques are available (as opposed to segmented versions) to obtain an entire slice in one heartbeat, further allowing for increased coverage of the myocardium in one breath-hold. Motion-corrected viability imaging with high signal intensity as well as wideband viability imaging allows for improved fidelity of the images as well as compensating for motion and metallic artifact respectively.

Further advances have relied on refining the correct TI time which, as can be surmised, is a critical component to the whole procedure; as mentioned, it is chosen to optimally “null” the myocardium (i.e., the time at which normal myocardium crosses the “zero” point of signal intensity) where the difference in signal intensity between normal and infarcted tissue is maximized. With a TI time that is too short, the normal myocardium will be below the zero point which will cause two issues (a) differences between signal intensities of infarcted and normal myocardium will not be maximized and (b) as the image intensity is a function of the magnitude of the magnetization vector, normal myocardium may become hyperenhanced and scar tissue may become nulled if the TI is shortened enough. On the other hand, if the TI time is too long, the normal myocardium will be shades of gray with the scar tissue having high signal as well; as one can see, the contrast between the two tissues will be reduced. Finally, as mentioned already, as gadolinium concentration decreases from the myocardium as time progresses, the TI will have to be adjusted upwards the longer the time after injection.

To make better choices of TI times, two advances have improved the process: (1) “TI scouts” have been developed which obtain images at various increments of TI. The imager can choose the TI based on this scout as to image which appears optimal. (2) A phase-sensitive inversion recovery approach can be used which provides consistent contrast between normal and scarred tissue over a wide range of TIs. This “auto viability” technique maintains signal polarity; the inversion recovery preparation pulse and phase reference acquisition are interleaved requiring 2 heartbeats.

There are a few pitfalls with viability imaging. In patients who cannot hold their breath or with arrhythmias, using certain viability sequences, image quality can be degraded although with single-shot viability imaging and motion-corrected versions, this is less of an issue. In addition, ghosting artifacts can occur from tissue which have long  $T_1$  values, such as pericardial effusion.

### 1.8.5.7 Multiparametric Mapping (Fig. 1.8)

One of the strengths of CMR is the ability to characterize tissue such as discrete fibrosis or tumor characterization.  $T_1$ ,  $T_2$ , and  $T_2^*$  star mapping has emerged as extensions of this capability which allows for spatially assessing the relaxation times of each one of these spin properties to assess for diffuse fibrosis (extracellular volume), myocardial edema, or iron deposition respectively. A disproportionate accumulation of collagen in the heart is an important factor in the etiologies of heart failure, diastolic dysfunction, and sudden cardiac death or as a result of valve lesions such as aortic stenosis and this generalized increase in collagen can be measured by the  $T_1$  relaxation time. Similarly, assessment of myocardial edema in regions near infarcts or in inflammatory states such as myocarditis would be useful to identify and this can be measured by  $T_2$  mapping. By the analysis of  $T_2^*$  in patients who may have iron overload (thalassemia, sickle cell disease, etc.), the amount of myocardial iron present can be measured.

There are multiple papers which describe these techniques in great detail which is beyond the scope of this chapter and the reader is referred to them [75–77]. The general concept behind, for example,  $T_1$  mapping, is acquiring many images with different  $T_1$  weightings, and the signal intensities in each are fit to the equation for  $T_1$  relaxation. To be more specific, the magnetization of the tissues/spins are either inverted or nulled with a radiofrequency pulse, and the  $T_1$ -weighted images acquired at different  $T_1$  times or times after the inversion or saturation. By doing this over multiple heartbeats and allowing for the tissue to relax, in between a series of tissue excitations, a  $T_1$  relaxation curve can be created. When this is performed prior to gadolinium administration (native  $T_1$  relaxation time) and after gadolinium (post contrast  $T_1$  relaxation), with a blood hematocrit, the extracellular volume may be calculated as a percent by:

$$ECV = (1 - \text{hematocrit}) \frac{\frac{1}{\text{postcontrast } T_1 \text{ myo}} - \frac{1}{\text{native } T_1 \text{ myo}}}{\frac{1}{\text{postcontrast } T_1 \text{ blood}} - \frac{1}{\text{native } T_1 \text{ blood}}}$$

An estimate of the hematocrit from the images, also termed “synthetic hematocrit,” has been touted to be a good substitute for a blood drawn hematocrit [78] but this is con-

troversial [79]. Similar techniques are used for  $T_2$  and  $T_2^*$  star but without the use of gadolinium. In the CMR protocol,  $T_1$  mapping is performed prior to gadolinium administration and then approximately 15 min afterwards or generally a few minutes after viability imaging.

$T_1$  mapping has found utility in multiple areas of pediatric congenital and acquired heart disease. For example, in tetralogy of Fallot, expansion of the extracellular space in both the right and left ventricles is present [80, 81] and expansion of left ventricular extracellular space in adult tetralogy of Fallot patients has been linked to adverse events [82].

Similarly,  $T_2$  mapping for edema has found utility in the adult world in acute ischemia and in both the pediatric and adult world as one of the criteria for myocarditis [83]. Generally, values over 55–60 ms at 1.5 T are considered abnormal.

**$T_2^*$  for Myocardial Iron Assessment** In brief, the sequence obtains multiple images of the same short axis slice at various echo times utilizing a gradient echo sequence. With longer TEs, the myocardium and liver become increasingly dark. Because iron is ferromagnetic, the magnetic properties of the myocardium and liver change with increasing iron concentration, decreasing the measured  $T_2^*$  (which makes the myocardium even darker) relative to normal myocardium. Values <20 ms are considered at risk for decreased ventricular function. Chelation therapy is generally modified in these patients using this information.

The combination of these techniques of multiparametric mapping can be utilized in a whole host of other diseases. Literature on amyloidosis, Fabry's disease, and non-ischemic cardiomyopathy has all been published.

## 1.9 Other Sections of the CMR Protocol

There are a number of other techniques in CMR that are not infrequently used but do not fit into the generalized protocol. They should be inserted at appropriate points in the protocol.

### 1.9.1 Coronary Artery Imaging (Fig. 1.6) [84, 85]

For CMR to be implemented successfully to image the coronary arteries, two main technical challenges need to be overcome; that of cardiac motion and respiratory motion. The magnitude of both motions greatly exceeds coronary artery diameters and in the absence of motion suppression algorithms, would cause blurring and possibly missing the coronary arteries all together. There are multiple other challenges as well but these two present the most complex ones. Various

techniques have been used in the past to overcome these motion-related problems and a history of how modern coronary imaging is performed by CMR is beyond the scope of this chapter; suffice it to note that it has been a long road to the present-day high-quality, high-resolution imaging of the coronary arteries.

To compensate for coronary motion, high-quality ECG or vector gating is required; peripheral pulse gating would not be adequate. In addition, if arrhythmias were present and “arrhythmia rejection” algorithms not used, image degradation will be present. In either case, cardiac motion is compensated for by imaging during the “quiescent phase” of the cardiac cycle which is generally mid to late diastole or if the patient has a high heart rate (generally >100 beats/min), end-systole. End-systole is advantageous as well in that this is the phase where the coronaries are most filled with blood. To determine the “quiescent phase” of the cardiac cycle, it has been our practice to perform a 4-chamber view and left ventricular outflow tract high temporal resolution cine (30–60 phases depending upon the heart rate), focusing on the atrio-ventricular groove and aortic annular motion respectively. When both of these regions are motionless should be considered the beginning of the “quiescent phase.” In addition, the length of the “quiescent phase” is measured in both views as well and is timed only as both structures remain motionless; this is helpful in determining how long the “shot time” for each heartbeat is (i.e., the amount of time it takes to acquire the lines of  $k$ -space).

To compensate for respiratory motion, a number of approaches have been used in the past including breath-holding, chest wall bellows, etc.; however, in the current era, the state of the art is utilizing navigator pulses. A navigator is used to track motion of a structure and, in this particular instance, is used to determine respiratory motion. Most navigators in use today for coronary imaging track the right dome of the diaphragm; however, the left hemidiaphragm and the anterior chest wall have also been used. Lines of  $k$ -space accepted into image reconstruction are only those that occur when the diaphragm is within certain defined boundaries (i.e., within 2 mm of the end-expiratory position of the diaphragm). Efficiency is the amount of lines of  $k$ -space accepted divided by the total lines of  $k$ -space. The overwhelming effect of respiration on cardiac motion is in the supero-inferior dimension and at end-expiration, the ratio between cardiac and diaphragmatic displacement ranges from 0.6 to 0.7 and this “tracking factor” is used to shift slice position coordinates. Newer sequences in development currently track the actual motion of the heart and as such, data from every heartbeat is acquired yielding an efficiency of 100% [18].

Finally, two other major pre-pulses are used to suppress the signal from surrounding tissue. As fat has a relatively short  $T_1$ , a frequency selective fat prepulse can be used to saturate the signal from fat surrounding the coronaries.

Because the coronaries also course near the epimyocardium, cardiac muscle needs to be suppressed as well. Unfortunately, blood and myocardium have similar  $T_1$  relaxation properties; however, their  $T_2$  relaxation differs significantly.  $T_2$  preparation pulses are used to enhance the contrast between the blood of the coronaries and the myocardium (it also suppresses deoxygenated venous blood); magnetization transfer contrast is used to image coronary veins.

Uses in congenital heart disease fall into three basic categories: (a) anomalous coronary artery imaging such as anomalous left coronary artery from the pulmonary artery or anomalous coronary arteries from the opposite sinus, (b) patient who have had coronary manipulation surgically such as transposition of the great arteries after arterial switch or the Ross procedure, and (c) acquired coronary artery disease such as Kawasaki's disease or with familial hypercholesterolemia.

### 1.9.2 Perfusion Imaging (Fig. 1.9)

Perfusion imaging of the myocardium with CMR using contrast has the advantage of no radiation, increased spatial resolution (compared to nuclear techniques), and provides functional information. Essentially, the concept of myocardial perfusion imaging is simply the relative changes in myocardial signal intensity are assessed during a bolus administration of gadolinium contrast agent under both pharmacological stress (typically either regadenoson, adenosine, or much less commonly in pediatrics, dipyridamole) and physical stress such as exercise on an MRI-compatible supine ergometer and at rest. The contrast agent causes increased myocardial signal intensity in proportion to the amount of contrast agent passing through each region of myocardium which is, in turn, proportional to the amount of coronary blood flow. Normally perfused myocardium will have a more rapid and intense signal increase under pharmacologic stress as compared with rest, while areas supplied by coronary arteries with flow-limiting stenosis will have slower and less intense rise in signal intensity under stress conditions.

Myocardial perfusion imaging is generally performed as a  $T_1$ -weighted, segmented gradient-echo or steady-state free precession implementation.  $T_1$  weighting is improved by a preparatory radiofrequency pulse at the beginning of the sequence; inversion recovery preparation has been utilized and provides the greatest contrast between normal and abnormal myocardium; however, because it is sensitive to arrhythmias, a saturation recovery preparatory pulse is now generally utilized that renders the magnetization insensitive to arrhythmias, and allowing quantitative assessment of results. In general, a stack of 3–6 short axis slices and, if possible, 4-chamber and long axis views of the ventricle (depending upon the disease and parameters chosen) are acquired under pharmacologic stress and then, approximately 15–20 min later, repeated at rest which is finally fol-

lowed by delayed enhancement (see above) 10 min afterwards. Images are obtained for every beat or every other beat, depending on the sequence.

Analysis of the images depend upon the relative changes in signal intensity (either qualitative or semiquantitative) to assess for ischemia. Qualitatively, the assessment is performed as a cine and visual analysis is performed of the relative signal intensity in regions of myocardium; a reduced rate of increase in signal intensity or an absolute decrease in signal intensity relative to normal myocardium is abnormal. This can be either because of (a) hypoperfusion, (b) infarction, or (c) artifact. To determine the difference between these, stress and rest perfusion images are combined with delayed enhancement imaging. If the region of abnormal signal intensity corresponds to infarcted regions of the ventricle, then the reason for abnormal signal intensity is obvious. If it does not, then hypoperfusion and ischemia are the reason if the stress images show the defect and the rest images do not. It is most likely an artifact if both rest and stress images show the defect (but not always) and there is a typical artifact pattern (susceptibility artifact, Gibbs ringing, or excessive motion of the heart). The visual analysis is simple, relatively fast, and has comparable sensitivity and specificity to nuclear techniques. Semiquantitative and quantitative approaches are more time-consuming which make it less suitable for routine use; however, it is used in some centers and in some studies, which improved the accuracy over visual analysis. Quantitative assessment is complex using an input arterial function; however, automated quantitative perfusion imaging is being tested at some centers [86].

Perfusion CMR has been investigated since 1990; however, because of software and hardware advances, it has gained the greatest clinical use since ~2000. Since that time, there have been numerous single-center studies demonstrating its clinical utility and accuracy. There is limited data in the literature; unfortunately, in patients with congenital heart disease, however, alternatives such as nuclear imaging and cardiac catheterization expose children to radiation; using CMR myocardial perfusion imaging for some of these applications has obvious potential benefits. Potential applications in congenital heart disease include patients who have had coronary artery manipulation (e.g., transposition of the great arteries after arterial switch procedure or patients after the Ross procedure), anomalous coronary arteries, assessment of cardiac tumors, and Kawasaki's disease. Perfusion imaging is safe in pediatrics and this data was recently published in the past few years [87].

### 1.9.3 Myocardial Strain

Relatively recently, in the echocardiographic world, strain has become a hot topic; however, it should be noted the CMR was the first noninvasive imaging modality to assess strain. As early as 1988, Zerhouni et al. demonstrated how to use "myocardial tagging" to assess strain in the heart [88]. Other



methodologies have since developed such as “displacement encoding with stimulated echoes (DENSE)” [89], strain encoded CMR or “SENC” [90], and myocardial velocimetry using phase contrast techniques (see below) [91]. These are dedicated sequences for strain. Relatively recently, feature and tissue tracking can be applied to regular cine imaging to extract global, longitudinal, and radial strains [92–95]. Regional strain has been found to inversely correlate with measures of ventricular fibrosis [96]. Regional strain can be utilized to assess for dyssynchrony as well.

A couple of protocols for specific disease states are worth mentioning that use the techniques noted above.

### 1.9.4 Tumor/Mass Characterization (Figs. 1.8, 1.9, and 1.10)

Characterization of tumors and masses on CMR is very useful as a high likelihood of what the mass is can be obtained. Many cardiac tumors and masses can be differentiated from each other by their tissue characteristics as well as their location, symptoms, and the patient’s age. For example, a lipoma will be signal intense on  $T_1$ -weighted images and become signal poor after fat saturation. A hemangioma will become signal intense during perfusion imaging and may be indistinguishable from the ventricular cavity on the image which is one of its characteristics. Tumor characterization by CMR includes  $T_1$ - and  $T_2$ -weighted images, images with fat saturation, gradient echo imaging, perfusion (e.g., for hemangiomas), delayed enhancement imaging,  $T_1$ -weighted images after gadolinium administration, and myocardial tagging. If time permits, functional imaging can be used to assess for effects of the tumor such as obstruction to flow and decreased cardiac output. A multicenter pediatric registry of tumors in children and their characteristics was published in 2011 [97].

### 1.9.5 Arrhythmogenic Right Ventricular Dysplasia

With fatty or fibrofatty replacement of myocardium, mostly of the right ventricle, arrhythmias can generally result (e.g., left bundle branch block tachycardia). In its severest form, the right ventricle can become dilated and function poorly with dyskinetic wall regions. In addition, there can be right ventricular conduction delay on ECG, inverted T waves, and Epsilon waves. As imaging is only one of multiple criteria in the 2010 Task Force manuscript, it cannot be utilized in and of itself to make a diagnosis but must be combined with other criteria [98]. There are criteria for arrhythmogenic right ventricular dysplasia in adults and have been utilized successfully; however, when applied to the pediatric population, there is a question of how useful it truly is [99]. The CMR findings in adults with arrhythmogenic right ventricular dysplasia vary

from study to study but in general, there is (1) fatty substitution of the myocardium, (2) ectasia of the RVOT, (3) dyskinetic bulges or dyskinesia of RV wall motion, (4) a dilated RV, (5) a dilated RA, and (6) fixed RV wall thinning with decreased RV wall thickening. The protocol includes simply cine for ventricular function to assess wall motion and ventricular volumes, phase-encoded velocity mapping of the aortic and pulmonary valves, and delayed enhancement which was shown to be helpful in a couple of studies; solely right ventricular volume and regional wall abnormalities are in the 2010 Task Force criteria.  $T_1$ -weighted imaging is not utilized anymore for evidence of fatty substitution of the myocardium by CMR; it is not one of the criteria and must be done by biopsy.

### 1.9.6 Other Techniques

Because of space limitations, techniques which will not be discussed in this chapter but the reader should be aware of are:

- XMR—the combination of CMR and cardiac catheterization
- Interventional CMR—performing intervention in the CMR suite
- Exercise CMR—utilizing a “CMR-friendly” exercise bicycle or other technique to obtain ventricular function and flow parameters during exercise
- Fetal CMR—utilizing CMR for evaluation of the heart in utero
- BOLD and other  $T_2$  techniques for oxygen saturation
- Details of CMR at 3 T as applied to pediatrics and congenital heart disease
- Although it was mentioned above details of four-dimensional velocity mapping (Fig. 1.26)

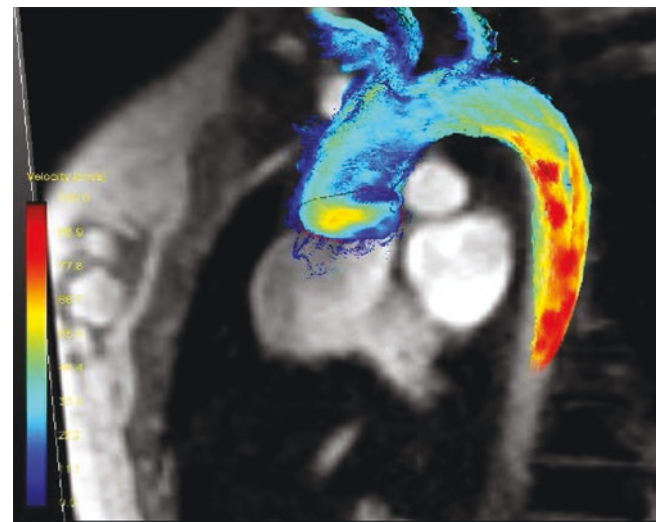


**Fig. 1.26** Four-dimensional flow in the candy cane view of the normal aorta by utilizing a stack of 3-dimensional phase-encoded velocity maps. Color code of the velocity is in the lower left of the image

## References

- Ridgway JP. Cardiovascular magnetic resonance physics for clinicians: part I. *J Cardiovasc Magn Reson*. 2010;12(1):71.
- Campbell-Washburn AE, Ramasawmy R, Restivo MC, et al. Opportunities in interventional and diagnostic imaging by using high-performance low-field-strength MRI. *Radiology*. 2019;293:384–93.
- Bandettini WP, Shanbhag SM, Mancini C, et al. A comparison of cine CMR imaging at 0.55 T and 1.5 T. *J Cardiovasc Magn Reson*. 2020;22:37.
- Simonetti OP, Finn JP, White RD, Laub G, Henry DA. “Black blood” T2-weighted inversion-recovery MR imaging of the heart. *Radiology*. 1996;199:49–57.
- Carr JC, Simonetti OP, Bundy JM, Li D, Pereles S, Finn JP. Cine MR angiography of the heart with segmented true fast imaging with steady-state precession. *Radiology*. 2001;219:828–34.
- Fogel MA, Gupta K, Baxter MS, Weinberg PM, Haselgrove J, Hoffman EA. Biomechanics of the deconditioned left ventricle. *Am J Physiol Heart Circ Physiol*. 1996;40:H1193–206.
- Fogel MA, Gupta KB, Weinberg PW, Hoffman EA. Regional wall motion and strain analysis across stages of Fontan reconstruction by magnetic resonance tagging. *Am J Physiol Heart Circ Physiol*. 1995;38:H1132–52.
- Fogel MA, Weinberg PM, Fellows KE, Hoffman EA. A Study in ventricular - ventricular interaction: single right ventricles compared with systemic right ventricles in a dual chambered circulation. *Circulation*. 1995;92:219–30.
- Young AA, Axel L, Dougherty L, et al. Validation of tagging with MR imaging to estimate material deformation. *Radiology*. 1993;188:101–8.
- Menteer J, Weinberg PM, Fogel MA. Quantifying regional right ventricular function in tetralogy of fallot. *J Cardiovasc Magn Reson*. 2005;7:753–61.
- Shankaranarayanan A, Simonetti OP, Laub G, Lewin JS, Duerk JL. Segmented k-space and real-time cardiac cine MR imaging with radial trajectories. *Radiology*. 2001;221:827–36.
- Li F. Golden-angle radial MRI: basics, advances, and applications. *J Magn Reson Imaging*. 2022;56:45–62.
- Atkinson DJ, Edelman RR. Cineangiography of the heart in a single breath hold with a segmented turboFLASH sequence. *Radiology*. 1991;178:357–60.
- Xue H, Kellman P, Larocca G, et al. High spatial and temporal resolution retrospective cine cardiovascular magnetic resonance from shortened free breathing real-time acquisitions. *J Cardiovasc Magn Reson*. 2013;15:102.
- Pruessmann KP, Weiger M, Scheidegger MB, Boesiger P. SENSE: sensitivity encoding for fast MRI. *Magn Reson Med*. 1999;42:952–62.
- Kellman P, Epstein FH, McVeigh ER. Adaptive sensitivity encoding incorporating temporal filtering (TSENSE). *Magn Reson Med*. 2001;45:846–52.
- Jaspan ON, Fleisher R, Lipton ML. Compressed sensing MRI: a review of the clinical literature. *Br J Radiol*. 2015;88:20150487.
- Heerfordt J, Whitehead KK, Bastiaansen JAM, et al. A Similarity-driven Multi-dimensional Binning Algorithm (SIMBA) for free-running motion-suppressed whole-heart MRA. *Magn Reson Med*. 2021;86:213–29.
- Cheng JY, Hanneman K, Zhang T, et al. Comprehensive motion-compensated highly-accelerated 4D flow MRI with ferumoxytol enhancement for pediatric congenital heart disease. *J Magn Reson Imaging*. 2016;43:1355–68.
- Nguyen KL, Ghosh R, Griffin L, et al. Four-dimensional multi-phase, steady-state MRI with ferumoxytol enhancement: early multicenter feasibility in pediatric congenital heart disease. *Radiology*. 2021;300:162–73.
- Nguyen KL, Yoshida T, Kathuria-Prakash N, et al. Multicenter safety results for off-label diagnostic use of ferumoxytol in MRI. *Radiology*. 2019;293:554–64.
- Fogel MA, Pawlowski TW, Harris MA, et al. Comparison and usefulness of cardiac magnetic resonance versus computed tomography in infants six months of age or younger with aortic arch anomalies without deep sedation or anesthesia. *Am J Cardiol*. 2011;108:120–5.
- Shariat M, Mertens L, Seed M, et al. Utility of feed-and-sleep cardiovascular magnetic resonance in young infants with complex cardiovascular disease. *Pediatr Cardiol*. 2015;36:809–12.
- Malviya S, Voepel-Lewis T, Eldevik OP, Rockwell DT, Wong JH, Tait AR. Sedation and general anaesthesia in children undergoing MRI and CT: adverse events and outcomes. *Br J Anaesth*. 2000;84:743–8.
- Fogel MA, Weinberg P, Parave E, Harris C, Montenegro L, Concepcion M. Safety and efficacy of deep sedation in infants, children and adolescents undergoing cardiac magnetic resonance. *J Pediatr*. 2008;152:534–9.
- Malviya S, Voepel-Lewis T, Tait AR. Adverse events and risk factors associated with the sedation of children by nonanesthesiologists. *Anesth Analg*. 1997;85:1207–13.
- Bluemke DA, Breiter SN. Sedation procedures in MR imaging: safety, effectiveness, and nursing effect on examinations. *Radiology*. 2000;216:645–52.
- Shepherd JK, Hall-Craggs MA, Finn JP, Bingham RM. Sedation in children scanned with high-field magnetic resonance: experience at the Hospital for Sick Children, Great Ormond Street. *Br J Radiol*. 1990;63:794–7.
- Vade A, Sukhani R, Dolenga M, Habisohn-Schuck C. Choral hydrate sedation of children undergoing CT and MR imaging: safety as judged by American Academy of Pediatrics guidelines. *Am J Roentgenol*. 1995;165:905–9.
- Volle E, Park W, Kaufmann HJ. MRI examination and monitoring of pediatric patients under sedation. *Pediatr Radiol*. 1996;26:280–1.
- Lawson GR. Sedation of children for magnetic resonance imaging. *Arch Dis Child*. 2000;82:150–4.
- Didier D, Ratib O, Beghetti M, et al. Morphologic and functional evaluation of congenital heart disease by magnetic resonance imaging. *J Magn Reson Imaging*. 1999;10:639–55.
- Nayak KS, Hargreaves BA, Hu BS, Nishimura DG, Pauly JM, Meyer CH. Spiral balanced steady-state free precession cardiac imaging. *Magn Reson Med*. 2005;53:1468–73.
- Scheffler K, Lehnardt S. Principles and applications of balanced SSFP techniques. *Eur Radiol*. 2003;13:2409–18.
- Lorenz CH, Walker ES, Morgan VL, Klein SS, Graham TP Jr. Normal human right and left ventricular mass, systolic function, and gender differences by cine magnetic resonance imaging. *J Cardiovasc Magn Reson*. 1999;1:7–21.
- Marcus JT, DeWaal LK, Götte MJ, van der Geest RJ, Heethaar RM, Van Rossum AC. MRI-derived left ventricular function parameters and mass in healthy young adults: relation with gender and body size. *Int J Card Imaging*. 1999;15:411–9.
- Sandstede J, Lipke C, Beer M, Hofmann S, Pabst T, Kenn W, Neubauer S, Hahn D. Age- and gender-specific differences in left and right ventricular cardiac function and mass determined by cine magnetic resonance imaging. *Eur Radiol*. 2000;10:438–42.
- Mostbeck GH, Caputo GR, Higgins CB. MR measurement of blood flow in the cardiovascular system. *AJR Am J Roentgenol*. 1992;159:453–61.
- Chatzimavroudis GP, Oshinski JN, Franch RH, Walker PG, Yoganathan AP, Pettigrew RI. Evaluation of the precision of magnetic resonance phase velocity mapping for blood flow measurements. *J Cardiovasc Magn Reson*. 2001;3:11–9.

40. Brenner LD, Caputo GR, Mostbeck G, et al. Quantification of left-to-right atrial shunts with velocity-encoded cine nuclear magnetic resonance imaging. *J Am Coll Cardiol*. 1992;20:1246–50.
41. Rebergen SA, Niezen RA, Helbing WA, et al. Cine gradient-echo MR imaging and MR velocity mapping in the evaluation of congenital heart disease. *Radiographics*. 1996;16:467–81.
42. John AS, Dill T, Brandt RR, Rau M, Ricken W, Bachmann G, Hamm CW. Magnetic resonance to assess the aortic valve area in aortic stenosis: how does it compare to current diagnostic standards? *J Am Coll Cardiol*. 2003;42:519–26.
43. Schlosser T, Malyar N, Jochims M, Breuckmann F, Hunold P, Bruder O, Erbel R, Barkhausen J. Quantification of aortic valve stenosis in MRI-comparison of steady-state free precession and fast low-angle shot sequences. *Eur Radiol*. 2007;17:1284–90.
44. Westenberg JJ, Roes SD, Ajmone Marsan N, Binnendijk NM, Doornbos J, Bax JJ, Reiber JH, de Roos A, van der Geest RJ. Mitral valve and tricuspid valve blood flow: accurate quantification with 3D velocity-encoded MR imaging with retrospective valve tracking. *Radiology*. 2008;249:792.
45. Firmin DN, Nayler GL, Klipstein RH, Underwood SR, Rees RS, Longmore DB. In vivo validation of MR velocity imaging. *J Comput Assist Tomogr*. 1987;11:751–6.
46. Caputo GR, Kondo C, Masui T, Geraci SJ, Foster E, O'Sullivan MM, Higgins CB. Right and left lung perfusion: *in vitro* and *in vivo* validation with oblique-angle, velocity-encoded cine MR imaging. *Radiology*. 1991;180:693–8.
47. Markl M, Kilner PJ, Ebberts T. Comprehensive 4D velocity mapping of the heart and great vessels by cardiovascular magnetic resonance. *J Cardiovasc Magn Reson*. 2011;13:7.
48. Markl M, Frydrychowicz A, Kozerke S, Hope M, Wieben O. 4D flow MRI. *J Magn Reson Imaging*. 2012;36:1015–36.
49. Cheng JY, Zhang T, Alley MT, Uecker M, Lustig M, Pauly JM, Vasanawala SS. Comprehensive multi-dimensional MRI for the simultaneous assessment of cardiopulmonary anatomy and physiology. *Sci Rep*. 2017;7:5330.
50. Rebergen SA, Chin JGJ, Ottenkamp J, van der Wall EE, de Roos A. Pulmonary regurgitation in the late postoperative follow-up of tetralogy of Fallot: volumetric quantification by MR velocity mapping. *Circulation*. 1993;88:2257–66.
51. Beerbaum P, Korperich H, Barth P, et al. Non-invasive quantification of left-to-right shunt in pediatric patients. Phase-contrast cine magnetic resonance imaging compared with invasive oximetry. *Circulation*. 2001;103:2476–82.
52. Harris MA, Weinberg PM, Whitehead KK, Fogel MA. Usefulness of branch pulmonary artery regurgitant fraction to estimate the relative right and left pulmonary vascular resistances in congenital heart disease. *Am J Cardiol*. 2005;95:1514–7.
53. Steffens JC, Bourne MW, Sakuma H, O'Sullivan M, Higgins CB. Quantification of collateral blood flow in coarctation of the aorta by velocity encoded cine magnetic resonance imaging. *Circulation*. 1994;90(2):937–43.
54. Whitehead KK, Gillespie MJ, Harris MA, Fogel MA, Rome JJ. Noninvasive quantification of systemic to pulmonary collateral flow: a major source of inefficiency in patients with superior cavopulmonary connections. *Circ Cardiovasc Imag*. 2009;2:405–11. Epub 2009 Jul 8.
55. Tzemos N, Therrien J, Yip J, Thanassoulis G, Tremblay S, Jamorski MT, Webb GD, Siu SC. Outcomes in adults with bicuspid aortic valves. *JAMA*. 2008;300:1317–25.
56. Gleeson TG, Mwangi I, Horgan SJ, Cradock A, Fitzpatrick P, Murray JG. Steady-state free-precession (SSFP) cine MRI in distinguishing normal and bicuspid aortic valves. *J Magn Reson Imaging*. 2008;28:873–8.
57. Vasanawala SS, Hanneman K, Alley MT, Hsiao A. Congenital heart disease assessment with 4D flow MRI. *J Magn Reson Imaging*. 2015;42:870–86.
58. Houriez-Gombaudo-Saintonge S, Mousseaux E, Bargiotas I, De Cesare A, Diertenbeck T, Bouaou K, Redheuil A, Soulat G, Giron A, Gencer U, Craiem D, Messas E, Bollache E, Chenoune Y, Kachenoura N. Comparison of different methods for the estimation of aortic pulse wave velocity from 4D flow cardiovascular magnetic resonance. *J Cardiovasc Magn Reson*. 2019;21:75.
59. Rengier F, Delles M, Eichhorn J, et al. Noninvasive pressure difference mapping derived from 4D flow MRI in patients with unrepaired and repaired aortic coarctation. *Cardiovasc Diagn Ther*. 2014;4:97–103.
60. Rodríguez-Palomares JF, Dux-Santoy L, Guala A, et al. Aortic flow patterns and wall shear stress maps by 4D-flow cardiovascular magnetic resonance in the assessment of aortic dilatation in bicuspid aortic valve disease. *J Cardiovasc Magn Reson*. 2018;20:28.
61. Kamphuis VP, Elbaz MSM, van den Boogaard PJ, et al. Disproportionate intraventricular viscous energy loss in Fontan patients: analysis by 4D flow MRI. *Eur Heart J Cardiovasc Imaging*. 2019;20:323–33.
62. Tandon A, Hashemi S, Parks WJ, Kelleman MS, Sallee D, Slesnick TC. Improved high-resolution pediatric vascular cardiovascular magnetic resonance with gadofosveset-enhanced 3D respiratory navigated, inversion recovery prepared gradient echo readout imaging compared to 3D balanced steady-state free precession readout imaging. *J Cardiovasc Magn Reson*. 2017;18:74.
63. Piccini D, Littmann A, Nelles-Vallespin S, Zenge MO. Respiratory self-navigation for whole-heart bright-blood coronary MRI: methods for robust isolation and automatic segmentation of the blood pool. *Magn Reson Med*. 2012;68:571–9.
64. Kwong RY, Korlakunta H. Diagnostic and prognostic value of cardiac magnetic resonance imaging in assessing myocardial viability. *Top Magn Reson Imaging*. 2008;19:15–24.
65. Kim RJ, Wu E, Rafael A, et al. The use of contrast-enhanced magnetic resonance imaging to identify reversible myocardial dysfunction. *N Engl J Med*. 2000;343:1445–53.
66. Wu E, Judd RM, Vargas JD, Klocke FJ, Bonow RO, Kim RJ. Visualisation of presence, location, and transmural extent of healed Q-wave and non-Q-wave myocardial infarction. *Lancet*. 2001;357:21–8.
67. Simonetti OP, Kim RJ, Fieno DS, et al. An improved MR imaging technique for the visualization of myocardial infarction. *Radiology*. 2001;218:215–23.
68. Moon JC, Reed E, Sheppard MN, et al. The histologic basis of late gadolinium enhancement cardiovascular magnetic resonance in hypertrophic cardiomyopathy. *J Am Coll Cardiol*. 2004;43:2260–4.
69. Babu-Narayan SV, Goktekin O, Moon JC, et al. Late gadolinium enhancement cardiovascular magnetic resonance of the systemic right ventricle in adults with previous atrial redirection surgery for transposition of the great arteries. *Circulation*. 2005;111:2091–8.
70. Babu-Narayan SV, Kilner PJ, Li W, et al. Ventricular fibrosis suggested by cardiovascular magnetic resonance in adults with repaired tetralogy of fallot and its relationship to adverse markers of clinical outcome. *Circulation*. 2006;113:405–13.
71. Wald RM, Haber I, Wald R, Valente AM, Powell AJ, Geva T. Effects of regional dysfunction and late gadolinium enhancement on global right ventricular function and exercise capacity in patients with repaired tetralogy of fallot. *Circulation*. 2009;119:1370–7.
72. Choudhury L, Mahrholdt G, Wagner A, et al. Myocardial scarring in asymptomatic or mildly symptomatic patients with hypertrophic cardiomyopathy. *J Am Coll Cardiol*. 2002;40:2156–64.
73. Teraoka K, Hirano M, Ookubo H, et al. Delayed contrast enhancement of MRI in hypertrophic cardiomyopathy. *Magn Reson Imaging*. 2004;22:155–61.



74. Jcc M, McKenna W, McCrohon JA, Elliott PM, Smith GC, Pennell DJ. Toward clinical risk assessment in hypertrophic cardiomyopathy with gadolinium cardiovascular magnetic resonance. *J Am Coll Cardiol*. 2003;41:1561–7.
75. Taylor AJ, Salerno M, Dharmakumar R, Jerosch-Herold M. T1 mapping: basic techniques and clinical applications. *J Am Coll Cardiol Img*. 2016;9:67–81.
76. O'Brien A, Gil KE, Varghese J, et al. T2 mapping in myocardial disease: a comprehensive review. *J Cardiovasc Magn Reson*. 2022;24:33.
77. Triadyaksa P, Oudkerk M, Sijens PE. Cardiac T2\* mapping: techniques and clinical applications. *J Magn Reson Imaging*. 2020;52:1340–51.
78. Treibel TA, Fontana M, Maestrini V, et al. Automatic measurement of the myocardial interstitium: synthetic extracellular volume quantification without hematocrit sampling. *J Am Coll Cardiol Img*. 2016;9:54–63.
79. Raucci FJ, Parra DA, Christensen JT, et al. Synthetic hematocrit derived from the longitudinal relaxation of blood can lead to clinically significant errors in measurement of extracellular volume fraction in pediatric and young adult patients. *J Cardiovasc Magn Reson*. 2017;19:58.
80. Kozak MF, Redington A, Yoo SJ, Seed M, Greiser A, Grosse-Wortmann L. Diffuse myocardial fibrosis following tetralogy of Fallot repair: a T1 mapping cardiac magnetic resonance study. *Pediatr Radiol*. 2014;44:403–9.
81. Yim D, Riesenkampff E, Caro-Dominguez P, et al. Assessment of diffuse ventricular myocardial fibrosis using native T1 in children with repaired tetralogy of Fallot. *Circ Cardiovasc Imag*. 2017;10:e005695.
82. Broberg CS, Huang J, Hogberg I, et al. Diffuse LV myocardial fibrosis and its clinical associations in adults with repaired tetralogy of fallot. *J Am Coll Cardiol Img*. 2016;9:86–7.
83. Ferreira VM, Schulz-Menger J, Holmvang G, Kramer CM, Carbone I, Sechtem U, et al. Cardiovascular magnetic resonance in nonischemic myocardial inflammation: expert recommendations. *J Am Coll Cardiol*. 2018;72:3158–76.
84. Danias PG, Stuber M, Botnar RM, Kissinger KV, Edelman RR, Manning WJ. Relationship between motion of coronary arteries and diaphragm during free breathing: lessons from real-time MR imaging. *AJR Am J Roentgenol*. 1999;172:1061–5.
85. Oncel D, Oncel G, Türkoğlu I. Accuracy of MR coronary angiography in the evaluation of coronary artery stenosis. *Diagn Interv Radiol*. 2008;14:153–8.
86. Xue H, Davies RH, Brown LAE, et al. Automated inline analysis of myocardial perfusion MRI with deep learning. *Radiol Artif Intell*. 2020;2:e 200009.
87. Biko D, Collins RT, Partington S, Harris MA, Whitehead KK, Keller M, Fogel MA. Magnetic resonance myocardial perfusion imaging: safety and indications in pediatrics and young adults. *Pediatr Cardiol*. 2018;39:275–82.
88. Zerhouni EA, Parish DM, Rogers WJ, Yang A, Shapiro EP. Human heart tagging with MR imaging: a method for noninvasive assessment of myocardial motion. *Radiology*. 1988;169:59–63.
89. Zhong X, Spottiswoode BS, Meyer CH, et al. Imaging three-dimensional myocardial mechanics using navigator-gated volumetric spiral cine DENSE MRI. *Magn Reson Med*. 2010;64:1089–97.
90. Neizel M, Lossnitzer D, Korosoglou G, et al. Strain-encoded (SENC) magnetic resonance imaging to evaluate regional heterogeneity of myocardial strain in healthy volunteers: comparison with conventional tagging. *J Magn Reson Imaging*. 2009;29:99–105.
91. Petersen SE, Jung BA, Wiesmann F, et al. Myocardial tissue phase mapping with cine phase-contrast MR imaging: regional wall motion analysis in healthy volunteers. *Radiology*. 2006;238:816–26.
92. Wehne GJ, Jing L, Haggerty CM, Suever JD, Chen J, Hamlet SM, Feindt JA, Mojsejenko WD, Fogel MA, Fornwalt BK. Comparison of left ventricular strains and torsion derived from feature tracking and DENSE. *J Cardiovasc Magn Reson*. 2018;20:63.
93. Muser D, Castro SA, Santangeli P, Nucifora G. Clinical applications of feature-tracking cardiac magnetic resonance imaging. *World J Cardiol*. 2018;10:210–21.
94. Schuster A, Hor KN, Kowallick JT, Beerbaum P, Kutty S. Cardiovascular magnetic resonance myocardial feature tracking. Concepts and clinical applications. *Circ Cardiovasc Imag*. 2016;9:e004077.
95. Sobh DM, Batouty NM, Tawfik AM, et al. Left ventricular strain analysis by tissue tracking - cardiac magnetic resonance for early detection of cardiac dysfunction in children with end-stage renal disease. *J Mag Reson Med*. 2021;54:1476–85.
96. Haggerty C, Suever J, Pulenthiran A, Mejia-Spiegeler A, Wehner G, Jing L, Charnigo R, Fornwalt B, Fogel M. Association between left ventricular mechanics and diffuse myocardial fibrosis in patients with repaired tetralogy of fallot: a cross-sectional study. *J Cardiovasc Magn Reson*. 2017;19:100.
97. Beroukhim RS, Prakash A, Buechel ERV, Cava JR, Dorfman AL, Festa P, et al. Characterization of cardiac tumors in children by cardiovascular magnetic resonance imaging: a multicenter experience. *J Am Coll Cardiol*. 2011;58:1044–54.
98. Marcus FI, McKenna WJ, Sherrill D, et al. Diagnosis of arrhythmogenic right ventricular cardiomyopathy/dysplasia. Proposed modification of the task force criteria. *Circulation*. 2010;121:1533–41.
99. Fogel MA, Weinberg PM, Harris M, Rhodes L. Usefulness of magnetic resonance imaging for the diagnosis of right ventricular dysplasia in children. *Am J Cardiol*. 2006;97(8):1232–7.





## 2.1 Introduction

Magnetic resonance imaging (MRI) is a safe diagnostic tool, and several 100 million diagnostic studies have been performed safely up to now. However, there have been at least 17 published cases of patient deaths associated with MRI scanning, 10 cases with implanted pacemakers [1, 2], 2 patients with an insulin pump, 1 patient with a neurostimulator, 1 patient with an aneurysm clip [3], and 3 persons were killed by an oxygen tank that was brought into the scanner room. The loud noises (up to 120 dBA) induced by the fast switching gradient fields make ear protections mandatory for all patient. The sources of all these risks are the electromagnetic fields of the MRI scanner.

In the publication from Delfino et al. [4], a good overview of the distribution of different kinds of safety incidents related to MRI could be found. The authors searched in the MAUDE database (database from the FDA for medical adverse events) for MR-related events between 1 January 2008 and 31 December 2017. From the 1548 events, 59% were thermal events, 11% mechanical events (most not MR related like finger pinching at the moving patient bed, falls, or moving of heavy items by the technologist), 9% projectiles, and 6% acoustic (e.g., reported tinnitus or hearing loss of patients/staff in the magnet room due to missing or badly placed hearing protection during examinations).

With over 25 million MR scans per year (2017) in the USA, the reported 1548 events are small, knowing that the number of unreported cases may be larger. MRI is a safe diagnostic tool, and the goal must be to avoid any adverse events. Among the 1548 events, there were still a larger portion of preventable events. The author of this chapter agrees with Delfino et al. [4] concluding: “Our shared safety goal should be to bring the preventable adverse event rate to zero.”

Medications or contrast agents used during CMR imaging may also pose significant risks. Until 2011, over 400 biopsy-confirmed cases of nephrogenic systemic fibrosis (NFS) associated with linear gadolinium-based contrast agent (GBCA) have been reported in patients with severe renal impairment [5, 6].

Besides these known and preventable risks, there are no known short- or long-term side effects attributed to the MRI magnetic field strengths currently used in clinical practice. It should be noted that MRI, like ultrasound, does not use any ionizing radiation, thus avoiding the risk of carcinogenesis.

## 2.2 Safety Risks from MRI Scanner

MRI uses three electromagnetic fields to acquire the images. A strong static magnetic field also called  $B_0$  is about 30,000 (1.5 T scanner) or 60,000 (3 T scanner) times the earth magnetic field (0.05 mT) and is used to align the spins of the proton of the hydrogen atom. For the spatial localization of the signal, fast switching magnetic fields, so-called gradient fields, are used. The nonionizing radiofrequency (RF) field also called  $B_1$  field is used to excite the hydrogen protons. The frequency of the RF field depends upon the main magnetic field ( $B_0$ ) and is of the order of those used by common radio waves. However, the used power is much stronger and need to be controlled to avoid any negative effects on the patient and electronic equipment.

Each of these three electromagnetic fields may pose safety risk. The risk may significantly increase if implants are present, and this applies also for any device/equipment which has not been tested and approved to enter the MR scanner room. Possible interactions are summarized in Table 2.1.

R. Luechinger (✉)  
Institute for Biomedical Engineering, ETH and University Zurich,  
Zurich, Switzerland  
e-mail: [luechinger@biomed.ee.ethz.ch](mailto:luechinger@biomed.ee.ethz.ch)

**Table 2.1** Overview of potential risks from the different electromagnetic fields used in clinical MRI

Electromagnetic field	Typical range	Potential safety risks
<b>Main magnetic field</b> (always on!)	≤7 T most common 1.5 T and 3 T	Magnetic force and torque on: <ul style="list-style-type: none"> <li>– Ferromagnetic implants</li> <li>– Ferromagnetic devices, tools, beds, etc.</li> </ul>
		Magneto hydrodynamic effect
		Interaction/damage of active implants (e.g., hearing aid)
		Damage of magnetic storage devices, watches, etc.
<b>Gradient field</b> (on only during scanning)	<100 mT/m <300 mT/m/ms	Noise
		Peripheral nerve stimulation
		Induced voltages in conducting implants
		Heating of conducting implants
		Interaction/damage of active implants
		Vibrations
<b>RF field</b> (on only during scanning)	≤300 MHz (42 MHz/T) <25 kW peak	RF-induced burns next to: <ul style="list-style-type: none"> <li>– Extended implants</li> <li>– Long wires or coils on the skin</li> <li>– Large loops built with the legs or arms of the patient (burns at skin to skin contact)</li> </ul>
		Interference/damage of active implants
		Interference with electric devices in the room

**Fig. 2.1** The main magnetic field will attract any ferromagnetic devices converting them into dangerous projectiles

### 2.3 Force and Torque Effects

The magnetic field of MR systems will increase over a short distance from earth magnetic field to the field at the isocenter of the magnet. During the planning of an MR system installation, it has to be ensured that the 9 gauss line (0.9 mT) is inside the magnet room, or if not possible, then those rooms are only accessible to trained staff. In fields lower than 10 gauss, pacemaker and ICD will not switch mode, and no interaction should be expected. By using active shielded magnets (nowadays the commonly used magnets), the room can be smaller, but the magnetic field will increase faster. Ferromagnetic materials can be brought closer to the magnet without any noticeable force, but if the magnet is approached too close, the magnetic attraction gets high very fast. Magnetic forces can be nearly zero at 2 m away from the cover, but at the cover, they can be more than 100× the gravitational force (“weight”) of the device, turning ferromagnetic devices into projectiles. A ferromagnetic item can reach a speed of over 50 km/h over a distance of <2 m! Therefore, it is absolutely essential that no ferromagnetic devices or item is taken into the scanner room (Fig. 2.1), preferable not

even into the MRI area. Monitoring devices, IV poles, etc. have to be tested and labeled as MR conditional before use in the MR room.

Some medical devices, like infusion pumps or ventilation devices, are only allowed to enter limited magnetic fields. To avoid these devices becoming projectiles, infusion pumps should be stored in a special container. These containers and larger equipment that need to be in the magnet room should include a continuous monitoring of the magnetic field strength with an acoustic alarm if the approved limit is approached. If such monitoring of the field is not included, attaching the item with a chain to the room wall could prevent movement closer to the magnet more than allowed.

Patients have to be very carefully screened to exclude ferromagnetic implants or ferromagnetic foreign bodies. Four cases of fatal accidents associated with magnetic force and torque effects have been reported up to date. In 2001, a 6-year-old boy was killed by a projectile ferromagnetic oxygen tank. The same happened in 2018 in India and 2021 in South Korea to two adults. In 1992, a patient with a ferromagnetic aneurysm clip died during preparation for MRI, laying on the patient bed connected to the MR scanner [3]. Another high-risk issue involves ferromagnetic splinter in the eye which could lead to blindness because of damage to critical organs from motion or rotation of splinter in the strong magnetic field. If there is any suspicion of metallic splinter in the eye, an X-ray of the eye should be obtained to exclude the splinter.

## 2.4 Magnetohydrodynamic Effect

Blood is a conductive liquid. If blood is moving orthogonal to a magnetic field, charge separation occurs, which results in a voltage orthogonal to the magnetic field and the flow direction. These voltages may be a potential limitation for MRI at very high magnetic fields (>10 T). However, at field strengths currently used in clinical practice (7 T or lower), there are no known adverse effects from the magnetohydrodynamic effect. Nevertheless, the voltages will affect the surface ECG particularly causing distortion of the ST segments. Higher magnetic field strength will produce stronger effects as shown by Chakeres et al. for magnetic field strengths of up to 8 T [7].

The alteration of the ECG may interfere with R-wave detection in cardiac-triggered scans resulting in a poor image quality. In addition, the diagnostic value of the ECG in a static magnetic field is limited, since the S-T segment is potentially unreliable. This has to be considered in case of patient undergoing stress MRI.

---

## 2.5 Gradient Noise

MR scanners may produce noise levels of up to 120 dB(A) [8]. Unprotected exposure to noise levels over 80 dB(A) can lead to temporary rise in hearing thresholds. Therefore, ear protections are mandatory for all MR examinations. Earplugs combined with headphones are preferable. If staff or other persons have to stay in the scanner room during imaging, ear protection is also mandatory for them.

---

## 2.6 Peripheral Nerve Stimulation

Fast switching gradients induce currents in the body, which may stimulate nerves. However, stimulation of cardiac nerves requires 5–10× stronger gradients compared to peripheral nerves (gradient slope <1 ms). Therefore, strong gradient systems have to be limited in such a way that the mean peripheral nerve stimulation threshold will not be exceeded. By limiting the gradient system to the mean peripheral nerve stimulation, cardiac stimulation can be avoided. For very long gradient slopes >10 ms, the graphs in the IEC 60601-2-33 ed. 4 standard (main safety standard for MR system) indicate that this may no longer be true. This will be of relevance for very powerful body gradient systems which became available for research in the last few years. However, more advanced evaluations [9] indicate that there is still a large safety margin even for longer gradient slopes.

Conducting implants may influence the likelihood of nerve stimulation, which has to be considered if such implants are next to the heart, for example, pacemaker leads.

## 2.7 RF Heating

The energy of the RF field is partly deposited in the body tissues with the concern for body heating during imaging. The specific absorption rate (SAR) is the measure of the absorption of electromagnetic energy in the body per weight (typically measured in watts per kilogram [W/kg]). The maximum allowed energy absorbed per volume is limited by international standards (IEC 60601-2-33) and controlled by the MR scanners. The maximal allowed whole-body SAR (in first level control mode) is up to 4 W/kg, which should limit the rise of the body core temperature to 1.3°C. Normal operating mode limits the whole-body SAR to 2 W/kg. This mode is recommended for patients with cardiocirculatory impairments, cerebral vascular impairments, and diabetes to compensate for the impaired thermoregulation in these patients. Normal operating mode is also used for pregnant women. If the MR unit goes to the limits for deposited RF energy, patients may feel the heating effects, especially if the thorax is in the isocenter of the MR scanner.

Implants may lead to strong local tissue heating and may cause thermal injuries, particularly at the ends of long and thin implants. In 2003, a lumbar spine MRI scan at 1 T resulted in a 2–3 cm lesion at the tip of an intracerebral electrode of a neurostimulator, resulting in severe permanent disability [10]. As mentioned above, Delfino et al. [4] found 906 heating events (out of the 1548 events) reported between 2008 and 2017 to the FDA, which were further divided as 39% (348 events) root cause unclear, 28% (257) contact with an object (like MR coils (138 events), ECG electrodes/leads (39), patient clothing/blankets (21), orthopedic implants (8), pulse oximeters (7), tattoos/permanent makeup (6), dermal patches (3)), 16% (147) skin-to-skin contact, and 10% (97) bore contact. The distribution may be surprising; the largest numbers of events are for coil contact, bore contact, and skin-to-skin contact. In most of these cases, padding between the skin and the other object or skin could prevent the events. The needed padding is described in detail in the MR vendor's manuals and must be followed. To predict if a given situation will lead to RF burn is very difficult, but it is much easier to prevent this potentially dangerous situation.

Cardiac and thoracic imaging has a higher risk for RF burns; with the thorax in the RF transmit coil, more RF energy is needed compared to head or lower extremity scanning. Monitoring cables, coil cables, and patients filling up the bore due to a larger body size may even further increase the risk.

Why does RF burns happen? A high current density flow getting in contact with tissue may result in high local heating. For example, if a person has a transdermal patch with a thin aluminum foil inside, currents run in the aluminum and propagate out at both ends of the foil. The next worse conductive material is the skin. Since the con-

ductivity of the skin is lower compared to aluminum, the current will be converted in a small area to heat, and this may be high enough to produce a burn. The same may be true for a person sweating in the MRI scanner. If the skin touches the bore, there will be a thin film of sweat, and at the end of this film, the current will enter the skin. With padding, there will be an increased distance to the transmit coil reducing the E fields and therefore the currents. In addition, padding may also lead to multiple small areas of sweat with dry gaps resulting in further reduced currents.

For longer implants oriented along the E field (parallel to the main magnetic field), currents will start to flow in the implant, and at both ends, they will leave the implant resulting in local heating of the tissue next to the ends of the implants. The amount of heating depends strongly on various parameters (length of the implant, the shape of the implant at the end, orientation of the implant, location inside the body, etc.). In the study from Delfino et al. [4], “only” eight cases of burns induced by implants could be found. This is certainly also a result of good screening of patients and awareness of the problem, but there is also a high likelihood that there were many more cases which either not reported or even not recognized. Since there are only limited temperature-sensitive nerves inside the body, the heating can’t be felt by the patient. And if tissue will be damaged at a small location at the end of the implant, this may not as easily be recognized as a skin burn. Even skin burns may only get visible hours after the MR investigations.

Additionally, isolated cable or wires on the skin may be another potential risk. In one case in Germany, a badly connected ECG cable resulted in a fire inside the MR system [11]. A growing problem is metallic fibers in cloth. Silver wires in sport wear and underwear can lead to RF burns in MR [12]. In 2010 in Switzerland, a woman had severe skin burns at her arms because she was scanned in her blouse which had thin metal fibers embedded in the fabric. This case highlights the importance of patients changing into hospital gowns before scanning.

## 2.8 Additional Safety Risks Due to Implants

Any active or passive implant in the patient has to be carefully checked under which condition it is considered safe for MRI. Risks of RF heating will be reduced if the implant is out of the transmitting RF coil, but they are still exposed to the magnetic force and torque effects from the static magnetic field.

To define compatibility of an implant with respect to MR imaging, the FDA developed labels in 1997 which were revised in 2005 by the American Society for Testing and




Materials International (ASTM): The current set of terms are “MR safe,” “MR conditional,” and “MR unsafe.”

It is strongly recommended to use only the wording and signs shown in Table 2.2.

**Passive implants** may interact mainly with the main magnetic field (force and torque effects) and RF field which may induce heating. Most of currently implanted stents, heart valves, sternal wires, cardiac closure and occluder devices, filters, embolization coils, and screws are MR conditional. Most of them are tested up to 3 T. However, it should be emphasized that such general statements are dangerous. For example, most of the aneurysm clips are nonmagnetic; however, an aneurysm clip implanted in 1968 and imaged in 1992 was MR-unsafe and resulted in a fatal outcome [3]. For many implants, a 6-week waiting period between implantation and MRI is recommended. These 6 weeks are mainly because tissue ingrowth needs about 6–8 weeks. After that time, the implant is stable. If an implant should be allowed to undergo MRI directly after implantation, implant manufacturer needs to prove that there is no additional risk of dislocation during the initial ingrowth period. Patel MR et al. [13] showed in a study with 66 patients that with 97 bare metal or drug eluting stents, no additional risk of an early MRI could be seen compared to a control group. This indicates that for implants which show only low magnetic interactions and are well fixated in the tissue, the 6-week waiting period may not be required, especially if strong forces already act on the implant originating from blood flow or muscles. For known implants, it is recommended to refer to the manufacturer’s product information or reference manuals [14].

The American Heart Association published in *Circulation* an overview on cardiovascular devices [15]: **Stents** are mainly made out of non-magnetic or weakly magnetic material. All tested coronary artery stents are nonferromagnetic and can be scanned at 3 T or less at any time after implantation. Nonmagnetic peripheral stents can also be scanned at 3 T or less at any time. Weak magnetic peripheral stents

**Table 2.2** Terminology used for labeling of implants

MR safe	An item that poses no known hazards resulting from exposure to any MR environment. MR safe items are composed of materials that are electrically nonconductive, nonmetallic, and nonmagnetic	
MR conditional	An item with demonstrated safety in the MR environment within defined conditions including conditions for the static magnetic field, the time-varying gradient magnetic fields, and the radiofrequency fields	
MR unsafe	An item which poses unacceptable risks to the patient, medical staff, or other persons within the MR environment	



should be determined on a case-by-case basis. If the scan can be delayed, it may be prudent to wait until 6 weeks after implantation. Peripheral stents may reach a length of over 10 cm and may be overlapped even longer. Such length may lead to RF heating. However, if the vessel with the stent is not occluded, blood flow will also produce an additional cooling reducing the risk of RF heating. Implant labels will take these effects into account, and it is likely that longer stents may request a SAR limitation to normal operating mode or even lower, particularly if the stent is inside the RF body coil or near to it.

Most **aortic stent grafts** show only limited interactions with MRI and are MR conditional. But years ago, there were stent grafts implanted which showed high magnetic forces. The safety cannot be demonstrated for such a device, but in individual cases, after risk-to-benefit evaluation and with an informed consent of the patient, scan could be performed using 1.5 T MRI scanner.

**Prosthetic heart valves, annuloplasty rings, and sternal wires** are made out of various mainly nonmagnetic or weakly magnetic materials. Some of the annuloplasty rings contain no metal and are therefore MR safe. The rest of the tested valves, rings, and sternal wires are MR conditional [14]. Based on the available literature in a review [15] and a reference manual [14], the presence of a prosthetic heart valve or annuloplasty ring should not be considered a contraindication to an MR examination at 3 T or less any time after implantation. MR examination of patients with sternal wires is generally considered to be safe.

**Cardiac closure, left atrial appendage occluder devices, and inferior vena cava filters** are made out of nonmagnetic or only weak ferromagnetic material, and up to now, none of the tested devices have been labeled as MR unsafe [14]. Therefore, patients with nonferromagnetic cardiac closure, occluder devices, or inferior vena cava filters may undergo MR procedures with up to 3 T at any time after implantation. In case of weakly ferromagnetic devices, MRI examination in the first 6 weeks should be considered on a case-by-case basis.

Further information on safety of implants can be obtained on:

<http://www.mrisafety.com>

<https://magresource.com/>

**Active implants** may interact with the different electromagnetic fields of an MR unit, and safety evaluations are much more demanding. Due to the steadily increasing number of implants, it is not possible to give general advice on safety of every implant.

Some adjustable shunts in the brain and other adjustable devices have been labeled as MRI conditional and

may therefore be imaged in MRI, but they need to be readjusted after MRI. There are other types of active devices that may still be considered an absolute contraindication. Scanning any kind of active devices like pacemakers, implantable cardioverter-defibrillators (ICDs), neurostimulators, and insulin and other drug pumps is more demanding. Different devices will have different restrictions. Devices need to be reprogrammed, or medication needs to be removed from the pump reservoir, and additional monitoring may be needed. In regards to pacemakers, a first MR conditional pacing system was approved by the FDA in April 2011 for non-thoracic imaging at 1.5 T [16]. With additional testing and experience labels were extended for whole body scanning and partly also approved for 3 T. At present, all major pacemaker, CRT, and ICD vendors have MR conditional devices on the market, but labels and restrictions differ between vendors and partly even within a vendor. Therefore, verifying the label of each pacing system is required. The implant manufacturer provides IFUs and webpages to simplify the search for the correct label. Important: Only pacemaker and leads together from same vendor are labeled as MR conditional system. If a pacemaker from a MR conditional pacing system from one vendor is combined with the leads from a MR conditional system from another vendor, this should work fine for pacing, but such a system will not be considered MR conditional. This does not mean that MRI is a high risk for such a mixed system, but the safety profile is unknown; therefore, scanning would be off label.

A lead no longer connected to a device or a broken lead is a contraindication for MRI. The major risks to scan active cardiac devices in MRI are RF heating of the tissue around the lead tip [17], inappropriate inhibition and/or stimulation [18], and stimulation of the heart by the gradients. In addition during MRI, device therapies may be turned off, and the patient may not be protected by the device. A good overview over the potential risk of pacemaker, CRT, or ICDs and also guidelines how such patient can be scanned safely are given in 2017 HRS consensus statement [19, 20]. These publications gave also guidelines to scan off-label devices which are not MR conditional.

A MR conditional label does not mean that there is no risk for the patient; rather the risk is acceptable for a clinical examination. If a device has no MR conditional label, the physician must make a risk to benefit evaluation. In addition, for most devices, a reprogramming may be needed before and after the MR examination. Some devices may only need the reprogramming some days before the MRI, and the device will only switch to the MR mode when it detects the strong magnetic field, and a few days after the MRI, the “MRI mode” will be disabled.

Table 2.3 summarizes the classification of different passive and active implants in risk classes.

**Table 2.3** Overview over the risk of MRI in patients with implants or other foreign parts in their bodies

	Absolute contraindication	Any implant known to be MR unsafe Unknown active device Unknown ferromagnetic implant Unknown aneurysm clips Metallic fragment in the eye or near sensitive tissue (larger nerves or blood vessels)
	Relative contraindication Scanning only possible after risk-to-benefit analysis and written informed consent	Active implants (pacemaker and ICD which has not been tested → see guidelines [19, 20]) Implants with magnets: cochlear implant, dental implants, medication pumps: removable devices – if all parts can be removed → scanning is OK if all parts can be removed before entering the magnet room. If parts with magnets can't be removed: risk of rotation and demagnetization of the device magnet. Follow instruction from implant manufacturer Long wires or bars (>8–15 cm → risk of sever RF burns). Reduce the SAR of the used sequences to reduce the risk
	Relative safe: Most of the cardiac devices mentioned on the right are safe to be scanned 6 weeks or more after implantation <b>Warning:</b> Safety cannot be guaranteed if not tested or new devices may be MR unsafe! Long thin implants (>8 cm) may heat up strongly and SAR restriction may be needed	Stent, coils, grafts, valve, filters, occluder, sternal wires, and orthopedic implants (plates, screws)
	Safe to scan: Devices where the label can be found and the label will be followed	Any MR conditional devices or implants
	Safe to scan at any time and without any restrictions	Patients without any implant or with MR safe implants. Patient not anesthetized and no restriction of thermal regulation

## 2.9 Gadolinium-Based MR Contrast Agents

In addition to the rare allergic reactions caused by these GBCA, another complication was observed since 2000 with serious outcomes [21]. Several aspects on MR contrast agents are discussed in the *ACR Manual on Contrast Media* edition from 2021 [6].

### 2.9.1 Nephrogenic Systemic Fibrosis (NSF)

In 2006, Grobner et al. proposed an association between NSF and GBCA administration [22]. NSF involves fibrosis of the skin and connective tissues, which can lead to contractures and joint immobility, later on involving other organs like the lungs, liver, muscles, and the heart, in some cases leading to a fatal outcome. NSF develops over a period of days and weeks.



About 5% of patients with NSF may show a rapidly progressive and severe course. More than 580 cases have been reported to the registry so far. NSF only occurred in patients with renal dysfunction, typically with a glomerular filtration rate (GFR) of  $<30$  mL/min/1.73 m<sup>2</sup>, and/or in patients on hemodialysis. In case of suspected NSF, skin biopsy should be done to confirm or exclude the diagnosis. Evidence for an effective treatment of NSF is not available to date.

After regulatory authorities have issued guidelines on the use of gadolinium-containing contrast agents, the number of new cases of NSF reduced to almost zero. However, it is important that these guidelines should be followed in the future.

## 2.9.2 Types of GBCM

Linear chelates for gadolinium like Magnevist, Omniscan, and OptiMARK show an increased risk for NSF, while macrocyclic chelates for gadolinium were associated with few, if any, unconfounded cases of NSF. The exact patho-mechanism by which GBCA may trigger NSF is not known. In patients with severe renal impairment, GBCA are eliminated slower, and Gd<sup>3+</sup> ions may be released into the body from the chelate complex, e.g., by transmetallation with ions from the body (e.g., zinc, iron, calcium, magnesium). Free Gd<sup>3+</sup> can accumulate in tissue and cause toxicity leading to fibrosis.

## 2.9.3 Regulatory Position

### 2.9.3.1 FDA

FDA required in December 2017 a new class warning and other safety warnings for all GBCA (<https://www.fda.gov/media/109825/download>; last accessed 11.1.2022). It states that a small amount of the Gd may stay in the body for month to years after injection. The safety warning included the requirement to update the patient medication guide, which must be read by the patient before administering GBCA. The healthcare professionals should consider the retention characteristics of each agent when choosing a GBCA. These patients include those requiring multiple lifetime doses, pregnant women, children, and patients with inflammatory conditions. Minimize repeated GBCA imaging studies when possible, particularly closely spaced MRI studies. However, do not avoid or defer necessary GBCA MRI scans.

FDA clearly states that the linear GBCA result in more retention and retention for a longer time than macrocyclic GBCAs. Among the linear contrast agents, the gadolinium levels remaining in the body are higher after administration of Omniscan (gadodiamide) or OptiMARK (gadoversetamide) than after Eovist (gadoxetate disodium), Magnevist (gadopentetate dimeglumine), or MultiHance (gadobenat dimeglumine). Gadolinium levels in the body are lowest

after administration of the macrocyclic Dotarem (gadoterate meglumine), Gadavist (gadobutrol), and ProHance (gadoteridol), and the gadolinium levels are also similar across these agents.

Based on that, the FDA-approved contrast agents approved by Dec. 2017 can be classified in three categories. See Table 2.4.

FDA states also that the only known adverse health effect related to gadolinium retention is the rare condition of NSF that occurs in a small subgroup of patients with preexisting kidney failure. FDA has also received reports of adverse events involving multiple organ systems in patients with normal kidney function. A causal association between these adverse events and gadolinium retention could not be established.

In addition, FDA urges patients and healthcare professionals to report side effects from GBCAs to the FDA MedWatch program.

### 2.9.3.2 Position of the American College of Radiology (ACR)

The ACR guidelines [6] gave the following recommendations based on a slightly different grouping of the contrast agent:

#### Group I: Agents associated with the greatest number of NSF cases

- Gadodiamide (Omniscan®—GE Healthcare)
- Gadopentetate dimeglumine (Magnevist®—Bayer HealthCare Pharmaceuticals)
- Gadoversetamide (OptiMARK®—Guerbet)

#### Group II: Agents associated with few, if any, unconfounded cases of NSF

- Gadobenat dimeglumine (MultiHance®—Bracco Diagnostics)

**Table 2.4** Overview of the gadolinium levels after administration of the contrast agents approved Dec. 2017 by the FDA. Alphabetical order within a group

Gadolinium level remaining in the body	Brand name	Generic name	Chemical structure
Highest	Omniscan	Gadodiamide	Linear
	OptiMARK	Gadoversetamide	Linear
Moderate	Eovist	Gadoxetate disodium	Linear
	Magnevist	Gadopentetate dimeglumine	Linear
	MultiHance	Gadobenat dimeglumine	Linear
Lowest	Dotarem	Gadoterate meglumine	Macrocyclic
	Gadavist	Gadobutrol	Macrocyclic
	ProHance	Gadoteridol	Macrocyclic

- Gadobutrol (Gadavist®—Bayer HealthCare Pharmaceuticals; Gadovist® in many countries)
- Gadoteric acid (Dotarem®—Guerbet, Clariscan®—GE Healthcare)
- Gadoteridol (ProHance®—Bracco Diagnostics)

**Group III: Agents for which data remains limited regarding NSF risk, but for which few, if any unconfounded cases of NSF have been reported**

- Gadoxetate disodium (Eovist®—Bayer HealthCare Pharmaceuticals; Primovist® in many countries)

**Group II Agents**

Based on the most recent scientific and clinical evidence, the ACR Committee on Drugs and Contrast Media considers the risk of NSF among patients exposed to standard or lower than standard doses of group II GBCAs to be sufficiently low or possibly nonexistent such that assessment of renal function with a questionnaire or laboratory testing is optional prior to intravenous administration. As in all instances, group II GBCAs should only be administered if they are deemed necessary by the supervising radiologist, and the lowest dose needed for diagnosis should be used.

**Group I Agents**

The ACR Committee on Drugs and Contrast Media concludes that patients receiving group I GBCAs should be considered at risk of developing NSF if any of the following conditions apply to the patient:

- On dialysis (of any form)
- Severe or end-stage chronic kidney disease (CKD 4 or 5, eGFR <30 mL/min/1.73 m<sup>2</sup>) without dialysis
- Acute kidney injury

**Group III Agents**

There is insufficient real-life data to determine the risk of NSF from administration of group III agents, despite an alternative excretion pathway for hepatobiliary agents. Thus, it is important to identify patients at risk of developing NSF; see above. Further details can be found in the ACR guidelines [6] and may differ for outpatients versus inpatients.

**2.9.3.3 Position of the European Medicines Agency (EMA)**

In July 2017, EMA reviewed the use of GBCAs and restrict the use of some linear GBCAs and suspend the authorizations of others. The two intravenous linear GBCA gadoxetic acid (Primovist®—Bayer HealthCare Pharmaceuticals) and gadobenic acid (MultiHance®—Bracco Diagnostics) can continue to be used for liver scans because they are taken up in the liver and meet an important diagnostic need. In addition, gadopentetic acid (Magnevist®—Bayer HealthCare

Pharmaceuticals) given intra-articularly (into the joint) can continue to be used for joint scans because the dose of gadolinium used for joint injections is very low.

For clinical body imaging including cardiac scans, only the following three macrocyclic GBCA are still allowed in Europe: gadoteric acid (Dotarem®—Guerbet), gadobutrol (Gadovist®—Bayer HealthCare Pharmaceuticals), and gadoteridol (ProHance®—Bracco Diagnostics). These three products can be used in their current indications but in the lowest doses that enhance images sufficiently and only when unenhanced body scans are not suitable. The review of the literature concluded that even with the macrocyclic GBCA, there is small gadolinium deposition in the brain, which can be confirmed with mass spectrometry. But up to now, no adverse neurological effects have been attributed to this gadolinium deposition.

The EMA document can be downloaded from: [https://www.ema.europa.eu/en/documents/referral/gadolinium-article-31-referral-emas-final-opinion-confirms-restrictions-use-linear-gadolinium-agents\\_en.pdf](https://www.ema.europa.eu/en/documents/referral/gadolinium-article-31-referral-emas-final-opinion-confirms-restrictions-use-linear-gadolinium-agents_en.pdf) (last access 12.1.2022).

**2.10 Stress Medication for CMR**

The use of stress medication (coronary vasodilator—adenosine and regadenoson or sympathomimetic drug—dobutamine) can be an additional risk for cardiac MRI patients. Different studies presented the safety profile of the two procedures [23–25]. Monitoring of the patient is mandatory for any MR investigation using stress medication, ECG or pulse oximetry plus blood pressure (every minute in case of adenosine/regadenoson and for each step in case of dobutamine). The patients have to be screened for the specific contraindication of the used stress medication [26]. In the study from Wahl et al. [24], the following side effects have been listed (seen in over 1000 patients undergoing a high-dose dobutamine stress CMR investigation): sustained ventricular tachycardia (0.1%), non-sustained ventricular tachycardia (0.4%), paroxysmal atrial fibrillation (1.6%), transient second degree AV block 2:1 (0.2%), severe increase in blood pressure (>240/120 mmHg) (0.5%), decrease in systolic blood pressure >40 mmHg (0.5%), and nausea (3.1%).

A defibrillator and all medications for emergency treatment must be available at the CMR site. Evacuation of a patient from the magnet room and emergency procedures should be practiced before the first patient is tested and periodically thereafter. It must be clear which emergency procedures are allowed inside the magnet room and for which procedures the patient must be evacuated from the magnet room. Only MR safety trained and screened staff are allowed to perform any emergency procedures inside the magnet room.

## 2.11 Pregnancy and MRI

### 2.11.1 Pregnancy of Healthcare Practitioner

ACR Guidance Document on MR Safe Practices: Update 2019 [27] mentioned based on the literature that pregnant healthcare practitioners are permitted to work in and around the MR environment throughout all stages of their pregnancy. However, local guidelines must be followed. For example, in Switzerland, the mother protection law from 2015 forbids a pregnant worker to enter with any body part a field larger than 40 mT. This disallows most of the work inside the magnet room.

### 2.11.2 Pregnancy of Patient

ACR Guidance Document on MR Safe Practices: Update 2019 [27] reviewed the influence of MRI on pregnancy and stated that the vast majority of data today has failed to show that exposure to MR has deleterious effects on the developing fetus, and the preponderance of research studies has failed to discover any reproducible harmful effects of exposure of the mother or developing fetus in the 3 T or weaker magnetic fields used in routine clinical MRI scanning. Nevertheless, if pregnancy is established, the decision to proceed with a non-contrast MR study at 1.5 T should be based on the medical benefits weighed against unknown potential risk.

An MRI investigation which can be postponed after the end of pregnancy should be rescheduled. If ultrasound can provide adequate information, MRI should not be performed; however, MRI should be preferred over imaging modalities using ionizing radiation.

If GBCA are needed, the decision should be reevaluated. GBCA are known to cross the human placenta and can accumulate in the fetus [28]. No adequate and well-controlled teratogenic studies of the effects on pregnant women have been performed. The release of gadolinium as seen in NFS patients may be a potential risk. Because it is unclear how gadolinium-based contrast agents will affect the fetus, these agents should be administered only with extreme caution. A study from Canada including 1.4 million pregnancies [29] indicated that there was an increase in stillbirth or neonatal death and increased risk for rheumatologic, inflammatory, or infiltrative skin conditions in the newborn after GBCA administration in the first trimester. However, the number of women which underwent MRI with GBCA was small. The reason why the risk of GBCA higher than expected during the first weeks of pregnancy is not yet established [30]. Pregnant patients should only be scanned after written informed consent and limiting the MRI protocol to a whole-body SAR of 2 W/kg (normal operating mode).

## 2.12 Patient Screening

MRI is a very safe diagnostic tool; however, there is potential for harm as described above. Screening procedures during preparation of patients for MRI would prevent the vast majority of those adverse events. Each patient should fill out a standardized screening form to identify any contraindications or safety issues related to MR imaging. However, since patient may overlook important points, the questionnaire should be followed by an interview by a physician or MR technologist specifically trained in MR safety. Implants with high safety risks like pacemakers or other active implants should be thoroughly investigated during this interview. Besides medical implants, metallic fragments especially in the eyes can lead to severe injuries. During screening, the patients should also be reminded not to take any ferromagnetic material inside the scanner room such as coins, keys, watches, credit cards, etc.

If there are any doubts about the safety of an MR examination, the MRI investigation should be either postponed until it could be verified that the study can be performed safely or the examination should be performed with an alternative modality. In the rare case that no alternative exists, the benefit of the MR examination should clearly outweigh the possible risks.

---

## 2.13 Patient Monitoring and Emergency Situations

Patients undergoing MRI may need monitoring, for example, in case of stress medication or electronic devices as discussed above. The built-in heart rate and pulse oximetry sensors of MR scanners are often not monitoring devices (a monitoring device must still work in case of a power failure at the MR system); therefore, additional dedicated monitoring devices are needed. Only MRI-approved monitoring devices are allowed within the MRI suit. A defibrillator and all medications for emergency treatment should be available at the MR site. It must be decided in advance which emergency treatment is allowed in the magnet room and for which treatment the patient must be evacuated out of the magnet room. In case of doubt, the patient must be moved out of the magnet room. Most of emergency equipment is not approved to be used in room of the MR system.

---

## 2.14 Conclusion

MRI is a very safe diagnostic tool, but there are potential risks particularly if a patient with implants or other foreign bodies needs to undergo an MRI. The large number and types of medical implants make it impossible to give general

advice on MR safety. For detailed information on a specific device, the reader is advised to consult the manufacturer's product information, reference list, or dedicated web pages on MRI safety.

With well-trained staff, screening for implants, and awareness of general safety precautions, the vast majority of accidents can be prevented. Our shared safety goal should be to avoid any preventable adverse event.

### Practical Pearls

- MRI is a safe diagnostic tool if staff is well trained and patients are thoroughly screened before entering the MR room.
- If there are any doubts about the safety of an MR examination, the MRI investigation should be either postponed until it could be verified that the study can be performed safely or the examination should be performed with an alternative modality.
- If contrast agents are needed, it should be used at lowest dose, and depending on the type of contrast agent, the kidney function needs to be checked.
- In case of stress tests, emergency equipment and physician with ACLS expertise must be present (also true if non-MR conditional pacemaker/ICD are scanned).
- Emergency situations should be practiced, and all staff must be trained in emergency procedures.
- Hearing protections are mandatory for all patients.

### References

1. Irnich W, Irnich B, Bartsch C, Stertmann WA, Gufler H, Weiler G. Do we need pacemakers resistant to magnetic resonance imaging? *Europace*. 2005;7(4):353–65.
2. Duru F, Luechinger R, Candinas R. MR imaging in patients with cardiac pacemakers. *Radiology*. 2001;219(3):856–8.
3. Klucznik RP, Carrier DA, Pyka R, Haid RW. Placement of a ferromagnetic intracerebral aneurysm clip in a magnetic field with a fatal outcome. *Radiology*. 1993;187(3):855–6.
4. Delfino JG, Krainak DM, Flesher SA, Miller DL. MRI-related FDA adverse event reports: a 10-yr review. *Med Phys*. 2019;46(12):5562–71. <https://doi.org/10.1002/mp.13768>.
5. Zou Z, Ma L. Nephrogenic systemic fibrosis: review of 408 biopsy-confirmed cases. *Indian J Dermatol*. 2011;56(1):65–73. <https://doi.org/10.4103/0019-5154.77556>.
6. ACR Committee on Drugs and Contrast Media. ACR manual on contrast media. Reston, VA: ACR; 2021. [https://www.acr.org/-/media/ACR/Files/Clinical-Resources/Contrast\\_Media.pdf](https://www.acr.org/-/media/ACR/Files/Clinical-Resources/Contrast_Media.pdf).
7. Chakeres DW, Kangarlu A, Boudoulas H, Young DC. Effect of static magnetic field exposure of up to 8 Tesla on sequential human vital sign measurements. *J Magn Reson Imaging*. 2003;18(3):346–52. <https://doi.org/10.1002/jmri.10367>.
8. De Wilde JP, Rivers AW, Price DL. A review of the current use of magnetic resonance imaging in pregnancy and safety implications for the fetus. *Prog Biophys Mol Biol*. 2005;87(2–3):335–53. <https://doi.org/10.1016/j.pbiomolbio.2004.08.010>.
9. Klein V, Davids M, Schad LR, Wald LL, Guerin B. Investigating cardiac stimulation limits of MRI gradient coils using electromagnetic and electrophysiological simulations in human and canine body models. *Magn Reson Med*. 2021;85(2):1047–61. <https://doi.org/10.1002/mrm.28472>.
10. Henderson JM, Tkach J, Phillips M, Baker K, Shellock FG, Rezaei AR. Permanent neurological deficit related to magnetic resonance imaging in a patient with implanted deep brain stimulation electrodes for Parkinson's disease: case report. *Neurosurgery*. 2005;57(5):E1063. <https://doi.org/10.1227/01.neu.0000180810.16964.3e>; discussion E1063.
11. Kugel H, Bremer C, Puschel M, Fischbach R, Lenzen H, Tombach B, et al. Hazardous situation in the MR bore: induction in ECG leads causes fire. *Eur Radiol*. 2003;13(4):690–4.
12. Pietryga JA, Fonder MA, Rogg JM, North DL, Bercovitch LG. Invisible metallic microfiber in clothing presents unrecognized MRI risk for cutaneous burn. *AJNR Am J Neuroradiol*. 2013;34(5):E47–50. <https://doi.org/10.3174/ajnr.A2827>.
13. Patel MR, Albert TS, Kandzari DE, Honeycutt EF, Shaw LK, Sketch MH Jr, et al. Acute myocardial infarction: safety of cardiac MR imaging after percutaneous revascularization with stents. *Radiology*. 2006;240(3):674–80. <https://doi.org/10.1148/radiol.2403050740>.
14. Shellock FG. Reference manual for magnetic resonance safety, implants, and devices. Los Angeles, CA: Biomedical Research Publishing Group; 2020.
15. Levine GN, Gomes AS, Arai AE, Bluemke DA, Flamm SD, Kanal E, et al. Safety of magnetic resonance imaging in patients with cardiovascular devices: an American Heart Association scientific statement from the Committee on Diagnostic and Interventional Cardiac Catheterization, Council on Clinical Cardiology, and the Council on Cardiovascular Radiology and Intervention: endorsed by the American College of Cardiology Foundation, the North American Society for Cardiac Imaging, and the Society for Cardiovascular Magnetic Resonance. *Circulation*. 2007;116(24):2878–91.
16. Wilkoff B, Sommer T, Taborsky M, Vymazal J, Kanal E, Heuer H, et al. Worldwide randomized clinical trial to evaluate new pacemaker system designed for use during magnetic resonance imaging. *Heart Rhythm*. 2009;
17. Luechinger R, Zeijlemaker VA, Pedersen EM, Mortensen P, Falk E, Duru F, et al. In vivo heating of pacemaker leads during magnetic resonance imaging. *Eur Heart J*. 2005;26(4):376–83; discussion 25–7.
18. Luechinger R, Duru F, Candinas R, Boesiger P. Safety considerations for magnetic resonance imaging of pacemaker and ICD patients. *Herzschr Elektrophys*. 2004;15(1):73–81.
19. Sommer T, Bauer W, Fischbach K, Kolb C, Luechinger R, Wiegand U, et al. MR imaging in patients with cardiac pacemakers and implantable cardioverter defibrillators. *RöFo*. 2017;189(3):204–17. <https://doi.org/10.1055/s-0043-102029>.
20. Indik JH, Gimbel JR, Abe H, Alkimi-Teixeira R, Birgersdotter-Green U, Clarke GD, et al. 2017 HRS expert consensus statement on magnetic resonance imaging and radiation exposure in patients with cardiovascular implantable electronic devices. *Heart Rhythm*. 2017;14(7):e97–e153. <https://doi.org/10.1016/j.hrthm.2017.04.025>.
21. Cowper SE, Robin HS, Steinberg SM, Su LD, Gupta S, LeBoit PE. Scleromyxoedema-like cutaneous diseases in renal-dialysis patients. *Lancet*. 2000;356(9234):1000–1.
22. Grobner T. Gadolinium—a specific trigger for the development of nephrogenic fibrosing dermopathy and nephrogenic systemic fibrosis? *Nephrol Dial Transplant*. 2006;21(4):1104–8. <https://doi.org/10.1093/ndt/gfk062>.
23. Duran SR, Huffaker T, Dixon B, Gooty V, Abou Zahr R, Arar Y, et al. Feasibility and safety of quantitative adenosine stress perfusion cardiac magnetic resonance imaging in pediatric heart trans-

- plant patients with and without coronary allograft vasculopathy. *Pediatr Radiol.* 2021;51(8):1311–21. <https://doi.org/10.1007/s00247-021-04977-1>.
24. Wahl A, Paetsch I, Gollesch A, Roethemeyer S, Foell D, Gebker R, et al. Safety and feasibility of high-dose dobutamine-atropine stress cardiovascular magnetic resonance for diagnosis of myocardial ischaemia: experience in 1000 consecutive cases. *Eur Heart J.* 2004;25(14):1230–6. <https://doi.org/10.1016/j.ehj.2003.11.018>.
25. Karamitsos TD, Ntusi NA, Francis JM, Holloway CJ, Myerson SG, Neubauer S. Feasibility and safety of high-dose adenosine perfusion cardiovascular magnetic resonance. *J Cardiovasc Magn Reson.* 2010;12:66. <https://doi.org/10.1186/1532-429X-12-66>.
26. Kramer CM, Barkhausen J, Bucciarelli-Ducci C, Flamm SD, Kim RJ, Nagel E. Standardized cardiovascular magnetic resonance imaging (CMR) protocols: 2020 update. *J Cardiovasc Magn Reson.* 2020;22(1):17. <https://doi.org/10.1186/s12968-020-00607-1>.
27. Safety ACRCOM, Greenberg TD, Hoff MN, Gilk TB, Jackson EF, Kanal E, et al. ACR guidance document on MR safe practices: updates and critical information 2019. *J Magn Reson Imaging.* 2020;51(2):331–8. <https://doi.org/10.1002/jmri.26880>.
28. Oh KY, Roberts VH, Schabel MC, Grove KL, Woods M, Frias AE. Gadolinium chelate contrast material in pregnancy: fetal biodistribution in the nonhuman primate. *Radiology.* 2015;276(1):110–8. <https://doi.org/10.1148/radiol.15141488>.
29. Ray JG, Vermeulen MJ, Bharatha A, Montanera WJ, Park AL. Association between MRI exposure during pregnancy and fetal and childhood outcomes. *JAMA.* 2016;316(9):952–61. <https://doi.org/10.1001/jama.2016.12126>.
30. Bird ST, Gelperin K, Sahin L, Bleich KB, Fazio-Eynullayeva E, Woods C, et al. First-trimester exposure to gadolinium-based contrast agents: a utilization study of 4.6 million U.S. pregnancies. *Radiology.* 2019;293(1):193–200. <https://doi.org/10.1148/radiol.2019190563>.





# Gadolinium-Based Contrast Agents

# 3

Menhel Kinno and Joanne Sutter

## Abbreviations

ACR	American College of Radiology
AKI	Acute kidney injury
CKD	Chronic kidney disease
CMR	Cardiac magnetic resonance imaging
FDA	Food and Drug Administration
GBCA	Gadolinium-based contrast agents
Gd <sup>3+</sup>	Gadolinium
MRI	Magnetic resonance imaging
NSF	Nephrogenic systemic fibrosis
SPIO	Superparamagnetic iron oxide

## 3.1 Introduction

Gadolinium-based contrast agents (GBCA) were first approved for use in MRI by the US Food and Drug Administration (FDA) in 1988. The indication for GBCA use is to improve the diagnostic and prognostic value of magnetic resonance imaging (MRI). GBCA are used in approximately one third of all general radiology MRI studies, with an estimated 50 million doses administered annually worldwide and over 500 million doses administered since its introduction [1]. While the use of GBCA is generally considered safe, there are important considerations and complications that have been recognized with their use, leading to precautions with administration. This chapter will cover the basic physics behind gadolinium as a contrast agent, its specific use in cardiac magnetic resonance imaging (CMR), and review known associated adverse effects.

M. Kinno (✉)

Loyola University Chicago, Maywood, IL, USA

J. Sutter

Cardiology, Rush University Medical Center, Chicago, IL, USA

## 3.2 Basic Structure and Physics of Gadolinium-Based Contrast Media

Gadolinium (Gd<sup>3+</sup>) is a rare heavy metal in the lanthanide series of the periodic table. It has 7 unpaired electrons, each of which contributes to a strong magnetic moment, equivalent to 657 times the magnetic moment of a proton, making the atom paramagnetic. In other words, it adds to the external magnetic field. This increases the rate of longitudinal relaxation of nearby protons, thereby shortening their T1 relaxation time [2]. The Gd<sup>3+</sup> ion has nine binding sites available, which makes the free form of gadolinium salt biologically toxic, as these binding sites can bind to other ions and interact with calcium-dependent biological processes [3]. As such, organic ligands are used as chelators to bind to eight of the nine binding sites, leaving only one site available for water to interact with, and, therefore, improving its pharmacologic and toxicologic properties.

Classes of GBCA are organized based on their chelator properties and divided into linear and macrocyclic based on the molecular structure of the organic ligand. In general, macrocyclic GBCA are considered more thermodynamically stable and more kinetically inert, leading to longer half-lives in comparison to linear GBCA [4]. GBCA can also be further subcategorized into ionic and nonionic based on their net charge in solution, as well as their primary mode of clearance, whether renal, hepatobiliary, or both. The majority of GBCA are extracellular agents, though gadofosveset trisodium (Ablavar/Vasovist) has a high affinity for protein binding, making it primarily an intravascular agent [5]. It was originally approved by the FDA for use in evaluating aortoiliac disease but has since been withdrawn from the market by its manufacturer in 2017 due to poor sales [6]. Gadobenate dimeglumine (Magnevist) also demonstrates a higher affinity of protein binding but to a lesser degree. The American College of Radiology (ACR) has also organized GBCA into three groups based on their propensity for causing nephrogenic systemic fibrosis, or NSF, with group 1 agents being

**Table 3.1** Gadolinium-based contrast agents used in magnetic resonance imaging

Generic name	Brand name (manufacturer)	Structure	Charge	ACR group	Type	Clearance	FDA approval
Gadodiamide	Omniscan (GE Healthcare)	Linear	Nonionic	I	Extracellular	Renal	Multi
Gadoversetamide	OptiMARK (Mallinckrodt)	Linear	Nonionic	I	Extracellular	Renal	Multi
Gadopentetate dimeglumine	Magnevist (Bayer Healthcare)	Linear	Ionic	I	Extracellular	Renal	Multi
Gadobenate dimeglumine	MultiHance (Bracco Diagnostics)	Linear	Ionic	II	Extracellular	Renal (95%)/hepatobiliary (5%)	Pediatric
Gadoteridol	ProHance (Bracco Diagnostics)	Macrocyclic	Nonionic	II	Extracellular	Renal	Multi
Gadobutrol	Gadavist/Gadovist (Bayer Healthcare)	Macrocyclic	Nonionic	II	Extracellular	Renal	Cardiac/pediatric
Gadoterate meglumine	Dotarem/Clariscan (Guerbet)	Macrocyclic	Ionic	II	Extracellular	Renal	Multi
Gadoxetate disodium	Eovist/Primovist (Bayer Healthcare)	Linear	Ionic	III	Extracellular	Hepatobiliary	Multi
Gadofosveset trisodium	Ablavar/Vasovist (Lantheus Medical)	Linear	Ionic	III	Intravascular	Renal	Aortoiliac disease (discontinued)

associated with the greatest number of NSF cases; group 2 agents being associated with few, if any, cases of NSF; and group 3 agents having limited data regarding NSF risk [7]. The currently available GBCA and their respective categories have been summarized in Table 3.1.

It is important to recognize that in contrast-enhanced MRI, the GBCA is not imaged directly. Rather its paramagnetic effect on the nearby protons results in a shorter T1 relaxation time and leads to higher signal intensity on T1-weighted sequences. Furthermore, GBCA does not only shorten T1 but also T2 relaxation times. The effects of GBCA on T1 and T2 relaxation times are determined by its relaxivity (R1 and R2, which are the inverse of T1 and T2, respectively) and its concentration. At lower concentrations, the signal intensity is proportional to the concentration of gadolinium. However, this relationship does not stay proportional at higher concentrations. In fact, the signal intensity becomes inversely proportional to the gadolinium concentration, meaning signal intensity begins to decrease at even higher gadolinium concentrations. This is because gadolinium also shortens T2 relaxation, and at higher concentrations, the T2 shortening effect is substantial enough to overcome the T1 shortening effect and cause signal loss. This has implications in CMR as this impacts the ability to quantify blood flow on perfusion studies [2].

Due to their extracellular properties, GBCA are useful in the evaluation of biological processes that expand the extracellular space. Imaging of the initial perfusion of normal myocardium will demonstrate increased signal intensity as GBCA enter the microvasculature. However, normal myocardium is primarily composed of intact myocytes with limited extracellular space. Therefore, GBCA is expected to wash out the healthy myocardial tissue. In acute infarction

with associated necrosis, gadolinium enters the cells due to cell membrane rupture. In processes that expand the extracellular space, GBCA lingers and localizes to those areas, where it can be identified on late gadolinium enhancement images. These processes include chronic scar, where the healthy tissue has been replaced with fibrosis, and infiltrative processes such as amyloidosis, where amyloid fibrils are deposited in the extracellular space and expand the territory of GBCA deposition.

### 3.3 Utilization of GBCA in Cardiovascular MRI

GBCA are used in approximately 92% of CMR studies, which is significantly more than in general radiology MRI studies [8]. Their use in CMR was only recently approved by the FDA in 2019, with gadobutrol (Gadavist/Gadovist) gaining specific approval [9]. However, the utility of GBCA in CMR has been widely accepted in the medical community prior to this approval, and the technical off-label use of other GBCA in CMR has been common practice. While non-contrast CMR has many applications, such as the assessment of basic structure and function, the addition of GBCA provides significantly more information, which has led to the increased use in CMR compared to general radiology studies.

The distributive properties of each GBCA are related to their specific chelating agent. All currently available GBCA are extracellular agents. This property is exploited in the assessment of scar and infiltrative processes with late gadolinium enhancement imaging. Contrast-enhanced imaging allows for accurate assessment of cardiovascular anatomy,

both of large vessels such as the aorta and pulmonary vessels and smaller vessels such as coronary arteries. Contrast can be used to assess perfusion of the myocardium to evaluate for ischemia, as well as perfusion of the larger vasculature to define any anomalous connections or shunts. Contrast enhancement also aids in tissue characterization of cardiac masses, particularly with perfusion to assess for vascularity and late gadolinium enhancement to assess for fibrosis and infiltration [10].

Standard doses of GBCA for use in CMR are 0.1–0.3 mmol/kg of body weight. Lower doses of 0.1 mmol/kg are recommended for perfusion studies to mitigate the occurrence of dark rim artifact, which tends to occur when the brighter contrast of blood pool is juxtaposed to the darker, not yet perfused, myocardium. Lower doses also have a more linear relationship between contrast agent concentration and signal intensity, which can be exploited in semiquantitative analyses of perfusion studies [11].

### 3.4 Adverse Events

Adverse events with GBCA are rare, with rates ranging in the literature between 0.07% and 2.4% [7]. Most reactions are mild and physiologic, with patients describing a sensation of cold, warmth, or pain at the injection site, nausea, vomiting, headache, or dizziness. Allergic-like reactions are uncommon, with rates reported in the literature between 0.004% and 0.7%. Severe life-threatening reactions such as anaphylaxis are extremely rare, with reported rates of 0.001–0.01% [12, 13]. Fatal reactions have been reported but are exceedingly rare [14]. Other complications described include extravasation, nephrogenic systemic fibrosis, and brain deposition of gadolinium.

#### 3.4.1 Allergic-Like Reactions

Allergic-like reactions manifest similarly to true allergic reactions seen with other drugs and allergens. However, an antigen-antibody interaction is not always identified, and therefore the reactions are termed “allergic-like.” The pathogenesis of these reactions is unclear, but several mechanisms have been postulated, with most involving the activation of immune modulators such as histamine, complements, and the kinin system. These reactions seem to occur independent of dose or concentration [15].

The biggest risk factor for a patient developing an allergic-like reaction is having a prior allergic-like reaction to the same agent. The estimated increased risk for these patients is approximately eightfold. Patients with allergies or asthma may have a slightly increased risk compared to the general population, but given the extremely low overall reaction rate,

special procedures for these patients are not recommended. Gadobenate dimeglumine (Magnevist) has a specific contraindication from the FDA for use in patients with prior allergic-like reactions. There is no evidence to suggest cross-reactivity between GBCA and iodinated contrast media [7].

Most institutions, including ours, recommend a premedication regimen of diphenhydramine and prednisone for patients with a history of allergic-like reaction to GBCA for subsequent exposures. We prescribe prednisone 50 mg by mouth 13, 7, and 1 h prior to administration and diphenhydramine 50 mg by mouth 1 h prior to administration. Currently, there is no evidence to support the use of a different GBCA to prevent recurrence of an allergic-like reaction.

#### 3.4.2 Nephrogenic Systemic Fibrosis

Nephrogenic systemic fibrosis or sclerosis (NSF) is a rare but serious disorder characterized by fibrosis of the skin and other tissues throughout the body in patients with renal dysfunction. It initially presents as pruritus and skin thickening but can progress rapidly and result in contractures and joint immobility. Fatal cases have been reported as well. The association of NSF with GBCA was first described in 2006, at which time guidelines were established to restrict the use of GBCA in patients with renal dysfunction [16]. Since the implementation of these restrictions, there has been a dramatic decrease in the number of cases of NSF. One study evaluating the incidence of NSF at two institutions reported the incidence pre-adoption of these restrictions as 0.057% (37 cases out of 65,240 patients) and the incidence post-adoption as 0% (0 cases out of 25,167 patients) [17]. The risk of NSF appears to be even lower with the use of group 2 GBCA, with one systematic review and meta-analysis citing an incidence of NSF in patients with stage 4 or 5 CKD of 0% [18].

The exact mechanism of GBCA leading to NSF in patients with renal dysfunction remains unknown. The postulated hypothesis is that renal dysfunction prolongs the circulating half-life of GBCA, which leads to increased opportunity for dissociation of the gadolinium ions from their chelating ligands. The free gadolinium ions then bind to anions such as phosphate and become insoluble, leading to their deposition in skin and soft tissue which causes a fibrotic reaction [19].

Risk factors for NSF include the use of Group 1 or 3 GBCA and severe renal impairment, which includes patients on any form of dialysis, severe or end-stage chronic kidney disease (CKD stage 4 or 5, with an eGFR <30), or acute kidney injury (AKI). Given the low to nonexistent risk of NSF with group 2 agents, the ACR Committee on Drugs and Contrast Media and National Kidney Foundation (NKF) consensus statement considers the assessment of renal function optional prior to the administration of these agents [7].

For other agents (groups 1 and 3), the current ACR/NKF consensus statement recommends checking the eGFR within 2 days of the planned study for inpatients or outpatients with most recent prior eGFR <45 or no prior GFR but risk factors for renal dysfunction. Risk factors include a need for prior dialysis, history of renal transplant, single kidney, kidney surgery, renal cancer, or history of CKD or AKI. For outpatients without risk factors and either no prior eGFR or most recent prior eGFR >60, repeating the eGFR is not required prior to the study. In patients with end-stage renal disease on chronic dialysis, group 1 GBCA are considered contraindicated. Groups 2 and 3 GBCA can be administered in this population if clinically indicated, without needing to change the frequency of dialysis. However, for elective MRI studies, it is prudent to perform the study prior to scheduled dialysis, particularly if hemodialysis, as it improves the clearance of GBCA [1, 7].

### 3.4.3 Brain Deposition of Gadolinium

Brain deposition of gadolinium was first described in 2014, when high MRI signal intensity was noted on unenhanced T1-weighted images of the dentate nucleus and globus pallidus of patients who had undergone multiple contrast-enhanced MRIs in the past [20]. The signal intensity appears to correlate to the number of contrast administrations. The mechanism of the deposition and its propensity for specific areas of the brain is unknown. The deposition has been observed to occur despite an intact blood-brain barrier and in the absence of clinically evident neurological disease. There is no association with renal disease, as is the case with NSF. Similarly, there is no apparent association between the class of GBCA and brain deposition, with deposits observed with linear and macrocyclic agents alike.

Despite the observation of gadolinium deposition in the brain, the clinical significance of this remains unclear. To date, there has been no demonstration that gadolinium deposition in the dentate nucleus or globus pallidus leads to disruption of the functions provided by these areas [21]. However, this has not yet been substantiated in long-term, prospective studies. In 2015, the FDA published a safety communication to announce the active investigation into the risk and clinical significance of these deposits but has not restricted the use of these agents based on the current data [22].

### 3.4.4 Extravasation

Extravasation of contrast is rare and not specific to GBCA. In a systematic review of GBCA, the rate of extravasation was 0.045% [23]. In animal studies, gadopentetate dimeglumine (Magnevist) and gadoteridol (ProHance) seem to be less

toxic to the skin and subcutaneous tissues than iodinated contrast media [24, 25]. Progression to compartment syndrome with GBCA is extremely rare and likely limited by the smaller volumes typically injected for MRI compared to CT studies. More peripherally placed IVs increase the risk of extravasation.

Symptoms of extravasation vary and are typically related to the amount of agent extravasated. Patients may experience swelling, stinging, or burning, while others may be asymptomatic. On physical exam, the area may appear edematous and erythematous and exhibit tenderness to palpation. Patients with extravasation should be examined for complications and warned of signs and symptoms of progression to more serious complications, such as paresthesias, decreased motion, or skin ulceration. Treatment options include elevation of the affected limb above the heart to promote resorption of the extravasated fluid and decrease capillary hydrostatic pressure, as well as warm or cold compresses. However, there is no evidence to support the efficacy of these strategies [26]. Injection of agents, such as corticosteroids or hyaluronidase, or aspiration of the extravasated fluid has not demonstrated benefit and is not recommended [27, 28].

---

## 3.5 Issues with Specific GBCAs

### 3.5.1 Transient Dyspnea

Severe, transient respiratory motion-related artifact has been described in the arterial phase of dynamic T1-weighted gradient echo imaging with the administration of gadoxetate disodium (Eovist/Primovist). This phenomenon appears to be specific to gadoxetate disodium compared to other GBCA, with a study from one institution describing more subjective shortness of breath with this agent compared to gadobenate dimeglumine (Magnevist) [29]. The frequency of this event varies in the literature from 4% to 14%. It is thought to be a physiologic reaction without associated bronchospasm, which suggests that prophylaxis with corticosteroids is unlikely to be beneficial. Risk factors for this reaction include prior reaction and COPD. It is also thought to be related to the volume of contrast administered [30, 31]. Gadoxetate disodium is a hepatospecific GBCA and is used exclusively for liver MRI.

### 3.5.2 Serum Calcium Measurement

Linear nonionic GBCA, such as gadoversetamide (OptiMARK) and gadodiamide (Omniscan), have been shown to interfere with total serum calcium lab values when assessed by the ortho-cresolphthalein assay. The agents specifically interfere with the assay itself, leading to falsely low

serum calcium lab values, but do not cause actual reductions in serum calcium. This effect is not seen with other GBCA [32, 33].

## 3.6 Special Populations

### 3.6.1 Children

CMR is an important modality in the pediatric population with congenital heart disease given its ability to define cardiac anatomy and function without the use of radiation. The majority of these studies benefit from the use of GBCA to enhance signal intensity for better definition of complex anatomy. The different GBCA have variable viscosity and osmolality profiles, which can lead to variable intravascular fluid shifts, particularly in patients with smaller volumes of distribution such as children. However, the overall volumes of GBCA administered for standard MRI studies are small, which limit the risk of clinically significant fluid shifts in this population [7].

Several retrospective studies have observed similar rates of allergic-like reactions in children as seen in adults [34]. Reported rates of NSF are also low and related to renal dysfunction [35]. While there is no specific evidence to support this recommendation, many institutions avoid the use of GBCA in neonates due to renal immaturity. Currently, only gadobutrol (Gadavist/Gadovist) and gadobenate dimeglumine (MultiHance) are FDA approved for the use in pediatric patients, with a recommended dose of 0.1 mmol/kg. For pediatric patients with a prior reaction to GBCA, a similar premedication regimen of prednisone and diphenhydramine is recommended, with prednisone 0.5–0.7 mg/kg PO (up to 50 mg) given 13, 7, and 1 h prior to contrast injection and diphenhydramine 1.25 mg/kg PO (up to 50 mg) given 1 h prior to contrast injection [7].

### 3.6.2 Pregnant or Women of Child-Bearing Age

Gadopentetate dimeglumine (Magnevist) has been shown to freely cross the placenta, and this distribution is assumed for all GBCA. There are no known adverse effects to human fetuses when GBCA have been given to pregnant women. A single cohort study of 26 women exposed to GBCA during their first trimester of pregnancy showed no evidence of teratogenesis or mutagenesis in their progeny [36]. There is a theoretical risk of gadolinium chelates accumulating in the amniotic fluid, conferring a potential risk of the toxic-free gadolinium ions dissociating and increasing the risk of NSF in the mother or child. However, this risk has not been studied prospectively nor substantiated in retrospective reviews.

In one large retrospective study from Canada, a cohort of mothers undergoing any MRI with the use of GBCA was compared to a control cohort of mothers who did not undergo any MRI at all. The study reported a higher risk of rheumatological, inflammatory, and infiltrative conditions in the children born to mothers in the MRI with GBCA group. However, the reported risk in the control group was also unusually high compared to the general population. Furthermore, the study reported an increased risk of stillbirth or neonatal death in the MRI with GBCA group compared to the control group. However, the rates of stillbirth or neonatal death were still overall very low [37]. Given these problematic findings, additional studies are warranted.

Since the risk in this population remains unclear, the current ACR recommendation is to use caution when considering the administration of GBCA to pregnant or potentially pregnant patients. The use of GBCA must be considered critical, with the potential benefits of use justifying the potential unknown risk to the fetus. Group 2 GBCA are preferred in this population given the lower risk of NSF. Obtaining informed consent from these patients prior to GBCA administration is also recommended [7].

### 3.6.3 Breastfeeding Women

GBCA are excreted into breast milk, predominantly in its stable and chelated form, at <0.04% of the intravascular dose given to the mother. Less than 1% of the contrast ingested by the infant is then absorbed from the GI tract, resulting in an expected systemic dose of <0.0004% of the dose given to the mother. Given the very small percentage of the GBCA that is excreted into breast milk and then absorbed by the infant's gut, the available data suggests that it is safe for a mother and infant to continue breastfeeding after receiving such an agent [38]. However, an informed decision to temporarily stop breastfeeding should be left up to the mother after these facts are communicated. If she remains concerned, she may abstain from breastfeeding from the time of contrast administration for a period of 12–24 h. There is no additional value in stopping breastfeeding beyond 24 h, as the dose given to the mother has been eliminated by that time. The mother can be advised to pump prior to the study to feed the baby during the abstinent period and to pump and dump breast milk until she feels comfortable resuming feeds. Note the taste of the breast milk may be altered by GBCA, which can affect feeds during the 24 h following contrast administration [39].

### 3.6.4 Sickle Cell Disease

In vitro studies have found that applying a strong external magnetic field, such as in an MRI scanner, can cause fully



deoxygenated, sickled red blood cells to align perpendicularly to the field [40]. This can theoretically increase the propensity toward vaso-occlusive crises in sickle cell patients undergoing MRI. However, these studies were performed in the absence of GBCA, and *in vivo* studies have not demonstrated any increased risk of vaso-occlusive complications in patient with sickle cell disease [41]. Nevertheless, the FDA updated the package inserts for gadoversetamide (OptiMARK), gadobenate dimeglumine (Magnevist), and gadoteridol (ProHance) to recommend the use of caution when administering these agents to patient with sickle cell disease.

### 3.7 Other Non-gadolinium-Based Contrast Imaging Agents

#### 3.7.1 Superparamagnetic Iron Oxide Nanoparticles

The lingering concerns with the use of gadolinium as a contrast agent have led to the development of non-gadolinium-based contrast agents. Superparamagnetic iron oxide (SPIO) nanoparticles are composed of an iron oxide core and outer biocompatible shell. There are four different categories of SPIO nanoparticles based on their size: large (>200 nm), standard (60–150 nm), ultrasmall (USPIO, 10–40 nm), and monocrySTALLINE (10–30 nm) agents. SPIO nanoparticles have ferromagnetic properties related to their higher relaxation rates, similar to GBCA. However, their dominant effect is largely on T2 relaxation, and therefore, they are mainly T2 accelerators. Of note, two SPIO nanoparticles gained FDA approval as liver agents, ferucarbotran (Resovist), and ferumoxides (Feridex). However, their commercial use was limited, and as a result, the manufacturers of both agents discontinued production and sales in 2012 [42].

Ferumoxytol is an intravenous drug with FDA approval for the treatment of iron deficiency anemia in patients with CKD. It is an ultrasmall SPIO nanoparticle whose outer carbohydrate shell is degraded in order to be incorporated into the hematopoietic pathway as iron. It has a long intravascular half-life with a safe profile for use in patients with renal dysfunction and high relaxivity, making it a promising alternative for use as an MRI contrast agent [43]. The dose required for imaging is one-fifth to half of therapeutic dosing. Currently, its use in diagnostic imaging is off-label pending systematic studies of its dosage, safety, and application in MRI.

#### 3.7.2 Manganese-Based Contrast Agent

Historically, manganese was the first element used *in vivo* as an MRI contrast agent, as it has excellent cardiac, hepatic, and renal uptake and significant paramagnetic effects with

high T1 relaxativity. It is important to note that manganese is an essential trace element required as a cofactor and enzyme activator for multiple biological processes and plays a role in stabilizing mitochondrial membranes from oxidative stress. However, at high doses, manganese strongly competes with the myocardial uptake of calcium, resulting in significant cardiovascular toxicity and cardiac arrest in animal studies which halted its further development as a contrast agent. Interestingly, as a calcium analogue, manganese can cross myocardial L-type voltage-gated calcium channels and sodium-calcium exchangers, making it an intracellular myocardial contrast agent [44]. Subsequent work has focused on overcoming the potential toxicity and allowing for its utilization in the assessment of stunned and viable myocardium, which has shown promising results [45].

#### 3.7.3 Molecular Imaging

Molecular imaging refers to the imaging of biological processes at the cellular and subcellular level. It requires the use of molecular contrast agents targeted toward the cells or tissues of interest [46]. In cardiovascular imaging, examples of clinical applications include the imaging of atherosclerotic plaques and myocardial injury by targeting cells undergoing apoptosis. Initial molecular MRI contrast agents consisted of MRI contrast agents conjugated to antibody ligands but have since evolved to include small proteins, peptides, and small molecule probes. Targets for these contrast agents have traditionally been cell surface antigens. However, an area of increased interest has been the development of probes that can be internalized following interaction with specific cell surface receptors [47]. While molecular imaging and its role in CMR is certainly promising, its current use remains experimental within the realm of clinical research.

### 3.8 Conclusion

GBCA are routinely utilized in cardiac MRI to assess perfusion and better delineate vascular structures. GBCA also aid in tissue characterization and scar identification. Although GBCA, especially ACR group 2 agents, have an excellent safety profile, there are still important adverse reactions and risks to be considered when GBCA are administered. The risk of NSF has been dramatically reduced with the adoption of renal function screening protocols when ACR group 1 or 3 GBCA is administered, as well as the increased utilization of ACR group 2 agents. Despite the lack of evidence that gadolinium deposition in the brain leads to clinically evident dysfunction, it is important to limit the use of GBCA, particularly in the pediatric population, to only when it is deemed clinically necessary.

## References

- Weinreb JC, et al. Use of intravenous gadolinium-based contrast media in patients with kidney disease: consensus statements from the American College of Radiology and the National Kidney Foundation. *Kidney Med.* 2000;3(1):142–50.
- Lee VS. *Cardiovascular MRI: physical principles to practical protocols.* Philadelphia, PA: Lippincott Williams & Wilkins; 2006.
- Rogosnitzky M, et al. Gadolinium-based contrast agent toxicity: a review of known and proposed mechanisms. *BioMetals.* 2016;29(3):365–76.
- Idee JM, et al. Role of thermodynamic and kinetic parameters in gadolinium chelate stability. *J Magn Reson Imaging.* 2009;30(6):1249–58.
- Goyen M. Gadofosveset-enhanced magnetic resonance angiography. *Vasc Health Risk Manag.* 2008;4(1):1–9.
- US Food and Drug Administration. n.d.. <https://www.accessdata.fda.gov/scripts/cder/daf/index.cfm?event=BasicSearch.process>.
- American College of Radiology. ACR manual on contrast media version 2021. Reston, VA: ACR. <https://www.acr.org/Clinical-Resources/Contrast-Manual>. Accessed 26 Jan 2021.
- Bruder O, et al. European Cardiovascular Magnetic Resonance (EuroCMR) registry – multi national results from 57 centers in 15 countries. *J Cardiovasc Magn Reson.* 2013;15:9.
- US Food and Drug Administration. n.d.. [https://www.accessdata.fda.gov/drugsatfda\\_docs/label/2019/201277s0171bl.pdf](https://www.accessdata.fda.gov/drugsatfda_docs/label/2019/201277s0171bl.pdf).
- Paiman EHM, et al. When should we use contrast material in cardiac MRI? *J Magn Reson Imaging.* 2017;46(6):1551–72.
- Gerber BL, et al. Myocardial first-pass perfusion cardiovascular magnetic resonance: history, theory, and current state of the art. *J Cardiovasc Magn Reson.* 2008;10(1):18.
- Murphy KJ, et al. Adverse reactions to gadolinium contrast media: a review of 36 cases. *AJR.* 1996;167(4):847–9.
- Runge VM. Safety of approved MR contrast media for intravenous injection. *J Magn Reson Imaging.* 2000;12(2):205–13.
- Jordan RM, et al. Fatal reaction to gadopentetate dimeglumine. *AJR.* 1995;164(3):743–4.
- Bush WH, et al. Acute reactions to intravascular contrast media: types, risk factors, recognition, and specific treatment. *AJR.* 1991;157:1153–61.
- Marckmann P, et al. Nephrogenic systemic fibrosis: suspected causative role of gadodiamide used for contrast-enhanced magnetic resonance imaging. *J Am Soc Nephrol.* 2006;17:2359–62.
- Altun E, et al. Nephrogenic systemic fibrosis: change in incidence following a switch in gadolinium agents and adoption of a gadolinium policy – report from two US universities. *Radiology.* 2009;253(3):689–96.
- Woolen SA, et al. Risk of nephrogenic systemic fibrosis in patients with stage 4 or 5 chronic kidney disease receiving a group II gadolinium-based contrast agent: a systematic review and meta-analysis. *JAMA Intern Med.* 2020;180(2):223–30.
- Abraham JL, et al. Dermal inorganic gadolinium concentrations: evidence for in vivo transmetallation and long-term persistence in nephrogenic systemic fibrosis. *Br J Dermatol.* 2008;158:273–80.
- Kanda T, et al. High signal intensity in the dentate nucleus and globus pallidus on unenhanced T1-weighted MR images: relationship with increasing cumulative dose of a gadolinium-based contrast material. *Radiology.* 2014;270:834–41.
- Gulani V, et al. Gadolinium deposition in the brain: summary of evidence and recommendations. *Lancet Neurol.* 2017;16(7):564–70.
- US Food and Drug Administration. n.d.. <https://www.fda.gov/media/93095/download>.
- Behzadi AH, et al. MRI and CT contrast media extravasation: a systemic review. *Medicine (Baltimore).* 2018;97(9):e0055.
- McAlister WH, et al. The effect of Gd-dimeglumine on subcutaneous tissues: a study with rats. *AJNR Am J Neuroradiol.* 1990;11(2):325–7.
- Cohan RH, et al. Extravascular toxicity of two magnetic resonance contrast agents: preliminary experience in the rat. *Investig Radiol.* 1991;26(3):224–6.
- Hastings-Tosima MT, et al. Effect of warm and cold applications on the resolution of IV infiltrations. *Res Nurs Health.* 1993;16(3):171–8.
- Park KS, et al. Methods for mitigating soft-tissue injury after subcutaneous injection of water soluble contrast media. *Investig Radiol.* 1993;28(4):332–4.
- Rowlett J. Extravasation of contrast media managed with recombinant human hyaluronidase. *Am J Emerg Med.* 2012;30(9):2102–3.
- Davenport MS, et al. Matched within-patient cohort study of transient arterial-phase respiratory motion related artifact in MRI of the liver: Gd-EOB-DTPA vs GD-BOPTA. *Radiology.* 2014;272:123–31.
- Pietryga JA, et al. Respiratory motion artifact affecting hepatic arterial phase imaging with gadoxetate disodium: examination recovery with a multiple arterial phase acquisition. *Radiology.* 2014;271(2):426–34.
- Bashir MR, et al. Respiratory motion artifact affecting hepatic arterial phase imaging with gadoxetate disodium is more common in patients with a prior episode of arterial phase motion associated with gadoxetate disodium. *Radiology.* 2015;274:141–8.
- Lin J, et al. Interference of magnetic resonance imaging contrast agents with the serum calcium measurement technique using colorimetric reagents. *J Pharm Biomed Anal.* 1999;21:931–43.
- Brown JJ, et al. Measurement of serum calcium concentration after administration of four gadolinium-based contrast agents to human volunteers. *AJR.* 2007;189(6):1539–44.
- Dillman JR, et al. Frequency and severity of acute allergic-like reactions to gadolinium-containing IV contrast media in children and adults. *AJR.* 2007;189:1533–8.
- Weller A, et al. Gadolinium and nephrogenic systemic fibrosis: an update. *Pediatr Nephrol.* 2014;29:1927–37.
- De Santis M, et al. Gadolinium periconceptional exposure: pregnancy and neonatal outcome. *Acta Obstet Gynecol Scand.* 2007;86(1):99–101.
- Ray JG, et al. Association between MRI exposure during pregnancy and fetal and childhood outcomes. *JAMA.* 2016;316(9):952–61.
- Kubik-Huch RA, et al. Gadopentetate dimeglumine excretion into human breast milk during lactation. *Radiology.* 2000;216:555–8.
- Webb JAW, et al. The use of iodinated and gadolinium contrast media during pregnancy and lactation. *Eur Radiol.* 2005;15:1234–40.
- Brody AS, et al. Induced alignment of flowing sickle erythrocytes in a magnetic field: a preliminary report. *Investig Radiol.* 1985;20(6):560–6.
- Dillman JR, et al. Safety of gadolinium-based contrast material in sickle cell disease. *J Magn Reson Imaging.* 2011;34(4):917–20.
- Bietenbeck M, et al. Remote magnetic targeting of iron oxide nanoparticles for cardiovascular diagnosis and therapeutic drug delivery: where are we now? *Int J Nanomedicine.* 2016;11:3191–203.
- Bashir MR, et al. Emerging applications for ferumoxytol as a contrast agent in MRI. *J Magn Reson Imaging.* 2015;41:884–98.
- Spath NB, et al. Manganese-enhanced MRI of the myocardium. *Heart.* 2019;105(22):1695–700.
- Spath NB, et al. Assessment of stunned and viable myocardium using manganese-enhanced MRI. *Open Heart.* 2021;8(1):e001646.
- Sosnovik DE, et al. Molecular magnetic resonance imaging in cardiovascular medicine. *Circulation.* 2007;115:2076–86.
- Kelly KA, et al. In vivo phage display selection yields atherosclerotic plaque targeted peptides for imaging. *Mol Imaging Biol.* 2006;8:201–7.



# Introduction to Congenital Heart Disease Anatomy

# 4

Pierangelo Renella and J. Paul Finn

## 4.1 Introduction

Imaging of the complex anatomy associated with many forms of congenital heart disease (CHD) requires knowledge of the morphology of the various cardiac chambers, valves, and extra-cardiac vasculature. For the cardiac diagnostician, assembling together the pieces of disordered anatomy is best done with the so-called segmental approach. This approach breaks down the cardiovascular anatomy sequentially, considering first the position of the abdominal viscera, next the cardiac atria, then the looping pattern of the ventricles, and, finally, the position of the semilunar valves and anatomic orientation of the great arteries. In this manner, the various forms of CHD may be precisely identified and the proper management applied by the clinician. The large field of view, good spatial and temporal resolution cine imaging, coupled with three-dimensional multiplanar reconstruction and volume rendering capability of angiographic images, as well as the lack of ionizing radiation exposure, make cardiac magnetic resonance (CMR) the ideal imaging modality for the initial evaluation and serial follow-up of patients with CHD. This holds particularly true for adult and postoperative patients who may have suboptimal echocardiographic imaging windows. This chapter introduces the segmental approach

to the diagnosis of CHD vis-à-vis CMR imaging. Each “segment” of the cardiovascular system is described with particular attention paid to the distinguishing features of normal structures so that abnormal features may be more clearly identified. Salient examples of pathology in each segment are also presented with their relevant clinical features.

## 4.2 Viscero-Atrial Anatomy and Morphology

The specific arrangement of the various thoracoabdominal organs is commonly described as the viscerο-atrial “situs.” Situs may be classified as *solitus* (normal arrangement), *inversus*, or *ambiguous* (Fig. 4.1) [2, 3]. In viscerο-atrial situs solitus, the abdominal and thoracic organs are arranged in the normal fashion, with the liver on the right side, and the spleen and stomach on the left. In addition, the right-sided lung is normally trilobed with an eparterial bronchus, while the left-sided lung has two lobes and a hyperarterial bronchus. In viscerο-atrial situs solitus, the morphologically left atrium is left-sided and posterior to the morphologically right atrium. Conversely, the morphologically right atrium resides rightward and anterior to the morphologically left atrium.

**Supplementary Information** The online version contains supplementary material available at [https://doi.org/10.1007/978-3-031-29235-4\\_4](https://doi.org/10.1007/978-3-031-29235-4_4).

P. Renella (✉)  
Department of Radiology Sciences, David Geffen School of Medicine, Ronald Reagan UCLA Medical Center, Los Angeles, CA, USA  
Department of Pediatric Cardiology, UC-Irvine College of Medicine, Children’s Hospital Orange County, Orange, CA, USA  
University of California Los Angeles (UCLA), Los Angeles, CA, USA  
Division of Pediatric Cardiology, CHOC Children’s Hospital, Orange, CA, USA  
e-mail: [prenella@mednet.ucla.edu](mailto:prenella@mednet.ucla.edu)

J. P. Finn  
Department of Radiology Sciences, David Geffen School of Medicine, Ronald Reagan UCLA Medical Center, Los Angeles, CA, USA  
University of California Los Angeles (UCLA), Los Angeles, CA, USA  
Department of Radiology, Diagnostic Cardiovascular Imaging Section, UCLA, Los Angeles, CA, USA  
e-mail: [pfinn@mednet.ucla.edu](mailto:pfinn@mednet.ucla.edu)

**Fig. 4.1** Types of viscerotri-atrial situs [1]. Shown are the three types of spatial arrangement of the visceral organs and the cardiac atria. Situs *solitus* is the normal configuration with the stomach and spleen on the left side of the body and the liver on the right. Situs *inversus* is the mirror image of situs *solitus*. The term situs *ambiguus* is applied when there is ambiguity with respect to the specific sidedness of the organs, and the atrial morphology cannot be precisely determined. RA right atrium, LA left atrium

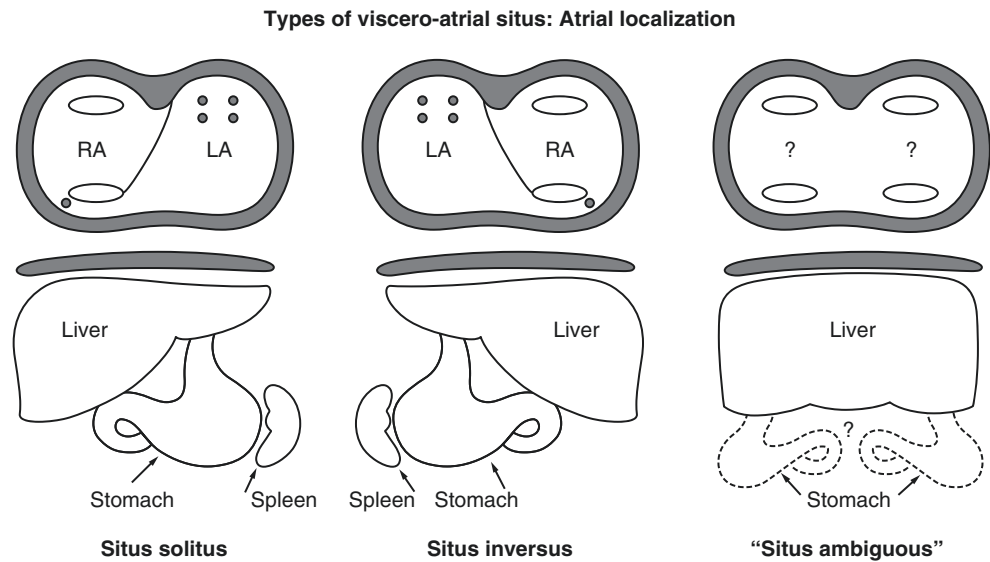


**Table 4.1** Morphological features of the right and left atria

Left atrium	Right atrium
Thin “finger-like” appendage	Broad pyramidal shaped appendage
Smooth wall	Pectinate muscles
Pulmonary venous connections	Crista terminalis
Ostium secundum	Coronary sinus ostium
	Connection of the inferior vena cava
	Connection of the superior vena cava

Morphological features of left and right atria are presented in Table 4.1. Situs “inversus” refers to the mirror image of the normal arrangement. The third category, in which elements of both situs *solitus* and *inversus* coexist in the same patient, is termed situs *ambiguus* (Fig. 4.1). Several different permutations of the thoracic and abdominal organ locations are possible in situs *ambiguus*, including the presence of two morphologically left or right atria and/or two morphologically left or right bronchi. The liver may be either on the left side or transverse in location. The stomach may be found on either side of the abdominal cavity [3, 4].

#### 4.2.1 Heterotaxy Syndrome

In the heterotaxy syndrome, various aberrations of thoracoabdominal organ right-left orientation may be seen (Fig. 4.2). There exist several published definitions of heterotaxy. A unified definition was proposed by the International Nomenclature Committee for Pediatric and Congenital Heart Disease Nomenclature Working Group

[3]. According to this definition, heterotaxy is “... an abnormality where the internal thoraco-abdominal organs demonstrate abnormal arrangement across the left-right axis of the body.” This definition excludes patients with pure situs *inversus* and includes patients with situs *ambiguus*. Heterotaxy may be associated with either the absence of a spleen (asplenia) or with multiple spleens (polysplenia). Asplenia has also been labeled “bilateral right-sidedness,” and polysplenia has been referred to as “bilateral left-sidedness.” For example, a patient with heterotaxy and asplenia (i.e., bilateral right-sidedness) may have bilateral morphologically right-sided bronchi and atria, while in heterotaxy with polysplenia, there may be bilateral morphologically left-sided bronchi and atria. Considerable anatomic variation can exist among patients with asplenia or polysplenia.

Heterotaxy syndrome is uncommon, occurring in only approximately 1% of patients with congenital heart disease (CHD) [5]. However, when present, it is often associated with severe cardiac abnormalities (Table 4.2). The 1-year survival without surgical intervention is poor (<15% in asplenia and <50% in polysplenia) [6, 7]. In spite of specialized palliative medical and surgical strategies, approximately one-third of patients will die or require orthotopic heart transplantation within 35 years of Fontan surgery [8].

Transthoracic echocardiography and cardiac catheterization have long been successfully applied in patients with heterotaxy syndrome. CMR has been also shown to be of value in this patient population and, in fact, may be superior in terms of precise localization of the thoracoabdominal organs, bronchial anatomy, cardiac chamber morphology, and connections of the pulmonary and systemic veins often encountered in these patients [9, 10].



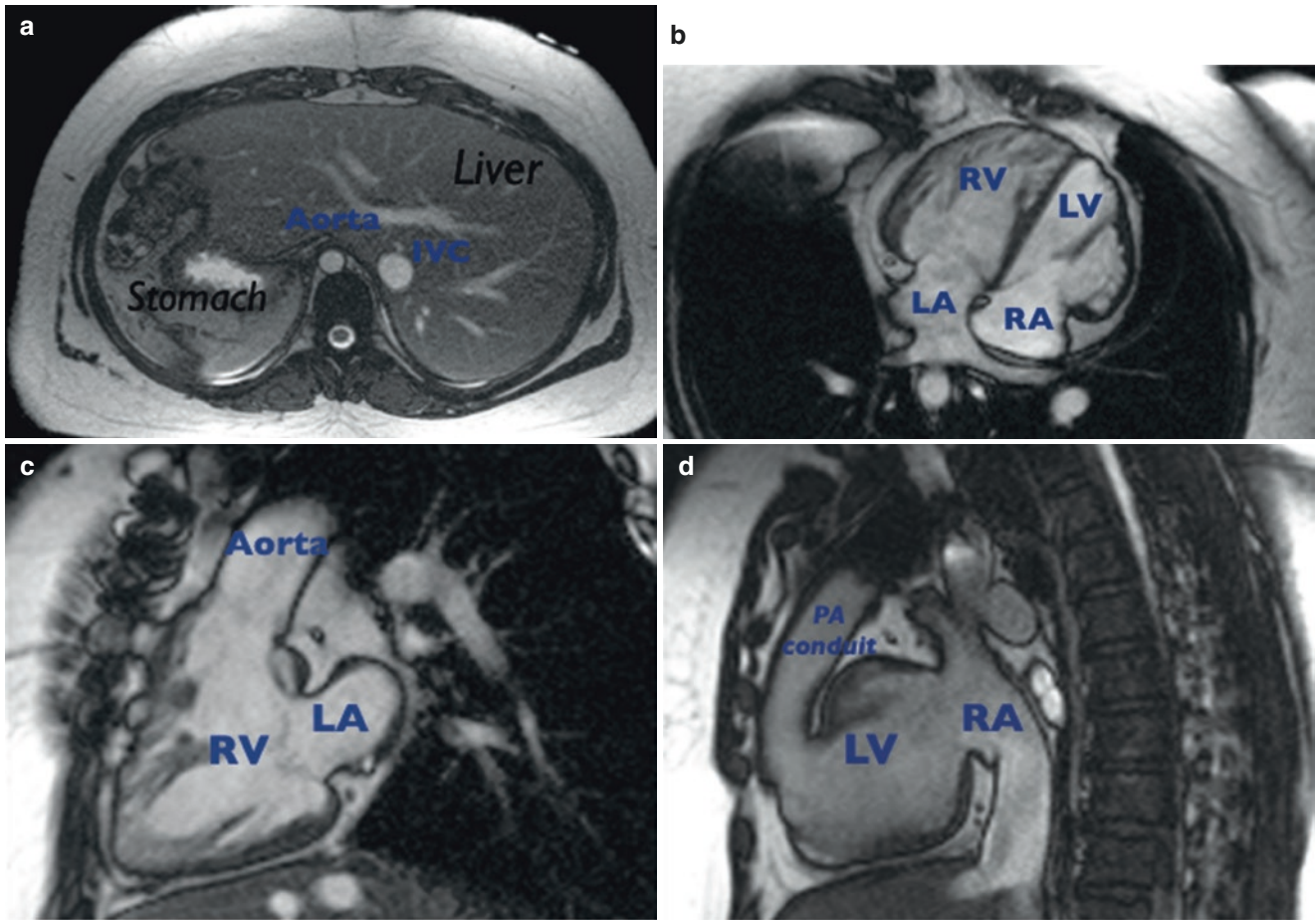


**Fig. 4.2** Heterotaxy syndrome with visero-atrial situs inversus (MR steady-state free precession imaging). (a) SSFP image in the axial plane through abdomen demonstrating visceral situs *inversus* (left-sided liver and right-sided stomach). Note also that the IVC is on the left and the aorta is on the right. (b) SSFP image of atrioventricular discordance in a patient with l-loop transposition of the great arteries. In this patient, there is visero-atrial situs inversus with discordant connections of the

atrial to their respective ventricles. (c) Same patient as in (b) depicting abnormal atrioventricular and ventriculo-arterial discordance (“double discordance”). The RV connects to the anteriorly and leftward positioned (l-malposed) aorta. (d) Same patient as in (b). This patient has undergone surgical LV to PA conduit placement to bypass native sub-pulmonary stenosis. IVC inferior vena cava, LV left ventricle, RV right ventricle, LA left atrium, RA right atrium, PA pulmonary artery



**Table 4.2** Cardiac malformations associated with heterotaxy syndrome

Anatomic feature	Asplenia (“bilateral right-sidedness”)	Polysplenia (“bilateral left-sidedness”)
Liver position	Transverse (76–91%)	Transverse (50–67%)
Lung lobes	Bilaterally trilobed (81–93%)	Bilaterally bilobed (72–88%)
Bronchial morphology	Bilaterally eparterial (95%)	Bilaterally hyparterial (68–88%)
Superior vena cava	Bilateral (46–71%)	Bilateral (33–50%)
Inferior vena cava	Interrupted with azygos continuation (rare)	Interrupted with azygos continuation (58–100%)
Pulmonary veins	Total anomalous connection (64–72%)	Anomalous drainage (normal connection) due to atrial septal malalignment (37–50%)
Atrial morphology	Common atrium (57%)	Common atrium (25–30%)
Cardiac crux	AV canal defects (84–92%)	AV canal defects (80%)
Ventricles	Functional single ventricle (44–55%)	Functional single ventricle (37%)
Cardiac position	Dextrocardia (36–41%)	Dextrocardia (33–42%)
Ventriculo-arterial connection	Double outlet right ventricle (82%); transposition of the great arteries (9%)	Double outlet right ventricle (17–37%)

Adapted from Bartram et al. [5]

### 4.3 Venous-Atrial Connections

Two distinct venous systems connect to the cardiac atria: the *systemic* veins (inferior vena cava, superior vena cava, hepatic veins, coronary sinus) and the *pulmonary* veins (Fig. 4.3). The systemic veins carry deoxygenated blood to the morphologically right atrium. Conversely, the pulmonary veins carry oxygenated blood to the morphologically left atrium. In fact, as already reviewed in Table 4.1, the very connections of the coronary sinus (CS) and inferior vena cava (IVC) to the right atrium help define it as the morphologically right atrium (Table 4.1). Similarly, the connections of the pulmonary veins are one of the distinguishing features of a morphologically left atrium.

#### 4.3.1 Systemic Venous Connections

The superior vena cava (SVC) forms from both brachiocephalic (innominate) veins. There is usually a single right SVC, although it is possible to have a single left SVC (with an absent right SVC) or bilateral SVCs (with or without a bridging vein). The right SVC normally courses anterior to the right pulmonary artery and against the posterolateral aspect of the ascending aorta before connects to the roof of the morphologically right atrium (Fig. 4.3a) [11].

The IVC receives systemic venous drainage from the lower body, including the retroperitoneum, portal circulation, and lower extremities (Fig. 4.3b). After traversing superiorly, it courses within the liver and through the diaphragmatic hiatus to reach the floor of the right atrium [11]. This normally occurs on the right side of the body but may be on the left or even midline, depending on the atrial situs. In atrial situs inversus, for example, the IVC may connect to a morphologically right atrium located on the left side of midline. The intrahepatic portion of the IVC may be absent (interrupted) as a normal variant or in the heterotaxy syndrome, particularly the polysplenia subtype (as described above). In this case, the IVC blood would continue to the SVC via the more posteriorly located azygos vein [12, 13].

The coronary sinus (CS) is the confluence of the majority of the coronary venous drainage and opens normally to the morphologically right atrium (Fig. 4.3c). It may also receive a persistent left superior vena cava (LSVC) or an anomalously connected pulmonary vein (or veins). In rare instances, the CS may be “unroofed” and thus open directly into the morphologically left atrium, resulting in an abnormal right-to-left shunt. Complete atresia of the CS ostium has also been reported [11].

The hepatic veins typically drain to the IVC directly and/or the floor of the morphologically right atrium (Fig. 4.3d). In the case of an interrupted IVC with azygos continuation, the hepatic veins will connect directly to the floor of the morphologically right atrium. Naturally, when there is viscerocranial situs inversus, the hepatic veins may be found left of midline. In situs ambiguous, the hepatic veins may drain in the midline to a common atrium of indeterminate morphology or have separate connections to one or both atria.

#### 4.3.1.1 Total Anomalous Systemic Venous Connection

Very rarely all the systemic veins connect anomalously to the morphologically left atrium. This is known as total anomalous systemic venous connection. In this lesion, there is usually a single left SVC connecting to an unroofed CS, such that venous drainage from the upper body drains directly to the left atrium. In addition, the IVC is interrupted with continuation via the azygos vein to the left SVC. Finally, the hepatic veins also anomalously connect to the floor of the left atrium. Most often, this condition occurs in the setting of heterotaxy and complex cyanotic CHD [12]. In isolation, this defect would be expected to cause profound cyanosis. However, arterial saturation may be somewhat improved by a bidirectional atrial level shunt (e.g., in the setting of a common atrium). An example of a variant of this lesion is depicted in Fig. 4.4. Surgical repair may consist of an intra-atrial baffle constructed to direct the IVC, SVC, and CS flow appropriately to the right atrium [12].

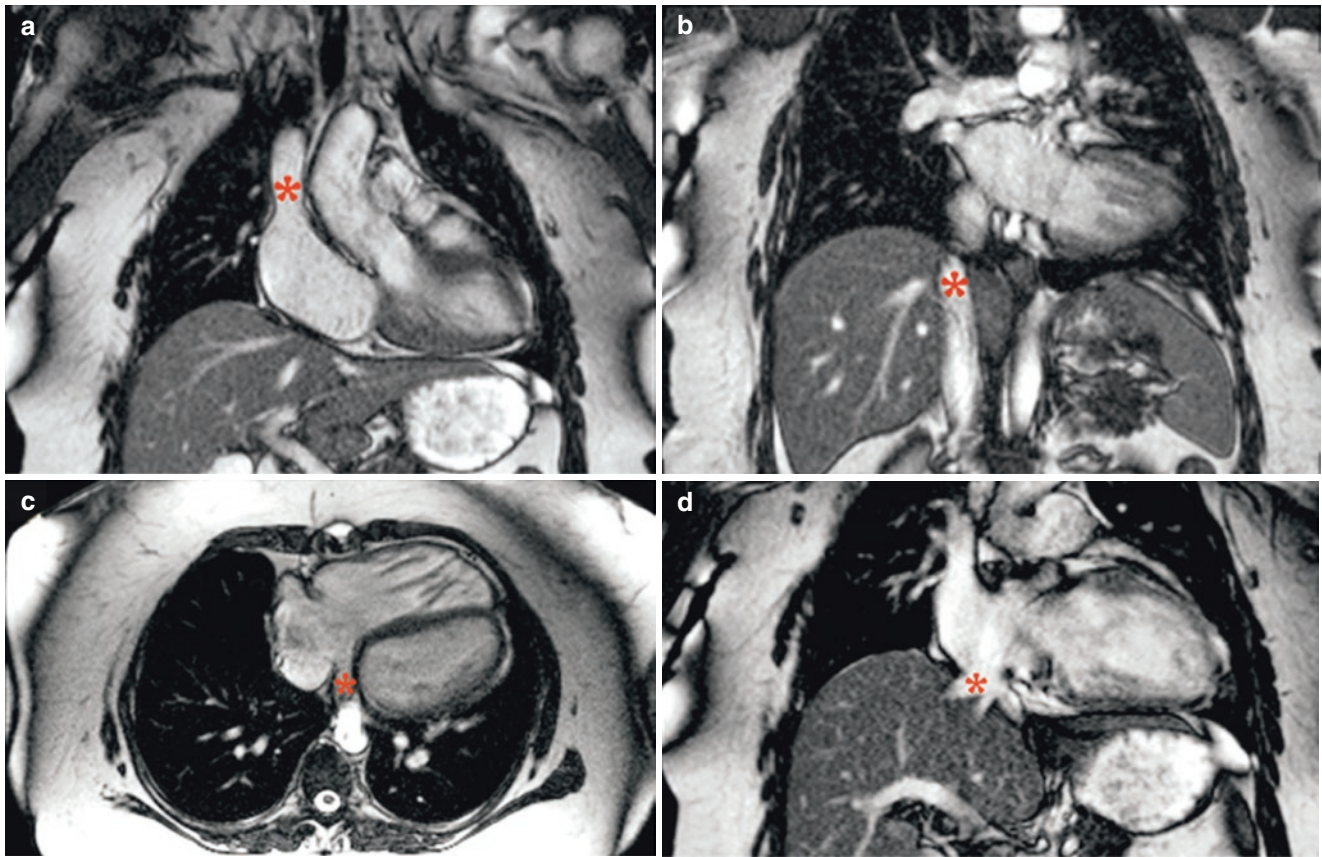
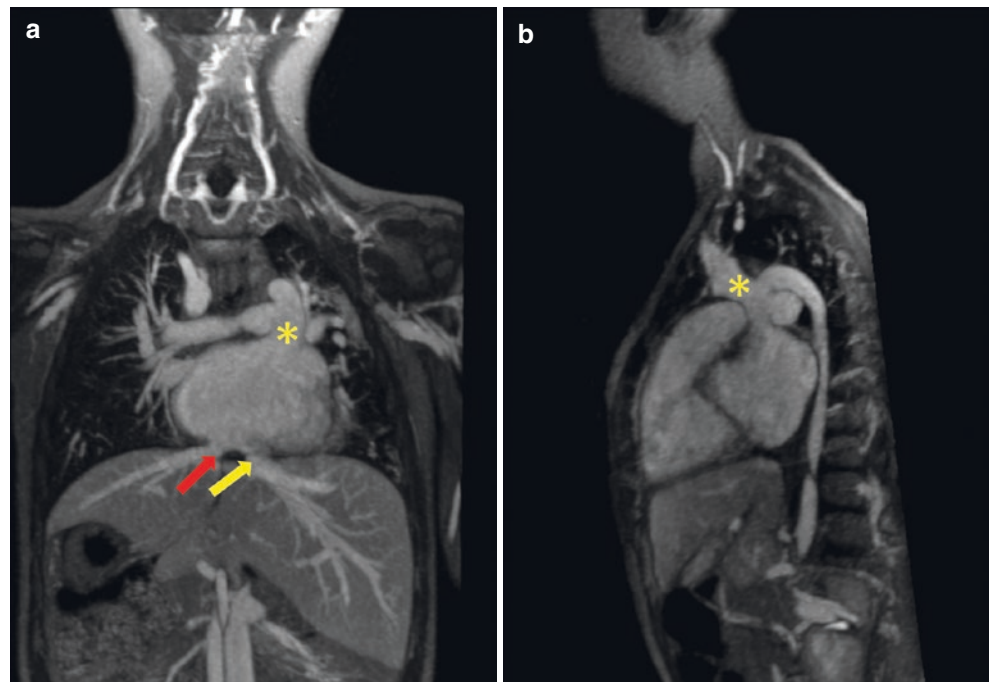


**Fig. 4.3** Normal systemic and pulmonary veno-atrial connections. (a) The superior vena cava (SVC) carries venous drainage from the upper body to the morphologically right atrium (*asterisk*). (b) The inferior vena cava (IVC) carries lower body venous drainage to the morphologically right atrium (RA), and indeed, this IVC connection is one of the defining features of an RA (*asterisk*). (c) The coronary sinus (CS) ostium is another defining feature of a morphologically RA. It carries the coronary venous blood (*asterisk*). (d) The hepatic veins either connect to the IVC and/or directly to the floor of the RA (*asterisk*)

**Fig. 4.4** Total anomalous systemic connection. Contrast-enhanced MRA maximum intensity projections in the coronal and sagittal planes. (a, b) Left superior vena cava receiving a dilated azygos vein (due to interruption of the inferior vena cava) with direct connection to the left-sided atrium (yellow asterisks). The right hepatic vein connects to the left-sided atrium (yellow arrow). In this patient, the only systemic vein not to connect to the left-sided atrium is the right hepatic vein (red arrow). Its connection is to the right-sided atrium



### 4.3.2 Pulmonary Venous Connections

In the normal heart, venous drainage from the lungs returns via the pulmonary veins to the morphologically left atrium. In the normal configuration, two pulmonary veins (one upper and one lower) from each lung course to the morphologically left atrium. The right upper and lower pulmonary veins course posteriorly to the right atrium and SVC, while the left upper and lower pulmonary veins course just anterior to the descending thoracic aorta. The right upper pulmonary vein is usually formed by branches from the right upper and right middle lobes of the lung. The right upper and right middle pulmonary veins typically join together prior to connecting to the left atrium. However, as a normal variant, the right middle branch may enter the left atrium separately. In addition, it is not uncommon for the two left-sided pulmonary veins to join the atrium as a single common vein [11]. Of clinical interest, the cardiac end of each pulmonary vein contains myocardial cells rather than smooth muscle cells [11]. This area of the pulmonary veins has been implicated in abnormal electrical circuits predisposing patients to atrial fibrillation. As such, the proximal pulmonary veins are potential targets of transcatheter radiofrequency ablation therapy for atrial fibrillation [14]. Pre-procedural planning for treatment of atrial fibrillation via transcatheter ablation often includes CMR imaging [15].

During embryological development of the pulmonary veins, there exist connections between the primitive pulmonary and splanchnic venous plexi. If the common pulmonary vein fails to connect to the posterior morphologically left atrium, these pulmonary and splanchnic connections persist, resulting in anomalous pulmonary venous connections of various types [16]. In the case of total anomalous pulmonary venous connection (TAPVC), all the pulmonary veins retain their embryonic connections to the systemic venous system and do not connect directly to the morphologically left atrium. These connections may become obstructed and present either at birth, or within the first part of infancy, with cyanosis and rapid clinical deterioration. In fact, “obstructed” TAPVC is one of the few surgical emergencies in pediatric

cardiology. In partial anomalous pulmonary venous connection (PAPVC), at least one, but not all, of the pulmonary veins connect abnormally.

Three general categories of TAPVC are described based on which systemic veins the anomalous pulmonary veins maintain an embryonic connection to Fig. 4.5. In decreasing order of frequency, these are (1) supracardiac, (2) cardiac, and (3) infradiaphragmatic. When the pulmonary venous connections consist of some combination of these categories, the designation of “mixed” TAPVC is given. The “mixed” form of TAPVC is the least common, occurring in only 8% of patients [18]. “Supracardiac” TAPVC occurs in approximately 50% of the cases and consists of pulmonary venous blood being redirected via a “vertical vein” (to usually the innominate vein) on its way to the right SVC or to a left SVC directly [16]. The “cardiac” form of the disease typically involves drainage of the pulmonary veins directly to the coronary sinus. The “infradiaphragmatic” form of TAPVC is described in detail below.

#### 4.3.2.1 Infradiaphragmatic Total Anomalous Pulmonary Venous Connection (TAPVC)

Although a relatively uncommon form of TAPVC, when the connection of the pulmonary venous confluence to the systemic circulation is via an infradiaphragmatic route, the risk of obstruction and subsequent early clinical deterioration is relatively high. In infradiaphragmatic TAPVC, the pulmonary venous blood courses via a “vertical vein” running parallel to the aorta, through the diaphragm (at the esophageal hiatus), connects to the portal venous system, and then into the hepatic circulation (via the ductus venosus), on its way to the right atrium (Fig. 4.6). This roundabout pathway back to the heart creates multilevel resistance to blood flow. In particular, the more common sites of obstruction are at the level of the vertical vein as it passes through the diaphragm, from closure of the ductus venosus, and/or due to high resistance intrahepatic connections [16]. Additionally, due to the complete mixing of pulmonary and systemic venous blood in the right atrium, patients may be profoundly cyanotic.



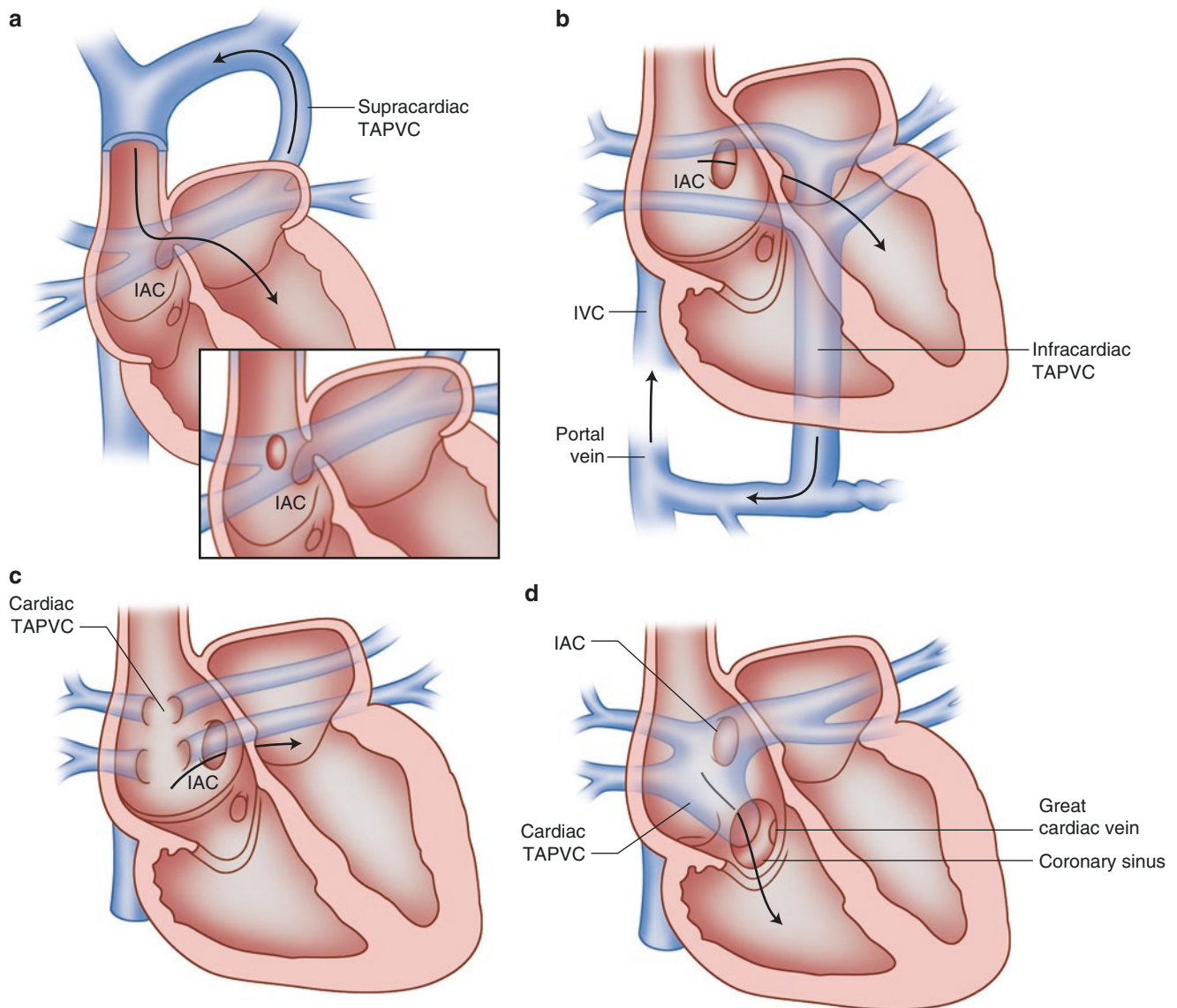
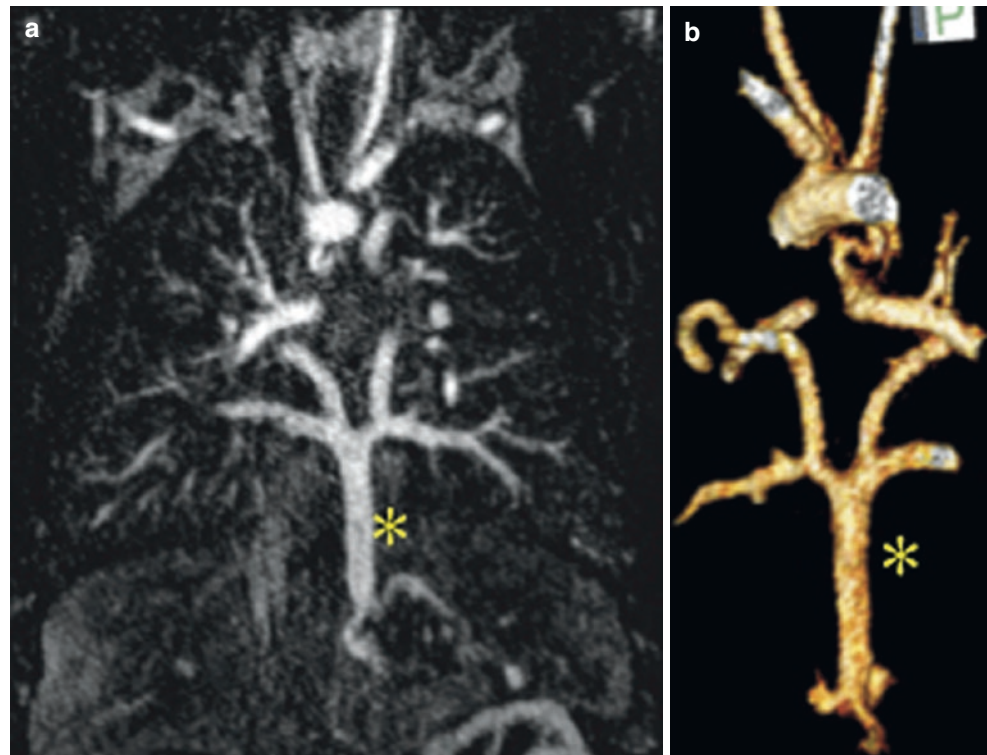


**Fig. 4.5** Total anomalous pulmonary venous connection (TAPVC) [17]. This diagram depicts the three general categories of TAPVC. (a) Supracardiac TAPVC: the pulmonary venous blood returns to the heart via a vertical vein to the innominate vein and ultimately to the SVC and right atrium. (b) Infracardiac (infradiaphragmatic) TAPVC: a particularly insidious subtype of TAPVC due to its relatively higher propensity for pulmonary venous obstruction and clinical deterioration in the neo-

natal period. (c) Cardiac TAPVC shown with direct anomalous pulmonary venous connections to the right atrium (d) and with the more common scenario involving anomalous drainage to the right atrium via direct connection of the pulmonary vein confluence with the coronary sinus. *IAC* interatrial communication, *TAPVC* total anomalous pulmonary venous connection. (Copyright 1985 by the Texas Heart Institute, Houston. Illustration by Bill Andrews)



**Fig. 4.6 (a, b)** Infradiaphragmatic TAPVC. Infant boy with infradiaphragmatic TAVPC. The *left* panel (a) is a coronal projection of a high-resolution contrast-enhanced MR angiogram showing all four pulmonary veins joining a confluence and coursing caudally through the diaphragm via a vertical vein (*asterisk*) toward the liver. It then drains into the portal circulation and subsequently to the IVC. The panel on the *right* (b) is a posterior projection of a volume rendered image of the MR angiogram



#### 4.4 Atrioventricular Connections and Ventricular Morphology

The accurate diagnosis of complex CHD depends on correctly identifying the morphology of the heart chambers, the atrioventricular connections, and their specific locations within the chest cavity. The anatomic components that identify the right and left atria are reviewed above (Table 4.1). Like the atria, the left and right ventricles also each have distinguishing morphological features (Table 4.3). Notably, the shape of the morphologically left ventricle (LV) resembles a prolate ellipsoid or “bullet” shape (Fig. 4.7a). It has a smooth basal septal surface (*asterisk*), and the mitral valve apparatus attaches to the free wall rather than the ventricular septum (“septophobic” attachments). The shape of the morphologically right ventricle (RV) is a complex pyramidal shape [19, 20]. It has three distinct parts: (1) inflow portion, (2) body and apex, and an (3) outflow or “infundibulum.” There is a moderator band located toward the apex, and the tricuspid valve apparatus attaches to both the ventricular septum (“septophilic” attachments) and the RV free wall (Fig. 4.7b–d).

After establishing the morphology of the atria and ventricles, attention can then be directed to how the chambers connect. In the normal configuration, a given ventricle typically receives inflow of blood only from its respective atrium via one of the two atrioventricular (AV) valves, the mitral or

**Table 4.3** Morphological features of the ventricles

Left ventricle	Right ventricle
Smooth basal septal surface	Muscular infundibulum (outflow tract)
Fine trabeculations	Coarse trabeculations
Guarded by mitral valve	Guarded by tricuspid valve
Prolate ellipsoid (“bullet”) shape	Complex pyramidal shape
	Moderator band
	Relatively thin free wall

tricuspid valve. Normally, the left atrium connects to the LV via the mitral valve, and the right atrium connects to the RV via the tricuspid valve.

Aberrations of these connections are the basis of some forms of CHD. For example, in double inlet left ventricle (DILV), both atrioventricular valves connect to a single morphologically left ventricle (see below). The LV would then give off either the aorta or the pulmonary artery. In these cases, there also exists a small outflow chamber that receives blood from the single left ventricle via a bulboventricular foramen that then connects to the other great artery. This outflow chamber does not have a direct atrioventricular connection (see below) and thus is not labeled a true ventricle in the strict sense.

In the very rare case of a double inlet right ventricle (DIRV), the opposite applies. That is, the single morphologically RV receives the inflow of both the left (“mitral”) and

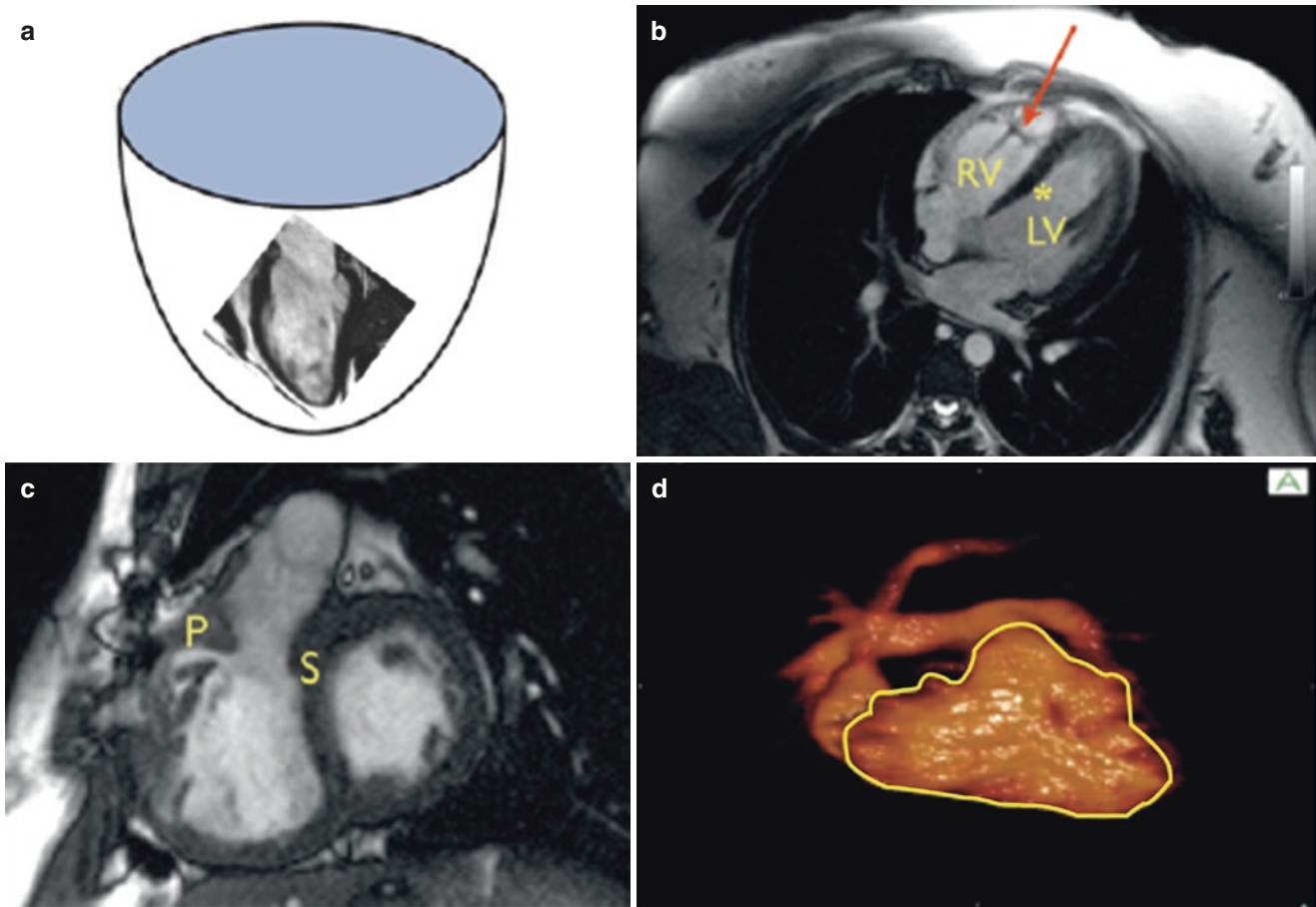


**Fig. 4.7** Normal left and right ventricular morphology. (a, b) The shape of the morphologically left ventricle most closely approximates the shape of a prolate ellipsoid (“bullet” shape). Other distinguishing features include a smooth basal septal surface (*asterisk*) and attachments of the mitral valve to the free wall rather than to the ventricular septum. (b) The shape of the morphologically right ventricle is a complex pyramidal shape with an inflow portion, a body and apex, and an outflow portion (infundibulum). The presence of the moderator band

(*arrow*) is a very reliable feature of a morphologically right ventricle. (c) Other distinguishing features include coarse trabeculations of the ventricular wall, septal band (*S*), parietal band (*P*), and attachments of the tricuspid valve to the ventricular septum as well as the free wall (“septophilic” attachments). (d) “Cast” of the right ventricle from a 3D volume rendered high resolution cardiac MR angiogram highlighting the complex geometry typical of an RV (yellow outline)

right (“tricuspid”) AV valves and connects to one of the great arteries. Just as in the case of DILV, in DIRV, there also exists a diminutive outflow chamber that connects to the other great artery. DILV and DIRV have also been referred to as types of “univentricular atrioventricular connections.”

Conversely, in the case of complete atrioventricular canal defect (AVCD), there are two distinct ventricles with one common AV valve rather than separate mitral and tricuspid valves (see below). When the common AV valve directs blood equally to the two ventricles, it is referred to as a “balanced” AVCD. This results in both ventricles being of adequate size. In “unbalanced” AVCD, however, the common AV valve orifice is directed preferentially toward one of the ventricles, causing the other to become hypoplastic and often not able to handle a full cardiac output. Thus, many patients

with unbalanced AVCD are not be candidates for standard surgical closure of the defect and may in fact require “single ventricle” surgical palliation [21].

#### 4.4.1 Unbalanced Right-Dominant Complete Atrioventricular Canal Defect (AVCD)

As described above, the complete form of the atrioventricular canal defect (AVCD), also known as “atrioventricular canal” or “atrioventricular septal defect,” is due to incomplete differentiation of the crux of the heart. This creates a primum atrial septal defect (ASD), an inlet ventricular septal defect (VSD), and failure of formation of the right and left halves of the atrioventricular canal which become the mitral and tricuspid valves

[22]. Physiologically, this can result in a large left-to-right shunt and congestive heart failure. AVCD commonly occurs as part of more complex CHD, extracardiac defects, and genetic syndromes. For example, approximately one-half of AVCD patients have Down syndrome [23, 24]. AVCD may also be combined with conotruncal defects (such as tetralogy of Fallot) in some patients, particularly in those with Down syndrome [24, 25]. In general, there are four basic types of AVCD: (1) complete, (2) intermediate, (3) transitional, and (4) partial (Fig. 4.8) [26]. In the complete form, the AV valve has one large common orifice and five or six rudimentary leaflets, along with significant primum ASD and inlet VSD components. In the intermediate form, there remain significant ASD and VSD components, but the AV valve has midline tissue dividing it into two distinct orifices. The transitional form is similar to the intermediate form, except that the VSD component is made smaller by dense attachments of the AV valve leaflets to the crest of the ventricular septum. The partial AVCD is characterized by simply a primum ASD and a cleft mitral valve, but no VSD. The tricuspid valve is usually normal. Note that all forms of AVCD, except the complete form, feature a “cleft” in the mitral valve that points toward the interventricular septum. In addition, based on the alignment of the common AV valve with the ventricles, the flow of blood may

be directed either equally to the two ventricles (“balanced” AVCD) or may favor one ventricle over the other (“unbalanced” AVCD). Unbalanced AVCD can be either right- or left-dominant, depending on which ventricle is larger (Fig. 4.9). A “balanced” complete AVCD is presented in Movie 4.1.

#### 4.4.2 Double Inlet Left Ventricle (DILV)

Double inlet left ventricle (DILV) is the most common form of “single ventricle” and occurs due to the persistence of the primitive state of the bulboventricular loop and failure of the atria to properly align themselves with the AV valves [27]. This results in the morphologically left ventricle receiving the inflow of both atria. In the majority of cases, the outflow of the left ventricle usually occurs via a transposed pulmonary artery, and the aorta arises from a rudimentary outflow chamber positioned anterior and leftward of the left ventricle (Fig. 4.10) [28]. Blood from the LV reaches the great artery arising from the outflow chamber via a bulboventricular foramen. This outflow pathway is prone to obstruction in the sub-valvar, valvar, and supra-valvar areas, as well as distally along length of the vessel. For example, in cases where the aorta arises from the diminutive outflow chamber, there is an

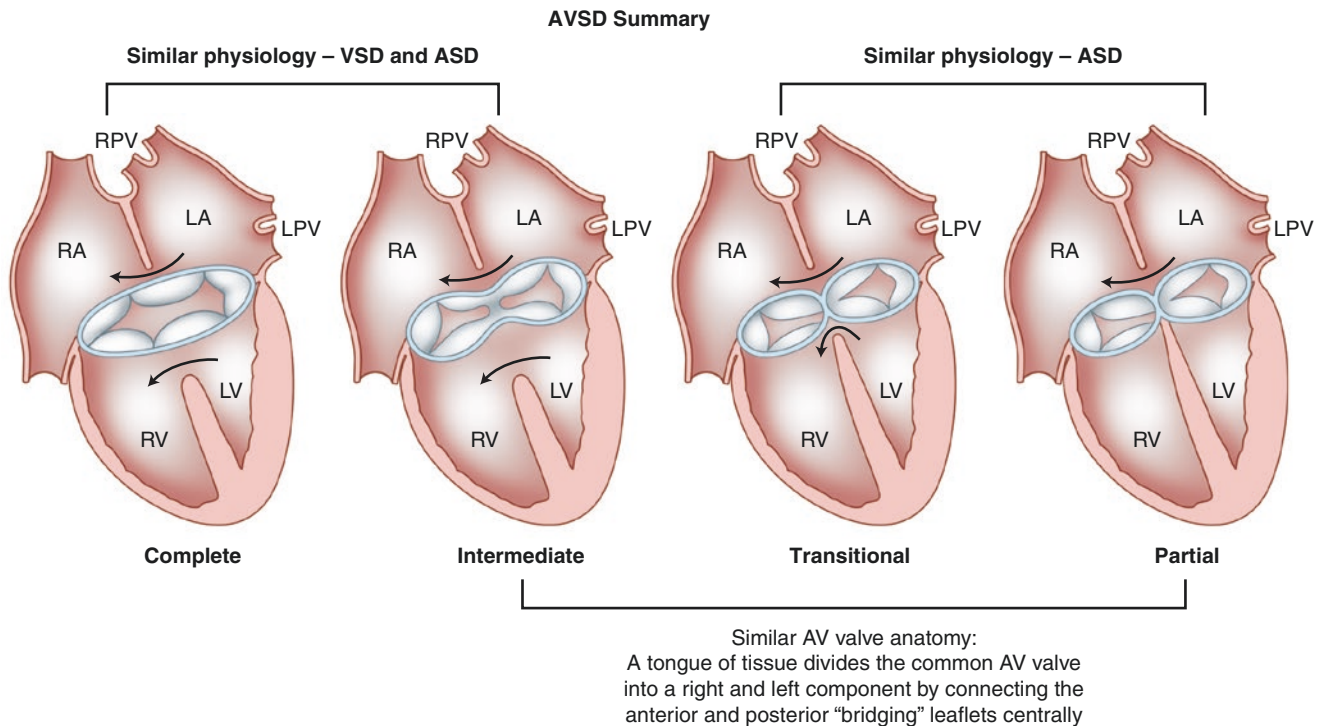


**Fig. 4.8** Summary of atrioventricular canal defects (AVCD) [26]. The four basic types of atrioventricular canal defects (AVCD). The “complete” AVCD features large primum ASD and inlet VSD components with a truly single common AV valve orifice. The “intermediate” form is similar to the complete form, but the AV valves have separate orifices, even though there remains a “cleft” in the mitral valve. The “transi-

itional” AVCD is similar to the intermediate form, but the AV valves have separate orifices, there is a mitral valve cleft, and there is a relatively smaller VSD component. In the “partial” form of AVCD, there is no VSD component, the tricuspid valve is normal, and the mitral valve is cleft. *ASD* atrial septal defect, *VSD* ventricular septal defect, *AV* atrioventricular



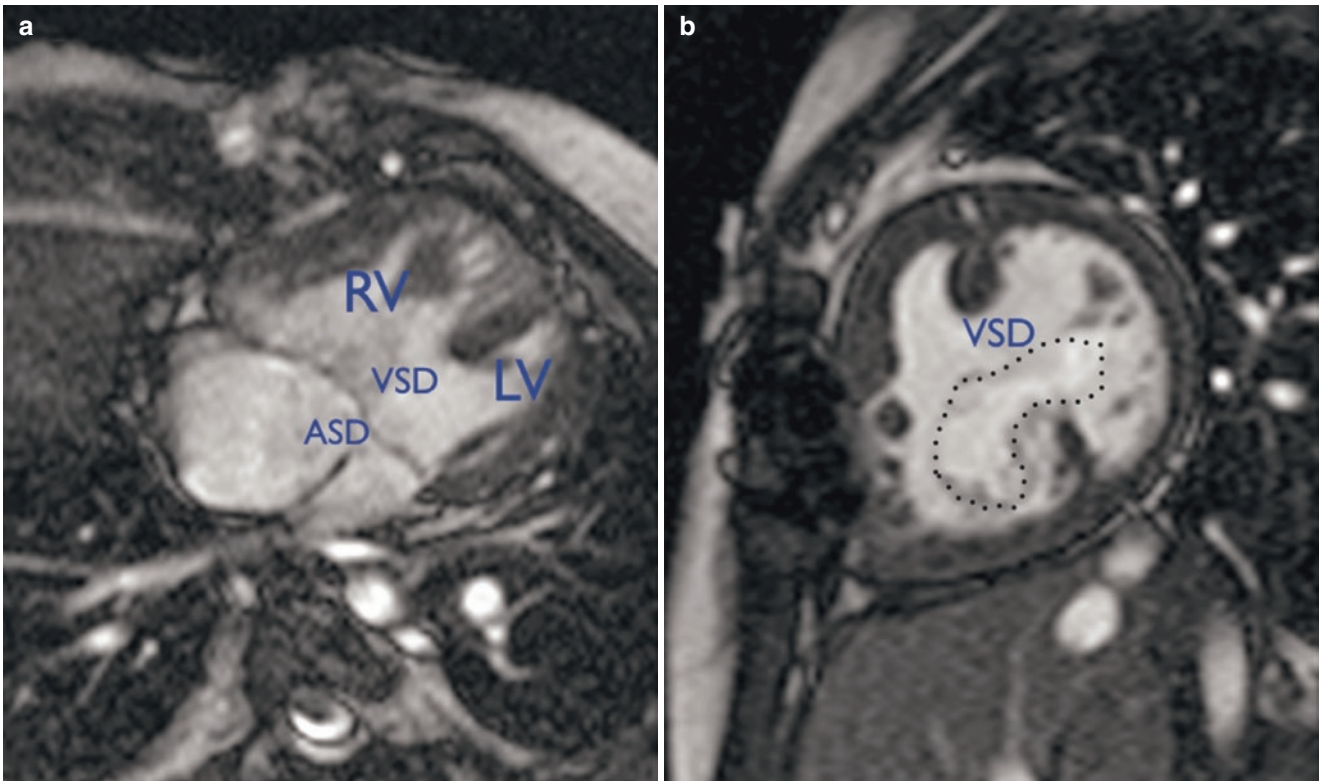


**Fig. 4.9** Unbalanced right-dominant AVCD. (a) SSFP MR imaging in the horizontal long axis (“four chamber”) view of a right-dominant AVCD. Clearly shown is the primum ASD, the large inlet VSD, and the common AV valve which spans across the cardiac crux and separates the ASD superiorly and the VSD inferiorly. Note the size discrepancy

between the ventricles with the RV being dominant. (b) SSFP MR imaging in the short axis plane. The common AV valve is disproportionately aligned with the RV, thus resulting in LV hypoplasia. SSFP steady-state free precession, ASD atrial septal defect, VSD ventricular septal defect, AV atrioventricular, RV right ventricle, LV left ventricle

increased risk of associated coarctation. In approximately 15% of cases, the great arteries are oriented normally, the so-called Holmes heart, with the aorta arising from the LV and the pulmonary artery from the outflow chamber. It is also possible to encounter a double inlet right ventricle (DIRV), but this lesion is considerably rarer.

Physiologically, all types of “functionally single ventricle” exhibit total mixing of venous and arterial blood at the atrial and/or ventricular levels. Depending on the balance of pulmonary versus systemic blood flow, the patient may be deeply cyanotic, less cyanotic but in congestive heart failure

from a large left-to-right shunt, or have relatively well-balanced systemic and pulmonary circulations with mild cyanosis but not in congestive heart failure.

Management of patients with single ventricle anatomy consists of a staged surgical strategy with the goal of separating the systemic venous circulation from the heart. First, the superior vena cava is anastomosed directly to the branch pulmonary arteries. Later, this strategy culminates in the Fontan surgery where the inferior vena cava is also redirected to the branch pulmonary arteries using an artificial conduit (see Fig. 4.11 and Movie 4.2).



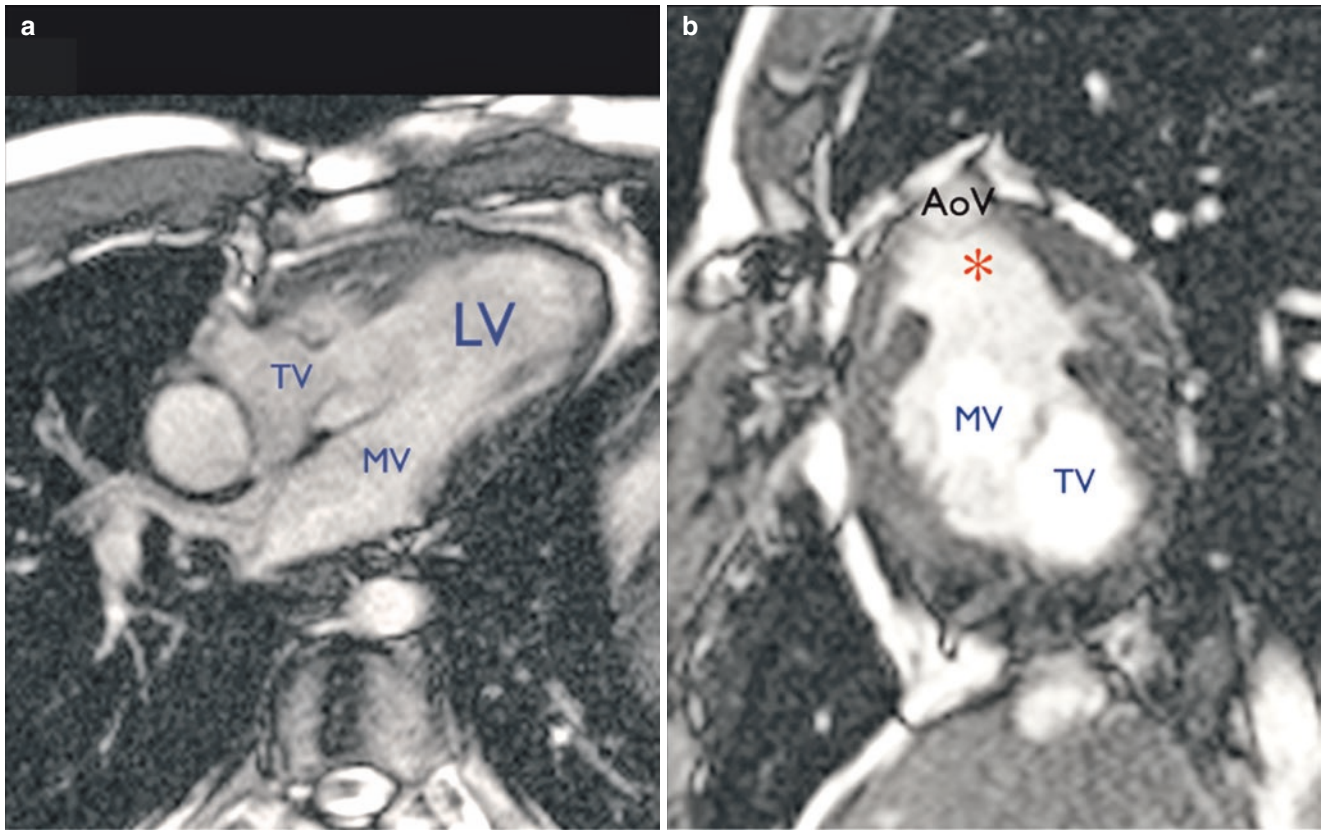


**Fig. 4.10** Double inlet left ventricle (DILV) [28]. (a) SSFP MR imaging in the horizontal long axis (“four chamber”) view of a patient with DILV. Both the left AV or “mitral” (MV) and right AV or “tricuspid” valves (TV) are aligned with the single left ventricle (LV). (b) SSFP MR imaging in the short axis plane. Note that both atrioventricular

are clearly aligned with the left ventricle (LV). The aortic valve (AoV) arises from the anterior and leftward diminutive “outflow chamber” (asterisk), as there is no true right ventricle in this lesion. AV atrioventricular

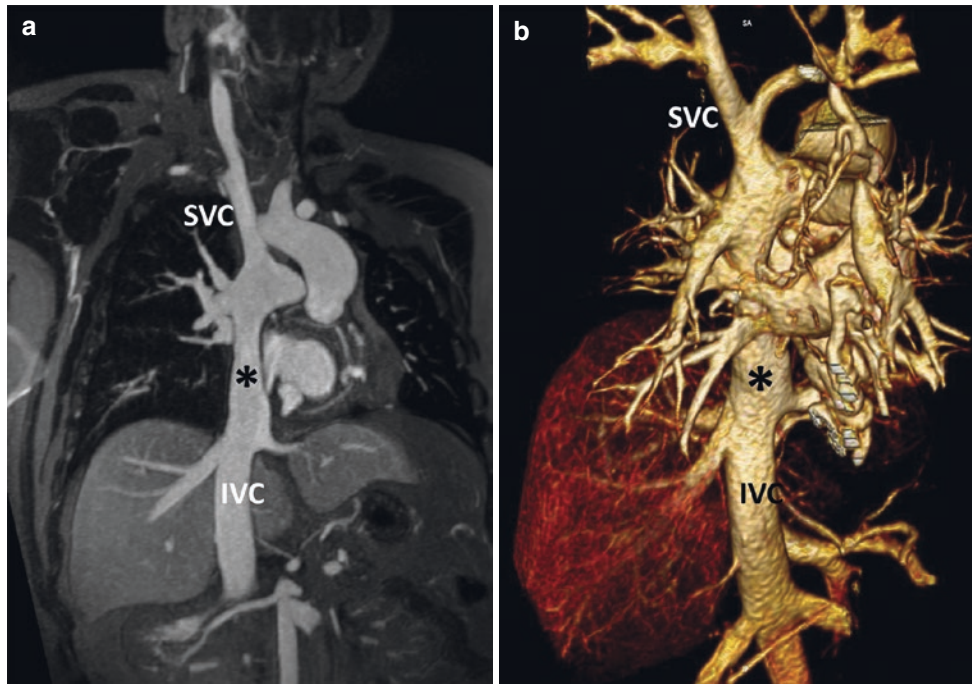


**Fig. 4.11** Fontan circulation in two adult patients with single ventricle anatomy who have undergone surgical Fontan completion. (a) Ferumoxytol-enhanced MR angiogram 3D multiplanar reconstruction in the coronal plane demonstrating connections of the superior vena cava (SVC) and the inferior vena cava (IVC) to the branch pulmonary arteries. The extracardiac artificial Fontan conduit connecting the IVC

to the pulmonary circulation is noted by the black asterisk. The native SVC was directly anastomosed to the branch pulmonary arteries during a prior surgery. (b) Posterior projection of a 3D volume rendered ferumoxytol-enhanced MR angiogram in a different patient with situs inversus who required a *left*-sided Fontan connection. The black asterisk again denotes the Fontan conduit

## 4.5 Ventriculo-Arterial Connections

Embryologically, both the aortic and pulmonary valves become associated with a “pedestal” of tissue known as the conus arteriosus overlying the morphologically RV. According to one prominent theory, beginning at approximately 30–34 days of gestation, the conus under the aortic valve begins to resorb. This allows for the aortic valve to move into its conventional position posterior and rightward of the pulmonary valve. When the subaortic conus persists and the sub-pulmonary conus resorbs instead, the aortic valve position is anterior and rightward of the pulmonary valve and becomes associated with the RV, leaving the pulmonary valve to connect to the LV. If the ventricles are normally looped, this “dextro-transposition” of the aortic valve may lead to a condition known as d-loop or complete transposition of the great arteries (TGA) (see below) [29]. Alternatively, when both sides of the conus fail to resorb, association of both the aortic and pulmonary valves with the RV occurs and is termed “double outlet right ventricle.”

### 4.5.1 D-Loop Transposition of the Great Arteries (D-Loop TGA, Complete TGA)

In d-loop TGA, the aorta is positioned anterior and rightward of the pulmonary artery and is connected to the morphologically RV, while the pulmonary artery arises more posteriorly and leftward from the LV (Fig. 4.12 and Movie 4.3). It is the most commonly encountered type of “discordance” of the ventriculo-arterial connections, occurring in approximately 2.4 in 10,000 live births [30]. D-loop TGA is often found in isolation with no other associated cardiac or extracardiac pathology. The most common subtype is “simple” d-loop TGA. That is, the ventricles are normally looped, and there are no associated ventricular septal defects (VSD) or other cardiac abnormalities. A VSD may be present in approximately one-half of patients and has been termed “complex” d-loop TGA. With a VSD present, there may be associated pulmonary valve stenosis/atresia, sub-valvar pulmonary stenosis, or coarctation of the aorta [31].

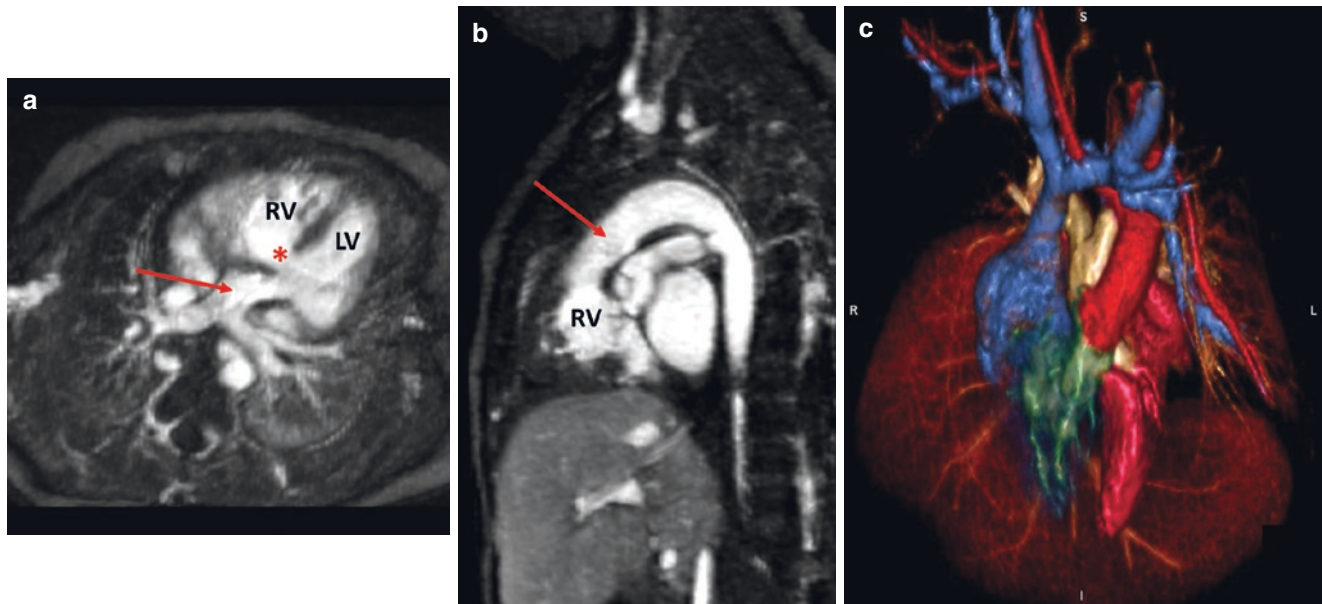


**Fig. 4.12** D-loop transposition of the great arteries (d-TGA) in a neonate. Ferumoxylol-enhanced MR angiogram 3D multiplanar reconstruction in the axial and sagittal planes (**a**, **b**). (**a**) The pulmonary artery (red arrow) arises posteriorly from the left ventricle (LV). There is a ventricular septal defect (VSD) present as noted by the red asterisk. (**b**)

The aorta (red arrow) arises anteriorly from the right ventricle (RV). (**c**) Anterior projection of a colorized 3D volume rendering in the same patient demonstrating the anterior aorta arising from the RV (both colored in red). The more posterior pulmonary artery is shown colored in gold

Physiologically, deoxygenated blood from the RV is distributed to the systemic circulation via the transposed aorta. Oxygenated blood is sent back to the lungs, resulting in inefficient gas exchange. As a result, profound cyanosis may occur, particularly in the absence of adequate intermixing between the two circulations. Mixing usually occurs via an atrial septal defect, VSD, and/or patent ductus arteriosus. Inadequate mixing will eventually lead to worsening cyanosis and death if not promptly addressed.

#### 4.5.2 L-Loop Transposition of the Great Arteries (“Congenitally Corrected” Transposition)

In contrast to d-loop TGA, the l-loop variety is considerably less common, occurring in approximately 2–7 in 100,000 live births or 0.5% of all CHD [30, 32]. L-loop TGA is characterized by “doubly discordant” atrioventricular and ventriculo-arterial connections. As the name implies the ventricles are l-looped. This allows for the alignment of the morphologically RV with the morphologically left atrium and vice versa for the right atrium and LV. The aortic valve in this condition is most often positioned anterior and leftward of

the pulmonary valve and is connected to the right ventricle. As such, patients are not typically cyanotic because oxygenated blood from the left atrium courses to the aorta, albeit via a “systemic” right ventricle. It is for this reason that l-loop TGA has been referred to as “congenitally corrected” or “physiologically corrected” transposition.

The vast majority of l-loop TGA patients have associated cardiac structural abnormalities. These include VSD, left ventricular outflow tract (sub-pulmonary) stenosis, Ebstein’s malformation of the tricuspid valve, mitral valve dysplasia, and a 2% per year incidence of spontaneous complete heart block [32]. In addition, dextrocardia or mesocardia may be seen in association with l-loop TGA [33].

#### 4.6 Arterial Malformations (Vascular Rings and Slings)

Certain malformations of the aorta and pulmonary arteries exist that may lead to external tracheal and/or esophageal compression [34]. The most common types are presented in Table 4.4. A complete vascular “ring” occurs when various components of the aortic arch and ligamentum arteriosum completely encircle the trachea and esophagus causing vari-



**Table 4.4** Most common vascular malformations causing external tracheal and/or esophageal compression

Left aortic arch with aberrant right subclavian artery (incomplete vascular ring)
Double aortic arch (complete vascular ring)
Right aortic arch with aberrant left subclavian artery (from a diverticulum of Kommerell) and left ligamentum arteriosum (complete vascular ring)
Left pulmonary artery sling

Adapted from Kussman et al. [35]

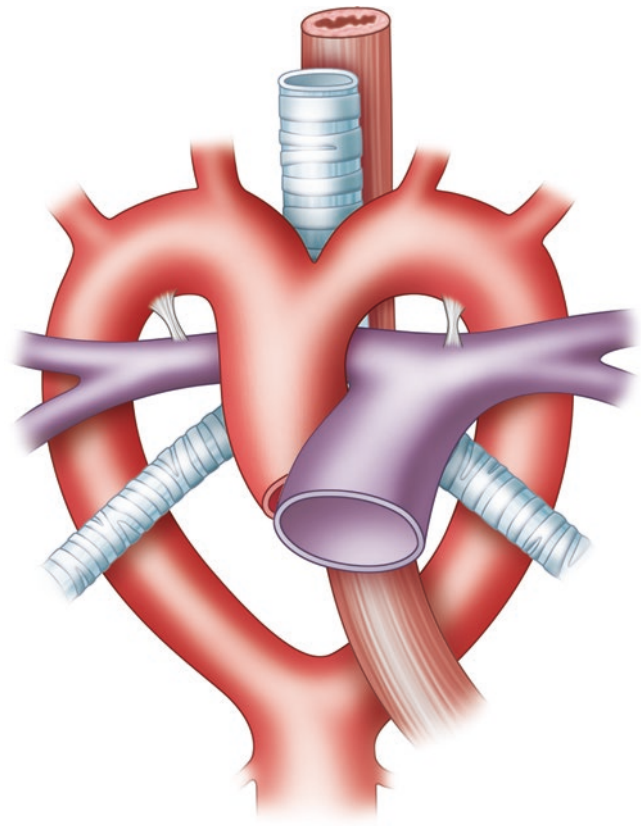
able degrees of external compression of these structures. With incomplete vascular rings, and in the case of a vascular “sling,” tracheal and/or esophageal compression can occur, but the involved vascular components do not completely encircle the trachea and esophagus.

Vascular rings and slings arise from aberrations in the complex sequence of formation and regression of the six pairs of embryonic aortic arches that connect the truncus arteriosus and aortic sac with the paired dorsal aortae. This process has been well described elsewhere [34, 36]. Edwards proposed a simplified model of the various types of vascular rings and slings by way of a conceptual “hypothetical double arch with bilateral ductus arteriosus” model (Fig. 4.13) [37]. The Edwards model may be further simplified into a series of line drawings, as shown in Fig. 4.14 [34]. By imagining the regression of specific segments of this double arch, one may arrive at the various types of existing aortic arch anomalies (Fig. 4.14).

Although aortic arch anomalies consist of less than 1% of all CHD, they may cause varying degrees of tracheal and/or esophageal compression and can be diagnosed early in life. Some cases are not diagnosed until adulthood and others may never be diagnosed at all. In the patient with significant wheezing, stridor, feeding intolerance, and/or recurrent airway obstruction, it is important to maintain a high index of suspicion for vascular malformations, particularly when other more common causes have been ruled out [35].

#### 4.6.1 Complete Vascular Rings

The most common complete vascular ring is the double aortic arch. In this lesion, the two aortic arches persist and surround the trachea and esophagus (Fig. 4.14a). In only 5% of cases are both arches patent, however. In up to 80% of the time the right arch is patent and the left arch is atretic. The left arch is patent and the right arch atretic in the remainder of cases [38]. It is important to remember that atretic arch segments are not usually visualized by imaging techniques

**Fig. 4.13** Edwards' hypothetical “double aortic arch with bilateral ductus arteriosus” model [34]

and must be inferred based upon the appearance of vascular outpouchings or based on knowledge of their typical location. This also holds true for the ductus arteriosus portion of vascular rings.

The second most common complete vascular ring is formed by a right aortic arch with aberrant left subclavian artery and a left ductus arteriosus (Fig. 4.14c and Movie 4.4). In this lesion, the ring is formed by the left common carotid artery, the transverse aortic arch, a posterior aberrant left subclavian artery, and the left-sided ductus arteriosus. The left subclavian artery arises from a remnant of the left fourth arch called the diverticulum of Kommerell, which encircles the esophagus posteriorly [38].

#### 4.6.2 Incomplete Vascular Ring

A left aortic arch with an aberrant right subclavian artery is the most common aortic arch variant with an incidence of approximately 0.5% in the general population (Fig. 4.14b)



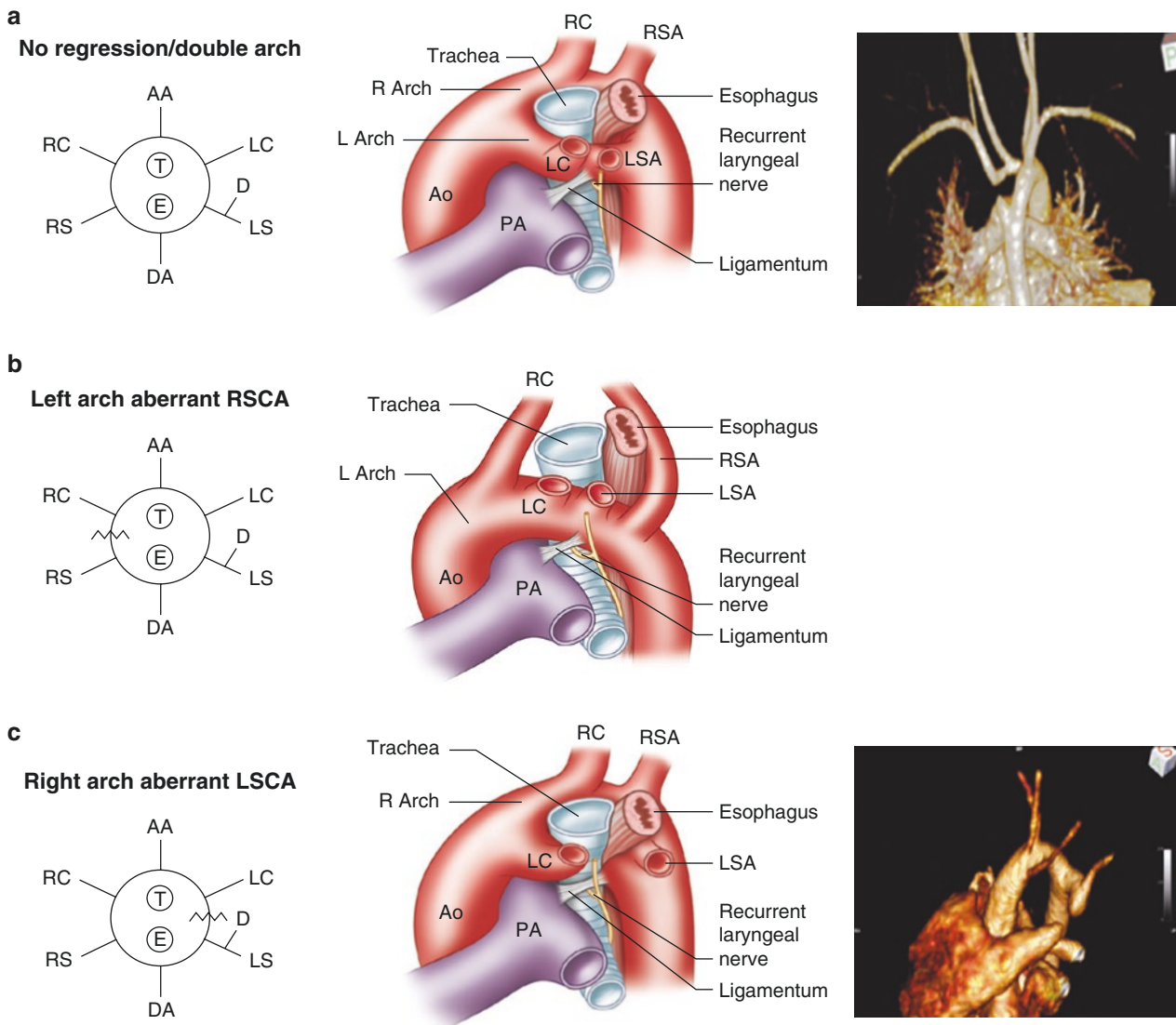


**Fig. 4.14** Vascular rings [34, 38]. Line diagram illustrating the origin of various types of vascular rings and slings (derived from Edwards' double arch model shown in Fig. 4.13). (a) The double aortic arch is the most common type of vascular ring. In this lesion, neither of the dorsal aortae regresses. The *right most* panel is a 3D volume rendered MR angiogram of a double aortic arch with an atretic left arch. The atretic

arch does not fill with contrast, and thus its presence must be inferred. (b) Left aortic arch with aberrant right subclavian artery is an incomplete ring and, as such, infrequently causes symptoms. (c) Right aortic arch with aberrant left subclavian artery is the second most common type of vascular ring. The *right most* panel is a 3D volume rendered MR angiogram of this lesion

[39]. This variation of aorta anatomy forms an incomplete vascular ring as the aberrant right subclavian compresses the esophagus posteriorly as it traverses toward the right arm. This anatomic variant only rarely has any clinical consequences.

### 4.6.3 Left Pulmonary Sling

In left pulmonary artery sling, the left branch pulmonary artery arises more distally than normal, branching directly off of the right pulmonary artery. The left pulmonary artery then courses around the right bronchus and then between the trachea and esophagus in order to reach the left lung hilum (Fig. 4.15). Approximately half of patients may have associated complete tracheal rings rather than the normal “C-” shaped tracheal rings. Posterior tracheal compression from the left pulmonary artery in conjunction with tracheal luminal narrowing by the complete tracheal rings often manifests as stridor, wheezing, and recurrent pneumonia in the neonatal period [40].

### 4.6.4 Coarctation of the Aorta

Narrowing of the aortic isthmus is termed coarctation of the aorta and occurs in 6–8% of infants born with CHD [41]. Severe coarctation most often presents in the first 1–2 weeks of life. After the patent ductus arteriosus closes, there may be inadequate blood flow to the lower body leading to circulatory shock. The typical location of the narrowing is “juxtaductal,” which is the area of the aortic isthmus opposite the

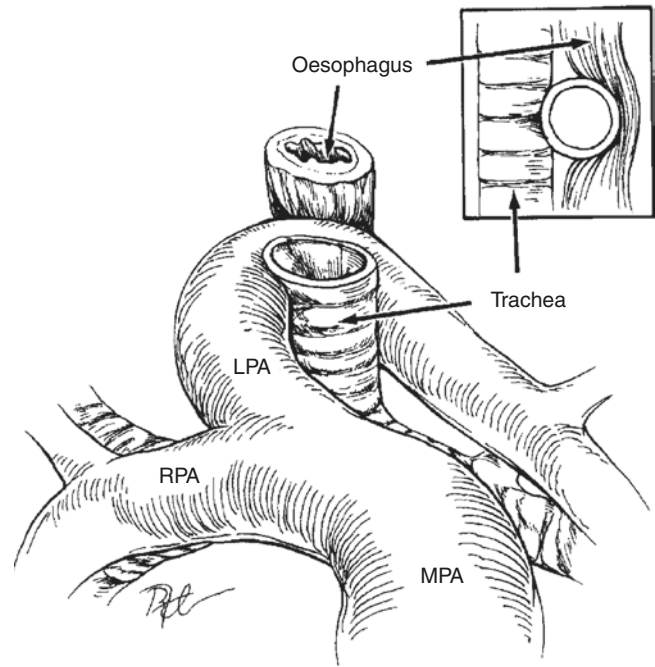


**Fig. 4.15** Left pulmonary artery sling [38]. The left pulmonary artery arises more distally off the right pulmonary artery and makes an acute turn, coursing in between the trachea and esophagus to reach the left lung hilum. This causes the classic anterior compression of the esophagus seen on conventional upper GI imaging

insertion of the ductus arteriosus (Fig. 4.16). There is often an associated long-segment narrowing of the transverse aortic arch proximal to the area of coarctation. Other associated defects include bicuspid aortic valve, ventricular septal defects, and mitral valve abnormalities.

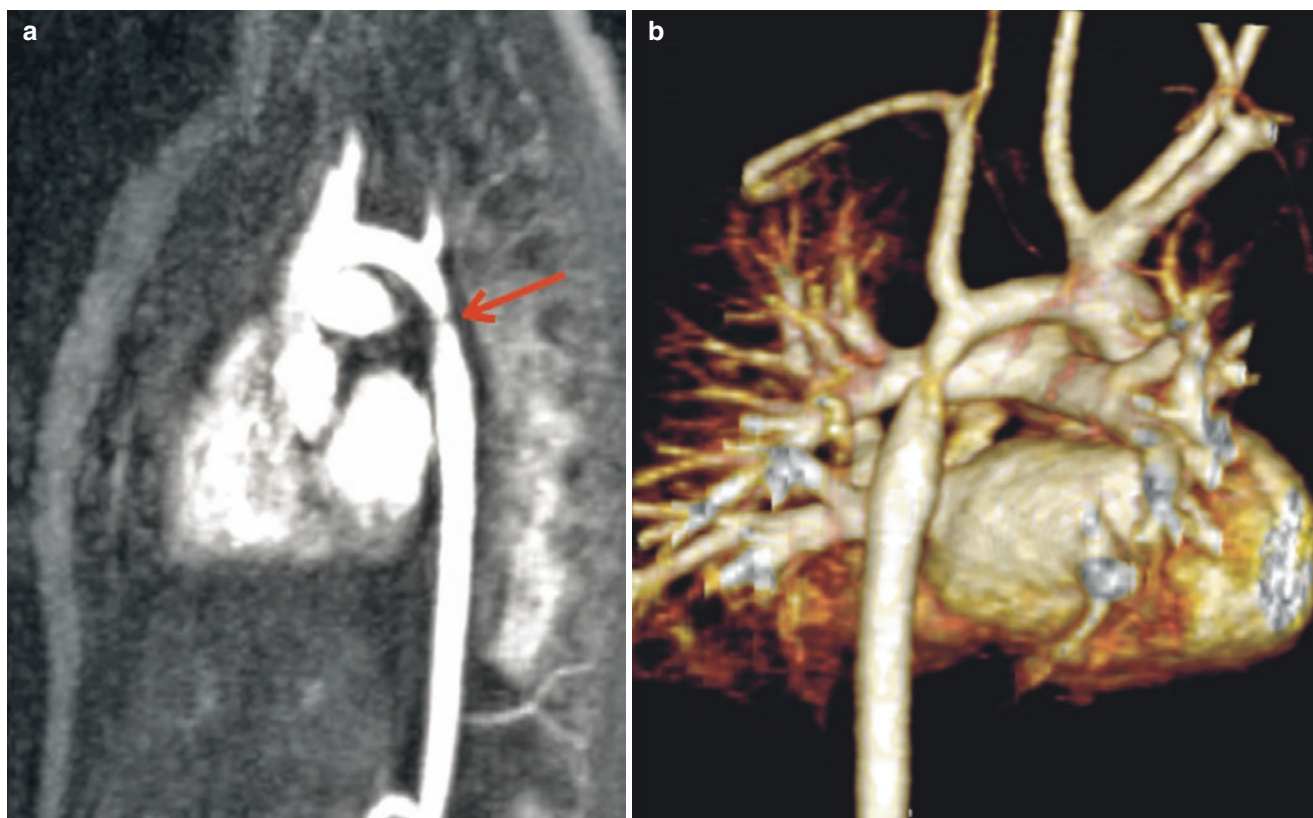


**Fig. 4.16** Coarctation of the aorta. (a) MR contrast-enhanced angiogram 3D multiplanar reconstruction in the sagittal plane demonstrating a juxtaductal coarctation of the aorta (*red arrow*) in a neonate. (b) 3D volume rendered MR contrast-enhanced angiogram of the same

#### 4.7 Conclusion

CMR imaging is ideally suited for the characterization of congenital anatomic and physiologic aberrations of the cardiovascular system. The advantages of CMR over other imaging modalities include its noninvasive nature, absence of ionizing radiation, the use of a non-iodinated contrast agent, comprehensive view of both the intracardiac structures and extra-cardiac vasculature, quantification of blood flow, and myocardial tissue characterization. Continuing technical developments in the areas of image processing speed, increased spatial resolution, and machine learning will ensure CMR's integral role in the comprehensive assessment of patients with congenital heart disease [42, 43].

#### Practical Pearls

- CMR imaging allows for a comprehensive assessment of intracardiac structures, extra-cardiac vasculature, and blood flow.
- The noninvasive nature of CMR and the lack of ionizing radiation and iodinated contrast make CMR imaging advantageous for congenital heart disease patients who require serial lifelong imaging studies.

- In the initial diagnosis and serial evaluation of congenital heart disease, CMR should be considered complimentary to other traditional imaging techniques such as echocardiography and cardiac catheterization.
- CMR in congenital heart disease is ideally performed and interpreted in concert with specially trained radiologists, cardiologists, and cardiothoracic surgeons.

#### References

1. Praagh RV, Praagh SV. Morphologic anatomy. In: Keane JF, Flyer DC, Lock J, editors. *Nadas' pediatric cardiology*. 2nd ed. Philadelphia, PA: Saunders Elsevier; 2006. p. 27–37.
2. Praagh RV. Segmental approach to diagnosis. In: Keane JE, Flyer DC, Lock J, editors. *Nadas' pediatric cardiology*. 2nd ed. Philadelphia, PA: Saunders Elsevier; 2006. p. 39–46.
3. Jacobs JP, Anderson RH, Weinberg PM, Walters HL III, Tchervenkov CI, Del Duca D, et al. The nomenclature, definition and classification of cardiac structures in the setting of heterotaxy. *Cardiol Young*. 2007;17(Suppl 2):1–28. <https://doi.org/10.1017/S1047951107001138>.
4. Cohen MS, Anderson RH, Cohen MI, Atz AM, Fogel M, Gruber PJ, et al. Controversies, genetics, diagnostic assessment, and outcomes relating to the heterotaxy syndrome. *Cardiol Young*. 2007;17(Suppl 2):29–43. <https://doi.org/10.1017/S104795110700114X>.
5. Bartram U, Wirbelauer J, Speer CP. Heterotaxy syndrome -- asplenia and polysplenia as indicators of visceral malposition and com-

- plex congenital heart disease. *Biol Neonate*. 2005;88(4):278–90. <https://doi.org/10.1159/000087625>.
6. Peoples WM, Moller JH, Edwards JE. Polysplenia: a review of 146 cases. *Pediatr Cardiol*. 1983;4(2):129–37. <https://doi.org/10.1007/BF02076338>.
  7. Van Mierop L, Gessner I, Schiebler GL. Asplenia and polysplenia syndrome. *Birth Defects*. 1972;8:74–84.
  8. Poh CL, Cordina RL, Iyengar AJ, Zannino D, Grigg LE, Wheaton GR, et al. Pre- and post-operative determinants of transplantation-free survival after Fontan. The Australia and New Zealand experience. *Int J Cardiol Heart Vasc*. 2021;35:100825. <https://doi.org/10.1016/j.ijcha.2021.100825>.
  9. Geva T, Vick GW III, Wendt RE, Rokey R. Role of spin echo and cine magnetic resonance imaging in presurgical planning of heterotaxy syndrome. Comparison with echocardiography and catheterization. *Circulation*. 1994;90(1):348–56. <https://doi.org/10.1161/01.cir.90.1.348>.
  10. Hong YK, Park YW, Ryu SJ, Won JW, Choi JY, Sul JH, et al. Efficacy of MRI in complicated congenital heart disease with visceral heterotaxy syndrome. *J Comput Assist Tomogr*. 2000;24(5):671–82. <https://doi.org/10.1097/00004728-200009000-00002>.
  11. Edwards WD. Cardiac anatomy and examination of cardiac specimens. In: Allen HD, Driscoll D, Shaddy RE, Feltes TF, editors. *Moss and Adams' heart disease in infants, children, and adolescents*. Philadelphia, PA: Lippincott Williams & Wilkins; 2008. p. 2–33.
  12. Mazzucco A, Bortolotti U, Stellin G, Gallucci V. Anomalies of the systemic venous return: a review. *J Card Surg*. 1990;5(2):122–33. <https://doi.org/10.1111/j.1540-8191.1990.tb00749.x>.
  13. Celentano C, Malinger G, Rotmensch S, Gerboni S, Wolman Y, Glezerman M. Prenatal diagnosis of interrupted inferior vena cava as an isolated finding: a benign vascular malformation. *Ultrasound Obstet Gynecol*. 1999;14(3):215–8. <https://doi.org/10.1046/j.1469-0705.1999.14030215.x>.
  14. Pappone C, Rosanio S, Oreto G, Tocchi M, Gugliotta F, Vicedomini G, et al. Circumferential radiofrequency ablation of pulmonary vein ostia: a new anatomic approach for curing atrial fibrillation. *Circulation*. 2000;102(21):2619–28. <https://doi.org/10.1161/01.cir.102.21.2619>.
  15. Beinart R, Nazarian S. Role of magnetic resonance imaging in atrial fibrillation ablation. *Curr Treat Opt Cardiovasc Med*. 2014;16(6):316. <https://doi.org/10.1007/s11936-014-0316-3>.
  16. Stein P. Total anomalous pulmonary venous connection. *AORN J*. 2007;85(3):509–20. [https://doi.org/10.1016/S0001-2092\(07\)60123-9](https://doi.org/10.1016/S0001-2092(07)60123-9); quiz 21–4.
  17. Reardon MJ, Cooley DA, Kubrusly L, Ott DA, Johnson W, Kay GL, et al. Total anomalous pulmonary venous return: report of 201 patients treated surgically. *Tex Heart Inst J*. 1985;12(2):131–41.
  18. Keane JF, Flyer DC. Total anomalous pulmonary venous return. In: Keane JF, Lock JE, Flyer DC, editors. *Nadas' pediatric cardiology*. 2nd ed. Philadelphia, PA: Saunders Elsevier; 2006. p. 773–81.
  19. Dorosz JL, Bolson EL, Waiss MS, Sheehan FH. Three-dimensional visual guidance improves the accuracy of calculating right ventricular volume with two-dimensional echocardiography. *J Am Soc Echocardiogr*. 2003;16(6):675–81. [https://doi.org/10.1016/s0894-7317\(03\)00226-8](https://doi.org/10.1016/s0894-7317(03)00226-8).
  20. Kuhl HP, Schreckenber M, Rulands D, Katoh M, Schafer W, Schummers G, et al. High-resolution transthoracic real-time three-dimensional echocardiography: quantitation of cardiac volumes and function using semi-automatic border detection and comparison with cardiac magnetic resonance imaging. *J Am Coll Cardiol*. 2004;43(11):2083–90. <https://doi.org/10.1016/j.jacc.2004.01.037>.
  21. Owens GE, Gomez-Fifer C, Gelehrter S, Owens ST. Outcomes for patients with unbalanced atrioventricular septal defects. *Pediatr Cardiol*. 2009;30(4):431–5. <https://doi.org/10.1007/s00246-008-9376-z>.
  22. Rogers HM, Edwards JE. Incomplete division of the atrioventricular canal with patent inter-atrial foramen primum, persistent common atrioventricular ostium; report of five cases and review of the literature. *Am Heart J*. 1948;36(1):28–54. [https://doi.org/10.1016/0002-8703\(48\)90545-6](https://doi.org/10.1016/0002-8703(48)90545-6).
  23. Dunlop KA, Mulholland HC, Casey FA, Craig B, Gladstone DJ. A ten year review of atrioventricular septal defects. *Cardiol Young*. 2004;14(1):15–23. <https://doi.org/10.1017/s1047951104001040>.
  24. Geva T, Ayres NA, Pignatelli RH, Gajarski RJ. Echocardiographic evaluation of common atrioventricular canal defects: a study of 206 consecutive patients. *Echocardiography*. 1996;13(4):387–400. <https://doi.org/10.1111/j.1540-8175.1996.tb00910.x>.
  25. Laursen HB. Congenital heart disease in Down's syndrome. *Br Heart J*. 1976;38(1):32–8. <https://doi.org/10.1136/hrt.38.1.32>.
  26. Cetta F, Minich L, Edwards WD, Dearani JA, Puga FJ. Atrioventricular septal defects. In: Allen HD, Driscoll D, Shaddy RE, Feltes TF, editors. *Moss and Adams' heart disease in infants, children, and adolescents*. 7th ed. Philadelphia, PA: Lippincott Williams & Wilkins; 2008. p. 647–67.
  27. Lev M, Liberthson RR, Kirkpatrick JR, Eckner FA, Arcilla RA. Single (primitive) ventricle. *Circulation*. 1969;39(5):577–91. <https://doi.org/10.1161/01.cir.39.5.577>.
  28. Keane JF, Flyer D. Single ventricle. In: Keane JF, Lock J, Flyer DC, editors. *Nadas' pediatric cardiology*. 2nd ed. Philadelphia, PA: Saunders Elsevier; 2006. p. 743–51.
  29. Fulton DR, Flyer D. D-transposition of the great arteries. *Nadas' pediatric cardiology*. 2nd ed. Philadelphia, PA: Saunders Elsevier; 2006. p. 645–61.
  30. Botto LD, Correa A, Erickson JD. Racial and temporal variations in the prevalence of heart defects. *Pediatrics*. 2001;107(3):E32. <https://doi.org/10.1542/peds.107.3.e32>.
  31. Blume ED, Altmann K, Mayer JE, Colan SD, Gauvreau K, Geva T. Evolution of risk factors influencing early mortality of the arterial switch operation. *J Am Coll Cardiol*. 1999;33(6):1702–9. [https://doi.org/10.1016/s0735-1097\(99\)00071-6](https://doi.org/10.1016/s0735-1097(99)00071-6).
  32. Hornung TS, Calder L. Congenitally corrected transposition of the great arteries. *Heart*. 2010;96(14):1154–61. <https://doi.org/10.1136/hrt.2008.150532>.
  33. Van Praagh R, Van Praagh S. Anatomically corrected transposition of the great arteries. *Br Heart J*. 1967;29(1):112–9. <https://doi.org/10.1136/hrt.29.1.112>.
  34. Powell AJ, Mandell V. Vascular rings and slings. In: Keane JF, Lock J, Flyer DC, editors. *Nadas' pediatric cardiology*. 2nd ed. Philadelphia, PA: Saunders Elsevier; 2006. p. 811–23.
  35. Kussman BD, Geva T, McGowan FX. Cardiovascular causes of airway compression. *Paediatr Anaesth*. 2004;14(1):60–74. <https://doi.org/10.1046/j.1460-9592.2003.01192.x>.
  36. Kellenberger CJ. Aortic arch malformations. *Pediatr Radiol*. 2010;40(6):876–84. <https://doi.org/10.1007/s00247-010-1607-9>.
  37. Edwards JE. Anomalies of the derivatives of the aortic arch system. *Med Clin North Am*. 1948;32:925–49. [https://doi.org/10.1016/s0025-7125\(16\)35662-0](https://doi.org/10.1016/s0025-7125(16)35662-0).
  38. Dodge-Khatami A, Tulevski II, Hitchcock JF, de Mol BA, Bennink GB. Vascular rings and pulmonary arterial sling: from respiratory collapse to surgical cure, with emphasis on judicious imaging in the hi-tech era. *Cardiol Young*. 2002;12(2):96–104. <https://doi.org/10.1017/s1047951102000239>.
  39. Edwards JE. Malformations of the aortic arch system manifested as vascular rings. *Lab Invest*. 1953;2(1):56–75.
  40. Fiore AC, Brown JW, Weber TR, Turrentine MW. Surgical treatment of pulmonary artery sling and tracheal stenosis. *Ann Thorac Surg*. 2005;79(1):38–46. <https://doi.org/10.1016/j.athoracsur.2004.06.005>; discussion 38–46.
  41. Beekman RH. Coarctation of the aorta. In: Allen HD, Driscoll D, Shaddy RE, Feltes TF, editors. *Coarctation of the aorta*. 7th



- ed. Philadelphia, PA: Lippincott Williams & Wilkins; 2008. p. 987–1005.
42. Kocaoglu M, Pednekar AS, Wang H, Alsaied T, Taylor MD, Rattan MS. Breath-hold and free-breathing quantitative assessment of biventricular volume and function using compressed SENSE: a clinical validation in children and young adults. *J Cardiovasc Magn Reson*. 2020;22(1):54. <https://doi.org/10.1186/s12968-020-00642-y>.
43. Nguyen KL, Ghosh RM, Griffin LM, Yoshida T, Bedayat A, Rigsby CK, et al. Four-dimensional multiphase steady-state MRI with ferumoxytol enhancement: early multicenter feasibility in pediatric congenital heart disease. *Radiology*. 2021;300(1):162–73. <https://doi.org/10.1148/radiol.2021203696>.



## 5.1 Introduction

Congenital venous anomalies of the thorax may be encountered in patients with documented congenital heart disease, those patients with abnormal echocardiographic findings (e.g., dilated right ventricle or pulmonary hypertension), or, unexpectedly, in patients having CT scan or magnetic resonance examination of the thorax for other reasons. These anomalies can range from the clinically important (partial anomalous pulmonary venous connection) to the clinically inconsequential (persistent left superior vena cava), and it is essential for the physician to be able to identify these anomalies (plus associated intracardiac and extracardiac defects) in order to decide whether further imaging and investigation are warranted.

Cardiac magnetic resonance imaging can detect the simple and the complex thoracic venous anomalies. It has the advantages of wide field of view, multiplanar capability without being restricted by anatomic limitations, ability to assess both structure and function, ability to reliably measure flow through the use of phase-contrast mapping, the ability to rapidly acquire 3-D imaging with MR angiography [1], and the lack of ionizing radiation. There are some disadvantages

of cardiac magnetic resonance imaging to consider, and these include metal-related artifact (an important factor in patients with treated congenital heart disease), the amount of time required for imaging, the cost of cardiac magnetic resonance imaging, concerns about claustrophobia, and patient sedation. Even though pacemakers and ICDs had been a contraindication to MR imaging in the past, newer implantable devices and scanning protocols have now permitted the use of MR imaging in many of these patients.

There have also been concerns about the use of gadolinium and nephrogenic systemic fibrosis (NSF), but recently introduced agents appear to carry smaller risks of NSF (Chap. 2). Nevertheless, gadolinium-enhanced MR angiography may not be necessary in all cases. Adequate visualization of anomalous veins has been demonstrated to be possible without the use of gadolinium [2, 3], and there have been recent reports of novel techniques without the use of intravenous contrast agent that image the pulmonary veins and arteries just as well as contrast-enhanced MRA [4].

Congenital thoracic venous anomalies are classified as pulmonary venoatrial anomalies (Table 5.1) or systemic venous anomalies (Table 5.2). The pulmonary venoatrial anomalies are the more likely to be of clinical significance and to have associated cardiac defects. It is, nevertheless, still important to identify the systemic venous anomalies because they may be confused with more important pulmonary venous anomalies and may lead to unnecessary further imaging and investigation.

---

**Supplementary Information** The online version contains supplementary material available at [https://doi.org/10.1007/978-3-031-29235-4\\_5](https://doi.org/10.1007/978-3-031-29235-4_5).

---

H. Kafka (✉)  
Department of Cardiology, Queen's University, Kingston Health Sciences Centre, Kingston, ON, Canada

R. H. Mohiaddin  
Cardiovascular Imaging, Royal Brompton and Harefield Hospitals, Guy's and St Thomas' NHS Foundation Trust, London, UK

National Heart and Lung Institute, Imperial College London, London, UK  
e-mail: [R.Mohiaddin@rbht.nhs.uk](mailto:R.Mohiaddin@rbht.nhs.uk)

**Table 5.1** Pulmonary venoatrial anomalies

1. Partial anomalous pulmonary venous connection
(a) Right-sided veins
• Superior vena cava or right atrium
• Scimitar
• Azygos
(b) Left-sided veins
• Left innominate
• Inferior vena cava, superior vena cava, azygos
2. Total anomalous pulmonary venous connection
(a) Supracardiac
• Left innominate vein
• Right atrium/right superior vena cava
• Coronary sinus
(b) Infradiaphragmatic
• Portal vein
• Inferior vena cava
3. Pulmonary vein number anomalies
4. Cor triatriatum
(a) Classic
(b) Subtotal
5. Central and peripheral pulmonary vein stenosis
(a) Central
(b) Peripheral

**Table 5.2** Anomalies of systemic thoracic veins

1. Superior vena cava
(a) Persistent left superior vena cava
(b) Absent right superior vena cava
(c) Superior vena cava to left atrium
2. Inferior vena cava
(a) Interrupted inferior vena cava
(b) Duplicate inferior vena cava
(c) Inferior vena cava to left atrium
3. Anomalous left innominate vein
(a) Retroaortic
(b) Duplicated
4. Azygos system
(a) Absent azygos vein
(b) Azygos lobe

## 5.2 Pulmonary Venoatrial Anomalies

### 5.2.1 Pulmonary Vein Development and Anatomy

In humans, the lungs, larynx, and tracheobronchial tree are derived from the foregut. In early stages of development, the lungs are enmeshed by the splanchnic plexus. As pulmonary differentiation progresses, part of the splanchnic plexus forms the pulmonary vascular bed. Initially, there is no direct connection between the heart and the pulmonary vascular bed, with the pulmonary vascular bed draining through the splanchnic plexus via the umbilicovitelline and cardinal system of veins. Eventually, the pulmonary veins connect with

the left atrium by establishing connection with the common pulmonary vein which arises from the left atrium, while the initial connection between the pulmonary portion of the splanchnic plexus and the cardinal and umbilicovitelline systems involutes. The pulmonary vascular bed then drains by four individual major pulmonary veins into the common pulmonary vein which drains into the left atrium. Eventually, the common pulmonary vein becomes part of the left atrium resulting in the anatomic arrangement that we recognize with four individual pulmonary veins connected directly to the left atrium. Defects in the development of the common pulmonary vein provide the basis for most anomalies of the pulmonary veins [5]. Pulmonary venous anomalies can be classified as anomalies in number of pulmonary veins; anomalies in the connections of the pulmonary veins; and stenotic pulmonary vein connections. Atresia of the common pulmonary vein, while the pulmonary to systemic venous connections are still present, can give rise to total anomalous pulmonary venous connection or partial anomalous pulmonary venous connections. Stenosis of the common pulmonary vein would result in cor triatriatum, whereas abnormal absorption of the common pulmonary vein into the left atrium will give rise to stenosis of the individual pulmonary veins or lead to an abnormal number of pulmonary veins [5].

### 5.2.2 Partial Anomalous Pulmonary Venous Connection (PAPVC)

Partial anomalous pulmonary venous connection involves one or more of the pulmonary veins (but not all) connected to a systemic vein. The common types of PAPVC are right-sided pulmonary veins to the superior vena cava and/or right atrium; right-sided pulmonary veins to the inferior vena cava; and left-sided pulmonary veins to the left innominate vein (Fig. 5.1). There have been reports of unusual sites of connection, such as to the azygos vein or the coronary sinus [5–7]. Patients may even have combinations of connections with a right pulmonary vein to the right superior vena cava and the left pulmonary vein to the left innominate [3]. PAPVC results in a left to right shunt with volume loading of the right ventricle. The hemodynamic importance of any PAPVC is linked to the amount of lung draining anomalously into the systemic venous circulation. Patients with a small shunt may never develop symptoms or any hemodynamic consequence. Patients with larger shunts may present with dyspnea and echocardiographic evidence of a dilated right ventricle and pulmonary hypertension. MRI is ideally suited to assess right ventricular size and function with SSFP cine imaging and to provide a reliable measure of the left to right shunting through the use of phase-contrast mapping.

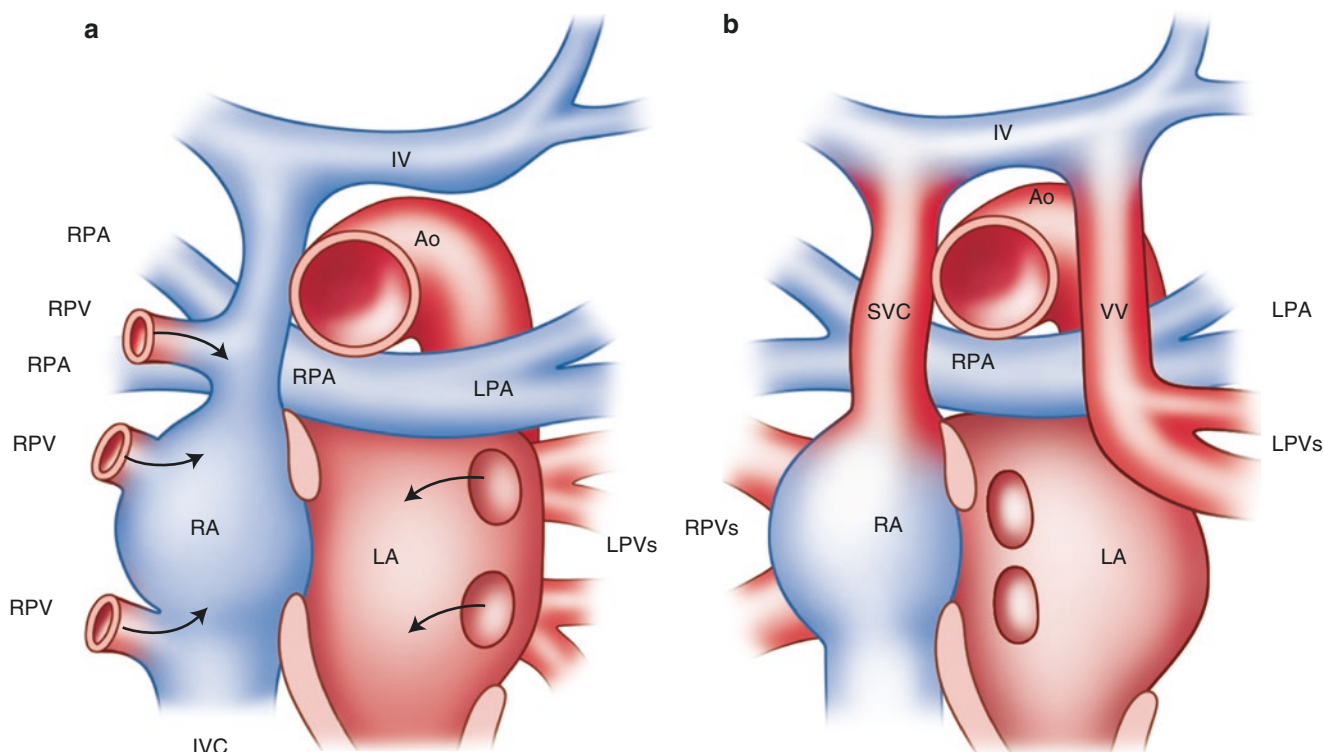


**Fig. 5.1** Partial anomalous pulmonary venous connections. (a) Depicts the commonest locations of anomalous right pulmonary vein (RPV) connections into the superior vena cava (SVC), right atrium (RA), or inferior vena cava (IVC). (b) Demonstrates the commonest type of anomalous left pulmonary vein (LPV) connection with the LPV drain-

ing to a vertical vein (VV) which is connected to the innominate (IV) or brachiocephalic vein and thence to the SVC. Ao aorta, LA left atrium, LPA left pulmonary artery, RPA right pulmonary artery. (From Ammass et al. JACC 1997 [6], with permission)

### 5.2.2.1 Right Partial Anomalous Pulmonary Venous Connection

#### Right PAPVC to the Superior Vena Cava or Right Atrium

The most common type of partial anomalous pulmonary venous connection encountered clinically is that where one or more pulmonary veins from the right lung attach into the superior vena cava and/or the right atrium. This type of PAPVC is frequently associated with the sinus venosus defect (see Chap. 6), reported in 42–87% of patients with right PAPVC [3, 6, 8, 9]. The sinus venosus defect is an interatrial communication due to the unroofing of the common wall between the right superior vena cava and the right upper pulmonary vein (Fig. 5.2). Patients with sinus venosus defect have been reported to have as high as a 95% prevalence of a right-sided PAPVC of the right pulmonary vein [3]. The relationship between sinus venosus defects and PAPVC from the right lung is so strong that the finding of one on echocardiography, transesophageal echocardiography, CT, or MRI mandates a careful search for the other. Although sinus venosus defect is the most common association with PAPVC,

secundum atrial septal defect has been described with PAPVC as well [2, 3], and it may be worthwhile to consider imaging for PAPVC in such patients before device closure of the secundum ASD [2, 3, 10]. Less frequent associated anomalies include tetralogy of Fallot and double outlet right ventricle.

#### 5.2.2.2 Scimitar Syndrome

There may be anomalous connection of the pulmonary veins from the right lung (occasionally just those from right middle lobe and right lower lobe) into the inferior vena cava, above or below the diaphragm. Connections into the hepatic vein have been described. The drainage pattern of the pulmonary veins in the right lung is changed and has been described as having a “fir tree” configuration [5]. This anomalous right pulmonary venous connection is referred to as the scimitar syndrome (Fig. 5.3) and is associated with other anomalies: hypoplasia of the right lung; anomalies of the bronchial system; anomalous arterial connection to the right lung; hypoplasia of the right pulmonary artery; and pulmonary sequestration. There is no association with sinus venosus defect, and the atrial septum is frequently intact. Unlike the



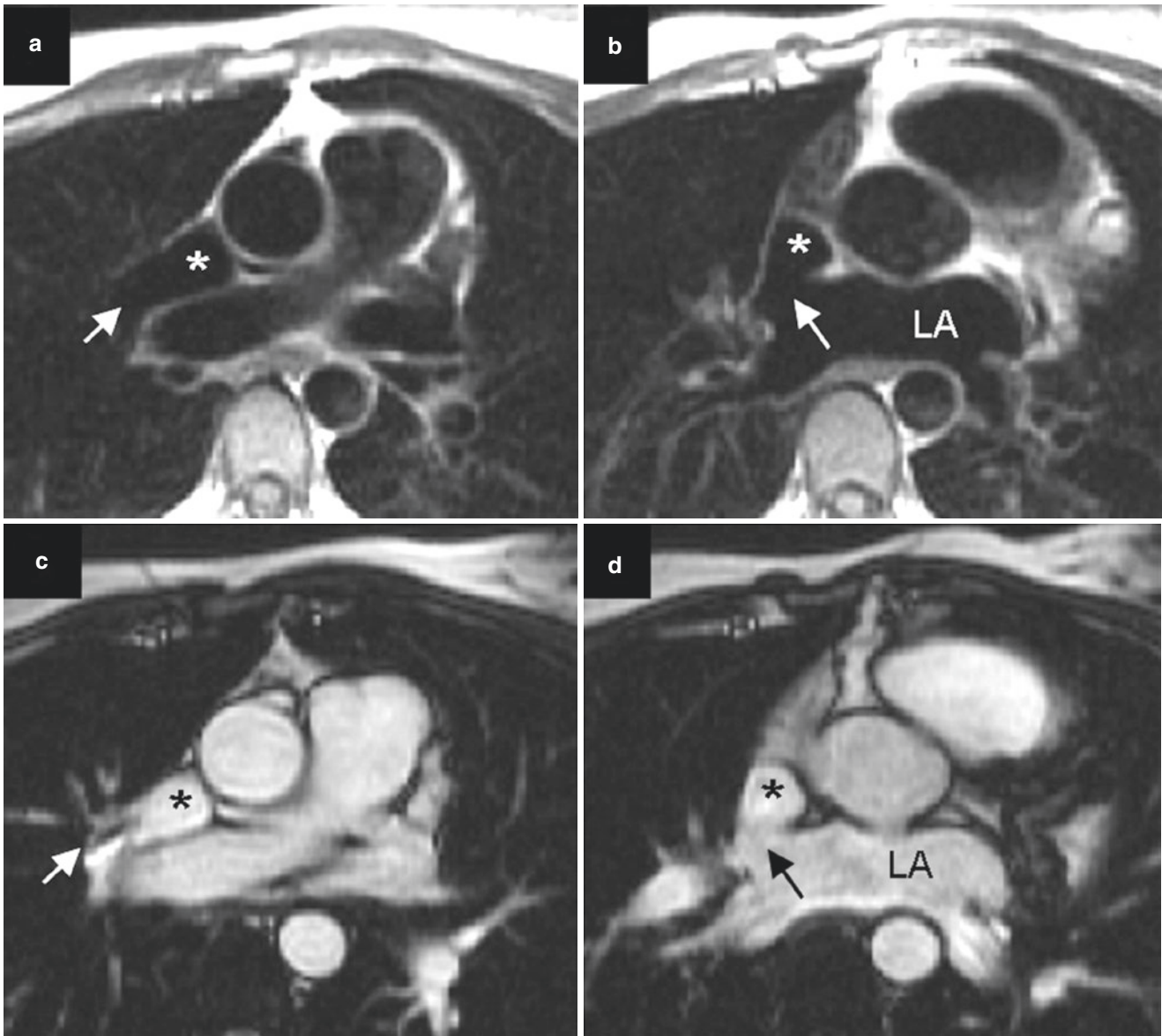


**Fig. 5.2** PAPVC with sinus venosus defect. Forty-six-year-old woman with partial anomalous pulmonary venous connection and sinus venosus defect. *LA* left atrium. Asterisk indicates superior vena cava (SVC). (a) Turbo spin-echo image shows connection of right upper pulmonary vein (*arrow*) to SVC. (b) Slice 20 mm caudal to (a) clearly shows sinus venosus defect (*arrow*). (c, d) Steady-state free precession cine still

images at same levels as (a) and (b) also show sinus venosus defect (*arrow*, d). Arrow in (c) indicates anomalous connection of upper pulmonary vein to the SVC. (Reprinted with permission from the American Journal of Roentgenology 2009; 192: 259–266 Kafka H and Mohiaddin RH [3])

other previously described PAPVC, the scimitar syndrome more likely represents developmental abnormality of the right lung [5]. A pseudo-scimitar syndrome has been described where there is a single pulmonary vein, draining the entire right lung that follows a meandering course toward the diaphragm but then turns cephalad and connects to the left atrium. Although the course is aberrant, there is an appropriate connection back to the left atrium, and so there is no clinical consequence to this lesion. There may be lung hypoplasia with this pseudo-scimitar syndrome as well [9,

11]. The significance of the pseudo-scimitar syndrome lies in its differentiation from a true anomalous connection and avoidance of additional imaging and intervention.

### 5.2.2.3 Azygos Vein

Anomalous connection of a right pulmonary vein to the azygos vein has been described [5, 7, 9] and is uncommonly seen (Fig. 5.4). Even anomalous connection of an upper left pulmonary vein to the azygos vein has been reported. These reports stress the importance of imaging the more cephalad

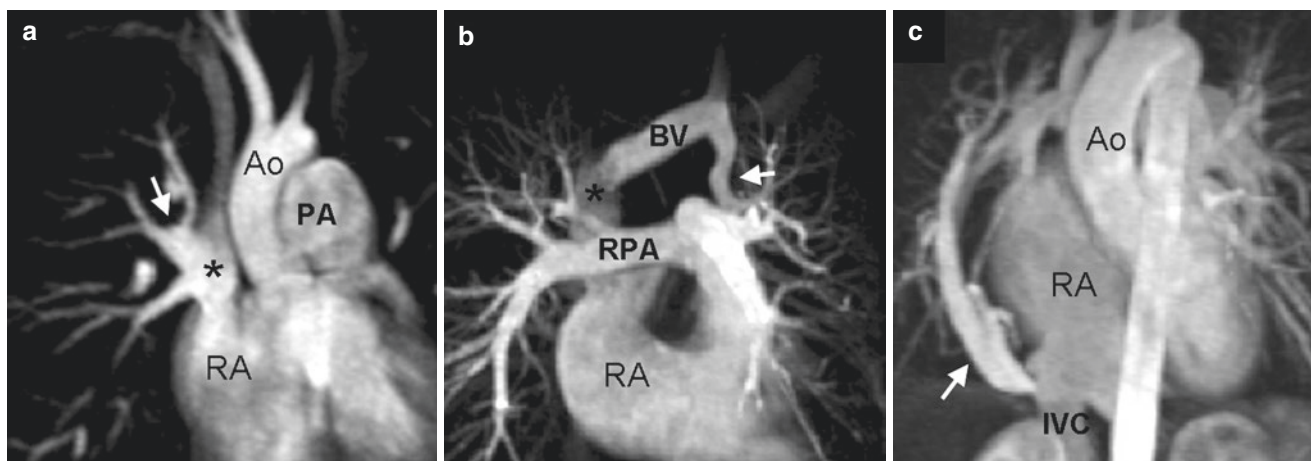


**Fig. 5.3** PAPVC CE-MRA. Contrast-enhanced MR angiography maximum-intensity-projection coronal images in three patients with partial anomalous pulmonary venous connection. *Ao* aorta, *RA* right atrium. (a) 18-year-old woman with anomalous connection of right pulmonary vein (arrow) to superior vena cava (SVC) (asterisk). *PA* pulmonary artery. (b) 63-year-old woman with anomalous connection of left upper pulmonary vein to vertical vein (arrow) that drains into brachio-

cephalic vein (BV) and from there into SVC (asterisk). *RPA* right pulmonary artery. (c) 45-year-old woman with anomalous scimitar vein. Image shows that all right pulmonary veins are connected to an anomalous vein (arrow) that, in turn, drains into inferior vena cava (IVC). (Reprinted with permission from the American Journal of Roentgenology 2009; 192: 259–266 Kafka H and Mohiaddin RH [3])

aspect of the SVC to avoid missing an anomalous connection to the azygos vein or a high connection to the SVC in the region of the azygos.

#### 5.2.2.4 Left Pulmonary Vein Anomalous Connection

The partial anomalous connection of left pulmonary veins, the vein from the left upper lobe or from the entire left lung, is usually through a vertical vein up to the left innominate vein (Figs. 5.1 and 5.3). The left PAPVC has been reported less commonly in the clinical situation but may be more common in the asymptomatic adult [9]. This surprising result may simply reflect the fact that patients with left PAPVC tend to have a smaller hemodynamic burden from the left to right shunting and are less likely to present clinically and only be detected incidentally during scans for other indications. Left PAPVC is not associated with sinus venosus defects, but secundum atrial septal defects are frequently seen [2, 3]. Left PAPVC can be an isolated incidental finding [9], and if the anomalous drainage involves just the left upper lobe, there may not be enough of a left to right shunt to be of any clinical significance, and no treatment would be required. Less frequent sites of left PAPVC are to the coronary sinus, inferior vena cava, right superior vena cava, left subclavian vein, and azygos vein [5].

#### 5.2.2.5 Imaging for PAPVC

Transthoracic echocardiography can detect sinus venosus defect and anomalous pulmonary venous connections in the young. However, in the older patient, transthoracic echocar-

diography cannot reliably detect sinus venosus defect or anomalous pulmonary venous connections. Transesophageal echocardiography is better capable of detecting the sinus venosus defect and most of the anomalous venous connections. Even so, several reports have indicated that even in the best of hands, transesophageal echocardiography may not detect all the anomalous pulmonary venous connections that were noted at surgery [6]. Furthermore, reliance on vein counting with two pulmonary veins on each side connected to the left atrium to rule out any anomalous connection is fraught with error since 40% of patients do not have this typical configuration (see Sect. 5.2.4). Cardiac magnetic resonance imaging enjoys the advantage of a wide field of view that allows it to detect anomalous connections in the upper superior vena cava that may not be visible to transesophageal echocardiography. Furthermore, the cardiac magnetic resonance imaging is not limited to any prespecified planes, allowing it to detect anomalous connections above and below the diaphragm and follow these connections along their course. In fact, the scan coverage should be extended superiorly to include the supraclavicular veins and inferiorly to the kidney level in order to detect all the anomalous veins [9]. In addition to the spin-echo images, SSFP cine imaging produces better delineation of blood-tissue borders (Fig. 5.2) and is able to demonstrate turbulent flow. Contrast-enhanced magnetic resonance angiography provides a rapid 3D image of the anomalous veins (Fig. 5.4). Phase-contrast mapping provides reproducible measurement of systemic and pulmonary flow, as well as measurement of differential flow to the lungs. These significant advantageous

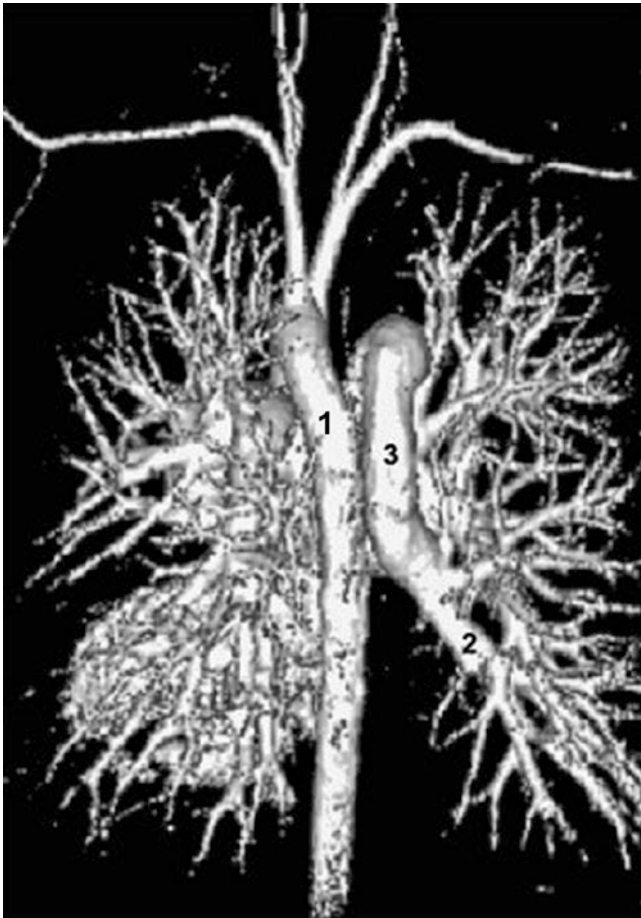


**Fig. 5.4** PAPVC azygos vein connection. 3D contrast-enhanced MRA. Surface-rendered image in the posteroanterior view. (1) Descending thoracic aorta. (2) Anomalous right middle and lower pulmonary vein. (3) Dilated azygos vein. (Adapted from *International Journal of Cardiology* 135 (2009), Locca D, Hughes M, Mohiaddin R [7]. With permission from Elsevier)

of cardiac magnetic resonance imaging make it the preferred imaging modality in these patients [2, 3, 12, 13]. Multislice CT with contrast will demonstrate the anomalous pulmonary venous connections, but it does not provide the same functional information about the degree of shunting or ventricular performance available from cardiac magnetic resonance imaging, and it does require the use of radiation and iodinated contrast [9].

#### 5.2.2.6 Image Guided Management Decision-Making in Patients with PAPVC

The management of patients with these partial anomalous pulmonary venous connections depends primarily on the symptoms, the presence of associated defects, and the degree of hemodynamic consequence of the shunts, both those arising from the anomalous pulmonary venous connection and those due to associated sinus venosus defects or atrial septal defects. Imaging will help determine the presence of

associated defects and can assess the presence of right ventricular volume overload with a dilated right ventricle and abnormal interventricular septal motion. Specifically, phase-contrast MR mapping will be able to accurately calculate the flow through the pulmonary artery and the aorta in order to determine the degree of left to right shunting [2, 3]. Furthermore, in patients with a single PAPVC and secundum ASD, phase-contrast MR mapping will be able to calculate the individual flow through the PAPVC compared to the ASD in order to determine the contribution of each in the left to right shunt [10]. If the preponderance of the left to right shunt is through the ASD, device closure of just the ASD may be sufficient for the patient [10]. In the patient with scimitar syndrome and no interatrial connection, phase-contrast MR mapping will be able to determine the relative pulmonary blood flow to each lung in order to determine the hemodynamic consequence of the anomalous pulmonary venous connection. Often, the flow to the right lung may represent only a quarter or third of total pulmonary blood flow because of the other associated pulmonary defects [5].

For years, the only definitive therapy for clinically significant PAPVC was surgical repair, but recent advances in transcatheter techniques have provided nonsurgical options for closure of PAPVC, both with and without SVD [10, 14]. The type of surgical repair depends on the anatomy of the connection [8]. For the right PAPVC to the superior vena cava with sinus venosus defect, the superior vena cava is divided above the anomalous pulmonary vein(s), and the tip of the right atrial appendage is anastomosed to the superior vena cava. A pericardial patch is sutured to the margin of the sinus venosus defect in order to channel blood flow from the anomalous pulmonary vein(s) into the left atrium through the sinus venosus defect. The sinus venosus defect may need to be enlarged in order to accommodate the pulmonary venous flow. Another approach is to make an incision into the superior vena cava over the insertion of the anomalous pulmonary veins and to create an atrial septal defect, if none is already present. A pericardial patch is used to baffle the blood from the anomalous pulmonary veins into the left atrium through the sinus venosus defect or newly created atrial septal defect. The superior vena cava incision is repaired with a patch of pericardium in order to minimize the superior vena cava narrowing at that site [8]. For the patient with a left PAPVC requiring surgery, the vertical vein between the innominate vein and the pulmonary vein is divided and implanted into the left atrial appendage. For the patient with the scimitar type of right PAPVC to the inferior vena cava, the surgery is more complex. An atrial septal defect is created, and a long baffle of pericardium is placed into the lumen of the inferior vena cava to channel the flow from the anomalous pulmonary vein to the right atrium and through the newly created atrial septal defect into the left atrium. Often it is necessary to enlarge the inferior vena cava with a pericardial patch in



an effort to prevent vena cava obstruction [8]. These operations can be generally carried out with very low mortality and morbidity risks and good long-term outlook [8]. However, the repair of the anomalous pulmonary venous connection in scimitar syndrome is associated with a high incidence of late postoperative pulmonary venous obstruction. The value of MR imaging postoperatively is to look for stenotic lesions at anastomosis sites [15], assess for narrowing in the superior vena cava or inferior vena cava, and rule out any baffle leaks or residual interatrial communication. Cardiac magnetic resonance imaging will be especially valuable in the assessment of obstruction along the extensive baffle used in scimitar syndrome repair.

For the transcatheter closure of PAPVC, it is necessary to have a connection to the left atrium, either in the common situation of SVD [14], less common situation of secundum ASD, or in the rare situation of dual drainage to both the vena cava and the left atrium [10]. Detailed imaging is critical in preparation for such a procedure in order to provide a map of all the pulmonary venous connections. The procedure is performed under TEE guidance and involves the use of a covered stent. Early case reports of transcatheter closure have been positive, and it has been used in an increasing number of cases with suitable anatomy [10, 14]. Follow-up with cardiac MR can detect any residual shunting and confirm successful reduction of right ventricular size.

### 5.2.3 Total Anomalous Pulmonary Venous Connection (TAPVC)

In total anomalous pulmonary venous connection, the pulmonary veins have no direct connection with the left atrium. The pulmonary veins connect to a systemic vein, and, therefore, an interatrial communication is mandatory in order to maintain life. Usually, TAPVC is an isolated anomaly, but it has been associated with other defects, such as tetralogy of Fallot, transposition of the great arteries, truncus arteriosus, and tricuspid atresia. Patients with asplenia have a high incidence of TAPVC.

#### 5.2.3.1 Supracardiac and Infradiaphragmatic TAPVC

The anomalous connections can be generally classified as those which are supracardiac (left innominate vein, right superior vena cava, coronary sinus, right atrium) without pulmonary venous obstruction and those which are infradiaphragmatic (to portal vein or IVC) with pulmonary venous obstruction (Fig. 5.5) and those which are mixed with pulmonary veins draining to at least two different locations [12]. The most common site of connection is to the left innominate vein. In this situation, the pulmonary veins from both lungs connect into a pulmonary venous confluence that is

posterior to the left atrium. A vertical vein from this chamber courses cephalad, passing anterior to the aortic arch and joins the left innominate vein which continues in its usual course to the right-sided superior vena cava. In another supracardiac variant, the anomalous vessel arises from the right side of the pulmonary venous confluence and passes cephalad to enter the superior vena cava posteriorly. There can also be a direct connection between the pulmonary venous confluence and the coronary sinus which will be significantly dilated because of the increased flow or a direct connection to the right atrium [12]. Infradiaphragmatic anomalous connections involve the vein from the common vessel posterior to the left atrium descending through the diaphragm and then connecting to the portal vein. It may connect to a hepatic vein or connect directly to the inferior vena cava. Such infradiaphragmatic connections usually have some component of obstruction [5].

#### 5.2.3.2 Management of Patients with TAPVC

Total anomalous pulmonary venous connection will result in significant right ventricular volume overload with signs and symptoms related to that, and the imaging needs to differentiate it from other causes of right heart overload such as atrial septal defect and PAPVC. There will be decreased left ventricular volume and decreased systemic output. In the cases with pulmonary venous obstruction (usually subdiaphragmatic), the elevated pulmonary venous pressure may lead to pulmonary edema. Diagnosis is usually made in the first months of life. The only long-term effective therapy for TAPVC involves a surgical repair. Essentially, a side-to-side anastomosis is made between the pulmonary venous confluence and the left atrium. The anomalous connection is then closed, as is the interatrial connection. Postoperative complications have involved the late stenosis of the left atrial-pulmonary venous confluence anastomosis [15] and residual patch leaks.

#### 5.2.3.3 Imaging for TAPVC

In these patients, echocardiography will show features of right ventricular volume overload, and there will be difficulty in demonstrating the pulmonary veins. The pulmonary venous confluence can be identified as a chamber posterior to the small left atrium, and the course of the pulmonary veins should be tracked.

Cardiac magnetic resonance imaging has the advantage of the wider field of view and can provide a comprehensive assessment of the pulmonary venous confluence and its connections (Fig. 5.6). It is especially of benefit to define the level of obstruction in patients with infradiaphragmatic connection. However, in infants, the windows available to echocardiography are such that a comprehensive and diagnostic study can usually be undertaken in TAPVC. The major role of MRI in total anomalous pulmonary venous connection is to



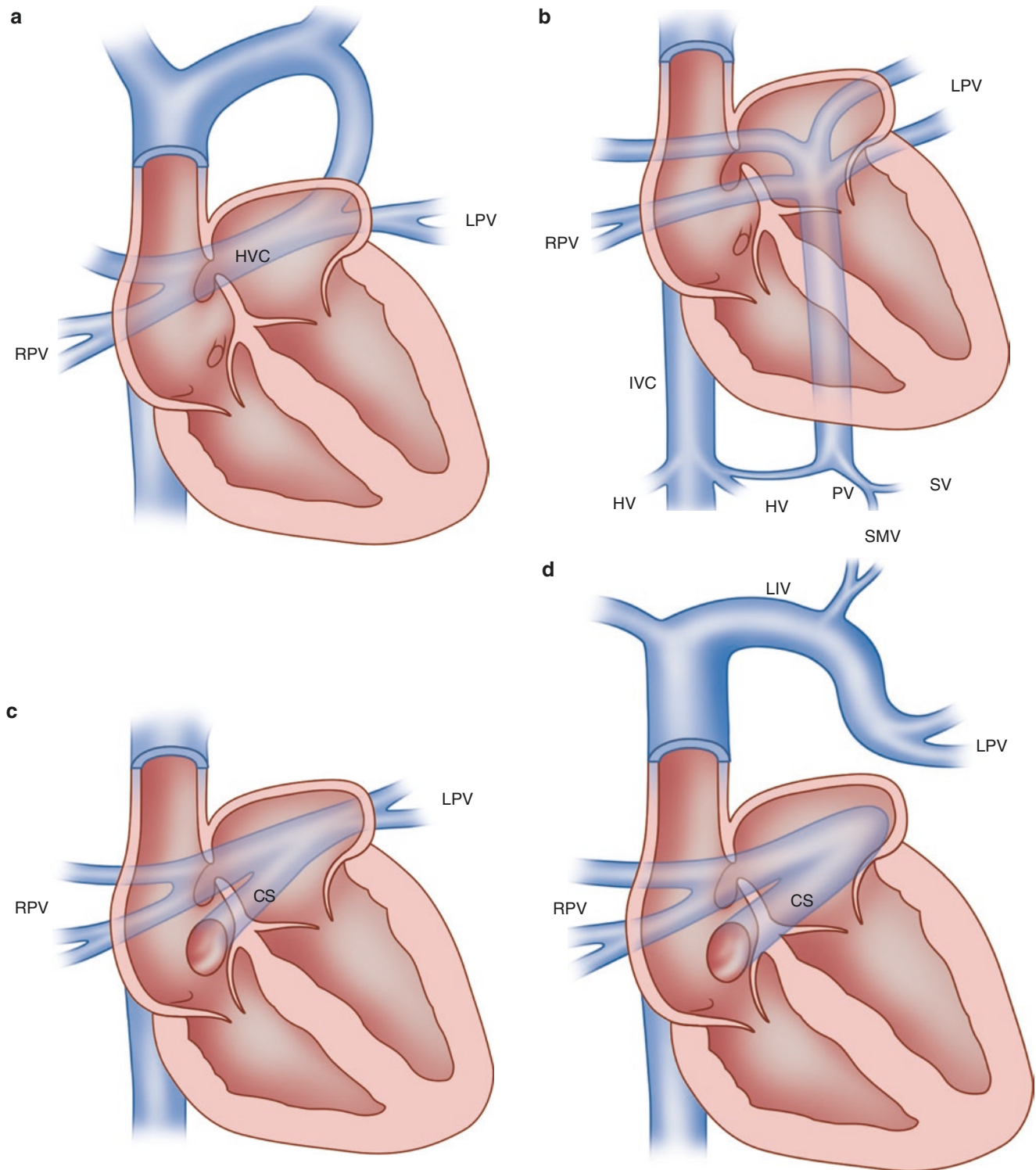


**Fig. 5.5** Diagram of common types of totally anomalous pulmonary venous connection (TAPVC). (a) Supracardiac TAPVC to the left innominate vein. The individual pulmonary veins form a horizontal pulmonary venous confluence (HVC) that connects to the left innominate vein by way of a vertical vein. (b) Infradiaphragmatic TAPVC to the portal vein. The pulmonary veins form a vertical confluence that descends below the diaphragm and typically joins the portal vein (PV). Pulmonary venous blood then drains into the inferior vena cava (IVC) via the ductus venosus or the hepatic sinusoids. The individual pulmo-

nary veins may join the vertical vein at different levels. (c) TAPVC to the coronary sinus (CS). (d) Mixed-type TAPVC. In the example shown, the left pulmonary veins (LPV) connect to the left innominate vein (LIV), and the right pulmonary veins (RPV) connect with the CS. HV hepatic vein, LA left atrium, RA right atrium, SMV superior mesenteric vein, SV splenic vein. (Adapted with permission from Chapter 37 (Figure 37.15) Tal Geva and Stella Van Pragh in Moss and Adams' Heart Disease in Infants, Children and Adolescents. 7th Edition Philadelphia Lippincott Williams & Wilkins; 2008 [5])

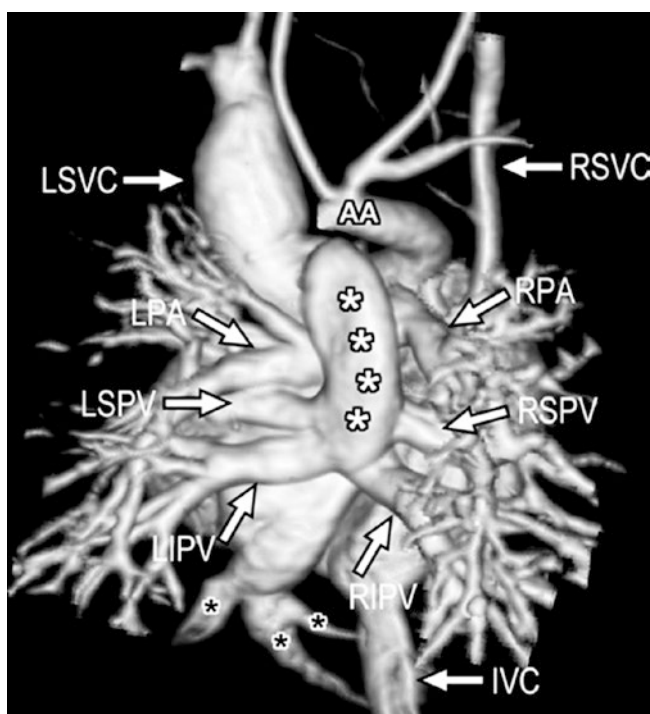


**Fig. 5.6** One-month-old girl with total anomalous pulmonary venous connection, asplenia, complete atrioventricular septal defect, double-outlet right ventricle, and bilateral superior venae cavae. Contrast-enhanced volume-rendered MR image in posterior view confirms drainage of all pulmonary veins into a common pulmonary vein (white asterisks) that drains into a markedly dilated left superior vena cava (LSVC). Small right superior vena cava (RSVC) and inferior vena cava (IVC) drain into right atrium. Note portions of distal aortic arch and descending thoracic aorta have been removed on posterior image. Black asterisks show hepatic veins. *LSVC* left superior vena cava, *LSPV* left superior pulmonary vein, *RSPV* right superior pulmonary vein, *RIPV* right inferior pulmonary vein, *LIPV* left inferior pulmonary vein, *RPA* right pulmonary artery, *LPA* left pulmonary artery, *AA* aortic arch. (Reprinted with permission from the American Journal of Roentgenology 2009; Dillman et al., 192: 1272 [12])

assess the patient following surgical repair for follow-up, assess for associated conditions, and rule out late complications (Fig. 5.7). SSFP imaging can track the connections as well as quantifying chamber size and ventricular performance, assessing the dimensions of the orifice connecting the left atrium to the pulmonary venous confluence, and detecting any residual patch leaks. Phase-contrast mapping can help in the search for evidence of any persistent shunting.

#### 5.2.4 Variation in the Number of Pulmonary Veins

The typical distribution of pulmonary veins of two pulmonary veins on the right and two pulmonary veins on the left is seen in 60–70% [16]. Recently, because of increased imaging by cardiac magnetic resonance imaging and CT

angiography in preparation for radiofrequency ablation, significant variations in pulmonary vein number and course have been noted [16]. On the left, the most common variant is a common trunk that drains into the left atrium in 15%. This can be a short or long left common trunk, the former being more common. The variations on the right are less frequent but more complex, comprising accessory veins in addition to the superior and inferior right pulmonary veins. These variations have included an accessory middle lobe vein connected directly to the left atrium, two accessory middle lobe veins connected directly to the left atrium, accessory right upper pulmonary vein, and a right top pulmonary vein [16]. Although abnormal number of pulmonary veins and variations of connection to the left atrium should not lead to any hemodynamic impairment, variations in the anatomy are important to document in preparation for pulmonary vein isolation procedures in the treatment of atrial fibrillation.

#### 5.2.5 Cor Triatriatum

##### 5.2.5.1 Cor Triatriatum and Subtotal Cor Triatriatum

Failure of incorporation of the common pulmonary vein into the left atrium will give rise to cor triatriatum. In the classic form of cor triatriatum, all the pulmonary veins enter an accessory atrial chamber that is attached to the left atrium through a narrowed orifice. There are variants where the accessory chamber receives all the pulmonary veins and does not communicate with the left atrium. In that case, there may be total anomalous pulmonary venous connection or an anomalous connection directly to the right atrium. In subtotal cor triatriatum, the accessory atrial chamber does not receive all of the pulmonary veins. The other pulmonary veins either connect normally or there is a partial anomalous pulmonary venous connection [5, 7].

##### 5.2.5.2 Management of Patients with Cor Triatriatum

Cor triatriatum will give rise to pulmonary venous hypertension because of the obstruction to the pulmonary venous flow, and patient presentation will mimic that of mitral stenosis with symptoms of dyspnea and evidence of pulmonary hypertension or even pulmonary edema. The only long-term effective treatment for clinically significant cor triatriatum involves surgical excision of the left atrial membrane. This is done through a right atrial approach with a high success rate, and there have been no reports of recurrence of the left atrial membrane after successful surgical excision.

##### 5.2.5.3 Imaging for Cor Triatriatum

Expected findings associated with cor triatriatum would include right ventricular hypertrophy and dilatation as well as

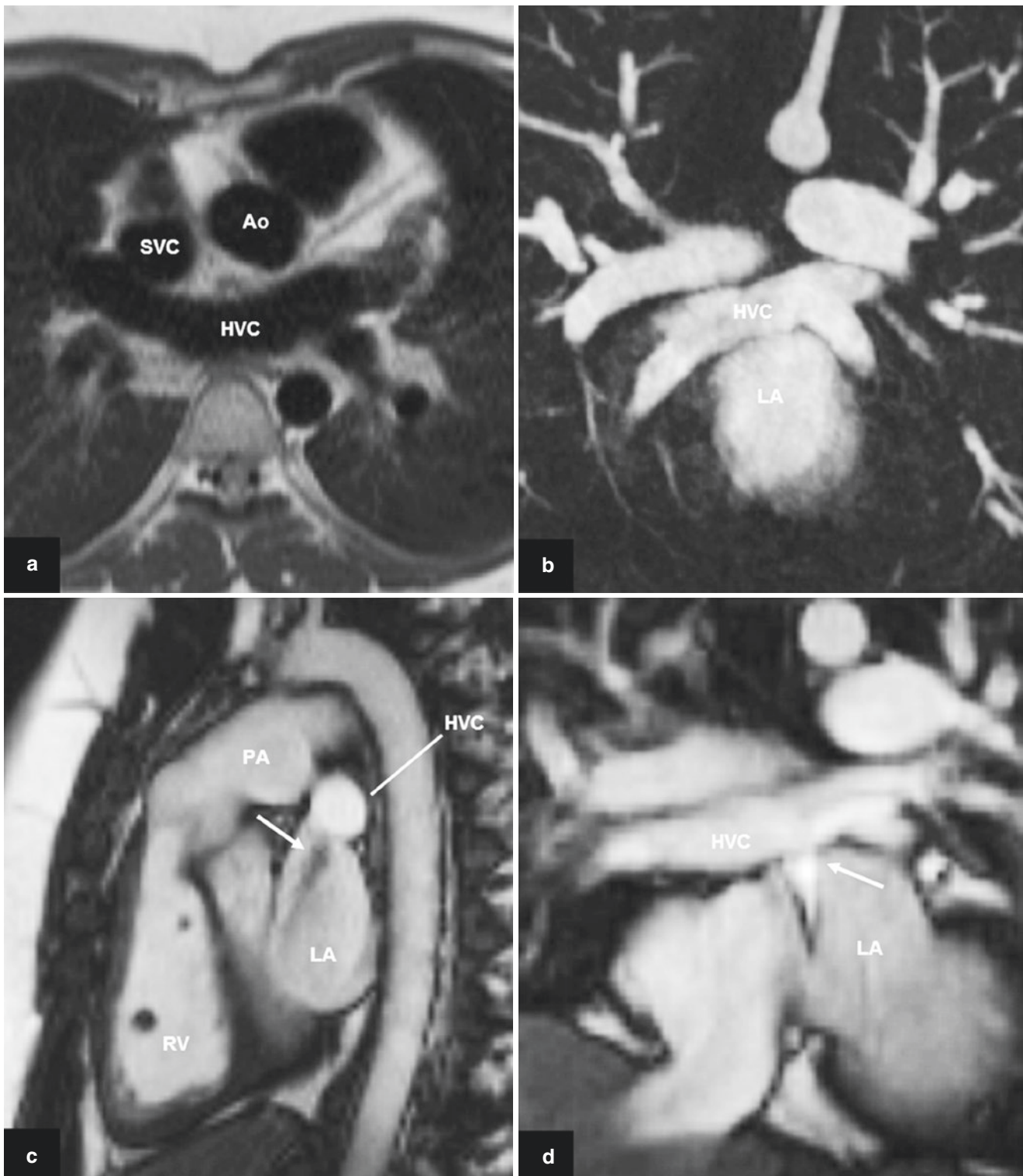


**Fig. 5.7** Twenty-year-old woman who had repair of a supracardiac TAPVC in infancy and is assessed for increasing dyspnea and X-ray evidence of heart failure. (a) Single-shot turbo spin-echo axial image demonstrating the posterior location of the horizontal pulmonary venous confluence (HVC). (b) Contrast-enhanced magnetic resonance angiography: maximum intensity projection (mip) coronal image. This demonstrates the connections of the four pulmonary veins into the

HVC. (c) Sagittal still image from SSFP cine confirming the superior location of the HVC and stenosis of the orifice between the HVC and the left atrium (LA). Note the hypertrophied right ventricle (RV). (d) Coronal still image from SSFP cine demonstrating the stenotic orifice and the turbulent flow into the LA (arrow) from the HVC. SSFP cines for (c) and (d) are available as supplemental files Movies 5.1 and 5.2



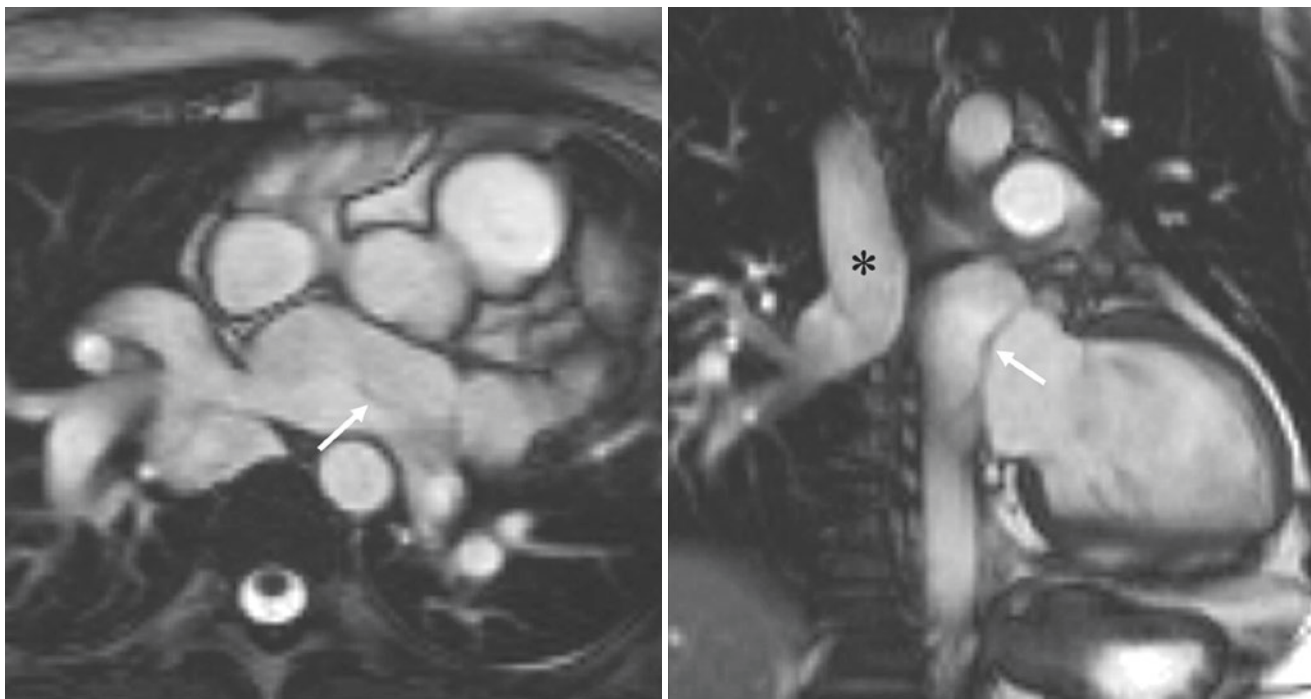


**Fig. 5.8** Cor triatriatum. Cine MRI images (balanced steady-state free precession sequences) acquired in transaxial plane through the left atrium (left) and in the left ventricular outflow tract (right). Arrow indicates cor triatriatum membrane. Note the anomalous right pulmonary venous connection to the azygos vein (asterisk). The movement of the

membrane and the flow through the membrane can be better appreciated in the cine loops (supplemental Movies 5.3 and 5.4). (Adapted from *International Journal of Cardiology* 135 (2009), Locca D, Hughes M, Mohiaddin R. With permission from Elsevier [7])

right atrial enlargement. Echocardiography will be able to detect dilated right ventricle and dilated pulmonary artery as well as right ventricular hypertrophy. The apical four-chamber view may be able to delineate the cor triatriatum membrane, and transesophageal echocardiography should be able to clearly demonstrate the membrane and the orifice size.

Cardiac magnetic resonance imaging will be able to demonstrate the membrane, the size of the orifice, and right-sided consequences of the stenosis within that membrane leading to right ventricular hypertrophy and a dilated right atrium. SSFP cine imaging will demonstrate the membrane and can be used to assess right-sided hypertrophy and dilatation (Fig. 5.8). SSFP cine imaging will detect the jet through the membrane, and phase-contrast mapping can be used to better delineate the stenosis and gradient. Magnetic resonance angiography will confirm pulmonary venous connections and rule out anomalous connections.

### 5.2.6 Pulmonary Vein Stenosis

Stenosis in the pulmonary veins at their junction with the left atrium may be a consequence of abnormal incorporation of

the common pulmonary vein. Congenital pulmonary vein stenosis is of two general types: a localized stenosis where the pulmonary vein has a narrowing at its junction with the left atrium or a diffuse narrowing of the lumen of the pulmonary vein for some distance. This latter more peripheral stenosis can be considered a hypoplasia of the pulmonary vein [5]. Pulmonary vein stenosis, depending on the amount of lung drained by the stenotic vein(s), can give rise to pulmonary hypertension. Echocardiography will be useful to document the pulmonary hypertension but may have difficulty in adequately characterizing the region of stenosis. Cardiac magnetic resonance imaging and MR angiography, as well as CT angiography [9], will be able to localize the stenosis and allow careful measurement of the residual lumen (Fig. 5.9). In the adult patient, pulmonary vein stenosis is more likely to be an acquired lesion, as a late complication of repair of PAPVC with stenosis at the site of pulmonary vein reimplantation [15] or due to scarring at the site of radiofrequency ablation used for pulmonary vein isolation in the treatment of atrial fibrillation. It must be kept in mind that malignancy and fibrosing mediastinitis may cause acquired pulmonary vein stenosis [16] and complete imaging of adjoining structures will be necessary in such cases.



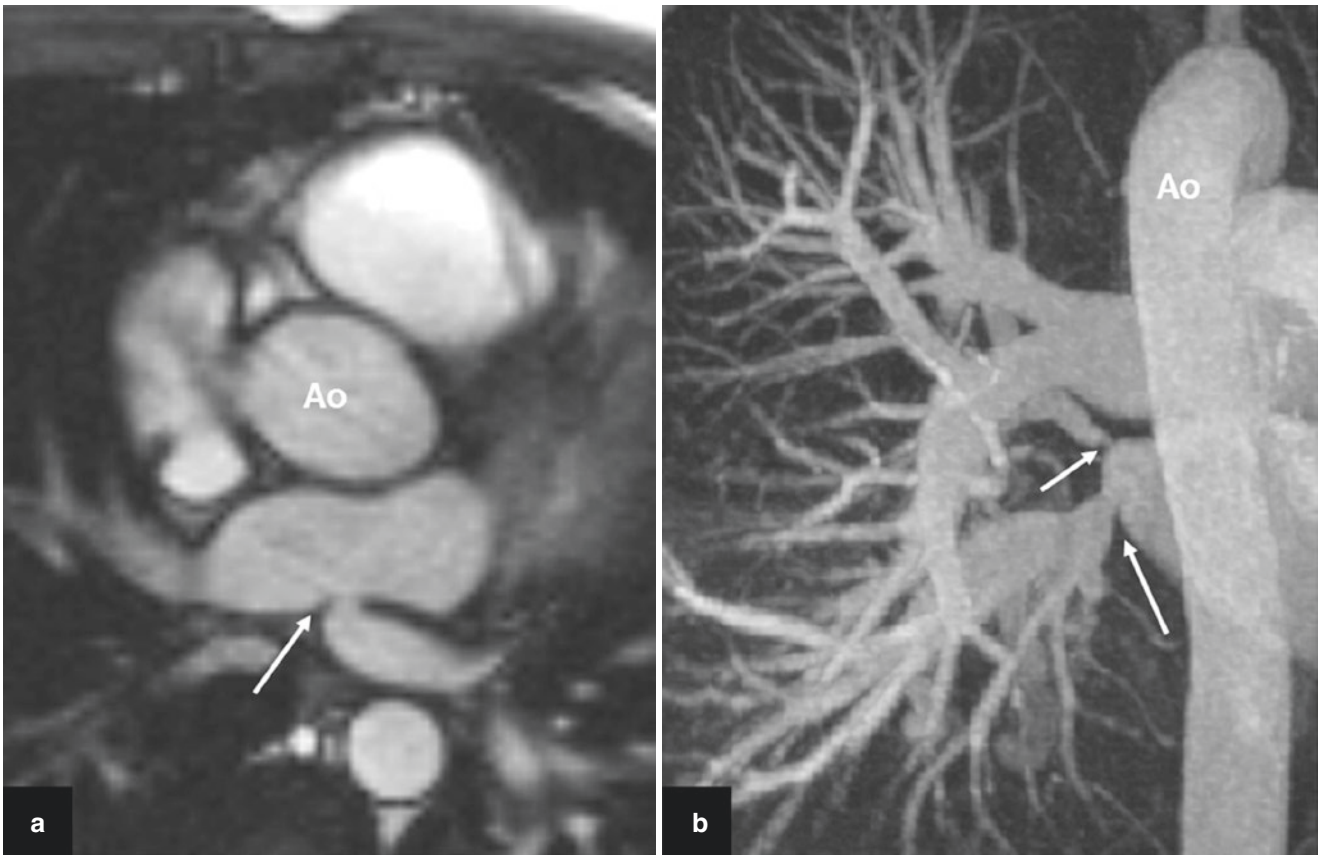


**Fig. 5.9** Pulmonary vein stenosis. (a) 25-year-old woman with dyspnea. Still axial image from a SSFP cine demonstrates stenosis (arrow) at the connection of the left lower pulmonary vein to the left atrium. This can be better appreciated on the SSFP cine and corresponding phase-contrast flow study (supplemental files Movies 5.5 and 5.6). (b)

34-year-old woman with dyspnea and dilated pulmonary artery on echocardiography. Contrast-enhanced MR angiography coronal image. Arrows point to the stenoses of the right lower and right upper pulmonary veins at the left atrium. *Ao* aorta

### 5.2.7 CMR Sequences and Protocols for Pulmonary Venous Imaging

Our standard approach to the imaging of thoracic venous anomalies has been previously described [2, 3]. We use multislice single-shot spin-echo images (HASTE) in three orthogonal planes to define the cardiac anatomy and supplement this with SSFP multislice images that provide a better definition of the blood-tissue borders. Turbo spin-echo imag-

ing can often better delineate edges of atrial septal defects or sinus venosus defects (Fig. 5.2). Right and left ventricular volumes and systolic function are evaluated by using ECG-gated SSFP cine images. These SSFP cine images also can demonstrate turbulent flow and help better focus the next imaging plane. The cine phase-contrast velocity flow maps are used to enhance and define the anomalous flow patterns (Fig. 5.10) and provide the calculation of differential flows and the pulmonary to systemic blood flow ratio. Contrast-

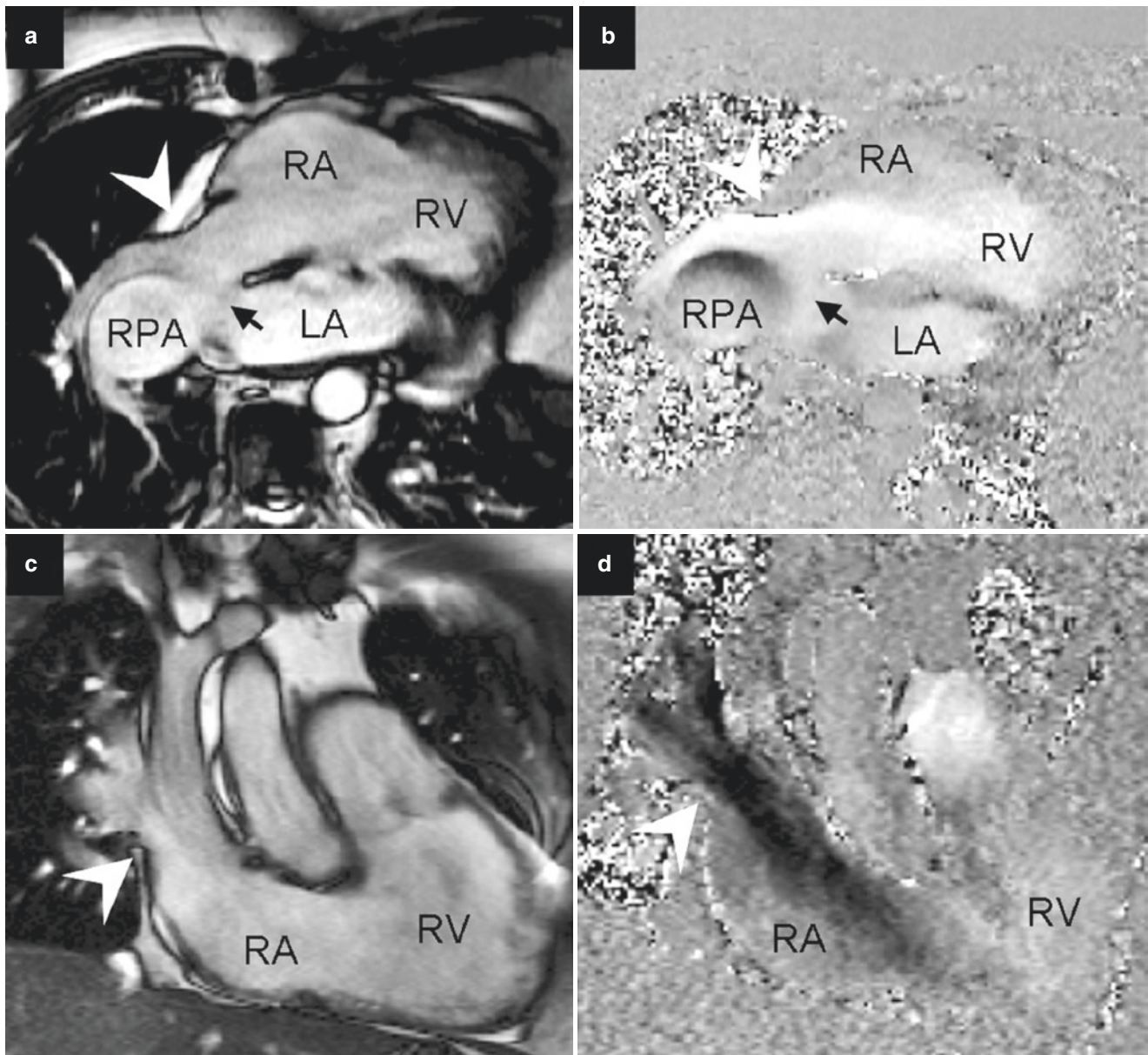


**Fig. 5.10** PAPVC flow studies. Fifty-seven-year-old man with sinus venosus defect and right partial anomalous pulmonary venous connection. LA left atrium, RA right atrium, RPA right pulmonary artery, RV right ventricle. (a, b) Oblique axial steady-state free precession cine image (a) shows anomalous connection of right upper pulmonary vein (arrowhead). Sinus venosus defect (arrow) is also evident at this level. Bright white signal in this velocity flow map (b) confirms flow from pulmonary vein into RA. (c, d) Coronal steady-state free precession

cine image (c) shows connection of right pulmonary vein to RA–superior vena cava junction (arrowhead). Dark signal in this velocity flow map (d) shows flow (arrowhead) from anomalous pulmonary vein into RA. The cines from which these stills are derived can be viewed as supplemental files (Movies 5.7 and 5.8). (Reprinted with permission from the American Journal of Roentgenology 2009; 192: 259–266 Kafka H and Mohiaddin RH [3])

enhanced MR angiography is obtained in the coronal plane during breath-hold at end inspiration before and after the IV administration of gadolinium. We time the bolus to the arrival of the contrast agent in the ascending aorta. Alternative 3D imaging approach is navigator echo and ECG-gated 3D-SSFP sequence. However, there is usually a drop of oxygenated blood signal in the pulmonary veins, and this approach is less robust for depicting pulmonary venous anatomy unless it is acquired post-contrast where a good blood signal is maintained. Our standard imaging parameters for the protocol are summarized in Table 5.3.

Transverse imaging is well suited to detect the connections between anomalous pulmonary veins and the right atrium, the superior vena cava or the inferior vena cava, because of the excellent cross-sectional visualization of the caval veins and the right atrium. The ascending vein of a left PAPVC or supracardiac TAPVC will be identified in the axial view. Once these have been identified, optimal imaging planes can be selected and enhanced with cine SSFP imaging in order to better visualize the actual areas of connection. Contrast-enhanced magnetic resonance angiography can be used to confirm the course and connections of the anomalous veins. Finally cine phase-contrast velocity flow mapping allows the calculation of the pulmonary systemic shunt ratio (Qp:Qs). Once the presence of an anomalous pulmonary

**Table 5.3** Imaging parameters

	TE (ms)	TR (R-R) (ms)	FOV (mm)	Pixel size (mm)	Slice thickness (mm)
HASTE	42	700–1000	340–400	2.7 × 1.7	6.0
SSFP	1.13	40	340–400	1.7 × 1.7	7.0
TSE	29	700–1000	340–400	2.2 × 1.3	6.0
CE-MRA	1.19	2.85	360–400	1.1 × 0.9	1.3
Phase-contrast velocity flow mapping	3.9	75	340–400	2.5 × 1.3	6.0

*SSFP* steady-state free precession, *TSE* turbo spin echo, *CE-MRA* contrast-enhanced magnetic resonance angiography

venous connection is established, it is necessary to perform complete cardiac imaging, not only to assess the hemodynamic burden on the right ventricle but also to look for associated defects, especially the sinus venosus defect. The best views for the sinus venosus defect are transverse and sagittal planes because they are perpendicular to the border between the superior vena cava and the left atrium. Specifically, SSFP cine imaging in these planes will provide a better delineation of blood tissue borders (Fig. 5.11).



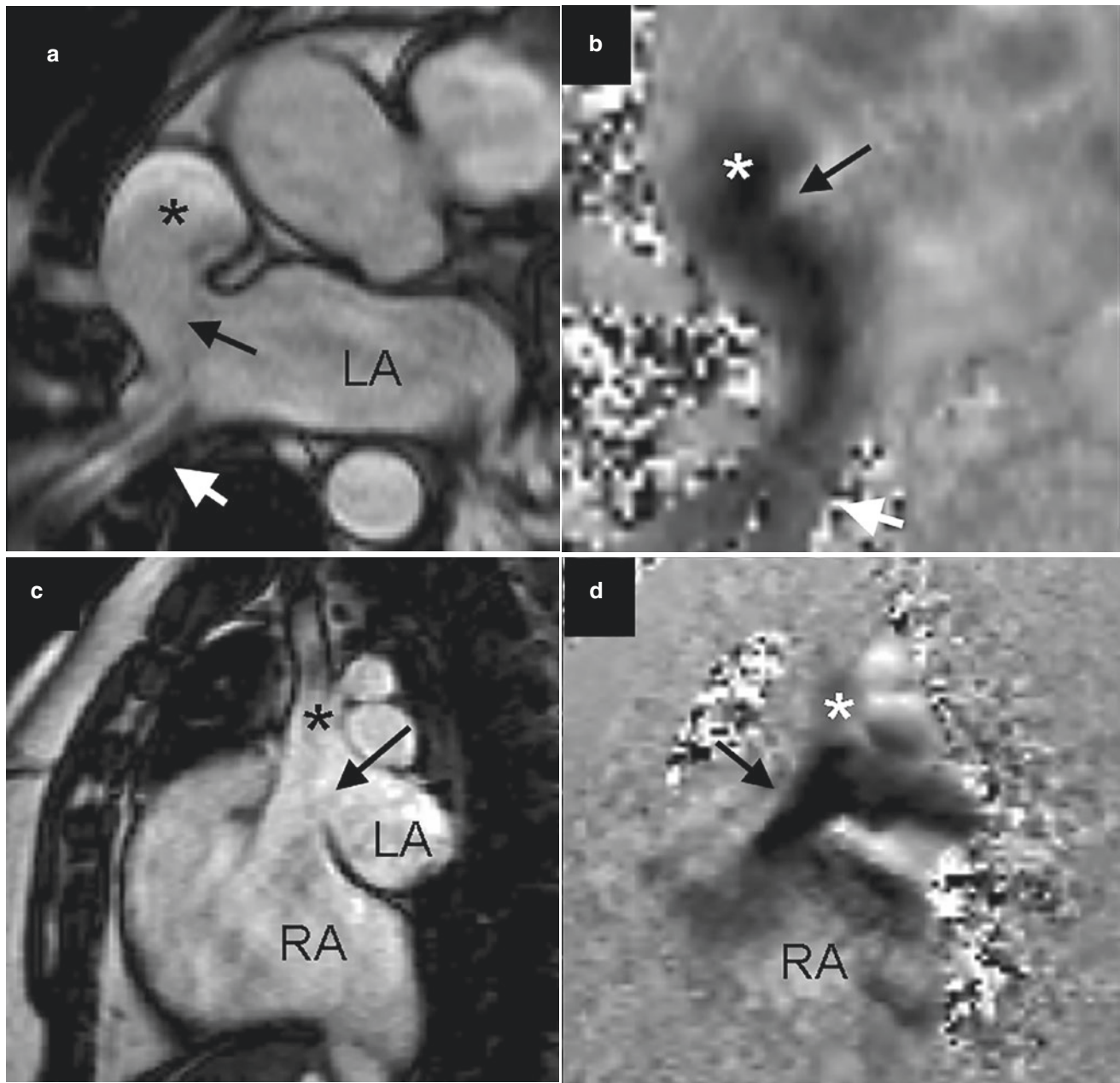


**Fig. 5.11** Sinus venus defect with PAPVC—velocity flow maps. (a, b) Transverse images in 32-year-old man with sinus venus defect. Steady-state free precession cine image (a) shows sinus venus defect (black arrow) between left atrium (LA) and superior vena cava (SVC) (asterisk). Corresponding in-plane velocity flow map (b) shows dark inflow from pulmonary vein (white arrow) into LA crossing sinus venus defect and entering the SVC. (c, d) Sagittal images in 35-year-old woman with sinus venus defect. Steady-state free precession cine frame (c) shows superior nature of sinus venus defect (arrow) between LA and SVC (asterisk). Corresponding in-plane velocity flow

map (d) shows dark inflow from LA across sinus venus defect (arrow) into right atrium (RA). (e, f) Coronal images in 18-year-old woman with sinus venus defect. FLASH image (e) shows bright flow disturbance in SVC (asterisk) related to flow through sinus venus defect. Through-plane velocity flow map (f) in same position as (e) shows sinus venus defect as dark region of flow (arrow) from LA. Ao aorta. (f) is available to be viewed as a cine in the supplemental files (Movie 5.9). (Reprinted with permission from the American Journal of Roentgenology 2009; 192: 259–266 Kafka H and Mohiaddin RH [3])



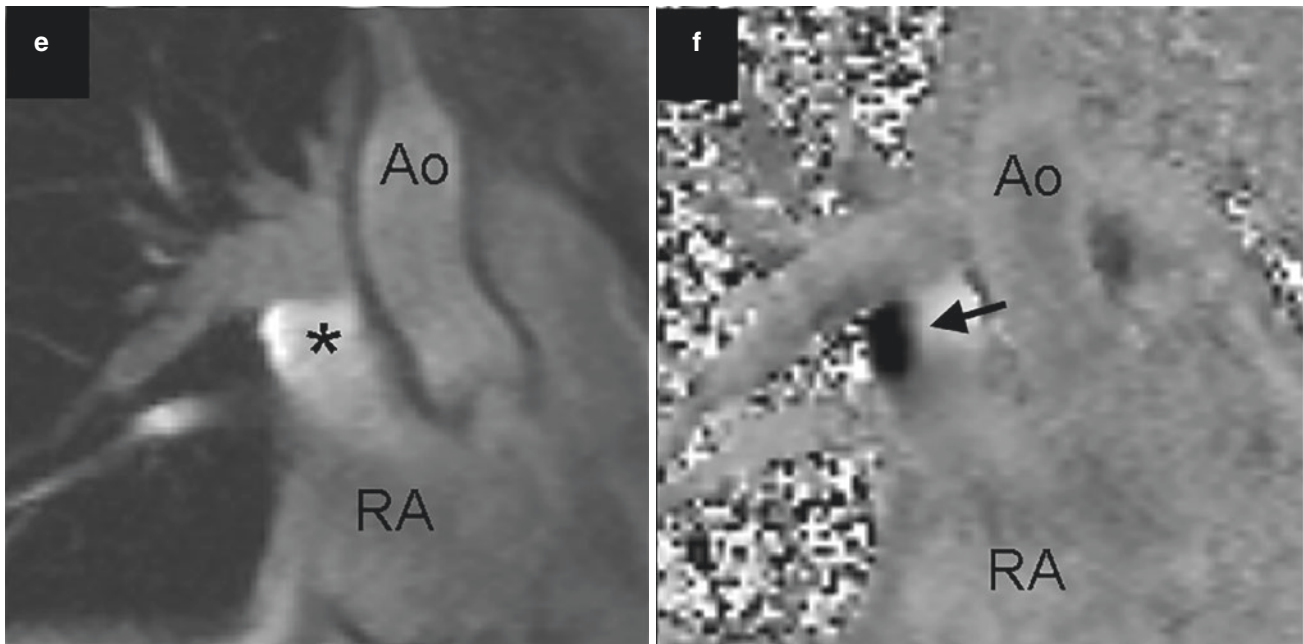


**Fig. 5.11** (continued)

### 5.3 Thoracic Systemic Vein Anomalies

#### 5.3.1 Thoracic Systemic Vein Development and Anatomy

The superior vena cava (SVC) courses from the junction of the right and left innominate veins to the right atrium. It is developed from the most proximal portion of the right anterior cardinal vein and the right common cardinal vein. The left innominate vein develops at the seventh week of gestation, with the involution of the left superior vena cava [5]. The left horn of the sinus venosus and the adjacent part of the left common cardiac vein go on to form the coronary sinus. The right posterior cardinal vein gives rise to the root of the azygos vein.

The azygos vein is formed by the suprarenal segment of the right supracardinal vein and the cephalic remnant of the right posterior cardinal vein [5]. The azygos and hemiazygos systems can be thought of as forming an H-shaped network of veins, with the azygos providing the right-sided aspect of the H while the hemiazygos provides the left lower segment and the accessory hemiazygos provides the left upper segment [17]. The azygos vein starts in the right lumbar region and passes through the aortic opening of the diaphragm to enter the thorax on the right of the aorta as it continues to receive drainage from the right lower ten intercostal veins. At the level of T4, it passes anteriorly to form a right-sided arch that joins to the posterior aspect of the SVC. The hemiazygos vein starts at the left lumbar region and ascends along the left side of the spine to the level of T8. Then, turning right, it

passes behind the aorta and terminates in the azygos vein. The accessory hemiazygos (left upper hemiazygos) collects the left intercostal veins that did not drain into the left superior intercostal vein and either connects to the lower hemiazygos or crosses over to the right to join the azygos vein. Where there is no connection to the hemiazygos or to the azygos vein, the accessory hemiazygos may connect directly to the left innominate vein.

The inferior vena cava (IVC) is the largest vein in the body. The inferior vena cava starts at the junction of the common iliac veins (the infrarenal IVC) and travels cephalad, receiving the drainage from the renal veins, and courses posterior to the liver (hepatic IVC) where the hepatic veins join to form the suprahepatic IVC with direct drainage into the right atrium. The development of the IVC is a complex process of five venous systems involving the posterior cardinals, the right supracardinals, the subcardinals, the hepatic segment of the inferior vena cava, and the hepatic veins.

In the normal systemic venous system, all systemic venous blood enters the right atrium via the right-sided inferior vena cava and the right-sided superior vena cava which are connected to the left side by the left common iliac vein, the left renal vein, the hemiazygos vein, and the left innominate vein. In general, the anomalies of the systemic thoracic veins are unlikely to be of hemodynamic consequence. However, their identification is important because of associated cardiac and noncardiac anomalies and to differentiate the systemic venous anomalies from the more important pulmonary venous anomalies that may require more imaging and investigation.

## 5.3.2 Superior Vena Cava

### 5.3.2.1 Persistent Left Superior Vena Cava

A persistent left superior vena cava is the most common congenital thoracic venous anomaly and results from the failure of the involution of the left anterior and left common cardinal veins. In the vast majority of cases, the persistent left superior vena cava drains into the right atrium through the coronary sinus. In a small number, it may drain into the left atrium by means of an unroofed coronary sinus. In many cases, the left innominate vein may still be present to connect the left superior vena cava to the right superior vena cava [5]. The size of the left superior vena cava has been noted to vary greatly and appears to be related to the presence and size of the left innominate vein. The left superior vena cava is commonly found in conjunction with other defects such as tetralogy of Fallot and atrioventricular septal defects but can be often present as an isolated finding. The left superior vena cava descends anterior to the aortic arch and to the left pulmonary artery, running along the posterior wall of the left atrium and into the left atrioventricular groove to drain through the coronary sinus and into the right atrium. Because of its drainage through the coronary sinus into the right atrium, there is enlargement of the coronary sinus. In fact, the echocardiographic finding of a dilated coronary sinus may often be the first indication of a persistent left superior vena cava and can be confirmed with an injection of agitated saline into the left arm to demonstrate bubble contrast in the dilated coronary sinus on echocardiography. No treatment is necessary for persistent left superior vena cava, but, once identified, it will be necessary to ensure that there are no other associated congenital defects and that there is clear documentation of a left superior vena cava. The presence of left superior vena cava will have future implications for the patient if consideration is ever given to insertion of a pacemaker or ablation catheter through the left subclavian vein [18]. There have been rare reports of a persistent left superior vena cava communicating with the left atrium by connection to the left atrial appendage or left pulmonary vein or through an unroofed coronary sinus. Such right to left shunts are rarely of hemodynamic consequence and are unlikely to be a cause of cyanosis. However, there is the potential for right to left thromboembolism, and it will be necessary to identify and document such a finding in order to limit any instrumentation of the left neck and upper limb veins [11, 19].

Cardiac MRI can quickly identify the presence and the course of the left superior vena cava (Fig. 5.12). On axial imaging, a persistent left superior vena cava can be confused with an anomalous left pulmonary vein (Fig. 5.13). Phase-contrast velocity flow maps will demonstrate that the flow is directed caudad with a persistent left superior vena cava and cephalad with an anomalous left pulmonary vein draining into the left innominate vein. The simple presence of a left

superior vena cava cannot account for a dilated right ventricle or other features of right-sided volume overload. In such a situation, it is important to seek out associated defects and especially to rule out the presence of an unroofed coronary sinus.

### 5.3.2.2 Absent Right Superior Vena Cava

This is a rare anomaly and has been reported with equal frequency in the presence of associated cardiac defects or with a normal heart. The right innominate vein drains, via the left innominate vein, to the left superior vena cava, and the azygos vein is connected to the left superior vena cava. There is no clinical consequence to this finding, but it is important to document the absent right superior vena cava in order to prevent problems at cardiac catheterization or with central line placement.

### 5.3.2.3 Superior Vena Cava to Left Atrium

There have been rare reports of the right superior vena cava draining to the left atrium [5] and can be a cause of unexplained cyanosis, with right to left shunting. This connection is due to a sinus venosus defect in conjunction with atresia of the superior vena cava orifice. If there is a patent but stenotic SVC orifice, then the superior vena cava would drain into both the right atrium and the left atrium. The standard imaging approach used to detect sinus venosus defect will demonstrate the sinus venosus defect and the SVC stenosis or atresia in this situation.

### 5.3.2.4 Inferior Vena Cava

#### Interrupted Inferior Vena Cava

The term interrupted inferior vena cava usually refers to the situation with the absence of the hepatic segment of the inferior vena cava. The infrahepatic venous drainage continues via the azygos vein and drains into the superior vena cava, either right or left sided. The hepatic veins drain separately into the right atrium. Rarely, the IVC may continue to bilateral superior venae cavae through bilateral azygos veins [5, 20]. Another variant may involve atresia of the suprahepatic vena cava. In that case, the hepatic veins must drain into the hepatic inferior vena cava and up through the azygos system. Interrupted left-sided IVC has been described with a dilated hemiazygos vein draining normally into the azygos at T8, or draining into a persistent left superior vena cava, or draining to the upper hemiazygos vein and from there into the left innominate vein following its usual course to the right superior vena cava [11]. Interrupted IVC will not result in any physiologic abnormality because abdominal venous return is assured. Its significance lies in its frequent association with other findings such as persistent left SVC, but especially with the heterotaxy syndrome and polysplenia. In fact, interrupted IVC is considered one of the features of the polysple-

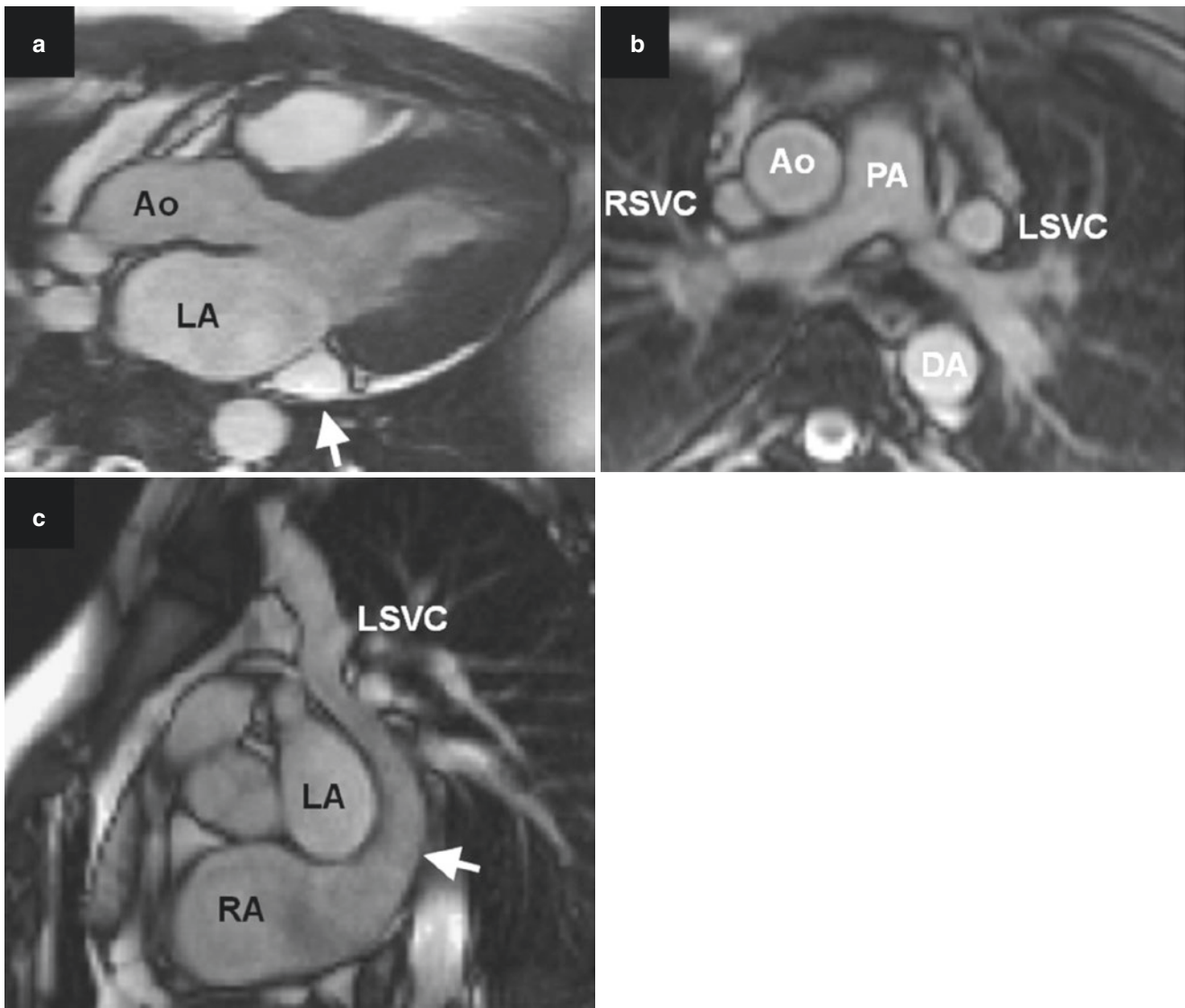


**Fig. 5.12** Left superior vena cava. (a) Still image from SSFP cine LVOT view demonstrating dilated coronary sinus (white arrow) posterior to the left atrium (LA). (b) Still image from SSFP cine transverse view. The left superior vena cava (LSVC) is seen anterior to the left pulmonary artery. (c) Still image from SSFP cine sagittal oblique dem-

onstrates the LSVC entering the dilated coronary sinus (white arrow) and flowing into the right atrium (RA). The cine from which this still is derived is available as a supplemental file (Movie 5.10). *Ao* ascending aorta, *DA* descending aorta, *RSVC* right superior vena cava, *PA* main pulmonary artery

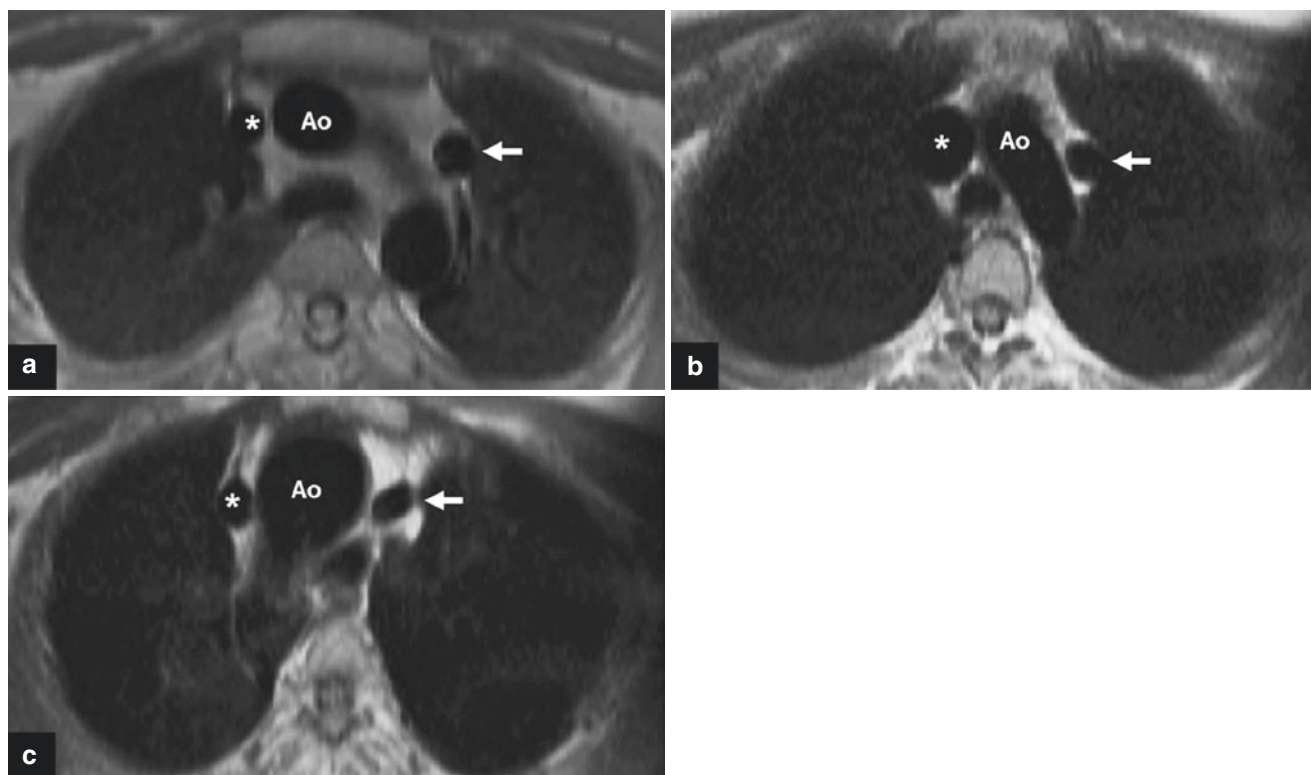


**Fig. 5.13** Left-sided vertical vein. Single-shot turbo spin-echo axial images from three different patients illustrating three different causes of a left-sided vein (arrow). (a) Persistent left superior vena cava is the cause of the left-sided vein in this patient—see Fig. 5.12. (b) Partial anomalous pulmonary venous connection with a vertical vein (arrow)

connecting upper left pulmonary vein with the innominate vein. Note the large size of the SVC (\*)—see Fig. 5.3. (c) Retroaortic innominate vein (arrow) along its vertical course before crossing under the aortic arch to join the superior vena cava. Note the right aortic arch—see Fig. 5.16. *Ao* aorta. \* superior vena cava

nia syndrome. It may be found in the absence of other anomalies [20], and it may complicate cardiac catheterization via the route from the femoral veins. Obviously, this anomalous anatomy will have an effect on cardiac interventions such as Fontan procedure that involves surgical diversion of IVC flow [5].

Cardiac magnetic resonance imaging will reveal that the intrahepatic segment of the IVC is absent but there may be hepatic veins attached to the suprahepatic IVC, draining into the right atrium. The most striking feature will be that of the markedly dilated azygos vein and the appearance of two vascular arches, the aortic arch and the azygos arch (Fig. 5.14). The finding of an interrupted IVC requires careful scrutiny to detect associated cardiac and extracardiac lesions.

#### Duplicated IVC

As previously postulated by Geva, the bilateral nature of the development of the IVC with five venous systems that contribute to the formation of the IVC can explain the presence of bilateral inferior venae cavae above and below the liver [5]. Bilateral suprahepatic inferior venae cavae can be fre-

quently found in cases of visceral heterotaxy with asplenia (Fig. 5.15). There is no clinical significance to this finding, except for its association with other defects.

#### Inferior Vena Cava Connection to the Left Atrium

Although cases of IVC connection to the left atrium have been reported in previous reviews [1], the IVC probably was connected to a left sided, but morphologically right atrium with the absence of the septum secundum, resulting in drainage of the inferior vena cava into the pulmonary veins [5]. This right to left shunting gives rise to cyanosis and to the risk of paradoxical embolization. Treatment requires surgical diversion of the inferior vena caval blood into the right atrium.

#### 5.3.3 Azygos Vein Anomalies

The absence of the azygos vein is rare [11] and has been described with the hemiazygos vein draining most of the right and left intercostal veins. The most common congenital



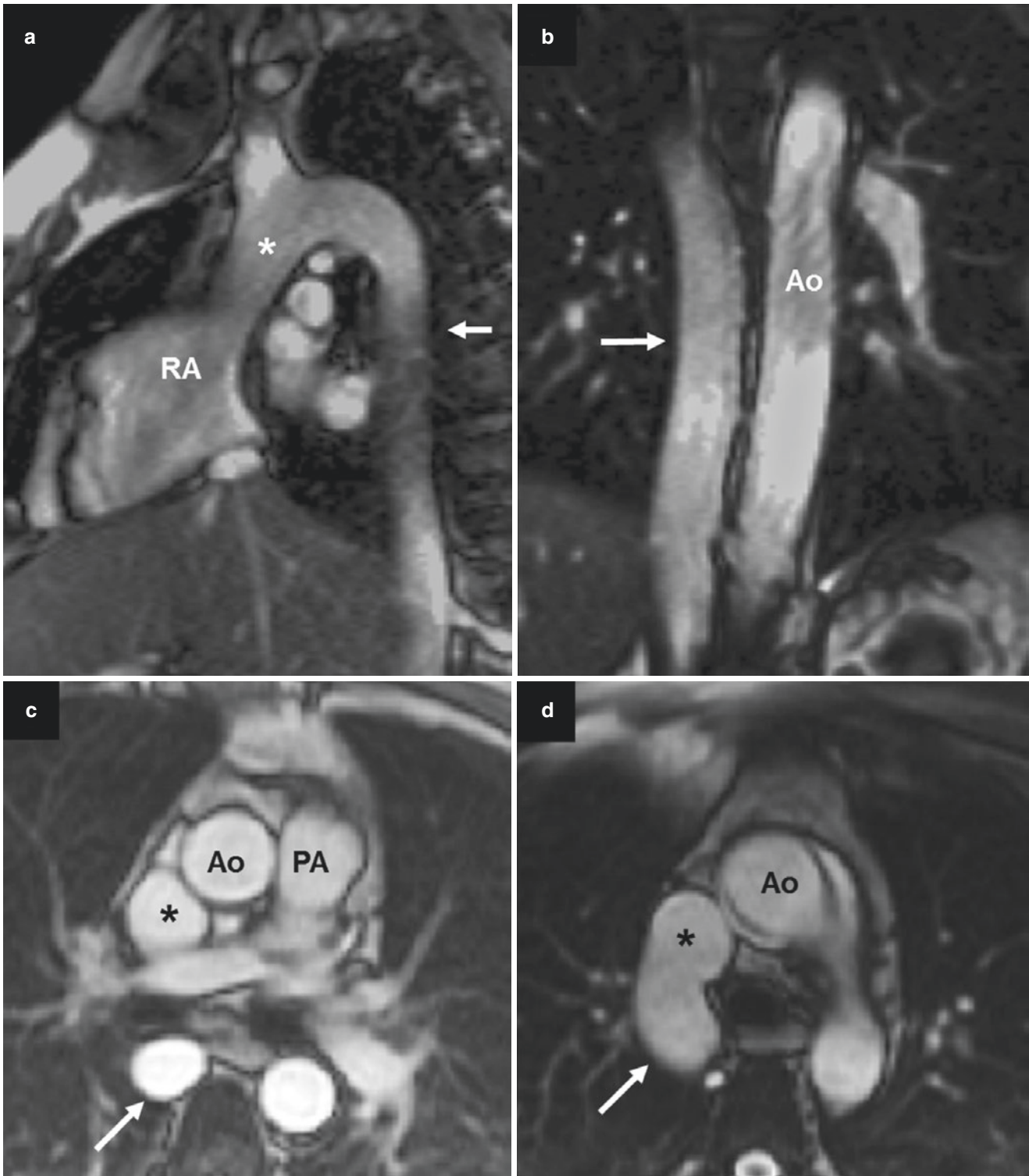


**Fig. 5.14** Interrupted IVC with azygos continuation. Adult female presented with PSVT. She was referred for ablation, but the right atrium could not be accessed via the femoral vein route. On MR imaging, she was found to have an interrupted IVC with azygos continuation. (a) SSFP bright blood sagittal image demonstrating the dilated azygos vein (arrow) and azygos arch connecting to the superior vena cava (\*). Note the absence of the intrahepatic IVC. (b) SSFP bright blood coronal

image demonstrating the double arch appearance with the dilated azygos vein (arrow) on the right of the aorta (Ao). (c) SSFP bright blood axial image at the level of the pulmonary artery (PA) bifurcation demonstrating the dilated azygos vein (arrow) and superior vena cava (\*). (d) SSFP bright blood axial image caudal to plane of (c), demonstrating the azygos arch and the aortic arch. SSFP sagittal plane cine is available as supplemental file (Movie 5.11)

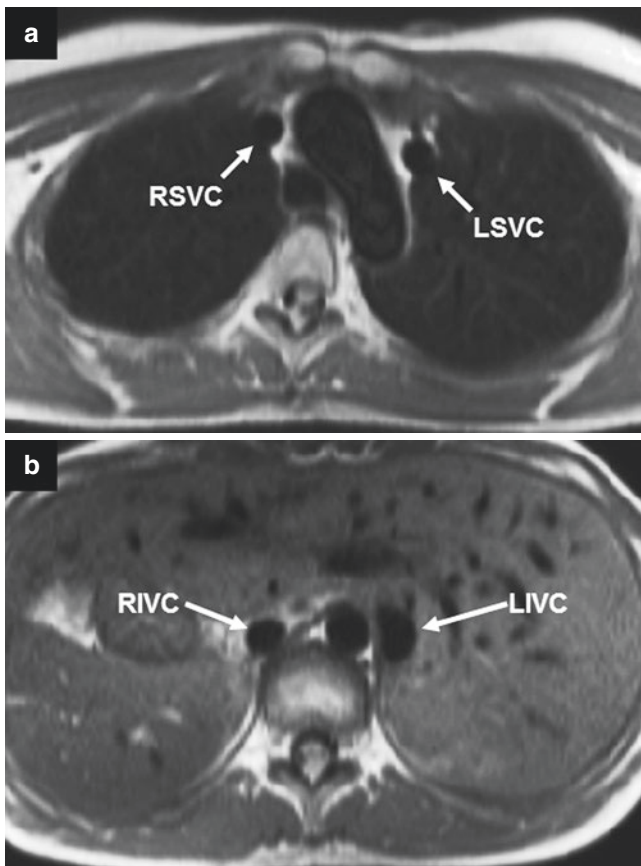


**Fig. 5.15** Duplicated IVC. Sixteen-year-old woman with double outlet right ventricle, right atrial isomerism, and asplenia. (a) Single-shot turbo spin-echo axial image at the level of the aortic arch demonstrating both a right superior vena cava (RSVC) and a persistent left superior vena cava (LSVC). (b) Single shot turbo spin-echo axial image below the diaphragm demonstrating both a right inferior vena cava (RIVC) and a left inferior vena cava (LIVC). Note the liver on the left extending across the abdomen

lesion directly affecting the azygos vein is the azygos lobe. The azygos lobe is a small accessory lobe above the hilum of the right lung. This occurs due to failure of the azygos vein to migrate over the apex of the lung during embryologic development. It is present in 1% of people and results in no venous impairment. Its only significance is to identify it as a normal variant and to not proceed to further imaging when it is detected [11]. The most striking congenital anomalies affecting the azygos vein are linked to interrupted IVC (see

above). More commonly, in the patient with congenital heart disease, the finding of a dilated azygos vein will be due to impaired drainage through the inferior vena cava or superior vena cava as a result of dilated pulmonary artery [21] or post-operative complications following Mustard repair, Fontan procedure, or repair of PAPVC.

### 5.3.4 Anomalous Course of the Left Innominate Vein

The normal left innominate vein courses from left to right, anterior to the aortic arch, joining the right innominate to form the superior vena cava. In retroaortic innominate vein, after the left subclavian and left common jugular veins form the innominate vein, it turns to run inferiorly and then makes a right turn behind the ascending aorta and reaches the superior vena cava below the insertion of the azygos vein (Fig. 5.16). This is a rare anomaly and has no direct clinical consequence but is usually associated with cardiac defects such as tetralogy of Fallot, atrioventricular septal defect, and coarctation of the aorta [5]. It is important to identify a retroaortic innominate vein in these patients because it may interfere with planned surgery for correction of the other defects. Care needs to be taken not to confuse the appearance of a persistent left SVC or anomalous connection of the pulmonary vein to the left innominate vein with that of a retroaortic innominate vein (Fig. 5.13). A duplicated innominate vein has been described. This has both an anterior and a retroaortic component and forms a ring that encircles the aorta [5].

### 5.3.5 CMR Sequences and Protocols for Thoracic Systemic Vein Imaging

The approach and imaging parameters described in Sect. 5.2.7 for pulmonary venous imaging apply equally to CMR imaging of thoracic systemic veins. Careful attention to the initial transverse images will provide clues to anomalies of the SVC, IVC, innominate vein, and azygos vein. Those transverse images can then be used for choosing the optimal planes for better visualization of the identified anomalies and to instigate a search for associated anomalies.

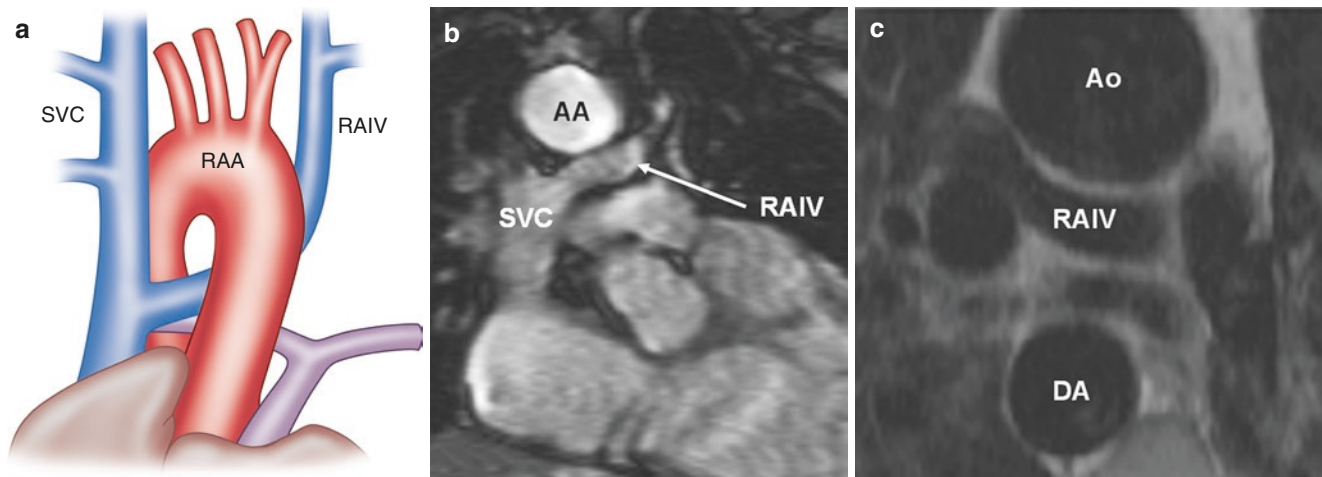


**Fig. 5.16** Retroaortic innominate vein. (a) Diagram showing a retroaortic innominate vein (RAIV) associated with a right aortic arch (RAA). (b) Coronal view demonstrating the RAIV passing under the aortic arch (AA) to connect to the superior vena cava (SVC). (c) Axial single-shot turbo spin echo showing the RAIV posterior to the ascend-

ing aorta (Ao). Note the descending aorta (DA) on the right. (a is adapted with permission from Chapter 38 (Figure 38.15) Geva T and Van Praagh S in Moss and Adams' Heart Disease in Infants, Children and Adolescents. 7th Edition Philadelphia Lippincott Williams & Wilkins; 2008 [5])

## 5.4 Conclusion

Venoatrial anomalies comprise a diverse set of abnormalities affecting both the pulmonary venous and the systemic thoracic venous systems. One standard cardiac magnetic resonance imaging approach (Sect. 5.2.7) can be used for the evaluation of these anomalies and has the additional advantage of being able not only to assess for associated intracardiac and extracardiac anomalies but also to provide physiologic information about cardiac function and the extent of intravascular shunting, all during one cardiovascular examination. Although echocardiography still forms the basis of imaging in congenital heart disease, cardiac magnetic resonance imaging is especially of value in the imaging of these venous anomalies because the anatomic constraints of echocardiography do not apply to MR imaging and its ability to encompass a wide field of view and visualize venous structures and their course in multiple planes.

### Practical Pearls

- Every patient with unexplained pulmonary hypertension or dilated right ventricle needs to have cardiac magnetic resonance imaging to rule out PAPVC, sinus venosus defect, unroofed coronary sinus, cor triatriatum, and pulmonary vein stenosis.
- Every patient with a right-sided PAPVC needs careful evaluation for sinus venosus defect. Every patient with sinus venosus defect needs careful evaluation for PAPVC. Consider evaluation for PAPVC in patient with secundum ASD who is being proposed for ASD closure.

- A persistent left SVC will cause a dilated coronary sinus but not a dilated right ventricle. The presence of a dilated right ventricle in the setting of a persistent left SVC requires a careful search for an unroofed coronary sinus, or other sources of right ventricular volume overload.
- A left-sided vertical vein is not always a persistent left SVC. The presence of a left-sided vertical vein requires sufficient imaging to differentiate it from a left PAPVC.

## References

1. Rahmani N, White CS. MR imaging of thoracic veins. *Magn Reson Imaging Clin N Am.* 2008;16:249–62.
2. Hatipoglu S, Almogheer B, Mahon C, Houshmand G, Uygur B, Giblin GT, Krupickova S, Baksi J, Alpendurada F, Prasad SK, Babu-Narayan SV, Gatzoulis MA, Mohiaddin RH, Pennell DJ, Izgi C. Clinical significance of partial anomalous pulmonary venous connections (isolated and atrial septal defect associated) determined by cardiovascular magnetic resonance. *Circ Cardiovasc Imaging.* 2021;14:e012371.
3. Kafka H, Mohiaddin RH. Cardiac MRI and pulmonary MR angiography of sinus venosus defect and partial anomalous pulmonary venous connection in cause of right undiagnosed ventricular enlargement. *AJR.* 2009;192:259–66.
4. Pennig L, Wagner A, Weiss K, Lennartz S, Grunz JP, Maintz D, Laukamp KR, Hieckthier T, Naehle CP, Bunck AC, Doerner J. Imaging of the pulmonary vasculature in congenital heart disease without gadolinium contrast: intraindividual comparison of a novel Compressed SENSE accelerated 3D modified REACT with 4D contrast-enhanced magnetic resonance angiography. *J Cardiovasc Magn Reson.* 2020;22:8. <https://doi.org/10.1186/s12968-019-0591-y>.
5. Geva T, Van Praagh S. Anomalies of the pulmonary veins. Abnormal systemic venous connections. In: Allen HD, Gutgesell HP, Clark EB, Driscoll DJ, editors. Moss and Adams' heart dis-

- ease in infants, children and adolescents. 7th ed. Philadelphia, PA: Lippincott Williams & Wilkins; 2008. p. 761–817.
6. Ammash NM, Seward JB, Warnes CA, Connolly HM, O’Leary PW, Danielson GK. Partial anomalous pulmonary venous connection: diagnosis by transesophageal echocardiography. *J Am Coll Cardiol.* 1997;29:1351–8.
  7. Locca D, Hughes M, Mohiaddin R. Cardiovascular magnetic resonance diagnosis of a previously unreported association: cor triatriatum with right partial anomalous pulmonary venous return to the azygos vein. *Int J Cardiol.* 2009;135:e80–2.
  8. Alsoufi B, Cai S, Van Arsdell GS, Williams WG, Caldarone CA, Coles JG. Outcomes after surgical treatment of children with partial anomalous pulmonary venous connection. *Ann Thorac Surg.* 2007;84:2020–6.
  9. Romberg EK, Stanescu AL, Bhutta ST, Otto RK, Ferguson MR. Computed tomography of pulmonary veins: review of congenital and acquired pathologies. *Pediatr Radiol.* 2021;52:2510. <https://doi.org/10.1007/s00247-021-05208-3>.
  10. Wilson W, Horlick E, Benson L. Successful transcatheter occlusion of an anomalous pulmonary vein with dual drainage to the left atrium. *Catheter Cardiovasc Interv.* 2015;85:1212–6.
  11. Demos TC, Posniak HV, Pierce KL, Olson MC, Muscato M. Venous anomalies of the thorax. *AJR.* 2004;182:1139–50.
  12. Dillman JR, Yarram SG, Hernandez RJ. Imaging of pulmonary venous developmental anomalies. *AJR.* 2009;192:1272–85.
  13. Valente AM, Sena K, Powell AJ, del Nido PJ, Geva T. Cardiac magnetic resonance imaging evaluation of sinus venosus defects: comparison to surgical findings. *Pediatr Cardiol.* 2007;28:51–6.
  14. Abdullah HAM, Alsalkhi HA, Khalid KA. Transcatheter closure of sinus venosus atrial septal defects with anomalous pulmonary venous drainage: innovative technique with long-term follow-up. *Catheter Cardiovasc Interv.* 2018;95:743–7.
  15. Ho YC, Chen SSM, Mohiaddin RH. Late stenosis after repair of anomalous pulmonary venous drainage and the value of cardiovascular magnetic resonance for assessment of this important complication. *Pediatr Cardiol.* 2013;34:480–2.
  16. Varona Porres D, Morenza OP, Pallisa E, Roque A, Andreu J, Martinez M. Learning from the pulmonary veins. *Radiographics.* 2013;33:999–1022.
  17. Mozes G, Gloviczki P. Venous embryology and anatomy. In: Bergan JJ, editor. *The vein book.* Oxford: Elsevier; 2007. p. 15–26.
  18. Keeble W, Mohiaddin R. Technical failure to perform cardiac resynchronization therapy: use of cardiac magnetic resonance imaging techniques to clarify a left-sided superior vena cava and coronary sinus morphology. *Can J Cardiol.* 2008;24:589–90.
  19. Sonovane SK, Milner DM, Singh SP, Aal AKA, Shahir KS, Chaturvedi A. Comprehensive imaging review of the superior vena cava. *Radiographics.* 2015;35:1873–92.
  20. Bartram U, Fischer G, Kramer HH. Congenitally interrupted inferior vena cava without other features of the heterotaxy syndrome: report of five cases and characterization of a rare entity. *Pediatr Dev Pathol.* 2008;11:266–73.
  21. Kafka H, Gatzoulis MA, Rubens MB. Superior vena cava obstruction due to markedly enlarged right pulmonary artery in Eisenmenger syndrome. *Eur Heart J.* 2007;28:1404.





# Septal Defects

# 6

Inga Voges and Sylvia Krupickova

## 6.1 Introduction

Atrial septal defects (ASD) are the second most common congenital heart anomalies and account for approximately 15% of all congenital heart defects worldwide [1]. Children and young adults are often asymptomatic; however, in the long term, many patients develop symptoms typically including dyspnea, reduced exercise capacity, and atrial rhythm disturbances [2]. Recent studies have also shown an increased mortality compared to a general population with improved survival if the ASD is closed earlier in life [3]. In this context, early detection of these septal defects is of great importance.

Ventricular septal defects (VSD) are the most common congenital cardiac defects with a global birth prevalence of about three per thousand (35% of all congenital heart defects worldwide) [1]. Large defects are closed surgically in the first year of life to avoid irreversible vascular changes from pulmonary overcirculation [4, 5]. Smaller and restrictive ventricular defects can be closed later in life depending on their hemodynamic relevance and associated findings.

**Supplementary Information** The online version contains supplementary material available at [https://doi.org/10.1007/978-3-031-29235-4\\_6](https://doi.org/10.1007/978-3-031-29235-4_6).

I. Voges (✉)

Department of Congenital Heart Disease and Pediatric Cardiology,  
University Hospital Schleswig-Holstein, Kiel, Germany

DZHK (German Centre for Cardiovascular Research),  
Kiel, Germany  
e-mail: [inga.voges@uksh.de](mailto:inga.voges@uksh.de)

S. Krupickova

Department of Paediatric Cardiology, Royal Brompton Hospital,  
Guy's and St Thomas' NHS Foundation Trust, London, UK

Imperial College, London, UK

CMR Unit, Royal Brompton Hospital, Guy's and St Thomas' NHS  
Foundation Trust, London, UK  
e-mail: [s.krupickova@rbht.nhs.uk](mailto:s.krupickova@rbht.nhs.uk)

Transthoracic and transesophageal echocardiography are the imaging modalities of choice to detect defects of the interatrial and interventricular septum but have well-known limitations. Cardiovascular magnetic resonance (CMR) has several advantages for the assessment of septal defects. Beside its ability to visualize cardiac structures in any view, it allows a quantification of the shunt and is able to clearly depict associated anomalies [6–8].

## 6.2 Definition and Morphology

### 6.2.1 Atrial Septal Defects

Five different ASD types are described: (1) patent foramen ovale, (2) secundum ASD, (3) primum ASD, (4) coronary sinus defect, and (5) superior and inferior sinus venosus defect.

Patent foramen ovale is a small communication between the left and right atrium that is nearly universally found during fetal life and in neonates after birth. In older and otherwise healthy children and adults, it is often an incidental finding with a decreasing incidence with age [9].

The secundum ASD is the most common ASD type and describes a defect that is located in the fossa ovalis (Fig. 6.1).

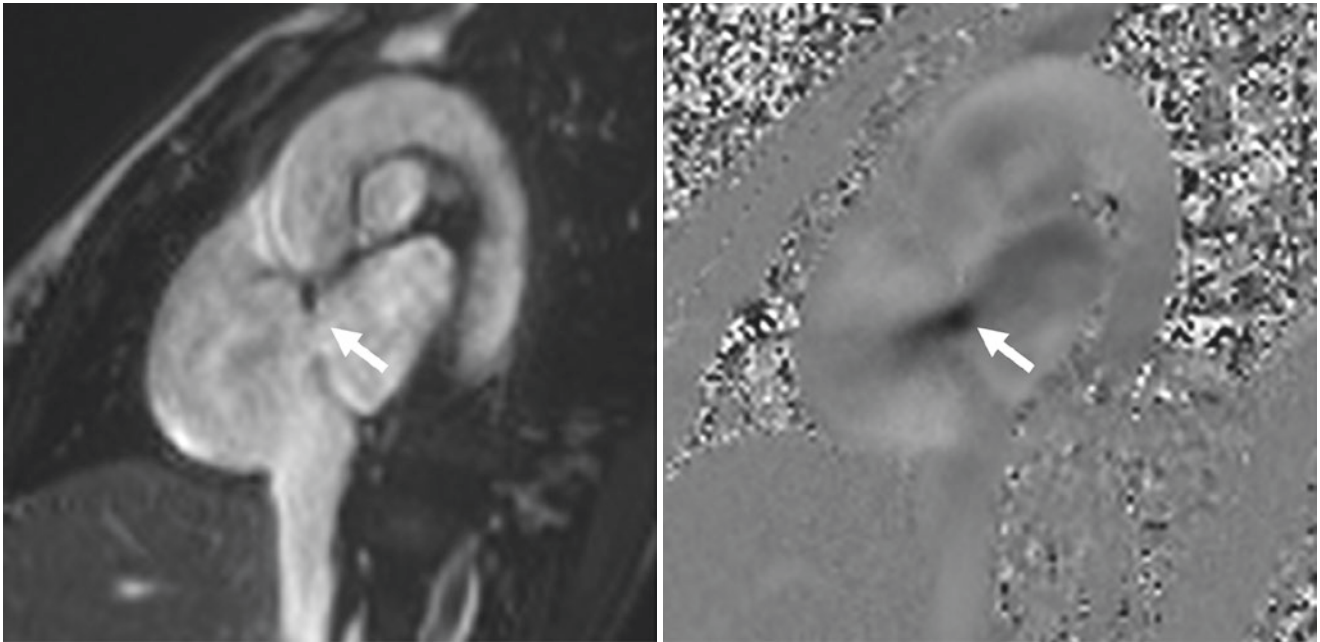


**Fig. 6.1** Secundum atrial septal defect. The right figure shows a cine image with a small defect in the area of the Fossa ovalis (white arrow). The left figure shows a phase image from phase-contrast CMR acquired in the same plane with left-to-right shunt across the interatrial septum

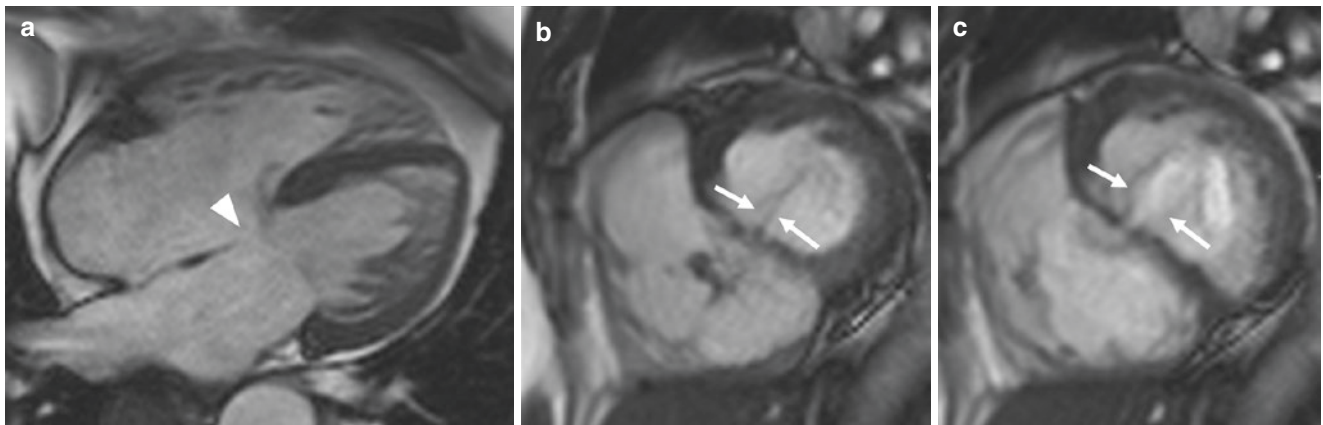


**Fig. 6.2** Primum atrial septal defect and mitral valve cleft. (a) In the 4ch-view, the defect (white arrowhead) is well seen and located directly above the atrioventricular valve. (b, c) Short axis images showing the mitral valve cleft in systole and diastole

In some patients, the defect can reach out beyond the fossa ovalis, and more than one defect can be found. In extreme cases, the atrial septum can be missing (so-called monoatrium).

A primum ASD involves the free margin of the atrial septum and the atrial surface of the conjoined leaflets of the common atrioventricular valve [10]. This type of ASD is typically associated with a mitral valve cleft (Fig. 6.2) [11].

The inferior and superior sinus venosus are located outside the fossa ovalis (Fig. 6.3). The superior sinus venosus defect is more common and occurs when the superior vena

cava overrides the atrial septum above the fossa ovalis with drainage of venous blood into both atria [11, 12]. An inferior sinus venosus defect can be found below the fossa ovalis at the orifice of the inferior vena cava [11, 12]. Both defects can be associated with an abnormal drainage of pulmonary veins.

The coronary sinus defect describes a defect at the site of the coronary sinus orifice that creates a direct communication between the right and left atrium (Fig. 6.4) [10–12]. It can also be located on the posteroinferior wall of the left atrium [11]. These defects can be associated with persistent left superior vena cava.

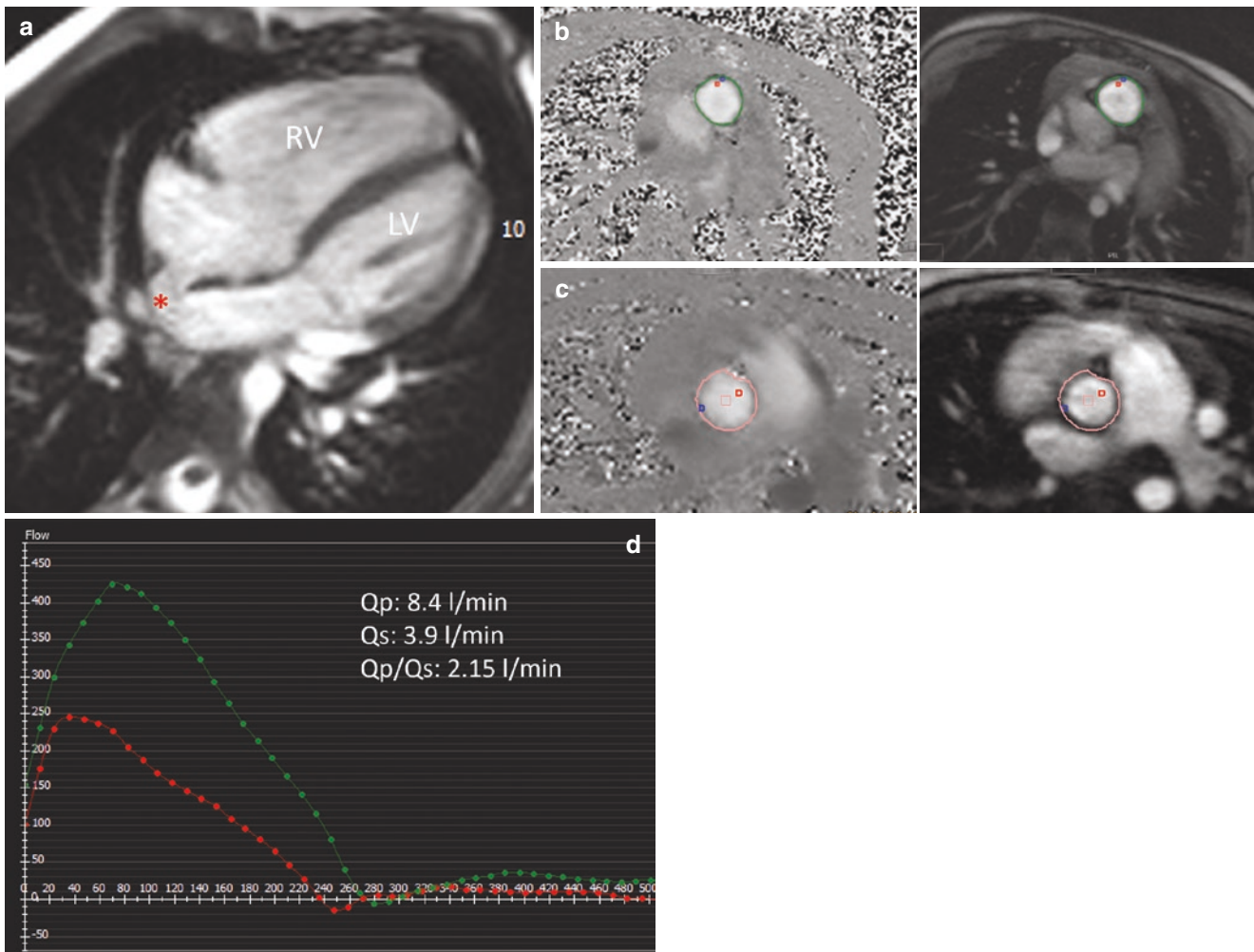


**Fig. 6.3** Superior sinus venosus defect (a,\*) with right heart volume overload in a 9-year-old girl. Phase-contrast flow measurement in the main pulmonary artery (b) and the ascending aorta (c) revealed a Qp/Qs of 2.15 L/min (d)

### 6.2.2 Ventricular Septal Defects

In the past, there was controversy regarding the classification of VSDs; however, the International Society for Nomenclature of Paediatric and Congenital Heart Disease has introduced a terminology that allows a detailed and standardized description of all types of VSDs [13]. This classification system takes into account the normal anatomy of the interventricular septum and divides the VSDs in four large groups by using a geographic approach: (1) central perimembranous defects, (2) inlet defects, (3) trabecular muscular defects, and (4) outlet defects [13].

Central perimembranous defects are the most common types of VSDs and are located in the area of the membranous septum. They are also known under the names perimembranous, membranous, subaortic, or infracristal VSDs. Central perimembranous defects are typically found at the antero-septal commissure behind the septal leaflet of the tricuspid

valve and below the commissure between the right and non-coronary cusps of the aortic valve [13].

Inlet defects open into the right ventricle (RV) and can be further subdivided into four different types according to their geography and borders [13, 14]. Another term to describe inlet defects is atrioventricular canal type of septal defect [15]. Inlet defects have distinct and separate right and left AV junctions that make them different to atrioventricular septal defects [13].

Trabecular muscular defects are located in the trabecular muscular septum with muscular borders [13]. Depending on their location within the septum, they can be further divided into midseptal, apical, posteroinferior, and anterosuperior defects [13]. These types of defects often close spontaneously.

Outlet defects open in the outlet of the RV and are cradled between the two limbs of the septal band [13, 16]. The 11th iteration of the international classification of diseases distinguishes further between outlet defects without malalignment,



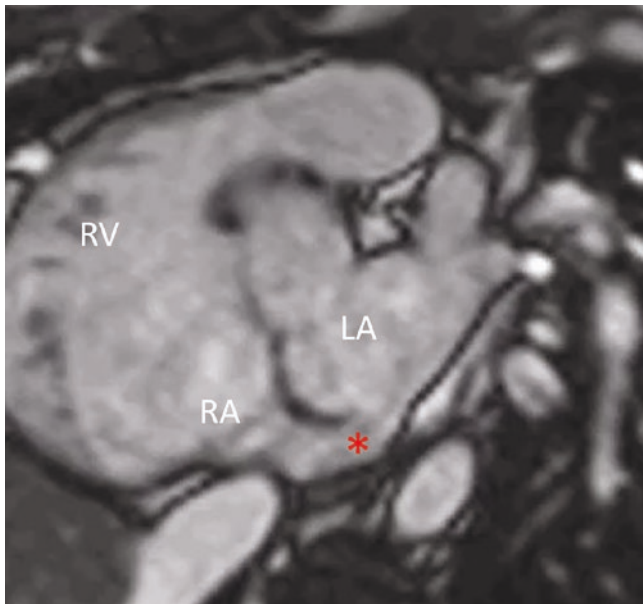


**Fig. 6.4** Coronary sinus defect (\*) in an adult patient who underwent cardiac surgery in childhood with closure of small secundum ASD and ligation of persistent left superior vena cava

outlet defects with anteriorly malaligned outlet septum, and outlet defects with posteriorly malaligned outlet septum [13].

### 6.3 Associated Anomalies

The indication for a CMR scan in patients with a secundum ASD is often to rule out an associated partial anomalous pulmonary venous return that might be otherwise missed [17]. The pulmonary veins can be well visualized on transaxial and coronal cine stacks and additional cross-cut cine images (Fig. 6.5). Contrast angiography is another useful way of delineating the pulmonary venous anatomy. In patients with a primum ASD, a cleft of the mitral valve is a typical associated finding that can cause significant mitral valve regurgitation with enlargement of the left atrium and left ventricle (LV). A volume overload of the right-sided heart chambers can lead to tricuspid valve regurgitation that, however, is commonly only mild. The coronary sinus ASD is often associated with a left persistent superior vena cava.

An isolated VSD can be associated with diverse cardiac or extracardiac anomalies as well as syndromes. Common car-

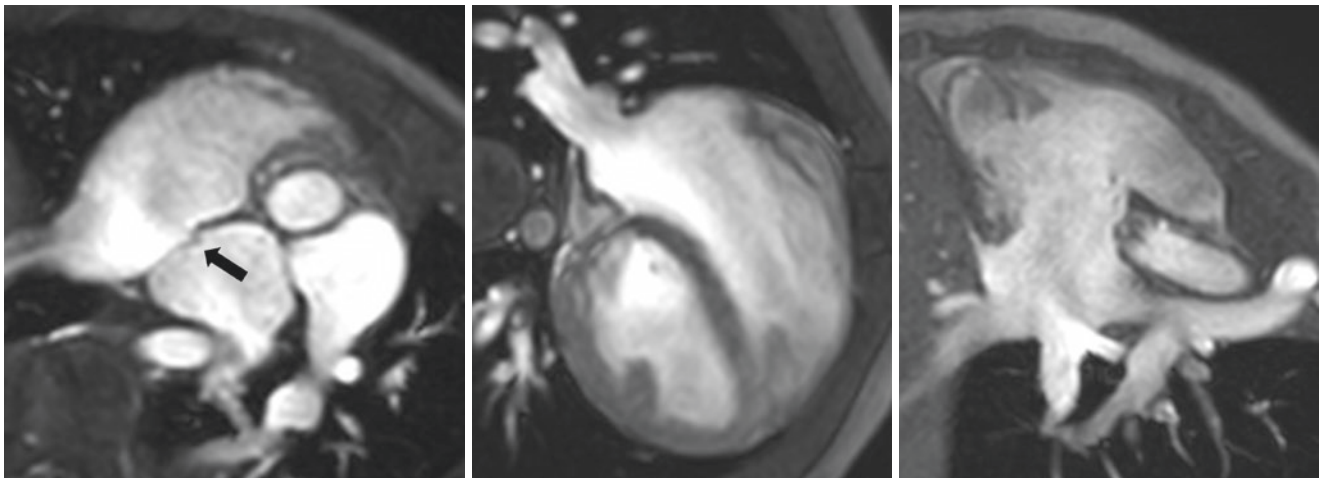


**Fig. 6.5** Patent foramen ovale (black arrow) and partial anomalous pulmonary venous drainage in a toddler. The entire right pulmonary veins drain into the right atrium (middle and right-sided image)



diac anomalies include aortic leaflet prolapse, aortic regurgitation, infundibular pulmonary stenosis, as well as ostium secundum ASD [18]. In addition, double-chamber RV is a well-known association, and the occurrence of infective endocarditis is relatively common [19]. Features of pulmonary hypertension such as enlarged pulmonary arteries can be found in patients with large VSDs.

## 6.4 Clinical Presentation

The clinical presentation of patients with an ASD can include a wide range of symptoms. Significant left to right shunt across the defect leads to right heart volume overload and increased pulmonary blood flow. In adults, this can result in heart failure, atrial arrhythmias due to right atrial enlargement, and pulmonary hypertension [20–22]. In children, heart failure is rarely seen, but pulmonary overcirculation can promote recurrent airway infections and dyspnea. Patients with a coronary sinus ASD and left persistent superior vena cava can present with reduced oxygen saturation due to right to left shunt across the defect.

Large ventricular septal defects are hemodynamically relevant and clinically present in the first weeks of life after pulmonary vascular resistance decreases. Typical symptoms and clinical findings are sweating during feeding, dyspnea, slow weight gain, and hepatomegaly. These large defects should be closed in the first months of life (normally in the first 6 months) to avoid pulmonary hypertension (Eisenmenger syndrome). Small defects normally do not cause any symptoms. However, a recent study has shown that a significant number of patients may develop left atrial and LV dilatation as well as LV dysfunction [19].

## 6.5 CMR Imaging

### 6.5.1 Indications

CMR imaging complements other imaging techniques and invasive hemodynamic assessments.

In patients with ASDs, CMR is of particular value for the assessment of the size of the right heart and for visualization of the pulmonary veins [23]. Beside detailed anatomical descriptions, CMR is able to accurately measure volumes and function of the dilated right heart structures and to quantify the degree of shunt [24].

In patients with VSDs, CMR allows an exact assessment of the potentially enlarged size of the LV and left atrium. Shunt quantification might help in the process of decision-making if the defect needs to be closed. Additional findings such as a double-chambered RV can anatomically be clearly described by CMR. Functional parameters derived from

CMR might have prognostic value in patients with post-tricuspid defects and Eisenmenger syndrome [25].

General indications for CMR in atrial and ventricular septal defects include poor echocardiographic acoustic windows, need to evaluate surrounding structures and associated vasculature which may be incompletely visualized by echocardiography (in particular, the pulmonary veins), and need for noninvasive quantification of pulmonary and systemic blood flow for shunt quantification. Goals for imaging include accurate assessment of ventricular volumes and function, the relationship of the defect to surrounding structures and resulting pathology, evaluation of associated anomalies, and assessment of intracardiac shunting.

CMR might be helpful for the presurgical or pre-interventional planning of closure of muscular VSDs (Fig. 6.6). However, CMR is less suitable for defects with thinner rims such as ASDs and perimembranous VSDs [26]. 3D imaging can be applied and used for 3D printing in complex cases [27].

### 6.5.2 Imaging Protocols

#### 6.5.2.1 CMR Techniques for the Anatomical Description of Septal Defects and Associated Findings

CMR is well suited to visualize defects of the atrial and ventricular septum. Spin-echo and 2-dimensional (2D) steady-state free precession (SSFP) pulse sequences are usually used for anatomical imaging. In complex cases, 3D imaging with ECG- and respiratory-navigated 3D SSFP or modified Dixon sequences might be useful for a detailed anatomical description [28]. Conventional contrast-enhanced magnetic resonance angiography and time-resolved dynamic contrast-enhanced magnetic resonance angiography give good information about the thoracic vessels including the pulmonary veins [29].

A secundum ASD can often be well visualized in the area of the fossa ovalis on a transaxial cine stack covering the entire heart. Furthermore, an atrial short axis stack with the use of a thin slice thickness (4–6 mm) should be applied to delineate the defect (Fig. 6.7c). Sometimes it can be difficult to distinguish between an ASD and a thin-walled but intact middle part of the interatrial septum. In those cases, it might be helpful to know that patients with an ASD have thickened edges of the septum adjacent to the defect (Fig. 6.7), whereas otherwise the septum thins gradually toward the thin-walled but intact septal part [31].

The primum ASD, sinus venosus defects, and coronary sinus ASD are also seen on transaxial stacks of 2D SSFP cine or spin-echo images as well as on an atrial short axis stack. As mentioned, the primum ASD defect is commonly associated with a mitral valve cleft that can be seen on short

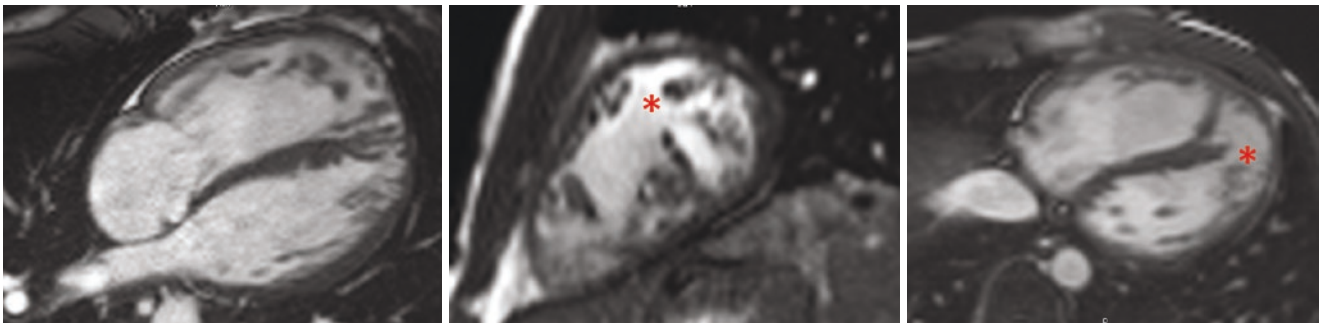


**Fig. 6.6** Large muscular ventricular septal defect (\*) in a male with unrepaired tetralogy of Fallot. There are a lack of septal rims toward the anterior and apical walls

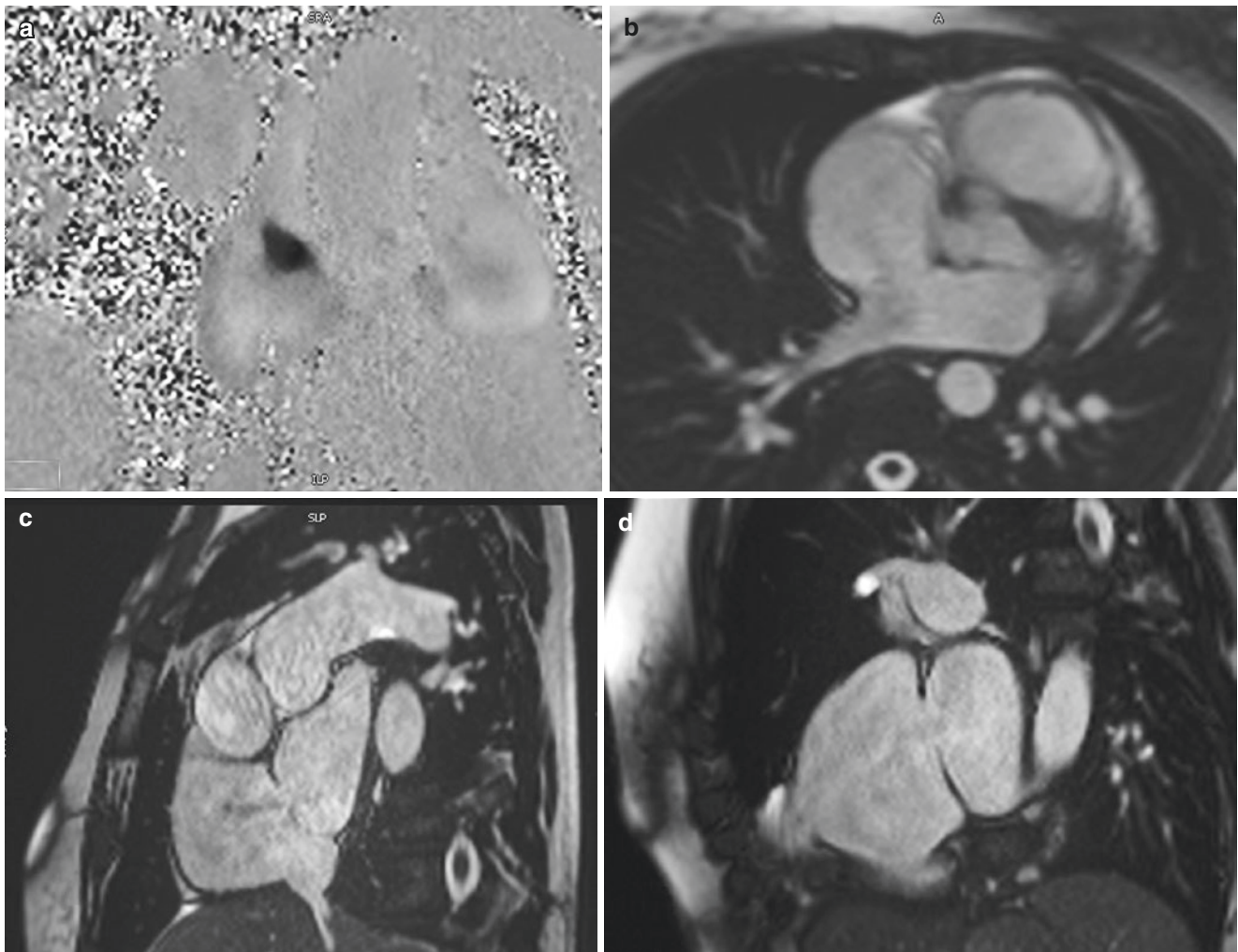


**Fig. 6.7** Female with a secundum ASD. (a) 2D phase-contrast image showing an en-face view of the defect [30]. (b–d) SSFP cine images illustrating the defect

axis stacks covering the atrioventricular valves (Fig. 6.2). The atrial short axis stack should include the entire atrial septum including the orifices of the caval veins. An additional coronal cine stack can be helpful in patients with a coronary sinus defect. In all situations, cross-cut images

through the defect using 2D SSFP pulse sequences can help for anatomical definition.

Ventricular septal defects are often well seen on trans-axial cine stacks. However, it might be of use to acquire images of the interventricular septum in a second plane

because small defects can be difficult to visualize. In addition, large defects can anatomically be better described. Dedicated 2D SSFP cine images can confirm the presence of a VSD.

Associated lesions, particularly aortic regurgitation and a double-chambered RV, can be visualized by acquiring LV and RV outflow tract views as well as aortic valve cine images.

For visualization of septal defects, it may be also helpful to use in-plane phase-contrast cine techniques that have longer repetition times than SSFP imaging. Additionally and carefully planned through-plane imaging might allow to acquire a direct en-face image of septal defects (Fig. 6.7a) [30].

CMR imaging in patients with septal defects is typically successful if information from previous imaging studies, in particular echocardiographic examinations, is available. Together with this information and a systematic scanning approach with thorough evaluation of the interventricular

and interatrial septum, the defect can typically be anatomically evaluated.

Late gadolinium enhancement (LGE) CMR may add valuable information in some occasions such as in patients with arrhythmias after surgical VSD closure to plan electrophysiology studies. LGE imaging is able to locate previous surgical areas and can give information about the extent of scar tissue and VSD patch material. An apical scar can sometimes be detected in older congenital heart disease patients and may suggest apical venting during a previous surgery. Nowadays, apical venting is typically not performed anymore. Other surgical approaches have been used and might be detected by LGE imaging (Fig. 6.8). Dark blood and gray blood LGE are newer techniques and might help to detect scar tissue adjacent to the blood pool in certain cases [32, 33]. Imaging atrial scar requires specialized sequences for the visualization of scar tissue in the thin atrial wall [34, 35].

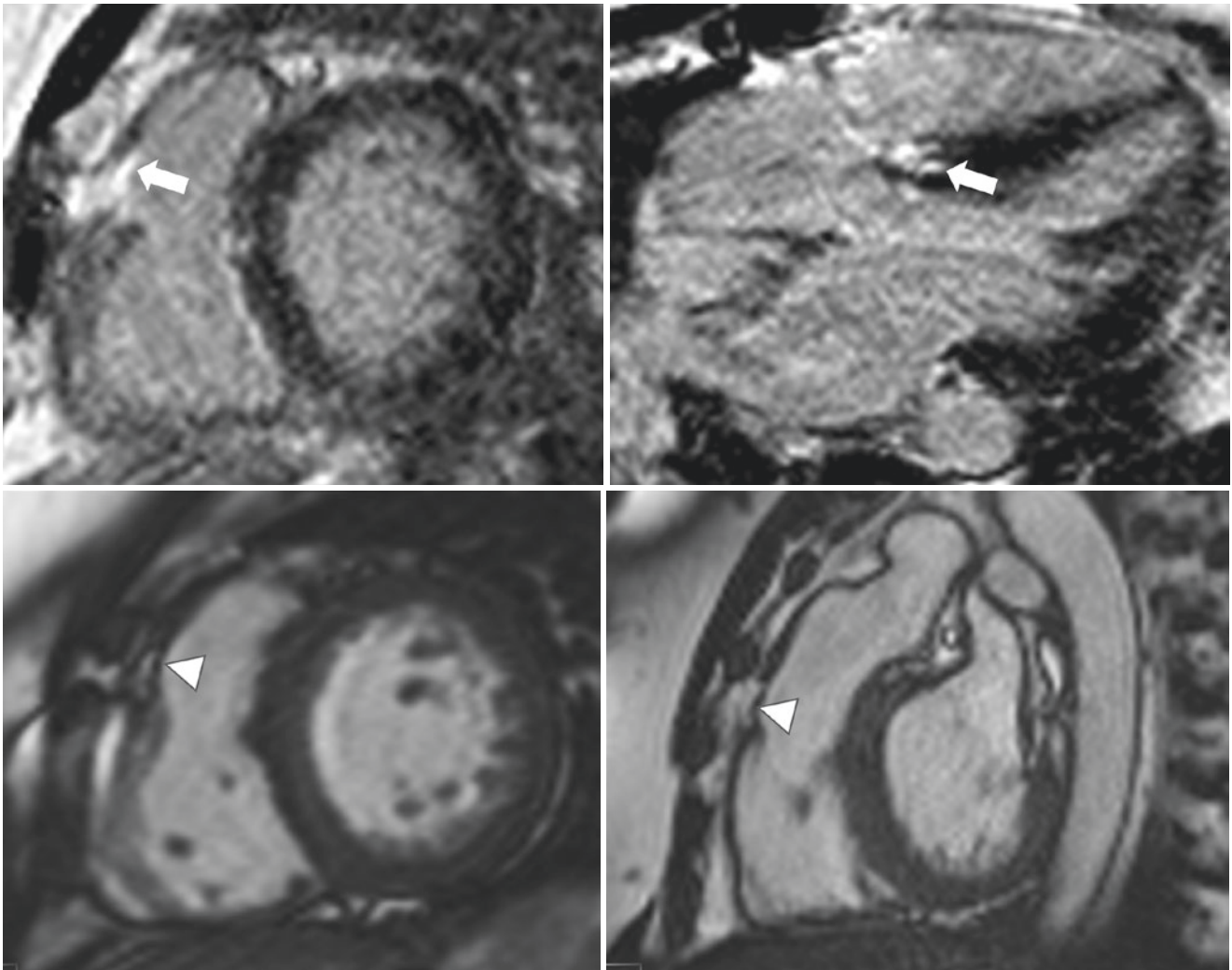


**Fig. 6.8** Adult patient after surgical VSD closure in childhood. The upper row of images shows LGE in the surgical areas (RV free wall and interventricular septum; white arrows). The lower row of images shows

a thin-walled area in the RV free wall corresponding to the area of LGE (white arrowhead)



### 6.5.2.2 CMR Techniques for the Hemodynamic Assessment of Septal Defects

The intracardiac shunt in patients with an ASD or VSD is typically a left-to-right shunt. This results in volume overload and enlargement of the right atrium and RV in patients with an ASD and in left heart volume overload in patients with a VSD. Ventricular volumetry should be performed in all patients from short axis or transaxial cine stacks to quantify the biventricular size and systolic function. Atrial size can be calculated from short axis cine images cutting the interatrial septum in an orthogonal plane similar to those views used for ventricular volumetry [36]. Another option for the measurement of atrial volumes is the monoplane or biplane-area-length method [37].

CMR allows to measure the shunt across the interatrial and interventricular septum. Shunt calculation can be performed by subtracting the LV stroke volume (LVSV) from the RV stroke volume (RVSV), both derived from ventricular volumetry: Shunt volume = RVSV – LVSV [38]. There are, however, several limitations with this method. The aortic or pulmonary regurgitant volume will increase the end-diastolic volume which will affect the calculation of the stroke volume and, in turn, calculation of the shunt (Qp:Qs). If this method is used to calculate the Qp:Qs in the setting of valvular regurgitation, the regurgitant volume must be taken into account and the stroke volume adjusted appropriately. This method is also not useful in the setting of large unrepaired ventricular septal defects in which there is equalization of

RV and LV pressures and, in turn, equalization of stroke volume. As with any volumetric technique, accurate assessment of the endocardial borders during ventricular volumetry is crucial to obtain correct measurements which impact clinical decision-making.

Another option that should be used in all patients with septal defects is the calculation of the ratio of pulmonary to systemic blood flow (Qp/Qs) from 2D or 4D phase-contrast cine imaging (Fig. 6.3) [6, 38, 39]. Typically defects with a Qp/Qs  $\geq 1.5$  should be considered for interventional or surgical closure.

Generally, phase-contrast cine imaging uses velocity-induced phase shifts to distinguish flowing blood from stationary tissue. Protons moving in the direction of a magnetic field gradient acquire changes in phase or phase shifts, and this phase shift is proportional to its velocity. In clinical routine, 2D phase-contrast cine imaging is more commonly applied than 4D flow imaging. This sequence produces two sets of data: magnitude images providing the anatomic information and phase images including the velocity information [37].

When using 2D phase-contrast cine imaging, image planning should be performed on cine images perpendicular to each other. For aortic flow measurement, the scanning plane should be placed at the level of the sinotubular junction and for pulmonary flow measurements slightly above the pulmonary valve (Fig. 6.9). Aortic flow measurements at the level of the sinotubular junction exclude the coronary blood flow

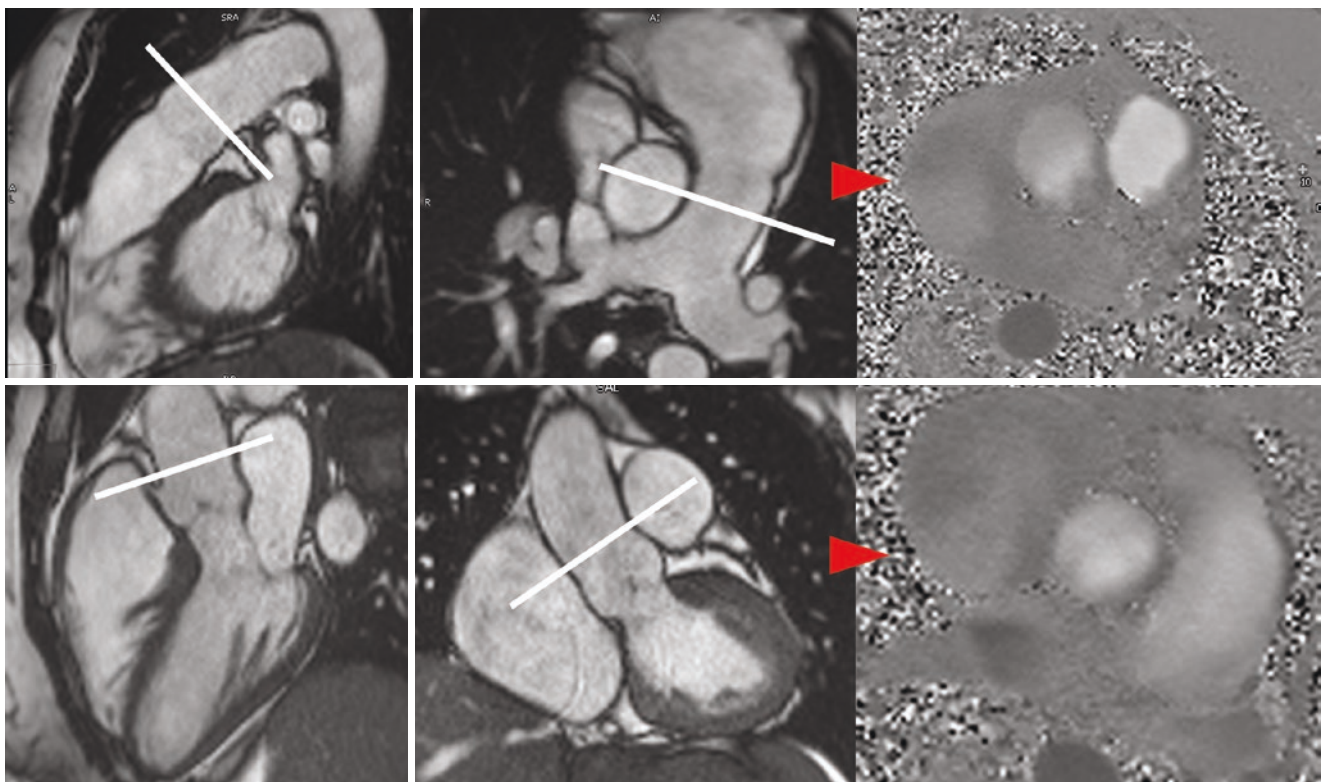


**Fig. 6.9** The upper row of images shows the planning of the pulmonary flow measurement, and the lower row demonstrates the scanning planes of aortic flow measurements



which may slightly impact the Qp:Qs measurement (coronary blood flow: ~5% of LV output). Apart from the correct planning of the scanning planes, the setting of the so-called velocity encoding value (VENC) is of importance. Ideally, the VENC should only be slightly higher than the velocity in the examined vessel. Peak velocities that are higher than the VENC cause aliasing (wrapping around of velocity information within a voxel), whereas VENC settings that are much higher than the peak velocity can result in small phase differences, low contrast to stationary tissue, and low signal-to-noise ratio [40, 41]. For aortic and pulmonary artery flow measurements in patients without aortic or pulmonary valve

disease, a VENC of 150–200 cm/s is typically used. For in-plane interatrial flow, the VENC is set up lower due to low velocities of the shunt (less than 100 cm/s).

4D flow CMR is an extension of the conventional 2D phase-contrast cine imaging technique. It has been developed to obtain a more comprehensive access to blood flow. Unlike 2D phase-contrast cine imaging, 4D flow CMR measures all three directional components of blood flow velocities relative to 3D dimensions of a specific volume throughout the cardiac cycle. Studies have shown that 4D flow CMR allows an accurate and highly reproducible measurement of Qp:Qs [42]. It also allows a visualization of the septal defect (Fig. 6.10).

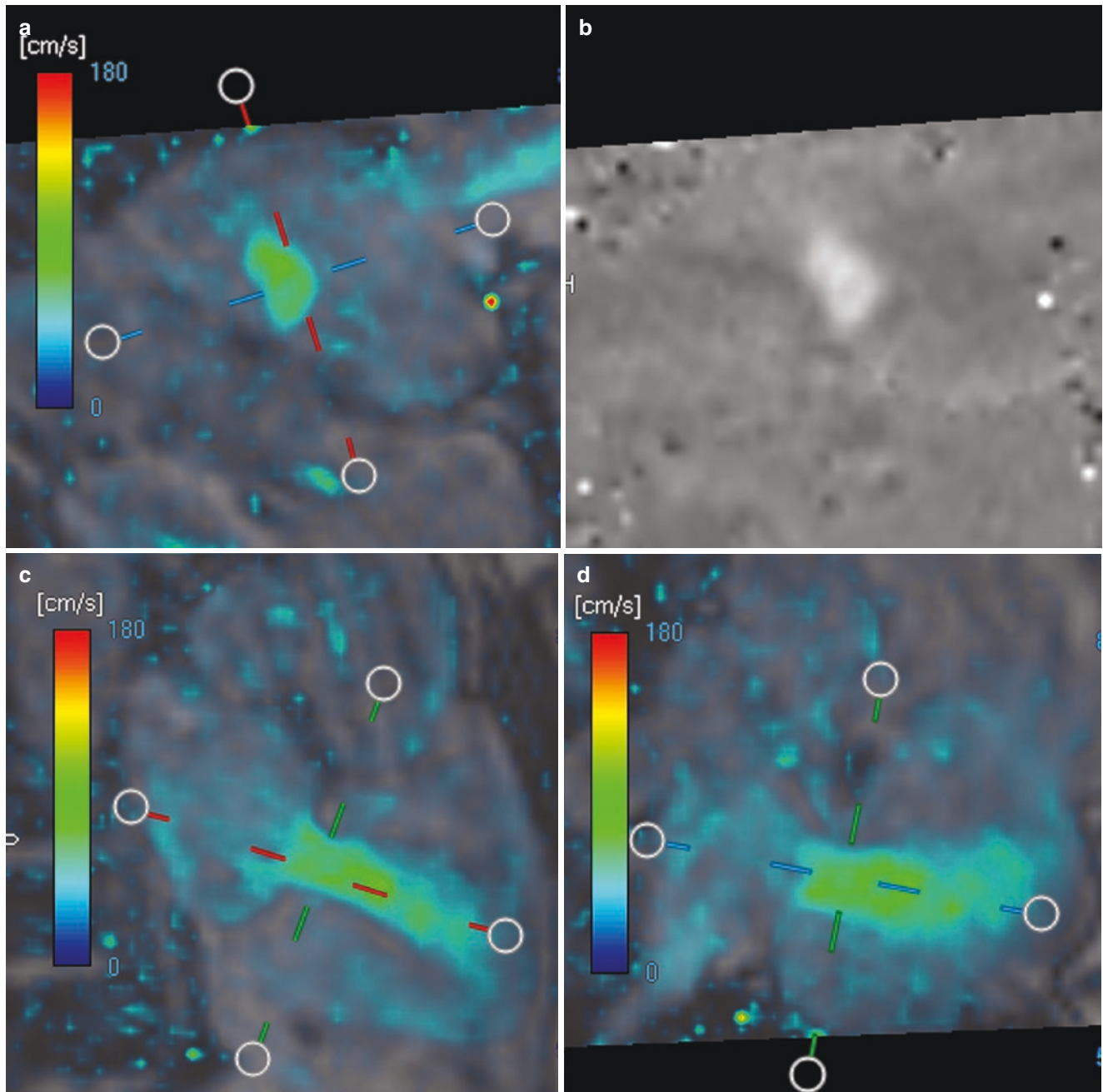


**Fig. 6.10** Visualization of a secundum ASD using 4D flow. (a, b) Direct en-face view of the defect (navigation crosshair). (c, d) Left to right shunt across the defect (navigation crosshair)

## 6.6 Discussion

CMR imaging has established its place in the noninvasive evaluation of patients with congenital heart disease. In patients with septal defects, CMR normally complements echocardiography and can give important information on the hemodynamic relevance of a defect by providing exact measurements of the ventricular size and the amount of shunt. This is reflected by the typical referral indications which include the measurement of biventricular volumes and ejection fraction as well as calculation of Qp:Qs by 2D and 4D phase contrast CMR. In addition, the assessment of associated findings such as a mitral valve cleft or an abnormal pulmonary venous drainage in patients with ASDs can be easily performed by CMR.

CMR is often used in adult patients in whom echocardiographic windows are poor and additional hemodynamic and quantitative data are needed. However, CMR is not only well suited for adults with septal defects but is increasingly used in children to investigate the hemodynamic relevance of a defect and its potentially associated anomalies.

In summary, CMR is an appealing technique because it can be crucial in clinical decision-making by allowing a detailed anatomic delineation of the defect from 2D- and 3D data sets together with accurate hemodynamic data.

## 6.7 Limitations and Pitfalls

When assessing patients with septal defects, a standard protocol should be used and should be available in advance (please see Table 6.1). Ideally, information of the clinical evaluation and previous imaging studies should be provided before the CMR scan for an accurate image planning and acquisition. Small defects can sometimes be missed on anatomical images; in those cases, previous data can be crucial. For shunt calculation, physicians should be aware of potential pitfalls and limitations of phase-contrast imaging to avoid errors in flow measurements [43]. In small children and uncooperative patients, sedation or general anesthesia may be necessary to complete CMR examination.

**Table 6.1** CMR sequence list for the assessment of patients with septal defects

Localizer scans	Transaxial, coronal, sagittal, short axis, HLA, VLA, and 3ch stacks and planes
Black blood imaging (e.g., TSE, HASTE)	Transaxial, coronal, and sagittal planes
Cine imaging	Transaxial cine stack, HLA, VLA, 3ch, SA stack including the atria (in patients with ASD), LVOT, RVOT, RV-VLA, additional planes to localize the defect, aortic valve (in patients with VSD and AI)
Phase-contrast cine imaging	Through-plane flow measurement through aortic root or sinotubular junction and main pulmonary artery; serial in-plane velocity-encoded and through plane velocity-encoded acquisitions along regions of interest to localize defects and quantify size and flow
First-pass perfusion imaging	Not routinely performed
Late gadolinium enhancement	Typically in the same planes as cine imaging, can be of additional use
Three-dimensional (3D) whole heart techniques (e.g., bSSFP, mDixon) or contrast-enhanced angiography	Coronal or transaxial plane to visualize the pulmonary veins and other thoracic vessels

## 6.8 Conclusions

Septal defects are the most common congenital heart defects in children and adults, and CMR has become an established technique for evaluating those patients. With the growing number of adults with congenital heart disease, it is of importance that physicians performing and interpreting CMR studies have a good understanding of CMR techniques to examine these patients [44]. Standard imaging protocols together with an interdisciplinary approach between imaging specialists, technicians, and cardiologists should ensure that the requested information for each specific lesion can be detected.

### Practical Pearls

- Clinical information and data from previous imaging studies should be available prior to the CMR scan

- A structured scanning protocol should guide technicians and physicians during the CMR examination
- Combinations of pulse sequences used for anatomical imaging (spin-echo sequences, 2D SSFP, 3D SSFP) should be used for delineation of the defect and to visualize associated anomalies
- Angiographic techniques with and without contrast (3D SSFP, 3D mDixon, CE-MRA) can help to detect anomalous pulmonary venous drainage
- 2D- or 4D phase-contrast CMR should be used for shunt calculation

## References

1. Liu Y, Chen S, Zühlke L, et al. Global birth prevalence of congenital heart defects 1970-2017: updated systematic review and meta-analysis of 260 studies. *Int J Epidemiol.* 2019;48:455–63.
2. Karunanithi Z, Nyboe C, Hjørtdal VE. Long-term risk of atrial fibrillation and stroke in patients with atrial septal defect diagnosed in childhood. *Am J Cardiol.* 2017;119:461–5.
3. Nyboe C, Karunanithi Z, Nielsen-Kudsk JE, et al. Long-term mortality in patients with atrial septal defect: a nationwide cohort-study. *Eur Heart J.* 2018;39:993–8.
4. Kidd L, Driscoll DJ, Gersony WM, et al. Second natural history study of congenital heart defects. Results of treatment of patients with ventricular septal defects. *Circulation.* 1993;87(2 Suppl):138–51.
5. Moller JH, Patton C, Varco RL, et al. Late results (30 to 35 years) after operative closure of isolated ventricular septal defect from 1954 to 1960. *Am J Cardiol.* 1991;68(15):1491–7.
6. Beerbaum P, Körperich H, Gieseke J, et al. Rapid left-to-right shunt quantification in children by phase-contrast magnetic resonance imaging combined with sensitivity encoding (SENSE). *Circulation.* 2003;16(108):1355–61.
7. Kilner PJ. Imaging congenital heart disease in adults. *Br J Radiol.* 2011;84(Spec Issue 3):S258–68.
8. Gatehouse PD, Keegan J, Crowe LA, et al. Applications of phase-contrast flow and velocity imaging in cardiovascular MRI. *Eur Radiol.* 2005;15:2172–84.
9. Hagen PT, Scholz DG, Edwards WD. Incidence and size of patent foramen ovale during the first 10 decades of life: an autopsy study of 965 normal hearts. *Mayo Clin Proc.* 1984;59:17–20.
10. Naqvi N, McCarthy KP, Ho SY. Anatomy of the atrial septum and interatrial communications. *J Thorac Dis.* 2018;10(Suppl 24):S2837–47.
11. Wald RM, Powell AJ. Simple congenital heart lesions. *J Cardiovasc Magn Reson.* 2006;8:619–31.
12. Menillo AM, Lee LS, Pearson-Shaver AL. Atrial septal defect. In: *StatPearls.* Treasure Island, FL: StatPearls Publishing; 2021.
13. Lopez L, Houyel L, Colan SD, et al. Classification of ventricular septal defects for the eleventh iteration of the international classification of diseases—striving for consensus: a report from the International Society for Nomenclature of Paediatric and Congenital Heart Disease. *Ann Thorac Surg.* 2018;106:1578–89.
14. Spicer DE, Anderson RH, Backer CL. Clarifying the surgical morphology of inlet ventricular septal defects. *Ann Thorac Surg.* 2013;95:236–41.
15. Van Praagh R, Geva T, Kreutzer J. Ventricular septal defects: how shall we describe, name and classify them? *J Am Coll Cardiol.* 1989;14:1298–9.
16. Mostefa-Kara M, Bonnet D, Belli E, et al. Anatomy of the ventricular septal defect in outflow tract defects: similarities and differences. *J Thorac Cardiovasc Surg.* 2015;149:682–8.
17. Hatipoglu S, Almogheer B, Mahon C, et al. Clinical significance of partial anomalous pulmonary venous connections (isolated and atrial septal defect associated) determined by cardiovascular magnetic resonance. *Circ Cardiovasc Imaging.* 2021;14:e012371.
18. Glen S, Burns J, Bloomfield P, et al. Prevalence and development of additional cardiac abnormalities in 1448 patients with congenital ventricular septal defects. *Heart.* 2004;90:1321–5.
19. Karonis T, Scognamiglio G, Babu-Narayan SV, et al. Clinical course and potential complications of small ventricular septal defects in adulthood: late development of left ventricular dysfunction justifies lifelong care. *Int J Cardiol.* 2016;208:102–6.
20. Perloff JK. Surgical closure of atrial septal defect in adults. *N Engl J Med.* 1995;333:513–4.
21. Gatzoulis MA, Freeman MA, Siu SC, et al. Atrial arrhythmia after surgical closure of atrial septal defects in adults. *N Engl J Med.* 1999;340:839–46.
22. Campbell M, et al. Natural history of atrial septal defect. *Br Heart J.* 1970;32:820–6.
23. Budts W, Miller O, Babu-Narayan SV, Li W, et al. Imaging the adult with simple shunt lesions: position paper from the EACVI and the ESC WG on ACHD. Endorsed by AEPC (Association for European Paediatric and Congenital Cardiology). *Eur Heart J Cardiovasc Imaging.* 2021;22:e58–70.
24. Leiner T, Bogaert J, Friedrich MG, et al. SCMR Position Paper on clinical indications for cardiovascular magnetic resonance. *J Cardiovasc Magn Reson.* 2020;22:76.
25. Jensen AS, Broberg CS, Rydman R, et al. Impaired right, left, or biventricular function and resting oxygen saturation are associated with mortality in Eisenmenger syndrome: a clinical and cardiovascular magnetic resonance study. *Circ Cardiovasc Imaging.* 2015;8:e003596.
26. Pushparajah K. Non-invasive imaging in the evaluation of cardiac shunts for interventional closure. *Front Cardiovasc Med.* 2021;8:651726.
27. Greil G, Tandon AA, Silva Vieira M. 3D whole heart imaging for congenital heart disease. *Front Pediatr.* 2017;5:36.
28. Kourtidou S, Jones MR, Moore RA, et al. mDixon ECG-gated 3-dimensional cardiovascular magnetic resonance angiography in patients with congenital cardiovascular disease. *J Cardiovasc Magn Reson.* 2019;21:52.
29. Körperich H, Gieseke J, Esdorn H, et al. Ultrafast time-resolved contrast-enhanced 3D pulmonary venous cardiovascular magnetic resonance angiography using SENSE combined with CENTRA-keyhole. *J Cardiovasc Magn Reson.* 2007;9:77–87.
30. Thomson LE, Crowley AL, Heitner JF, et al. Direct en face imaging of secundum atrial septal defects by velocity-encoded cardiovascular magnetic resonance in patients evaluated for possible transcatheter closure. *Circ Cardiovasc Imaging.* 2008;1:31–40.
31. Wang ZJ, Reddy GP, Gotway MB, et al. Cardiovascular shunts: MR imaging evaluation. *Radiographics.* 2003;23 Spec:S181–94.
32. Holtackers RJ, Van De Heyning CM, Nazir MS, et al. Clinical value of dark-blood late gadolinium enhancement cardiovascular magnetic resonance without additional magnetization preparation. *J Cardiovasc Magn Reson.* 2019;21:44.
33. Fahmy AS, Neisius U, Tsao CW, et al. Gray blood late gadolinium enhancement cardiovascular magnetic resonance for improved detection of myocardial scar. *J Cardiovasc Magn Reson.* 2018;20:22.

34. Schulz-Menger J, Bluemke DA, Bremerich J, et al. Standardized image interpretation and post-processing in cardiovascular magnetic resonance - 2020 update: Society for Cardiovascular Magnetic Resonance (SCMR): Board of Trustees Task Force on Standardized Post-Processing. *J Cardiovasc Magn Reson*. 2020;22:19.
35. Craft J, Li Y, Bhatti S, Cao JJ. How to do left atrial late gadolinium enhancement: a review. *Radiol Med*. 2021;126:1159–69.
36. Maceira AM, Cosín-Sales J, Roughton M, et al. Reference right atrial dimensions and volume estimation by steady state free precession cardiovascular magnetic resonance. *J Cardiovasc Magn Reson*. 2013;15:29.
37. Nacif MS, Barranhas AD, Turkbey E, et al. Left atrial volume quantification using cardiac MRI in atrial fibrillation: comparison of the Simpson's method with biplane area-length, ellipse, and three-dimensional methods. *Diagn Interv Radiol*. 2013;19:213–20.
38. Devos DG, Kilner PJ. Calculations of cardiovascular shunts and regurgitation using magnetic resonance ventricular volume and aortic and pulmonary flow measurements. *Eur Radiol*. 2010;20:410–21.
39. Powell AJ, Tsai-Goodman B, Prakash A, et al. Comparison between phase-velocity cine magnetic resonance imaging and invasive oximetry for quantification of atrial shunts. *Am J Cardiol*. 2003;91:1523–5.
40. Lotz J, Meier C, Leppert A, Galanski M. Cardiovascular flow measurement with phase-contrast MR imaging: basic facts and implementation. *Radiographics*. 2002;22:651–71.
41. Reiter U, Reiter G, Fuchsjäger M. MR phase-contrast imaging in pulmonary hypertension. *Br J Radiol*. 2016;89:20150995.
42. Urmeneta Ulloa J, Álvarez Vázquez A, Martínez de Vega V, et al. Evaluation of cardiac shunts with 4D flow cardiac magnetic resonance: intra- and interobserver variability. *J Magn Reson Imaging*. 2020;52:1055–63.
43. Kilner PJ, Gatehouse PD, Firmin DN. Flow measurement by magnetic resonance: a unique asset worth optimising. *J Cardiovasc Magn Reson*. 2007;9:723–8.
44. Kilner PJ, Geva T, Kaemmerer H, et al. Recommendations for cardiovascular magnetic resonance in adults with congenital heart disease from the respective working groups of the European Society of Cardiology. *Eur Heart J*. 2010;31:794–805.





# Right Ventricular Anomalies

# 7

Frédérique Bailliard

## 7.1 Introduction

In congenital heart disease, the right ventricle (RV) plays a disproportionately important role in pathophysiology. Unfortunately, the right ventricle has notoriously been difficult to image functionally and structurally by echocardiography for the following reasons:

- The anterior position of the RV in the chest can result in poor acoustic echocardiographic windows, preventing accurate assessments of the RV free wall, or of an unusually positioned outflow tract.
- The right ventricular outflow tract (RVOT) formed by the outlet septum, the ventriculo-infundibular fold, and the septomarginal trabeculations can be difficult to conceptualize, particularly when malformed, and even more so when the great arteries are malpositioned.
- The complex anatomy of the RV cavity precludes simple mathematical models for providing quantitative functional data that is accurate and reproducible.

Cardiovascular magnetic resonance (CMR) imaging, not limited by the location of the RV in the chest, nor by its anat-

omy, has the ability to provide high-resolution anatomical and functional data for morphologically abnormal right ventricles, or those affected by abnormal pressure or volume loading conditions.

In this chapter, an overview of CMR imaging of the abnormal right ventricle is provided, with reference to specific lesions. We will provide a methodical, fundamental imaging protocol (Table 7.1), with appropriate modifications guided by the pathophysiology and surgical techniques for individual lesions. We will discuss four principal subtypes of “abnormal RV”:

- The RV with abnormal great artery position: double-outlet RV
- The RV with abnormal division of the trabeculations: double-chambered RV
- The RV with abnormal pulmonary outlet: pulmonary atresia with intact ventricular septum
- The RV with abnormal afterload: pulmonary arterial hypertension and Eisenmenger syndrome

**Supplementary Information** The online version contains supplementary material available at [https://doi.org/10.1007/978-3-031-29235-4\\_7](https://doi.org/10.1007/978-3-031-29235-4_7).

F. Bailliard (✉)  
Bailliard Henry Pediatric Cardiology, Raleigh, NC, USA  
Department of Pediatrics, Duke University, Durham, NC, USA  
e-mail: [frederique.bailliard@duke.edu](mailto:frederique.bailliard@duke.edu), [fbailliard@bhpcardio.com](mailto:fbailliard@bhpcardio.com)

**Table 7.1** Example of the standard sequences and views of a routine congenital cardiac scan with additional images (marked with an asterisk) to complete a comprehensive “RV assessment,” in the order of workflow

	Sequence	Planning	1° purpose	2° purpose
Scout	Single-shot bSSFP images	Contiguous slices in all three radiological planes covering all relevant anatomy	Isocentering of the heart in the scanner	Preview of thoracic anatomy May be used for planning should other images be unable to be obtained
Axial stack	Respiratory-navigated, ECG-gated, “black-blood” images (HASTE or TSE)	Coverage from liver to neck	Planning subsequent cine imaging planes	Provides a map of thoracic anatomy
	Contiguous axial slices	Include aortic arch and proximal head and neck vessels Include systemic and pulmonary veins		
Ventricular long axis (RVLA, LVLA)	Breath-held, ECG-gated, bSSFP cine images	From axial stack Place perpendicular plane through long axis of ventricle, from mid-atrioventricular (AV) valve to ventricular apex	Planning the true four-chamber image	Assessment of anterior and inferior myocardium, AV valves, ventricular sizes
AV valves	Breath-held, ECG-gated, bSSFP cine image	From axial stack Place perpendicular plane parallel to, and on apical side of AV valve Check orientation is parallel to the vertical axis of the AV valves on RVLA and LVLA views The image should include base of aortic valve in systole	Planning the four-chamber and LV outflow tract (LVOT) images	Subjective evaluation of AV valve morphology and function
Four-chamber view	Breath-held, ECG-gated, bSSFP cine image	From AV valves and VLA views Place perpendicular plane across both AV valve orifices From LVLA cine check that this plane passes through mid-mitral valve and LV apex From RVLA check that the plane passes through mid-tricuspid valve and RV apex	Subjective assessment of atrial volumes, biventricular volumes and function, ventricular wall motion, AV valve regurgitation	Planning short axis (SA) stack
Short-axis (SA) stack	Breath-held, ECG-gated, bSSFP cine image	From end-diastolic frame of four-chamber cine Place perpendicular plane at hinge points of both AV valves, with special care to include the entire basal ventricular blood pool From VLA views, check the first slice is perpendicular to AV valve hinge points Contiguous slices are then placed to cover the entire ventricular mass to the apex	Provides the images required for segmentation of ventricular volumes	Assessment of the ventricular septum, ventricular myocardial morphology, wall motion abnormalities, and outflow tracts

(continued)

**Table 7.1** (continued)

	Sequence	Planning	1° purpose	2° purpose
MR angiogram	Breath-held, not ECG-gated	Isotropic voxels	Angiographic views of large and small thoracic vessels. Images less subject to artifact caused by low velocity or turbulent flow	Subjective determination of preferential blood flow
		Planned on axial TSE stack, for sagittally orientated raw data Include anteroposterior chest wall, lung fields Image acquisition triggered with bolus-tracking to ensure maximum signal in structure of interest Two acquisitions routinely acquired	The second pass acquisition allows assessment of systemic and pulmonary venous anatomy	Can be expanded to perform time-resolved angiography or four-dimensional angiography
3D bSSFP	Free breathing, respiratory navigated, ECG-gated	Planned on axial TSE stack for sagittally oriented raw data	Provides high-resolution images of intracardiac anatomy, including coronary arteries	Planning further imaging planes in patients with complex anatomy
	Data acquisition optimized to occur during cardiac standstill Signal improved following gadolinium injection	Include entire heart, pulmonary arteries and veins, aortic arch	Allows multiplanar reformatting	
	Signal improved in tachycardic patients by triggering acquisition with every second heartbeat	Respiratory navigator placed mid-right dome of diaphragm, avoiding cardiac region of interest		
Delayed enhancement	Free breathing, single-shot true-FISP inversion recovery images	Copy image position and parameters of the SA stack Adjust inversion time (TI) to null normal myocardium	Screen for myocardial fibrosis or scar	Determine if segmented, breath-held delayed enhancement should be performed
LV outflow tract	Breath-held, ECG-gated, bSSFP cine image	From the AV valves cine	Outflow tract morphology, subjective assessment of semilunar valve function	Planning phase contrast velocity mapping Planning “en-face” view of semilunar valve
		Place a perpendicular plane through both basal aortic valve and mid-mitral valve orifice Check orientation passes through LV apex using LVLA cine Cross-cut this view to obtain two orthogonal cine views of LVOT		
RV outflow tract	Breath-held, ECG-gated, bSSFP cine image	From axial stack	Outflow tract morphology	Planning phase contrast velocity mapping
		Place perpendicular plane through the pulmonary trunk Cross-cut this view to obtain two orthogonal cine views of RVOT	Subjective assessment of semilunar valve function	Planning “en-face” view of semilunar valve
RV in/out	Breath-held, ECG-gated, bSSFP cine image	From four-chamber cine and RVOT sagittal cine Place a perpendicular plane across the TV in four-chamber cine Ensure the plane crosses the RVOT in the RVOT sagittal cine	Assess RV free wall motion Additional profile of infundibulum	

(continued)

**Table 7.1** (continued)

	Sequence	Planning	1° purpose	2° purpose
Branch PA	Breath-held, ECG-gated, bSSFP cine images	Images 1 and 2: From MRA, create MPR of the sagittal and coronal view of the RPA and of the LPA	Assess the dynamic nature of the branch PAs	
		Image 3: From images 1 and 2, plan the axial image of the confluence of the branches	Assess the PA confluence	
Great artery flow	Non-breath-held, ECG-gated, through-plane phase contrast flow velocity mapping	From the orthogonal outflow tract images	Vessel flow volume	Calculate pulmonary blood flow to systemic blood flow ratio (Qp:Qs)
		Place a perpendicular plane across the vessel of interest	Calculate regurgitant fractions (RF%)	Evaluate the presence and location of shunts
		Place plane just distal to valve leaflets in systole, to avoid turbulent areas of flow	Validate ventricular stroke volume measurements	Calculate flow velocity
		Optimize velocity encoding to maximize accuracy and prevent aliasing		
Branch PA flow	Non-breath-held, ECG-gated, through-plane phase contrast flow velocity mapping	From orthogonal views of the branch PA	Assess the ratio of net forward branch PA flow	Calculate flow velocity
		Place perpendicular plane across the RPA and the LPA	Assess regurgitant fraction of each PA	Validate MPA flow

## 7.2 Right Ventricular Imaging and Analysis

With any anatomic or functional assessment of the RV, the accuracy and reproducibility of imaging critically depend on image position, the technical quality of the images (temporal and spatial resolution), and the post-processing techniques. Much subjectivity, and therefore poor reproducibility, can be introduced by imprecise or non-systematic methods of post-processing and measurement, even in the setting of excellent image quality.

Planning the slice positions for acquisition of a short-axis stack of images to cover the RV begins with careful acquisition of long-axis images utilized to plan the stack. The RV long-axis view must transect the right-sided atrioventricular valve (AVV) and the RV apex. The short-axis stack is subsequently planned in a plane parallel to the right-sided atrioventricular valve (AVV) and perpendicular to the ventricular septum in order to minimize partial-volume effects caused by the myocardial-blood pool interface. In cases of dilated right ventricles, one must take care to acquire sufficient slices into the right atrium to obtain the entire basal ventricular volume, particularly in diastole. Inaccurate interpretation of ventricular volumes at the basal slices is frequently responsible for observer variation in short-axis stack volumetric analysis [1] and must not be overlooked at the time of image acquisition.

Post-processing of cine images to calculate ventricular volumes and systolic function is usually performed off-line, using commercially available software. The segmentation of the blood pool and myocardial border can be performed manually or by using a variety of automated signal thresholding techniques. A fundamental issue, particularly for the RV in

patients with congenital heart disease, is that of inclusion or noninclusion of the trabeculae in the blood pool. This is illustrated in Fig. 7.1. If a simple endocardial contour is drawn ignoring the trabeculae and therefore including them in the blood pool, the manual segmentation process is more efficient and more reproducible [2]. However, this leads to erroneously large volume estimates for the ventricles and prohibits internal validation of stroke volumes using great arterial flow volumes [3]. Calculation of the difference between stroke volumes and great arterial flow to quantify tricuspid regurgitation and the presence or absence of intracardiac shunts will therefore also be inaccurate. Including major trabeculae in the blood pool volume rather than myocardial volume eliminates one of the benefits of performing CMR.

Although the plane of image acquisition for volumetric analysis has conventionally been the short-axis stack [4, 5], there may be limitations when using this imaging plane. In complex congenital heart disease, conventional anatomic landmarks used for planning of the short axis stack may be lost, making axial stacks much simpler to acquire. Another limitation arises in right ventricles impaired by excessive afterload (e.g., pulmonary arterial hypertension) (see Sect. 7.6.2) when the loss of systolic contraction in the radial plane often exceeds that in the longitudinal plane [6]. In these severely depressed ventricles, the small changes between end-systolic and end-diastolic volumes may be more readily detected in the longitudinal plane than in the short-axis plane. Finally, in the short-axis plane, suboptimal visualization of the valvular attachments in the RV inflow and outflow tracts may make it difficult to distinguish atrial from ventricular volumes. These issues could all impair the accuracy and reproducibility of volumetric analysis using short-axis images [7, 8].



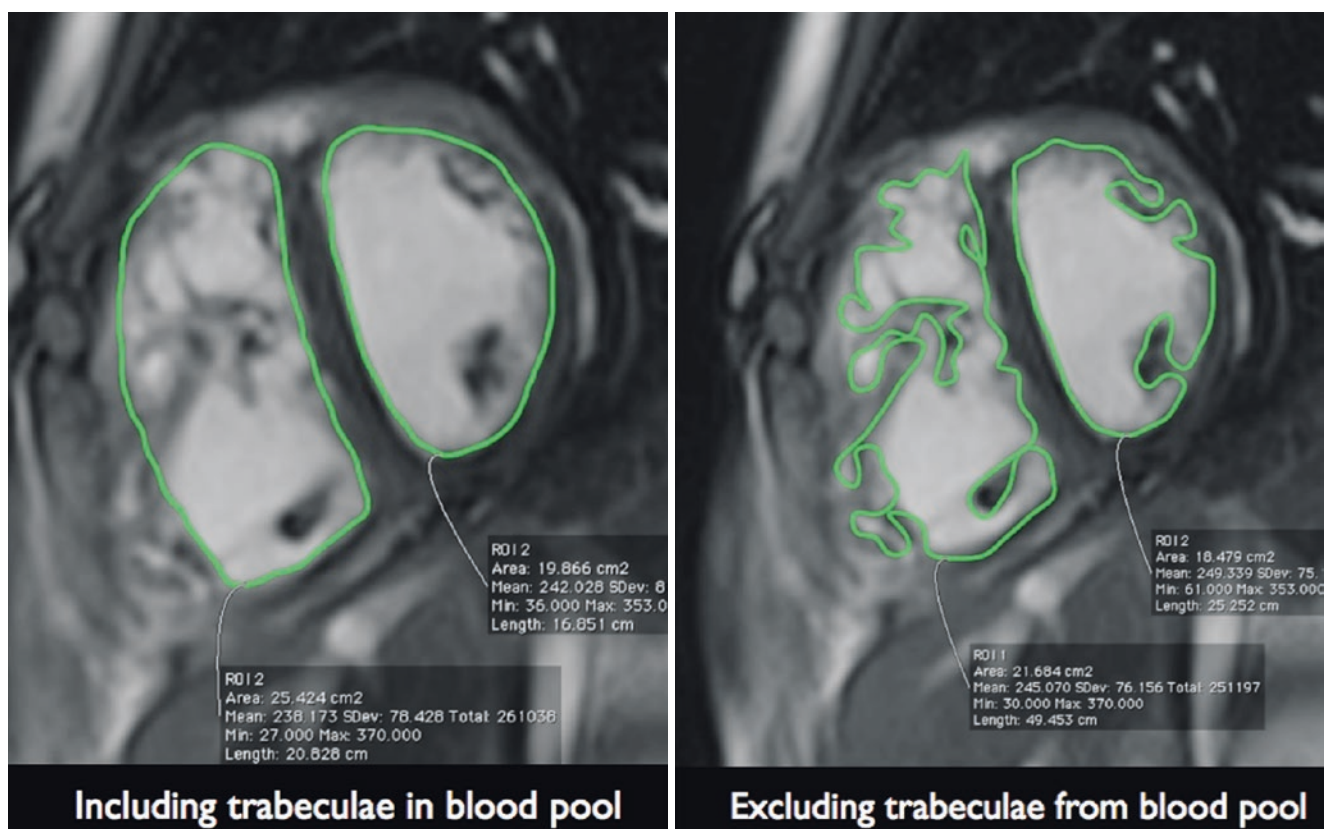


**Fig. 7.1** A diagrammatic illustration of the varying modes of manual segmentation of the right and left ventricles, for volumetric analysis, using a representative mid-short-axis cine view

Conversely, in the axial image plane, through-plane motion of the myocardium, with loss of clarity of the myocardial–blood pool interface, can render the inferior border of the right ventricle difficult to accurately identify [7]. Moreover, any inconsistency in the patient’s breath-holding position during acquisition of an axial stack will alter diaphragmatic position and therefore increase the likelihood that slices are not contiguous, significantly impairing accuracy. Although the reproducibility of volumetric analysis from axial stacks of images has been portrayed in groups of normal patients, and in a group of patients with repaired tetralogy of Fallot, it has not been evaluated in more complex congenital heart disease nor has it been directly compared to measurement reproducibility from meticulously planned and segmented short-axis images.

The post-processing software used greatly influences the accuracy and reproducibility of ventricular volumetric assessment, particularly for the right ventricle. This applies to the issue of manual segmentation versus thresh-holding techniques [9]. Viewing software permitting the display of multiple cines simultaneously that also allows the relative position of each cine (or slice) to be marked in relation to the other is disproportionately important [10]. This slice-positioning tool enables the exact position of any short- or long-axis slice to be visualized in relation to the inflow and outflow tract in systole and diastole. While this technique greatly improves

accuracy, there remains individual subjectivity with manual segmentation techniques. One method to minimize inter-observer variability is to actively archive images that include the manually drawn regions of interest to allow comparison with future manual segmentation in serial studies.

Published standard protocols [4, 5] endorse the use of a short-axis stack for ventricular volumetric analysis. However, for isolated clinical scenarios such as pulmonary arterial hypertension (Sect. 7.6.2), an axial stack is used for volumetric analysis.

## 7.3 The RV with Abnormal Great Artery Position: Double-Outlet Right Ventricle (DORV)

### 7.3.1 Definition of DORV

Although patients with double-outlet right ventricle (DORV) can exist in the setting of heterotaxy, single ventricles, and atrioventricular septal defects, the following discussion will be limited to those patients with situs solitus and balanced ventricles and atrioventricular valves.

The term DORV describes congenital malformations in which greater than 50% of the circumference of both of the

great arteries arises from the RV in the presence of a ventricular septal defect (VSD). It accounts for 1–1.5% of all congenital heart disease. Echocardiography establishes the commitment of the great arteries to the right ventricle in the more extreme forms of DORV. In more subtle cases, with even slight deviation from the traditional imaging planes, the two-dimensional images of echocardiography can be misleading and give the appearance of DORV when in fact only one great artery arises from the RV [11]. Clinicians have therefore used other morphologic criteria such as the absence of atrioventricular to semilunar valve continuity and/or the presence of bilateral infundibulum to solidify the diagnosis of DORV. Unfortunately, these criteria do not equivocally establish the diagnosis: DORV with subpulmonary VSD may exist with mitral-pulmonary continuity and thus without bilateral infundibulum [12]. It is this relationship of the ventricular septal defect to the great arteries that defines the physiology of patients with DORV and is the basis for the most commonly used classification of DORV, first described by Lev et al. [13]. It is important to note that in spite of the Lev classification, DORV is a continuum of anomalies with physiology of tetralogy of Fallot on one end and physiology of transposition of the great arteries on the other end. Lesions in the middle of the spectrum may not easily be described by the Lev classification, complicating the surgical decision-making [14]. In the past, the diagnosis of the more difficult cases of DORV could only be confirmed by surgical inspection.

Today, multiplanar reconstructions (MPRs) of intracardiac anatomy provided by CMR imaging have provided clinicians with a tool to accurately determine not only the relationship of the great arteries to the RV but also to describe the location of the ventricular septal defect. More recently, three-dimension printing has provided yet an additional representation of the heart, solidifying diagnoses and optimizing surgical planning [15]. The major variations of DORV are discussed below.

### 7.3.2 DORV with Subaortic Ventricular Septal Defect (VSD) and Pulmonary Stenosis(PS)

#### 7.3.2.1 Anatomy

DORV with a subaortic VSD accounts for two thirds of cases of DORV and is part of the continuum of tetralogy of Fallot (TOF). The great arteries lie side by side with the aorta rightward of the pulmonary artery (PA) and slightly posterior, thus similar to a normal heart. The rarely restrictive VSD sits between the limbs of the septomarginal trabeculations with the outlet septum attached to the anterior limb of the septomarginal trabeculations, which isolates the pulmonary artery from the left ventricle (LV) [12]. As in patients with TOF, the severity of pulmonary stenosis will determine the degree of hypoxemia and therefore both the type and timing of surgical

repair. Associated lesions, easily identified even in the neonate by echocardiography, include arch anomalies, additional ventricular septal defects, branch pulmonary artery hypoplasia, and anomalous coronary arteries.

#### 7.3.2.2 Surgery

Surgical intervention consists of closing the VSD with a patch incorporating the aorta into the left ventricle. If the aorta is significantly rightward and/or anterior, the distance between the tricuspid and pulmonary valve may be less than the aortic root diameter. In this case, a baffle from the LV to the aorta passing between the tricuspid valve and pulmonary valve will be compromised [14]. Depending on the degree and location of the pulmonary stenosis, repair will also comprise of a combination of infundibular resection, right ventricular outflow tract (RVOT) patch augmentation, pulmonary valvotomy, transannular patch, and branch pulmonary artery augmentation.

#### 7.3.2.3 Imaging

Most infants with DORV/subaortic VSD/PS will not require preoperative CMR imaging in addition to echocardiography. Rarely, a patient with an unexpected or complex preoperative course will prompt CMR imaging. This may be a focused exam guided by the preoperative course and query with examples as follow.

1. If the feasibility of an intracardiac repair is questioned, the essential sequence is the three-dimensional balanced steady-state free precession (3D bSSFP) whole-heart sequence. By acquiring data with isotropic voxels and using MPRs, the distance between the tricuspid and pulmonary valves can be measured, thereby allowing an assessment of the likelihood of successful intracardiac baffling. MPRS are created to prescribe complex nontraditional imaging planes for bSSFP cine images depicting the dynamic relationship of the VSD, the aorta, and the pulmonary and tricuspid valves.
2. In patients who have mild pulmonary stenosis, in whom deferring surgical repair is favored, documenting the pulmonary blood flow, and therefore risk of developing pulmonary hypertension, may be desirable. In these patients, the exam should focus on obtaining an accurate measure of the ratio of pulmonary to aortic blood flow ( $Q_p:Q_s$ ) and of ventricular volumes. Branch pulmonary artery flow should be obtained as validation of values obtained from the main pulmonary artery flow.
3. In the event that the branch pulmonary artery anatomy is questioned, if only one 3D sequence may be obtained due to time constraints, magnetic resonance angiography (MRA) is the preferred sequence over the 3D bSSFP whole-heart sequence. In the setting of significant pulmonary stenosis, the 3D bSSFP whole heart is at risk of dephasing artifact from turbulent flow in the pulmonary trunk.

When performing MRA in patients with DORV, a prior understanding of the physiology and shunting across the VSD is necessary to anticipate the path of contrast and allow appropriately timed triggering of image acquisition. For example, in patients with near-critical pulmonary stenosis, contrast in the RV will fill the ascending aorta prior to the pulmonary arteries, and branch PA imaging may be best obtained on the second pass of the MRA sequence. Should a patent ductus arteriosus (PDA) be present, a delayed triggering of image acquisition in the ascending aorta will be optimal.

Although coronary artery anatomy may be shown by the 3D bSSFP whole-heart sequence, CMR imaging cannot reliably define coronary arteries in neonates. Neonatal coronary imaging is best attained with cardiac catheterization or CT angiography.

In the older child or adult, CMR plays an important role in the long-term assessment of patients with DORV/subaortic VSD/PS. There is the potential for residual pulmonary stenosis, pulmonary regurgitation, and branch pulmonary artery stenosis. Serial, systematic evaluation of residual lesions and their hemodynamic consequence should utilize a “RV assessment” protocol obtained by addition of certain relevant images to a basic protocol (Table 7.1). The RV inflow/outflow cine profiles the tricuspid valve and the RV free wall. It also provides an additional dynamic view of the RVOT. This view often portrays aneurismal motion of the RVOT, as defined by systolic expansion of the outflow tract. Cine imaging of the branch pulmonary arteries in orthogonal planes defines the cyclic pulsatility of the vessels and areas of focal narrowing. Through-plane phase-encoded flow velocity mapping of each of the branch pulmonary arteries allows evaluation of the net ratio of forward flow to each lung. Of note, in the presence of turbulent flow in a pulmonary artery due to stenosis, phase-encoded velocity mapping will be unreliable. In this situation, flow volume quantification is more accurately ascertained by summing through-plane flow volumes in the four pulmonary veins.

The remainder of a basic congenital heart disease protocol should be followed, assessing the findings in the context of past surgical intervention and the current pathology. Ventricular compliance can be assessed by the flow pattern across the pulmonary valve. A noncompliant right ventricle becomes a conduit for blood flow during atrial systole, and through-plane phase-encoded velocity mapping of the pulmonary artery may demonstrate antegrade flow in late diastole. As ventricular compliance decreases, the pulmonary regurgitant fraction may decrease.

With abnormal RV loading, the hemodynamic effect on the LV must be considered. Patients with severe pulmonary regurgitation exhibit smaller left ventricular volumes as a result of decreased right ventricular output [15]. LV filling has been shown to improve after percutaneous pulmonary valve implantation [16]. Thus one should not ignore the clinical implication of RV abnormalities on left-sided hemodynamics which must be followed just as meticulously.

### 7.3.3 DORV with Subaortic VSD Without Pulmonary Stenosis

#### 7.3.3.1 Imaging

Infants with DORV and a subaortic VSD without pulmonary stenosis rarely have indications for preoperative CMR imaging. The anatomy is straightforward and can be delineated by echocardiography. The physiology is that of a large VSD. Uncomplicated surgical closure of the defect is expected to result in normal physiology and anatomy without significant residua.

Postoperative assessments using CMR would be indicated if clinical and echocardiographic screening suggested hemodynamic compromise. The protocol suggested above would apply.

### 7.3.4 DORV with Subpulmonary VSD

#### 7.3.4.1 Anatomy

DORV with subpulmonary VSD accounts for one quarter of cases of DORV. It is frequently referred to as the “Taussig-Bing” variety of DORV, although this term has also been used to describe complete transposition of the great arteries with subpulmonary VSD [12]. The aorta and pulmonary artery lie side by side with the aorta rightward of the pulmonary artery or may lie in anterior-posterior orientation with the aorta anterior and slightly rightward [17]. The VSD sits between the limbs of the septomarginal trabeculations, but in contrast with the subaortic VSD, the outlet septum attaches to the ventriculo-infundibular fold or to the posterior limb of the septomarginal trabeculations therefore isolating the aorta from the left ventricle. Associated findings include a constellation of left heart anomalies: coarctation of the aorta, straddling of the mitral valve, and subaortic stenosis. Pulmonary stenosis is rare. As many as 27% of patients with DORV and subpulmonary VSD have coronary artery anomalies [17]. The streaming effect of oxygenated blood from the left ventricle into the pulmonary artery results in physiology resembling that of transposition of the great arteries. Depending on the size of the VSD and associated mixing lesions (atrial septal defect, PDA), patients will present with varying degrees of cyanosis.

Echocardiography is expected to provide sufficient information for operative planning during early infancy. Rarely, a patient will require preoperative CMR imaging to further delineate the degree of aortic arch anomalies and subaortic stenosis. The relevant images will be obtained by following the basic protocol with additional images as necessary (Table 7.2). MR angiography will demonstrate focal or tubular narrowing of the aortic arch. Additional long-axis cine images of the aortic arch may be useful to demonstrate areas of flow acceleration. These may be planned from MPRs using the 3D data set or by prescribing a perpendicular plane through the ascending and descending aorta from axial images.



**Table 7.2** Preoperative images often obtained in addition to the “RV assessment” protocol given in Table 7.1, for patients with DORV/–subpulmonary VSD

	Sequence	Planning	Purpose
Aortic outflow tract	Breath-held, ECG-gated, bSSFP cine images	Image 1: From axial stack, place perpendicular plane through the aorta and angle this toward apex of the RV	Replaces the LV outflow tract view
		Image 2: Cross-cut image 1 with a perpendicular plane	Assessment of subaortic stenosis if present Allows planning of aortic flow
Aortic arch	Breath-held, ECG-gated, bSSFP cine image	From TSE axial stack	Subjective assessment of degree of obstruction
		Place a perpendicular plane across the ascending aorta and ensure it passes through the descending aorta	Assessment of area of flow acceleration
Atrial septal defect flow	Non-breath-held, ECG-gated, through-plane phase contrast flow velocity mapping	From four-chamber and short-axis stack	Profiles the size of the atrial septal defect
		Place a perpendicular plane on the right atrial side of the atrial septum, parallel to the septum	
		Ensure the plane is parallel to the septum in the short-axis plane	

### 7.3.4.2 Surgery

The preferred surgical repair in some centers consists of an arterial switch operation (ASO) with closure of the VSD by baffling the native pulmonary trunk, now neo-aorta, into the LV [18]. Alternatively, patients may undergo oversewing of the pulmonary trunk, baffling of the LV to the aorta incorporating the pulmonary trunk in the LV, with an RV to PA conduit completing the repair (Rastelli procedure) [19]. Patients with great arteries in the anteroposterior relationship have greater mortality when undergoing ASO than those with side-by-side great arteries. It is postulated to be due to a higher prevalence of coronary artery anomalies in patients with anteroposterior great arteries and, for some centers, results in a greater number of patients undergoing the Rastelli procedure [18].

### 7.3.4.3 Imaging

The long-term assessment of patients with DORV/subpulmonary VSD is guided by the past surgical intervention and associated residual lesions. Patients with a history of ASO and Rastelli procedure should be assessed routinely for the development or progression of branch pulmonary artery or RV-PA conduit stenosis, respectively (see Fig. 7.2a, b, and Movies 7.1 and 7.2). An RV assessment protocol as described

above should be followed. Reimplantation of the coronary arteries carries a risk of coronary dysfunction as demonstrated by abnormal coronary flow reserve in patients after ASO [20, 21]. Short- and long-axis cine images of the LV should be closely evaluated for wall motion abnormalities. If found, segmented, breath-held delayed enhancement imaging, to optimize spatial resolution and sensitivity for detection of myocardial fibrosis or scar, should be performed.

## 7.3.5 DORV/Noncommitted VSD (ncVSD)

### 7.3.5.1 Anatomy

A noncommitted VSD is a more unusual location for a VSD in DORV and accounts for approximately 10% of patients with DORV [12]. The noncommitted VSD may be restrictive and does not sit between the limbs of the septomarginal trabeculations as in other types of DORV. Instead, the VSD may be perimembranous, with inlet extension, or may be muscular [11, 22]. The great arteries generally lie side by side with the aorta slightly posterior. Associated anomalies include pulmonary stenosis, straddling atrioventricular valves, subaortic stenosis, LV hypoplasia, and coarctation of the aorta [22, 23]. Depending on the size of the VSD and degree of great artery obstruction, patients can present with cyanosis or pulmonary overcirculation.

### 7.3.5.2 Surgery

The remoteness of the VSD from both of the great arteries complicates the surgical repair. The aorta is located not only rightward of the pulmonary artery but high in the right ventricle, and in the past, these patients were committed to a single-ventricle palliation [22]. Nowadays, patients successfully undergo biventricular repair by enlargement of the VSD and tunneling the left ventricle to the aorta or ASO with tunneling the left ventricle to the native pulmonary artery [22–24]. In centers which prefer the intracardiac repair to the ASO, as many as 50–100% of patients will require VSD enlargement [23, 24]. Straddling atrioventricular valves and the location of chordal attachments play an important role in the surgical management of these patients. Attachments to the crest of the ventricular septum complicate VSD enlargement but do not always preclude it. In contrast, attachments of the tricuspid valve crossing the subaortic pathway are more likely to prevent biventricular repair [23]. The complexity of either surgical option frequently results in patients undergoing repair at an older age predisposing patients to the need for palliative procedures such as pulmonary artery band for overcirculation and aortopulmonary shunts for hypoxemia as neonates [11, 23, 24].

### 7.3.5.3 Imaging

Preoperative CMR imaging in patients with DORV/ncVSD will focus on the feasibility of intracardiac repair which can be determined by following the “RV assessment” protocol.



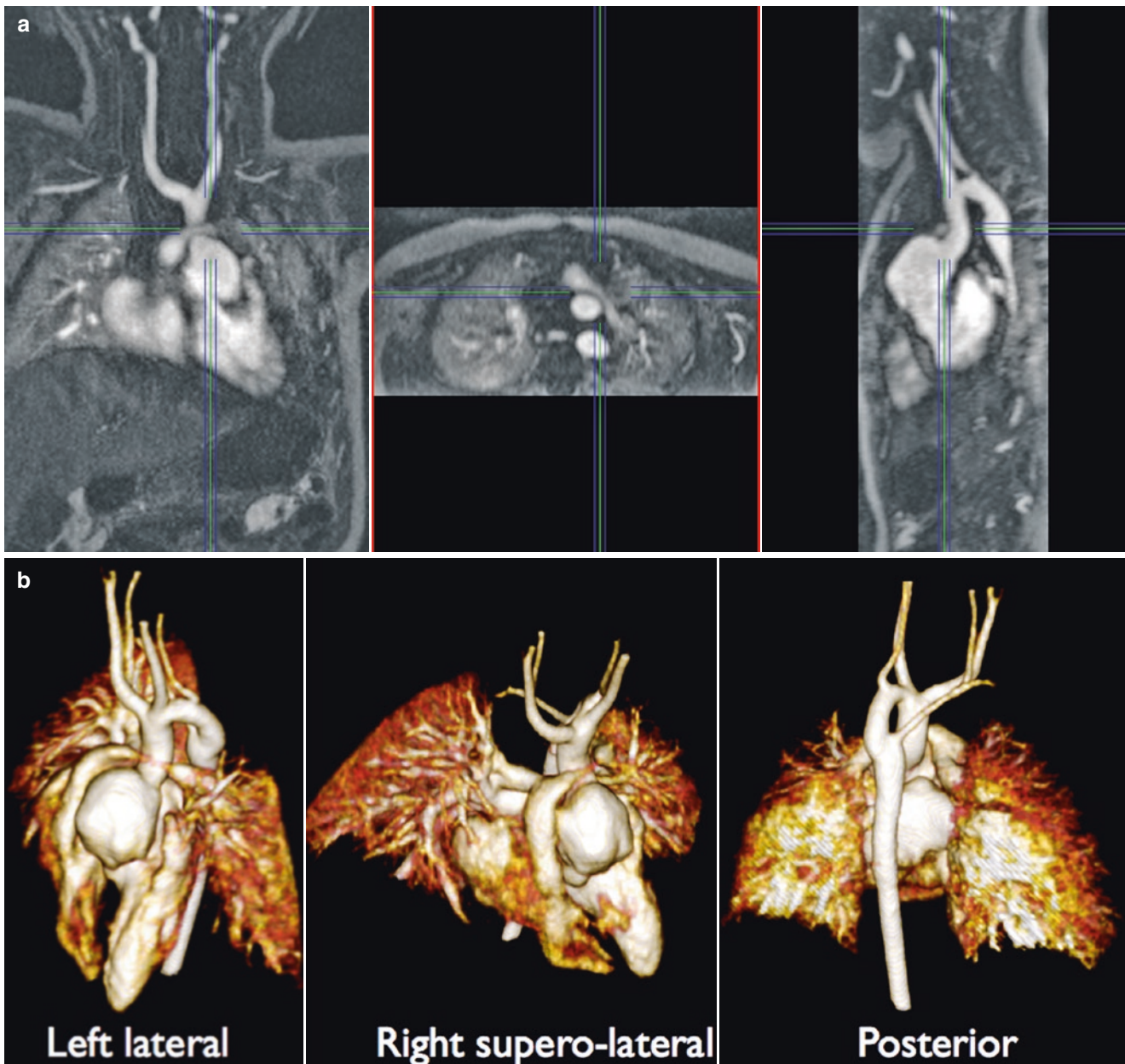


**Fig. 7.2** (a) From the raw data described in Movie 7.1, this is a representative view using 3D image viewing software. The three planes focus on the severely stenotic left pulmonary artery, and the image demonstrates the value of isotropic data for assessing complex anatomy. (b) Three views from different aspects of a 3D volume-rendered model, using data

derived from the MR angiogram of the above patient; an infant following repair of DORV with subpulmonary VSD, involving arterial switch operation with Le Compte maneuver and VSD closure. This image demonstrates the pertinence of 3D data, allowing visualization of the RV outflow tract, the narrowed branch pulmonary arteries and the aortic arch

The distance between the tricuspid and pulmonary valves may be measured from the 3D bSSFP whole-heart sequence. The VSD will be seen in the same sequence and will additionally be profiled by the short-axis cine images. The atrio-ventricular valve apparatus should carefully be evaluated for chordal attachments to the crest of the septum, using long- and short-axis bSSFP cine views. Critical attention must be focused on the technical quality of the images to achieve optimal spatial resolution in order to sensitively visualize the fine fibrous structures of the chordae tendinae. The degree

and location of aortic and pulmonary stenosis will be seen in both 3D datasets and bSSFP cine images.

Postoperatively, patients who have undergone tunneling of the LV to the aorta will likely have an elongated, akinetic left ventricular outflow tract (LVOT). Up to 30% of these patients are at risk of developing subaortic stenosis [23, 25]. The preferred method of imaging the LV outflow tract involves a combination of cine imaging and 3D datasets. Cine images in orthogonal planes will demonstrate the contractility of the LVOT and the 3D bSSFP sequence by allowing multiplanar

reconstructions that will profile the length and narrowing of the outflow tract. Patients who undergo repair by ASO and tunneling of the LV to the native pulmonary trunk will need to be imaged to evaluate the potential for branch pulmonary artery stenosis and for evidence of coronary artery anomalies. As above, concerns regarding coronary artery integrity and/or wall motion abnormalities should prompt segmented, breath-held delayed enhancement imaging.

### 7.3.6 DORV/Doubly Committed VSD

A doubly committed VSD in DORV occurs in approximately 10% of patients with DORV [12]. A thin, fibrous raphe separates the rightward aorta from the pulmonary trunk. Patients present with early signs of congestive heart failure due to unrestricted pulmonary blood flow. Surgical repair consists of closing the VSD to the aorta. Preoperatively, there are rarely indications for CMR.

Uncomplicated surgical closure of the defect is expected to result in normal physiology and anatomy without significant residua. Postoperative assessments using CMR would be indicated if clinical and echocardiographic screening suggested hemodynamic compromise. The protocols suggested above would apply.

## 7.4 The RV with Abnormal Division of the Trabeculations: Double-Chambered Right Ventricle (DCRV)

### 7.4.1 Anatomy

The double-chambered RV (DCRV) is a rare anomaly created by hypertrophied muscle bundles that divide the trabeculated apex of the RV. Various origins of the muscle bundles have been described including a hypertrophied moderator band with a high insertion site on the septal surface and anomalous muscle bundles arising from the supraventricular crest [26]. Others describe DCRV as occurring from hypertrophied septoparietal trabeculations that create a muscular shelf, either in a high and horizontal position or in a low and oblique plane [27]. In all cases, the resultant physiology is of a high-pressure proximal chamber and a low-pressure distal chamber, both containing apical trabeculations, thus distinguishing the obstruction of DCRV from the infundibular obstruction of tetralogy of Fallot [27]. DCRV, in 70–90% of patients, is associated with an existing or preexisting perimembranous VSD [26–28].

### 7.4.2 Imaging

In small children with pristine echocardiographic acoustic windows, the diagnosis may easily be made using modified

subcostal right ventricular views. In older children and adults, limited views of the right ventricle may result in poor detection of obstructive right ventricular muscle bundles, particularly when the high-velocity jet of the obstruction is mistaken for shunting across the VSD. In a recent retrospective review of 32 adult patients with DCRV, transthoracic echocardiography correctly identified a DCRV in only 5% of patients [28]. Missed diagnoses have been reported in multiple patients, leading to inappropriate surgical and medical management [29]. Suspicion of the presence of DCRV, based on physical exam and on an unexpectedly hypertrophied RV on echocardiography, should prompt additional imaging by a modality that provides unrestricted views of the right ventricle such as CMR or transesophageal echocardiography. The degree of obstruction across the hypertrophied muscle bundles will determine timing of surgical intervention. Progression of the obstruction occurs at a highly variable rate; patients have required surgical resection anytime between infancy and adulthood [26, 27].

CMR imaging should follow the “RV assessment” protocol with additional images focused on the intracavitary anatomy (Table 7.3). Cine imaging of the right ventricular obstruction will identify the location of maximal obstruction

**Table 7.3** Images often obtained in addition to the “RV assessment” protocol given in Table 7.1, for patients with double-chambered RV

	Sequence	Planning	Purpose
RV cavity	Breath-held, ECG-gated, “black-blood” images (HASTE or TSE). Contiguous, high-resolution slices	From scouts	Define location of muscle bands including attachments
		Stacks covering the RV in sagittal, axial, and coronal planes	Help plan cine imaging of obstruction
RV obstruction cine	Breath-held, ECG-gated, bSSFP cine images	Image 1: From TSE axial stack. Place perpendicular plane through the RV outlet by scrolling through axial stack	Obtain dynamic profile of area of obstruction
		Image 2: Orthogonal view through image 1	Help plan phase contrast velocity mapping of obstruction
RV obstruction flow	Non-breath-held, ECG-gated, through-plane phase contrast flow velocity mapping	From orthogonal cine views of the RV obstruction Place a perpendicular plane just distal to point of maximal jet acceleration Venc at least 4 m/s, or greater based on estimate of gradient	Obtain peak velocity to estimate gradient across the obstruction, with Bernoulli equation

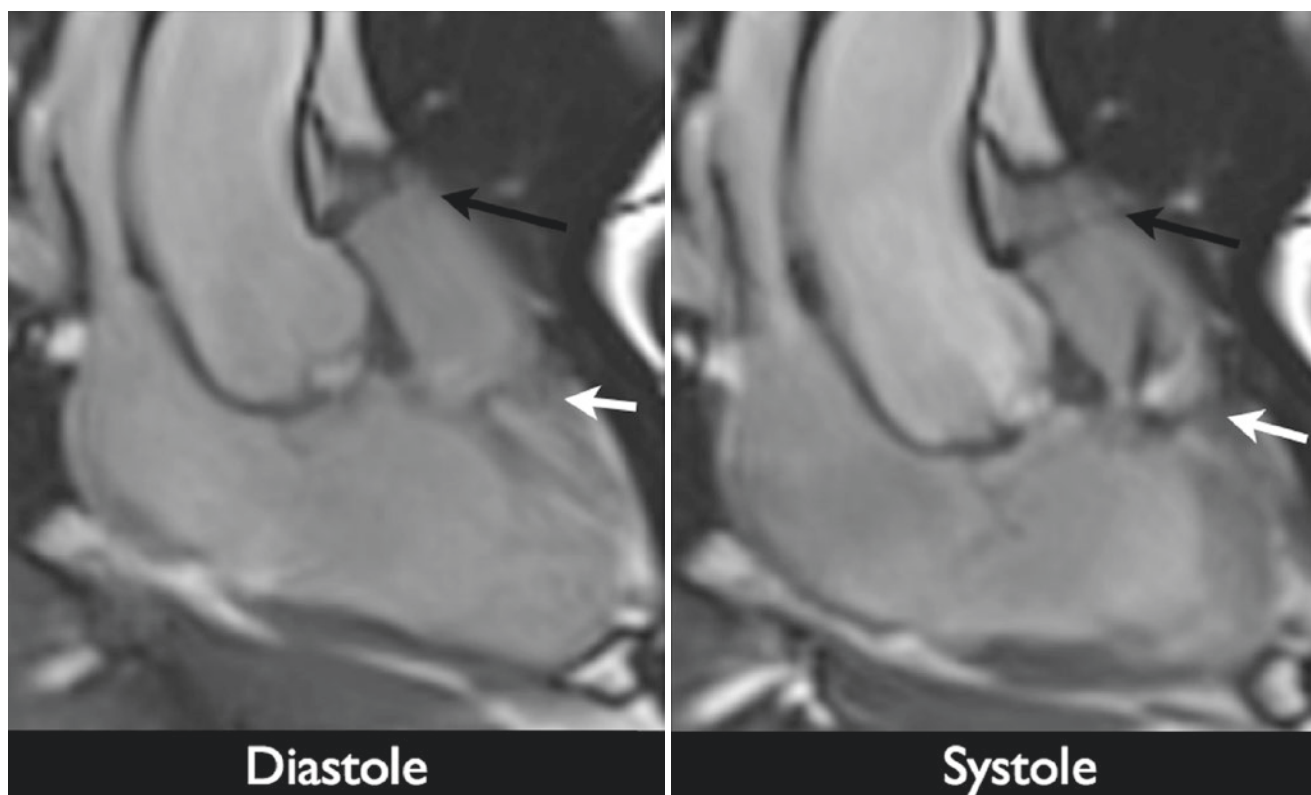


**Fig. 7.3** A segmented, bSSFP cine, showing a skewed sagittal view of the right ventricle that includes both inflow and outflow tracts. This adult patient has unoperated, double-chambered right ventricle, associated with a perimembranous ventricular septal defect. Persistent, native, septoparietal fibromuscular bands occupy a high horizontal position,

and may need to be obtained from nontraditional oblique planes through the RV cavity (Fig. 7.3 and Movies 7.3, 7.4 and 7.5). The peak gradient across the area of greatest obstruction can be obtained by applying the Bernoulli equation to velocity data obtained from phase contrast velocity mapping of the area, potentially obviating the need for cardiac catheterization. In the presence of a VSD, the size and extension of the defect should be profiled by a short-axis or axial stack through the ventricles. The 3D bSSFP dataset will allow multiplanar reconstruction of the obstruction and of the VSD. MR angiography will unlikely provide additional preoperative information and may be removed from the protocol.

Surgical repair consists of an atrial approach, although in more complicated cases, a ventriculotomy may be necessary. Resection of the muscle bundles carries excellent mid- and long-term outcomes [26, 30]. Nonetheless, the potential for postoperative residual or recurrent obstruction requires long-term follow-up [26]. CMR imaging should be performed as described above with a focus on profiling the anatomy of the resected area and quantifying the right ventricular pressure gradient.

proximal to the infundibular region, and give rise to dynamic obstruction. The level of the obstruction is shown with a white arrow; the level of the pulmonary valve is shown with a *black arrow*. The unobstructed infundibular region lies between these levels

## 7.5 The RV with Abnormal Pulmonary Outlet: Pulmonary Atresia with Intact Ventricular Septum (PA/IVS)

### 7.5.1 Anatomy

Accounting for less than 2.5% of congenital heart disease [31] PA/IVS presents a spectrum of right ventricular anomalies from a severely hypoplastic RV to a near-normal volume RV. Bull et al. classified patients with PA/IVS based on the tripartite nature of the RV that consists of an inlet, a trabecular apex, and an infundibulum [32]. It is myocardial overgrowth of one or more of these components that results in the characteristic hypoplastic and thick-walled RV. Muscular overgrowth of the infundibulum only occurs in the setting of apical overgrowth; thus, patients with muscular pulmonary atresia will likely have unipartite ventricles. Valvar atresia, which occurs in 75% of patients with PA/IVS [33], is associated 50% of the time with a well-developed infundibulum. The remainder of patients will have some degree of stenosis [34]. It has been postulated that the embryological insult in PA/IVS occurs later in development than in tetralogy of



Falot with pulmonary atresia (TOF/PA). As a result, and in contrast to patients with TOF/PA, the pulmonary valve, branch pulmonary arteries, and ductus arteriosus in patients with PA/IVS will frequently be of near normal size and morphology [35]. Occasionally, one may find discontinuous pulmonary arteries supplied by bilateral ducti and, more infrequently, multiple aortopulmonary collateral vessels. Other associated findings include an obligatory right to left shunt at the atrial septum, which if absent results in fetal death. The tricuspid valve is frequently both hypoplastic and dysplastic, but only the degree of hypoplasia correlates with right ventricular size. In fact, patients may have a severely dysplastic valve in the setting of a normal-sized RV [31]. In addition to nonspecific tricuspid valve dysplasia, up to 10% of patients will have true Ebstein's anomaly [33].

There is a high prevalence of important coronary artery abnormalities in patients with PA/IVS. From two large population-based studies, between 8 and 23% of patients with PA/IVS have right ventricular-dependent coronary circulation (RVDCC) at presentation [34, 36]. RVDCC is defined as atresia or severe stenosis of a coronary artery at its orifice or along its course, with coronary perfusion maintained by communication of the distal coronary to the RV cavity. Coronary perfusion pressure is therefore dependent on elevated right ventricular pressure. In these patients, any procedure that results in a decrease in right ventricular pressure, such as relief of the right ventricular outflow tract obstruction, results in reduced coronary perfusion. In addition to RVDCC, as many as 45–55% of patients with PA/IVS have RV to coronary artery fistulae, defined as communications between the epicardial coronary arteries and the right ventricular cavity but without stenosis. In 80% of the time, both coronary arteries are involved [34, 36]. Over time, the elevated right ventricular systolic pressure promotes myointimal thickening of the fistulous connections and can progress to clinically significant stenosis or interruption of the coronary artery from the aortic origin, therefore developing RVDCC [37]. For this reason, patients with coronary artery fistulae should undergo relief of the elevated RV pressure in a timely fashion in order to prevent the development of RVDCC.

### 7.5.2 Surgery

The options and timing of interventions are varied and may be staged, depending on the functionality of the RV and its potential for growth. Patients with valvar atresia and mild infundibular hypoplasia will likely undergo an RV decompression procedure such as percutaneous catheter-based pulmonary valvotomy or a combination of surgical procedures such as RVOT patch augmentation, transannular patch placement, and/or infundibular resection. In the event that



**Fig. 7.4** A segmented, bSSFP cine, showing a four-chamber view from an adult patient following “one and a half ventricle” repair of PA/IVS. This patient has a pulmonary valve homograft and a bidirectional cavo-pulmonary anastomosis. The right ventricle is hypoplastic with impaired systolic function (RV ejection fraction 47%) and severe diastolic dysfunction. Note the sharp shift of the interventricular septum toward the left during diastole

the RV remains unable to sustain adequate forward pulmonary blood flow, an aortopulmonary shunt may be placed. The goal is to promote right ventricular growth and eventually complete a biventricular repair. Patients in this pathway that fail to develop adequate RV stroke volume will undergo a bidirectional cavo-pulmonary connection and remain with “one and a half ventricle” physiology (Fig. 7.4 and Movie 7.6). The principle of the one and a half ventricle is to unload an RV inadequate to maintain full cardiac output while at the same time avoiding the dreaded complications of the Fontan physiology. Patients with a tripartite ventricle, without significant tricuspid valve dysplasia, may successfully undergo biventricular repair in the neonatal period. Patients with unipartite ventricles and those with RVDCC, regardless of RV size, will begin single-ventricle palliation. It is important to realize that patients with RVDCC, until completion of the Fontan, will have coronary blood flow supplied by deoxygenated blood from the RV. These patients therefore have an additional risk of developing myocardial dysfunction, and Fontan completion will be performed as early as technically possible.

Overall 5-year survival in the modern era is 80%, with only 55–72% of patients having reached a definitive surgical endpoint by that time [38]. In a prospective study of 408 patients with PA/IVS from 33 institutions between 1987 and 1997, 60% were predicted to undergo biventricular repair based on preoperative imaging, but only 30% were able to do so. The authors found a statistically significant increased mortality of 54 versus 31% in those neonates who did not follow their predicted clinical course, thus



emphasizing the need for accurate preoperative imaging and planning [38].

### 7.5.3 Imaging

#### 7.5.3.1 Neonatal Period

Echocardiography establishes the diagnosis of PA/IVS in infancy. In the extremely severe cases of RV hypoplasia, and in patients with a very mildly hypoplastic RV with normal tricuspid valve, choosing the appropriate surgical intervention may be straightforward. In contrast, in borderline cases, determining the ability of a RV to eventually sustain systemic venous return can be extremely difficult. Complicated formulas utilizing the variables of right-sided structures, such as tricuspid valve area, RV end-diastolic volume (EDV), RV length, and RV outflow diameter, have been created in attempts to predict the optimal surgical management [39]. Others have relied on tricuspid valve annulus Z-score to estimate the potential for RV growth and successfully assign patients to a univentricular or biventricular repair. Unfortunately, there traditionally has been significant overlap between patient groups classified by tricuspid valve Z-scores and type of successful surgical intervention. To date, there is no unifying Z-score that can be utilized to predict the appropriate surgical course [38, 40, 41].

One of the difficulties in isolating a tricuspid valve Z-score as a predictor of outcome has been the significant inter-observer and intra-observer variability in the method of obtaining tricuspid valve measurements by echocardiography [41]. CMR imaging has the potential to overcome the limitations of echocardiography that have negatively impacted studies of predictors of outcome but has not been studied in this setting. It is conceivable that by providing CMR-derived, reproducible measurements of tricuspid valve area, RV volumes, ejection fraction, and atrial shunting, multicenter trials could arrive at a more robust management algorithm.

In the current era, CMR would therefore unlikely alter planning in the neonatal period and is usually not performed. Patients suspected of having coronary anomalies will undergo cardiac catheterization to identify coronary artery blood supply and obtain a risk assessment of right ventricular decompression prior to intervention.

#### 7.5.3.2 CMR After RV Decompression

CMR will provide more useful information in patients who have undergone RV decompression followed by a period of RV growth. In these patients, measurements of tricuspid valve area, RV volumes and forward pulmonary blood flow may be useful to document progression of RV output and function (Fig. 7.4). The “RV assessment” protocol should be followed, with RV volume assessment using a short axis or

axial long axis stack (for centers not using slice positioning tools during post-processing), of 2D cine images. Ventricular segmentation with exclusion of trabeculations from the ventricular volumes should be performed consistently and meticulously and indexed to body surface area to provide accurate comparisons of volumes over time. The tricuspid valve should be adequately profiled both in the long axis and short axis. Valve orifice area can be planimetered at the tips of leaflets from an “en-face” view. The volume of pulmonary blood flow can be quantified and the contribution from multiple sources (e.g., both forward flow across the RVOT and via a cavo-pulmonary connection) defined, using through-plane phase contrast flow volumetry. Pulmonary venous flow volumes can be ascertained to estimate total pulmonary flow and to quantify any collateral flow. Should the atrial septal communication need to be imaged, the 3D bSSFP whole-heart sequence may provide adequate delineation of the septal defect, but because the atrial septum is thin, the image resolution is not always sufficient. Instead, an “en-face” view of the atrial septum imaged by through-plane phase-encoded velocity mapping will demonstrate the defect size, the direction of shunt through the cardiac cycle and the estimated net shunt through the defect (Fig. 7.5). The image plane can be planned from the four-chamber cine view and atrial short axis cine views by prescribing a perpendicular image plane, parallel to the atrial septum. The image plane is best prescribed on the left atrial side of the defect when net shunting is right to left and on the right atrial side when net shunting is left to right.

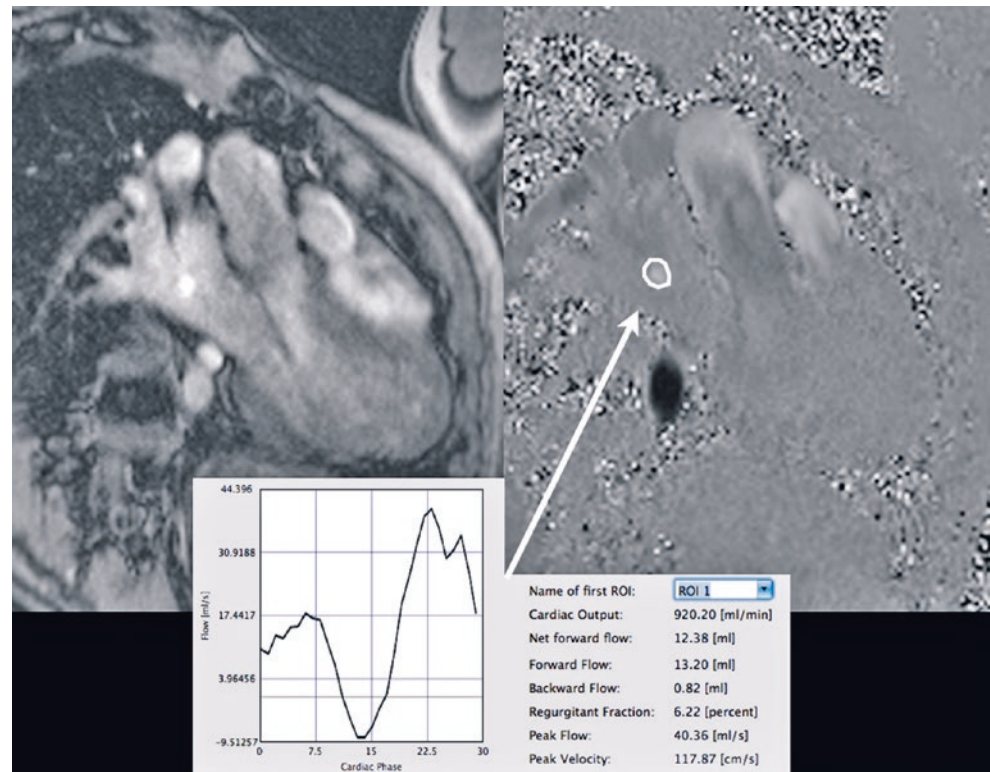
#### 7.5.3.3 CMR After Biventricular Repair

It is expected that 50% of patients with PA/IVS will successfully undergo biventricular repair [38], although most series to date have reported at most, one third of patients with PA/IVS completing a biventricular pathway [25, 36, 39]. CMR is a valuable tool for routine, serial RV assessment. It has been shown that restrictive RV physiology persists in patients with PA/IVS after biventricular repair [42], which can be demonstrated by the presence of antegrade diastolic pulmonary flow on phase contrast flow mapping (Fig. 7.6). Additional support for restrictive physiology can be demonstrated with abnormal tricuspid valve inflow pattern, a dilated right atrium and vena cavae, and RV fibrosis assessed by delayed-enhancement imaging. Branch PA size, particularly at the site of previous aortopulmonary shunts or surgical arterioplasties should be assessed.

#### 7.5.3.4 CMR in the Single Ventricle (Table 7.4)

CMR imaging provides valuable clinical information prior to completion of a bidirectional cavo-pulmonary connection (BCPC) or total cavo-pulmonary connection (TCPC). Prior to BCPC, the basic imaging protocol (Table 7.1) should be

**Fig. 7.5** This is the magnitude and matching phase contrast flow velocity image, planned perpendicular to the atrial septum in order to measure the through-plane flow through a small residual ASD in an adult following biventricular repair of PA/IVS. The region of interest (ASD) is circled (white arrow). The flow data is illustrated and shows phasic, but net right atrial to left atrial flow



followed paying particular attention to LV function (particularly in the setting of RVDCC), the patency of the atrial communication, the size of the branch pulmonary arteries, and the presence of bilateral superior vena cavae. The atrial septum can be profiled by cine imaging or phase-encoded velocity mapping with an “en-face” view as described above. Prior to completion of a TCPC, to assess pulmonary hemodynamics, a jugular venous pressure, reflective of pulmonary artery pressure, can be obtained under general anesthetic at the time of CMR.

Although 3D imaging using a bSSFP sequence may preclude the need for MRA, angiographic views can identify significant collateral vessels and further delineate the surgical anastomoses. MRA acquisition early after bolus administration in the upper extremities will likely be confounded by signal loss from a T2\* effect in the superior vena cava and pulmonary arteries. In this case, the T1 shortening effects of the contrast will only be useful for imaging during the second pass acquisition. Administration of gadolinium contrast for MRA should therefore ideally be administered in a lower extremity vein and triggered in the LV to opacify the inferior

vena cava and the aorta during the first acquisition. The second pass acquisition of the MRA will then provide imaging of the BCPC.

Through-plane phase-encoded velocity mapping of the pulmonary arterial flow volume, compared to total pulmonary venous flow volume, can be obtained to calculate the degree of systemic arterial to pulmonary collateral flow [43, 44]. An acceptable alternative method of measuring the amount of systemic arterial to pulmonary collateral flow is by measuring the discrepancy between ascending and descending aorta flow [43]. Should there be suspicion of supradiaphragmatic systemic venous to pulmonary venous collaterals, which can develop in patients after the BCPC in patients with elevated PA pressure, both methods could be performed to quantify the contribution of each group of collaterals (Table 7.4).

Routine, serial, surveillance CMR studies are valuable in patients with single-ventricle palliation of PA/IVS to ensure patency of the Fontan circuit, evaluate collateral flow, quantify atrioventricular valve regurgitation, and follow ventricular systolic function.

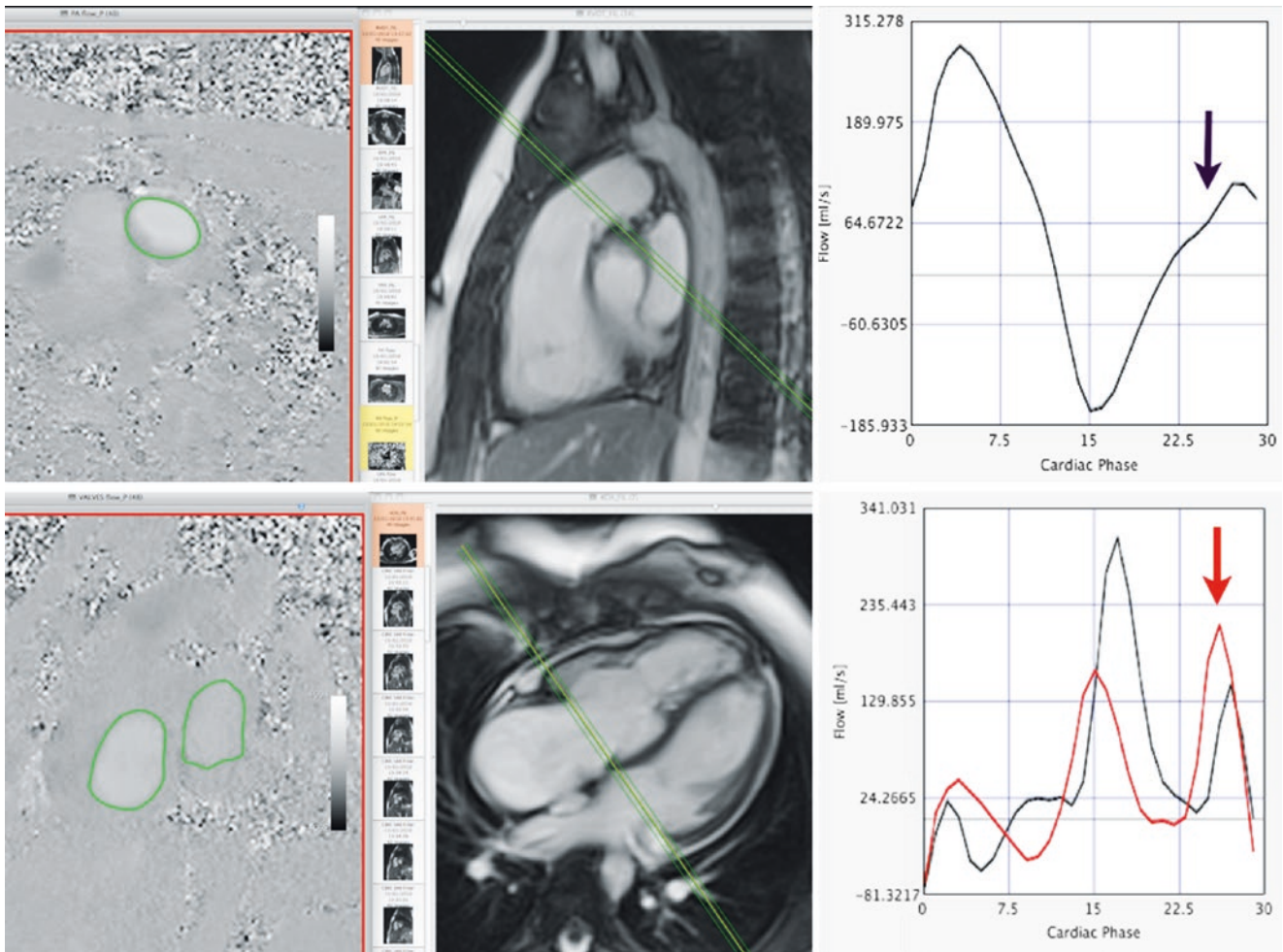


**Fig. 7.6** Phase contrast flow velocity maps, measuring through-plane flow in both the pulmonary and tricuspid valves, with image planes marked in the neighboring cine image. This data is from an adult patient, with restrictive RV physiology, following biventricular repair of PA/IVS. There is forward flow in the pulmonary artery in late diastole,

limiting the regurgitant fraction from the RV-PA homograft valve, marked with a *black arrow*. There is reversal of the usual E/A ratio, seen in the trans-tricuspid valve flow map, (*red graph*, superimposed on the *black*, trans-mitral flow map), marked with a *red arrow*

**Table 7.4** Images often obtained in addition to the “RV assessment” protocol given in Table 7.1, for patients with PA/IVS undergoing single-ventricle palliation

	Sequence	Planning	Purpose
Tricuspid valve	Breath-held, ECG-gated, bSSFP cine images	Perpendicular plane from four-chamber and RVLA, parallel to TV 5 mm contiguous slices from right atrium into ventricle	En-face view Identify dysplastic leaflets Measure inflow and regurgitant orifices
SVC flow	Non-breath-held, ECG-gated, through-plane phase contrast flow velocity mapping	From 3D whole heart Ensure orthogonal planes Close to the SVC-RA junction to avoid exclusion of azygos flow	Assessment of proportion of Qp supplied by BCPC
Pulmonary venous flow	Non-breath-held, ECG-gated, through-plane phase contrast flow velocity mapping	From 3D whole heart Ensure orthogonal planes of each of the pulmonary veins	Assessment of collateral flow
Descending aorta flow	Non-breath-held, ECG-gated, through-plane phase contrast flow velocity mapping	From 3D whole heart Ensure orthogonal planes of aorta at the diaphragm	Assessment of collateral flow
Atrial septal communication	Non-breath-held, ECG-gated, through-plane phase contrast flow velocity mapping	From four-chamber and short-axis stack Place a perpendicular plane on the left atrial side of the atrium septum, parallel to the septum Ensure the plane is parallel to the septum in the short-axis plane	Profiles the size of the atrial septal communication



## 7.6 The RV with Abnormal Afterload: Pulmonary Arterial Hypertension (PAH)

### 7.6.1 Classification and Diagnosis

The diagnosis of pulmonary arterial hypertension (PAH) is suspected by echocardiography based on tricuspid valve regurgitation velocity, a flattened ventricular septum in systole and right ventricular hypertrophy when long-standing. The diagnosis of PAH is confirmed by right heart catheterization demonstrating a mean pulmonary artery pressure greater than or equal to 20 mmHg, as of the *sixth World Symposium on Pulmonary Hypertension* in 2019. Pulmonary vascular resistance and pulmonary artery wedge pressure are utilized to determine if pulmonary hypertension is pre- or postcapillary and therefore help identify an etiology [45].

As of 2019, the classification system defined by the *sixth World Symposium on Pulmonary Hypertension* comprises of five groups, each with its own subgroups, based on similar clinical presentations and historical response to treatment. Group 1 clusters patients with pulmonary arterial hypertension including patients with idiopathic pulmonary hypertension (IPAH) and patients with irreversible pulmonary arterial hypertension due to a chronic congenital systemic-pulmonary shunt or Eisenmenger syndrome. Patients with pulmonary hypertension owing to long-standing left heart disease, including left-sided congenital heart disease, fall under Group 2. Group 3 encompasses pulmonary hypertension attributable to primary lung disease. Pulmonary hypertension in Group 4 is caused by pulmonary artery obstructions, and Group 5 combines all multifactorial etiologies and unclear causes [46].

Committing a patient to the diagnosis of PAH is ominous with the natural history predicting a 3-year survival of 35–45% in IPAH and 77% in Eisenmenger syndrome [47]. Over the past 30 years, the routine use of anticoagulants and targeted therapies such as prostanoids, phosphodiesterase inhibitors, and endothelin-receptor antagonists, has resulted in an overall 40% decrease in mortality [48]. In most centers, various combinations of the 6-min walk distance test, New York Heart Association Functional Classification, N-terminal prohormone of brain natriuretic peptide (NT-proBNP), echocardiography, and cardiac catheterization are used every 3–6 months to escalate treatment when specific goals are not met, prior to irreversible clinical deterioration. CMR focusing on the RV has more recently been included in routine evaluations.

### 7.6.2 Imaging

The frequency of evaluations of patients with PAH has prompted the need for noninvasive standardized modalities that can provide reproducible diagnostic markers. As previously discussed, until CMR became more widely available, the geometry of the RV precluded the ability to accurately measure not only subtle but also significant changes in volume and function. As the chamber most directly affected by the pathophysiology of pulmonary hypertension, CMR has therefore become an invaluable tool for diagnosis and prognosis of children and adults with suspected pulmonary hypertension [49–51]. Many studies exist to identify variables predictive of pulmonary artery pressure measured by catheterization and identify prognostic factors. The most robust studies focus on volumetric analysis. A decrease in RV ejection fraction and LV stroke volume has been found to correlate with an increased risk of mortality in children [52]. An adult study demonstrated that increased RV volumes, decreased RV stroke volume, and decreased LV volume independently predict treatment failure and mortality [53]. A meta-analysis of 22 studies confirmed that RV function and ventricular volumes predict both clinical worsening and mortality [54].

Additional variables have also been studied. The degree of pulmonary artery dilatation by CMR has been found to be proportional to the degree of pulmonary hypertension [55, 56]. But there are some controversies with respect to pulmonary artery size as Boerritger et al. [57] have shown that pulmonary arteries continue to dilate in PAH, even in the setting of resolving hypertension by cardiac catheterization measurements (Fig. 7.8 and Movie 7.8). Similarly, an increase in pulmonary artery elastance coupled with a decrease in right ventricular contractility, or ventriculo-arterial uncoupling, has been found in pediatric patients who fail to respond to nitric oxide [58]. Further findings such as myocardial fibrosis have also generated an interest in the prognosis of pulmonary hypertension [59, 60]. Finally, RV mechanics as evaluated by myocardial strain has provided insight into the progression of RV dysfunction in PAH and correlates with disease severity [61, 62] (Fig. 7.7 and Movie 7.7).

More innovative approaches have combined cardiac catheterization and CMR in the diagnosis and management of PHA. Cardiac catheterization relies on the Fick equation or thermodilution to estimate pulmonary blood flow which, with mean PA pressure, is then utilized to calculate pulmo-



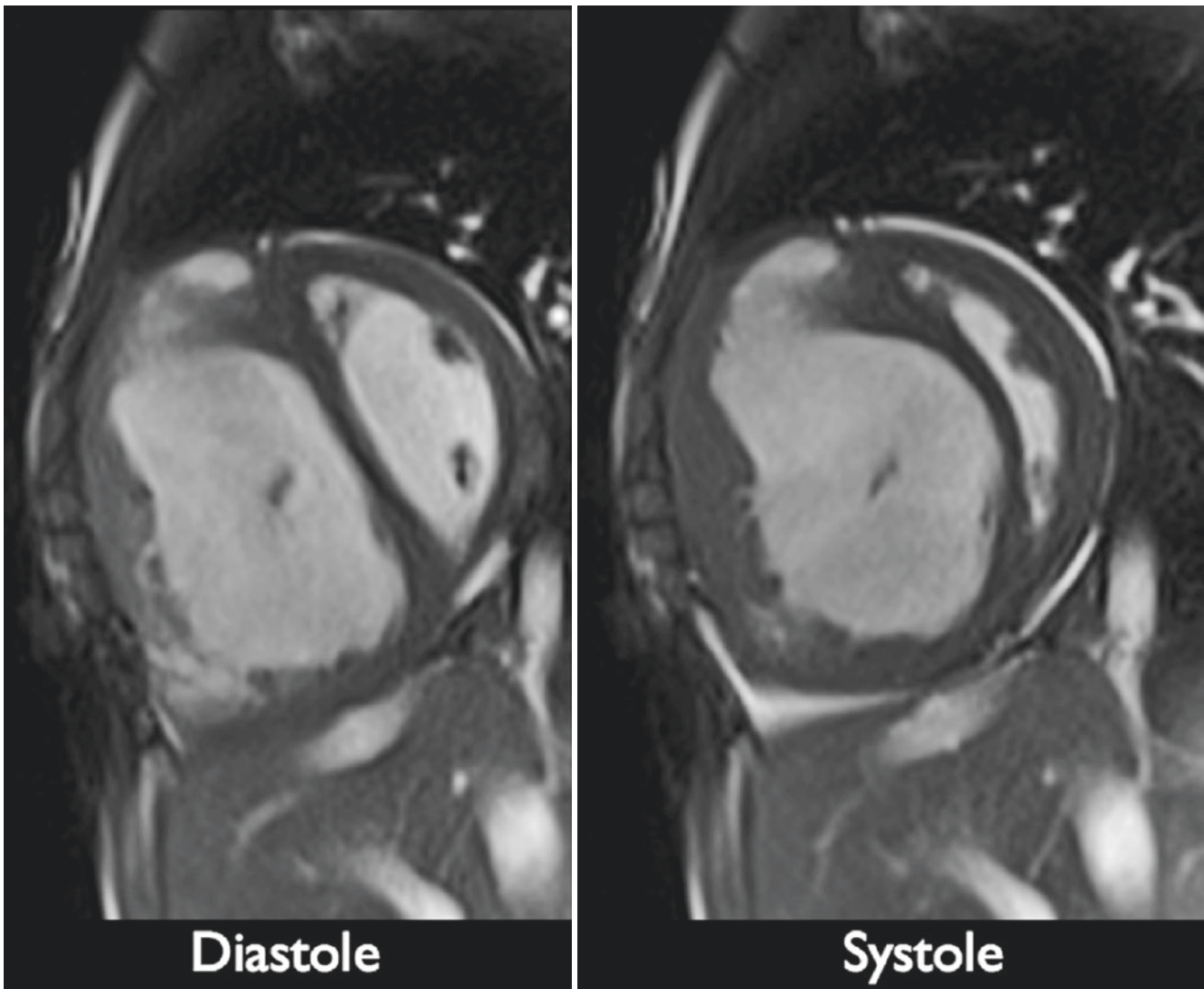


**Fig. 7.7** This is a segmented, breath-hold bSSFP cine view in the mid-ventricular short-axis plane, from an 11-year-old patient with idiopathic pulmonary hypertension. There is severe hypertrophy and dilatation of

the right ventricle. The right ventricular systolic function is globally, severely reduced. There is bowing of the septum toward the left ventricle throughout the cardiac cycle and interventricular dyssynchrony

nary vascular resistance and cardiac output. Studies have shown that both methods of calculating pulmonary blood flow become less reliable in the setting of critically ill patients [63, 64]. In contrast, phase-encoded velocity mapping in CMR provides a direct measurement of vessel blood volume. When combined with near simultaneous measurements of pulmonary artery pressure obtained by catheterization, the two allow a very precise measure of pulmonary vascular resistance. Centers with the ability to perform hybrid procedures using simultaneous catheterization and

CMR can use both modalities to evaluate pulmonary vasoreactivity and guide treatment management (Fig. 7.8 and Movie 7.8) [65].

The CMR study of a patient with severe PAH can be technically challenging since dyspneic patients will frequently be unable to remain supine for extended periods and may be unable to breath-hold comfortably and reliably. The essence of the CMR evaluation of these patients is rapid acquisition of critically relevant data. Real-time radial k-t SENSE imaging has been shown to provide

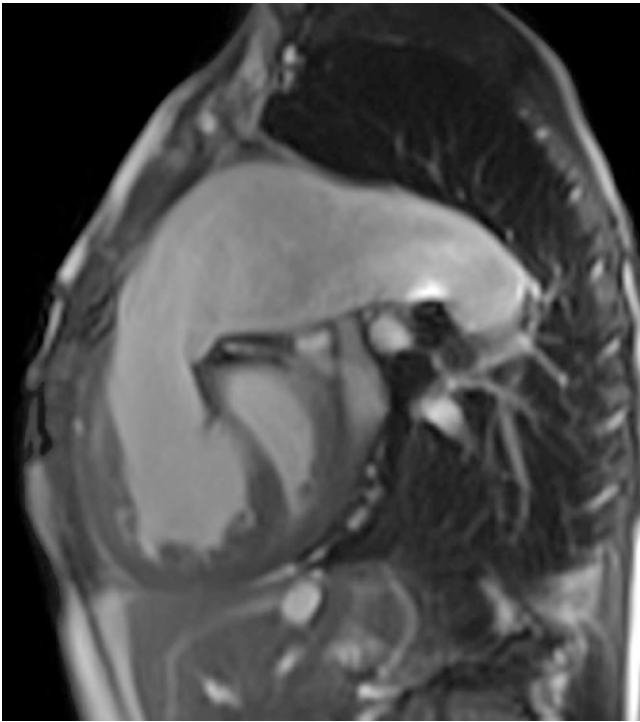


**Fig. 7.8** This is a segmented, breath-hold bSSFP cine, showing a sagittal view of the RV outflow tract, dilated MPA and proximal LPA from 16-year-old patient with Eisenmenger physiology, following chronic pulmonary overcirculation due to an ASD and a large muscular VSD. The spatial and temporal resolution of the image has been lowered to give a shorter breath-hold duration because of the poor breath-holding capacity of the patient

accurate volumetric data in abnormal right ventricles and can be extremely useful in this patient population [66]. As sequence development continues to steadily progress, approaches such as higher-resolution real-time imaging will allow CMR imaging of sicker and younger patients. A typical protocol in a lab performing hybrid procedures is detailed in Table 7.5 and, when performed routinely, can be completed in 15–20 min. Because a detailed anatomical evaluation is unnecessary, the examination can focus on real-time imaging of biventricular function and on non-breath-held, phase-encoded velocity mapping to quantify pulmonary blood flow. As mentioned above, because longitudinal shortening is affected later than transverse shortening [61], axial stacks may potentially provide more accurate volumetric analysis and should be considered.

The role of CMR in patients with PAH is therefore developing. It enables accurate measurements of PVR in centers with the ability to perform hybrid procedures by providing direct measurements of pulmonary artery blood flow. CMR also offers reliable, objective markers of the progression of disease by allowing direct quantification of biventricular cardiac output and biventricular volumes over time.

**Table 7.5** Example of the standard sequences and views of a routine cardiac scan for assessment of PAH, in the order of workflow

	Sequence	Planning	Purpose
Scout	Single shot b-SSFP images	Contiguous axial, sagittal, coronal slices. Coverage from liver to neck in all three radiological planes	Ensures isocentering of the heart in the scanner
RVLA, LVLA	Single shot b-SSFP images. Non-breath-held	From scout images Place a perpendicular image plane through the long axis of the ventricle from mid-AV valve to the ventricular apex	Planning the true four-chamber image
Four-chamber view	Breath-held, ECG-gated, bSSFP cine image	From RVLA, LVLA Place perpendicular plane through both AV valve orifices in each image From LVLA cine, check that the plane passes through mid-mitral valve and LV apex From RVLA, check that the plane passes through the mid tricuspid valve and RV apex	Subjective assessment of atrial volumes, biventricular volumes and function, ventricular wall motion, AV valve regurgitation
Axial cine stack	Radial k-t SENSE Non-breath-held	From the sagittal and coronal scout images Plan contiguous 7–10 mm thick slices in the axial plane, covering the entire ventricular mass from diaphragm to outflow tracts	Alternative to short-axis cine stack. Provides the images required for segmentation of RV volumes
Short axis cine stack	Radial k-t SENSE Non-breath-held	From end-diastolic frame of four-chamber cine Place perpendicular plane at hinge points of both AV valves, with special care to include the entire basal ventricular blood pool Contiguous slices are placed to cover entire ventricular mass from base to apex	Alternative to axial cine stack. Provides the images required for segmentation of biventricular volumes

**Table 7.5** (continued)

	Sequence	Planning	Purpose
LV outflow tract	Radial k-t SENSE	Image 1: From sagittal scout. Place a perpendicular plane through both basal aortic valve and mid-mitral valve orifice. Check orientation passes through LV apex on LVLA	Outflow tract morphology, subjective assessment of semilunar valve function
	Non-breath-held	Image 2: Cross-cut image 1 to obtain two orthogonal cine views of the LVOT	Plan AO flow
RV outflow tract	Radial k-t SENSE	Image 1: From axial scout. Place a perpendicular plane through the pulmonary trunk and angle toward apex on RVLA	Outflow tract morphology, subjective assessment of semilunar valve function
	Non-breath held	Image 2: Cross-cut image 1 to obtain two orthogonal views of the RVOT	Plan MPA flow
MPA flow	Non-breath-held, ECG-gated, through-plane phase contrast velocity mapping	From the two orthogonal RVOT images	Calculate regurgitant fractions (RF%)
		Place a perpendicular plane across the MPA	Validate ventricular stroke volume measurements
		The plane should be just distal to the valve leaflets in systole and avoid turbulent areas of flow	Calculate PVR with simultaneous catheter-obtained pressure
		Optimize velocity encoding to maximize accuracy and prevent aliasing	
Aorta flow	Non-breath-held, ECG-gated, through-plane phase contrast velocity mapping	From the two orthogonal LVOT images	Validate ventricular stroke volume measurements
		Place a perpendicular plane across the proximal ascending aorta	
		The plane should be just distal to the valve leaflets in systole	
		Optimize velocity encoding to maximize accuracy and prevent aliasing	
Branch PA cine	Radial k-t SENSE. Non-breath held	From axial, sagittal, and coronal scout, optimize image plane to obtain two orthogonal planes of each branch pulmonary artery	Plan branch PA flow
Branch PA flow	Non-breath-held, ECG-gated, through-plane phase contrast velocity mapping	Place perpendicular image plane on two orthogonal views of each of the branch pulmonary arteries	Validate ventricular stroke volume measurements
			Calculate PVR with simultaneous catheter-obtained pressure
			Validate MPA flow

## 7.7 Conclusion

The abnormal right ventricle is a highly variable entity, potentially posing diagnostic and management challenges to the clinician. Prior to the advent of CMR in the clinical arena, the anatomy and physiology of abnormal right ventricles were difficult to define, and the pathophysiology was frequently underestimated.

However, clinicians with access to CMR possess a powerful resource for decision support, which is adaptable to various RV abnormalities. The use of 3D balanced SSFP imaging is ideal to understand the complex anatomy and resultant physiology of abnormal RV, particularly DORV. The ability to quantify intracardiac shunts can help to stratify risk and optimize the timing of surgical interventions. The chronic postoperative management of patients with PA/IVS, DCRV, and DORV is guided by objective analysis of regurgitant valves, stenoses, RV size, and function. Patients with PAH

may be evaluated noninvasively for disease progression and treatment response.

In nearly all cases, attaining the full clinical potential of a CMR examination requires the presence of a cardiologist experienced in congenital and acquired heart disease in order to assimilate knowledge of the natural history of disease and the details of interventions. During the scan, continuous assessment of images as they are acquired is necessary to guide a scan beyond a basic RV assessment protocol, based on the unique hemodynamic issues of the patient. The final key to a successful scan is systematic, consistent, and meticulous post-processing to give accurate and reproducible assessment of RV volumes, vessel measurements, and flow analysis.

As CMR techniques evolve and a reliable body of RV data continues to develop, a greater understanding of the complex RV will ensue, allowing refinement of clinical and surgical management protocols.

## Practical Pearls

- Prepare carefully for the scan by reviewing and thoroughly understanding the patient's entire past medical history and presenting query. This will minimize the risk of overlooking relevant findings and help explain unexpected findings that may require additional image acquisition.
- Pay close attention to patient comfort in the scanner and to communication, so that cooperation and breath-holding capability are maximized. There are no shortcuts to a comprehensive congenital scan.
- Patient comfort and behavior permitting always perform a comprehensive assessment protocol for the scan, aiming to acquire morphologic data in 3D, ventricular functional data and arterial flow data for every scan. Unexpected findings occur frequently with congenital disease and presumed "redundant" data may be necessary at the reporting stage to resolve these.
- Take care to optimize the sequences used, by maximizing the temporal and spatial resolution of the images, particularly in images obtained for volumetric and flow analysis. Modify these resolutions for patient body size and heart rate.
- Carefully plan acquisition of cine image stacks for volumetric analysis. Include the whole ventricle in the stack in systole and diastole, and modify slice position to minimize partial voluming of ventricular septum and free walls.
- Establish a consistent and systematic approach to post-processing to minimize inter-observer variability in serial studies.
- Use slice-positioning tools to accurately analyze basal slices for segmentation.
- Utilize arterial and venous flow volumes as well as left ventricular volumes for quality assurance and to improve the accuracy of right ventricular volumetric analysis. Ensure that all volumetric and flow data make hemodynamic sense in the context of the patient's history.
- Always look for non-RV causes of RV abnormality, such as anomalous pulmonary venous drainage, intracardiac shunts, and valvar regurgitation.

## References

1. Luijnenburg SE, Robbers-Visser D, Moelker A, Vliegen HW, Mulder BJM, Helbing WA. Intra-observer and inter-observer variability of biventricular function, volumes and mass in patients with congenital heart disease measured by CMR imaging. *Int J Cardiovasc Imaging*. 2010;26:57–64.
2. Winter MM, Bernink FJP, Groenink M, Bouma BJ, van Dijk AP, Helbing WA, Tijssen JG, Mulder BJ. Evaluating the systemic right ventricle by CMR: the importance of consistent and reproducible delineation of the cavity. *J Cardiovasc Magn Reson*. 2008;10:40–8.
3. Devos D, Kilner P. Calculations of cardiovascular shunts and regurgitation using magnetic resonance ventricular volume and aortic and pulmonary flow measurements. *Eur Radiol*. 2010;20:410–21.
4. Kramer C, Barkhausen J, Bucciarelli-Ducci C, Flamm S, Kim R, Nagel E. Standardized cardiovascular magnetic resonance imaging (CMR) protocols: 2020 update. *J Cardiovasc Magn Reson*. 2020;22:17–45.
5. Leiner T, Bogaert J, Friedrich MG, Mohiaddin R, Muthurangu V, Myerson S, Powell AJ, Raman SV, Pennell DJ. SCMR position paper (2020) on clinical indications for cardiovascular magnetic resonance. *J Cardiovasc Magn Reson*. 2020;22:76–113.
6. Kind T, Mauritz GJ, Marcus JT, van de Veerendonk M, Westerhof N, Vonk-Noordegraaf A. Right ventricular ejection fraction is better reflected by transverse rather than longitudinal wall motion in pulmonary hypertension. *J Cardiovasc Magn Reson*. 2010;12:35–46.
7. Alfakih K, Plein S, Bloomer T, Jones T, Ridgway J, Sivanathan M. Comparison of right ventricular volume measurements between axial and short axis orientation using steady-state free precession magnetic resonance imaging. *J Magn Reson Imaging*. 2003;18:25–32.
8. Fratz S, Schuhbaeck A, Buchner C, Busch R, Meierhofer C, Martinoff S, Hess J, Stern H. Comparison of accuracy of axial slices versus short axis slices for measuring ventricular volumes by cardiac magnetic resonance in patient with corrected tetralogy of Fallot. *Am J Cardiol*. 2009;103:1764–9.
9. Bradlow WM, Hughes ML, Keenan NG, Bucciarelli-Ducci C, Assomull R, Gibbs JS, Mohiaddin RH. Measuring the heart in pulmonary arterial hypertension (PAH): implications for trial study size. *J Magn Reson Imaging*. 2010;31:117–24.
10. Rosset A, Spadola L, Ratib O. OsiriX: an open-source software for navigating in multidimensional DICOM images. *J Digit Imaging*. 2004;17(3):205–16.
11. Mahle WT, Martinez R, Silverman N, Cohen M, Anderson R. Anatomy, echocardiography, and surgical approach to double outlet right ventricle. *Cardiol Young*. 2004;18(Suppl 3):39–51.
12. Wilkinson JL. Double outlet ventricle. In: Anderson RH, Baker EJ, Macartney FJ, Rigby ML, Shinebourne EA, Tynan M, editors. *Paediatric cardiology*. 2nd ed. London: Churchill Livingstone; 2002. p. 1353–81.
13. Lev M, Bharati S, Meng CC, Liberthson RR, Paul MH, Idriss F. A concept of double-outlet right ventricle. *J Thorac Cardiovasc Surg*. 1972;64:271–81.
14. Jonas R. Double outlet right ventricle. In: Jonas RA, Dinardo J, Laussen PC, Howe R, LaPierre R, Matte G, editors. *Comprehensive surgical management of congenital heart disease*. London: Arnold Publishers; 2004. p. 413–28.
15. Yoo SJ, Hussein N, Peel B, Coles J, van Arsdell GS, Honjo O, Haller C, Lam CZ, Seed M, Barron D. 3D Modeling and printing in congenital heart surgery: entering the stage of maturation. *Front Pediatr*. 2021;9:621672.
16. Lurz P, Puranik R, Nordmeyer J, Muthurangu V, Hansen MS, Schievano S, Marek J, Bonhoeffer P, Taylor AM. Improvement in left ventricular filling properties after relief of right ventricle to pulmonary artery conduit obstruction: contribution of septal motion and interventricular mechanical delay. *Eur Heart J*. 2009;30:2266–74.
17. Uemura H, Yagihar T, Kawashima Y, Nishigaki K, Kamiya T, Ho SY, Anderson RH. Coronary arterial anatomy in double-outlet right ventricle with subpulmonary VSD. *Ann Thorac Surg*. 1995;59:591–7.
18. Takeuchi K, McGowan F, Moran AM, Zurakowski D, Mayer JE, Jonas RA, del Nido PJ. Surgical outcome of double-outlet right ventricle with subpulmonary VSD. *Ann Thorac Surg*. 2001;71:49–53.



19. Brown JW, Ruzmetov M, Okada Y, Jiay P, Turrentine MW. Surgical results in patients with double outlet right ventricle: a 20-year experience. *Ann Thorac Surg.* 2001;72:1630–5.
20. Bengel FM, Hauser M, Duvernoy CS, Kuehn A, Ziegler SI, Stollfuss JC, Beckmann M, Sauer U, Muzik O, Schwaiger M, Hess J. Myocardial blood flow and coronary flow reserve late after anatomical correction of transposition of the great arteries. *J Am Coll Cardiol.* 1998;32(7):1955–61.
21. Gagliardi MG, Adorisio R, Crea F, Versacci P, Di Donato R, Sanders SP. Abnormal vasomotor function of the epicardial coronary arteries in children five to eight years after arterial switch operation. *J Am Coll Cardiol.* 2005;46(8):1565–72.
22. Lacour-Gayet F, Haun C, Ntalakoura K, Belli E, Houyet L, Marcsek P, Wagner F, Weil J. Biventricular repair of double outlet right ventricle with non-committed ventricular septal defect (VSD) by VSD rerouting to the pulmonary artery and arterial switch. *Eur J Cardiothorac Surg.* 2002;21:1042–8.
23. Belli E, Serraf A, Lacour-Gayet F, Hubler F, Zoghby J, Houyel L, Planche C. Double-outlet right ventricle with non-committed ventricular septal defect. *Eur J Cardiothorac Surg.* 1999;15:747–52.
24. Artrip JH, Sauer H, Campbell DN, Mitchell MB, Haun C, Almodovar MC, Hraska V, Lacour-Gayet F. Biventricular repair in double outlet right ventricle: surgical results based on the STS-EACTS international nomenclature classification. *Eur J Cardiothorac Surg.* 2006;29:545–50.
25. Rychik J, Jacobs ML, Norwood WI. Early changes in ventricular geometry and ventricular septal defect size following Rastelli operation or intraventricular baffle repair for conotruncal anomaly. A cause for development of subaortic stenosis. *Circulation.* 1994;90(5 Pt 2):II13–9.
26. Telagh R, Alex-Mekishvili V, Hetzer R, Lange PE, Berger F, Abdul-Khalik H. Initial clinical manifestations and mid-long-term results after surgical repair of double-chambered right ventricle in children and adults. *Cardiol Young.* 2008;18:268–74.
27. Alva C, Ho SY, Lincoln CR, Rigby ML, Wright A, Anderson RH. The nature of the obstructive muscular bundles in double-chambered right ventricle. *J Thorac Cardiovasc Surg.* 1999;117:1180–9.
28. Hoffman P, Wojcik AW, Rozanski J, Siudalska H, Jakubowska E, Wlodarska EK, Kowalski M. The role of echocardiography in diagnosing double chambered right ventricle in adults. *Heart.* 2004;90:789–93.
29. Kilner PJ, Sievers B, Meyer GP, Ho SY. Double-chambered right ventricle or sub-indundibular stenosis assessed by cardiovascular magnetic resonance. *J Cardiovasc Magn Reson.* 2002;4:373–9.
30. Hachiro Y, Takagi N, Koyanagi T, Morikawa M, Abe T. Repair of double-chambered right ventricle: surgical results and long-term follow-up. *Ann Thorac Surg.* 2001;72:1520–2.
31. Fricker FJ, Zuberbuhler JR. Pulmonary atresia with intact ventricular septum. In: Anderson RH, Baker EJ, Macartney FJ, Rigby ML, Shinebourne EA, Tynan M, editors. *Paediatric cardiology.* 2nd ed. London: Churchill Livingstone; 2002. p. 1177–89.
32. Bull C, de Leval MR, Mercanti C, Macartney FJ, Anderson RH. Pulmonary atresia and intact ventricular septum: a revised classification. *Circulation.* 1982;66(2):266–72.
33. Shinebourne EA, Rigby ML, Carvalho JS. Pulmonary atresia with intact ventricular septum: from fetus to adult. *Heart.* 2008;84:1350–7.
34. Dyamenahalli U, McCrindle BW, McDonald C, Trivedi KR, Smallhorn JF, Benson LN, Coles J, Williams WC, Freedom RM. Pulmonary atresia with intact ventricular septum: management of, and outcomes for, a cohort of 210 consecutive patients. *Cardiol Young.* 2004;14:299–308.
35. Kutsche LM, Van Mierop LHS. Pulmonary atresia with and without ventricular septal defect: a different etiology and pathogenesis for the atresia in the 2 types? *Am J Cardiol.* 1983;51:932–5.
36. Daubeney P, Delany DJ, Anderson RH, Sandor GG, Slavik Z, Keeton BR, Webber SA. Pulmonary atresia with intact ventricular septum: range of morphology in a population based study. *J Am Coll Cardiol.* 2002;39:1670–9.
37. Freedom RM, Nykanen DG. Pulmonary atresia and intact ventricular septum. In: Adams F, Allen M, Moss A, editors. *Moss and Adams' heart disease in infants, children, and adolescents: including the fetus and young adult.* 6th ed. Philadelphia, PA: Lippincott Williams and Wilkins; 2001. p. 845–79.
38. Ashburn DA, Blackstone EH, Wells WJ, Jonas RA, Pigula FA, Manning PB, Lofland GK, Williams WG, McCrindle BW. Determinants of mortality and type of repair in neonates with pulmonary atresia and intact ventricular septum. *J Thorac Cardiovasc Surg.* 2004;127(4):1000–8.
39. Yoshimura N, Yamaguchi M, Ohashi H, Oshima Y, Oka S, Yoshida M, Murakami H, Tei T. Pulmonary atresia with intact ventricular septum: strategy based on right ventricular morphology. *J Thorac Cardiovasc Surg.* 2003;126(5):1417–26.
40. Hannan RL, Zabinsky JA, Eng M, Stanfill RM, Ventura RA, Rossi AF, Nykanen DG, Zahn EM, Burker RP. Midterm results for collaborative treatment of pulmonary atresia with intact ventricular septum. *Ann Thorac Surg.* 2009;87:1227–33.
41. Bull C, Kostelka M, Sorensen K, de Leval M. Outcome measures for the neonatal management of pulmonary atresia with intact ventricular septum. *J Thorac Cardiovasc Surg.* 1994;107:359–66.
42. Liang XC, Lam WWM, Cheung EWY, Wong SJ, Cheung YF. Restrictive right ventricular physiology and right ventricular fibrosis as assessed by cardiac magnetic resonance and exercise capacity after biventricular repair of pulmonary atresia and intact ventricular septum. *Clin Cardiol.* 2010;33(2):104–10.
43. Grosse-Wortmann L, Al-Otay A, Yoo SJ. Aortopulmonary collaterals after bidirectional cavopulmonary connection or Fontan completion: quantification with MRI. *Circ Cardiovasc Imaging.* 2009;2:219–25.
44. Whitehead K, Gillespie MJ, Harris MA, Fogel MA, Rome JJ. Non-invasive quantification of systemic-to-pulmonary collateral flow: a major source of inefficiency in patients with superior cavopulmonary connections. *Circ Cardiovasc Imaging.* 2009;2:405–11.
45. Simonneau G, Montani D, Celermajer DS, Denton CP, Gatzoulis MA, Krowka M, Williams PG, Souza R. Haemodynamic definitions and updated clinical classification of pulmonary hypertension. *Eur Respir J.* 2019;53(1):1801913.
46. Simonneau G, Robbins IM, Beghetti M, Channick RN, Delcroix M, Denton CP, Elliott G, Gaine SP, Gladwin MT, Jing ZC, Korwka MJ, Langlenben D, Nakanishi N, Souza R. Updated clinical classification of pulmonary hypertension. *J Am Coll Cardiol.* 2009;54:s43–54.
47. Hopkins WE, Ochoa LL, Richardson GW, Trulock EP. Comparison of the hemodynamics and survival of adults with severe primary pulmonary hypertension or Eisenmenger syndrome. *J Heart Lung Transplant.* 1996;15:100–5.
48. Galie N, Manes A, Negro L, Palazzini M, Bacchi-Reggiani ML, Branzi A. A meta-analysis of randomized controlled trials in pulmonary arterial hypertension. *Eur Heart J.* 2009;30:394–403.
49. Fratz S, Chung T, Greil GF, Samyn MM, Taylor AM, Valsangiacomo Buechel ER, Yoo SJ, Powell AJ. Guidelines and protocols for cardiovascular magnetic resonance in children and adults with congenital heart disease: SCMR expert consensus group on congenital heart disease. *J Cardiovasc Magn Reson.* 2013;15(1):51.
50. Latus H, Meierhofer C. Role of cardiovascular magnetic resonance in pediatric pulmonary hypertension-novel concepts and imaging biomarkers. *Cardiovasc Diagn Ther.* 2021;11(4):1057–69.
51. Lechartier B, Chaouat A, Aubert JD, Schwitzer J, Swiss Society for Pulmonary Hypertension (SSPH). Magnetic resonance imaging in pulmonary hypertension: an overview of current applications and future perspectives. *Swiss Med Wkly.* 2022;152:w30055.

52. Moledina S, Pandya B, Bartsota M, Mortensen KH, McMillan M, Quyam S, Taylor AM, Haworth SG, Schulze-Neick I, Muthurangu V. Prognostic significance of cardiac magnetic resonance imaging in children with pulmonary hypertension. *Circ Cardiovasc Imaging*. 2013;6(3):407–14.
53. Van Wolferen SA, Marcus JT, Boonstra A, Marques KMJ, Bronzwaer JGF, Spreeuwenberg MD, Postmus PE, Vonk-Noordegraaf A. Prognostic value of right ventricular mass, volume and function in idiopathic pulmonary arterial hypertension. *Eur Heart J*. 2007;28:1250–7.
54. Alabed S, Shahin Y, Garg P, Alandejani F, Johns CS, Lewis RA, Condliffe R, Wild JM, Kiely DG, Swift AJ. Cardiac-MRI predicts clinical worsening and mortality in pulmonary arterial hypertension: a systematic review and meta-analysis. *JACC Cardiovasc Imaging*. 2021;14(5):931–42. <https://doi.org/10.1016/j.jcmg.2020.08.013>. Epub 2020 Sep 30. Erratum in: *JACC Cardiovasc Imaging*. 2021 Apr;14(4):884.
55. Swift AJ, Rajaram S, Condliffe R, Capener D, Hurdman J, Elliot CA, Wild JM, Kiely DG. Diagnostic accuracy of cardiovascular magnetic resonance imaging of right ventricular morphology and function in the assessment of suspected pulmonary hypertension results from the ASPIRE registry. *J Cardiovasc Magn Reson*. 2012;14(1):40.
56. Creuzé N, Hoette S, Montani D, Günther S, Lau E, Ternacle J, Savale L, Jaïs X, Parent F, Girerd B, Sitbon O, Simonneau G, Rochitte CE, Souza R, Humbert M, Chemla D. Usefulness of cardiovascular magnetic resonance indices to rule in or rule out precapillary pulmonary hypertension. *Can J Cardiol*. 2015;31(12):1469–76.
57. Boerritger B, Mauritz GJ, Marcus JT, Helderma F, Postmus PE, Westerhof N, Vonk-Noordegraaf A. Progressive dilatation of the main pulmonary artery is a characteristic of pulmonary arterial hypertension and is not related to changes in pressure. *Chest*. 2010;138:1395–401.
58. Aggarwal M, Grady RM, Choudhry S, Anwar S, Egtesady P, Singh GK. Potts shunt improves right ventricular function and coupling with pulmonary circulation in children with suprasystemic pulmonary arterial hypertension. *Circ Cardiovasc Imaging*. 2018;11(12):e007964.
59. Remy-Jardin M, Ryerson CJ, Schiebler ML, Leung ANC, Wild JM, Hoeper MM, Alderson PO, Goodman LR, Mayo J, Haramati LB, Ohno Y, Thistlethwaite P, van Beek EJR, Knight SL, Lynch DA, Rubin GD, Humbert M. Imaging of pulmonary hypertension in adults: a position paper from the Fleischner society. *Radiology*. 2021;298(3):531–49.
60. Ascha M, Renapurkar RD, Tonelli AR. A review of imaging modalities in pulmonary hypertension. *Ann Thorac Med*. 2017;12(2):61–73.
61. Dambrauskaitė V, Delcroix M, Claus P, Herbots L, D'hooge J, Bijmens B, Rademakers F, Sutherland GR. Regional right ventricular dysfunction in chronic pulmonary hypertension. *J Am Soc Echocardiogr*. 2007;20(10):1172–80.
62. de Siqueira ME, Pozo E, Fernandes VR, Sengupta PP, Modesto K, Gupta SS, Barbeito-Caamaño C, Narula J, Fuster V, Caixeta A, Sanz J. Characterization and clinical significance of right ventricular mechanics in pulmonary hypertension evaluated with cardiovascular magnetic resonance feature tracking. *J Cardiovasc Magn Reson*. 2016;18(1):39.
63. Dhingra VK, Fenwick JC, Walley KR, Chittock DR, Ronco JJ. Lack of agreement between thermodilution and Fick cardiac output in critically ill patients. *Chest*. 2002;122:990–7.
64. Van Grondelle A, Ditchey RV, Groves BM, Wagner WW, Reeves JT. Thermodilution method overestimates low cardiac output in humans. *Am J Physiol*. 1983;245(4):H690–2.
65. Muthurangu V, Taylor A, Andriantsimivona R, Hegde S, Miquel ME, Tulloh R, Baker E, Hill DLG, Razavi RS. Novel method of quantifying pulmonary vascular resistance by use of simultaneous invasive pressure monitoring and phase-contrast magnetic resonance flow. *Circulation*. 2004;110:826–34.
66. Muthurangu V, Lurz P, Critchely JD, Deanfield JE, Taylor AM, Hansen M. Real-time assessment of right and left ventricular volumes and function in patients with congenital heart disease by using high spatiotemporal resolution radial k-t SENSE. *Radiology*. 2008;248(3):782–91.



# Pulmonary Hypertension

# 8

Daniel Knight and Vivek Muthurangu

## 8.1 Introduction

Pulmonary hypertension (PH) is a rare condition of elevated blood pressure in the pulmonary arteries. A diagnosis of PH is associated with a sevenfold increase in mortality, irrespective of aetiology [1]. There are numerous potential causes of PH which share similarities with respect to symptoms but not their prognoses and treatments. Whilst the abnormalities in pulmonary arterial haemodynamics are diagnostic and of modest prognostic significance, the impact on right ventricular function is ultimately the principal determinant of outcome [2]. Thus, a comprehensive assessment of the right ventricle (RV) and the pulmonary vasculature is fundamental in the management of PH. Echocardiography is a first-line screening tool for PH and also provides useful information about right heart size and function. However, the complex geometries and position in the thorax of the RV and pulmonary circulation confer difficulties for cardiac ultrasound. Cross-sectional imaging techniques overcome these limitations, with cardiovascular magnetic resonance (CMR) imaging being particularly well-placed for the assessment of patients with PH. Furthermore, the ability to acquire three-dimensional datasets is particularly advantageous for the investigation of patients with PH due to congenital heart disease (CHD). Accordingly, CMR has become an important tool for both clinical and research purposes in PH. The aim of this chapter is to provide an overview of how contemporary CMR imaging can be used to assess PH.

---

D. Knight (✉)  
Royal Free London NHS Foundation Trust, London, UK  
e-mail: [dan.knight@nhs.net](mailto:dan.knight@nhs.net)

V. Muthurangu  
University College London, London, UK  
e-mail: [v.muthurangu@ucl.ac.uk](mailto:v.muthurangu@ucl.ac.uk)

## 8.2 Definition and Clinical Classification

Pulmonary hypertension is defined haemodynamically as a mean resting pulmonary artery pressure (mPAP) of greater than 20 mmHg [3]. However, abnormally raised mPAP alone is insufficient to identify pulmonary vascular disease as other causes of mPAP >20 mmHg include elevated pulmonary arterial wedge pressure (PAWP) or high cardiac output (CO) states. Therefore, both PAWP and CO are mandatorily measured on right heart catheterization (RHC) studies, enabling the calculation of pulmonary vascular resistance (PVR) and the distinction between pre-capillary PH, isolated post-capillary PH (IpcPH) and combined pre- and post-capillary PH (CpcPH) (Table 8.1).

Pathologically, pre-capillary PH (also called pulmonary arterial hypertension, PAH) is a disease of the vasculature with widespread pulmonary arterial remodelling characterized by excessive intimal proliferation, progressive distal pulmonary arterial luminal narrowing, occlusion, and pruning, the consequence of which is elevated PVR. Hence, for a given amount of pulmonary arterial blood flow, a progressive increase in PVR causes increased mean pulmonary arterial pressure. Concomitantly, the central pulmonary arteries become stiff and dilated causing an increase in systolic PA pressure. This increased right ventricular afterload is accompanied by RV structural remodelling, including hypertrophy and dilatation with consequent RV dysfunction.

Clinically, PH is categorized into five groups based upon underlying aetiology [3]. These groups are (1) pulmonary arterial hypertension (PAH); (2) PH associated with left heart disease; (3) PH associated with lung diseases and/or hypoxia; (4) PH associated with pulmonary artery obstructions (including chronic thromboembolic PH (CTEPH) and other pulmonary artery obstructions); and (5) PH with unclear and/or multifactorial mechanisms. Pulmonary arterial hypertension associated with congenital heart disease (PAH-CHD) is classified in group 1 and has several clinical subtypes, including PAH with congenital systemic-to-

**Table 8.1** Haemodynamic definitions of PH

Definitions	Characteristics	Clinical groups <sup>a</sup>
Pre-capillary PH	mPAP >20 mmHg PAWP ≤15 mmHg PVR >2 WU	1, 3, 4 and 5
Isolated post-capillary PH (IpcPH)	mPAP >20 mmHg PAWP >15 mmHg PVR ≤2 WU	2 and 5
Combined pre- and post-capillary PH (CpcPH)	mPAP >20 mmHg PAWP >15 mmHg PVR >2 WU	2 and 5

Adapted from [3] and [4]

mPAP mean pulmonary arterial pressure, PAWP pulmonary arterial wedge pressure, PVR pulmonary vascular resistance, WU wood units

<sup>a</sup>group 1, pulmonary arterial hypertension (PAH); group 2, PH associated with left heart disease; group 3, PH associated with lung diseases and/or hypoxia; group 4, PH associated with pulmonary artery obstructions; group 5, PH with unclear and/or multifactorial mechanisms

pulmonary shunts; Eisenmenger syndrome; repaired defects; and PAH with small or coincidental defects [5]. Whilst pulmonary vascular disease is encountered in patients with Fontan circulation, elevated mPAP is most frequently post-capillary in origin. Furthermore, PH due to CHD can arise in other WHO groups. For example, group 2 PH can result from congenital mitral stenosis or cor triatriatum and group 4 PH due to congenital pulmonary artery stenosis. Segmental PH, whereby abnormally elevated pressures are found only in discrete areas of the pulmonary vasculature perfused by aorto-pulmonary collaterals, can be found in cases of complex CHD such as pulmonary or tricuspid atresia [6].

### 8.3 Epidemiology

The overall prevalence of PH is estimated at approximately 1% of the global population and increases with age up to 10% of individuals aged over 65 years [7]. Groups 2 and 3 are the commonest and second commonest clinical PH subtypes with 1-year mortalities of 41% and 46%, respectively [1]. Pulmonary arterial hypertension (group 1 PH) is a relatively rare disorder with an estimated prevalence of 10 to 52 cases per million [8]. It should be noted, however, that these estimates of incidence and prevalence of PH are based upon the previous long-standing haemodynamic definition of resting mPAP ≥25 mmHg [9].

Registry data of patients with PAH suggest the proportion of PAH due to CHD ranges from 10% to 20% [8]. The global prevalence of PAH-CHD has previously been estimated to be about 25 people per million in the entire adult population [7]. However, a contemporary nationwide cross-sectional registry study estimated the prevalence of PAH in patients with CHD at 3.2%, resulting in an estimated prevalence of PAH-

CHD of approximately 100 per million in the general population [10]. Patients with PAH-CHD have a more favourable prognosis than those with idiopathic PAH [11]. Nevertheless, patients with PAH-CHD are more symptomatic and have at least double the risk of mortality than CHD patients without PAH [12, 13].

### 8.4 Symptoms and Signs

The clinical presentation of PH relates to underlying RV dysfunction and, in the initial stages, tends to be related to exertion. Dyspnoea is the commonest symptom, with fatigue and exercise intolerance, pre-syncope, syncope, and angina also being manifest. Given the non-specific nature of symptoms coupled with the relative rarity of PH, late diagnosis is not uncommon with patients having previously consulted a number of healthcare professionals prior to a final diagnosis being established. Chest pain may manifest with mechanisms including RV ischaemia [14], left main stem compression [15], or co-morbid coronary artery disease. Ankle oedema and abdominal distension due to ascites reflect decompensated right heart failure. More rarely, mechanical complications of severe pulmonary arterial dilatation include hoarse voice resulting from left recurrent laryngeal nerve compression and wheeze secondary to large airways compression. Haemoptysis can result from rupture of engorged hypertrophied bronchial arteries that form systemic to pulmonary collateral vessels.

Clinical examination findings of raised RV afterload include a left parasternal heave and a loud pulmonary component of the second heart sound. Elevated jugular venous pressure (JVP) reflects right atrial pressure. Murmurs of tricuspid regurgitation and pulmonary regurgitation may be present. Peripheral oedema, ascites, and hepatomegaly are suggestive of RV decompensation. Signs of underlying PH aetiology should also be sought, for example: clinical stigmata of systemic sclerosis including telangiectasia, sclerodactyly, digital ulceration, calcinosis, and Raynaud's phenomenon; fine inspiratory crackles could suggest the presence of interstitial lung disease; features of chronic liver disease such as jaundice, spider naevi and palmar erythema; and finger clubbing, which has a differential diagnosis that includes cyanotic congenital heart disease, pulmonary veno-occlusive disease, interstitial lung disease, chronic lung infections and liver cirrhosis.

### 8.5 Treatment Strategies

Targeted PAH therapies work by lowering pulmonary pressures and target three separate pathways. The nitric oxide pathway may be targeted by phosphodiesterase type 5 inhibi-



tors (PDE-5i, such as sildenafil and tadalafil) or soluble guanylate cyclase (sGC) stimulators (such as riociguat). The endothelin pathway is targeted by endothelin receptor antagonists (ERA) that include bosentan, ambrisentan and macitentan. The prostacyclin pathway can be targeted with oral selective prostacyclin IP receptor agonists (selexipag) or prostacyclin analogues (epoprostenol, iloprost and treprostinil) which have modes of administration including intravenous, inhaled and subcutaneous. Epoprostenol is the only treatment shown to reduce mortality in idiopathic PAH in a single randomized controlled trial [16]. These separate pathways are synergistic and should be concomitantly targeted in a manner analogous to the treatment strategies in systemic hypertension and heart failure. This approach is supported by the AMBITION trial, which showed that initial combination therapy with tadalafil and ambrisentan resulted in a significantly lower risk of clinical-failure events than monotherapy in treatment-naïve PAH patients [17]. Calcium channel blockers are reserved for the small proportion of idiopathic PAH patients with a favourable response to acute vasodilator testing.

The successful management of PAH-CHD requires a multidisciplinary team input in specialist centres. Patients with Eisenmenger syndrome and likely also other PAH-CHD benefit from advanced PAH therapies [18]. A comprehensive review of targeted therapies in PAH-CHD is beyond the scope of this text and is summarized in relevant published guidelines [5]. There is insufficient evidence to support the use of PAH therapies in groups 2 or 3 PH, with treatment in these groups aimed at the underlying cause. Furthermore, little evidence exists for targeted PH therapy in group 5 PH. Suitable patients with chronic thromboembolic PH and appropriate distribution and burden of disease may benefit from interventions such as pulmonary endarterectomy or balloon pulmonary angioplasty.

## 8.6 Role of CMR in PH

The key aspects of PH management include making the diagnosis, establishing the underlying cause, risk stratification for the evaluation of disease severity, monitoring disease progression and assessing response to treatment. The well-established roles of CMR in each of these facets of PH management will be reviewed in this chapter. This will be divided into relevant components of a CMR study in PH (Table 8.2), starting with the most important aspect of CMR assessment of ventricular function and remodelling followed by CMR measures of RV afterload and vascular physiology. The role of CMR in shunt assessment will be reviewed and, finally, novel CMR techniques that provide new non-invasive insights into PH.

**Table 8.2** CMR imaging protocol in patients with PH

<b>Core protocol (excluding localizer and scout images)</b>
<i>Single-plane cine images</i>
– Four-chamber
– RV long-axis
– LV long-axis
<i>Volumetric assessment: with a minimum temporal resolution of 40 ms</i>
– Short-axis (with 7–10 mm spacing between slices, depending upon adult or paediatric patients)
– Transaxial (with 5–8 mm spacing between slices, depending upon adult or paediatric patients)
<i>Phase-contrast MR imaging</i>
– Ascending aorta
– Main and branch pulmonary arteries
<i>Additional protocol (depending upon clinical indication(s) and incident versus follow-up studies)</i>
– MR angiography and perfusion
– Myocardial tissue characterization (especially in adults and in patients with connective tissue disease-associated PH and/or previous acquired left-sided heart disease)

### 8.6.1 Ventricular Function and Remodelling

#### 8.6.1.1 Volumetric Assessment

Cardiovascular magnetic resonance is the reference standard technique for quantification of cardiac chamber size and function in terms of both accuracy and reproducibility [19]. An abundance of studies have shown that CMR-derived metrics of RV function and biventricular cavity size are prognostic in both adults and children with PH [20–22]. Additionally, a meta-analysis of CMR studies has shown that volumetric indices of RV size and function predict clinical worsening as well as mortality, an important composite endpoint in PAH clinical trials [23]. Conventionally, the left ventricular (LV) stack of cine images on CMR is acquired in the LV short-axis imaging plane. Conversely, a transaxial stack of cine images offers improved reproducibility for RV volumetric analysis [24, 25]. This is likely due to the removal of through-plane longitudinal motion (which confers difficulty in delineating RV cavity volumes especially in the basal short-axis cine slices) and easier identification of the tricuspid and pulmonary valves. For these reasons, a transaxial stack of cine images is recommended for dedicated RV volumetric analysis [26].

The importance of CMR-derived volumetric parameters in both risk stratification and monitoring the response to targeted PAH treatment has become increasingly recognized. Indexed RV end-systolic volume (ESVi) adjusted for age and sex, for example, improves risk stratification for 1-year mortality when used in conjunction with either the Registry to Evaluate Early And Long-term PAH disease management (REVEAL) 2.0 risk score calculator or a modified French Pulmonary Hypertension Registry (FPHR) approach [27]. Additionally, risk assessment of patients

with idiopathic PAH at 1-year follow-up based upon CMR-derived metrics has been shown to be at least equal to that based upon invasive RHC assessment [28]. Changes in CMR-derived RV ejection fraction (RVEF) with targeted PAH therapy but not PVR have been shown to be associated with survival in patients with PH [29]. Furthermore, deterioration of RV function can still occur after targeted PAH therapy despite reduction in PVR. A change in stroke volume (SV) of 10 mL measured on CMR has been demonstrated to be clinically relevant in patients with PH [30]. This is advantageous as a non-invasive tool for serial patient follow-up and has subsequently been utilized as a primary endpoint in the Right vEntricular remodelling in Pulmonary Arterial hypertension (REPAIR) study [31]. This multi-centre trial evaluated the effects of macitentan, an endothelin receptor antagonist, on RV and haemodynamic outcomes in patients with PAH. This growing body of evidence supporting the role of CMR in the management of patients with PAH has culminated in the inclusion of CMR-derived RVEF, indexed SV and RV ESVi in the comprehensive PAH risk assessment tool in the 2022 European Society of Cardiology (ESC) and European Respiratory Society (ERS) PH guidelines [3].

### 8.6.1.2 Deformation Imaging

Strain (the fractional change in the length of a myocardial segment) and strain rate (the rate of deformation over time) are markers of biventricular myocardial deformation and

enable assessment of wall motion in three directions, namely, longitudinal, circumferential and radial. Feature tracking applied to conventionally acquired cine images is a commercially available approach to strain analysis by CMR, analogous to speckle-tracking software applied to echocardiography images and with similar findings (Fig. 8.1). Impairment in strain can detect ventricular dysfunction before changes in global ejection fraction, with evidence of abnormal resting and exercise RV longitudinal strain despite normal RVEF in patients with PAH [32]. Peak global circumferential RV strain rate has also been shown to be impaired in patients with PH and preserved RVEF, with RV global longitudinal strain, global longitudinal strain rate and global circumferential strain rate all independently predictive of outcome [33].

Beyond RV assessment, abnormalities in LV myocardial mechanics in patients with PH and preserved LVEF have also been shown by feature tracking and tissue phase mapping techniques [34–36]. These changes could reflect the importance of ventricular interdependence as well as LV cardiomyocyte atrophy and contractile dysfunction as potential pathophysiological mechanisms of LV dysfunction in PH [37, 38]. Deformation analysis also allows a deeper insight into right atrial function, which is itself not conventionally measured clinically. Indeed, right atrial (RA) dysfunction as evidenced by impaired right atrial strain is associated with decompensated haemodynamics and RV function in PH [39, 40].

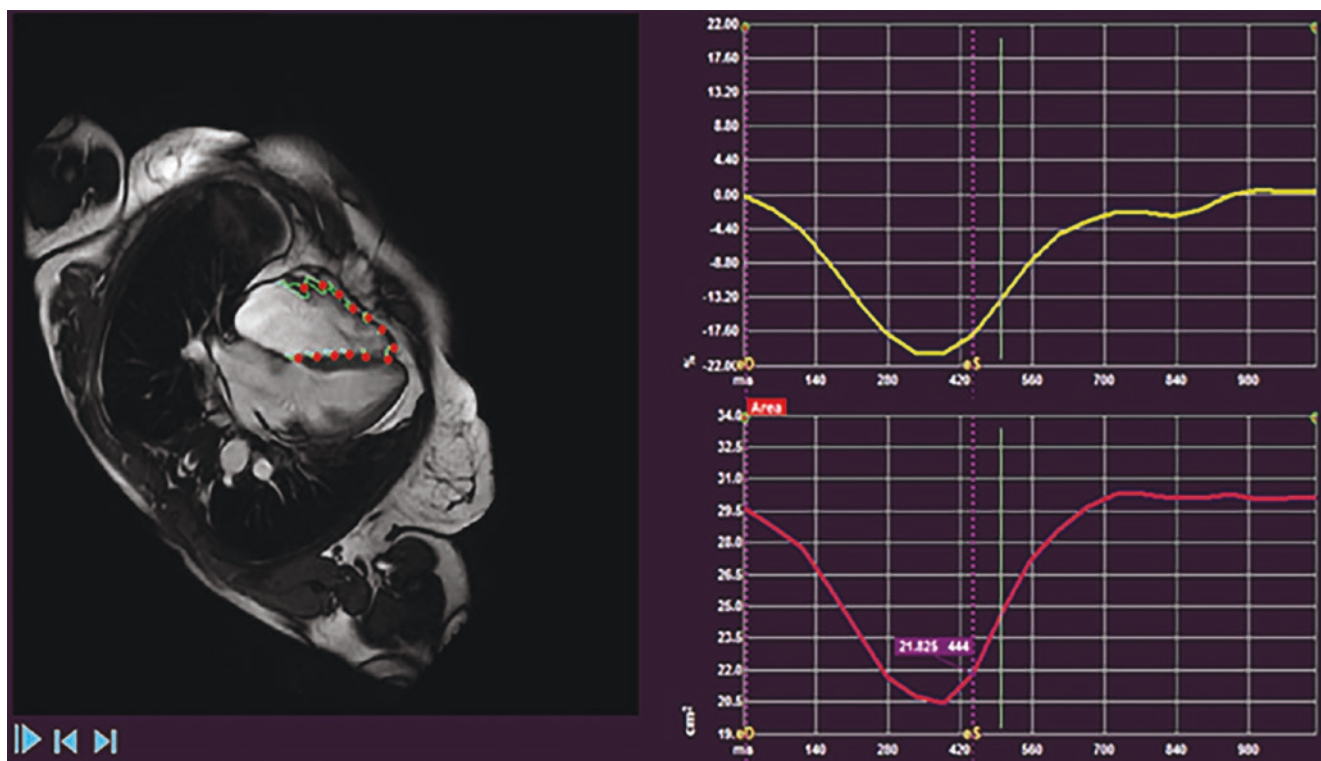


**Fig. 8.1** Right ventricular strain analysis by CMR feature tracking in a patient with PH. (Reproduced from [80])

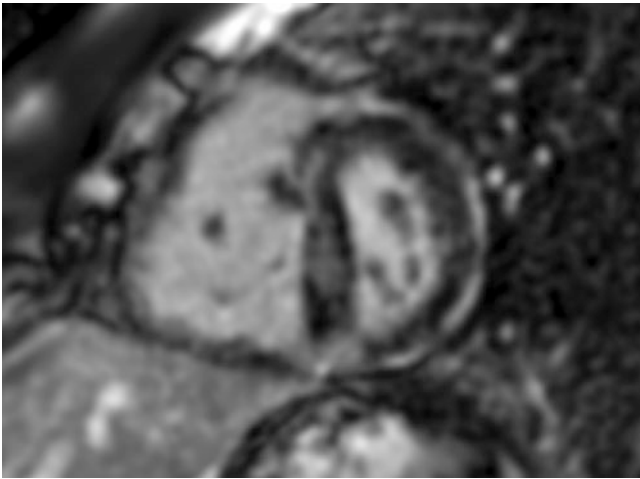


**Fig. 8.2** Prominent inferior RV insertion point and mid-septal mid-wall late gadolinium enhancement in a patient with PH

### 8.6.1.3 Myocardial Tissue Characterization

Late gadolinium enhancement (LGE) is well described in PH at the RV insertion points and the mid-wall of the interventricular septum (Fig. 8.2). Autopsy studies have suggested that these findings may represent exaggerated myocardial disarray and plexiform fibrosis, possibly as a consequence of RV hypertrophy and abnormal interventricular septal dynamics [41]. However, whilst RV insertional LGE is suggestive of the presence of PH and has been shown to predict clinical worsening in this condition, it does not provide additive prognostic information to CMR-derived RVEF [42, 43]. It is also a non-specific finding that is present in other pathologies such as hypertrophic heart muscle disease and so is not diagnostic for PH as an isolated finding.

Non-contrast (native) myocardial T1 mapping and extracellular volume (ECV) quantification have also been studied in PH, albeit their clinical utility is less well-established [44–50]. Perhaps unsurprisingly and akin to the description of insertional LGE in PH, native myocardial T1 is particularly elevated at the RV insertion points and is associated with measures of abnormal interventricular septal dynamics [46, 48]. Whilst RV insertion point T1 correlates with severity of PH, it has not shown prognostic capacity in PH and also does not discriminate between patients with or without PH [44, 48]. Overall, multiparametric myocardial mapping is more challenging in the thin-walled RV. Nevertheless, RV ECV has been described as significantly higher in patients with PH versus patients with LV systolic dysfunction without PH [45]. Furthermore, whilst RV ECV was related to RV dilatation and dysfunction, it was independently associated with clinical diagnosis and thus may describe changes in the RV myocardium beyond conventional CMR-derived functional metrics.

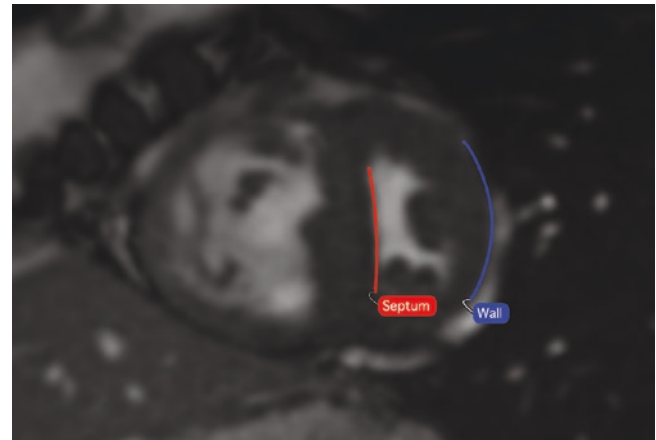


**Fig. 8.3** Abnormal interventricular septal dynamics on a short-axis mid-ventricular cine image in a patient with PH. Note the septum bows towards the left ventricle at end-systole, indicative of raised RV afterload

### 8.6.2 Measures of Afterload and Vascular Physiology

#### 8.6.2.1 Interventricular Septal Configuration

The interventricular septal dynamics are highly revealing of loading conditions of the RV (Fig. 8.3). Many studies have shown significant correlations between CMR measures of interventricular septal curvature and invasively derived mPAP and PVR in both adults and children [51–56]. Furthermore, measures of septal curvature have been shown to track changes in pulmonary haemodynamics during vasodilator testing, providing a potential non-invasive method for assessing response to therapy in PH [54].

Sophisticated CMR analysis has also enabled a more detailed evaluation of the mechanistic basis behind these deleterious interventricular septal dynamics and their impact on cardiac function. Deformation analysis using tagged CMR cine images shows a ‘post-systolic’ RV contractile phase of the RV [57]. This causes relatively higher RV versus LV pressures with consequent leftward bowing and deviation of the interventricular septum during LV isovolumic relaxation period [53, 58]. This discordant pattern of biventricular contraction and relaxation gives rise to ventricular interdependence, manifesting as impaired LV filling in early diastole and ultimately reducing LV stroke volume. This may be a reason underlying why CMR indices of LV early diastolic function are so important with respect to functional capacity and clinical worsening in patients with PH [36].

#### 8.6.2.2 Pulmonary Arterial Geometry

The pulmonary arterial tree is characterized by its low pressure and low resistance as well as a high degree of distensibility. The relative area change of the pulmonary artery (PA) represents its elasticity, is inversely proportional to stiffness

and is simple to measure at CMR, reflecting the advantages of CMR as a non-invasive, dynamic, cross-sectional imaging modality. Relative area change is calculated as the percentage increase in PA area during the cardiac cycle. There is a curvilinear relationship between mPAP and PA relative area change, reflecting hysteresis of vessel biomechanics. Irrespective of this non-linear relationship, the stiffness of the proximal pulmonary arterial tree is associated with more severe PH and is an independent predictor of outcome in PAH [21, 59, 60]. It should also be noted that changes in stiffness as PH progresses are associated with vessel remodelling. However, there are currently no specific reference ranges or diagnostic clinical thresholds for relative area change in PH.

### 8.6.2.3 Magnetic Resonance Angiography and Perfusion

The demonstration of pulmonary arterial thromboembolic changes or mismatched pulmonary perfusion defects coupled with elevated pulmonary arterial pressures is required in order to diagnose chronic thromboembolic PH (CTEPH). Conventionally, non-invasive imaging of the pulmonary vasculature is performed using computed tomography pulmonary angiograms (CTPA) and nuclear ventilation/perfusion (V/Q) scans. Alternatively, anatomical assessment of the proximal pulmonary arterial tree can be provided by magnetic resonance angiography (MRA), and MRI can also be used to visualize pulmonary parenchymal perfusion (Fig. 8.4). The advantages of MRI include the absence of ionizing radiation that is encountered with CTPA and V/Q scans along with providing an alternative modality for

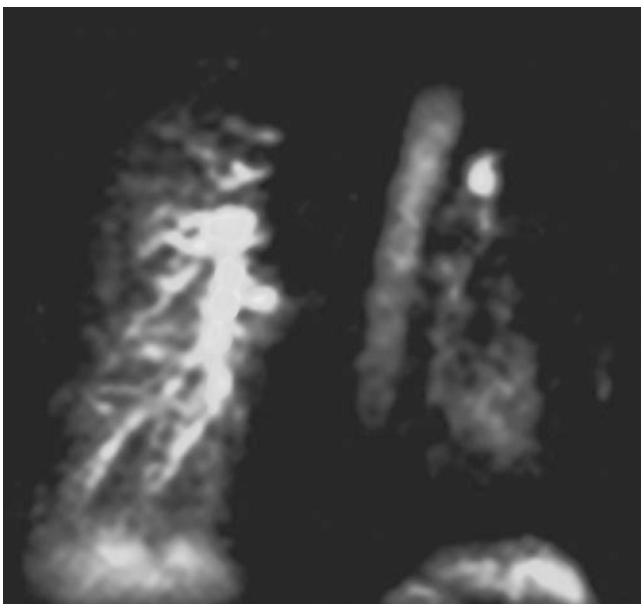


**Fig. 8.4** Magnetic resonance pulmonary perfusion in a patient with chronic thromboembolic PH. Note the lack of perfusion in the majority of the left lung

patients who cannot receive the iodinated contrast agents required for CTPA. However, a particular limitation to be considered of both MRA and MRI-based perfusion imaging is the long breath-hold times which are particularly challenging for breathless patients.

The V/Q scan still remains the preferred imaging test for CTEPH screening, with a normal study effectively excluding the condition [61]. Nevertheless, retrospective studies of three-dimensional dynamic contrast-enhanced lung perfusion MRI have shown promise for diagnosing CTEPH, with a similar sensitivity when compared with planar V/Q scans and a higher sensitivity when compared with single photon emission computed tomography (SPECT) scans [62, 63]. The results of ongoing prospective studies of dynamic contrast-enhanced MRI-derived pulmonary perfusion to fully assess their diagnostic performance in clinical practice are awaited to determine the place of this technique in the diagnostic pathway of CTEPH [64]. Contrast-enhanced MRA has shown promise in imaging the proximal pulmonary arteries, but CTPA remains the non-invasive test of choice [65, 66].

## 8.6.3 Quantitative Shunt Assessment

### 8.6.3.1 The Role of Phase-Contrast MR

The quantification of blood flow velocity and volume is an important part of the routine assessment of PH by CMR. Cardiac output is reduced in PH, and abnormal flow characteristics are seen in pulmonary vessels due to the altered mechanical properties of the pulmonary vascular bed. Great vessel flow is quantified by velocity-encoded phase-contrast MRI (PCMR), can be acquired during free-breathing and has been extensively validated. However, swirling rather than laminar or plug flow patterns occurs in dilated pulmonary arteries which can result in inaccuracies in through-plane flow quantification. Therefore, proximal branch PA flows as well as main PA flow should be acquired in PH studies to provide corroborative data. Great vessel flow assessment by PCMR allows the calculation of cardiac output, shunt flow ( $Q_p:Q_s$ ), right and left lung perfusion ratios, collateral flow and aortic and pulmonary valvular regurgitation. Furthermore, biventricular stroke volume assessment by cine imaging combined with great vessel flow evaluation by PCMR permits the quantification of atrioventricular valvular regurgitation.

## 8.6.4 Novel CMR Techniques to Assess PH

### 8.6.4.1 4D Flow and Vortices

Three-dimensional spatial encoding combined with three-directional velocity-encoded PCMR, termed 4D flow, offers



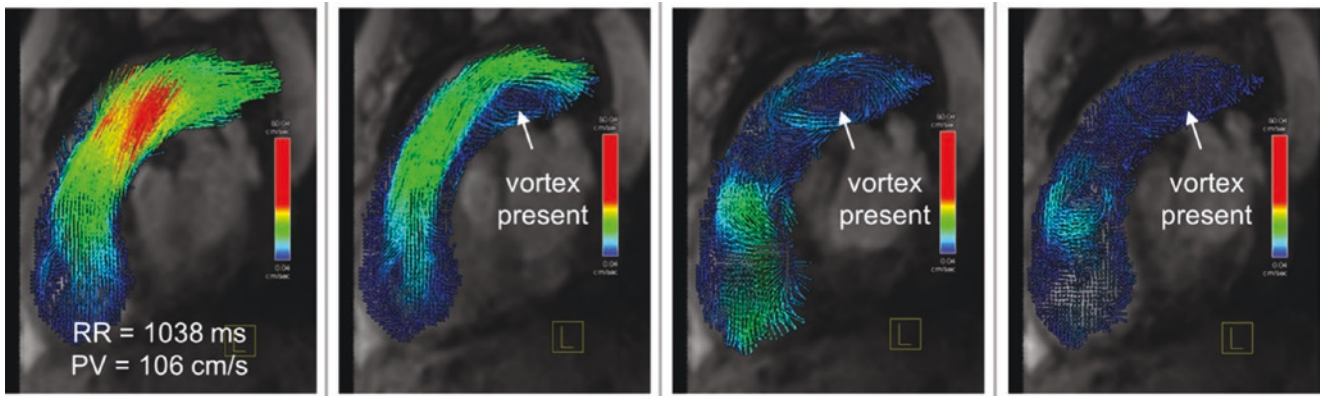


**Fig. 8.5** Velocity colour-encoded three-dimensional vector representation of vortical blood flow along the main pulmonary artery in a patient with known PH (images from left to right correspond to systole through to diastole). (Reproduced from [69])

the abilities to measure and visualize the temporal evolution of complex blood flow patterns, namely, vortices, within an acquired 3D volume. Abnormal flow characteristics are demonstrated in the right heart and pulmonary circulation in patients with PH, with a change in flow from laminar or plug to a helical flow pattern (Fig. 8.5). The duration of abnormal vortical flow in the main PA correlates with mPAP and has been demonstrated as a non-invasive estimate of PA pressure [67–70].

#### 8.6.4.2 Wave Intensity Analysis

Abnormal PA wave reflections contribute to increased RV afterload, the most obvious in clinical practice being the mid-systolic notching of the PA flow velocity waveform. Abnormal wave reflections can be quantified using wave intensity analysis (WIA) [71, 72]. This allows the measurement of the magnitude, timing, direction (forward or backward) and type (compression or expansion waves) of vascular waves. Traditionally, WIA has been limited by the requirement for invasively derived pressure waveforms with simultaneous measurement of flow. Instead, high temporal resolution PCMR-derived flow and area waveforms can be used to non-invasively quantify travelling waves in the pulmonary arteries. For example, CMR-based WIA has demonstrated that the size of the backwards compression wave is increased in PH and discriminates between CTEPH subtypes [73]. Furthermore, CMR-derived WIA indices have been shown to be predictive of functional worsening in children with PAH [74].

#### 8.6.4.3 MR-Augmented Right Heart Catheterization

Whilst a plethora of CMR metrics can be used to indicate the presence of PH or provide surrogates of pulmonary haemodynamics, pressure can only be directly obtained by invasive RHC. However, there are limitations of the measurement of CO by RHC by both thermodilution and Fick methods, such

as the presence of shunts and valvular insufficiency. Alternatively, phase-contrast magnetic resonance (PCMR) provides the reference standard for flow analysis which can be combined with concurrent invasive pressure data [75]. Moreover, CMR has the advantages of freedom from radiation, a pertinent point in children and patients who require repeated procedures, and soft-tissue visualization which is of particular utility in complex anatomy. Therefore, attention has grown in RHC under MRI guidance (MR-RHC).

Combined MR-RHC is not a novel concept but has been relatively slow to clinically adopt, largely due to reliance on expensive infrastructure and relatively long procedure times [75, 76]. More recently, MR-RHC has been performed safely in conventional CMR environments with clinically acceptable procedure times including in patients with PH [77–79]. Combined MR-RHC also has the convenient benefit of acquiring important additional data such as cardiac chamber size and function quantification in a single comprehensive procedure.

## 8.7 Conclusion

Numerous studies confirm the clinical importance and utility of CMR in patients with PH. It is the reference standard imaging modality for the assessment of biventricular volumes and function as well as for the non-invasive quantification of blood flow. This is particularly valuable in PH given that the response of the RV to elevated afterload is of greater prognostic significance than the change in afterload itself. Nevertheless, the clinical evaluation of PH still requires the direct measurement of pulmonary haemodynamics for diagnosis and the assessment of response to PH-targeted therapies. There are many CMR measures that provide estimates of PA pressure but, ultimately, cannot replace the requirement for RHC. However, combining CMR with invasive pressure measurement by RHC has emerged as a clinically

feasible technique. This permits the accurate quantification of pulmonary vascular resistance, provides a comprehensive assessment of PH and affords potential for more novel assessments of afterload such as wave intensity analysis and impedance spectra. It is likely that the role of CMR will continue to grow and evolve in the field of PH, including the increasing use of CMR-derived biomarkers as endpoints in clinical trials of PH therapies.

## References

- Mathai SC, Ryan JJ. The growing burden of pulmonary hypertension in the modern era: a zebra no more? *Circ Cardiovasc Qual Outcomes*. 2018;11(2):e004536.
- Chin KM, Kim NH, Rubin LJ. The right ventricle in pulmonary hypertension. *Coron Artery Dis*. 2005;16(1):13–8.
- Humbert M, Kovacs G, Hoeper MM, Badagliacca R, Berger RMF, Brida M, et al. 2022 ESC/ERS guidelines for the diagnosis and treatment of pulmonary hypertension. *Eur Heart J*. 2022;43(38):3618–731.
- Simonneau G, Montani D, Celermajer DS, Denton CP, Gatzoulis MA, Krowka M, et al. Haemodynamic definitions and updated clinical classification of pulmonary hypertension. *Eur Respir J*. 2019;53(1):1801913.
- Baumgartner H, De Backer J, Babu-Narayan SV, Budts W, Chessa M, Diller GP, et al. 2020 ESC guidelines for the management of adult congenital heart disease. *Eur Heart J*. 2021;42(6):563–645.
- Dimopoulos K, Diller GP, Opatowsky AR, D'Alto M, Gu H, Giannakoulas G, et al. Definition and management of segmental pulmonary hypertension. *J Am Heart Assoc*. 2018;7(14):e008587.
- Hoeper MM, Humbert M, Souza R, Idrees M, Kawut SM, Sliwa-Hahnle K, et al. A global view of pulmonary hypertension. *Lancet Respir Med*. 2016;4(4):306–22.
- Hoeper MM, Simon RGJ. The changing landscape of pulmonary arterial hypertension and implications for patient care. *Eur Respir Rev*. 2014;23(134):450–7.
- Hoeper MM, Bogaard HJ, Condliffe R, Frantz R, Khanna D, Kurzyna M, et al. Definitions and diagnosis of pulmonary hypertension. *J Am Coll Cardiol*. 2013;62(25 Suppl):D42–50.
- van Riel AC, Schuurin MJ, van Hesse ID, Zwinderman AH, Cozijnsen L, Reichert CL, et al. Contemporary prevalence of pulmonary arterial hypertension in adult congenital heart disease following the updated clinical classification. *Int J Cardiol*. 2014;174(2):299–305.
- Benza RL, Miller DP, Barst RJ, Badesch DB, Frost AE, McGoon MD. An evaluation of long-term survival from time of diagnosis in pulmonary arterial hypertension from the REVEAL registry. *Chest*. 2012;142(2):448–56.
- Lowe BS, Therrien J, Ionescu-Ittu R, Pilote L, Martucci G, Marelli AJ. Diagnosis of pulmonary hypertension in the congenital heart disease adult population impact on outcomes. *J Am Coll Cardiol*. 2011;58(5):538–46.
- Verheugt CL, Uiterwaal CS, van der Velde ET, Meijboom FJ, Pieper PG, van Dijk AP, et al. Mortality in adult congenital heart disease. *Eur Heart J*. 2010;31(10):1220–9.
- Gómez A, Bialostozky D, Zajarias A, Santos E, Palomar A, Martínez ML, et al. Right ventricular ischemia in patients with primary pulmonary hypertension. *J Am Coll Cardiol*. 2001;38(4):1137–42.
- Galiè N, Saia F, Palazzini M, Manes A, Russo V, Bacchi Reggiani ML, et al. Left main coronary artery compression in patients with pulmonary arterial hypertension and angina. *J Am Coll Cardiol*. 2017;69(23):2808–17.
- Barst RJ, Rubin LJ, Long WA, McGoon MD, Rich S, Badesch DB, et al. A comparison of continuous intravenous epoprostenol (prostaglandin) with conventional therapy for primary pulmonary hypertension. *N Engl J Med*. 1996;334(5):296–301.
- Galiè N, Barberà JA, Frost AE, Ghofrani HA, Hoeper MM, McLaughlin VV, et al. Initial use of ambrisentan plus tadalafil in pulmonary arterial hypertension. *N Engl J Med*. 2015;373(9):834–44.
- Dimopoulos K, Inuzuka R, Goletto S, Giannakoulas G, Swan L, Wort SJ, et al. Improved survival among patients with Eisenmenger syndrome receiving advanced therapy for pulmonary arterial hypertension. *Circulation*. 2010;121(1):20–5.
- Schulz-Menger J, Bluemke DA, Bremerich J, Flamm SD, Fogel MA, Friedrich MG, et al. Standardized image interpretation and post-processing in cardiovascular magnetic resonance –2020 update: Society for Cardiovascular Magnetic Resonance (SCMR): board of trustees task force on standardized post-processing. *J Cardiovasc Magn Reson*. 2020;22(1):19.
- Moledina S, Pandya B, Bartsota M, Mortensen KH, McMillan M, Quayam S, et al. Prognostic significance of cardiac magnetic resonance imaging in children with pulmonary hypertension. *Circ Cardiovasc Imaging*. 2013;6(3):407–14.
- Swift AJ, Capener D, Johns C, Hamilton N, Rothman A, Elliot C, et al. Magnetic resonance imaging in the prognostic evaluation of patients with pulmonary arterial hypertension. *Am J Respir Crit Care Med*. 2017;196(2):228–39.
- van Wolferen SA, Marcus JT, Boonstra A, Marques KM, Bronzwaer JG, Spreeuwenberg MD, et al. Prognostic value of right ventricular mass, volume, and function in idiopathic pulmonary arterial hypertension. *Eur Heart J*. 2007;28(10):1250–7.
- Alabed S, Shahin Y, Garg P, Alandejani F, Johns CS, Lewis RA, et al. Cardiac-MRI predicts clinical worsening and mortality in pulmonary arterial hypertension: a systematic review and meta-analysis. *JACC Cardiovasc Imaging*. 2021;14(5):931–42.
- Alfakih K, Plein S, Bloomer T, Jones T, Ridgway J, Sivanathan M. Comparison of right ventricular volume measurements between axial and short axis orientation using steady-state free precession magnetic resonance imaging. *J Magn Reson Imaging*. 2003;18(1):25–32.
- Atalay MK, Chang KJ, Grand DJ, Haji-Momenian S, Machan JT, Sheehan FH. The transaxial orientation is superior to both the short axis and horizontal long axis orientations for determining right ventricular volume and ejection fraction using Simpson's method with cardiac magnetic resonance. *ISRN Cardiol*. 2013;2013:268697.
- Kramer CM, Barkhausen J, Flamm SD, Kim RJ, Nagel E. Standardized cardiovascular magnetic resonance (CMR) protocols 2013 update. *J Cardiovasc Magn Reson*. 2013;15:91.
- Lewis RA, Johns CS, Cogliano M, Capener D, Tubman E, Elliot CA, et al. Identification of cardiac magnetic resonance imaging thresholds for risk stratification in pulmonary arterial hypertension. *Am J Respir Crit Care Med*. 2020;201(4):458–68.
- van der Bruggen CE, Handoko ML, Bogaard HJ, Marcus JT, Oosterveer FPT, Meijboom LJ, et al. The value of hemodynamic measurements or cardiac MRI in the follow-up of patients with idiopathic pulmonary arterial hypertension. *Chest*. 2021;159(4):1575–85.
- van de Veerdonk MC, Kind T, Marcus JT, Mauritz GJ, Heymans MW, Bogaard HJ, et al. Progressive right ventricular dysfunction in patients with pulmonary arterial hypertension responding to therapy. *J Am Coll Cardiol*. 2011;58(24):2511–9.
- van Wolferen SA, van de Veerdonk MC, Mauritz GJ, Jacobs W, Marcus JT, Marques KM, et al. Clinically significant change in stroke volume in pulmonary hypertension. *Chest*. 2011;139(5):1003–9.
- Vonk Noordegraaf A, Channick R, Cottrell E, Kiely DG, Marcus JT, Martin N, et al. The REPAIR study: effects of macitentan on RV

- structure and function in pulmonary arterial hypertension. *JACC Cardiovasc Imaging*. 2021;15(2):240–53.
32. Lin ACW, Seale H, Hamilton-Craig C, Morris NR, Strugnell W. Quantification of biventricular strain and assessment of ventriculo-ventricular interaction in pulmonary arterial hypertension using exercise cardiac magnetic resonance imaging and myocardial feature tracking. *J Magn Reson Imaging*. 2019;49(5):1427–36.
  33. de Siqueira ME, Pozo E, Fernandes VR, Sengupta PP, Modesto K, Gupta SS, et al. Characterization and clinical significance of right ventricular mechanics in pulmonary hypertension evaluated with cardiovascular magnetic resonance feature tracking. *J Cardiovasc Magn Reson*. 2016;18(1):39.
  34. Homsí R, Luetkens JA, Skowasch D, Pizarro C, Sprinkart AM, Gieseke J, et al. Left ventricular myocardial fibrosis, atrophy, and impaired contractility in patients with pulmonary arterial hypertension and a preserved left ventricular function: a cardiac magnetic resonance study. *J Thorac Imaging*. 2017;32(1):36–42.
  35. Kallianos K, Brooks GC, Mukai K, Seguro de Carvalho F, Liu J, Naeger DM, et al. Cardiac magnetic resonance evaluation of left ventricular myocardial strain in pulmonary hypertension. *Acad Radiol*. 2018;25(1):129–35.
  36. Knight DS, Steeden JA, Moledina S, Jones A, Coghlan JG, Muthurangu V. Left ventricular diastolic dysfunction in pulmonary hypertension predicts functional capacity and clinical worsening: a tissue phase mapping study. *J Cardiovasc Magn Reson*. 2015;17:116.
  37. Gan C, Lankhaar JW, Marcus JT, Westerhof N, Marques KM, Bronzwaer JG, et al. Impaired left ventricular filling due to right-to-left ventricular interaction in patients with pulmonary arterial hypertension. *Am J Physiol Heart Circ Physiol*. 2006;290(4):H1528–33.
  38. Manders E, Bogaard HJ, Handoko ML, van de Veerdonk MC, Keogh A, Westerhof N, et al. Contractile dysfunction of left ventricular cardiomyocytes in patients with pulmonary arterial hypertension. *J Am Coll Cardiol*. 2014;64(1):28–37.
  39. Leng S, Dong Y, Wu Y, Zhao X, Ruan W, Zhang G, et al. Impaired cardiovascular magnetic resonance-derived rapid semiautomated right atrial longitudinal strain is associated with decompensated hemodynamics in pulmonary arterial hypertension. *Circ Cardiovasc Imaging*. 2019;12(5):e008582.
  40. Tello K, Dalmer A, Vanderpool R, Ghofrani HA, Naeije R, Roller F, et al. Right ventricular function correlates of right atrial strain in pulmonary hypertension: a combined cardiac magnetic resonance and conductance catheter study. *Am J Physiol Heart Circ Physiol*. 2020;318(1):H156–h64.
  41. Bradlow WM, Assomull R, Kilner PJ, Gibbs JS, Sheppard MN, Mohiaddin RH. Understanding late gadolinium enhancement in pulmonary hypertension. *Circ Cardiovasc Imaging*. 2010;3(4):501–3.
  42. Freed BH, Gomberg-Maitland M, Chandra S, Mor-Avi V, Rich S, Archer SL, et al. Late gadolinium enhancement cardiovascular magnetic resonance predicts clinical worsening in patients with pulmonary hypertension. *J Cardiovasc Magn Reson*. 2012;14(1):11.
  43. Swift AJ, Rajaram S, Capener D, Elliot C, Condliffe R, Wild JM, et al. LGE patterns in pulmonary hypertension do not impact overall mortality. *JACC Cardiovasc Imaging*. 2014;7(12):1209–17.
  44. Chen YY, Yun H, Jin H, Kong H, Long YL, Fu CX, et al. Association of native T1 times with biventricular function and hemodynamics in precapillary pulmonary hypertension. *Int J Cardiovasc Imaging*. 2017;33(8):1179–89.
  45. Mehta BB, Auger DA, Gonzalez JA, Workman V, Chen X, Chow K, et al. Detection of elevated right ventricular extracellular volume in pulmonary hypertension using accelerated and navigator-gated look-locker imaging for cardiac T1 estimation (ANGIE) cardiovascular magnetic resonance. *J Cardiovasc Magn Reson*. 2015;17:110.
  46. Reiter U, Reiter G, Kovacs G, Adelsmayr G, Greiser A, Olschewski H, et al. Native myocardial T1 mapping in pulmonary hypertension: correlations with cardiac function and hemodynamics. *Eur Radiol*. 2017;27(1):157–66.
  47. Roller FC, Wiedenroth C, Breithecker A, Liebetrau C, Mayer E, Schneider C, et al. Native T1 mapping and extracellular volume fraction measurement for assessment of right ventricular insertion point and septal fibrosis in chronic thromboembolic pulmonary hypertension. *Eur Radiol*. 2017;27(5):1980–91.
  48. Saunders LC, Johns CS, Stewart NJ, Oram CJE, Capener DA, Puntmann VO, et al. Diagnostic and prognostic significance of cardiovascular magnetic resonance native myocardial T1 mapping in patients with pulmonary hypertension. *J Cardiovasc Magn Reson*. 2018;20(1):78.
  49. Spruijt OA, Vissers L, Bogaard HJ, Hofman MB, Vonk-Noordegraaf A, Marcus JT. Increased native T1-values at the interventricular insertion regions in precapillary pulmonary hypertension. *Int J Cardiovasc Imaging*. 2016;32(3):451–9.
  50. Wang J, Zhao H, Wang Y, Herrmann HC, Witschey WRT, Han Y. Native T1 and T2 mapping by cardiovascular magnetic resonance imaging in pressure overloaded left and right heart diseases. *J Thorac Dis*. 2018;10(5):2968–75.
  51. Bouchard A, Higgins CB, Byrd BF 3rd, Amparo EG, Osaki L, Axelrod R. Magnetic resonance imaging in pulmonary arterial hypertension. *Am J Cardiol*. 1985;56(15):938–42.
  52. Dellegrottaglie S, Sanz J, Poon M, Viles-Gonzalez JF, Sulica R, Goyenechea M, et al. Pulmonary hypertension: accuracy of detection with left ventricular septal-to-free wall curvature ratio measured at cardiac MR. *Radiology*. 2007;243(1):63–9.
  53. Marcus JT, Gan CT, Zwanenburg JJ, Boonstra A, Allaart CP, Gotte MJ, et al. Interventricular mechanical asynchrony in pulmonary arterial hypertension: left-to-right delay in peak shortening is related to right ventricular overload and left ventricular underfilling. *J Am Coll Cardiol*. 2008;51(7):750–7.
  54. Pandya B, Quail MA, Steeden JA, McKee A, Odille F, Taylor AM, et al. Real-time magnetic resonance assessment of septal curvature accurately tracks acute hemodynamic changes in pediatric pulmonary hypertension. *Circ Cardiovasc Imaging*. 2014;7(4):706–13.
  55. Roeleveld RJ, Marcus JT, Faes TJ, Gan TJ, Boonstra A, Postmus PE, et al. Interventricular septal configuration at mr imaging and pulmonary arterial pressure in pulmonary hypertension. *Radiology*. 2005;234(3):710–7.
  56. Swift AJ, Rajaram S, Hurdman J, Hill C, Davies C, Sproson TW, et al. Noninvasive estimation of PA pressure, flow, and resistance with CMR imaging: derivation and prospective validation study from the ASPIRE registry. *JACC Cardiovasc Imaging*. 2013;6(10):1036–47.
  57. Mauritz GJ, Marcus JT, Westerhof N, Postmus PE, Vonk-Noordegraaf A. Prolonged right ventricular post-systolic isovolumic period in pulmonary arterial hypertension is not a reflection of diastolic dysfunction. *Heart*. 2011;97(6):473–8.
  58. Marcus JT, Vonk Noordegraaf A, Roeleveld RJ, Postmus PE, Heethaar RM, Van Rossum AC, et al. Impaired left ventricular filling due to right ventricular pressure overload in primary pulmonary hypertension: noninvasive monitoring using MRI. *Chest*. 2001;119(6):1761–5.
  59. Gan CT, Lankhaar JW, Westerhof N, Marcus JT, Becker A, Twisk JW, et al. Noninvasively assessed pulmonary artery stiffness predicts mortality in pulmonary arterial hypertension. *Chest*. 2007;132(6):1906–12.
  60. Ray JC, Burger C, Mergo P, Safford R, Blackshear J, Austin C, et al. Pulmonary arterial stiffness assessed by cardiovascular magnetic resonance imaging is a predictor of mild pulmonary arterial hypertension. *Int J Cardiovasc Imaging*. 2019;35(10):1881–92.
  61. Kim NH, Delcroix M, Jais X, Madani MM, Matsubara H, Mayer E, et al. Chronic thromboembolic pulmonary hypertension. *Eur Respir J*. 2019;53(1):1801915.



62. Johns CS, Swift AJ, Rajaram S, Hughes PJC, Capener DJ, Kiely DG, et al. Lung perfusion: MRI vs. SPECT for screening in suspected chronic thromboembolic pulmonary hypertension. *J Magn Reson Imaging*. 2017;46(6):1693–7.
63. Rajaram S, Swift AJ, Telfer A, Hurdman J, Marshall H, Lorenz E, et al. 3D contrast-enhanced lung perfusion MRI is an effective screening tool for chronic thromboembolic pulmonary hypertension: results from the ASPIRE registry. *Thorax*. 2013;68(7):677–8.
64. Lasch F, Karch A, Koch A, Derlin T, Voskrebenezv A, Alsady TM, et al. Comparison of MRI and VQ-SPECT as a screening test for patients with suspected CTEPH: CHANGE-MRI study design and rationale. *Front Cardiovasc Med*. 2020;7:51.
65. Ley S, Kauczor HU, Heussel CP, Kramm T, Mayer E, Thelen M, et al. Value of contrast-enhanced MR angiography and helical CT angiography in chronic thromboembolic pulmonary hypertension. *Eur Radiol*. 2003;13(10):2365–71.
66. Ley S, Ley-Zaporozhan J, Pitton MB, Schneider J, Wirth GM, Mayer E, et al. Diagnostic performance of state-of-the-art imaging techniques for morphological assessment of vascular abnormalities in patients with chronic thromboembolic pulmonary hypertension (CTEPH). *Eur Radiol*. 2012;22(3):607–16.
67. Reiter G, Reiter U, Kovacs G, Kainz B, Schmidt K, Maier R, et al. Magnetic resonance-derived 3-dimensional blood flow patterns in the main pulmonary artery as a marker of pulmonary hypertension and a measure of elevated mean pulmonary arterial pressure. *Circ Cardiovasc Imaging*. 2008;1(1):23–30.
68. Reiter G, Reiter U, Kovacs G, Olschewski H, Fuchsjäger M. Blood flow vortices along the main pulmonary artery measured with MR imaging for diagnosis of pulmonary hypertension. *Radiology*. 2015;275(1):71–9.
69. Reiter U, Kovacs G, Reiter C, Kräuter C, Nizhnikava V, Fuchsjäger M, et al. MR 4D flow-based mean pulmonary arterial pressure tracking in pulmonary hypertension. *Eur Radiol*. 2021;31(4):1883–93.
70. Schäfer M, Barker AJ, Kheyfets V, Stenmark KR, Crapo J, Yeager ME, et al. Helicity and vorticity of pulmonary arterial flow in patients with pulmonary hypertension: quantitative analysis of flow formations. *J Am Heart Assoc*. 2017;6(12):e007010.
71. Lau EM, Abelson D, Dwyer N, Yu Y, Ng MK, Celermajer DS. Assessment of ventriculo-arterial interaction in pulmonary arterial hypertension using wave intensity analysis. *Eur Respir J*. 2014;43(6):1804–7.
72. Su J, Manisty C, Parker KH, Simonsen U, Nielsen-Kudsk JE, Mellekjaer S, et al. Wave intensity analysis provides novel insights into pulmonary arterial hypertension and chronic thromboembolic pulmonary hypertension. *J Am Heart Assoc*. 2017;6(11):e006679.
73. Quail MA, Knight DS, Steeden JA, Taelman L, Moledina S, Taylor AM, et al. Noninvasive pulmonary artery wave intensity analysis in pulmonary hypertension. *Am J Physiol Heart Circ Physiol*. 2015;308(12):H1603–11.
74. Schäfer M, Wilson N, Ivy DD, Ing R, Abman S, Browne LP, et al. Noninvasive wave intensity analysis predicts functional worsening in children with pulmonary arterial hypertension. *Am J Physiol Heart Circ Physiol*. 2018;315(4):H968–h77.
75. Razavi R, Hill DL, Keevil SF, Miquel ME, Muthurangu V, Hegde S, et al. Cardiac catheterisation guided by MRI in children and adults with congenital heart disease. *Lancet*. 2003;362(9399):1877–82.
76. Kuehne T, Yilmaz S, Schulze-Neick I, Wellnhofer E, Ewert P, Nagel E, et al. Magnetic resonance imaging guided catheterisation for assessment of pulmonary vascular resistance: in vivo validation and clinical application in patients with pulmonary hypertension. *Heart*. 2005;91(8):1064–9.
77. Knight DS, Kotecha T, Martinez-Naharro A, Brown JT, Bertelli M, Fontana M, et al. Cardiovascular magnetic resonance-guided right heart catheterization in a conventional CMR environment—predictors of procedure success and duration in pulmonary artery hypertension. *J Cardiovasc Magn Reson*. 2019;21(1):57.
78. Rogers T, Ratnayaka K, Khan JM, Stine A, Schenke WH, Grant LP, et al. CMR fluoroscopy right heart catheterization for cardiac output and pulmonary vascular resistance: results in 102 patients. *J Cardiovasc Magn Reson*. 2017;19(1):54.
79. Ratnayaka K, Kanter JP, Faranesh AZ, Grant EK, Olivieri LJ, Cross RR, et al. Radiation-free CMR diagnostic heart catheterization in children. *J Cardiovasc Magn Reson*. 2017;19(1):65.
80. Alabed S, Garg P, Johns CS, Alandejani F, Shahin Y, Dwivedi K, et al. Cardiac magnetic resonance in pulmonary hypertension—an update. *Curr Cardiovasc Imaging Rep*. 2020;13(12):30.





# Tetralogy of Fallot

# 9

Michael A. Quail, Vivek Muthurangu,  
and Andrew M. Taylor

## 9.1 Introduction

Tetralogy of Fallot (TOF) is the most common form of cyanotic congenital heart disease, occurring in 1 in 3600 live births [1]. Complete repair of TOF was devised over 50 years ago (first reported by Lillehei in 1954) and can result in complete intra-cardiac repair in early infancy [2]. There are excellent short- and medium-term survival rates, and increasingly the 25-year actuarial survival for patients repaired before their fifth birthday is greater 90% of the expected survival rate [3] though the annualized risk of death triples in the third postoperative decade [4]. Late morbidity and mortality, in particular related to pulmonary incompetence, have been observed in many patients long after total repair.

Initially, pulmonary incompetence was believed to be a relatively benign condition, with few problems associated with right ventricular volume loading. However, it has become clear that chronic pulmonary incompetence and right ventricular (RV) volume loading can cause RV dysfunction, which can in turn lead to symptoms of reduced exercise tolerance, increased risk of atrial and ventricular tachyarrhythmia, and sudden death. This has led to an

**Supplementary Information** The online version contains supplementary material available at [https://doi.org/10.1007/978-3-031-29235-4\\_9](https://doi.org/10.1007/978-3-031-29235-4_9).

M. A. Quail  
Cardiovascular Imaging and Adult Congenital Heart Disease, Great Ormond Street Hospital for Children, London, UK  
e-mail: [Michael.Quail@gosh.nhs.uk](mailto:Michael.Quail@gosh.nhs.uk)

V. Muthurangu  
Cardiovascular Imaging and Physics, UCL Institute of Cardiovascular Science, University College London, London, UK  
e-mail: [v.muthurangu@ucl.ac.uk](mailto:v.muthurangu@ucl.ac.uk)

A. M. Taylor (✉)  
Cardiovascular Imaging, UCL Institute of Cardiovascular Science and Great Ormond Street Hospital for Children, London, UK  
e-mail: [a.taylor76@ucl.ac.uk](mailto:a.taylor76@ucl.ac.uk)

increasing proportion of patients requiring operative replacement of incompetent and/or stenosed pulmonary valves and conduits.

The accurate quantification of pulmonary incompetence and stenosis and their effects on the right and left ventricles and great vessel anatomy/pathology is therefore crucial: Data that can be provided by cardiovascular magnetic resonance (CMR) imaging. In this chapter, we will provide an overview of TOF, its treatment and its assessment with CMR. Ultimately, CMR may enable improvements in the management of late complications through appropriate surveillance and treatment and may extend the survival and quality of life of patients.

## 9.2 Morphology

Morphologically, the principal defect of this condition is antero-cephalad deviation of the muscular outlet septum resulting in the tetrad of ventricular septal defect (VSD), pulmonary outflow tract obstruction, overriding aorta, and RV hypertrophy (Fig. 9.1). In TOF, the malaligned outlet septum serves to narrow the sub-pulmonary outflow tract and simultaneously create an interventricular defect that is overridden by the aortic valve apparatus.

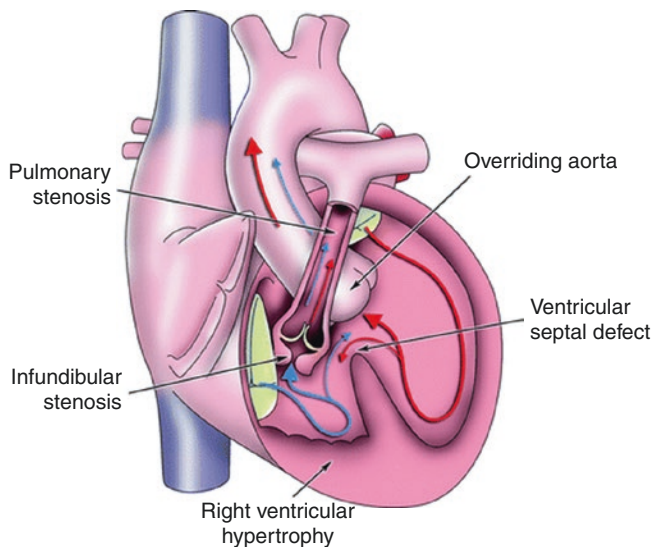


**Fig. 9.1** Schematic diagram of unrepaired TOF (copyright belongs to Gemma Price)

The VSD in TOF is usually nonrestrictive and subaortic; however, it may occasionally extend into the sub-pulmonary region. Its inferior and anterior borders are comprised of the limbs of the septomarginal trabeculation, while the superior border is formed from the deviated outlet septum and posteriorly the anteroseptal leaflet of the tricuspid valve.

Obstruction of the right ventricular outflow tract (RVOT) in TOF is most frequently in the form of infundibular stenosis (45%) with obstruction rarely isolated to the pulmonary valve alone (10%), and more usually a combination of the two (15%). In its most severe form, the pulmonary valve is atretic (15%) [5]. The deviated outlet septum combined with hypertrophied septoparietal trabeculations contributes significantly to subvalvular obstruction and inevitably requires division at surgery. The pulmonary valve is frequently stenotic with thickened and tethered leaflets requiring valvotomy or placement of a transannular patch if the annulus diameter is deemed inadequate (Fig. 9.2). However, the resultant sequelae of pulmonary incompetence are now recognized to be a significant problem later in life. Stenosis of the origin of the left and/or right pulmonary arteries (PAs) is a common finding and may require resection if localized or placement of a separate patch is more diffusely hypoplastic. In a proportion of patients, there may be pulmonary atresia, particularly at an infundibular or valvular level and associated major aortopulmonary collateral arteries (MAPCAs). The preferred approach in this situation may be the placement of a right ventricle to pulmonary artery (RV-PA) conduit.

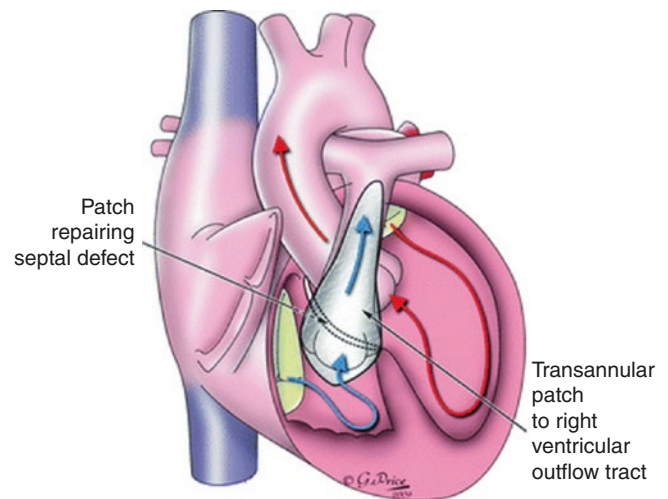


**Fig. 9.2** Schematic diagram of repaired TOF (copyright belongs to Gemma Price)

The individual components of the tetrad clearly show marked variability, especially the nature of pulmonary stenosis and the extent of the VSD; these variations account for the spectrum of clinical severity, and their surgical treatment can significantly influence later outcomes.

### 9.2.1 Associated Anomalies

Significant associated cardiac defects are uncommon. The most frequent associated lesions include right-sided aortic arch, atrial septal defect, patent ductus arteriosus, atrioventricular septal defects, and additional VSDs. Less commonly, there may be a persistent left-sided superior vena cava, anomalous origin of the left anterior descending coronary artery, or aortopulmonary collaterals if severe pulmonary stenosis. Associated syndromic conditions in which TOF may occur as a major manifestation include DiGeorge syndrome (22q11.2 deletion) and Alagille syndrome (JAG1 mutation); however, the condition more often occurs as an isolated defect.

## 9.3 Clinical Presentation

The clinical presentation of TOF in infancy varies depending on the degree of RVOT obstruction. Typically, the infant will present with cyanosis due to right-to-left shunt, and diagnosis is then established by echocardiography. Surgery is usu-

ally performed around 3–6 months as cyanosis progresses, often without a prior palliative shunt procedure. In the infant with TOF and pulmonary atresia, severe cyanosis is seen immediately after birth.

The complications observed in patients beyond the immediate postoperative period relate to surgical residua and progression of the “unnatural” history of the disease. Common problems requiring re-intervention include severe pulmonary regurgitation, residual outflow tract obstruction, and conduit failure. Less commonly a residual VSD, particularly at the posteroinferior margin of the patch, and severe tricuspid regurgitation require reoperation. Pulmonary regurgitation, in contrast to other residua, is remarkably well tolerated. However, over time, it produces its deleterious effects through volume overload of the right ventricle. It is associated with pathological RV dilatation and dysfunction, decreased exercise tolerance, sudden cardiac death, and ventricular arrhythmia associated with prolonged QRS duration. Pulmonary valve replacement (PVR) can ameliorate the volume overload imposed by pulmonary regurgitation. However, the optimal timing for this procedure remains unclear, as homograft prostheses have a limited life span and further reoperations may be required should these fail.

### 9.3.1 Primary Surgical Repair

Early primary repair is preferred because it shortens the period the patient is exposed to hypoxemia, right ventricular (RV) pressure overload, and subsequent RV hypertrophy. It is performed with a low perioperative mortality, with reported midterm survival in the modern era of 97% at 7 years of postoperative follow-up [3].

The surgical approach has also shifted from a transventricular approach to a trans-atrial/trans-pulmonary approach, with the aim of preserving RV structure and myocardial function and reducing the potential side effects of an RV ventriculotomy (coronary artery damage, RV contractile reduction, scar arrhythmia).

### 9.3.2 Late Surgical Treatment: Pulmonary Valve Replacement

Surgical pulmonary valve replacement (SPVR) can be performed using a variety of valve materials including cadaveric homografts and man-made conduits with excellent outcomes [6]. Additional procedures may also be necessary and can be performed during the same cardiopulmonary bypass including resection of residual trabeculations, extensive enlargement of pulmonary arteries, closure of a patent foramen ovale, residual atrial and/or ventricular septal defects, tricuspid valve annuloplasty, and aortic valve replacement.

PVR is now commonly performed with a degree of RVOT refashioning [7] to reduce RVOT aneurismal dilatation and optimally align the RVOT and new pulmonary trunk.

### 9.3.3 Percutaneous Pulmonary Valve Replacement

In patients who develop stenosis of their surgical PVR (homograft or conduit stenosis), percutaneous transcatheter stenting is possible. This can prolong conduit life and postpone reoperation. However bare-metal stenting can potentially convert the pressure-overloaded ventricle to one of volume overload through relief of obstruction and introduction of free pulmonary incompetence.

In 2000, percutaneous pulmonary valve replacement (PPVR) was described, whereby a new pulmonary valve was placed into a dysfunctional RV-PA prosthetic conduit [8]. Over the following decade, this technology has been accepted into clinical practice, with over many thousands of devices now implanted throughout the world [9–11]. Multiple devices can be used in this setting including the Melody™ (Medtronic Inc., Minneapolis, MN, USA) (Fig. 9.3) and Edwards SAPIEN transcatheter heart valve [12]. This method offers a minimally invasive alternative to open-heart surgery for RVOT/pulmonary trunk dysfunction in children and adults by restoring acceptable RV loading conditions, in particular when compared to bare-metal stenting of pulmonary conduit stenosis [13].

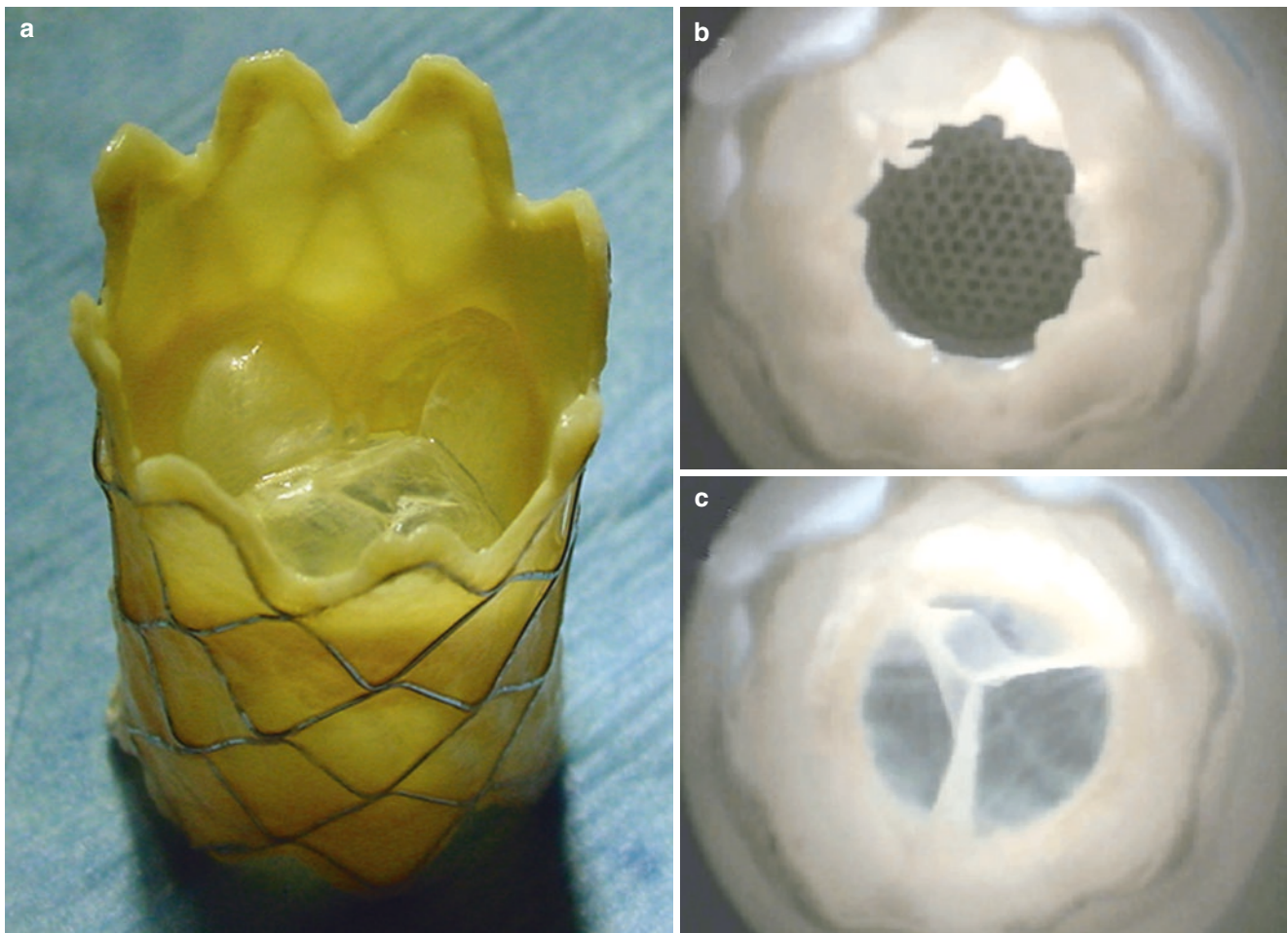


**Fig. 9.3** PPVI device (a). Device viewed in water bath showing the valve open during forward flow (b) and closed during reverse flow (c) note tri-leaflet morphology of the valve

It must be noted that one complication of the Melody device is infective endocarditis (IE) that occurs more frequently than in patients undergoing SPVR—survival free of IE by Kaplan–Meier at 5 years of 98.7% for homografts vs. 84.9% for Melody [14].

#### 9.4 CMR Imaging

As patients with congenital heart disease in general, and TOF in particular, are increasingly surviving longer, appropriate follow-up and surveillance for complications are becoming more important. In this regard, echocardiography has been the mainstay of investigation—providing important information regarding intracardiac anatomy, assessing valvular competence, and ventricular function. However, the technique is limited by postoperative restriction of acoustic windows, inability to provide sufficient hemodynamic infor-

mation, and because extracardiac anatomy, such as branch PAs, can be difficult to assess.

CMR has become an important modality in the assessment of TOF because the technique can provide three-dimensional (3D) anatomy of the right-sided cardiac and vascular structures crucial to adequate clinical assessment. CMR can provide reliable serial hemodynamic information noninvasively and, unlike echocardiography, can quantify pulmonary regurgitation volume and flow in branch PAs. CMR can also provide myocardial tissue fingerprinting, using focal late-gadolinium enhancement to assess areas of myocardial scarring, and T1 mapping and extracellular volume (ECV) imaging to assess diffuse fibrosis.

Ultimately, CMR provides a large field of view and unlimited choice of imaging planes and is much less operator dependent than echocardiography. A current limitation of CMR is its inability to measure hemodynamic pressures.



### 9.4.1 Indications

CMR is primarily used for the assessment of patients with TOF late after primary repair for the assessment of significant residual lesions that are identified at routine follow-up. Patients also undergo CMR assessment routinely before transfer from pediatric to adult congenital cardiac services to provide baseline anatomic and functional information. The exact frequency of serial scans remains to be determined; repeat scans are usually performed early if significant lesions are present, particularly where surgical or catheter intervention may be required.

### 9.4.2 CMR Sequences

#### 9.4.2.1 3D Imaging

The 3D capabilities of CMR play a key role for pediatric and adult patients with congenital heart disease. There are two conventional methods of acquiring 3D data. One uses angiographic techniques with gadolinium-based contrast agents that can be injected via any peripheral vein. The other uses a 3D balanced-SSFP sequence, which is respiratory and cardiac gated, but does not require contrast [15]. Both data sets are acquired in such a way to give isotropic voxels, so that the images can be viewed with the same spatial resolution in any anatomical plane. These data can be used during the scan to plan image planes for further scanning as well as during the reporting phase to assess 3D relationships between structures, quantify vessel size, and view morphology. The high-signal, isotropic 3D images that are achieved using gadolinium-contrast angiography allow complex modeling of structures so that interventional techniques can be optimized [16].

Gadolinium-enhanced MR angiography is particularly useful in the assessment of complex pulmonary vascular anatomy associated with TOF (Movie 9.1), where the pulmonary vascular bed may be supplied with blood flow from other sources, such as surgically created shunts or aortopulmonary collateral vessels. Delineation of all sources of pulmonary blood supply and the size and morphology of the pulmonary arteries are essential as surgical and transcatheter procedures are often required to augment effective pulmonary blood flow or to eliminate sources of excessive pulmonary blood flow [17]. Gadolinium contrast-enhanced MR angiography relies on the T1 shortening effect of dilute gadolinium. A 3D data set is acquired at the peak of the gadolinium bolus. Sequences are designed to ensure that tissues without gadolinium enhancement are suppressed, resulting in prominence of contrast-enhanced vessels. Images are acquired in a single breath-hold, without cardiac synchroni-

zation. This results in two significant limitations: image blurring due to cardiac motion reduces the ability of this technique to visualize intracardiac anatomy, and the size of individual vessels represents an average size over the cardiac cycle which can lead to underestimation of systolic dimensions. A further disadvantage of gadolinium-enhanced MR angiography is that fast-moving turbulent blood causes signal dropout, leading to overestimation of stenoses.

#### 9.4.2.2 Cine Imaging

Cine imaging using balanced-SSFP, or fast gradient echo sequences, gives multiphase data that shows myocardial or valve motion over the entire cardiac cycle. These cines may have up to 40 frames per cardiac cycle, a temporal resolution adequate for accurate physiological representation. The balanced-SSFP sequences are now used as standard, as they provide improved blood pool homogeneity throughout the cardiac cycle. Balanced-SSFP images have significantly higher contrast-to-noise ratios allowing better detection of the endocardial border than traditional gradient echo sequences [18]. The technique lends itself particularly to assessment of TOF allowing qualitative assessment of cardiac chambers, pulmonary valvular function, and vascular anatomy.

Cine images are acquired in equal-width slices perpendicular to the long axis of the heart, from base to apex, in order to assess cardiac function and measure the ventricular volumes (Fig. 9.4). The post-processing of cine images to calculate ventricular volumes and function is performed offline, using commercially available or open-source software. The segmentation of the blood pool and myocardial border can be performed manually, or by using automated signal thresholding techniques. There is currently a wide range of software available and a wide variation in segmenting practice and procedures. A fundamental issue, particularly for pediatric patients and those with congenital disease, is that of inclusion or noninclusion of the trabeculae in the blood pool. If a simple endocardial contour is drawn and the trabeculae ignored and included in the blood pool, the manual segmentation process is more efficient and more reproducible [19]. However, this leads to erroneously large volume estimates for the ventricles and prohibits internal validation of stroke volumes using great arterial flow volumes.

#### 9.4.2.3 Flow Assessment

Accurate quantification of flow volume is crucial in patients with known or suspected congenital heart disease. For volume quantification, we favor a free-breathing, velocity encoded phase-contrast sequence with a temporal resolution of at least 30 frames per cardiac cycle. Slice positioning and velocity encoding must be optimized [20]. If these param-

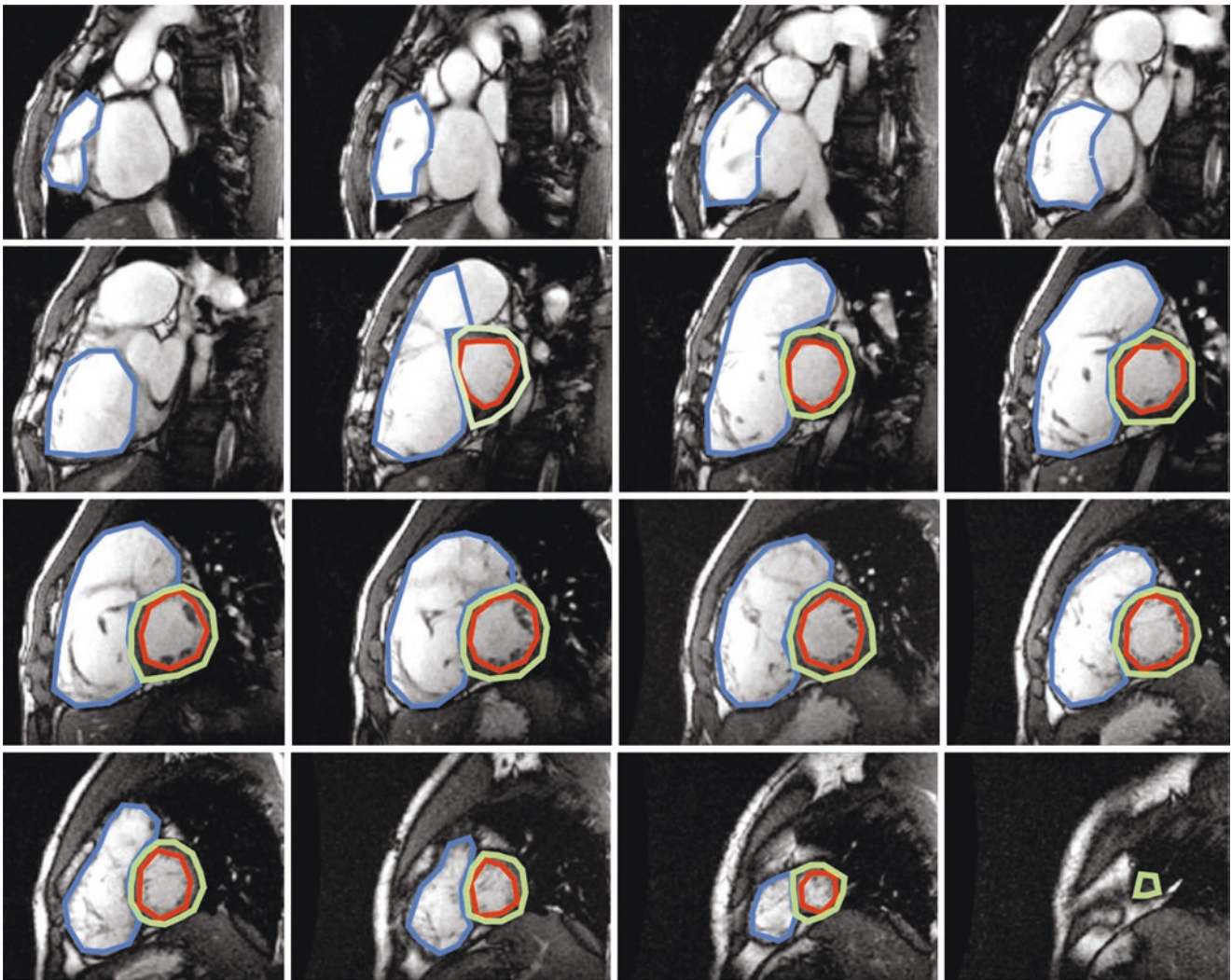


**Fig. 9.4** Short-axis, b-SSFP imaging stack through the ventricles of a patient with TOF, starting at the base (left to image) passing from left to right top to bottom toward the apex (right bottom image). This is the

diastolic stack—red contour LV end-diastolic volume (EDV), blue—RV EDV, green LV mass contour

ters are rigorously controlled, flow can be assessed in large and small arteries and systemic and pulmonary veins. Aortic and pulmonary valve regurgitant volumes can be directly measured (Fig. 9.5). Phase contrast flow sequences also enable the profiling of flow acceleration jets, with velocity estimation. More importantly, with appropriate combinations of arterial and venous flow volume assessment, the technique allows accurate assessment of interatrial, interventricular, arterial, and venous shunt volumes. In the context of atrioventricular valve regurgitation, knowledge of the ventricular stroke volume, combined with knowledge of the forward arterial flow volume from that ventricle allows for calculation of mitral or tricuspid valve regurgitant fraction. For every patient in whom ventricular function is quantified, the practice of our unit is to undertake great arterial flow vol-

ume assessment to guide the volumetric analysis. This greatly enhances the accuracy and reproducibility of our reporting procedure.

#### 9.4.2.4 Black-Blood Imaging

Black-blood spin-echo pulse sequences are seldom used in the CMR protocol nowadays, however, can still play a role in the assessment of TOF. They are good for the morphology of the blood vessels and cardiac chambers, in particular when turbulent flow at the site of stenosis reduces the accuracy of b-SSFP or MR angiography images. Black-blood imaging is also good at elucidating the relationship between airway and blood vessels. In TOF, this allows accurate assessment of branch PA abnormalities including hypoplasia, stenosis, and non-confluence, which are otherwise missed by echocardiography.



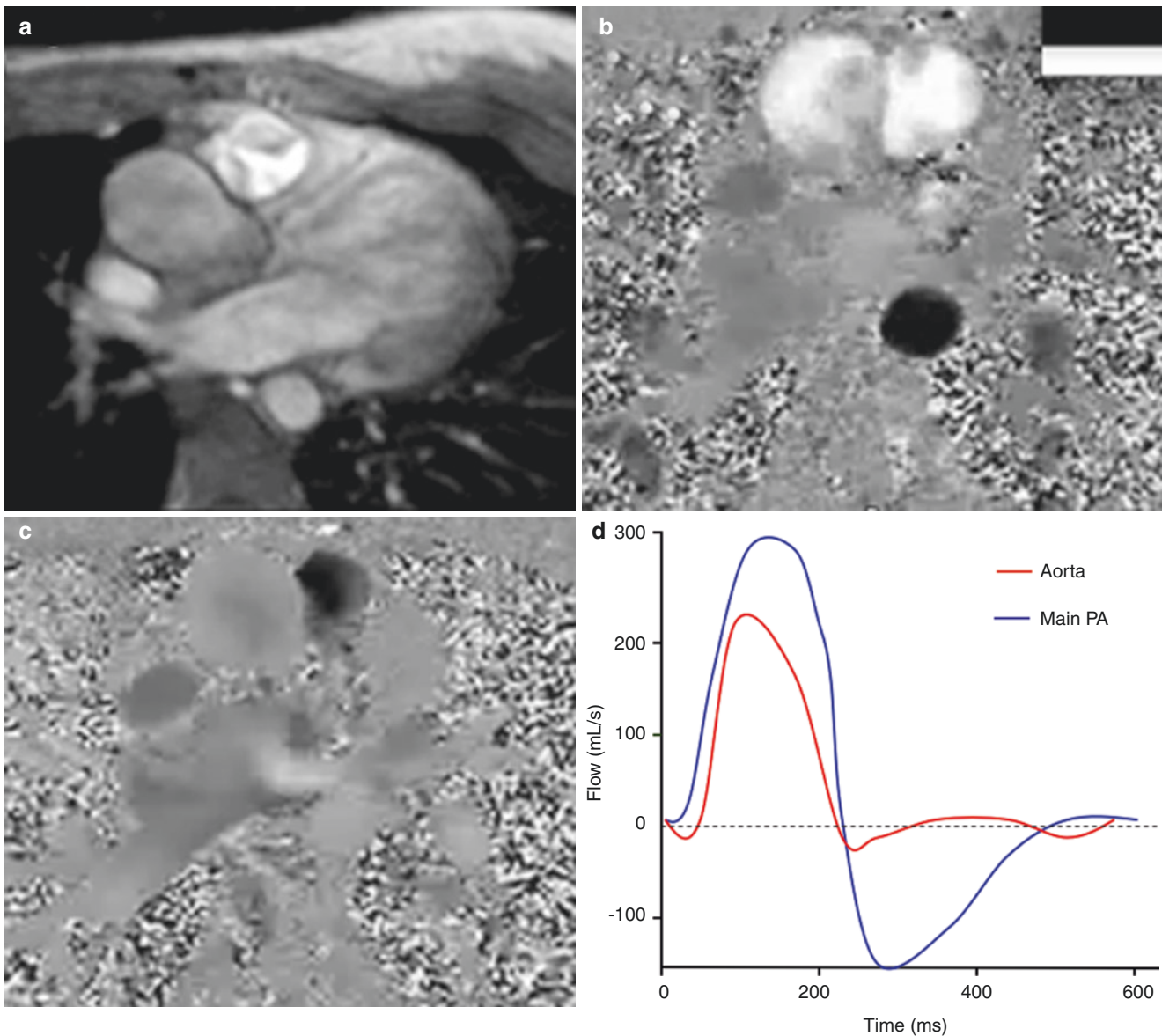


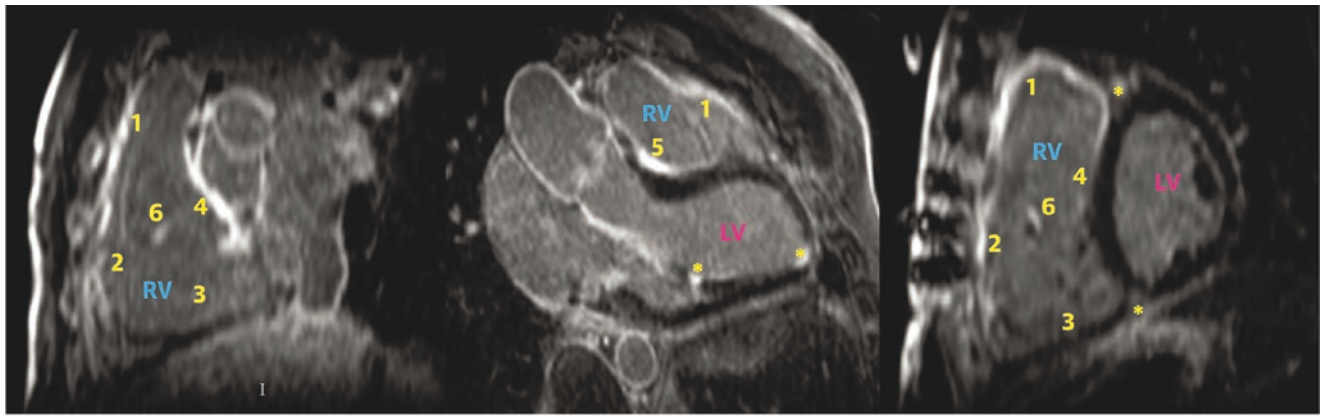
**Fig. 9.5** MR phase contrast velocity mapping in pulmonary regurgitation—(a) diastolic, modulus image showing non-coaptation of the valve leaflets, (b) systolic phase contrast image with *white* forward flow

(note *black* flow in the descending aorta posteriorly), (c) diastolic phase contrast showing pulmonary regurgitation (*black*), (d) flow curve over the cardiac cycle

Following treatment of PA stenoses by intravascular stenting, or following PPVR, gradient echo sequences suffer from serious metal artifacts due to T2\* field inhomogeneity. Though spin-echo is less susceptible to metal artifacts, this does not necessarily lead to a better assessment of stents and may possibly lead to false reassurance as to their patency [21]. CT imaging may be required to definitively exclude intra-stent stenosis.

#### 9.4.2.5 Tissue Characterization

Late-gadolinium enhancement (LGE) demonstrates large focal areas of fibrosis or other myocardial abnormality and is frequently observed in patients with TOF (Fig. 9.6) [22]. This is particularly so in areas that reflect the surgical repair—RVOT scar, site of VSD repair, and ventriculotomy site; however, areas of LGE are also seen remote to sites of surgery. Importantly, LGE correlates to RV systolic function



1	Anterior wall of RVOT (0-3)	4	RV surface of septum (0-3)	Minimal RV LGE	≤2
2	Anterior wall of RV (0-3)	5	VSD patch region (0-3)	Mild RV LGE	3 or 4
3	Inferior wall of RV (0-3)	6	Trabecular bands (0-3)	Moderate RV LGE	5-7
				Severe RV LGE	≥8

**Fig. 9.6** Example of severe RV LGE extent. The RV is divided into six segments (yellow numbers 1–6). Regions of RV LGE were scored according to linear extent (0 1/4 no enhancement, 1 1/4 up to 2 cm, 2 1/4 up to 3 cm, 3 1/4 3 or more cm in length) and number of trabeculations enhanced including the moderator band (0 1/4 no enhancement, 1

1/4 1 trabeculation, 2 1/4 2–4). From Ghonim S, et al. *JACC Cardiovascular Imaging* 2022; Feb;15(2):257–268. doi: 10.1016/j.jcmg.2021.07.026 used under the terms of the Creative Commons Attribution 4.0 International License (<http://creativecommons.org/licenses/by/4.0/>)

and dilatation and, ultimately, may provide some prognostic information for timing PVR in repaired TOF.

Other forms of tissues characterization using either T1 mapping [23] or ECV imaging [24] remain in their infancy for use in routine TOF CMR assessment. Large-scale studies to understand the role of tissue fingerprinting in TOF are required.

#### 9.4.2.6 Stress CMR Imaging

Stress CMR imaging can be performed either with exercise (specifically designed MR bicycle) or dobutamine administration and has been used as means of assessing global RV function in response to increased workload. An abnormal ventricular response to dobutamine stress has been associ-

ated with adverse outcome in patients with repaired TOF [25] after midterm (8.9 years) follow-up in 100 patients. In normal subjects, RV ejection fraction increases during stress while in patients with TOF RV function remains unchanged or reduced during stress. The responses of subjects with chronic pulmonary incompetence to stress may be able to provide important prognostic indicators to help with the timing of pulmonary valve replacement in this patient population. Importantly, the use of real-time imaging to assess flow and function [26] during exercise may mean that such studies can now be carried out, without the need for pharmacological stress or the need to breath-hold during exercise, making exercise MR more acceptable to the patient.



**Table 9.1** Routine clinical imaging protocol

	Sequence	Planning	Purpose
Scout	Single shot b-SSFP	48 images in 3 orthogonal planes—16 in each plane	Isocentering To set up subsequent image planes
Ventricular long-axis (RV and LV)	b-SSFP cine images, breath-held, ECG gated	Orthogonal plane through long axis of ventricle from AV valve to ventricular apex, planned from axial scout images	AV valve function, assessment of ventricular volumes
AV valves	b-SSFP cine images, breath-held, ECG gated	Orthogonal plane parallel to AV valve, planned from axial stack	Planning four-chamber
Four-chamber view	b-SSFP cine images, breath-held, ECG gated	Orthogonal plane across AV valve orifices, planned from AV valves image	Atrial/ventricular size and function, AV valve regurgitation
Short-axis stack	b-SSFP cine images, breath-held, ECG gated	Orthogonal plane at AV valve hinge points with inclusion of basal blood pool, planned from end-diastolic frame of four-chamber cine	Ventricular volume calculation, assessment of septum, and outflow tracts
MR angiography	Gadolinium injection. Breath held, no ECG gating	Planned on axial scout images	Angiographic views of large and small vessels. Second pass allows assessment of systemic and pulmonary venous anatomy
LV and RV outflow tracts	b-SSFP cine images, breath-held, ECG gated	LV planned from AV valves cine. RV planned from axial stack	Outflow tract morphology, subjective assessment of semilunar valve function
Bi-ventricular LGE	2D fast low angle shot inversion recovery with myocardial nulling	Short axis stack, 4-chamber and RVOT images copied from appropriate planes	Focal scar imaging
3D b-SSFP	Free breathing, respiratory navigated, ECG-gated. Data acquisition in diastole	Planned on axial scout images for sagittal orientation	High-resolution intracardiac anatomy Visualize position of coronary artery origins, and proximal course
Great vessel flow	Through-plane velocity mapping, ECG gated, non-breath-held	Planned from outflow tract images (aortic root, pulmonary trunk). AV values and 3D whole heart (branch PAs, SVC, IVC). Measure pulmonary venous flow if aortopulmonary collateral flow needed	Vessel flow volume/velocity, calculation of regurgitant fraction and volume. Evaluate shunts

*b-SSFP* balanced steady-state free precession, *RV* right ventricle, *LV* left ventricle, *AV* atrioventricular, *LGE* late gadolinium, *RVOT* right ventricular outflow tract, *PAs* pulmonary arteries, *SVC* superior vena cava, *IVC* inferior vena cava

### 9.4.3 Clinical Imaging Protocol (Table 9.1)

## 9.5 CMR Findings in TOF

### 9.5.1 Pulmonary Valve and RV Assessment

The MR assessment of TOF requires comprehensive evaluation of the entire heart; however, emphasis is rightly placed on the evaluation of the RV and pulmonary valve. The RV outflow tract is visualized by aligning a plane that passes through the pulmonary trunk (or conduit) and the RV inferiorly from the axial stack. An alternative RVOT plane is a sagittal or sagittal-oblique view through the pulmonary trunk and descending aorta. Pulmonary incompetence can be assessed using a plane perpendicular to the RVOT views described, just above the pulmonary valve.

#### 9.5.1.1 Pulmonary Incompetence

Pulmonary incompetence to some degree is a predominant feature of TOF late after repair. CMR can image the regurgi-

tant jet in three dimensions and can quantify the regurgitant volume or describe it as a regurgitant fraction. This quantification is important in clinical decision-making regarding catheter or surgical valve replacement.

Turbulence of blood regurgitating through the pulmonary valve in diastole causes de-phasing and signal loss in gradient echo cine imaging (Movie 9.2). This facilitates a qualitative gradation of the regurgitant jet: grade 1, signal loss close to the valve; grade 2, signal loss extending into the proximal chamber; grade 3, signal loss filling the whole of the proximal chamber; and grade 4, signal loss in the receiving chamber throughout the relevant half of the cardiac cycle. The most accurate assessment of PR however is achieved by through-plane velocity-encoded phase-contrast imaging. Instantaneous flow volumes in the PA are calculated by multiplying the PA contour area (drawn manually) with the spatial average flow within this contour (Fig. 9.5). Total forward and retrograde (regurgitant) flow in a cardiac cycle can be calculated by integrating the instantaneous flow volumes for all frames. This technique has been validated in TOF by comparing it to the differ-

ences in left and right stroke volume, which can also be used to quantify pulmonary regurgitation if there is no other valve regurgitation or shunt. The regurgitant fraction is calculated by dividing pulmonary retrograde flow by pulmonary forward flow  $\times 100$ .

### 9.5.1.2 Pulmonary Stenosis and RVOT Obstruction

Pulmonary stenosis and RVOT obstruction are significant and common residual lesions following TOF repair. Using MR velocity mapping and the modified Bernoulli equation, the gradient across a stenosis can be calculated. This technique is comparable to Doppler echocardiography but is not limited by acoustic windows, allowing measurement of the velocity jet in any plane. Imaging is usually performed using a combination of through-plane (perpendicular to jet) and in-plane (parallel to jet) imaging. The latter is used to initially define the jet, with subsequent through-plane images at the site of maximum velocity.

### 9.5.1.3 Systolic Ventricular Function

Systolic ventricular function in TOF is based on CMR ventricular volumetric assessment. The complex geometry of the RV means that no single imaging plane is well suited to RV assessment. We recommend the use of the short axis; however, the interface between right ventricle and right atrium can be difficult to assess, and long-axis imaging may help.

### 9.5.1.4 Diastolic Ventricular Function

Diastolic ventricular function can also be assessed using CMR. Though the late forward flow of so-called restrictive physiology can be seen, RV time-volume curves can be created using either cine ventricular volume data or by combining phase contrast velocity maps of flow through the tricuspid and pulmonary valve. These have not only been used to demonstrate impaired diastolic function in the RV and LV of patients with TOF but also how early diastolic filling can improve following relief of conduit stenosis [27]. Again, further studies of diastolic properties, with both CMR and echocardiography, are required to define the prognostic use of this information.

## 9.5.2 Unrepaired TOF

In the assessment of the patient with unrepaired TOF, the anatomical diagnosis will usually have been made previously by echocardiography. CMR will therefore aim to confirm the characteristic morphology (Fig. 9.7) and assist

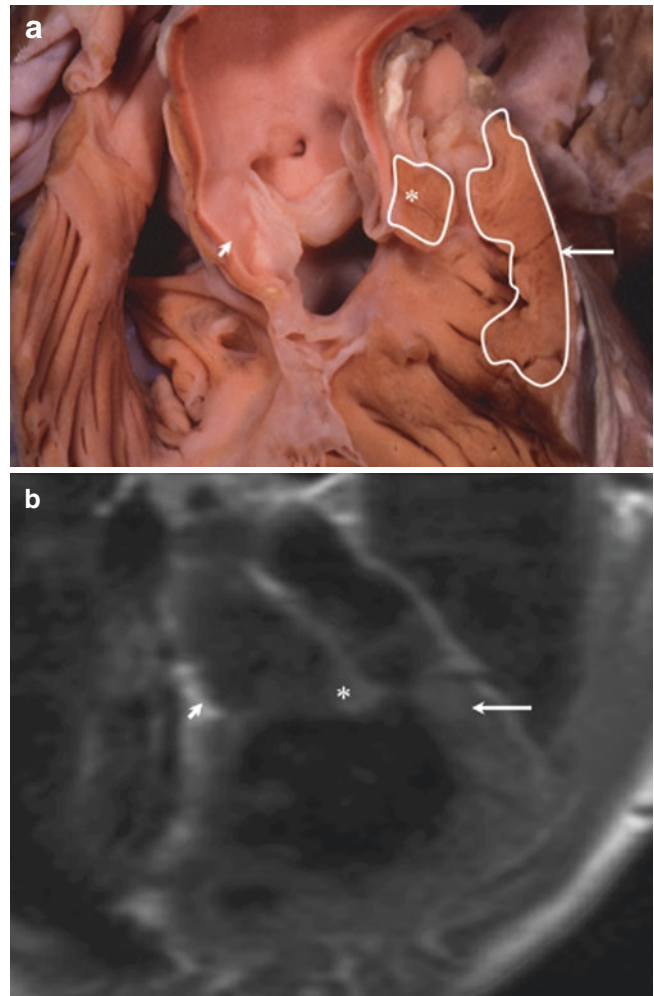


**Fig. 9.7** Unrepaired TOF in neonate. (a) Histological specimen showing VSD, overriding aorta (arrowhead), infundibular stenosis (asterisks), and RV hypertrophy (arrow). (b) Comparison CMR image—black-blood coronal oblique view

preoperative planning by defining any additional complex anatomy and physiology that may influence the surgical procedure. *Assessment should include:*

- RV outflow tract obstruction—Is narrowing of the sub-pulmonary infundibulum fixed or dynamic?
- Pulmonary valve morphology—Is valve sparing surgery possible?
- Quantify peak velocity across RV outflow tract.
- Identify and measure any branch pulmonary stenosis/hypoplasia.
- Identify and measure any palliative shunts.
- Measure differential lung perfusion.
- Quantify ventricular volumes, mass, and function.

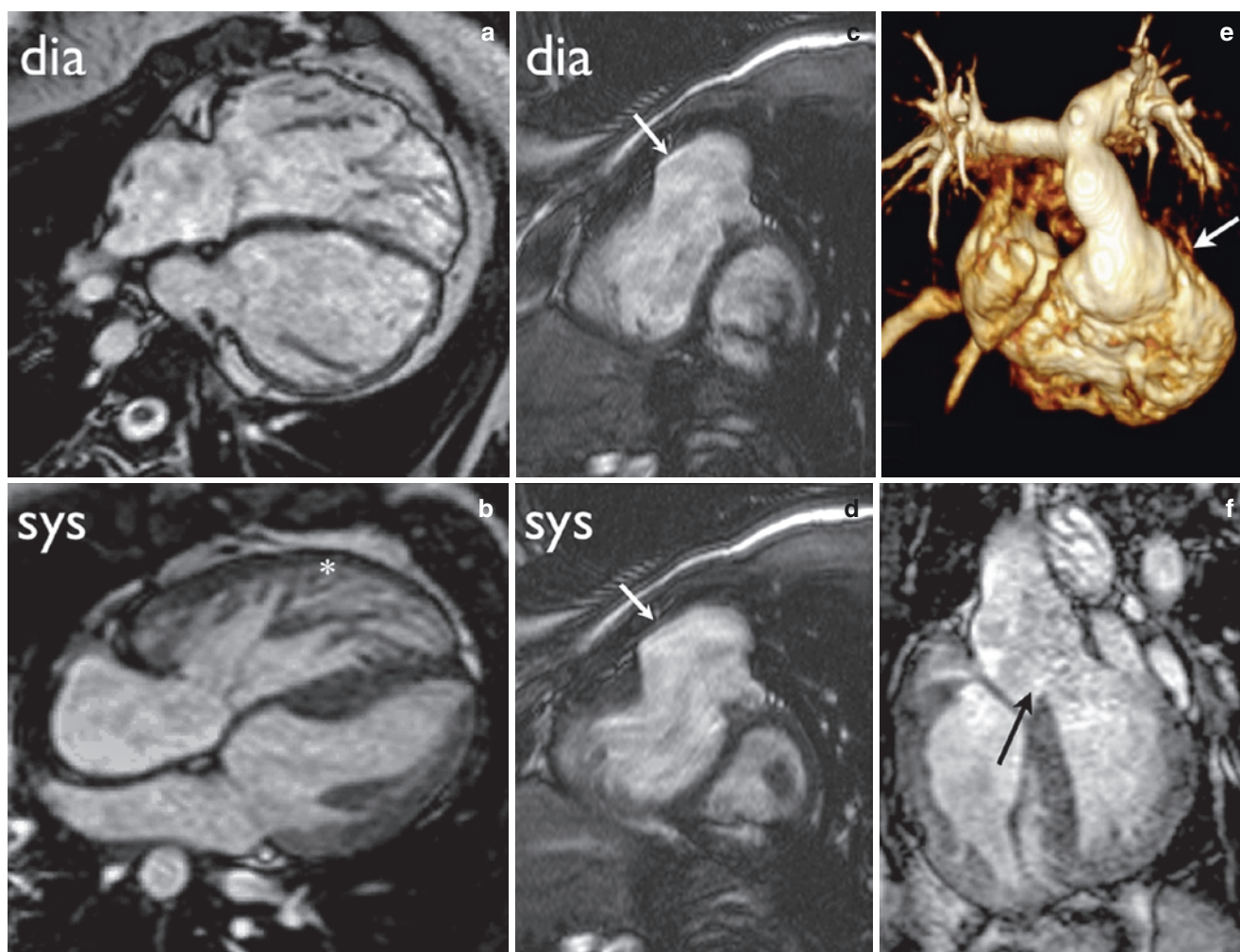


**Fig. 9.8** Repaired TOF in an adolescent. (a, b) Four-chamber b-SSFP image showing RV dilatation in diastole (*dia*) and RV hypertrophy in systole (*sys*,\*). (c, d) b-SSFP image showing dilated and aneurysmal RVOT (*arrow*) following transannular patch repair in oblique sagittal

view (c) diastole and (d) systole—note the paradoxical increase in aneurysm size during systole. (e) 3D MR angiogram reconstruction of RVOT aneurysm (*arrow*). (f) b-SSFP image through an intact VSD patch (*arrow*)

- Check aortic root for dilation.
- Exclude additional VSDs.

### 9.5.3 Repaired TOF

Patients who have undergone surgical repair of TOF will have had repair of VSD and relief of the RVOT obstruction. The latter may have involved surgical resection of infundibular muscle bundles and/or the insertion of a transannular patch if the annular diameter was deemed inadequate. Significant pulmonary regurgitation is almost always encountered following this procedure, though mild/moderate regurgitation is well tolerated. Pulmonary regurgitation may be increased by proximal or distal pulmonary artery stenosis, and chronic severe/free pulmonary regurgitation may lead to RV dilatation and dysfunction. The CMR study aims to comprehensively define the hemodynamic status of the patient (Fig. 9.8).

*The following should be considered:*

- Describe RV outflow tract and pulmonary trunk anatomy (Fig. 9.9 and Movie 9.2).
- Identify any RV outflow tract aneurysm (Fig. 9.8 and Movie 9.2).
- Quantify pulmonary valve regurgitation (Fig. 9.5).
- Assess proximal and distal pulmonary arteries for stenoses (Fig. 9.9 and Movie 9.1).
- Assess biventricular function, volume, and mass (Fig. 9.4 and Movie 9.3).
- Assess for LGE in both ventricles and the RVOT (Fig. 9.6).
- Check for the presence of MAPCAs.
- Measure Qp:Qs—assess for residual shunts, e.g., residual VSD and MAPCAs.
- Check aortic root for dilatation.
- Assess course of coronary arteries, which may be in proximity PPVR implantation sites, important to know prior to SPVR (Movie 9.4).





**Fig. 9.9** Variations in pulmonary trunk and branch pulmonary artery anatomy. Rapid prototyping models (reconstructed from CMR contrast-enhanced angiography data) of 12 patients with TOF assessed 10–15 years after early complete repair

## 9.6 Clinical Use of CMR

The most commonly encountered complication of repaired TOF is severe RV dilatation and dysfunction secondary to free pulmonary incompetence. The dilemma of when to treat patients with free pulmonary incompetence, presenting late after repair of right ventricular outflow tract obstruction, is one that faces all congenital heart disease clinicians. Although there is clear data to suggest that, in the long term, pulmonary incompetence is detrimental, leading to an increased incidence of adverse events (death, sustained arrhythmias, increasing symptoms), the conventional thinking has been that the benefit of treating free pulmonary incompetence is outweighed by the potential risk of surgical pulmonary valve replacement and the lack of longevity of this treatment (conduit dysfunction within 10–15 years that exposes patients to multiple operations over their life) (Fig. 9.10) [28]. PVR has therefore often been left until patients develop symptoms; however, once symptoms develop, there is the potential that symptomatic improvement after surgery may be limited due to the fact that the right ventricle has been chronically exposed to pulmonary incompetence.

More recently, there has been a shift in this risk/benefit continuum. Operative mortality and morbidity are now small with modern operative methods and postoperative care [6], and conduit life can now be extended using new non-invasive percutaneous approaches to treat conduit dysfunction.

### 9.6.1 The Use of CMR to Select Patients with Severe Pulmonary Incompetence for PVR

Current data from CMR assessment of patients with severe pulmonary incompetence have demonstrated elevated RV end-diastolic and end-systolic volumes and reduced RV ejection fraction compared to normal. Furthermore, there is increasing evidence that RV function may be irreversibly compromised by such long-term changes. This is exemplified by three findings that have been demonstrated by CMR. Firstly, RV ejection fraction has been shown to be significantly lower in patients with both RV pressure and volume overload as compared with RV pressure overload alone. Secondly, an abnormal RV response to stress has been demonstrated in patients with TOF and pulmonary incompetence. And finally, there appears to be no, or limited, improvement in RV function (ejection fraction at rest) following PVR. Indeed, one of the few studies to demonstrate an improvement in RV ejection fraction following PVR was in patients with moderately dilated right ventricles [29].

Despite this lack of marked improvement in RV function by correcting pulmonary incompetence, PVR does reduce RV dimensions (Fig. 9.11), and if performed before an RV EDV index of 160 mL/m<sup>2</sup> or an RV ESV index of 80 mL/m<sup>2</sup> RV dimensions can be normalized in the majority of patients [30–32]. These numbers form the basis for both the AHA/ACC [33] and ESC [34] guidelines for when to consider PVR in patients with repaired TOF (Table 9.2). These num-



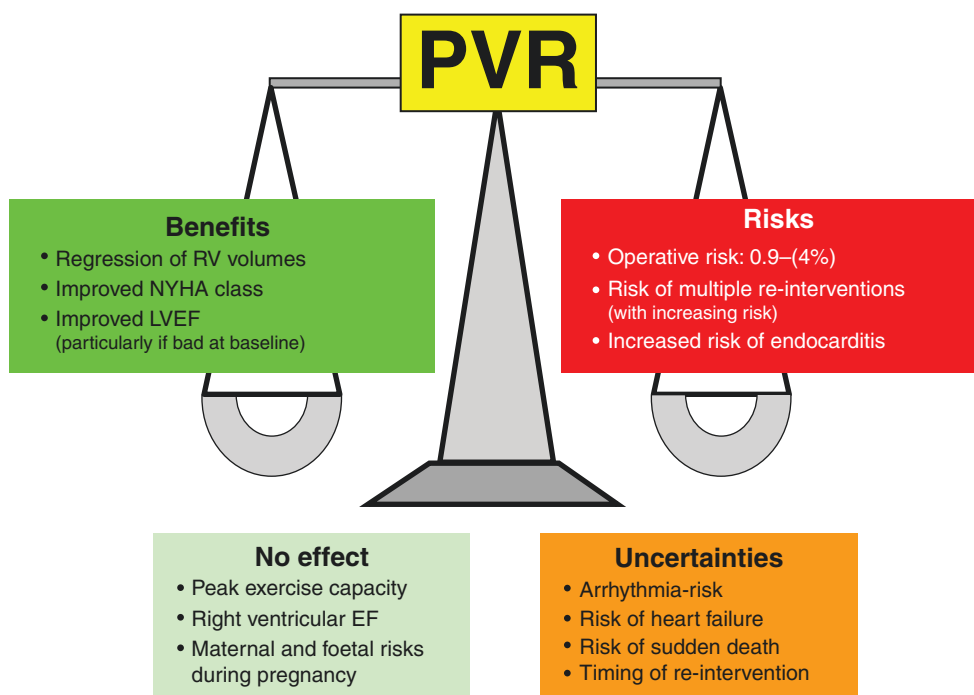


**Fig. 9.10** Risks, benefits, and uncertainties about pulmonary valve replacement (PVR). *LVEF* left ventricular ejection fraction, *NYHA* New York Heart Association, *RV* right ventricular. With permission

from Greutmann M. *European Heart Journal* 2016; 37:836–839 doi:10.1093/eurheartj/ehv634

bers need to be taken with caution as they represent studies done in patients of varying age groups, with varying original operations and varying PVR surgery (RVOT aneurysmal reduction or not). Furthermore, as there is limited standardization for the measurement of RV volumes, the quantitative measure of RV dimensions can vary between centers. It may be that as the RV dilates, interaction through the septum reduces LV filling [27] and reduces LV function. Importantly, there are suggestions that this may be happening at even moderate RV dilatation, because following PVR, LV EDV increases with a subsequent increase in LV function in some studies [29, 35]. Furthermore, a recent systematic review of outcomes shows that impaired right and left ventricular function is the most consistent independent predictor of disease progression in repaired ToF [36]. Hence, large-scale prospective studies are still necessary to provide important information to guide optimal clinical decision making in this area. Research is required to define CMR prognostic factors for PVR timing, and importantly, other information from echocardiography, exercise testing, assessment of neurohormonal activation, ECG data, and stress CMR may be useful for decision-making [29].

There is increasing evidence from systematic review that LGE may act as marker of progressive impairment of myocardial function with higher amount of right ventricular LGE related to higher right ventricular volumes, lower ejection fraction, and a higher pulmonary regurgitant fraction [37].

Importantly, LGE in TOF patients appears to correlate with the onset of arrhythmias, with a recent [38].

## 9.6.2 Which Treatment Option?

Once a PVR has been clinically justified, there is now a choice between surgery and PPRI for approximately 15–20% of patients with TOF. Technical suitability for PPVR can be defined by CMR using the protocol previously defined, but with focus on three main areas:

### 9.6.2.1 RVOT/Pulmonary Trunk Size and Distensibility

PPVR can be performed in RVOT/pulmonary trunks that range from 14 to 22 mm. At the lower end of the spectrum, conduits need to be of an adequate size to allow for sufficient opening without residual gradients. At the upper end, the device can only be expanded to a maximal diameter of 22 mm—any larger and valve leaflet coaptation may fail, or the device may embolize. This precludes PPVI in dilated anatomies (Fig. 9.9). Conduit sizes can be gleaned from operative reports; however, conduits can become smaller (or larger) over time, and in order to have a full understanding of the anatomy of the outflow tract, CMR with 3D capabilities is crucial. Although the CMR-derived 3D reconstructions can be used to define size, it is important to realize that these

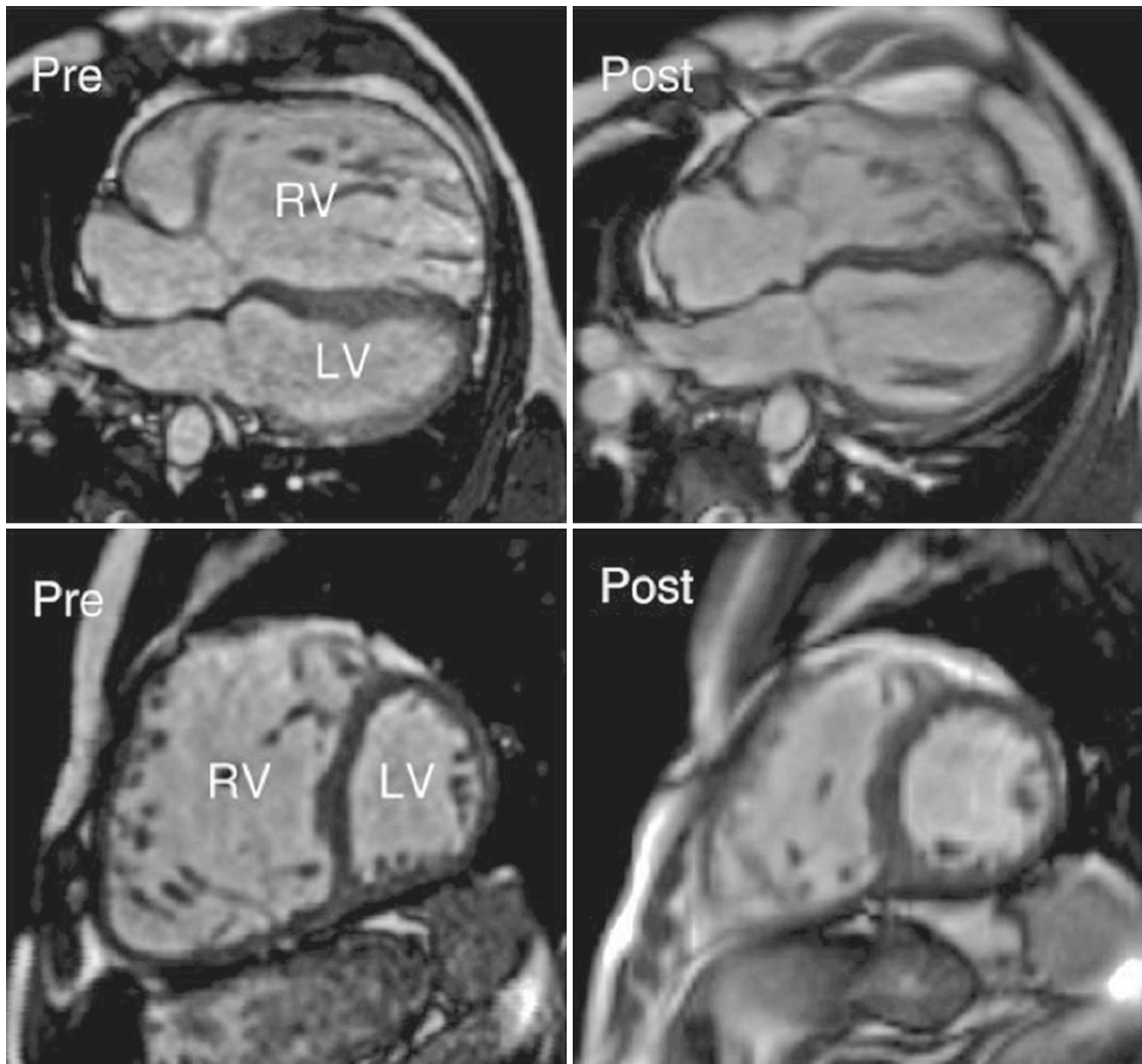


**Fig. 9.11** Response to surgical PVR after 1 year. Four-chamber and short-axis views showing marked RV volume reduction and increased LV volumes

reconstructions are performed on data acquired in diastole, or from non-ECG-gated data and, thus, maximal dimensions of very distensible anatomies may be underestimated. Cine imaging of the RVOT/pulmonary trunk in both long and short axes overcomes this problem, enabling the measurement of the maximum diameter of the site at which PPVI may be attempted. If the results of MRI are doubtful or borderline, balloon sizing of the RVOT can be performed at the time of catheterization.

#### 9.6.2.2 RVOT/Pulmonary Morphology

The 3D information from CMR can be used to visualize the best site for device anchorage in the RVOT/pulmonary trunk. Furthermore, certain shapes are not suitable for safe implantation of the device [16]. A morphological classification has been created according to measurements of 3D reconstructions of the RVOT [39]. Importantly, a pyramidal morphology, meaning that the RVOT funnels down toward the pulmonary bifurcation, is not suitable for PPVr because

**Table 9.2** Summary of international guidelines for pulmonary valve replacement

PVR indication	Class	Level of evidence
<b>ESC 2020 [34]</b>		
PVR is recommended in symptomatic patients with severe PR and/or at least moderate RVOTO	I	C
In patients with no native outflow tract, catheter intervention (PPVR) should be preferred if anatomically feasible	I	C
PVR should be considered in asymptomatic patients with severe PR and/or RVOTO when one of the following criteria is present: 1. Decrease in objective exercise capacity 2. Progressive RV dilation to RVESVi $\geq 80$ mL/m <sup>2</sup> , and/or RVEDVi $\geq 160$ mL/m <sup>2</sup> , and/or progression of TR to at least moderate 3. Progressive RV systolic dysfunction 4. RVOTO with RVSP $> 80$ mmHg	IIa	C
<b>ACC 2018 [33]</b>		
Moderate or greater PR and cardiovascular symptoms not otherwise explained	I	B
Moderate or greater PR and any two of the following: 1. Mild or moderate RV or LV systolic dysfunction 2. Severe RV enlargement (RVEDV $\geq 160$ mL/m <sup>2</sup> , RVESVi $\geq 80$ mL/m <sup>2</sup> , or RVEDV $\geq 2 \times$ LVEDV) 3. RVSP due to RVOT obstruction $\geq 2/3$ systemic pa 4. Progressive reduction in objective exercise tolerance	IIa	B
Moderate or greater PR and sustained ventricular tachyarrhythmias	IIb	C

PVR pulmonary valve replacement, PR pulmonary regurgitation, RVOTO right ventricular outflow tract obstruction, PPVR percutaneous pulmonary valve replacement, RV right ventricle, RVESVi right ventricular end-systolic volume, indexed for BSA, RVEDVi right ventricular end-diastolic volume, indexed for BSA, LV left ventricle, RVSP right ventricular systolic pressure, pa pressure

**ESC**

## Class

I—Evidence and/or general agreement that a given treatment or procedure is beneficial, useful, effective

II—Conflicting evidence and/or a divergence of opinion about usefulness/efficacy of the given treatment or procedure

a—Weight of evidence/opinion is in favor of usefulness/efficacy

b—Usefulness/efficacy is less well established by evidence/opinion

## Level of evidence

A—Data derived from multiple randomized clinical trial or meta-analyses

B—Data derived from a single randomized clinical trial or large non-randomized studies

C—Consensus of opinion of the experts and/or small studies, retrospective studies, registries

of the high risk of device dislodgement. Ideal RVOT/pulmonary trunk shapes comprise conduits with parallel borders or conduits with a narrowing in the midportion since this provides a safe landing zone for the stent [39].

### 9.6.2.3 Proximity of the Proximal Coronary Arteries

The proximity of the proximal coronary arteries to the RVOT/pulmonary trunk has to be assessed (Movie 9.4). On CMR 3D whole-heart b-SSFP images, the anatomical relationship of the coronary arteries and the proposed implantation site can be judged. In addition, aortic root angiography is performed at the time of catheterization. On biplane projection, the relationship between the coronaries and the pulmonary artery can be judged. In case the CMR assessment or aortic root angiography cannot fully rule out the risk for coronary compression, simultaneous high-pressure balloon inflation in the implantation site and selective coronary angiography are performed [40]. Importantly, when angiography and simultaneous balloon inflation are performed, it is crucial to expand the RVOT to a therapeutic size. This maneuver is only meaningful when the conduit is expanded with a high-pressure balloon up to the diameter that will be reached post-PPVI.

### 9.6.3 Acute Hemodynamic Results and Implications for Biventricular Function Following PPVI

CMR performed before and within 1 month of the procedure, with analysis of biventricular function and calculation of great vessel blood flow, has shown an improvement in effective RV and LV stroke volume in both patients with predominantly pulmonary stenosis and those with predominantly regurgitation [9, 35]. In patients with predominantly pulmonary stenosis, this is due to decreased RV ESV and improved RV ejection fraction after marked relief of after-load. By contrast, RV ejection fraction remains unchanged in patients with predominantly pulmonary regurgitation, with the improvement in RV and LV effective stroke volume due to abolishment of pulmonary regurgitation [35].

## 9.7 New Developments

### 9.7.1 Development of New Percutaneous Devices

Because of the wide variation in patient morphology, size, and dynamics of the right ventricular outflow tract (RVOT)/pulmonary trunk (Fig. 9.9), only ~15–20% of patients with a hemodynamic and clinical indication for PPVI can be treated with the current device. Thus, 85% of patients with pulmonary dysfunction still require open-heart surgery for treatment. The majority of these patients are those with dilated, dynamic RVOT/pulmonary trunk anatomy (patients with TOF and previous RVOT patches) in whom the current per-



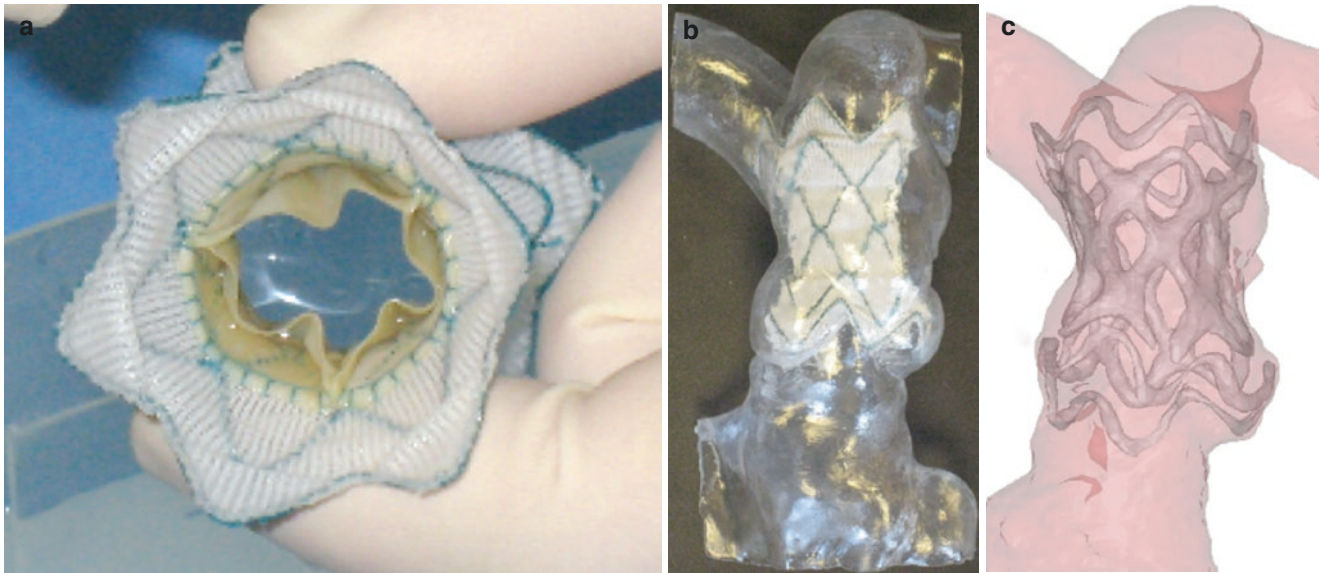


**Fig. 9.12** New percutaneous device for implantation into the dilated outflow tract. (a) Nitinol device, (b) preimplantation in rapid prototyping model, (c) 3D CT reconstruction postimplantation with device in situ in “first-in-man” case

cutaneous device is too small. Over the last decade, several new devices have been developed which can be implanted into the dilated outflow tract either percutaneously with self-expandable devices using the Venus p-valve (MedTech, Shanghai, China) [41] or The Harmony™ Transcatheter Pulmonary Valve (Medtronic Inc., Minneapolis, MN, USA) [42, 43] or using a hybrid surgical approach [44]. The Harmony™ device underwent a successful “first-in-man” implantation [42] in 2010. For this procedure, advanced cardiovascular imaging, in combination with patient-specific computer modeling, is crucial to achieve procedural success (Fig. 9.12).

### 9.7.2 4D Flow CMT in TOF

A recent systematic review of 26, 4D flow CMR studies has shown that this technique has huge potential in the assessment of TOF (Fig. 9.13) [45], with use in retrospective flow measurement (with optimization of valve tracking), and assessment of velocity mapping (very time-consuming and often inaccurate on 2D velocity mapping), while presenting novel information for intracardiac kinetic energy quantification, and vortex visualization in both ventricles, outflow tracts, and great vessels. Such information shows promise and may further support the optimization of PVR timing and advanced interventions to treat arrhythmias, though prospec-

tive, randomized, multicentered studies are required to validate these new parameters. The main disadvantages of 4D flow assessment are the long acquisition, reconstruction, and post-processing time, all on which may be supported by new computing and AI algorithms.

### 9.7.3 The Use of AI in CMR

AI offers the potential to change many aspects of congenital heart disease imaging [46]. At present, there are only a few clinically validated examples of AI applications in this field: however, AI has the potential to affect all parts of the patient journey (Fig. 9.14), from improved and automated patient booking, protocolization, and reporting to reduced CMR sequence, reconstruction, and post-processing times, to speed up CMR scanning to support the acquisition of high-quality, complex images.

Importantly, developments in AI will help move clinical practice to an era of precision patient management, where information from big data (clinical, laboratory, genetic, ECG, imaging, and outcome data) is used to create knowledge that is then drilled down to meet the specific needs of the individual patient in real time. Ultimately, this will improve patient outcomes, patient and clinician experience, and hopefully free up clinician time from many of the mundane processes that we currently need to carry out.



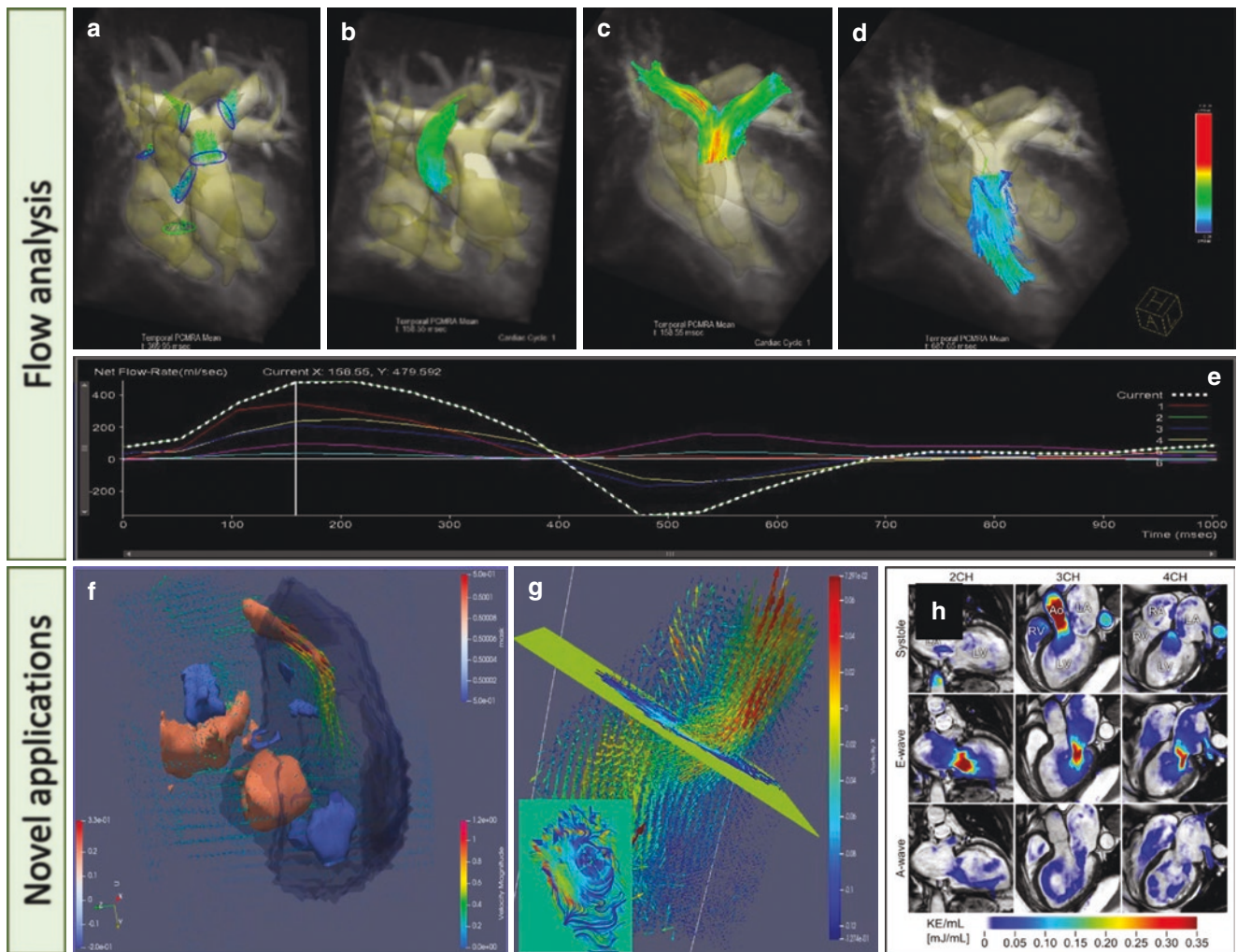


**Fig. 9.13** 4D flow analysis applications. (a) Manually placed seed positions; (b) particle streamline visualization of the ascending aorta; (c) main pulmonary and branches forward flow; (d) main pulmonary artery regurgitation; (e) flow analysis: net flow across cardiac cycle; (f) 3D vortex core extraction in the right ventricle; (g) 2D visualization of

vortices in the right ventricle; (h) kinetic energy mapping from Kanski et al. JCMR (2015) 17:111 DOI 10.1186/s12968-015-0211-4 used under the terms of the Creative Commons Attribution 4.0 International License (<http://creativecommons.org/licenses/by/4.0/>)

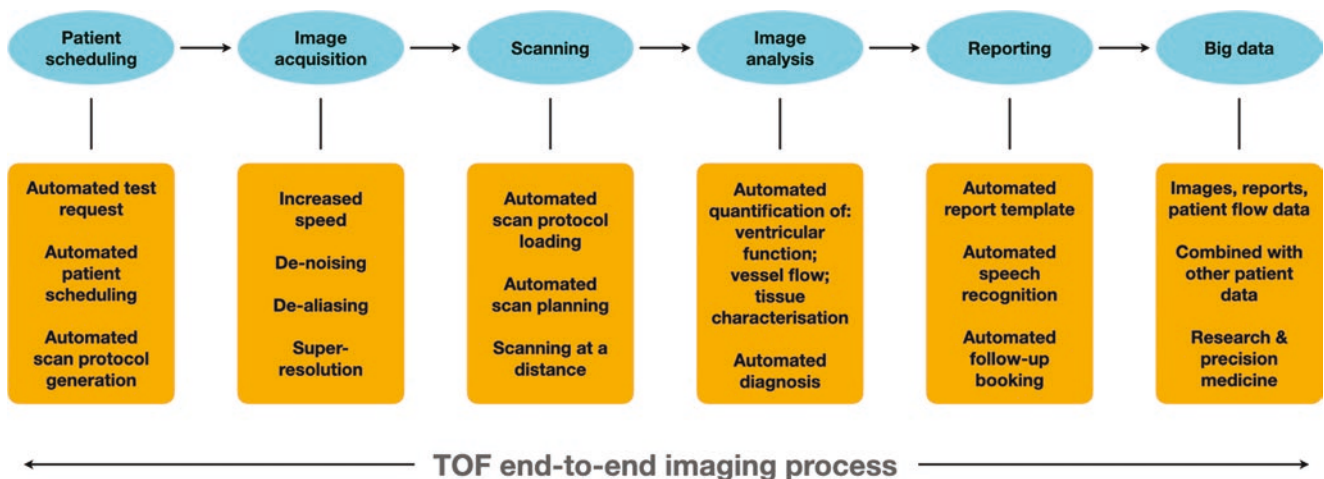


**Fig. 9.14** Aspects of the TOF radiological pathway for CMR imaging where artificial intelligence (AI) or machine learning (ML) may play a role

## 9.8 Discussion

In this chapter, we have emphasized the advantages of CMR imaging over other modalities to demonstrate its many strengths in the comprehensive assessment of TOF. However, it is prudent to mention that there are clearly clinical situations in which other modalities are indeed superior and preferable.

Echocardiography is a very effective bedside imaging tool and is used as the sole modality for the initial diagnosis of TOF in infancy and indeed the majority of later clinical follow-up. It could rightly be considered that CMR is an adjunct to this primary imaging modality in the management of TOF.

In patients who have been treated previously with metallic stents, aneurysm clips, or pacemakers, CT imaging is the preferable imaging modality. CT delineates RVOT and branch pulmonary artery morphology very well, and it has a very rapid acquisition time, which is valuable for critically ill patients. As patients with TOF survive longer, the burden of acquired ischemic heart disease will increase, and it is here that CT imaging of the coronary arteries is superior to CMR. However, the technique cannot quantify vascular flow and, of course, uses ionizing radiation.

In our institution, we have observed an increase in the use of cross-sectional imaging modalities with a resultant decrease in diagnostic cardiac catheterizations. Cardiac catheterization is still necessary when therapeutic interventions are required or when intravascular pressures must be discerned. However, the fluoroscopic projections are not suitable for the characterization of complex 3D malformations or ventricular function.

### 9.8.1 Conclusion

The tremendous advance in cross-sectional cardiovascular imaging has changed the landscape in the long-term follow-up and clinical decision-making in TOF. The wealth of reliable, reproducible hemodynamic information provided by CMR studies justifies its recognition as the gold standard. The data provided by CMR in TOF continues to advance our understanding of the disease and will continue to help us manage patients more effectively. Large, multicenter studies such as the INDICATOR Cohort [47] will be necessary to enhance our understanding of the unnatural life course, pathology, and optimal times for intervention in TOF patients.

### Practical Pearls

- TOF is common, and its routine assessment should be familiar to all CMR imagers.
- Protocolized follow-up for repaired TOF is important and should include CMR as outlined in the clinical imaging protocol.

- Debate remains about the exact timing of PVR in TOF, but an indexed RV end-diastolic volume between 160 and 200 mL/m<sup>2</sup>, in the presence of severe pulmonary incompetence, seems appropriate.
- CMR can be used to select treatment options (watchful waiting, surgical PVR, or percutaneous PVR).
- CMR provides excellent longitudinal data to track hemodynamic deterioration, responses to therapy, and changes in myocardial fibrosis.

## References

1. Apitz C, Webb GD, Redington AN. Tetralogy of Fallot. *Lancet*. 2009;374(9699):1462–71.
2. Murphy JG, Gersh BJ, Mair DD, et al. Long-term outcome in patients undergoing surgical repair of tetralogy of Fallot. *N Engl J Med*. 1993;329(9):593–9.
3. Smith CA, McCracken C, Thomas AS, et al. Long-term outcomes of tetralogy of Fallot. A study from the Pediatric cardiac care consortium. *JAMA Cardiol*. 2019;4(1):34–41. <https://doi.org/10.1001/jamacardio.2018.4255>.
4. Chiu SN, Wang JK, Chen HC, et al. Long-term survival and unnatural deaths of patients with repaired tetralogy of Fallot in an Asian cohort. *Circ Cardiovasc Qual Outcomes*. 2012;5:120–5. <https://doi.org/10.1161/CIRCOUTCOMES.111.963603>.
5. Park MK. *Pediatric cardiology for practitioners*. 3rd ed. St. Louis, MI: Mosby; 1996.
6. Suleiman T, Kavinsky CJ, Skerritt C, Kenny D, Ilbawi MN, Caputo M. Recent development in pulmonary valve replacement after tetralogy of Fallot repair: the emergence of hybrid approaches. *Front Surg*. 2015;2:22. <https://doi.org/10.3389/fsurg.2015.00022>.
7. Ghez O, Tsang VT, Frigiola A, et al. Right ventricular outflow tract reconstruction for pulmonary regurgitation after repair of tetralogy of Fallot. Preliminary results. *Eur J Cardiothorac Surg*. 2007;31(4):654–8.
8. Bonhoeffer P, Boudjemline Y, Saliba Z, et al. Percutaneous replacement of pulmonary valve in a right-ventricle to pulmonary-artery prosthetic conduit with valve dysfunction. *Lancet*. 2000;356(9239):1403–5.
9. Khambadkone S, Coats L, Taylor A, et al. Percutaneous pulmonary valve implantation in humans: results in 59 consecutive patients. *Circulation*. 2005;112(8):1189–97.
10. McElhinney DB, Hellenbrand WE, Zahn EM, et al. Short- and medium-term outcomes after transcatheter pulmonary valve placement in the expanded multicenter US melody valve trial. *Circulation*. 2010;122:507–16. <https://doi.org/10.1161/CIRCULATIONAHA.109.921692>.
11. Eicken A, Ewert P, Hager A, et al. Percutaneous pulmonary valve implantation: two-Centre experience with more than 100 patients. *Eur Heart J*. 2011;32:1260–5. <https://doi.org/10.1093/eurheartj/ehq520>.
12. Kenny D, Hijazi ZM, Kar S, et al. Percutaneous implantation of the Edwards SAPIEN transcatheter heart valve for conduit failure in the pulmonary position: early phase I results from an international multicenter clinical trial. *J Am Coll Cardiol*. 2011;58:2248–56. <https://doi.org/10.1016/j.jacc.2011.07.040>.
13. Lurz P, Nordmeyer J, Muthurangu V, et al. Comparison of bare metal stenting and percutaneous pulmonary valve implantation for treatment of right ventricular outflow tract obstruction: use of an x-ray/magnetic resonance hybrid laboratory for acute physiological assessment. *Circulation*. 2009;119(23):2995–3001.
14. Van Dijk I, Budts W, Cools B, et al. Infective endocarditis of a transcatheter pulmonary valve in comparison with surgical

- implants. *Heart*. 2015;101(10):788–93. <https://doi.org/10.1136/heartjnl-2014-306761>.
15. Sorensen TS, Korperich H, Greil GF, et al. Operator-independent isotropic three-dimensional magnetic resonance imaging for morphology in congenital heart disease: a validation study. *Circulation*. 2004;110(2):163–9.
  16. Schievano S, Coats L, Migliavacca F, et al. Variations in right ventricular outflow tract morphology following repair of congenital heart disease: implications for percutaneous pulmonary valve implantation. *J Cardiovasc Magn Reson*. 2007;9(4):687–95.
  17. Geva T, Greil GF, Marshall AC, Landzberg M, Powell AJ. Gadolinium-enhanced 3-dimensional magnetic resonance angiography of pulmonary blood supply in patients with complex pulmonary stenosis or atresia: comparison with x-ray angiography. *Circulation*. 2002;106(4):473–8.
  18. Barkhausen J, Ruehm SG, Goyen M, Buck T, Laub G, Debatin JF. MR evaluation of ventricular function: true fast imaging with steady-state precession versus fast low-angle shot cine MR imaging: feasibility study. *Radiology*. 2001;219(1):264–9.
  19. Winter MM, Bernink FJ, Groenink M, et al. Evaluating the systemic right ventricle by CMR: the importance of consistent and reproducible delineation of the cavity. *J Cardiovasc Magn Reson*. 2008;10:40.
  20. Taylor A, Dymarkowski S, Bogaert J. Valvular heart disease. In: Bogaert J, Dymarkowski S, Taylor A, Muthurangu V, editors. *Clinical cardiac MRI*. Heidelberg: Springer; 2012. p. 465–509. ISBN: 978-3-642-23035-6.
  21. Nordmeyer J, Gaudin R, Tann OR, et al. MRI may be sufficient for noninvasive assessment of great vessel stents: an in vitro comparison of MRI, CT, and conventional angiography. *Am J Roentgenol*. 2010;195(4):865–71.
  22. Babu-Narayan SV, Kilner PJ, Li W, et al. Ventricular fibrosis suggested by cardiovascular magnetic resonance in adults with repaired tetralogy of Fallot and its relationship to adverse markers of clinical outcome. *Circulation*. 2006;113(3):405–13.
  23. Yiğit H, Ergün E, Öztekin PS, Koşar PN. Can T1 mapping be an alternative of post-contrast magnetic resonance sequences in patients with surgically corrected tetralogy of Fallot? *Anatol J Cardiol*. 2020;24(6):377–81.
  24. Al-Wakeel-Marquard N, Ferreira da Silva T, Jeuthe S, et al. Measuring myocardial extracellular volume of the right ventricle in patients with congenital heart disease. *Sci Rep*. 2021;11(1):2679. <https://doi.org/10.1038/s41598-021-81440-z>.
  25. van den Bosch E, Cuypers JAAE, et al. Ventricular response to dobutamine stress cardiac magnetic resonance imaging is associated with adverse outcome during 8-year follow-up in patients with repaired tetralogy of Fallot. *Eur Heart J Cardiovasc Imaging*. 2020;21(9):1039–46. <https://doi.org/10.1093/ehjci/jez241>.
  26. Lurz P, Muthurangu V, Schievano S, et al. Feasibility and reproducibility of biventricular volumetric assessment of cardiac function during exercise using real-time radial k-t SENSE magnetic resonance imaging. *J Magn Reson Imaging*. 2009;29(5):1062–70.
  27. Lurz P, Puranik R, Nordmeyer J, et al. Improvement in left ventricular filling properties after relief of right ventricle to pulmonary artery conduit obstruction: contribution of septal motion and inter-ventricular mechanical delay. *Eur Heart J*. 2009;30(18):2266–74.
  28. Greutmann M. Tetralogy of Fallot, pulmonary valve replacement, and right ventricular volumes: are we chasing the right target? *Eur Heart J*. 2016;37:836–9. <https://doi.org/10.1093/eurheartj/ehv634>.
  29. Frigiola A, Tsang V, Bull C, et al. Biventricular response after pulmonary valve replacement for right ventricular outflow tract dysfunction: is age a predictor of outcome? *Circulation*. 2008;118(14 Suppl):S182–90.
  30. Oosterhof T, van Straten A, Vliegen HW, et al. Preoperative thresholds for pulmonary valve replacement in patients with corrected tetralogy of Fallot using cardiovascular magnetic resonance. *Circulation*. 2007;116(5):545–51.
  31. Therrien J, Provost Y, Merchant N, Williams W, Colman J, Webb G. Optimal timing for pulmonary valve replacement in adults after tetralogy of Fallot repair. *Am J Cardiol*. 2005;95(6):779–82.
  32. Buechel ER, Dave HH, Kellenberger CJ, et al. Remodelling of the right ventricle after early pulmonary valve replacement in children with repaired tetralogy of Fallot: assessment by cardiovascular magnetic resonance. *Eur Heart J*. 2005;26(24):2721–7.
  33. Stout KK, Daniels CJ, Aboulhosn JA, et al. 2018 AHA/ACC guideline for the management of adults with congenital heart disease: executive summary: a report of the American College of Cardiology/American Heart Association task force on Clinical practice guidelines. *Circulation*. 2019;139:e637–97.
  34. Baumgartner H, De Backer J, Babu-Narayan SV, et al. ESC scientific document group. 2020 ESC guidelines for the management of adult congenital heart disease. *Eur Heart J*. 2021;42(6):563–645. <https://doi.org/10.1093/eurheartj/ehaa554>.
  35. Coats L, Khambadkone S, Derrick G, et al. Physiological consequences of percutaneous pulmonary valve implantation: the different behaviour of volume- and pressure-overloaded ventricles. *Eur Heart J*. 2007;28(15):1886–93.
  36. Mohamed I, Stamm R, Keenan R, Boris Lowe B, Coffey S. Assessment of disease progression in patients with repaired tetralogy of Fallot using cardiac magnetic resonance imaging: a systematic review. *Heart Lung Circ*. 2020;29(11):1613–20. <https://doi.org/10.1016/j.hlc.2020.04.017>.
  37. Secchi F, Lastella G, Monti CB, Barbaro U, Capra D, Zanardo M, Sardaneli F. Late gadolinium enhancement in patients with tetralogy of Fallot: a systematic review. *Eur J Radiol*. 2021;136:109521. <https://doi.org/10.1016/j.ejrad.2021.109521>.
  38. Ghonim S, Gatzoulis MA, Ernst S, et al. Predicting survival in repaired tetralogy of Fallot. A lesion-specific and personalized approach. *JACC Cardiovasc Imaging*. 2022;15(2):257–68. <https://doi.org/10.1016/j.jcmg.2021.07.026>.
  39. Schievano S, Migliavacca F, Coats L, et al. Percutaneous pulmonary valve implantation based on rapid prototyping of right ventricular outflow tract and pulmonary trunk from MR data. *Radiology*. 2007;242(2):490–7.
  40. Sridharan S, Coats L, Khambadkone S, Taylor AM, Bonhoeffer P. Images in cardiovascular medicine. Transcatheter right ventricular outflow tract intervention: the risk to the coronary circulation. *Circulation*. 2006;113(25):e934–5.
  41. Cao QL, Kenny D, Zhou D, et al. Early clinical experience with a novel self-expanding percutaneous stent-valve in the native right ventricular outflow tract. *Catheter Cardiovasc Interv*. 2014;84:1131–7. <https://doi.org/10.1002/ccd.25544>.
  42. Schievano S, Taylor AM, Capelli C, et al. First-in-man implantation of a novel percutaneous valve: a new approach to medical device development. *EuroIntervention*. 2010;5(6):745–50.
  43. Gillespie MJ, Benson LN, Bergersen L, et al. Patient selection process for the harmony transcatheter pulmonary valve early feasibility study. *Am J Cardiol*. 2017;120(8):1387–92. <https://doi.org/10.1016/j.amjcard.2017.07.034>.
  44. Chen Q, Turner M, Caputo M, Stoica S, Marianeschi S, Parry A. Pulmonary valve implantation using self-expanding tissue valve without cardiopulmonary bypass reduces operation time and blood product use. *J Thorac Cardiovasc Surg*. 2013;145:1040–5. <https://doi.org/10.1016/j.jtcvs.2012.05.036>.
  45. Elsayed A, Gilbert K, Scadeng M, Cowan BR, Pushparajah K, Young AA. Four-dimensional flow cardiovascular magnetic resonance in tetralogy of Fallot: a systematic review. *J Cardiovasc Magn Reson*. 2021;23(1):59. <https://doi.org/10.1186/s12968-021-00745-0>.
  46. Taylor AM. The role of artificial intelligence in paediatric cardiovascular magnetic resonance imaging. *Pediatr Radiol*. 2021;52(11):2131–8. <https://doi.org/10.1007/s00247-021-05218-1>.
  47. Geva T, Mulder B, Gauvreau K, et al. Preoperative predictors of death and sustained ventricular tachycardia after pulmonary valve replacement in patients with repaired tetralogy of Fallot enrolled in the INDICATOR cohort. *Circulation*. 2018;138(19):2106–15. <https://doi.org/10.1161/CIRCULATIONAHA.118.034740>.





# Ebstein's Anomaly and Other Tricuspid Valve Anomalies

# 10

Steve W. Leung and Mushabbar A. Syed

## 10.1 Introduction

Tricuspid valve is affected by a wide variety of abnormalities both congenital and acquired. The clinical impact of these abnormalities also varies widely depending upon the lesion and its impact on right heart function. Congenital anomalies of the tricuspid valve are rare and include:

- Ebstein's anomaly
- Tricuspid atresia
- Tricuspid stenosis/hypoplasia
- Tricuspid regurgitation

Among all congenital tricuspid valve defects, tricuspid atresia is more common and is usually diagnosed at or soon after birth. Ebstein's anomaly is less common, and due to its variable, clinical presentation may not be diagnosed until adulthood.

**Supplementary Information** The online version contains supplementary material available at [https://doi.org/10.1007/978-3-031-29235-4\\_10](https://doi.org/10.1007/978-3-031-29235-4_10).

S. W. Leung  
Division of Cardiovascular Disease, Department of Medicine and Radiology, University of Kentucky, Lexington, KY, USA  
e-mail: [steve.leung@uky.edu](mailto:steve.leung@uky.edu)

M. A. Syed (✉)  
Cardiovascular Imaging, Division of Cardiology,  
Loyola University Medical Center, Maywood, IL, USA  
e-mail: [masyed@lumc.edu](mailto:masyed@lumc.edu)

## 10.2 Tricuspid Valve Anatomy

The tricuspid valve is the largest of the four cardiac valves and is located between the right atrium and right ventricle. The tricuspid valve complex consists of leaflets, the fibrous tricuspid annulus, the chordae tendinae, papillary muscles, and the right atrial and right ventricular (RV) myocardium. The tricuspid annulus is an asymmetric, saddle-shaped ellipsoid that is dynamic in nature and can change markedly with loading conditions and during cardiac cycle, e.g., 30% decrease in annular area during systole [1]. Leaflets are usually semicircular or triangular and are attached to the annulus at their base. Typically, tricuspid valve consists of three leaflets: anterior or superior, posterior or inferior, and septal with anterior leaflet being the largest and most mobile while septal being the smallest and least mobile. Septal leaflet lies against the septum and is apically displaced from the mitral annulus. Variations in the structural orientation of tricuspid leaflets and occurrence of accessory leaflets have been reported with one study of 36 adult hearts showed that the number of leaflets can vary from routine three to as many seven [2]. The anterior papillary muscle provides chordae to the anterior and posterior leaflets, and the medial papillary muscle provides chordae to the posterior and septal leaflets. The septal wall gives chordae to the anterior and septal leaflets without the presence of a formal septal papillary muscle.

## 10.3 Ebstein's Anomaly

Ebstein's anomaly is a rare congenital heart disease that affects approximately 1 in 200,000 live births and <1% of all congenital heart diseases [3]. The anomaly was originally described in 1866 by Dr. Wilhelm Ebstein in a patient with progressive tricuspid insufficiency due to a congenital malformation [4]. Until 1950s, the diagnosis of Ebstein's anomaly was mainly based on autopsy findings. It was not



until 1951 when Soloff et al. first described a method of diagnosing Ebstein's anomaly while the patient is still alive by invasive angiogram [5]. In the 1970s, with the development of M-mode, two-dimensional, and Doppler echocardiography, echocardiography became the primary modality in diagnosing Ebstein's anomaly [6]. However, echocardiography is highly dependent on operator experience, the availability of good acoustic windows, and spatial resolution distal to the probe. Due to the position of the right ventricle being directly behind the sternum and its complex geometry, imaging the right ventricle with echocardiogram is often difficult (Movie 10.1).

Over the past two decades, cardiac magnetic resonance imaging (CMR) has emerged as a versatile technique for the assessment of cardiac function, morphology, vascular anatomy, and flow in patients with congenital heart disease. Patients who have limited echocardiographic windows can have clearer pictures with CMR, and the right ventricle can be visualized more easily. Quantification of right ventricular volume and function and identification of other associated lesions can be obtained within the same imaging session in the management of this special population.

## 10.4 Definition

Ebstein's anomaly encompasses a wide spectrum of anatomic and functional abnormalities of the morphologic tricuspid valve and right ventricle. The classic description involves the apical displacement of basal attachments of the septal and posterior leaflets of tricuspid valve secondary to failed delamination of the tricuspid valve leaflets from the endocardium during fetal development leading to atrialization of the right ventricle. Apical displacement of the septal leaflet of  $>20$  mm or  $\geq 8$  mm/m<sup>2</sup> indexed to body surface area relative to the mitral valve in the apical four-chamber view is considered diagnostic [6].

## 10.5 Morphology

Ebstein's anomaly is characterized by the congenital malformations of the right ventricle and tricuspid valve. These malformations include adherence of the septal and posterior leaflets to the myocardium, apical displacement of the tricuspid annulus, redundancy/fenestration and tethering of the anterior leaflet, dilation of the atrialized portion of the right ventricle, and dilation of the right atrioventricular (AV) junction [7]. The posterior leaflet is the most frequently affected leaflet, followed by the septal and anterior leaflets. Depending on the severity of the tethering, patients can present as a neonate or late into adult life. Due to the developmental malformation of the tricuspid valve, patients can

have tricuspid regurgitation or occasionally tricuspid stenosis.

The amount of tethering also determines whether the valve can be repaired or replaced by the Carpentier classification [8].

- Type A: right ventricular volume is adequate.
- Type B: large atrialized right ventricle with mobile anterior leaflet of the tricuspid valve.
- Type C: severely restricted anterior leaflet of the tricuspid valve.
- Type D: almost complete atrialization of the right ventricle except for a small infundibular component.

Patients with Type A, B, and C leaflets are likely to benefit from surgical repair. Type D patients require valve replacement.

## 10.6 Associated Anomalies

The most common anomaly associated with Ebstein's anomaly is interatrial connection such as atrial septal defects and patent foramen ovale, which occurs in upwards of 80% of patients with Ebstein's anomaly. There are numerous other abnormalities that are associated with Ebstein's anomaly aside from atrial septal defects (Table 10.1). Ebstein's anomaly, generally an isolated process, has been described in patients with Down's syndrome, Marfan syndrome, Noonan syndrome, and left ventricular (LV) non-compaction.

**Table 10.1** Anatomical anomalies associated with Ebstein's anomaly

<i>Septal defects</i>
Atrial septal defect
Patent foramen ovale
Ventricular septal defect
<i>Aortic valve/aorta</i>
Bicuspid or atretic aortic valve
Aortic coarctation
Subaortic stenosis
Corrected transposition of the great arteries
Patent ductus arteriosus
<i>Pulmonic valve/pulmonary artery</i>
Pulmonary stenosis
Pulmonary atresia
Hypoplastic pulmonary arteries
Hypertensive pulmonary vascular disease
<i>Mitral valve</i>
Parachute mitral valve
Cleft anterior leaflet of the mitral valve
Mitral valve prolapse
<i>Other</i>
Left ventricular outflow obstruction
Tetralogy of Fallot
Left ventricular non-compaction

## 10.7 Clinical Presentation

Due to the wide spectrum of the severity of the tricuspid malformation, clinical presentation can range from intra-uterine fetal demise to incidental finding in an asymptomatic adult patient. Patients who present during their first year of life usually have more severe cardiac disease and present with severe heart failure and cyanosis. In contrast, children and adults more often present with incidental murmurs and arrhythmias such as Wolff–Parkinson–White syndrome [9].

Symptomatic patients may present with right ventricular failure from worsening tricuspid regurgitation and atrial arrhythmia. Common presenting symptoms include:

- Dyspnea on exertion
- Fatigue and lack of appetite
- Abdominal distention due to ascites
- Peripheral edema
- Palpitations

Due to the high prevalence of septal defects, patients may present later in life with pulmonary hypertension, paradoxical emboli, and Eisenmenger physiology.

The electrocardiogram in patients with Ebstein's anomaly often has interventricular conduction delay or right bundle branch block. The P-waves may indicate marked right atrial enlargement often described as Himalayan P-waves. Since there is a higher prevalence of pre-excitation in this population, delta waves can be seen in some patient's ECGs. Due to the atrialization of the right ventricle, right ventricular hypertrophy is rare and if present other associated anomalies should be considered.

Most cases of Ebstein's anomaly discovered have been sporadic, but there have been some familial cases. Neonates whose mothers were exposed to lithium have been reported to develop Ebstein's anomaly.

## 10.8 Cardiac Magnetic Resonance Imaging

### 10.8.1 Indications

Echocardiography has been the main tool in the diagnosis of Ebstein's anomaly. However, in patients with poor echocardiographic windows, CMR can be an alternative method in making the diagnosis. In patients with known Ebstein's anomaly, CMR can provide valuable information in quantifying right ventricular size and function, along with severity of tricuspid regurgitation. Serial CMR can be performed to serially monitor right ventricular size and function, as well as severity of tricuspid regurgitation. Since patients with Ebstein's anomaly often have other associated anomalies,

CMR can provide great visualization of great vessel abnormalities and quantify intracardiac shunt ratio. Per the most recent ACC/AHA guidelines, serial CMR is recommended to follow these patients. The interval varies based on the patient's physiologic stage of disease.

### Physiologic Stages A–D

Frequency of testing	Stage A (mo)	Stage B (mo)	Stage C (mo)	Stage D (mo)
TTE	12–24	12–24	12	12
CMR/CCT	60	36	24–36	12–24

Physiological stage	
A	NYHA I symptoms
	No hemodynamic or anatomic sequelae
	No arrhythmias
	Normal exercise capacity
	Normal renal/hepatic/pulmonary function
B	NYHA II symptoms
	Mild hemodynamic sequelae (mild aortic enlargement, mild ventricular enlargement, mild ventricular dysfunction)
	Mild valvular disease
	Trivial or small shunt (not hemodynamically significant)
	Arrhythmia not requiring treatment
	Abnormal objective cardiac limitation to exercise
C	NYHA III symptoms
	Significant (moderate or greater) valvular disease; moderate or greater ventricular dysfunction (systemic, pulmonic, or both)
	Moderate aortic enlargement
	Venous or arterial stenosis
	Mild or moderate hypoxemia/cyanosis
	Hemodynamically significant shunt
	Arrhythmias controlled with treatment
	Pulmonary hypertension (less than severe)
	End-organ dysfunction responsive to therapy
D	NYHA IV symptoms
	Severe aortic enlargement
	Arrhythmias refractory to treatment
	Severe hypoxemia (almost always associated with cyanosis)
	Severe pulmonary hypertension
	Eisenmenger syndrome
	Refractory end-organ dysfunction

<sup>a</sup>Adapted from 2018 ACC/AHA Guideline for the Management of Adults with Congenital Heart Disease [10]

### 10.8.2 Goals of Imaging

1. To determine the extent of apical displacement of the tricuspid valve and assess mobility of the anterior leaflet (Carpentier classification)
2. To accurately assess right ventricular size and function
3. To identify tricuspid regurgitation and quantify severity
4. To identify associated lesions such as atrial septal defect, ventricular septal defect, and calculate the amount of shunt (Qp:Qs ratio)
5. To determine aortic or pulmonary artery anomalies
6. To identify right ventricular outflow tract obstructions

### 10.8.3 CMR Sequences and Imaging Protocols

A sample CMR scanning protocol is listed in Table 10.2.

#### 10.8.3.1 Scout Imaging

Scout imaging in various planes can help quickly identify any significant right ventricular enlargement and any apparent associated lesions in the aorta or pulmonary artery such as coarctation or hypoplastic pulmonary artery. Since most patients who present have enlarged right heart, the cardiac anatomy is likely to be distorted. The scout images can then help with accurate prescription of the long- and short-axis cines and ensure adequate coverage of the ventricles for quantification of size and function.

#### 10.8.3.2 Cine Imaging—Diagnosis, Chamber Size and Function, and Septal Defects

For the diagnosis of Ebstein's anomaly, four-chamber steady-state free precession (SSFP) cine can identify the extent of apical displacement of the tricuspid valve compared to the mitral valve (Fig. 10.1 and Movie 10.2). The diagnosis can be made if the apical displacement of the tricuspid valve compared to the mitral valve is  $>20$  mm or  $\geq 8$  mm/m<sup>2</sup> indexed to body surface area. The identification of the tricuspid leaflets and the amount of tethering can be useful in determining type of surgical treatment. However, due to the complex shape and thin tricuspid valve leaflet and relatively limited spatial resolution of CMR, it may be difficult to visualize leaflet adherence to the myocardium.

The short-axis cines from base to apex are routinely used for calculating LV and RV size and function (Fig. 10.2) [11]. Alternatively, axial plane cines can also be used for calculating RV size and function; however, the method of acquiring RV size and function in serial follow-up studies should be consistent with the first study [12].

To identify septal defects, four-chamber stack of cines through the atrial and ventricular septum extending from the superior vena cava to the level of atrioventricular (AV) valves should be obtained for interatrial or interventricular connections (Fig. 10.3).

#### 10.8.3.3 In Plane Phase Contrast Imaging: Evaluation of Abnormal Flow

SSFP cine imaging can often miss valvular regurgitation or flow through septal defects as the sequence is designed to suppress flow for better delineation of endocardial borders. Therefore, ECG-gated, free-breathing, in-plane phase contrast imaging can be helpful in clearly identifying any tricuspid regurgitation or flow through septal defects in patients with Ebstein's anomaly. Qualitatively, tricuspid regurgitation can be evaluated by in-plane phase contrast imaging in the four-chamber view or right atrial/ventricular two-chamber view with the axis parallel to the predicted tricuspid regurgi-

**Table 10.2** Imaging protocol example

• Scout (localizers) scan: in three-plane (axial, sagittal, and coronal), axial stack, four-chamber, short-axis plane
• SSFP cine images:
Short-axis, multislice stack from base to apex
Three-chamber, two-chamber, four-chamber views
Two-chamber of the right atrium/right ventricle
LVOT and RVOT
Four-chamber view, stack for full volume coverage (for identification of septal defects)
<i>Optional: axial plane, cine stack from top to bottom of the right ventricle</i>
• First pass contrast-enhanced MRA of pulmonary arteries and aorta
• In-plane phase contrast flow imaging (ECG-gated, free-breathing)
Four-chamber view
LVOT
RVOT
<i>Optional: two-chamber view of the right atrium/ventricle</i>
• Through-plane phase contrast imaging (ECG-gated, free-breathing) of the main pulmonary artery (Qp) and ascending aorta (Qs)
• Late gadolinium enhancement imaging in short-axis stack, two-chamber, three-chamber, four-chamber views (usually 10–20 min post-contrast)
• <i>Optional: through-plane phase contrast of static gel phantom with identical acquisition parameters as Qp and Qs</i>

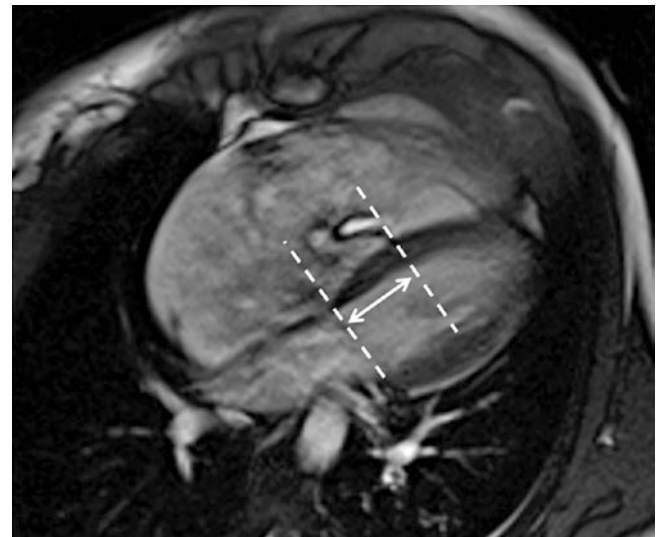


**Fig. 10.1** Still frame in an SSFP four-chamber view shows the apical displacement (*double arrow*) of the tricuspid valve compared to the mitral valve. End-diastolic frame is used for measuring the apical displacement

tant jet (Movie 10.3). The velocity encoding (VENC) setting should be at least 150 cm/s. For septal defects, the appropriate four-chamber view of the suspected area of the defect should be evaluated with in-plane phase contrast. Due to slow flow in the atrium, the VENC setting is usually set at 50–100 cm/s. Since patients with Ebstein's anomaly can also have left or right ventricular outflow tract (LVOT or RVOT)



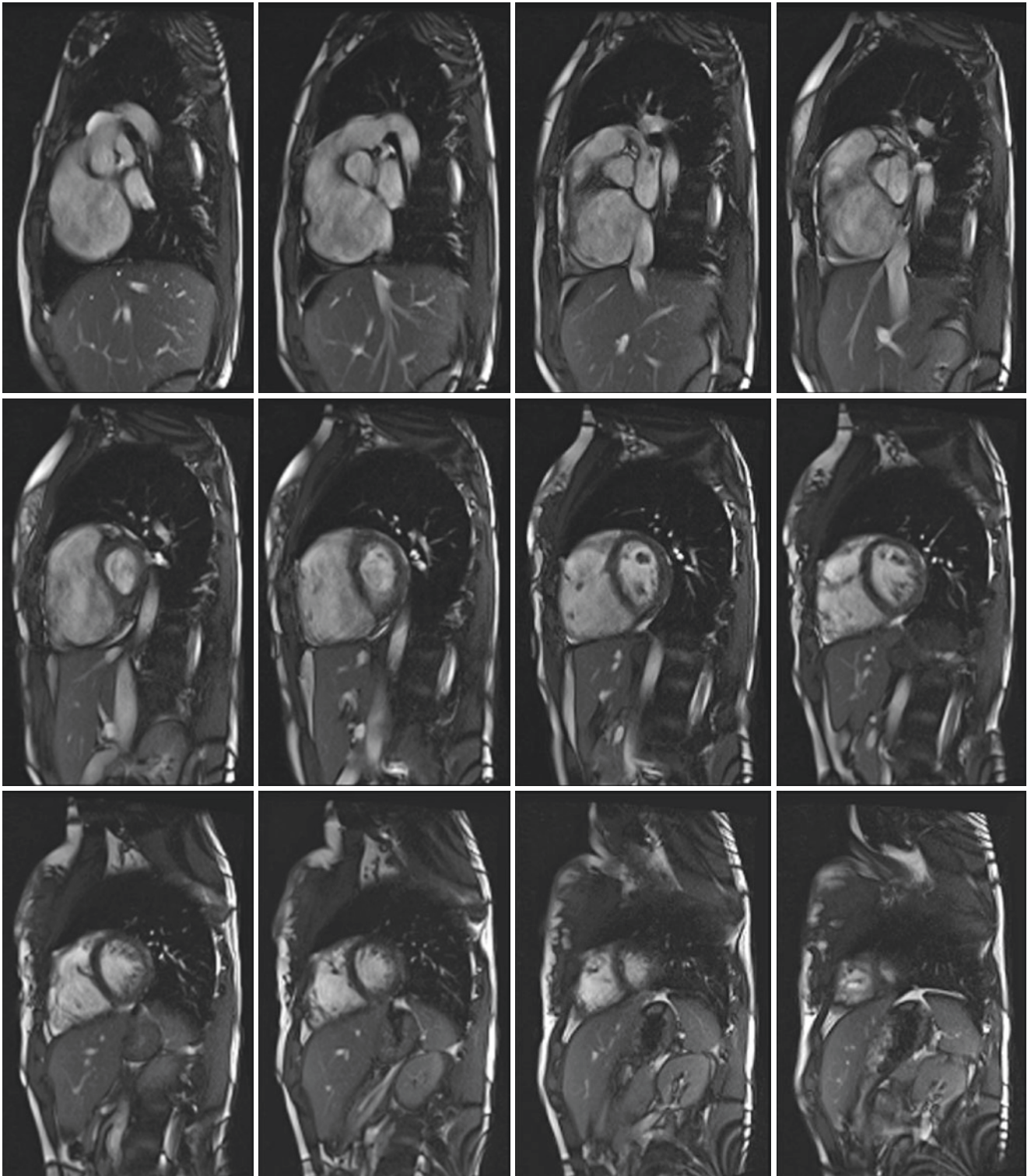


**Fig. 10.2** Still frame of short-axis stack for evaluation of ventricular size and function



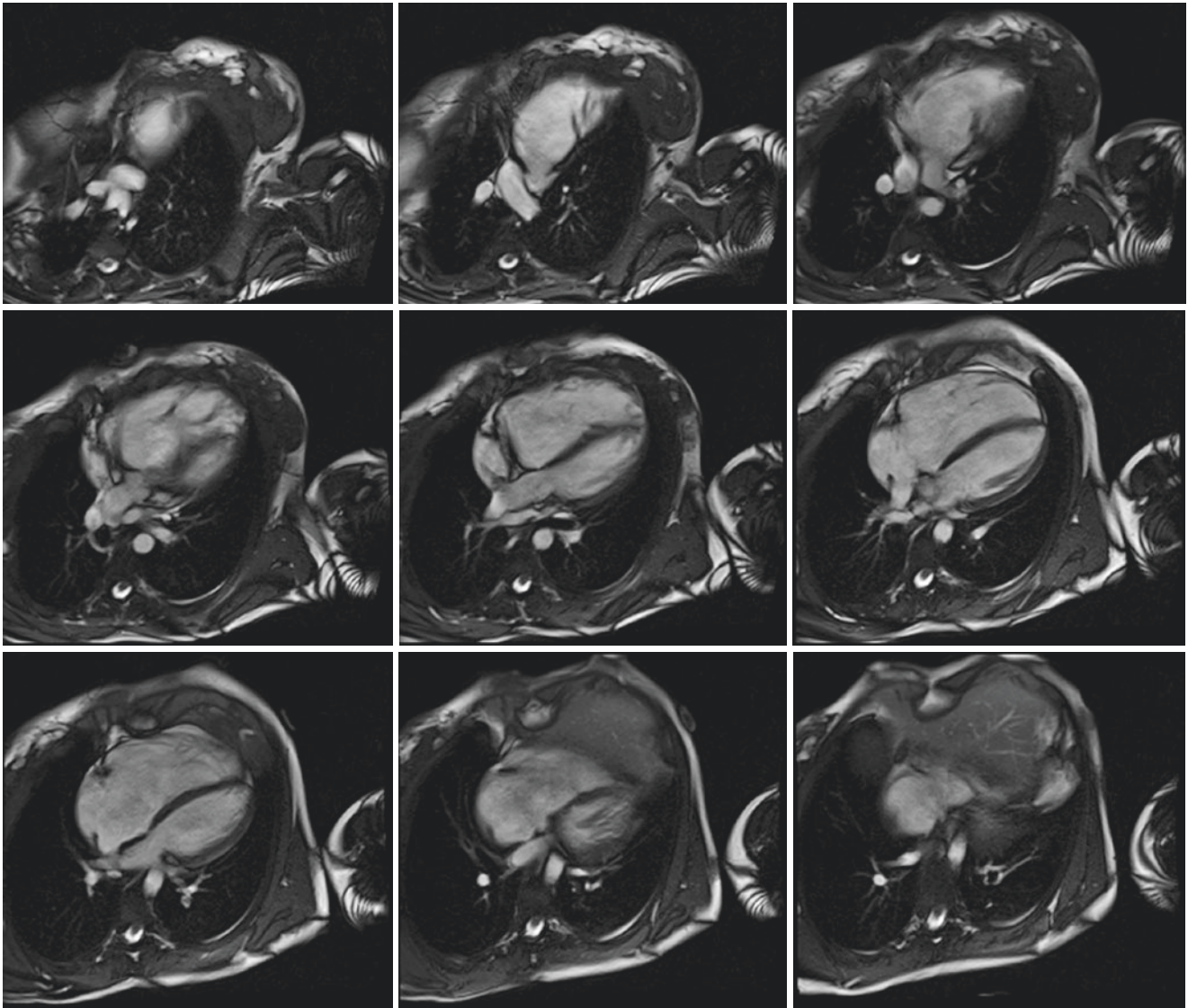


**Fig. 10.3** Still frame of four-chamber stack for evaluation of septal defects

obstruction, LVOT and RVOT in-plane phase contrast can help identify any significant turbulent flow suggestive of obstruction across the outflow tracts (Fig. 10.4 and Movie 10.4).

Occasionally, patients with Ebstein's anomaly have tricuspid stenosis. Severe tricuspid stenosis has been identified as a right atrium to right ventricle gradient of  $>5$  mmHg during diastole by Doppler echocardiography. In-plane phase contrast imaging in a four-chamber or right-sided two-chamber orientation can identify increased velocity through the tricuspid valve during diastole as a sign of tricuspid stenosis. Initial VENC of 100 cm/s should be used. If the jet aliases during diastole, then the gradient across the tricuspid valve is  $>4$  mmHg by using the simplified Bernoulli's equation ( $\text{gradient} = 4v^2$ ). Be aware that in patients with significant tricuspid regurgitation that there can be increased

velocities or gradients due to increase flow, and not due to anatomic tricuspid stenosis.

#### 10.8.3.4 Through-Plane Phase Contrast: Quantification of Tricuspid Regurgitation

Patients with Ebstein's anomaly often develop significant tricuspid regurgitation. In echocardiography, severe tricuspid regurgitation is determined by color jet size, vena contracta width  $>0.7$  cm<sup>2</sup>, and systolic reversal of flow in the hepatic veins. In CMR, there have not been established criteria for severe tricuspid regurgitation; however, in general, valvular regurgitant fraction  $>40\%$  is considered severe. Unlike the aortic and pulmonic valves, the tricuspid annulus goes through significantly complex motion during systole, which renders direct measurements by through-plane phase con-



**Fig. 10.4** Still frame of right ventricular outflow tract SSFP cine for evaluation of right ventricular outflow tract obstruction

trast CMR of the tricuspid valve difficult. For best results, a short-axis plane can be prescribed using four-chamber cine SSFP to align the imaging plane with the valve annulus at end-systole. Additionally, the tricuspid regurgitant volume and regurgitant fraction can be measured indirectly from effective pulmonary flow and right ventricular stroke volume.

Effective pulmonary flow ( $Q_p$ ) can be obtained by ECG-gated, free-breathing, through-plane phase contrast imaging of the main pulmonary artery cross section above the pulmonary valve. Often, this prescription can be obtained from a perpendicular slice from the right ventricular outflow tract view (sagittal plane) above the pulmonary valve (Fig. 10.5) starting at VENC of 150 cm/s. The resultant velocity images should be immediately assessed for aliasing (low VENC setting) and repeated if necessary by increasing the VENC setting. Also check the magnitude images for appropriate vessel shape (arteries should be round) and phase wrap artifacts. Phase wrap does not significantly affect the precision of the measurements as long as wrap is not superimposed on the vessel of interest. Right ventricular stroke volume (RVSV) is obtained by subtracting the right ventricular end-systolic

volume (RVESV) from the right ventricular end-diastolic volume (RVEDV). RVESV and RVEDV are obtained from either the short-axis stack or axial stack SSFP cine images. Tricuspid regurgitant volume ( $RV_{TR}$ ) can then be calculated by:

$$RV_{TR} = Q_p - (RVEDV - RVESV) = Q_p - RVSV.$$

Regurgitant fraction (RF) can be obtained by:

$$RF\% = (RV_{TR} / RVSV) \times 100\%.$$

This method can only be used if there is no interventricular shunt.

Without phase contrast flow measurements,  $RV_{TR}$  can also be calculated by:

$$RV_{TR} = RVSV - (LVEDV - LVESV) = RVSV - LVSV.$$

This can only be performed if there are no other significant valvular regurgitations (aortic, mitral, or pulmonic) or interventricular shunt.

#### 10.8.3.5 Through-Plane Phase Contrast: Quantification of Shunt Ratio

Since patients with Ebstein's anomaly frequently have associated atrial or ventricular septal defects, shunt ratio quantification ( $Q_p/Q_s$ ) can be helpful in determining need for closure of these defects. Shunt ratio quantification should be obtained from through-plane phase contrast.

$Q_p$  prescription has been described above. Through-plane phase contrast of an appropriate axial slice above the aortic valve can be obtained for effective systemic flow ( $Q_s$ ) (Fig. 10.6). The VENC for flow measurement in ascending aorta is usually set at 200 cm/s.

With phase contrast imaging, flow acquisition can be erroneous due to background phase offset errors from non-compensated eddy currents [13]. This error can be corrected by obtaining phase contrast images from static gel phantoms post-acquisition with heart rate simulator simulating a heart rate similar to the time of  $Q_p$  and  $Q_s$  acquisition or background phase correction based on a regional of interest in the static chest wall. The correction should then be used to adjust the original data. It's important to note that the table position should not be reset prior to obtaining the phantom images, as this can cause positioning errors in finding the original flow positions and acquisition of the correct background phase offset errors.

#### 10.8.4 Contrast-Enhanced Magnetic Resonance Angiography

Patients with Ebstein's anomaly can have associated pulmonary artery or aortic anomalies. Contrast-enhanced magnetic



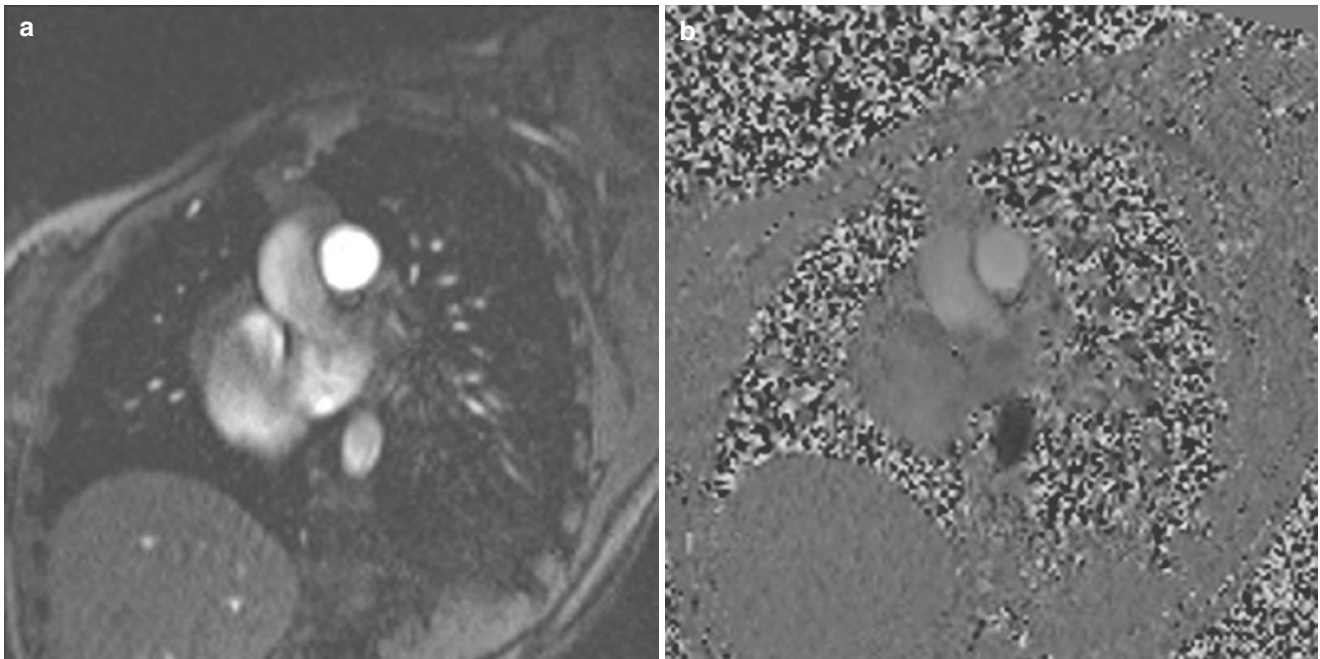


**Fig. 10.5** Still frame of the main pulmonary artery just above the pulmonic valve for effective pulmonary flow ( $Q_p$ ) quantification. (a) Magnitude image for anatomy and (b) is corresponding phase image. Vessel of interest should be circular to quantify flow

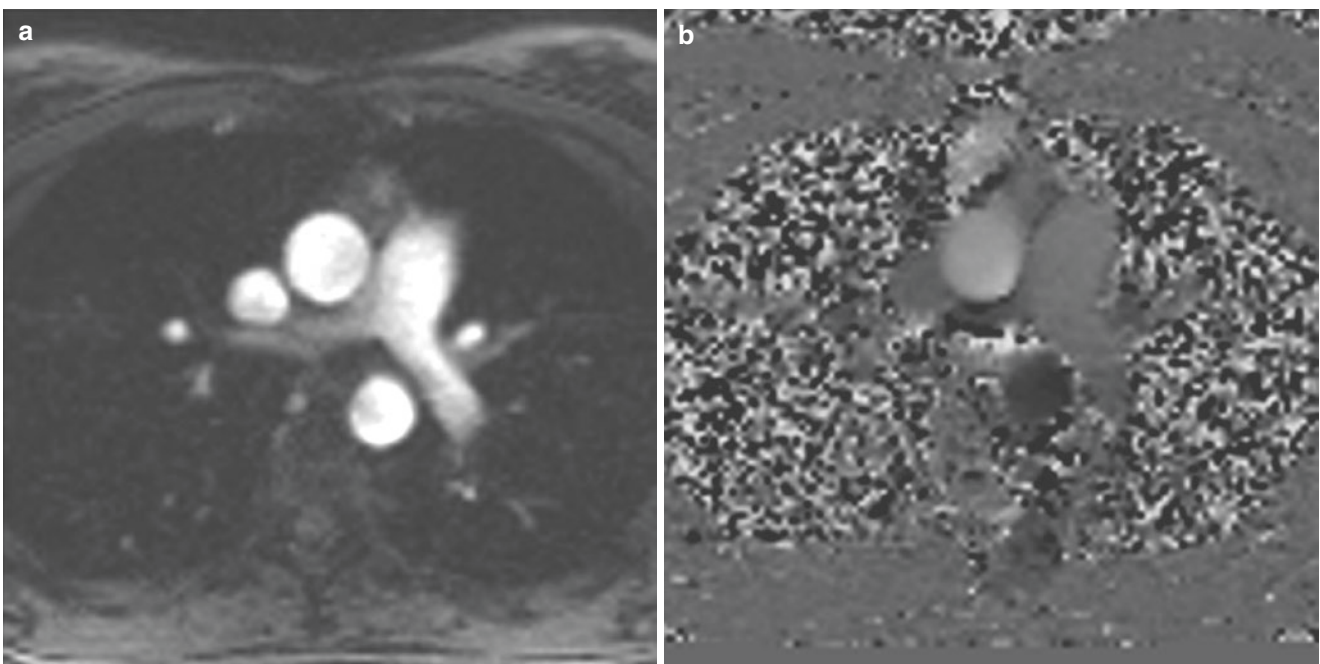


**Fig. 10.6** Still frame of the ascending aorta at pulmonary artery bifurcation for effective systemic flow ( $Q_s$ ) quantification. (a) Magnitude image for anatomy and (b) is corresponding phase image. Vessel of interest should be circular to quantify flow

resonance angiography (MRA) can provide a three-dimensional view to detect hypoplastic pulmonary arteries, coarctation of the aorta, and transposition of the great arteries. It can also provide accurate vascular measurements for planning surgical treatment of these anomalies.

### 10.8.5 Late Gadolinium Enhancement Imaging

Late gadolinium enhancement imaging has been quite useful in detecting scar or fibrosis in patients with myocardial infarction and various cardiomyopathies. In patients with Ebstein's anomaly, late gadolinium enhancement can be used to identify fibrotic changes of the atrialized ventricular wall [14]. RV septal late gadolinium enhancement and elevated LV extracellular volume in patients with Ebstein's anomaly are associated with worse LV and RV function and NYHA class [15]. In patients with tricuspid stenosis or right ventricular dysfunction, late gadolinium imaging can also identify right atrial and right ventricular thrombus.

## 10.9 CMR in Comparison with Other Imaging Modalities

Echocardiography remains the primary method of diagnosing Ebstein's anomaly and identifying tricuspid leaflet deformities for possible surgical correction. Due to the higher spatial resolution, the tethering of the tricuspid leaflet can be more easily identified. Doppler echocardiography can also be helpful in evaluation of tricuspid regurgitation severity. However, in cases where there are limited acoustic windows and/or poor spatial resolution in deep structures, CMR is helpful in providing essential information. Since structures are more clearly defined and volumetric measurements are more reliable and reproducible than echocardiography, CMR is important in serial imaging to follow patients with established diagnosis of Ebstein's anomaly. Since patients with Ebstein's anomaly may have various associated vascular anomalies, CMR can help identify these other findings that may have been missed on echocardiography.

With the development of multi-slice computed tomography (CT) with electrocardiographic gating, CT scan has also become useful in evaluation of congenital heart disease. Since cardiac CT can provide excellent spatial resolution, complete volumetric coverage, and functional analysis, it can be a valuable tool when echocardiography and CMR cannot be performed adequately. This can be due to inadequate acoustic windows or suboptimal right ventricular visualization for echocardiography, contraindication to CMR due to metallic implants, patients unable to lay flat for pro-

longed periods of time, or unable to hold their breaths repeatedly. However, at this time, cardiac CT cannot adequately quantify the amount of tricuspid regurgitation unless there is no other concomitant valvular regurgitation or intracardiac shunts. Since cardiac function evaluation with CT requires high doses of radiation, this should be limited to as the last resort especially in young patients or women of child-bearing age.

## 10.10 Limitations and Common Pitfalls

For patients with Ebstein's anomaly who are referred for CMR imaging, prior imaging studies should be reviewed to develop a plan of scanning to reduce scanning time. One of the limitations of CMR is that image acquisition can take a prolonged period of time. Some patients are unable to tolerate such prolonged scans due to claustrophobia, fatigue, back pain, or other issues. If a patient has known atrial septal defect that has been adequately evaluated by echocardiography, one can consider skipping the four-chamber cine stack. If a patient does not have RVOT or LVOT obstruction on Doppler echocardiography, one can consider skipping these imaging planes to reduce acquisition time.

Other limitations include patient cooperation in following breathing commands, which can limit the clarity in the SSFP cine images and late gadolinium enhancement images. The spatial resolution limits visualization of the tricuspid valve leaflet as clearly as echocardiography. Despite the common use of phase contrast for flow measurements, it is important to perform background offset error correction to obtain more accurate flow quantification data.

## 10.11 Tricuspid Atresia

Tricuspid atresia is a form of cyanotic congenital heart disease characterized by the complete agenesis of the tricuspid valve. In a 2019 study, it was estimated that about 404 babies in the United States are born with tricuspid atresia with an incidence of 1 in every 9751 live births [16]. In the current era, the majority of patients are diagnosed during pregnancy or soon after birth with echocardiogram as the first-line imaging modality. In most patients, the tricuspid inlet appears as a dimple in the right atrium, and in rare form, there is fusion of partial delaminated leaflets and the formation of membrane (Ebstein type). Tricuspid atresia is associated with hypoplastic right ventricle, atrial septal defect, ventricular septal defect, and pulmonary obstruction. This lesion has been classified based on the relationship of the great arteries, presence of a VSD and degree of pulmonary obstruction [17].



- Type I (70–80%): Normal anatomy of the great arteries
- Subgroup a—Intact ventricular septum with pulmonary atresia
  - Subgroup b—Small VSD with pulmonary stenosis (PS)/ hypoplasia
  - Subgroup c—Large VSD without PS
- Type II (12–25%): D-transposition of the great arteries (D-TGA)
- Subgroup a—VSD with pulmonary atresia
  - Subgroup b—VSD with PS or hypoplasia
  - Subgroup c—VSD without PS
- Type III (3–6%): Malposition defects of the great arteries other than D-TGA (e.g., truncus arteriosus, atrioventricular septal defects, and double outlet right ventricle)

Echocardiography is diagnostic for tricuspid atresia with limited role for other imaging modalities. CMR is primarily used in the follow-up of these patients after Fontan surgery and is discussed in detail in the Single Ventricle and Fontan Procedures chapter.

## 10.12 Other Tricuspid Valve Anomalies

Isolated congenital tricuspid stenosis is an extremely rare congenital heart malformation. The condition is a result of hypoplasia and thickening of the tricuspid valve, deformity of the chordae, or malformation of the entire subvalvular apparatus including parachute valve [18]. It is commonly associated with patent foramen ovale or atrial septal defect [19–21]. They are also associated with right-sided hypoplasia including right ventricular hypoplasia and pulmonic stenosis or atresia. SSFP cine in the long-axis views of the right atrium/right ventricle can be helpful in identifying the cause of tricuspid stenosis (Fig. 10.7 and Movie 10.5). The tricuspid gradient can be identified by ECG-gated, free-breathing, in-plane phase contrast imaging in the long axis through the tricuspid valve as described above. Due to the tricuspid annular plane systolic excursion, multiple cross sections through the tricuspid valve with no skip may be required to obtain a planimetry of the valve opening and optimal through-plane phase contrast to obtain the maximal gradient through the valve. A short-axis plane using four-chamber cine SSFP to align the imaging plane with the valve annulus at end-systole usually provides the best result for gradient estimation.

Congenital tricuspid regurgitation is generally due to Ebstein's anomaly. Isolated congenital tricuspid regurgitation is even less common. The valvular insufficiency can be caused by tricuspid leaflet prolapse, hypoplastic or cleft leaflets, absence of papillary muscle or chordae, or annular dilation [21–24]. Functional causes include right ventricular outflow tract obstruction or right ventricular dysfunction [18].

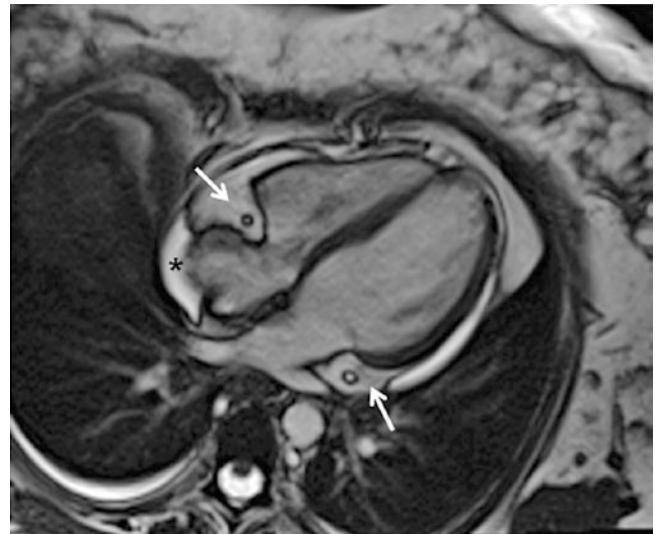


**Fig. 10.7** Still frame of four-chamber SSFP cine demonstrating small tricuspid valve annulus. There is small pericardial effusion (*asterisk*) and prominent intrapericardial fat (*arrows*)

In these patients, CMR can be used to calculate regurgitant volume and fraction similar to the methods mentioned in Ebstein's anomaly. SSFP cine imaging of the tricuspid valve in long-axis views can be helpful in identifying tricuspid valve prolapse and other causes of tricuspid regurgitation. Right ventricular volumes can also be followed over time.

The role of CMR in these cases is similar to patients with Ebstein's anomaly. In patients who do not have optimal acoustic windows for echocardiography, the need to evaluate other associated anomalies, or serial follow-up of right-sided volumes, CMR can be beneficial.

## 10.13 Conclusions

Ebstein's anomaly and congenital tricuspid anomalies are rare congenital heart defects that affect less than 1% of all congenital heart diseases. Although echocardiography is the primary modality for diagnosis of these rare anomalies, it is limited in evaluation of the right ventricular size and function. Adult patients who present with little to no symptoms would need to be followed for years prior to the necessary surgical correction due to right ventricular enlargement and failure. CMR not only provides the capability to diagnose these rare anomalies but also can provide accurate serial measurements of right ventricular volume and function and severity of tricuspid regurgitation. Many of these patients also present with various associated anomalies that can be detected readily by a comprehensive CMR study. In patients with associated shunts, quantification of pulmonary artery to aorta flow ratio ( $Q_p/Q_s$ ) can be performed to assess the severity of these shunts.

## Practical Pearls

- Review of prior imaging studies (especially echocardiographic images) is extremely helpful in planning scanning protocol to minimize scan time.
- Echocardiography is usually the first-line imaging modality for the diagnosis of tricuspid valve anomalies. CMR has a complimentary role for the evaluation of right ventricle and other associated anomalies.
- CMR can be used to evaluate tricuspid valvular regurgitation/stenosis, accurate measurements of right and left ventricular size and function, associated anomalies such as septal defects and great vessel abnormalities, and quantification of shunt ratio.
- Serial CMR imaging for assessment of right ventricular size and function should be performed in the same orientation as the initial study (short-axis stack or axial plane stack cines).
- Interatrial and interventricular communication can be difficult to see on SSFP cine images. ECG-gated, free-breathing, in-plane phase contrast flow imaging is helpful in these situations.
- 3D contrasted MRA can be helpful in defining any aortic or pulmonary artery abnormalities.
- Flow quantification for Qp, Qs, and tricuspid regurgitation measurements should be carefully planned.

## References

1. Yucel E, Bertrand PB, Churchill JL, Namasivayam M. The tricuspid valve in review: anatomy, pathophysiology and echocardiographic assessment with focus on functional tricuspid regurgitation. *J Thorac Dis.* 2020;12:2945–54.
2. Lama P, Tamang BK, Kulkarni J. Morphometry and aberrant morphology of the adult human tricuspid valve leaflets. *Anat Sci Int.* 2016;91:143–50.
3. Attenhofer Jost CH, et al. Ebstein's anomaly. *Circulation.* 2007;115(2):277–85.
4. Ebstein W. Ueber einen sehr seltenen fall von insuffizienz der valvula tricuspidatis, bedingt durch eine angeborene hochgradige Missbildung derselben. *Arch Anat Physiol.* 1866;33:238–54.
5. Soloff LA, Stauffer HM, Zatuchni J. Ebstein's disease: report of the first case diagnosed during life. *Am J Med Sci.* 1951;222(5):554–61.
6. Shiina A, et al. Two-dimensional echocardiographic spectrum of Ebstein's anomaly: detailed anatomic assessment. *J Am Coll Cardiol.* 1984;3(2 Pt 1):356–70.
7. Edwards WD. Embryology and pathologic features of Ebstein's anomaly. *Prog Pediatr Cardiol.* 1993;2(1):5–15.
8. Carpentier A, et al. A new reconstructive operation for Ebstein's anomaly of the tricuspid valve. *J Thorac Cardiovasc Surg.* 1988;96(1):92–101.
9. Celermajer DS, et al. Ebstein's anomaly: presentation and outcome from fetus to adult. *J Am Coll Cardiol.* 1994;23(1):170–6.
10. Stout KK, Daniels CJ, Aboulhosn JA, et al. 2018 AHA/ACC Guideline for the Management of Adults With Congenital Heart Disease: A Report of the American College of Cardiology/American Heart Association Task Force on Clinical Practice Guidelines. *Circulation.* 2019;139(14):e698–e800
11. Grothues F, et al. Interstudy reproducibility of right ventricular volumes, function, and mass with cardiovascular magnetic resonance. *Am Heart J.* 2004;147(2):218–23.
12. Alfakih K, et al. Comparison of right ventricular volume measurements between axial and short axis orientation using steady-state free precession magnetic resonance imaging. *J Magn Reson Imaging.* 2003;18(1):25–32.
13. Holland BJ, Printz BF, Lai WW. Baseline correction of phase-contrast images in congenital cardiovascular magnetic resonance. *J Cardiovasc Magn Reson.* 2010;12:11.
14. Nakamura I, et al. Ebstein anomaly by cardiac magnetic resonance imaging. *J Am Coll Cardiol.* 2009;53(17):1568.
15. Yang D, Li X, Sun JY, Cheng W, Greiser A, Zhang TJ, Liu H, Wan K, Luo Y, An Q, Chung YC, Han Y, Chen YC. Cardiovascular magnetic resonance evidence of myocardial fibrosis and its clinical significance in adolescent and adult patients with Ebstein's anomaly. *J Cardiovasc Magn Reson.* 2018;20(1):69.
16. Mai CT, Isenburg JL, Canfield MA, et al. For the National Birth Defects Prevention Network. National population-based estimates for major birth defects, 2010-2014. *Birth Defects Res.* 2019;111:1–16. <https://doi.org/10.1002/bdr2.1589>.
17. Rao PS. A unified classification of tricuspid atresia. *Am Heart J.* 1980;99:799–804.
18. Dearani JA, Danielson GK. Congenital heart surgery nomenclature and database project: Ebstein's anomaly and tricuspid valve disease. *Ann Thorac Surg.* 2000;69(4 Suppl):S106–17.
19. Chuah SY, Hughes-Nurse J, Rowlands DB. A successful pregnancy in a patient with congenital tricuspid stenosis and a patent oval foramen. *Int J Cardiol.* 1992;34(1):112–4.
20. Khan AN, Boatman J, Anderson AS. Management of new-onset congestive heart failure in a patient with complex congenital heart disease. *Congest Heart Fail.* 2002;8(1):54–6.
21. Krishnamoorthy KM. Balloon dilatation of isolated congenital tricuspid stenosis. *Int J Cardiol.* 2003;89(1):119–21.
22. Kobza R, et al. Aberrant tendinous chords with tethering of the tricuspid leaflets: a congenital anomaly causing severe tricuspid regurgitation. *Heart.* 2004;90(3):319–23.
23. Motoyoshi N, et al. Cleft on tricuspid anterior leaflet. *Ann Thorac Surg.* 2001;71(4):1350–1.
24. Katogi T, et al. Surgical management of isolated congenital tricuspid regurgitation. *Ann Thorac Surg.* 1998;66(5):1571–4.



# Abnormalities of Left Ventricular Inflow and Outflow

# 11

Tal Geva and Puja Banka

## 11.1 Introduction

Congenital abnormalities of left ventricular inflow and outflow include abnormalities of the left atrium, mitral valve (supravalvar, valvar, and subvalvar), and abnormalities of the left ventricular outflow tract, the aortic valve, and supravalvar area. Cardiac magnetic resonance imaging (CMR) has become an important adjunctive tool in evaluating and following patients with this group of anomalies. This chapter reviews the role of CMR in the care of patients with congenital abnormalities of left ventricular inflow and outflow. In addition to describing the morphologic abnormalities and their clinical presentations, the indications and limitations of CMR in each condition are discussed, and a suggested CMR examination protocol is provided.

## 11.2 Abnormalities of Left Ventricular Inflow

### 11.2.1 Left Atrium

#### 11.2.1.1 Definitions

Abnormalities of the left atrium include congenital left atrial aneurysm and cor triatriatum. The former is characterized by intrinsic left atrial enlargement out of proportion to the hemodynamic load on the left atrium. The latter is characterized by a dividing “membrane” within the left atrium resulting in a proximal pulmonary venous chamber and a distal supramitral chamber containing the appendage.

#### 11.2.1.2 Congenital Left Atrial Aneurysm

##### Morphologic and Functional Abnormalities

Congenital left atrial aneurysm is a rare anomaly associated with dysplasia of the left atrial myocardium [1]. This anomaly, also called giant left atrium, is characterized by a markedly dilated left atrium with thinning or partial absence of the myocardium. The left atrial enlargement is out of proportion to its hemodynamic load. The diagnosis is made in the absence of an inflammatory or degenerative process [2].

##### Associated Anomalies

The etiology and morphogenesis of congenital left atrial aneurysm are poorly understood. This lesion is generally found as an isolated condition, and the presence of associated cardiac anomalies that can cause left atrial dilation usually excludes it from the differential diagnosis.

##### Clinical Presentation

Congenital left atrial aneurysm often presents as an incidental finding on radiographic imaging done for other reasons [3]. In some cases, however, patients present with tachyarrhythmias, cardiac arrest, pericardial tamponade from rupture of the aneurysm, systemic embolization of atrial

**Supplementary Information** The online version contains supplementary material available at [https://doi.org/10.1007/978-3-031-29235-4\\_11](https://doi.org/10.1007/978-3-031-29235-4_11).

T. Geva (✉)

Department of Pediatrics, Harvard Medical School,  
Boston, MA, USA

Department of Cardiology, Boston Children’s Hospital,  
Boston, MA, USA  
e-mail: [tal.geva@cardio.chboston.org](mailto:tal.geva@cardio.chboston.org)

P. Banka

Department of Pediatrics, Harvard Medical School, Boston, MA,  
USA

Department of Cardiology, Boston Children’s Hospital,  
Boston, MA, USA  
e-mail: [puja.banka@cardio.chboston.org](mailto:puja.banka@cardio.chboston.org)

thrombi, respiratory distress, or heart failure [2, 4]. Since the aneurysm can increase in size over time, long-term follow-up is generally recommended to monitor its size and associated complications. Surgical resection may be considered, especially in symptomatic patients [2].

### CMR of Congenital Left Atrial Aneurysm

The aneurysm can be visualized by several techniques including transthoracic and transesophageal echocardiogram, computed tomography, and conventional angiography. CMR can be adjunctive to these diagnostic modalities by providing comprehensive visualization of the aneurysm, imaging of adjacent structures, and measurements of the aneurysm volume [2]. Other causes for left atrial enlargement, such as mitral valve abnormalities or intracardiac shunts, can be excluded. In addition, CMR can be used to assess for thrombus within the aneurysm. Indications for CMR in patients with suspected or known congenital left atrial aneurysm include confirmation of the diagnosis, longitudinal assessment of aneurysm size, and evaluation for thrombus within the aneurysm [4]. CMR examination in a patient suspected of having congenital left atrial aneurysm may include the following:

- Electrocardiogram (ECG)-triggered, breath-hold cine steady-state free precession (SSFP) in the following planes:
  - Axial and coronal planes through the entirety of the aneurysm to allow measurements of aneurysm size and visualization of potential thrombi
  - Left ventricle (LV) two-chamber (vertical long-axis)
  - Four-chamber stack (horizontal long-axis)
  - LV three-chamber view parallel to the left ventricular outflow
  - Ventricular short-axis stack with 12–14 equidistant slices covering the entire length of both ventricles to evaluate ventricular volumes and function and to exclude other causes of left atrial enlargement
- ECG-triggered, breath-hold turbo (fast) spin echo sequence with blood suppression for assessment of left atrial wall thickness
- ECG-triggered, free-breathing cine phase contrast flow measurements in the proximal ascending aorta, main pulmonary artery, and, in selected cases, across the atrioventricular (AV) valves to assess for shunts
- ECG-triggered, breath-hold, phase sensitive late gadolinium enhancement (LGE) imaging with a long inversion time (e.g., 600 ms) for evaluation of possible thrombi

When CMR is used to follow patients longitudinally, care must be taken to make measurements of the aneurysm that are comparable from one scan to the next. For linear measurements, therefore, prescribed planes should either be eas-

ily reproducible between scans (e.g., axial or coronal planes), or care should be taken to duplicate the plane used on prior examinations. Alternatively, left atrial volume can be calculated using the summation of discs technique, and this can be followed over time.

### 11.2.1.3 Cor Triatriatum

#### Morphologic and Functional Abnormalities

Cor triatriatum is a rare lesion comprising approximately 0.1–0.4% of congenital heart disease cases. The lesion is considered a form of stenosis of the common pulmonary vein due to a fibromuscular “membrane” or “diaphragm” that divides the left atrium into two chambers: a proximal chamber that receives the pulmonary veins and a distal chamber that communicates with the left atrial appendage and the mitral valve (Fig. 11.1; Movies 11.1 and 11.2) [5]. Several developmental theories for this lesion have been proposed, but the most commonly accepted hypothesis is incomplete incorporation of the common pulmonary vein to the posterior aspect of the developing left atrium [5]. Some variants of cor triatriatum, however, are not consistent with this explanation. Examples include cases in which the proximal chamber receives only some of the pulmonary veins, a condition termed subtotal cor triatriatum.

In typical cor triatriatum, the partitioning left atrial membrane forms a windsock, which is directed toward the mitral valve. The opening in the windsock-like membrane varies in size from few millimeters to about 1 cm. The distal chamber that communicates with the left atrial appendage and the mitral valve also has the fossa ovalis lying between it and the right atrium. In most cases, neither the proximal nor the distal chambers communicate with the right atrium. In some cases, the distal (supramitral) chamber communicates with the right atrium through a patent foramen ovale or a secundum atrial septal defect. Rarely, the proximal (pulmonary venous) chamber communicates with the right atrium. In the latter case, the possibility of a sinus venosus defect should be considered.

The hemodynamic burden due to cor triatriatum is obstruction to pulmonary venous return causing pulmonary venous and arterial hypertension. From a hemodynamic standpoint, cor triatriatum can be viewed as a form of mitral stenosis.

#### Associated Anomalies

Cor triatriatum can be seen in isolation or with a number of other congenital heart defects, including partially anomalous pulmonary venous connection and secundum atrial septal defect [5].

#### Clinical Presentation

The clinical presentation of this lesion is similar to that of mitral stenosis and depends on the size of the opening in the membrane separating the two left atrial chambers. Rarely,



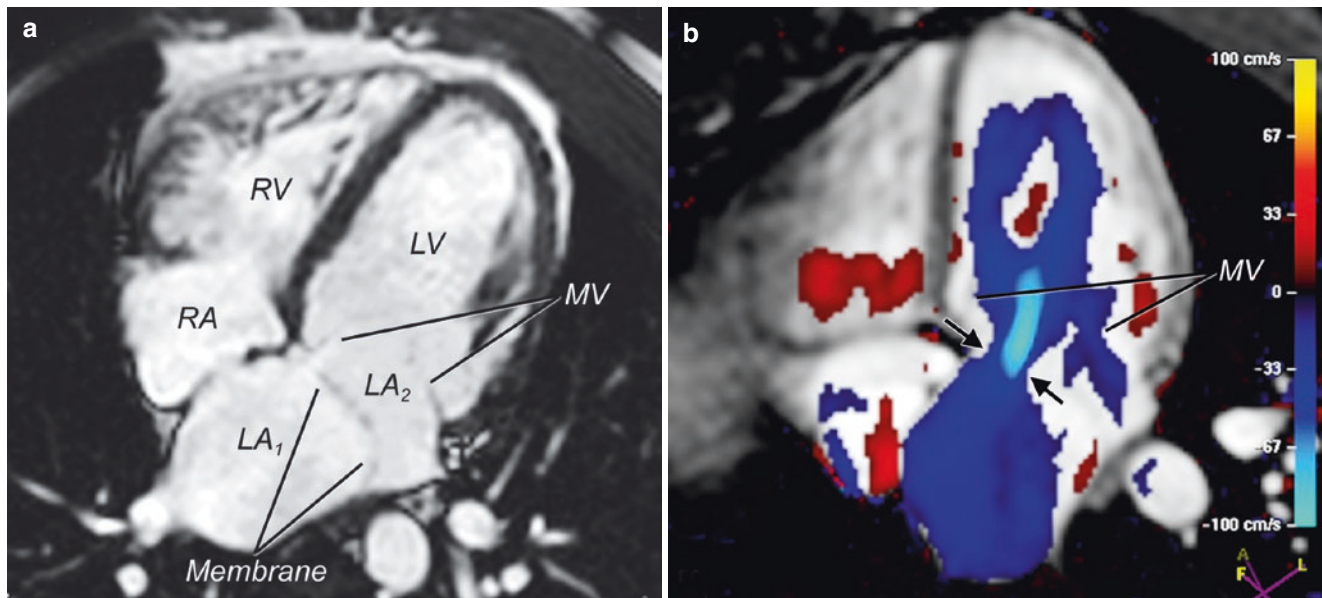


**Fig. 11.1** Cor triatriatum. (a) Cine SSFP image in a four-chamber plane showing the cor triatriatum membrane dividing the left atrium into two chambers, a proximal chamber that receives the pulmonary veins ( $LA_1$ ) and a distal chamber that communicates with the mitral

valve and left atrial appendage ( $LA_2$ ). (b) In-plane cine phase contrast flow mapping in the four-chamber plane demonstrating flow across the defect in the cor triatriatum membrane (arrows). LV left ventricle, MV mitral valve, RA right atrium, RV right ventricle

the pulmonary venous chamber can decompress through a defect between the proximal chamber and the right atrium. When the communication between the two left atrial chambers is small, patients develop signs and symptoms of pulmonary venous obstruction such as pulmonary edema and hypertension or decreased cardiac output. If, however, the opening is large, symptoms may be minimal or absent. Older patients can also exhibit embolic phenomenon from thrombus formation in the atrium.

### CMR of Cor Triatriatum

Given its ubiquitous availability, excellent spatial and temporal resolutions, and its ability to evaluate the hemodynamic burden of cor triatriatum by Doppler, echocardiography is the primary imaging modality used in this condition. CMR can be helpful in two circumstances: (1) as a substitute for transesophageal echocardiography in patients with poor acoustic windows when transthoracic echocardiography does not provide adequate data [6] and (2) to evaluate associated defects such as anomalous pulmonary venous connections [7]. CMR can also be used to measure intracardiac shunts, as well as right ventricular size and function. The following CMR examination protocol can be used in patients with cor triatriatum:

- ECG-triggered, breath-hold cine SSFP in the following planes:
  - LV two-chamber (vertical long-axis)
  - Right ventricle (RV) two-chamber (vertical long-axis)

- Extended four-chamber covering the entire left atrium (Fig. 11.1a; Movie 11.1)
- LV three-chamber view parallel to the left ventricular outflow
- Ventricular short-axis stack to evaluate ventricular volumes and function
- Gadolinium-enhanced magnetic resonance angiogram (MRA) to assess for anomalous pulmonary venous connections and other associated anomalies
- ECG-triggered, free-breathing cine phase contrast flow measurements in the proximal ascending aorta, main pulmonary artery, and, in selected cases, across the AV valves to assess for shunts. In-plane flow velocity mapping in the four-chamber plane can provide additional information regarding the location and size of the opening within the cor triatriatum membrane (Fig. 11.1b; Movie 11.2).
- Optional sequences:
  - ECG-triggered, breath-hold turbo (fast) spin echo sequence with blood suppression for further imaging of the cor triatriatum membrane
  - ECG-triggered, respiratory-navigated, free breathing three-dimensional isotropic SSFP for evaluation of the coronary arteries
  - In patients with possible myocardial scar, LGE imaging performed 10–20 min after contrast administration in the following planes: ventricular short-axis, four-chamber, LV two- and three-chamber, and RV two-chamber

## 11.2.2 Mitral Valve

### 11.2.2.1 Definitions

The normal mitral valve has a saddle-shaped annulus, two leaflets with a larger anterior and a smaller posterior leaflet, and primary and secondary chordal attachments to two left ventricular papillary muscles. Each of these components of the valve apparatus plays an important role in valve function, and abnormalities at any level of the valve can result in obstruction to inflow (mitral stenosis) or to incompetence (mitral regurgitation).

### 11.2.2.2 Mitral Stenosis

#### Morphologic and Functional Abnormalities

Congenital mitral stenosis comprises a diverse group of valve morphologies, function, and natural history and is often associated with additional left heart obstructive lesions [8, 9]. Common to all forms of congenital mitral stenosis is anatomic abnormality of one or more components of the valve anatomy leading to narrowing of left ventricular inflow. Abnormalities at any level of the valve apparatus can result in obstruction to left ventricular inflow.

- *Supramitral stenosis*: In this anomaly, fibrous tissue develops on the left atrial aspect of the mitral annulus and leaflets, resulting in a restricted inflow orifice and thickened, poorly mobile leaflets [10, 11]. The fibrous tissue often adheres to the atrial surface of the valve leaflets, and the location of the effective flow orifice varies between the annular plane and the leaflet tips.
- *“Typical” congenital mitral stenosis*: This anatomic variant involves the valve leaflets, chordae tendineae, and papillary muscles. The leaflets are thickened and can be myxomatous, the leaflet margins are rolled, the chordae tendineae are short (in some cases the leaflets insert directly onto the papillary muscles), the interchordal spaces are narrowed, and the papillary muscles are closely spaced and can be displaced toward the base of the ventricle (Fig. 11.2; Movie 11.3) [11, 12].
- *Parachute mitral valve*: All chordae tendineae insert into a single papillary muscle head, forming a parachute-like deformity (Fig. 11.3) [12]. A second, usually hypoplastic, papillary muscle may be present but does not receive chordae tendineae. In patients without an AV canal defect, the posteromedial muscle usually receives the chordae tendineae, and the anterolateral papillary muscle is either absent or underdeveloped. In patients with an AV canal defect, the anterolateral papillary muscle is usually dominant [11].
- *Mitral arcade*: This rare anomaly consists of short, thick, and poorly differentiated chordae tendineae with fusion between the papillary muscles and the thickened, myxo-

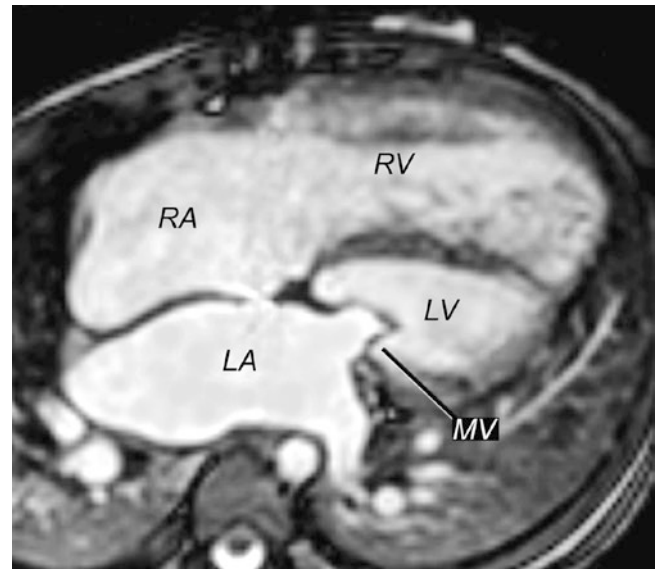


**Fig. 11.2** Congenital mitral stenosis. Cine SSFP image in a four-chamber plane showing a hypoplastic mitral valve annulus with thickened leaflets and restricted leaflet motion (MV). The left ventricle (LV) is also hypoplastic. LA left atrium, RA right atrium, RV right ventricle

matous, and rolled leaflet margins. The interchordal spaces are either completely or nearly completely obliterated with a bridge of fibrous tissue between the papillary muscles [13–15]. The valve annulus size is usually normal. The mitral valve in this anomaly has also been described as “hammock valve.”

- *Double-orifice mitral valve*: An abnormal tensor apparatus can result in two or more functional orifices of the mitral valve. This anomaly is often associated with common AV canal but can be seen in isolation or with other congenital heart defects. The hemodynamic implications of double-orifice mitral valve are variable, depending on associated abnormalities of the valve and its tensor apparatus [16]. In some patients, this is an incidental finding with no mitral stenosis or regurgitation.

#### Associated Anomalies

Mitral stenosis is seldom an isolated anomaly. Although it has been reported in association with almost any other cardiac anomaly, mitral stenosis is most often accompanied by other left heart obstructive lesions, including left ventricular outflow tract obstruction, aortic stenosis, coarctation, and left ventricular hypoplasia [11].

#### Clinical Presentation

The clinical presentation and course of congenital mitral stenosis are highly variable and depend on the degree of obstruction and the presence, type, and severity of associated cardiovascular anomalies [9]. Patients with mild congenital

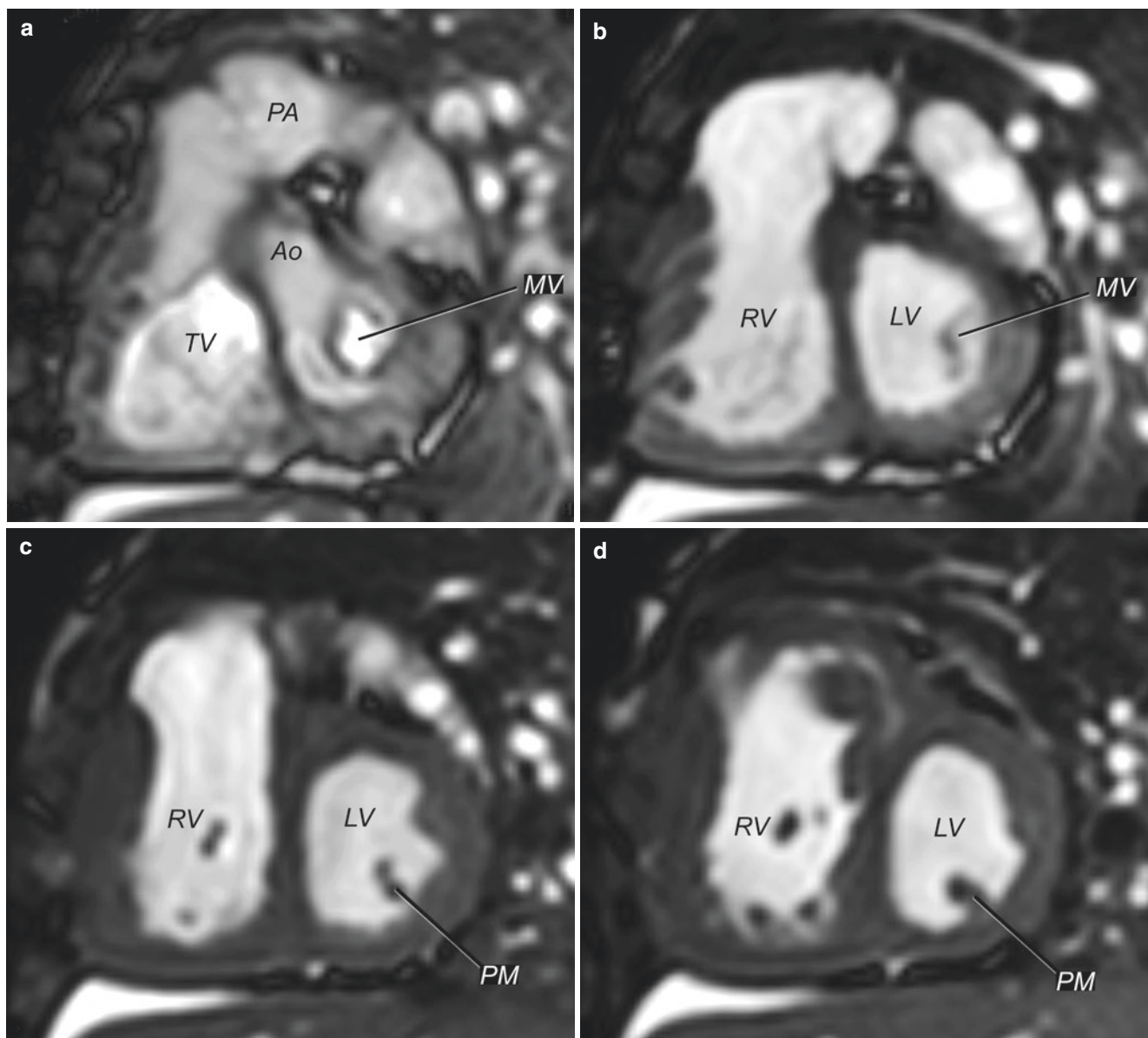


**Fig. 11.3** Parachute mitral valve. Contiguous slices (a–d) from a cine SSFP ventricular short-axis stack showing a hypoplastic mitral valve (MV) with attachments to a single, dominant posteromedial papillary

muscle (PM). The anterolateral papillary muscle is poorly developed. Ao aorta, LV left ventricle, PA pulmonary artery, RV right ventricle, TV tricuspid valve

mitral stenosis may be asymptomatic, and the lesion may not progress. Patients with moderate or severe mitral stenosis exhibit signs and symptoms of left atrial and pulmonary hypertension, including tachypnea and dyspnea, pulmonary edema, and poor growth. Manifestations of long-standing mitral stenosis include hemoptysis, supraventricular tachyarrhythmias, and right heart failure related to severe pulmonary hypertension. When present, associated left heart obstructive lesions such as left ventricular outflow obstruction, coarctation of the aorta, left ventricular hypoplasia, and endocardial fibroelastosis play an important role in determining the clinical course and prognosis.

### CMR of Mitral Stenosis

Echocardiography is the primary diagnostic tool in the evaluation of congenital mitral stenosis. The benefit of CMR is as an adjunctive technique, particularly in patients with poor acoustic windows, to assess valve morphology [17], evaluate the hemodynamic burden on the atria and ventricles, and assess associated anomalies and for longitudinal follow-up. There is also some experience in adults in using CMR to assess the severity of mitral stenosis. One report utilized CMR for mitral valve planimetry in patients with rheumatic heart disease [18]. Another report found good correlation between velocity-encoded cine phase contrast flow and



Doppler echocardiography in the assessment of transmitral peak velocity [19]. Published data in patients with congenital mitral stenosis are limited [17], and these techniques have not yet been validated for infants and children. Small structures, multilevel obstructions, and fast heart rates are some of the challenges in the pediatric age group.

The goals of CMR in patients with congenital mitral stenosis include detailed evaluation of mitral valve morphology (annulus, leaflets, chordae tendineae, and papillary muscles), mitral valve function (stenosis and regurgitation), left atrial size, left ventricular size and function, presence and severity of associated anomalies (e.g., subvalvar aortic stenosis, coarctation, endocardial fibroelastosis), degree of pulmonary hypertension, and right ventricular size and function. These objectives can be realized with the following CMR examination protocol:

- ECG-triggered, breath-hold cine SSFP in the following planes:
  - LV two-chamber (vertical long-axis)
  - RV two-chamber (vertical long-axis)
  - Extended four-chamber covering the entire mitral valve
  - LV three-chamber view parallel to the left ventricular outflow
  - Ventricular short-axis stack to evaluate ventricular volumes and function
- Gadolinium-enhanced 3D MRA to assess for coarctation of the aorta and other associated anomalies
- ECG-triggered, free-breathing cine phase contrast flow measurements in the AV valves, proximal ascending aorta, and main pulmonary artery. In-plane flow velocity mapping in the ventricular long-axis plane across the mitral valve can provide additional information about location of flow acceleration within the mitral valve.
  - Flow velocity mapping in a short-axis plane of the mitral valve is hampered by through-plane annular motion in the base-to-apex direction. For best results, we prescribe the short-axis plane using a four-chamber cine SSFP to align the imaging plane with the valve annulus at end-systole.
- Optional sequences:
  - ECG-triggered, breath-hold turbo (fast) spin echo sequence with blood suppression in patients with metallic artifacts from implanted devices and to visualize supramitral stenotic tissue.
  - ECG-triggered, respiratory-navigated, free breathing three-dimensional isotropic SSFP for evaluation of the coronary arteries.
  - In patients with suspected endocardial fibroelastosis (Fig. 11.4), LGE imaging in the ventricular short-axis, four-chamber, and LV two- and three-chamber planes.

### 11.2.2.3 Mitral Regurgitation

#### Morphologic and Functional Abnormalities

Isolated congenital mitral regurgitation is rare. In the majority of cases, mitral regurgitation is found in association with other congenital or acquired cardiovascular anomalies. As with obstructive lesions, mitral regurgitation can result from abnormalities at any level of the valve apparatus.

- *Annular dilatation*: This is a common mechanism contributing to mitral regurgitation in patients with left ventricular dilatation due to chronic volume load (e.g., left-to-right shunt through a ventricular septal defect or patent ductus arteriosus, aortic regurgitation) or dilated cardiomyopathy. In addition to preventing systolic coaptation between the anterior and posterior leaflets, left ventricular dilatation also causes displacement of the papillary muscles, which further contributes to mitral regurgitation.
- *Congenital perforation*: This rare anomaly comprises a congenital defect within one of the leaflets of the mitral valve resulting in regurgitation [20].
- *Mitral arcade*: As described in the section on mitral stenosis, mitral arcade can also result in regurgitation [15].
- *Cleft mitral valve*: A cleft refers to a split anterior leaflet with each component of the leaflet attaching to a different papillary muscle group (Fig. 11.5; Movies 11.4 and 11.5) [21]. It is differentiated from a commissure in that the latter is defined as a split between leaflets with both leaflets attaching to the same papillary muscle. Although, in most cases, cleft anterior mitral leaflet is associated with one of several types of common AV canal (e.g., primum atrial septal defect and complete common AV canal), it can rarely present either as an isolated anomaly or in association with cardiac defects other than AV canal (e.g., conotruncal anomalies) [21]. Regurgitation typically emanates from the region of the cleft itself.
- *Mitral valve prolapse*: Although mitral valve prolapse usually presents in adolescents and adults, it can infrequently manifest in infancy and childhood [22]. In most cases, mitral valve prolapse is associated with one of several forms of connective tissue disorder (e.g., Marfan syndrome and Ehlers–Danlos syndrome). Elongated chordae tendineae and redundant, myxomatous leaflets characterize mitral valve prolapse (Fig. 11.6; Movies 11.6 and 11.7). Regurgitation results from ineffective coaptation between the anterior and posterior leaflets. In severe cases, ruptured chordae result in a flail leaflet and severe regurgitation.
- *Papillary muscle dysfunction*: Mitral regurgitation can result from papillary muscle dysfunction due to myocardial ischemia or infarction. Examples include congenital anomalies such as anomalous origin of the left coronary



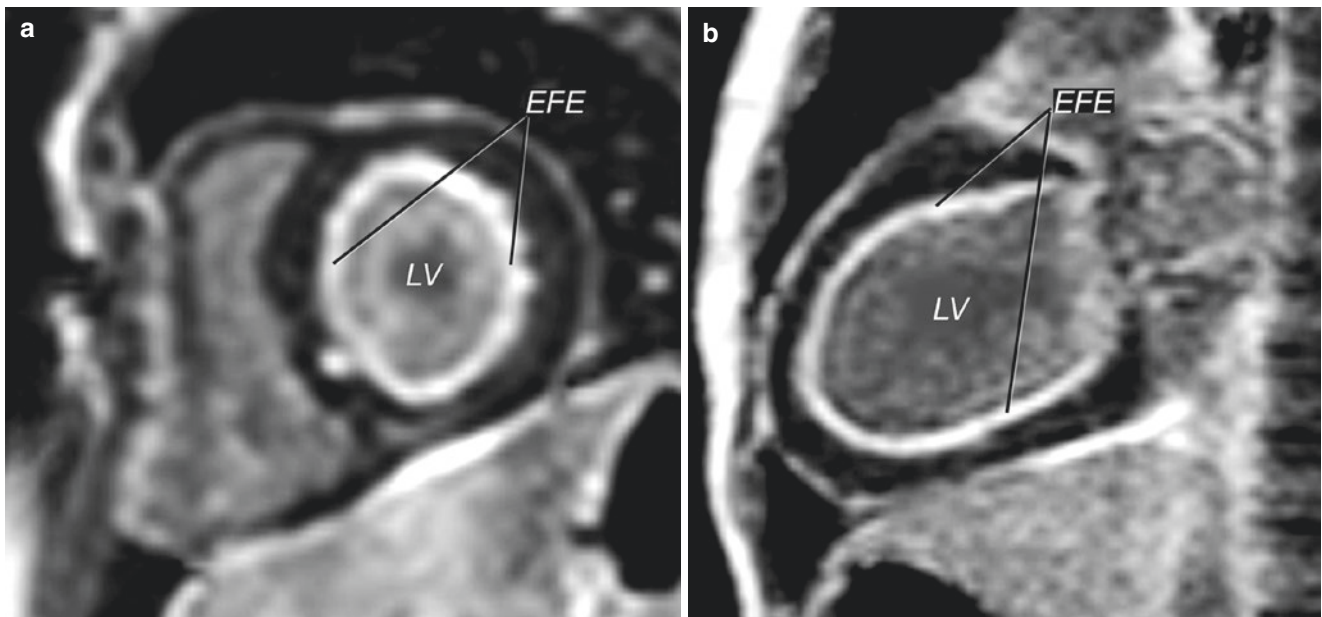


**Fig. 11.4** Endocardial fibroelastosis. Late gadolinium enhancement (LGE) imaging in a ventricular short-axis (a) and left ventricular two-chamber (b) planes showing hyperenhancement along the endo-

cardial surface of the left ventricle (LV) consistent with endocardial fibroelastosis (EFE)

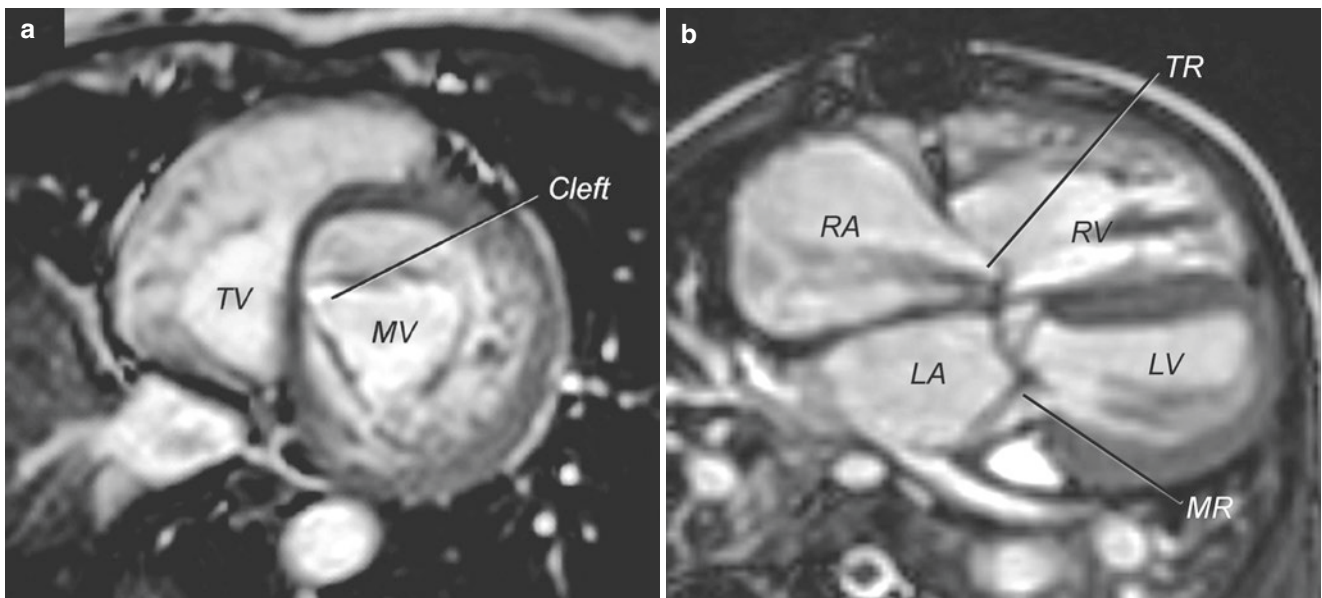


**Fig. 11.5** Cleft mitral valve. Cine SSFP images in a ventricular short-axis plane (a) showing a cleft in the anterior leaflet of the mitral valve extending to the ventricular septum. On four-chamber views (b) in a patient after atrioventricular canal defect repair, there is a posteriorly

directed mitral regurgitation jet (MR) through a residual cleft and a medial tricuspid regurgitation jet (TR). LA left atrium, LV left ventricle, MV mitral valve, RA right atrium, RV right ventricle, TV tricuspid valve

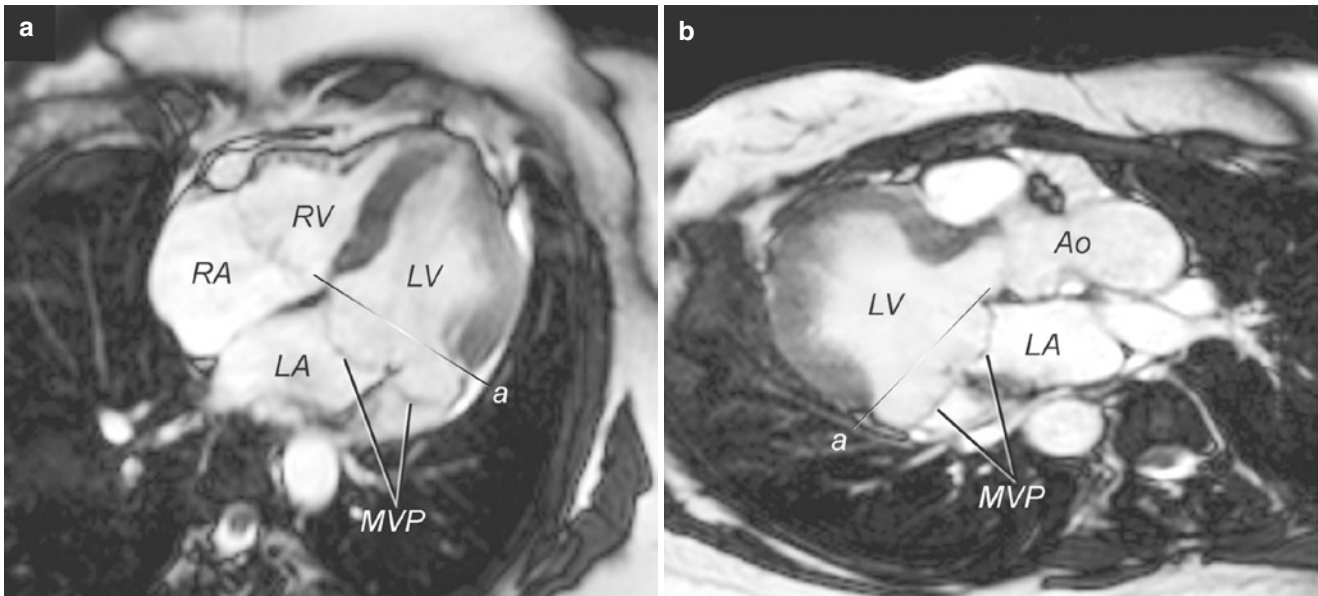


**Fig. 11.6** Mitral valve prolapse. Cine SSFP images in four-chamber (a) and ventricular three-chamber (b) planes showing bileaflet mitral valve prolapse (MVP) past the plane of the annulus aorta (Ao) (a) and

associated jet of mitral regurgitation. LA left atrium, LV left ventricle, RA right atrium, RV right ventricle

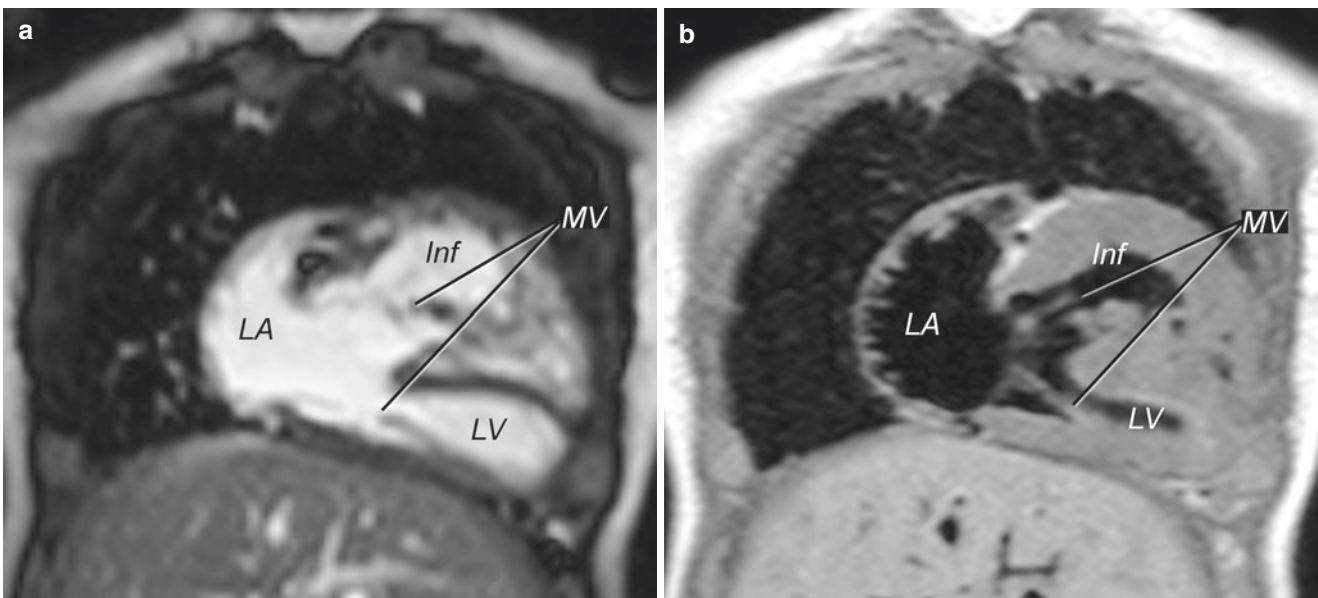


**Fig. 11.7** Straddling mitral valve. Cine SSFP (a) and turbo (fast) spin echo (b) images in a coronal plane in a patient with superior–inferior ventricles and a horizontal ventricular septum. The mitral valve (MV)

overrides the septum and has straddling attachments to the right ventricular infundibulum (Inf). LA left atrium, LV left ventricle

artery from the main pulmonary artery [23] and acquired conditions such as coronary insufficiency due to complications of Kawasaki disease [24].

- **Straddling mitral valve:** This anomaly is defined as having attachments of the mitral valve chords to both sides of the interventricular septum (Fig. 11.7). The mitral valve straddles the ventricular septum through an anterior, outlet ventricular septal defect, and usually a conoventricular-

type defect. The straddling portion of the valve attaches to the infundibular portion of the right ventricle [25]. Frequently, the anterior leaflet is divided by an accessory commissure [25]. The degree of mitral regurgitation is usually mild.

In addition to congenital anomalies of the mitral valve, mitral regurgitation can complicate the course of acquired

heart disease in children. Examples include endocarditis, systemic lupus erythematosus, and drug-induced valvulitis.

### Associated Anomalies

Cleft mitral valve is usually associated with primum atrial septal defect or other forms of common AV canal defect, a topic covered elsewhere in this book. Straddling mitral valve is associated with conotruncal anomalies such as transposition of the greater arteries or double-outlet right ventricle. It is also found in complex anomalies in which the ventricles are malposed, resulting in superior–inferior ventricles with or without crisscross atrioventricular relations [25, 26]. Fraiese et al. found dextrocardia in 6 of 46 cases of straddling mitral valve (13%) [25].

### Clinical Presentation

The clinical manifestations of mitral regurgitation depend on the severity and duration of the regurgitation and on associated anomalies. Patients with mild regurgitation may be asymptomatic with only a holosystolic high-frequency murmur at the cardiac apex. Severe acute mitral regurgitation generally presents with signs and symptoms of acute left atrial hypertension such as pulmonary arterial hypertension and edema, dyspnea or respiratory failure, left ventricular dysfunction, and decreased cardiac output. With chronic mitral regurgitation, the symptoms are more gradual in onset, occurring once ventricular dysfunction and/or pulmonary hypertension occurs. Supraventricular tachyarrhythmias can also complicate the clinical course of patients with mitral regurgitation.

### CMR of Mitral Regurgitation Lesions

CMR is a particularly useful tool for quantitative assessment of the degree of mitral regurgitation and the hemodynamic load on the left ventricle and atrium. The ability to measure flow rates and biventricular volumes allow CMR to provide quantitative information that is not readily or reliably available by echocardiography. In the absence of intracardiac shunts or additional regurgitant lesions, mitral regurgitation volume and fraction can be calculated either by comparison of ventricular stroke volumes, AV valve inflows (Fig. 11.8), mitral versus aortic or pulmonary valve flows, or a combination of these measurements. Assessment of mitral regurgitation volume and fraction by several methods is recommended so that results can be compared for consistency.

Although data in children are limited, studies in adults have shown that CMR-derived mitral inflow and regurgitation values are highly reproducible [27, 28] and correlate well with other noninvasive [29] and invasive [30] measures of regurgitation. There has also been some interest in calculating anatomic regurgitant orifice for longitudinal follow-up using CMR flow mapping in adults [31], but the utility of this technique in pediatric patients has not been evaluated.

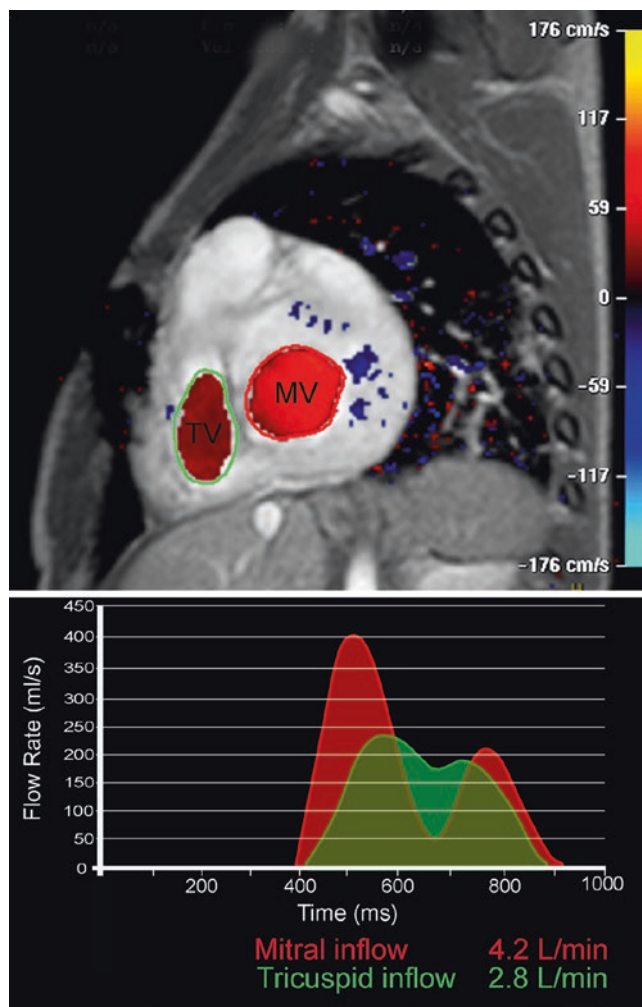


**Fig. 11.8** Measurement of mitral regurgitation. *Top panel:* Cine phase contrast through-plane flow mapping perpendicular to the atrioventricular valve inflows. A region of interest is prescribed encompassing the mitral (red) and tricuspid (green) valve inflows. *Bottom panel:* For each AV valve, the area under the diastolic phase of the cardiac cycle represents the antegrade flow across that valve, in this case, 4.2 L/min across the mitral and 2.8 L/min across the tricuspid valve, respectively. Mitral regurgitation fraction is calculated as follows:  $(\text{mitral inflow} - \text{tricuspid inflow}) / \text{mitral inflow} \times 100 = 33\%$ . *MV* mitral valve, *TV* tricuspid valve

The goals of CMR in patients with mitral regurgitation include evaluation of valve morphology and function, measurements of the hemodynamic burden (mitral regurgitation volume and fraction, left ventricular size and function, and left atrial size), and assessment of associated anomalies. These objectives can be realized with the following CMR examination protocol:

- ECG-triggered, breath-hold cine SSFP in the following planes:
  - LV two-chamber (vertical long-axis)
  - Extended two-chamber covering the entire mitral valve.



- LV two-chamber view parallel to the left ventricular outflow.
- Ventricular short-axis stack to evaluate ventricular volumes and function.
- Additional cine SSFP acquisitions for evaluation of mitral valve leaflets or subvalvar support apparatus
- ECG-triggered, free-breathing cine phase contrast flow measurements in the AV valves, proximal ascending aorta, and main pulmonary artery. In-plane flow velocity mapping in the ventricular long-axis plane across the mitral valve can provide additional information about location of flow acceleration within a valve.
  - Flow velocity mapping in a short-axis plane of the mitral valve is hampered by through-plane annular motion in the base-to-apex direction. For best results, we prescribe the short-axis plane using a four-chamber cine SSFP to align the imaging plane with the valve annulus at end-systole.
- Optional sequences:
  - Gadolinium-enhanced 3D MRA to assess for associated anomalies of the great vessels and veins

## 11.3 Abnormalities of Left Ventricular Outflow

### 11.3.1 Obstructive Lesions

#### 11.3.1.1 Definition

Obstructive left ventricular outflow lesions include subaortic stenosis, aortic valve stenosis, and supra-avalvar aortic stenosis. Subaortic stenosis is defined as obstruction in the left ventricular outflow below the aortic valve annulus. Aortic valve stenosis occurs at the level of the annulus and leaflets. Supra-avalvar aortic stenosis involves the aortic sinotubular junction and may extend to the ascending aorta.

#### 11.3.1.2 Morphologic and Functional Abnormalities

The left ventricular outflow tract includes the subaortic region, aortic valve, and supra-avalvar area. The subaortic outflow is bound by the membranous and infundibular segments of the ventricular septum and by the anterior leaflet of the mitral valve. In cross section, the geometry of the subaortic outflow is oval. The normal aortic valve consists of three pocket-like cusps, each approximately equal in size with dividing commissures, adhering to a crown shaped fibrous annulus. The normal aortic root, which contains the aortic valve, comprises three sinuses, named sinuses of Valsalva, with the left and right coronary arteries arising from their respective sinuses. The junction between the aortic root and ascending aorta is called the sinotubular junction and is the site of supra-avalvar aortic stenosis. As with the mitral valve,

structural abnormalities causing obstruction of the left ventricular outflow can occur at any level or in combination:

- *Discrete subaortic stenosis*: A fibromuscular “membrane” or “ridge” forms below the aortic valve, sometimes extending up and adherent to the ventricular surface of aortic and mitral valve leaflets (Fig. 11.9). The morphology of the left ventricular outflow is characterized by elongation of the aortic–mitral intervalvular fibrosa and an acute angle between the ventricular septum and proximal ascending aorta (called aorto-septal angle) [32]. The etiology of discrete subaortic stenosis is unknown, but it has been speculated that the aforementioned abnormal geometry of the left ventricular outflow tract results in increased flow shear stress, which can promote proliferation of obstructive fibrous tissue [33, 34].
- *Tunnel-type subaortic stenosis*: The left ventricular outflow tract is diffusely narrowed, usually due to septal hypertrophy, resulting in long-segment obstruction [35]. This lesion can be seen in patients with hypertrophic cardiomyopathy.
- *Subaortic stenosis due to posterior deviation of the conal septum*: In patients with a posterior malalignment conoventricular septal defect, the deviated conal septum protrudes into the subaortic outflow, causing subaortic obstruction [36]. This type of subvalvar aortic stenosis is typically found in patients with type B interrupted aortic arch [37].
- *Subaortic stenosis due to AV valve attachments*: Subvalvar aortic stenosis is seen in some patients with a common AV canal (usually primum atrial septal defect), isolated cleft mitral valve and transposition of the great arteries or double-outlet right ventricle, straddling mitral valve, and, rarely, straddling tricuspid valve.
- *Valvar aortic stenosis*: Decreased effective aortic valve flow area can result from annular hypoplasia, leaflet thickening, and commissural underdevelopment and/or fusion. In most cases of congenital aortic valve stenosis, the mechanism of obstruction includes a combination of these abnormalities. Unicommissural or bicommissural aortic valves are common variants of congenital aortic stenosis (Fig. 11.10; Movies 11.8 and 11.9) [38–40].
- *Supra-avalvar aortic stenosis*: Supra-avalvar aortic stenosis is located above the level of the aortic valve, most commonly at the sinotubular junction (Fig. 11.11; Movie 11.10) [41].

#### 11.3.1.3 Associated Anomalies

Left ventricular outflow tract obstruction is often seen in conjunction with other left heart obstructive lesions such as mitral stenosis, coarctation, or Shone syndrome. Discrete subvalvar aortic stenosis is associated with aortic valve stenosis (29%), membranous ventricular septal defect (23%),



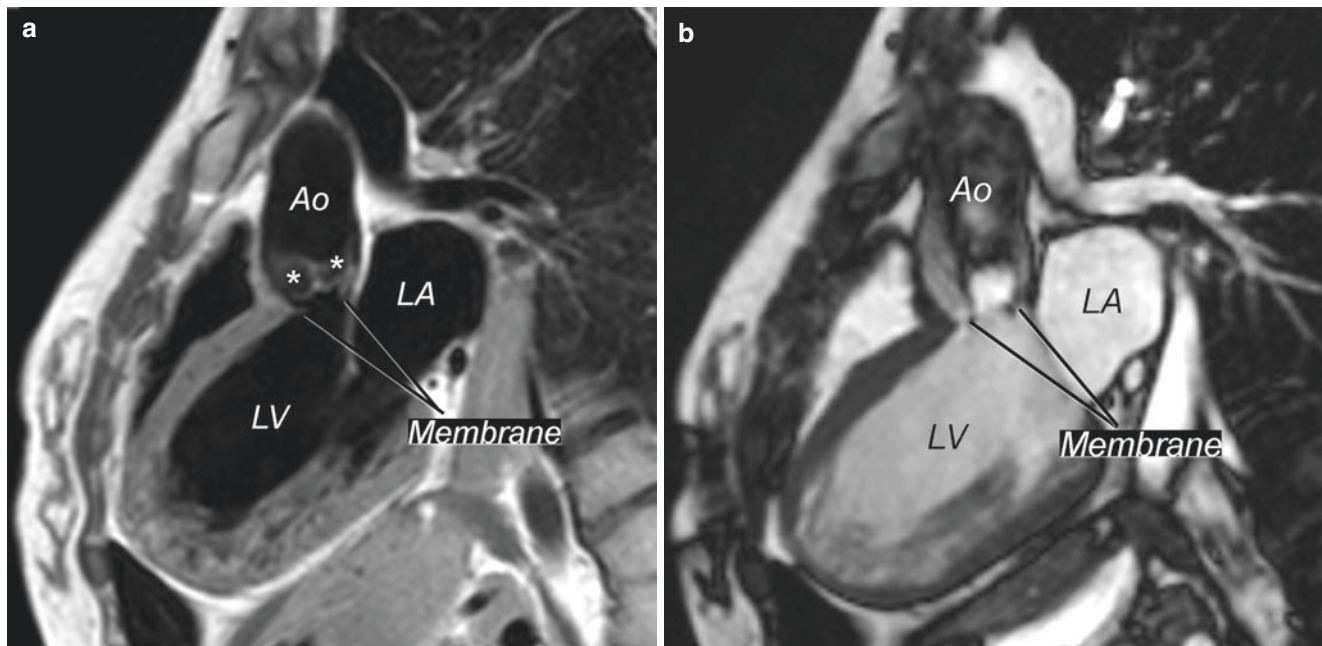


**Fig. 11.9** Discrete subaortic stenosis. (a) Turbo (fast) spin echo sequence with blood suppression in a left ventricular three-chamber plane parallel to the outflow tract demonstrating a discrete subvalvar membrane immediately below the aortic valve leaflets (\*). (b) Cine

SSFP image in the same plane as in panel A demonstrating systolic dephasing consistent with stenosis beginning at the level of the subaortic membrane. *Ao* aorta, *LA* left atrium, *LV* left ventricle

coarctation (14%), double-chambered right ventricle (8%), and interrupted aortic arch (3%) [42]. Supravalvar aortic stenosis may be associated with Williams syndrome or with the autosomal dominant familial form of the disease [43, 44].

#### 11.3.1.4 Clinical Presentation

The clinical presentation of obstructive lesions of the left ventricular outflow tract depends on the severity of obstruction, the rate at which it develops, age, and associated anomalies. Neonates with severe aortic outflow obstruction and closing or closed ductus arteriosus can present in shock with poor perfusion, weak pulses, lethargy, lactic acidemia, and oliguria or anuria. When the ductus arteriosus is patent or the degree of obstruction is not critical, neonates and infant may present with a systolic murmur, tachypnea, cyanosis, and feeding difficulties. The only manifestation of mild or moderate obstruction is a systolic heart murmur. Older patients may present with exertional symptoms such as chest pain with exercise or diminished exercise capacity. Sudden cardiac death is rare [45].

#### 11.3.1.5 CMR of Left Ventricular Outflow Obstruction

CMR allows for anatomic assessment of the morphology of the left ventricular outflow tract and aortic valve, assessment of the hemodynamic burden on the aorta and ventricles, and evaluation of associated anomalies. Although there are no

detailed published studies on the use of CMR in patients with subvalvar or supravalvar aortic stenosis, several reports have described CMR evaluation in patients with bicommissural and unicommissural aortic valves. CMR has been shown to have excellent sensitivity and specificity in detecting and characterizing bicommissural [46, 47] and unicommissural [48] aortic valves in adults.

Several groups have reported on the use of CMR for assessment of aortic valve stenosis based on the continuity equation and planimetry [49, 50]. Furthermore, CMR allows for excellent visualization of thoracic vasculature [51] and can therefore allow for assessment of aortic dimensions in patients with bicommissural aortic valve and dilatation of the ascending aorta (Fig. 11.12) [52]. Research has also focused on analysis of flow patterns and wall stress in the aorta with the hope that it will lead to identification of patients at risk for aortic dissection [53–55].

The goals of CMR in patients with left ventricular outflow obstruction include anatomic and functional evaluations of the location of the obstructive lesion(s), the mechanism of obstruction, the hemodynamic burden of the anomaly, and assessment of associated anomalies. These objectives can be realized with the following CMR examination protocol:

- ECG-triggered, breath-hold cine SSFP in the following planes:
  - LV and RV two-chamber (vertical long-axis)

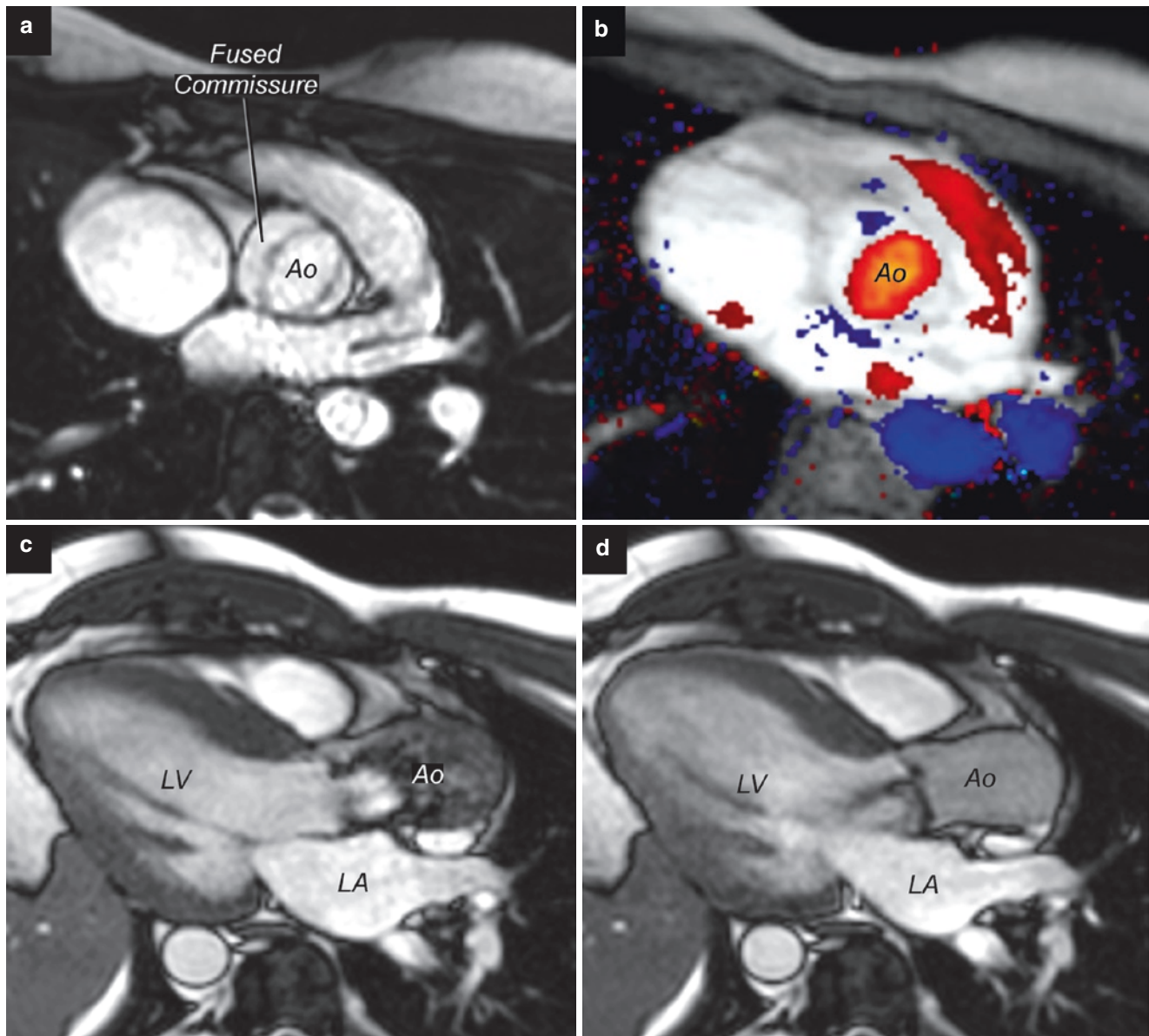


**Fig. 11.10** Valvar aortic stenosis and regurgitation. (a) Cine SSFP image in a plane perpendicular to the aortic root demonstrating a bicuspid aortic valve with fusion of the right and noncoronary cusps. (b) Cine phase contrast through-plane flow mapping perpendicular to the aortic root demonstrating the eccentric antegrade flow jet across the

bicuspid valve. (c) Systolic cine SSFP image in a left ventricular (LV) three-chamber view parallel to the outflow tract showing a dephasing jet consistent with valvar aortic stenosis. (d) Diastolic cine SSFP image in a left ventricular three-chamber view parallel to the outflow tract showing an aortic regurgitation jet. *Ao* aorta, *LA* left atrium

- Extended two-chamber covering the left ventricular inflow and outflow.
- LV three-chamber view parallel to the left ventricular outflow for visualization of the subvalvar area and aortic valve. This view allows measurement of aortic valve annulus diameter.
- Oblique coronal plane parallel to the left ventricular outflow; complements the previous view.
- Short-axis stack perpendicular to the aortic root for assessment of aortic valve morphology and measurements of aortic root diameters (systolic frame).
- Short-axis stack perpendicular to the widest segment of the ascending aorta (usually oblique axial plane) for measurements of the ascending aorta diameter (systolic frame) (Fig. 11.12).
- Ventricular short-axis for measurements of biventricular size, function, and mass.
- Gadolinium-enhanced 3D MRA to assess for coarctation of the aorta and other associated anomalies
- ECG-triggered, free-breathing cine phase contrast flow measurements in the proximal ascending aorta and main pulmonary artery. In-plane flow velocity mapping parallel



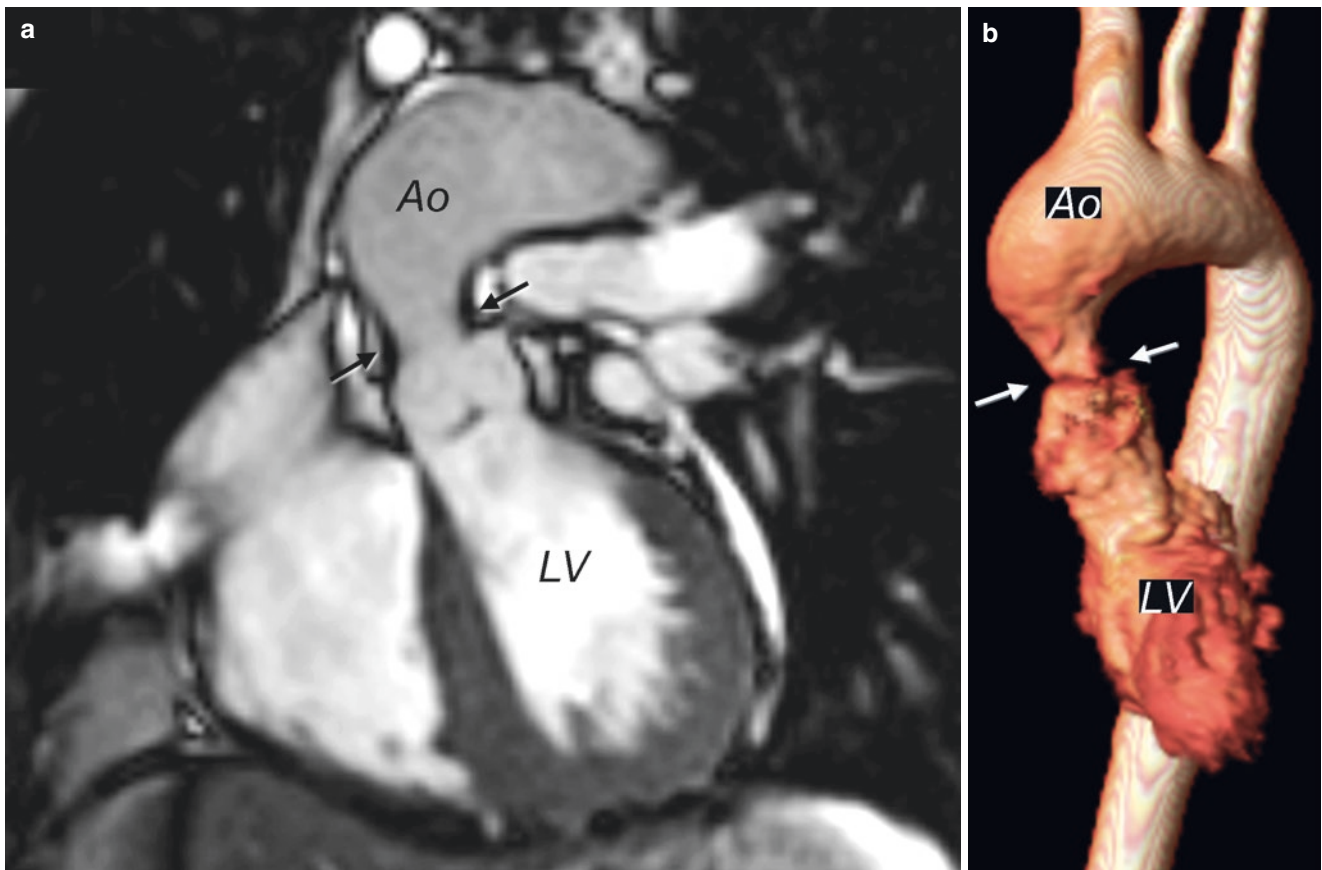


**Fig. 11.11** Supravalvar aortic stenosis. (a) Cine SSFP image in an oblique coronal plane parallel to the left ventricle (LV) outflow tract demonstrating supravalvar aortic stenosis with narrowing at the sinotubular junction (arrows). (b) Corresponding gadolinium-enhanced three-dimensional magnetic resonance angiogram. Ao aorta, LV left ventricle

bular junction (arrows). (b) Corresponding gadolinium-enhanced three-dimensional magnetic resonance angiogram. Ao aorta, LV left ventricle

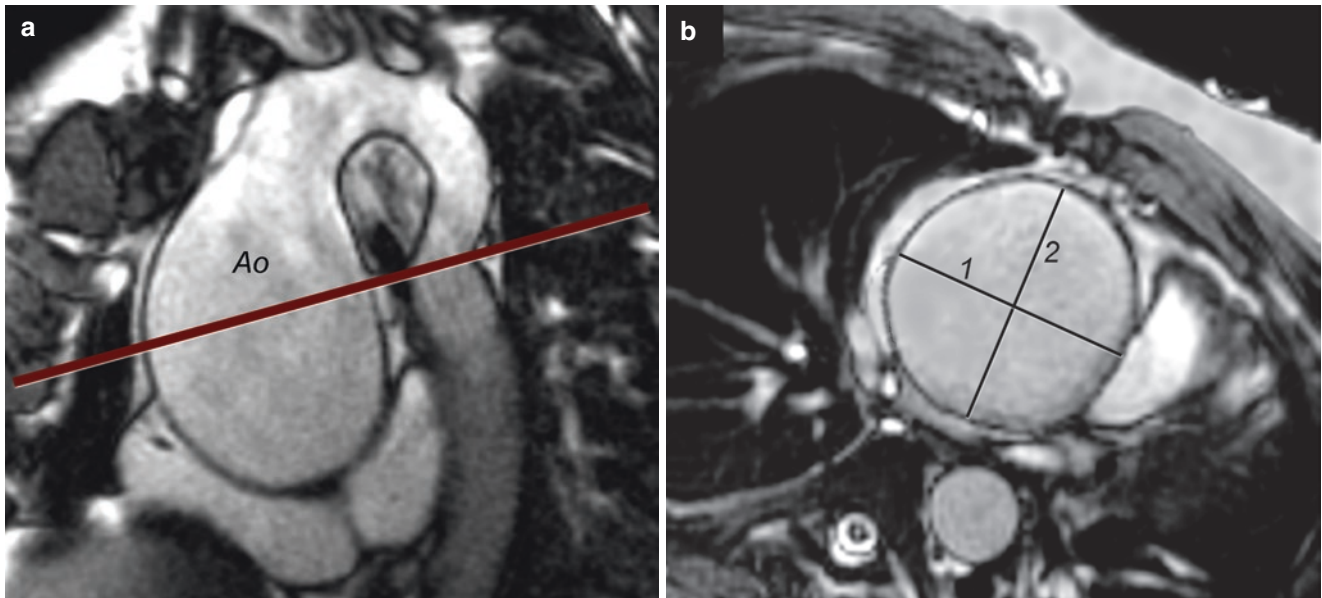


**Fig. 11.12** Dilated ascending aorta. (a) Cine SSFP image in an oblique sagittal plane parallel to the ascending aorta (Ao) and aortic arch. The most dilated portion of the ascending aorta is selected and an imaging plane is prescribed perpendicular to this region (line). (b) Cine SSFP

imaging perpendicular to the widest portion of the ascending aorta as prescribed in panel A. The diameter of the ascending aorta is measured in two orthogonal planes (1 and 2) on a systolic frame

- to the left ventricular outflow allows (1) visualization of the location of flow acceleration and (2) assessment of peak velocity and estimation of the peak gradient. In cases with more than mild left ventricular outflow obstruction, high-velocity turbulent flow can preclude reliable flow measurements in the proximal ascending aorta. In this circumstance, the phase contrast imaging plane can be positioned proximal to the obstructive lesion in the left ventricular outflow (Fig. 11.13a) or, in selected cases, in the distal ascending aorta before the origin of the right innominate artery.
- In patients with suspected endocardial fibroelastosis (Fig. 11.4) or myocardial scar, LGE imaging performed

10–20 min after contrast administration in the ventricular short-axis, LV two- and three-chamber, and four-chamber lanes.

- Optional sequences:
  - ECG-triggered, breath-hold turbo (fast) spin echo sequence with blood suppression in patients with metallic artifacts from implanted devices or to visualize a discrete subaortic membrane (Fig. 11.9)
  - ECG-triggered, respiratory-navigated, free breathing three-dimensional isotropic SSFP for evaluation of the coronary arteries

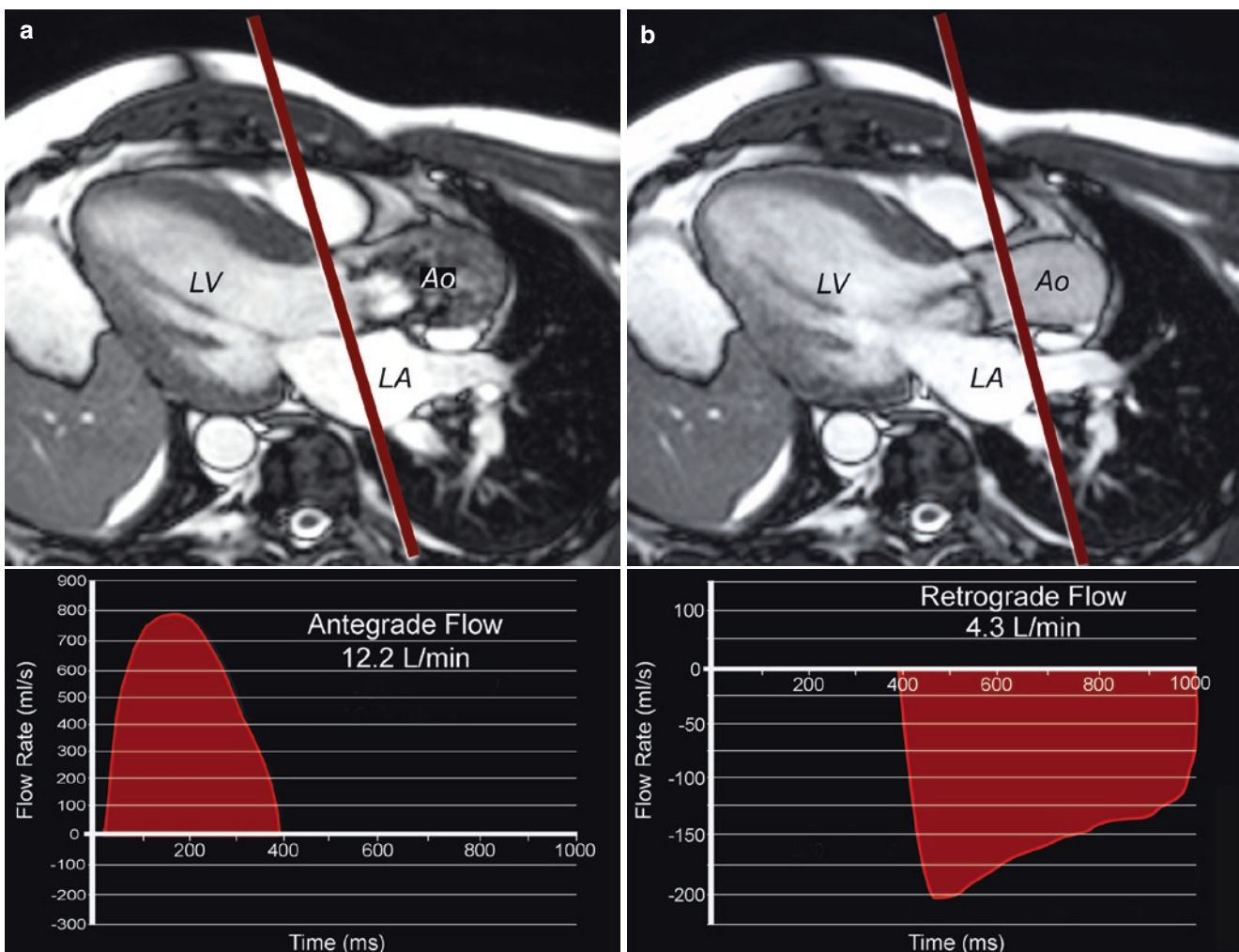


**Fig. 11.13** Measuring aortic flow in mixed aortic valve disease (stenosis and regurgitation). (a) Antegrade flow across the left ventricular outflow is measured below the aortic valve. *Top panel:* The imaging plane (LV, left ventricle; LA, left atrium; Ao, aorta) for subsequent cine phase contrast flow mapping is prescribed from cine SSFP diastolic image in the ventricular three-chamber plane. *Bottom panel:* The area under the diastolic phase of the cardiac cycle represents the retrograde flow in the aortic root (4.3 L/min). Net aortic flow is, therefore, antegrade flow—retrograde flow = 7.9 L/min. Aortic regurgitation fraction is calculated as retrograde flow/antegrade flow  $\times$  100 = 35%.

tic root is measured above the aortic valve. *Top panel:* The imaging plane (LV, left ventricle, LA, left atrium, Ao, aorta) for subsequent cine phase contrast flow mapping is prescribed from cine SSFP diastolic image in the ventricular three-chamber plane. *Bottom panel:* The area under the diastolic phase of the cardiac cycle represents the retrograde flow in the aortic root (4.3 L/min; regurgitation volume). Net aortic flow is, therefore, antegrade flow—retrograde flow = 7.9 L/min. Aortic regurgitation fraction is calculated as retrograde flow/antegrade flow  $\times$  100 = 35%.



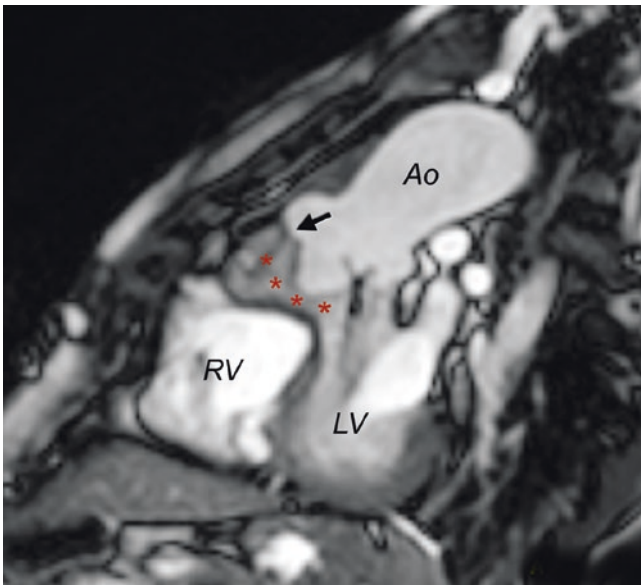


**Fig. 11.14** Aortico-left ventricular tunnel. Cine SSFP image in an oblique sagittal plane parallel to the left ventricular outflow tract demonstrating a defect in the aortic wall (*arrow*) and the tunneling flow (\*) into the left ventricle. *Ao* aorta, *LV* left ventricle, *RV* right ventricle

### 11.3.2 Regurgitant Lesions

#### 11.3.2.1 Definitions

Aortic valve regurgitation can be an isolated anomaly or associated with other anomalies of the left ventricular outflow or other congenital heart diseases. Aortico-left ventricular tunnel is a rare congenital cardiac anomaly that results in regurgitation of blood from the ascending aorta to the left ventricle adjacent to the aortic valve.

#### 11.3.2.2 Morphologic and Functional Abnormalities

Regurgitation at the level of the left ventricular outflow tract can result from several morphologic abnormalities.

- *Unicommissural or bicommissural aortic valve*: Although bicommissural aortic valve disease is often associated with stenosis, mixed lesions and pure aortic regurgitation are seen in a proportion of patients. In one large series of patients undergoing aortic valve surgery, 75% had aortic stenosis, 13% had regurgitation, and 10% had mixed valve disease [56]. Regurgitation results from leaflet tissue deficiency, redundancy and prolapse, restriction of diastolic motion, and root dilatation [39, 57].
- *Aortic valve prolapse*: Prolapse of one or more leaflets of an otherwise normal tricommissural aortic valve can be seen in patients with conal septal (subpulmonary, outlet) ventricular septal defect and, less frequently, in membranous ventricular septal defect [58]. The prolapsing leaflet can create a windsock-like deformity and restrict or even close the ventricular septal defect.

- *Congenital leaflet perforation*: This is a rare congenital anomaly of the aortic valve resulting in severe regurgitation [59].
- *Iatrogenic aortic regurgitation*: The most common cause of iatrogenic aortic regurgitation in congenital heart disease is due to transcatheter balloon dilatation of congenital aortic stenosis [60]. A therapeutic tear in the anterior aspect of the stenotic valve is common, and the ensuing regurgitation may progress over time.
- *Acquired aortic regurgitation*: Bacterial endocarditis is a leading cause of acquired, non-iatrogenic aortic regurgitation in children. It is not only associated with bicommissural aortic valve and subvalvar aortic stenosis but can also occur with or without associated congenital heart disease [61].
- *Aortico-left ventricular tunnel*: This is a rare paravalvar communication between the aorta and the left ventricle (Fig. 11.14; Movie 11.11) [62]. The tunnel most commonly originates above the origin of the right coronary artery and courses posterior to the right ventricular outflow tract to enter the left ventricle immediately below the aortic valve [62].

#### 11.3.2.3 Clinical Presentation

As with mitral regurgitation, the clinical presentation of aortic regurgitation in children depends on the severity and duration of the lesion as well as associated anomalies. Patients who develop acute severe aortic regurgitation can present with signs and symptoms of heart failure. Patients with chronic or slowly progressing aortic regurgitation may be asymptomatic until the compensatory mechanisms of the left ventricle fail and systolic dysfunction occurs.

#### 11.3.2.4 CMR of Aortic Regurgitation

The primary goals of CMR include quantification of the regurgitation volume and fraction, assessment of the hemodynamic burden on the left ventricle, and visualization of the mechanism of valve dysfunction. Although cases of aortico-left ventricular tunnel have typically been diagnosed by echocardiography and conventional X-ray angiography, Humes et al. reported on CMR diagnosis of this rare anomaly [63]. More frequently, however, CMR has been used to quantify aortic regurgitation in children and adults [64–66]. Several studies found good correlation between CMR and other noninvasive [29, 66] and invasive [67] measures of aortic regurgitation as well as good reproducibility [68]. As noted previously, there are also published data demonstrating the ability of CMR to assess valve morphology [46–48], although studies evaluating the ability of CMR to delineate the mechanism of valve regurgitation are limited.

The CMR protocol for evaluation of aortic regurgitation is essentially identical to that of obstructive lesions in the left

ventricular outflow. In patients with both stenosis and regurgitation in the left ventricular outflow, flow measurements should be performed both below and above the areas of turbulent flow (Fig. 11.13). In this circumstance, antegrade flow is measured from the systolic phase of the cardiac cycle obtained in the left ventricular outflow below the aortic valve. The retrograde (regurgitation) flow is measured from the diastolic phase of the cardiac cycle obtained at the level of the sinotubular junction. In the absence of mitral regurgitation or ventricular septal defect, the antegrade flow can also be obtained by measurement of left ventricular stroke volume from end-diastolic and end-systolic volumes. The phase contrast and volumetric measurements can then be compared for consistency.

## 11.4 Abnormalities of Combined Left Ventricular Inflow and Outflow

### 11.4.1 Definitions

Multiple left heart obstructions encompass a wide range of congenital anomalies affecting the mitral valve, left ventricle, left ventricular outflow tract, and thoracic aorta. Schwartz et al. defined multiple left heart obstructive lesions as having two or more of the following areas of obstruction or hypoplasia: (1) *mitral valve*: mitral stenosis (mean gradient  $>3$  mmHg), mitral annulus hypoplasia, or parachute mitral valve; (2) *left ventricular outflow tract*: subaortic stenosis or diameter less than normal aortic annulus; (3) *aortic valve*: aortic valve stenosis (maximum instantaneous Doppler gradient  $\geq 20$  mmHg) or aortic valve annulus hypoplasia; (4) *aortic arch*: aortic arch hypoplasia, isthmic hypoplasia, coarctation, or interrupted aortic arch; or (5) *left ventricle*: left ventricular-to-right ventricular long-axis ratio  $<0.8$  or subnormal LV end-diastolic volume. Hypoplasia for each parameter was defined by a measurement with a Z-score smaller than  $-2.0$  [69]. *Morphologic and Functional Abnormalities*

Several patterns of multiple left heart obstructive lesions are recognized:

- *Hypoplastic left heart syndrome*: This most severe form of multiple left heart obstructions is characterized by severe hypoplasia or atresia of the mitral and/or aortic valves and marked hypoplasia of the left ventricle, often with endocardial fibroelastosis.
- *Shone syndrome*: Shone syndrome consists of the following four anatomic obstructions (Fig. 11.15): (1) supramitral membrane; (2) parachute mitral valve; (3) discrete subaortic stenosis; and (4) aortic coarctation. It is worth noting that in Shone's original report not all patients exhibit all four lesions [70].

- *Multiple left heart obstructive lesions*: Included in this category are the many patients with more than one level of left heart obstruction as defined above but not fulfilling criteria for Shone syndrome [69].

#### 11.4.1.1 Clinical Presentation

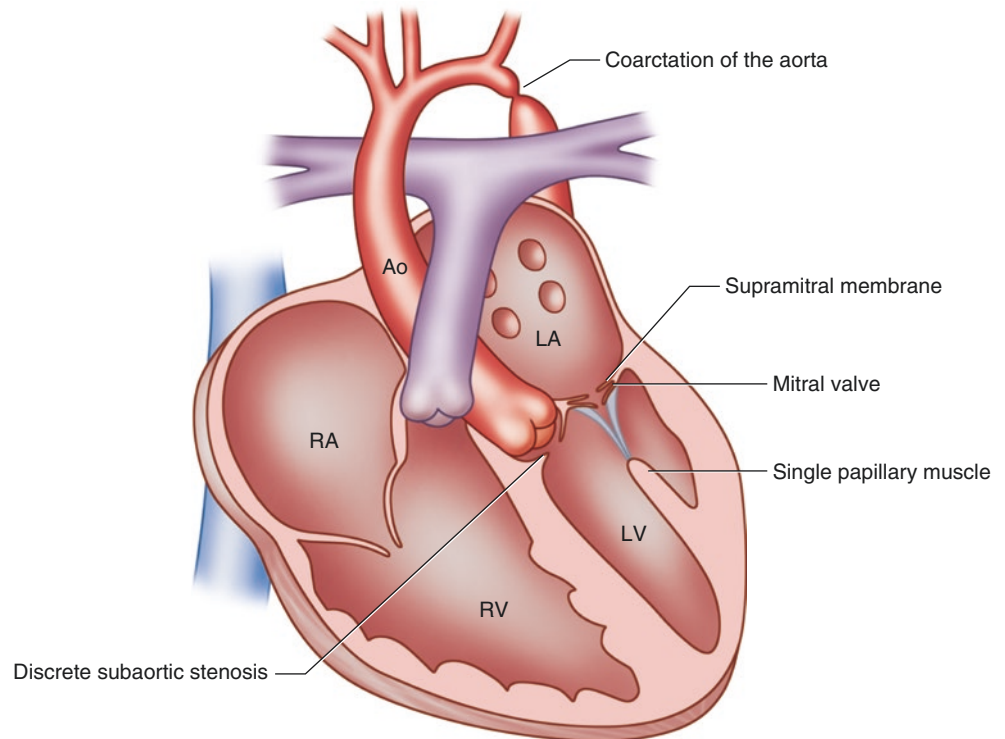
The clinical presentation, course, and prognosis of patients with obstructions at multiple levels of left ventricular inflow and outflow vary considerably. The location and severity of the obstructive lesions as well as associated defects, such as patent ductus arteriosus and atrial septal defect, are important determinants of initial clinical course. At one end of the clinical spectrum are newborns with hypoplastic left heart syndrome presenting with cyanosis and cardiovascular collapse as the patent ductus arteriosus closes. At the other end of the spectrum are asymptomatic patients with slowly progressing coarctation of the aorta, mild mitral or aortic valve stenosis, and normal left ventricular size and function. Prematurity and associated genetic and major noncardiac congenital defects adversely affect prognosis.

#### 11.4.1.2 CMR Evaluation of Combined Left Ventricular Inflow and Outflow Obstructions

CMR offers important advantages in the evaluation of patients with multiple left heart obstructive lesions, Shone syndrome, and hypoplastic left heart syndrome. As noted above in the sections on individual lesions, CMR allows for visualization of mitral and aortic valve morphology and quantification of valve function, assessment of the hemodynamic burden, and evaluation of any associated lesions.

Of particular importance in this group of patients is the ability of CMR to aid in clinical decision making with regard to single versus biventricular management strategies. Although echocardiography has been used effectively to predict a successful biventricular outcome in patients with aortic stenosis [71] and with multiple left heart obstructive lesions [69], its ability to accurately measure the size and function of the hypoplastic, abnormally shaped left ventricle has been questioned [72]. CMR has particular strengths in quantitative evaluation of left ventricular volumes, mass, ejection fraction, and stroke volume. Additional important information provided by CMR includes evaluation of endocardial fibroelastosis, flow measurements through the left heart, and assessment of associated anomalies [72]. Therefore, the goals of the preoperative CMR examination in the infant with a borderline left ventricle include measurements of biventricular size and function, visualization of valve anatomy, quantification of valve flow and regurgitation on both sides of the heart, and assessment of associated anomalies. These objectives can be realized with the following CMR examination protocol:

**Fig. 11.15** Shone syndrome. Schematic representation of Shone syndrome depicting a supramitral membrane, parachute mitral valve with a single papillary muscle, discrete subaortic stenosis, and coarctation of the aorta. *Ao* aorta, *LA* left ventricle, *LV* left ventricle, *RA* right atrium, *RV* right ventricle



- ECG-triggered, breath-hold cine SSFP in the following planes:
  - LV and RV two-chamber (vertical long-axis).
  - Four-chamber stack covering the left ventricular inflow and outflow
  - LV three-chamber view parallel to the left ventricular outflow for visualization of the subvalvar area and aortic valve
  - Oblique coronal plane parallel to the left ventricular outflow (optional)
  - Short-axis stack perpendicular to the aortic root for assessment of aortic valve morphology
  - Ventricular short-axis stack for measurements of biventricular size, function, and mass
- ECG-triggered, breath-hold turbo (fast) spin echo sequence with blood suppression for evaluation of the aortic arch (optional)
- Gadolinium-enhanced 3D MRA to assess for coarctation of the aorta and other associated thoracic vascular anomalies
- ECG-triggered, free-breathing cine phase contrast flow measurements in the proximal ascending aorta, main pulmonary artery, and AV valves
- LGE imaging performed 10–20 min after contrast administration in the ventricular short-axis, four-chamber, and LV two- and three-chamber planes
- Optional sequences:
  - ECG-triggered, breath-hold turbo (fast) spin echo sequence with blood suppression for evaluation of intracardiac or extracardiac anomalies not clearly seen by cine SSFP.
  - Additional flow measurements (case-specific). Examples include differential pulmonary blood flow in patients with pulmonary artery or pulmonary vein anomalies or measurements of systemic-to-pulmonary collateral flow.

### Practical Pearls

- Anatomic and physiologic evaluations by CMR are inseparable in patients with abnormalities of left ventricular inflow and outflow.
- Measurements of left and right ventricular volumes and function, as well as flow across the atrioventricular and semilunar valves, are essential in most patients.
- The CMR protocol should be designed to allow internal validation of shunts and valve regurgitation fractions. For example, in patients with mitral regurgitation, the CMR protocol should allow quantification of the degree of regurgitation by both ventricular stroke volume differential and by comparison of mitral inflow to net aortic outflow.
- Due to through-plane annular motion of the atrioventricular valves in the base-to-apex direction, assessment of

atrioventricular valve inflows is best prescribed using horizontal and vertical ventricular long-axis views, with the plane aligned with the valve annulus at end-systole.

- In patients with mixed aortic valve disease (aortic stenosis and regurgitation), flow measurements should be obtained both below the level of stenosis and above the valve for accurate determination of valve function.
- Myocardial delayed enhancement imaging is particularly important in patients with left ventricular outflow tract obstruction and borderline left ventricular size for identification of endomyocardial fibrosis.

## References

- Victor S, Nayak VM. Aneurysm of the left atrial appendage. *Tex Heart Inst J*. 2001;28:111–8.
- Chowdhury UK, Seth S, Govindappa R, Jagia P, Malhotra P. Congenital left atrial appendage aneurysm: a case report and brief review of literature. *Heart Lung Circ*. 2009;18:412–6.
- Park JS, Lee DH, Han SS, Kim MJ, Shin DG, Kim YJ, Shim BS. Incidentally found, growing congenital aneurysm of the left atrium. *J Korean Med Sci*. 2003;18:262–6.
- Wang D, Holden B, Savage C, Zhang K, Zwischenberger JB. Giant left atrial intrapericardial aneurysm: noninvasive preoperative imaging. *Ann Thorac Surg*. 2001;71:1014–6.
- Van Praagh R, Corsini I. Cor triatriatum: pathologic anatomy and a consideration of morphogenesis based on 13 postmortem cases and a study of normal development of the pulmonary vein and atrial septum in 83 human embryos. *Am Heart J*. 1969;78:379–405.
- Rumancik WM, Hernanz-Schulman M, Rutkowski MM, Kiely B, Ambrosino M, Genieser NB, Naidich DP. Magnetic resonance imaging of cor triatriatum. *Pediatr Cardiol*. 1988;9:149–51.
- Locca D, Hughes M, Mohiaddin R. Cardiovascular magnetic resonance diagnosis of a previously unreported association: cor triatriatum with right partial anomalous pulmonary venous return to the azygos vein. *Int J Cardiol*. 2009;135:e80–2.
- McElhinney DB, Sherwood MC, Keane JF, del Nido PJ, Almond CSD, Lock JE. Current management of severe congenital mitral stenosis: outcomes of transcatheter and surgical therapy in 108 infants and children. *Circulation*. 2005;112:707–14.
- Selamet Tierney ES, Graham DA, McElhinney DB, Trevey S, Freed MD, Colan SD, Geva T. Echocardiographic predictors of mitral stenosis-related death or intervention in infants. *Am Heart J*. 2008;156:384–90.
- Toscano A, Pasquini L, Iacobelli R, Di Donato RM, Raimondi F, Carotti A, Di Ciommo V, Sanders SP. Congenital supravalvar mitral ring: an underestimated anomaly. *J Thorac Cardiovasc Surg*. 2009;137:538–42.
- Ruckman RN, Van Praagh R. Anatomic types of congenital mitral stenosis: report of 49 autopsy cases with consideration of diagnosis and surgical implications. *Am J Cardiol*. 1978;42:592–601.
- Marino BS, Kruge LE, Cho CJ, Tomlinson RS, Shera D, Weinberg PM, Gaynor JW, Rychik J. Parachute mitral valve: morphologic descriptors, associated lesions, and outcomes after biventricular repair. *J Thorac Cardiovasc Surg*. 2009;137:385–93.e384.
- Collins RT 2nd, Ryan M, Gleason MM. Images in cardiovascular medicine. Mitral arcade: a rare cause of fatigue in an 18-year-old female. *Circulation*. 2010;121:e379–83.
- Layman TE, Edwards JE. Anomalous mitral arcade: a type of congenital mitral insufficiency. *Circulation*. 1967;35:389–95.
- Losada E, Moon-Grady AJ, Strohsnitter WC, Wu D, Ursell PC. Anomalous mitral arcade in twin-twin transfusion syndrome. *Circulation*. 2010;122:1456–63.
- Baño-Rodrigo A, Van Praagh S, Trowitzsch E, Van Praagh R. Double-orifice mitral valve: a study of 27 postmortem cases with developmental, diagnostic and surgical considerations. *Am J Cardiol*. 1988;61:152–60.
- Hamilton-Craig C, Anscombe R, Platts D, Burstow D, Slaughter R. Congenital mitral stenosis by multimodality cardiac imaging. *Echocardiography*. 2009;26:284–7.
- Lanjewar C, Ephrem B, Mishra N, Jhankariya B, Kerkar P. Planimetry of mitral valve stenosis in rheumatic heart disease by magnetic resonance imaging. *J Heart Valve Dis*. 2010;19:357–63.
- Søndergaard L, Ståhlberg F, Thomsen C. Magnetic resonance imaging of valvular heart disease. *J Magn Reson Imaging*. 1999;10:627–38.
- Stos B, Hatchuel Y, Bonnet D. Mitral valvar regurgitation in a child with Sweet's syndrome. *Cardiol Young*. 2007;17:218–9.
- Van Praagh S, Porras D, Oppido G, Geva T, Van Praagh R. Cleft mitral valve without ostium primum defect: anatomic data and surgical considerations based on 41 cases. *Ann Thorac Surg*. 2003;75:1752–62.
- Geva T, Sanders SP, Diogenes MS, Rockenmacher S, Van Praagh R. Two-dimensional and Doppler echocardiographic and pathologic characteristics of the infantile Marfan syndrome. *Am J Cardiol*. 1990;65:1230–7.
- Ben Ali W, Metton O, Roubertie F, Pouard P, Sidi D, Raïsky O, Vouhe PR. Anomalous origin of the left coronary artery from the pulmonary artery: late results with special attention to the mitral valve. *Eur J Cardiothorac Surg*. 2009;36:244–8; discussion 248–249.
- Takao A, Niwa K, Kondo C, Nakanishi T, Satomi G, Nakazawa M, Endo M. Mitral regurgitation in Kawasaki disease. *Prog Clin Biol Res*. 1987;250:311–23.
- Fraisse A, del Nido PJ, Gaudart J, Geva T. Echocardiographic characteristics and outcome of straddling mitral valve. *J Am Coll Cardiol*. 2001;38:819–26.
- Milo S, Siew Yen H, Macartney FJ, Wilkinson JL, Becker AE, Wenink ACG, De Groot ACG, Anderson RH. Straddling and over-riding atrioventricular valves: morphology and classification. *Am J Cardiol*. 1979;44:1122–34.
- Fujita N, Chazouilleres AF, Hartiala JJ, O'Sullivan M, Heidenreich P, Kaplan JD, Sakuma H, Foster E, Caputo GR, Higgins CB. Quantification of mitral regurgitation by velocity-encoded cine nuclear magnetic resonance imaging. *J Am Coll Cardiol*. 1994;23:951–8.
- Hartiala JJ, Mostbeck GH, Foster E, Fujita N, Dulce MC, Chazouilleres AF, Higgins CB. Velocity-encoded cine MRI in the evaluation of left ventricular diastolic function: measurement of mitral valve and pulmonary vein flow velocities and flow volume across the mitral valve. *Am Heart J*. 1993;125:1054–66.
- Gelfand EV, Hughes S, Hauser TH, Yeon SB, Goepfert L, Kissinger KV, Rofsky NM, Manning WJ. Severity of mitral and aortic regurgitation as assessed by cardiovascular magnetic resonance: optimizing correlation with Doppler echocardiography. *J Cardiovasc Magn Reson*. 2006;8:503–7.
- Hundley WG, Li HF, Willard JE, Landau C, Lange RA, Meshack BM, Hillis LD, Peshock RM. Magnetic resonance imaging assessment of the severity of mitral regurgitation: comparison with invasive techniques. *Circulation*. 1995;92:1151–8.
- Buchner S, Debl K, Poschenrieder F, Feuerbach S, Riegger GA, Luchner A, Djauidani B. Cardiovascular magnetic resonance for direct assessment of anatomic regurgitant orifice in mitral regurgitation. *Circ Cardiovasc Imaging*. 2008;1:148–55.



32. Kleinert S, Geva T. Echocardiographic morphometry and geometry of the left ventricular outflow tract in fixed subaortic stenosis. *J Am Coll Cardiol.* 1993;22:1501–8.
33. Cape EG, VanAuker MD, Sigfússon G, Tacy TA, del Nido PJ. Potential role of mechanical stress in the etiology of pediatric heart disease: septal shear stress in subaortic stenosis. *J Am Coll Cardiol.* 1997;30:247–54.
34. Leichter DA, Sullivan I, Gersony WM. “Acquired” discrete subvalvular aortic stenosis: natural history and hemodynamics. *J Am Coll Cardiol.* 1989;14:1539–44.
35. Suri RM, Dearani JA, Schaff HV, Danielson GK, Puga FJ. Long-term results of the Konno procedure for complex left ventricular outflow tract obstruction. *J Thorac Cardiovasc Surg.* 2006;132:1064–71.e1062.
36. Suzuki T, Ohye RG, Devaney EJ, Ishizaka T, Nathan PN, Goldberg CS, Gomez CA, Bove EL. Selective management of the left ventricular outflow tract for repair of interrupted aortic arch with ventricular septal defect: management of left ventricular outflow tract obstruction. *J Thorac Cardiovasc Surg.* 2006;131:779–84.
37. Geva T, Hornberger LK, Sanders SP, Jonas RA, Ott DA, Colan SD. Echocardiographic predictors of left ventricular outflow tract obstruction after repair of interrupted aortic arch. *J Am Coll Cardiol.* 1993;22:1953–60.
38. Campbell M, Kauntze R. Congenital aortic valvular stenosis. *Br Heart J.* 1953;15:179–94.
39. Siu SC, Silversides CK. Bicuspid aortic valve disease. *J Am Coll Cardiol.* 2010;55:2789–800.
40. Mookadam F, Thota VR, Lopez AM, Emani UR, Tajik AJ. Unicuspid aortic valve in children: a systematic review spanning four decades. *J Heart Valve Dis.* 2010;19:678–83.
41. Williams JCP, Barratt-Boyes BG, Lowe JB. Supravalvular aortic stenosis. *Circulation.* 1961;24:1311–8.
42. Geva A, McMahan CJ, Gauvreau K, Mohammed L, del Nido PJ, Geva T. Risk factors for reoperation after repair of discrete subaortic stenosis in children. *J Am Coll Cardiol.* 2007;50:1498–504.
43. Youn HJ, Chung WS, Hong SJ. Demonstration of supravalvular aortic stenosis by different cardiac imaging modalities in Williams syndrome. *Heart.* 2002;88:438.
44. Beitzke A, Becker H, Rigler B, Stein JI, Suppan C. Development of aortic aneurysms in familial supravalvular aortic stenosis. *Pediatr Cardiol.* 1986;6:227–9.
45. Brown DW, Dipilato AE, Chong EC, Gauvreau K, McElhinney DB, Colan SD, Lock JE. Sudden unexpected death after balloon valvuloplasty for congenital aortic stenosis. *J Am Coll Cardiol.* 2010;56:1939–46.
46. Gleeson TG, Mwangi I, Horgan SJ, Cradock A, Fitzpatrick P, Murray JG. Steady-state free-precession (SSFP) cine MRI in distinguishing normal and bicuspid aortic valves. *J Magn Reson Imaging.* 2008;28:873–8.
47. Buchner S, Hulsmann M, Poschenrieder F, Hamer OW, Fellner C, Kobuch R, Feuerbach S, Riegger GAJ, Djavidani B, Luchner A, Debl K. Variable phenotypes of bicuspid aortic valve disease: classification by cardiovascular magnetic resonance. *Heart.* 2010;96:1233–40.
48. Debl K, Djavidani B, Buchner S, Poschenrieder F, Heinicke N, Schmid C, Kobuch R, Feuerbach S, Riegger G, Luchner A. Unicuspid aortic valve disease: a magnetic resonance imaging study. *Rofo.* 2008;180:983–7.
49. Sing-Chien Y, van Geuns R-J, Meijboom FJ, Kirschbaum SW, McGhie JS, Simoons ML, Kilner PJ, Roos-Hesselink JW. A simplified continuity equation approach to the quantification of stenotic bicuspid aortic valves using velocity-encoded cardiovascular magnetic resonance. *J Cardiovasc Magn Reson.* 2007;9:899–906.
50. Pouleur A-C, Polain L, de Waroux J-B, Pasquet A, Vanoverschelde J-LJ, Gerber BL. Aortic valve area assessment: multidetector CT compared with cine MR imaging and transthoracic and transesophageal echocardiography. *Radiology.* 2007;244:745–54.
51. Valsangiacomo Büchel ER, DiBernardo S, Bauersfeld U, Berger F. Contrast-enhanced magnetic resonance angiography of the great arteries in patients with congenital heart disease: an accurate tool for planning catheter-guided interventions. *Int J Cardiovasc Imaging.* 2005;21:313–22.
52. Debl K, Djavidani B, Buchner S, Poschenrieder F, Schmid F-X, Kobuch R, Feuerbach S, Riegger G, Luchner A. Dilatation of the ascending aorta in bicuspid aortic valve disease: a magnetic resonance imaging study. *Clin Res Cardiol.* 2009;98:114–20.
53. Hope MD, Hope TA, Meadows AK, Ordovas KG, Urbania TH, Alley MT, Higgins CB. Bicuspid aortic valve: four-dimensional MR evaluation of ascending aortic systolic flow patterns. *Radiology.* 2010;255:53–61.
54. Barker A, Lanning C, Shandas R. Quantification of hemodynamic wall shear stress in patients with bicuspid aortic valve using phase-contrast MRI. *Ann Biomed Eng.* 2010;38:788–800.
55. den Reijer PM, Sallee D, van der Velden P, Zaaijer E, Parks WJ, Ramamurthy S, Robbie T, Donati G, Lamphier C, Beekman R, Brummer M. Hemodynamic predictors of aortic dilatation in bicuspid aortic valve by velocity-encoded cardiovascular magnetic resonance. *J Cardiovasc Magn Reson.* 2010;12:4.
56. Sabet HY, Edwards WD, Tazelaar HD, Daly RC. Congenitally bicuspid aortic valves: a surgical pathology study of 542 cases (1991 through 1996) and a literature review of 2,715 additional cases. *Mayo Clin Proc.* 1999;74:14–26.
57. Boodhwani M, de Kerchove L, Glineur D, Rubay J, Vanoverschelde J-L, Noirhomme P, El Khoury G. Repair of regurgitant bicuspid aortic valves: a systematic approach. *J Thorac Cardiovasc Surg.* 2010;140:276–84.e271.
58. Chiu S-N, Wang J-K, Lin M-T, Wu E-T, Lu FL, Chang C-I, Chen Y-S, Chiu I-S, Lue H-C, Wu M-H. Aortic valve prolapse associated with outlet-type ventricular septal defect. *Ann Thorac Surg.* 2005;79:1366–71.
59. Walley VM, Black MD. Erosion and perforation of a cusp by nodular calcification: an unusual cause of insufficiency in a congenital bicuspid aortic valve. *Can J Cardiol.* 1991;7:202–4.
60. Brown DW, Dipilato AE, Chong EC, Lock JE, McElhinney DB. Aortic valve reinterventions after balloon aortic valvuloplasty for congenital aortic stenosis: intermediate and late follow-up. *J Am Coll Cardiol.* 2010;56:1740–9.
61. McMahon CJ, Ayres N, Pignatelli RH, Franklin W, Vargo TA, Bricker JT, El-Said HG. Echocardiographic presentations of endocarditis, and risk factors for rupture of a sinus of Valsalva in childhood. *Cardiol Young.* 2003;13:168–72.
62. Martins JD, Sherwood MC, Mayer JE Jr, Keane JF. Aortico-left ventricular tunnel: 35-year experience. *J Am Coll Cardiol.* 2004;44:446–50.
63. Humes RA, Hagler DJ, Julsrud PR, Levy JM, Feldt RH, Schaff HV. Aortico-left ventricular tunnel: diagnosis based on two-dimensional echocardiography, color flow Doppler imaging, and magnetic resonance imaging. *Mayo Clin Proc.* 1986;61:901–7.
64. Søndergaard L, Lindvig K, Hildebrandt P, Thomsen C, Ståhlberg F, Joen T, Henriksen O. Quantification of aortic regurgitation by magnetic resonance velocity mapping. *Am Heart J.* 1993;125:1081–90.
65. Honda N, Machida K, Hashimoto M, Mamiya T, Takahashi T, Kamano T, Kashimada A, Inoue Y, Tanaka S, Yoshimoto N. Aortic regurgitation: quantitation with MR imaging velocity mapping. *Radiology.* 1993;186:189–94.
66. Ley S, Eichhorn J, Ley-Zaporozhan J, Ulmer H, Schenk JP, Kauczor HU, Arnold R. Evaluation of aortic regurgitation in congenital heart disease: value of MR imaging in comparison to echocardiography. *Pediatr Radiol.* 2007;37:426–36.

67. Sondergaard L, Lindvig K, Hildebrandt P, Thomsen C, Stahlberg F, Joen T, Henriksen O. Quantification of aortic regurgitation by magnetic resonance velocity mapping. *Am Heart J.* 1993;125:1081–90.
68. Dulce MC, Mostbeck GH, O’Sullivan M, Cheitlin M, Caputo GR, Higgins CB. Severity of aortic regurgitation: interstudy reproducibility of measurements with velocity-encoded cine MR imaging. *Radiology.* 1992;185:235–40.
69. Schwartz ML, Gauvreau K, Geva T. Predictors of outcome of biventricular repair in infants with multiple left heart obstructive lesions. *Circulation.* 2001;104:682–7.
70. Shone JD, Sellers RD, Anderson RC, Adams P Jr, Lillehei CW, Edwards JE. The developmental complex of “parachute mitral valve,” supra-ventricular ring of left atrium, subaortic stenosis, and coarctation of aorta. *Am J Cardiol.* 1963;11:714–25.
71. Colan SD, McElhinney DB, Crawford EC, Keane JF, Lock JE. Validation and re-evaluation of a discriminant model predicting anatomic suitability for biventricular repair in neonates with aortic stenosis. *J Am Coll Cardiol.* 2006;47:1858–65.
72. Grosse-Wortmann L, Yun T-J, Al-Radi O, Kim S, Nii M, Lee K-J, Redington A, Yoo S-J, van Arsdell G. Borderline hypoplasia of the left ventricle in neonates: insights for decision-making from functional assessment with magnetic resonance imaging. *J Thorac Cardiovasc Surg.* 2008;136:1429–36.



# Single Ventricle and Fontan Procedures

# 12

Sylvia Krupickova, Inga Voges, and Raad H. Mohiaddin

## 12.1 Introduction

Fontan procedures are palliative surgical reconstructions performed for children born with only one effective ventricle or two that cannot be separated functionally. They entail the connection of the pulmonary vascular resistance downstream of the systemic vascular resistance, flow through both being delivered, in series, by the functionally one ventricle, but at the cost of elevated systemic venous pressure (Fig. 12.1). This aims to eliminate shunting and the associated ventricu-

lar volume loading and to achieve full pulmonary oxygenation.

There is a great range of morphology in congenital heart disease. Whenever possible, the surgeon aims to achieve a repair dividing the heart into two sides with one side providing the systemic circulation and the other side providing the pulmonary circulation. However, in some instances, morphological features may make this impossible or too high risk (Table 12.1); in these cases, palliation by a Fontan procedure is considered.

---

**Supplementary Information** The online version contains supplementary material available at [https://doi.org/10.1007/978-3-031-29235-4\\_12](https://doi.org/10.1007/978-3-031-29235-4_12).

---

S. Krupickova (✉)  
Department of Paediatric Cardiology, Royal Brompton Hospital,  
London, UK

Cardiovascular Magnetic Resonance Unit, Royal Brompton  
Hospital and Imperial College, London, UK  
e-mail: [s.krupickova@rbht.nhs.uk](mailto:s.krupickova@rbht.nhs.uk)

I. Voges  
Department of Congenital Heart Disease and Paediatric  
Cardiology, University Hospital Schleswig-Holstein,  
Kiel, Germany

R. H. Mohiaddin  
Cardiovascular Imaging, Royal Brompton and Harefield Hospitals,  
Guy's and St Thomas' NHS Foundation Trust, London, UK

National Heart and Lung Institute, Imperial College London,  
London, UK  
e-mail: [r.mohiaddin@rbht.nhs.uk](mailto:r.mohiaddin@rbht.nhs.uk)

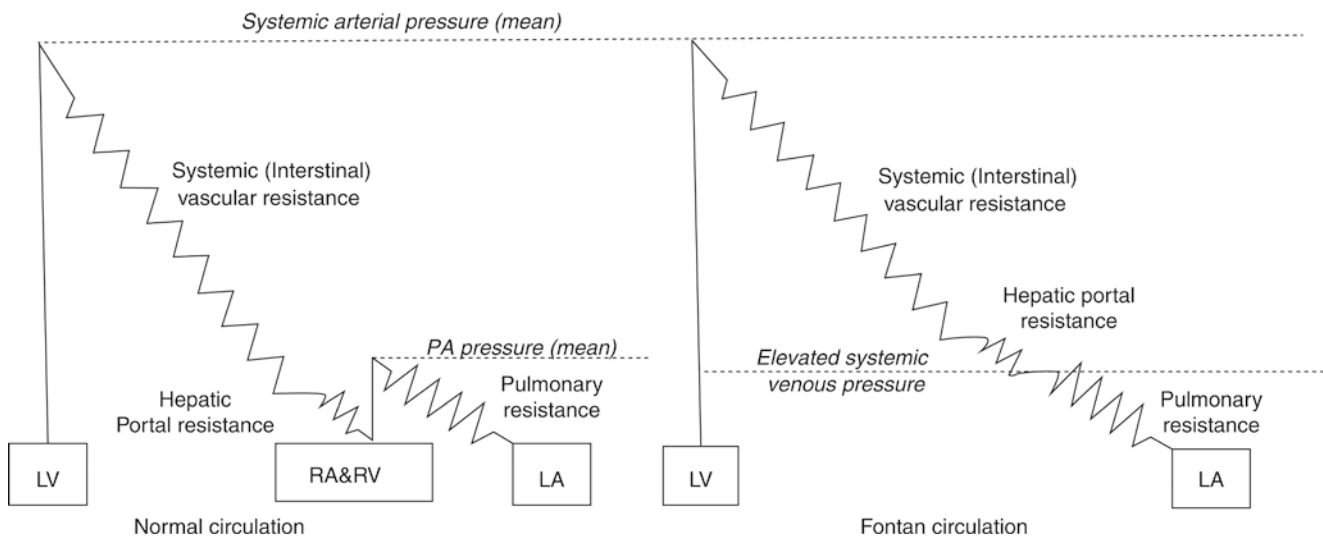


**Fig. 12.1** Schematic diagrams indicating the relative vascular pressures and resistance of a normal biventricular circulation (*left*) compared to a Fontan circulation (*right*). Pressures (mean where pulsatile) are indicated by the *vertical heights*. Vascular resistances are represented by *zigzag lines*. Because of the low pulmonary relative to sys-

temic resistance, a Fontan circulation adds relatively little to the systemic ventricular afterload. The more critical issue is the height of the systemic venous pressure and its effect on the hepatic portal and systemic, notably intestinal, and microvessels upstream. *LV*, left ventricle; *RA*, right atrium; *RV*, right ventricle; *LA*, left atrium

**Table 12.1** Examples of types of congenital heart disease which may be palliated by the Fontan circulation

Ventricular septal defect
(a) with significant straddling of the atrioventricular valve chordal apparatus
(b) where there is almost the complete ventricular septal deficiency
Atrioventricular septal defect
(a) unbalanced defect
(b) where the ventricular component is very large
Pulmonary atresia with intact ventricular septum
Tricuspid atresia
Hypoplastic left heart syndrome
Mitral atresia
Double-inlet left/right ventricle
Double-outlet right ventricle
(a) with noncommitted ventricular septal defect
(b) with mitral stenosis
Severe Ebstein malformation (following oversewing of the tricuspid valve)
Complex forms of congenital heart disease where there is only one good-sized ventricle
Complex forms of congenital heart disease where there are two ventricles but division into a biventricular circulation is too high risk

## 12.2 Definition

In a Fontan circulation, the systemic venous return is connected to the pulmonary arteries without the interposition of an adequate ventricle [1]. As Fontan surgery is used on a vast range of patients, initial intervention depends on the presenting morphology. Typically, preliminary palliative surgery is

performed to limit (pulmonary artery banding) or supplement (Blalock–Tausig shunt) blood flow to the lungs. Only a minority of children do not require surgery after birth as they have balanced circulation. Sufficient intracardiac mixing is also important, with an atrial septostomy or surgical septectomy being required in the first few days of life. More complex surgical procedures might be required after birth, e.g., Norwood procedure in patients with hypoplastic left heart syndrome.

Bidirectional Glenn is performed as the second stage of palliation. In this procedure, the superior vena cava is anastomosed onto the pulmonary artery. Timing of this procedure is debated [2], but it appears that about 6 months of age is ideal.

At the age of 3–4 years, the third and final stage of palliation is performed completing Fontan circulation. Completion of the Fontan aims to eliminate shunting and the associated volume loading of the dominant ventricle and desaturation of the arterial blood. The procedure involves connection of the pulmonary arteries downstream of the systemic veins so that the single effective ventricle delivers flow through the systemic then the pulmonary resistances in series.

Elevated systemic venous and hepatic portal pressure is needed to propel the blood forward through the relatively low resistance of the pulmonary vessels (Fig. 12.2). The most critical and unavoidable pathophysiological consequence of Fontan surgery, however, is the height of the systemic venous pressure and its effects on the microvessel upstream.

Fontan reconstruction should achieve nearly normal arterial saturation and avoids chronic volume overload but



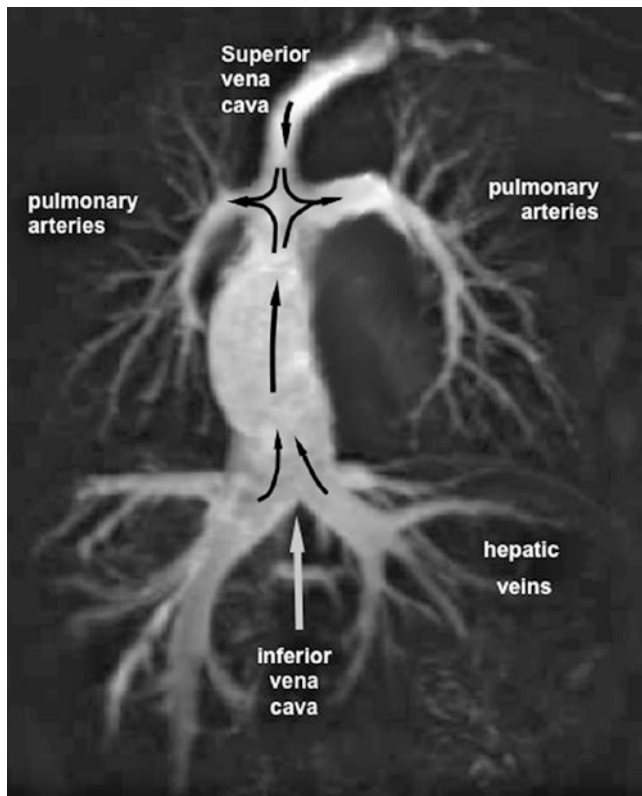


**Fig. 12.2** The hepato-cavopulmonary flow paths after a lateral tunnel TCPC Fontan connection, illustrated by a magnetic resonance contrast angiogram. It is important that hepatic venous blood flows via the IVC pathway to both lungs as it carries a factor which prevents the formation of pulmonary arteriovenous malformations, a potential cause of desaturation (see Fig. 12.9b)

at the cost of significant elevation of the systemic venous and hepatic portal pressure, typically to about 12–15 mmHg at rest. Patients with Fontan circulation usually have slightly decreased cardiac output at rest and limited capacity to increase output on exercise. A small fenestration is surgically created between tunnel and atrial cavity at the time of Fontan completion to offload the pressure in Fontan pathways and avoid abdominal hypertension in patients with preoperatively higher pulmonary artery pressure. This is however at the expense of lower saturations.

### 12.3 Preoperative Criteria

In order for a Fontan circulation to work successfully, there are certain requirements that ideally should be fulfilled:

1. Good ventricular function
2. Low (i.e., normal) pulmonary vascular resistance
3. No or mild atrioventricular valve regurgitation

4. Unobstructed ventricular outflow
5. Good-sized branch pulmonary arteries without stenoses
6. Unobstructed pulmonary venous return
7. Low amount of aortopulmonary collateral arteries

### 12.4 Morphology of Different Fontan Circulations

Fontan operations have undergone several modifications and refinements in the decades since Fontan and Baudet published their initial results in humans in 1971 [3]. It is important when imaging a patient with a Fontan circulation that details of what procedure has been performed are known.

Until the end of the 1980s, the right atrium was routinely included between the caval veins and the pulmonary arteries (Fig. 12.3a). Initially, atrial inflow and outflow valves were inserted, but they were not found to function satisfactorily (Fig. 12.4a). In patients with atriopulmonary Fontan connections, the right atrium tends to become dilated and subject to arrhythmias. The peaks of pressure caused by the contraction of a right atrium included in a Fontan circulation are propagated, detrimentally, upstream to the systemic and hepatic veins as well as beneficially downstream to pulmonary arteries. The work put into this part of the circulation by right atrial contraction not only fails to contribute usefully, the extra energy being largely dissipated in turbulent flow, but the turbulence itself slightly increases the local resistance to flow through the cavity and adjacent vessels. This was part of the rationale put forward by Marc de Leval and colleagues, for total cavopulmonary connection (TCPC) [4] (Fig. 12.3b) which has emerged as a superior technique.

TCPC excludes part or all of the right atrial cavity from the elevated pressure of the cavopulmonary flow path, which may help to avoid the atrial distension which predisposes to arrhythmias, blood flow stagnation and thrombosis. It also allows the coronary sinus to drain to the low-pressure part of the right atrium and then to the left atrium via an atrial septal defect. The superior caval vein is connected to the pulmonary artery (bidirectional cavopulmonary anastomosis, bidirectional Glenn). There are two variants to connect the inferior caval vein: the lateral tunnel (Fig. 12.3b) which consists of a prosthetic conduit and a portion of the lateral atrial wall and the extra cardiac conduit (Fig. 12.3c) consisting of a tube graft between the transected inferior caval vein and the pulmonary artery.

Fenestration of a TCPC was a further modification introduced in 1990 as a transitional or final stage, slightly alleviating systemic venous congestion and augmenting filling of the systemic ventricle [5]. This aids in the postoperative course, maintaining cardiac output if pulmonary vascular resistance is labile. Occasionally, a small fenestration may

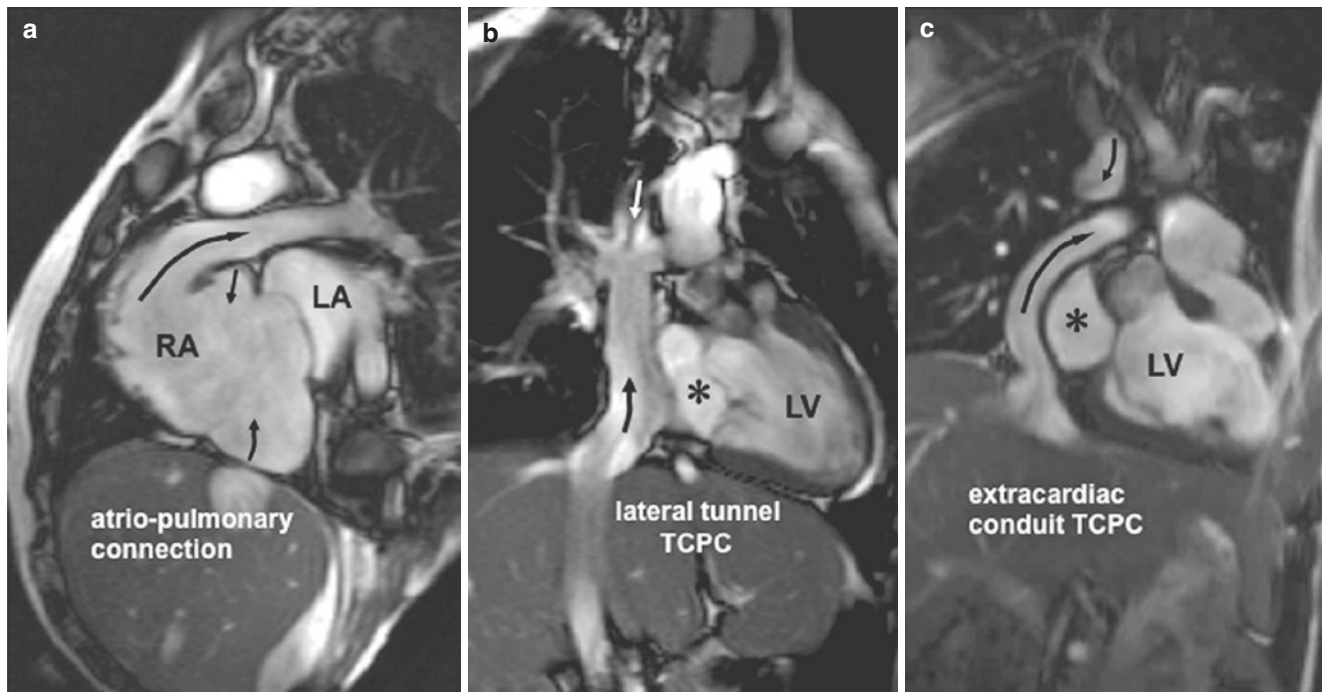


**Fig. 12.3** Three types of Fontan connection illustrated by CMR cine images, (a) atrio-pulmonary connection, (b and Movie 12.1) lateral tunnel, and (c) extracardiac conduit. b and c can both be called total cavopulmonary connection (TCPC). The TCPC avoids the progressive right

atrial distension which can predispose to atrial arrhythmias, stagnation and thrombosis, and the coronary sinus drains to the low-pressure part of the right atrium, which is marked \*. Arrows show the direction of blood flow

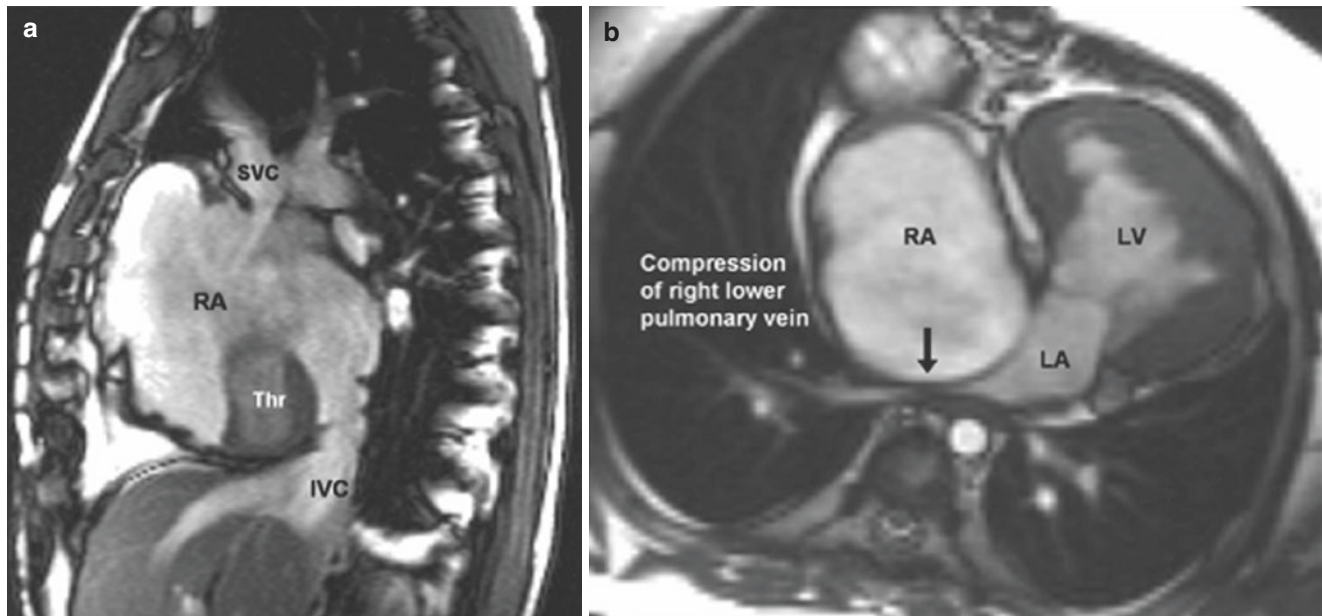


**Fig. 12.4** Complications of early atrio-pulmonary Fontan procedures. (a and Movie 12.2) This sagittal cine image shows dilated right atrium (RA) with a large thrombus attached to its floor. The solidified, ineffective leaflets of homograft atrial inflow valves can be seen in this case, mildly restricting inflow from the SVC and IVC. For this reason, atrial inflow valves were not included in later variants of the operation. (b and

Movie 12.3) The dilated right atrium (RA) upstream of an atrio-pulmonary Fontan connection causing compression of the right lower pulmonary vein (arrow), which then tends to exacerbate right atrial pressure and distension. SVC, superior vena cava; Thr, thrombus; IVC, inferior vena cava; LV, left ventricle; LA, left atrium

close spontaneously. If the hemodynamics assessed during catheterization is favorable, it can be closed by an occlusion device in a few months following surgery. A small fenestration, however, can be useful for the electrophysiologist providing access to the atria if electrophysiological procedures are needed in the future for arrhythmia.

## 12.5 Optimal Morphology of the Fontan Circulation

Marc de Leval and colleagues as well as other groups have gone on to apply computational fluid dynamic modeling to studies of the geometries and fluid dynamics of TCPC, either by lateral tunnel or extra cardiac conduit [6]. There is little doubt that the dimensions and shapes of the connections matter. The factors likely to optimize cavopulmonary flow and minimize systemic venous congestion include:

1. Avoidance of stenosis. Each flow path (IVC and SVC to RPA and LPA) and the junctions between them must have adequate cross-sectional area for the flow carried.
2. Avoidance of sharp angulations at the suture lines of the cavopulmonary anastomoses. Abrupt changes of direction predispose to flow separation and turbulence.
3. Avoidance of opposing or competing streams from the upward flowing IVC and the downward flowing SVC. In other words, they should not collide head on, but be slightly offset relative to one another. It is important, however, that hepatic venous blood contributes, via the IVC pathway, to both lungs as it carries a factor which prevents the formation of pulmonary arteriovenous malformations, a potential cause of progressive desaturation.
4. Minimization of flow separation, flow disturbance, and regions of stagnation that might predispose to thrombosis by maintaining uniform diameters and smooth contours through the cavopulmonary flow paths.
5. The minimization of energy dissipation, avoidance of potentially arrhythmogenic and thrombogenic atrial scarring and distension.

## 12.6 Causes of Failure in the Fontan Circulation

With improvement in surgical technique and better selection of patients, the operative mortality for completion of Fontan is now less than 5%. Patients, however, frequently run into complications in the long term [7].

There are several factors that may contribute to failure of a Fontan circulation. They include:

1. *Elevated resistance of the cavo-(atrio)-pulmonary vasculature*, including stenosis at surgical connections, hypoplasia, or stenosis of pulmonary arteries, thromboembolic obstruction, and pulmonary vein compression due to right atrial distension after atriopulmonary connection (Fig. 12.4b). In addition, there may be abnormal microvasculature either due to high pulmonary blood flow earlier in life or intrinsic anomalies, sildenafil might be of benefit in some cases [8].
2. *Atrial arrhythmias* (sinus node dysfunction or atrial re-entry tachycardia) particularly late after atriopulmonary connection. It is important to establish whether there are any treatable hemodynamic lesions such as anastomotic or pulmonary arterial stenosis which may be exacerbating atrial distension and making the patient prone to arrhythmia. Moreover, heterotaxy syndrome is associated with conduction system abnormalities. Patients with left atrial isomerism are predisposed to sinus node dysfunction and atrioventricular block due to lack of normal sinus node. On the other hand, patients with right atrial isomerism have dual sinus nodes and dual atrioventricular nodes and therefore are prone to supraventricular tachycardia [9].
3. *Thromboembolism*. Pathophysiology of prothrombotic state in Fontan patients is quite complex and includes endothelial dysfunction, blood flow abnormalities due to complex Fontan pathways, and absent subpulmonary pumping chamber; liver disease caused by chronic venous congestion resulting in coagulation abnormalities (Fig. 12.4a). Atrial arrhythmias and higher age increase this risk further. Unfortunately, there are no randomized studies in the literature to guide the physician to the best anticoagulation treatment. Vitamin K antagonists are strongly recommended in patients with known thromboembolic event or with history of atrial arrhythmias (Class I recommendation) according to the most recent 2018 Guidelines of American College of Cardiology and American Heart Association. Acetylsalicylic acid may be considered (Class IIb) in Fontan adults without previous thromboembolic event or atrial arrhythmias. There is currently insufficient data on safety and efficacy of NOACs (non-vitamin K antagonist oral anticoagulants) [10].
4. *Ventricular dysfunction*. The underlying congenital malformation, volume loading of the systemic ventricle prior to completion of Fontan reconstruction, the surgical procedure itself, and the abnormal pre- and after-loading of the ventricle following Fontan surgery may all contribute to ongoing ventricular dysfunction. Survival rate is significantly higher in dominant left ventricle when compared to the right ventricle (left ventricle 92%, 82%, and 78% vs. right ventricle 90%, 68%, and 63% at 10, 20, and 25 years, respectively,  $p = 0.005$ ). Atrioventricular valve regurgitation precedes ventricular dysfunction in most



cases and both progress over time, especially right ventricular dysfunction [11]. Outflow to the aorta via a ventricular septal defect/or an infundibulum can be subject to progressive obstruction and should be carefully assessed.

Both systolic and diastolic ventricular function is important, and indeed it may be that diastolic dysfunction is responsible for poor outcome in some patients [12]. It is the author's preference that most patients with a Fontan circulation should be on an ACE inhibitor although there is little direct evidence to support this [13].

5. *Systemic venous and hepatic portal congestion* and complications following from these. Elevation of systemic venous pressure to near critical levels is an inevitable consequence of Fontan surgery and can have damaging consequences for the microvessels and tissues of the organs upstream, notably the liver and the intestines. Ascites, hepatic edema and hepatic fibrosis, and, less commonly, cirrhosis and hepatic carcinoma have been reported as sequel. Protein-losing enteropathy is a further, relatively uncommon complication related to portal and lymphatic congestion. Plastic bronchitis, probably due to pulmonary lymphatic congestion and exudates is an uncommon but potentially fatal complication.

## 12.7 Role of Cardiovascular Magnetic Resonance

Cardiovascular magnetic resonance (CMR) enables the non-invasive assessment of the anatomical structures without ionizing radiation, and it enables ventricular functional assessment, quantification of flow, and assessment of ventricular fibrosis.

CMR can be used to help assess the suitability for the Fontan procedure to be performed in a particular patient, as well as having an important role in the assessment of the Fontan patient. Cine and 3D CMR acquisitions can be helpful in guiding interventions on Fontan patients, including those in the electrophysiology laboratory.

### 12.7.1 Assessment Pre-Fontan Completion

#### 12.7.1.1 Goals of Imaging

As detailed above, there are certain requirements for a Fontan circulation to work. Imaging should be targeted to help answer whether the patient meets these criteria.

Patients undergoing pre-Fontan assessment are usually 3–4 years old, and therefore they require general anesthesia or sedation. As the structures are small, sequences need to be modified appropriately, often necessitating smaller slice thickness on cine images. An example of a protocol used in a pre-Fontan patient is outlined in Table 12.2.

**Table 12.2** Comprehensive imaging protocol for pre- and post-Fontan patient

Sequence		Technical notes
Multislice scouts	Transaxial, coronal, and sagittal multislice	Bright blood SSFP in all three planes, dark-blood stack in transaxial plane to assist tissue characterization.
Transaxial cine stack	Cover the chest from neck to diaphragm	SSFP, 5 mm thickness, no gaps. All cines breath held and ECG gated.
Vertical long axis (VLA)	Cine (SSFP)	
Horizontal long axis (HLA)	Cine (SSFP)	
Short axis	Cine stack (SSFP)	
Four chamber	(If there are four)	
Outflow tract	Cines (SSFP)	
Aortic arch (if aortic coarctation suspected or history of aortic reconstruction)	Cine (SSFP)	
CMR contrast angiography	Conventional angiography or time-resolved angiography	
3D SSFP of the whole heart and great arteries	Free-breathing, ECG-gated, diaphragm-navigated acquisition	
Flow velocity acquisitions	Through-plane, breath hold acquisitions	For accurate shunt calculations, post-acquisition phantom correction may be needed.
Aortic flow	Velocity mapping	Venc 120–150 cm/s
SVC flow	Velocity mapping. Left SVC may be present.	Venc 80 cm/s
IVC flow	Velocity mapping. At diaphragm or above to include hepatic flow, proximal and distal to fenestration if present	Venc 80 cm/s
Branch pulmonary artery flows (RPA and LPA)	Velocity mapping	Venc 80 cm/s or 120 cm/s if suspected stenosis.
Early gadolinium imaging (optional)	In selected slice(s) to confirm or exclude suspected thrombus	Inversion recovery
Late gadolinium enhancement (optional)	For possible ventricular fibrosis or infarction	Inversion recovery



Important features which can be answered with CMR include:

- Detailed anatomy including situs, AV and VA connections, ventricular morphology, systemic and pulmonary venous return, and anatomy of the aortic arch
- Ventricular function (stroke volume and ejection fraction)
- Atrioventricular valve regurgitation(s) and regurgitation fraction
- Ventricular outflow
- Branch pulmonary arteries (dimensions and split net flow ratio between right and left lungs)
- Pulmonary venous return
- Interatrial communication
- Aortic arch patency
- Identification of venovenous collaterals and aortopulmonary collaterals and their hemodynamic impact

CMR study can be combined with measurement of internal jugular venous pressure after the CMR scan under the same general anesthesia. This allows estimation of the pressure in the pulmonary arteries. Care needs to be taken if there are bilateral superior caval veins and no bridging vein or if there is stenosis of superior caval vein or proximal pulmonary branches. Although this is a common practice, there is some evidence that internal jugular venous pressure might not be the best parameter to predict post-Fontan outcome. Venovenous collaterals are developed as consequence of pressure difference between superior and inferior caval veins in patients with bidirectional Glenn. Recent study has shown that venovenous decompressing grade but not jugular venous

pressure correlates with length of stay after Fontan completion and early- and medium-term outcome [14]. Jugular venous pressure might be an underestimate of true pulmonary vascular resistance as the superior caval vein offloading allows venous decompression. Therefore, careful assessment of venovenous collaterals on gadolinium enhanced CMR angiography is important.

Aortopulmonary collaterals can be visualized on contrast-enhanced angiography (conventional or time-resolved). Several studies showed association of their amount with length of hospital stay and pleural drainage after Fontan completion. Therefore, some units prefer their closure prior to Fontan surgery. The amount of aortopulmonary collaterals can be calculated by subtraction of superior and inferior caval venous flow from aortic flow or subtraction of pulmonary venous flow from pulmonary right and left artery flow [15–17].

Flow assessment is an important part of pre-Fontan evaluation. Numerous through-plane flows are acquired using 2D phase contrast imaging or 4D flow acquisition. 4D flow is now routinely used in many centers for flow measurements in pre-Fontan and Fontan patients although the relatively long scan times are still a limiting factor. Different to 2D phase contrast CMR, the imaging data cover a 3D volume that allows assessment of flow volumes and velocities in retrospect within every vessel of the acquired volume. More recently, commercially available CMR software has embedded tools that allow analysis of 4D flow image data. In addition to simple flow measurements, 4D flow enables to visualize the flowing blood during the cardiac cycle with several approaches such as pathlines or streamlines (Fig. 12.5; Movie 12.5). Another advantage of 4D flow is the

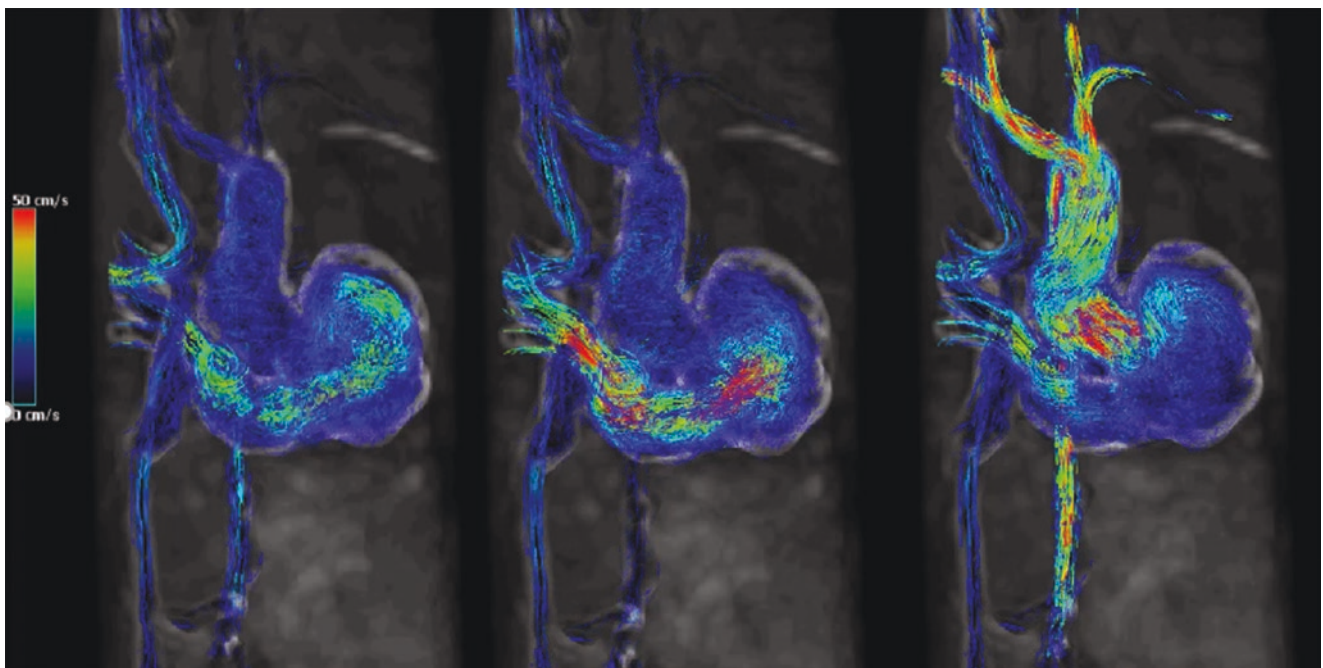


**Fig. 12.5** 4D flow with streamline visualization in a child with complex single ventricle anatomy after Fontan completion. The streamlines show the blood flow in the Fontan pathways, the ventricle, and the thoracic aorta

assessment of advanced hemodynamic markers (e.g., kinetic energy, vorticity, and helicity) that are still mainly used for research purposes but might have the potential to become future imaging biomarkers [18, 19].

Historically, all children undergoing completion of Fontan have had diagnostic cardiac catheterization to detail anatomy and measure pulmonary artery pressure and transpulmonary gradient (pulmonary artery pressure minus left atrial pressure) prior to the procedure. Many units have changed this practice, but there is no consensus in diagnostic approach in this group of patients so far. Whereas some units still perform catheterization in all patients, another ones prefer to perform CMR together with internal jugular venous measurement in the majority of the patients and reserve invasive catheterization only for the most risky patients [20] with poor ventricular function, high suspicion of increased pulmonary vascular resistance, or need for intervention on aortic arch or pulmonary branches to optimize the findings prior to Fontan procedure. An alternative approach preferred by some clinicians is aggressive closure of aortopulmonary collaterals before proceeding to Fontan. As no randomized trials are published so far, it is difficult to comment, which from these approaches is the most beneficial for the patients.

So far, CMR has been shown to be safe and effective and less costly alternative to routine catheterization in the evaluation of selected patients before the bidirectional cavopulmonary anastomosis operation [21, 22].

Examples of CMR findings in the preoperative Fontan patient are illustrated in Figs. 12.6 and 12.7. Points to be included in the report are shown in Table 12.3.

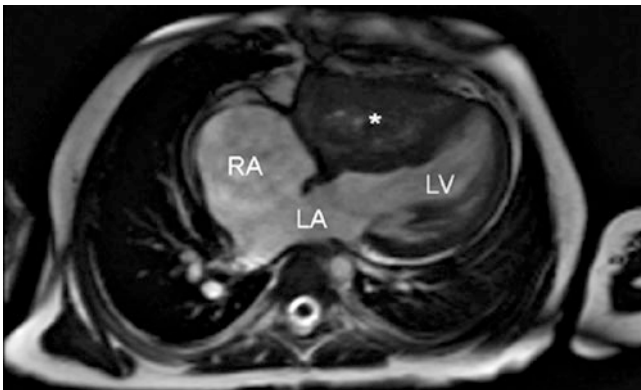


**Fig. 12.6** CMR cine image acquired prior to a Fontan procedure in a 5-year-old child with Ebstein's malformation. Previous Starne's procedure (oversewing of the tricuspid valve) and atrial septectomy. Four chamber view shows thrombus in the right ventricle. The interatrial communication is widely patent. \*thrombus in the right ventricle. RA, right atrium; LA left atrium; LV, left ventricle

## 12.7.2 Assessment Post-Fontan Completion

### 12.7.2.1 Goals of Imaging

Detailed complex anatomy of Fontan patient can be described using several sequences including multislice scouts, transaxial cine stack, tailored cines, 3D SSFP, and contrast-enhanced magnetic resonance angiogram (MRA). As detailed above, there are several factors that may contribute to failure of a Fontan circulation. CMR can be used as a tool to assess for many of these [23].

#### 1. Elevated resistance of the cavo-(atrio)-pulmonary vasculature

Assessment of:

- (a) the pulmonary arteries for anastomotic stenoses, branch pulmonary artery stenoses, or hypoplasia, split net flow between right and left lungs, which allows to assess clinical significance of potential unilateral narrowing
- (b) thrombosis in the Fontan pathways (Fig. 12.4a)
- (c) pulmonary vein stenosis or pulmonary vein compression caused by right atrial distension after atriopulmonary connection (Fig. 12.4b)

#### 2. Thromboembolism:

- (a) A stack of transaxial SSFP cines, for example 5 mm slice thickness with no gaps, is a good way to look for evidence of thrombus in cavo-atriopulmonary pathways, backed up by early gadolinium inversion recovery imaging (inversion time 450 ms) of any suspected thrombus, which should then appear as dark signal void relative to bright blood signal.

#### 3. Ventricular function:

- (a) Volumetric measurement is performed from a short-axis cine stack. If a second, usually small ventricle is present and communicating with the dominant ventricle, combined ventricular volume measurement is usually performed. Separate volume and function measurements might be useful, e.g., in case of two well-developed ventricles or if small ventricle is dysfunctional and assessment of contractility of dominant ventricle is desirable.

Increased total functional indexed end-diastolic ventricular volume was found to be the strongest independent predictor of death or transplant. Moreover, patients with ventricular dilatation and worse global circumferential strain are at highest risk [24]. Cardiac strain measured by CMR feature tracking was recently found to be an early indicator of sys-



**Fig. 12.7** Cardiac magnetic resonance scan pre-Fontan of a 2.5-year-old child with tricuspid atresia, ventriculo-arterial discordance and interrupted aortic arch. Previous aortic arch repair and pulmonary artery banding, followed by Damus–Kaye–Stansel procedure and right modified Blalock–Taussig shunt. Followed by bidirectional cavopulmonary anastomosis. **(a)** Four chamber view showing absent right connection (tricuspid atresia) and dominant left ventricle. The interatrial communi-

cation is widely patent. **(b)** Unobstructed cavopulmonary anastomosis (arrowed). The left pulmonary artery (LPA) is uniformly of lower caliber than the right (RPA). **(c)** Critical narrowing of the Damus–Kaye–Stansel anastomosis (arrowed). **(d)** Residual coarctation of the aorta just distal to the left subclavian artery. **(e)** Varicose dilatation of the anterior jugular veins in the neck. Ao, aorta

**Table 12.3** Points to include in the report for pre- and post-Fontan patient

Underlying anatomy (situs, AV and VA connections, ventricular morphology, systemic and pulmonary venous anatomy, and aortic arch)
Any Fontan pathway stenosis (SVC-PA and IVC-PA anastomoses)
Fontan pathway thrombosis
Branch pulmonary artery size and stenosis
Pulmonary vein narrowing
Ventricular function
Interatrial communication
Any atrioventricular valve regurgitation
Any aortic valve regurgitation
Any outflow tract +/- aortic arch obstruction
Anatomy and calculated amount of aortopulmonary collaterals
Descriptiton of venovenous collaterals
Presence and hemodynamic impact of fenestration
Extracardiac anomalies (e.g., scoliosis, pleural effusions, hematomegaly, splenomegaly, and abnormalities of the kidneys)



tolic ventricular decline even when ejection fraction, cardiac index, and clinical status are still preserved [25].

- (b) Long-axis cines should be acquired aligned with each ventricular inflow and outflow tract looking for evidence of regurgitation or stenosis which should be assessed further if found (Fig. 12.8).

4. *Assessment of collaterals and fenestration:*

- (a) systemic veins to pulmonary veins collaterals (Fig. 12.9c)  
 (b) aortopulmonary collaterals  
 (c) fenestration

*Gadolinium enhanced MRA* is used to assess great vessels and collaterals. Two three-dimensional data sets are usually acquired. These can be assessed using multiplanar reconstruction (MPR) in any plane. Measurements of vessels in perpendicular view can be also performed. 3D reconstructions represent a valuable tool for presenting the data to the clinicians.

Noncontrast ECG and respiratory navigator-gated 3D SSFP imaging is another way of 3D data acquisition. This sequence is particularly useful for assessment of intracardiac anatomy, aorta, and Fontan pathways.

*Flow analysis* is very helpful when assessing the postoperative Fontan patient. Differential flow in the right and left pulmonary arteries can be an indicator of stenoses, although there can be other explanations. One of them is a marked variability of flow from the caval veins toward the right and

left pulmonary arteries [23]. Most current CMR systems are subject to background phase offset errors that can affect measurements of flow. Post-acquisition correction using an acquisition in a static phantom may be needed. Unilateral pulmonary venous obstruction can also result in differential pulmonary artery blood flow, with reduced pulmonary artery flow on the side with pulmonary venous obstruction.

Although less issue than pre-Fontan, aortopulmonary collaterals and venovenous collaterals need to be assessed anatomically and using calculations mentioned above [16].

Evaluation of myocardial fibrosis by *late gadolinium enhancement* may be informative in patients with impaired ventricular function. Myocardial fibrosis has been shown to be common in Fontan survivors and associated with adverse ventricular mechanics and a higher prevalence of non-sustained ventricular tachycardia [26].

Patients undergoing post-Fontan assessment have usually undergone multiple previous surgical and catheterization procedures that may have involved coils, devices, or stenting procedures. These can affect image quality, some earlier devices causing significant artifacts [27]. Sequences need to be changed appropriately; GRE (gradient echo sequence) is usually used. Contrast-enhanced MRA might be helpful in some cases.

Examples of CMR findings in the postoperative Fontan patient are illustrated in Figs. 12.4, 12.8, 12.9, and 12.10. Comprehensive imaging protocol for postoperative Fontan patient is outlined in Table 12.2. Protocols must be individualized for each particular patient as the underlying anatomy and surgical technique may vary considerably. Figure 12.11

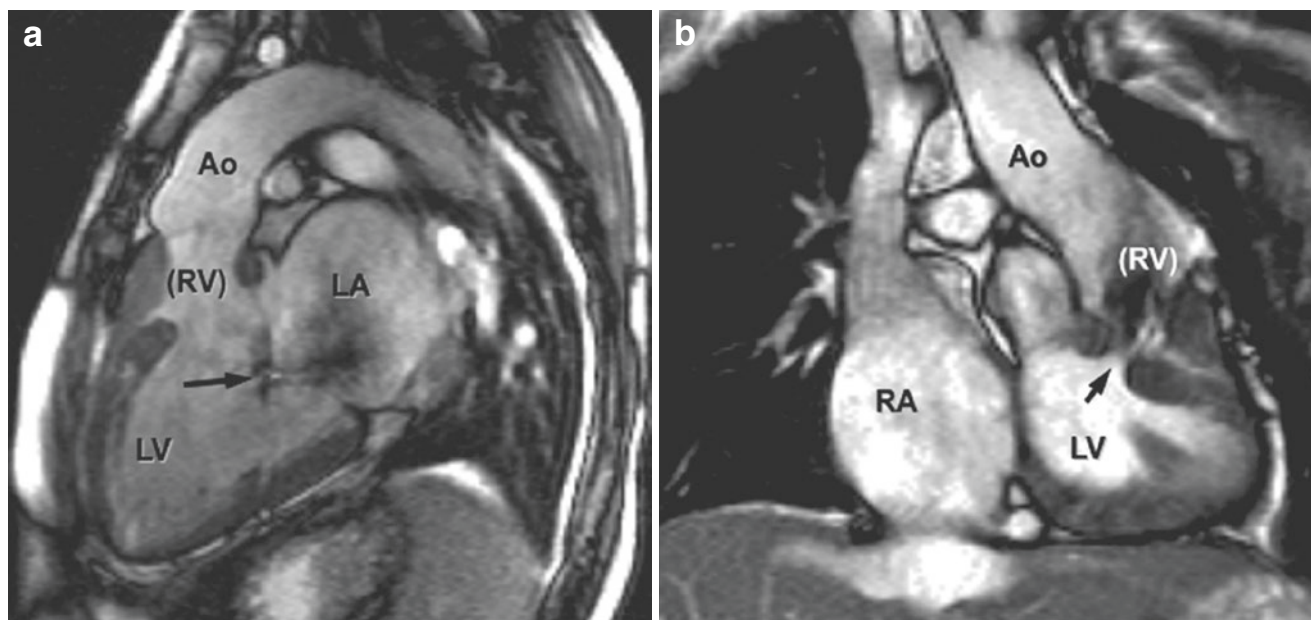


**Fig. 12.8** Problems with the left ventricular inflow valve or the outflow tract after Fontan procedure. (a) Mitral regurgitation (arrow) contributes to back pressure in the pulmonary vessels and so back to the systemic veins. In this particular patient who also had a pleural effu-

sion, treatment of fluid retention alleviated the regurgitation. (b) Left ventricular outflow obstruction after Fontan operation caused by a moderately restrictive VSD and hypertrophy of the infundibulum of the rudimentary, subaortic right ventricle



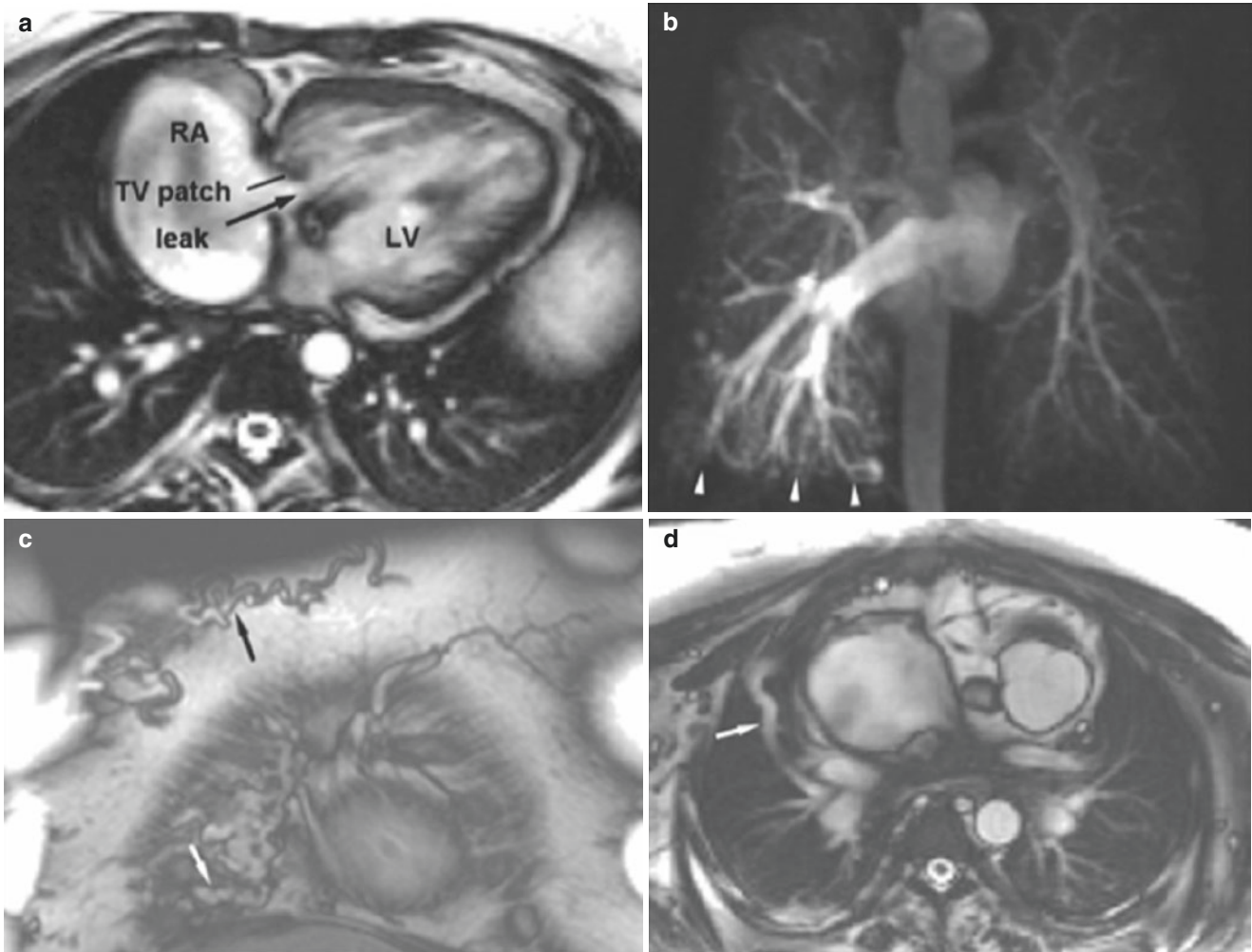


**Fig. 12.9** Desaturating shunts in three different patients. (**a**, Movie 12.4) A diastolic leak through the detachment of a patch placed across the right atrioventricular valve of a patient with double-inlet left ventricle and an atriopulmonary Fontan connection. (**b**) Magnetic resonance contrast angiogram showing evidence of right pulmonary

arteriovenous malformations (*arrows*) in a patient after Kawashima operation in whom hepatic venous return was flowing to the left lung but not the right. (**c**, **d**) Subcutaneous (*black arrow*) and intrathoracic (*white arrows*) branches of systemic venous to pulmonary venous collateral veins

shows all sites of through-plane flows which are acquired as part of the protocol. Points to be included in the report are described in Table 12.3.

### 12.7.3 Cardiac Magnetic Resonance Imaging for Guiding Intervention in Fontan Patients

Patients following the Fontan procedure are at risk of developing atrial arrhythmias which can be particularly difficult to

treat. They may require repeat electrophysiological interventions or repeat surgery. If no fenestration is left, access into the atrial mass is not possible at cardiac catheterization without creation of a fenestration in the wall of the conduit/lateral tunnel.

CMR can have a role in identifying or excluding the presence of thrombus pre-procedure, and 3D CMR acquisitions, for example by SSFP, can allow a “road map” of the cardiovascular pathways to be reconstructed which can be superimposed on the angiographic image to guide the interventionist.

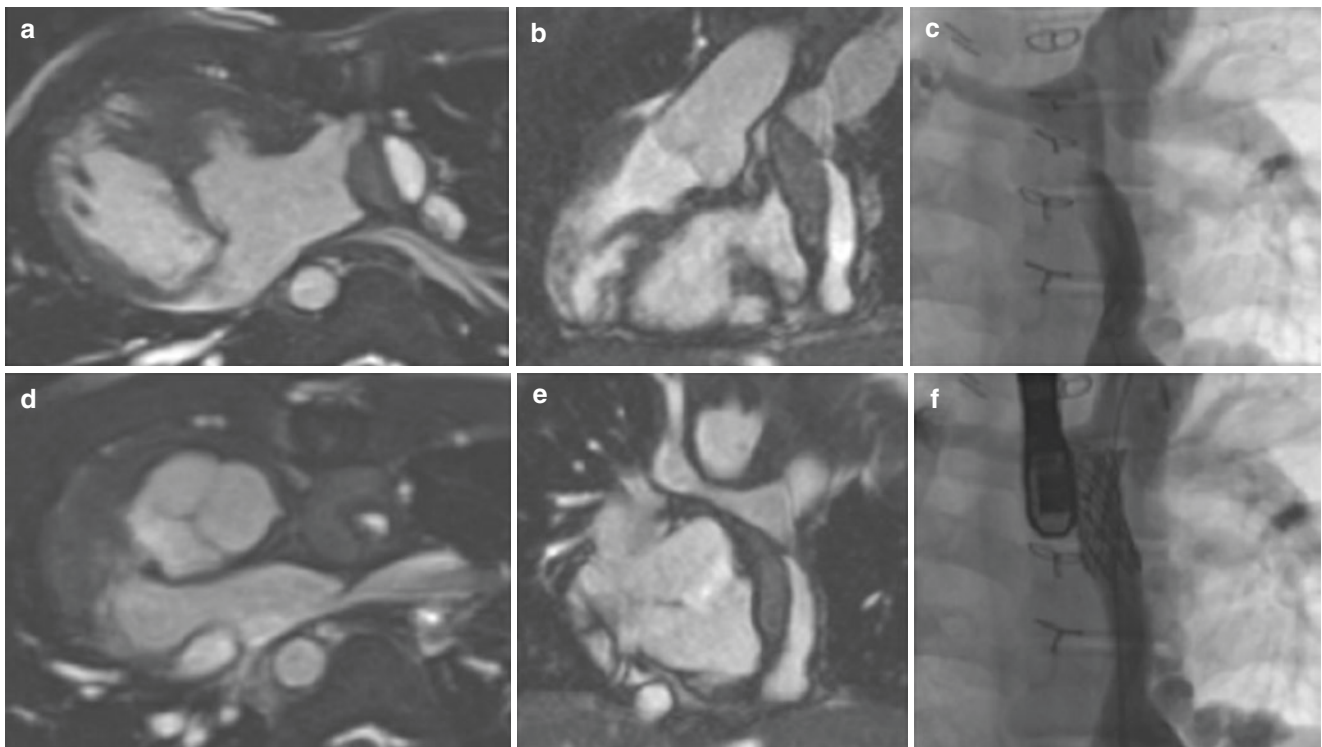


**Fig. 12.10** A 15-year-old patient with situs inversus, dextrocardia, bilateral superior caval veins, atrioventricular discordance with a single-outlet and pulmonary atresia, large perimembranous ventricular septal defect, and right aortic arch was found to have incidental finding of dissection of the TCPC conduit at routine CMR scan (a

and d show short axis and b and e long axis of the dissected conduit). Figure d shows very narrowed true lumen of the conduit at insertion to the pulmonary artery. Patient underwent cardiac catheterization (c). Figure f shows successful stent implantation into the conduit

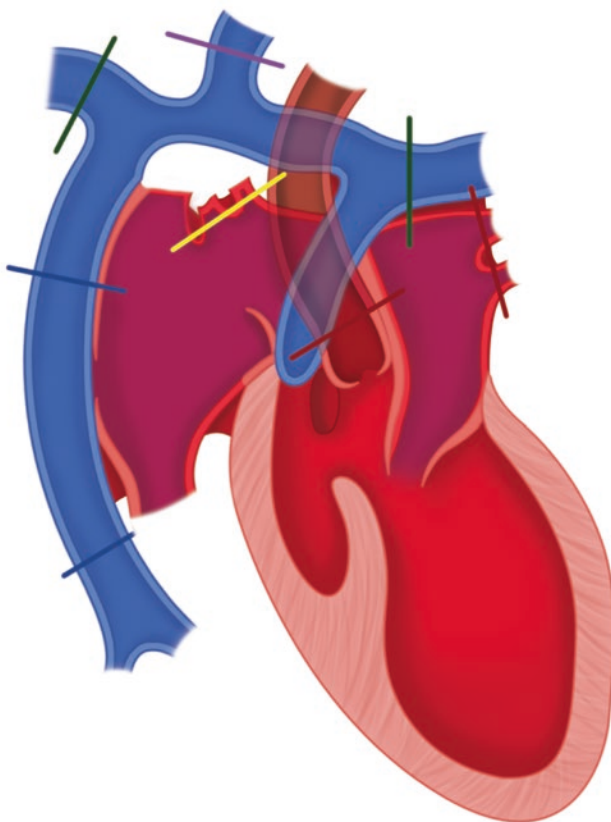


**Fig. 12.11** Sites of through-plane flows which are acquired as part of a comprehensive protocol of a pre- and post-Fontan patient

## 12.8 Discussion, Limitations, and Common Pitfalls

CMR's noninvasiveness and freedom from ionizing radiation are particularly relevant as patients often now have completion of Fontan at 3–4 years of age, with a life-long need for serial assessment. Multiple procedures using ionizing radiation can significantly increase the risk of malignancies later in life and should be avoided. In addition, CMR allows fairly easy quantification of ventricular function, flow analysis and myocardial viability.

However, patients may have intracardiac or pulmonary devices, stents, or coils that can cause artifacts. They are also susceptible to arrhythmia, and some Fontan patients have pacing systems which makes study by CMR challenging.

Computed tomography (CT) offers excellent spatial resolution and relatively unrestricted access in much shorter acquisition times than CMR. This can be beneficial for children as there is no need for an anesthetic, newer technology has greatly reduced ionizing radiation dose making CT angiography a more viable option for young children in specific cases.

Computed tomography is superior for imaging the epicardial coronary arteries and their relation to adjacent structures or conduits. As with CMR contrast angiography, the route of contrast passage relative to the cavopulmonary connections needs consideration. Given its high spatial resolution, CT

angiography is likely to depict small vessels such as aortopulmonary collateral arteries more clearly. Angiography, similarly with direct injection into collateral vessels, provides superior imaging of collateral vessels and their connections.

Transthoracic and/or transesophageal echocardiography still remains the first-line cardiovascular imaging modality in patients with congenital heart disease due to its availability and portability for bedside use. Although imaging is frequently very good in young patients, suboptimal acoustic access can be problematic in older patients particularly following cardiovascular surgery. Echocardiography is usually preferable to CMR for the identification of small baffle shunts, structural abnormalities of valve leaflets, and their suspensory apparatus, assessment of gradients (when adequate Doppler angle gained), and infective endocardial vegetations.

## 12.9 Conclusion

The range of procedures known as Fontan operations is palliative procedures, not corrections, and there is no such thing as a “perfect” Fontan operation. Patients invariably have complications at some point. Follow-up needs to be lifelong, by cardiologists with specific knowledge of the peculiarities of Fontan pathophysiology. Expert imaging, including CMR, is an important aspect of assessment of the preoperative and postoperative Fontan patient. A potential cascade of complications underlines the importance of excellent pre-Fontan management and decision-making, careful selection and planning for surgery, excellent surgical technique, and from then on, appropriate diagnostic follow-up and management. CMR is an excellent imaging technique, which allows serial follow-up scans and assessment of morphology, function, and risk stratification of patients with adverse outcome.

**Acknowledgments** We would like to thank Dr. Philip Kilner and Dr. Anna Seale for their valuable contribution to the first edition of this chapter and for giving us their permission to revise and update the chapter.

## References

- Gewillig M. The Fontan circulation. *Heart*. 2005;91(6):839–46.
- Cleuziou J, Schreiber C, Cornelsen JK, Horer J, Eicken A, Lange R. Bidirectional cavopulmonary connection without additional pulmonary blood flow in patients below the age of 6 months. *Eur J Cardiothorac Surg*. 2008;34(3):556–61.
- Fontan F, Baudet E. Surgical repair of tricuspid atresia. *Thorax*. 1971;26(3):240–8.
- de Leval MR, Kilner P, Gewillig M, Bull C. Total cavopulmonary connection. *J Thorac Cardiovasc Surg*. 1989;97(4):636.
- Bridges ND, Lock JE, Castaneda AR. Baffle fenestration with subsequent transcatheter closure. Modification of the Fontan operation for patients at increased risk. *Circulation*. 1990;82(5):1681–9.
- Hsia TY, Migliavacca F, Pittaccio S, et al. Computational fluid dynamic study of flow optimization in realistic models of the total cavopulmonary connections. *J Surg Res*. 2004;116(2):305–13.
- Rychik J, Atz AM, Celermajer DS, Deal BJ, Gatzoulis MA, Gewillig MH, Hsia TY, Hsu DT, Kovacs AH, McCrindle BW, Newburger JW, Pike NA, Rodefeld M, Rosenthal DN, Schumacher KR, Marino BS, Stout K, Veldtman G, Younoszai AK, d’Udekem Y; American Heart Association Council on Cardiovascular Disease in the Young and Council on Cardiovascular and Stroke Nursing. Evaluation and management of the child and adult with Fontan circulation: a scientific statement from the American Heart Association. *Circulation*. 2019;CIR0000000000000696. <https://doi.org/10.1161/CIR.0000000000000696>.
- Reinhardt Z, Uzun O, Bhole V, et al. Sildenafil in the management of the failing Fontan circulation. *Cardiol Young*. 2010;20(5):522–5.
- Ozawa Y, Asakai H, Shiraga K, Shindo T, Hirata Y, Hirata Y, Inuzuka R. Cardiac rhythm disturbances in heterotaxy syndrome. *Pediatr Cardiol*. 2019;40(5):909–13.
- Stout KK, Daniels CJ, Aboulhosn JA, et al. 2018 AHA/ACC guideline for the management of adults with congenital heart disease: a report of the American College of Cardiology/American heart association task force on clinical practice guidelines. *J Am Coll Cardiol*. 2019;73(12):e81–e192.
- Moon J, Shen L, Likosky DS, Sood V, Hobbs RD, Sassalos P, Romano JC, Ohye RG, Bove EL, Si MS. Relationship of ventricular morphology and atrioventricular valve function to long-term outcomes following Fontan procedures. *J Am Coll Cardiol*. 2020;76(4):419–31.
- Akagi T, Benson LN, Green M, et al. Ventricular performance before and after Fontan repair for univentricular atrioventricular connection: angiographic and radionuclide assessment. *J Am Coll Cardiol*. 1992;20(4):920–6.
- Kouatli AA, Garcia JA, Zellers TM, Weinstein EM, Mahony L. Enalapril does not enhance exercise capacity in patients after Fontan procedure. *Circulation*. 1997;96(5):1507–12.
- Hughes ML, Broadhead M, McEwan A, Tann O, Krupickova S, Muthurangu V. Pre-operative grade of decompressing systemic venous collaterals, but not jugular venous pressure, predicts short- and medium-term outcome after completion of the total cavopulmonary connection. *JACC Cardiovasc Imaging*. 2019;12(6):1109–11.
- Grosse-Wortmann L, Al-Otay A, Yoo SJ. Aortopulmonary collaterals after bidirectional cavopulmonary connection or Fontan completion: quantification with MRI. *Circ Cardiovasc Imaging*. 2009;2(3):219–25.
- Grosse-Wortmann L, Drolet C, Dragulescu A, Kotani Y, Chaturvedi R, Lee KJ, Mertens L, Taylor K, La Rotta G, van Arsdell G, Redington A, Yoo SJ. Aortopulmonary collateral flow volume affects early postoperative outcome after Fontan completion: a multimodality study. *J Thorac Cardiovasc Surg*. 2012;144:1329–36.
- Odenwald T, Quail MA, Giardini A, Khambadkone S, Hughes M, Tann O, Hsia TY, Muthurangu V, Taylor AM. Systemic to pulmonary collateral blood flow influences early outcomes following the total cavopulmonary connection. *Heart*. 2012;98:934–40.
- Rizk J. 4D flow MRI applications in congenital heart disease. *Eur Radiol*. 2021;31(2):1160–74.
- Warmerdam E, Krings GJ, Leiner T, Grotenhuis HB. Three-dimensional and four-dimensional flow assessment in congenital heart disease. *Heart*. 2020;106(6):421–6.
- Prakash A, Khan MA, Hardy R, Torres AJ, Chen JM, Gersony WM. A new diagnostic algorithm for assessment of patients with single ventricle before a Fontan operation. *J Thorac Cardiovasc Surg*. 2009;138(4):917–23.
- Brown DW, Gauvreau K, Powell AJ, et al. Cardiac magnetic resonance versus routine cardiac catheterization before bidirectional Glenn anastomosis in infants with functional single ventricle: a prospective randomized trial. *Circulation*. 2007;116(23):2718–25.

22. Jones BO, Ditchfield MR, Cahoon GD, et al. Cardiac magnetic resonance imaging prior to bidirectional cavopulmonary connection in hypoplastic left heart syndrome. *Heart Lung Circ*. 2010;19(9):535–40.
23. Kilner PJ, Geva T, Kaemmerer H, Trindade PT, Schwitter J, Webb GD. Recommendations for cardiovascular magnetic resonance in adults with congenital heart disease from the respective working groups of the European Society of Cardiology. *Eur Heart J*. 2010;31(7):794–805.
24. Meyer SL, Clair NS, Powell AJ, Geva T, Rathod RH. Integrated clinical and magnetic resonance imaging assessments late after Fontan operation. *J Am Coll Cardiol*. 2021;77(20):2480–9.
25. Meyer SL, Ridderbos FJS, Wolff D, Eshuis G, van Melle JP, Ebels T, Berger RMF, Willems TP. Serial cardiovascular magnetic resonance feature tracking indicates early worsening of cardiac function in Fontan patients. *Int J Cardiol*. 2020;303:23–9.
26. Rathod RH, Prakash A, Powell AJ, Geva T. Myocardial fibrosis identified by cardiac magnetic resonance late gadolinium enhancement is associated with adverse ventricular mechanics and ventricular tachycardia late after Fontan operation. *J Am Coll Cardiol*. 2010;55(16):1721–8.
27. Garg R, Powell AJ, Sena L, Marshall AC, Geva T. Effects of metallic implants on magnetic resonance imaging evaluation of Fontan palliation. *Am J Cardiol*. 2005;95(5):688–91.





## 13.1 Introduction

Transposition of the great arteries (TGA) is a form of conotruncal abnormalities in which the aorta arises from the morphological right ventricle (RV) and pulmonary artery arises from the morphological left ventricle (ventriculoarterial discordance). TGA encompasses two distinct defects, complete TGA and congenitally corrected TGA. Complete TGA has a prevalence of 0.31/1000 live births [1] and represents ~3–5% of all congenital heart disease [2]. It is the ninth most common congenital heart defect and the second most common cyanotic lesion after tetralogy of Fallot [1]. Complete TGA occurs in the setting of D-looped ventricles in situs solitus or L-looped ventricles in situs inversus. Congenitally corrected TGA is rarer, recognized in 0.02–0.07 per 1000 live births [3], or less than 1% of congenital heart defects [2].

Whereas patients with congenitally corrected TGA can survive unrecognized into adulthood, patients with complete TGA present with varying degrees of cyanosis in infancy and almost always require early surgical intervention. Beginning in the late 1950s, surgical treatment for patients with complete TGA was revolutionized with the advent of the Senning and Mustard atrial shunt procedures. Although the arterial switch procedure was first described in

1976, it only became the corrective procedure of choice in the 1980s.

The role of cardiac magnetic resonance imaging (CMR) in these defects is dictated by the specific cardiac anatomy and by the reparative surgical interventions present (if any). In cases of congenitally corrected TGA, CMR can be instrumental in discriminating between the morphologic right and left ventricles, in characterizing abnormalities of viscerio-atrial situs and in describing the associated cardiac anomalies that are nearly universally present. In the patients with complete TGA, almost all of whom will have had corrective surgery early in life; CMR can assess patency of conduits and baffles and presence of residual defects. Furthermore, when the morphologic RV is in the systemic position, it is prone to failure over time. Traditional methods of right ventricular function assessment are less accurate in this setting, and ventricular function and reserve may be better assessed by CMR in such cases.

## 13.2 Definitions and Morphology

### 13.2.1 Developmental Terms

- **Bulboventricular looping:** During normal embryologic development, the heart tube undergoes a bending and rightward rotation (dextro=D-looping). This normal D-looping indicates that the right ventricular inflow lies to the right of the left ventricle. L-looping (levo=L) is the abnormal leftward rotation of the heart tube, with the result that the right ventricular inflow becomes situated to the left of the left ventricle.
- **Conotruncal development:** In the primitive heart tube, the truncus arteriosus is the common origin for the aorta and pulmonary artery. Ventriculo-arterial connections are formed through growth or regression of muscular tissue,

**Supplementary Information** The online version contains supplementary material available at [https://doi.org/10.1007/978-3-031-29235-4\\_13](https://doi.org/10.1007/978-3-031-29235-4_13).

J. R. Wilson  
Advanced Cardiac Imaging, Overlake Hospital,  
Bellevue, WA, USA

M. A. Syed (✉)  
Cardiovascular Imaging, Division of Cardiology, Loyola  
University Medical Center, Maywood, IL, USA  
e-mail: [masyed@lumc.edu](mailto:masyed@lumc.edu)

the conus, beneath each of the eventual semilunar valves. Growth of the conus beneath the pulmonic valve directs it anteriorly, while regression of conus beneath the aortic valve directs it posteriorly and creates fibrous continuity between the aortic and the mitral valve.

### 13.2.2 Transposition of Great Arteries (TGA)

Transposition refers to ventriculoarterial discordance, when the morphologic RV leads to the aorta and the left ventricle to the pulmonary artery. The aorta is situated posterior and to the right in normal individuals. The direction of transposition (dextro- or levo-) refers to the rotation of the aorta relative to the pulmonary artery. By definition, the aorta follows the right ventricle in transposition syndromes.

- D-TGA or complete TGA (Fig. 13.1): Dextro-TGA signifies rightward rotation of the aorta and pulmonary artery (counterclockwise viewed from below). The aortic valve becomes displaced anteriorly and to the right of the pulmonic valve due to growth of conus tissue beneath the

aortic valve and resorption of tissue beneath the pulmonic valve (Fig. 13.2). In most cases, the ventricles are D-looped, so atrioventricular (AV) concordance is preserved. The aorta overlies a systemic right ventricle (which lies to the right of the left ventricle) that is in turn connected to the right atrium. Systemic and pulmonary circulations are arranged in a parallel circuit with one another; thus, a shunt, e.g. septal defect, is required for mixing of oxygenated and deoxygenated blood for survival of baby.

- L-TGA or congenitally corrected TGA, ventricular inversion, or double discordance—atrioventricular discordance and ventriculoarterial discordance (Fig. 13.3): In this condition, left and right ventricle positions are switched. Venous blood returns from the body into the right atrium and then passes through the mitral valve into the morphological left ventricle, also called subpulmonic ventricle. Blood then enters the lungs through the main pulmonary artery. Pulmonary venous blood returns to the left atrium and then through the tricuspid valve into the morphological RV, which acts as the systemic ventricle. Blood then exits through the aorta. The great arteries are

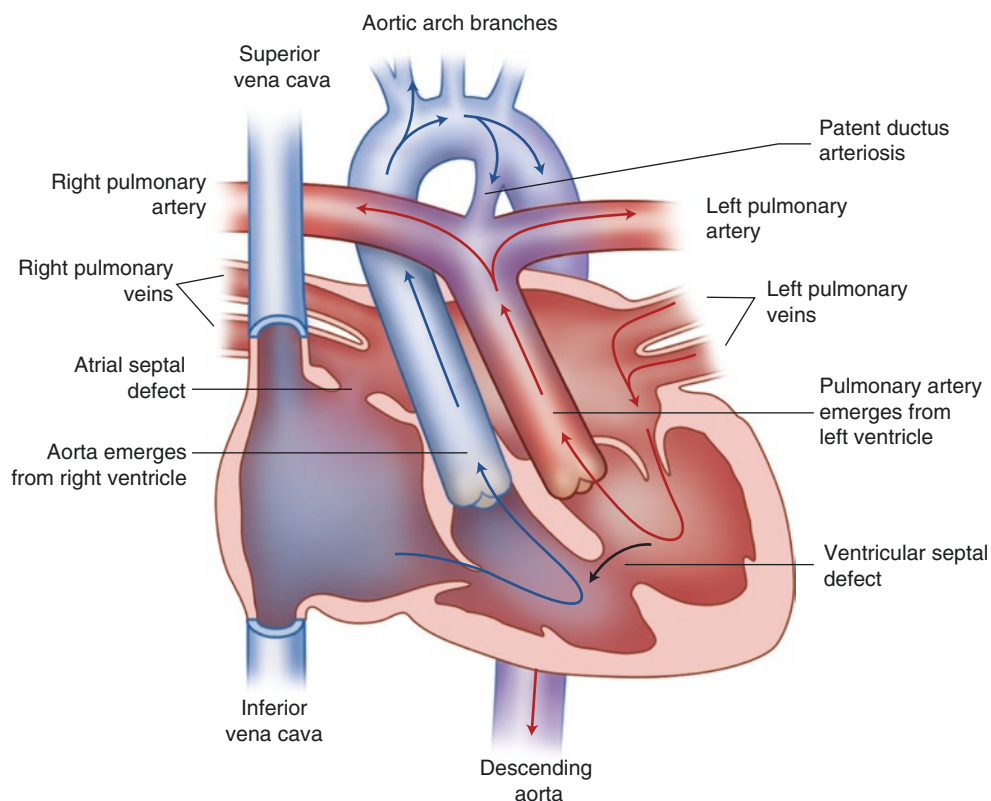


**Fig. 13.1** Complete transposition of the great arteries (complete TGA, D-TGA). Schematic showing the arterial connections and flow of blood in the case of unrepaired complete TGA. The right atrium leads into the morphologic right ventricle and the left atrium into the morphologic left ventricle (atrioventricular concordance). The aorta arises from the morphologic (systemic) right ventricle, whereas the pulmonary artery origi-

nates from the morphologic left ventricle (ventriculoarterial discordance). In the unrepaired patient, the systemic and pulmonary circulations run in parallel. In order for blood in the systemic circulation to oxygenate, mixing must occur through one or more communications, such as a ventricular septal defect, atrial septal defect, or patent ductus arteriosus

typically arranged side by side in patients with congenitally corrected TGA, rather than anterior and posterior. Systemic and pulmonary circulations are arranged in a series circuit with one another, analogous to normal individuals.

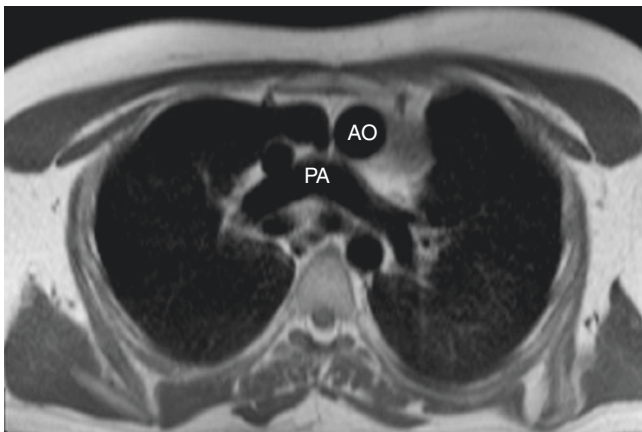
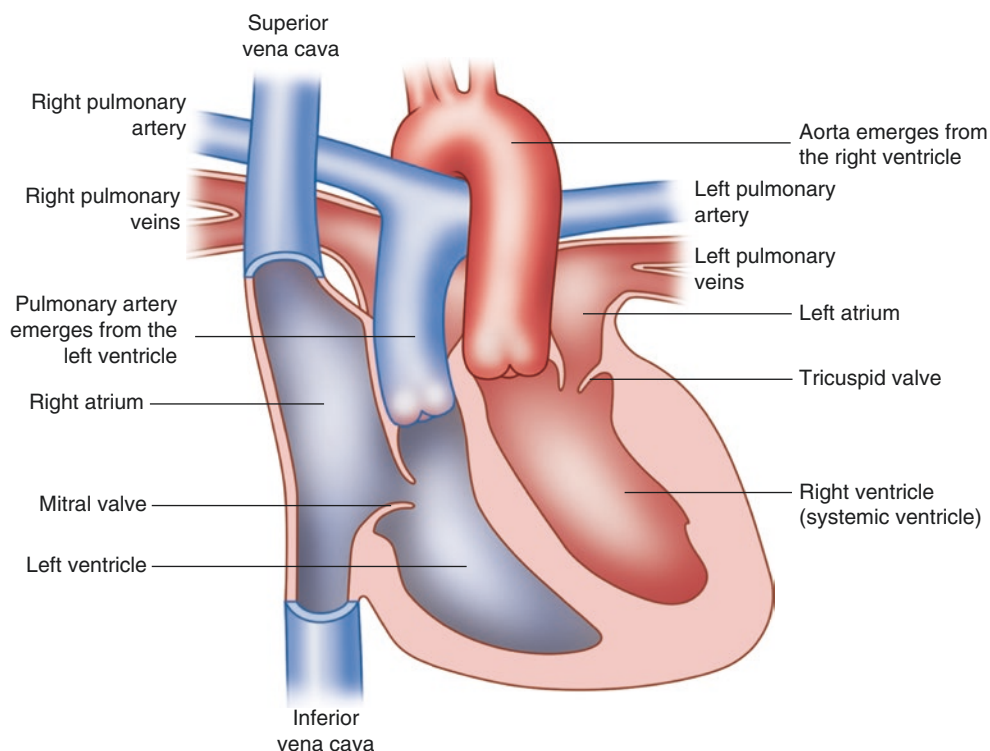


**Fig. 13.2** Axial black blood image of a patient with complete transposition of the great arteries (complete TGA, D-TGA). In normal individuals, the aorta lies slightly posterior and to the right of the pulmonary artery. In most cases of complete TGA, the aorta is anterior and to the right of the pulmonary artery; however this spatial relationship is variable. This example, in which the aorta (AO) lies anterior and to the left of the pulmonary artery (PA), demonstrates the variability in the relationship of the great arteries in transposition syndromes. The diagnosis of transposition should rely on the presence of ventriculoarterial discordance rather than on the position of the aorta

### 13.2.3 Corrective Surgeries for Complete TGA

- Atrial baffle procedures (Senning and Mustard operation, also called atrial switch procedures; Fig. 13.4): Performed with either autograft (Senning) or synthetic (Mustard) baffle material, atrial baffle operations involve removal of the interatrial septum and creation of a partition which directs systemic venous return from the superior and inferior venae cavae into the left atrium and the pulmonary venous return into the right atrium. The baffle runs in an oblique coronal orientation and is roughly shaped like a pair of pants. One leg of the pants is in each of the venae cavae, and the waistband surrounds the nonsystemic (mitral) atrioventricular valve. The excluded portions of the common atrium form the return pathway for the pulmonary veins to the systemic circulation through the morphologic RV.
- Arterial switch procedure (Jatene operation; Fig. 13.5): The aorta and main pulmonary arteries are transected at the level of the sinotubular junction. The coronary artery ostia with buttons are removed from the original aortic root and reimplanted in the previous main pulmonary artery root (the “neo-aorta”). The main pulmonary artery is brought forward and anastomosed to the previous aortic root, while the aorta is relocated posterior to the branch pulmonary arteries and anastomosed to the neo-aorta. As a result, the right pulmonary artery runs anterior to the ascending aorta in its new position. The Lecompte maneuver may also be performed during the surgery to avoid

**Fig. 13.3** Congenitally corrected transposition of the great arteries (congenitally corrected TGA, L-TGA). Schematic demonstrating the arterial connections and flow of blood in the case of congenitally corrected TGA. The right atrium leads into the morphologic left ventricle and the left atrium into the morphologic right ventricle (atrioventricular discordance). The aorta arises from the morphologic (systemic) right ventricle, whereas the pulmonary artery originates from the morphologic left ventricle (ventriculoarterial discordance). Because of the “double discordance,” the systemic and pulmonary circulations are in series with one another, as in normal individuals, but the right ventricle becomes the systemic ventricle



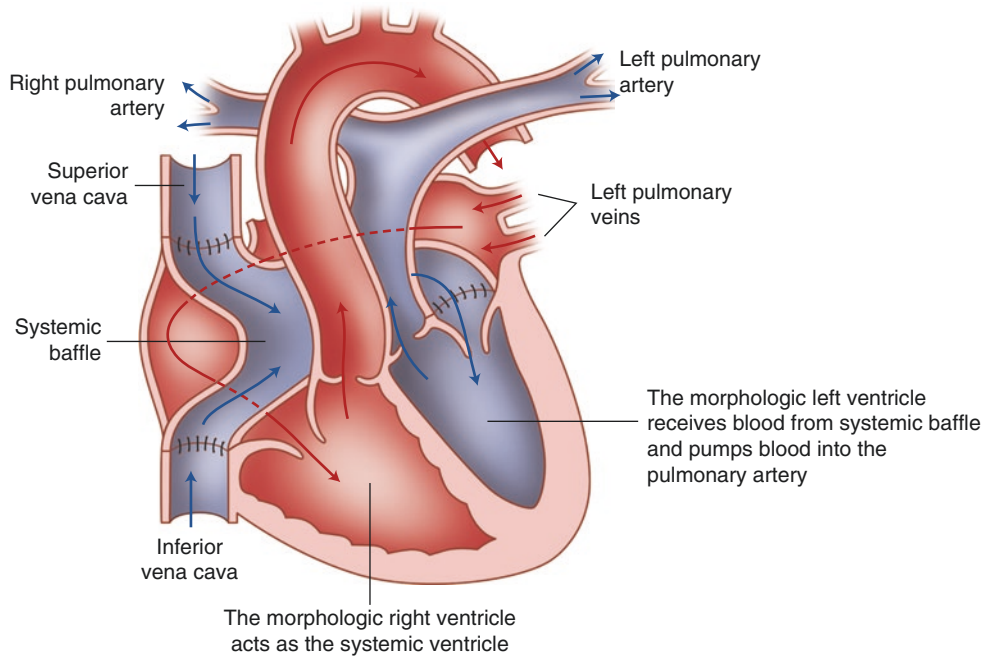


**Fig. 13.4** Complete TGA with atrial baffle procedure (Mustard or Senning). This schematic illustrates the flow of blood in patients with complete TGA who have undergone repair with atrial baffle procedures. The interatrial septum is removed creating a single combined atrium. The systemic baffle (the shunt for blood returning from the systemic venous circulation) is shaped like a “pair of pants” with one “leg,”

or limb, connected to the superior vena cava and the other to the inferior vena cava. The “waist” of the pants is sutured to the mitral valve annulus. Blood returning from the pulmonary circulation enters the systemic right ventricle by flowing through the areas of the combined atria that are excluded by the systemic baffle

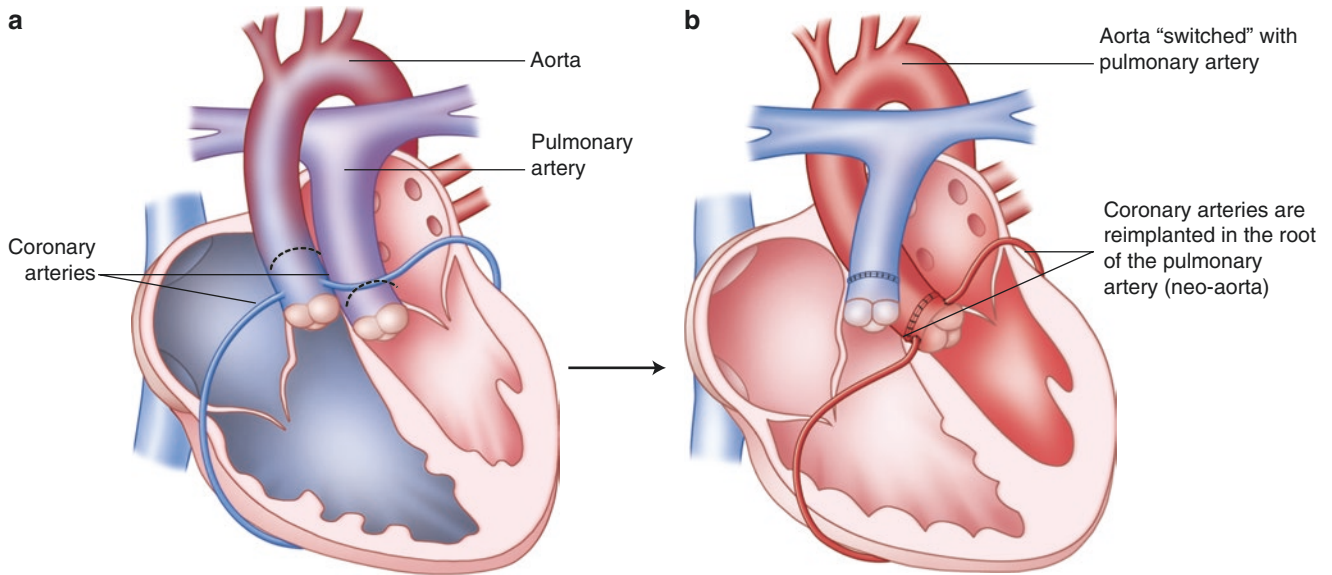
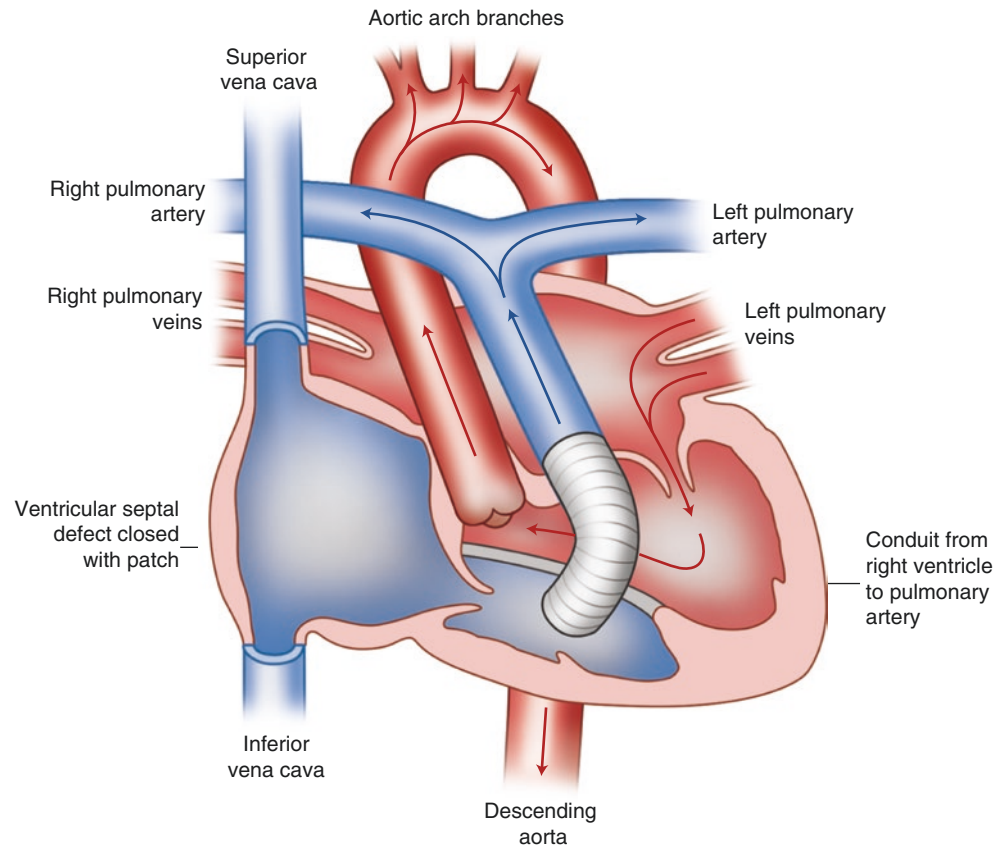


**Fig. 13.5** Complete transposition of the great arteries with arterial switch procedure (Jatene operation). The arterial switch procedure is currently the favored approach for surgical correction of complete TGA. The coronary arteries and a cuff of aortic tissue surrounding the ostia are detached from the aorta and reimplanted in the root of the pulmonary artery. The aorta and pulmonary artery are transected and the pulmonary artery and the right main pulmonary artery are brought anterior to the aorta (see panel a). Note the new position of the right pulmonary artery in panel b is different than the normal anatomic position beneath the aortic arch. The pulmonary artery is anastomosed to

the remaining rim of aortic tissue superior to the aortic valve. The aorta is anastomosed to the root of the pulmonary artery with the reimplanted coronary arteries, now termed the neo-aortic root. Residual shunts are repaired. The normal relationship of the pulmonary and systemic circulations is restored with the left ventricle in the systemic position. Blood returning from the lungs passes into the left atrium, through the mitral valve into the left ventricle, and out into the systemic circulation through the pulmonary valve and neo-aorta, which is now anastomosed to the aorta (panel b)



**Fig. 13.6** Complete transposition of the great arteries (TGA) with Rastelli procedure. The Rastelli procedure is used as a primary surgical correction in the minority of patients with complete TGA who have a ventricular septal defect (VSD), and often stenosis in the pulmonary outflow. It involves patching and sometimes enlarging the VSD in such a manner as to create a left ventricular outflow through the VSD to reach the aorta. After resecting obstructions, the right ventricle is connected to the main pulmonary artery with a valved conduit. The morphologic left ventricle is now in the systemic position (correcting the ventriculoarterial discordance)



distortion of the branch pulmonary arteries in the process of switching the great vessels by relocating the aorta posterior to the pulmonary artery such that both branch pulmonary arteries drape anterior to the aorta.

- Rastelli procedure (Fig. 13.6): Used in the minority of patients (<10%), who have pulmonary outflow tract stenosis and a ventricular septal defect (VSD), blood flow is directed from the left ventricle through the ventricular septal defect to the aorta. The normal flow of blood on the right side is reestablished by oversewing the pulmonary outflow tract and placing a conduit between the RV and the pulmonary artery.

### 13.3 Associated Anomalies

In contrast to other conotruncal abnormalities such as tetralogy of Fallot, chromosome 22q11.2 deletions are not seen in patients with complete TGA. Males are affected twice as often as females in both complete and congenitally corrected TGA [3–5]. There are no associated syndromes with TGA, nor is there a familial form [4, 5]. In

**Table 13.1** Conditions associated with transposition syndromes

Complete TGA	Congenitally corrected TGA
Ventricular septal defect (VSD): 45–50%, can be present in any region of the ventricular septum	Ventricular septal defect (VSD): 70–80% typically perimembranous
Left ventricular (subpulmonic) outflow tract obstruction: 25%	Left ventricular outflow tract obstruction (pulmonic/subpulmonic stenosis): 30–70%
Patent ductus arteriosus usually present at birth	Patent ductus arteriosus: 10%
Anomalies of coronary artery origin and course: ~30%	Atrioventricular (AV) node and his bundles: abnormal position and course common. Presentation with heart block progress to AV block at ~2%/year
Coarctation of the aorta: ~5%	Coarctation of the aorta: ~5% Abnormalities of the systemic atrioventricular valve: 80–90%, usually an apically displaced valve, but without other features of a typical Ebstein's anomaly

both forms of TGA, there are few extracardiac anomalies reported, but associated cardiac anomalies are common (Table 13.1) [2, 5].

## 13.4 Clinical Presentation

### 13.4.1 Complete TGA

Clinical presentation and age of presentation are usually determined by the presence or absence of a ventricular septal defect (VSD). In the absence of a VSD, newborns will present with cyanosis, either within the first day or as the ductus arteriosus closes during the first week [2]. In the remainder, the presenting signs and symptoms depend upon the degree of mixing between systemic and pulmonary blood pools. With VSD present, children may present between 4 and 8 weeks old with poor feeding, tachypnea, and tachycardia, with cyanosis less prominent [6]. The presence of VSD with subpulmonic stenosis can mimic tetralogy of Fallot. In other cases, it may be difficult to distinguish complete TGA from double outlet right ventricle [5].

The majority of children with complete TGA will have undergone corrective surgery, since unrepaired there is a 90% mortality in the first year of life. Dyspnea, fatigue, and arrhythmias are common presenting complaints for late complications following corrective surgery. Arrhythmias may be poorly tolerated in patients with marginal hemodynamics. Exercise capacity is usually decreased due to a combination of factors, one of which is often sinus node dysfunction. Additionally, specific complications arise in association with the various corrective surgeries.

Long-term survival after atrial baffle procedures (Mustard and Senning operations) in experienced centers is up to 77% at 25 years [7]. In addition to systemic (morphologic RV) ventricular dysfunction and tricuspid valve regurgitation, pulmonic stenosis or subpulmonic obstruction may arise when enlargement of the systemic ventricle distorts these left-sided structures. Other important long-term sequelae include baffle leak or stenosis and pulmonary hypertension. Baffle stenosis, typically of the upper limb of the two-legged systemic baffle, presents with facial fullness, upper extremity edema, or subtle mental status changes mimicking a superior vena cava syndrome when severe. Stenosis of the lower limb of the systemic baffle may present as edema, ascites or hepatic dysfunction. When pulmonary return is compromised, pulmonary hypertension may develop. Hemodynamically significant baffle stenosis is relatively common and likely under-recognized, although often managed without intervention [8].

First performed in 1976, the arterial switch procedure is the preferred surgical management in uncomplicated complete TGA infants. Survival following this procedure is around 90% at 10 years, and quality-of-life scores are better for children who have undergone arterial switch procedures than those who have had atrial baffle procedures [2, 9]. The most common late complication following arterial switch operations is main pulmonary artery or branch pulmonary

artery stenosis, sometimes as a result of neo-aortic root dilatation. Other complications include coronary insufficiency, coronary ostial narrowing, and coronary kinking leading to myocardial ischemia. Ventricular dysfunction, semilunar valve regurgitation, and arrhythmias are also relatively common.

Survival following the Rastelli procedure is approximately 60% at 20 years [10]. Late complications include left- or right-sided outflow tract or conduit obstruction, residual VSD, hypertrophy or chamber enlargement, aortic regurgitation, and aortic root dilatation.

### 13.4.2 Congenitally Corrected TGA

Despite the fact that most (80–90%) patients with congenitally corrected TGA have associated anomalies [4], in the majority of patients congenitally corrected TGA remains unrecognized until adulthood. Two-thirds of patients with associated abnormalities and one-quarter without will develop heart failure by age 45 [2]. Compromise of the systolic function of the systemic RV probably develops due to a combination of myocardial supply-demand mismatch and regurgitation of the systemic atrioventricular valve. Other presenting features depend upon the associated abnormalities. Patients with subpulmonic/pulmonic stenosis and a VSD may present with variable degrees of cyanosis. Presentation with AV block or atrial tachyarrhythmia is common.

## 13.5 CMR Imaging

### 13.5.1 Indications and Goals of Imaging

Lifelong follow-up is needed as residual lesions and sequelae are common. The basic indications for CMR in patients with congenital heart disease are when the echocardiographic assessment is suboptimal or ambiguous. In infants presenting with complete TGA, echocardiography typically provides sufficient information and adjunctive CMR imaging is rarely required. However, surgeries for complete TGA are never curative. Thus, the primary indication for CMR is in long-term follow-up after corrective surgery and in monitoring systemic right ventricular function, where routine surveillance is often indicated [9, 11]. CMR will often be obtained for further information when clinicians are contemplating surgical or catheter-based interventions, and it is useful for imagers to be familiar with indications for reoperation procedures [9].

For patients with unrecognized congenitally corrected TGA presenting prior to diagnosis, CMR may be initially requested for further evaluation of ventricular dysfunction or dextrocardia. It is important for the imager to be familiar

with the findings in transposition in order to make the diagnosis. Goals in this setting include establishing viscerocardiac anatomy, segmental cardiac anatomy, course of great vessels, quantifying ventricular function particularly of the systemic right ventricle, and the degree of tricuspid regurgitation. Once the diagnosis of TGA has been established, the presence of associated anomalies, such as subpulmonic stenosis or stenosis of pulmonary valve, should be explored.

In the postsurgical patient, there is often limited visualization of heart and blood vessels by echocardiography while CMR does not have these limitations [12]. In these patients, knowledge of the type of prior surgical procedures performed is critical to the imaging assessment. In patients with congenitally corrected TGA or complete TGA with atrial baffle operations, periodic assessment of the systemic right ventricular systolic function and the severity of systemic atrioventricular valve (tricuspid valve) regurgitation are indicated. Systemic atrioventricular valve dysfunction in transposition represents an entity comparable to mitral valve regurgitation in patients without transposition syndromes. It is essential that tricuspid repair or replacement be performed before the ejection fraction of the systemic RV falls below 45%. Competence of the surgically created baffles (after Mustard/Senning operations) and conduits (after Rastelli operation) should be assessed during follow-up. Shunts, whether from baffle leak or residual VSD, are another indication for intervention when the Qp/Qs is greater than 1.5:1, when they result in progressive dysfunction or chamber dilatation or when they cause symptoms. For patients with prior arterial switch operations, the presence of main pulmonary artery or branch pulmonary artery obstruction, as well as the size of the neo-aortic root, should be assessed during follow-up. Regurgitation of the semilunar valves should also be evaluated. Additionally, all adult patients should have the patency of the coronary arteries evaluated at least once [9], which may be accomplished by CMR in some cases or cardiac computed tomography (CT).

Approximately 1% of patients with prior atrial switch procedures will undergo heart transplantation [7]. As part of the evaluation prior to cardiac transplantation, CMR imaging goals include describing the atrio-visceral situs and venous return abnormalities, which complicate transplantation surgery. A large fraction of patients with transposition syndromes will require pacemaker implantation [2, 7]. In patients referred prior to pacemaker placement, the indication includes assessing the feasibility of a transvenous approach. Additionally, evaluation for small baffle leaks or residual VSD is indicated in this setting, as the presence of these increases the risks of paradoxical embolism during instrumentation.

Physiologic assessments such as stress tests are sometimes indicated for evaluation of symptoms like exercise intolerance or for evaluation for ischemia following arterial switch procedures. In patients with poor exercise tolerance, a

dobutamine or exercise stress protocol can evaluate whether systolic function can be augmented. Because of the long-term risks for coronary artery insufficiency following arterial switch procedures and because presentation can be clinically silent, intermittent surveillance for ischemia by CMR stress or other modalities has been suggested [13]. This topic is discussed in more detail in the Stress MRI in Congenital Heart Disease chapter.

### 13.5.2 CMR Sequences and Imaging Protocols

As with clinical presentation and CMR indications, details of specific sequences will depend upon what form of TGA is present, which prior surgical procedures have been performed, if any, and the clinical setting; therefore the imaging protocol should be individualized. An example of CMR imaging protocol used in our institution is shown in Table 13.2.

**Table 13.2** CMR protocol for imaging transposition of great arteries

<i>Sequences common to all transposition syndromes:</i>	
1. Localizer scout images	
2. Static multislice SSFP in axial, coronal and sagittal planes covering the whole chest	
3. Electrocardiogram (ECG) gated, expiratory breath-held SSFP cine images	
(a) Two- and four-chamber views	
(b) Short-axis stack from base to apex	• A 7 mm slice thickness with a 3 mm interslice gap. Use the same spacing for late gadolinium enhancement
(c) Outflow views: Oblique sagittal and oblique coronal views of the systemic and subpulmonic outflow tracts (“right ventricular outflow tract” and “left ventricular outflow tract” or “three-chamber” views)	
(d) Contiguous axial SSFP cine stack from aortic arch to diaphragm	
4. Contrast magnetic resonance angiography (MRA)	Bolus-timed MRA is typically used to study great vessels. High temporal resolution MRA images can track the bolus to evaluate abnormal connections (septal defects and baffle patency)
5. Phase contrast velocity-encoded cines. In-plane images (breath-held) in four-chamber, LVOT and RVOT orientations to assess valvular function. Through-plane images of ascending aorta, main pulmonary artery and branch pulmonary arteries for shunt and flow quantification	
6. Late gadolinium enhancement (LGE)	
(a) TI scout: Use a mid-ventricular slice to acquire the correct TI time to null normal myocardium	
(b) Inversion recovery LGE imaging in short-axis and long-axis planes (similar to cine images)	
<i>Additional sequences specific to clinical setting:</i>	
<i>In complete TGA:</i>	
Following atrial baffle procedures:	
1. SSFP cine images	
(a) Contiguous oblique coronal views parallel to the SVC and IVC to evaluate systemic baffle function	

(continued)

**Table 13.2** (continued)

(b) Contiguous oblique sagittal views through the pulmonary baffle
2. Phase contrast velocity-encoded cines
(a) In-plane images (breath-held) in regions of suspected narrowing or flow acceleration on SSFP images, initial VENC of 100 cm/s is appropriate for baffle evaluation
(b) Through-plane images (breath-held) to transect regions of suspected flow acceleration, increasing VENC by 50 cm/s until aliasing disappears (for peak velocity assessment)
(c) If shunt or baffle leak suspected: Through-plane systemic and pulmonary flow (free breathing) assessments for shunt fraction quantification. Systemic flow obtained with through-plane images above the sinotubular junction. Pulmonary flow obtained with through-plane images transecting the main pulmonary artery
Following Rastelli operation:
1. SSFP cine images
(a) Contiguous oblique coronal and sagittal images parallel to the outflow tracts (parallel left and right ventricular outflow tract views)
(b) Cine of the prosthetic valve within the RVOT conduit is obtained orthogonal to the RVOT views
2. Phase contrast velocity-encoded cines
(a) If residual VSD or other shunt is suspected, free breathing systemic and pulmonary flow images are obtained for shunt fraction quantification as described above
(b) If flow acceleration is suspected in the right ventricular outflow tract or pulmonary arteries from in-plane LVOT & RVOT images, then through-plane images are acquired oriented to transect confirmed flow accelerations. Initial VENC of 200 cm/s is appropriate for arterial flows, increasing by 50 cm/s until aliasing disappears
Following arterial switch procedure:
1. Phase contrast velocity-encoded cines
(a) In-plane images of the aortic root, main pulmonary artery and branch pulmonary arteries
(b) Through-plane images to transect regions of flow acceleration on in-plane images
2. Isotropic respiratory-navigated three-dimensional SSFP coronary MRA to evaluate proximal vessels
3. Pharmacologic stress testing with myocardial perfusion imaging, if ischemia suspected
Stress and resting first-pass perfusion imaging obtained in representative basal, mid, and apical short-axis slices
<i>In unoperated congenitally corrected TGA:</i>
1. SSFP cine images
(a) Contiguous coronal SSFP cine stack from anterior chest wall through descending aorta to delineate the relationship of the great vessels
2. Phase contrast velocity-encoded cines
(a) In-plane images in regions of suspected VSD or stenosis on SSFP images
(b) If VSD is present, through-plane systemic and pulmonary flow assessments for shunt fraction quantification as described above
3. If VSD suspected, GRE cine images with saturation bands can be helpful to localize VSD and characterize direction of jet. Care must be taken to orient saturation band to cover just one side of the heart

### 13.5.2.1 Static Multislice SSFP in Axial, Coronal, and Sagittal Planes Covering the Whole Chest

Images obtained in the three anatomical reference planes allow for localization of structures and can be used to prescribe further images. A series of ECG-gated, breath-held axial, coronal, and sagittal images with close spacing of slices covering the entire thorax (slice thickness of 5 mm obtained every 3–5 mm, for example) provides sufficient detail to identify the relationship of the great vessels and to determine abdominal visceral situs. As an alternative to steady state free precession (SSFP) sequences, some centers prefer to use dark blood techniques for these images.

### 13.5.2.2 SSFP Cine Images

Cine images using SSFP-based sequences will typically be obtained in more than one imaging plane to sufficiently delineate the complex anatomy of TGA syndromes. Cine images are ECG-gated and should ideally be breath-held, except in the assessment of ventricular interdependence.

### Complete TGA Following Atrial Baffle Operation

Contiguous, axial, or parallel four-chamber cine stacks from the aortic arch to the lower heart border provide information on ventricular function, systemic atrioventricular valve competence, and venous and arterial anatomy (Figs. 13.7

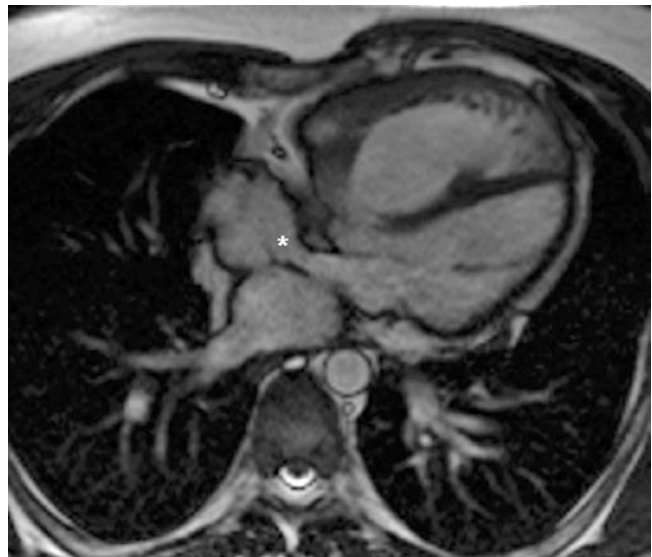


**Fig. 13.7** Complete transposition of the great arteries following atrial baffle procedure. Still frame of an axial SSFP cine showing the systemic baffle to the left ventricle. The *asterisk* is located in the confluence of the superior and inferior limbs, which attach to the superior and inferior vena cavae, respectively (anastomoses not shown). The waist of the systemic baffle attaches to the mitral valve annulus



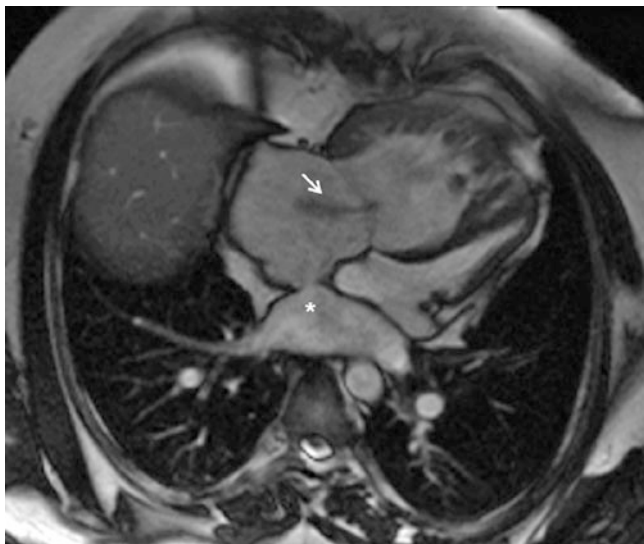


**Fig. 13.8** Complete transposition of the great arteries following atrial baffle procedure. Still frame of a four chamber SSFP cine loop through the pulmonary baffle. Pulmonary veins can be seen draining into the posterior portion of the atrium, then through the pulmonary baffle (*asterisk*) to enter into the systemic right ventricle. The tricuspid valve is typically dysmorphic and is prone to regurgitation (*arrow*)

and 13.8; Movies 13.1 and 13.2). From these images or from the axial static SSFP images, oblique coronal SSFP cines may be obtained to evaluate baffle function. These should be oriented parallel to the SVC and IVC planes. A contiguous stack of straight coronal and/or sagittal cines is an alternative initial approach [14, 15]. In the majority of cases, oblique sagittal or oblique coronal views optimally visualize the full extent of the systemic venous baffle, with double oblique views less frequently required, whereas axial or oblique coronal views are best for the pulmonary venous pathway [16]. A short-axis stack should be obtained for quantification of the systolic function and chamber dimensions of the systemic RV. Short-axis slices are usually obtained with a 7 mm slice thickness and a 3 mm inter-slice gap such that 10 short-axis slices can be obtained through the ventricle from base to apex. Left ventricular (LV) outflow tract cines should be obtained for evaluation of subpulmonic stenosis. Additional cine views include the two-chamber/vertical long-axis and right ventricular outflow tract cines for further qualitative assessment of ventricular and valvular function.

#### Complete TGA Following Rastelli Operation

As the pertinent postsurgical anatomy following the Rastelli operation is around the outflow tracts and pulmonary arteries, pulmonary artery cines to evaluate for stenosis in axial plane usually replace the oblique coronal cines. Each of the branch pulmonary arteries should have cine images prescribed parallel to blood flow and orthogonal to the axial scouts or cines. Pulmonary artery bifurcation is usually seen

on axial cine. Cine of the prosthetic valve within the right ventricular outflow tract (RVOT) conduit should be obtained orthogonal to the RVOT views. More than one RVOT view (parallel RVOT views) may be needed to evaluate the RV to main pulmonary artery conduit (Movie 13.3). Similarly, parallel views may be needed to evaluate the left ventricular outflow tract (LVOT) as it tunnels through the repaired VSD (Movie 13.4). Contiguous parallel four-chamber or axial cine stacks can assess qualitative evaluation of ventricular function and evaluate for residual VSD. The long-axis views and short-axis stack are obtained as above.

#### Complete TGA Following Arterial Switch Operation

Cine views should be obtained in several imaging planes, focusing primarily on the outflow tracts, neo-aortic root and pulmonary arteries. Contiguous axial cine stacks from the lower heart border or mid-ventricle to the aortic arch, parallel three-chamber (LVOT) cines, and parallel RVOT cines allow for dynamic assessment surrounding the sites of surgical anastomoses. A cine view of the bifurcation of the main pulmonary artery should be obtained. Aortic valve cine should be obtained parallel to the aortic cusps to evaluate morphology. Assessment of ventricular function is obtained from short-axis cine stack and two- and four-chamber views. A contiguous parallel coronal cine stack from the posterior aspect of the sternum through the descending aorta is also recommended by some [17].

#### Congenitally Corrected TGA

The typical individual long-axis cines (two-, three-, and four-chamber) and short-axis cine stack should be obtained for qualitative and quantitative left ventricular function. Cines in a coronal orientation can demonstrate the parallel arrangement of the great vessels and provide additional information on semilunar valve function. A contiguous stack of cines oriented perpendicular to the line of coaptation of this valve can assess valvular morphology. Additional contiguous axial or parallel four-chamber cine stacks allow for assessing regurgitation and for the presence of an associated ventricular septal defect. Coverage should extend through the outflow tracts, as most VSDs in congenitally corrected TGA are perimembranous. Right-sided outflow tract and pulmonary artery cines are also indicated given the frequency with which pulmonic stenosis and subpulmonic obstructions are associated.

#### 13.5.2.3 Phase Contrast (Velocity-Encoding) Imaging

##### Estimating Stenosis Severity

Volumetric coverage with SSFP cine images in more than one imaging plane allows for identification of regions of flow acceleration and anatomic narrowing and guides the acquisition of phase contrast imaging. This is particularly useful in

exploring baffle stenosis, although other areas of flow acceleration may include the subpulmonic outflow tract, main pulmonary artery, branch pulmonary arteries, or along the ventricular septum at the site of a residual or unrecognized VSD. In-plane velocity-encoded images, with the frequency encoding direction parallel to the jet or blood flow, can help to further localize the jet envelopes if not well seen on SSFP images.

Through-plane phase contrast images should be obtained in a plane perpendicular to the jet or blood flow near the orifice. An initial velocity encoding (VENC) level of 100 cm/s is appropriate for evaluating baffles, increased in increments of 50 cm/s if aliasing exists. The estimated peak gradient across the defect, obtained using the modified Bernoulli's equation, will not exceed  $4 \times (\text{VENC})^2$  where the VENC is the level at which aliasing disappears. Flow curves in combination with peak velocity can provide additional useful information for estimating stenosis severity (Table 13.3).

These criteria must be interpreted in the clinical context.

For interrogating arterial or outflow tract stenosis, in-plane followed by through-plane phase contrast imaging with an initial VENC level of 200 cm/s is appropriate. Further characterization of gradients follows principles outlined above; perpendicularly transect the jet near the orifice and increase the VENC level on subsequent acquisitions if needed until aliasing disappears. In-plane and through-plane phase contrast imaging can be attempted for the valved conduit to assess for stenosis in patients with prior Rastelli operations; however susceptibility artifacts may compromise interpretation when stented bioprosthetic valves are used.

### Flow Quantification

The ratio of pulmonary to systemic blood flow ( $Q_p/Q_s$ ) is an important indicator of the need for surgical intervention in patients with TGA as in other conditions. An abnormal  $Q_p/Q_s$  may elucidate a need for further imaging for a VSD or baffle leak. A  $Q_p/Q_s$  of 1.5:1 or greater is an indication for repair of a baffle leak [4, 9, 11, 18]. Slice prescriptions for assessing pulmonary flows can be based on RVOT or pulmonary artery images and should be a cross section of the main pulmonary artery between the pulmonic valve and the bifurcation. Aortic flow measurement is obtained as a cross sec-

tion of the aorta above the sinotubular junction and can be prescribed from coronal views. Flow quantification measurements are usually non-breath-held, ECG-gated acquisitions with an initial velocity encoding (VENC) value in the through plane between 150 and 200 cm/s. Quantitative flows through the great vessels also provide estimates of regurgitant volumes across the semilunar valves. Subtracting stroke volume assessed by phase contrast from the stroke volume obtained by volumetric assessment of ventricular size provides another means of calculating atrioventricular valve regurgitant volumes and fractions.

### 13.5.2.4 Contrast Angiography (MRA)

Contrast-enhanced MRA can provide a qualitative, three-dimensional overview of complex anatomy. Contrast-enhanced MRA acquisitions are usually bolus-timed to study specific anatomy. This technique is useful in the evaluation of main or branch pulmonary artery stenosis following arterial switch procedures or in the setting of congenitally corrected TGA. Dynamic angiography, or three-dimensional time-resolved contrast-enhanced MRA, is a three-dimensional fast gradient echo sequence obtained once pre-contrast then repeated successively about every 5 s (high temporal resolution) during contrast administration. Since successive images are acquired as the contrast bolus moves through the circulation, it is potentially useful to detect shunt and baffle stenosis. However, mild stenosis may be missed by dynamic angiography, and thus it is probably best used as an adjunct to other imaging sequences [15].

### 13.5.2.5 Noncontrast Angiography

Three-dimensional noncontrast MRA is acquired with a bright blood SSFP-based sequence that is diaphragm-navigated and ECG-gated. The standard acquisition window covers the entire heart and mediastinum. It requires no breath holding or gadolinium contrast, but acquisition times are lengthy. There is potential utility in the assessment of all transposition syndromes. Since it is ECG-gated, it is more useful for measurements of the aortic root than non ECG-gated contrast-enhanced MRA and should be considered for follow-up evaluations of patients after arterial switch procedures. It can be helpful in the assessment of pulmonary artery stenosis. While it can also be useful for assessing baffles, care must be taken to position the diaphragm navigator such that the saturation effect of the navigator band does not interfere with signal in the pulmonary venous pathways.

By including fat saturation, noncontrast diaphragm-navigated three-dimensional acquisitions can also be modified for coronary angiography to assess for anomalies of coronary origins and potentially rule out proximal stenoses or kinking in patients following arterial switch procedures [19].

**Table 13.3** Estimating severity of baffle stenosis by characteristics of velocity-encoding images when anatomic narrowing is also present [15]

Estimated severity	Flow curve	Peak velocity (m/s)
Mild	Pulsatile, peaking in early diastole	<1
Moderate	Pulsatile	1–1.5
Severe	Damped curve, continuous flow	>1.5

### 13.5.2.6 Late Gadolinium Enhancement (LGE)

LGE has been evaluated in limited numbers of patients with transposition syndromes, and the significance of the finding in this population is debated [19, 20, 21]. Nonetheless, in patients who are receiving gadolinium-based contrast for other imaging sequences such as contrast MRA, LGE images should be obtained in the short- and long-axis orientations used for SSFP cine images. In patients with prior arterial switch procedures in whom coronary ostial narrowing and coronary kinking is a potential late complication, LGE may have some clinical utility. In one small series, LGE was seen in 2 out of 16 pediatric patients who had prior arterial switch procedures. However, both of these patients had previously known or suspected peri-surgical myocardial infarctions, so it is unclear how LGE findings affected patient management [19]. The prognostic utility of LGE in patients with transposition syndromes needs further study.

### 13.5.2.7 Stress Myocardial Perfusion Imaging

First-pass myocardial perfusion imaging has established efficacy in patients being evaluated for atherosclerotic coronary artery disease. Typical protocols use vasodilator medications (regadenoson, adenosine, and dipyridamole) for stress imaging. SSFP, echo planar, and FLASH imaging sequences have been used. Stress and rest cine acquisitions are obtained in three representative short-axis slices (base, mid, and apex); gadolinium contrast is infused during both acquisitions. CMR stress protocols may be reasonable alternatives to nuclear stress testing in order to avoid repetitive radiation exposures over long-term follow-up [22].

## 13.5.3 CMR Findings

Abnormalities of atrio-visceral situs and ventricular orientation should be assessed in all patients with transposition syndromes (Figs. 13.9 and 13.10). Regurgitation of atrioventricular valves is common, more so when the morphologic RV is the systemic ventricle.

### 13.5.3.1 Congenitally Corrected TGA: Unoperated

The trabecular pattern and position of the atrioventricular valve are features which help to distinguish the morphologic right from left ventricle. The morphologic RV has increased trabeculations. A moderator band may be visible. The tricuspid valve has a septal attachment that is apically displaced relative to the mitral valve, and the ventricles usually associate with their respective atrioventricular valve [2]. Fibrous continuity exists between the mitral valve and the semilunar valve in the morphologic left ventricle but not RV. Atrioventricular and semilunar valve



**Fig. 13.9** SSFP image of a patient with congenitally corrected transposition of the great arteries and dextrocardia. The systemic right ventricle is posterior and is identified by its coarse trabecular pattern and its association with the morphologic tricuspid valve, demonstrated by the apical position of its septal attachment relative to the mitral valve (*arrows*)

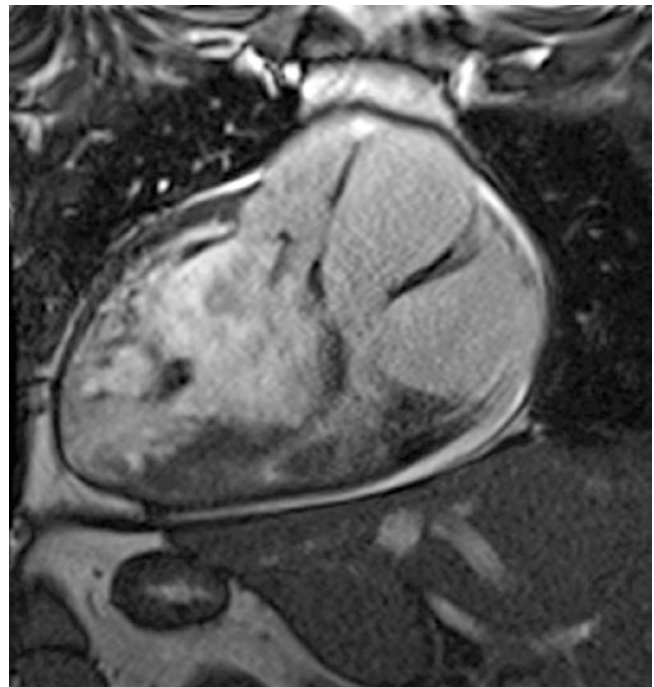


**Fig. 13.10** Coronal view of a patient with congenitally corrected transposition of the great arteries (*TGA*), dextrocardia, and situs inversus. The outflow tracts are seen in a side-by-side configuration, which is typical in congenitally corrected TGA. Regurgitation is seen in the systemic semilunar (aortic) valve. The liver is seen on the left





**Fig. 13.11** Still frame of first-pass perfusion imaging in a parallel four-chamber orientation in patient with congenitally corrected TGA and situs inversus. Contrast enhancement of the nonsystemic ventricle outlines several non-enhancing masses consistent with thrombi along the base of the interventricular septum (*arrows*)

regurgitation can be seen in many cases. By quantifying stroke volumes for both ventricles, the regurgitant fraction of a single regurgitant valve can be calculated by subtracting the ventricular stroke volumes from one another, divided by the stroke volume of the regurgitant ventricle. The typical orientation of the outflow tracts in congenital TGA is side by side (Movie 13.5). When ventricular function is abnormal, perfusion imaging can demonstrate coexisting pathologies (Fig. 13.11; Movie 13.6). Other associated abnormalities include malformations of the systemic atrioventricular valve, ventricular septal defect, left ventricular outflow tract obstruction, and pulmonic stenosis (Movie 13.7). Abnormalities of coronary origin and course can also be seen.

### 13.5.3.2 Complete TGA: Unrepaired

Patients with complete TGA present early in infancy, and the role of CMR in these patients is limited. Echocardiography is the main modality for evaluating these patients. The majority of newly diagnosed patients will undergo arterial switch procedures; however many adult patients will have undergone atrial switch operations.

### 13.5.3.3 Complete TGA Following Atrial Baffle Operations

Baffle leaks, fenestrations, or stenosis can be identified by flow artifact on SSFP images or by anatomic narrowing on three-dimensional imaging and confirmed with velocity-encoded images [8, 16]. While there is no standard definition of baffle stenosis, an internal dimension of <10 mm in either major or minor axis has been used by some to define ana-

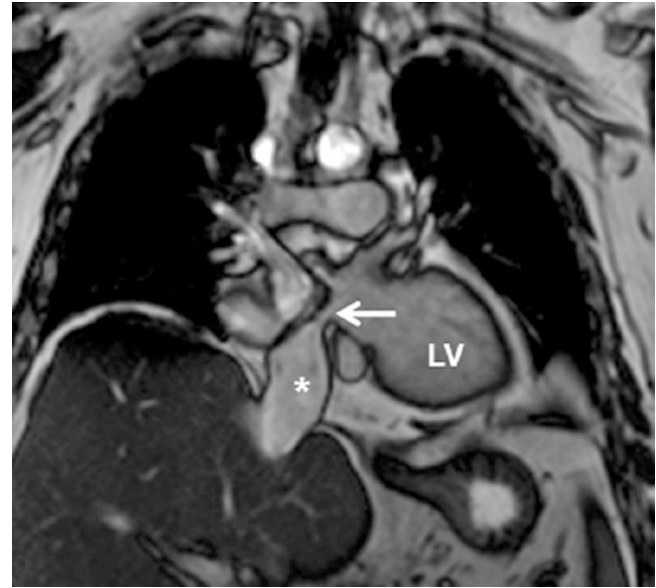


**Fig. 13.12** Still frame of a coronal SSFP cine in a patient with complete transposition of the great arteries following an atrial baffle procedure. Anatomic narrowing of the inferior limb of the systemic baffle is seen (*arrow*) with concomitant dilation of the inferior vena cava (*asterisk*). LV, left ventricle

tomic narrowing [8] (Fig. 13.12). If present this finding should prompt further investigation to determine hemodynamic significance, such as azygous vein dilation >5 mm or flow reversal in the azygous system on axial images (Fig. 13.13). The typical arrangement of the aorta is anterior and to the right of the pulmonary artery in patients with complete TGA (D-TGA).

### 13.5.3.4 Complete TGA Following Rastelli Operation

The course of the left ventricular outflow tract as it passes from the posterior morphologic left ventricle to the anteriorly displaced aortic valve can be traced (Fig. 13.14a). The left ventricular outflow tract may be stenotic. Residual VSD can be seen along the VSD patch/conduit. The RVOT conduit (Fig. 13.14b) can be incompetent, stenotic, or aneurysmal. The native pulmonic valve may be present, or a valved conduit may have been used.

### 13.5.3.5 Complete TGA Following Arterial Switch Operation

During the arterial switch operation, the pulmonary artery is moved anterior to the aorta. In this position, the pulmonary arteries can be especially susceptible to obstruction, especially when there is enlargement of the neo-aortic root. The morphologic pulmonic valve remains attached to the left ventricle and therefore is vulnerable to regurgitation. Occasionally, stenosis of the coronary arteries or coronary kinking may be suspected by MRA.



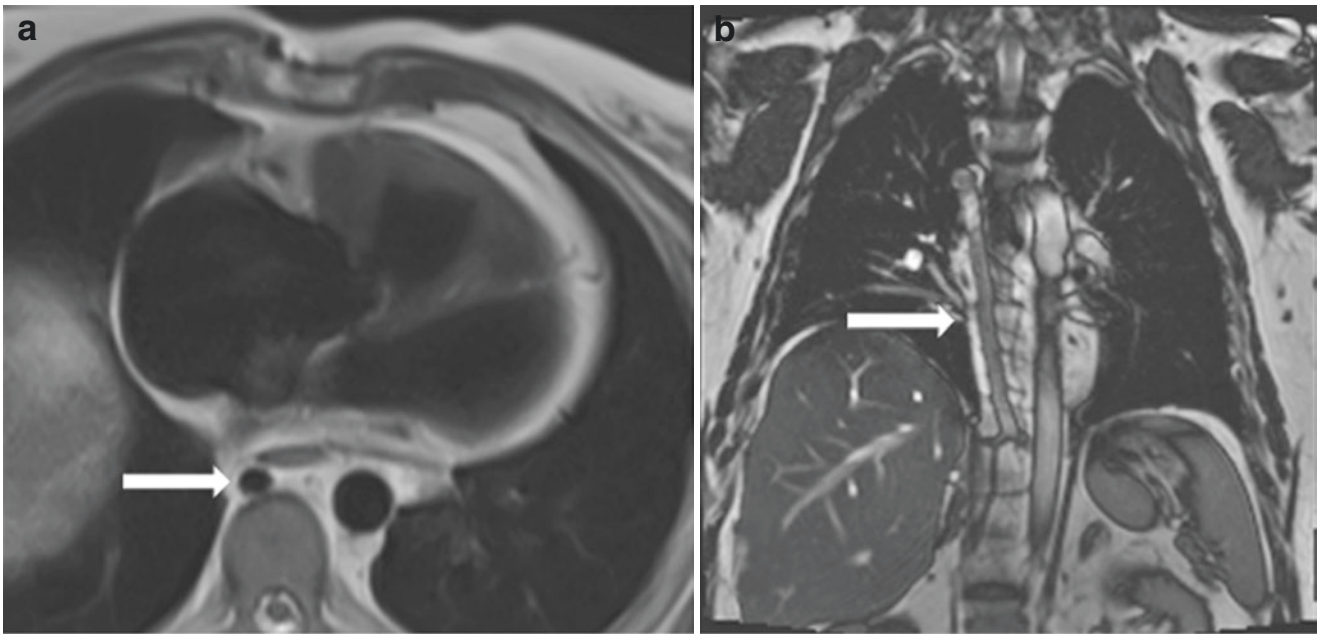


**Fig. 13.13** Baffle stenosis in a patient with complete transposition of the great arteries. Axial black blood image (a) and coronal SSFP image (b) demonstrate a dilated azygous vein (arrows), suggesting baffle stenosis

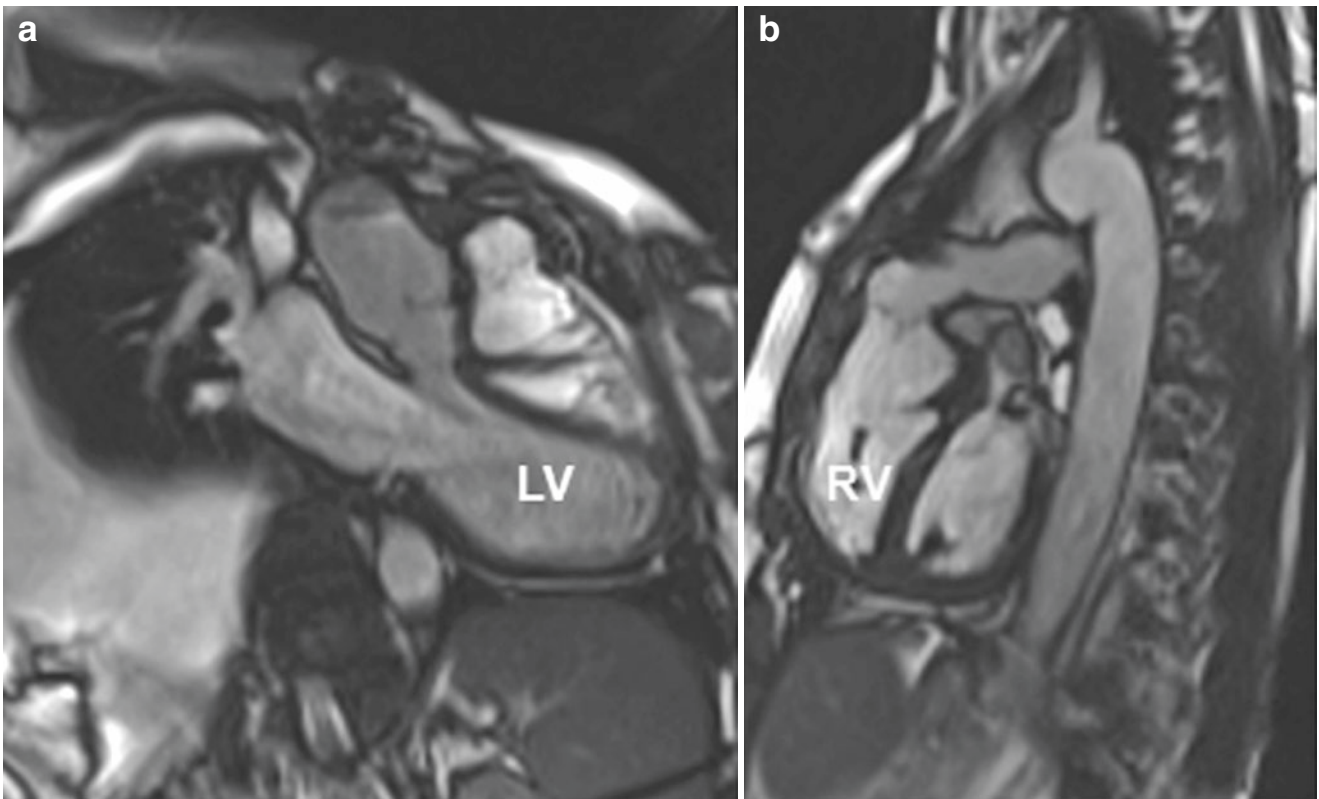


**Fig. 13.14** SSFP images in a patient with complete transposition of the great arteries following a Rastelli operation. (a) The left ventricular outflow tract courses through a patched ventricular septal defect (LV indicates left ventricle). (b) The right ventricular outflow tract is formed by a conduit from the right ventricle (RV) to the main pulmonary artery

## 13.6 Discussion

While CMR has been considered adjunctive to echocardiography in the evaluation of transposition syndromes according to society guidelines [9, 11, 17], a more central role of CMR in the management of congenital heart disease is rapidly evolving. This is illustrated by the change in the European Society of Cardiology (ESC) guidelines for management of grown-up congenital heart patients from 2003 to 2010. The 2003 ESC guidelines indicate that CMR is “rarely required if transesophageal echocardiography is available” in the evaluation of complete transposition following atrial baffle procedure [23]. In 2010, the ECS became the first major society to issue separate guidelines specific to the use of CMR in adults with congenital heart disease. In these guidelines, CMR should be employed in scenarios when it “usually informs management more effectively” such as in the evaluation of systemic and pulmonary veins, quantification of RV volumes and ejection fraction, shunt quantification, conduit function, and evaluation of the great vessels [17].

Echocardiography has several advantages relative to CMR, chiefly that it is portable, readily available, and inexpensive. While availability is sometimes cited as an advantage of echocardiography relative to CMR, all patients with transposition syndromes should be followed at specialized centers, where CMR should also be available [9]. Periodic echocardiographic surveillance of systemic right ventricular function is a Class I indication by current ACC/AHA guidelines, generally every 1–2 years [9, 24]. At least one institution has implemented a combined approach to longitudinal monitoring of patients after atrial baffle procedures, using transthoracic echocardiography (TTE) routinely but with CT or MRI every 4–5 years adjunctively [8]. When initial TTE windows are suboptimal, echo contrast with either microbubbles or agitated saline can be employed, or the patient can be referred for further imaging with either transesophageal echocardiography (TEE), CMR, or CT. There are no published data comparing efficacy or accuracy of TEE to CMR or CT to CMR in the management of transposition syndromes. The decision as to which modality to use when questions remain after TTE depends upon clinical setting and the discretion of the clinician.

CMR has been the gold standard in assessing ejection fraction in patients with systemic right ventricles in several studies. Accurate measurement of ventricular function is especially critical in patients with systemic right ventricles, as deterioration in function is a major source of morbidity and mortality. Echocardiography-derived measures of myocardial function, including myocardial performance index [25] and global longitudinal strain rate [26], correlate with right ventricular ejection fraction as assessed by CMR in patients with systemic right ventricles. However, it is not

clear that this offers more prognostic information than ejection fraction alone. TTE derived parameters have shown mixed efficacy to directly predict surrogates of clinical condition. While tricuspid annular peak systolic excursion and a *qualitative* assessment of global systemic right ventricular systolic function by TTE correlate with NYHA class, maximal exercise capacity and NT-proBNP levels, parameters such as peak systolic velocity, tissue Doppler-derived strain, and diastolic parameters did not [27].

There are important limitations to echocardiography. CMR is regarded to be superior to TTE and TEE in the assessment of great arteries and veins [9] and in the quantification of ventricular masses and volumes [18]. Inadequate sonographic windows have often been cited as a major limitation of TTE, but it is difficult to determine how often this is the case. One prospective study of echocardiography in adult patients with systemic RVs excluded 8% of their initial sample because of inadequate transthoracic windows [27]. A retrospective study of 12 patients with prior atrial baffle procedures demonstrated limitations to viewing systemic baffles by TTE in most patients studied: there was inadequate visualization of the common baffle in 4 patients (33%), of the SVC limb in 7 patients (58%), and of the IVC limb in 8 patients (67%) [28]. Finally, TTE with Doppler has been shown to be inferior to a combination of other modalities (75% CMR, 15% CT, 10% invasive) in detecting superior limb baffle stenosis, but the reasons for this discrepancy were not stated [8]. TEE was not performed in any of these studies, however.

Noninvasive CT coronary angiography may have an expanding role in imaging patients with complete TGA treated by arterial switch operations. Many of the patients treated with arterial switch operations are now adults, in whom assessment of coronary artery patency is warranted [9]. MRA of coronary arteries can be challenging and is generally best suited for evaluation of proximal vessels and anomalies of coronary origins. Given its high negative predictive value, CT coronary angiography is an attractive alternative to invasive catheterization in patients who are otherwise low atherosclerotic risk and asymptomatic. Like CMR, it has the advantage of unhindered anatomic assessment of the great vessels and venous anatomy. Assessments of baffle leaks and baffle stenosis are also possible by CT angiography [8, 10]. However, CT may not be suitable for lifelong surveillance of congenital heart disease patients due to radiation effects.

### 13.6.1 Areas of Emerging Data

Patients with systemic RVs who are asymptomatic by self-report often have dramatically decreased peak oxygen con-

sumption and exercise tolerance, so clinical condition can be difficult to judge by history alone. Several studies have used dobutamine stress CMR protocols to unmask subclinical defects in patients with systemic RVs. The prognostic utility of such studies has not been well described, however. Additionally, abnormal resting blood flow distribution in the main and branch pulmonary arteries as measured by CMR has been found to correlate with poor cardiopulmonary response to exercise. The two exams have complementary information that may help to decide functional significance of stenoses in pulmonary arteries [29].

### 13.7 Limitations and Common Pitfalls

The frequency of contraindications to CMR is difficult to determine in patients with transposition syndromes. Long-term follow-up of patients with prior atrial switch procedures indicates that around a third of patients will require permanent pacemaker implantation, most as adults [7]. In congenitally corrected patients, ~2% per year will develop atrioventricular node dysfunction [2]; presumably a large fraction of those patients will require pacemaker implantation. Presence of pacemaker is not a contraindication for CMR; however device-related artifacts may affect adequate visualization of cardiac structures. One study of systemic right ventricular function excluded 34% of enrolled patients from CMR analysis for unstated reasons. Furthermore, atrial dysrhythmias are common and may complicate ECG gating and image quality.

Evaluation for baffle leaks requires care and an understanding of phase contrast techniques, but reliance on one CMR method of assessing baffle function is not recommended. Atrial baffles generally have fairly low-pressure gradients, and care must be taken in selecting the VENC settings. Unrestricted baffle leaks may be missed if they generate too little turbulence and therefore dephasing to be identified on SSFP cine images. Reversal of azygous vein flow was only present in 53% of patients with hemodynamically significant SVC baffle stenosis in one cohort [8]. Mild baffle stenosis is less well characterized by contrast MRA compared to the reference standard phase contrast mapping [15]. Similarly, while navigated 3D SSFP noncontrast MRA may be useful for assessing baffles, the saturation effect of the navigator band can potentially decrease signal in the pulmonary venous pathways. None of these techniques have been extensively evaluated against invasive methods.

Finally, for quantification of volumes and mass in the systemic right ventricular, extensive trabeculations may complicate delineation of muscle from cavity and therefore potentially decrease reproducibility and accuracy.

### 13.8 Conclusion

Transposition of the great arteries (TGA) refers to ventriculoarterial discordance and encompasses two distinct entities, complete TGA and congenitally corrected TGA. Whereas the former is usually associated with cyanosis and therefore nearly always identified and surgically corrected in infancy, the latter may not be diagnosed until adulthood. Associated cardiac anomalies are common, but syndromic associations are absent. Three surgical procedures are commonly performed to correct complete TGA, and the method used informs the role of CMR in long-term follow-up. Periodic monitoring of systemic right ventricular function for patients with congenitally corrected TGA or complete TGA treated with atrial baffle procedures is required, with careful attention to the severity of regurgitation of the systemic atrioventricular valve. Stenosis or obstructions in the subpulmonic outflow tract through the branch pulmonary arteries can be seen in any form of TGA, but is especially common following arterial switch operations. CMR is especially useful following atrial baffle repairs and Rastelli procedures, where the complex, distorted anatomy can be especially challenging to evaluate by echocardiography. CMR exam should be performed under supervision of a physician familiar with imaging and interpretation of congenital heart disease in both preoperative and postoperative settings.

#### Practical Pearls

- Consider the diagnosis of congenitally corrected TGA in the presence of dextrocardia with situs solitus.
- For the postsurgical patient, knowledge of the type of prior surgical procedures performed is critical to the imaging assessment.
- Multiple breath-held sequences can be fatiguing, especially in patients who often have some degree of exercise intolerance or systolic dysfunction. The choice of which cine slice orientations to obtain first should be tailored to address the most pressing indication for a CMR study. For example, if systolic function is paramount, short-axis cine stacks should be acquired early, whereas if a baffle stenosis is likely, coronal and axial stacks should be prioritized.
- Azygous vein enlargement (>5 mm) and flow reversal can be clues to the presence of baffle stenosis. Flow reversal indicates a superior baffle or vena cava obstruction. These determinations usually do not require separate acquisitions as the azygous vein is frequently well seen on axial localizers and Qs phase contrast images.
- Aortic root measurements require ECG-gated imaging with either cine or 3D MRA protocols, for example following arterial switch operations.



## References

- Hoffman JI, Kaplan S. The incidence of congenital heart disease. *J Am Coll Cardiol*. 2002;39:1890–900.
- Warnes CA. Transposition of the great arteries. *Circulation*. 2006;114(24):2699–709.
- Keane JF, Flyer D. Corrected transposition of the great arteries. In: Nadas' pediatric cardiology. 2nd ed. Philadelphia: Saunders; 2006.
- Baumgartner H, et al. ESC guidelines for the management of grown-up congenital heart disease (new version 2010): the task force on the management of grown-up congenital heart disease of the European Society of Cardiology (ESC). *Eur Heart J*. 2010;31(23):2915–57.
- Fulton DR, Flyer DC. D-transposition of the great arteries. In: Nadas' pediatric cardiology. 2nd ed. Philadelphia: Saunders; 2006.
- Rao PS. Diagnosis and management of cyanotic congenital heart disease: part I. *Indian J Pediatr*. 2009;76(1):57–70.
- Oechslin E, Jenni R. 40 years after the first atrial switch procedure in patients with transposition of the great arteries: long-term results in Toronto and Zurich. *Thorac Cardiovasc Surg*. 2000;48(4):233–7.
- Bottega NA, et al. Stenosis of the superior limb of the systemic venous baffle following a Mustard procedure: an under-recognized problem. *Int J Cardiol*. 2010;154(1):32–7.
- Warnes CA, et al. ACC/AHA 2008 guidelines for the management of adults with congenital heart disease: a report of the American College of Cardiology/American Heart Association task force on practice guidelines (Writing Committee to develop guidelines on the management of adults with congenital heart disease). Developed in collaboration with the American Society of Echocardiography, Heart Rhythm Society, International Society for Adult Congenital Heart Disease, Society for Cardiovascular Angiography and Interventions, and Society of Thoracic Surgeons. *J Am Coll Cardiol*. 2008;52(23):e1–121.
- Cook SC, et al. Usefulness of multislice computed tomography angiography to evaluate intravascular stents and transcatheter occlusion devices in patients with d-transposition of the great arteries after Mustard repair. *Am J Cardiol*. 2004;94(7):967–9.
- Silversides CK, et al. Canadian Cardiovascular Society 2009 consensus conference on the management of adults with congenital heart disease: complex congenital cardiac lesions. *Can J Cardiol*. 2010;26(3):e98–117.
- Cohen MS, et al. Multimodality imaging guidelines of patients with transposition of great arteries: a report from the American Society of Echocardiography developed in collaboration with the Society of Cardiovascular Magnetic Resonance and the Society of Cardiovascular Computed Tomography. *J Am Soc Echocardiogr*. 2016;29:571–621.
- Skinner J, Hornung T, Rumball E. Transposition of the great arteries: from fetus to adult. *Heart*. 2008;94(9):1227–35.
- Dorfman AL, Geva T. Magnetic resonance imaging evaluation of congenital heart disease: conotruncal anomalies. *J Cardiovasc Magn Reson*. 2006;8(4):645–59.
- Johansson B, et al. 3-dimensional time-resolved contrast-enhanced magnetic resonance angiography for evaluation late after the Mustard operation for transposition. *Cardiol Young*. 2010;20(1):1–7.
- Fogel MA, Hubbard A, Weinberg PM. A simplified approach for assessment of intracardiac baffles and extracardiac conduits in congenital heart surgery with two- and three-dimensional magnetic resonance imaging. *Am Heart J*. 2001;142(6):1028–36.
- Kilner PJ, et al. Recommendations for cardiovascular magnetic resonance in adults with congenital heart disease from the respective working groups of the European Society of Cardiology. *Eur Heart J*. 2010;31(7):794–805.
- Therrien J, et al. Canadian Cardiovascular Society consensus conference 2001 update: recommendations for the management of adults with congenital heart disease part III. *Can J Cardiol*. 2001;17(11):1135–58.
- Taylor AM, et al. MR coronary angiography and late-enhancement myocardial MR in children who underwent arterial switch surgery for transposition of great arteries. *Radiology*. 2005;234(2):542–7.
- Babu-Narayan SV, et al. Late gadolinium enhancement cardiovascular magnetic resonance of the systemic right ventricle in adults with previous atrial redirection surgery for transposition of the great arteries. *Circulation*. 2005;111(16):2091–8.
- Fratz S, et al. Myocardial scars determined by delayed-enhancement magnetic resonance imaging and positron emission tomography are not common in right ventricles with systemic function in long-term follow up. *Heart*. 2006;92(11):1673–7.
- Prakash A, et al. Magnetic resonance imaging evaluation of myocardial perfusion and viability in congenital and acquired pediatric heart disease. *Am J Cardiol*. 2004;93(5):657–61.
- Deanfield J, et al. Management of grown up congenital heart disease. *Eur Heart J*. 2003;24(11):1035–84.
- Cheitlin MD, et al. ACC/AHA guidelines for the clinical application of echocardiography. A report of the American College of Cardiology/American Heart Association task force on practice guidelines (Committee on Clinical Application of Echocardiography). Developed in collaboration with the American Society of Echocardiography. *Circulation*. 1997;95(6):1686–744.
- Salehian O, et al. Assessment of systemic right ventricular function in patients with transposition of the great arteries using the myocardial performance index: comparison with cardiac magnetic resonance imaging. *Circulation*. 2004;110(20):3229–33.
- Chow PC, et al. New two-dimensional global longitudinal strain and strain rate imaging for assessment of systemic right ventricular function. *Heart*. 2008;94(7):855–9.
- Winter MM, et al. Echocardiographic determinants of the clinical condition in patients with a systemic right ventricle. *Echocardiography*. 2010;27(10):1247–55.
- Fogel MA, Hubbard A, Weinberg PM. Mid-term follow-up of patients with transposition of the great arteries after atrial inversion operation using two- and three-dimensional magnetic resonance imaging. *Pediatr Radiol*. 2002;32(6):440–6.
- Giardini A, et al. Effect of abnormal pulmonary flow distribution on ventilatory efficiency and exercise capacity after arterial switch operation for transposition of great arteries. *Am J Cardiol*. 2010;106(7):1023–8.





## 14.1 Introduction

Aortic congenital anomalies are common and comprised of a heterogeneous group of conditions that may be due to either embryological or vessel wall architectural defects. Imaging is crucial for diagnosis, management, follow-up, and reassessment after intervention of these conditions. Cardiovascular magnetic resonance (CMR) is a valuable noninvasive imaging method for providing detailed anatomical, functional, and hemodynamic information on a wide spectrum of aortic anomalies and intra- and extracardiac associated abnormalities. The technique is radiation free and is ideally suited for diagnoses as well as serial follow-up pre and post-interventions such as a dilated aortic root in Marfan syndrome and aortic coarctation. This chapter reviews the role of CMR in the management of a wide spectrum of congenital aortic anomalies and provides CMR scanning protocols and clinical reporting of the anomalies both in the native and post-repair states.

**Supplementary Information** The online version contains supplementary material available at [https://doi.org/10.1007/978-3-031-29235-4\\_14](https://doi.org/10.1007/978-3-031-29235-4_14).

S. S. M. Chen (✉)  
Cardiovascular Magnetic Resonance Unit, The Royal Brompton Hospital, London, UK

Adult Congenital Heart Disease, The Prince Charles Hospital, Brisbane, Australia

R. H. Mohiaddin  
Cardiovascular Imaging, Royal Brompton and Harefield Hospitals, Guy's and St Thomas' NHS Foundation Trust, London, UK

National Heart and Lung Institute, Imperial College London, London, UK  
e-mail: [r.mohiaddin@imperial.ac.uk](mailto:r.mohiaddin@imperial.ac.uk)

## 14.2 Aortic Anomalies

Aortic anomalies consist of a spectrum of conditions. The anomalies are usually due to abnormality either in embryological development or in the architecture of the vessel wall. Abnormal persistence or regression of the branchial arches during embryogenesis, for example, may result in a double aortic arch and vascular ring [1]. Architectural defects due to genetic mutations such as Marfan syndrome [2] or biochemical derangements as seen in the aortic matrix in the context of a bicuspid aortic valve [3] may result in aortic aneurysms that are susceptible to dissection or rupture. These aortic abnormalities may be associated with other cardiac defects that may also require treatment and follow-up.

Diagnosis, instigation of treatment, and subsequent follow-up are therefore crucial. Definition of the anatomy is needed for diagnosis of the abnormality and its hemodynamic effects, its relationship to its surrounding structures, and its associated cardiac anomalies. An important component of assessment is the impact of the anomaly on the heart. For example, what is the severity and therefore effect of coarctation of the aorta (CoA) on the heart? Is there left ventricular hypertrophy and left ventricular impairment, or is the dilated aortic root in Marfan syndrome causing aortic regurgitation? Detailed structural and functional information is vital not only for diagnosis but to help guide management decisions, feasibility of a particular type of intervention, and in the post-repair phase, follow-up for residual defects, complications of repair, and recurrent disease.

### 14.2.1 CMR and Other Imaging Modalities for Aortic Anomaly Assessment

High-quality and informative imaging is a valuable part of the process of diagnosis and management and can be provided easily by CMR [4]. Traditionally, chest X-ray (although rarely used for diagnosis alone), cardiac catheterization, and

echocardiography were used to image the aorta. More recently, cardiac CT angiography (CTA) has become more available and is very useful for assessing the aorta.

CMR is perhaps the most ideal imaging technique as it is able to provide high-quality and detailed examination of the anatomy and function of the entire aorta, its branches, relationship to the surrounding mediastinal structures, and associated anomalies. It is noninvasive and does not use radiation or iodinated contrast agents, both of which are ideal attributes for serial follow-up. Its ability to image in multiple planes is an advantage as it allows accurately aligned images to be obtained and therefore accurate depiction of the anomaly. The duration of study time is longer compared to other modalities but may be shortened if the operator is experienced. The main contraindications for CMR are the presence of metallic devices, i.e., drug infusion pump, non-MRI-compatible devices including defibrillators, permanent pacemakers, and biventricular pacing for cardiac resynchronization therapy or other metallic objects in particular regions of the body such as the eye. Several reports have described feasibility of safely performing CMR in selected patients with non-MRI conditional pacemakers and defibrillators. MRI conditional pacemaker and defibrillator models are also clinically available, and patients with these devices may be able to undergo routine CMR. Other potential difficulties may be overcome. Claustrophobia may be helped by using partial sedation or alternative positioning, for example, entering the scanner feet first or using glasses that reflect out toward the control room. Careful counselling prior to scanning can be very valuable in alleviating anxiety. Similarly in our experience, children excluding the very young (<4 years old) may undergo CMR study without sedation or anesthesia if they and their parents have been well prepared and counselled prior to study. Play therapists are extremely useful in the preparation including venous cannulation of these children. In the presence of impaired renal function or if venous cannulation was not possible, imaging that usually requires contrast agent enhancement such as angiography may be done using an alternative CMR sequence, 3D whole heart balanced steady-state precession with fat suppression (3D whole heart), done without the use of contrast agents.

In comparison, apart from echocardiography, other imaging modalities usually have the disadvantages of the need to use radiation and iodinated contrast agents and/or are invasive. These modalities are:

- Chest X-ray: It is easily available and quick to perform. Widening of the mediastinum raises the suspicion of aortic dilatation and evidence of a CoA by the presence of rib notching or the “3 sign,” which is the silhouette formed by a dilated left subclavian artery above, and dilated distal descending aorta below the level of CoA [5] may be detected. However, specific diagnosis and detailed examination of all the various anomalies or serial follow-up of an enlarging aneurysm cannot be achieved using X-ray alone.
- Cardiac catheterization and aortography: Aortography allows examination of the structure and size of the thoracic aorta and its branches. Cardiac catheterization’s particular advantage over CMR and the other modalities is its ability to provide information of pressure gradients crucial, for example, in CoA. It also allows the opportunity to intervene at the same time if appropriate, for example, closing a patent ductus arteriosus (PDA) or stent implantation for CoA. However, although the coronary anatomy can be examined, other associated anomalies may not be easy to assess. Furthermore, it is invasive and may have complications of vascular injury, inducing ventricular arrhythmia, stroke, or distal embolization and ideally should not be used alone for serial follow-up.
- CTA: It is a quick study compared to CMR and therefore more suitable in acute settings such as aortic dissection and for children who may tolerate a short period of time in a CT scanner, but not the longer duration required to perform a CMR study. CTA is useful as an alternative to CMR for patients with non-MRI-compatible pacemakers. As with CMR, CTA is able to provide detailed structural information of the aorta, its branches, its relationship to other structures in the mediastinum, other coexisting cardiac anomalies, and the size and location of the defects. Compared to CMR, CTA is better in the assessment of the coronary arteries and their course and lumen, in identifying calcification which can be a useful tool in assessing, for example, a PDA prior to surgery [6, 7], and when studying the integrity of an aortic stent which has the potential to cause metallic artifacts on CMR. CTA, however, is not the ideal modality for serial follow-up for conditions such as aortic aneurysm because of the risk of complications from accumulative doses of radiation and iodinated contrast agents. Radiation may be reduced using prospective ECG-gated imaging which is good for structural assessment but not for functional analysis of the ventricles and valves, which may also be abnormal in aortic anomalies. Retrospective ECG-gating, with higher doses of radiation, must be used instead. The temporal resolution achieved using retrospective ECG-gating, however, is less than CMR, and therefore ventricular volume and function assessment is inferior in comparison [8].
- Echocardiography: As with CMR, it is noninvasive, does not use radiation, and is highly informative on anatomy and function. It is more widely available and has a shorter duration of study time, and bedside imaging is possible using portable machines and should be used in most instances, as the first imaging modality of choice for diag-

nosis and follow-up. Estimation of pulmonary vascular and right ventricular systolic pressure relevant in PDA assessment, for example, can be done on echocardiography but not easily on CMR. However, compared to CMR, good-quality imaging is dependent on an adequate echocardiographic window, patient's body habitus, and presence of lung disease such as asthma. The aorta is not easily visualized in its entirety and especially in an adult. Detailed examination of aneurysms or stenosis in the arch or proximal descending aorta and arch vessel anomalies cannot be done easily on echo, but excellent imaging of these regions can be achieved using CMR. Echocardiography is limited also in its ability to assess aortic dissection and rupture. Similarly, the pulmonary artery and its branches are best assessed by CMR. Transesophageal echocardiography can provide more detailed examination compared to transthoracic echocardiography but is semi-invasive and require at least partial sedation.

## 14.2.2 Indications and Goals for CMR Imaging

CMR is indicated for diagnosis, planning management strategies, serial follow-up for progression of disease or the development of complications, and reassessment after intervention. Imaging has to demonstrate the anatomy and functional significance of the anomaly and be precise in the alignment of the imaging planes so that measurements of aortic dimensions including aneurysms and stenosis may be as accurate as possible and reproducible in subsequent repeated studies for follow-up. Assessment for associated anomalies and cardiac function must also be performed.

## 14.2.3 CMR Assessment of the Aorta

A suggested protocol (to be altered accordingly to suit the particular condition under assessment) is tabulated on Table 14.1.

### 14.2.3.1 Anatomical Imaging

- The aorta may be examined using any or all of the sequences in the suggested protocol. The entire aorta is imaged, from the left ventricular outflow tract to the descending aorta at diaphragm level. A cross-sectional plane through the aortic valve for valve morphology is also recommended. The “hockey stick” or “candy cane” image of the aorta (Fig. 14.1a) gives an overview of the aorta but may not necessarily be completely aligned in all the segments of the aorta as the aorta is rarely in one plane. Therefore, separate specifically aligned images to

**Table 14.1** Suggested CMR protocol

Sequences	Parameters
Localizers: true fast imaging with steady-state precession	TR 337.1, TE 1.16, slice thickness 8 mm, matrix 2.4 × 1.6 mm
Half-Fourier acquisition single-shot turbo spin echo (HASTE) multislice imaging in a transverse orientation	TR 700, TE 42, slice thickness 6 mm, matrix 2.3 × 1.3 mm
Steady-state free precession (SSFP) multislice imaging in the transverse, coronal, and sagittal oblique orientations	TR 292.2, TE 1.22, slice thickness 6 mm, matrix 2.0 × 1.3 mm
SSFP cine imaging	TR 40.2, TE 1.13, slice thickness 7 mm, matrix 1.7 × 1.7 mm, temporal resolution 25 frames
Phase contrast flow and velocity quantification: in-plane and through-plane flow	In-plane: TR 61, TE 3.09, slice thickness 6 mm, matrix 2.5 × 1.3 mm, temporal resolution 20 frames Through-plane: TR 60, TE 2.32, slice thickness 10 mm, matrix 2.5 × 1.3 mm, temporal resolution 20 frames
Turbo spin echo (TSE) imaging	TR 700, TE 29, slice thickness 6 mm, matrix 2.2 × 1.3 mm
Contrast-enhanced magnetic resonance angiography (MRA)	TR 2.85, TE 1.19, slice thickness 1.3 mm, matrix 1.1 × 0.9 × 1.3 mm
3D whole heart balanced steady-state precession with fat suppression (3D whole heart)	TR 275.81, TE 1.63, slice thickness 1.5 mm, matrix 1.5 × 1.0 × 1.0 mm

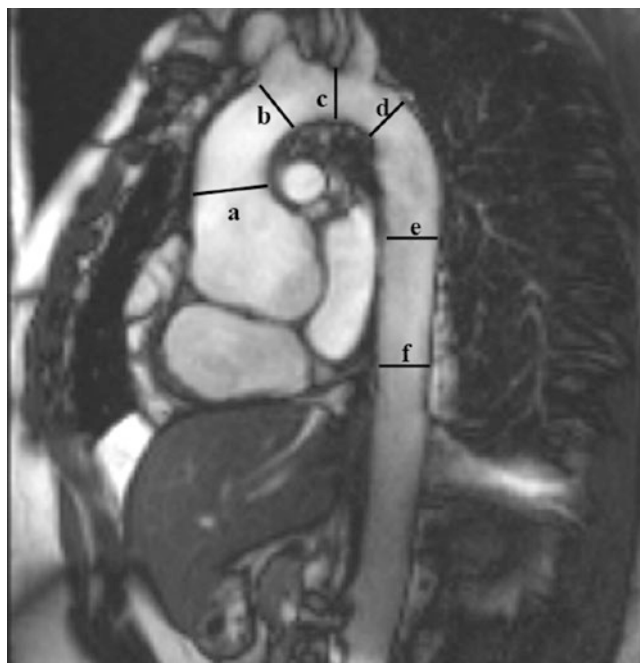


**Fig. 14.1** Sites of aortic measurements: *a* = ascending aorta at the level of the pulmonary artery, or at its widest dimension if dilated; *b* = proximal arch just before the origin of the right brachiocephalic artery; *c* = mid aortic arch, between the origins of the left common carotid and subclavian arteries; *d* = distal arch; *e* = mid-descending thoracic aorta, between *d* and *f*; *f* = descending aorta at the diaphragm

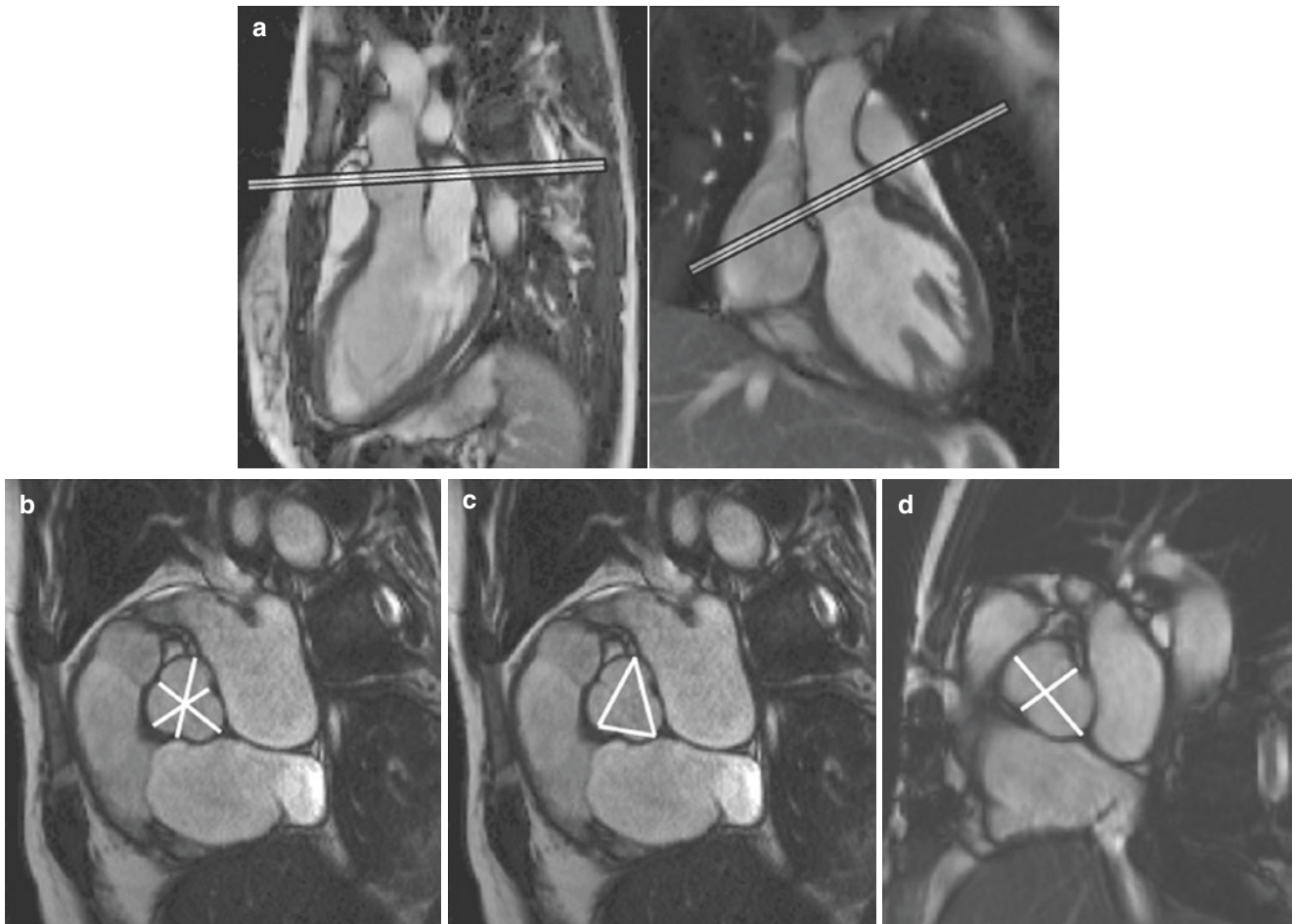


**Fig. 14.2** (a) Two slice imaging without a gap transecting the aortic sinus at its widest dimension, in the sagittal and oblique coronal orientations to obtain the image in (b–d). (b) Diastolic cusp-commissure measurements of the aortic root in its cross-sectional orientation. (c)

Diastolic cusp-cusp measurements of the aortic root in its cross-sectional orientation. (d) Diastolic cusp-cusp and cusp-commissure measurements of the aortic root of a bicuspid aortic valve in its cross-sectional orientation

the aortic segments (ascending aorta, arch, and descending aorta) may be necessary for accurate assessment and measurement. Cross-sectional or orthogonal planes to the sites in Fig. 14.1a is recommended for more accurate measurements of aortic dimensions.

- Careful alignment of the imaging plane is crucial. The aorta is usually circular in the cross-sectional plane, and the most accurate measurement of aortic diameters is at its widest point, that is, through the middle of the vessel. Several orthogonal planes through the area of interest may be required to obtain the most accurately aligned imaging plane. This is particularly important for repeated studies over years, for patients with conditions such as CoA and aortic aneurysms with regular follow-up studies for disease progression. It is difficult to attribute differences in measurement as true changes in dimensions if the imaging planes are not exactly the same. This is particularly relevant and important to clinical management decisions with regard to reintervention as a result of the

CMR study. It is recommended that previous studies should be available at the time of the present study and comparative images acquired.

- Aortic root: A diastolic cross-sectional plane through the widest diameter of the aortic sinus is recommended for the measurement of aortic root dimension [9] (Fig. 14.2a). To account for through-plane movement that may cause inaccuracies in measuring the diameters, it is recommended that two consecutive slices without an interslice gap are acquired.
- Dark blood sequences using half-Fourier acquisition single-shot turbo spin echo (HASTE) and T1-weighted turbo spin echo (TSE) sequences are useful for vessel wall inspection, for example, in aortic dissection.
- Metallic artifacts (due to stents, for example) preclude detailed examination of the aorta on steady-state free precession (SSFP) cine and multislice imaging (Fig. 14.3). Dark blood and fast low-angle shot imaging (FLASH) sequences can be used in this circumstance, although



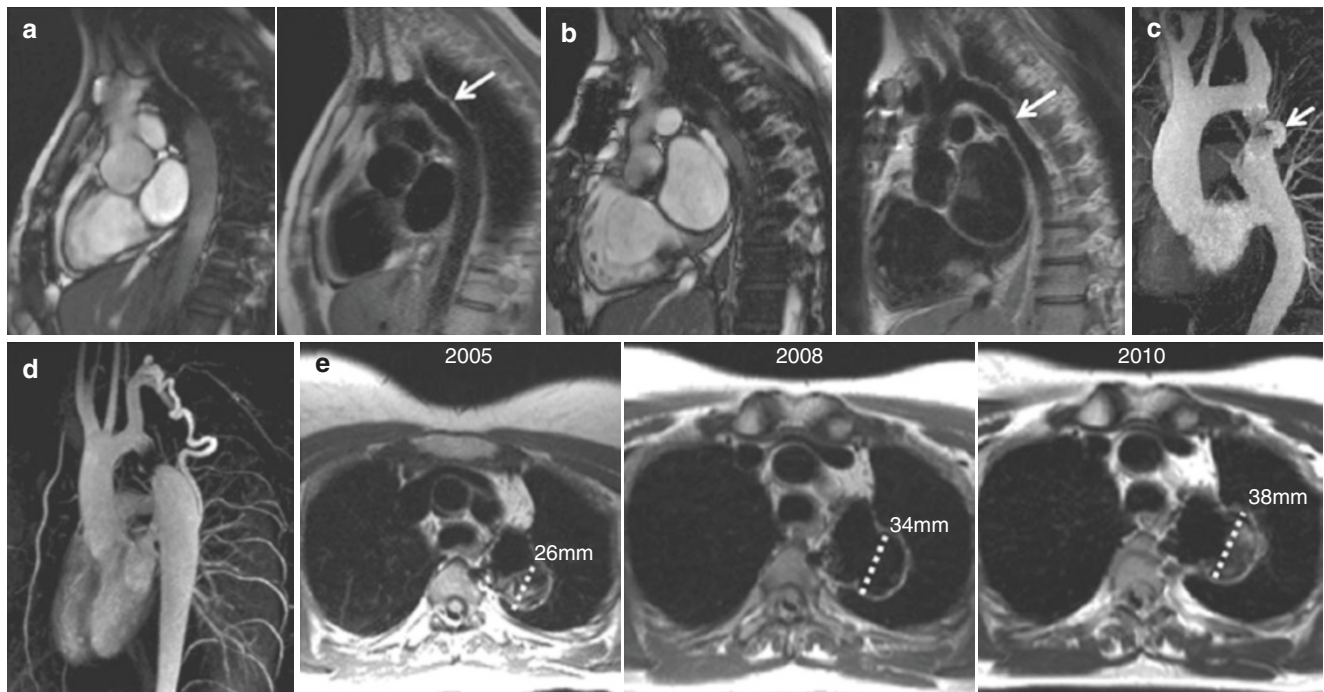


**Fig. 14.3** Imaging after stent implantation in CoA. (a, b) SSFP images on the left and TSE images on the right. Metallic artifact precludes detailed examination on SSFP, but the aortic lumen is well visualized in TSE. A small aneurysm (*arrowed*) in the proximal stent is seen on TSE but not on SSFP in (a), and narrowing of the descending aorta distal to the stent (*arrowed*) is visualized on TSE but not easily on SSFP in (b).

(c) An aneurysm seen in the stent (*arrowed*) on MRA. (d) Collateral on MRA supporting the suspicion of stenosis within the stent. (e) Serial CMR studies 2005–2010 to assess progression of an aneurysm at the site of a stent. TSE imaging in similar planes show increasing dimensions

FLASH is also susceptible to metallic artifact. A stent cannot be seen on dark blood images, but the lumen of the vessel is visible, and therefore some assessment of the diameter of the lumen can be made. Complications such as an in-stent aneurysm cannot be seen on cine imaging but may be visualized on TSE or HASTE imaging (Fig. 14.3a, e).

- Contrast or non-contrast-enhanced magnetic resonance angiography (MRA) is useful for its three-dimensional assessment, particularly for planning of intervention.

#### 14.2.3.2 Function

- Judgment on the severity of the lesions such as stenosis or the relationship of the vessel to and its impact on its surrounding structures may be made using cine imaging, phase contrast flow, and velocity mapping.
- Again, careful alignment of the imaging plane to the jet, whether in the long axis or transacted planes, is crucial for accurate assessment.
- MRA is useful for the detection of collateral vessels, for example, in the severe CoA.

#### 14.2.4 Reporting a CMR Study

Important features to include are:

- Detailed description of the aortic abnormality: Anatomical detail and dimensions, location, and severity of and impact of the anomaly on its surrounding structures (e.g., trachea compression from a vascular sling) should be reported.
- Aortic dimensions: Measurements may be made on images acquired using any of the sequences described previously. For consistency and repeatability, measurements should be made on the same type of sequence on subsequent follow-up studies. Documentation of where the measurements were made and on which sequence especially in the presence of a stent should ideally be made in the report. Previous documentation is useful for repeated studies over years for accurate assessment of progression of stenosis or increasing aneurysm size. If previous record is not available, then it is recommended that measurements of the previous study at similar locations to the current study are performed by the same reporter (Fig. 14.3e). Maximum extra-luminal dimen-

sions perpendicular to the aortic wall are recommended [9]. The intraluminal diameter does not always reflect the external aortic diameter when there is intraluminal thrombus, wall inflammation, or dissection. Both diameters, external and internal, are useful in these circumstances. Cine SSFP and dark blood spin echo images such as HASTE or TSE are recommended for these measurements. Figure 14.1 illustrates the recommended sites of measurement from the ascending aorta to the descending aorta at the diaphragm. The ascending aorta is best measured in its cross-sectional plane at the level of the RPA (Fig. 14.1b) or at the widest diameter if dilated. Measurement of the aortic root at the sinus level is recommended from the cross-sectional image described above using the diastolic cusp-commissure diameters (Fig. 14.2b) as they correspond closer with respect to age and body surface area compared to other measurements using diastolic cusp-cusp or systolic cusp-commissure or the widest diameters measured from the left ventricular outflow tract images in the coronal and sagittal oblique orientations [10]. Diastolic cusp-cusp diameters may also be measured for an overall assessment of aortic root dimensions (Fig. 14.2c). For a bicuspid aortic valve, the aortic sinus may be measured using the diastolic cusp-cusp and commissure-commissure diameters (Fig. 14.2d). Normal values for aortic root dimensions in adult males and females and in children by CMR have been reported previously and can be used as a reference [10–12].

- Associated anomalies: Coexisting congenital defects such as ventricular septal defect or bicuspid aortic valve and/or consequences of the disease such as aortic valve regurgitation or left ventricular hypertrophy.
- Cardiac function: Dimensions, ejection fraction, and hypertrophy of the right and left ventricles must be reported.

### 14.3 Coarctation of the Aorta

Coarctation of the aorta (CoA) is a narrowing in the aortic lumen (Movie 14.1). It is usually discrete, commonly located distal to the left subclavian artery and opposite the ligamentum arteriosum but may also be found in the aortic arch and descending thoracic or abdominal aorta or as complete interruption of the aorta [11]. More diffuse narrowing may be present and usually in association with other congenital anomalies such as a bicuspid aortic valve, ventricular septal defect, Shone's syndrome (subvalvular, valvular, and supra-valvular aortic stenosis and mitral valve abnormality), or complex congenital heart disease, for example, transposition of the great arteries. CoA is present in about 7% of congenital heart disease with a male preponderance of 1.5:1 [5]. The

region of coarctation is related to posterior infolding of the aorta, seen as a ridge that protrudes into the lumen. It is likely that CoA represents a more diffuse arteriopathy, as cystic medial necrosis is present not only at the site of coarctation but also in the aorta proximal and distal to coarctation [13]. These aortic wall abnormalities may account for aneurysmal dilatation in the descending aorta distal to the site of coarctation and aneurysms found around the site of previous repair. Other associated abnormalities are aneurysms of the circle of Willis (in 10%) and Turner syndrome.

The mode of presentation depends on the severity of the lesion. In the more severe cases, patients present soon after birth commonly with heart failure, or, in the less severe, with hypertension, claudication in the lower limbs during exercise, or nonspecific symptoms of headache or epistaxis. After CoA repair, patients with recurrent or residual stenosis may present with hypertension or lower limb claudication. Aneurysms that develop after intervention are usually silent, unless there is dissection or rupture of the aneurysm.

Management is usually surgical repair for young children. Percutaneous balloon angioplasty and stent implantation (Fig. 14.3) may be an option for adults or older children and have the advantages of a smaller procedure without the use of cardiopulmonary bypass. There are various options for surgical repair: resection and end-to-end anastomosis (Fig. 14.4a), subclavian flap repair (Fig. 14.4b, c), patch repair using artificial material such as Dacron (Fig. 14.4d, e), interposition graft repair (Fig. 14.4f), and bypass graft repair (Fig. 14.4g, h). The most common complications after repair are stenosis (residual or recurrent or at suture lines, Fig. 14.4a, b, d) and aneurysm formation (Fig. 14.4c, e, f, h) [14]. In subclavian flap repair, residual stenosis is probably due to inadequate resection of the periductal tissue and may be seen on CMR as an indenting ridge at the site of previous repair (Fig. 14.4b) [15]. Aneurysms may form at the site of previous repair (Figs. 14.3a, c, e and 14.4c, e) or may occur at or/and around suture lines (Fig. 14.4f, h). Dacron patch repair, for example, is predisposed to aneurysm formation [13] in the aortic wall around the patch (Fig. 14.4e). Discrete aneurysms may form as a result of percutaneous balloon angioplasty or at the suture lines after interposition graft repair (Fig. 14.4f).

#### 14.3.1 CMR of CoA

The protocol may be followed as described previously but with additional attention to:

- Site of coarctation, native or post-repair: Precise alignment through the region of coarctation is crucial and should be done in at least two planes orthogonal to each other and aligned through the center of the aortic lumen.

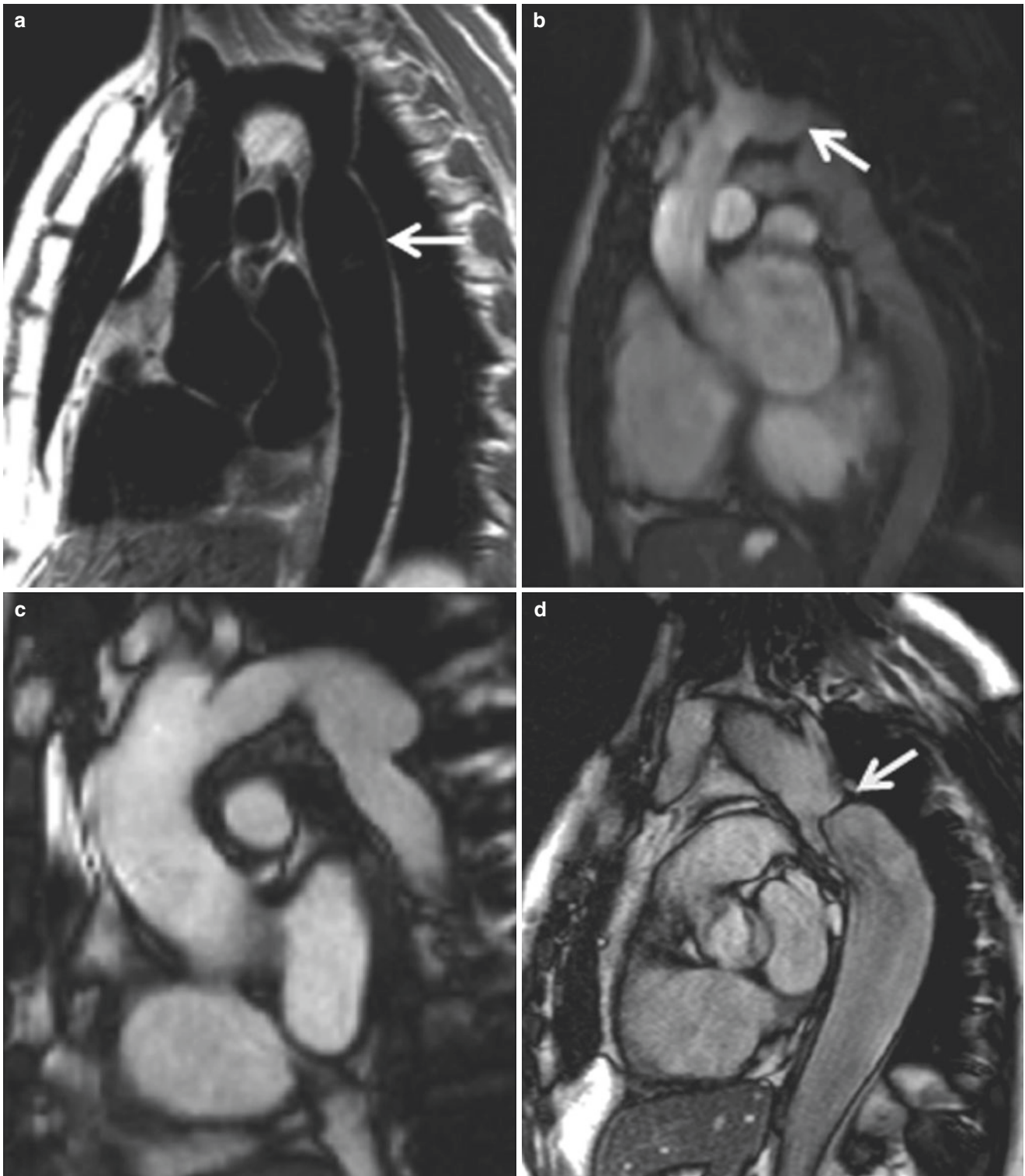


**Fig. 14.4** (a) Resection and end-to-end repair with post-stenotic dilatation (*arrowed*). (b, c) Subclavian flap repair showing a residual infolding ridge (b, *arrowed*) and aneurysm formation (c). (d, e) Patch repair with stenosis and jet formation, (d, *arrowed*) and aneurysm formation at the proximal suture line (e). (f) Interpositional graft repair with discrete aneurysms at the proximal and distal suture lines (*arrowed*). (g, h) Two bypass graft

repairs. In (g), the bypass is connected to the ascending aorta and the descending aorta at the diaphragm. In (h), the bypass is located just distal to the origin of the left subclavian artery and connected to the mid-descending thoracic aorta. There is a discrete aneurysm at the distal suture line (*arrowed*)



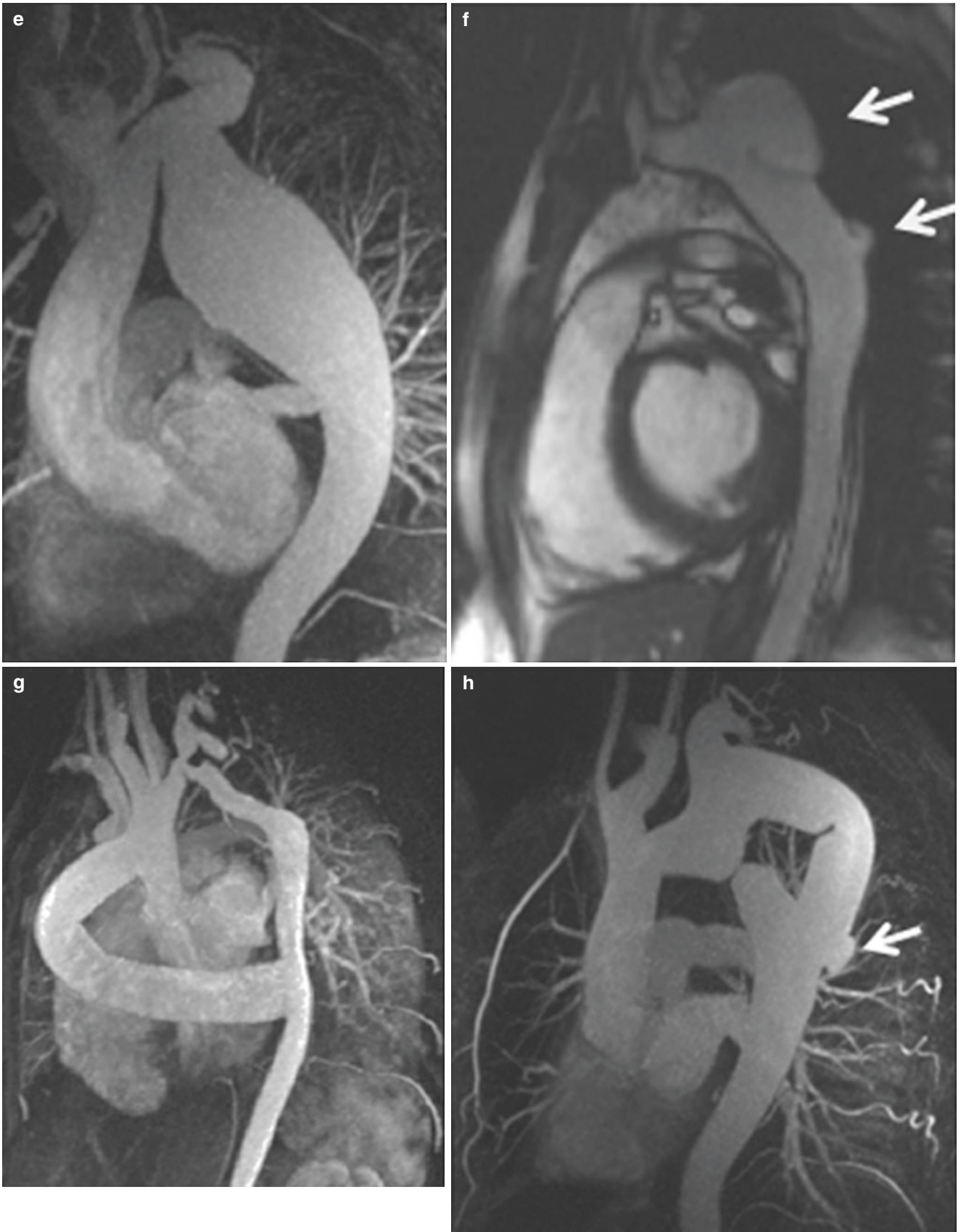


Fig. 14.4 (continued)



Any aneurysm formation should be interrogated, taking cross-sectional planes through the aneurysm at its widest points. Consider high temporal resolution imaging for small aneurysms.

- The aortic root and remaining thoracic aorta as described previously.
- Through-plane flow: Most commonly, done at the level just distal to the site of coarctation at the point of highest velocity as seen on the in-plane flow. This allows peak velocity measurement and also quantification of flow through the site of coarctation. Through-plane aortic flows at the level of coarctation and at the diaphragm can also be performed for comparative flow quantification at these sites [16].
- MRA: Important for detailed anatomical information on dimensions, anatomy, and assessment for collaterals (which are not so easily assessed on cine imaging alone).
- Stent: Metallic artifact may be problematic in imaging. As described previously, dark blood and FLASH sequences may be used. Instent aneurysm or stenosis in or near the stent, for instance, may be better visualized (Fig. 14.3a, b) on dark blood imaging. In addition, MRA may be useful for closer examination and measurement of an aneurysm at the site of the stent (Fig. 14.3c). MRA may also provide evidence of instent stenosis by demonstrating collateral flow (Fig. 14.3d). SSFP cine imaging is still useful, as in the case of aneurysms, it may demonstrate flow into the aneurysm (Movie 14.2).

### 14.3.2 Analysis of CoA

The following should be reported:

- Site of coarctation, native: Dimensions of the stenosis and its location. Intraluminal dimensions are recommended. The anatomy is also crucial, for example, angulation or tortuosity of the site can have important implications on the type of intervention needed. The dimension of the stenosis, presence or absence of collaterals, and peak recorded velocity through the stenosis (normal <1.5 m/s) can and should be used to assess severity of the stenosis. A diastolic tail or forward flow persisting into diastole is also indicative of severity, but is not always easy to see on through-plane flow mapping done distal to the site of CoA. Flow curves may be helpful in demonstrating a diastolic tail on the flow curve. The presence of collaterals can also be demonstrated by higher aortic flow at the level of the diaphragm compared to flow at the coarctation [16]. Associated aneurysm formation or anomalous neck vessels such as an anomalous origin of the right subclavian artery from the proximal descending aorta close to

the coarctation must also be reported as they must also be considered in planning management strategies.

- The aortic root and the remaining aorta: Measurement of the diameters of the aortic root and ascending aorta must be made as one or both segments of the aorta may be dilated, particularly in the presence of a bicuspid aortic valve. It is not uncommon to find dilatation of the descending aorta distal to the site of CoA even after successful repair (Figs. 14.3d and 14.4a). This is commonly referred to as “post-stenotic” dilatation.
- Left ventricle: Left ventricular hypertrophy indicates systemic hypertension and is another sign of severity of stenosis. Hypertension may also occur in the absence of stenosis and is a recognized complication of CoA.
- Associated anomalies: Bicuspid aortic valve, ventricular septal defect, left ventricular outflow obstruction from supra or/and subaortic valve stenosis, mitral valve abnormalities, and other anomalies.

Assessment after repair: As described above, but with special attention to:

- Site of coarctation: Detailed assessment of the repair site for restenosis and aneurysm formation (anatomy, dimensions, and severity). Serial CMR studies may be done to assess progression of an aneurysm, and it is therefore crucial that there is consistency in measurements. Stents may be difficult to assess because of metallic artifact. Dark blood sequences should be used to assess for intra-stent aneurysm. Stenosis proximal or distal to the stent may not be visualized adequately on SSFP cine imaging but may be seen on dark blood imaging (Fig. 14.3b). MRA is useful to assess for any aneurysm formation as measurements and detailed assessment of its anatomy can be made. Evidence for stenosis may be indicated on MRA by the presence of collaterals (Fig. 14.3d).

## 14.4 Aortic Aneurysms

Aortic aneurysms secondary to congenital defects affect, predominantly, the aortic root and ascending aorta. Marfan syndrome is the most common genetic cause of aortic aneurysm, and its estimated prevalence is between 1 in 5000 and 1 in 10,000 [2]. Intrinsic wall architecture abnormality from mutations in the fibrillin 1 gene cause aneurysmal dilatation of the aorta, predominantly in the aortic root. A bicuspid aortic valve also predisposes to aortic aneurysms, previously reported to be about 60% in the ascending aorta, and 40% in the aortic root by echocardiography study [17] and appear to be due to multiple mechanisms, including high ascending aortic wall shear stress [18]. Cystic medial degeneration, fibrillin 1 gene defect that is also found in the

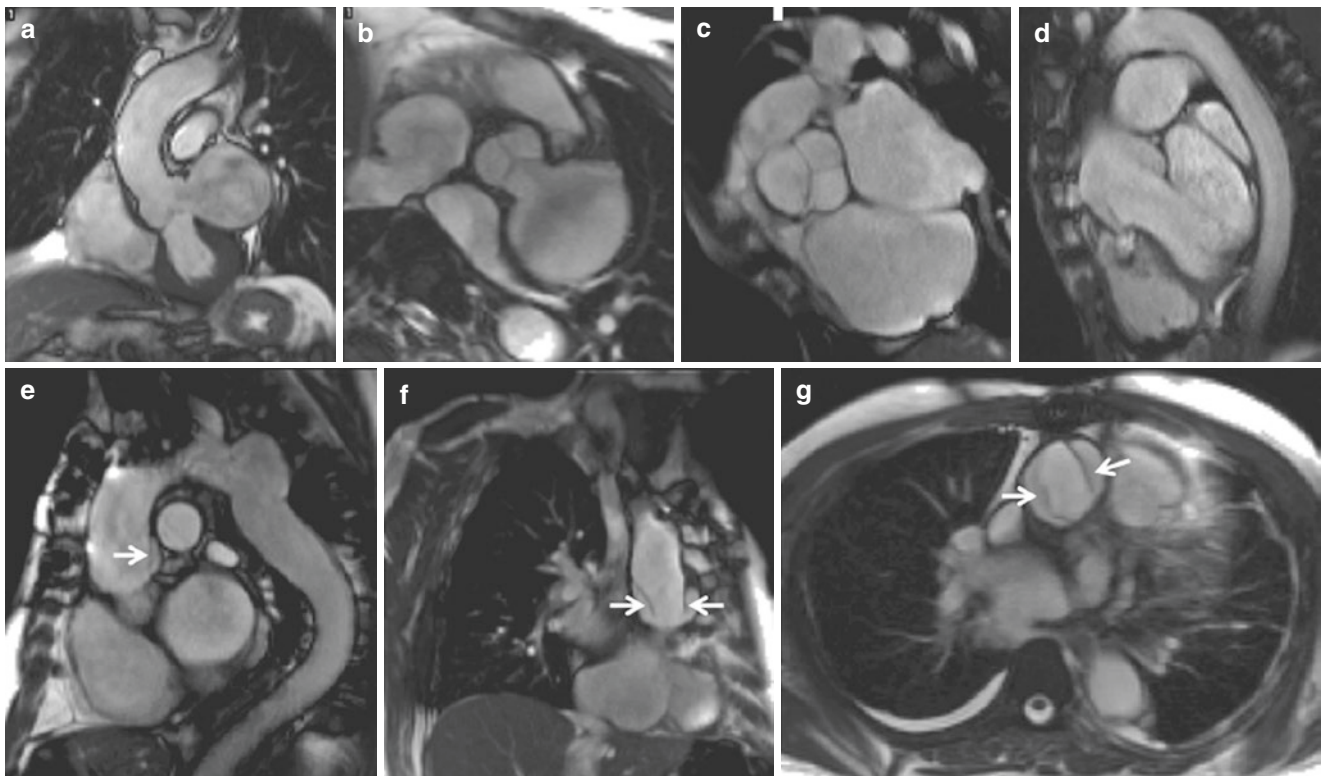


**Fig. 14.5** (a–d) Left sinus of valsalva aneurysm without rupture in (a, b). Right sinus of valsalva aneurysm with compression into and rupture into the RVOT in (c, d). (e–g) Bicuspid aortic valve with patch aneu-

rysm after CoA patch repair and dissection in the ascending aorta (e). (f) Is a slice from a coronal stack through the area of dissection, and (g) from a transaxial stack, the dissection flaps are arrowed in images e–g

main pulmonary artery of these patients, and ‘post-stenotic’ dilatation of the ascending aorta due to jet flow from a stenotic aortic valve and other causes have all been proposed [2, 3, 19].

Aneurysm of the sinus of Valsalva differs from aortic root dilatation as it is enlargement of one aortic sinus (Fig. 14.5a–d), between the aortic annulus and the sinotubular junction, and accounts for 0.14–0.23% of Western surgical series and 0.46–3.5% of Asian surgical series [20]. It is due to a weakness in the aortic wall from congenital absence of elastic lamellae causing disruption of the aortic media in the sinus and the media adjacent to the aortic annulus [21]. The most common aortic sinus involved is the right sinus (65–85%) and less commonly, the noncoronary sinus accounting for 10–30% and the left sinus in less than 5% of cases [22].

Arch and descending aortic aneurysms in the context of congenital heart disease are rarer and mostly due to complications of previous repair. CoA is the main cause, and aneurysms (Figs. 14.3 and 14.4) can be found at the site of previous repair or as a ‘post-stenotic’ dilatation in the descending aorta and is thought to be due to flow disturbance from the stenosis (native or recurrent). CoA is described in more detail earlier in this chapter.

#### 14.4.1 Associated Cardiac Defects

1. Marfan syndrome: mitral regurgitation due to either mitral valve prolapse or annular dilatation.
2. Bicuspid aortic valve: aortic stenosis or/and regurgitation, CoA (Fig. 14.5e).
3. Aneurysm of the sinus of Valsalva: most commonly, a ventricular septal defect (30–60%), aortic regurgitation (up to 30%), bicuspid aortic valve, CoA, pulmonary stenosis, and atrial septal defect [20]. Coronary artery anomalies may rarely coexist.
4. Coarctation of the aorta: bicuspid aortic valve in up to 85% of patients and associated aortic stenosis or/and regurgitation and ventricular septal defect. CoA may occur as part of complex congenital heart disease, in which other defects such as transposition of the great arteries may be present.

#### 14.4.2 Complications

The main complications of aortic aneurysms are aortic regurgitation due to annular dilatation from an aortic root

aneurysm and aortic dissection or rupture. Clinical presentation in the acute setting of dissection and rupture is usually with chest pain radiating to the back or, more dramatically, with hemodynamic compromise with or without heart failure. Dissection may also present more insidiously, with chronic back pain, or incidentally found on follow-up imaging. Aortic regurgitation presents either with a murmur found on clinical examination or in the more severe cases, with heart failure.

Other complications are more specific to the underlying condition. In aneurysm of the sinus of Valsalva, obstruction to the right ventricular outflow tract (RVOT) (Fig. 14.5c), coronary artery ostium, or rarely the left ventricular outflow tract may occur, depending on the particular sinus involved. A right sinus aneurysm usually ruptures into the RVOT (Fig. 14.5d) or more rarely the pulmonary artery, the non-coronary sinus into the right atrium, and the left sinus into the left ventricular outflow tract. Coronary artery tear or dissection and thrombus formation may also present following rupture of a sinus of Valsalva aneurysm.

#### 14.4.3 Management

Surgical repair with or without aortic valve replacement (for concurrent aortic valve disease) is the treatment of choice for aortic aneurysms. For smaller aneurysms of the aortic root and ascending aorta that do not need surgical repair, medical therapy may be instituted [19]. A more recent innovation for Marfan syndrome is the bespoke external aortic root support (EARS), a support structure that is wrapped around the external surface of the aorta from the level of the annulus to just beyond the right brachiocephalic artery [23–25] (Fig. 14.6). The support structure is fashioned after a computer derived model adjusted specifically to the patient's aortic measurements made from preliminary CMR images

acquired according to a dedicated protocol. Initial results have shown reduction in the aortic root dimensions at 1-year follow-up [23].

#### 14.4.4 CMR of Aortic Aneurysms

Early detection and intervention of aortic aneurysms result in more successful management and better prognosis [9]. Baseline imaging should be performed at the time of diagnosis of the underlying condition and then repeated imaging at a time frequency appropriate for the condition, for example, annual imaging for Marfan syndrome [9]. More frequent imaging should be done if the aneurysm is increasing in size. CMR is the modality of choice for patients with hemodynamically stable chronic aortic dissection who require regular follow-up imaging for surveillance. A patient with acute aortic dissection and unstable hemodynamic should not undergo CMR as the study is longer in duration than that of cardiac CT or transesophageal echocardiography. Furthermore, monitoring of and quick access to the patient should there be any deterioration in hemodynamics are difficult within the confines of a CMR scanner. Although access to the patient in a CT scanner may also be similarly difficult, a CT scan is much quicker to perform in comparison to a CMR study.

In addition to that already described for imaging of the aorta, particular attention should also be given to:

- Dissection or rupture: A stack of transaxial slices from the aortic arch to the aortic root or in another orientation aligned with the area of interest is useful (Fig. 14.5f, g) to assess the extent of dissection.
- Localized aneurysm: This may occur after repair of CoA, for example, as a discrete aneurysm (usually a pseudoaneurysm) at the suture line of an interpositional graft

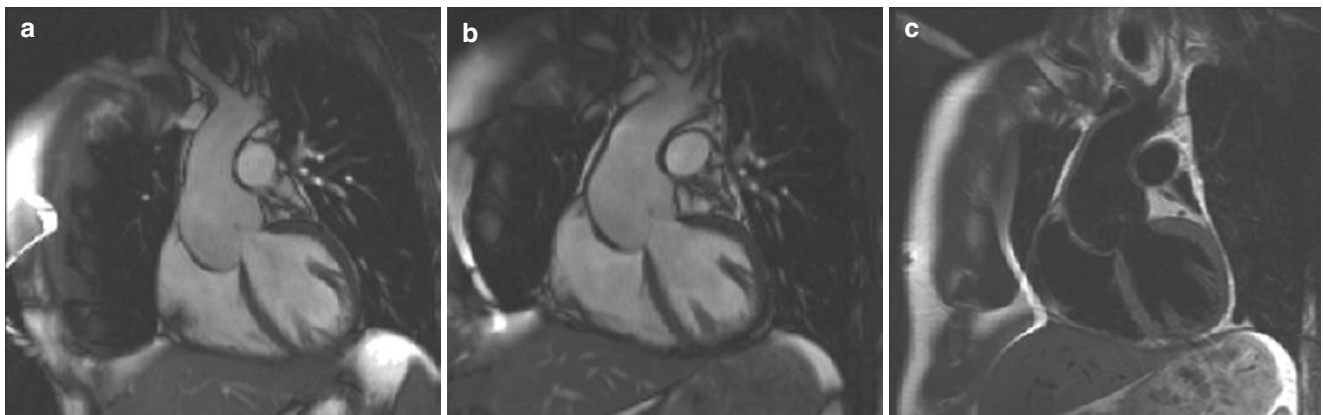


**Fig. 14.6** (a) Marfan syndrome with dilated aortic root, unrepaired. (b, c) Same patient as (a), post-EARS insertion. The device is seen as a thickened layer of aortic wall, seen in the SSFP image (b), and better seen on TSE imaging in (c)

(Fig. 14.4). Images carefully aligned to the widest points of the aneurysm are useful for measurements. High spatial and temporal resolution SSFP may be helpful if the aneurysm is small.

- Aortic valve: For functional assessment particularly of aortic regurgitation in aortic root aneurysm.
- Flow mapping: May be helpful in rupture to visualize leakage better or to visually assess the amount of leakage.
- Dissection flap: May be assessed using either SSFP cine imaging, TSE or MRA.
- Thrombus in dissection: May be seen on SSFP, TSE, and MRA, or, alternatively, in the early phase after contrast injection.
- Imaging for complications such as RVOT obstruction from a right sinus of Valsalva aneurysm.

#### 14.4.5 Analysis of Aortic Aneurysms

The following should be reported:

- Dimensions of the aorta: It is useful to record the location of the measurements as a reference for repeated studies in the future. Either the external or internal aortic dimensions can be used, but the key is consistency especially as most of these patients will have repeated studies for follow-up. If there is intramural thrombus, the internal and external diameters will be quite different. TSE imaging is useful in this instance for measurement of the internal diameter.
- Aneurysm: The shape of the aneurysm should be described (e.g., asymmetrical, fusiform, or saccular). Measurements will depend on its form. The widest and the longest (for aneurysms apart from aortic root aneurysm) dimensions are recommended. Discrete aneurysms should also be similarly measured and described.
- Dissection and rupture: The extent of the dissection including branch artery involvement, intramural hematoma, relative widths of the false and true lumen, and leakage from rupture should be described. The chamber or region that the aneurysm has ruptured into, if it is contained or not, persistent leakage from the aorta and the impact on the surrounding structures should also be reported.
- Aortic valve structure and function. Severity of stenosis and/or regurgitation should be reported.

Assessment after repair:

- The site of repair and the aorta: report on dimensions, presence of further or new dissection, intramural hematoma, and any new aneurysm formation.
- Assessment of aortic valve replacement if that has also been done at the time of aortic aneurysm repair.

### 14.5 Truncus Arteriosus

Truncus arteriosus is a single arterial trunk arising from the heart that divides into the pulmonary, systemic, and coronary artery circulations and results from failed septation of the aortopulmonary septum [1]. It accounts for <1% of all congenital heart anomalies. The truncal valve is tricuspid in 70% of patients, bicuspid in 21%, and quadricuspid in 9% (Fig. 14.7a). A subarterial ventricular septal defect is invariably present and is usually large and nonrestrictive. Other associated anomalies are right aortic arch (30%), interrupted aortic arch (10%) in association with a patent ductus arteriosus (PDA) (Fig. 14.7b), coronary artery abnormalities, and the DiGeorge syndrome.

Classification according to Collette and Edwards [26] is commonly used (Fig. 14.8). In type 1 (48–68%), the main pulmonary artery arises from the common arterial trunk and branches into the right and left pulmonary arteries (Movie 14.3 and Fig. 14.7c–e); in type 2 (29–48%), the main pulmonary artery is absent, and the right and left pulmonary arteries arise separately but close to each other on the posterior aspect of the common arterial trunk (Fig. 14.7f); and in type 3 (6–10%), the branch pulmonary arteries arise separately and further away from each other. There is complete absence of the pulmonary arteries in type 4. The lungs are perfused by aortopulmonary collaterals, and type 4 is no longer considered as part of the spectrum of truncus arteriosus but, instead, a variant of pulmonary atresia.

Patients present early in infancy with cyanosis or heart failure. Rarely, survival without repair may occur and is mainly due to the development of pulmonary hypertension. However, it is uncommon to survive beyond the third decade without intervention.

Surgical repair involves detachment of the pulmonary arteries from the arterial trunk, closure of the ventricular septal defect, connection of the pulmonary arteries to the right ventricle using a valved or valveless conduit, and repair of the truncal valve if regurgitant.

#### 14.5.1 CMR of Truncus Arteriosus

In addition to the previously described suggested protocol, imaging of:

- Common arterial trunk and pulmonary arteries, prior to repair: Two planes perpendicular to each other aligned to the left ventricular outflow tract for assessment of the outflow tract and truncal valve function. A cross section through the truncal valve to define valve morphology should be done. Planes aligned to the pulmonary arteries



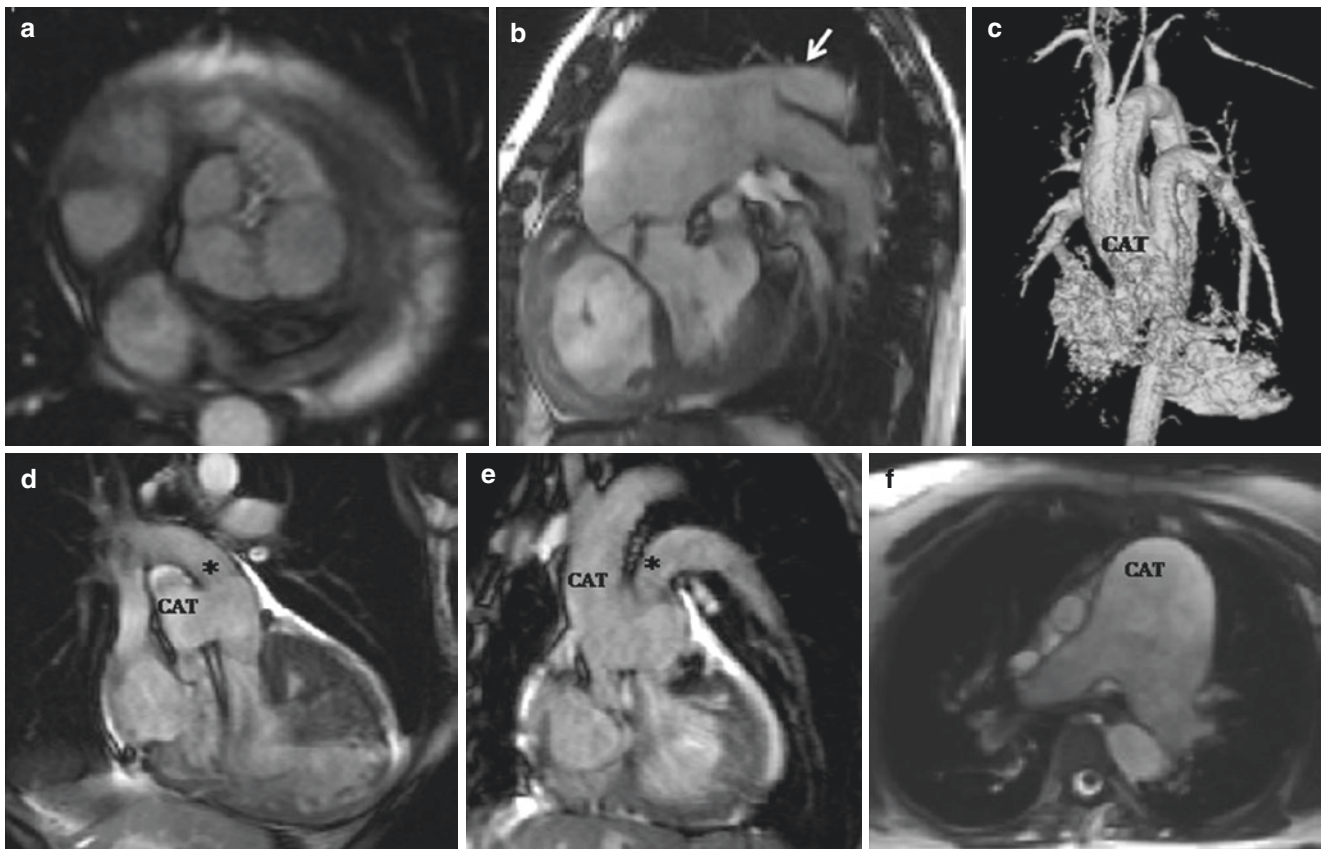


**Fig. 14.7** (a) Quadricuspid tricuspid leaflet. (b) Truncus arteriosus type 2 with interrupted arch and PDA (arrowed). (c–e) Surface-rendered 3D reconstruction after contrast-enhanced MRA of truncus arteriosus type 1 in (c). There is a short main pulmonary arising from the common

trunk (labelled *CAT*) and then dividing into the right pulmonary artery (labelled \* in d) and left pulmonary artery (labelled \* in e). (f) Truncus arteriosus type 2 with the pulmonary arteries arising separately from the posterior aspect of the common truncus (labelled *CAT*)

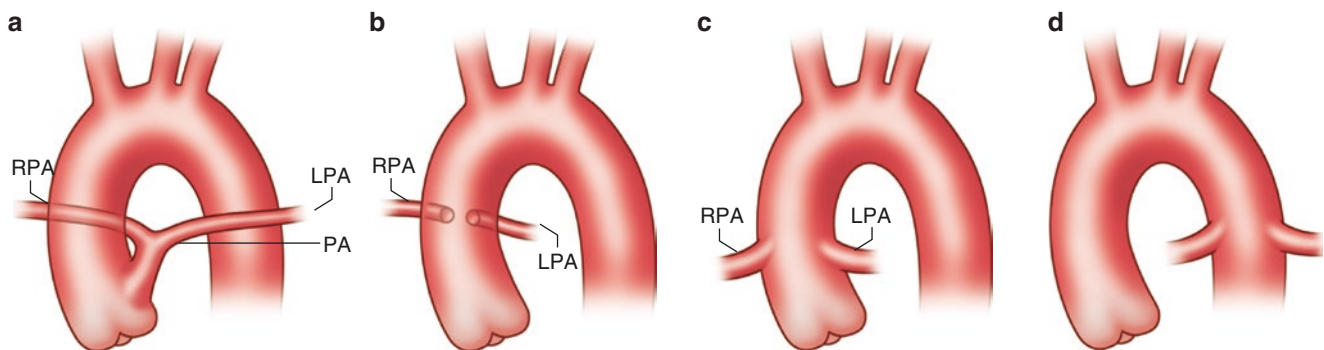


**Fig. 14.8** Classification of truncus arteriosus. Type 1 (a) the main pulmonary artery arises from the common arterial trunk. Type 2 (b) separate but close origins of the left and right pulmonary arteries from the common arterial trunk. Type 3 (c) separate but distant origins of the left

and right pulmonary arteries from the common arterial trunk. Type 4 (d) absence of the pulmonary arteries with aortopulmonary collaterals supplying blood flow to the lungs. *RPA* right pulmonary artery, *LPA* left pulmonary artery, *PA* pulmonary artery

for anatomical assessment of the pulmonary arteries and phase contrast flow mapping are useful if there is pulmonary stenosis to evaluate the severity of stenosis.

- MRA: May be helpful to further delineate pulmonary artery anatomy and, if present, CoA.
- Ventricular septal defect.
- Associated aortic interruption and PDA with phase contrast flow mapping for shunt direction and quantification.
- After repair: Interrogation of the RVOT to assess pulmonary homograft valve function and homograft conduit stenosis. Careful assessment of the pulmonary arteries and

flow mapping should be done if there is pulmonary arterial stenosis. The function of the truncal valve or the replaced valve and the truncal root dimension should all be assessed.

### 14.5.2 Analysis of Truncus Arteriosus

The following should be reported:

- Definition of the type of truncus arteriosus.
- Pulmonary artery: Morphology and function. If there is stenosis, report on its location and severity.
- Dimensions of the common arterial trunk.
- Truncal valve morphology and function.
- Ventricular septal defect: Report on the size, location, shunt direction, and quantification.

Assessment after repair:

- Pulmonary homograft valve and conduit: Report on the competency of the valve and if there is any stenosis in the conduit.
- Pulmonary arteries: Location and severity of pulmonary arterial stenosis should be reported.
- Truncal valve: Assessment of the function of the native or replaced valve.
- Arterial trunk: Report on its dimensions.
- Residual ventricular septal defect and other anomalies such as CoA or a patent ductus arteriosus.

## 14.6 Aortopulmonary Window

An aortopulmonary window is a rare congenital anomaly and result from a defect in the aorticopulmonary septum [1]. The pulmonary artery and aorta have separate pulmonary and aortic valves. The defect is usually located midway between the level of the aortic and pulmonary valves and the pulmonary bifurcation (Fig. 14.9) and may be circular or helical in shape. This defect may occur in isolation or in

association with CoA, aortic interruption, tetralogy of Fallot, and anomalous origin of one branch pulmonary artery, usually the right, from the ascending aorta [25].

Aortopulmonary window causes a left to right shunt. Large defects present early in childhood with heart failure. Late presentation with pulmonary hypertension and cardiac failure is rarer. Repair is usually with a direct suture or patch closure. There are reports of a limited number of small defects that have been closed using a percutaneous device.

### 14.6.1 CMR of Aortopulmonary Window

In addition to the protocol already described:

- Aortopulmonary window: A large defect should be easily seen on the initial multislice images and followed by appropriately aligned SSFP cine and phase contrast flow mapping for shunt direction and quantification. If the defect is small and not easily seen on the multislice images, then a stack of thin sliced (5-mm-thick) SSFP cine images in a transverse orientation taken from the level of the pulmonary bifurcation down to the level of the aortic and pulmonary valve should be done. If the defect cannot be seen on those images, a stack in the sagittal oblique orientation, aligned parallel to the wall of the ascending aorta, may be helpful.

### 14.6.2 Analysis of an Aortopulmonary Window

The following should be reported:

- Aortopulmonary window: The size and location of the defect including shunt size and direction and any associated anomalies should be reported.
- Evidence of pulmonary hypertension: Dilated branch pulmonary arteries with limited expansion, right ventricular hypertrophy, and septal flattening in systole.
- After repair: Report on any residual defect and shunt size.

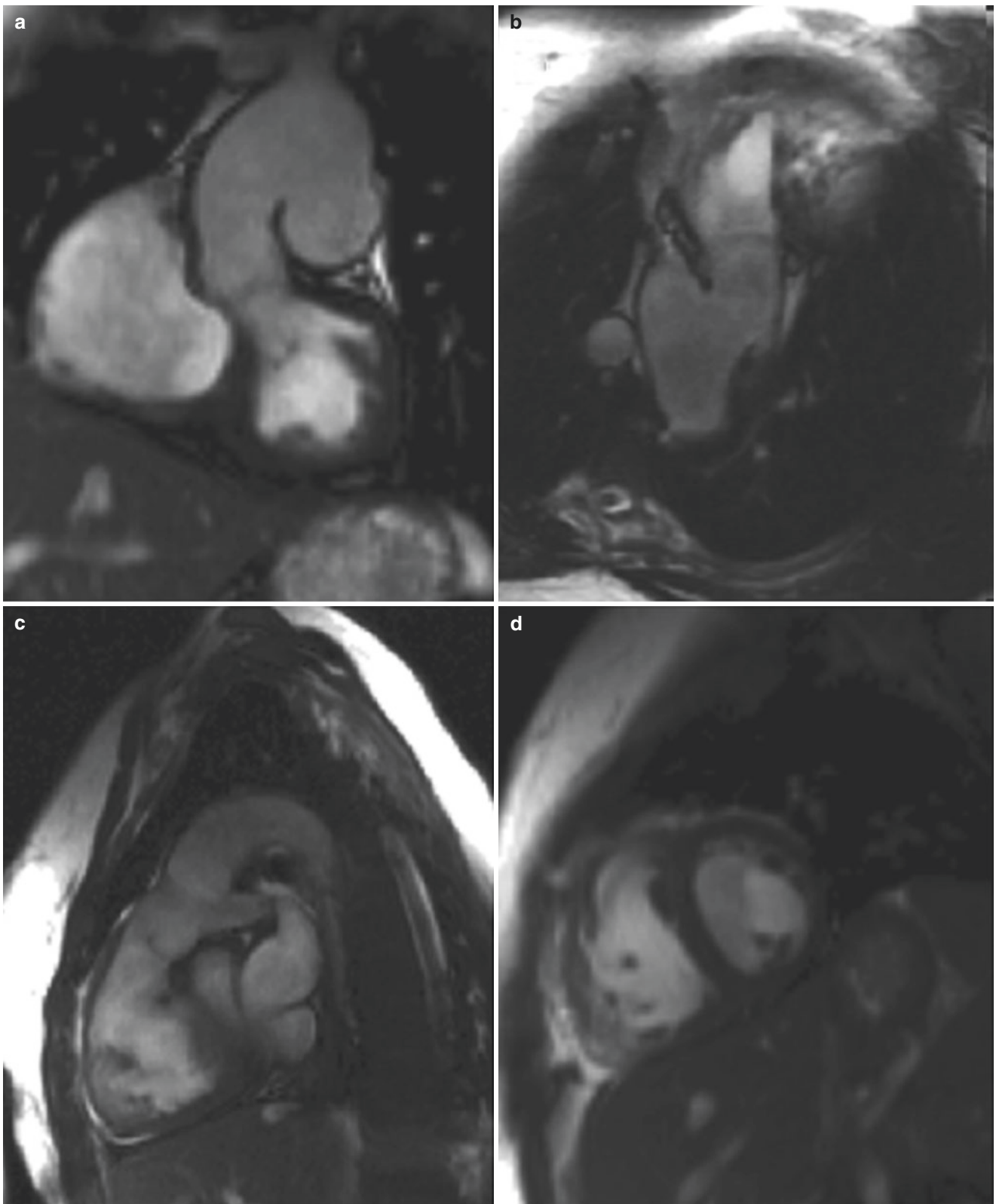


**Fig. 14.9** Aortopulmonary window seen in coronal (a), transaxial (b), and sagittal oblique (c) orientations (SSFP imaging). Right ventricular hypertrophy on short-axis SSFP (d) imaging, suggestive of pulmonary hypertension

## 14.7 Patent Ductus Arteriosus

A PDA is a vascular connection between the proximal descending aorta and the pulmonary artery, usually near the origin of the left pulmonary artery. It forms from the left sixth aortic arch [1] and, in fetal life, functions as a conduit for the portion of blood flow that passes between the right ventricle and the descending aorta. The duct normally closes after birth but may persist in preterm babies because of immaturity or in term babies due to a combination of structural, genetic, and environmental factors [27]. The incidence of PDA in term babies is about 5–10% of all congenital heart disease. It may occur as an isolated finding or as part of a group of other congenital anomalies. A PDA is usually on the left, but occasionally, a right sided PDA can occur particularly if the aortic arch is also right sided.

Presentation of a PDA depends on the size of the duct and the shunt. A duct may be silent and only discovered as an incidental finding, for example, on transthoracic echocardiography performed for other reasons. A continuous murmur is heard on clinical examination. Infective endarteritis can complicate a small PDA and in those with more significant shunts, heart failure, arrhythmia, and pulmonary hypertension (Fig. 14.10) may present later in life [27, 28]. In the most severe cases, there is differential cyanosis of the lower limbs.

Other intracardiac shunts such as an atrial or ventricular septal defect may coexist with a PDA. A PDA may also occur in the context of complex congenital heart disease such as pulmonary atresia or hypoplastic left heart syndrome.

Treatment for a PDA is either surgical ligation or clip or percutaneous device closure using coils or an Amplatzer (or other similar) device.

### 14.7.1 CMR of PDA

The transaxial, coronal, and sagittal SSFP multislice localizer stacks should be used to locate the PDA prior to SSFP cine imaging. It should be possible to see it on one or more of these stacks but may be difficult if it is small in size. If it is not obvious on the initial stacks, look also for a hint of it on the coronal SSFP stack, as a bright spot in the main pulmonary artery as it passes below the aortic arch.

Once a PDA is visualized on the initial stacks, cine imaging should be performed first to delineate the structure of the PDA and its relation to its surrounding structures.

- PDA: Ideally, at least two images in different orientations should be acquired. An in-plane flow map to demonstrate the direction of the shunt is useful; however, a through-

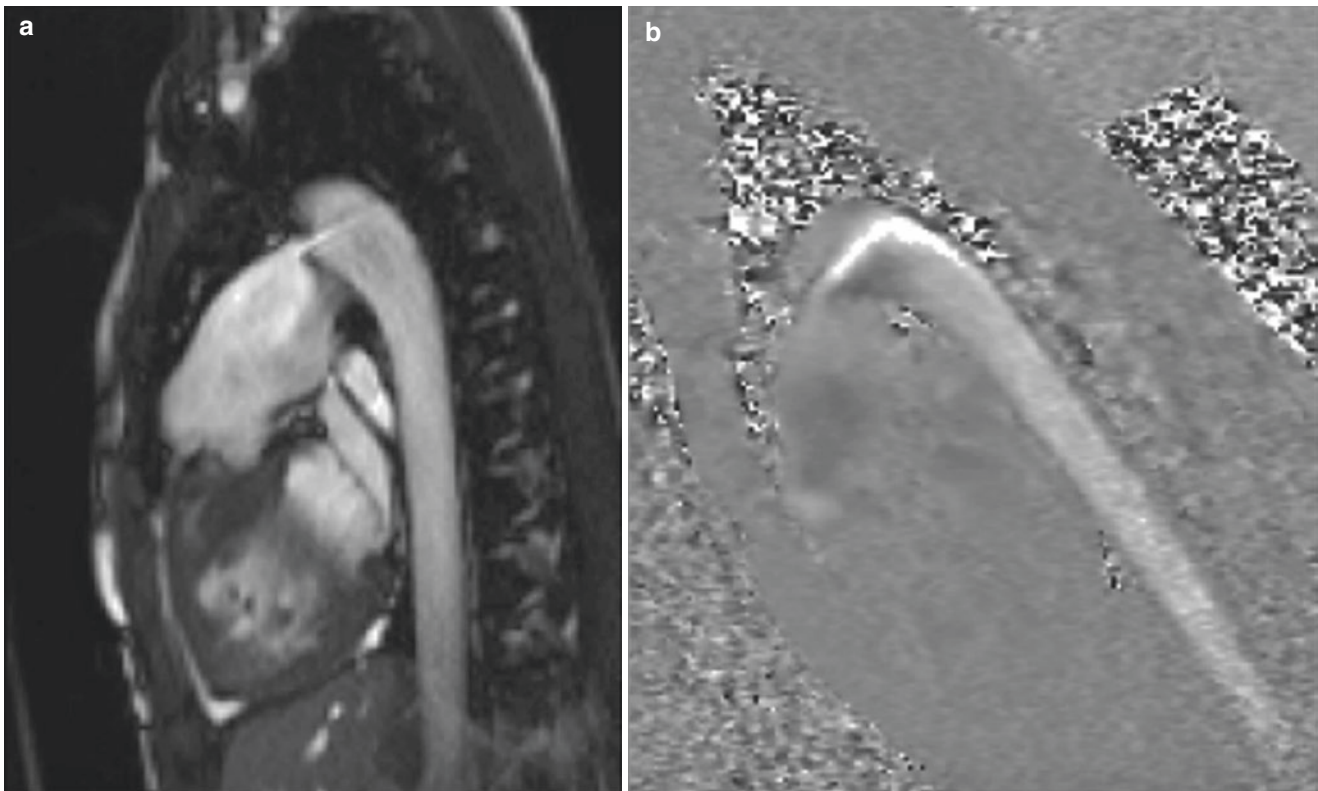


**Fig. 14.10** Patent ductus arteriosus with Eisenmenger physiology. There is reversed flow into the descending aorta on SSFP (a) and flow mapping (b) and RV hypertrophy



plane flow map through the PDA is not essential. Shunt quantification is done by through-plane ascending aortic to main pulmonary artery flow ratio.

- If a PDA cannot be easily seen on the initial transaxial, coronal, and sagittal stacks, it is probably small and may be difficult to find on CMR. In this instance, a stack of SSFP cine imaging in the transaxial orientation from the aortic arch to the main pulmonary artery, done using thin slices of 5 mm without gaps, can be very useful to pick up a small PDA. If this stack fails to show a PDA, then a similar stack but in a sagittal oblique orientation, aligned perpendicular to the descending aorta and the left pulmonary artery as seen in the transaxial orientation can be used. If a PDA cannot be seen on these images, then ensure that the aortic and pulmonary artery through-plane flows for shunt quantification are done to confirm the presence (in this case then, a small PDA) or absence of a PDA.
- Repaired PDA: Metallic artifact from the clip or device may preclude detailed examination of the site of repair. FLASH imaging may be used to try and overcome the problem with the artifacts. Shunt quantification should be done to assess for a residual defect.

### 14.7.2 Analysis of a PDA

The following should be reported:

- PDA: Size, structure, and dimensions of the PDA. These are useful in clinical decisions on management and the type of intervention.
- Shunt direction and quantification.
- Evidence for pulmonary hypertension: dilated branch pulmonary arteries with limited expansion, right ventricular hypertrophy, and septal flattening in systole.
- Biventricular volumes and function: Overloading of the left ventricle may be present and indicates a more significant shunt.

Assessment after repair:

- Assess for a residual PDA and improvement in ventricular function if there was pre-surgical impairment.

## 14.8 Vascular Rings and Sling

The aortic arch, its branches, and the pulmonary arteries are the result of the embryologic development or regression of the six paired aortic arches that are connected to the ventral and dorsal aortas. Of these arches, the third, fourth, and sixth pairs normally develop into the carotid arteries, the aortic

arch, and the proximal right pulmonary artery, left pulmonary artery, and ductus arteriosus, respectively [1]. Abnormalities in the pattern of regression or persistence of these arches result in vascular rings and sling.

Vascular rings are rare with a prevalence of <1% of all congenital heart defects. It forms a ring around the esophagus and trachea and causes respiratory and feeding difficulties by compression. It may be complete or partial, depending on whether the esophagus and trachea are fully surrounded by the ring or not [29].

Complete vascular ring (Fig. 14.11a, b): A double aortic arch (Movie 14.4) is the most common complete vascular ring (40%) and results from persistence of the right aortic arch. Both arches with their respective arch branches fuse dorsally to form the descending aorta. The second most common complete ring is a right aortic arch with a persistent left ligamentum arteriosum. The ring is formed by the ascending aorta anteriorly, the arch on the right, an aberrant left subclavian artery that arises as the fourth arch vessel and passes posterior to the esophagus and trachea, and on the left, is a persistent ligamentum arteriosum between the descending aorta and the left pulmonary artery.

Partial vascular rings (Fig. 14.11c, d) include an aberrant origin of the right brachiocephalic artery from a more leftward position on the arch and causes compression as it passes anteriorly toward the right and anomalous origin of the right subclavian artery as the fourth neck vessel on a left sided aortic arch and passing posterior to the esophagus (or anomalous left subclavian artery origin from a right sided aortic arch, Movie 14.5 and Fig. 14.12a).

A vascular sling is an anomalous left pulmonary artery origin from the right pulmonary artery and causes compression as it passes between the trachea and the esophagus during its course to the left lung (Fig. 14.12b).

Symptoms and clinical presentation depend on the severity of trachea and esophageal compression and are mainly related to respiratory compromise. Dysphagia is less common. Associated anomalies are tetralogy of Fallot, transposition of the great arteries, CoA, and ventricular septal defects.

Surgery is not commonly indicated. If needed, division can be done of the smaller of the arches in double aortic arch or the ligamentum arteriosum for a right aortic arch ring and, for a vascular sling, division and reimplantation of the left pulmonary artery.

### 14.8.1 CMR of a Vascular Ring or Sling

Diagnosis is possible using CMR, but most rings are diagnosed on clinical symptoms and by barium esophagography. CMR is extremely useful in examining the relationship between the vascular ring and the surrounding structures.

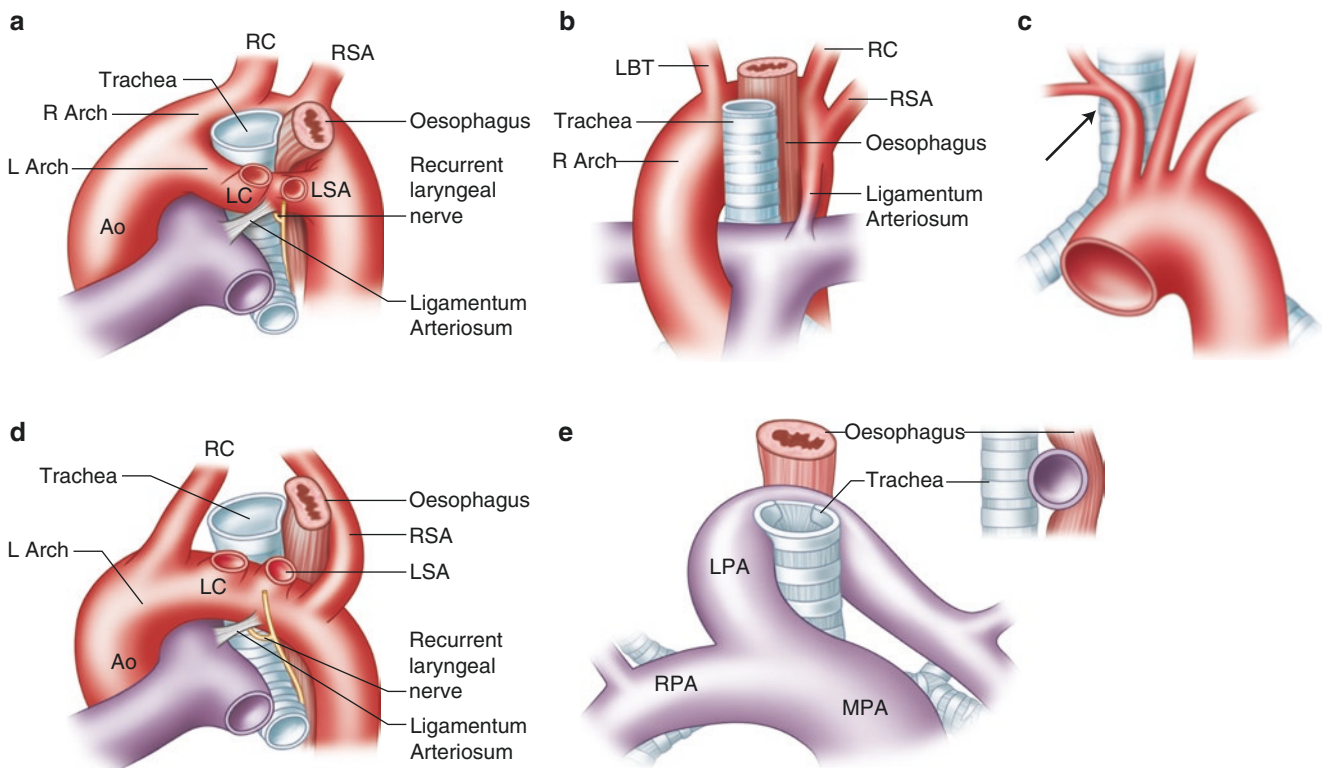


**Fig. 14.11** Complete and partial vascular rings. (a) Double aortic arch. (b) Right aortic arch and a persistent ligamentum arteriosum. (c) Compression of the trachea by a more leftward origin of the right brachiocephalic artery (arrowed). (d) Anomalous origin of the right subclavian artery from the proximal descending aorta with a retroesophageal

and tracheal course. (e) Left pulmonary artery arising from a right pulmonary artery. *RC* right carotid artery, *LC* left carotid artery, *RSA* right subclavian artery, *LSA* left subclavian artery, *LBT* left brachiocephalic trunk, *Ao* ascending aorta, *LPA* left pulmonary artery, *RPA* right pulmonary artery, *MPA* main pulmonary artery

- SSFP cine imaging: unless the anomaly can be visualized in a single plane (and often it is not as vessels may be tortuous and traverse more than one plane), a stack of images is recommended (Fig. 14.12d). Orientation may be in the transaxial or coronal (or both) whichever follows the course of the vessel best. Thin slices of 5 mm without gaps are recommended as vessels may be small in diameter. Cine imaging may be advantageous over a 3D whole heart or SSFP multislice imaging as assessment may also be made (to a degree) of the effect of systolic expansion of the anomalous vessels on the trachea and esophagus.
- 3D whole heart: This method may be useful and may be used as an adjunct to cine imaging.

- MRA: this is not essential but may be useful if there is concurrent stenosis in the vessels of interest.

## 14.8.2 Analysis of a Vascular Ring or Sling

The following should be reported:

- The morphology and course of the vascular ring or sling.
- The relationship of the vascular ring or sling to its surrounding structures and the degree of compression.
- After repair: report on any evidence of residual compression.

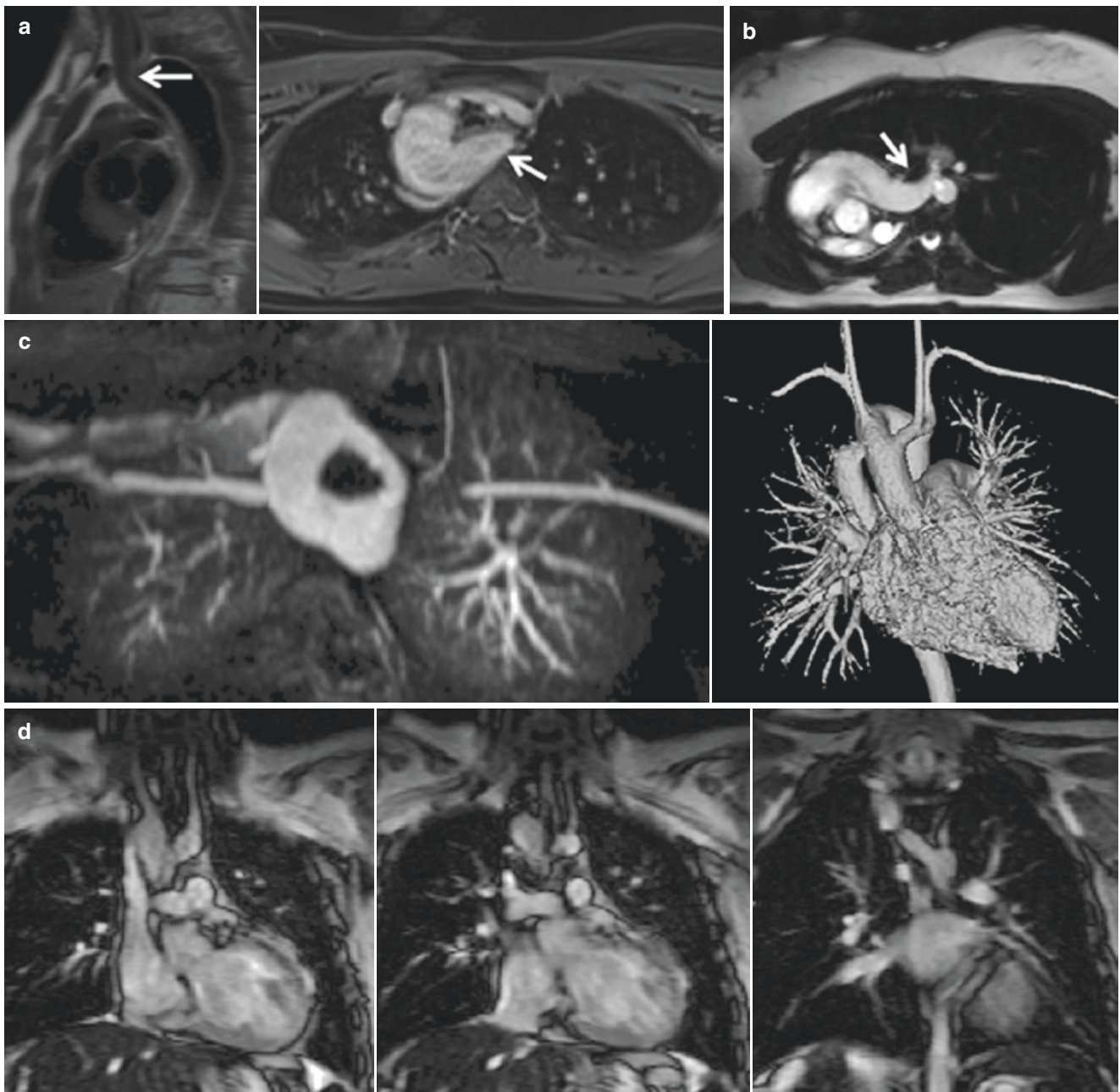


**Fig. 14.12** (a) Right aortic arch with a Kommerell diverticulum at the origin of an anomalous left subclavian artery. The left subclavian artery courses behind the esophagus and trachea (*arrowed*), causing compression (HASTE and SSFP multislice imaging). (b) Unusual left pulmonary artery sling causing esophageal and tracheal compression

(*arrowed*). (c) Double aortic arch. Contrast-enhanced (near transaxial orientation) image showing a complete vascular ring on the left and a surface-rendered 3D reconstruction after contrast-enhanced MRA on the right. (d) SSFP multislice imaging showing a double aortic arch

### 14.9 Limitations and Common Pitfalls

CMR is somewhat limited by the image degrading effect of metallic artifacts, but this can be overcome to a degree as described earlier in the chapter. Tortuous aortas and branch vessels may be difficult to image on SSFP cine imaging, but MRA largely compensates. The most com-

mon pitfall is inaccurate measurements due to misalignment of the imaging planes, and reproducibility in measurements of studies done over time may be difficult. Again, by careful planning of the planes prior to imaging and using previous studies as a guide, reproducibility and accuracy of measurements and therefore assessment may be improved.



## 14.10 Conclusion

Aortic anomalies comprise a heterogeneous group of defects and can be assessed in detail using CMR for diagnosis and in planning management strategies, surveillance, and follow-up for residual or progressive and/or recurrent abnormalities. Its ability to image the aorta in all orientations and projections is an advantage as detailed and accurate assessment of can be made. In addition, phase contrast and velocity mapping allow measurement of blood flow, useful in quantification of severity of the lesions. CMR is a versatile imaging modality for the evaluation of the aorta with the added advantages of its noninvasive nature and the lack of radiation and use of iodinated contrast agents.

## References

- Moore KL, Persaud TVN. The developing human, clinically orientated embryology. 7th ed. Philadelphia: Saunders; 2003. p. 329–80.
- Pearson GD, Devereux R, Loeys B, Maslen C, Milewicz D, Pyeritz R, Ramirez F, Rifkin D, Sakai L, Svensson L, Wessels A, Van Eyk J, Dietz HC. Report of the National Heart, Lung and Blood Institute and National Marfan Foundation Working Group on research in Marfan syndrome and related disorders. *Circulation*. 2008;118:785–91.
- Fedak PW, de Sa MP, Verma S, Nili N, Kazemian P, Butany J, Strauss BH, Weisel RD, David TE. Vascular matrix remodelling in patients with bicuspid aortic valve malformations: implications for aortic dilatation. *J Thorac Cardiovasc Surg*. 2003;126:797–806.
- Leiner T, Bogaert J, Friedrich MG, Mohiaddin R, Muthurangu V, Myerson S, Powell AJ, Raman SV, Pennell DJ. SCMR position paper (2020) on clinical indications for cardiovascular magnetic resonance. *J Cardiovasc Magn Reson*. 2020;22:76. <https://doi.org/10.1186/212968-020-00682-4>.
- Aboulhosn J, Child JS. Left ventricular outflow obstruction: sub-aortic stenosis, bicuspid aortic valve, supraaortic stenosis, and coarctation of the aorta. *Circulation*. 2006;114:2412–22.
- Warnes CA, Williams RG, Bashore TM, Child JS, Connolly HM, Dearani JA, del Nido P, Fasules JW, Graham TP Jr, Hijazi AM, Hunt SA, King ME, Landzberg MJ, Miner PD, Radford MJ, Walsh EP, Webb GD. ACC/AHA 2008 guidelines for the management of adults with congenital heart disease: a report of the American College of Cardiology/American Heart Association task force on practice guideline (writing committee to develop guidelines on the management of adults with congenital heart disease): developed in collaboration with the American Society of Echocardiography, Heart Rhythm Society, International Society for Adult Congenital Heart Disease, Society for Cardiovascular Angiography and Interventions, and Society of Thoracic Surgeons. *Circulation*. 2008;118:e714–833.
- Morgan-Hughes GJ, Marshall AJ, Roobottom C. Morphologic assessment of patent ductus arteriosus in adults using retrospectively ECG-gated multidetector CT. *AJR Am J Roentgenol*. 2003;181:749–54.
- Hoey ETD, Kanagasigam A, Sivanathan MU. Sinus of valsalva aneurysms: assessment with cardiovascular MRI. *AJR Am J Roentgenol*. 2010;194:W494–504.
- Hiratzka LF, Bakris GL, Beckman JA, Bersin RM, Carr VF, Casey DE Jr, Eagle KA, Hermann LK, Isselbacher EM, Kazerooni EA, Kouchoukos NT, Lytle BW, Milewicz DM, Reich DL, Sen S, Shinn JA, Svensson LG, Williams DM, American College of Cardiology Foundation/American Heart Association Task Force on Practice Guidelines, American Association for Thoracic Surgery, American College of Radiology, American Stroke Association, Society of Cardiovascular Anesthesiologists, Society for Cardiovascular Angiography and Interventions; Society of Interventional Radiology, Society of Thoracic Surgeons, Society for Vascular Medicine. ACCF/AHA/AATS/ACR/ASA/SCA/SCAI/SIR/STS/SVM guidelines for the diagnosis and management of patients with Thoracic Aortic Disease: a report of the American College of Cardiology Foundation/American Heart Association Task Force on Practice Guidelines, American Association for Thoracic Surgery, American College of Radiology, American Stroke Association, Society of Cardiovascular Anesthesiologists, Society for Cardiovascular Angiography and Interventions, Society of Interventional Radiology, Society of Thoracic Surgeons, and Society for Vascular Medicine. *Circulation*. 2010;121(13):e266–369.
- Burman ED, Keegan J, Kilner PJ. Aortic root measurement by cardiovascular magnetic resonance: specification of planes and lines of measurement and corresponding normal values. *Circ Cardiovasc Imaging*. 2008;1:104–13.
- Davis AE, Lewandowski AJ, Holloway CJ, Ntobeko ABN, Banerjee R, Nethononda R, Pitcher A, Francis JM, Myerson SG, Leeson P, Donovan T, Neubauer S, Rider OJ. Observational study of regional aortic size referenced to body size: production of a cardiovascular magnetic resonance nomogram. *J Cardiovasc Magn Reson*. 2014;16:9. <https://doi.org/10.1186/1532-429X-16-9>.
- Voges I, Jerosch-Herold M, Hedderich J, Pardun E, Hart C, Gabbert DD, Hansen JH, Petko C, Kramer HH, Rickers C. Normal values of aortic dimensions, distensibility, and pulse wave velocity in children and young adults: a cross-sectional study. *J Cardiovasc Magn Reson*. 2012;14:77. <https://doi.org/10.1186/1532-429X-14-77>.
- Isner JM, Donaldson RF, Fulton D, Bhan I, Payne DD, Cleveland RJ. Cystic medial necrosis in coarctation of the aorta: a potential factor contributing to adverse consequences observed after percutaneous balloon angioplasty of coarctation sites. *Circulation*. 1987;75:689–95.
- Chen SS, Dimopoulos K, Alonso-Gonzalez R, Lioudakis E, Teixeira-Fernandez E, Alvarez-Barredo M, Kempny A, Diller G, Uebing A, Shore D, Swan L, Kilner PJ, Gatzoulis MA, Mohiaddin RH. Prevalence and prognostic implication of restenosis or dilatation at the aortic coarctation repair site assessed by cardiovascular MRI in adult patients late after coarctation repair. *Int J Cardiol*. 2014;173(2):209–15. <https://doi.org/10.1016/j.ijcard.2014.02.012>.
- Rocchini AP. Coarctation of the aorta and interrupted aortic arch. In: Moller JH, Hoffman IE, editors. *Pediatric cardiovascular medicine*. Philadelphia: Churchill Livingstone; 2000. p. 567–93.
- Steffens JC, Bourne MW, Sakuma H, O'Sullivan M, Higgins CB. Quantification of collateral blood flow in coarctation of the aorta by velocity encoded cine magnetic resonance imaging. *Circulation*. 1994;90:937–43.
- Nistri S, Sorbo MD, Palisi M, Scognamiglio R, Thiene G. Aortic root dilatation in young men with normally functioning bicuspid aortic valves. *Heart*. 1999;82:19–22.
- Mohiaddin RH. WSS for predicting BAV aortopathy growth. Good as gold or a sheer Wall street speculation? *J Am Coll Cardiol Img*. 2022;15(1):43–5.
- Isselbacher EM. Thoracic and abdominal aortic aneurysms. *Circulation*. 2005;111:816–28.
- Ring WS. Congenital heart surgery nomenclature and database project: aortic aneurysm, sinus of valsalva aneurysm, and aortic dissection. *Ann Thorac Surg*. 2000;69:S147–63.
- Edwards JE, Burchell HB. The pathological anatomy of deficiencies between the aortic root and the heart, including aortic sinus aneurysms. *Thorax*. 1957;12:125–39.



22. Swan L. Sinus of valsalva aneurysms. In: Gatzoulis MA, Webb GD, Daubeney PEF, editors. *Diagnosis and management of adult congenital heart disease*. London: Churchill Livingstone; 2003. p. 239–44.
23. Pepper J, Golesworthy T, Utley M, Chan J, Ganeshalingam S, Lamperth M, Mohiaddin R, Treasure T. Manufacturing and placing a bespoke support for the Marfan aortic root: description of the method and technical results and status at one year for the first ten patients. *Interact Cardiovasc Thorac Surg*. 2010;10:360–5.
24. Dormand H, Mohiaddin RH. Cardiovascular magnetic resonance in Marfan syndrome. *J Cardiovasc Magn Reson*. 2013;15:33. <https://doi.org/10.1186/1532-429X-15-33>.
25. Izgi C, Newsome S, Alpendurada F, Nyktari E, Boutsikou M, Pepper J, Treasure T, Mohiaddin R. External aortic root support to prevent aortic dilatation in patients with Marfan syndrome. *J Am Coll Cardiol*. 2018;72:1095–105. <https://doi.org/10.1016/j.jacc.2018.06.053>.
26. Collett RW, Edwards JE. Persistent truncus arteriosus; a classification according to anatomic types. *Surg Clin North Am*. 1949;29:1245–70.
27. Schneider DJ, Moore JW. Patent ductus arteriosus. *Circulation*. 2006;114:1873–82.
28. Gersony WM, Apfel HD. Patent ductus arteriosus and other aortopulmonary anomalies. In: Moller JH, Hoffman IE, editors. *Pediatric cardiovascular medicine*. Philadelphia: Churchill Livingstone; 2000. p. 323–34.
29. Park MK. *Paediatric cardiology for practitioners*. 4th ed. Philadelphia: Mosby; 1984. p. 241–6.



Theodore Murphy, Rory O’Hanlon,  
and Raad H. Mohiaddin

## 15.1 Introduction

In order to plan optimal management and treatment strategies in patients with a suspected inherited cardiomyopathy, the key initial factor is to establish the diagnosis and underlying etiology at an early stage. While many patients will present with symptoms and demonstrable ventricular dysfunction on echocardiography, often the underlying cause is not apparent, thus necessitating many “routine” invasive and noninvasive investigations such as angiography, echocardiography, Holter monitoring, treadmill testing, and nuclear studies. There has been considerable progress in recent years in the development of imaging technologies which are now able to characterize a much wider number of cardiomyopathic processes than ever before in a noninvasive manner. Gadolinium-enhanced cardiac magnetic resonance imaging (CMR) and more recently parametric mapping have dramatically changed the noninvasive work-up of patients with a suspected cardiomyopathy. In a single-scan setting, it is now possible to provide a comprehensive assessment of both ischemic and nonischemic cardiomyopathies providing detailed information on cardiac anatomy, function, tissue

characterization, assessment of epicardial and microvascular perfusion, valvular flows, and coronary and peripheral angiography (Fig. 15.1). This comprehensive examination can be completed in a short period of time, typically 30–45 min, without the need for prolonged breath holds or ionizing radiation. This establishes a definitive diagnosis with the greatest degree of clarity, helps guide and monitor therapeutic response, and assists in optimal risk stratification. Gadolinium-based contrast agents are remarkably safe, and the incidence of adverse reactions or nephrogenic systemic sclerosis (NSF) is exceedingly low. Follow-up imaging to monitor progression and response to interventions can be performed safely and without any concern regarding cumulative radiation exposure.

In this chapter we will primarily focus on the inherited/congenital cardiomyopathies with a defined genetic basis. There will be scope for the discussion of non-inherited cardiomyopathies as there is often a phenotypic overlap since patients often do not present with a known genetic diagnosis; rather they present with symptoms or are incidentally found to have an abnormal clinical exam or screening test and are subsequently found to have a hypertrophied or dilated heart warranting further investigation.

**Supplementary Information** The online version contains supplementary material available at [https://doi.org/10.1007/978-3-031-29235-4\\_15](https://doi.org/10.1007/978-3-031-29235-4_15).

T. Murphy  
Cardiovascular Magnetic Resonance Unit, Royal Brompton  
Hospital and National Heart and Lung Institute, Imperial College  
London, London, UK

R. O’Hanlon  
Centre for Cardiovascular Magnetic Resonance, Dublin, Ireland

R. H. Mohiaddin (✉)  
Cardiovascular Imaging, Royal Brompton and Harefield Hospitals,  
Guy’s and St Thomas’ NHS Foundation Trust, London, UK

National Heart and Lung Institute, Imperial College London,  
London, UK  
e-mail: [r.mohiaddin@imperial.ac.uk](mailto:r.mohiaddin@imperial.ac.uk)

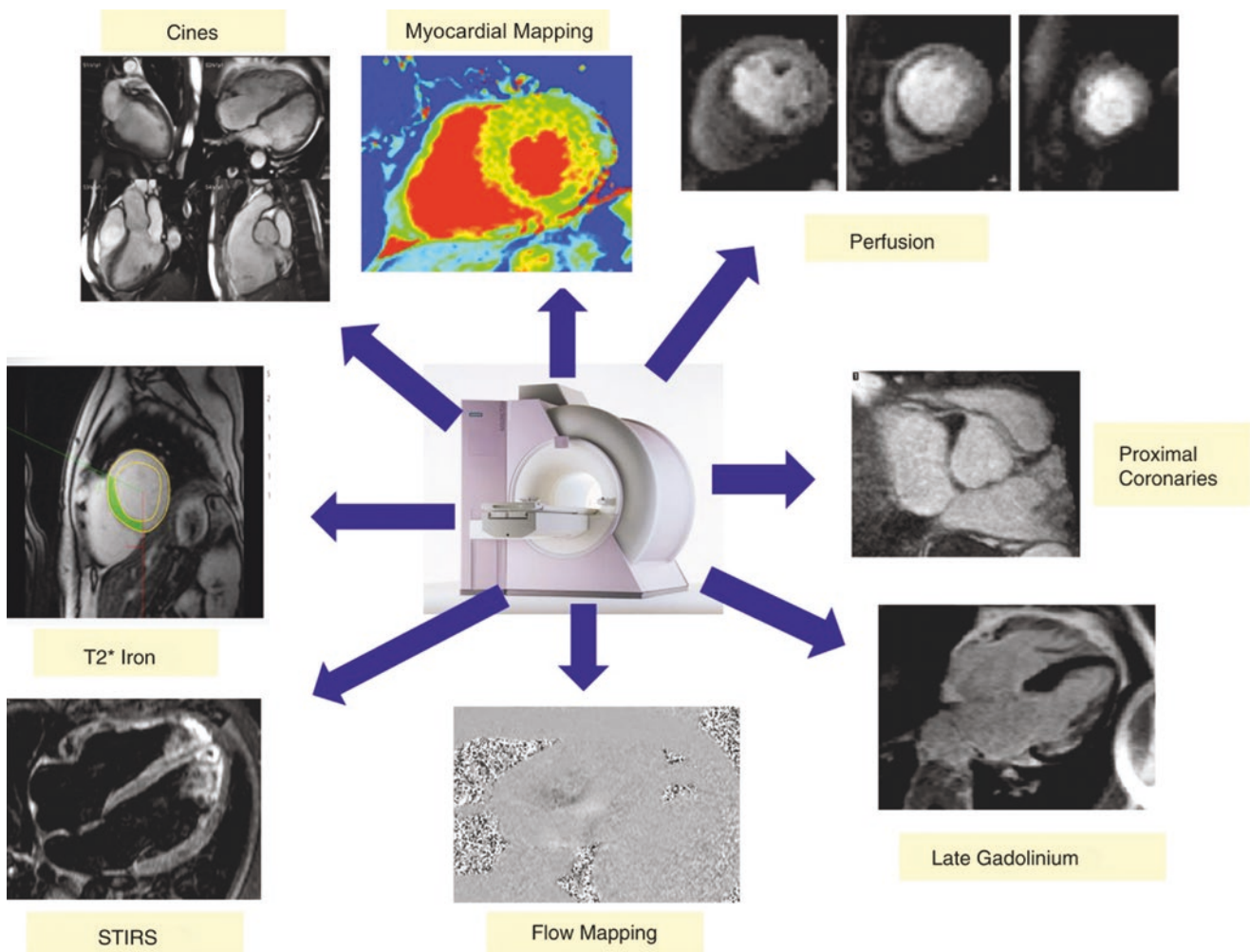


**Fig. 15.1** Typical CMR sequences and post-processing tools available for routine use. In a single-scan setting typically taking no more than 35–40 min, a complete evaluation of cardiac structure, function, myo-

cardial characterization, myocardial perfusion, and valvular assessment can be performed.

## 15.2 CMR Techniques

In the CMR work-up of a suspected cardiomyopathy, a wide range of sequences are acquired following dedicated protocols as outlined by the Society of Cardiovascular Magnetic Resonance [1]. Initial dark blood single shot scout images are acquired in transaxial, coronal, and sagittal imaging planes. Following this, dynamic cine images of the heart are acquired along its long and short axis using balanced steady-state free precession (bSSFP) cine imaging. Cine images can be acquired in any given imaging plane without the limitation of acoustic windows as seen with echocardiography. CMR is validated as the gold-standard imaging tool to quantify biventricular volumes and function using short-axis cine images of the left ventricle (LV) and right ventricle (RV) acquired from the base to the apex. The availability of normalized values for CMR-measured dimensions, cor-

rected for age, sex and body surface area helps to establish subtle ventricular abnormalities and provides a more suitable method for follow-up of serial measurements given the superior interstudy reproducibility over other imaging modalities [2, 3].

Tissue characterization can also be performed by the use of both intrinsic and extrinsic contrast imaging sequences. T1- and T2-weighted turbo-spin echo (TSE) sequences are useful to assess the pericardium where the clinical question concerns constrictive vs. restrictive cardiomyopathy. Short tau inversion recovery (STIR) imaging with a triple inversion protocol nulls signal from fat, is T2-weighted, and is used to identify areas of increased myocardial water content, indicative of myocardial edema and inflammation which are seen in conditions such as acute myocarditis, cardiac sarcoidosis, and acute myocardial infarction. Native T1 mapping is used to characterize interstitial fibrosis using a modified look-

locker inversion recovery pulse sequence (MOLLI sequence) or a shortened MOLLI (ShMOLLI) sequence [1]. Myocardial T2\*-weighted imaging exploits the loss of signal owing to greater field inhomogeneities and is used to assess myocardial iron, since iron is ferromagnetic and leads to a dose-dependent breakdown in field homogeneity which can be quantified [4]. Valvular heart disease is assessed using velocity flow mapping. Similar to echocardiography's tissue Doppler velocity imaging, myocardial tagging can quantify cardiac deformation and assess contraction and relaxation in the radial, longitudinal, and circumferential directions [5]. Myocardial feature tracking using vendor specific software can also facilitate the assessment of myocardial strain and deformation from routinely acquired cine images [6]. Perfusion can be assessed at the microvascular level and is an important adjunct in the assessment of suspected inherited cardiomyopathies. Following administration of intravenous gadolinium contrast into a peripheral vein (0.1–0.2 mmol/kg body weight), the passage of the contrast through the right heart, the left heart, and the myocardium can be followed, providing information about regional myocardial perfusion at rest and perfusion reserve during administration of adenosine. Imaging performed immediately (1–3 min) following intravenous gadolinium contrast agent is a sensitive tool to detect intracardiac thrombi by providing the best delineation between the enhanced blood pool and myocardium on one side and the avascular dark thrombus on the other side. Late gadolinium enhancement (LGE) imaging is then performed approximately 5–20 min after gadolinium administration. Due to its volume of distribution and washout kinetics, it accumulates in areas of increased extracellular space (interstitial expansion). The presence of LGE is indicative of abnormal myocardial interstitium typically due to the presence of myocardial fibrosis or infarction. The distribution and patterns of LGE guide both accurate diagnosis and risk stratification in both ischemic and nonischemic cardiomyopathies.

---

## 15.3 Hypertrophic Cardiomyopathy

Hypertrophic cardiomyopathy (HCM) is a common inherited cardiac disorder previously thought to have a prevalence of around 1 in 500 in the general population. However, more contemporaneous studies report an increased prevalence of up to 1 in 200. This is thought to be due to four reasons: (1) pathogenic sarcomeric genes being more common in the general population than previously thought, (2) increased availability of genetic testing defining a new subset of patients without clinical expression or LV hypertrophy (genotype-positive, phenotype-negative), (3) appropriate recognition of alternative HCM phenotypes being facilitated by advanced imaging (i.e.,

CMR), and (4) prior prevalence studies not accounting for the familial nature of the disease [7, 8].

Histopathology in phenotypical expression of HCM reveals hypertrophied myocytes arranged in a disorganized and chaotic fashion with a varying amount of interstitial fibrosis [9]. The disease is characterized by marked heterogeneity with respect to clinical manifestation, natural history, prognosis, the association with an increased risk of sudden cardiac death (SCD), and progression to heart failure (HF).

The recently published AHA/ACC 2020 guidelines on the diagnosis and treatment of hypertrophic cardiomyopathy defines HCM as a disease state in which morphologic expression is confined solely to the heart. HCM is characterized predominantly by left ventricular hypertrophy in the absence of another cardiac, systemic, or metabolic disease capable of producing the degree of hypertrophy evident in a given patient and for which a disease-causing sarcomere (or sarcomere-related) variant is identified, or genetic etiology remains unresolved [10].

### 15.3.1 CMR in the Diagnosis of HCM

(See Movies 15.1, 15.2, 15.3, 15.4, 15.5, 15.6, 15.7, and 15.8)

There are a number of important challenges in the noninvasive evaluation of HCM particularly accurate diagnosis, assessment of disease severity, risk stratification in addition to screening family members, guiding lifestyle, and therapeutic strategies. The question regarding the diagnosis arises not infrequently in the assessment of athletes with variable degrees of presumed physiological hypertrophy or in patients with long-standing hypertension and asymmetrical hypertrophy. In addition, there are many phenocopies of HCM including lysosomal storage diseases (Fabry's disease) and infiltrative cardiomyopathies (amyloidosis, sarcoidosis) all of which can present with ECGs and echocardiograms that mimic HCM, although the management of each differs greatly from the other.

For the purposes of this review, the role of CMR in diagnosis of HCM will refer to typical sarcomeric HCM. The majority of patients with sarcomeric protein gene mutations have an asymmetrical pattern of hypertrophy, most commonly affecting the interventricular septum. CMR-indexed LV volumes are typically small with hyperdynamic systolic function. Progression to left ventricular dilatation and systolic failure occurs in a minority of patients [11]. Although the usual clinical diagnostic criteria for HCM is a maximal LV wall thickness greater than or equal to 15 mm, genotype-phenotype correlations have shown that virtually any wall thickness (including those within normal range) are compatible with the presence of a HCM mutant gene. The ECG can



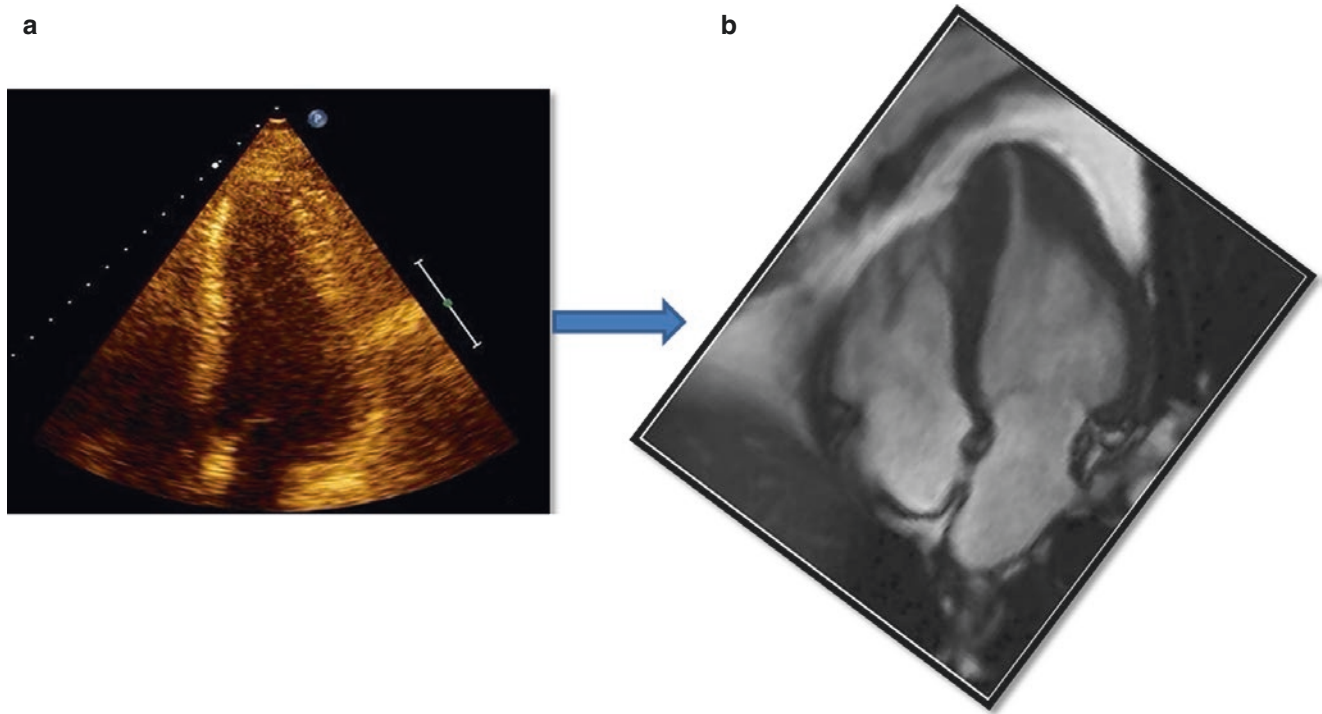


**Fig. 15.2** Apical HCM “missed” by echocardiography (a) but easily visualized using CMR (b)

be normal or at least unremarkable, without the typical deep T-wave inversions or large QRS complexes (approximately 5–10% of cases), and any pattern of hypertrophy is described including concentric hypertrophy, reinforcing the diagnostic challenges that exist [12, 13]. The heterogeneity of the phenotypical expression of HCM results in many different morphological subtypes identified, namely, classic reverse curvature septum, neutral HCM, sigmoid HCM, apical HCM, mid-cavity HCM, and genotype +ve phenotype-negative HCM. Although not diagnostic of HCM, a number of additional morphologic abnormalities, which can be readily seen with CMR, are associated with phenotypical expression of HCM. These include hypertrophied and apically displaced papillary muscles, myocardial crypts, anomalous insertion of the papillary muscle, left ventricular apical aneurysm, elongated mitral valve leaflets, and right ventricular (RV) hypertrophy.

Two-dimensional echocardiography is the first line test to diagnose HCM. However, the available acoustic windows and the orientation of the heart in the mediastinum often limit the quality of images obtained by echocardiography. Furthermore, certain areas of the myocardium are not visualized well with echocardiography, and detection of subtle areas of abnormal hypertrophy can be missed. CMR images can be acquired in any given plane; meaning that oblique views are avoided and hypertrophied areas can be visualized and measured with confidence and accuracy (Fig. 15.2). A study comparing CMR versus echocardiography in the eval-

uation of patients with HCM demonstrated a measurement discrepancy occurring in 15% of the patients at diagnostic or prognostic cutoffs [14].

An important strength of CMR compared to other imaging modalities is the ability to determine myocardial tissue characteristics in vivo using the late gadolinium enhancement (LGE) technique in addition to parametric mapping (T1, T2, T2\*, and ECV.) In patients with HCM, the pattern of replacement fibrosis is distinct to that seen in CAD or patients with DCM. Typically, it is patchy, mid-wall with multiple foci and most commonly found in regions of hypertrophy. Several patterns of LGE are seen with a diffuse trans-septal or RV septal pattern at one end of the spectrum and a confluent pattern that may affect the interventricular junction or be multifocal at the other end of the spectrum. Hypertrophied hearts may appear phenotypically the same by echocardiography or based on cine imaging alone. Incorporating LGE imaging and parametric mapping, to what may seem like phenotypically similar conditions by echocardiography or CMR imaging alone, may confer an alternative diagnoses (Fig. 15.3) [15–17]. This can be particularly useful in cases with possible concentric left ventricular hypertrophy seen in atypical HCM, hypertensive heart disease, cardiac amyloid, hemochromatosis and athletic remodeling. Additionally CMR strain imaging may also further help distinguish ambiguous cases [18].

There is growing interest in HCM individuals who are genotype-positive and phenotype-negative, focusing on

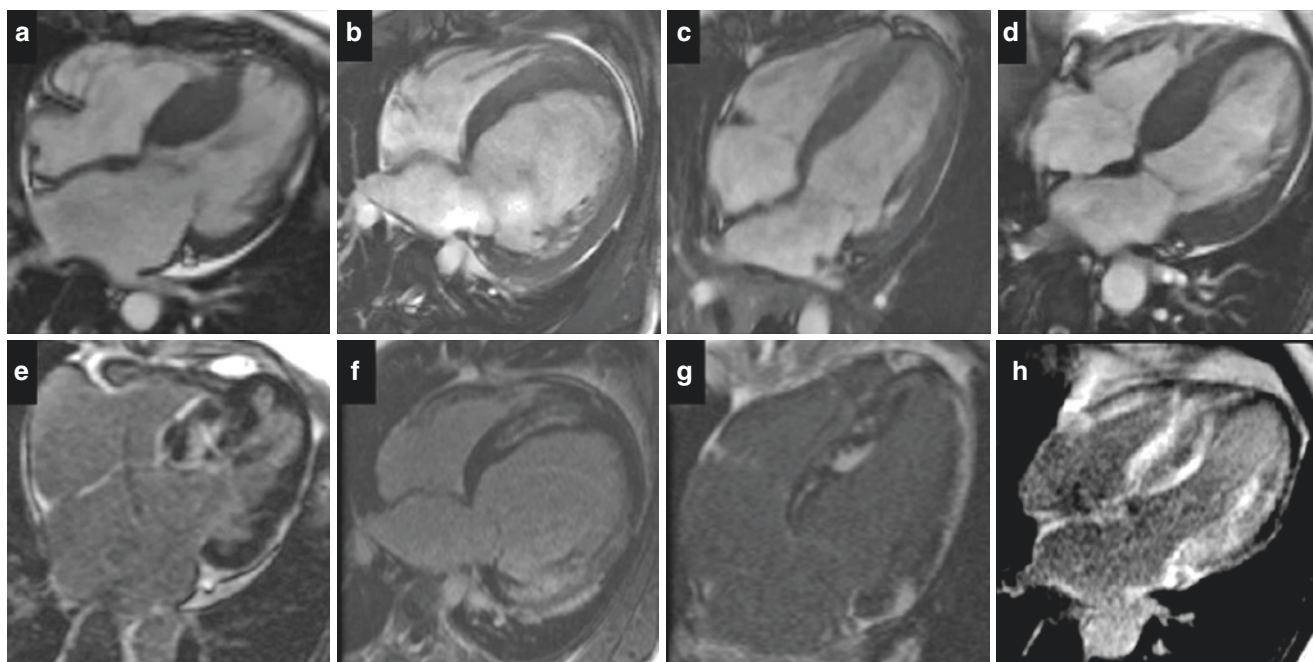


**Fig. 15.3** Four-chamber SSSP images of different patterns of left ventricular hypertrophy (**a–d**) and corresponding late gadolinium enhancement images (LGE) (**e–h**). Hypertrophic cardiomyopathy (**a, e**) typically shows patchy mid-wall LGE in the regions of maximal hypertrophy. Fabry's (**b, f**) shows mid-wall LGE in the basal lateral wall and

septum. Sarcoidosis (**c, g**) typically shows focal LGE scarring which is typically patchy and involving the basal and lateral segments. Cardiac amyloidosis (**d, f**) showing diffuse subendocardial LGE with “sparing” of the epicardium and septum characteristically referred to as a “zebra” pattern

morphological changes, perfusion abnormalities, and altered parametric values. Recent work has identified novel left ventricular morphological features in individuals who are genotype-positive, phenotype-negative in comparison to normal controls. A novel model looking at morphological findings including the presence of an anterobasal hook, multiple myocardial crypts, and the ratio of various ventricular dimensions was able to predict the genotype status with an area under the curve of 0.92 [0.87–0.97] [19]. In addition, contemporary work has illustrated regional and global impaired myocardial perfusion occurs in genotype-positive, phenotype-negative individuals, occurring before the development of hypertrophy or fibrosis suggesting that perfusion abnormalities may predate left ventricular hypertrophy [20]. T1 mapping has also shown to be altered in individuals who are genotype-positive, phenotype-negative and may help discriminate between hypertensive heart disease and HCM [21].

As demonstrated, the use of conventional assessment algorithms when assessing patients with suspected HCM may erroneously misdiagnose patients with important clinical implications. Subsequently, CMR has become much more prominent in the most recent 2014 European and 2020 American guidelines and carries a class 1 indication for individuals who have suspected hypertrophic cardiomyopathy and inadequate echocardiographic windows in order to confirm the diagnosis.

### 15.3.2 CMR in the Prognosis and Management of HCM

There are several challenges in the clinical management of HCM, but one of the most commonly presented questions concerns the decision regarding ICD implantation. There are seven established clinical risk factors to help stratify the risk of sudden cardiac death and to identify those who may benefit from an ICD [10]. They include the following: family history of SCD, unexplained syncope, left ventricular (LV) wall thickness >30 mm, occurrence of non-sustained ventricular tachycardia (NSVT), impaired left ventricular systolic function (LVEF <50%), extensive LGE on CMR imaging, and the presence of left ventricular apical aneurysm. Of note four of the seven risk factors are optimally assessed with CMR, namely, to accurately determine the ejection fraction, wall thickness, in addition to identifying the presence of an apical aneurysm and or extensive LGE.

In patients with HCM, maximal LV wall thickness measurements can be underestimated or overestimated with echocardiography compared to CMR imaging. In one study CMR identified 83% of the population as having left ventricular hypertrophy >30 mm in contrast to only 48% having significant hypertrophy on echocardiography [22]. Another study with 353 HCM patients who had both a CMR and an echocardiogram demonstrated echocardiography both under and overestimated the peak wall thickness in 36% and 46%

of cases respectfully. Furthermore, echocardiography underestimated the LVEF in 88% of cases with the median difference of LVEF of 12%. In the same population, echocardiography only identified 30% of left ventricular apical aneurysms identified on CMR [23]. CMR has now become the gold standard in assessing individuals with HCM as it has the added benefit of better identifying these key binary risk factors highlighted in the risk stratification process, facilitating earlier diagnosis and treatment where indicated.

In addition to these morphological risk factors, tissue characterization with LGE is also one of the most useful tools in determining the SCD risk of an individual, and over the last 10 years there has been much research in this domain [24–26] (Figs. 15.4 and 15.5). A study involving 1293 HCM patients demonstrated that those patients with a burden of LGE  $\geq 15\%$  of the total myocardium were associated with a twofold increase in SCD event risk and an estimated likelihood of a SCD event of 6% at 5 years [27]. Subsequent, to this growing body of evidence, the 2020 AHA/ACC

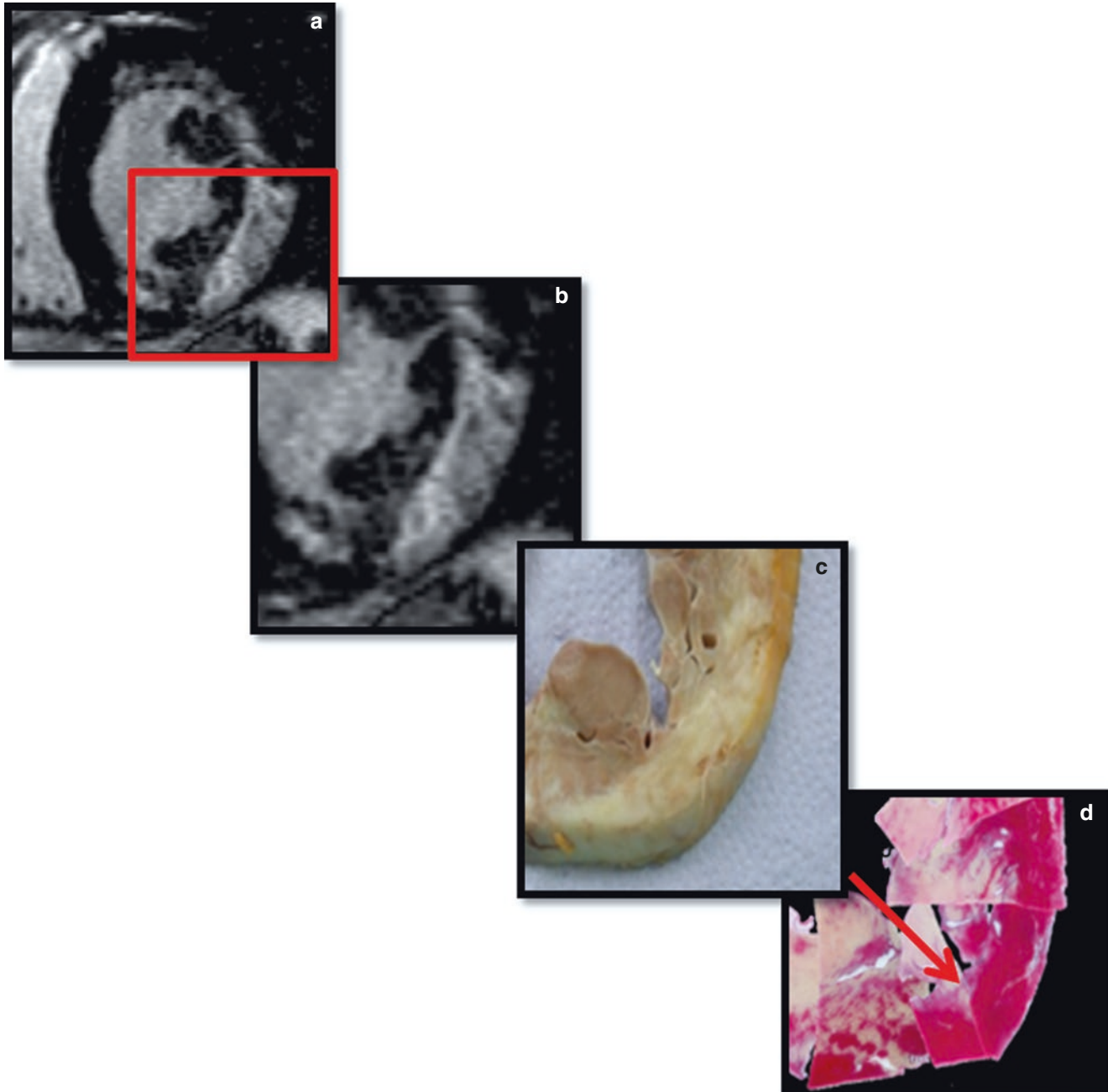


**Fig. 15.4** Comparison of in vivo late gadolinium enhancement (LGE) images (a, b) matching macroscopic assessment from autopsy (c) and confirmed as myocardial replacement fibrosis on histology sections stained with Picrosirius red (d)



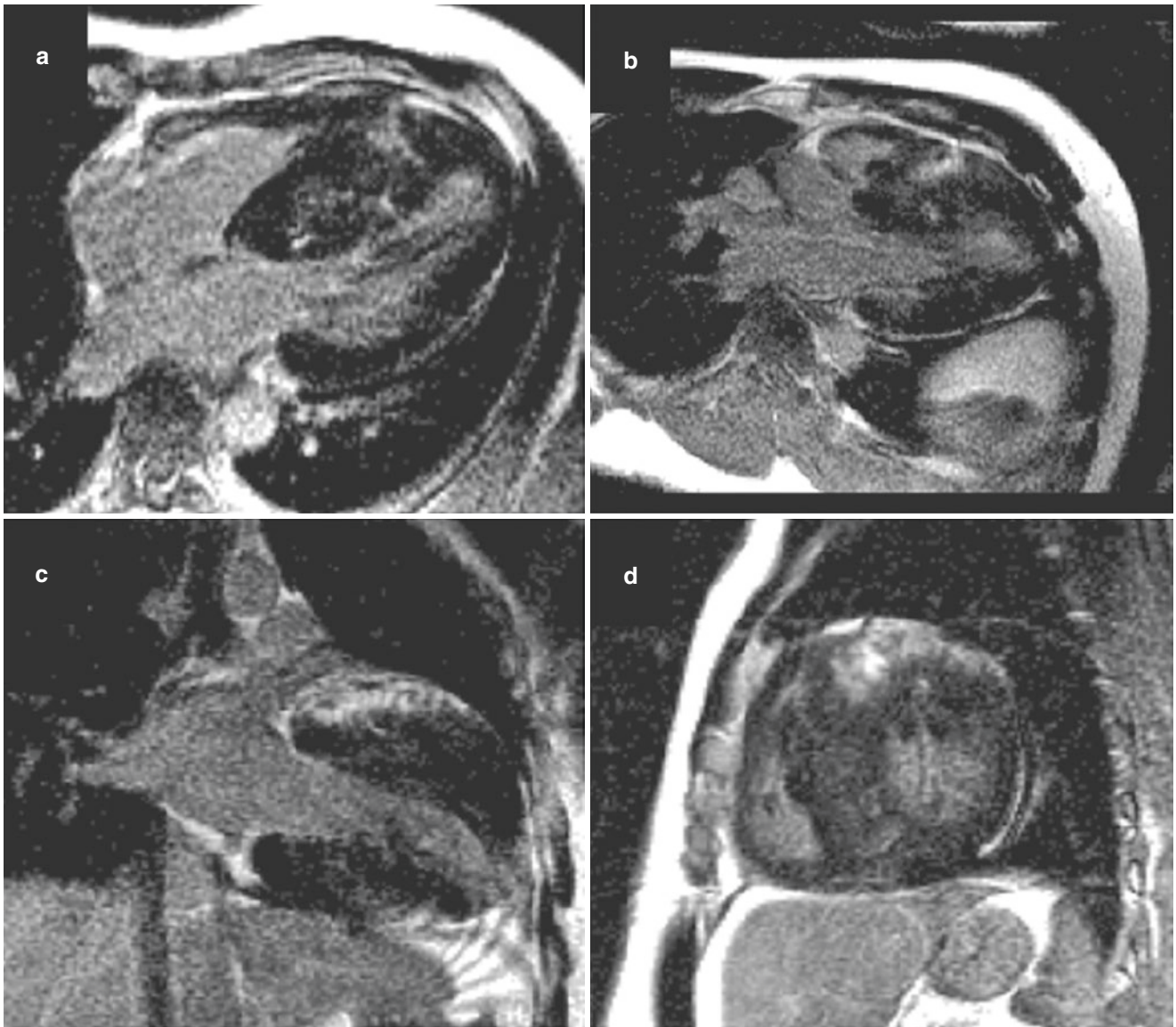


**Fig. 15.5** LGE images in a patient with HCM in four-chamber, three-chamber, two-chamber, and short-axis views (**a–d**) at the time of the baseline scan. Follow-up scanning 4 years later shows marked increase in the severity of LGE in the anterior, septal, and inferior walls (**e–h**)



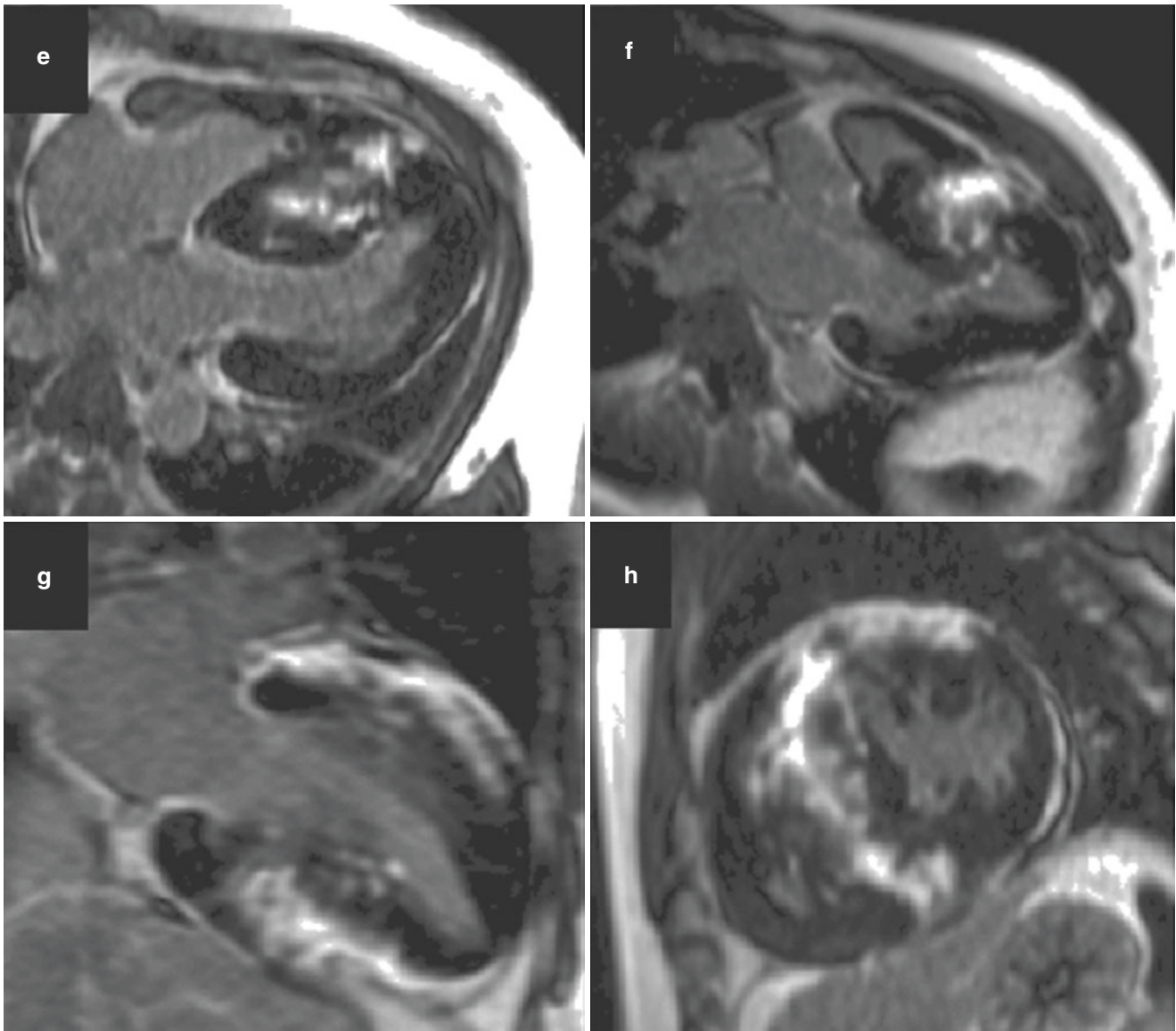


**Fig. 15.5** (continued)

Guidelines now recommend that the presence of a significant burden of LGE can act as an arbitrator in cases that are ambiguous regarding the insertion of an ICD. Although the cutoff value for determining significant LGE is debated, what is apparent is that the higher the burden of LGE, the higher the adverse event risk [28].

From a prognostic perspective, the established risk factors identified by CMR have a varying impact on the clinical decision-making process. Maximum left ventricular wall thickness is known to have an increased risk of sudden cardiac death and in a large meta-analysis was found to have a HR of 3.17 for increased risk of sudden cardiac death [29, 30]. The presence of a left ventricular aneurysm in a HCM patient is similarly associated with an increased risk of sudden cardiac death with an event rate of almost 5%/year

reported and an adverse event rate of 6.4%/year, which is more than threefold greater than that of those without aneurysms [31]. Furthermore, there is also an increased risk of thromboembolism with a rate of over 1% a year. Crucially, identifying the presence of an apical aneurysm should alert the treating physician of a more severe pathological process, and early identification may lower the threshold for possible intervention with effective treatment modalities such as anticoagulation, catheter ablation, and/or ICD implantation [32]. Accurate determination of LVEF is vital as LVEF is one of the strongest prognostic risk factors. Indeed patients with LVEF <50% have more progressive and are associated increased adverse events. In a study of 188 patients with HCM and an EF of <50% followed up over an extended period of time, 20% of the patients had appropriate ICD ther-

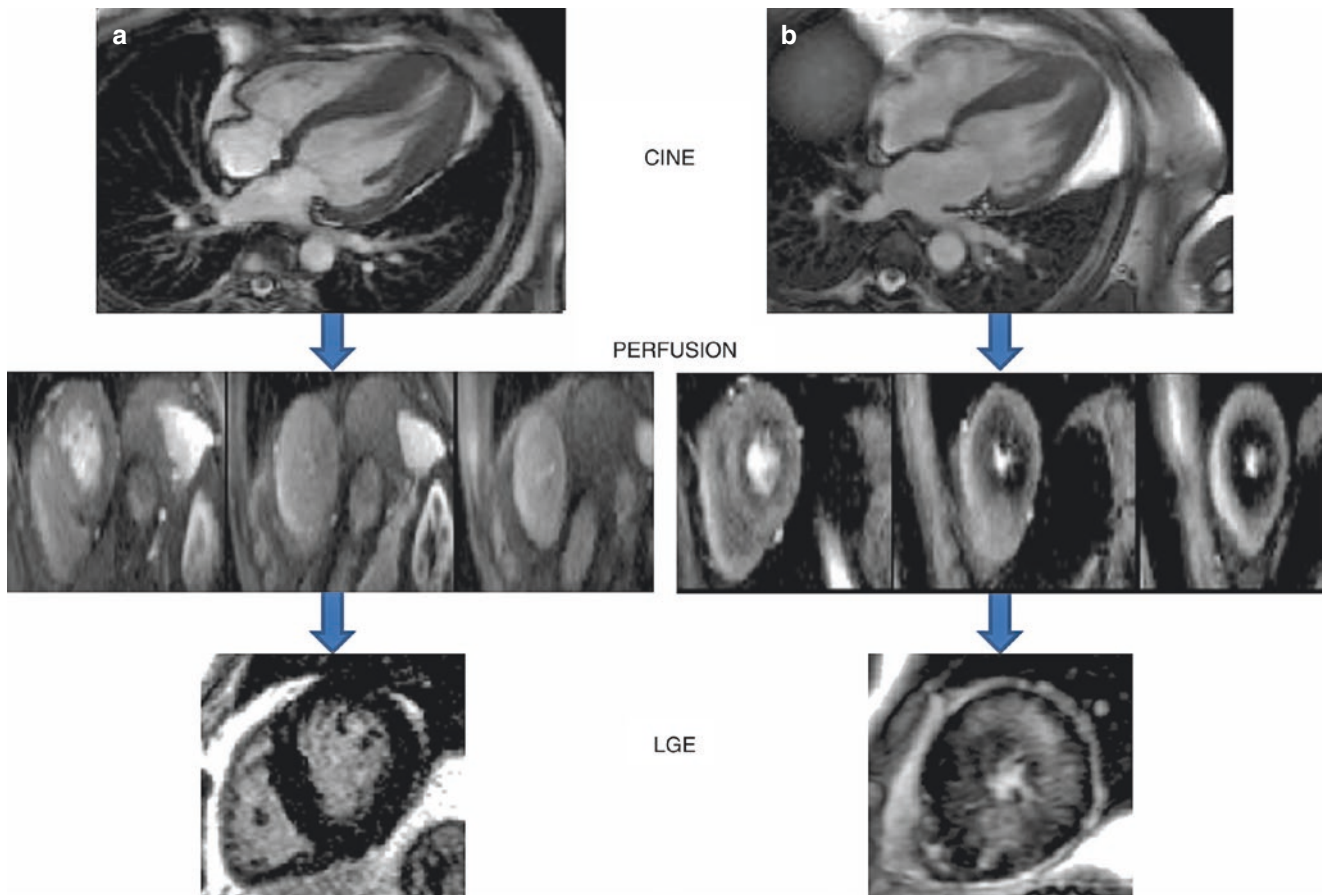


**Fig. 15.6** Two cases of mid to apical HCM (**a, b**) appearing phenotypically similar on cine imaging. By performed adenosine stress perfusion followed by LGE imaging, two very different phenotypes emerge. Patient A demonstrates preserved microvascular perfusion at basal, mid, and apical ventricular levels without evidence of myocardial fibro-

sis on LGE imaging. Patient B shows a similar pattern of hypertrophy but with marked circumferential microvascular perfusion abnormalities (dark regions) at basal, mid, and apical ventricular levels and evidence of diffuse fibrosis in the regions of maximal hypertrophy

apathy preventing potentially lethal malignant arrhythmias, and interestingly over two thirds of these events occurred in those with LVEF between 35% and 49%. Furthermore, the authors of this study inferred that timely identification of systolic impairment and intervention with ICD, cardiac resynchronization therapy, or transplant was associated with a fourfold increase in outcome in comparison with historical studies, illustrating the importance of accurate and early identification of high-risk morphological features [33].

Additional novel CMR biomarkers such as myocardial strain, myocardial perfusion defects, and left atrial function and structure have been shown to be possibly associated with negative prognostic indicators, although further work is needed to further clarify these early findings (Fig. 15.6) [34–36].

The use of parametric mapping extends beyond the diagnostic process and is now identifying early markers of the disease process. A recent study demonstrating prolonged native T1 and increased ECV was found in HCM patients without LGE, which suggests that early interstitial fibrosis

precedes focal fibrosis and LGE which may in the future facilitate earlier diagnosis and treatment [37].

The role of CMR in HCM encompasses more than just the initial diagnostic and prognostic algorithm and is recommended for interval surveillance of disease progression. CMR with LGE is recommended in the 2020 AHA/ACC Guidelines as a class 2b indication for periodic longitudinal surveillance (every 3–5 years) in those individuals without an ICD or to assess for any morphological change [10]. The consensus is that the progression or development of one or more of these high-risk morphological features identified by CMR is likely to have a significant impact on any future clinical decisions. Additionally, CMR is useful in planning septal reduction procedures and by reliably characterizing specific features of the LVOT anatomy that may be contributing to the underlying obstruction.

Future work enhancing and improving the role of CMR in HCM is occurring at the diagnostic, prognostic, and throughout the lifespan of the disease process. Key registries such as the HCMR registry will provide a wealth of information in

the future to help understand and treat this heterogeneous and complex condition [38]. In summary, CMR provides a robust single imaging modality to diagnose HCM, out-rule phenocopies, accurately risk stratify, and provide ongoing longitudinal high quality care to individuals with HCM.

## 15.4 Dilated Cardiomyopathy

Dilated cardiomyopathy (DCM) is one of the most common cardiomyopathies worldwide and has many causes. It is characterized mainly by systolic dysfunction with ventricular dilatation in one or both ventricles (Movies 15.9 and 15.10). The ESC 2021 Heart Failure guidelines subdivide DCM into two different subtypes – DCM and hypokinetic non-dilated cardiomyopathy (HNDC) based on the presence or absence of ventricular dilatation. DCM is defined as LV dilatation and systolic dysfunction in the absence of known abnormal loading conditions or significant CAD. HNDC is defined as LV or biventricular global systolic dysfunction (LVEF <45%) *without* dilatation in the absence of known abnormal loading conditions or significant CAD. DCM and HNDC can be considered “familial” if two or more first- or second-degree relatives have DCM or HNDC, or a first-degree relative has autopsy-proven DCM and sudden death at <50 years of age [39]. For the purposes of this text, DCM will refer to both subtypes (DCM and HNDC). DCM can be primary (genetic, mixed or predominantly familial nongenetic, or acquired) or secondary (e.g., infiltrative, autoimmune, toxins, pregnancy). It is important to remember that identification of an acquired cause of DCM does not exclude an underlying pathogenic gene variant, and this should still be assessed as the acquired cause may be the catalyst resulting in the genetic phenotypical expression [40]. DCM is classified as idiopathic once all nongenetic detectable agents are excluded. Prevalence in the general population remains unclear and is likely underestimated due to significant heterogeneity in diagnostic criteria and incomplete family screening historically [41]. DCM disorder develops at any age, in either sex, and in people of any ethnic origin. In many cases, the disease is inherited and is called familial dilated cardiomyopathy; patients without any inheritance pattern are classified as having sporadic DCM. The familial type is thought to account for 30–50% of idiopathic DCM cases of which 40% have a genetic cause identified [42, 43].

### 15.4.1 CMR in the Diagnosis of DCM

CMR is a fundamental tool in the diagnosis, prognosis, and optimization of therapeutic treatments in the DCM population. CMR cine imaging provides accurate and reproducible measurements on biventricular volumes, mass, and function

overcoming limitations specific to other imaging modalities. Consequently, CMR is the recommended imaging modality of choice in patients with nondiagnostic or sub-optimal echocardiography (ESC class 1 recommendation) [39].

After accurate determination of left ventricular volume and systolic function, the next diagnostic question is to determine the absence of significant coronary artery disease. Furthermore, this differentiation carries important therapeutic implications in terms of possible revascularization and decisions regarding ICD therapy. CMR with LGE can effectively rule in or out significant coronary artery disease by identifying myocardial scar in a coronary distribution in either a subendocardial or transmural pattern [44]. Accordingly, the updated 2021 ESC Heart Failure guidelines support the use of CMR with LGE in DCM patients to distinguish between ischemic and nonischemic myocardial fibrosis (class 2a recommendation) [39]. The reporting cardiologist must be cognizant that there may be “bystander coronary artery disease,” where an individual may have a small subendocardial infarction that does not explain the severity of systolic impairment and dilatation. In this scenario it may be useful to consider further imaging with perfusion sequences or invasive coronary angiography if clinically appropriate. In the potential rare setting of true myocardial hibernation secondary to significant ischemia in the absence of infarction, perfusion imaging can assess for significant coronary artery disease.

The nonischemic late gadolinium pattern in DCM is typically diffuse, seen in the septal mid-wall or with subepicardial enhancement. However, in most cases 60–70% of DCM there is no LGE [45]. In individuals with borderline low LVEF and mildly increased ventricular volumes without LGE (e.g., athletic remodeling vs. early DCM), native T1 mapping can be used to help aid the in the diagnostic process as T1 values are prolonged in DCM and have been reliably shown to help discriminate between normal and myopathic myocardium [46–48]. Of note if low T1 values are recorded, T2\* sequences should be performed to assess for any evidence of myocardial iron overload, which on echocardiography can occasionally appear with a DCM-like phenotype (Fig. 15.7).

### 15.4.2 CMR in the Prognosis and Management of DCM

Risk stratification for DCM has traditionally focused on conventional markers such as ejection fraction to predict SCD risk and the need for ICD implantation. Unfortunately, the current risk stratification model appears ineffective at accurately determining those who are at increased risk and who may benefit from implantation, leading physicians and researchers to seek alternative markers to guide the decision-



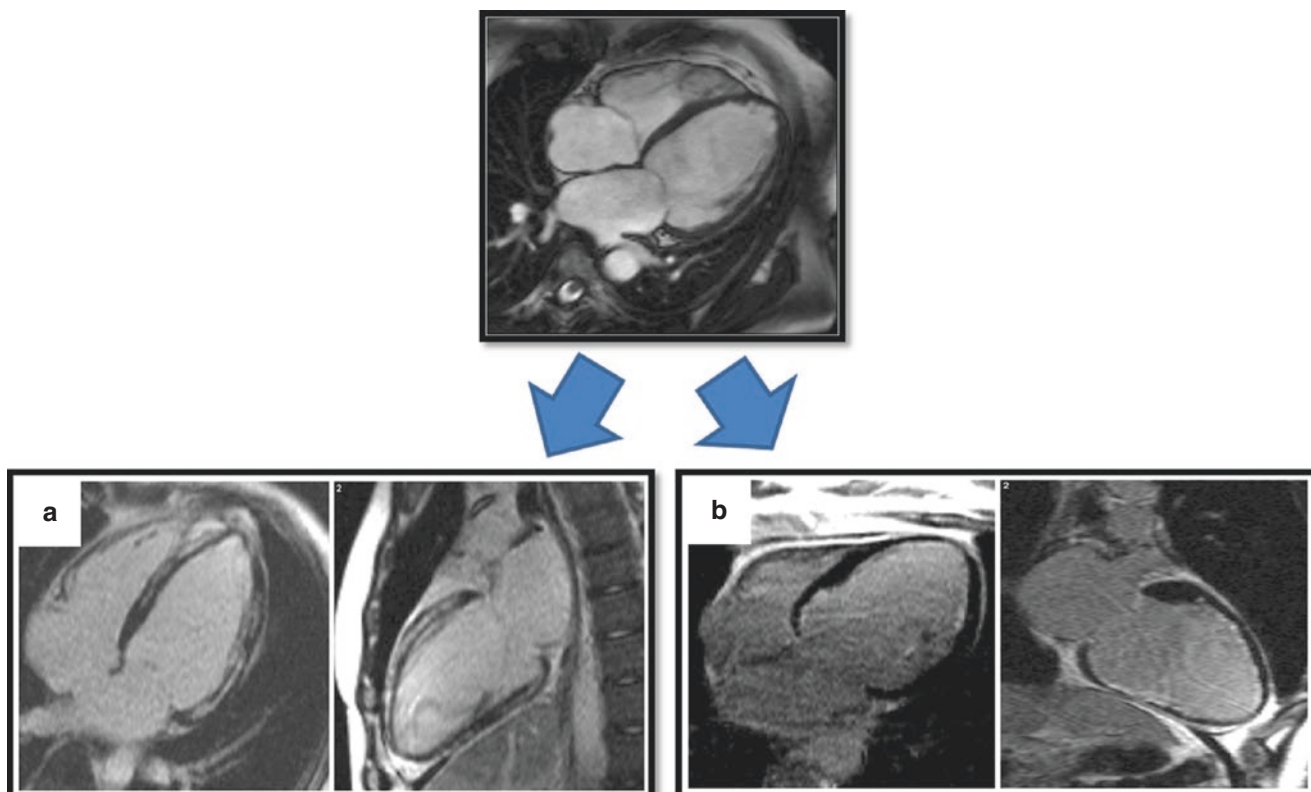


**Fig. 15.7** Dilated cardiomyopathy appearing “phenotypically” one disease on cine imaging (*top row*). Late gadolinium-enhanced images (*bottom row*) demonstrating two different disease processes leading to similar phenotype. Mid-wall fibrosis is seen in example (a) consistent

with DCM, whereas extensive subendocardial fibrosis is seen in example (b), consistent with prior myocardial infarction, and diagnostic of an ischemic etiology

making process. This was highlighted by the DANISH Trial, which demonstrated that ICDs in primary prevention in DCM did not reduce total mortality despite lowering the risk of SCD [49]. Utilizing CMR may result in improved prognostic stratification, leading to better patient selection of those who would benefit from ICD therapy, improving outcomes while also decreasing adverse events for those who are unlikely to benefit from an ICD.

Histologically, DCM is characterized by progressive interstitial fibrosis and degeneration of myocytes. Replacement fibrosis is also often seen, and unlike in CAD, there is mid-wall rather than subendocardial fibrosis, due to involvement of the circumferential fiber layer (Fig. 15.8). This finding carries important prognostic implications and has been found to represent an important substrate for inducible ventricular arrhythmias independent of ejection fraction [50]. There are a number of prospective studies evaluating the independent prognostic value of myocardial fibrosis in DCM [51, 52]. The first of these studies was published by Assomul et al. following 101 consecutive patients with DCM for a mean of  $658 \pm 355$  days. Mid-wall fibrosis (seen in 35% of patients) was an independent predictor of major adverse cardiac events, including all-cause death and hospitalization

for a cardiovascular event (HR 3.4;  $p = 0.01$ ). Multivariate analysis showed mid-wall fibrosis as the sole significant predictor of death or hospitalization. Mid-wall fibrosis also predicted secondary outcome measures of sudden cardiac death (SCD) or ventricular tachycardia (HR 5.2,  $p = 0.01$ ). Mid-wall fibrosis remained predictive of SCD/VT after correction for baseline differences in left ventricular ejection fraction between those with and without fibrosis. More recently Alba et al. performed a large multinational retrospective study of 1672 DCM patients followed for an average of 2.3 years [45]. After adjustment for other clinical risk factors, LGE presence was independently associated with a 1.5-fold increased risk of all-cause mortality, heart transplantation, or left ventricular assist device implant and a 1.8-fold increased risk of malignant arrhythmic event. Specifically, presence of LGE was associated with an annual mortality risk of 4.0% versus only 1% in patients without LGE. Similarly the annual risk of SCD or appropriate ICD shock was 4.0% versus only 1.5% in patients without LGE. A recent meta-analysis by Becker et al. reported the presence of LGE was associated with a 3.4-fold unadjusted increased mortality and a 4.5-fold unadjusted increase risk for arrhythmic events [53]. Interestingly, in a study of 847 individuals with DCM, there



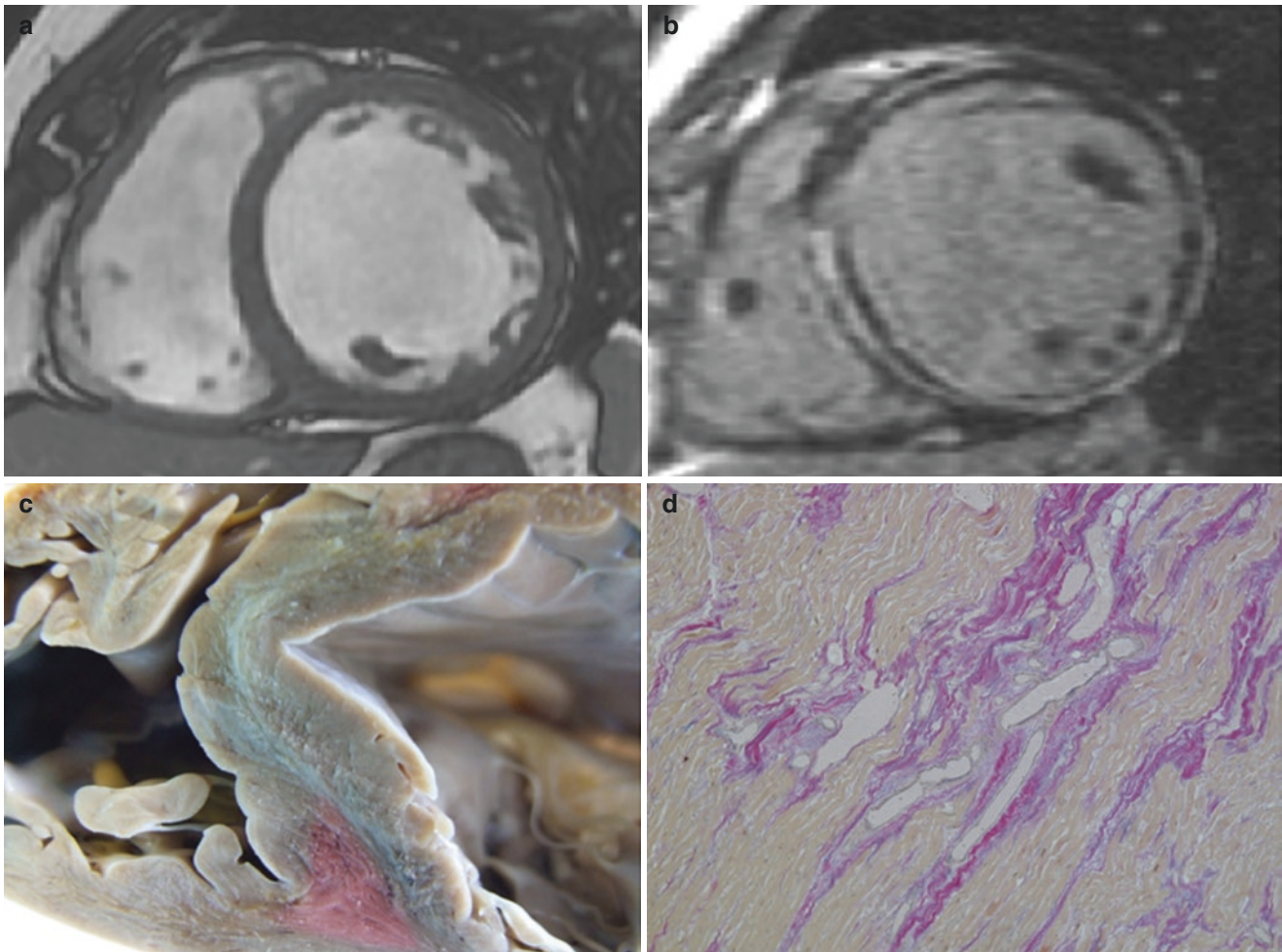


**Fig. 15.8** Dilated cardiomyopathy. Cine image (a) showing dilated LV with wall thinning and mild increase in lateral wall trabeculation. Late gadolinium images (b) show typical mid-wall enhancement, confirmed macroscopically (c), and microscopically as myocardial fibrosis (d)

does not appear to be a linear relationship between volume of LGE and increasing risk (unlike with HCM). The presence of even a small amount of septal LGE is associated with a large increase in the risk of death and SCD events and slightly increased with concomitant septal and free-wall LGE [54].

Based on these findings, a large multicenter registry called the DERIVATE study evaluated 1508 DCM patients with a novel risk score that included male sex, LVEDVI  $>120.5$  ml/m<sup>2</sup>, and the presence of  $\geq 3$  segments with LGE mid-wall enhancement [55]. This score made it possible to reclassify approximately 1/3 of patients who met the current criteria for ICD implantation as low-risk patients, while also providing a net reclassification improvement of 64%. These findings were confirmed in a validation cohort of 508 individuals. This study demonstrated that this CMR-based risk score provided incremental prognostic value beyond the current standard of care and infers that CMR has a key role in prognostic stratification and ICD selection. A recent study has further demonstrated that T1 mapping and calculation of the ECV add prognostic value in the majority of DCM

patients without LGE [56]. Future prospective trials such as the CMR GUIDE trial and the ReCONSIDER study will help determine the magnitude of CMR in improving clinical outcomes [57, 58].

## 15.5 Arrhythmogenic Ventricular Cardiomyopathy (AVC)

Arrhythmogenic cardiomyopathy (AVC) is a primary heart muscle disorder presenting clinically with ventricular arrhythmias, sudden death, or heart failure. It is characterized pathologically by progressive myocardial loss with fibrous or fibrofatty replacement caused by abnormal cell connections through the desmosome [59, 60]. Traditionally, AVC was thought to have regional or global alteration in the function of the right ventricle with or without anomalies of the left ventricle and was subsequently known as arrhythmogenic right ventricular cardiomyopathy (ARVC). However, it is now known that this cardiomyopathy can present with iso-

lated abnormalities in either the right or the left ventricle or indeed in a biventricular pattern. Therefore, in order to define the broader spectrum of disease, the term “arrhythmogenic ventricular cardiomyopathy” AVC has been proposed.

The estimated prevalence of AVC in the general population ranges from 1 in 2000 to 1 in 5000; men are more frequently affected than women, with an approximate ratio of 3:1. The condition is a major cause for SCD in the young and athletes. Dysfunctional desmosomes resulting in defective cell adhesion proteins, such as plakoglobin (JUP), desmoplakin (DSP), plakophilin-2 (PKP-2), and desmoglein-2 (DSG-2), consequently cause loss of electrical coupling between cardiac myocytes, leading to myocyte cell death, fibrofatty replacement, and arrhythmias. LV or RV dilatation and functional impairment often result in regional wall motion abnormalities and regional aneurysmal dilatation (Movies 15.11 and 15.12). Subtle changes are typically confined to the inflow tract, outflow tract, or apex of the RV, the so-called triangle of dysplasia which has now evolved into the “quadrangle of dysplasia” to include the left ventricular inferolateral wall, the most frequently involved LV region [61].

The traditional diagnosis of ARVC involved the use of a 2010 task force criteria, which used major and minor criteria based on electrocardiographic, morphological, histological, clinical, and genetic findings. The cornerstone of the diagnosis was based on accurate assessment for any regional or global morphological changes in the right ventricle, with or without changes in the left ventricle [62]. Echocardiography traditionally was the most extensively used imaging tool to evaluate these individuals. However, the RV is difficult to completely evaluate with echocardiography owing to near field signal dropout and its crescent shape; furthermore, predominant left ventricular AC can be particularly difficult to diagnose on echocardiography alone. Given the evolution of ARVC to AVC, the proposed 2020 Padua criteria provide a working framework to improve the diagnosis of AVC. This criteria introduces myocardial tissue characterization with LGE as a key part of the diagnostic criteria, in addition to ECG abnormalities and ventricular arrhythmia features for the diagnosis of the left ventricular phenotype [63].

CMR has a much better diagnostic performance for AVC when compared with echocardiography. In a study of 102 patients with AVC, the diagnostic performance of echocardiography was low in contrast to CMR with a sensitivity of 50% and specificity 70%, positive predictive value 80%, and negative predictive value 37% [64]. In a study of 200 AVC patients who had a CMR, there were three main patterns of disease expression: (1) *classic*; defined as isolated RV disease or LV involvement in the presence of notable RV enlargement and/or dysfunction; (2) *left-dominant*; prominent LV manifestations in the setting of relatively mild right-sided disease; and (3) *biventricular*; characterized by equal bilateral ventricular involvement [65]. 5% had left-dominant

disease, and 56% showed a biventricular pattern. Classic disease expression was observed in 39%, of which 59% had LV involvement. Of note 80% had CMR evidence of LGE in the LV. The inferolateral wall was most commonly affected (85%) in subepicardial and mid-wall locations. Other locations include the inferoseptal junction, anterolateral wall, and anterior wall (Fig. 15.9).

CMR is not only fundamental in the diagnosis of AVC but also helps prognosticate the severity of the disease while simultaneously guiding decisions regarding implantable defibrillators. A study by Zorzi et al. demonstrated that the presence of major morphological criteria and of moderate-severe RV dysfunction was significantly higher in those with malignant arrhythmic events [66]. Furthermore, it is becoming increasingly apparent that involvement of the left ventricle is associated with a worse prognosis in comparison to abnormalities limited to the right ventricle [67]. In a study of 140 AVC patients with a median follow-up of 5 years, 34% had major events. However, none occurred in patients with a normal CMR. Patients with LV involvement (LV-dominant and biventricular) had a worse prognosis than those with RV only ( $p < 0.0001$ ). A RV only presentation was more frequent in patients without major events than others (OR: 0.3; 95% CI: 0.2 to 0.7;  $p = 0.03$ ). By contrast, those with cardiac events had more often a LV-dominant (OR: 4.3; 95% CI: 1.5 to 12.0;  $p = 0.004$ ) or a biventricular (OR: 2.6; 95% CI: 1.3 to 5.4;  $p = 0.04$ ) presentation. Overall, a LV involvement was found in 36 of 48 patients (75%) with events and in 32 of 92 (35%) without (OR: 5.6; 95% CI: 2.6 to 12.3;  $p < 0.0001$ ) [68]. Of note the 5-year ARVC risk score underestimated the risk when the LV was involved. Consequently, the authors recommend ICD implantation in those who have evidence of left ventricular disease and no ICD in those with normal CMR studies and to use the 5-year ARVC risk score to assess risk for those with RV only disease [69].

In predominant left ventricular AVC, diffuse disease may result in left ventricular heart failure, and ventricular arrhythmias may or may not be present. Consequently, it can be difficult to differentiate from DCM particularly in from the hypokinetic non-dilated cardiomyopathy subclass (HNDC) [70]. From an imaging perspective, patients with predominant left ventricular AC are more likely to have focal areas of hypokinesia in contrast to global hypokinesia, subepicardial LGE in contrast to either no LGE or septal mid-wall fibrosis, and an inverse relationship between the extent of the LGE and LVEF seen in the AVC but not in the HNDC phenotype [71, 72].

CMR is cornerstone to the diagnosis, risk assessment, and management in patients with AVC. CMR has an excellent negative predictive value and can better identify those at greater risk of cardiac arrhythmias who may benefit from ICD implantation.



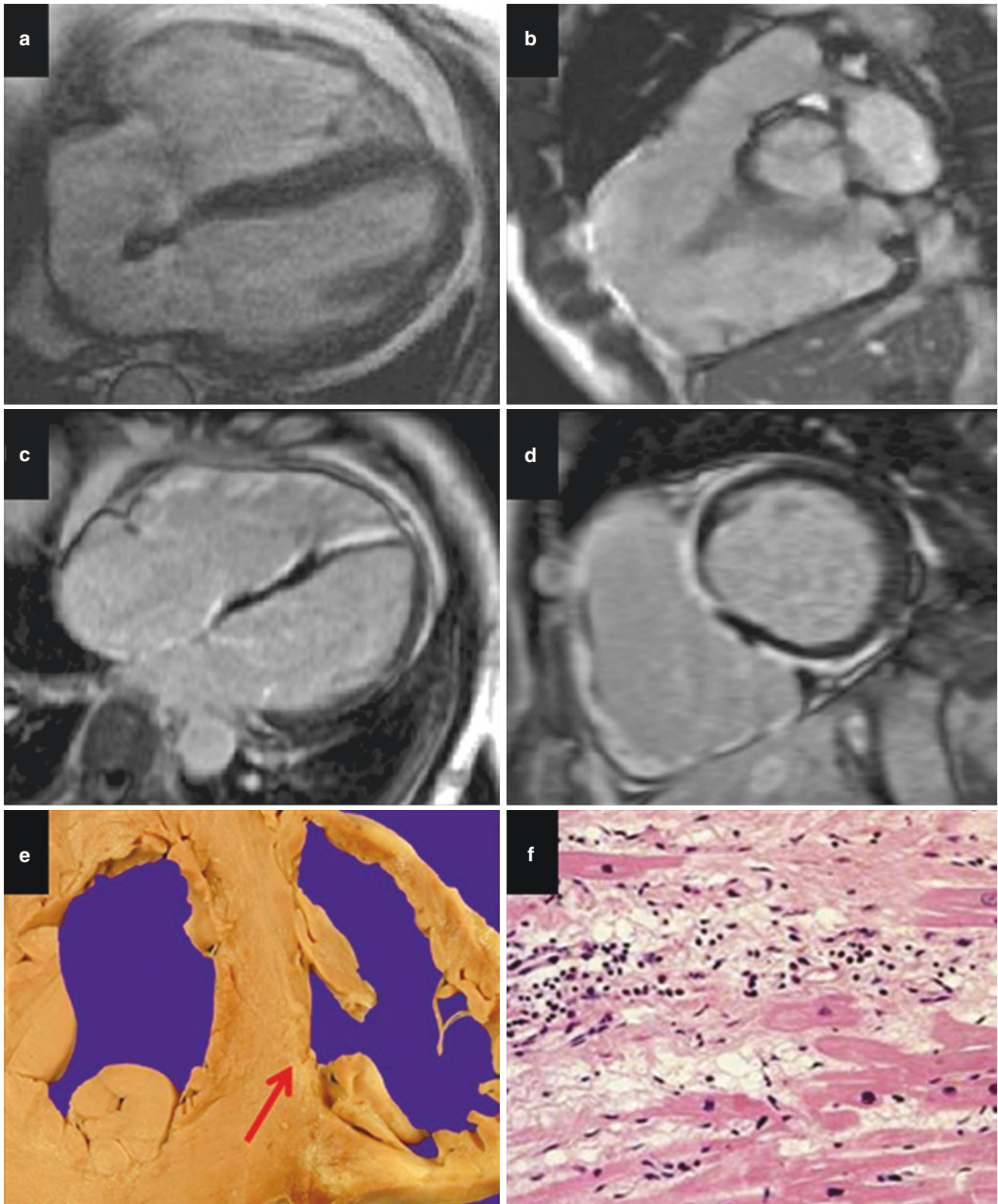


**Fig. 15.9** Arrhythmogenic right ventricular cardiomyopathy. Four-chamber and RVOT view cine images show a markedly dilated RV (a) with local aneurysmal in the RVOT (b). Corresponding LGE imaging shows extensive fibrosis in the RV walls and in the septum, preferen-

tially in the RV septal wall extending to the LV inferior and anterior epicardial regions (c, d). A representative postmortem heart showing RV septal fibrosis (red arrow) confirmed as ARVC on microscopy showing typical fibrofatty replacement (e, f)

## 15.6 Left Ventricular Noncompaction (LVNC)

Left ventricular noncompaction (LVNC) is a rare primary genetic cardiomyopathy first described over 30 years ago and is hypothesized to be a result of arrested compaction of the developing myocardium [73]. Morphologically LVNC is typically characterized by a bilayered appearance of the myocardium, with excessive trabeculations and deep intertrabecular recesses [74, 75] (Movies 15.13, 15.14, and 15.15). Based on the unique morphological features, LVNC was initially defined as a distinct cardiomyopathy with early studies suggesting that LVNC may be an aggressive cardiomyopathy with increased risk of heart failure, cerebrovascular events, and arrhythmias [76, 77]. However, as the cardiology community's knowledge and understanding of this cardiomyopathy grew, there has been significant debate as to whether or not LVNC is a distinct cardiomyopathy or morphological feature of remodeling [78, 79]. Indeed, in 2008 the ESC position statement defined LVNC as an "unclassified cardiomyopathy"; however, more recently this has been clarified in the 2021 ESC Guidelines on Heart Failure which states *LVNC is not to be treated as a separate disease entity, but as a separate rare presentation of a genetic susceptibility to either HCM or DCM* [39, 73]. The reasoning is due to the overlap that exists in families with DCM and HCM phenotypes, as commonly individuals with features of LVNC are found in families where other affected relatives have typical DCM or HCM.

CMR is key in clarifying the diagnosis of LVNC and carries a class 1 recommendation for the diagnosis and characterization of myocardial tissue in suspected cases [39]. There are currently four different CMR criteria for the diagnosis of LVNC; by assessing the ratio between noncompacted and compacted myocardium at end diastole (Petersen method) or at end systole (Stacey method) or by assessing the mass ratio between total and trabeculated mass (Jacquier method) or by fractal dimension (Captur method) [80–83]. As expected, using different criteria results in varying prevalence of indi-

viduals fulfilling the CMR criteria of LVNC. One single-center study demonstrated that applying the different criteria to 700 patients referred for CMR for various indications found that the prevalence of increased trabeculations using the Petersen, Stacey, Jacquier, and Captur criteria was 39%, 23%, 25%, and 3%, respectively [84]. Furthermore, there was also absence of a correlation between the diagnosis of LVNC by any of the criteria and any clinical outcomes. In terms of guiding prognosis, a study of 339 patients who met echocardiographic or CMR diagnostic criteria for LVNC illustrated that those with preserved systolic function and noncompaction limited to the apex have a benign prognosis with the 5-year survival being the same as the general population. Increased age, lower left ventricular ejection fraction, and noncompaction extending beyond the left ventricular apex to the mid-basal segments were associated with increased mortality among patients meeting LVNC criteria [85]. In light of the multiple clinical criteria for the diagnosis of LVNC and the high prevalence of individuals meeting imaging-based criteria, with nonsignificant clinical outcomes in otherwise normal studies, diagnosing LVNC on increased trabeculations in an otherwise normal CMR is challenging. Indeed some have proposed that there is no need to routinely quantify the extent of trabeculations, unless there is a known high pretest probability for LVNC because, firstly, a clinical diagnosis would be very unlikely, and secondly there seems to be no evidence of incremental prognostic value [86]. In individuals who have increased trabeculations and a high pretest probability, with confirmed genetic mutations, there is no association between increased trabeculation and a poorer prognosis. However, as expected, evidence of LGE and impaired systolic function has been demonstrated to be associated with a more malignant trajectory [87, 88]. The authors suggest therefore that a clinical diagnosis of LVNC based on increased trabeculations alone should be avoided unless there is a high pretest probability and instead should be interpreted in the clinical context, regarding family history, arrhythmias, and history of neuromuscular disease and symptoms (Figs. 15.10 and 15.11).



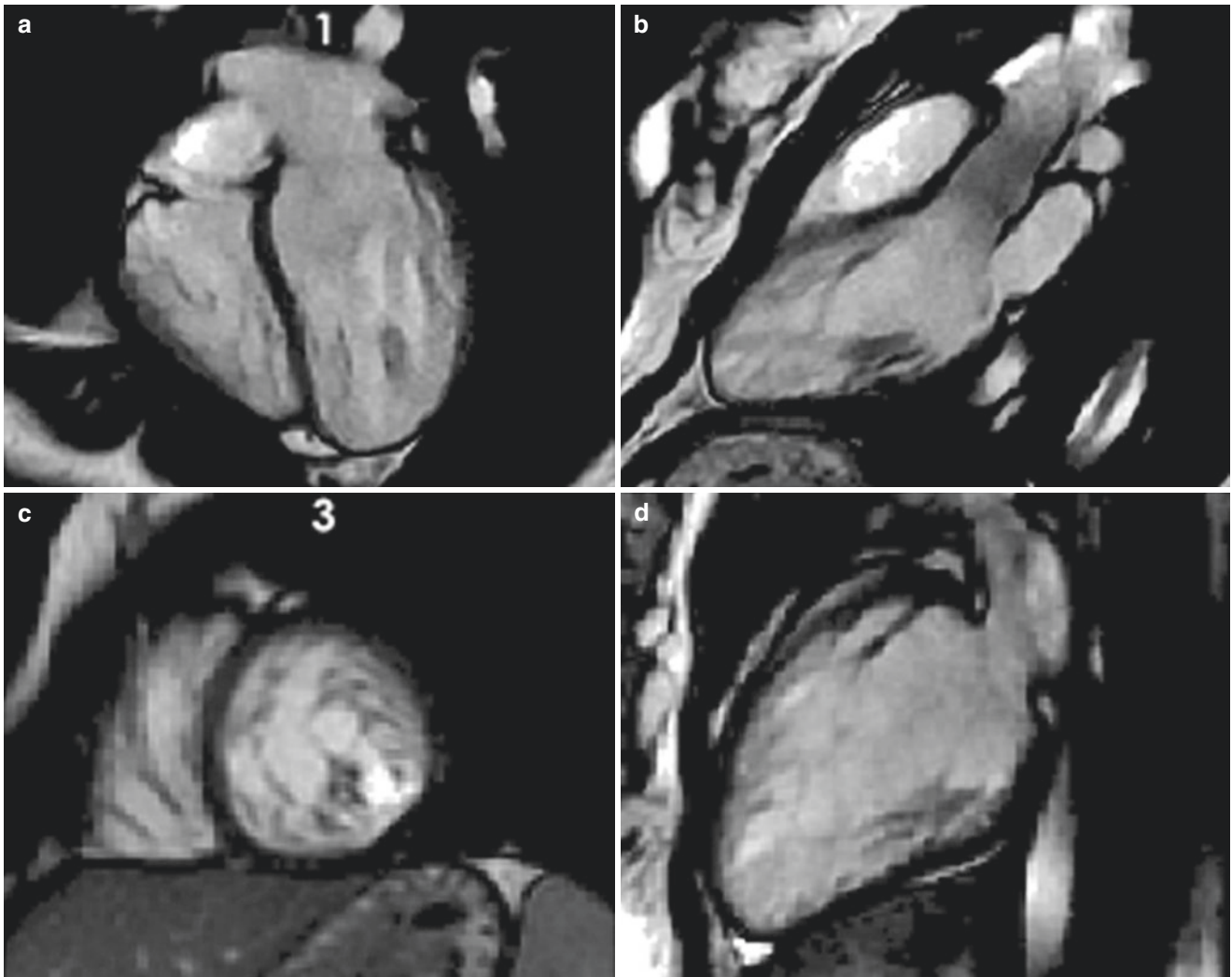


**Fig. 15.10** Left ventricular non compaction (LVNC). Representative cine images in four-chamber, three-chamber, two-chamber, and short-axis imaging planes (**a–d**) demonstrating marked increase in trabecular

meshwork, with a noncompact trabecular to compact trabecular ratio  $>2.3:1$  at end diastole. The apical regions are easily visualized using CMR

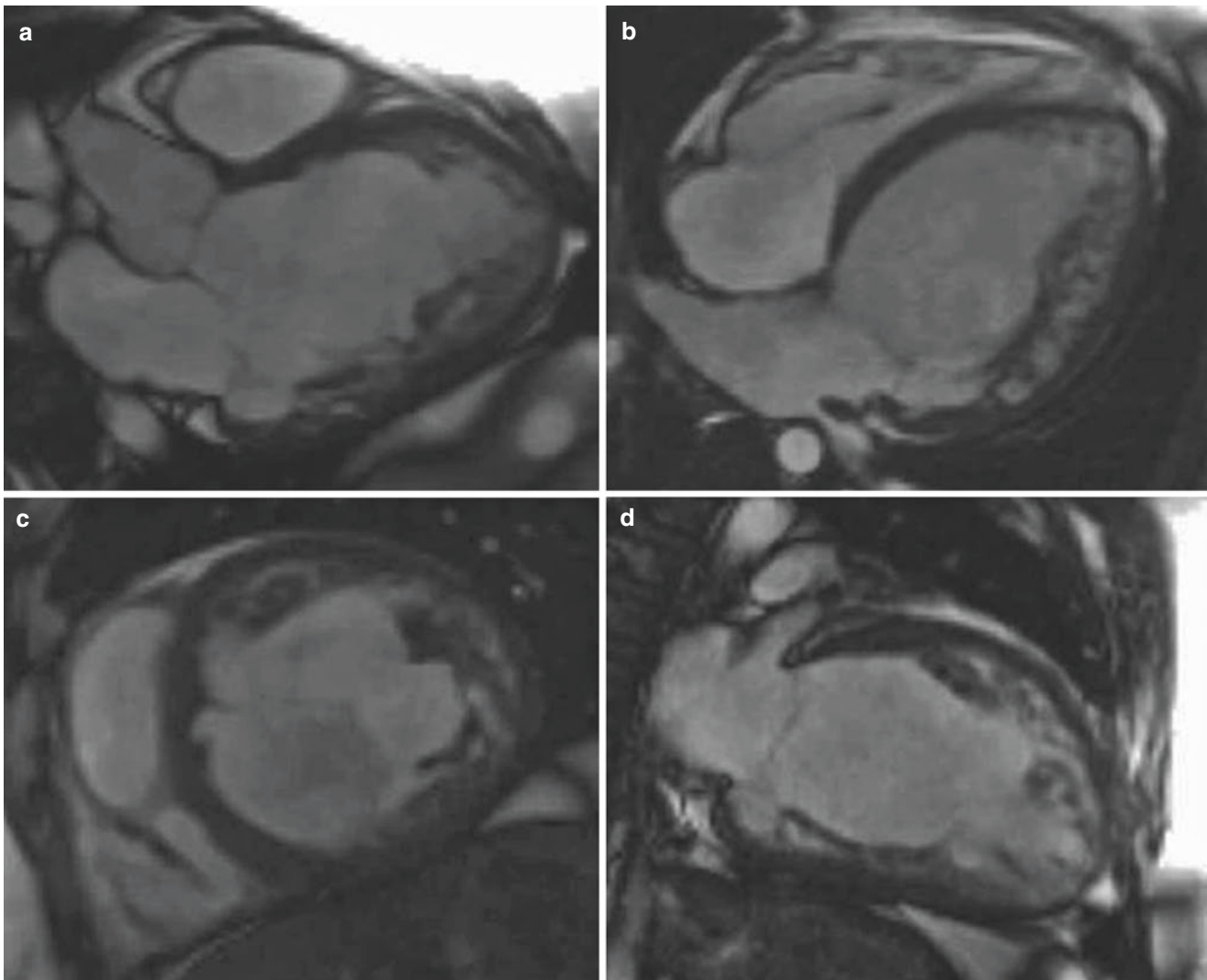


**Fig. 15.11** Left ventricular non compaction (LVNC). Representative cine images in three-chamber, four-chamber, two-chamber, and short-axis imaging planes (a–d). This example demonstrates the more “tradi-

tionally” described trabecular pattern in LVNC with predominant noncompact trabeculations seen in the lateral and apical walls

### 15.7 CMR in the Diagnosis and Evaluation of Muscular Dystrophies (MD)

Muscular dystrophies (MD) encompass a rare heterogeneous group of genetic diseases with many overlapping, yet distinct, phenotypes, most often relating to muscular weakness secondary to progressive muscular degeneration. Various inheritance patterns are seen including X-linked, autosomal dominant or autosomal recessive. Common to all MDs is cardiac involvement with the severity of the presentation dependent on the genetic basis of the MD phenotype. Examples of manifestation of cardiac disease include heart failure, arrhythmias, and conduction abnormalities [89]. However, patients often have subclinical cardiac abnormalities for many years that are not diagnosed resulting in patients

presenting symptomatically with advanced cardiac pathology. A recent registry publication illustrated that 30% of patients with Duchene muscular dystrophy had not had an echocardiogram and only 40% of those diagnosed with a cardiomyopathy were on cardioprotective medications [90]. Furthermore, there is an increasing body of evidence that suggests that cardiac evaluation and treatment before symptoms improve mortality [91–93]. This highlights the need for early, accurate diagnosis to facilitate timely commencement of cardioprotective therapies to improve outcomes. While echocardiography has traditionally been used as the initial imaging modality of choice, there is increasing evidence that the use of CMR aides early and prognostically relevant information that would not be available with echocardiography [94]. It is important to be cognizant that these patients often

have respiratory incompetence and may not tolerate lying flat for long periods of time; furthermore in those patients that require ventilatory support, the suitability and practicality of performing a study must be carefully considered.

There are three main types of MD in which CMR has been shown to be of use: dystrophinopathies (Duchenne and Becker), myotonic dystrophies (myotonic dystrophy type 1 and type 2 and LMNA gene), and mitochondrial myopathies. Of these three types, most of the research to date has focused on Duchenne muscular dystrophy (DMD) and Becker muscular dystrophy (BMD).

DMD and BMD are X-linked recessive disorders affecting males primarily and female carriers with milder symptoms [95]. Cardiomyopathy is the principal cause of death, and cardiac manifestations are present in 60–75% of patients with BMD and almost every patient with DMD [96–98]. CMR has been shown to identify cardiac involvement in patients with normal echocardiograms. In one study of BMD patients, 53% had an impaired ejection fraction on echocardiography, yet 73% had LGE on CMR imaging [99]. Typically, LGE is subepicardial or mid-wall and progresses to transmural and is located in the inferolateral left ventricular wall [100]. Additional studies have demonstrated that in a study of 314 DMD patients, LGE is present in 30%. It occurs early and is progressive, increasing with age and decreasing systolic function suggesting that the time course and LGE may be an important clinical biomarker in the management of DMD-associated cardiac disease [101]. A CMR study of 88 DMD/BMD patients demonstrated that an impaired LVEF  $\leq 45\%$  and a transmural pattern of LGE independently predicted the occurrence of adverse cardiac events. Furthermore, in patients with an LVEF  $>45\%$ , LGE was of additive prognostic value [102]. Secondary to the clear benefit of utilizing CMR in this population, the 2017 American Heart Association scientific statements comment that periodic use of advanced tissue imaging modalities such as CMR in the care of DMD/BMD patients is reasonable particularly in those with poor echocardiographic views or for assessing myocardial fibrosis (class 2a; level of evidence B) [89]. Female carriers who present without muscle weakness are also found to have a high burden of dilated cardiomyopathy, with LV dysfunction present in 14–40% of DMD with CMR demonstrating LGE in a similar pattern to males in 35–60% of DMD carriers and 19–20% of BMD carriers [101].

Myotonic dystrophy type 1 is caused by a CTG triplet repeat manifesting with myotonia, cataracts, diabetes, and cardiac arrhythmias. Conduction abnormalities are the primary cardiac complication, although CMR can demonstrate abnormalities with dilatation, hypertrophy, systolic impairment, and LGE. LGE is seen in approximately 10–30% of MD individuals typically in the mid-myocardial septal and basal inferolateral wall [103, 104]. There is also an associa-

tion of increased post-contrast T1 values in DM individuals which likely represents the diffuse myocardial fibrosis [105].

It is apparent that CMR has a growing role in the diagnosis and management of MDs; the long-term prognostic relevance of these findings remains to be determined, but with the increasing use of CMR in this population, this is expected in the near future.

---

## 15.8 Iron-Related Cardiomyopathies

There are two main types of iron overload-related cardiomyopathies. Primary iron overload is seen in the context of hereditary hemochromatosis, and secondary iron overload is seen in the context of multiple blood transfusions required for management of hereditary anemias (thalassemia/sickle cell disease) or acquired anemias (e.g., myelodysplastic syndromes). Iron overload cardiomyopathy can manifest in a restrictive, mildly hypertrophied fashion before possibly evolving into a dilated phenotype with progression of the disease. Crucially myocardial iron overload can be prevented by either chelation therapy or venesection depending on the underlying etiology. Indeed the use of CMR with T2\* is attributed as a key contributor to the improvement of outcomes in thalassemia patients and has demonstrated a prognostic role guiding treatment regarding chelation therapy [106, 107]. CMR with T2\* allows quantitative assessment of myocardial iron overload with a clear inverse correlation between systolic function and severity of myocardial iron overload, with increased iron deposition associated with decreasing systolic function [108, 109]. The typical T2\* value for iron load assessment is  $<20$  ms; however, this is a conservative value in order to ensure optimal specificity rather than sensitivity. Recent studies have demonstrated that T1 mapping is more sensitive and at the T2\* range of 20–30ms may help identify small values of myocardial iron accumulating and potentially guide more timely interventions with the hope of improving outcomes [110, 111].

---

## 15.9 Conclusion

CMR is a comprehensive and single imaging modality used to diagnose inherited cardiomyopathies, to differentiate phenotypes, and to provide key prognostic information. CMR utilizes various imaging approaches including high-resolution cine imaging, T1- and T2-weighted images, myomapping (T1, T2, T2\*), stress perfusion, and late gadolinium imaging to provide diagnostic and prognostic information to the referring clinician. The use of CMR imaging is increasing at a phenomenal rate internationally and is now recommended in many guidelines as the imaging technique of

choice. Unique insights into disease manifestation and progression are being acquired, and in the future CMR may hopefully provide more data on genotype-phenotype correlations beyond what standard imaging currently provides.

### Practical Pearls

- In a single-scan setting, CMR can acquire high-resolution cine images with a wide field of view; can characterize tissue to define fat, edema, infarction, fibrosis, and infiltration; and can assess epicardial and microvascular blood flow using perfusion imaging.
- CMR is increasingly appreciated as the gold-standard imaging modality of choice in the assessment and risk stratification in inherited cardiomyopathies.
- CMR accurately, in a single scan, diagnoses HCM, out-rules HCM phenocopies, and provides additional risk stratification information including the presence and burden of LGE and/or presence or absence of left ventricular apical aneurysms.
- The presence of LGE mid-wall fibrosis is an important independent marker of risk in patients with DCM and may help guide the decision-making regarding ICD implantation.
- LVNC is not to be treated as a separate disease entity but as a separate rare presentation of a genetic susceptibility to either HCM or DCM. Furthermore, a clinical diagnosis of LVNC based on increased trabeculations alone should be avoided unless there is a high pretest probability and should be interpreted in the clinical context.
- CMR is cornerstone to the diagnosis, risk assessment, and management in patients with AVC with an excellent negative predictive value and can better identify those at increased risk of cardiac arrhythmias who may benefit from ICD implantation.
- CMR has a growing role in the diagnosis and management of cardiac manifestations of MDs; the long-term prognostic relevance of these findings remains to be determined but is expected in the near future.
- CMR with T2\* and native T1 mapping is key to diagnosing and managing iron overload-related cardiomyopathies.

### References

1. Kramer C, Barkhausen J, Bucciarelli-Ducci C, Flamm S, Kim R, Nagel E. Standardized cardiovascular magnetic resonance imaging (CMR) protocols: 2020 update. *Journal of Cardiovascular Magnetic Resonance*. 2020;22:17.
2. Petersen S, Khanji M, Plein S, Lancellotti P, Bucciarelli-Ducci C. European Association of Cardiovascular Imaging expert consensus paper: a comprehensive review of cardiovascular magnetic resonance normal values of cardiac chamber size and aortic root in adults and recommendations for grading severity. *Eur Heart J Cardiovasc Imaging*. 2019;20:1321–31.
3. Maceira AM, Prasad SK, Khan M, Pennell DJ. Normalized left ventricular systolic and diastolic function by steady state free precession cardiovascular magnetic resonance. *J Cardiovasc Magn Reson*. 2006;8:417–26.
4. Anderson LJ, Holden S, Davis B, et al. Cardiovascular T2-star (\*) magnetic resonance for the early diagnosis of myocardial iron overload. *Eur Heart J*. 2001;21:2171–9.
5. Rademakers FE, Bogaert J. Cardiac dysfunction in heart failure with normal ejection fraction: MRI measurements. *Prog Cardiovasc Dis*. 2006;49:215–27.
6. Muser D, Castro S, Santangeli P, Nucifora G. Clinical applications of feature-tracking cardiac magnetic resonance imaging. *World J Cardiol*. 2018;10:210–21.
7. Maron BJ, Gardin JM, Flack JM, et al. Prevalence of hypertrophic cardiomyopathy in a general population of young adults: echocardiographic analysis of 4111 subjects in a CARDIA study. *Circulation*. 1995;92:785–9.
8. Semsarian C, Ingles J, Maron M, Maron B. New perspectives on the prevalence of hypertrophic cardiomyopathy. *J Am Coll Cardiol*. 2015;65:1249–54.
9. Shirani J, Pick R, Roberts W, Maron B. Morphology and significance of the left ventricular collagen network in young patients with hypertrophic cardiomyopathy and sudden cardiac death. *J Am Coll Cardiol*. 2000;35:36–44.
10. Ommen S, Mital S, Burke M, Day S, Deswal A, Elliott P, et al. 2020 AHA/ACC Guideline for the Diagnosis and Treatment of Patients With Hypertrophic Cardiomyopathy. *J Am Coll Cardiol*. 2020;76:e159–240.
11. Kubo T, Kitaoka H, Okawa M, Matsumura Y, Hitomi N, Yamasaki N, et al. Lifelong left ventricular remodeling of hypertrophic cardiomyopathy caused by a founder frameshift deletion mutation in the cardiac myosin-binding protein C gene among Japanese. *J Am Coll Cardiol*. 2005;46:1737–43.
12. Klues HG, Schiffrers A, Maron BJ. Phenotypic spectrum and patterns of left ventricular hypertrophy in hypertrophic cardiomyopathy: morphologic observations and significance as assessed by two-dimensional echocardiography in 600 patients. *J Am Coll Cardiol*. 1995;26:1699–708.
13. Parato V, Antoncicchi V, Sozzi F, Marazia S, Zito A, Maiello M, et al. Echocardiographic diagnosis of the different phenotypes of hypertrophic cardiomyopathy. *Cardiovasc Ultrasound*. 2015;14:30.
14. Hindieh W, Weissler-Snir A, Hammer H, Adler A, Rakowski H, Chan R. Discrepant measurements of maximal left ventricular wall thickness between cardiac magnetic resonance imaging and echocardiography in patients with hypertrophic cardiomyopathy. *Circ Cardiovasc Imaging*. 2017;10:e006309.
15. Geske J, Ommen S, Gersh B. Hypertrophic cardiomyopathy. *JACC Heart Fail*. 2018;6:364–75.
16. Haaf P, Garg P, Messroghli D, Broadbent D, Greenwood J, Plein S. Cardiac T1 mapping and extracellular volume (ECV) in clinical practice: a comprehensive review. *J Cardiovasc Magn Reson*. 2016;18:89.
17. Swoboda P, McDiarmid A, Erhayiem B, Broadbent D, Dobson L, Garg P, et al. Assessing myocardial extracellular volume by T1 mapping to distinguish hypertrophic cardiomyopathy from athlete's heart. *J Am Coll Cardiol*. 2016;67:2189–90.
18. Neisius U, Myerson L, Fahmy A, Nakamori S, El-Rewaidy H, Joshi G, et al. Cardiovascular magnetic resonance feature tracking strain analysis for discrimination between hypertensive heart disease and hypertrophic cardiomyopathy. *PLoS One*. 2019;14:e0221061.



19. van der Velde N, Huurman R, Hassing H, Budde R, van Slegtenhorst M, Verhagen J, et al. Novel morphological features on CMR for the prediction of pathogenic sarcomere gene variants in subjects without hypertrophic cardiomyopathy. *Front Cardiovasc Med.* 2021;8:727405.
20. Hughes R, Camaioni C, Augusto J, Knott K, Quinn E, Captur G, et al. Myocardial perfusion defects in hypertrophic cardiomyopathy mutation carriers. *J Am Heart Assoc.* 2021;10:e020227.
21. Hinojar R, Varma N, Child N, Goodman B, Jabbour A, Yu C, et al. T1 mapping in discrimination of hypertrophic phenotypes: hypertensive heart disease and hypertrophic cardiomyopathy. *Circ Cardiovasc Imaging.* 2015;8:e003285.
22. Bois J, Geske J, Foley T, Ommen S, Pellikka P. Comparison of maximal wall thickness in hypertrophic cardiomyopathy differs between magnetic resonance imaging and transthoracic echocardiography. *Am J Cardiol.* 2017;119:643–50.
23. Husselbury T, Godec T, Murphy T, Hughes R, Omahony C, Moon J et al. Multi-modality imaging in hypertrophic cardiomyopathy: intermodal discrepancies in key prognostic parameters. *Eur Heart J.* 2021;42.
24. O'Hanlon R, Grasso A, Roughton M, Moon J, Clark S, Wage R, et al. Prognostic significance of myocardial fibrosis in hypertrophic cardiomyopathy. *J Am Coll Cardiol.* 2010;56:867–74.
25. Klopotoski M, Kukuła K, Malek L, Spiewak M, Polanska-Skrzypczyk M, Jamiolkowski J, et al. The value of cardiac magnetic resonance and distribution of late gadolinium enhancement for risk stratification of sudden cardiac death in patients with hypertrophic cardiomyopathy. *J Cardiol.* 2016;68:49–56.
26. Mentias A, Raeisi-Giglou P, Smedira N, Feng K, Sato K, Wazni O, et al. Late gadolinium enhancement in patients with hypertrophic cardiomyopathy and preserved systolic function. *J Am Coll Cardiol.* 2018;72:857–70.
27. Chan R, Maron B, Olivetto I, Pencina M, Assenza G, Haas T, et al. Prognostic value of quantitative contrast-enhanced cardiovascular magnetic resonance for the evaluation of sudden death risk in patients with hypertrophic cardiomyopathy. *Circulation.* 2014;130:484–95.
28. Todiere G, Nugara C, Gentile G, Negri F, Bianco F, Falletta C, et al. Prognostic role of late gadolinium enhancement in patients with hypertrophic cardiomyopathy and low-to-intermediate sudden cardiac death risk score. *Am J Cardiol.* 2019;124:1286–92.
29. Elliott P, Gimeno Blanes J, Mahon N, Poloniecki J, McKenna W. Relation between severity of left-ventricular hypertrophy and prognosis in patients with hypertrophic cardiomyopathy. *Lancet.* 2001;357:420–4.
30. Liu Q, Li D, Berger A, Johns R, Gao L. Survival and prognostic factors in hypertrophic cardiomyopathy: a meta-analysis. *Sci Rep.* 2017;7:11957.
31. Rowin E, Maron B, Haas T, Garberich R, Wang W, Link M, et al. Hypertrophic cardiomyopathy with left ventricular apical aneurysm. *J Am Coll Cardiol.* 2017;69:761–73.
32. Papanastasiou C, Zegkos T, Karamitsos T, Rowin E, Maron M, Parcharidou D, et al. Prognostic role of left ventricular apical aneurysm in hypertrophic cardiomyopathy: a systematic review and meta-analysis. *Int J Cardiol.* 2021;332:127–32.
33. Rowin E, Maron B, Carrick R, Patel P, Koethe B, Wells S, et al. Outcomes in patients with hypertrophic cardiomyopathy and left ventricular systolic dysfunction. *J Am Coll Cardiol.* 2020;75:3033–43.
34. Kim E, Lee S, Chang S, Jang S, Kim S, Park S, et al. Prevalence and clinical significance of cardiovascular magnetic resonance adenosine stress-induced myocardial perfusion defect in hypertrophic cardiomyopathy. *J Cardiovasc Magn Reson.* 2020;22:30.
35. Smith B, Dorfman A, Yu S, Russell M, Agarwal P, Ghadimi Mahani M, et al. Relation of strain by feature tracking and clinical outcome in children, adolescents, and young adults with hypertrophic cardiomyopathy. *Am J Cardiol.* 2014;114:1275–80.
36. Farhad H, Seidelmann S, Vigneault D, Abbasi S, Yang E, Day S, et al. Left atrial structure and function in hypertrophic cardiomyopathy sarcomere mutation carriers with and without left ventricular hypertrophy. *J Cardiovasc Magn Reson.* 2017;19:107.
37. Xu J, Zhuang B, Sirajuddin A, Li S, Huang J, Yin G, et al. MRI T1 mapping in hypertrophic cardiomyopathy: evaluation in patients without late gadolinium enhancement and hemodynamic obstruction. *Radiology.* 2020;294:275–86.
38. Kramer C, Appelbaum E, Desai M, Desvigne-Nickens P, DiMarco J, Friedrich M, et al. Hypertrophic Cardiomyopathy Registry: the rationale and design of an international, observational study of hypertrophic cardiomyopathy. *Am Heart J.* 2015;170:223–30.
39. McDonagh T, Metra M, Adamo M, Gardner R, Baumbach A, Böhm M, et al. 2021 ESC guidelines for the diagnosis and treatment of acute and chronic heart failure. *Eur Heart J.* 2021;42:3599–726.
40. Bondue A, Arbustini E, Bianco A, Ciccarelli M, Dawson D, De Rosa M, et al. Complex roads from genotype to phenotype in dilated cardiomyopathy: scientific update from the Working Group of Myocardial Function of the European Society of Cardiology. *Cardiovasc Res.* 2018;114:1287–303.
41. Petretta M, Pirozzi F, Sasso L, Paglia A, Bonaduce D. Review and Metaanalysis of the frequency of familial dilated cardiomyopathy. *Am J Cardiol.* 2011;108:1171–6.
42. Ganesh S, Arnett D, Assimes T, Basson C, Chakravarti A, Ellinor P, et al. Genetics and genomics for the prevention and treatment of cardiovascular disease: update. *Circulation.* 2013;128:2813–51.
43. McNally E, Mestroni L. Dilated cardiomyopathy. *Circ Res.* 2017;121:731–48.
44. Assomull R, Shakespeare C, Kalra P, Lloyd G, Gulati A, Strange J, et al. Role of cardiovascular magnetic resonance as a gatekeeper to invasive coronary angiography in patients presenting with heart failure of unknown etiology. *Circulation.* 2011;124:1351–60.
45. Alba A, Gaztañaga J, Foroutan F, Thavendiranathan P, Merlo M, Alonso-Rodriguez D, et al. Prognostic value of late gadolinium enhancement for the prediction of cardiovascular outcomes in dilated cardiomyopathy. *Circ Cardiovasc Imaging.* 2020;13:e010105.
46. Puntmann V, Voigt T, Chen Z, Mayr M, Karim R, Rhode K, et al. Native T1 mapping in differentiation of normal myocardium from diffuse disease in hypertrophic and dilated cardiomyopathy. *JACC Cardiovasc Imaging.* 2013;6:475–84.
47. Dass S, Suttie J, Piechnik S, Ferreira V, Holloway C, Banerjee R, et al. Myocardial tissue characterization using magnetic resonance noncontrast T1 mapping in hypertrophic and dilated cardiomyopathy. *Circ Cardiovasc Imaging.* 2012;5:726–33.
48. Mordi I, Carrick D, Bezerra H, Tzemos N. T1 and T2 mapping for early diagnosis of dilated non-ischaemic cardiomyopathy in middle-aged patients and differentiation from normal physiological adaptation. *Eur Heart J Cardiovasc Imaging.* 2015;17:797–803.
49. Køber L, Thune J, Nielsen J, Haarbø J, Videbæk L, Korup E, et al. Defibrillator implantation in patients with nonischemic systolic heart failure. *N Engl J Med.* 2016;375:1221–30.
50. Nazarian S, Bluemke D, Lardo A, Zviman M, Wu K, Watkins S, et al. Magnetic resonance assessment of the substrate for inducible ventricular tachycardia in patients with non-ischemic dilated cardiomyopathy. *Heart Rhythm.* 2005;2:S81.
51. Assomull R, Prasad S, Lyne J, Smith G, Burman E, Khan M, et al. Cardiovascular magnetic resonance, fibrosis, and prognosis in dilated cardiomyopathy. *J Am Coll Cardiol.* 2006;48:1977–85.
52. Wu K, Weiss R, Thiemann D, Kitagawa K, Schmidt A, Dalal D, et al. Late gadolinium enhancement by cardiovascular magnetic resonance heralds an adverse prognosis in nonischemic cardiomyopathy. *J Am Coll Cardiol.* 2008;51:2414–21.

53. Becker M, Cornel J, van de Ven P, van Rossum A, Allaart C, Germans T. The prognostic value of late gadolinium-enhanced cardiac magnetic resonance imaging in nonischemic dilated cardiomyopathy. *JACC Cardiovasc Imaging*. 2018;11:1274–84.
54. Halliday B, Baksi A, Gulati A, Ali A, Newsome S, Izgi C, et al. Outcome in dilated cardiomyopathy related to the extent, location, and pattern of late gadolinium enhancement. *JACC Cardiovasc Imaging*. 2019;12:1645–55.
55. Guaricci A, Masci P, Muscogiuri G, Guglielmo M, Baggiano A, Fusini L, et al. CarDiac magnEtic Resonance for prophylactic Implantable-cardioVerter defibrillATor ThErapy in Non-Ischaemic dilated CardioMyopathy: an international Registry. *Europace*. 2021;23:1072–83.
56. Li S, Zhou D, Sirajuddin A, He J, Xu J, Zhuang B, et al. T1 mapping and extracellular volume fraction in dilated cardiomyopathy. *JACC Cardiovasc Imaging*. 2022;15:578.
57. Selvanayagam J, Hartshorne T, Billot L, Grover S, Hillis G, Jung W, et al. Cardiovascular magnetic resonance-GUIDEd management of mild to moderate left ventricular systolic dysfunction (CMR GUIDE): Study protocol for a randomized controlled trial. *Ann Noninvasive Electrocardiol*. 2017;22:e12420.
58. Gatzoulis K, Dilaveris P, Arsenos P, Tsiachris D, Antoniou C, Sideris S, et al. Arrhythmic risk stratification in nonischemic dilated cardiomyopathy: the ReCONSIDER study design – a two-step, multifactorial, electrophysiology-inclusive approach. *Hellenic J Cardiol*. 2021;62:169–72.
59. Thiene G, Nava A, Corrado D, Rossi L, Pennelli N. Right ventricular cardiomyopathy and sudden death in young people. *N Engl J Med*. 1988;318:129–33.
60. Sommariva E, Brambilla S, Carbuicchio C, Gambini E, Meraviglia V, Dello Russo A, et al. Cardiac mesenchymal stromal cells are a source of adipocytes in arrhythmogenic cardiomyopathy. *Eur Heart J*. 2015;37:1835–46.
61. Corrado D, Basso C, Thiene G, McKenna W, Davies M, Fontaliran F, et al. Spectrum of clinicopathologic manifestations of arrhythmogenic right ventricular cardiomyopathy/dysplasia: a multicenter study. *J Am Coll Cardiol*. 1997;30:1512–20.
62. Marcus F, McKenna W, Sherrill D, Basso C, Bauce B, Bluemke D, et al. Diagnosis of arrhythmogenic right ventricular cardiomyopathy/dysplasia: proposed modification of the task force criteria. *Eur Heart J*. 2010;31:806–14.
63. Corrado D, Perazzolo Marra M, Zorzi A, Beffagna G, Cipriani A, Lazzari M, et al. Diagnosis of arrhythmogenic cardiomyopathy: the Padua criteria. *Int J Cardiol*. 2020;319:106–14.
64. Borgquist R, Haugaa K, Gilljam T, Bundgaard H, Hansen J, Eschen O, et al. The diagnostic performance of imaging methods in ARVC using the 2010 task force criteria. *Eur Heart J Cardiovasc Imaging*. 2014;15:1219–25.
65. Sen-Chowdhry S, Syrris P, Ward D, Asimaki A, Sevdalis E, McKenna W. Clinical and genetic characterization of families with arrhythmogenic right ventricular dysplasia/cardiomyopathy provides novel insights into patterns of disease expression. *Circulation*. 2007;115:1710–20.
66. Zorzi A, Rigato I, Pilichou K, Perazzolo Marra M, Migliore F, Mazzotti E, et al. Phenotypic expression is a prerequisite for malignant arrhythmic events and sudden cardiac death in arrhythmogenic right ventricular cardiomyopathy. *Europace*. 2015;18:1086–94.
67. Pinamonti B, Dragos A, Pyxaras S, Merlo M, Pivetta A, Barbati G, et al. Prognostic predictors in arrhythmogenic right ventricular cardiomyopathy: results from a 10-year registry. *Eur Heart J*. 2011;32:1105–13.
68. Aquaro G, De Luca A, Cappelletto C, Raimondi F, Bianco F, Botto N, et al. Prognostic value of magnetic resonance phenotype in patients with arrhythmogenic right ventricular cardiomyopathy. *J Am Coll Cardiol*. 2020;75:2753–65.
69. Cadrin-Tourigny J, Bosman L, Nozza A, Wang W, Tadros R, Bhonsale A, et al. A new prediction model for ventricular arrhythmias in arrhythmogenic right ventricular cardiomyopathy. *Eur Heart J*. 2019;40:1850–8.
70. Mirmomen S, Bradley A, Arai A, Sirajuddin A. Arrhythmogenic left ventricular cardiomyopathy. *BJR Case Rep*. 2020;6:20190079.
71. Corrado D, van Tintelen PJ, McKenna WJ, Hauer RNW, Anastatakis A, Asimaki A, Basso C, et al. International experts arrhythmogenic right ventricular cardiomyopathy: evaluation of the current diagnostic criteria and differential diagnosis. *Eur Heart J*. 2020;41:1414–27.
72. Cipriani A, Bauce B, De Lazzari M, Rigato I, Bariani R, Meneghin S, et al. Arrhythmogenic right ventricular cardiomyopathy: characterization of left ventricular phenotype and differential diagnosis with dilated cardiomyopathy. *J Am Heart Assoc*. 2020;9:e014628.
73. Elliott P, Andersson B, Arbustini E, Bilinska Z, Cecchi F, Charron P, et al. Classification of the cardiomyopathies: a position statement from the European society of cardiology working group on myocardial and pericardial diseases. *Eur Heart J*. 2007;29:270–6.
74. Towbin J, Lorts A, Jefferies J. Left ventricular non-compaction cardiomyopathy. *Lancet*. 2015;386:813–25.
75. Arbustini E, Weidemann F, Hall J. Left ventricular noncompaction. *J Am Coll Cardiol*. 2014;64:1840–50.
76. Chin T, Perloff J, Williams R, Jue K, Mohrmann R. Isolated noncompaction of left ventricular myocardium. A study of eight cases. *Circulation*. 1990;82:507–13.
77. Maron B, Towbin J, Thiene G, Antzelevitch C, Corrado D, Arnett D, et al. Contemporary definitions and classification of the cardiomyopathies. *Circulation*. 2006;113:1807–16.
78. Oechslin E, Jenni R. Left ventricular noncompaction. *J Am Coll Cardiol*. 2018;71:723–6.
79. Ross S, Semsarian C. Clinical and genetic complexities of left ventricular noncompaction. *JAMA Cardiol*. 2018;3:1033.
80. Petersen S, Selvanayagam J, Wiesmann F, Robson M, Francis J, Anderson R, et al. Left ventricular non-compaction. *J Am Coll Cardiol*. 2005;46:101–5.
81. Stacey R, Andersen M, St. Clair M, Hundley W, Thohan V. Comparison of systolic and diastolic criteria for isolated LV non-compaction in CMR. *JACC Cardiovasc Imaging*. 2013;6:931–40.
82. Jacquier A, Thuny F, Jop B, Giorgi R, Cohen F, Gaubert J, et al. Measurement of trabeculated left ventricular mass using cardiac magnetic resonance imaging in the diagnosis of left ventricular non-compaction. *Eur Heart J*. 2010;31:1098–104.
83. Captur G, Muthurangu V, Cook C, Flett A, Wilson R, Barison A, et al. Quantification of left ventricular trabeculae using fractal analysis. *J Cardiovasc Magn Reson*. 2013;15:36.
84. Ivanov A, Dabiesingh D, Bhumireddy G, Mohamed A, Asfour A, Briggs W, et al. Prevalence and prognostic significance of left ventricular noncompaction in patients referred for cardiac magnetic resonance imaging. *Circ Cardiovasc Imaging*. 2017;10:e006174.
85. Vaidya V, Lyle M, Miranda W, Farwati M, Isath A, Patlolla S, et al. Long-term survival of patients with left ventricular noncompaction. *J Am Heart Assoc*. 2021;10:e015563.
86. Petersen S, Neubauer S. Excessive trabeculations and prognosis. *Circ Cardiovasc Imaging*. 2017;10:e006908.
87. Grigoratos C, Barison A, Ivanov A, Andreini D, Amzulescu M, Mazurkiewicz L, et al. Meta-analysis of the prognostic role of late gadolinium enhancement and global systolic impairment in left ventricular noncompaction. *JACC Cardiovasc Imaging*. 2019;12:2141–51.
88. Amzulescu M, Rousseau M, Ahn S, Boileau L, de Meester de Ravenstein C, Vancraeynest D et al. Prognostic impact of hypertrabeculation and noncompaction phenotype in dilated cardiomyopathy. *JACC Cardiovasc Imaging*. 2015;8:934–946.
89. Feingold B, Mahle W, Auerbach S, Clemens P, Domenighetti A, Jefferies J, et al. Management of cardiac involvement associ-

- ated with neuromuscular diseases: a scientific statement from the American Heart Association. *Circulation*. 2017;136:e200–31.
90. Spurney C, Shimizu R, Morgenroth L, Kolski H, Gordish-Dressman H, Clemens P. Cooperative international neuromuscular research group duchenne natural history study demonstrates insufficient diagnosis and treatment of cardiomyopathy in duchenne muscular dystrophy. *Muscle Nerve*. 2014;50:250–6.
  91. Matsumura T, Tamura T, Kuru S, Kikuchi Y, Kawai M. Carvedilol can prevent cardiac events in duchenne muscular dystrophy. *Intern Med*. 2010;49:1357–63.
  92. Ramaciotti C, Heistein L, Coursey M, Lemler M, Eapen R, Iannaccone S, et al. Left ventricular function and response to enalapril in patients with duchenne muscular dystrophy during the second decade of life. *Am J Cardiol*. 2006;98:825–7.
  93. Duboc D, Meune C, Lerebours G, Devaux J, Vaksman G, Bécane H. Effect of perindopril on the onset and progression of left ventricular dysfunction in duchenne muscular dystrophy. *J Am Coll Cardiol*. 2005;45:855–7.
  94. Almogheer B, Antonopoulos A, Azzu A, Al Mohdar S, Vlachopoulos C, Pantazis A, et al. Diagnostic and prognostic value of cardiovascular magnetic resonance in neuromuscular cardiomyopathies. *Pediatr Cardiol*. 2021;43:27–38.
  95. Ishizaki M, Kobayashi M, Adachi K, Matsumura T, Kimura E. Female dystrophinopathy: review of current literature. *Neuromuscul Disord*. 2018;28:572–81.
  96. Rajdev A, Groh W. Arrhythmias in the muscular dystrophies. *Card Electrophysiol Clin*. 2015;7:303–8.
  97. Beynon R, Ray S. Cardiac involvement in muscular dystrophies. *QJM*. 2008;101:337–44.
  98. Ho R, Nguyen M, Mather P. Cardiomyopathy in becker muscular dystrophy: overview. *World J Cardiol*. 2016;8:356.
  99. Yilmaz A, Gdynia H, Baccouche H, Mahrholdt H, Meinhardt G, Basso C, et al. Cardiac involvement in patients with Becker muscular dystrophy: new diagnostic and pathophysiological insights by a CMR approach. *J Cardiovasc Magn Reson*. 2008;10:50.
  100. Verhaert D, Richards K, Rafael-Fortney J, Raman S. Cardiac involvement in patients with muscular dystrophies. *Circ Cardiovasc Imaging*. 2011;4:67–76.
  101. Hor K, Taylor M, Al-Khalidi H, Cripe L, Raman S, Jefferies J, et al. Prevalence and distribution of late gadolinium enhancement in a large population of patients with Duchenne muscular dystrophy: effect of age and left ventricular systolic function. *J Cardiovasc Magn Reson*. 2013;15:107.
  102. Florian A, Ludwig A, Engelen M, Waltenberger J, Rösch S, Sechtem U, et al. Left ventricular systolic function and the pattern of late-gadolinium-enhancement independently and additively predict adverse cardiac events in muscular dystrophy patients. *J Cardiovasc Magn Reson*. 2014;16:81.
  103. Hermans M, Faber C, Bekkers S, de Die-Smulders C, Gerrits M, Merkies I, et al. Structural and functional cardiac changes in myotonic dystrophy type 1: a cardiovascular magnetic resonance study. *J Cardiovasc Magn Reson*. 2012;14:48.
  104. Chmielewski L, Bietenbeck M, Patrascu A, Rösch S, Sechtem U, Yilmaz A, et al. Non-invasive evaluation of the relationship between electrical and structural cardiac abnormalities in patients with myotonic dystrophy type 1. *Clin Res Cardiol*. 2019;108:857–67.
  105. Turkbey E, Gai N, Lima J, van der Geest R, Wagner K, Tomaselli G, et al. Assessment of cardiac involvement in myotonic muscular dystrophy by T1 mapping on magnetic resonance imaging. *Heart Rhythm*. 2012;9:1691–7.
  106. Modell B, Khan M, Darlison M, Westwood M, Ingram D, Pennell D. Improved survival of thalassaemia major in the UK and relation to T2\* cardiovascular magnetic resonance. *J Cardiovasc Magn Reson*. 2008;10:42.
  107. Pepe A, Meloni A, Rossi G, Midiri M, Missere M, Valeri G, et al. Prediction of cardiac complications for thalassemia major in the widespread cardiac magnetic resonance era: a prospective multicentre study by a multi-parametric approach. *Eur Heart J Cardiovasc Imaging*. 2017;19:299–309.
  108. Marsella M, Borgna-Pignatti C, Meloni A, Caldarelli V, Dell'Amico M, Spasiano A, et al. Cardiac iron and cardiac disease in males and females with transfusion-dependent thalassemia major: a T2\* magnetic resonance imaging study. *Haematologica*. 2011;96:515–20.
  109. Anderson L. Cardiovascular T2-star (T2\*) magnetic resonance for the early diagnosis of myocardial iron overload. *Eur Heart J*. 2001;22:2171–9.
  110. Torlasco C, Cassinerio E, Roghi A, Faini A, Capecchi M, Abdel-Gadir A, et al. Role of T1 mapping as a complementary tool to T2\* for non-invasive cardiac iron overload assessment. *PLoS One*. 2018;13:e0192890.
  111. Meloni A, Martini N, Positano V, De Luca A, Pistoia L, Sbragi S, et al. Myocardial iron overload by cardiovascular magnetic resonance native segmental T1 mapping: a sensitive approach that correlates with cardiac complications. *J Cardiovasc Magn Reson*. 2021;23:70.



Andrew Crean

## 16.1 Introduction

Anomalies of the coronary arteries are paradoxically among the simplest and yet most difficult of subjects to understand in congenital heart disease. Disconcertingly, even the definition of what constitutes an “anomalous” vessel has been disputed in the past. Prevalence data for coronary anomalies vary widely between published reports, undoubtedly reflecting institutional bias and degree of enthusiasm for the topic.

While the identification of one of the many published anomalies is rarely difficult with modern imaging methods, the clinical relevance of the uncovered abnormality is often unclear, forcing patients and their physicians to live with an unsettling degree of uncertainty at times [1–3].

The purpose of this chapter is first to establish what is meant by normal and anomalous coronary anatomy, then to describe the principal subtypes of anomaly, and finally to review the strengths and weaknesses of potentially applicable CMR imaging protocols.

## 16.2 Definition

Recognition of “abnormal” assumes knowledge of “normal”—a statement which appears facile but reflects the debate that has occurred on this topic. Leonardo da Vinci (1452–1519) was among the first to publish a description of normal coronary anatomy in which he not only described separate right and left coronary ostia but also pointed out that the normal coronary tree diminishes progressively in size from base of the heart to apex [4].

**Supplementary Information** The online version contains supplementary material available at [https://doi.org/10.1007/978-3-031-29235-4\\_16](https://doi.org/10.1007/978-3-031-29235-4_16).

A. Crean (✉)  
University of Ottawa Heart Institute, Ottawa, ON, Canada  
e-mail: [acrean@ottawaheart.ca](mailto:acrean@ottawaheart.ca)

Works by other historical authors, however, elaborated on cases with single coronary arteries, and it would be another 200 years before Morgagni would clearly establish the normality of a dual coronary system in the human [5]. A further leap forward occurred in the 1960s with the advent of selective invasive coronary angiography and subsequent publications on coronary variants and anomalies in large cohorts.

Finally, the era of multi-detector row computed tomography (MDCT) has opened Pandora’s box with significant numbers of coronary artery anomalies (CAAs) being uncovered for the first time in adult patients with widely varying degrees of symptomatology (and in many cases, atypical symptoms or no symptoms at all).

Angelini et al. suggested over 20 years ago that recognition of CAAs must stem from an appreciation of normal coronary anatomy and proposed the following guiding principles [6], which remain valid today:

1. A coronary artery is defined as any artery or arterial branch that carries blood to the cardiac parenchyma.
2. The name and nature of a coronary artery or branch are defined by that vessel’s distal vascularization territory, not by its origin.
3. The sinuses of Valsalva are identified not by the coronary arteries but rather by their own topographic location.
4. “Normal” should mean “what is commonly observed”.
5. “Abnormal” or “anomalous” should be employed for any form observed in less than 1% of the general (human) population. Thus, an abnormality which occurs in a population with an observed frequency of greater than 1% is better described as a (normal) variant than an anomaly.
6. Classification schemes are helpful for cataloguing CAAs but not for clinical prognostication.
7. Normally (i.e., in >1%) the human coronary arteries have two or three coronary ostia.
8. The proximal segment of a coronary artery arises at a nearly orthogonal angle from the aortic wall.



9. The coronary ostia are typically equal to, or larger in size, than the proximal segment of the related coronary artery.
10. The course of the coronary arteries is mostly epicardial.
11. The coronary arteries normally terminate in the capillary network.
12. All myocardial segments should have a congenitally adequate arterial circulation with respect to basal and exercise requirements.

### 16.3 Morphology

Many complex classification schemes bedevil this topic—a nice summary was published by Jacobs et al. [7]. A simplified structure for the classification of anomalies is commonly employed clinically: (1) anomalies of origin, (2) anomalies of course, and (3) anomalies of termination. Although this scheme provides anatomic neatness, it has little bearing on

the clinical importance of selected anomalies as will be discussed below. Nonetheless it is an appropriate starting point.

### 16.4 Coronary Anomalies Associated with Other Conditions

Coronary artery anomalies may occur alone or in conjunction with other cardiac abnormalities and malformations. Most commonly an incidental recognition of an anomaly in an otherwise well individual is usually an isolated finding. Several important anomalies occur reliably in association with major congenital malformations. These range from the expected clockwise rotation of the aortic root common to most cases of tetralogy of Fallot to the varied coronary patterns (including single coronary artery, Fig. 16.1) associated with transposition of the great arteries as well as the coronary-cameral fistulas (Fig. 16.2) seen in children with pulmonary atresia with intact interventricular septum (PA-IVS) [8].

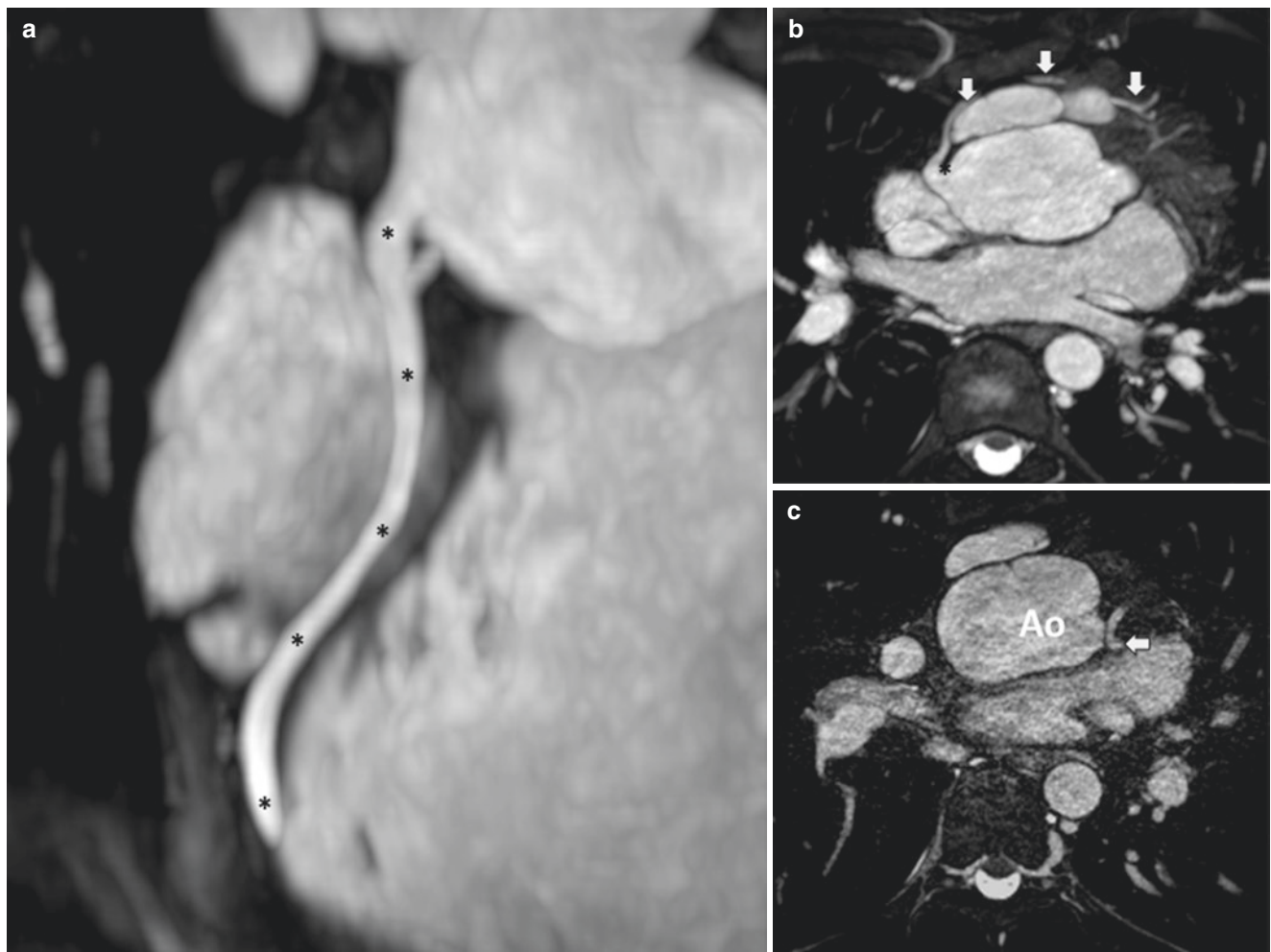


**Fig. 16.1** Single coronary system in a patient with *d*-transposition of the great arteries following arterial switch surgery. (a) Coronary MRA demonstrates a large right coronary artery (asterisks) arising normally from the right coronary sinus. (b) A large marginal branch is seen to emerge from the right coronary artery (asterisk) and pass anteriorly over the front of the right ventricular outflow tract (arrows). (c)

Ultrahigh-resolution MRA (0.5 mm isotropic) demonstrates that the vessel (arrow) in the expected position of the left anterior descending coronary artery does not connect to the aortic root (Ao) but instead forms the left coronary system as a direct extension of the RCA marginal branch shown in b

**Fig. 16.2** Coronary-cameral fistulae in a patient with pulmonary atresia and intact ventricular septum. Volume-rendered images from multiple angles demonstrating multiple fistulous connections from the right (white arrow) and left (grey arrow) coronary arteries to the hypoplastic right ventricle (RV). Note the multiple areas of coronary stenosis and aneurysmal expansion (asterisks) that are frequent in this condition

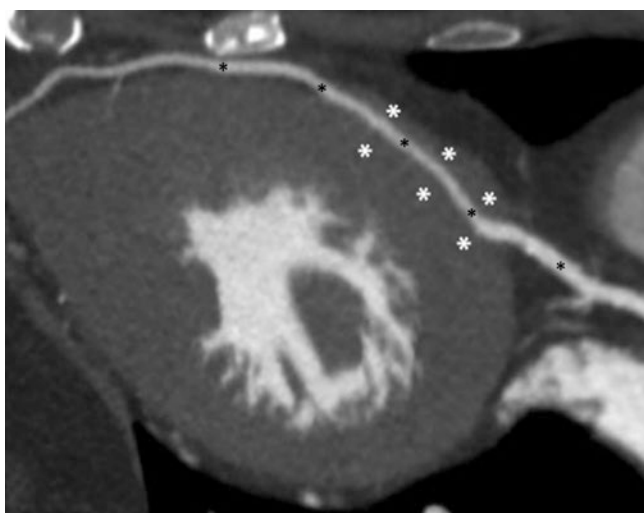
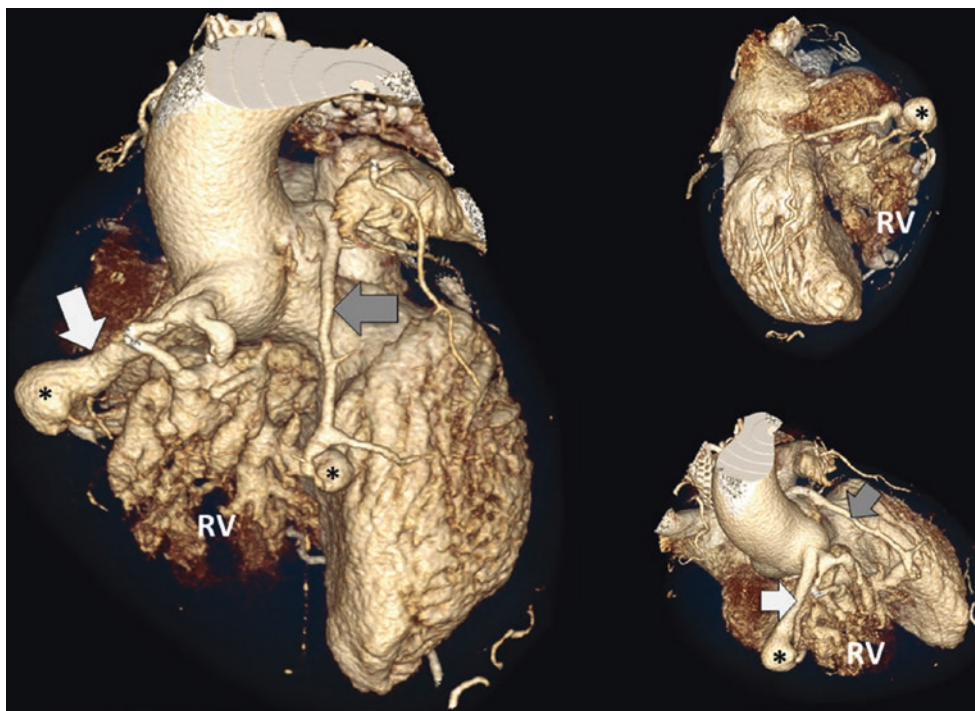


**Fig. 16.3** Reformat from cardiac gated CT demonstrating a relatively long segment of myocardial bridging in a patient with hypertrophic cardiomyopathy. The left anterior descending coronary artery (black asterisks) is shown, with its midportion passing through a “tunnel” of left ventricular muscle (white asterisks)

Not surprisingly there is a moderate association with aortic valve disease in up to 20% of cases of coronary anomaly in angiographic series [9], and it is possible that this represents an underestimate of the true incidence of associated valvular pathology. Prospective registries with newer cross-sectional imaging techniques will be ideally placed to resolve this [10].

Coronary abnormalities may also be seen in heart muscle disease, principally hypertrophic cardiomyopathy (HCM), in

which an excessive degree of myocardial bridging is not infrequently seen (Fig. 16.3). This is more correctly regarded as a variant than an anomaly since it occurs with a frequency well in excess of 1%. Bridging has been claimed to result in demonstrable myocardial ischemia in the absence of atherosclerotic disease [11]. Although coronary “milking” is a systolic phenomenon, there is evidence to suggest impact on diastolic coronary flow also [12]. On occasion this may be sufficiently severe as to warrant surgery.

Sometimes overlooked, also, are the *acquired* coronary anomalies, including aneurysms, that may develop as a result of systemic illness particularly Behcet and Kawasaki diseases. Although not congenital (except perhaps by virtue of genetic predisposition), they are likely to be encountered by most CMR imagers and are included here for completeness.

## 16.5 Clinical Presentation

The frequency of CAAs is debated, and it seems likely that many individuals with coronary anomalies never present during their lifetime. The literature is biased with series of either otherwise healthy individuals who experienced sudden cardiac death or those with symptoms of myocardial ischemia. The diagnosis is established in some cases by invasive angiography and in others by autopsy alone. Extreme populations are often over represented (e.g., military recruits or athletes who undergo extreme levels of conditioning and physical exertion) making it difficult to know whether outcomes in these groups are truly representative of those in the general (more sedentary) population with the same or similar

anomaly [13–15]. The one consistent finding, however, has been that there is a higher incidence of coronary anomalies in victims of sudden death than is seen in *routine* autopsy series [16, 17]. It is this fact that generates the most angst for physicians attempting to counsel these patients.

One retrospective surgical series of 36 patients documented preoperative symptoms of angina, shortness of breath, or syncope in 81%, but importantly, abnormalities of perfusion were only identifiable in 43% [18]. In contrast, another small series demonstrated inducible perfusion defects by nuclear perfusion imaging in 80% of subjects with an inter-arterial vessel [19]. However, it is the lack of reproducible ischemia in survivors of sudden cardiac death with known coronary anomalies that has led to some arguing in favor of surgical repair upon identification, regardless of stress test results. This is held to be particularly true for

anomalous left coronary artery from the opposite sinus (ALCAOS, Fig. 16.4) which appears to have a much stronger association with sudden death than its counterpart anomalous right coronary artery from the opposite sinus (ARCAOS) [2]. With regard to the latter diagnosis, there is generally a lower threshold for operating on asymptomatic children than there is in adults, unless myocardial ischemia can be demonstrated.

At the Texas Heart Institute almost 2000 angiograms were reviewed for evidence of CAA. In this study approximately 5% of men and 8% of women had an identifiable anomaly [9]. The commonest anomalies were as shown in Table 16.1.

Thus, a total of 5.6% of the patients had an identifiable CAA—a much higher figure than the 1.3% detected in the large angiographic series from the Cleveland Clinic [20]. Furthermore, in a recent paper from the Netherlands looking

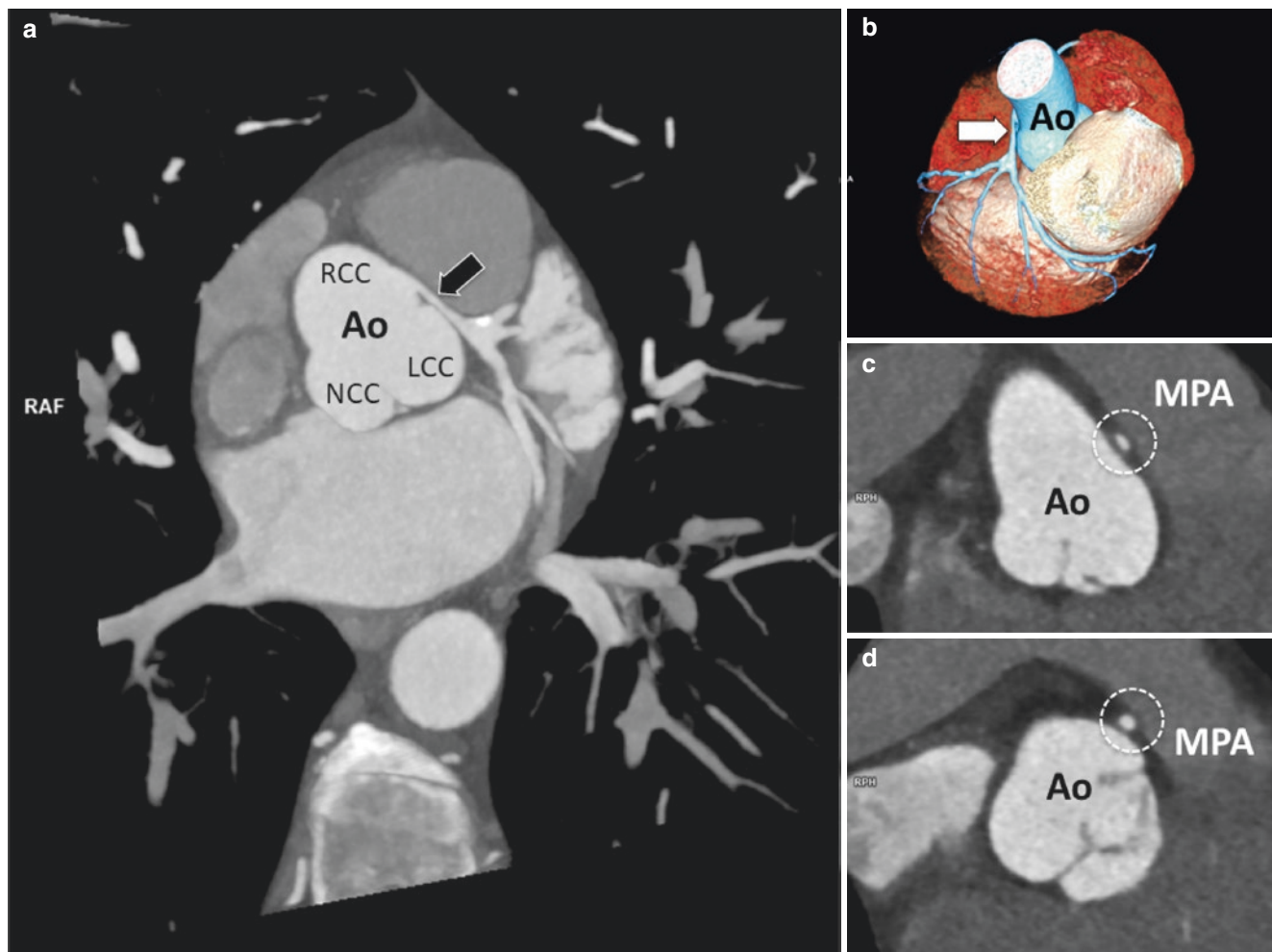


**Fig. 16.4** Anomalous left coronary artery the opposite sinus (ALCAOS). (a) maximum intensity projection image showing the left main coronary artery (arrow) arising from the right coronary cusp (RCC) and passing between the aortic root (AO) and the main pulmonary artery (MPA). Note that it appears relatively narrowed at this location. (b) Volume-rendered image again showing attenuation (arrow) of proximal left main artery—the main pulmonary artery has been

removed to improve visibility. (c) Cross section of the left main coronary artery immediately beyond the ostium. Observe that the shape of the vessel is oval and somewhat slit-like (circle). (d) Cross section of the left main coronary artery as it emerges from between the aortic root and the pulmonary artery; the vessel now has a normal circular appearance and a larger cross-sectional area. This was also confirmed at the time of surgical repair



**Table 16.1** Frequency of coronary anomalies in the Texas Heart Institute angiographic series [9]

Anomaly	Percentage
Ectopic RCA from left cusp	0.92
Fistulas	0.87
Absent left main coronary artery	0.67
Circumflex arising from the right cusp	0.67
Left coronary artery from the right cusp	0.15
Low origin of the RCA	0.1
Other anomalies	0.27

at a little under 2000 patients examined by dual source CT, the incidence of anomalies was identical to the Cleveland angiographic series at 1.3% [21]. The true incidence of coronary anomalies remains uncertain and is a question likely to be answered by large CT registries in the future.

## 16.6 How Good Is CMR for the Detection of the Course of Anomalous Coronary Vessels?

### 16.6.1 Anomalies of Origin

These are generally simple to identify by CMR since the vessels are usually of a reasonable size, and the number of options for their origin is relatively limited. By far the commonest abnormality is origin of one coronary from the opposite sinus. Careful imaging of the aortic root with thin slice cine, black blood, or angiographic images usually uncovers the abnormality in a matter of minutes. Slightly more challenging are rarer coronary origins such as that of the left or right coronary artery from the pulmonary artery. The first clue to the presence of this condition is the unusually dilated nature of most of the coronary arterial branches—enlarged because of increased volume flow as blood passes down a pressure gradient from the coronary with an aortic origin to that connecting to the pulmonary artery. Multiple small fistulous branches anastomose between left and right coronary systems including septal branches, giving the appearances of twinkling lights or “Christmas tree septum” on Doppler echocardiography (Fig. 16.5). Once recognized, the search for the coronary origin from the pulmonary artery is then straightforward.

The other very rare anomalies of origin cannot be dealt with here. Suffice it to say that most CMR practitioners may never encounter one in an entire career. However, the best way of ensuring that a rare anomaly (coronary or otherwise) is not missed is to ensure that every CMR protocol includes full thoracic coverage in either axial, sagittal, or coronal planes (or all three) with thin slice overlapping SSFP single-shot single-phase acquisitions. These can be run in quiet respiration and are a very rapid method of acquiring a comprehensive overview of the heart and great vessels.

### 16.6.2 Anomalies of Course

At this point it is appropriate to consider what precisely is meant by an “anomalous” coronary course. When a coronary artery arises anomalously, it may travel along four principal courses and these are not all of equal clinical importance. The vessel may pass:

1. Inter-arterial between the aorta and pulmonary trunk (Fig. 16.6).
2. Retroaortic (Fig. 16.7).
3. Transseptal (Fig. 16.8), i.e., the proximal portion is tunneled through the septal myocardium (below the level of the pulmonary valve).
4. Pre-pulmonic or preaortic in certain congenital conditions (Fig. 16.9).

Of these four, it is the inter-arterial course that has generally been regarded as “malignant.”

Historically the concern has been that the vessel might be compressed during systole as it crosses between the aorta and pulmonary artery, resulting in ischemia and arrhythmic death. Most authors now consider this mechanism to be too simplistic, and greater emphasis is put on the shape of the ostium and the relationship of the most proximal portion of the artery to the aortic wall. In many cases the vessel takes a very oblique angle from its origin and actually travels within the wall of the aortic root for the first few millimeters. This so-called “intramural” course has been shown on intravascular ultrasound (IVUS) studies to correspond to a very significant reduction in cross-sectional area of the vessel [22]. In these cases, it seems likely that supply-demand mismatch may occur in the subtended myocardium during exercise as intra-aortic pressure rises and the intramural segment is further compressed. Similarly, the extreme tangential origin of an intramural coronary artery results in deformation of the ostium which is often seen to be “slit-like” on both IVUS and cardiac CT (Fig. 16.10).

It should be emphasized that not all “inter-arterial” coronary arteries have malignant features as described above. Some may have no intramural component at all in which case the ostium as well is frequently normal. Although it might appear reasonable to assume that this subcategory of anomalous coronary is at far lower risk of adverse events than those with an initial intramural course, there are no prospective natural history studies available to confirm this. Indeed there is limited pathological evidence to the contrary—in one postmortem study of sudden cardiac death from the Royal Brompton Hospital in London UK, there were 13 cases of inter-arterial coronary anatomy, but an intramural course and slit-like origin were documented in only four of the cases at direct inspection [16].

The three remaining possible proximal coronary courses (including the intraseptal intramyocardial) are generally



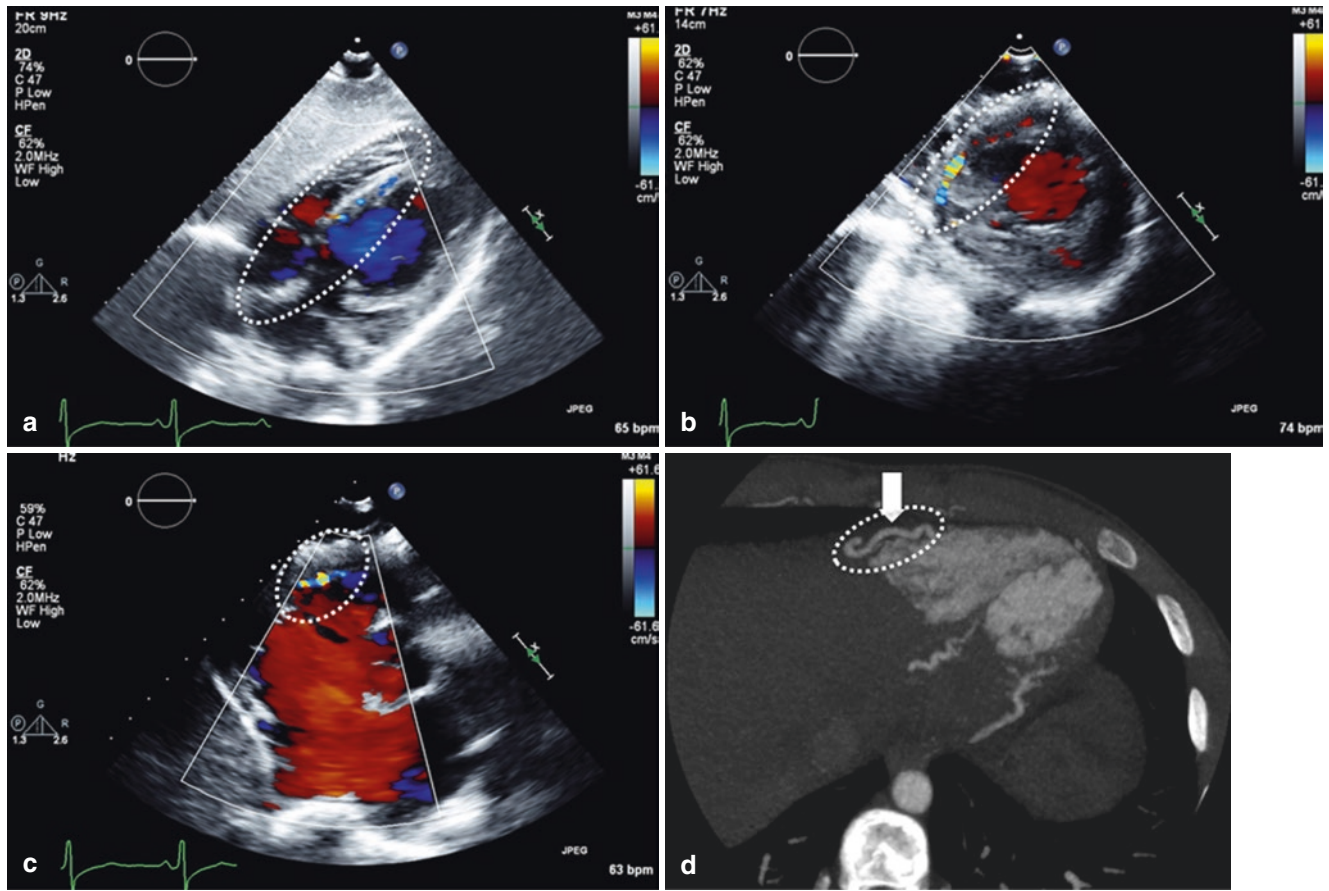


**Fig. 16.5** “Christmas tree lights” in anomalous coronary artery from the pulmonary artery. (a, b) Long- and short-axis echo views with color Doppler. Note the appearance of the septum where multiple Doppler colors are present due to the presence of collaterals which weave toward and away from the echo probe. (c) Off-axis view showing unusual color

Doppler signal along the free wall of the right ventricle. (d) Corresponding cardiac CT view which reveals the findings in (c) to be due to the presence of greatly enlarged marginal vessels (arrow) engorged due to collateral flow

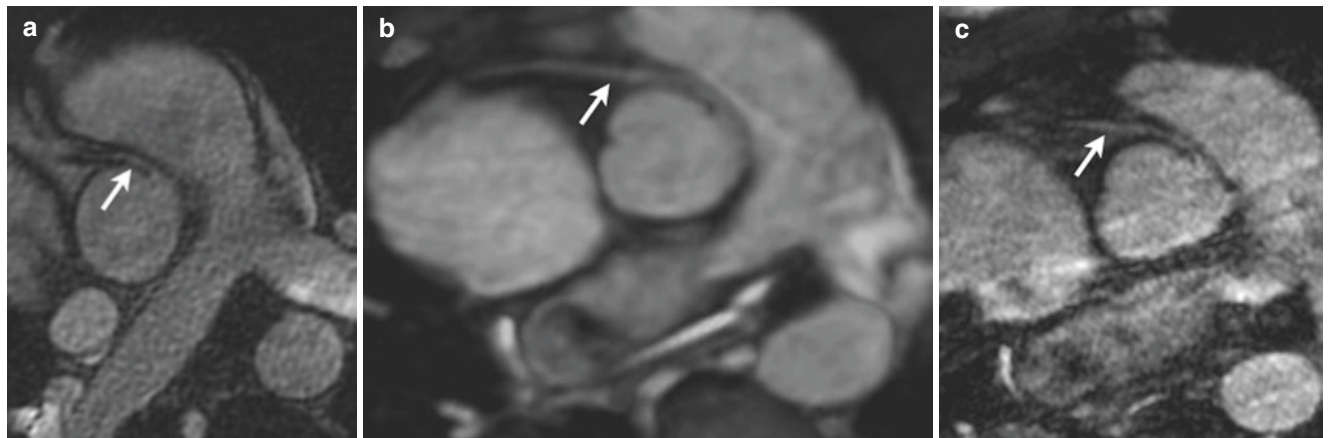


**Fig. 16.6** Inter-arterial course of the right coronary artery. The right coronary artery (arrow, all three panels) can be identified originating from the contra-lateral sinus. SSFP cine imaging (a) alone is often adequate for identification of inappropriate sinus origin—performed here with a voxel size of  $1.0 \times 1.0 \times 3$  mm. Whole heart coronary MRA (b)

demonstrates the same finding in this patient with clarity achieved by a  $1.5 \times 1.5 \times 1.5$  mm voxel size. The relationship of the proximal vessel to the aortic wall (intramural course—see text) is however more clearly defined with higher resolution MRA images (c) acquired at an isotropic 1.0 mm resolution

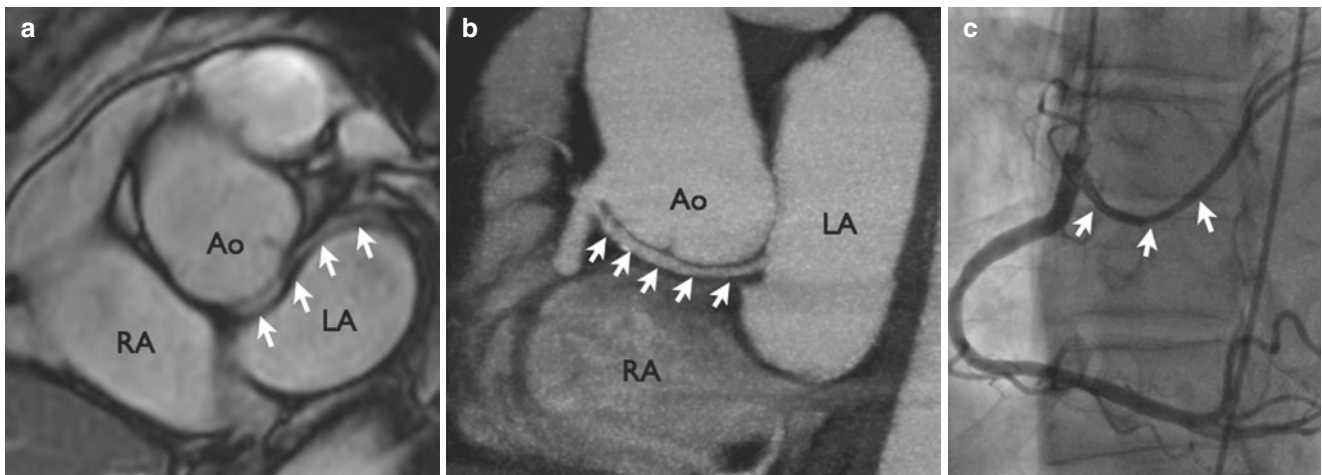


**Fig. 16.7** Retroaortic course of the circumflex artery (arrows a–c). A vessel (arrows) can be seen to take an unusual course infero-posterior to the aortic root on the freeze frame from a short-axis SSFP cine stack (a). Cardiac-gated tomography (b) in the same patient clearly shows its

origin from the right coronary artery. Although this anomalous vessel is readily identified by catheter angiography (c) its 3-dimensional course in space is much more clearly understood by a cross-sectional technique. *Ao* aorta, *LA* left atrium, *RA* right atrium

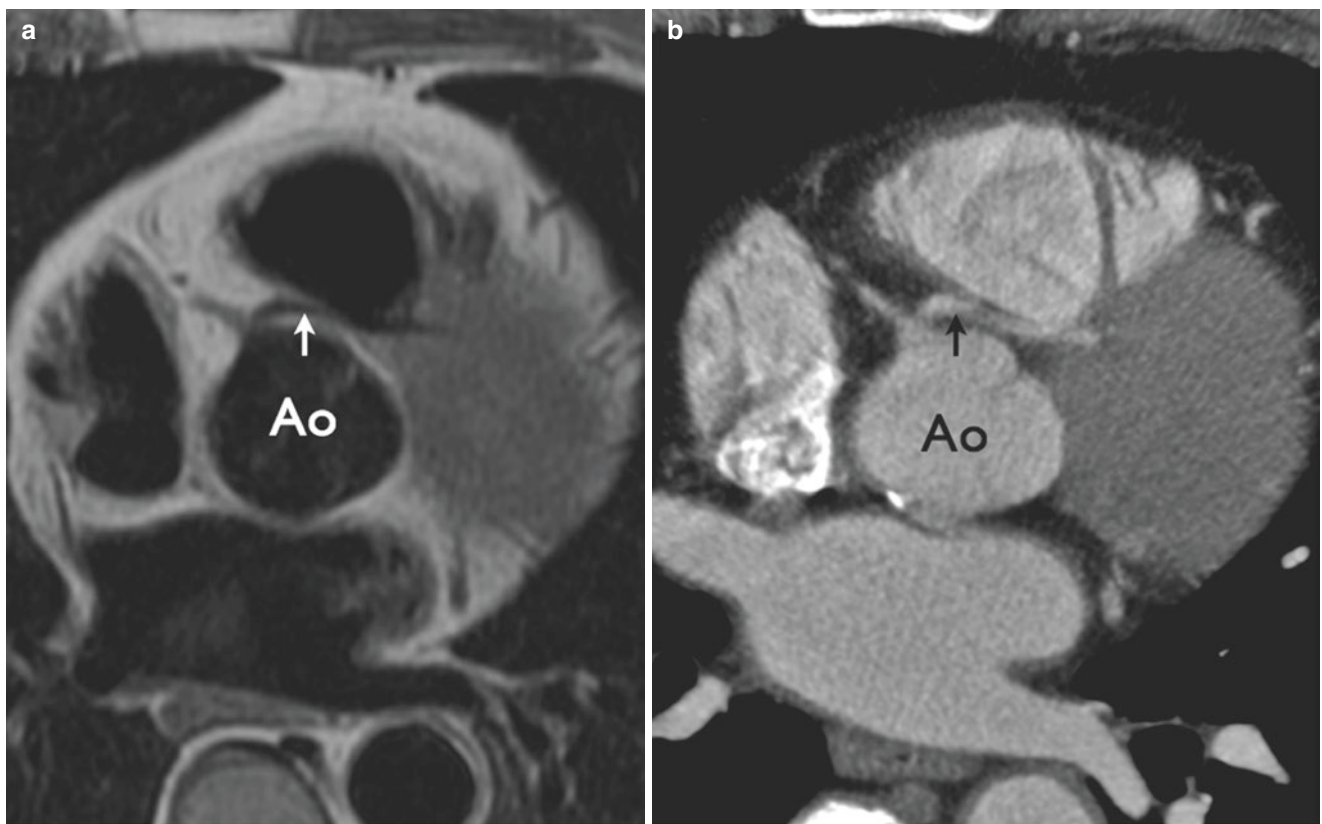


**Fig. 16.8** Transseptal course of the left main coronary artery. The left main coronary vessel (arrow) arises from a common ostium with the right coronary artery. Note however that it is clearly extramural in relation to the aortic root. It passes anterior to the aorta below the level of the pulmonary valve and dives into septal myocardium prior to gaining

a normal position in the anterior interventricular groove. A simple double inversion black blood technique (a) demonstrates the abnormality every bit as clearly as the companion slice from a cardiac-gated CT scan (b). *Ao* aorta

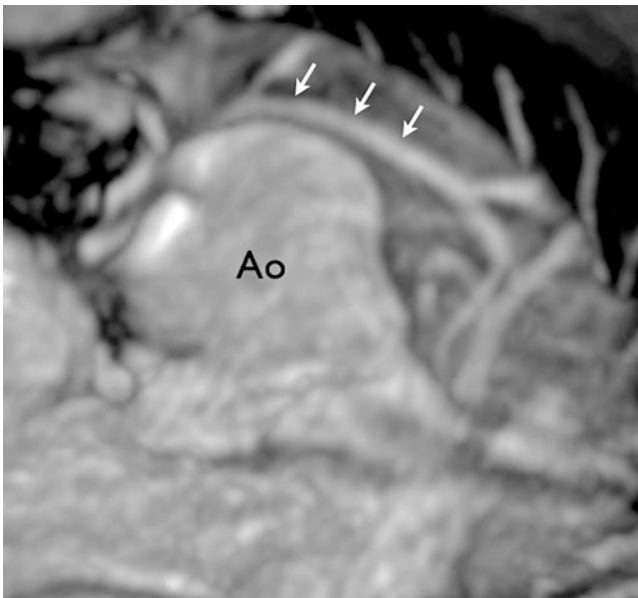


**Fig. 16.9** Preaortic course of the left main coronary artery. Coronary MR angiography demonstrates the pre-aortic course of the left main coronary artery (*arrows*) in a patient with transposition of the great arteries. This anomaly is considered benign

regarded as benign. Sporadic case reports of myocardial infarction in patients with these anomalies do arise, but whether this is due to the anomaly itself or simply ‘bystander’ atheromatous coronary disease is not always clear [23]. Alternatively, while it is sometimes postulated that “benign” anomalous vessels could nevertheless have altered flow profiles that lead to accelerated atheroma formation, few data exist to support this hypothesis.

Coronary MRA has historically been extremely successful at the identification of coronary anomalies. Table 16.2 summarizes the literature in this regard. In almost every series an extremely high diagnostic accuracy is demonstrated, and this is even more impressive considering that the early series were published almost 30 years ago when CMR was more limited and coronary MRA in relative infancy. Interestingly, in several cases coronary MRA was shown to be indubitably superior to conventional angiography which misclassified the course of the vessel.

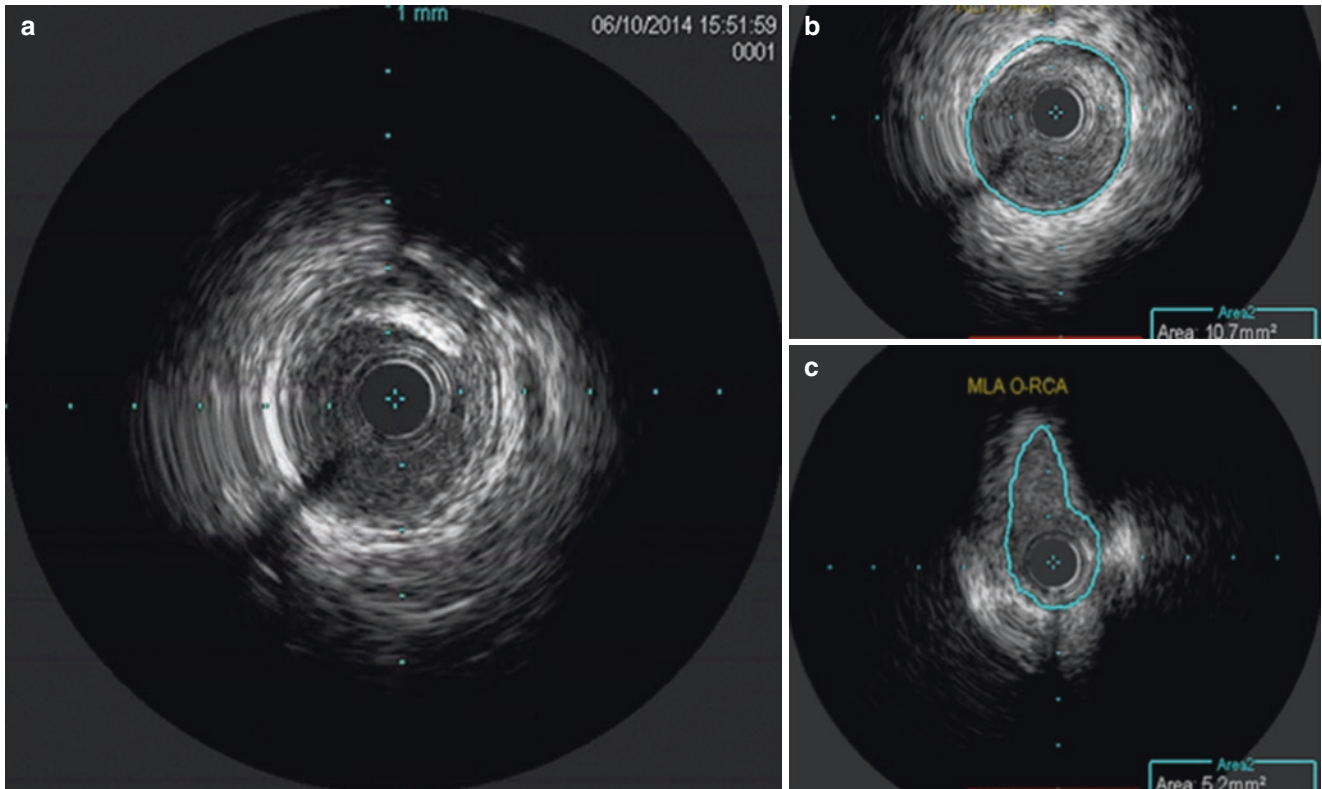


**Fig. 16.10** Intravascular ultrasound (IVUS) in the assessment of anomalous right coronary artery (RCA) from the opposite sinus. (a) The IVUS catheter (asterisk) has been introduced into the RCA distal to the narrowed proximal segment. (b) The catheter is slowly retracted (“pulled back”) toward the ostium—at the level shown, there is still a

normal circular shape to the lumen. (c) The catheter has now reached the proximal intramural segment of the RCA. At this level the lumen (outlined in blue) has now changed into a very abnormal oval shape—the so-called slit-like appearance



**Table 16.2** CMRA studies in coronary anomalies

Author	Year	Number of subjects	Field strength	Manufacturer	MRA sequence	Volume or targeted	Accuracy	Reference standard
McConnell [24]	1995	16	1.5	Siemens	Breath-hold gradient echo	Targeted	14/15 (1 excluded for poor image quality)	X-ray angiography
Post [25]	1995	36	1.5	Siemens	Breath-hold gradient echo	Targeted	36/36	X-ray angiography
Vliegen [26]	1997	12	1.5	Philips	Breath-hold gradient echo	Targeted	11/12	X-ray angiography
Bekedam [27]	1999	4	1.5	Philips	Breath-hold gradient echo	Targeted	4/4	X-ray angiography
White [28]	1999	8	1.5	GE	Breath-hold gradient echo	Targeted	8/8	X-ray angiography
Taylor [29]	2000	25			Navigated free-breathing gradient echo	3D volume or 2D targeted slices depending upon respiratory pattern	23/25 (included 9 normal controls in a blinded mix with 16 anomalous vessels)	X-ray angiography
Greil* [30]	2002	6	1.5	Philips	Navigated free-breathing gradient echo	3D volume	6/6	X-ray angiography
Bunce [31]	2003	26	1.5	Picker or Siemens	Navigated free-breathing gradient echo or SSFP	3D volume	26/26	X-ray angiography
Mavrogeni* [32]	2004	13	1.5	Philips	Navigated free-breathing gradient echo	3D volume	13/13	X-ray angiography
Su [33]	2005	65	1.5	Philips	Navigated free-breathing gradient echo	3D volume	62/65	No reference
Taylor† [34]	2005	16	1.5	Philips	Navigated free-breathing SSFP	Targeted 3D	N/A	No reference
Takemura* [35]	2007	35	1.5	Philips	Navigated free-breathing SSFP	3D volume (15/35) Targeted 3D (20/35)	N/A	No reference
Gharib [36]	2008	22	3.0	Philips	Navigated free-breathing gradient echo	3D volume	N/A	X-ray angiography (8/12 patients and 0/10 volunteers)
Beerbaum [37]	2009	40	1.5	Philips	Navigated free-breathing SSFP	3D volume	12/12 in those with reference	X-ray angiography in 17/40
Clemente [38]	2010	15	1.5	Philips	Navigated free-breathing SSFP	3D volume	15/15	No reference
Tangcharoen [39]	2011	58	1.5	Philips	Navigated free-breathing SSFP	3D volume	4/4	Surgical inspection
Rajiah [40]	2011	112	1.5	Siemens	Navigated free-breathing SSFP	3D volume	N/A	No reference

\*Pure population of Kawasaki's disease patients

†Pure population of patients with transposition of the great arteries following arterial switch surgery

### 16.6.3 Anomalies of Termination

Anomalous termination is less common than the other two kinds of anomaly discussed earlier. It is also potentially more difficult to detect and may require a high index of suspicion.

One clue is the presence of unexplained ventricular enlargement which should prompt consideration of abnormal coronary arterial drainage once the more common types of shunt have been excluded. One of the commonest anomalies of termination seen in clinical practice is that of the RCA or



circumflex artery draining to the coronary sinus (Fig. 16.11). As with the ALCAPA/ARCAPA lesions, the abnormally draining vessel is invariably dilated due to increased flow. Cine phase contrast imaging may be used to quantify the shunt but also to directly demonstrate the abnormal flow into the right atrium (usually best accomplished with slices parallel and on either side of the plane of the AV groove). Other small fistulas such as those sometimes seen draining into the

pulmonary arteries or the left ventricle are generally considered to be benign. Quantification of chamber enlargement as well as the degree of fistulous flow by CMR is often very useful in subsequent discussions regarding appropriate surgical or interventional management.

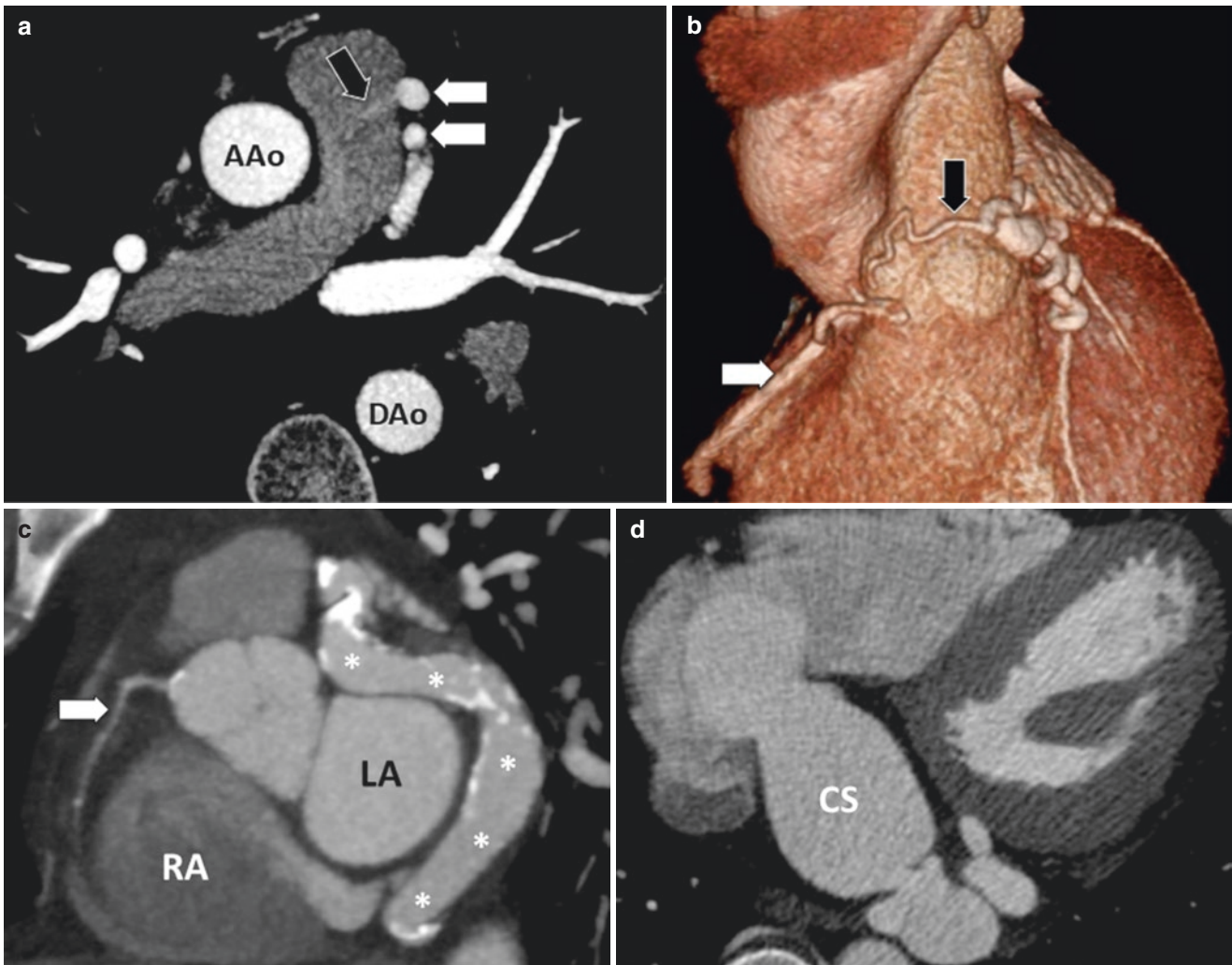


**Fig. 16.11** Anomalies of termination; coronary fistulae. (a) Axial CT image at the level of the main pulmonary artery. Two small contrast-filled vessels (white arrows) are seen lateral to the main pulmonary artery. Note that they have a similar density of contrast to the ascending and descending aorta and are therefore likely to be arterial structures. A small jet of contrast (black arrow) is seen passing into the relatively unenhanced main PA. The imager here was lucky; in practice it is difficult to get the timing just right to facilitate a contrast gradient of this sort, and small connections can be easily missed. When small arterial fistulae are suspected, it is often easier to use thin slice cine SSFP or gradient echo CMR imaging to visualize the associated flow disturbance, given that flow is occurring under diastolic aortic pressure, which is much higher than pulmonary arterial diastolic pressure. (b)

Same patient; volume-rendered CT image demonstrates more clearly a tortuous tangle of vessels with a feeder vessel (white arrow) arising from the left anterior descending artery (black arrow). (c) Circumflex artery to coronary sinus fistula, moderate size. The circumflex (asterisks) is significantly enlarged compared to the RCA (arrow) due to high-volume flow from high diastolic aortic pressure to low diastolic right atrial pressure. (d) Circumflex artery to coronary sinus fistula, large size. Here a large longstanding circumflex fistula has led to enormous dilatation of the coronary sinus (CS). Lesions of this sort recirculate additional volumes of blood through the heart and may cause biventricular enlargement. Accurate quantitation of this flow and its secondary effects on chamber enlargement is a very important role of CMR as part of management planning

## 16.7 The Role of Cardiovascular Magnetic Resonance

### 16.7.1 Indications

The commonest indication for coronary imaging in the congenital heart world is to delineate the origin and the proximal course of the coronary arteries. Particular indications to do this include the investigation of individuals with aborted sudden cardiac death, particularly if young or athletic. Other indications include postoperative follow-up after procedures which involve relocation or reimplantation of the coronary arteries such as the Ross procedure or the arterial switch operation in which there may exist concerns over the longer-term patency of the proximal vessel. Fortunately demonstrating the course and patency of a proximal coronary artery is considerably easier than the demonstration of percentage vessel stenosis by CMR, which remains a niche pursuit worldwide, in distinct con-

trast to the widespread adoption of coronary CT for this purpose.

### 16.7.2 Goals of Imaging

These may be summarized as:

1. To demonstrate the origin of each vessel (e.g., anomalous, ectopic, conjoint, etc.)
2. To characterize the origin of each vessel (e.g., slit-like orifice, intramural course, etc.)
3. To demonstrate the proximal course in relation to the surrounding vascular structures (aorta, pulmonary artery)
4. To demonstrate the physiological effects of an encountered coronary anomaly (e.g., myocardial ischemia or infarction, Fig. 16.12)
5. To demonstrate any secondary effects of specific anomalies (e.g., chamber enlargement in coronary fistula)

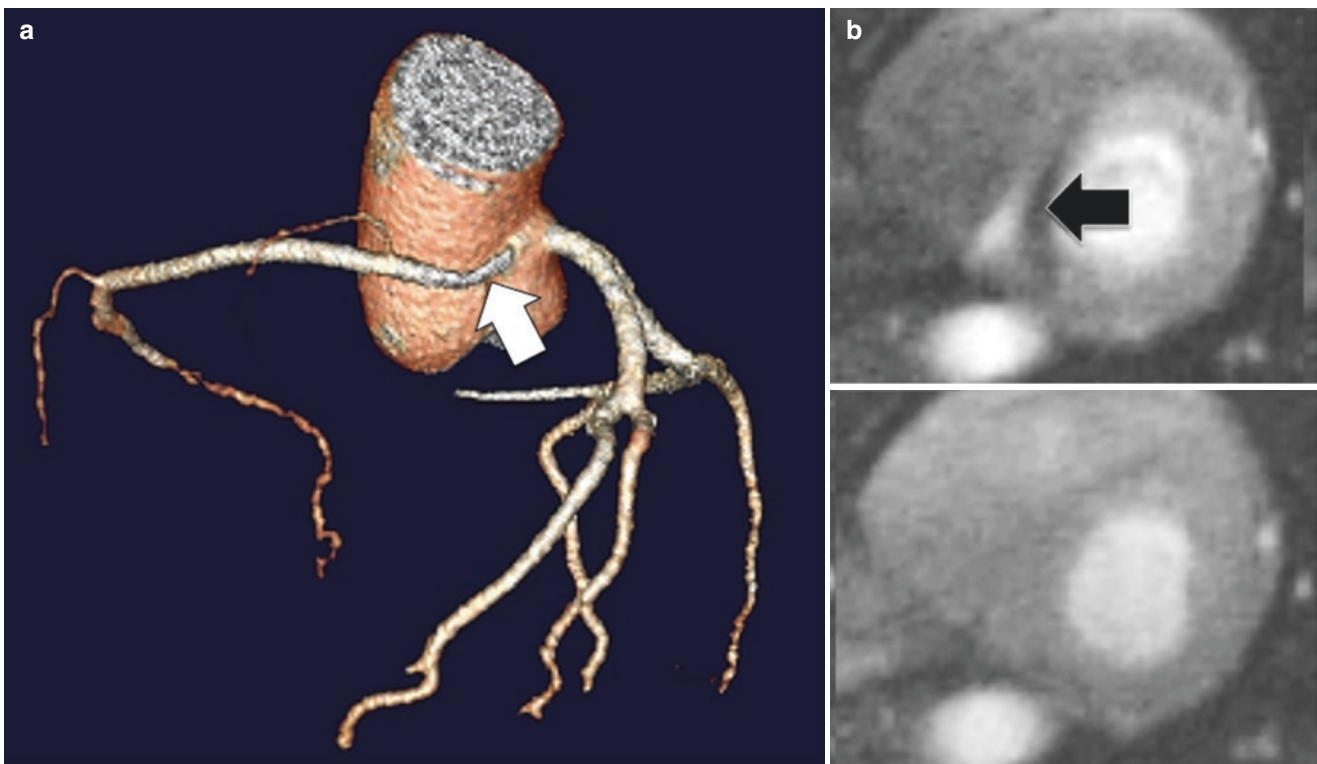


**Fig. 16.12** Inducible ischemia in anomalous right coronary artery from the opposite sinus (ARCAOS). (a) Volume-rendered coronary image demonstrating the narrowed appearance (arrow) of an intramural right coronary artery. (b) Dipyridamole stress/rest perfusion CMR

study. Upper panel reveals an inducible perfusion defect (arrow) in the basal inferior septum under stress conditions. At rest (bottom panel) the defect has entirely resolved

## 16.8 CMR Sequences and Imaging Protocols

### 16.8.1 Technical Considerations in Coronary MRA

Coronary imaging represents a significant challenge for CMR due to the constraints of the beating heart and the moving chest. Enormous research efforts have been made over the last 20 years to overcome these two practical limitations. The paragraphs that follow describe the principal approaches that have been taken to coronary MRA. We start however by suggesting that dedicated coronary MRA techniques are unnecessary in many cases and that work-horse DIR and SSFP sequences often suffice.

### 16.8.2 Everyday CMR Sequences for Coronary Identification

Coronary MR imaging is often felt to be a rather arcane and difficult topic that only the few can master. There is some truth to this when the goal of imaging is to compete with invasive angiography in pursuit of percent diameter stenosis within vessels themselves only a few millimeters in diameter. Fortunately, in the congenital world the clinical question is more straightforward—where do the coronaries arise, what is their proximal course, and are there adverse functional consequences as a result? In this regard, the majority of coronary anomalies are amenable to ready detection and

interpretation with everyday clinical CMR pulse sequences and techniques.

Basic coronary imaging may be performed with either dark blood breath-held double inversion recovery (DIR) sequences or with bright blood balanced steady-state free precession (SSFP) cine imaging. With either technique the key to optimum delineation of the vessel is a sufficiently small voxel size to allow visualization free of partial volume artifact (Fig. 16.13). Slice thickness, in particular, is ideally no more than 3–5 mm (contiguous slices), and optimum in-plane spatial resolution is around 1.0–1.3 mm. Small voxel size is important in order to try and comment on distortion of the vessel ostium in both native and surgically reimplemented vessels. The longer breath-hold times potentially required for this level of resolution may be reduced using higher parallel imaging factors, particularly for the SSFP approach since this is an intrinsically high signal technique.

Although many authors advocate the use of DIR techniques in this setting, the advantage of multiphase SSFP is undoubtedly that the human eye tracks a moving contour more readily than a static one—allowing easier visualization of the vessel as it travels in and out of the slice plane. The plane in which images should be acquired is debatable—the simplest approach is to plan a stack of axial slices through the aortic root to localize the coronaries. Subsequent non-standard imaging planes may be used to demonstrate a greater length of vessel in a single slice but are rarely required for diagnostic purposes.

Dedicated coronary imaging sequences include both contrast-enhanced vs noncontrast-enhanced, targeted vs

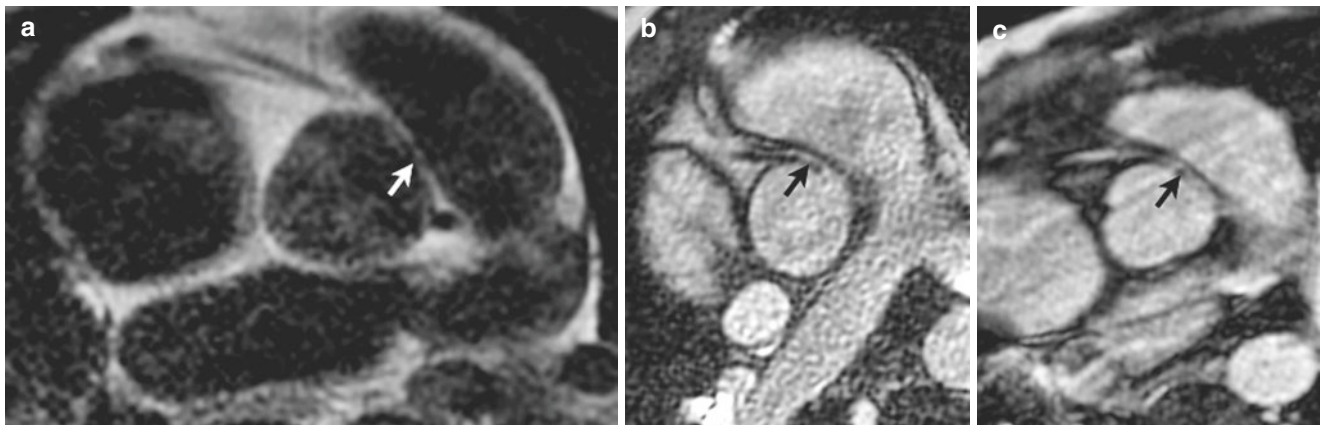


**Fig. 16.13** Comparison of three techniques for coronary visualization—example of an intramural course of an anomalous right coronary artery (*arrow*). Double inversion black blood imaging (**a**) is often perfectly adequate for demonstration of both the origin and proximal course of the coronary vessels. In this case, however, the proximal coronary segment was not clearly visualized with this technique. Thin slice SSFP imaging (**b**) is a good alternative which is simple to perform

and in this case clearly reveals the proximal intramural segment. Whole heart coronary MRA (**c**) is more time-consuming and technically challenging (see text). However the navigated 3D nature of the sequence allows for the acquisition of small isotropic data sets which may be post-processed in any plane of interest—something that is currently impossible with the first two techniques



whole heart acquisitions, and rectilinear  $k$ -space filling vs non-Cartesian methods. The fact that there are so many varying approaches may imply to the reader that none are perfect. Indeed, the cynic might suggest that the cardiac computed tomography (CT) revolution has rendered coronary MRA obsolete. While only the most ardent enthusiast would argue that CMR can compete with coronary CT, there have been genuine improvements in coronary MRA over the last few years which have led to it being a more widely used technique than previously. Furthermore, there remains an appropriate reluctance to subject young patients to ionizing radiation if similar information can be obtained by nonionizing techniques.

## 16.9 Advances in Coronary MRA in the Last Decade

Impediments to performance of coronary MRA have traditionally included the small size of the coronary arteries, the rapid cyclical motion due to cardiac contraction, and the cranio-caudal translation occurring as a result of respiration.

Historically simple free-breathing spin echo techniques were first applied to coronary imaging. At that time, lack of a method for dealing with either coronary or diaphragmatic motion rendered the images essentially nondiagnostic in most cases. Subsequently breath-held fast spin echo black blood methods such as the double inversion recovery sequence often provided (and still provide) perfectly adequate images for determining the origin and proximal course of the coronary vessels.

Before long there was a move toward techniques producing signal based on flowing blood. The early years of coronary MRA (cMRA) were based on use of first 2D and then 3D gradient echo sequences which were heavily dependent on inflow of blood to generate signal contrast. In later years there has been a shift toward use of the steady-state free precession (SSFP) pulse sequence which provides inherently high signal, relative T2 weighting, and an independence from inflow effects.

The principal challenges facing cMRA are those of small vessel size, rapid coronary motion, and respiratory diaphragmatic incursion and excursion, relatively poor contrast between blood-filled arteries and myocardium, presence of blood within coronary veins, and limited contrast between arteries and surrounding epicardial fat. Cardiac motion is generally handled through acquisition of  $k$ -space data lines in a relatively quiescent period of the cardiac cycle which at lower heart rates is usually in late diastole. The coronary rest period is less predictable at higher heart rates, falling in some cases in end systole. End systole is also generally preferable for data acquisition in patients with widely varying cycle

lengths as seen in atrial fibrillation where diastole is of inconstant duration.

Essentially two principal different methods of dealing with respiratory motion have been applied:

- Targeted volume (usually in a single breath-hold)
- Free-breathing navigated whole heart approach

The principal advantage of a targeted approach is the potential time saving, although in practice the required breath-holds of around 30 s are not always as easily achievable in patients as they were in the normal volunteers in which they were initially described. Some authors have addressed this through the implementation of non-Cartesian  $k$ -space filling regimes [41] which significantly reduce scan time (Fig. 16.14). Furthermore, the planning involves acquisition of a number of lower resolution scout images in order to orient the imaging plane. This can at times be rather fiddly although semiautomated three-point planning tools which allow the operator to define the course of the coronary artery of interest have been introduced by several of the vendors.

### 16.9.1 Navigated Whole Heart SSFP

The whole heart approach using a navigated free-breathing 3D SSFP sequence has found favor with many operators in recent years. Its advantages include the inherently high signal available (without exogenous contrast) which derives from its 3D nature (more signal than 2D techniques) and SSFP design (inflow independent unlike earlier gradient echo techniques). Importantly there is freedom from complex planning since an entire volume is generally acquired ensuring adequate coronary coverage (Movie 16.1).

Navigators are fundamental to the process of respiratory gating in the commercially available whole heart approaches. A navigator is simply a two-dimensional vertical “pencil beam” of echoes directed through the lung-liver interface, usually over the right diaphragmatic surface. This high temporal resolution pulse ensures that the position of the diaphragm is known in near real time. In this way the end-expiratory position of the diaphragm can be tracked, and image acquisition segmented to the appropriate phase of the cardiac cycle while the diaphragm is static (Movie 16.2). In practice, a small respiratory “acceptance window” is permitted (often 2–3 mm) on either side of the end-expiratory level around which data will still be acquired and used. Unfortunately, respiratory patterns may vary over the duration of the scan which can be as long as 15 min. More recently, compressed sensing techniques have been able to substantially shorten acquisition times, albeit with potential reduction in image quality [42, 43].



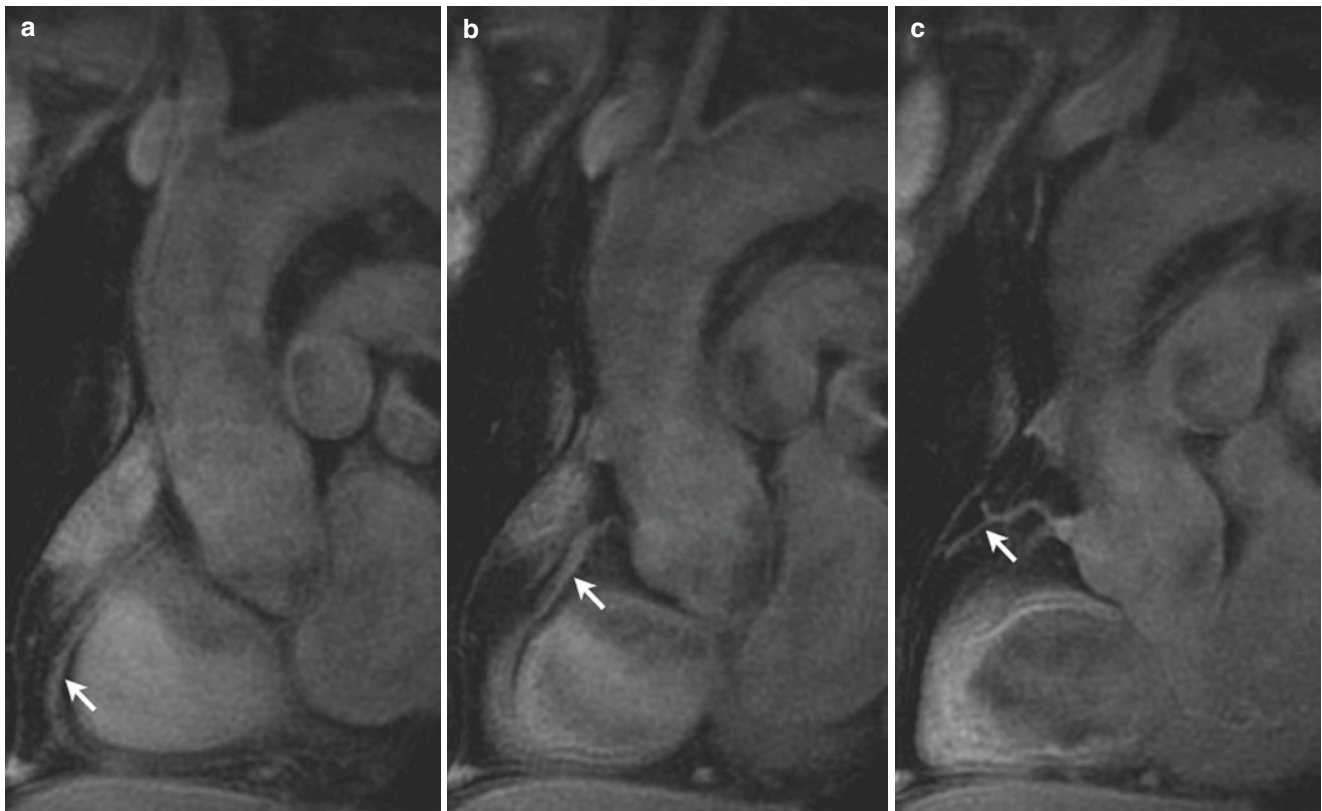


**Fig. 16.14** Non-Cartesian  $k$ -space filling for coronary MRA. One of the principal trade-offs in coronary MRA is the speed of acquisition versus the acquired spatial resolution. Non-Cartesian  $k$ -space filling approaches represent one attempt at resolving these conflicting require-

ments. Spiral  $k$ -space trajectories are efficient yet allow for high spatial resolution. The right coronary artery is easily visualized in this example (*arrow*, **a** and **b**). Note, however, that the small conus branch (*arrow*, **c**) is also unusually well depicted

Most vendors have the equivalent of a respiratory “gate and drift” mode which tracks the mean end-expiratory position of the diaphragm over time and adjusts the mean level of the respiratory acceptance window as required to maintain optimum navigator efficiency. Navigator efficiency of 40–50% is achievable and reasonable in most patients. Small numbers of highly experienced centers have been able to get efficiency rates as high as 70% or more on a regular basis, but this is difficult to achieve without fastidious attention to detail and the perfect patient. Navigator efficiency of less than 30% is usually due to poor technique or a widely varying patient respiratory pattern. Diaphragmatic restriction either by prone positioning or abdominal binding [44, 45]

may sometimes rescue an indifferent study when due to low navigator efficiency. We routinely apply an abdominal belt to promote shallow respiration with a gratifying reduction in scan time due to improved efficiency.

Use of a navigator makes it possible to routinely achieve a relatively high isotropic spatial resolution in the order of  $1 \times 1 \times 1$  mm voxel size (Fig. 16.15). This then allows for post-acquisition multiplanar reconstruction without any significant loss of image quality. This kind of spatial resolution is difficult to achieve in a breath-hold scan without advanced non Cartesian  $k$ -space filling methods (as shown in Fig. 16.13) or high levels of parallel processing (which adversely affects signal to noise ratio).

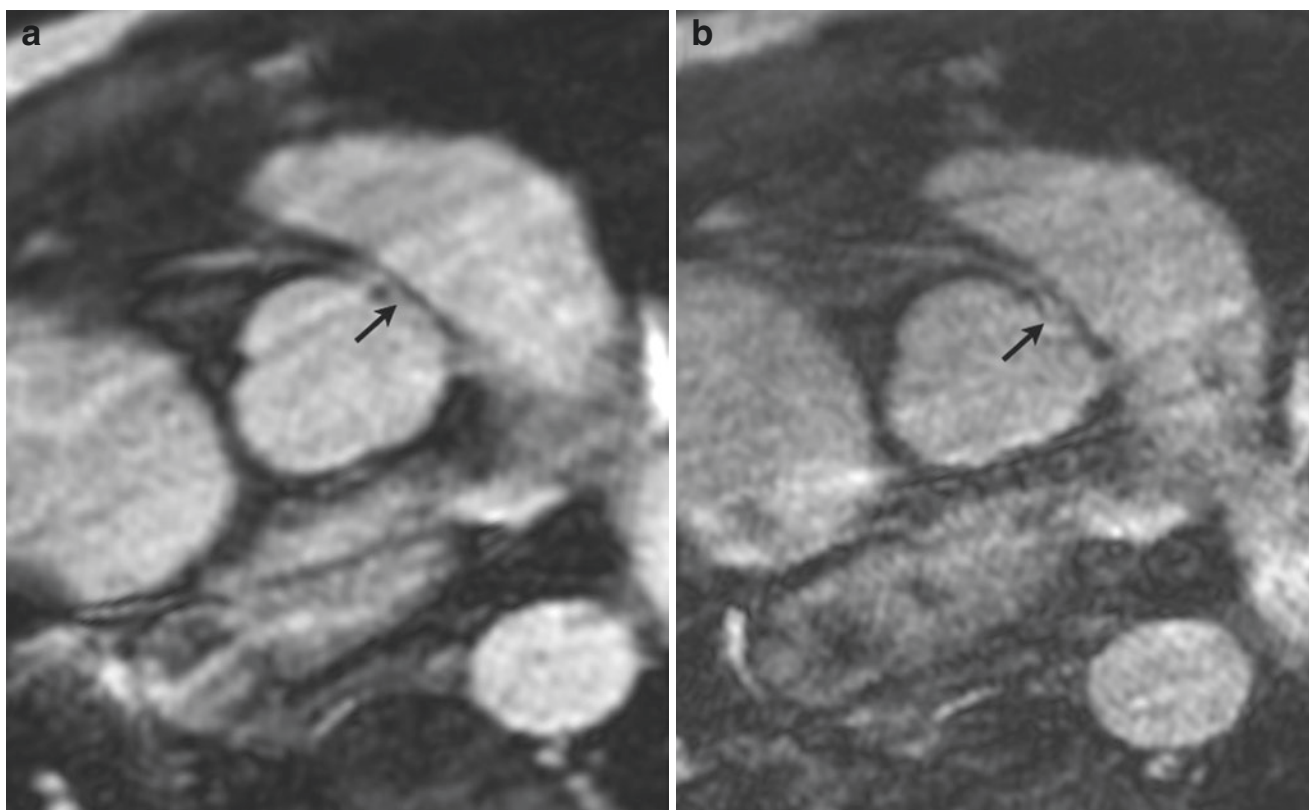


**Fig. 16.15** Trade-offs in coronary MRA—spatial resolution versus image noise. Whole heart coronary MRA achieves volumetric data sets through the acquisition of isotropic voxels. In theory the smaller the voxels the better for identification of these small coronary vessels. In reality, however, there is a trade-off between clarity and noise. Although vessel edges may be slightly less well defined at 1.5 mm isotropic reso-

lution (a), there is clearly better signal to noise than with 1.0 mm isotropic resolution (b). For the purposes of identifying and following the course of the coronary vessels, the former is usually more appropriate. The example shown here is of anomalous origin of the right coronary artery (arrow) from the left coronary cusp with proximal intramural course

## 16.10 Components of a Typical Whole Heart Sequence

A typical pulse schematic for a whole heart sequence is shown in Fig. 16.16. The individual portions of the pulse diagram are discussed briefly below.

### 16.10.1 T2 Preparation

Contrast between myocardium and coronary arteries is lower than ideal using a simple SSFP technique. However, myocardium has a relatively short T2 (50 ms) compared to blood (220 ms). By tipping the magnetization into the x-y plane and then resampling at a relatively short time interval with a refocusing pulse, much of the T2 signal decay will already have occurred for the myocardium but not for arterial blood—therefore the use of a T2 pre-pulse tends to suppress signal from myocardium. An additional advantage stems from the fact that deoxygenated blood has a shorter T2 time (roughly 35 ms) than oxygenated blood (220 ms) and thus a

T2 preparation pulse also serves to reduce the signal from coronary veins which is desirable to simplify image interpretation. The usual duration of this pre-pulse is 50–80 ms.

The effect of a T2 preparation pulse on recoverable signal from different cardiac components at progressive time points is shown in Fig. 16.17. Note that arterial blood has a much slower (i.e., less steep) T2 decay curve than either myocardium or blood within the coronary veins. Thus, early interrogation of available T2 signal with a refocusing pulse will maximize the signal intensity differences between these structures, favoring coronary arterial blood.

### 16.10.2 Navigator Pulse

The typical navigator, discussed earlier, is a two-dimensional selective excitation pulse (sometimes referred to as a “pencil beam”) which is positioned on the dome of the right hemidiaphragm in order to monitor the liver-lung interface during respiration. The navigator is first run in “scout mode” in which a free-breathing coronal set of images is acquired to determine the end-expiratory position of the heart from

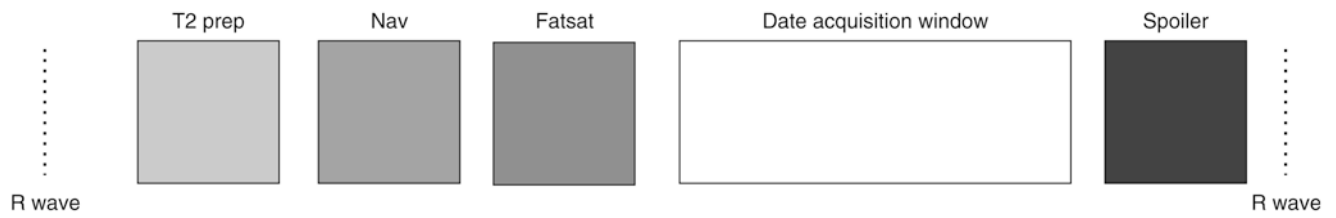


**Fig. 16.16** Typical pulse sequence schematic for whole heart coronary MRA (see text)

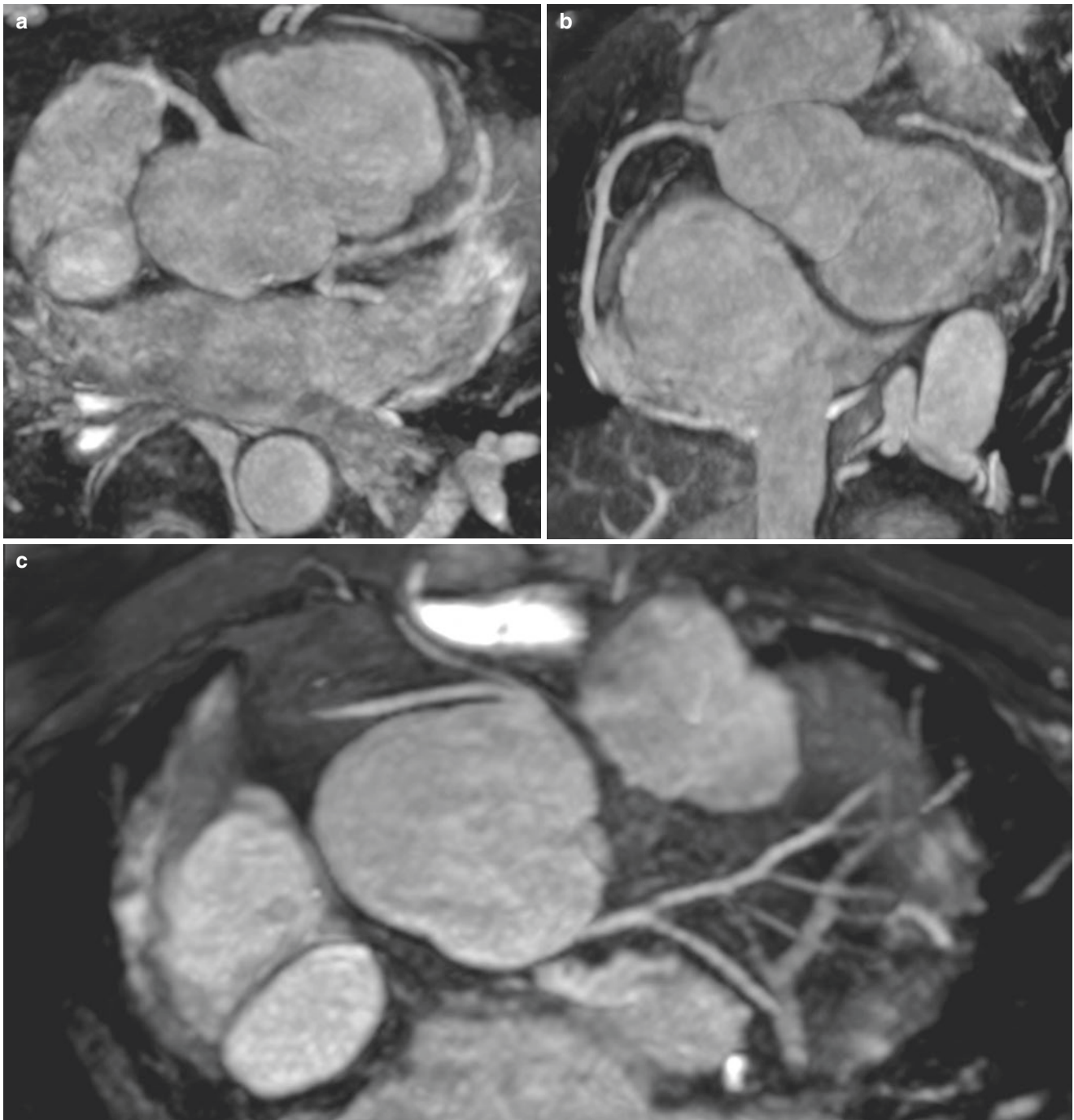


**Fig. 16.17** Examples of successful whole heart coronary MRA. Three separate examples (a–c) of good coronary definition achieved with use of a whole heart technique. Note that although the presence of gadolinium contrast agent is not required for the SSFP-based whole heart

sequence used at 1.5 T, where present in the blood pool it tends to produce slightly better image quality and our practice is therefore to run this sequence after the usual late gadolinium enhancement images have been acquired

which the axial stack is subsequently planned. A free-breathing axial stack is also required during setup to identify the dome of the diaphragm in this plane and place intersecting navigators on the dome in the end-expiratory position for the subsequent whole heart acquisition. The navigator pulse takes approximately 40 ms to run.

### 16.10.3 Fat Saturation Pulse

The coronary arteries are surrounded by epicardial fat which is usually high signal on many cMRA pulse sequences. To reduce this signal, a fat suppression pre-pulse is commonly applied prior to data acquisition. There is a spectral shift of approximately 3.5 parts per million between lipid and water, and this can be exploited to either saturate the lipid signal or instead selectively excite the water molecules to emphasize the signal within the coronary arteries. It should be noted that the distal coronary tree which is less often surrounded by fat benefits more from T2 preparation than from fat saturation per se.

### 16.10.4 Data Acquisition Window

The requirement to “freeze” coronary motion during image acquisition necessitates identification of that portion of the cardiac cycle when the coronary arteries appear relatively static. Since the RCA typically exhibits a wider arc of motion than the left coronary system, this vessel is usually employed as a marker to identify the coronary rest period.

A four-chamber cine reviewed image of the heart can be used which, when reviewed frame by frame, allows recognition of the first time point at which RCA motion stops and the duration (in milliseconds) until it begins moving again (Movie 16.3). This determines the period of time during each end-expiratory cardiac cycle that the operator will set for data acquisition during the whole heart MRA itself. The data

acquisition window can in theory equal the coronary rest period, which at slow heart rates may be as long as 150 ms. In practice, and at the more typical higher patient heart rates, an acquisition window of 50–60 ms usually produces excellent results. An incorrect selection of window starting point or duration will of course introduce coronary motion during data acquisition with predictable and uninterpretable results.

For fine-tuning of the window at higher heart rates, it may be necessary to use a four-chamber scout with a higher than normal temporal resolution. For example, improving the temporal resolution of the cine image to 10 ms frames and reconstructing 80 phases (rather than the more typical 35–50 ms), reconstructed at 25 phases permit very accurate delineation of the coronary rest period which would otherwise be difficult to achieve (Movie 16.4). (However, achieving this kind of temporal resolution with adequate spatial resolution in a single breath-hold requires the use of three- to four-time acceleration with parallel imaging.)

Finally, it should be remembered that diastolic length is a function of heart rate. As heart rate increases, systole remains unchanged in duration but diastole shrinks. Above 80 bpm there may be little or no available diastolic rest period in which to image. In this case we have learned from our contemporaries in the cardiac CT world that—with a sufficiently short acquisition window of around 50 ms—good images may be acquired in late systole when there is also a brief period of coronary rest. Although it is seldom done in clinical practice, the use of beta-blockers and sublingual nitrate is as pertinent to coronary MRA as it is to CTA.

With close attention to the foregoing details, the results from whole heart MRA are sometimes gratifyingly good (Fig. 16.18). Unlike other methods of visualizing the coronary arteries, whole heart MRA also has the advantage that the data set is an isotropic volume which can therefore be displayed in a number of ways, as with cardiac CT, including multiplanar reformats, curved reformats, and center line extractions (Fig. 16.19).



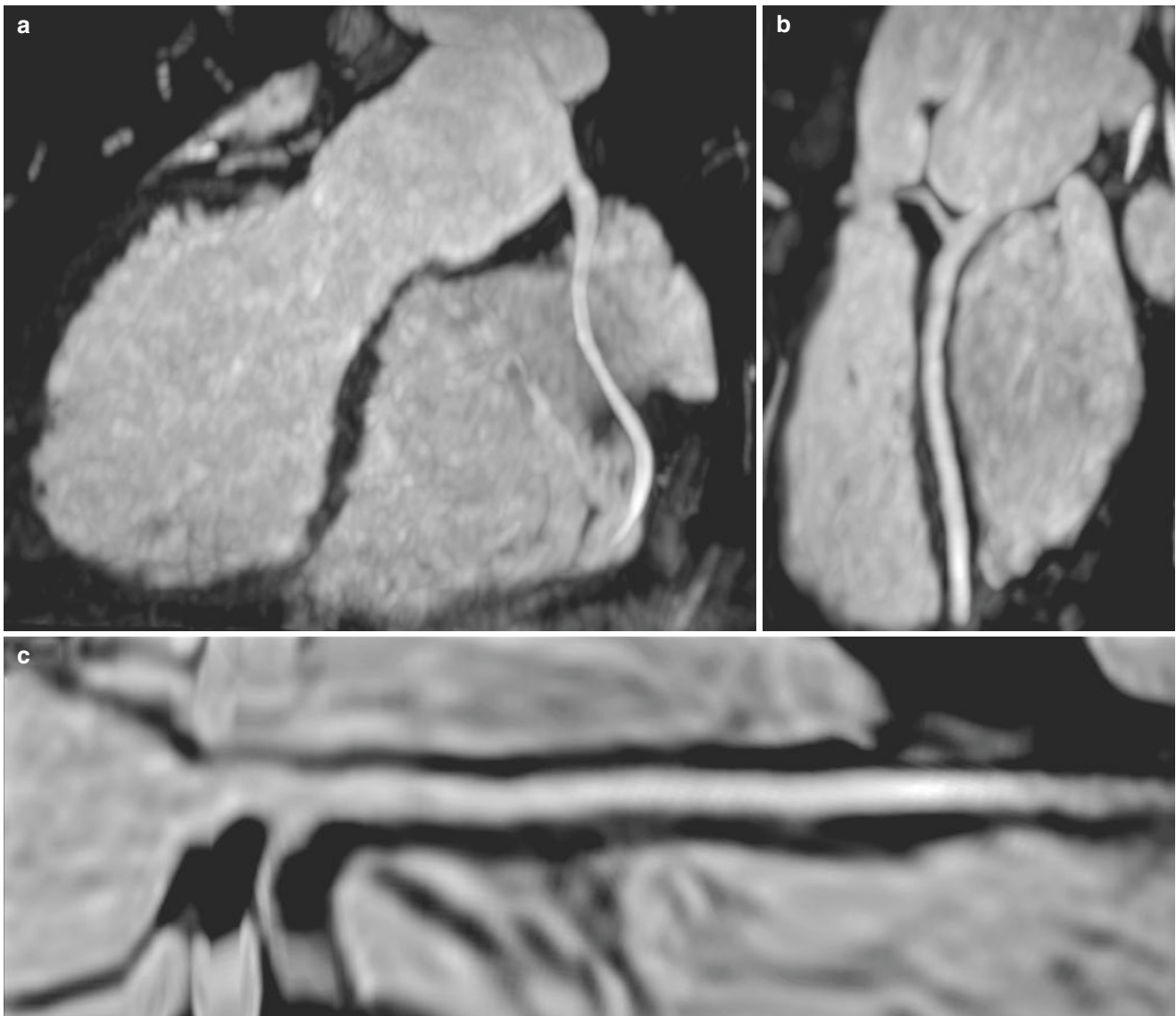


**Fig. 16.18** Post-processing of the volumetric data set. Since whole heart acquisitions are usually 3D isotropic volume acquisitions they may be post-processed in just the same way that thin slice CT data sets can be. This includes production of multiplanar coronary reformats (**a**, **b**) as well as straightened center line extractions (**c**)

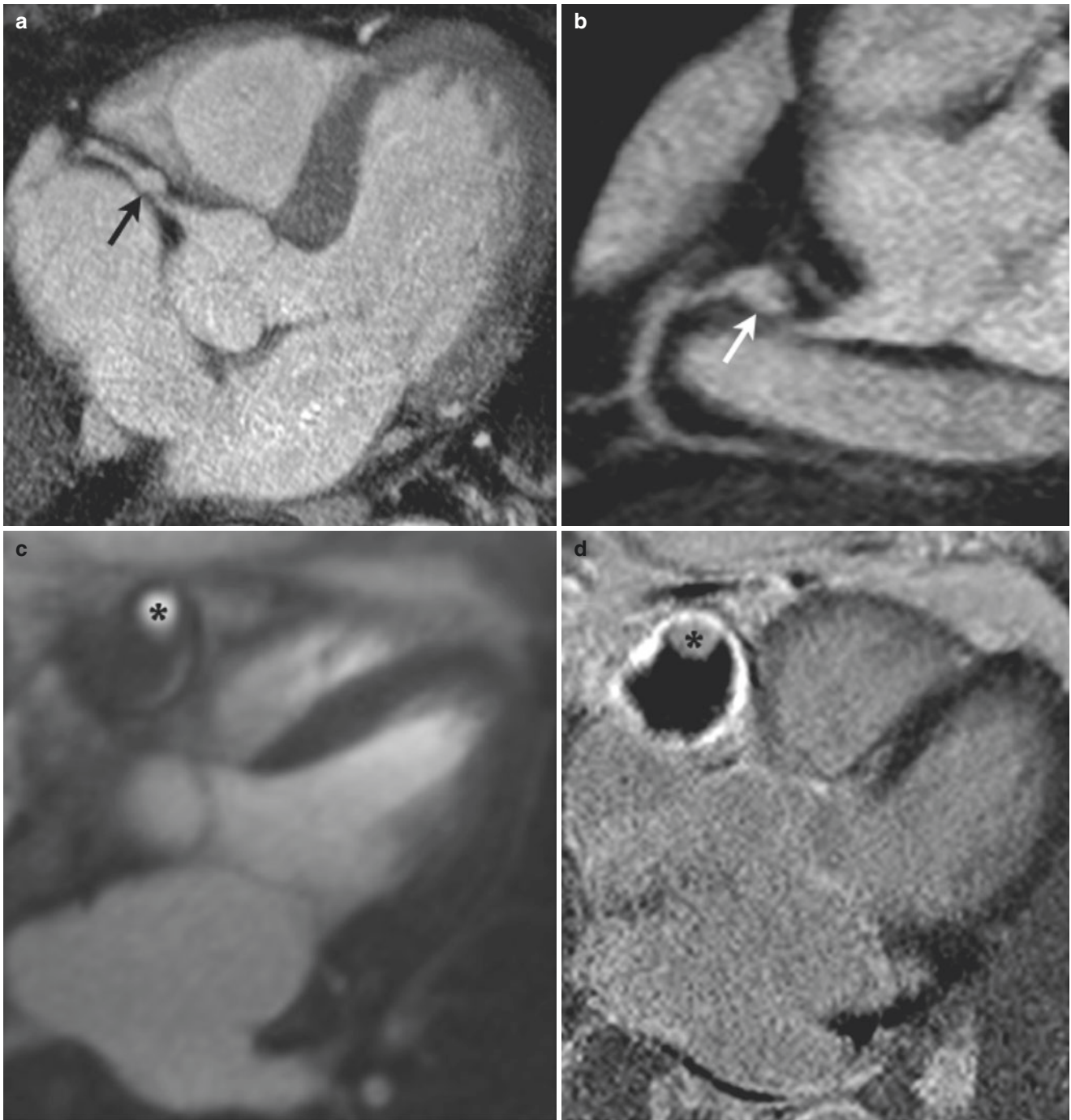


**Fig. 16.19** CMR in Kawasaki disease. Patient 1 has a small proximal right coronary artery aneurysm (*arrows, a, b*) that is well delineated by coronary MRA. Patient 2 has a much larger aneurysm lying in the right atrioventricular groove (*c, d*). Dynamic perfusion CMR (*c*) demonstrates an enlarged but centrally patent portion of the aneurysm (*aster-*

*isk*) which represents the ectatic right coronary artery. Late gadolinium enhancement images (*d*) reveal low signal thrombus posterior to the lumen. Note also the circumferential enhancement surrounding the aneurysm (*d*) which hints at the inflammatory etiology of the lesion

### 16.11 Stress CMR for Coronary Anomalies

Since the relevant clinical endpoint for patients with coronary anomalies is sudden cardiac death and since the mechanism is assumed to be ischemia-induced ventricular arrhythmia or infarction, it appears logical to extend the role of CMR beyond the simple identification of a coronary anomaly and seek to uncover the underlying ischemic pathophysiology as well.

CMR is ideally suited to the task [46–48]. Both dobutamine and vasodilator stress CMR have been validated in the setting of adult coronary disease, and neither poses a significant technical challenge in congenital heart disease. The unobstructed field of view and lack of ionizing radiation are both major benefits of a CMR-led approach to ischemia detection in this relatively young population who have—at times—complex and confusing anatomy.

Most stress CMR work is performed with vasodilator drugs adenosine, dipyridamole, or regadenoson. There is less published experience with dobutamine stress MR for coronary anomalies, although it has been applied to other questions in the congenital field and certainly regarded as safe and reasonable [49]. One paper reported high technical success rates with an aggressive protocol that involved graded infusion of dobutamine up to 40mcg/kg/min plus atropine as done in standard stress echocardiography [50]. However, a new wall motion abnormality was identified in only 1 out of 32 studies in a relatively heterogeneous congenital patient cohort. It is worth noting that two thirds of the studies were performed under general anesthesia. In the author's experience, high-dose dobutamine stress is often less well tolerated by patients than vasodilator stress and is more complicated to perform in the magnet environment unless done regularly.

Finally, the technique of late gadolinium enhancement which is now accepted as the reference standard for the identification of myocardial viability clearly merits incorporation into a standard CMR protocol for coronary assessment since infarction is assumed to be one of the modes of morbidity and patient attrition.

### 16.12 The Comprehensive CMR Examination For Suspected Coronary Anomalies

In general, there are three main categories of coronary anomaly patient: those in whom an anomaly is suspected, those in whom an anomaly has been surgically repaired, and those in whom the discovery of an anomaly is incidental during a study performed for another purpose. The aim of the examination must therefore be tailored to some extent to the background history and the current clinical question under consideration.

In general, a minimum CMR exam should include assessment of the coronary origin and proximal course adequate to categorize the anomaly as either high risk (inter-arterial, ALCAPA, ARCAPA) or a lower risk group (pre-pulmonic, retroaortic, intraseptal, etc.). Coronary aneurysms should be excluded in patients with childhood Kawasaki disease—a situation where CMR has been proved to be as accurate as catheter angiography [32]—or adult Behcet disease (Figs. 16.20 and 16.21). Coronary narrowing may be ostial as a result of reimplantation following the arterial switch procedure (Fig. 16.22), Ross operation, or Bentall procedure or may occur due to enlargement of adjacent vascular structures—this latter situation is sometimes encountered in the tetralogy variant with absent pulmonary valve when gross pulmonary arterial enlargement is the norm and can result in

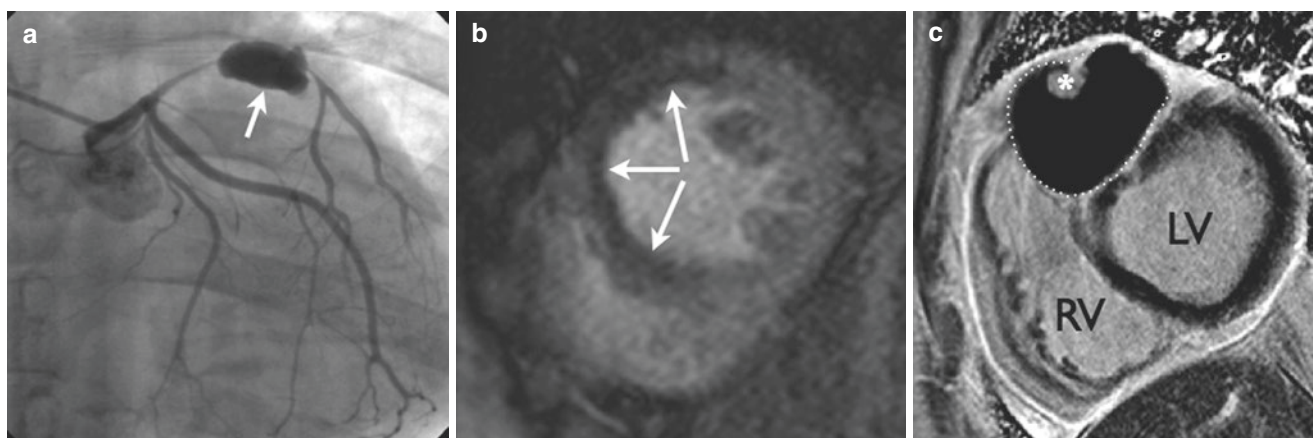


**Fig. 16.20** CMR in Behcet disease. Coronary angiography (a) shows a large aneurysm involving the mid portion of the left anterior descending coronary artery in this patient with confirmed Behcet disease. The vessel appears to taper both on its entrance into and exit from the aneurysm. The physiological significance of this is confirmed by adenosine

stress perfusion cardiac MRI (b) in which a substantial perfusion defect is visible in the antero-septum (white arrows). Late enhancement imaging (c) reveals a large portion of the aneurysm to contain low signal thrombus with a central patent core (asterisk) representing the native vessel. LV left ventricle, RV right ventricle



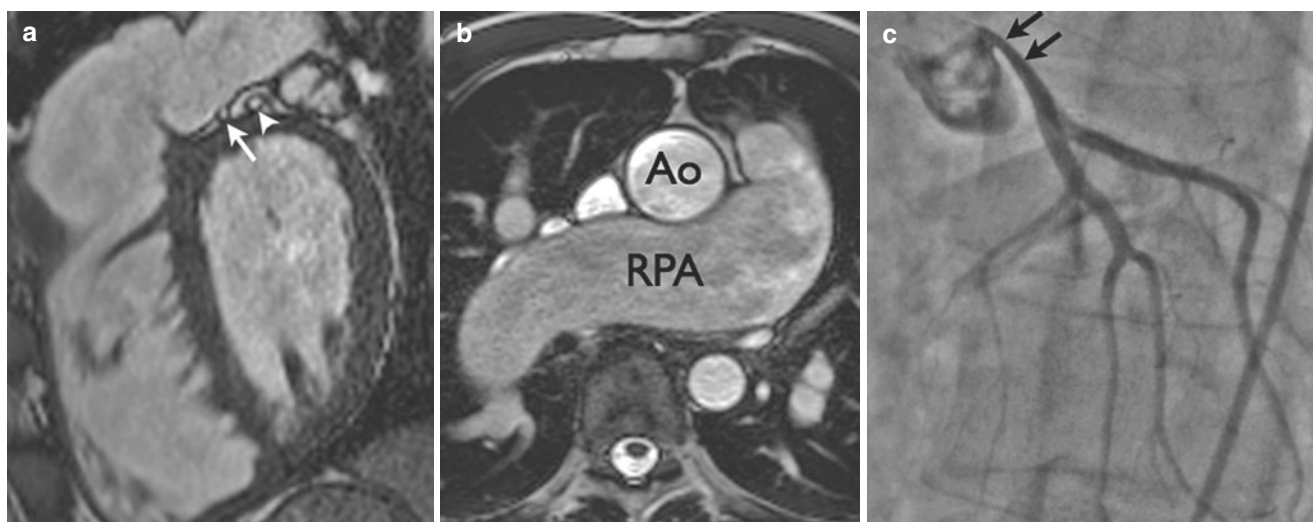


**Fig. 16.21** Compression of the left main coronary artery. This rare complication was seen in a patient with the tetralogy-absent pulmonary valve complex. In this condition life-long absence of the pulmonary valve results in severe pulmonary arterial enlargement. This 55-year-old manual worker presented with typical angina and subsequently had a strongly positive treadmill exercise test. Cine SSFP demonstrates his left main coronary artery (arrow, **a**) to be compressed between the

undersurface of the main and right pulmonary artery (**b**) and the heart. The left anterior descending portion (**a**, arrowhead) appears spared. Catheter angiography confirms significant extrinsic compression of the left main (arrows, **c**). Direct visualization of pulsatile coronary compression by the pulmonary artery was achieved using dynamic cardiac CT (Movie 16.5). Left main osteoplasty and pulmonary arterial plication was performed at open heart surgery with subsequent full relief of symptoms. *Ao* aorta, *RPA* right pulmonary artery

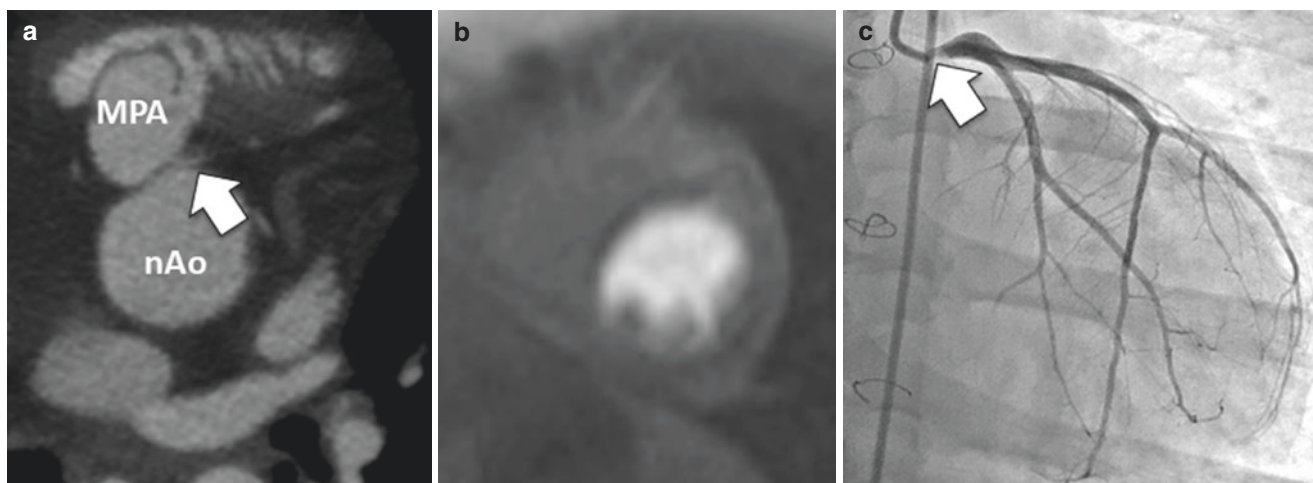


**Fig. 16.22** Late coronary stenosis following arterial switch for *d*-transposition. (**a**) Axial coronary CT image in a patient with exercise-induced chest pain; the origin of the left main coronary was not clearly seen. (**b**) Stress perfusion CMR indicated a large perfusion defect

(asterisks) in the territory of the same vessel. (**c**) Invasive coronary angiography confirmed a very tight ostial stenosis which required surgical repair. *MPA* main pulmonary artery, *nAo* neo aortic root

left main or left anterior descending coronary compression (Fig. 16.21, Movie 16.5).

Since myocardial infarction is a recognized complication both of many anomalies and a possible iatrogenic sequela of surgery, assessment of ventricular function and myocardial scar can also be considered mandatory (Figs. 16.23 and 16.24). One recent innovation has been the development of “black blood” LGE sequences where signal is suppressed

from the blood pool, to aid with identification of subendocardial scar which might otherwise be missed [51].

In some instances, there may be a more specific clinical question relating to known preexisting anatomy and planned percutaneous intervention. In patients with tetralogy of Fallot and significant pulmonary insufficiency, for example, an increasingly important role for CMR is to establish the relationship between the site of



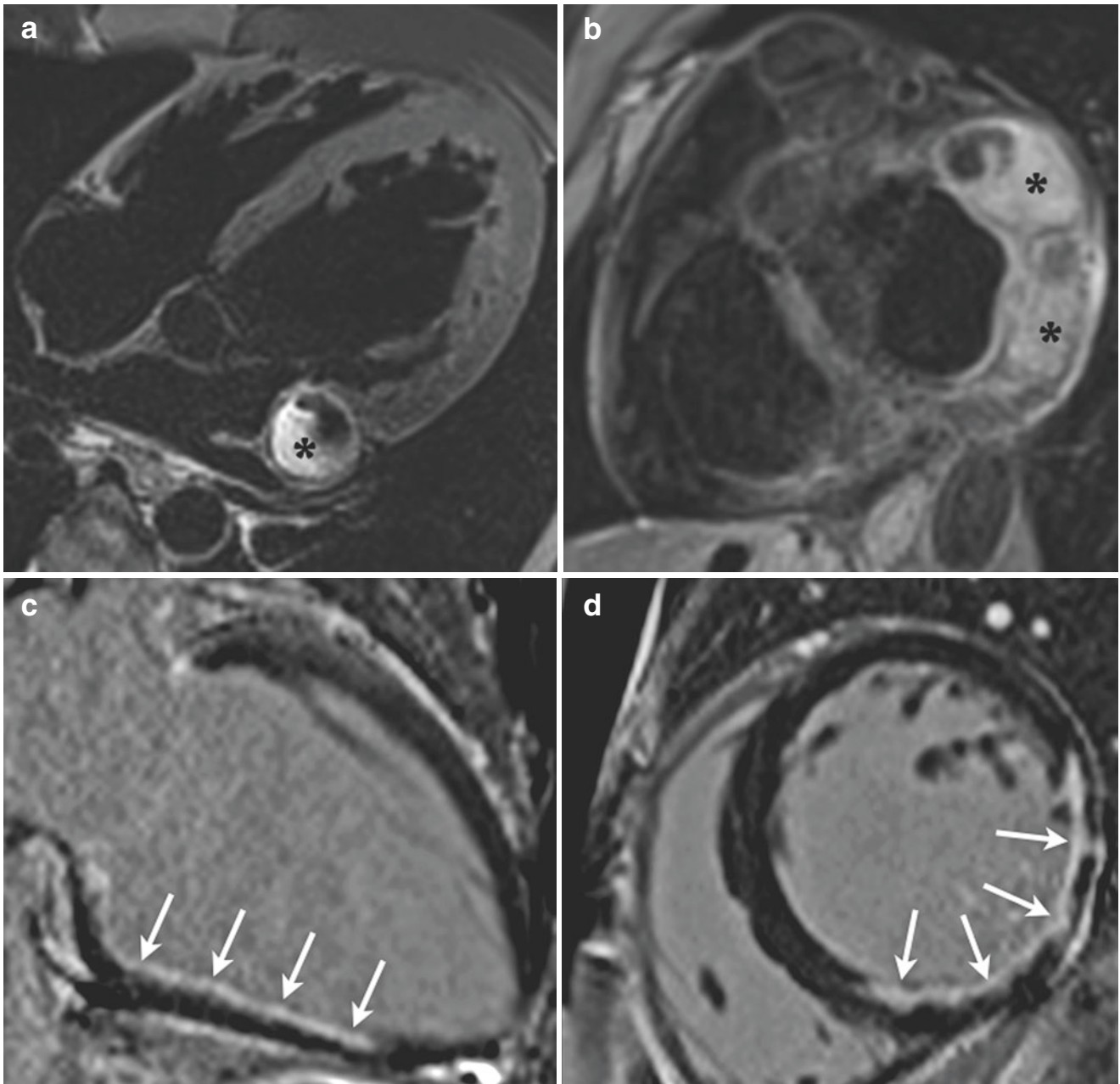


**Fig. 16.23** Example of myocardial scar secondary to Kawasaki disease. Several large aneurysms are evident in the left atrioventricular groove (**a, b, asterisks**). These inflammatory aneurysms contain thrombus which has the potential to embolize distally. This has occurred in this patient whose late enhancement (LGE) imaging depicts a subendo-

cardial area of infarction in the inferolateral wall (**c, d, arrows**). This was unknown prior to the CMR exam and highlights the importance of including LGE imaging as part of the CMR protocol in congenital or inflammatory coronary disease

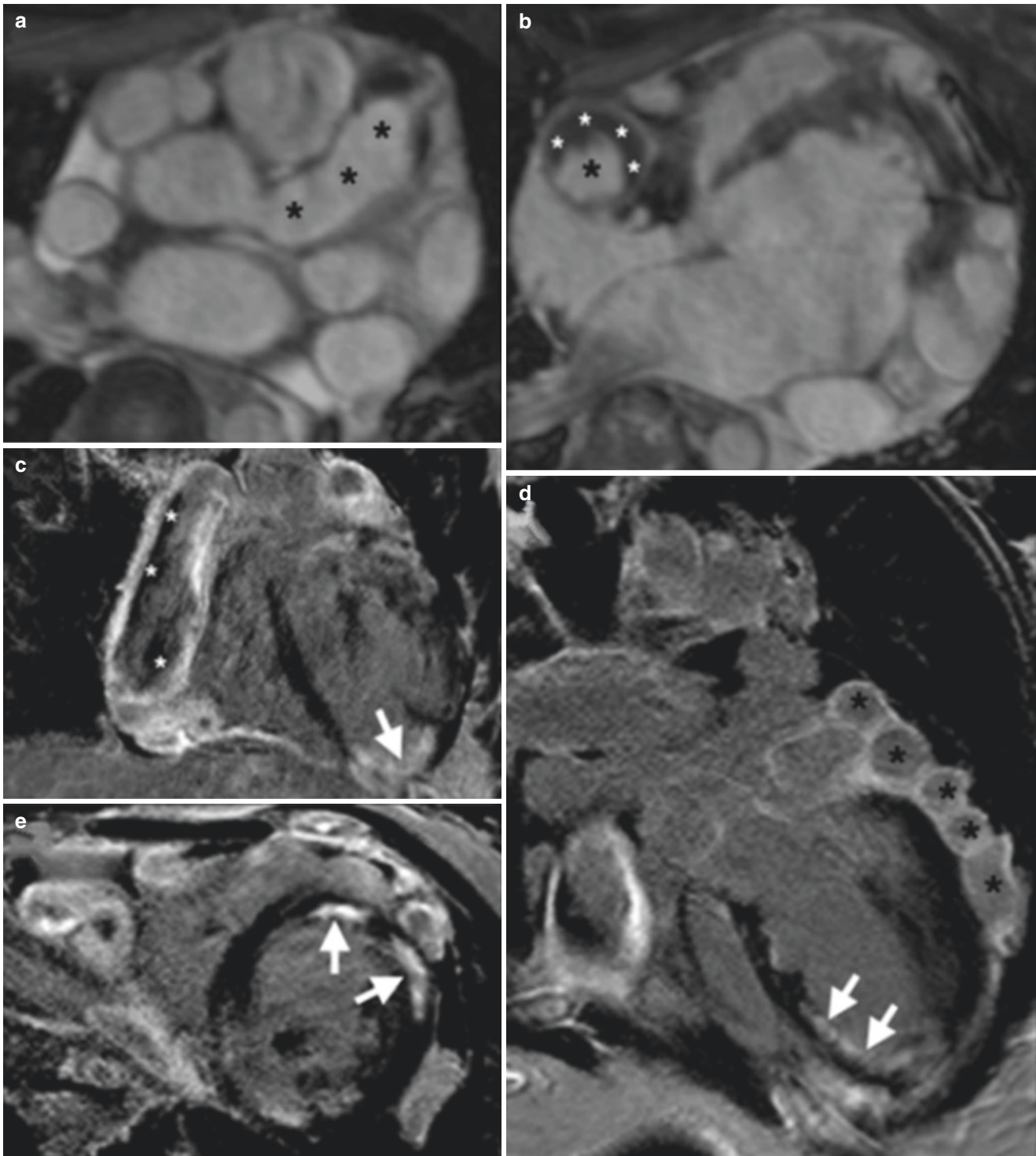


**Fig. 16.24** Unexplained diffuse coronary artery dilatation in Noonan syndrome. **(a)** Whole heart coronary MRA demonstrates diffuse dilatation of all coronary arterial structures (left main coronary artery highlighted, asterisks). **(b)** Right coronary artery aneurysm with patent lumen (black asterisk) but rim of thrombus (white asterisks). **(c)** Coronal LGE image shows a hugely dilated RCA (2 cm in diameter) with diffuse enhancement of the vessel wall (for reasons unknown) as

well as thrombus (asterisks) lining the vessel wall. Transmural scar is present at the LV apex (arrow), likely due to embolism. **(d)** Four-chamber LGE view with infarction in the mid- to distal septum. Note also multiple circular lesions (asterisks) adjacent to the LV wall which represent the dilated and convoluted left circumflex artery. **(e)** Short-axis LGE image showing embolic infarction in the mid-anterolateral LV wall.



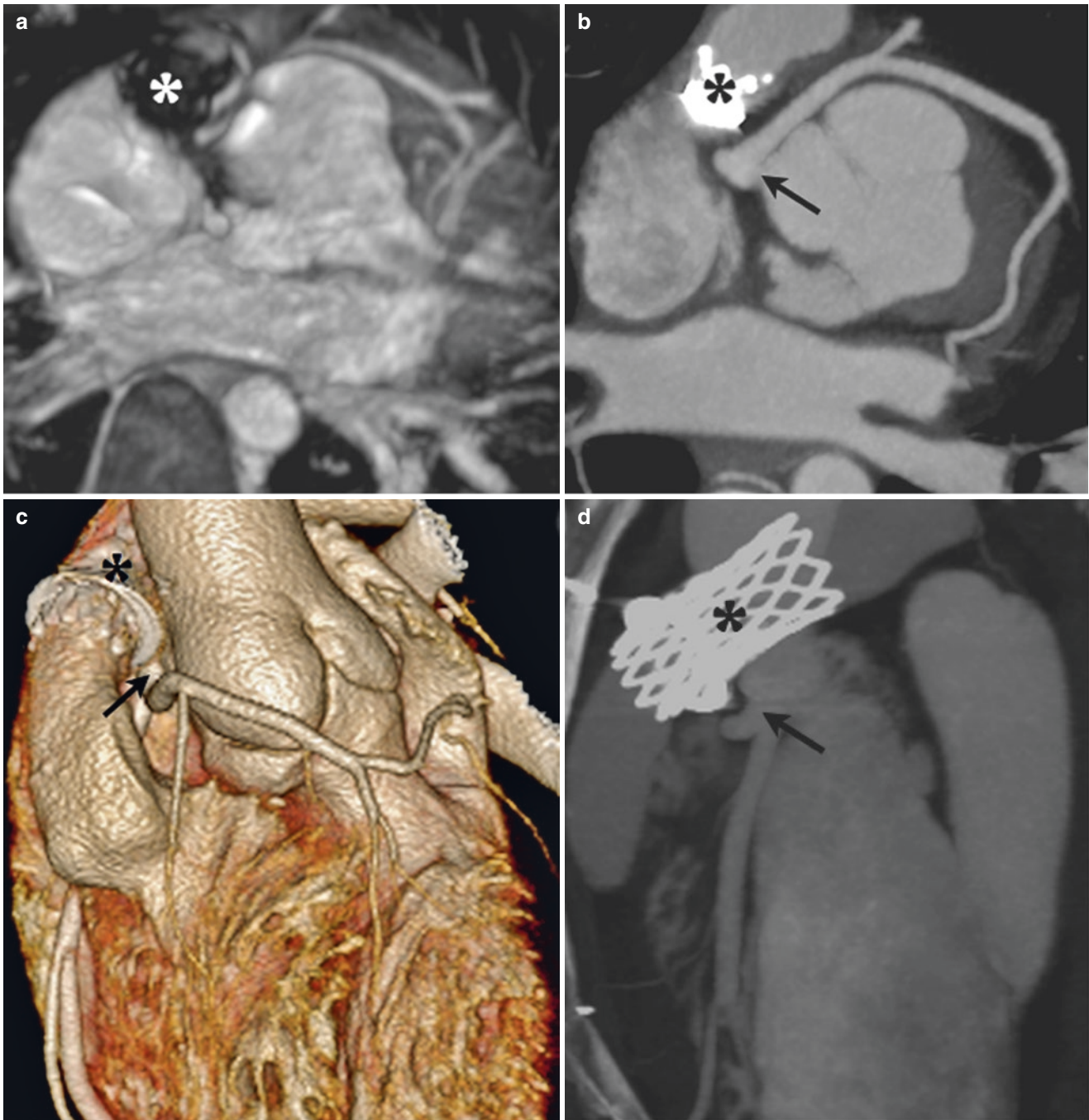


**Fig. 16.25** Suboptimal coronary visualization at CMR due to metal stent. This patient required re-stenting of an RV conduit which had previously been stented. One of the concerns of conduit stenting is any possible compression effect on adjacent coronary arteries. The origin of the anomalous left coronary artery (*arrow*) shown in (a) was obscured

by susceptibility artifact from the adjacent pre-existing stent (*asterisk*). This is one situation in which switching to cardiac CT is required—the relationship of the vessel to the conduit pre re-stenting (b) and post re-stenting (c, d) is clearly appreciated

“touchdown” for a percutaneous pulmonary valve in the main pulmonary artery and any adjacent coronary artery which might be at risk of compression by stent placement (Fig. 16.25).

### 16.13 Unoperated CAA

Unoperated patients may be particularly challenging since the question usually concerns not only the course of the anomalous artery but also its physiological consequences in

the form of myocardial ischemia or volume loading of a ventricle due to shunt flow. Standard anomalies of origin or course will not cause shunting (since termination is normal), although may cause ischemia. As discussed, there is limited practical experience, and no consensus on whether CMR is adequate for the detection of ischemia using any method in these cases. The three most common lesions leading to shunting as well as possible ischemia are the RCA to coronary sinus fistula, the ALCAPA, and the ARCAPA anomalies. The ALCAPA lesion is only rarely encountered *de novo* in an adult patient [48, 52–55]. However, its “sister” lesion—ARCAPA—is less often life threatening and occasionally

presents for the first time in adult life. Both lesions result in a bulk steal of blood from the contrary coronary artery down a diastolic pressure gradient from the aortic root to the pulmonary artery. The coronary arteries generally become severely dilated as a consequence of significantly increased flow, and increased size and tortuosity of coronary vessels are a sign that a coronary shunt lesion should be expected (Movie 16.6). Since multiple collateral pathways exist in this type of lesion, it is also common for the smaller intramyocardial vessels to be dilated, and this is usually most obvious in the interventricular septum (Fig. 16.26).

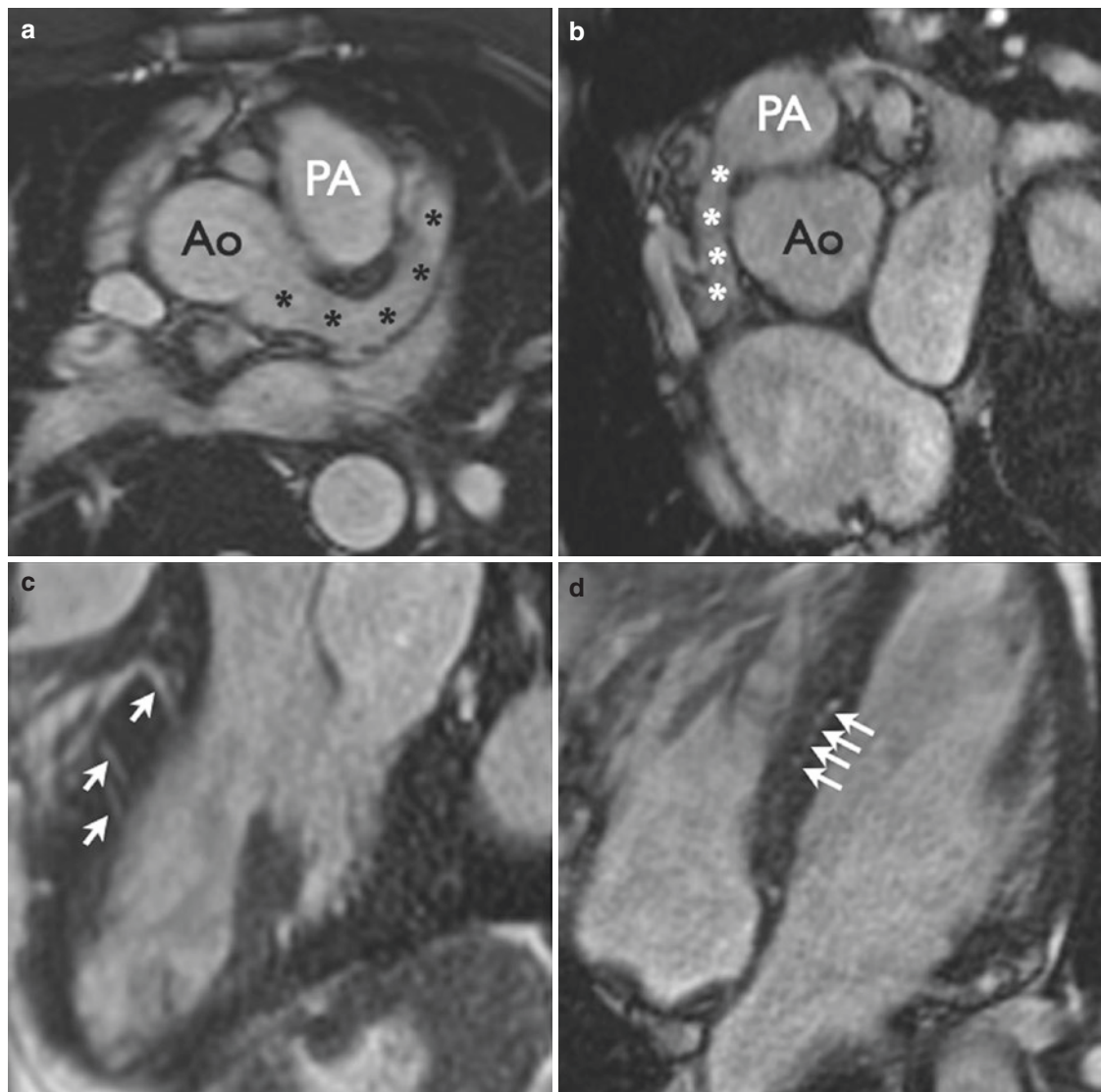


**Fig. 16.26** Anomalous right coronary artery from the pulmonary artery. The left main and left anterior descending coronary arteries (**a**, *asterisks*) are severely dilated. This is often a clue that there is a high pressure to low pressure shunt with high volume flow occurring down a pressure gradient. This is seen to be true on the short-axis SSFP image

(**b**) where the right coronary artery (*asterisks*) is observed to drain into the pulmonary artery (*PA*) rather than arise from the aorta (*Ao*). Multiple dilated collateral networks connect the left and right coronary systems, most often visible in the interventricular septum (**c**, **d**, *arrows*)



### 16.14 Operated CAA

Surgical repair of coronary anomalies depends on the nature of the anomaly itself [56]. Inter-arterial LMS or LAD lesions are generally treated with coronary artery bypass for which follow-up is conventional and generally beyond the scope of CMR except perhaps for assessment of LV function and myocardial perfusion. Only a true enthusiast would endeavor to image the bypassed coronary circulation by CMR instead

of CT or conventional angiography although the potential for this has been demonstrated by several groups [57–59]. One exception is imaging of the transposition patient who has undergone arterial switch where several groups have demonstrated the utility of CMR in children [60] and in adults [46].

Repaired ARCAPA/ALCAPA or coronary artery to coronary sinus fistula lesions are, however, eminently suitable for follow-up by CMR [61]. The chief focus of interest is the anastomotic site of the reimplanted anomalous artery into

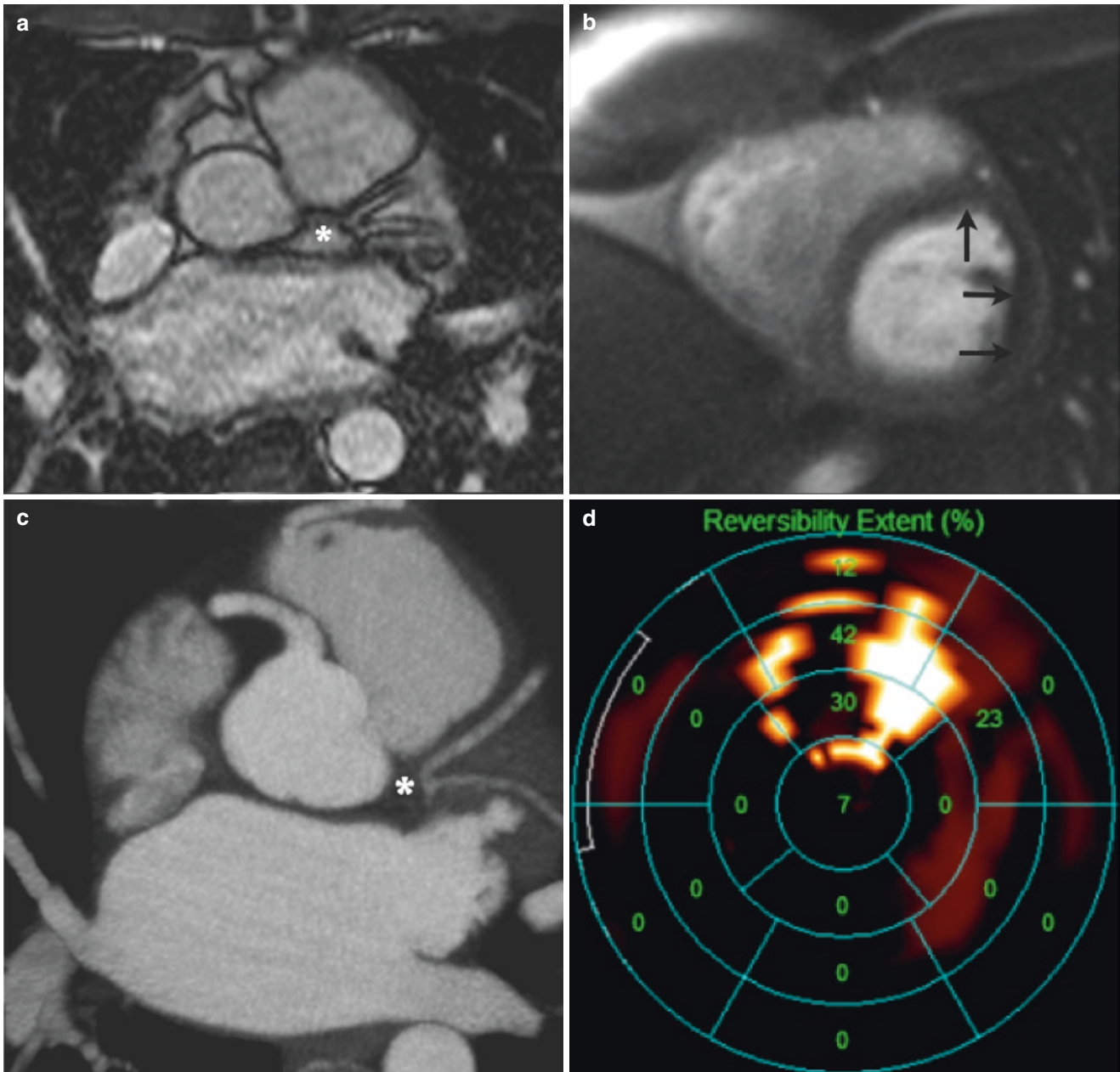


**Fig. 16.27** Postoperative chronic ischemia following ALCAPA repair. Routine imaging in this young adult following infantile repair of anomalous left coronary artery from the pulmonary artery (ALCAPA) demonstrated unexpected absence of the left main coronary segment (a, *asterisk*). Cardiac CT (c) was equally unable to visualize the re-

implanted left main segment at the aortic origin (*asterisk*). Stress perfusion CMR (b) and technetium MIBI (d) both confirmed the presence of a large area of reversible ischemia (arrows in (b)). The patient has been offered surgical revascularization

the aortic root since in some cases there may be asymptomatic post-surgical distortion or even atresia of the proximal vessel with demonstrable ischemia and/or scar (Fig. 16.27).

### 16.15 When the Going Gets Tough

Although the preference at our institution is to perform whole heart MRA for most coronary anomalies, simple cine SSFP or black blood imaging is acceptable where the principal question relates to the proximal course of the artery. At times, however, it can be difficult to comment on ostial narrowing or fully comprehend the course of complex tortuous fistulas even with good-quality coronary MRA and cine imaging—and in those instances, prompt transfer of the patient to the cardiac CT scanner is a wise action rather than a nihilistic expression of defeat [62]!

### 16.16 Limitations of CMR and Considerations for Imaging Coronary Anomalies

As Mark Twain is reported (without evidence) to have said: “to a man with a hammer everything looks like a nail.” However, no handyman relies upon a single tool, and the

same should apply to the cardiac imager. CMR may not always be the modality of choice to assess all cases of coronary anomaly, and the multiple multi-modality figures provided in this chapter speak for themselves in this regard.

Selection between CMR, CT, catheter angiography, echo, etc. depends partly on the age of the patient, partly on the question being asked and partly also on the physical condition of the patient. For example, young children are considered highly radiosensitive such that echo or CMR would usually be the preferred methods of investigation.

In contrast a sick patient or claustrophobic patient, or one immediately postoperative in whom a surgical complication is suspected, may not tolerate the prolonged examination times common to CMR. In this situation cardiac CT may be quicker and kinder as well as less susceptible to breathing artifacts. Alternatively, if an assessment of myocardial perfusion or scar is required, nuclear medicine and CMR are the modalities of choice.

Finally, the presence of metallic coils, calcified conduits, or stents within the thorax may limit the visibility of the coronary arteries by CMR and cardiac CT is usually an excellent alternative in this situation (Fig. 16.25).

Points to consider in selection of the most appropriate technique for depiction of a coronary anomaly and its potential consequences are given in Table 16.3.

**Table 16.3** Relative merits of imaging modalities in the assessment of coronary anomalies

	CMR	Cardiac CT	Echo	Invasive angiography
Spatial resolution	Good	Excellent	Excellent	Excellent
Temporal resolution	Good	Fair	Excellent	Excellent
Potential morbidity	Low	Low	None <sup>a</sup>	High
Coronary visibility	Good	Excellent	Poor (except children)	Excellent
Coronary course	Good to Excellent	Excellent	Poor	Fair/Difficult
Coronary origins	Excellent	Excellent	Fair (except children)	Excellent
Demonstration of small fistulae	Fair	Good	Fair	Excellent
Demonstration Of large fistulae	Excellent	Excellent	Fair	Fair (often incomplete opacification)
Wall motion abnormalities	Excellent	Fair	Excellent	Good
Scar demonstration	Excellent	Poor	Poor	Poor
Perfusion abnormality	Excellent	Not established	Good	Fair
Radiation exposure	None	Low to moderate <sup>b</sup>	None	Moderate
Dependence on patient window for image quality	None	Low (noise if obese)	High	Low
Suitability for sick patients or those unable to breath hold	Poor	Good	Excellent	Good to excellent
Identification of coronary thrombus	Excellent	Excellent	Poor	Poor
Claustrophobia	Can be problematic	Rarely problematic	Not problematic	Not problematic
Presence of metal	Can be problematic	Rarely problematic	Not problematic	Not problematic

<sup>a</sup>Unless intravenous contrast given

<sup>b</sup>Low if a prospective trigger technique is used, moderate if retrospective gating applied

## 16.17 Conclusion

Coronary anomalies may appear to be one of the more arcane topics for the CMR practitioner, but they appear surprisingly often in any busy cardiac practice, and a working knowledge of the principal types of anomaly is essential. Most anomalies are straightforward to image without great technical prowess or advanced imaging techniques. Ventricular function, myocardial perfusion, and scar are often intrinsic parts of the patient assessment since it is these aspects that in many cases will dictate subsequent management.

### Practical Pearls

Standard imaging sequences will likely be adequate for the demonstration of a coronary anomaly in more than 90% of patients, but if you do perform coronary MRA, then consider the following:

1. Coronary MRA requires a high degree of physician involvement at the scanner. If you delegate the study acquisition to an unsupervised technologist then expect poor-quality images unless you have extremely experienced CMR technologists.
2. A whole heart approach is often easier for the novice than a targeted approach.
3. A high temporal resolution cine scout for identifying the coronary rest period more than repays the brief time investment required to perform it.
4. Select a relatively narrow data acquisition window—no more than 70 ms at heart rates of 65 bpm or less and <50 ms at heart rates higher than this.  
Tighten the respiratory belt until the patient feels mildly uncomfortable when breathing in—this has the effect of limiting diaphragmatic excursion somewhat and in our experience and that of others [37] tends to increase navigator acceptance by 10–15%.
5. Consider giving sublingual nitrate and oral beta-blockers prior to acquisition
6. Don't forget that it's not just the vessel origin and course but also the consequences of the anomaly that should be sought (perfusion, LGE, etc.)
7. CMR may not be the imaging modality of choice in some circumstances
8. It is a sign of wisdom—not failure—to terminate the CMR study early and send the patient to the CT scanner occasionally!

## References

1. Brothers J, Gaynor JW, Paridon S, Lorber R, Jacobs M. Anomalous aortic origin of a coronary artery with an interarterial course: understanding current management strategies in children and young adults. *Pediatr Cardiol*. 2009;30(7):911–21.
2. Cheitlin MD, De Castro CM, McAllister HA. Sudden death as a complication of anomalous left coronary origin from the anterior sinus of valsalva, A not-so-minor congenital anomaly. *Circulation*. 1974;50(4):780–7.
3. Cheitlin MD. Finding asymptomatic people with a coronary artery arising from the wrong sinus of valsalva: consequences arising from knowing the anomaly to be familial. *J Am Coll Cardiol*. 2008;51(21):2065–7.
4. Boon B. Leonardo da vinci on atherosclerosis and the function of the sinuses of valsalva. *Neth Heart J*. 2009;17(12):496–9.
5. Morgagni G. The seats and causes of diseases investigated by anatomy; in five books.: Containing A great variety of dissections, with remarks. to which are added very accurate and copious indexes of the principal things and names therein contained. translated from the latin of john baptist morgagni, chief professor of anatomy, and president of the university at padua, by benjamin alexander, M. D. in three volumes. ... . London: printed for A. Millar; and T. Cadell.
6. Angelini P. Normal and anomalous coronary arteries: definitions and classification. *Am Heart J*. 1989;117(2):418–34.
7. Jacobs ML, Mavroudis C. Anomalies of the coronary arteries: nomenclature and classification. *Cardiol Young*. 2010;20(Suppl 3):15–9.
8. Anderson RH, Spicer D. Fistulous communications with the coronary arteries in the setting of hypoplastic ventricles. *Cardiol Young*. 2010 Dec;20(Suppl 3):86–91.
9. Angelini P, Fairchild VD, editors. Coronary artery anomalies: a comprehensive approach. Philadelphia: Lippincott Williams & Wilkins; 1999.
10. Brothers JA, Gaynor JW, Jacobs JP, Caldarone C, Jegatheeswaran A, Jacobs ML, et al. The registry of anomalous aortic origin of the coronary artery of the congenital heart surgeons' society. *Cardiol Young*. 2010;20(Suppl 3):50–8.
11. Gawor R, Kusmerek J, Plachcinska A, Bienkiewicz M, Drozd J, Piotrowski G, et al. Myocardial perfusion GSPECT imaging in patients with myocardial bridging. *J Nucl Cardiol*. 2011;18(6):1059–65.
12. Hakeem A, Cilingiroglu M, Leesar MA. Hemodynamic and intravascular ultrasound assessment of myocardial bridging: fractional flow reserve paradox with dobutamine versus adenosine. *Catheter Cardiovasc Interv*. 2010;75(2):229–36.
13. Thiene G, Carturan E, Corrado D, Basso C. Prevention of sudden cardiac death in the young and in athletes: dream or reality? *Cardiovasc Pathol*. 2010;19(4):207–17.
14. Maron BJ, Doerer JJ, Haas TS, Tierney DM, Mueller FO. Sudden deaths in young competitive athletes: analysis of 1866 deaths in the United States, 1980-2006. *Circulation*. 2009;119(8):1085–92.
15. Eckart RE, Scoville SL, Campbell CL, Shry EA, Stajduhar KC, Potter RN, et al. Sudden death in young adults: a 25-year review of autopsies in military recruits. *Ann Intern Med*. 2004;141(11):829–34.
16. Hill SF, Sheppard MN. Non-atherosclerotic coronary artery disease associated with sudden cardiac death. *Heart*. 2010;96(14):1119–25.
17. Baroldi G. In: Scomazzoni G, United States, Armed Forces Institute of Pathology (U.S.), editors. Coronary circulation in the normal and the pathologic heart. Washington: Armed Forces Institute of Pathology [for sale by the Supt. of Docs.]; 1967.
18. Davies JE, Burkhart HM, Dearani JA, Suri RM, Phillips SD, Warnes CA, et al. Surgical management of anomalous aortic origin of a coronary artery. *Ann Thorac Surg*. 2009;88(3):844–7; discussion 847–8.
19. De Luca L, Bovenzi F, Rubini D, Niccoli-Asabella A, Rubini G, De Luca I. Stress-rest myocardial perfusion SPECT for functional assessment of coronary arteries with anomalous origin or course. *J Nucl Med*. 2004;45(4):532–6.
20. Yamanaka O, Hobbs RE. Coronary artery anomalies in 126,595 patients undergoing coronary arteriography. *Catheter Cardiovasc Diagn*. 1990;21(1):28–40.



21. Zhang LJ, Yang GF, Huang W, Zhou CS, Chen P, Lu GM. Incidence of anomalous origin of coronary artery in 1879 Chinese adults on dual-source CT angiography. *Neth Heart J*. 2010;18(10):466–70.
22. Angelini P, Flamm SD. Newer concepts for imaging anomalous aortic origin of the coronary arteries in adults. *Catheter Cardiovasc Interv*. 2007;69(7):942–54.
23. Crean AM, Kilcullen N, Younger JF. Arrhythmic acute coronary syndrome and anomalous left main stem artery: culprit or innocent bystander. *Acute Card Care*. 2008;10(1):60–1.
24. McConnell MV, Ganz P, Selwyn AP, Li W, Edelman RR, Manning WJ. Identification of anomalous coronary arteries and their anatomic course by magnetic resonance coronary angiography. *Circulation*. 1995;92(11):3158–62.
25. Post JC, van Rossum AC, Hofman MB, Valk J, Visser CA. Protocol for two-dimensional magnetic resonance coronary angiography studied in three-dimensional magnetic resonance data sets. *Am Heart J*. 1995;130(1):167–73.
26. Vliegen HW, Doornbos J, de Roos A, Jukema JW, Bekedam MA, van der Wall EE. Value of fast gradient echo magnetic resonance angiography as an adjunct to coronary arteriography in detecting and confirming the course of clinically significant coronary artery anomalies. *Am J Cardiol*. 1997;79(6):773–6.
27. Bekedam MA, Vliegen HW, Doornbos J, Jukema JW, de Roos A, van der Wall EE. Diagnosis and management of anomalous origin of the right coronary artery from the left coronary sinus. *Int J Card Imaging*. 1999;15(3):253–8.
28. White CS, Laskey WK, Stafford JL, Ness Aiver M. Coronary MRA: use in assessing anomalies of coronary artery origin. *J Comput Assist Tomogr*. 1999;23(2):203–7.
29. Taylor AM, Thorne SA, Rubens MB, Jhooti P, Keegan J, Gatehouse PD, et al. Coronary artery imaging in grown up congenital heart disease: complementary role of magnetic resonance and x-ray coronary angiography. *Circulation*. 2000;101(14):1670–8.
30. Greil GF, Stuber M, Botnar RM, Kissinger KV, Geva T, Newburger JW, et al. Coronary magnetic resonance angiography in adolescents and young adults with Kawasaki disease. *Circulation*. 2002;105(8):908–11.
31. Bunce NH, Lorenz CH, Keegan J, Lesser J, Reyes EM, Firmin DN, et al. Coronary artery anomalies: assessment with free-breathing three-dimensional coronary MR angiography. *Radiology*. 2003;227(1):201–8.
32. Mavrogeni S, Papadopoulos G, Douskou M, Kaklis S, Seimenis I, Baras P, et al. Magnetic resonance angiography is equivalent to X-ray coronary angiography for the evaluation of coronary arteries in Kawasaki disease. *J Am Coll Cardiol*. 2004;43(4):649–52.
33. Su JT, Chung T, Muthupillai R, Pignatelli RH, Kung GC, Diaz LK, et al. Usefulness of real-time navigator magnetic resonance imaging for evaluating coronary artery origins in pediatric patients. *Am J Cardiol*. 2005;95(5):679–82.
34. Taylor AM, Dymarkowski S, Hamaekers P, Razavi R, Gewillig M, Mertens L, et al. MR coronary angiography and late-enhancement myocardial MR in children who underwent arterial switch surgery for transposition of great arteries. *Radiology*. 2005;234(2):542–7.
35. Takemura A, Suzuki A, Inaba R, Sonobe T, Tsuchiya K, Omuro M, et al. Utility of coronary MR angiography in children with Kawasaki disease. *AJR Am J Roentgenol*. 2007;188(6):W534–9.
36. Gharib AM, Ho VB, Rosing DR, Herzka DA, Stuber M, Arai AE, et al. Coronary artery anomalies and variants: technical feasibility of assessment with coronary MR angiography at 3 T. *Radiology*. 2008;247(1):220–7.
37. Beerbaum P, Sarikouch S, Laser KT, Greil G, Burchert W, Korperich H. Coronary anomalies assessed by whole-heart isotropic 3D magnetic resonance imaging for cardiac morphology in congenital heart disease. *J Magn Reson Imaging*. 2009;29(2):320–7.
38. Clemente A, Del Borrello M, Greco P, Mannella P, Di Gregorio F, Romano S, et al. Anomalous origin of the coronary arteries in children: diagnostic role of three-dimensional coronary MR angiography. *Clin Imaging*. 2010;34(5):337–43.
39. Tangcharoen T, Bell A, Hegde S, Hussain T, Beerbaum P, Schaeffter T, et al. Detection of coronary artery anomalies in infants and young children with congenital heart disease by using MR imaging. *Radiology*. 2011;259(1):240–7.
40. Rajiah P, Setser RM, Desai MY, Flamm SD, Arruda JL. Utility of free-breathing, whole-heart, three-dimensional magnetic resonance imaging in the assessment of coronary anatomy for congenital heart disease. *Pediatr Cardiol*. 2011;32(4):418–25.
41. Gui D, Tsekos NV. Dynamic imaging of contrast-enhanced coronary vessels with a magnetization prepared rotated stripe keyhole acquisition. *J Magn Reson Imaging*. 2007;25(1):222–30.
42. Nakamura M, Kido T, Kido T, Watanabe K, Schmidt M, Forman C, Mochizuki T. Non-contrast compressed sensing whole-heart coronary magnetic resonance angiography at 3T: a comparison with conventional imaging. *Eur J Radiol*. 2018;104:43–8. <https://doi.org/10.1016/j.ejrad.2018.04.025>; Epub 2018 Apr 27.
43. Hirai K, Kido T, Kido T, Ogawa R, Tanabe Y, Nakamura M, Kawaguchi N, Kurata A, Watanabe K, Yamaguchi O, Schmidt M, Forman C, Mochizuki T. Feasibility of contrast-enhanced coronary artery magnetic resonance angiography using compressed sensing. *J Cardiovasc Magn Reson*. 2020;22(1):15. <https://doi.org/10.1186/s12968-020-0601-0>.
44. Ishida M, Schuster A, Takase S, Morton G, Chiribiri A, Bigalke B, Schaeffter T, Sakuma H, Nagel E. Impact of an abdominal belt on breathing patterns and scan efficiency in whole-heart coronary magnetic resonance angiography: comparison between the UK and Japan. *J Cardiovasc Magn Reson*. 2011;13(1):71. <https://doi.org/10.1186/1532-429X-13-71>.
45. Ishida M, Schuster A, Takase S, Morton G, Chiribiri A, Bigalke B, et al. Impact of an abdominal belt on breathing patterns and scan efficiency in whole-heart coronary magnetic resonance angiography: comparison between the UK and Japan. *J Cardiovasc Magn Reson*. 2011;13:71.
46. Tobler D, Motwani M, Wald RM, Roche SL, Verocai F, Iwanochko RM, Greenwood JP, Oechslin EN, Crean AM. Evaluation of a comprehensive cardiovascular magnetic resonance protocol in young adults late after the arterial switch operation for d-transposition of the great arteries. *J Cardiovasc Magn Reson*. 2014;16(1):98. <https://doi.org/10.1186/s12968-014-0098-5>.
47. Deva DP, Torres FS, Wald RM, Roche SL, Jimenez-Juan L, Oechslin EN, Crean AM. The value of stress perfusion cardiovascular magnetic resonance imaging for patients referred from the adult congenital heart disease clinic: 5-year experience at the Toronto General Hospital. *Cardiol Young*. 2014;24(5):822–30. <https://doi.org/10.1017/S104795111300111X>; Epub 2013 Sep 18.
48. Laflamme E, Alonso-Gonzalez R, Roche SL, Wald RM, Swan L, Silversides CK, Thorne SA, Horlick EM, Benson LN, Osten M, Hickey E, Barron DJ, Colman JM, Oechslin E, Crean AM. Anomalous origin of a coronary artery from the pulmonary artery presenting in adulthood: experience from a tertiary center. *Int J Cardiol Congenit Heart Dis*. 2021;4:100169. <https://doi.org/10.1016/j.ijcchd.2021.100169>.
49. Fratz S, Chung T, Greil GF, Samyn MM, Taylor AM, Valsangiacomo Buechel ER, Yoo SJ, Powell AJ. Guidelines and protocols for cardiovascular magnetic resonance in children and adults with congenital heart disease: SCMR expert consensus group on congenital heart disease. *J Cardiovasc Magn Reson*. 2013;15(1):51. <https://doi.org/10.1186/1532-429X-15-51>.
50. Strigl S, Beroukhim R, Valente AM, Annese D, Harrington JS, Geva T, et al. Feasibility of dobutamine stress cardiovascular



- magnetic resonance imaging in children. *J Magn Reson Imaging*. 2009;29(2):313–9.
51. Song L, Ma X, Zhao X, Zhao L, DeLano M, Fan Y, Wu B, Lu A, Tian J, He L. Validation of black blood late gadolinium enhancement (LGE) for evaluation of myocardial infarction in patients with or without pathological Q-wave on electrocardiogram (ECG). *Cardiovasc Diagn Ther*. 2020;10(2):124–34. <https://doi.org/10.21037/cdt.2019.12.11>.
  52. Backer CL, Stout MJ, Zales VR, Muster AJ, Weigel TJ, Idriss FS, et al. Anomalous origin of the left coronary artery. A twenty-year review of surgical management. *J Thorac Cardiovasc Surg*. 1992;103(6):1049–57; discussion 1057–8.
  53. Belli E, Roussin R, Ly M, Roubertie F, Le Bret E, Basaran M, et al. Anomalous origin of the left coronary artery from the pulmonary artery associated with severe left ventricular dysfunction: results in normothermia. *Ann Thorac Surg*. 2010;90(3):856–60.
  54. Ben Ali W, Metton O, Roubertie F, Pouard P, Sidi D, Raisky O, et al. Anomalous origin of the left coronary artery from the pulmonary artery: late results with special attention to the mitral valve. *Eur J Cardiothorac Surg*. 2009;36(2):244–8; discussion 248–9.
  55. Karunadasa R, Buxton BF, Dick R, Calafiore P. Anomalous origin of left coronary artery from the pulmonary artery does the management in the adult differ from that of the infant? Four cases of the bland-white-garland syndrome. *Heart Lung Circ*. 2007;16(Suppl 3):S29–33.
  56. Mavroudis C, Dodge-Khatami A, Stewart RD, Jacobs ML, Backer CL, Lorber RE. An overview of surgery options for congenital coronary artery anomalies. *Futur Cardiol*. 2010;6(5):627–45.
  57. Wintersperger BJ, von Smekal A, Engelmann MG, Knez A, Penzkofer HV, Laub G, et al. Contrast media enhanced magnetic resonance angiography for determining patency of a coronary bypass. A comparison with coronary angiography. *Rofo*. 1997;167(6):572–8.
  58. Brenner P, Wintersperger B, von Smekal A, Agirov V, Bohm D, Kreuzer E, et al. Detection of coronary artery bypass graft patency by contrast enhanced magnetic resonance angiography. *Eur J Cardiothorac Surg*. 1999;15(4):389–93.
  59. Bunce NH, Lorenz CH, John AS, Lesser JR, Mohiaddin RH, Pennell DJ. Coronary artery bypass graft patency: assessment with true fast imaging with steady-state precession versus gadolinium-enhanced MR angiography. *Radiology*. 2003;227(2):440–6.
  60. Manso B, Castellote A, Dos L, Casaldaliga J. Myocardial perfusion magnetic resonance imaging for detecting coronary function anomalies in asymptomatic paediatric patients with a previous arterial switch operation for the transposition of great arteries. *Cardiol Young*. 2010;20(4):410–7.
  61. <https://www.sciencedirect.com/science/article/pii/S2666668521000938>.
  62. Schmitt R, Froehner S, Brunn J, Wagner M, Brunner H, Cherevatyy O, et al. Congenital anomalies of the coronary arteries: imaging with contrast-enhanced, multidetector computed tomography. *Eur Radiol*. 2005;15(6):1110–21.



Edward T. Martin

## 17.1 Introduction

Pericardial disease can be an important cause of morbidity and mortality in a clinical cardiology practice. However, patients with pericardial disease are not always encountered on a daily basis, and because pericardial disease can mimic other diseases, such as cardiovascular, pulmonary, and pleural processes a firm diagnosis may be difficult. Frequently, pericardial involvement can be the initial presentation of a systemic disease process. Disorders of the pericardium can also have a variety of etiologies, including congenital malformations along with infectious, infarction-related, metabolic, autoimmune, traumatic, neoplastic, and idiopathic processes. Additionally, accurate diagnosis of a pericardial disorder may require the use of multiple noninvasive tests or a noninvasive test coupled with an invasive study.

This chapter will focus on the ability of cardiac magnetic resonance imaging (CMR) to accurately assess pericardial diseases. It will compare and contrast CMR's ability to diagnose pericardial disorders to both echocardiography and computed tomography (CT). This chapter will also provide rationale for the appropriate use of CMR in a patient with suspected pericardial disease.

## 17.2 Anatomy/Physiology

The pericardium is a relatively avascular double-layered sac that surrounds the heart and extends superiorly to the origin of the great vessels and is attached to the sternum, the dorsal spine and the diaphragm. It consists of a visceral and parietal layer. In general, its combined thickness is less than 2 mm. The two layers create a potential space that normally contains 15–35 ml of serous fluid which is secreted by the visceral pericardium [1]. A variable amount of epicardial and pericardial fat is also present which can aid MRI and CT by providing enhanced tissue contrast. The pericardium is well innervated and can cause severe pain during inflammation and trigger vagally-mediated reflexes. From a physiologic perspective, the pericardium interacts with the pleural space and the ventricles. The pericardium is also involved in the interaction between the right and left ventricles. This interaction can be utilized in the diagnosis of pericardial constriction in the form of ventricular interdependence.

While the pericardium does not appear to be essential for the cardiovascular system to perform its normal physiologic function it does seem to have utility. It maintains the normal position of the heart, anchoring it to the central thorax, and may also provide a barrier to infection. It also secretes prostaglandins that regulate cardiac tone. Finally, the pericardium restrains cardiac volume and enhances mechanical interactions of the cardiac chambers. Despite these important functions, absence of the pericardium does not usually result in significant problems.

**Supplementary Information** The online version contains supplementary material available at [https://doi.org/10.1007/978-3-031-29235-4\\_17](https://doi.org/10.1007/978-3-031-29235-4_17).

E. T. Martin (✉)  
Department of Cardiovascular MRI, Oklahoma Heart Institute,  
Tulsa, OK, USA  
e-mail: [martin@oklahomaheart.com](mailto:martin@oklahomaheart.com)

### 17.3 MRI Examination for Pericardial Diseases

The pericardium is usually bordered by epicardial and pericardial fat, which has high signal on black blood T1-weighted images. Black blood imaging demonstrates the pericardium as a thin band of low signal due to its mainly fibrous structure and lack of water content. The normal pericardial thickness by MRI is between 1 and 3 mm and is best evaluated anatomically on axial imaging (Fig. 17.1). However, scanning in two perpendicularly oriented planes through the heart optimizes the depiction of the entire pericardium. The normal MRI pericardial thickness is somewhat larger than the normal anatomical thickness which is 1 mm or less [2–4]. Cardiac motion and limited spatial resolution in this area contribute to this phenomenon [5].

A cardiac examination designed for evaluation of pericardial disease will include the standard sequences used in essentially all cardiac MRI. These sequences can then be

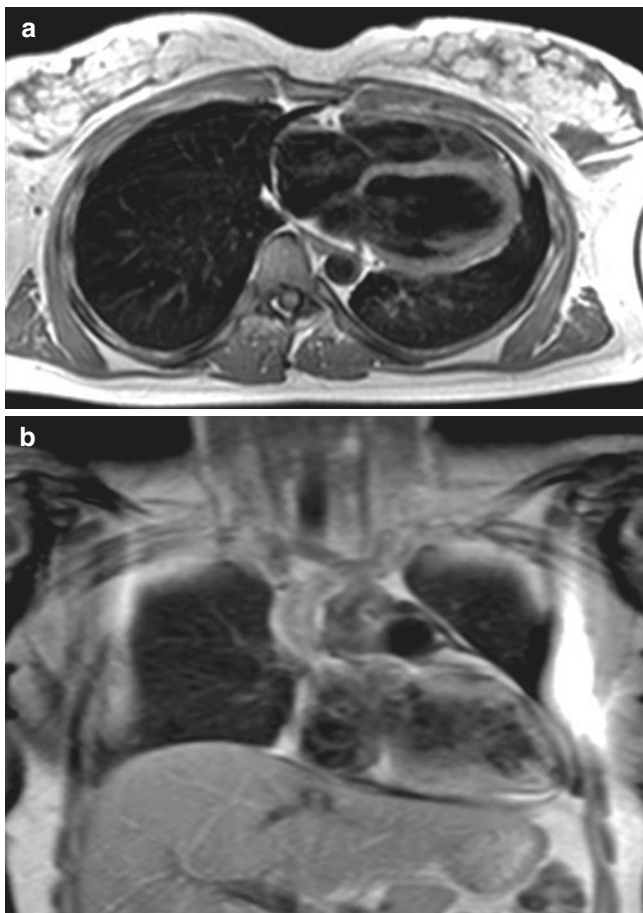


**Fig. 17.1** Normal pericardial appearance. (a) Black blood axial view of the heart. The pericardium is the thin black line surrounding the heart. (b) Black blood coronal view of the normal pericardium. Again, the pericardium is the thin black line seen at the outer edge of the heart extending superiorly to level of the main pulmonary artery

supplemented by real-time, delayed-enhancement and perfusion imaging depending on the clinical condition (Table 17.1).

The CMR exam will start with a morphological assessment of the heart, pericardium, and mediastinum using a black-blood, T1-weighted technique, using a fast-segmented sequence. The T2-weighted half-Fourier acquisition single-shot turbo spin-echo (HASTE) sequence can also be used as it allows dark blood imaging with a reduced acquisition time. There is slightly increased blurring with this technique relative to standard gated spin-echo techniques. However, the resistance of the single-shot sequence to respiratory motion artifact and cardiac arrhythmias, which frequently degrades spin-echo image quality, usually offsets this minimal disadvantage. The T2-weighted spin-echo CMR sequences are useful for depicting myocardial edema, pericardial edema, and fluid, as well as allowing one to differentiate pericardial cysts from other types of masses. Triple inversion recovery or double inversion recovery with fat saturation can also help in this instance as well.

Cine imaging through the entire myocardium in the short and long-axis planes as routinely performed for cardiac evaluation is appropriate for the imaging of suspected pericardial diseases. Balanced steady-state free precession (SSFP) gradient-echo sequences are now the standard technique used for cine imaging. They demonstrate improved image

**Table 17.1** Cardiac MRI strategies to evaluate the pericardium

Pericardial width/localization/extent (T1w/T2w spin-echo CMR/cine CMR)
Pericardial delineation (T1w/T2w spin-echo CMR/cine CMR, CMR/gadolinium-enhanced CMR)
Pericardial layer/fluid characterization (T1w/T2w spin-echo CMR/cine CMR/gadolinium-enhanced CMR)
Pericardial function
Motion pattern (cine CMR)
Fusion of pericardial layers and myocardial adherence (CMR tagging)
Pericardial masses (T1w/T2w spin-echo CMR/double IR with fat saturation/triple IR/cine CMR/gadolinium-enhanced CMR)
Cardiac morphology (spin-echo CMR, cine CMR)
Size and shape of ventricles
Myocardial morphology (restrictive cardiomyopathy)
Cardiac systolic function (cine CMR)
Regional and global systolic ventricular function
Cardiac filling (velocity-encoded CMR)
Ventricular coupling (real-time cine CMR)
Ventricular septal shape and septal motion patterns
Respiratory-related septal shift
Other findings (spin-echo CMR/cine CMR/gadolinium-enhanced CMR)
Myocardial enhancement (associated myocarditis or myocardial infiltrative or storage disease)
Caval vein size
Pleural effusion/ascites
Lung processes

quality in comparison with segmented gradient echo imaging techniques. The signal intensity in the SSFP technique depends upon the T2/T1 ratio. Therefore, structures with a high T2/T1 ratio such as fat, fluid, and intracavitary blood demonstrate similar high signal despite their significantly different T1 and T2 properties. Cine imaging allows one to view myocardial movement in relation to pericardial movement and differentiate normal pericardial movement from a stiff immobile pericardium seen in patients with constrictive pericarditis. The cine sequences are also used to qualitatively assess myocardial and valvular function.

MRI tagging sequences can be performed to aid in identifying adhesion of the visceral to parietal pericardium in constrictive pericarditis. In this sequence, a grid of saturation bands is placed over the heart in diastole, and their deformation in systole can provide information about regional cardiac motion. The grid lines remain unbroken, as opposed to demonstrating normal disruption caused by cardiac motion, in areas of pericardial adherence.

Velocity-encoded, phase contrast CMR is also used to evaluate diastolic cardiac function by looking at the inflow patterns of the mitral and tricuspid valves as well as the pulmonary and systemic veins to help rule out myocardial restriction from pericardial constriction.

Perfusion sequences using gadolinium contrast are used to evaluate the vascularity of cardiac and pericardial masses and can be obtained in multiple imaging planes with one injection. These are heavily T1-weighted imaging sequences that can provide information on perfusion and diffusion in the myocardium or in a mass.

The contrast-enhanced inversion-recovery technique with delayed enhancement (DE-CMR), also called late gadolinium enhancement (LGE) can be employed to identify pericardial enhancement in a similar manner to identifying infarcts in the myocardium. This enhancement represents inflammation and can diagnose pericarditis. This technique can better differentiate between inflammatory and constrictive forms of pericarditis. Because the myocardium is also being assessed, myopericarditis can also be diagnosed.

Newer MRI scanners are now able to perform real-time cine image acquisitions, which obtain images without breath-holding and without segmentation. These non-gated SSFP images are acquired in real time and can be used to assess ventricular coupling to aid in the diagnosis of pericardial constriction.

---

## 17.4 Congenital Abnormalities of the Pericardium

Congenital abnormalities of the pericardium are rare. Pericardial disorders are more commonly seen as post-operative sequelae in patients with congenital heart dis-

ease. The following section covers the pericardial disorders encountered in patients with congenital heart disease.

### 17.4.1 Congenital Absence of the Pericardium

Congenital absence of the pericardium is a rare entity. Complete or partial absence can occur with partial defects being more common. Other congenital abnormalities can also be seen and include anomalies of the chest wall, lungs, and diaphragm. Cardiac anomalies such as tetralogy of Fallot, atrial septal defect, mitral valve stenosis, and patent ductus arteriosus can also occur in concert with congenital absence of the pericardium [5, 6].

Patients with absence of the pericardium are usually asymptomatic, and the condition may be detected on routine chest radiograph as an abnormal left cardiac contour. Symptoms occur when cardiac structures become entrapped in the defect. Herniation of the left atrial appendage through a small defect may lead to infarction of the appendage, compression of the left coronary artery during exercise, and/or prolapse of the pulmonary trunk (Movie 17.1).

The diagnosis of congenital absence of the pericardium by CMR may be difficult because the partial defects of the pericardium predominantly occur on the left side of the heart where the pericardium is difficult to visualize because there is a minimal amount of fat in this location [7]. Therefore, the diagnosis may rely on other signs such as an abnormal location of cardiac structures with excessive levorotation or cardiac indentation at the location of the defect [5, 8]. Functional MRI assessment may also be of use in diagnosing pericardial defects by detecting excessive mobility of the cardiac apex which is normally stationary [9].

### 17.4.2 Pericardial Diverticulum

This is a rare condition where there is herniation through a defect in the parietal pericardium allowing communication into the pericardial space. The most typical location of these defects is at the cardiophrenic angles. These defects resemble cysts but differ because a complete wall cannot be identified in all parts of the abnormality [10].

### 17.4.3 Pericardial Cysts

Pericardial cysts are thin-walled, saccular, fluid-filled, and self-contained. They are usually classified as congenital, postinflammatory, or ecchinococcal. They do not communicate with other structures or the pericardium. They are most often found in the cardiophrenic space. Pericardial cysts



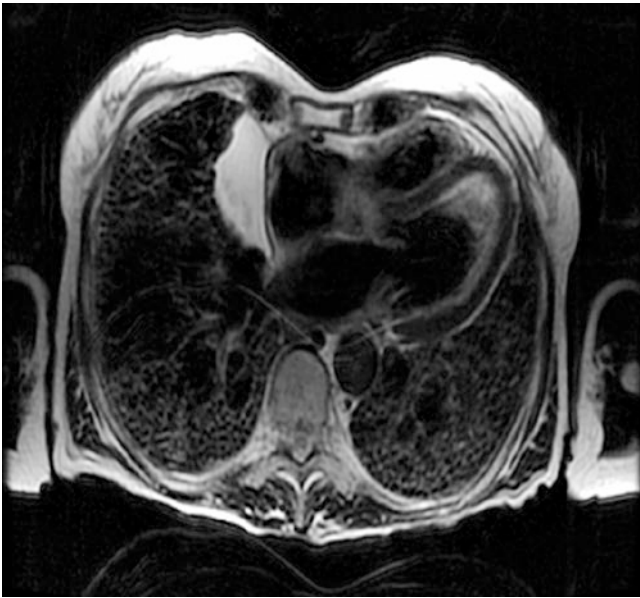


**Fig. 17.2** Pericardial cyst. T2-weighted axial image showing bright signal representing a pericardial cyst lateral to the right atrium

occur on the right side 70% of the time and may calcify. When they do occur on the left, they may mimic left ventricular aneurysms or a prominent left atrial appendage.

During CMR, cysts typically have low or intermediate signal intensity on T1-weighted images and homogeneous high intensity on T2-weighted images (Fig. 17.2). Triple inversion recovery sequences or double inversion recovery with fat saturation sequences may help display the cyst as bright while eliminating interfering fat signal. A line of low signal intensity may be seen surrounding the cyst representing parietal pericardium [2]. Cysts do not enhance with the administration of gadolinium chelates. Occasionally, a cyst may contain highly proteinaceous fluid, which may demonstrate high signal intensity on T1-weighted images. Pericardial cysts need to be distinguished from bronchogenic and thymic cysts as well as from coronary artery aneurysms. Pericardial cysts are distinguished from the latter in that they will exhibit no mass effect on the myocardium (Movie 17.2).

## 17.5 Pericarditis

Pericarditis is an inflammatory process of the pericardium that has multiple etiologies (Table 17.2). The initial presenting symptom is chest pain that worsens with inspiration or in

**Table 17.2** Causes of pericarditis

Infectious: viral, bacterial, fungal, tuberculosis, parasitic
Myocardial infarction (Dressler's syndrome)
Postpericardiotomy syndrome
Immunologic conditions including systemic lupus erythematosus or rheumatoid arthritis
Uremia
Malignancy—Breast, lung, lymphoma, mesothelioma, sarcoma, leukemia
Side effect of some medications (e.g. isoniazid, cyclosporine, hydralazine, warfarin, and heparin, tetracyclines)
Radiation induced
Aortic dissection
Trauma to the heart

the supine body position. Acutely, an inflamed pericardium contains highly vascular granulation tissue with fibrin deposits [11]. Chronically, the pericardium can become fibrosed and stiffened by fibroblasts and collagen. In this acute phase, there may also be a pericardial effusion and slight pericardial thickening. This process can be detected and evaluated by CMR. Response to treatment can be monitored by MRI as well (Fig. 17.3).

The pericardium can initially be assessed for thickening and fluid by both dark-blood fast spin-echo techniques and by white-blood cine techniques (Fig. 17.4). The DE-CMR technique has been described as being useful for detecting pericardial inflammation [11, 12]. The normal pericardium, being relatively avascular does not enhance. However, when the pericardium is inflamed acutely with vascularized granulation tissue the pericardium will enhance (Fig. 17.5).

Sometimes there is concomitant myocarditis with pericarditis and vice versa. In one CMR study for the detection of myocarditis, 9 of 20 patients with myocarditis also had pericardial enhancement [13]. With DE-CMR this phenomenon is easily diagnosed and characterized [12, 13] (Fig. 17.6).

The initial acute inflammatory reaction within the pericardium also contains an increase in free water content due to lymphocyte infiltration. This can cause T2 relaxation time prolongation. Therefore one can also use a short  $\tau$ -inversion recovery T2-weighted sequence looking for a hyperintense signal from the pericardium representing edema [14].

**Fig. 17.3** Pericardial assessment before and after treatment for pericarditis. (a) Axial white blood image of a thickened pericardium in a patient with pericarditis. (b) White blood axial image of the same patient after treatment with steroids and plaquenil. Note the reduction in pericardial thickness

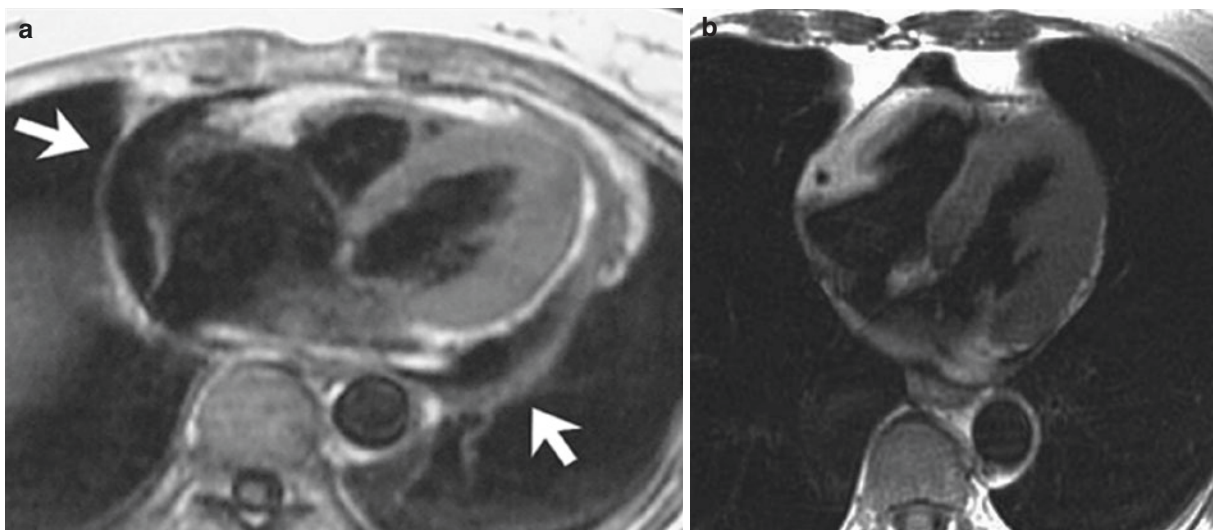
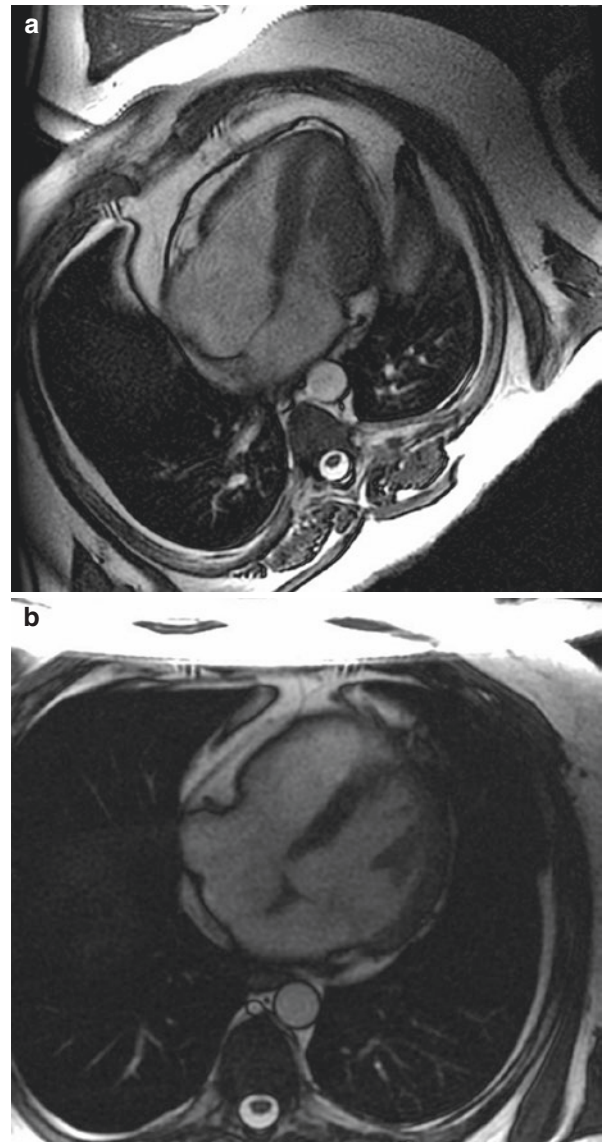


**Fig. 17.4** (a) Pericardial Effusion – Axial Black Blood MR image. White arrows point to black space surrounding the heart, which represents a pericardial effusion. (b) Pericardial Effusion – Four Chamber

Black Blood MR image. The white areas anterior to the right ventricular free wall and to the black space represent fat



**Fig. 17.5** Acute pericarditis. Pericardial enhancement is seen in a patient with acute pericarditis using the delayed enhancement sequence following the administration of gadolinium

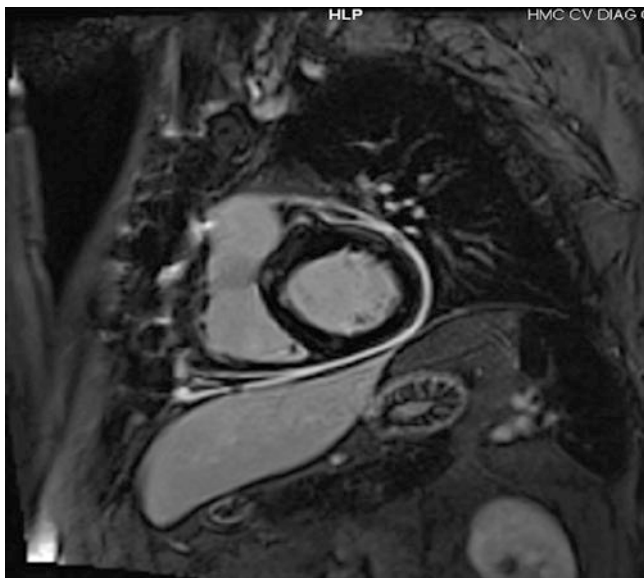


**Fig. 17.6** Myopericarditis. In addition to the ring enhancement of the pericardium small islands of gadolinium are seen in the myocardium especially in the anteroseptal and inferoseptal walls. This represents concomitant myocarditis along with pericarditis

## 17.6 Constrictive Pericarditis

As mentioned previously, chronic pericarditis is characterized by sclerosing pericarditis and chronic inflammation leading to fibrosis stiffened by fibroblasts and collagen.

Constrictive pericarditis is an uncommon and easily missed diagnosis. Patients with constrictive pericarditis usually present with dyspnea, elevated jugular venous pressure, edema, and ascites, especially when left ventricular systolic function is normal. The classic features of constrictive pericarditis include elevation and equalization of pressures in all four cardiac chambers during diastole with ventricular interdependence or coupling during respiration [1, 15].

Constrictive pericarditis must be distinguished from restrictive cardiomyopathy as both can cause restricted ventricular filling. CMR has been shown to be able to detect the hallmarks of constriction accurately and separate it from restrictive cardiomyopathy [16].

Chronic inflammation of the pericardium usually results in pericardial thickening. However, pericardial constriction can occur without pericardial thickening and a thickened pericardium does not always mean constriction [17, 18]. The typical presentation of constriction includes a thickened pericardium. Echo can usually detect this, but accurate measurements of pericardial thickness are difficult because of poor diagnostic windows, reverberations of reflected ultrasound, and calcific shadowing. MRI has none of these problems. Because the pericardium is outlined by epicardial fat and lung tissue, MRI can measure pericardial thickness more reliably and accurately than echo. Computed tomography is also very accurate at detecting pericardial thickness, fluid, and calcification.

CMR can detect a thickened pericardium by utilizing dark blood imaging sequences. Using spin-echo dark blood images, MRI was able to detect pericardial thickening in 88% of patients with proven constrictive pericarditis predominantly over the right ventricle [16]. Pericardial delineation may also be irregular [19]. A pitfall of this technique is that thickness will be inaccurate in the presence of a pericardial effusion. Therefore, this technique will need to be coupled with a white blood cine sequence. The cine sequence can also show adhesion of the visceral to parietal pericardium [20] (Movie 17.3). CMR tagging techniques can help visualize this adherence if the cine sequence is not adequate (Movie 17.4). Rather than the normal slippage of the pericardium over the myocardium during systole, there is adherence and tethering of the myocardium that impairs diastolic filling. Tagging may be especially helpful where the pericardium is of normal thickness [21].

Additional cardiac and vascular morphologic changes can also be easily detected by MRI. In constriction, the ventricles, especially the right, may appear elongated, flattened, and tubular; one or both atrioventricular grooves may be narrowed; unilateral or bilateral atrial enlargement can occur; and possibly dilatation of the vena cava or hepatic veins. Pleural effusions or ascites may also be seen. Finally, a sigmoid-shaped septum with abnormal motion may occur. These changes can be seen using standard MRI sequences (Fig. 17.7).



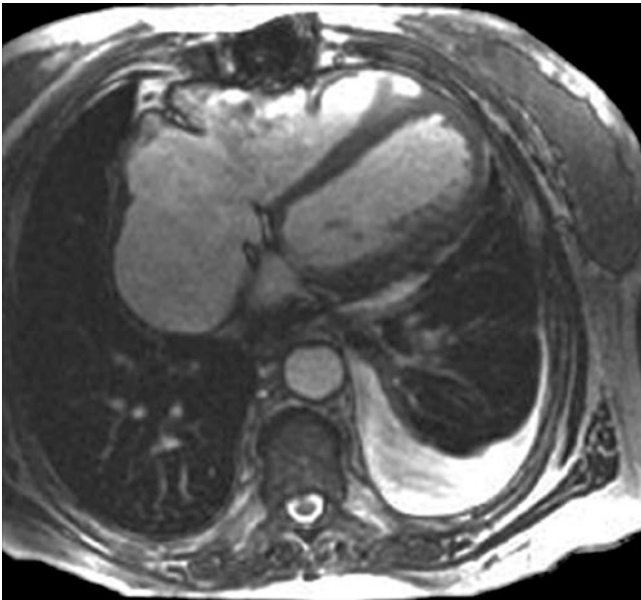


**Fig. 17.7** Cardiac morphologic changes in constrictive pericarditis. Morphologic changes seen in this patient with constrictive pericarditis include enlarged right atrium, inferior vena cava and a left sided pleural effusion

Because severe constriction can occur without pericardial thickening, functional assessments are necessary in order to completely evaluate the patient for constriction. Under normal conditions, the interventricular septum bows towards the right ventricular cavity throughout the entire cardiac cycle. The pericardium in constriction forms a noncompliant shell around the heart preventing it from expanding and leading to significant respiratory variation in blood flow. During inspiration, the negative pressure in the thoracic cavity will lead to increased blood flow into the right ventricle. This increased volume in the right ventricle will cause the interventricular septum to bulge towards the left ventricle, leading to decreased filling of the left ventricle. The opposite then occurs during expiration. This abnormal septal motion can be detected by cardiac MRI (Movie 17.5).

Using breath-hold cine sequences, cardiac MRI was able to detect early diastolic septal flattening with a sensitivity of 81% and a specificity of 100% for the diagnosis of constrictive pericarditis thus distinguishing it from restrictive cardiomyopathy [22]. Using real-time CMR, this effect has been demonstrated dynamically and again was useful in distinguishing constriction from restriction [23].

## 17.7 Pericardial Effusion and Tamponade

A pericardial effusion is an excess amount of fluid within the pericardial space of greater than 50 ml. Fluid usually results from inflammation due to an inflammatory or infec-



**Fig. 17.8** Pericardial and pleural effusions. This white blood axial image demonstrates bilateral loculated pleural effusions with a pericardial effusion

tious process, but it can also occur in trauma and fluid overload states like congestive heart failure and renal failure. Of the conditions that can cause pericardial effusions, those with a high incidence of progression to cardiac tamponade are bacterial and fungal infections, human immunodeficiency virus infections, neoplasms, and bleeding. Again, echocardiography is fairly useful at detecting pericardial effusions. However, loculated effusions as well as combined pleural and pericardial effusions can pose a diagnostic problem for echo. These problems are more easily distinguished by CMR (Fig. 17.8). CMR has also been shown to be superior to echo for detecting the distribution and amount of pericardial fluid or in effusions complicated by pericardial thickening [19].

CMR not only can identify effusions but it also may be able to characterize them as well. Uncomplicated or transudative effusions are usually low in signal intensity on T1-weighted images and high in signal intensity on T2-weighted images. Additionally, an SSFP cine sequence will have a uniformly high signal [24]. Exudative effusions have a high cell and protein content and therefore will display high signal on T1-weighted images and low signal on T2-weighted images. Hemorrhagic effusions can be suspected when the signal is high on T1-weighted images and cine imaging reveals a complex and inhomogeneous effusion with different signal intensities [25–28]. Air in the pericardial space is seen as a signal void. Finally, if both a pericardial and pleural effusion are seen in association with infiltration of adjacent structures and a tumor size greater than 5 cm then these findings are a highly specific but not sensitive sign of malignancy [29].



Cardiac tamponade is present when fluid or air accumulates within the pericardial space leading to cardiac chamber compression and decreased cardiac output. Usually, it is the time course of fluid accumulation that is most physiologically significant. Tamponade is best assessed by simultaneously measuring right atrial or ventricular pressure and intrapericardial pressure. Usually, invasive diagnostics are undertaken on the basis of noninvasive assessment. Evaluation is usually performed using echo because of the need for a rapid diagnosis in hemodynamically unstable patients. However, if the situation is nonemergent, CMR can be done to confirm equivocal echo findings.

According to the echo literature, significant hemodynamic compromise from an effusion is likely when there is observed right atrial and ventricular collapse during diastole. This can be observed by CMR either on cine imaging [30] or real-time cine imaging (Movie 17.6). Real-time imaging may have an advantage over standard cine imaging given that the degree of collapse may be variable in certain parts of the respiratory cycle. Real-time imaging can also demonstrate abnormal ventricular interdependence suggesting hemodynamic significance of the fluid accumulation [31].

## 17.8 Pericardial Masses

Pericardial masses usually are noticed initially by echocardiography. However, echo often does a poor job of localizing and characterizing the mass. Therefore, CMR is often needed to assess the mass and determine whether the mass is compromising surrounding structures. Masses can be categorized as cysts (described above), thrombi, or neoplasms.

### 17.8.1 Pericardial Hematomas

Pericardial hematomas are associated with trauma, cardiac surgery, mitral annular calcification, acute myocardial infarction, aortic valve disease, and aortic dissections. Localized pericardial and intramural hematomas can compress various myocardial structures and even lead to cardiac tamponade [32]. Adhesions between cardiac tissues and pericardium tend to contain hematomas and direct their spread along the paths of least resistance.

Hematomas can be identified and characterized by CMR. Fresh thrombus contains a large amount of hemoglobin resulting in high signal on both T1 and T2-weighted imaging. After about 1–2 weeks, deoxyhemoglobin and methemoglobin predominate in the thrombus resulting in increased signal on T1-weighted imaging and decreased on T2-weighted imaging.

### 17.8.2 Neoplasms

Benign tumors of the pericardium are rare and include teratomas, hemangiomas, and fibrous tumors of the pericardium. Primary malignant tumors are also rare. The most common is mesothelioma followed by sarcomas and teratomas [24, 33, 34]. However, the most common neoplasms of the pericardium are metastatic masses. The pericardium may also contain paraneoplastic involvement, causing thickening and consequent constriction without evidence of metastatic spread. Cardiac MRI is ideally suited to evaluate these masses because of its ability to characterize tissue, high spatial resolution, and large fields of view. The standard CMR sequences can be used to evaluate these masses (Fig. 17.9).

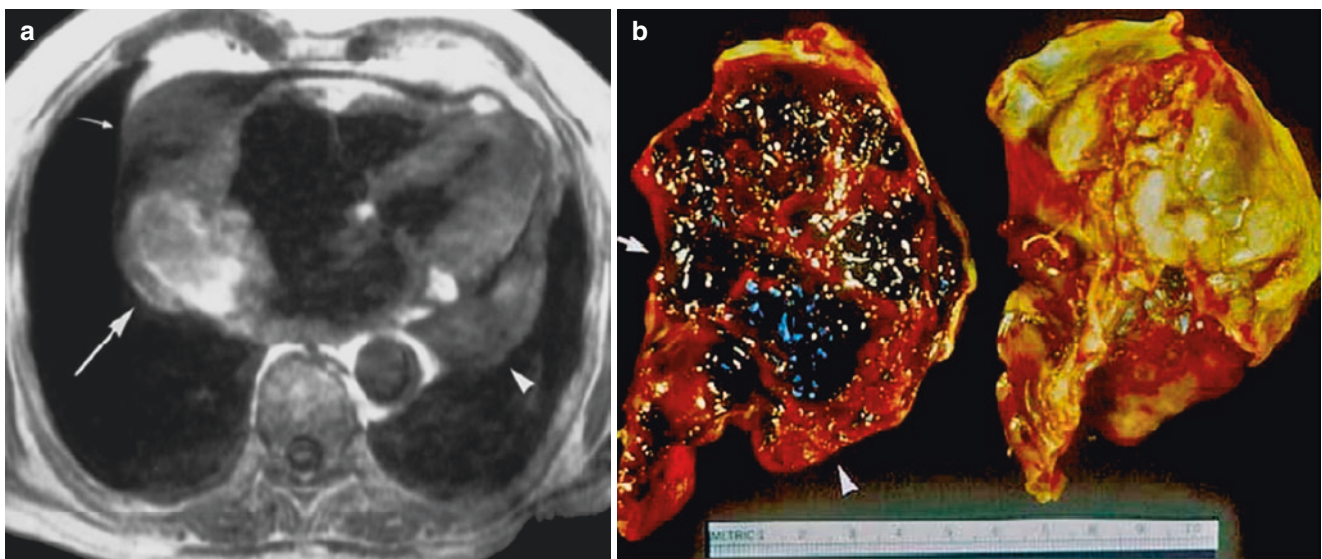


**Fig. 17.9** (a) Angiosarcoma – Axial Black Blood MR image. (b) Angiosarcoma – Autopsy photo. The white arrows on both figures point to the angiosarcoma

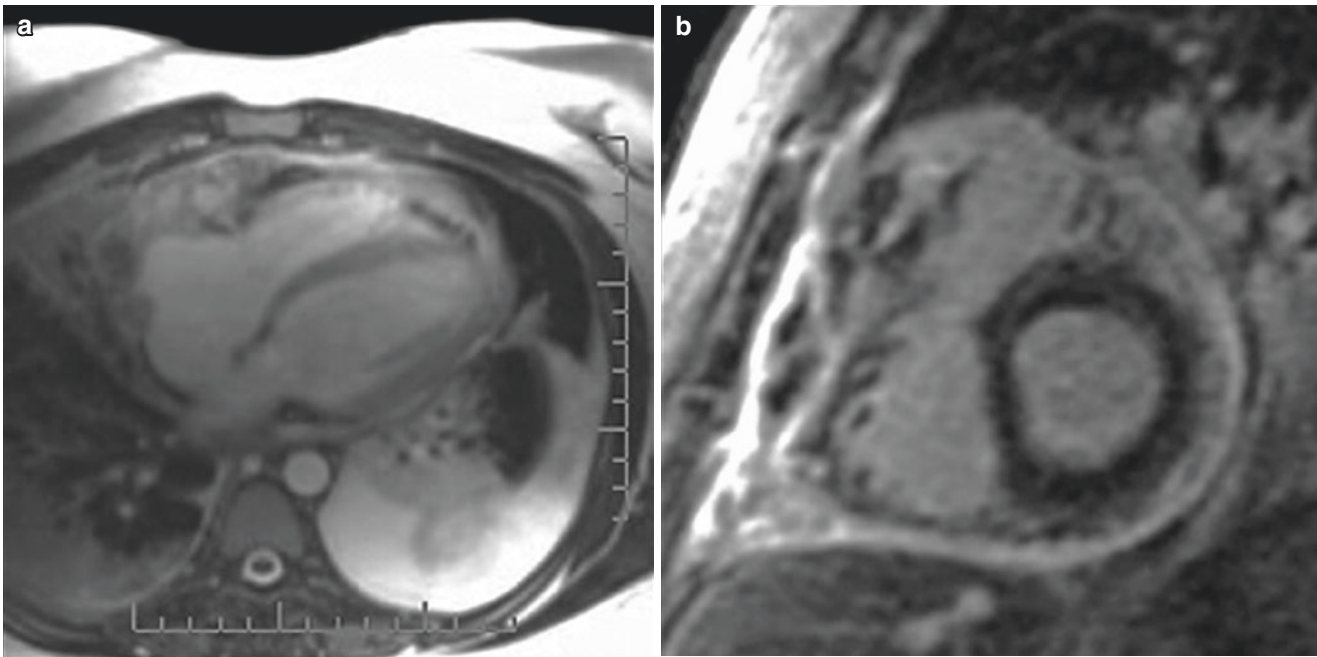


**Fig. 17.10** (a) Gadolinium Enhancement of an Angiosarcoma – Bright Blood Axial View. (b) Gadolinium Enhancement of an Angiosarcoma – Bright Blood Short Axis View. A pericardial effusion is also seen surrounding the heart

However, gadolinium administration is also very important as neoplasms, being vascular, will enhance with contrast (Fig. 17.10).

## 17.9 Comparison of Imaging Modalities

Echocardiography is usually the first-line noninvasive test used in patients with suspected pericardial disease. Echo is portable, cheap, and provides valuable anatomic and physiologic information. There is also a wealth of scientific data supporting its use. However, echo can be limited by poor acoustic windows, especially in patients who are obese; have had previous cardiothoracic surgery; have thoracic deformities or have lung disease. Echo is also hampered by small fields-of-view, poor tissue characterization, and limited views of the pericardium. Because of these important limitations, echo may not, by itself, be able to provide enough information for a definitive diagnosis.

Two additional noninvasive imaging techniques, CT and MRI, have emerged and have been found to be extremely valuable in providing additional information in pericardial disease patients that have undergone a nondiagnostic echocardiographic exam.

Computed tomography is a 3D, high-resolution noninvasive imaging technique that provides larger fields-of-view than echo. CT technique has excellent spatial and contrast resolution and therefore can assess pericardial thickness, fluid, calcification, and masses accurately. Computed tomog-

raphy is capable of high-resolution thin-section imaging using isotropic voxels and can be gated to the cardiac cycle, allowing cinematic displays of cardiac motion. However, despite this ability, CT has limited temporal resolution and thus may not provide adequate physiologic information. Because of the temporal resolution limitations real-time imaging may also not be possible. Computed tomography also uses ionizing radiation to obtain its images. In fact, gated CT examinations can result in a radiation dose that exceeds that of cardiac catheterization. Finally, CT examinations usually require the administration of iodinated contrast with its attendant risks of nephrotoxicity and potential allergic reactions.

CMR is a reliable method for the comprehensive assessment of the pericardium because it offers excellent spatial, temporal, and contrast resolution, as well as accurate functional and three-dimensional imaging with highly reproducible measurements. There are no limitations regarding acoustic windows, no ionizing radiation is used and no nephrotoxic contrast media is given. A gadolinium-based contrast agent is frequently administered, but it is widely regarded as significantly safer than iodinated contrast material. CMR also offers important advantages over both echo and CT.

CMR has larger fields-of-view than echo potentially providing a much easier and fuller anatomical assessment. The pericardial thickness is visible over the entire heart and pericardial fluid may be more reliably detected especially over the inferior wall with MRI. CMR can also accurately identify adherent areas of pericardium which can be an advantage in

patients headed to surgery for constriction. Lastly, image quality is not limited in patients with prior cardiothoracic surgery, concomitant lung disease, or who have anatomical deformities.

CMR has better temporal resolution than CT thus allowing for functional assessment and real-time imaging capabilities. This faster temporal resolution provides MRI with the ability to diagnose both pericardial constriction and tamponade. Tagging techniques with MRI can also aid in the identification of adherent areas of pericardium to myocardium. In addition, no radiation is used for obtaining images. Finally, and most importantly, MRI provides superior tissue characterization relative to both CT and echocardiography.

MRI is limited in very obese patients who cannot fit in the bore of the magnet and in people who are severely claustrophobic. MRI also cannot reliably be used in patients with contraindications, such as patients with certain implanted devices like pacemakers, implantable cardioverter defibrillators, or aneurysms clips to name a few. Despite these limitations, protocols do exist to safely image patients with pacemakers and defibrillators if the study is clinically necessary [35–39].

### 17.10 Uses and Appropriateness

In 2006 The American College of Cardiology Foundation's (ACCF) Committee on Appropriateness for cardiac CT and cardiac MRI deemed cardiac MRI "appropriate" for the evaluation of pericardial conditions, especially in the areas of pericardial masses and pericardial constriction [40]. In 2019 in its document on Appropriate Use Criteria for Multimodality Imaging, the ACCF again reaffirmed that cardiac MRI was "appropriate" for the evaluation of suspected pericardial disease, as well as for the re-evaluation of progression of pericardial effusion size or development of tamponade, or for progression of pericardial constriction [41].

The ACCF published an expert consensus document on cardiovascular MRI in 2010. This panel supported the use of CMR in the evaluation of pericardial disease patients because of its ability to provide a comprehensive structural and functional assessment of the pericardium. In addition, they highlighted the importance of MRI in identifying the physiological consequences of pericardial constriction [42].

The European Society of Cardiology Task Force on the Diagnosis and Management of Pericardial Diseases mentions CMR in its diagnostic pathway for acute pericarditis patients, if previous tests have proven inconclusive. They establish CMR as a class IIa indication (weight of evidence/opinion is in favor of usefulness/efficacy) [43]. CMR is also mentioned as useful for assessing the size and extent of simple and complex pericardial effusions and in helping to diagnose constrictive pericarditis [43].

A position paper on clinical indications for CMR was published by the Society of Cardiovascular Magnetic Resonance (SCMR) in 2020 [44]. CMR in pericardial diseases was given a class I indication (provides clinically relevant information and is usually appropriate; may be used as first-line imaging technique; usually supported by substantial literature or randomized controlled trials) for assessment of congenital anomalies of the pericardium, pericardial constriction, and pericardial inflammation. Routine CMR for pericardial effusions was given a class III indication (provides clinically relevant information but is infrequently used because information from other imaging techniques is usually adequate).

### 17.11 Conclusions

Because of the nature and certain limitations of noninvasive imaging studies, pericardial disease may prove difficult to diagnose with a single noninvasive imaging modality. Often an accurate diagnosis is the result of multiple noninvasive imaging studies in conjunction with invasive studies. Because of favorable inherent imaging characteristics, CMR can provide a structural and functional assessment of the pericardium in a broad range of pericardial disorders. These features support the use of CMR in either a primary or confirmatory role in the evaluation of patients with suspected pericardial disorders.

#### Practical Pearls

1. Because of the nature and certain limitations of noninvasive imaging studies, pericardial disease may prove difficult to diagnose with a single noninvasive imaging modality.
2. Echocardiography can be limited by poor acoustic windows, especially in patients who are obese; have had previous cardiothoracic surgery; have thoracic deformities or have lung disease. Echo is also hampered by small fields-of-view, poor tissue characterization, and limited views of the pericardium.
3. CMR has larger fields-of-view than echo potentially providing a much easier and fuller anatomical assessment. With CMR pericardial thickness is visible over the entire heart, pericardial fluid may be more reliably detected especially over the inferior wall, and image quality is not limited in patients with prior cardiothoracic surgery, concomitant lung disease, or who have anatomical deformities. CMR can also accurately identify adherent areas of pericardium.
4. CMR has better temporal resolution than cardiac CT thus allowing for functional assessment and real-time imaging capabilities. This faster temporal resolution provides



MRI with the ability to diagnose both pericardial constriction and tamponade.

- SMR position paper (2020) gave CMR class I indication for assessment of congenital anomalies of the pericardium, pericardial constriction, and pericardial inflammation. Routine CMR for pericardial effusions was given a class III indication.

## References

- Little WC, Freeman GL. Pericardial disease. *Circulation*. 2006;113:1622–32.
- Sechtem U, Tscholakoff D, Higgins CB. MRI of the abnormal pericardium. *AJR Am J Roentgenol*. 1986;147:245–52.
- Bogaert J, Duerinckx AJ. Appearance of the normal pericardium on coronary MR angiograms. *J Magn Reson Imaging*. 1995;5:579–87.
- Chako AC, Temany CM, Zerhouni EA. Effect of slice acquisition direction on image quality in thoracic MRI. *J Comput Assist Tomogr*. 1995;19:936–40.
- Bogaert J, Francone M. Cardiovascular magnetic resonance in pericardial diseases. *J Cardiovasc Magn Reson*. 2009;11:14.
- Letanche G, Gayet C, Souquet PJ, Mallet JJ, Bernard JP, Laine X, Touraine R. Agenesis of the pericardium: clinical, echocardiographic and MRI aspects. *Rev Pneumol Clin*. 1988;44:105–9.
- Gutierrez FR, Shackelford GD, McKnight RC, Levitt RG, Hartmann A. Diagnosis of congenital absence of left pericardium by MR imaging. *J Comput Assist Tomogr*. 1985;9:551–3.
- Abbas AE, Appleton CP, Liu PT, Sweeney JP. Congenital absence of the pericardium: case presentation and review of literature. *Int J Cardiol*. 2005;98:21–5.
- Psychidis-Papakyritsis P, de Roos A, Kroft LJM. Functional MRI of congenital absence of the pericardium. *AJR Am J Roentgenol*. 2007;189:W312–4.
- Carretta A, Negri G, Pansera M, Melloni G, Zannini P. Thoracoscopic treatment of a pericardial diverticulum. *Surg Endosc*. 2003;17:158–9.
- Taylor AM, Dymarkowski S, Verbeken EK, Bogaert J. Detection of pericardial inflammation with late-enhancement cardiac magnetic resonance imaging: initial results. *Eur Radiol*. 2006;16:569–74.
- Teraoka K, Hirano M, Yannbe M, Ohtaki Y, Ohkubo T, Abe K, Yamashina A. Delayed contrast enhancement in a patient with perimyocarditis on contrast-enhanced cardiac MRI: case report. *Int J Cardiovasc Imaging*. 2005;21:325–9.
- Yelgec NS, Dymarkowski S, Ganame J, Bogaert J. Value of MRI in patients with a clinical suspicion of acute myocarditis. *Eur Radiol*. 2007;17:2211–7.
- Sa MI, Kiesewetter CH, Jagathesan R, Prasad SK. *Circulation*. 2009;119:e183–6.
- Santamore WP, Bartlett R, Van Buren SJ, Dowd MK, Kutcher MA. Ventricular coupling in constrictive pericarditis. *Circulation*. 1986;74:597–602.
- Masui T, Finck S, Higgins CV. Constrictive pericarditis restrictive cardiomyopathy: evaluation with MR imaging. *Radiology*. 1992;182:369–73.
- Troughton RW, Asher CR, Klein AL. Pericarditis. *Lancet*. 2004;363:717–27.
- Talreja DR, Edwards WD, Danielson GK, et al. Constrictive pericarditis in 26 patients with histologically normal pericardial thickness. *Circulation*. 2003;108:1852–7.
- Mulvagh SL, Rokey R, Vick GWD, Johnston DL. Usefulness of nuclear magnetic resonance imaging for evaluation of pericardial effusions, and comparison with two-dimensional echocardiography. *Am J Cardiol*. 1989;64:1002–9.
- Mikolich JR, Martin ET. Constrictive pericarditis diagnosed by cardiac magnetic resonance imaging in a pacemaker patient. *Circulation*. 2007;115:e191–3.
- Kojima S, Yamada N, Gotto Y. Diagnosis of constrictive pericarditis by tagged cine magnetic resonance imaging. *N Engl J Med*. 1999;341:373–4.
- Giorgi B, Mollet NRA, Dymarkowski S, Rademakers FA, Bogaert J. Assessment of ventricular septal motion in patients clinically suspected of constrictive pericarditis, using magnetic resonance imaging. *Radiology*. 2003;228:417–24.
- Fancone M, Szymkowski S, Kalantzi M, Rademakers FE, Bogaert J. Assessment of ventricular coupling with real-time cine MRI and its value to differentiate constrictive pericarditis from restrictive cardiomyopathy. *Eur Radiol*. 2006;16:944–51.
- Grizzard JD, Ang GB. Magnetic resonance imaging of pericardial disease and cardiac masses. *Cardiol Clin*. 2007;25:111–40.
- Kastler B, Germain P, Dietemann JL, et al. Spin echo MRI in the evaluation of pericardial disease. *Comput Med Imaging Graph*. 1990;14(4):241–7.
- Wang ZJ, Reddy GP, Gotway MB, et al. CT and MR imaging of pericardial disease. *Radiographics*. 2003;23:S167–80.
- Glockner JF. Imaging of pericardial disease. *Magn Reson Imaging Clin N Am*. 2003;11(1):149–62; vii.
- Frank H, Globits S. Magnetic resonance imaging evaluation of myocardial and pericardial disease. *J Magn Reson Imaging*. 1999;10(5):617–26.
- Hoffmann U, Globits S, Schima W, et al. Usefulness of magnetic resonance imaging of cardiac and paracardiac masses. *Am J Cardiol*. 2003;92:890–5.
- Mikolich JR. Right ventricular diastolic collapse by cardiac magnetic resonance imaging. *Circulation*. 2008;118:e122–5.
- Francone M, Dymarkowski S, Kalantzi M, et al. Real-time cine MRI of ventricular septal motion: a novel approach to assess ventricular coupling. *J Magn Reson Imaging*. 2005;21(3):305–9.
- Kronzon I, Cohen ML, Winer HE. Cardiac tamponade by loculated pericardial hematoma: limitations of M-mode echocardiography. *J Am Coll Cardiol*. 1983;1:913–5.
- Gilkeson RC, Chiles C. MR evaluation of cardiac and pericardial malignancy. *Magn Reson Imaging Clin N Am*. 2003;11(1):173–86; viii.
- Syed IS, Feng D, Harris SR, Martinez MW, Misselt AJ, Breen JF, Miller DV, Araoz PA. MR imaging of cardiac masses. *Magn Reson Imaging Clin N Am*. 2008;16:137–64.
- Martin ET, Coman JA, Shellock FG, Pulling CC, Fair R, Jenkins K. Magnetic resonance imaging and cardiac pacemaker safety at 1.5 Tesla. *J Am Coll Cardiol*. 2004;43:1315–24.
- Nazarian S, Roguin A, Menekhem Zviman M, Lardo A, Timm L, et al. Clinical utility and safety of a protocol for noncardiac and cardiac magnetic resonance imaging of patients with permanent pacemakers and implantable-cardioverter defibrillators at 1.5 Tesla. *Circulation*. 2006;114:1277–84.
- Levine GN, Arai A, Bluemke D, Flamm S, Gomes A, Kanal E, Manning W, Martin ET, Smith JM, Wilke N, Shellock FS. Safety of magnetic resonance imaging in patients with cardiovascular devices: an American Heart Association scientific statement from the committee on diagnostic and interventional cardiac catheterization, council on clinical cardiology, and the council on cardiovascular radiology and intervention. *Circulation*. 2007;116:2878–91.
- Russo RJ, Costa HS, Silva PD et al. Assessing the Risk Associated with MRI in Patients with a Pacemaker or Defibrillator. *N Engl J Med*. 2017;376:755–64.



39. Nazarian S, Hansford R, Rahsepar AA, et al. Safety of Magnetic Resonance Imaging in Patients with Cardiac Devices. *N Engl J Med*. 2017;377:2555–64.
40. Hendel RC, Kramer CM, Patel MR, Poon M. ACCF/ACR/SCCT/SCMR/ASNC/NASCI/SCAI/SIR 2006 appropriateness criteria for cardiac computed tomography and cardiac magnetic resonance imaging. *J Am Coll Cardiol*. 2006;48:1475–97.
41. Doherty JU, Kort S, Mehran R, Schoenhagen P, Soman P. ACC/AATS/AHA/ASE/ASNC/HRS/SCAI/SCCT/SCMR/STS 2019 Appropriate Use Criteria for Multimodality Imaging in the Assessment of Cardiac structure and Function in Nonvalvular Heart Disease. *J Am Coll Cardiol*. 2019;73:488–16.
42. Hundley WG, Bluemke DA, Finn JP. ACCF/ACR/AHA/NASCI/SCMR 2010 expert consensus document on cardiovascular magnetic resonance. *Circulation*. 2010;121:2462–508.
43. Maisch B, Seferovic PM, Ristic AD, et al. Guidelines on the diagnosis and management of pericardial diseases. *Eur Heart J*. 2004;25:587–610.
44. Leiner T, Bogaert J, Friedrich MG, et al. SCMR position paper (2020) on clinical indications for cardiovascular magnetic resonance. *J Cardiovasc Magn Reson*. 2020;22:76. <https://doi.org/10.1186/s12968-020-00682-4>.



## 18.1 Introduction

Evaluation of cardiac mass or tumor has become a routine application for cardiovascular magnetic resonance (CMR) imaging. CMR is a versatile imaging modality that provides two-dimensional or three-dimensional imaging using a variety of pulse sequences for a comprehensive assessment of cardiac masses. Echocardiography is usually the first-line imaging modality used in patients suspected of a cardiac mass or tumor; however, this technique has several limitations, is highly dependent upon availability of good echocardiographic “windows” and even then may not be able to provide a comprehensive answer due to limited field of view and inability to characterize tissue. In this regard, CMR imaging has evolved as a reference standard method for the assessment of suspected cardiac tumors and is being increasingly used for confirmation, localization, and tissue characterization of cardiac masses discovered in other types of imaging. CMR imaging readily evaluates for the presence of tumor-related cardiovascular complications and is helpful in determining prognosis and treatment planning.

**Supplementary Information** The online version contains supplementary material available at [https://doi.org/10.1007/978-3-031-29235-4\\_18](https://doi.org/10.1007/978-3-031-29235-4_18).

M. A. Syed (✉)  
Cardiovascular Imaging, Division of Cardiology, Loyola  
University Medical Center, Maywood, IL, USA  
e-mail: [masyed@lumc.edu](mailto:masyed@lumc.edu)

R. H. Mohiaddin  
Cardiovascular Imaging, Royal Brompton and Harefield Hospitals,  
Guy’s and St Thomas’ NHS Foundation Trust, London, UK

National Heart and Lung Institute, Imperial College London,  
London, UK  
e-mail: [r.mohiaddin@rbht.nhs.uk](mailto:r.mohiaddin@rbht.nhs.uk)

In this chapter, we will focus on the common types of tumors that involve the heart. For pericardial tumors, the reader is referred to the chapter “Pericardial Diseases” that provides an overview of pericardial tumors. This chapter will focus on specific CMR techniques, imaging protocols, and appearance of common tumors. A sample imaging protocol is also provided.

## 18.2 Cardiac Tumors in Adults

Primary cardiac tumors are rare but can occur in all age groups with an estimated incidence of 0.02% in autopsy series [1]. Non-neoplastic masses or pseudo-tumors are seen more frequently than true tumors (Table 18.1). Pseudo-tumors are masses that may falsely appear like a tumor usually discovered on echocardiography and often referred to CMR for further assessment. The common pseudo-tumors include thrombi (Fig. 18.1), lipomatous hypertrophy of interatrial septum (Fig. 18.2), caseous variety of mitral annular calcification [2], prominent crista terminalis and cysts (Fig. 18.3) among other causes (Table 18.1).

Primary cardiac tumors can be benign or malignant (Table 18.2). Benign cardiac tumors remain extremely rare although relatively more common than primary malignant cardiac tumors. Of all primary cardiac tumors, 75% are histologically benign [3]. Myxomas represent approximately 50% of benign tumors, while rhabdomyomas (5–10%) and fibromas (4–6%) occur less commonly [4]. Most common benign tumors encountered in adults are myxomas followed by papillary fibroelastoma.

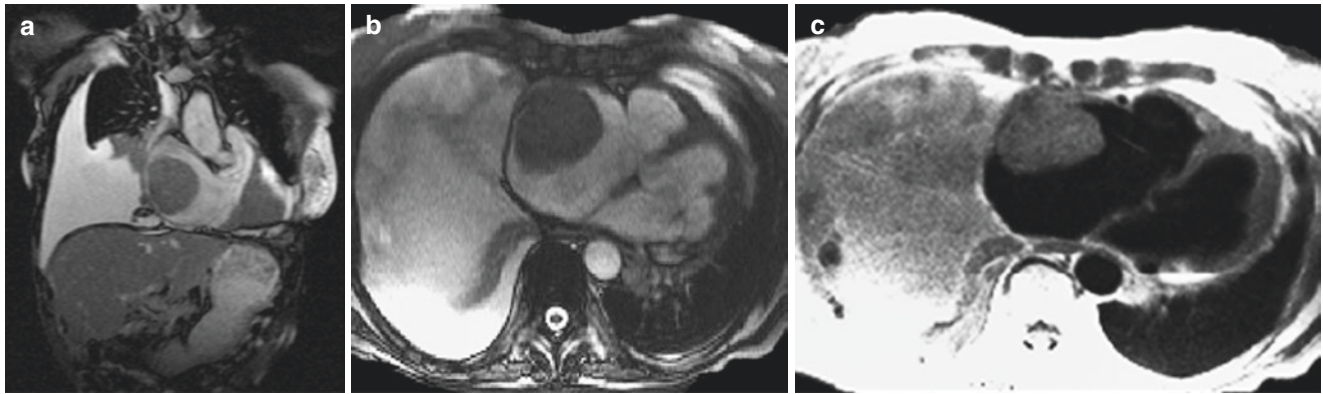
Secondary malignant cardiac tumors that metastasize to the heart are 40–50 times more common than primary cardiac tumors [5]. Spread to the heart occurs through direct extension from adjacent tumors, hematogenous and/or lymphatic spread, and transvenous invasion. Common tumors metastasizing to the heart are shown in Table 18.2. Direct extension occurs from lung, breast, esophageal, or

**Table 18.1** Pseudo-tumors

Thrombus
Cyst (pericardial, bronchogenic)
Lipomatous hypertrophy of interatrial septum
Caseous mitral annular calcification
Hypertrophied papillary muscle
Calcified hematoma
Inflammatory mass

other mediastinal tumors. Venous extension occurs through the inferior vena cava, superior vena cava, or pulmonary veins.

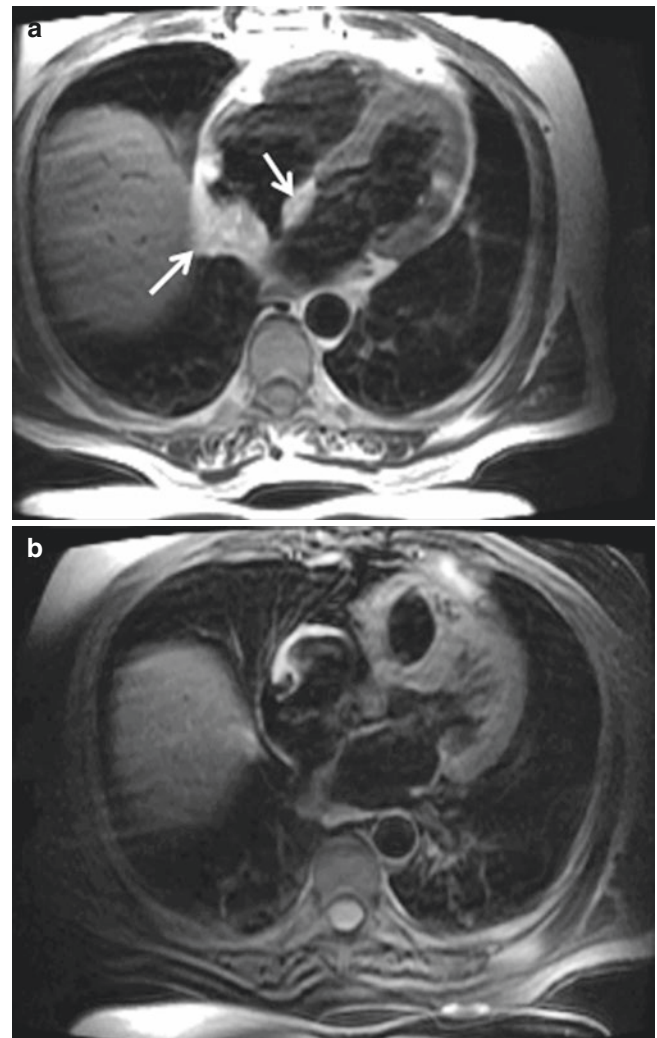
Primary malignant tumors account for approximately 15% of primary cardiac tumors and can broadly be divided into sarcomas, lymphomas, and pericardial malignancy [6]. Sarcoma is the most common primary cardiac malignant



**Fig. 18.1** Large mass in the right atrium. Mass has well-defined borders and is isointense with myocardium on black blood T2 image. It does not infiltrate right atrial wall and there is no associated pericardial

effusion. Right atrium is severely dilated. This is an example of a large thrombus in the right atrium in a patient with Ebstein's anomaly (**a** and **b** are SSFP images and **c** is black blood T2w spine-echo image)

**Fig. 18.2** Lipomatous hypertrophy of interatrial septum. The fatty mass is “dumb-bell” shaped and spares the fossa ovalis (**a**, arrows). On T1 weighted fat saturation image the fat is saturated and mass appears dark confirming fatty tissue (**b**)



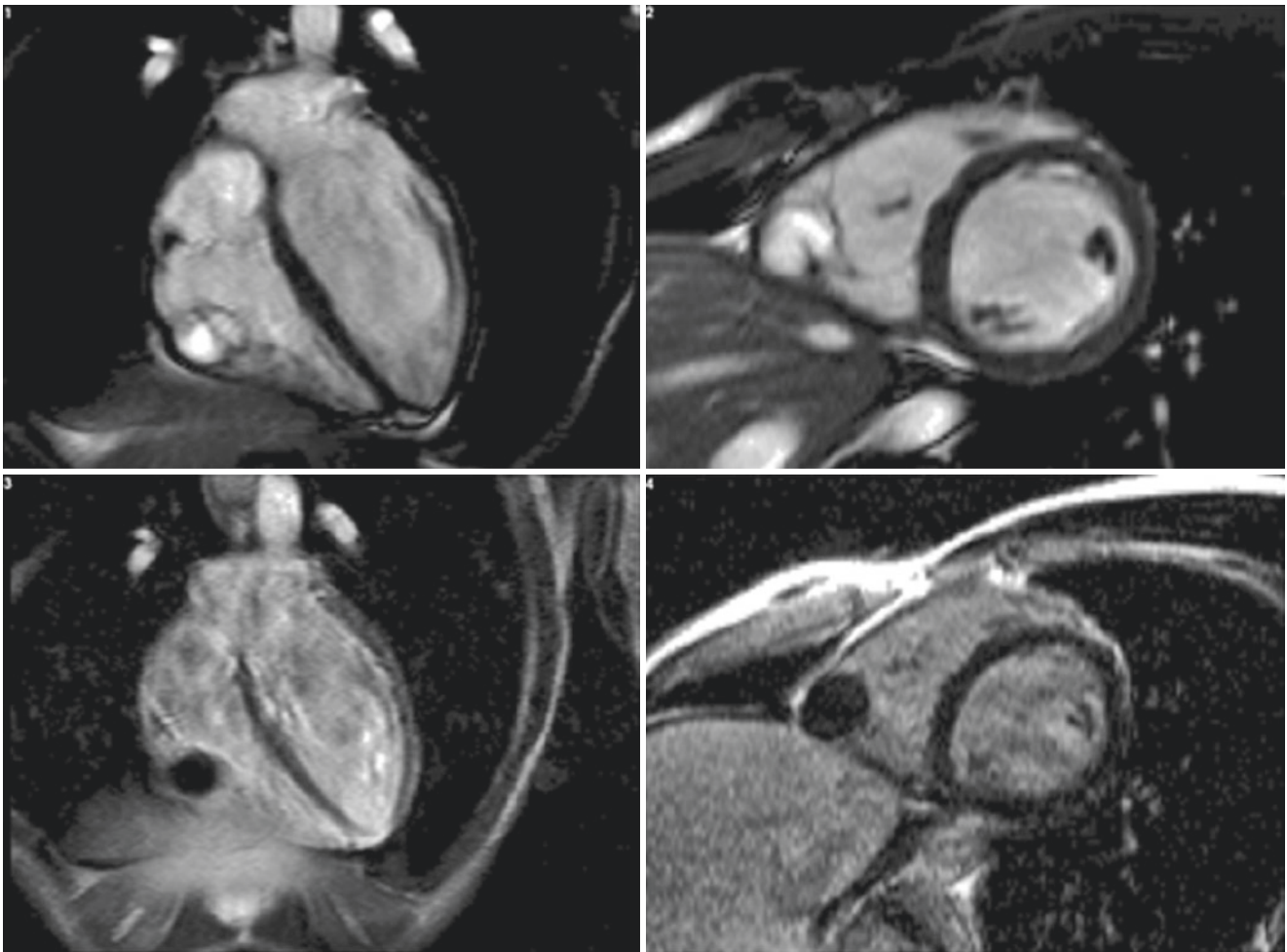


**Fig. 18.3** Hydatid cyst in the right ventricle. A cystic mass is seen on the cine SSFP images (*upper row*) and non-enhancing mass on post-contrast images (*bottom row*)

tumor and are extremely rare, usually described in isolated case reports or reviews. Virtually all types of sarcomas have been reported in the heart. Angiosarcomas are the most common form of cardiac sarcoma arising predominantly in the right atrium. Other most frequently described sarcomas include rhabdomyosarcomas (the most common primary cardiac malignancy in children), fibrosarcomas, and leiomyosarcomas.

According to one report, primary cardiac lymphoma histology has become the most common histology type after 1992, representing 39% of primary cardiac malignant tumors by 2003 [7]. Primary cardiac lymphomas are aggressive B-cell lymphomas with higher incidence in immunocompromised patients. The right atrium is the commonest site of origin with frequent involvement of more than one cardiac chamber and pericardial invasion.



**Table 18.2** Cardiac tumors

Benign tumors
Myxoma
Rhabdomyoma
Fibroelastoma
Fibroma
Lipoma
Hemangioma
Teratoma
Malignant tumors
<i>Primary</i>
Angiosarcoma
Rhabdomyosarcoma
Leiomyosarcoma
Fibrosarcoma
Liposarcoma
Lymphoma
Osteosarcoma
Other sarcomas
<i>Secondary</i>
Metastasis
Melanoma
Thyroid
Lung
Esophagus
Kidney
Breast
Lymphoma
Leukemia
Direct extension
Lung
Breast
Esophageal
Mediastinal
Venous extension
Renal
Hepatic
Adrenal cortex
Lung
Thyroid
Endometrium

### 18.3 Cardiac Tumors in Children

Cardiac tumors are also rare in children, with reported incidence of 0.03–0.08% [8, 9]. In a multicenter international CMR study of 78 cases in children, tumors were found in all cardiac chambers and extracardiac locations with most common location being the ventricular myocardium [10]. Most common tumor was fibroma (38%) followed by rhabdomyoma (18%), malignant (16%), hemangioma (12%), myxoma (4%), and teratoma (3%). Malignant tumors included osteosarcoma ( $n = 3$ ), rhabdomyosarcoma ( $n = 2$ ), and 1 case each of angiosarcoma, B-cell lymphoma, desmoplastic round cell tumor, melanoma, and medulloblastoma. Other series have reported rhabdomyomas as the most common cardiac tumor

in children which likely represents a referral bias to MR imaging as these tumors are usually diagnosed by echocardiography due to their typical appearance and not referred for MR imaging [11].

## 18.4 Clinical Presentation

Many tumors are found on cardiac imaging studies investigating other pathology and may remain clinically silent while others present with early symptoms. Symptoms of cardiac tumors are highly variable and are typically secondary to their effect on normal cardiac geometry and function. Symptoms also depend upon mass size and location. Arrhythmias, particularly sudden death and abnormal atrioventricular conduction, are common because of tumor disruption of the conduction system. Cardiac tumor should be considered in the differential diagnosis of any patient with an embolic phenomenon or signs or symptoms of inflow or outflow obstruction with left or right-sided heart failure.

### 18.4.1 Symptoms and Signs

- Heart failure: left and/or right ventricular failure can be caused by cardiac chamber obliteration by tumor or abnormal myocardial function secondary to intramyocardial tumor growth. Tumor growth can also cause left or right ventricular outflow tract obstruction (Fig. 18.4). Valve function can also be impaired due to tumor compression or growth causing stenosis or regurgitation.
- Palpitations: usually occurs due to myocardial irritation from tumor or involvement of the conduction system.
- Sudden death: usually related to malignant arrhythmias.
- Syncope: syncopal episodes might be related to associated arrhythmias or ventricular outflow obstruction.

### 18.4.2 Complications

- Congestive heart failure due to impairment of ventricular function
- Left or right ventricular inflow and/or outflow obstruction
- Conduction system involvement
- Peripheral embolism
- Tissue invasion

Prognosis of tumors is also variable and depends on many factors including whether they are benign or malignant. Benign tumors can generally be completely resected with good prognosis with minimal morbidity particularly before reaching the complication stage. Malignant tumors in gen-

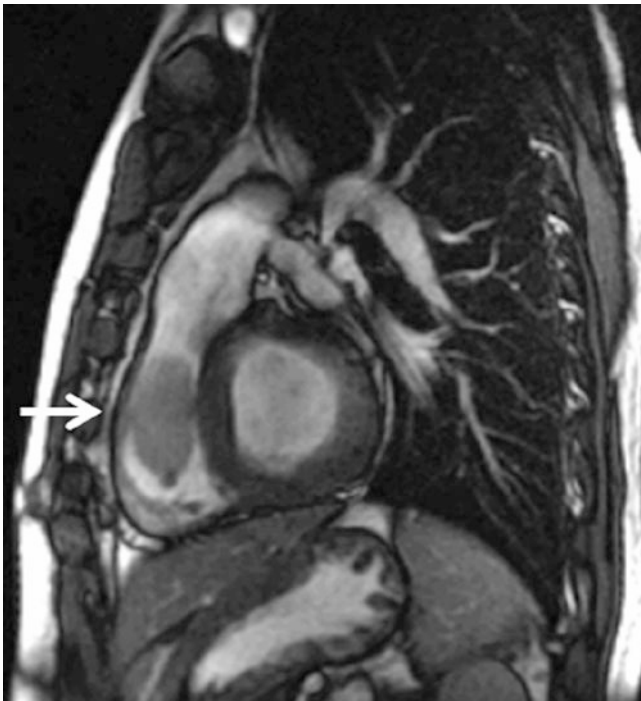


**Fig. 18.4** Cine SSFP sequence shows a large mass in the right ventricular outflow tract causing flow obstruction. This was metastatic malignant melanoma (*arrow*)

eral have a poor prognosis with median survival rates of around 12 months despite surgical debulking and aggressive chemotherapy [12].

## 18.5 Magnetic Resonance Imaging

### 18.5.1 Goals of CMR Imaging

The information provided by CMR imaging is not only important for diagnosis but also helps in determining prognosis and treatment planning including surgical resection [13]. Because most masses are not amenable to biopsy, the role of imaging becomes critical in their evaluation. The broad goals of CMR imaging in the evaluation of cardiac mass include:

1. Location
2. Size and shape
3. Tumor borders and extent/tissue invasion
4. Tissue characterization
5. Differentiating true tumor from pseudo-tumors
6. Evaluating impact on cardiac structure and function
7. Presence of pericardial or pleural effusion

### 18.5.2 CMR Sequences and Imaging Protocol

Cardiac mass may initially be discovered on echocardiography or chest imaging performed for non-cardiac causes. CMR is usually used for confirmation and further assessment of a mass. CMR not only provides accurate localization of a mass but a comprehensive evaluation by utilizing a variety of imaging techniques called “pulse sequences” before and after administration of gadolinium-based contrast agent (GBCA). It’s important to understand the strengths and limitations of each CMR sequence for appropriate utilization. A sample CMR imaging protocol is shown in Table 18.3.

#### 18.5.2.1 Cine Imaging

Mass localization is usually performed by cine bright-blood imaging with steady-state free precession (SSFP) sequence. The SSFP sequence is considered the “work-horse” for CMR imaging and is used to acquire cine images in different conventional or non-conventional planes, e.g. axial, coronal, sagittal, and/or oblique. SSFP sequence provides intrinsically high contrast between blood pool and adjacent myocardium or mass without the need for administering GBCA. Images are electrocardiography (ECG)-gated and acquired during breath holding. Free-breathing image acquisition is possible using accelerated MRI acquisition techniques in patients who are unable to hold their breath. Volumetric coverage of the heart is required to localize the mass and assess its size, shape, and relationship to other cardiovascular and extra-cardiac structures. We usually acquire this volumetric coverage in axial orientation with contiguous slices without inter-slice gap from pulmonary arteries to the diaphragm (Movie 18.1). In addition to delineation of the anatomic extent of the mass, cine imaging provides a quantitative assessment of myocardial and valve functional impairment or other complications associated with cardiac tumors. Cine images can be helpful in identifying specific tumor types that have a predilection for certain cardiac chambers or valves. Features like tumor attachment site, mobility, border definition, invasion of chamber walls or extracardiac structures, and presence of pericardial effusion help in further differentiating cardiac tumors. However, cine images are usually not adequate for tissue characterization of the mass, which requires the use of other sequences and administration of GBCA. It’s also worth noting that some tumors may display similar tissue features as myocardium or blood on SSFP imaging and can be missed.

#### 18.5.2.2 Black-Blood Imaging

Tissue characterization of a cardiac mass is based on its hydrogen proton density and tissue relaxation ( $T_1$  and  $T_2$ )

**Table 18.3** CMR protocol

Image	Sequence	Planning	Purpose
Three-plane localizers (axial, sagittal, coronal)	Single-shot SSFP	3–6 images in each three orthogonal planes	Heart localization & isocentering
Axial stack	Black blood HASTE or Single-shot ECG-gated, breath-held	Contiguous axial slices from above the clavicles to the diaphragm include the heart, systemic/pulmonary vessels, and proximal part of arch branches	Cardiac and extra-cardiac anatomy, mass localization
2-Chamber LV localizer	Single-shot SSFP ECG-gated, breath-held	Single slice, orthogonal plane through long axis of left ventricle from mitral valve to LV apex, planned from axial stack	Planning cine sequences
Short-axis localizers	Single-shot SSFP ECG-gated, breath-held	Multiple contiguous slices from AV valves to the ventricular apex	Planning cine sequences
2-Chamber LV	SSFP cine ECG-gated, breath-held	Single slice, copy image position from 2-chamber localizer	LV and mitral valve function assessment, mass localization
4-Chamber LV	SSFP cine ECG-gated, breath-held	Orthogonal plane across AV valves prescribed from short-axis localizers	AV valve function, mass localization
Axial stack (volumetric coverage)	SSFP cine ECG-gated, breath-held	Contiguous axial slices from the pulmonary arteries to the diaphragm to include the heart, systemic and pulmonary vessels	Mass localization, size, shape, extent, extra-cardiac involvement
LV and RV outflow tracts	SSFP cine ECG-gated, breath-held	LV planned from short-axis localizers. RV planned from axial stack	Outflow tract morphology, semilunar valve assessment, mass localization
Short-axis stack	SSFP cine ECG-gated, breath-held	Orthogonal plane parallel to AV valves prescribed from end-diastolic frame of 4 chamber cine, from above the AV valves to the apex	Ventricular volume and function assessment, mass localization
Black Blood	T1w, T2w, fat saturation	Use orientation where mass is best seen. Copy image position from cine slices	Mass tissue characterization
Perfusion (First pass during gadolinium injection)	Saturation recovery or SSFP ECG-gated, breath-held	Combination of short axis and long axis, 3–4 slices prescribed in orientation where mass is best seen	Mass vascularity/tissue characterization
Late gadolinium enhancement (10–15 min post contrast)	T1w, inversion recovery, TI time adjusted to null normal myocardium, ECG-gated, breath-held	Long-axis and short-axis views	Mass vascularity/tissue characterization
Late gadolinium enhancement (20 min post contrast)	T1w, inversion recovery, fixed TI 600 ms, ECG-gated, breath-held	Single slice, use orientation where mass is best seen.	Differentiate thrombus from tumor
<i>Optional: Flow</i>	In-plane and/or through-plane, ECG-gated, non-breath held	Outflow tract views or other views selected from cine images	Assessment of flow obstruction caused by the mass
<i>Optional: 3D MRA</i>	3D, non-ECG-gated, breath held	Coronal plane from right ventricle anteriorly to spine posteriorly	Assessment of systemic and/or pulmonary vascular involvement

properties. This type of imaging is acquired by using black-blood double inversion recovery fast spin echo sequence that is  $T_1$  or  $T_2$  weighted. These images are ECG-gated and acquired during breath holding. Fast imaging methods with half-Fourier acquisition usually cause blurring of cardiac structures and tumor as well as suboptimal suppression of blood pool signal and are therefore not recommended. Black-blood imaging provides high-resolution static images of the cardiac structures/mass and tissue characterization is based on different signal intensities from different cardiac structures. Fat saturation prepulses can be added to the black-blood sequence to characterize fatty masses, e.g. lipoma or lipomatous hypertrophy of interatrial septum (Fig. 18.2).

Malignant cells are usually larger in size and have higher intracellular water content compared to normal cells; malignant cells also have higher interstitial water content. These features translate into longer  $T_1$  and  $T_2$  relaxation times resulting in inherent contrast between tumors and normal tissues (Fig. 18.5) [14].

### 18.5.2.3 Perfusion Imaging

First-pass perfusion imaging is usually performed with  $T_1$ -weighted saturation recovery or SSFP sequence during the passage of GBCA through the myocardium after intravenous administration (Movie 18.2). This technique is well studied in stress MRI and has proven accuracy in the detection of

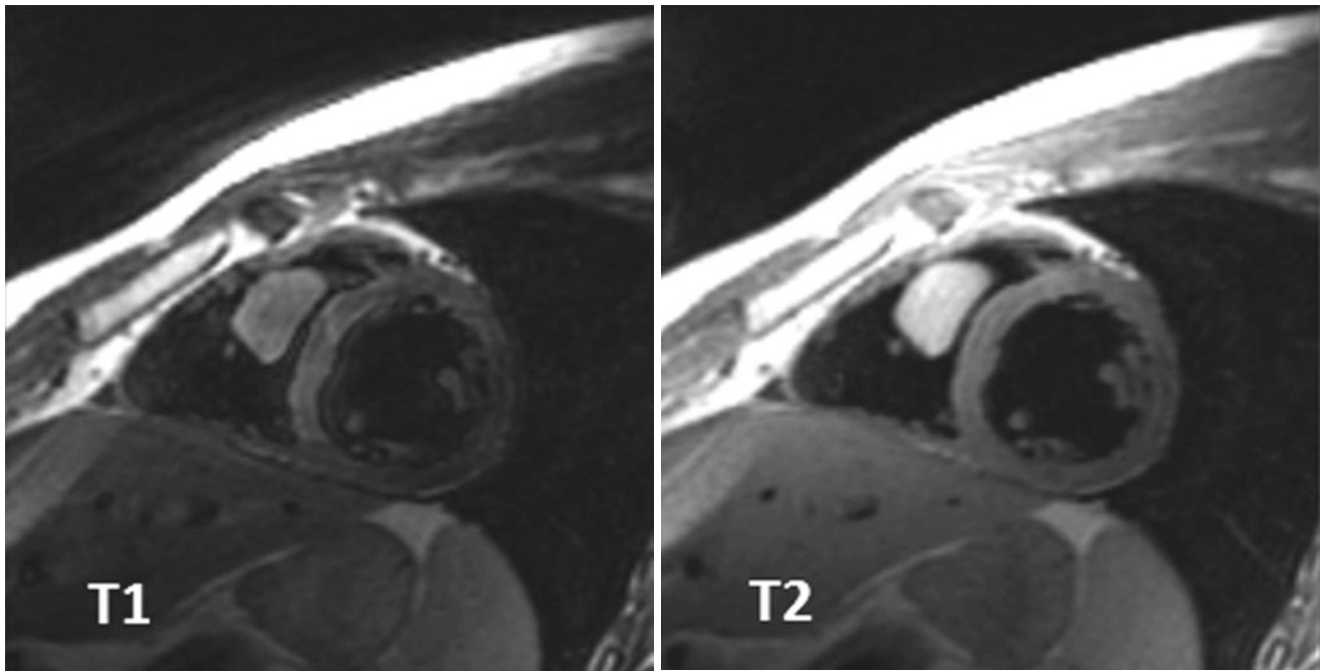


**Fig. 18.5** Black blood imaging of right ventricular tumor. Tumor is isointense on  $T_1$  and hyperintense on  $T_2$  images suggesting increased water content, which is a feature of malignant tumors (see text for details), in this case metastatic malignant melanoma

coronary artery stenosis. In the assessment of cardiac masses, CMR perfusion imaging at rest provides additional information for mass vascularity and tissue composition. Highly vascular tumors such as angiosarcoma, hemangioma, and some vascular malformations typically show significant contrast enhancement on first-pass perfusion imaging. First-pass perfusion imaging is also useful in differentiating cardiac tumors from thrombi. Thrombi are avascular structures and hence non-enhancing on perfusion imaging compared to tumors which are vascular and show different degrees of contrast enhancement.

#### 18.5.2.4 Late Gadolinium Enhancement

Late gadolinium enhancement (LGE) is typically performed with inversion recovery sequence, 10–20 min after administration of GBCA. GBCA are extra-cellular contrast agents and decrease tissue  $T_1$  relaxation. Malignant tumors have increased interstitial space and thus more volume of distribution for GBCA compared to normal tissues. LGE reflects uptake of GBCA within the areas of fibrosis, infarction, or expanded interstitium, such as in some benign and malignant tumors. Patchy delayed enhancement within a cardiac mass suggests regional variations in vascularity and is usually seen in malignant tumors and in up to 40–50% of benign tumors, e.g. myxoma [15].

LGE with long inversion time has been shown to be extremely sensitive for the detection of cardiac thrombi [16]. After completing the standard LGE imaging, we reimagine the slices with the mass by increasing inversion time to 600 ms.

Increasing the inversion time allows recovery of signal by virtually all tissues except thrombus which remains dark in these images.

#### 18.5.2.5 Optional Sequences

Masses causing flow obstruction across the valves or outflow tracts can be further interrogated by phase contrast velocity encoded flow imaging. This is analogous to the Doppler echocardiography and is acquired with ECG gating during free breathing. An in-plane flow image provides qualitative assessment of the site of flow obstruction or valve regurgitation. A through-plane flow image is then acquired to quantify gradients across the obstruction or to assess the severity of regurgitation.

Contrast-enhanced magnetic resonance angiography (CE-MRA) can be useful in the assessment of masses involving the vena cava, aorta, or pulmonary vessels. CE-MRA provides high-resolution, three-dimensional imaging of blood vessels infiltrated by the tumor and is helpful for surgical treatment planning. This sequence is non-ECG-gated and is acquired during breath holding.

## 18.6 CMR Findings in Cardiac Tumors

Kidaffas et al. published CMR-based diagnostic criteria that predict tumor type on the basis of their experience with 11 cases and review of literature [17]. Beroukhim et al. subsequently tested these diagnostic criteria in children in their



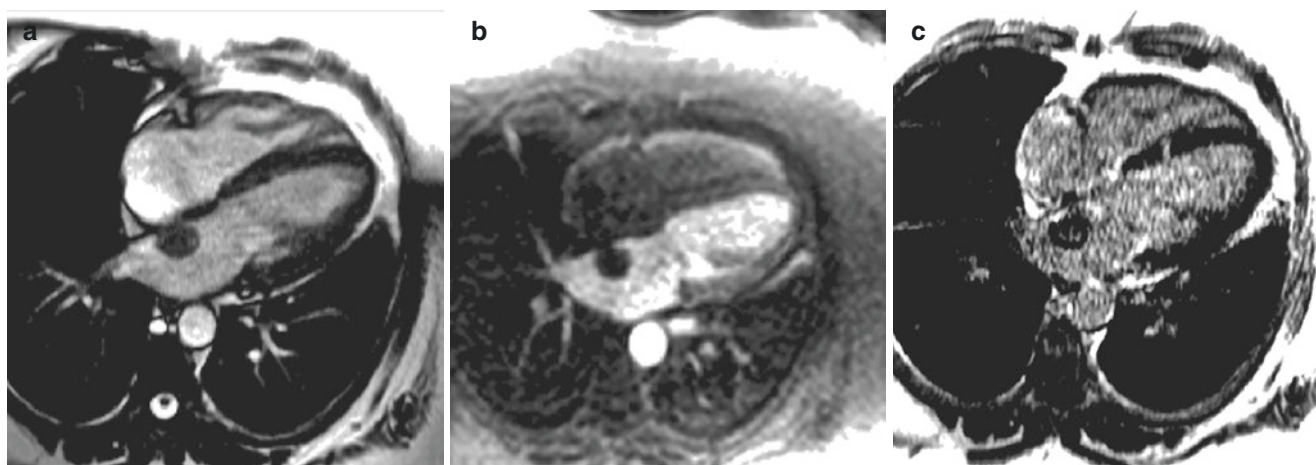


**Fig. 18.6** Left atrial myxoma. Atrial septum is the typical location where myxomas are attached by a stalk to the fossa ovalis. Myxoma appears heterogeneous on SSFP (a) due to the presence of areas of cal-

cification, hemorrhage, necrosis, and thrombus. Heterogeneous enhancement is seen on perfusion (b) and LGE images (c)

multicenter, international study [10]. Three reviewers blinded to the histologic diagnosis classified tumor type in 78 cases and correctly identified 97% of tumors. Incorrect diagnosis was related to atypical appearance on CMR images, suboptimal image quality, and lack of comprehensive examination. In a study of 55 adults with confirmed tumor histology, Hoffman et al. predicted malignancy with an area under the receiver-operator characteristic curve between 0.88 and 0.92 [15]. Tumor location, tissue composition and presence of pericardial or pleural effusion were predictors of malignancy.

CMR findings and tissue characteristics of common types of cardiac tumors are described below:

## 18.6.1 Benign Tumors

### 18.6.1.1 Myxoma

Myxomas usually arise from the endocardium and therefore can originate anywhere in the atria, ventricles, or valves; however, the vast majority (80%) develop from the left atrium, with the remainder from the right atrium (15–20%), and origin from ventricles or valves is rare [18]. Atrial septum is the typical location where myxomas are attached by a stalk to the fossa ovalis (Fig. 18.6). Myxomas are mostly solitary, range in size from 1 to 20 cm, but may occasionally be multiple, particularly in association with Carney complex (syndrome of myxoma, endocrine hyperfunction, and areas of skin pigmentation). Although benign, there are case reports of malignant transformation. They frequently are pedunculated masses and have organized thrombi on the surface. The clinical presentation consists of constitutional symptoms (fever, arthralgia, weight loss), embolic phenomenon, and cardiac obstruction typically involving the mitral

(left atrial myxoma) or tricuspid valve (right atrial myxoma).

Myxomas appear heterogeneous on SSFP due to the presence of areas of calcification, hemorrhage, necrosis, and thrombus [19]. They are generally hyperintense on T<sub>2</sub>-weighted images due to high extracellular water content and are isointense on T<sub>1</sub>-weighted images [13]. Heterogeneous enhancement is seen on perfusion and LGE images due to tissue heterogeneity and non-enhancing overlying thrombi.

### 18.6.1.2 Papillary Fibroelastoma

Papillary fibroelastomas (PFE) are the second most common benign cardiac tumor in adults. PFE also arise from endocardial surface but majority originate on the left-sided heart valves [20]. They are usually small, less than 1 cm, mobile pedunculated masses typically on the atrial surface of the mitral valve and aortic side of the aortic valve [21]. They are more common on aortic valves followed by mitral and less common on tricuspid and pulmonary valves. They resemble Lamb's excrescences histologically but tend to be larger, rounded, and away from the free edges of the valve. Most PFE are asymptomatic and are usually detected incidentally on echocardiography but have been associated with neurological symptoms related to embolic phenomenon. The differential diagnosis is usually with a valve vegetation, myxoma, or thrombus.

Small PFE are difficult to localize and characterize on CMR images due to their small size and rapid motion with valve leaflets. Therefore, their imaging requires high spatial and high temporal resolution sequences, e.g. SSFP. They have intermediate signal intensity similar to myocardium on T<sub>1</sub> on T<sub>2</sub> weighted images, although are difficult to visualize on black-blood static images due to moving out of imaging plane from motion [21]. Valvular regurgitation is usually not a feature of papillary fibroelastoma.

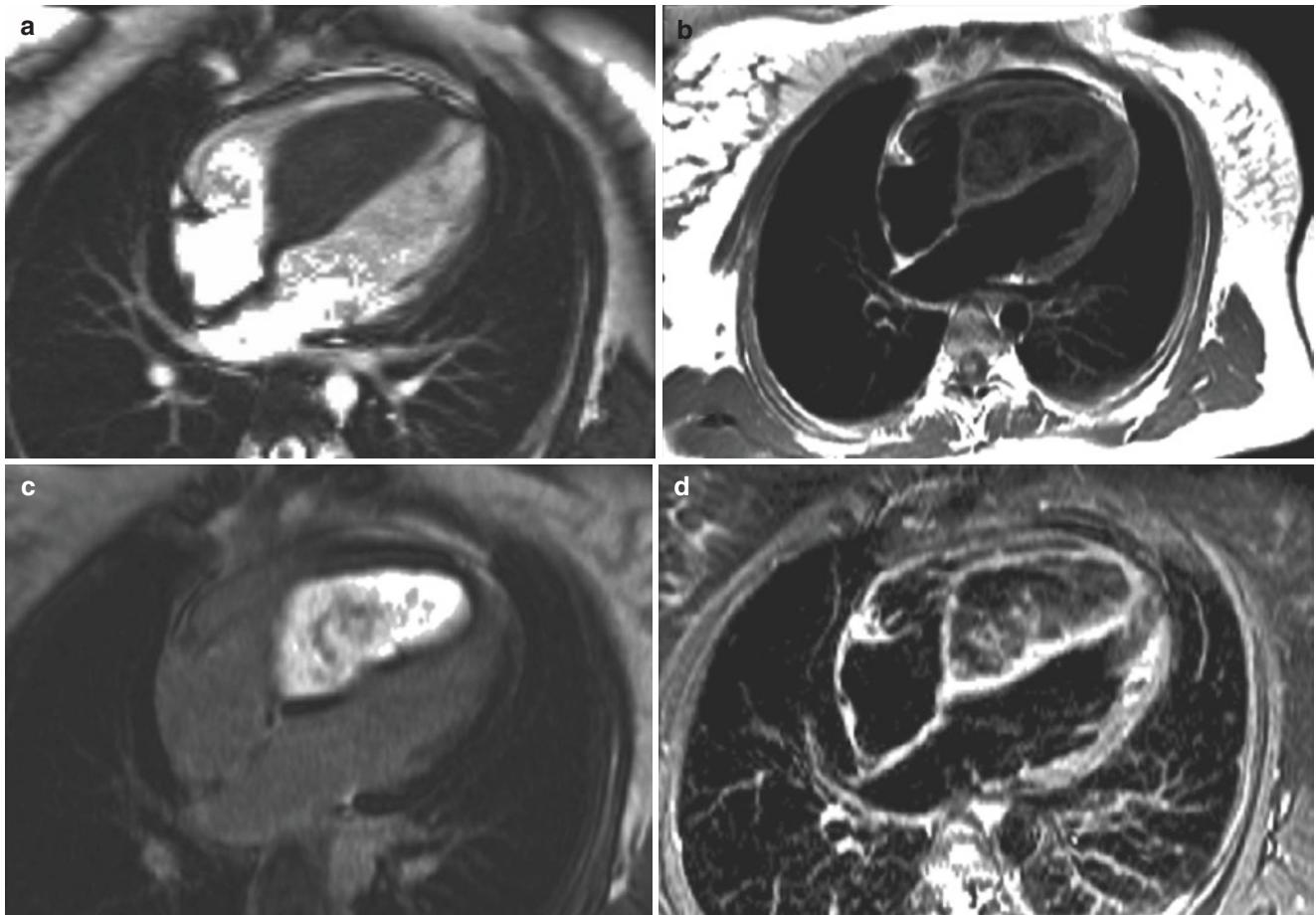


**Fig. 18.7** Fibroma in the right ventricle attached to the ventricular septum. (a) SSFP image, (b) T<sub>1</sub>w TSE, (c) LGE and (d) STIR T<sub>2</sub>w. Black blood images (b, d) show heterogeneous signal intensity and well-

defined borders with thin rim of myocardium. Late gadolinium enhancement (c) shows very high signal intensity mass due to high collagen content

### 18.6.1.3 Rhabdomyoma

In children, approximately 50% of rhabdomyomas occur in association with tuberous sclerosis where they occur as multiple intramural masses in the ventricular myocardium (left ventricle more than right ventricle) and most regress spontaneously [22]. Rhabdomyomas can sometimes produce obstructive or arrhythmic symptoms and require surgical excision. They are seen as multiple intramyocardial masses on SSFP with focal wall motion abnormality. They are isointense to myocardium on T<sub>1</sub> and mildly hyperintense on T<sub>2</sub>-weighted images. They typically show no or minimal enhancement after GBCA administration on perfusion and LGE images [23]. They have homogenous appearance on all sequences.

### 18.6.1.4 Fibroma

Fibromas are primarily seen in children due to their congenital origin. Fibromas are most often intramural tumors, arising within the interventricular septum or left ventricular free wall (Fig. 18.7). They have well-defined borders with thin

rim of myocardium. Fibromas have limited water content and show heterogeneous signal intensity on T<sub>1</sub> and T<sub>2</sub>-weighted images [10]. They are hypointense on perfusion imaging and have very high signal intensity on LGE due to high collagen content [24].

### 18.6.1.5 Lipoma

Cardiac lipomas are composed of encapsulated mature adipose tissue, similar to extracardiac lipomas. They usually occur on the epicardial surface of the heart, although myocardial or endocardial lipomas have been reported and can occasionally protrude into cardiac cavities [25]. Cardiac lipomas show high signal intensity similar to chest wall fat on T<sub>1</sub>-weighted sequences and signal void/drop out on fat saturation sequence. The CMR characteristics are very specific for this diagnosis obviating the need for further testing. Lipomatous hypertrophy of the atrial septum is sometimes confused with lipoma but can be distinguished by characteristic sparing of the fossa ovalis, which produces a dumb-bell-like appearance.

### 18.6.1.6 Other Benign Tumors

Less common benign tumors include hemangioma, paraganglioma, and cystic tumor of the atrioventricular nodal region [18].

Hemangioma are highly vascular tumors and are hyperintense on perfusion sequence with variable or weak enhancement on LGE sequence. CMR sequences may not be able to distinguish between highly vascular tumors which include hemangioma, angiosarcoma, vascular malformation, and paraganglioma [10].

Paragangliomas are extremely rare, originate for the neuroendocrine cells, and are typically seen in the posterior wall of left atrium, along the atrioventricular groove, or at the root of great vessels in the distribution of cardiac ganglia. They show marked high signal intensity on T<sub>2</sub>-weighted imaging, high vascularity on perfusion, and heterogeneous signal intensity on LGE due to central necrosis [26].

## 18.6.2 Malignant Tumors

### 18.6.2.1 Angiosarcoma

Angiosarcoma is the most common malignant tumor of the heart and accounts for less than 10% of all primary cardiac tumors [27]. Angiosarcoma is characterized by rapid growth, local invasion, and distant metastasis and has a predilection for the right atrium (>90%) but other cardiac chamber involvement has been reported (Fig. 18.8). Angiosarcoma grows rapidly and metastasis is usually present at the time of presentation with lung being the commonest site [28]. Pericardial effusion and tamponade are often present. CMR findings include broad base of attachment, lack of pedicle, presence of hemorrhage or necrosis, vascularity, and invasion of surrounding structures [13]. Heterogeneous signal intensity on T<sub>1</sub> and T<sub>2</sub>-weighted fast spin echo is consistent with areas of tumor tissue, necrosis, and hemorrhage in the tumor which is a feature of cardiac angiosarcoma [29]. Right atrial location is a distinguishing feature from other forms of sarcomas that tend to arise from the left atrium [30].

### 18.6.2.2 Lymphoma

Primary cardiac lymphoma is extranodal non-Hodgkin's lymphoma located in the heart and/or pericardium. This neoplasm has increased prevalence in immunocompromised patients and is rarely seen in immunocompetent patients. This is an aggressive neoplasm presenting with heart failure, pericardial effusion/tamponade, syncope, or arrhythmia.

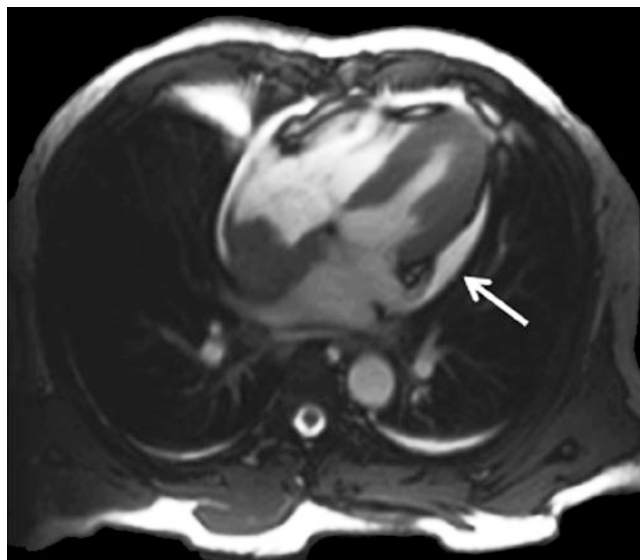


**Fig. 18.8** Angiosarcoma of the right atrium. Cine SSFP image shows infiltration of right atrial wall and pericardial effusion (*arrow*), which are signs of a malignant tumor

There are no pathognomonic imaging features (Fig. 18.9). Primary cardiac lymphoma typically involves the right heart chambers and/or pericardium. Pericardial effusion, outflow obstruction, and infiltration of adjacent tissues are usually seen. Histological and immunohistochemical examination of the involved tissue is always required to confirm diagnosis as chemotherapy ± radiation is the main therapeutic approach [31].

### 18.6.2.3 Other Sarcomas

Virtually all types of sarcomas have been reported in the heart (Fig. 18.10). In one review, undifferentiated sarcomas accounted for 25% of all primary cardiac tumors, however, with improved immunohistochemistry techniques this frequency is decreasing as they may now be assigned a specific subtype [32]. Leiomyosarcoma arise mostly in the left atrium infiltrating the pulmonary veins. Fibrosarcomas arise in the left atrium in 50%, either ventricle in 30%, and pericardium in 20%. Liposarcomas do not have a predilection for any cardiac chamber while osteosarcomas always originate from the left atrium invading into the pulmonary vein ostia and mitral valve [32]. The CMR tissue features of these sarcomas are non-specific with heterogeneous signal intensity on post-contrast imaging. Cardiac CT can better delineate the calcific components of osteosarcoma providing a complimentary role to CMR imaging.



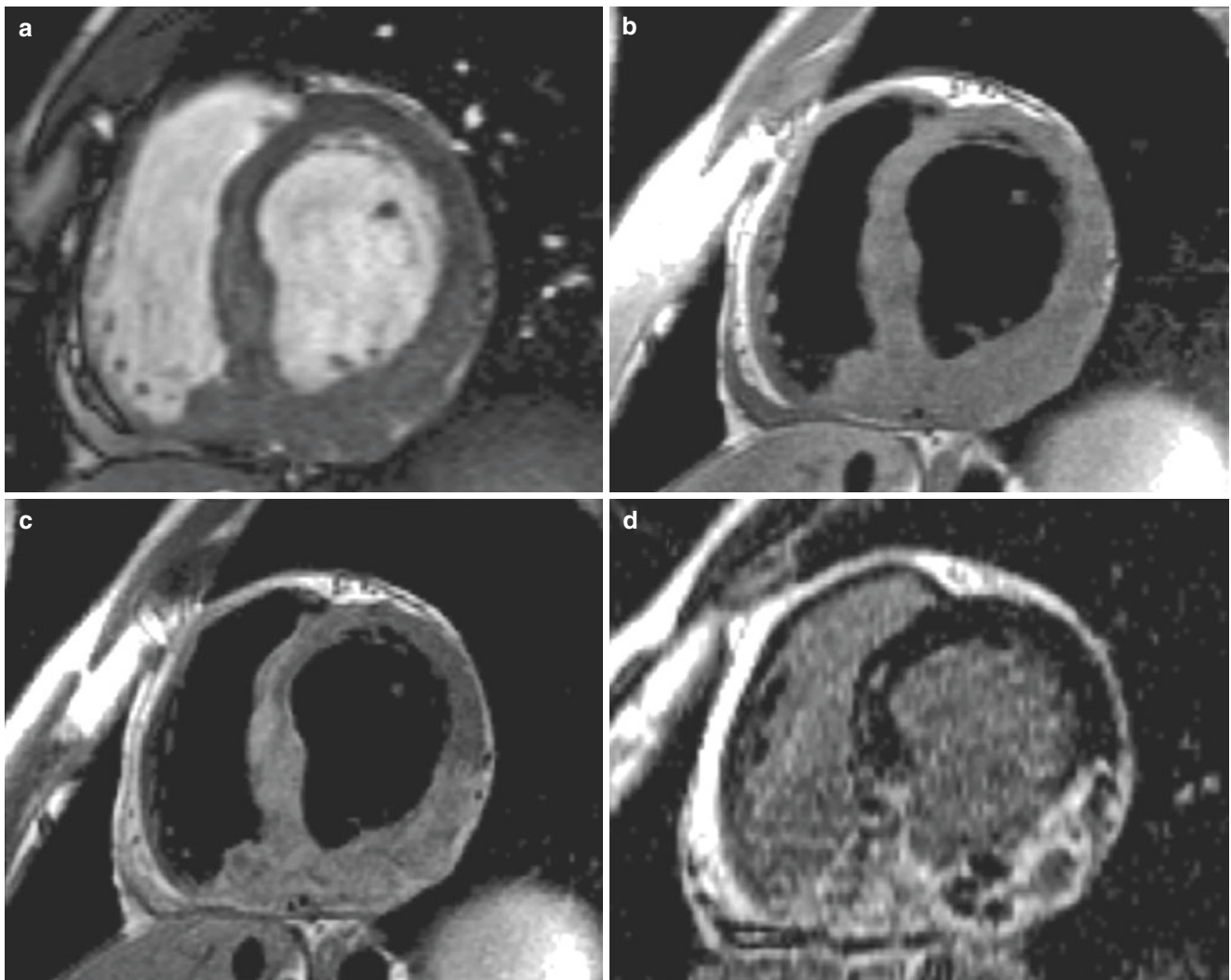


**Fig. 18.9** Lymphoma involving the left ventricle. Cine imaging (**a**) shows irregularly thickened myocardium in the septum, inferior and inferolateral segments, and a mass in the right ventricle adjacent to the inferior RV insertion site. T<sub>1</sub> black blood (**b**) does not show any significant signal intensity difference between the abnormal and normal myo-

cardium; however, T<sub>2</sub>-weighted image (**c**) shows increased signal intensity in the abnormal myocardial segments suggesting increased water content. Late gadolinium enhancement shows diffuse, patchy enhancement suggesting necrosis (**d**)



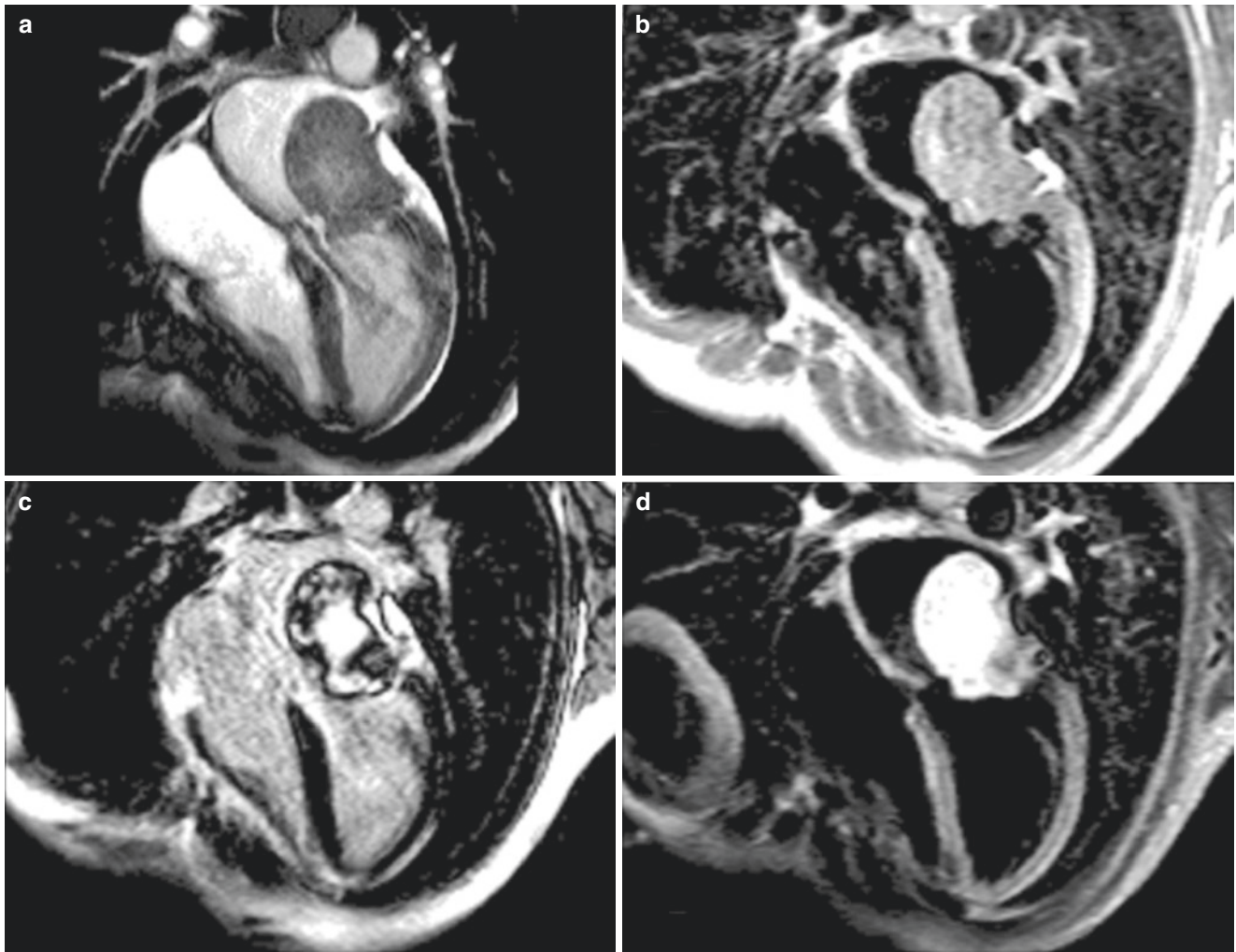


**Fig. 18.10** Sarcoma (undifferentiated) of the left atrium obstructing the mitral inflow (a). Black blood spin-echo imaging shows the mass isointense on  $T_1$  (b) and hyperintense on  $T_2$  spin-echo image (d). Patchy enhancement is seen on late gadolinium enhancement (c)

## 18.7 Comparison with Other Imaging Modalities

### 18.7.1 Echocardiography

Transthoracic echocardiography (TTE) is usually the first-line imaging modality used in the evaluation of cardiac masses. However, TTE has significant limitations from dependence upon availability of good acoustic windows particularly in patients with obesity, emphysema, and chest deformities. TTE also has limited field of view and ability to characterize tissue structure. TTE is therefore not a reliable method for characterizing the cardiac mass. The tissue characterization can be improved by utilizing contrast echocardiography to distinguish thrombus from tumor. Most malignant tumors have abnormal neovascularization with

increased blood supply, while thrombi are avascular. Mansencal et al. have shown that with microbubble contrast administration, a complete lack of enhancement is suggestive of thrombus; partial or incomplete enhancement suggests myxoma and complete enhancement suggests tumor [33].

Transesophageal echocardiography (TEE) is also routinely performed for cardiac mass evaluation. Compared to TTE, TEE can provide more detailed assessment of small masses, masses in atria particularly left atrial appendage, and masses associated with valves particularly fibroelastoma. However, TTE is better than TEE in evaluating mass in left ventricular apex. Despite using microbubble contrast agents, both TTE and TEE remain limited in their tissue characterization of cardiac masses and confident differentiation between thrombi and benign and malignant tumors may not be possible.

### 18.7.2 Computed Tomography

ECG-gated multidetector computed tomography (MDCT) has evolved into an important cardiac imaging technique, particularly for the assessment of coronary arteries. MDCT provides high spatial resolution and can be a valuable tool for assessing a cardiac mass, particularly when a patient can't undergo CMR due to contraindications. CT scanning is often performed during an evaluation for a possible thoracic malignancy where an incidental cardiac tumor may also be found. MDCT can be complimentary to CMR imaging, particularly in the evaluation of calcified masses [34]. The wide field of view and multiplanar reconstruction capabilities are useful in providing a detailed evaluation of cardiac and pericardial masses and adjacent structures [35]. Non-contrast images are diagnostic for detecting calcification, e.g. central calcification suggestive of a cardiac fibroma or identifying caseous variety of mitral annular calcification. Contrast-enhanced images may help identify the nature of the mass similar to contrast echocardiography and perfusion CMR, however, this requires specialized acquisition protocols for perfusion CT.

MDCT requires the use of iodinated contrast agents and exposure to radiation. The temporal resolution is also limited requiring the use of beta-blockers to slow the heart rate for better image quality. Imaging of the heart necessitates the use of MDCT scanners with ECG gating capabilities. The tissue characterization properties of CT are inferior to CMR; however, CT has an important role when MR imaging is contraindicated or not available.

### 18.7.3 Positron Emission Tomography

Positron emission tomography combined with computed tomography (PET-CT) is increasingly available and has become an important tool for assessment of myocardial ischemia, viability, and malignant disease. With the use of 2-[18F] Fluoro-2-deoxy-D-glucose (18-FDG) PET can distinguish benign from malignant lesions, accurately stage malignancies, and assess response to therapy [36]. An increased 18-FDG uptake by a mass is suggestive of a neoplasm; however, increased uptake can also be seen in the presence of brown fat, e.g. lipomatous hypertrophy of atrial septum [37]. PET-CT is not routinely utilized for cardiac mass evaluation, perhaps due to easy availability and use of echocardiography, MRI and CT imaging.

More recently PET-MRI system has become commercially available combining the advantages of both PET and MRI techniques, which may be uniquely suitable for cardiac tumor evaluation. PET-MRI can provide comprehensive

evaluation of tumor morphology, characterization, infiltration to adjacent structures, and local and M staging [38].

### 18.7.4 Angiography with Cardiac Catheterization

In the current era of high-resolution, three-dimensional non-invasive imaging, cardiac catheterization has limited role in the evaluation of patients with known intracardiac mass. Ventriculography is relatively contraindicated in patients with known intracardiac mass because of the risk of catheter-induced tumor embolization. In other patients, ventriculography might demonstrate filling defects suggestive of an intracavitary mass. If a mass is found as an incidental finding during angiography, strict care is required to minimize disruption of the mass to avoid causing a systemic embolic complication. In patients who are at high risk for concomitant coronary disease and are undergoing surgical treatment, coronary angiography is usually necessary. Coronary angiography may also demonstrate neovascularization of the cardiac mass [39].

---

## 18.8 CMR Role in Treatment Decision Making

Treatment of cardiac mass is dependent upon accurate localization and diagnosis. CMR can provide localization and tissue characterization non-invasively. Black-blood imaging, first-pass perfusion, and LGE with long inversion can accurately differentiate tumor from thrombus and obviate the need for additional invasive procedures. Fatty masses are well characterized by black-blood sequence with fat saturation prepulse. Vascularity of cardiac mass is suggestive of tumor and is evaluated by first-pass perfusion and LGE.

Malignant tumors (Fig. 18.11) can be differentiated from benign tumors by some specific features that include invasion of extra-cardiac tissues, infiltration of myocardial walls, involvement of more than one cardiac chamber, right-sided location, poor border definition, and the presence of pericardial effusion [40].

It's important to know that there may be significant overlap between biologic properties of different neoplasms, and therefore, decisions regarding chemotherapy or radiation treatment generally cannot be made solely on the basis of CMR imaging but rather require a tissue diagnosis. CMR imaging provides an excellent anatomical assessment of cardiac tumors and its relationship to extracardiac structures that is useful for surgical excision planning.

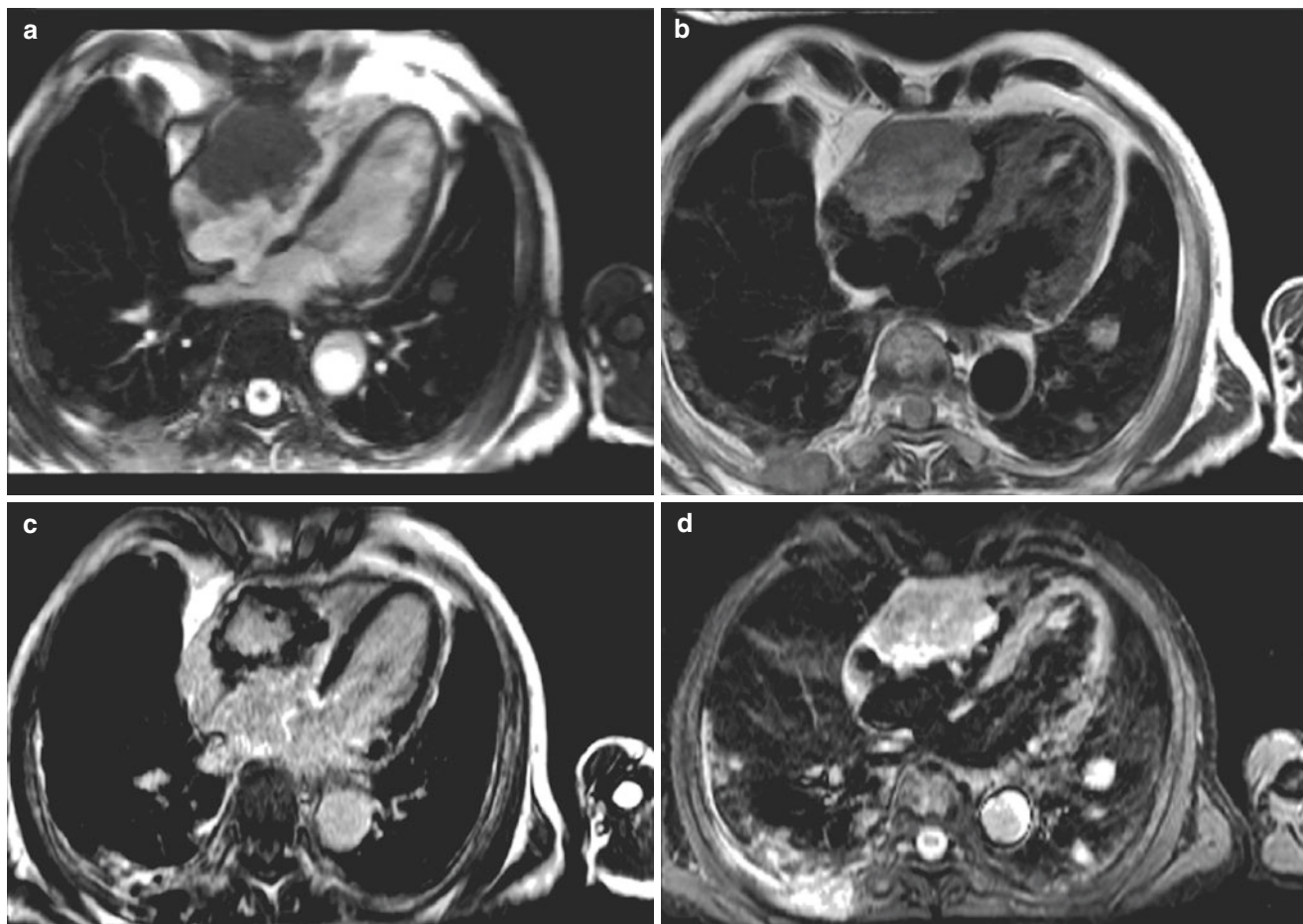


**Fig. 18.11** Cardiac metastasis from gastric carcinoma. Tumor involves the right atrium and right ventricle and is infiltrating the myocardium. Tumor is isointense on precontrast SSFP (a) and T1w spin-echo image

(b) and hyperintense on T2w STIR image (d). Patchy enhancement is present on late gadolinium enhancement imaging (c)

## 18.9 Conclusion

CMR imaging is currently considered the modality of choice for evaluating suspected cardiac tumors. A comprehensive CMR evaluation of cardiac tumors includes accurate localization, delineation of anatomical extent, assessment of associated functional consequences and complications, and characterization of cardiac mass tissue into pseudo-tumor, benign, and malignant neoplasm.

### Practical Pearls

- Echocardiography is usually the first-line imaging modality used for the assessment of suspected cardiac tumors but has several limitations.
- CT is generally reserved for patient with known contraindications to MRI.
- CMR provides comprehensive evaluation of cardiac masses with the use of SSFP cine, black-blood imaging, perfusion, and late gadolinium enhancement techniques.
- Goals of CMR imaging include confirmation & localization of mass, differentiating true tumor from pseudo-tumors, assessment of extent of tumor, tissue characterization for assessment of etiology, and evaluating impact on cardiac structure and function. A comprehensive imaging protocol is required for accurate diagnosis.
- Myxomas are the most common benign cardiac tumors.
- Primary malignant tumors are divided into sarcomas, lymphomas, and pericardial tumors.
- Secondary malignant cardiac tumors that metastasize to the heart are 40–50 times more common than primary cardiac tumors.
- Invasion of extra-cardiac tissues, myocardial infiltration, involvement of more than one cardiac chamber, right-sided location, poor border definition, and the presence of pericardial effusion are suggestive of malignant tumors. In some cases, malignancy cannot be definitively excluded by CMR alone.
- Treatment decisions for the use of chemotherapy or radiation require a tissue diagnosis.



- Knowledge of multimodality imaging is usually required to guide the appropriate use of TTE, TEE, CMR, and MDCT imaging as indicated.

## References

- Reynen K. Frequency of primary tumors of the heart. *Am J Cardiol.* 1996;77:107.
- Monti L, Renifilo E, Profili M, Balzarini L. Cardiovascular magnetic resonance features of caseous calcification of the mitral annulus. *J Cardiovasc Magn Reson.* 2008;10:25.
- Lam KY, Dickens P, Chan AC. Tumors of the heart. A 20-year experience with a review of 12,485 consecutive autopsies. *Arch Pathol Lab Med.* 1993;117:1027–31.
- Grebenc ML, Rosado-de-Christenson ML, Green CE, Burke AP, Galvin JR. Cardiac myxoma; imaging features in 83 patients. *Radiographics.* 2002;22:673–89.
- Chiles C, Woodard PK, Gutierrez FR, et al. Metastatic involvement of the heart and pericardium: CT and MR imaging. *Radiographics.* 2001;21:439–49.
- Molina JE, Edwards JE, Ward HB. Primary cardiac tumors: experience at the University of Minnesota. *Thorac Cardiovasc Surg.* 1990;38(Suppl 2):183.
- Ghbeis MB, Onitilo A, Greenlee R, Vidaillet H. Primary cardiac malignant tumors. Incidence, trends and survival. *Circulation.* 2008;118:S1098–9.
- Isaacs H Jr. Fetal and neonatal cardiac tumors. *Pediatr Cardiol.* 2004;25:252–73.
- Nadas AS, Ellison RC. Cardiac tumors in infancy. *Am J Cardiol.* 1968;21:363–6.
- Beourkhim RS, Prakash A, Valsangiacomo Buechel ER, et al. Characterization of cardiac tumors in children by cardiovascular magnetic resonance imaging. A multicenter experience. *J Am Coll Cardiol.* 2011;58:1044–54.
- Moss AJ, Allen HD. Moss and Adam's heart disease in infants, children, and adolescents: including the fetus and the young adult. 7th ed. Philadelphia: Wolters Kluwer Health/Lippincott Williams & Wilkins; 2008.
- Donsbeck AV, Ranchere D, Coindre JM, et al. Primary cardiac sarcomas: an immunohistochemical and grading study with long term followup of 24 cases. *Histopathology.* 1999;34:295–304.
- Sparrow PJ, Kurian JB, Jones TR, et al. MR imaging of cardiac tumors. *Radiographics.* 2005;25:1255–76.
- Mitchell DG, Burk DL Jr, Vinitzki S, et al. The biophysical basis of tissue contrast in extracranial MR imaging. *AJR Am J Roentgenol.* 1987;149:831–7.
- Hoffmann U, Globits S, Schima W, et al. Usefulness of magnetic resonance imaging of cardiac and paracardiac masses. *Am J Cardiol.* 2003;92:890–5.
- Weinsaft JW, Kim HW, Shah DJ, et al. Detection of left ventricular thrombus by delayed-enhancement cardiovascular magnetic resonance: prevalence and markers in patients with systolic dysfunction. *J Am Coll Cardiol.* 2008;52:148–57.
- Kiaffas MG, Powell AJ, Geva T. Magnetic resonance imaging evaluation of cardiac tumor characteristics in infants and children. *Am J Cardiol.* 2002;89:1229–33.
- Randhawa K, Ganeshan A, Hoey ETD. Magnetic resonance imaging of cardiac tumors: part 1, sequences, protocols and benign tumors. *Curr Probl Diagn Radiol.* 2011;40:158–68.
- Masui T, Takahashi M, Miura K, et al. Cardiac myxoma: identification of intratumoral hemorrhage and calcification on MR images. *Am J Roentgenol.* 1995;164:850–2.
- Gowda RM, Khan IA, Nair CK, et al. Cardiac papillary fibroelastoma: comprehensive analysis of 725 cases. *Am Heart J.* 2003;146:404–10.
- Wintersperger BJ, Becker CR, Gulbins H, et al. Tumors of the cardiac valves: imaging findings in magnetic resonance imaging, electron beam computed tomography, and echocardiography. *Eur Radiol.* 2000;10:443–9.
- Harding CO, Pagon RA. Incidence of tuberous sclerosis in patients with cardiac rhabdomyoma. *Am J Med Genet.* 1990;37:443–6.
- O'Donnell DH, Abbar S, Chaithiraphan V, et al. Cardiac tumors: optimal cardiac MR sequences and spectrum of imaging appearances. *AJR Am J Roentgenol.* 2009;193:377–87.
- Yan AT, Coffey DM, Li Y, et al. Images in cardiovascular medicine. Myocardial fibroma in gorlin syndrome by cardiac magnetic resonance imaging. *Circulation.* 2006;114:e376–9.
- Grebenc ML, de Christenson MLR, Burke AP, Green CE, Galvin JR. Primary cardiac and pericardial neoplasms: radiologic-pathologic correlation. *Radiographics.* 2000;20:1073–103.
- Syed IS, Feng D, Harris SR, et al. MR imaging of cardiac masses. *Magn Reson Imaging Clin N Am.* 2008;16:137–64.
- Dennig K, Lehmann G, Richter T. An angiosarcoma in the left atrium. *N Engl J Med.* 2000;342:443–4.
- Chul HK, Jane YD, Donna C, et al. Clinicopathologic study of 24 patients with primary cardiac sarcomas: a 10-year single institution experience. *Hum Pathol.* 2008;39:933–8.
- Di Bella G, Gaeta M, Patane L, Lentini S. Tissue characterization of a primary cardiac angiosarcoma using magnetic resonance imaging. *Rev Esp Cardiol.* 2010;63:1382–3.
- Araoz PA, Eklund HE, Welch TJ, Breen JF. CT and MR imaging of primary cardiac malignancies. *Radiographics.* 1999;19:1421–34.
- Anghel G, Zoli V, Petti N, et al. Primary cardiac lymphoma: report of two cases occurring in immunocompetent subjects. *Leuk Lymphoma.* 2004;45:781–8.
- Randhawa K, Ganeshan A, Hoey ETD. Magnetic resonance imaging of cardiac tumors: part 2, malignant tumors and tumor-like conditions. *Curr Probl Diagn Radiol.* 2011;40:169–79.
- Mansencal N, Revault-d'Allonnes L, Pelage JP, Farcot JC, Lacombe P, Dubourg O. Usefulness of contrast echocardiography for assessment of intracardiac masses. *Arch Cardiovasc Dis.* 2009;102:177–83.
- Roberts WT, Bax JJ, Davies LC. Cardiac CT and CT coronary angiography: technology and application. *Heart.* 2008;94:781–92.
- Rajiah P, Kanne JP, Kalahasti V, Schoenhagen P. Computed tomography of cardiac and paracardiac masses. *J Cardiovasc Comput Tomogr.* 2011;5:16–29.
- Israel O, Keidar Z, Bar-Shalom R. Positron emission tomography in the evaluation of lymphoma. *Semin Nucl Med.* 2004;34:166–79.
- Rao PM, Woodard PK, Patterson A, Peterson LR. Myocardial metastasis or benign brown fat? *Circ Cardiovasc Imaging.* 2009;2:e25–7.
- Fathala A, Abouziad M, AlSugair AA. Cardiac and pericardial tumors: a potential application of positron emission tomography-magnetic resonance imaging. *World J Cardiol.* 2017;9:600–8.
- Huang CY, Yu WC, Chen KC, Lin SJ. Coronary angiography of cardiac myxomas. *Clin Cardiol.* 2005;28:505–9.
- Luna A, Ribes R, Caro P, et al. Evaluation of cardiac tumors with magnetic resonance imaging. *Eur Radiol.* 2005;15:1446–55.





W. A. Helbing

## 19.1 Introduction

Since the first use of magnetic resonance imaging (MRI) for cardiac imaging, the potential of this technique to allow visualization and functional assessment of the heart during exercise has been recognized [1]. In patients with ischemic heart disease, assessment of ventricular function and myocardial perfusion with stress imaging has been widely applied and is a recommended tool in the diagnostic process and for prognostication [2, 3]. MR stress imaging has also been applied in patients with dilated or hypertrophic cardiomyopathy, valvular heart disease, and congenital heart disease [4–9]. In patients with congenital heart disease (CHD), stress imaging has mainly been used to determine global systolic function, contractile reserve and wall motion abnormalities, as well as to assess diastolic function and vascular function [4, 10–29]. Observations in these studies have helped to understand the pathophysiological processes. An important advantage of stress cardiovascular magnetic resonance (CMR) imaging is that all these parameters can be obtained in a single study. General and well-known disadvantages of CMR clearly also apply to stress imaging.

In this chapter, we will discuss the use, limitations, and potential future applications of CMR stress imaging in patients with CHD.

## 19.2 Stressors

### 19.2.1 Physical Exercise

The optimal stressor of the cardiovascular system is physical exercise, since it results in combined activation of cardiac, pulmonary, vascular, neurohormonal, muscular, and meta-

bolic systems involved in the adaptations to stress [8, 30]. Common tools to perform physical exercise during MRI procedures are a bicycle ergometer or handgrip exercise [8, 31]. Specific MR-compatible supine or upright bicycle ergometers have been used for exercise testing in combination with MRI. Supine ergometers are most widely used. These include cycling, stepper/up-down, and push-pull ergometers. The type of ergometer used should fit the circumstances in the bore of the MR scanner during exercise and CMR scanning. The posture of the patient during stress-testing should be considered, since posture has a significant effect on central hemodynamics, with lower cardiac output, higher stroke volumes, and lower heart rates in supine compared to upright position [32]. Supine exercise protocols currently lack standardization. Protocols used during stress imaging in patients with CHD have included (1) exercise to a certain percentage of their maximal exercise capacity or oxygen consumption [15, 16, 33, 34]; (2) symptom-limited exercise [35–37]; (3) exercise at 0.5 and 2.5 W/kg [24–26, 38]. Oxygen uptake-driven protocols are the preferred method, but have not found widespread application [34]. Clearly, physical exercise in the MR environment has several limitations. Maximal physical stress is dependent on the patient's motivation and cooperation, and cannot be used in patients with impairment of motor function. Hyperventilation during physical exercise hinders breath-hold during image acquisition. Rapid removal from the scanner should be warranted in case of the need for circulatory support or resuscitation. Actual image acquisition during physical exercise is challenging as it is limited by respiratory and physical motion artifacts. Therefore acquisition has commonly been performed directly after cessation of exercise, in- or outside the scanner [4, 15, 16, 26, 39]. Alternatively, scanner exercise combined with real-time imaging can be used. This allows scanning during rapid breathing [24, 25]. Combining ungated real-time CMR using highly accelerated sequences and retrospective synchronization of ECG and respiratory movements has been shown feasible, even in patients with complex CHD [13, 40].

W. A. Helbing (✉)  
Erasmus Medical Center, Department of Pediatrics,  
Division of Cardiology, and Department of Radiology,  
Rotterdam, The Netherlands  
e-mail: [w.a.helbing@erasmusmc.nl](mailto:w.a.helbing@erasmusmc.nl)

As an alternative stressor, mental stress imposed during cardiac MRI, reducing motion artifacts, has been shown to allow detailed assessment of stress physiology, exposing relationships, not seen at rest, of cardiovascular function with age, sex, and even endocrine function [41].

### 19.2.2 Pharmacological Stress

Pharmacological agents can be used to overcome the limitations of scanning combined with physical exercise. Differences in outcome between physical and pharmacological stress should be weighed against the differences regarding practical aspects [42, 43]. The most commonly used drugs are adenosine, dipyridamole, dobutamine, and regadenoson.

Adenosine and dipyridamole are coronary vasodilators that generate a reduced oxygen supply in myocardial areas supplied by stenotic coronary arteries, and are used for myocardial perfusion imaging [8, 44]. Adenosine is a naturally occurring substance in the body that causes coronary vasodilatation by activation of A<sub>2</sub> receptors. This results in increased blood flow in normal coronary arteries compared to stenotic coronary arteries (“steal phenomenon”), resulting in a perfusion mismatch. It does not necessarily cause ischemia. Adenosine has a very short half-life of only 2 s and therefore needs to be administered through continuous intravenous infusion. The adenosine dose rate used for stress-testing is 0.14 mg/kg/min over 6 min or until significant patient discomfort [5, 8, 45]. Common side effects are flushing, dyspnea, chest pain, gastrointestinal discomfort, headache, and light-headedness. Most side effects disappear shortly after discontinuation of adenosine administration and do not require medical treatment. Adenosine is contraindicated in patients with active restrictive airway disease, second or third-degree atrioventricular block, and in patients taking dipyridamole. Since theophylline and caffeine are adenosine receptor antagonists, abstinence of these substances is required 24–48 h before stress-testing with adenosine or dipyridamole. In patients with CHD, adenosine is increasingly used for stress imaging, particularly when coronary artery abnormalities are expected [46–51].

Dipyridamole inhibits reuptake of adenosine by vascular endothelial cells and indirectly causes coronary vasodilatation. Dipyridamole has a considerably longer half-life than adenosine and hemodynamic effects can persist up to 30 min. Dipyridamole is administered at a dose rate of 0.56–0.84 mg/kg over 3–6 min [52]. Side effects and contraindications for the use of dipyridamole are similar to those of adenosine [8].

Regadenoson is a selective A<sub>2A</sub> receptor agonist. Main advantages over adenosine are fewer negative chronotropic effects, longer hyperemia, and easier use through a single dose injected intravenously [53]. Furthermore, regadenoson has been preferred over adenosine in patients with increased

airway reactivity. In patients with suspected ischemic heart disease regadenoson stress CMR has been validated for risk stratification [54]. Few studies in CHD have reported the use of regadenoson [48, 55, 56].

Dobutamine increases myocardial oxygen demand similar to physical exercise, and is used to study contractile reserve and wall motion abnormalities [8]. Dobutamine is a synthetic catecholamine with positive inotropic and, to a lesser extent, chronotropic effects. In healthy children, positive inotropic effects occur from 1 to 2 µg/kg/min with dose-dependent increases in measures of systolic ventricular function [57], while chronotropic effects are seen from 5 to 10 µg/kg/min [58]. Dobutamine is also known to enhance diastolic function and to decrease preload and afterload [59]. In normal subjects, during dobutamine infusion, stroke volume increases, end-diastolic volume does not change, end-systolic volume decreases, and ejection fraction (EF) increases [60]. The half-life of dobutamine is only 2 min, requiring continuous infusion during stress CMR. In patients with CHD, different dosages have been used in CMR. Low or moderate dose dobutamine is used to assess cardiac contractile reserve. Dobutamine infusion is started at 2.5 or 5 µg/kg/min, and increased every 3–5 min with 2.5 or 5 µg/kg/min to 5–20 µg/kg/min [8]. High-dose dobutamine is used to detect wall motion abnormalities in patients with coronary artery abnormalities, as in patients with Kawasaki disease or after arterial switch operation for transposition of the great arteries. Infusion rates usually start at 10 µg/kg/min, and are increased every 3–5 min with 10 µg/kg/min until the heart rate is 85% of the maximal predicted heart rate for age or to 40 µg/kg/min maximum. If 85% of the maximal predicted heart rate for age is not reached at 40 µg/kg/min, atropine can be administered in conjunction with dobutamine to reach the target heart rate [8]. Heart rate, blood pressure, and (if possible) heart rhythm are continuously monitored during dobutamine stress-testing. Common minor side effects, such as headache, nausea, hypertension, hypotension, and hemodynamically insignificant arrhythmias, can occur in up to 20% of children [61, 62]. Major side effects, particularly arrhythmias (ventricular extrasystoles, bigeminy, supraventricular tachycardia) generally occur infrequently [28, 63, 64]. Dose-dependent complete heart block has been noted incidentally [28]. Side effects of both dobutamine and atropine can be treated with β-blockers or calcium antagonists (preferably not in children) that should be readily available during stress-testing. Dobutamine administration is contraindicated in patients with a mechanical obstruction of systemic ventricular filling or ejection, in patients with second- or third-degree atrioventricular block, and in patients with a history of sustained ventricular tachycardia [8].

Imaging during pharmacological stress commonly does not require major adjustments for sequence settings. In the

large majority of cases adjustment of heart rate settings is the most important difference compared to the settings at rest.

The majority of stress imaging studies in patients with CHD have been performed with pharmacological stress, mostly using dobutamine. Protocols used have varied, some have used high-dose dobutamine (20  $\mu\text{g}/\text{kg}/\text{min}$  or more) [29, 65–71]. In studies performing low-dose dobutamine stress imaging, different dobutamine dosages have been used, ranging from 5.0 to 20  $\mu\text{g}/\text{kg}/\text{min}$ . In our experience, a dobutamine dosage of 7.5  $\mu\text{g}/\text{kg}/\text{min}$  is safe, with a low incidence of only minor adverse effects [62]. Furthermore, it is important to elicit a significant cardiovascular stress response in patients [8, 10, 11, 22, 23]. Arrhythmias are side effects of special concern in the group of patients with CHD. Although the incidence of arrhythmias is low in the studies performed so far, most occurred with a dobutamine dosage of at least 10  $\mu\text{g}/\text{kg}/\text{min}$  [21, 28, 72, 73]. In patients after Fontan operation for a functionally univentricular heart, dobutamine administration at 7.5  $\mu\text{g}/\text{kg}/\text{min}$  provoked an increase in heart rate of more than 150% from baseline in 10 of 37 patients [23]. This was well tolerated and lowering the dobutamine dosage to 5  $\mu\text{g}/\text{kg}/\text{min}$  was sufficient to decrease the heart rate and successfully complete the study protocol, i.e. with images adequate for analysis [8].

## 19.3 Stress Imaging in Children and Patients with Congenital Heart Disease

### 19.3.1 Stress Echocardiography

Echocardiography in conjunction with stress has been reported in children with left-sided cardiac disease as early as in 1980 [33]. Stress echocardiography combined with dobutamine has been used to assess contractile reserve in children with thalassemia major, after Kawasaki disease, after chemotherapy for childhood cancer, or heart transplantation and patients with CHD [35–38, 60, 61, 65–67, 72–77]. Recent guidelines suggest that stress echocardiography, either with physical or pharmacological stress, is particularly useful in evaluating contractile reserve in CHD [78]. The common limitations of echocardiography apply to all these situations. The role of speckle tracking or 3D echocardiography combined with stress has hardly been explored.

### 19.3.2 Stress Cardiovascular Magnetic Resonance Imaging

Several groups have reported on the use of stress CMR imaging in >1200 patients with CHD. Table 19.1 is an overview of stress CMR studies that have been performed in patients

with different types of congenital heart defects. These studies have shown the feasibility and safety of stress CMR, have contributed to the understanding of the pathophysiology of the studied lesion, and some of the more recent studies have demonstrated prognostic value of stress CMR.

Studies in CHD have been performed predominantly in three patient groups: (a) patients with a pressure-overloaded right ventricle (congenitally corrected transposition of the great arteries (TGA), TGA after atrial switch procedures, pulmonary artery stenosis, Eisenmenger syndrome) [14, 16–21, 27, 28, 55, 56, 64, 79]; (b) patients with a volume-overloaded right ventricle (after correction for tetralogy of Fallot) [10, 15, 20, 22, 63, 70, 80–82]; and (c) patients with a Fontan circulation for univentricular heart defects [8, 24–26, 69, 84, 85, 89–93].

#### 19.3.2.1 Stress CMR in Pressure-Overloaded Right Ventricle

In patients with a right ventricle (RV) supporting the systemic circulation in a biventricular circulation, dobutamine stress CMR has demonstrated abnormal responses of the RV. In patients after atrial repair of TGA, a lack of functional reserve of the RV and prolonged recovery after exercise has been shown [16, 19]. In patients with congenitally corrected TGA (ccTGA), different stress responses of the systemic RV have been reported, in part relating to the treatment strategy. In operated ccTGA patients, impaired response of the systemic RV was noted, while a normal response in unoperated asymptomatic patients (also in direct comparison with healthy controls) may be found [17, 21]. As noted by Fratz et al. differences in systemic RV response to stress of atrially corrected TGA and ccTG may relate to inflow impairment related to the atrial baffle [28]. Dodge-Khatami has suggested that in unoperated ccTGA patients, with a favorable anatomy, dobutamine stress CMR might be helpful in identifying patients who will need anatomic correction [17]. Winter et al. have demonstrated that an abnormal response to stress, defined as lack of a decrease in RV end-systolic volume (ESV) or lack of an increase in RV EF, irrespective of the type of stressor, related to the later occurrence of major cardiac events [64].

The current treatment strategy for TGA is the arterial switch operation. Coronary artery flow may be compromised in these patients. Stress perfusion imaging using adenosine, dipyridamole or regadenoson has been shown to be feasible in children and adults with TGA to detect perfusion defects [27, 55, 56, 79].

In patients with pulmonary artery stenosis and in those with Eisenmenger syndrome, end-diastolic volume was found to be significantly larger compared to controls, but EF was normal at rest. With stress-testing, end-diastolic volume, ESV, and stroke volume all decreased, and EF did not change, clearly demonstrating the highly abnormal response of these

**Table 19.1** Overview of stress CMR studies performed in patients with congenital or acquired pediatric heart disease

Study	Stressor	Patients	Age	Adverse effects	Measurements	Outcome
Tulevski [19]	Dobutamine, 15 µg/kg/min max	12 patients after atrial switch for TGA	18–28 years	None	Biventricular volumes, function	No increase in RV SV and decrease in LV SV with stress-testing
Roest [16]	Supine bicycle exercise	10 patients after atrial switch for TGA	17–31 years	None	Biventricular volumes, function Ascending aorta flow	Prolonged SV recovery after supine bicycle exercise in patients after atrial switch for TGA
Oosterhof [14]	Dobutamine, 15 µg/kg/min max	39 patients after atrial switch for TGA	25 (4) years	None	Segmental and global ventricular function and volumes	Dobutamine stress and physical exercise not interchangeable for assessment of systolic and diastolic function in patients with after atrial switch for TGA
	Supine bicycle exercise					
Dodge-Khatami [17]	Dobutamine, 15 µg/kg/min max	13 patients with ccTGA	28 (12) years	None	Biventricular volumes, function	No increase in RV SV with DCMR. Five asymptomatic, unoperated patients had near normal volumes and adequate response to stress-testing
Van der Zedde [18]	Dobutamine, 15 µg/kg/min max	13 patients with ccTGA	17–65 years	None	Segmental and global ventricular function and volumes	At rest: TGA-patients have diminished segmental and global ventricular function During stress: ccTGA-patients no increase in segmental and global ventricular function
		17 patients after atrial switch for TGA				
Tulevski [21]	Dobutamine, 15 µg/kg/min max	47 patients with RV pressure overload (24 systemic RV; 23 subpulmonic RV)	26 (5) years	Dizziness, nausea ( <i>n</i> = 3). Arrhythmia ( <i>n</i> = 1)	Biventricular volumes, function	Clear heterogeneity in response to DCMR between different groups with chronic pressure-overloaded RV Impaired RV filling in surgically corrected TGA, decreased contractility in patients with chronic pressure-overloaded subpulmonic RV
Fratz [28]	Dobutamine, 10 µg/kg/min max	12 patients after atrial switch for TGA	15–28 years	Arrhythmias ( <i>n</i> = 3)	Biventricular function, mass	Non increase in SV during dobutamine stress in patients after atrial switch for TGA. Increased SV in patients with ccTGA
		11 patients with ccTGA			Aortic flow	
Winter [64]	Supine bicycle ergometry	39 patients with systemic RV in biventricular circulation	18–65	SVT in 1 patient (dobutamine stress)	Ventricular size and function	Patients with a systemic RV, who show no decrease in RV ESV or no increase in RV ejection fraction during stress, have a significantly higher risk of future cardiac events
	and Dobutamine 15 µg/kg/min					
Taylor [27]	Adenosine, 0.14 mg/kg/min	15 patients with congenital AS 2 patients after ASO for TGA	9–17 years	None	Biventricular volumes, function	Feasibility of adenosine stress-testing for assessment of biventricular function during single breath-hold cine CMR
Tobler [79]	Dipyridamole stress	27 patients with transposition of the great arteries	21 ± 3	None	Ventricular size and function	Adult ASO survivors have no evidence of myocardial ischemia, scar, or coronary ostial abnormality
					Late gadolinium enhancement	Asymptomatic and clinically stable adult ASO patient has low pre-test probability for inducible ischemia
					Whole heart CMR angiography (free-breathing navigated 3D SSFP)	

(continued)



**Table 19.1** (continued)

Study	Stressor	Patients	Age	Adverse effects	Measurements	Outcome
Noel [56]	Regadenoson	36 patients after ASO	15 ± 5 years	None	Stress/rest perfusion	Demonstrated perfusion defects, good agreement with cardiac catheterization Regadenoson useful coronary hyperemia agent in pediatric patients following arterial switch procedure when there is concern for ischemia Ability to administer as a single bolus with one IV advantageous in pediatrics
Wilkinson [55]	Regadenoson 8 µg/kg	36 patients with suspected coronary disease, less than 40 kg bodyweight	2 months to 14 years	20% minor adverse events	Stress/rest perfusion	Weight-based dosing of regadenoson for stress cardiac MRI is safe and feasible in infants and young children Regadenoson has integral role in outcome and treatment decisions for children with coronary artery disease
Roest [15]	Supine bicycle exercise	15 patients after TOF repair	14–24 years	None	Pulmonary regurgitation Biventricular volumes, function	Decrease in pulmonary regurgitation with supine bicycle exercise. Abnormal RV response, normal LV response to exercise
Tulevski [20]	Dobutamine, 5 µg/kg/min	13 patients with RV pressure overload (PS, PAH) 9 patients with RV pressure + volume overload (TOF)	27 (7) years	None	RV volumes, function	During DCMR: significant decrease in RV EDV and RV SV, no increase in EF. Impaired RV filling during stress in asymptomatic or minimally symptomatic patients
Van den Berg [10]	Dobutamine, 7.5 µg/kg/min max	36 patients after TOF repair	7–23 years	Bigeminy ( <i>n</i> = 1)	Biventricular volumes, function Pulmonary artery, tricuspid, and IVC flow	Abnormal relaxation with stress-testing in patients with end-diastolic forward flow
Van den Berg [22]	Dobutamine, 7.5 µg/kg/min max	51 patients after TOF repair	7–26 years	None	Biventricular volumes, function Pulmonary artery, and tricuspid flow	Biventricular functional reserve preserved in TOF repaired at young age, irrespective of RV volume
Parish [70]	Dobutamine 10 and 20 µg/kg/min	18 patients with tetralogy of Fallot				Excellent inter-observer agreement for volumetric assessment during stress MR except for LV-ESV at higher doses of dobutamine Axial geometry reproducible for RV parameters
Van den Bosch [80]	Dobutamine, 7.5 µg/kg/min	100 patients with tetralogy of Fallot	14–40 years	4% minor adverse effects: ventricular bigeminy, >50% increase in heart rate	Rest and stress biventricular size and function. Clinical endpoints	Abnormal ventricular response to dobutamine stress associated with adverse outcome in patients with repaired TOF
Luijnenburg [81]	Dobutamine 7.5 µg/kg/min	27 patients with tetralogy of Fallot	14 (4)	3 patients systolic blood pressure increase of >50%	Serial follow-up of Rest and stress ventricular size and function	Response to dobutamine stress normal, remained stable during the 5-year follow-up Smaller increase in RV EF during stress at baseline was predictive for a larger decrease in peak VO <sub>2</sub> during 5-year follow-up

(continued)

**Table 19.1** (continued)

Study	Stressor	Patients	Age	Adverse effects	Measurements	Outcome
Cuypers [63]	Dobutamine 7.5 and 20 µg/kg/min	30 patients with tetralogy of Fallot	36–46	In 5 patients: ventricular extrasystoles, ventricular bigeminy, nonsustained VT, blood pressure drop, anxiety	Rest and stress ventricular size and function	DSMR increase in RV EF and LV EF at a low dose, but no further increase at high dose
Lurz [82]	Supine bicycle exercise stress	17 patients who underwent PPVR	19 (6)	None	Rest and stress ventricular size and function	Patients with PR or PS are unable to augment total RVSV in response to exercise Patients with PR are able to augment effective RVSV due to a reduction in PR, which leads to an increased LVSV Following PPVI the RV can augment SV during exercise in both PR and PS patients In PR group, effective RVSV augmentation during exercise was similar pre- and post-PPVI
Steinmetz [83]	Supine in scanner bicycle exercise test	33 TOF patients, 35 matched controls	36 ± 11 years	None	Biventricular size and function. Pulmonary artery blood flow	Impaired exercise capacity in cTOF resulted from a reduction in not only RV, but also LV function. cTOF with good exercise capacity on CPET demonstrated higher LV reserve and pulmonary blood flow during incremental CMR-ET
Strigl [29]	Dobutamine, atropine 40 µg/kg/min max	28 patients with (suspected) coronary artery abnormalities	0.8–22 years	None	Ventricular size and function, wall motion abnormalities, Gadolinium enhancement	DSMR in pediatric patients is feasible and provides high-quality imaging of all ventricular wall segments with low interobserver variability
Doan [71]	Dobutamine 10–40 µg/kg/min, ±atropine	182 patients with anomalous origin of coronary artery	12–16 years	No major, 12.5% minor	Rest and stress first-pass perfusion, wall motion abnormalities (WMA), inter-observer agreement	DSCMR is feasible in pediatric patients with anomalous origin of coronary arteries AAOCA to assess hypoperfusion and wall motion
Schubert [12]	Supine step ergometer	20 patients with aortic coarctation	22 (14)	None	4D flow-based computational fluid dynamics of: Peak systolic pressure gradients, wall shear stress, secondary flow degree and normalized flow displacement. Stroke volume	Combination of MRI-ergometry with CFD allows assessing pressure gradients as well as flow profiles during physical exercise. May be alternative to cardiac catheterization with pharmacological stress-testing, provides hemodynamic information of aortic coarctation
Pedersen [26]	Supine bicycle exercise	11 patients after Fontan operation	11 (5)	None	Branch pulmonary artery and caval vein flow	During exercise: Unchanged flow distribution to the branch pulmonary arteries Increase in cardiac output predominantly by increase in heart rate
Hjortdal [25]	Supine bicycle exercise	11 patients after Fontan operation	12 (5)	None	Real-time aorta and IVC and SVC flow	Feasibility of the technique. Aortic and IVC flow increase with supine leg exercise. Inspiration facilitates IVC flow at rest, less during exercise

(continued)

**Table 19.1** (continued)

Study	Stressor	Patients	Age	Adverse effects	Measurements	Outcome
Hjortdal [24]	Supine bicycle exercise	14 Fontan patients	9 (5) years	None	Aortic and caval vein flow	A similar increase in flow rates in Fontan patients as in healthy controls
Robbers-Visser [23]	Dobutamine, 7.5 µg/kg/min max	32 patients after Fontan operation	8–22 years	Minor headache (n = 1)	Systemic ventricular volumes, function. Aortic and IVC flow	Abnormal decrease in EDV with stress-testing, adequate decrease in ESV, and increase in EF
Robbers-Visser [11]	Dobutamine, 7.5 µg/kg/min max	14 patients after Fontan operation	8–20 years	None	Branch pulmonary artery flow	Flow variables, distensibility, and wall shear stress is lower compared to controls; abnormal reaction to stress
Wong [69]	Dobutamine, 10 and 20 µg/kg/min	10 patients with HLHS	4–12 years	None	X-MR pressure volume loop analysis	Markers of systolic and diastolic function remained normal. Failure to adequately fill the ventricle implies a ceiling of maximal flow through the Fontan circuit despite low PVR
Van der Ven [84]	Dobutamine, 7.5 µg/kg/min	57 patients with TCPC (ILT and ECC)	10–16 years	None	Rest and stress atrial and ventricular size and function. Clinical endpoints	Dobutamine stress augmented atrial reservoir and pump function for Fontan patients Atrial early emptying reserve related to exercise capacity in ECC patients No other atrial or diastolic ventricular function parameter related to outcomes
Kamphuis [85]	Dobutamine, 7.5 µg/kg/min	10 patients with TCPC (Fontan circulation)	16.5 ± 3.8	2 patients with ventricular extrasystole	4D flow MRI during dobutamine stress Average ventricular kinetic energy, energy loss, and vorticity in systole, diastole, and total cardiac cycle	Intraventricular kinetic energy, viscous energy loss, and vorticity in Fontan patients increase during stress and have negative correlation with VO <sub>2</sub> max
Bossers [86]	Dobutamine, 7.5 µg/kg/min	69 patients with TCPC (Fontan circulation)	13 (4)	3 patients with ventricular extrasystole	Rest and stress ventricular size and function	Ventricular function is preserved in modern-day Fontan patients Decrease in EDVi with stress ECC patients have higher CI and EF during stress. Patients with a dominant RV lower systolic and diastolic function
Bossers [87]	Dobutamine, 7.5 µg/kg/min	29 patients with TCPC (Fontan circulation)	13 (2)	None	Rest and stress ventricular size and function, power loss in TCPC	Power loss inside TCPC structure is limited but increases with simulated exercise This relates to anatomy of TCPC In all flow conditions, ILT patients have lower Ploss than ECC patients
Van den Bosch [88]	Dobutamine, 7.5 µg/kg/min	92 patients with TCPC (Fontan circulation)	10–15 years	None	Rest and stress single ventricular size and function. Clinical endpoints	Fontan patients with good ventricular response to dobutamine stress have a lower risk of developing cardiac events during follow-up
Pushparajah [89]	Dobutamine 10 and 20 µg/kg/min	13 patients with HLHS and TCPC and exercise intolerance; 10 healthy controls	4–12 years	None	X-MR rest and stress invasive hemodynamic assessment and ventricular size and function	Cardiac output post-Fontan in HLHS at peak stress is blunted due to a limitation in preload which is not responsive to inhaled pulmonary vasodilators in the setting of normal PVR

(continued)

**Table 19.1** (continued)

Study	Stressor	Patients	Age	Adverse effects	Measurements	Outcome
Bruaene [90]	Exercise stress	10 TCPC patients	20 (4)	None	Rest and stress ventricular size and function. Arterial and venous pressure measurements	Before sildenafil, cardiac index increased throughout exercise, and SV index and EDV index decreased during exercise. ESV index remained unchanged
					Manipulation of vascular resistance with sildenafil	Total pulmonary resistance index increased, whereas systemic vascular resistance index decreased during exercise Sildenafil increased cardiac index and SV, especially at high-intensity exercise
Tang [91]	Exercise stress	47 patients with TCPC (Fontan circulation)	19 (6)	None	Flow in IVC, SVC, LPA, RPA, Fontan pathway, and azygous vein	Significant inverse correlation between TCPC diameter index, with indexed power loss with exercise
					CFD	Positive correlations for indexed power loss with exercise performance variables

Ages are given as ranges, or mean (standard deviation)

AS aortic stenosis, ASO arterial switch operation, CFD computational fluid dynamics, CMR cardiovascular magnetic resonance, ccTGA congenitally corrected transposition of the great arteries, D(S)CMR dobutamine (stress) CMR, ECC extracardiac conduit modification of TCPC (Fontan operation), EDV(i) end-diastolic volume (index), EF ejection fraction, ESV(i) end-systolic volume (index), HLHS hypoplastic left heart syndrome, ILT intra-atrial lateral tunnel modification of TCPC (Fontan operation), IVC inferior caval vein, LPA left pulmonary artery, LV left ventricle, PAH pulmonary arterial hypertension, PPVR percutaneous pulmonary valve replacement, PS pulmonary stenosis, RPA right pulmonary artery, RV right ventricle, SV stroke volume, SVC superior caval vein, TCPC total cavopulmonary connection, TGA transposition of the great arteries, (c)TOF (corrected) tetralogy of Fallot, VO<sub>2 max</sub> maximum oxygen uptake in exercise test, WSS wall shear stress, X-MR combined X-ray and MRI study

RVs to stress [21]. After relief of pulmonary stenosis with percutaneous valve implantation RV EF during physical stress improved, as did left ventricle (LV) stroke volume [82].

### 19.3.2.2 Stress CMR in Volume-Overloaded Right Ventricle

Various studies have reported on the biventricular stress response in patients with a volume-overloaded RV, mainly in the setting of surgical repair of tetralogy of Fallot (TOF) (Fig. 19.1). Roest et al. and Lurz et al. were among the first to use supine bicycle exercise and demonstrated a decrease in pulmonary regurgitation and a normal left ventricular function during stress [15, 82]. More recently, combined supine in scanner imaging and exercise testing revealed that impaired exercise capacity in cTOF results from a reduction in not only RV, but also LV function. Preserved exercise capacity related to higher LV reserve and pulmonary blood flow during stress [83]. In patients with isolated pulmonary regurgitation who had been operated with a transatrial transpulmonary approach, Van den Berg and coworkers using low-dose dobutamine stress CMR, showed well-preserved functional reserve in all (young) patients despite important pulmonary regurgitation and RV dilatation. With stress-testing, they could also demonstrate abnormal RV diastolic relaxation, that was not appreciated at rest in TOF patients with pulmonary artery end-diastolic forward flow [10, 22].

Stress CMR also revealed normal contractile reserve in TOF patients with RV volumes well above widely used size criteria for pulmonary valve replacement, challenging these cut-off values [22, 94, 95]. There has been some debate on the added value of higher dobutamine doses in TOF stress CMR. Increase of 20 µg/kg/min provoked abnormal RV-ESV response in some TOF patients, suggesting presence of ventricular systolic dysfunction not evident at rest or at lower doses [96]. This was not confirmed in a larger group of patients studied in another center [63]. Serial follow-up of stress CMR has shown that during a 5-year follow-up stress response remains stable in relatively young TOF patients treated according to current surgical strategies. In a relatively large group with medium-term follow-up after the baseline stress CMR, van den Bosch et al. have shown the relation between an abnormal ventricular response to stress (impaired functional reserve) and later adverse events in TOF patients [80].

### 19.3.2.3 Stress CMR in Fontan Patients

In patients with a Fontan circulation, stress CMR has been used to study pathophysiology and outcomes (Fig. 19.2). Pedersen, Hjortdal, and Robbers-Visser studied the systemic venous return, pulmonary arterial circulation, and systemic ventricular function in Fontan patients [11, 23–26]. Pedersen and Hjortdal performed branch pulmonary artery and caval vein flow measurements immediately after exercise or dur-



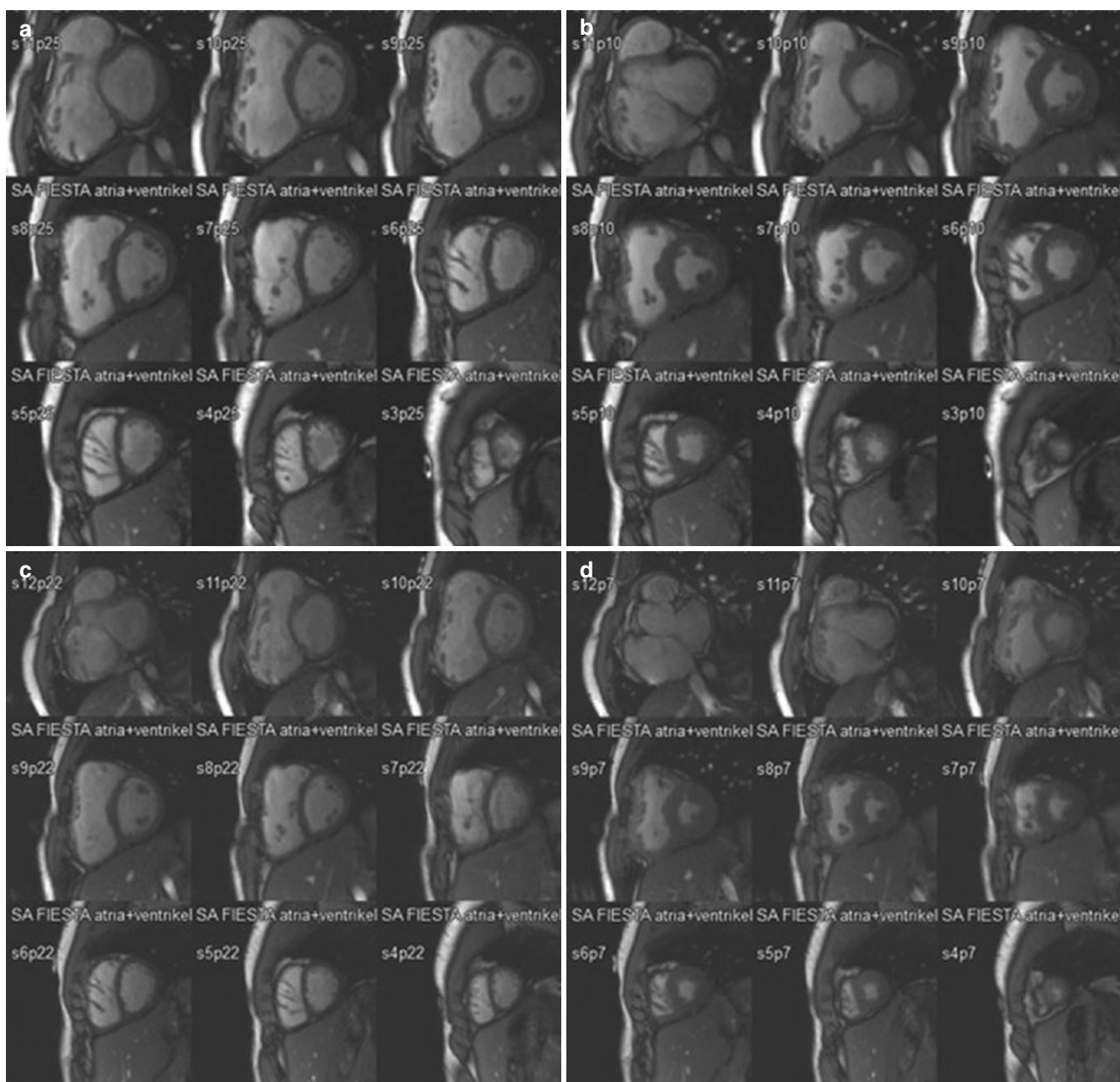


**Fig. 19.1** ED (a) and ES (b) still frames of b-SSFP cine series in short-axis orientation of heart at rest of 14 year old patient with surgically corrected tetralogy of Fallot. Left ventricle EDVi 83 ml/m<sup>2</sup>, ESVi 46, SVi 37, EF 45 % Right ventricle EDVi 146 ml/m<sup>2</sup>, ESVi 91, SVi 54, EF 37 %. Pulmonary regurgitation fraction: 31 %. ED (c) and ES (d) still frames of b-SSFP cine series in short-axis orientation of heart during

dobutamine stress of patient from (a) and (b). Left ventricle EDVi; 85 ml/m<sup>2</sup>, ESVi 31, SVi 53, EF 63%. Right ventricle EDVi 153 ml/m<sup>2</sup>, ESVi 75, SVi 75, EF 51%. Pulmonary regurgitation fraction: 29 %. ED end-diastolic, EF ejection fraction, ES end-systolic, *i* indexed to body surface area

ing exercise using real-time cardiovascular MRI [24–26]. In these studies, the technique was shown to be feasible and all children (mean age between 9 and 12 years old) were able to perform and complete the protocol [8]. An increase in cardiac output with stress in Fontan patients is predominantly caused by an increase in heart rate, not by an increase in stroke volume [23]. As postulated by these groups and confirmed in invasive studies, this response relates to a ceiling of

maximal flow through the Fontan circuit, resulting in ventricular inflow impairment [89]. This ceiling may be determined by limitations at different levels in the Fontan circulation. Energy loss in the Fontan construction connecting the caval veins to the pulmonary arteries is a potential limitation [97]. The size of the Fontan conduit and the vessels (IVC, SVC, PAs) connected to the conduit contribute to energy loss [91]. Energy loss increases with higher flows

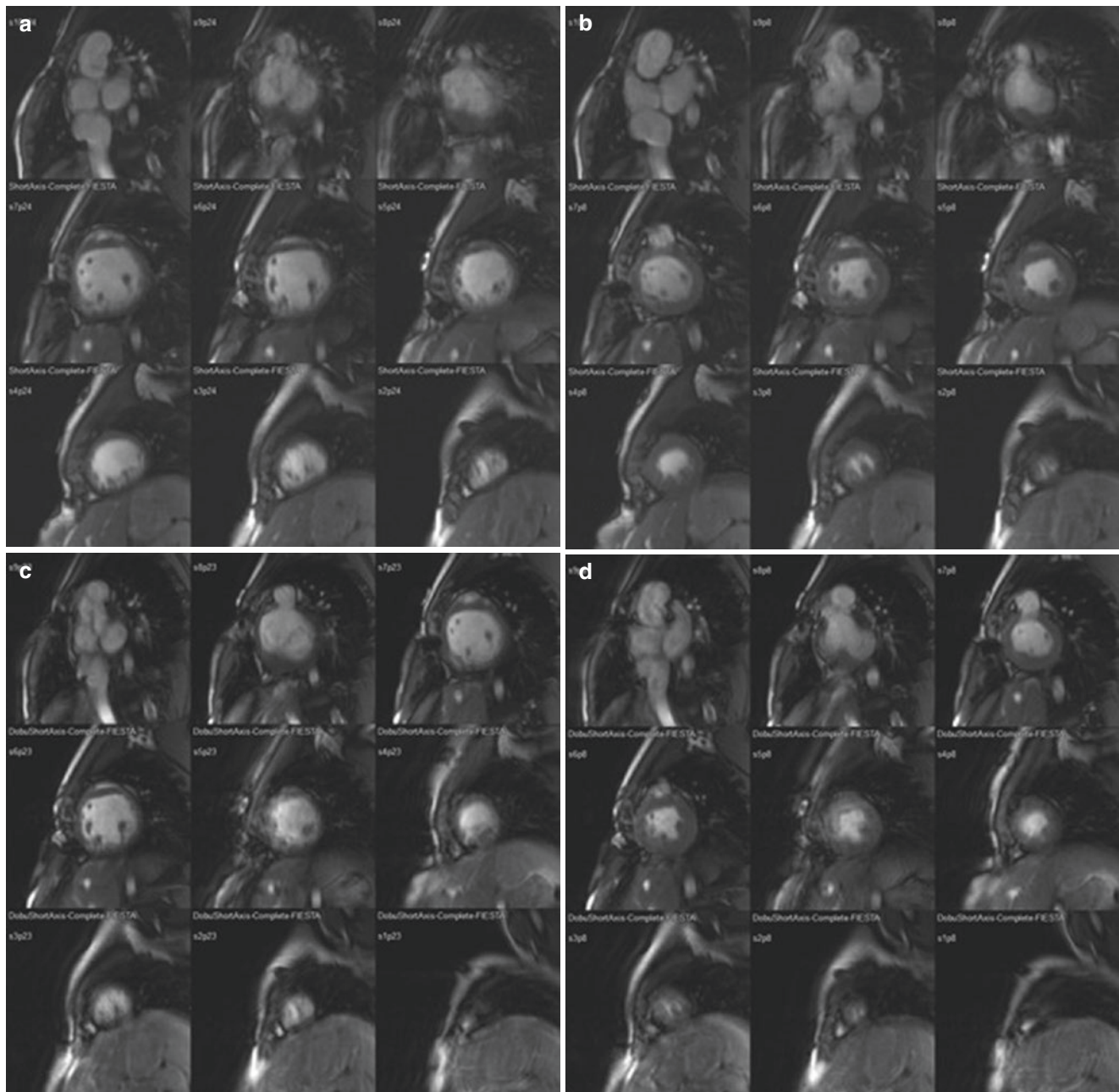


**Fig. 19.2** ED (a) and ES (b) still frames of b-SSFP cine series in short-axis orientation of heart at rest of 16 year old patient with univentricular heart and Fontan circulation. Single ventricle EDVi 86 ml/m<sup>2</sup>, ESVi 30, SVi 56, SVi 43, EF 49 %. ED (c) and ES (d) still frames of b-SSFP cine series

in short-axis orientation of heart during dobutamine stress of patient from Fig. 19.1a, b. Single ventricle EDVi 87 ml/m<sup>2</sup>, ESVi 44, EF 65%. *ED* end-diastolic, *EF* ejection fraction, *ES* end-systolic, *i* indexed to body surface area

through the Fontan connection [85, 87, 91, 97]. Another potential limiting factor in the increase of flow through Fontan circulation is the pulmonary arterial vasculature. Stress CMR has shown that PA stress response of flow, distensibility, and shear stress are abnormal in Fontan patients [11]. This is not responsive to pulmonary vasodilators [89]. Impaired atrial function may also result in ventricular inflow impairment. Resting atrial stroke volume was independently associated with lower peak VO<sub>2</sub> and Fontan failure in atrio-

pulmonary Fontan [98]. In the total cavopulmonary connection Fontan modification CMR showed that stress augments atrial reservoir and pump function for Fontan patients and atrial early emptying reserve related to exercise capacity in extracardiac conduit (ECC) patients [84]. Stress CMR has also been used to assess differences between the ECC and intra-atrial lateral tunnel (ILT) modifications of the total cavopulmonary connection Fontan circulation. EF and cardiac index (CI) during dobutamine were lower for ILT

patients, whereas other parameters were comparable. Patients with dominant LVs had smaller ESV and higher EF and contractility during rest and higher EF during dobutamine than patients with univentricular hearts with dominant RVs [86]. Recently, van den Bosch et al. demonstrated that normal single ventricular response (preserved functional reserve) to low-dose dobutamine stress is related to better medium-term outcomes [88].

The type of stressor should be taken into account when comparing or interpreting the results of stress studies. Coma-Canella et al. [99] showed a different response in healthy volunteers to physical exercise and to dobutamine stress. Global and regional EF increased more with dobutamine than with physical exercise. In the study by Oosterhof et al., the response to both types of stressors was comparable in healthy controls, while a discrepancy in response to physical exercise and low-dose dobutamine stress was noted in patients after intra-atrial correction for TGA [14]. The authors suggested that this disagreement was the result of differences in preload and afterload. However, both dobutamine and physical exercise increase contractility, and decrease preload and afterload [58, 100]. Comparison between the results of the use of different types of stressors is hampered by a lack of direct comparison in similar subjects in most studies. Therefore, it is hard to compare circulatory responses at identical metabolic loads resulting from various stress protocols.

## 19.4 Future Applications

Combining the advantages of CMR and testing the heart under load with stress CMR has proven value for patients with CHD, as discussed above. Further improvements in stress CMR could be obtained by improved standardization of both dobutamine as well as physical stress levels during stress CMR, allowing better comparison of results of scientific and clinical applications of these methods. This may require organizing consensus in the field.

Both stress CMR and cardiopulmonary exercise testing provide highly important information on cardiovascular physiology and prognosis in patients with CHD [64, 80, 88]. Combination of these methods has been shown feasible. If practical issues can be solved, this would be a highly powerful tool in clinical practice [101]. With improved fast real-time imaging and motion compensation this combined stress-testing might be feasible in the near future [13].

The combination of computational fluid dynamics and CMR during stress holds promise for improved understanding of pathophysiology as well as replacement of current invasive procedures [12]. CMR with stress might provide important input in biomechanical modeling the circulation of CHD [69, 102–104]. Assessment of myocardial strain has

been shown to contribute to prognostication of outcomes in CHD [105]. Strain during stress might be an additional important factor to be explored. The same is true for myocardial perfusion.

Remarkably, many of the stress CMR research has been done in populations with CHD resulting in abnormal loading conditions of the RV or in the single ventricular circulation. There is a potential role for these techniques in other types of CHD.

## 19.5 Conclusions

MRI of the heart during increased cardiac output generated by physical or pharmacological stress is a clinically feasible technique that provides increased insights into the pathophysiology of CHD. Stress CMR can be used to assess global systolic function, contractile reserve, and wall motion abnormalities, and also to assess diastolic function, vascular function and energy transfer, and loss in the heart and large vessels. In patients with systemic RVs in the biventricular circulation, with TOF and pulmonary regurgitation and in those with a Fontan circulation, stress CMR results have prognostic value. In patients with suspected coronary artery problems in the setting of CHD or acquired pediatric heart disease, stress CMR is feasible and clinically indicated. Improved standardization of dobutamine and physical stress protocols, including improved techniques for real-time imaging and handling of the effects of patient motion, are important for the more widespread use of this application of CMR.

## References

1. Pennell DJ, Underwood SR, Ell PJ, Swanton RH, Walker JM, Longmore DB. Dipyridamole magnetic resonance imaging: a comparison with thallium-201 emission tomography. *Br Heart J*. 1990;64(6):362–9.
2. Kwong RY, Ge Y, Steel K, Bingham S, Abdullah S, Fujikura K, et al. Cardiac magnetic resonance stress perfusion imaging for evaluation of patients with chest pain. *J Am Coll Cardiol*. 2019;74(14):1741–55.
3. Wolk MJ, Bailey SR, Doherty JU, Douglas PS, Hendel RC, Kramer CM, et al. ACCF/AHA/ASE/ASNC/HFSA/HRS/SCAI/SCCT/SCMR/STS 2013 multimodality appropriate use criteria for the detection and risk assessment of stable ischemic heart disease: a report of the American College of Cardiology Foundation Appropriate Use Criteria Task Force, American Heart Association, American Society of Echocardiography, American Society of Nuclear Cardiology, Heart Failure Society of America, Heart Rhythm Society, Society for Cardiovascular Angiography and Interventions, Society of Cardiovascular Computed Tomography, Society for Cardiovascular Magnetic Resonance, and Society of Thoracic Surgeons. *J Am Coll Cardiol*. 2014;63(4):380–406.
4. Roest AA, Kunz P, Lamb HJ, Helbing WA, van der Wall EE, de Roos A. Biventricular response to supine physical exercise in



- young adults assessed with ultrafast magnetic resonance imaging. *Am J Cardiol.* 2001;87(5):601–5.
5. Gulati A, Ismail TF, Ali A, Hsu LY, Gonçalves C, Ismail NA, et al. Microvascular dysfunction in dilated cardiomyopathy: a quantitative stress perfusion cardiovascular magnetic resonance study. *JACC Cardiovasc Imaging.* 2019;12(8 Pt 2):1699–708.
  6. Roberts PA, Lin ACW, Cowan BR, Young AA, Stewart R. Comparison of effects of losartan and metoprolol on left ventricular and aortic function at rest and during exercise in chronic aortic regurgitation. *Int J Cardiovasc Imaging.* 2018;34(4):615–24.
  7. Kim EK, Lee SC, Chang SA, Jang SY, Kim SM, Park SJ, et al. Prevalence and clinical significance of cardiovascular magnetic resonance adenosine stress-induced myocardial perfusion defect in hypertrophic cardiomyopathy. *J Cardiovasc Magn Reson.* 2020;22(1):30.
  8. Robbers-Visser D, Luijnenburg SE, van den Berg J, Moelker A, Helbing WA. Stress imaging in congenital cardiac disease. *Cardiol Young.* 2009;19(6):552–62.
  9. Schuster A, Paul M, Bettencourt N, Hussain ST, Morton G, Kutty S, et al. Myocardial feature tracking reduces observer-dependence in low-dose dobutamine stress cardiovascular magnetic resonance. *PLoS One.* 2015;10(4):e0122858.
  10. van den Berg J, Wielopolski PA, Meijboom FJ, Witsenburg M, Bogers AJ, Pattynama PM, et al. Diastolic function in repaired tetralogy of Fallot at rest and during stress: assessment with MR imaging. *Radiology.* 2007;243(1):212–9.
  11. Robbers-Visser D, Helderma F, Strengers JL, van Osch-Gevers L, Kapusta L, Pattynama PM, et al. Pulmonary artery size and function after Fontan operation at a young age. *J Magn Reson Imaging.* 2008;28(5):1101–7.
  12. Schubert C, Brüning J, Goubergrits L, Hennemuth A, Berger F, Kühne T, et al. Assessment of hemodynamic responses to exercise in aortic coarctation using MRI-ergometry in combination with computational fluid dynamics. *Sci Rep.* 2020;10(1):18894.
  13. Craven TP, Tsao CW, La Gerche A, Simonetti OP, Greenwood JP. Exercise cardiovascular magnetic resonance: development, current utility and future applications. *J Cardiovasc Magn Reson.* 2020;22(1):65.
  14. Oosterhof T, Tulevski II, Roest AA, Steendijk P, Vliegen HW, van der Wall EE, et al. Disparity between dobutamine stress and physical exercise magnetic resonance imaging in patients with an intra-atrial correction for transposition of the great arteries. *J Cardiovasc Magn Reson.* 2005;7(2):383–9.
  15. Roest AA, Helbing WA, Kunz P, van den Aardweg JG, Lamb HJ, Vliegen HW, et al. Exercise MR imaging in the assessment of pulmonary regurgitation and biventricular function in patients after tetralogy of fallot repair. *Radiology.* 2002;223(1):204–11.
  16. Roest AA, Kunz P, Helbing WA, Lamb HJ, Vliegen HW, van den Aardweg JG, et al. Prolonged cardiac recovery from exercise in asymptomatic adults late after atrial correction of transposition of the great arteries: evaluation with magnetic resonance flow mapping. *Am J Cardiol.* 2001;88(9):1011–7.
  17. Dodge-Khatami A, Tulevski II, Bennink GB, Hitchcock JF, de Mol BA, van der Wall EE, et al. Comparable systemic ventricular function in healthy adults and patients with unoperated congenitally corrected transposition using MRI dobutamine stress testing. *Ann Thorac Surg.* 2002;73(6):1759–64.
  18. van der Zedde J, Oosterhof T, Tulevski II, Vliegen HW, Mulder BJ. Comparison of segmental and global systemic ventricular function at rest and during dobutamine stress between patients with transposition and congenitally corrected transposition. *Cardiol Young.* 2005;15(2):148–53.
  19. Tulevski II, Lee PL, Groenink M, van der Wall EE, Stoker J, Pieper PG, et al. Dobutamine-induced increase of right ventricular contractility without increased stroke volume in adolescent patients with transposition of the great arteries: evaluation with magnetic resonance imaging. *Int J Card Imaging.* 2000;16(6):471–8.
  20. Tulevski II, Hirsch A, Dodge-Khatami A, Stoker J, van der Wall EE, Mulder BJ. Effect of pulmonary valve regurgitation on right ventricular function in patients with chronic right ventricular pressure overload. *Am J Cardiol.* 2003;92(1):113–6.
  21. Tulevski I, van der Wall EE, Groenink M, Dodge-Khatami A, Hirsch A, Stoker J, et al. Usefulness of magnetic resonance imaging dobutamine stress in asymptomatic and minimally symptomatic patients with decreased cardiac reserve from congenital heart disease (complete and corrected transposition of the great arteries and subpulmonic obstruction). *Am J Cardiol.* 2002;89(9):1077–81.
  22. van den Berg J, Strengers JL, Wielopolski PA, Hop WC, Meijboom FJ, de Rijke YB, et al. Assessment of biventricular functional reserve and NT-proBNP levels in patients with RV volume overload after repair of tetralogy of Fallot at young age. *Int J Cardiol.* 2009;133:364–70. <https://doi.org/10.1016/j.ijcard.2008.01.011>.
  23. Robbers-Visser D, Ten Harkel DJ, Kapusta L, Strengers JL, Dalinghaus M, Meijboom FJ, et al. Usefulness of cardiac magnetic resonance imaging combined with low-dose dobutamine stress to detect an abnormal ventricular stress response in children and young adults after fontan operation at young age. *Am J Cardiol.* 2008;101(11):1657–62.
  24. Hjortdal VE, Christensen TD, Larsen SH, Emmertsen K, Pedersen EM. Caval blood flow during supine exercise in normal and Fontan patients. *Ann Thorac Surg.* 2008;85(2):599–603.
  25. Hjortdal VE, Emmertsen K, Stenbog E, Frund T, Schmidt MR, Kromann O, et al. Effects of exercise and respiration on blood flow in total cavopulmonary connection: a real-time magnetic resonance flow study. *Circulation.* 2003;108(10):1227–31.
  26. Pedersen EM, Stenbog EV, Frund T, Houlied K, Kromann O, Sorensen KE, et al. Flow during exercise in the total cavopulmonary connection measured by magnetic resonance velocity mapping. *Heart.* 2002;87(6):554–8.
  27. Taylor AM, Dymarkowski S, De Meerleer K, Hamaekers P, Gewillig M, Mertens L, et al. Validation and application of single breath-hold cine cardiac MR for ventricular function assessment in children with congenital heart disease at rest and during adenosine stress. *J Cardiovasc Magn Reson.* 2005;7(5):743–51.
  28. Fratz S, Hager A, Busch R, Kaemmerer H, Schwaiger M, Lange R, et al. Patients after atrial switch operation for transposition of the great arteries can not increase stroke volume under dobutamine stress as opposed to patients with congenitally corrected transposition. *Circ J.* 2008;72(7):1130–5.
  29. Strigl S, Beroukhim R, Valente AM, Annese D, Harrington JS, Geva T, et al. Feasibility of dobutamine stress cardiovascular magnetic resonance imaging in children. *J Magn Reson Imaging.* 2009;29(2):313–9.
  30. Lafountain RA, da Silveira JS, Varghese J, Mihai G, Scandling D, Craft J, et al. Cardiopulmonary exercise testing in the MRI environment. *Physiol Meas.* 2016;37(4):N11–25.
  31. von Knobelsdorff-Brenkenhoff F, Dieringer MA, Fuchs K, Hezel F, Niendorf T, Schulz-Menger J. Isometric handgrip exercise during cardiovascular magnetic resonance imaging: set-up and cardiovascular effects. *J Magn Reson Imaging.* 2013;37(6):1342–50.
  32. Cheng CP, Herfkens RJ, Lightner AL, Taylor CA, Feinstein JA. Blood flow conditions in the proximal pulmonary arteries and vena cavae: healthy children during upright cycling exercise. *Am J Physiol Heart Circ Physiol.* 2004;287(2):H921–6.
  33. Alpert BS, Bloom KR, Olley PM. Assessment of left ventricular contractility during supine exercise in children with left-sided cardiac disease. *Br Heart J.* 1980;44(6):703–10.
  34. Barber NJ, Ako EO, Kowalik GT, Cheang MH, Pandya B, Steeden JA, et al. Magnetic resonance-augmented cardiopulmonary exercise testing: comprehensively assessing exercise intolerance in



- children with cardiovascular disease. *Circ Cardiovasc Imaging*. 2016;9(12):e005282.
35. Hauser M, Bengel FM, Kuhn A, Sauer U, Zylla S, Braun SL, et al. Myocardial blood flow and flow reserve after coronary reimplantation in patients after arterial switch and ross operation. *Circulation*. 2001;103(14):1875–80.
36. Kaplan JD, Foster E, Redberg RF, Schiller NB. Exercise Doppler echocardiography identifies abnormal hemodynamics in adults with congenital heart disease. *Am Heart J*. 1994;127(6):1572–80.
37. Cyran SE, Grzeszczak M, Kaufman K, Weber HS, Myers JL, Gleason MM, et al. Aortic “recoarctation” at rest versus at exercise in children as evaluated by stress Doppler echocardiography after a “good” operative result. *Am J Cardiol*. 1993;71(11):963–70.
38. Oyen EM, Ingerfeld G, Ignatzky K, Brode PE. Dynamic exercise echocardiography in children with congenital heart disease affecting the left heart. *Int J Cardiol*. 1987;17(3):315–25.
39. Pedersen EM, Kozerke S, Ringgaard S, Scheidegger MB, Boesiger P. Quantitative abdominal aortic flow measurements at controlled levels of ergometer exercise. *Magn Reson Imaging*. 1999;17(4):489–94.
40. La Gerche A, Claessen G, Van de Bruene A, Pattyn N, Van Cleemput J, Gewillig M, et al. Cardiac MRI: a new gold standard for ventricular volume quantification during high-intensity exercise. *Circ Cardiovasc Imaging*. 2013;6(2):329–38.
41. Jones A, Steeden JA, Pruessner JC, Deanfield JE, Taylor AM, Muthurangu V. Detailed assessment of the hemodynamic response to psychosocial stress using real-time MRI. *J Magn Reson Imaging*. 2011;33(2):448–54.
42. Berthe C, Pierard LA, Hiernaux M, Trotteur G, Lempereur P, Carlier J, et al. Predicting the extent and location of coronary artery disease in acute myocardial infarction by echocardiography during dobutamine infusion. *Am J Cardiol*. 1986;58(13):1167–72.
43. Picano E, Lattanzi F, Masini M, Distante A, L’Abbate A. High dose dipyridamole echocardiography test in effort angina pectoris. *J Am Coll Cardiol*. 1986;8(4):848–54.
44. Helbing WA, Luijnenburg SE, Moelker A, Robbers-Visser D. Cardiac stress testing after surgery for congenital heart disease. *Curr Opin Pediatr*. 2010;22(5):579–86.
45. Thomas DM, Minor MR, Aden JK, Lisanti CJ, Steel KE. Effects of adenosine and regadenoson on hemodynamics measured using cardiovascular magnetic resonance imaging. *J Cardiovasc Magn Reson*. 2017;19(1):96.
46. Hauser M, Bengel FM, Kuhn A, Sauer U, Nekolla SG, Eicken A, et al. Myocardial perfusion and coronary flow reserve assessed by positron emission tomography in patients after Fontan-like operations. *Pediatr Cardiol*. 2003;24(4):386–92.
47. Secinaro A, Ntsinjana H, Tann O, Schuler PK, Muthurangu V, Hughes M, et al. Cardiovascular magnetic resonance findings in repaired anomalous left coronary artery to pulmonary artery connection (ALCAPA). *J Cardiovasc Magn Reson*. 2011;13(1):27.
48. Noel CV, Krishnamurthy R, Moffett B, Krishnamurthy R. Myocardial stress perfusion magnetic resonance: initial experience in a pediatric and young adult population using regadenoson. *Pediatr Radiol*. 2017;47(3):280–9.
49. Ntsinjana HN, Tann O, Hughes M, Derrick G, Secinaro A, Schievano S, et al. Utility of adenosine stress perfusion CMR to assess paediatric coronary artery disease. *Eur Heart J Cardiovasc Imaging*. 2017;18(8):898–905.
50. Vijarnsorn C, Noga M, Schantz D, Pepelassis D, Tham EB. Stress perfusion magnetic resonance imaging to detect coronary artery lesions in children. *Int J Cardiovasc Imaging*. 2017;33(5):699–709.
51. Biko DM, Collins RT 2nd, Partington SL, Harris M, Whitehead KK, Keller MS, et al. Magnetic resonance myocardial perfusion imaging: safety and indications in pediatrics and young adults. *Pediatr Cardiol*. 2018;39(2):275–82.
52. Pezel T, Garot P, Hovasse T, Untersee T, Champagne S, Kinnel M, et al. Vasodilatation stress cardiovascular magnetic resonance imaging: feasibility, workflow and safety in a large prospective registry of more than 35,000 patients. *Arch Cardiovasc Dis*. 2021;114(6-7):490–503.
53. Rovere G, Meduri A, Savino G, Flammia FC, Lo Piccolo F, Carafa MRP, et al. Practical instructions for using drugs in CT and MR cardiac imaging. *Radiol Med*. 2021;126(3):356–64.
54. Abbasi SA, Heydari B, Shah RV, Murthy VL, Zhang YY, Blankstein R, et al. Risk stratification by regadenoson stress magnetic resonance imaging in patients with known or suspected coronary artery disease. *Am J Cardiol*. 2014;114(8):1198–203.
55. Wilkinson JC, Doan TT, Loar RW, Pednekar AS, Trivedi PM, Masand PM, et al. Myocardial stress perfusion MRI using regadenoson: a weight-based approach in infants and young children. *Radiol Cardiothorac Imaging*. 2019;1(4):e190061.
56. Noel CV, Krishnamurthy R, Masand P, Moffett B, Schlingmann T, Cheong BY, et al. Myocardial stress perfusion MRI: experience in pediatric and young-adult patients following arterial switch operation utilizing regadenoson. *Pediatr Cardiol*. 2018;39(6):1249–57.
57. Berg RA, Paddybury JF, Donnerstein RL, Klewer SE, Hutter JJ Jr. Dobutamine pharmacokinetics and pharmacodynamics in normal children and adolescents. *J Pharmacol Exp Ther*. 1993;265(3):1232–8.
58. Michelfelder EC, Witt SA, Khoury P, Kimball TR. Moderate-dose dobutamine maximizes left ventricular contractile response during dobutamine stress echocardiography in children. *J Am Soc Echocardiogr*. 2003;16(2):140–6.
59. Harada K, Tamura M, Ito T, Suzuki T, Takada G. Effects of low-dose dobutamine on left ventricular diastolic filling in children. *Pediatr Cardiol*. 1996;17(4):220–5.
60. De Wolf D, Suys B, Verhaeren H, Matthys D, Taeymans Y. Low-dose dobutamine stress echocardiography in children and young adults. *Am J Cardiol*. 1998;81(7):895–901.
61. Noto N, Ayusawa M, Karasawa K, Yamaguchi H, Sumitomo N, Okada T, et al. Dobutamine stress echocardiography for detection of coronary artery stenosis in children with Kawasaki disease. *J Am Coll Cardiol*. 1996;27(5):1251–6.
62. Robbers-Visser D, Luijnenburg SE, van den Berg J, Roos-Hesselink JW, Strengers JL, Kapusta L, et al. Safety and observer variability of cardiac magnetic resonance imaging combined with low-dose dobutamine stress-testing in patients with complex congenital heart disease. *Int J Cardiol*. 2011;147:214.
63. Cuypers JA, Menting ME, Konings EE, Oplić P, Utens EM, Helbing WA, et al. Unnatural history of tetralogy of Fallot: prospective follow-up of 40 years after surgical correction. *Circulation*. 2014;130(22):1944–53.
64. Winter MM, Scherptong RW, Kumar S, Bouma BJ, Tulevski II, Tops LF, et al. Ventricular response to stress predicts outcome in adult patients with a systemic right ventricle. *Am Heart J*. 2010;160(5):870–6.
65. Li W, Hornung TS, Francis DP, O’Sullivan C, Duncan A, Gatzoulis M, et al. Relation of biventricular function quantified by stress echocardiography to cardiopulmonary exercise capacity in adults with Mustard (atrial switch) procedure for transposition of the great arteries. *Circulation*. 2004;110(11):1380–6.
66. Apostolopoulou SC, Laskari CV, Tsoutsinos A, Rammos S. Doppler tissue imaging evaluation of right ventricular function at rest and during dobutamine infusion in patients after repair of tetralogy of Fallot. *Int J Cardiovasc Imaging*. 2007;23(1):25–31.
67. Brili SV, Alexopoulos NA, Barberis VI, Gatzoulis MA, Barbetseas J, Chrysouhou C, et al. Dobutamine stress echocardiography for the evaluation of cardiac reserve late after Fontan operation. *Hellenic J Cardiol*. 2007;48(5):252–7.
68. Stephensen SS, Steding-Ehrenborg K, Thilén U, Holm J, Hochbergs P, Arheden H, et al. Changes in blood volume shunting

- in patients with atrial septal defects: assessment of heart function with cardiovascular magnetic resonance during dobutamine stress. *Eur Heart J Cardiovasc Imaging*. 2017;18(10):1145–52.
69. Wong J, Pushparajah K, de Vecchi A, Ruijsink B, Greil GF, Hussain T, et al. Pressure-volume loop-derived cardiac indices during dobutamine stress: a step towards understanding limitations in cardiac output in children with hypoplastic left heart syndrome. *Int J Cardiol*. 2017;230:439–46.
  70. Parish V, Valverde I, Kutty S, Head C, Greil GF, Schaeffter T, et al. Higher dose dobutamine stress MR imaging in repaired Tetralogy of Fallot: observer variance of volumetric assessment compared with normal volunteers. *J Magn Reson Imaging*. 2013;38(6):1356–61.
  71. Doan TT, Molossi S, Sachdeva S, Wilkinson JC, Loar RW, Weigand JD, et al. Dobutamine stress cardiac MRI is safe and feasible in pediatric patients with anomalous aortic origin of a coronary artery (AAOCA). *Int J Cardiol*. 2021;334:42–8.
  72. Hui L, Chau AK, Leung MP, Chiu CS, Cheung YF. Assessment of left ventricular function long term after arterial switch operation for transposition of the great arteries by dobutamine stress echocardiography. *Heart*. 2005;91(1):68–72.
  73. Brili S, Stamatopoulos I, Barbetseas J, Chrysohoou C, Alexopoulos N, Misailidou M, et al. Usefulness of dobutamine stress echocardiography with Tissue Doppler imaging for the evaluation and follow-up of patients with repaired tetralogy of Fallot. *J Am Soc Echocardiogr*. 2008;21(10):1093–8.
  74. Lanzarini L, Bossi G, Laudisa ML, Klersy C, Arico M. Lack of clinically significant cardiac dysfunction during intermediate dobutamine doses in long-term childhood cancer survivors exposed to anthracyclines. *Am Heart J*. 2000;140(2):315–23.
  75. Hui L, Leung MP, Ha SY, Chau AKT, Cheung YF. Early detection of left ventricular dysfunction in patients with  $\beta$  thalassaemia major by dobutamine stress echocardiography. *Heart*. 2003;89(6):669–70.
  76. Donofrio MT, Kakavand B, Moskowitz WB. Evaluation of regional wall motion and quantitative measures of ventricular function during dobutamine stress echocardiography in pediatric cardiac transplantation patients. *J Am Soc Echocardiogr*. 2000;13(10):932–40.
  77. Larsen RL, Applegate PM, Dyar DA, Ribeiro PA, Fritzsche SD, Mulla NF, et al. Dobutamine stress echocardiography for assessing coronary artery disease after transplantation in children. *J Am Coll Cardiol*. 1998;32(2):515–20.
  78. Lancellotti P, Pellikka PA, Budts W, Chaudhry FA, Donal E, Dulgheru R, et al. The clinical use of stress echocardiography in non-ischaemic heart disease: recommendations from the European Association of Cardiovascular Imaging and the American Society of Echocardiography. *Eur Heart J Cardiovasc Imaging*. 2016;17(11):1191–229.
  79. Tobler D, Motwani M, Wald RM, Roche SL, Verocai F, Iwanochko RM, et al. Evaluation of a comprehensive cardiovascular magnetic resonance protocol in young adults late after the arterial switch operation for d-transposition of the great arteries. *J Cardiovasc Magn Reson*. 2014;16(1):98.
  80. van den Bosch E, Cuypers J, Luijnenburg SE, Duppen N, Boersma E, Budde RPJ, et al. Ventricular response to dobutamine stress cardiac magnetic resonance imaging is associated with adverse outcome during 8-year follow-up in patients with repaired Tetralogy of Fallot. *Eur Heart J Cardiovasc Imaging*. 2020;21(9):1039–46.
  81. Luijnenburg SE, Mekic S, van den Berg J, van der Geest RJ, Moelker A, Roos-Hesselink JW, et al. Ventricular response to dobutamine stress relates to the change in peak oxygen uptake during the 5-year follow-up in young patients with repaired tetralogy of Fallot. *Eur Heart J Cardiovasc Imaging*. 2014;15(2):189–94.
  82. Lurz P, Muthurangu V, Schuler PK, Giardini A, Schievano S, Nordmeyer J, et al. Impact of reduction in right ventricular pressure and/or volume overload by percutaneous pulmonary valve implantation on biventricular response to exercise: an exercise stress real-time CMR study. *Eur Heart J*. 2012;33(19):2434–41.
  83. Steinmetz M, Stümpfig T, Seehase M, Schuster A, Kowallick J, Müller M, et al. Impaired exercise tolerance in repaired tetralogy of fallot is associated with impaired biventricular contractile reserve: an exercise-stress real-time cardiovascular magnetic resonance study. *Circ Cardiovasc Imaging*. 2021;14(8):e011823.
  84. van der Ven JPG, Bossers SSM, van den Bosch E, Dam N, Kuipers IM, van Iperen GG, et al. Dobutamine stress testing for the evaluation of atrial and diastolic ventricular function in Fontan patients. *Open Heart*. 2021;8(1):e001487.
  85. Kamphuis VP, Elbaz MSM, van den Boogaard PJ, Kroft LJM, Lamb HJ, Hazekamp MG, et al. Stress increases intracardiac 4D flow cardiovascular magnetic resonance-derived energetics and vorticity and relates to VO(2)max in Fontan patients. *J Cardiovasc Magn Reson*. 2019;21(1):43.
  86. Bossers SS, Kapusta L, Kuipers IM, van Iperen G, Moelker A, Kroft LJ, et al. Ventricular function and cardiac reserve in contemporary Fontan patients. *Int J Cardiol*. 2015;196:73–80.
  87. Bossers SS, Cibis M, Gijzen FJ, Schokking M, Strengers JL, Verhaart RF, et al. Computational fluid dynamics in Fontan patients to evaluate power loss during simulated exercise. *Heart*. 2014;100(9):696–701.
  88. van den Bosch E, Bossers SSM, Robbers-Visser D, Boersma E, Roos-Hesselink JW, Breur H, et al. Ventricular response to dobutamine stress CMR is a predictor for outcome in Fontan patients. *JACC Cardiovasc Imaging*. 2019;12(2):368–70.
  89. Pushparajah K, Wong JK, Bellsham-Revell HR, Hussain T, Valverde I, Bell A, et al. Magnetic resonance imaging catheter stress haemodynamics post-Fontan in hypoplastic left heart syndrome. *Eur Heart J Cardiovasc Imaging*. 2016;17(6):644–51.
  90. Van De Bruaene A, La Gerche A, Claessen G, De Meester P, Devroe S, Gillijns H, et al. Sildenafil improves exercise hemodynamics in Fontan patients. *Circ Cardiovasc Imaging*. 2014;7(2):265–73.
  91. Tang E, Wei ZA, Whitehead KK, Khiabani RH, Restrepo M, Mirabella L, et al. Effect of Fontan geometry on exercise haemodynamics and its potential implications. *Heart*. 2017;103(22):1806–12.
  92. Robbers-Visser D, Jan ten Harkel D, Kapusta L, Strengers JL, Dalinghaus M, Meijboom FJ, et al. Usefulness of cardiac magnetic resonance imaging combined with low-dose dobutamine stress to detect an abnormal ventricular stress response in children and young adults after Fontan operation at young age. *Am J Cardiol*. 2008;101(11):1657–62.
  93. van den Bosch E, Bossers SSM, Kamphuis VP, Boersma E, Roos-Hesselink JW, Breur J, et al. Associations between blood biomarkers, cardiac function, and adverse outcome in a young Fontan Cohort. *J Am Heart Assoc*. 2021;10(5):e015022.
  94. Valsangiacomo Buechel ER, Dave HH, Kellenberger CJ, Dodge-Khatami A, Pretre R, Berger F, et al. Remodelling of the right ventricle after early pulmonary valve replacement in children with repaired tetralogy of Fallot: assessment by cardiovascular magnetic resonance. *Eur Heart J*. 2005;26(24):2721–7.
  95. Stout KK, Daniels CJ, Aboulhosn JA, Bozkurt B, Broberg CS, Colman JM, et al. 2018 AHA/ACC guideline for the management of adults with congenital heart disease: a report of the American College of Cardiology/American Heart Association Task Force on Clinical Practice Guidelines. *Circulation*. 2019;139(14):e698–800.
  96. Parish V, Valverde I, Kutty S, Head C, Qureshi SA, Sarikouch S, et al. Dobutamine stress MRI in repaired tetralogy of Fallot with chronic pulmonary regurgitation: a comparison with healthy volunteers. *Int J Cardiol*. 2013;166(1):96–105.

97. Khiabani RH, Whitehead KK, Han D, Restrepo M, Tang E, Bethel J, et al. Exercise capacity in single-ventricle patients after Fontan correlates with haemodynamic energy loss in TCPC. *Heart*. 2015;101(2):139–43.
98. Alsaied T, van der Ven JPG, Juggan S, Sleeper LA, Azcue N, Kroft LJ, et al. Relation of Fontan Baffle stroke volume to Fontan failure and lower exercise capacity in patients with an atriopulmonary Fontan. *Am J Cardiol*. 2019;124(1):151–7.
99. Coma-Canella I, Garcia Velloso MJ, Maceira A, Cabrera A, Villas A, Albaladejo V, et al. [Isotopic ventriculography in healthy young volunteers. Their response to different types of stress]. *Rev Esp Cardiol*. 1997;50(10):709–14.
100. Kimball TR, Mays WA, Khoury PR, Mallie R, Claytor RP. Echocardiographic determination of left ventricular preload, afterload, and contractility during and after exercise. *J Pediatr*. 1993;122(6):S89–94.
101. Barber NJ, Ako EO, Kowalik GT, Steeden JA, Pandya B, Muthurangu V. MR augmented cardiopulmonary exercise testing—a novel approach to assessing cardiovascular function. *Physiol Meas*. 2015;36(5):N85–94.
102. Ruijsink B, Zugaj K, Wong J, Pushparajah K, Hussain T, Moireau P, et al. Dobutamine stress testing in patients with Fontan circulation augmented by biomechanical modeling. *PLoS One*. 2020;15(2):e0229015.
103. Hellmeier F, Nordmeyer S, Yevtushenko P, Bruening J, Berger F, Kuehne T, et al. Hemodynamic evaluation of a biological and mechanical aortic valve prosthesis using patient-specific MRI-based CFD. *Artif Organs*. 2018;42(1):49–57.
104. Nordmeyer S, Lee CB, Goubergrits L, Knosalla C, Berger F, Falk V, et al. Circulatory efficiency in patients with severe aortic valve stenosis before and after aortic valve replacement. *J Cardiovasc Magn Reson*. 2021;23(1):15.
105. Meyer SL, St. Clair N, Powell AJ, Geva T, Rathod RH. Integrated clinical and magnetic resonance imaging assessments late after Fontan operation. *J Am Coll Cardiol*. 2021;77(20):2480–9.



Emanuela R. Valsangiacomo Buechel

## 20.1 Introduction

Performing cardiac magnetic resonance (CMR) in infants and neonates is different from adults in some imaging aspects as well as regarding specific referral indications. The overall examination setting requires adjustments of the imaging sequences due to the small patient size and fast heart rates. In young children with complex congenital heart disease

(CHD), CMR is mainly used for definitive diagnosis complementary to echocardiography; information is the base for discussion of treatment strategies and for planning surgical or catheter-guided interventions (Fig. 20.1).

Some peculiar aspects of paediatric cardiac imaging with inclusion of new CMR techniques that are advantageous for the paediatric population will be discussed in this chapter.

---

**Supplementary Information** The online version contains supplementary material available at [https://doi.org/10.1007/978-3-031-29235-4\\_20](https://doi.org/10.1007/978-3-031-29235-4_20).

---

E. R. Valsangiacomo Buechel (✉)  
Paediatric Heart Centre, University Children's Hospital Zurich,  
Zurich, Switzerland  
e-mail: [emanuela.valsangiacomo@kispi.uzh.ch](mailto:emanuela.valsangiacomo@kispi.uzh.ch)



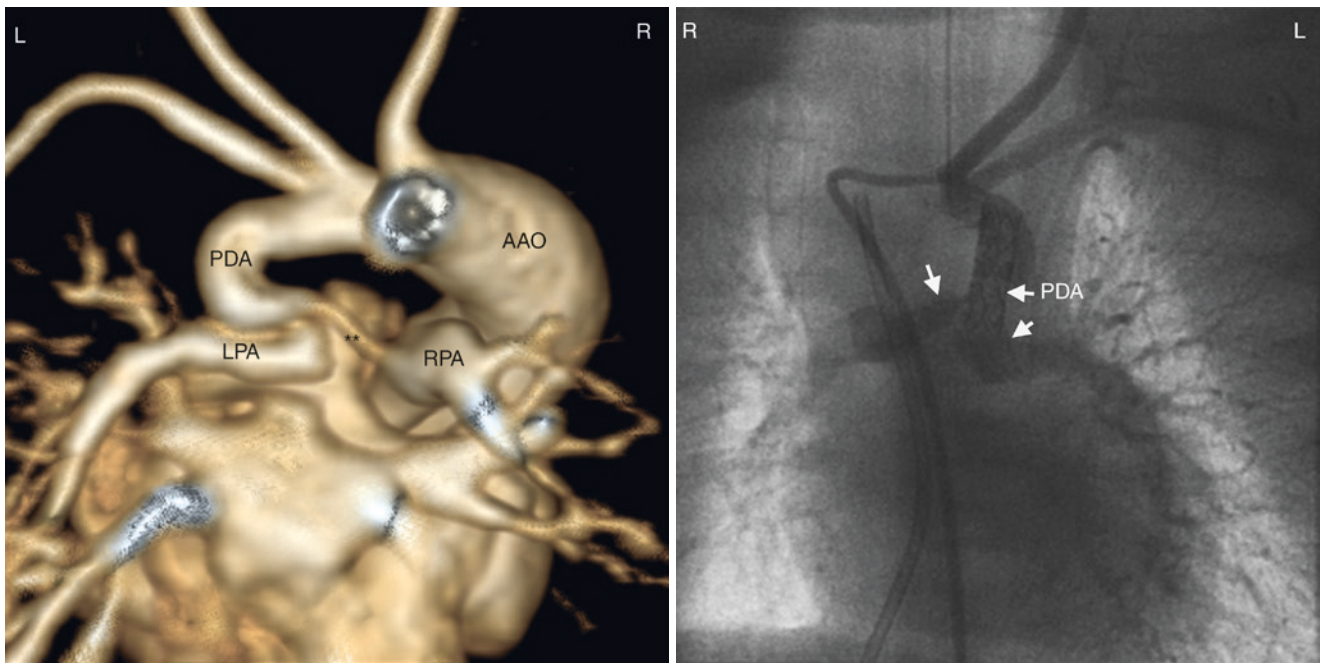


**Fig. 20.1** Newborn patient with pulmonary atresia and ventricular septal defect. Pulmonary perfusion is warranted by a patent ductus arteriosus. Surface rendered CE-MRA depicting a complex anatomical situation: ductus arteriosus is tortuous and perfuses the left pulmonary artery; both pulmonary arteries are connected by a severely hypoplastic and stenotic confluent segment (\*\*). On the base of this information

further treatment was planned, and the anatomy of pulmonary bifurcation was reconstructed by catheter-guided stenting (arrows) of the hypoplastic confluent segment. Another stent was placed in the ductus arteriosus to keep its patency (arrow). AAO ascending aorta, LPA left pulmonary artery, PDA patent ductus arteriosus, RPA right pulmonary artery

## 20.2 Fundamentals of Paediatric Imaging

### 20.2.1 Settings

Paediatric patients with complex cardiac anatomy that cannot be adequately assessed by echocardiography require advanced imaging with CMR [1]. At the time of first diagnosis, particularly in complex CHD, understanding all clinical questions that need to be answered by the examination and the ability to interpret each image as it is acquired, are essential factors to direct the scan appropriately. As children may not be compliant for a long examination time and the youngest ones require general anaesthesia, the CMR scan should be kept as short as possible (shorter than 60 min) and tailored to the specific questions that need to be answered. Recently, some technical advances with the development of accelerated sequences help to shorten the scan time. Ideally, CMR in young children should be performed by a cardiac imager together with/or supervised by an experienced paediatric cardiologist trained in cross-sectional imaging.

### 20.2.2 Sequences

CMR assessment of CHD in children can be performed with the same basic sequences applied in adults. However, high

heart rate and small patient size require some adjustment of the imaging parameters, targeted to improve both temporal and spatial resolution of the images [2]. High *spatial resolution* (in-plane resolution  $\sim 1 \text{ mm}^2$ ) can be achieved by using a small field of view, a sufficiently large matrix, and thin slices. A rectangular FOV (reducing the number of phases) and parallel imaging can be used for shortening the acquisition time. Recently, commercially available dedicated paediatric thoracic coils (phased-array, multi-channel) that can be placed directly on top of or underneath the child provide high signal-to-noise and improved image quality (Fig. 20.2).

High *temporal resolution* (20–40 ms) is particularly important for functional measurements such as ventricular function by steady-state free precession (SSFP) and blood flow quantification. For SSFP the true temporal resolution is calculated as the number of views per segment (VPS) (or lines of the  $k$ -space) that can be obtained by one repetition time:  $\text{TR} \times \text{VPS}$ . For velocity-encoded phase contrast cine (PC), the time is multiplied by a factor of two since the sequence is repeated twice for obtaining an anatomical image corresponding to each PC image:  $2 \times \text{TR} \times \text{VPS}$ . Temporal resolution can therefore be optimised by adjusting the number of VPS (between 2 and 8) to heart rate and keeping TR as low as possible.

In children, SSFP cine and contrast-enhanced MR angiography (CEMRA) are still the most used sequences for anatomical assessment. SSFP is the sequence of choice



**Fig. 20.2** Four-days old newborn examined in general anaesthesia. A new-generation light, flexible, multichannel phased-array coil is placed directly on the patient's chest. The newborn is wrapped in blankets and has a cold-pack around its head for maintaining body temperature

for measuring ventricular volume and ejection fraction; excellent reproducibility has been shown also in children, and specific paediatric normal values have been recently published [3].

CEMRA is considered one of the most striking and revolutionary sequence for vascular imaging in CHD. In our paediatric CMR program, CEMRA is being performed in >90% of all examinations. CEMRA acquires a stack of contiguous thin slices covering the entire chest, which corresponds to a 3D data set. In order to optimally visualise all intrathoracic vessels, CEMRA is usually performed in a *coronal plane* including the chest wall anteriorly and spine posteriorly. In CHD, all the intrathoracic vessels are of interest, as additional unexpected findings are not rare. Therefore, image acquisition is repeated three times, for visualisation of the arterial and the venous phase of contrast medium passage. The excellent SNR obtained after contrast medium injection allows the use of a small field of view (18–20 cm) and very thin slices (down to 1.4 mm). In small children, a double dose of Gadolinium (0.2 mmol/kg) is usually used [4]. In newborns, we recommend diluting the small amount of contrast medium with 3–5 ml of saline solution and to perform manual bolus injection. In small children, when injecting by using an automated injection pump, ensuring full patency of the I.V line is particularly important. In uncorrected CHD with right to left shunt, particular care needs to be taken for avoiding injection of air bubbles, since contrast medium cannot be injected through an air filter which would dampen the bolus effect.

Correct timing of image acquisition synchronised to the maximal signal intensity in the vessel of interest is crucial for obtaining excellent quality angiography data. The injection

rate should be set depending on the amount of contrast medium and targeting a total injection time of 10 s. In modern scanners, automated bolus detection or MR fluoroscopic triggering can be used for exact timing of image acquisition. We use a sequence with elliptic-centric *k*-space filling and a delay time of 5 s between bolus detection and image acquisition to start a breath-holding. If automated contrast medium detection is not available, we recommend using outcentric linear *k*-space filling and to start image acquisition simultaneously with contrast injection [2].

From the acquired 3D dataset, a specific vessel can be visualised in any oblique plane following sub-volume maximum intensity projection (MIP) reconstructions. Accurate measurements of the vessel diameters even in small children can be achieved, which is crucial for proper planning of further surgical or catheter-guided intervention [5].

Time-resolved 3D CEMRA shows the dynamic distribution of contrast medium into the vessels. This technique overcomes the need for bolus timing and has been successfully performed in free-breathing children with CHD [6]. The improved temporal resolution implies the trade-off of a significantly decreased spatial resolution, both in-plane and through-plane. The limited spatial resolution is a major limitation of this technique for assessment of small vascular structures [2].

Nephrogenic systemic fibrosis (NSF) is a well-known serious complication of Gadolinium-based contrast agents. NSF is exceedingly rare, and even more so in children compared to adults [7]. Nevertheless, screening of the renal function is mandatory before administration of contrast medium. Particularly in neonates and infants, who may have an immature renal function, contrast medium should be administered after careful consideration of the risks and benefits and only agents bound to a cyclic chelate should be used [7].

3D SSFP is an ECG-triggered and respiratory-navigated sequence enabling acquisition of a whole-chest 3D dataset without the use of contrast medium. 3D SSFP presents with an increased spatial resolution compared to anisotropic 2D and contrast-enhanced 3D imaging; however, in small children small voxel size and fast heart rate may result in decreased signal-to-noise ratio as well as blurred borders of anatomic structures. Image acquisition should be tailored to occur during end-diastole, the phase with the least cardiac motion, and in fast heart rate the RR interval increased to 6 or 8; i.e. image acquisition every sixth or eighth RR interval enables longer time for pre-pulse preparation. General anaesthesia with regular ventilation is an additional help for obtaining efficient image acquisition and sharp 3D SSFP images (Fig. 20.3).

3D cine SSFP images, a further development of 3D SSFP, have been successfully acquired with good spatial and temporal resolution in free-breathing infants [8, 9]. 3D cine SSFP provides data on ventricular volumes and function,

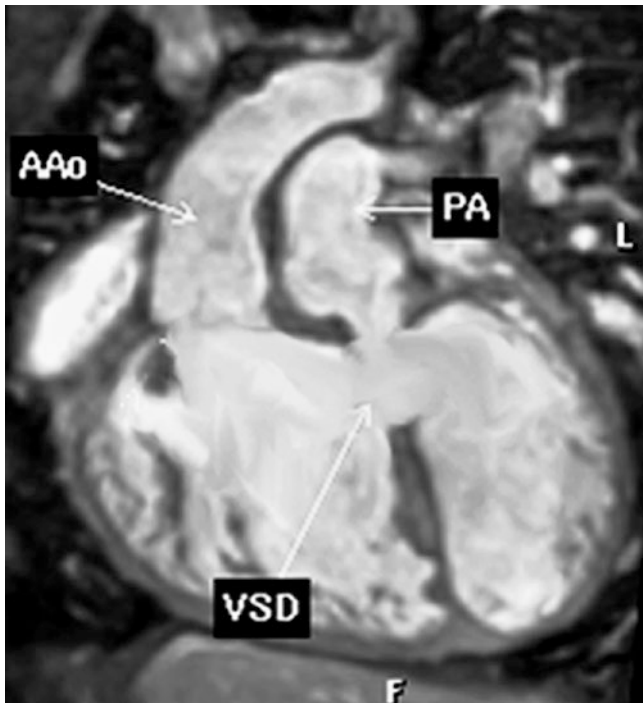


**Fig. 20.3** 3D SSFP image in a patient with double outlet right ventricle, depicting the intracardiac anatomy, with large VSD, transposed position of the ascending aorta, and overriding pulmonary artery with subvalvular narrowing (conus). (Courtesy of Dr. Greil, Dallas Texas). *AAO* ascending aorta, *PA* pulmonary artery, *VSD* ventricular septal defect

without the need for repetitive breath-holding and cumbersome planning procedures. Volumetric indices using 3D cine SSFP are slightly larger than with 2D cine SSFP, but show a comparable low variability [9, 10]. Thus, measurements cannot be considered interchangeable, and it is highly recommended to perform sequential measurements using the same sequence.

More recently, combination of parallel imaging, efficient *k*-space filling, temporal undersampling, and/or compressed sensitivity encoding algorithms, yielded a significant accel-

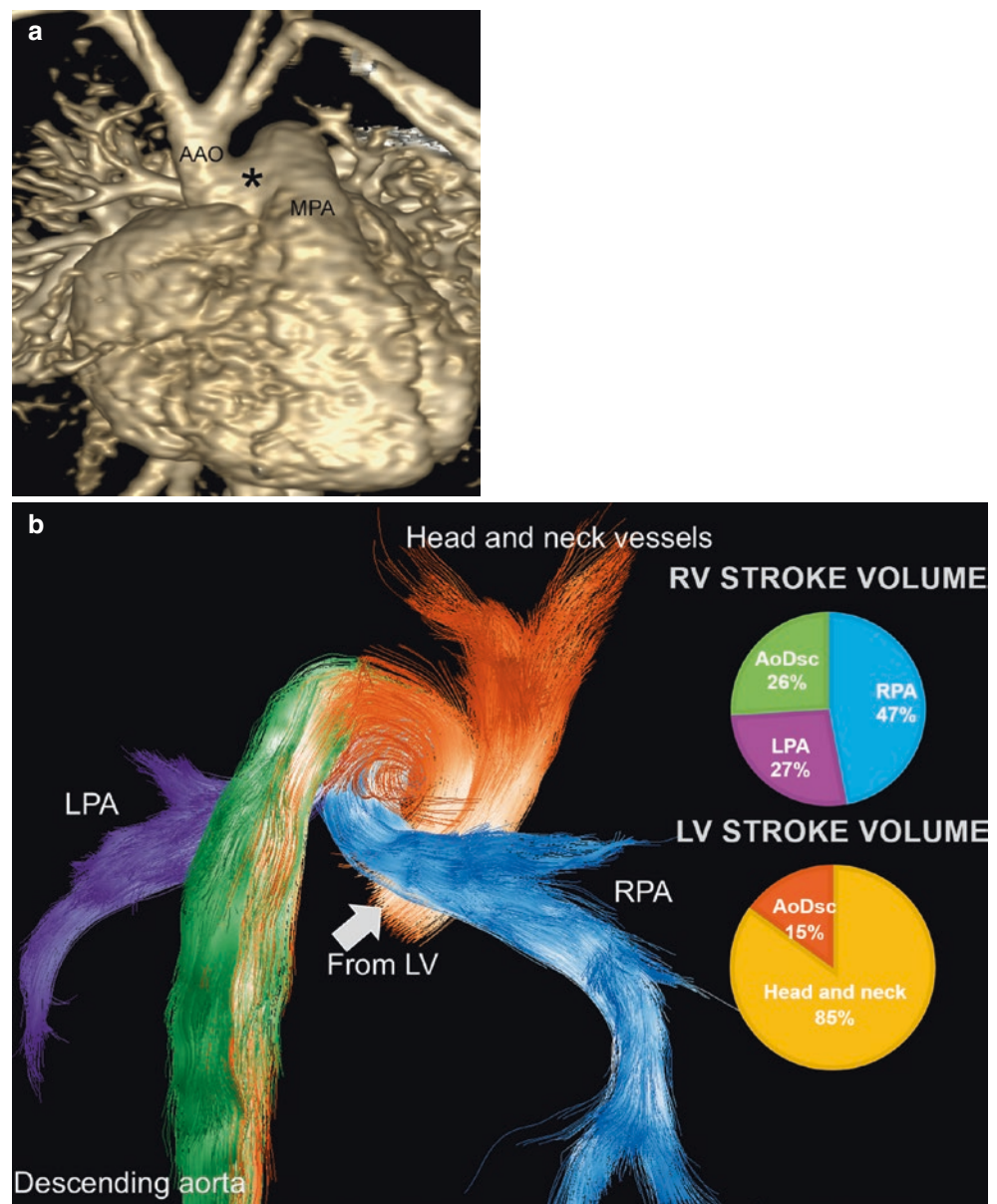
eration of image acquisition and eventually the development of real-time imaging [11, 12]. Although these newly developed sequences hold the potential for shorter and free-breathing data acquisition, their clinical application in young children still requires validation [13].

4D flow is being increasingly applied in children with CHD. 4D flow enables to visualise and quantify flow within the whole chest, as images are acquired as a large 3D volume. 4D flow image acquisition can be easily planned over the whole chest and it obviates the cumbersome selective image planning/acquisition over each single vessel of interest. Flow can be retrospectively quantified in each vessel of interest, for instance for clinical questions raised during surgical planning, and the reconstructed images help to understand complex mechanism of abnormal flow pattern [14]. As in other sequences, the physiological specifics of small children require appropriate parameters adaptations. We recommend an isotropic spatial resolution of 1.6 mm<sup>3</sup> in neonates and of 1.8 mm<sup>3</sup> in infants and young children; the targeted temporal resolution is 20–25 ms; velocity encoding is set at 160 cm/s, if higher velocities are expected velocity encoding is increased to 200 cm/s [15]. Flow visualisation and quantification requires a dedicated post processing and editing software; various solutions are commercially available. Flow can be visualised in form of velocity maps, colour-coded streamlines, velocity vectors, or path line tracking (Movie 20.1).

Flow quantification requires first multiplanar reformatting of the vessel of interest and secondly, similar to 2D flow, a correct plane positioning perpendicular to flow direction, using the double oblique technique. Flow quantification on 4D flow images has been shown to be accurate and precise not only in the arterial but also in the venous vessels [16, 17]. In children, 4D flow is very helpful in preoperative visualization and quantification of shunts (Movie 20.2), for complex abnormal flow conditions, such as in abnormal pulmonary veins, as well as in better understanding of flow in rare and complex CHD (Fig. 20.4).



**Fig. 20.4** Three-days old newborn investigated for complex conotruncal anatomy. Volume rendered CEMRA (a) reconstruction shows an interrupted aortic arch Type A and an aortopulmonary window (\*). 4D flow (posterior view) (b) visualizes the complex flow characteristics and quantify flow distribution in the different vascular structures. AAO ascending aorta, AoDsc descending aorta, LV left ventricle, LPA left pulmonary artery, MPA main pulmonary artery, RPA right pulmonary artery, RV right ventricle. (Courtesy of F.Callaghan, Zurich)



### 20.3 Anaesthesia and Sedation Considerations for CMR in Infants and Young Children

Younger children, mainly before school age (7–8 years), require either sedation or general anaesthesia for a successful CMR examination. The preference regarding these procedures may differ between centres.

If a *deep sedation* is performed, the patient can breathe spontaneously and the images are acquired during shallow free-breathing. This approach is primarily less invasive, but the airways remain unprotected with some risk of aspiration, airway obstruction, and hypoventilation. Thus, sedation in the CMR unit should always be performed and monitored by an

anaesthesiology team. From an imaging point of view, respiratory motion generates artefacts that deteriorate image quality and the negative diagnostic impact of such artefacts is more pronounced in younger children, in whom sharp images help better delineation of smaller vascular structures.

*General anaesthesia* (GA) with endotracheal intubation allows an adequate degree of sedation, in which the airways are protected and ventilation can be controlled [18]. Since children with CHD are considered high-risk patients for sedation and GA, most anaesthesiologists may prefer to examine under completely controlled ventilatory and hemodynamic conditions [19].

Working in the CMR unit may present some challenges for the anaesthesiology team. The procedure is performed in a





**Fig. 20.5** CMR-compatible anaesthesia equipment available in the examination room; the ventilatory system is integrated with a full monitoring system. The anaesthesiologist has full control on patient's conditions and can stop ventilation manually during image acquisition

noisy and unfamiliar environment, the ambient temperature is cool (20–22 °C) with risk of patient hypothermia, the access to the patient and the equipment may be limited, and reliable monitoring of the patient may not be warranted during the whole MR scan. Nowadays full MR compatible anaesthesia equipment, without mutual interference between scanner and monitoring system, is commercially available and should be present in every centre performing paediatric CMR. The respirator in the CMR unit should provide complete ventilation and respiratory gas monitoring, including plethysmography and end-tidal carbon dioxide analysis. Hemodynamic monitoring should include blood pressure, continuous ECG, and pulse oximetry (Fig. 20.5). In neonates, hypothermia can be avoided and body temperature maintained constant by placing commercially available hot-packs, preheated to body temperature, around the head, the pelvis, and the legs of the patients, and by covering the baby with a blanket (Fig. 20.2).

Repetitive safety instruction is mandatory for all medical personnel entering the MR unit; rigorous behaviour is crucial for avoiding any incident related to ferromagnetic medical equipment and objects in the MR environment. An additional crucial aspect for a successful and safe CMR examination consists of a close collaboration between the imaging team (cardiologist and/or radiologist) and the anaesthesiology team, with joint meticulous planning and tailoring of the examination to the patient's hemodynamic and respiratory status [18]. By following these recommendations, infants under 1 year, inpatients, and critically ill patients can undergo a CMR examination in GA without significant procedural complications or hemodynamic impairment [20, 21]. In a well-organised paediatric infrastructure, with an anaesthesi-



**Fig. 20.6** Infant examined in natural sleep following the feed-and-sleep method. The infant is embedded in a rigid cradle, which helps minimized movements

ology premedication clinic and dedicated beds in a day-clinic ward, CMR can be usually performed in an outpatients setting, and the patients discharged the same day of the examination. We recommend a short hospitalization for patients under 3 months of age, patients with a single ventricle physiology, and children with pulmonary hypertension or with unrepaired cyanotic CHD [19].

The *feed-and-sleep* approach obviates the use of GA or deep sedation and their related risks. This technique can be applied on selected infants younger than 6 months and consists of feeding the patient immediately before the CMR scan and wait for a deep sleep to occur [22]. The infants are placed in a vacuum immobiliser, which is transformed in a rigid cradle after removing the air from the bag, once the infant is sleeping. (Fig. 20.6). Feed-and-sleep can be performed with-

out complications and with sufficient diagnostic quality in a shorter time for use of the scanner room and without need for additional anaesthesia staff. Thus, eventually in selected cases that don't require cardiovascular or respiratory support, the feed-and-sleep method appears to be a safer, time- and staff-saving and therefore cost-efficient approach [22, 23].

## 20.4 Specific Clinical Applications in Children

At the time of first diagnosis, CMR is performed in all cases, in which echocardiographic information is insufficient. Main indications for performing CMR in neonates and infants are summarised in Table 20.1.

In this group of young patients, the main referral reason for CMR is anatomical delineation of the intrathoracic vascular anatomy, including the aorta, the pulmonary arteries, and the pulmonary veins, mainly in the context of complex CHD [1] [24] (Fig. 20.7). The information obtained can be used for discussion of further treatment strategy. The retrospective review of 100 consecutive neonatal cases (age < 1 month) examined in our institution demonstrated that in 70% of the cases the CMR findings were relevant for planning cardiac surgery (47%) or a catheter-guided intervention (23%). In 20% of the cases, findings requiring further intervention were ruled out, and in 5% compassionate care was decided, as CMR confirmed a dismal diagnosis. Infants with complex CHD and with univentricular heart are an important group in which CMR is used at time of first diagnosis. Later on, as soon as the patients are able to perform breath-holding, CMR is a standard of care during follow-up of all patients with Fontan physiology (see also chapter "Single Ventricle and Fontan Procedures") [1].

**Table 20.1** Common clinical indications for CMR in neonates and infants with CHD

Complex vascular anatomy
Aortic arch anomalies (interrupted aortic arch, coarctation, vascular rings)
Arterial blood supply to the lungs (pulmonary artery anatomy, aortopulmonary collateral arteries)
Pulmonary vein anomalies (anomalous connection, stenosis)
Complex CHD (Heterotaxy syndrome)
Quantification of ventricular volumes
Borderline hypoplasia of the left ventricle (hypoplastic left heart complex)
Borderline hypoplasia of the right ventricle
Follow-up after surgery or intervention
Shunt patency
Pulmonary artery stenosis
Restenosis or aneurysm of the aortic arch
Evaluation of tumours

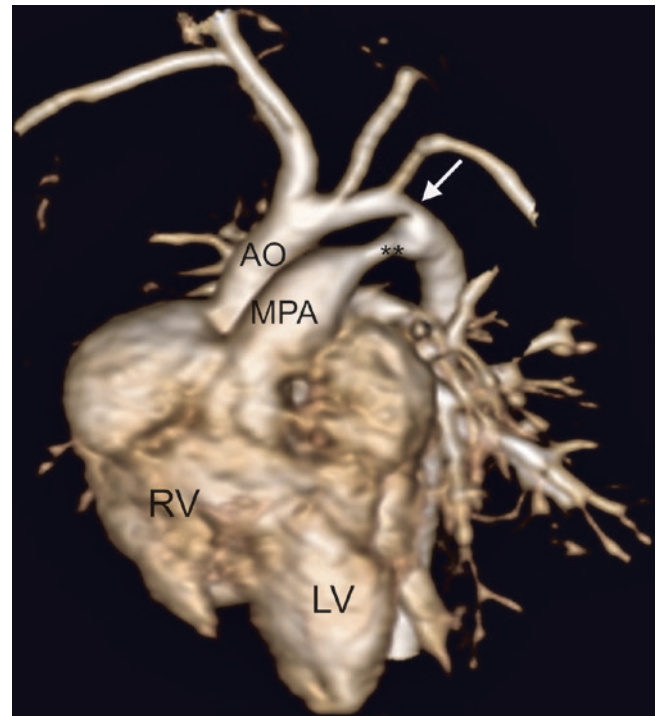


**Fig. 20.7** Newborn with heterotaxy syndrome, double-outlet right ventricle, transposition of the great arteries, subaortic conus and hypoplastic aortic arch with coarctation (arrow). A patent arterial duct (\*\*\*) provides continuity to the proximal descending aorta. AO ascending aorta, LV left ventricle, MPA main pulmonary artery, RV right ventricle

In older children, CMR is mainly performed for evaluating residual findings after cardiovascular surgery for planning or assessing the results of interventions. Due to the lack of radiation and the high reproducibility of the functional and anatomical measurements, CMR is the modality of choice for repetitive examinations in selected disease such as connective tissue disease—Marfan syndrome, Loeys-Dietz Syndrome—in which the size of the aorta requires a close follow-up.

Conotruncal anomalies, aortic arch anomalies, the pulmonary arteries, and the pulmonary veins are being discussed in different chapters of this book. Two very specific paediatric applications for preoperative assessment are discussed in the following paragraphs.

### 20.4.1 Heterotaxy Syndrome

Heterotaxy syndrome is frequently associated with complex CHD and is characterised by inconsistency of the situs of the thoracic and abdominal viscera (situs ambiguous), with similar shape of the atrial appendages (atrial isomerism), bronchial symmetry and splenic anomalies, including asplenia or polysplenia. The most common characteristics of cardiac defects occurring in heterotaxy syndrome are summarised in



**Table 20.2** Characteristics of complex CHD associated with heterotaxy syndrome

Defect	Right isomerism	Left isomerism
Bilateral superior venae cavae	45%	45%
Absence of coronary sinus	~100%	~60%
Interruption of the inferior vena cava	<2.5%	80%
Total anomalous pulmonary vein connection	50% (obstruction in 50%)	Rare
Atrioventricular connection	Univentricular in 70%	Biventricular in ~75%
Ventriculoarterial connection	Concordant only in 4%	Concordant in ~70%
Pulmonary atresia or stenosis	80%	30%
Left sided obstructive lesion	<5%	~30%
Heart block/bradycardia	Rare	~70%

TAPVC total anomalous pulmonary venous connection

Table 20.2. Hearts in left atrial isomerism tend to be biventricular and those with right atrial isomerism univentricular. In spite of any classification, a recent review of cases studied by cross-sectional imaging has shown an undefined variability of pattern; discordance between bronchopulmonary branching, atrial appendage arrangement, and splenic status occurs in up to 20% of patients with heterotaxy syndrome [25]. Thus, in patients with suspected heterotaxy syndrome the diagnostic approach should be individualised and based on a systematic segmental analysis. This can be done by acquiring a stack of cine images in an axial plane covering the whole chest or by 3D SSFP; at time of reading, the segmental analysis can be done by scrolling through the different planes.

Imaging and reporting these cases should include assessment of the abdominal situs, spleen—asplenia, polysplenia, thoracic situs—bronchi, morphology of the atrial appendages, cardiac position, cardiac segments, intracardiac anatomy (atrial defects, atrioventricular defects, ventricular defects, coronary sinus), ventriculoarterial alignment, systemic venous anatomy, pulmonary venous anatomy and site of connection, pulmonary arteries, and aortic arch.

The abdominal status can be easily defined on the coronal localiser images. More accurate visualisation of the spleen status is achieved by covering the upper abdomen when acquiring axial SSFP images. The thoracic status is determined by the bronchial anatomy; in addition to black-blood fast spin echo images, newly developed ultrashort echo time sequences are excellent techniques for showing the main stem bronchi and their relations to the branch pulmonary arteries (Fig. 20.8). In situs solitus, the course of the right bronchus is superior to the right pulmonary artery (eparterial bronchus), whereas the left bronchus runs inferiorly to the

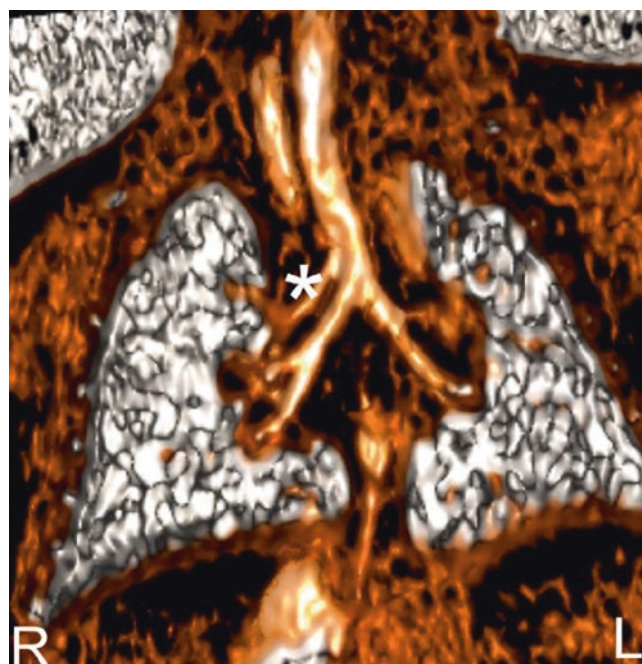


**Fig. 20.8** 3D reconstruction of the bronchial tree from a ultrashort Echo Time sequence dataset acquired in a newborn girl with right atrial isomerism. There is a bilateral right bronchial system; in addition, a tracheal bronchus (\*) has been depicted

left pulmonary artery (hyarterial bronchus). Symmetrical length of the bronchi and symmetrical superior-inferior relation between the main bronchi and the proximal pulmonary arteries are indicative for a situs ambiguus.

The unique diagnostic performance of CMR is achieved by combining several available sequences, including 2DSSFP, 3D SSFP, CEMRA, and 4D flow [25, 26] (Fig. 20.9).

Exact definition of the morphology of the atrial appendages remains challenging. The morphologically right atrial appendage has an external triangular shape with a broad base and the apex pointed upward; internally the prominent crista terminalis and the pectinate muscles can be identified. The left atrial appendage has a tubular finger-like shape with a narrow base, pointed anteriorly and downward (Fig. 20.10).

Anomalies of the pulmonary venous connection occur very frequently in heterotaxy syndrome and are considered major determinants of outcome. Pulmonary venous anomalies can be accurately depicted by CEMRA (Fig. 20.11) [27].

#### 20.4.2 Single Ventricle Lesions

Mostly, the initial diagnosis of single ventricle can be achieved by echocardiography. CMR is the second-line modality of choice for cases with additional anomalies of the

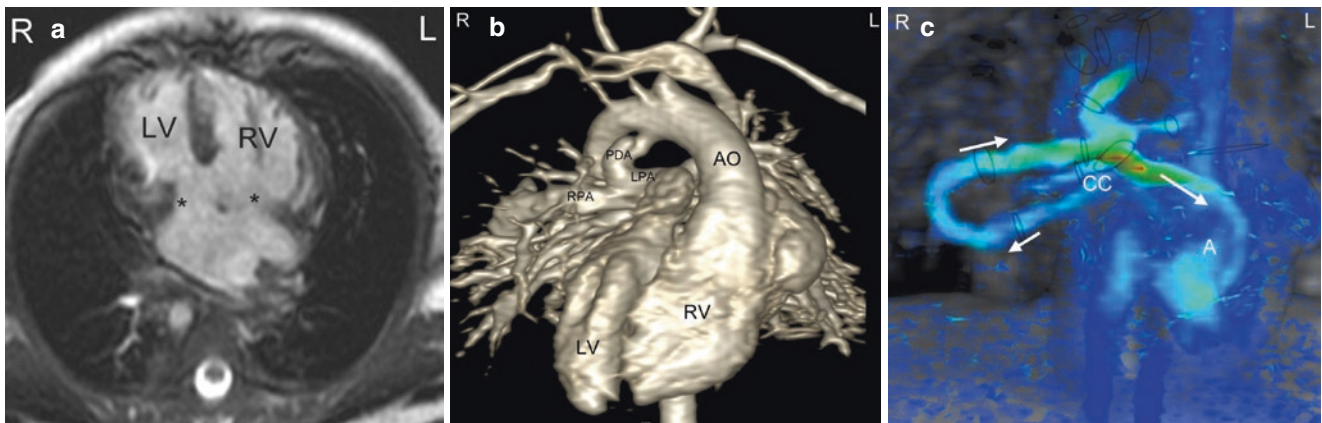


**Fig. 20.9** Newborn girl with heterotaxy syndrome, specifically right atrial isomerism, dextrocardia, ventricular inversion, ventriculo-arterial discordance, pulmonary atresia, total anomalous pulmonary venous connection and right aortic arch. The SSFP cine images (a) show the intracardiac anatomy, with a balanced atrioventricular defect (\*). The morphological right ventricle is left-sided and the morphological left ventricle is right-sided. Volume rendered reconstructed CEMRA images (b) provide clear visualization of the ventriculo-arterial discordance,

right aortic arch and pulmonary perfusion warranted by a patent ductus arteriosus. Pulmonary side branches are confluent. 4D flow (c) enables improved understanding of the flow direction of a complex form of total anomalous pulmonary vein connection of cardiac type. The collecting vein is running in a loop to the roof of the common atrium. A common atrium, AO ascending aorta, cc collector vein, LPA left pulmonary artery, LV left ventricle, PDA patent ductus arteriosus, RPA right pulmonary artery, RV right ventricle

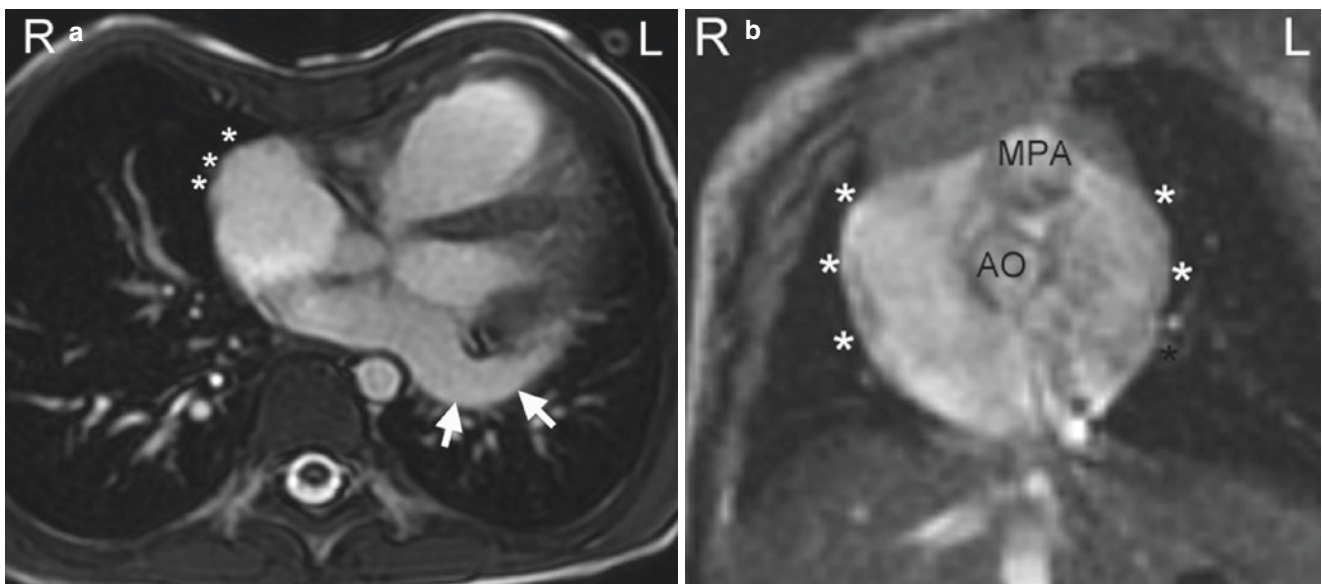


**Fig. 20.10** Morphology of the atrial appendages as seen in cross-sectional imaging (a). Normal situs. Right atrial appendage is marked with stars, left atrial appendage with an arrow. Right atrial isomerism.

Both atrial appendages appear as a symmetrical triangular shape (b) with a broad base, corresponding to the morphology of a right atrial appendage (\*)

pulmonary arteries, pulmonary veins, complex anomalies of the aortic arch, or in situs anomalies, as described above.

CMR is increasingly used for non-invasive diagnostics before Stage II (Glenn procedure) and before Stage III (Fontan completion). After previous patient selection, combining clinics and echocardiography, patients who do not require a catheter-guided intervention, can be safely evaluated without an invasive cardiac catheterisation [28, 29]. This approach has been shown to yield the same outcome in

a short- and mid-term follow-up, than in patients who had been invasively assessed [30]. The use of CMR for preoperative assessment significantly reduces the amount of radiation and the rate of adverse events [31].

Features to be assessed by imaging, i.e. combination of echocardiography and CMR, before the Glenn- or Fontan procedure are summarised in Table 20.3. Branch pulmonary artery stenosis or pulmonary vein stenosis, arch obstruction, and/or aortopulmonary collaterals can compromise the short-



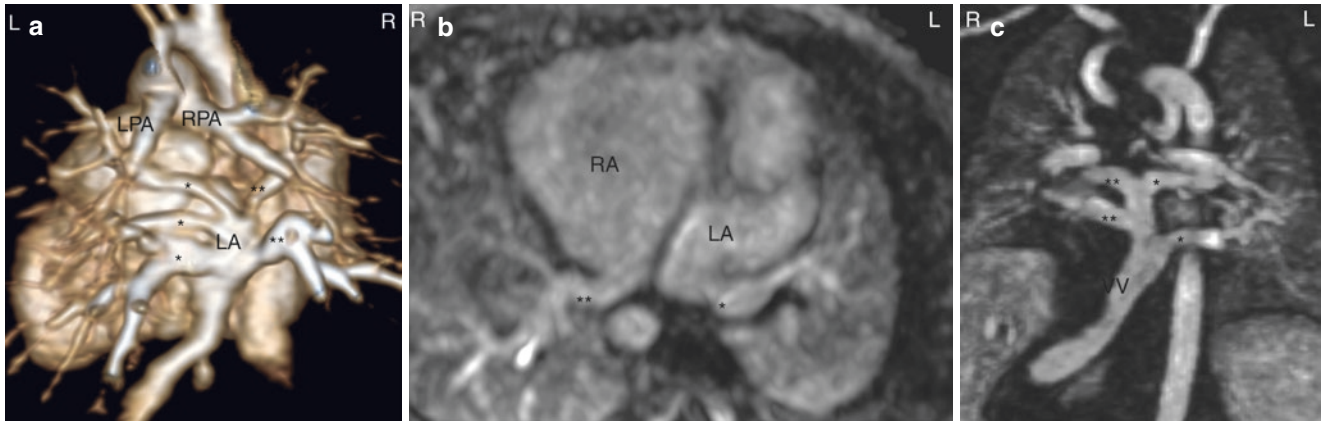


**Fig. 20.11** Pulmonary venous anomalies in heterotaxy syndrome. Newborn with right atrial isomerism. Echocardiography suspected stenosis of the pulmonary veins, due to turbulent flow. CEMRA (a) (in a view from posterior) demonstrates that all pulmonary veins connect to the left-sided atrium without anatomical narrowing. There are three segmental pulmonary veins draining the left lung (\*), and two right-sided pulmonary veins (\*\*). LA left atrium, LPA left pulmonary artery,

RPA right pulmonary artery. (b) Newborn with left atrial isomerism. CEMRA show that the left-sided pulmonary veins (\*) connect to the left-sided atrium (LA); the right-sided pulmonary veins (\*\*) connect to the right-sided atrium (RA). (c) Newborn with right atrial isomerism and total anomalous pulmonary venous connection as demonstrated in a CEMRA view from posterior. Right-sided pulmonary veins (\*\*), left-sided pulmonary veins (\*), VV vertical vein

**Table 20.3** Non-invasive imaging before staged palliation of patients with single ventricle

Non-invasive evaluation (echocardiography and CMR)	Findings requiring invasive pre-operative assessment and intervention
• Ventricular size and function	• Severe ventricular dysfunction
• Valve function	• Severe AV-valve regurgitation
• Pulmonary arteries	• Pulmonary artery stenosis
• Pulmonary veins	• Pulmonary veins stenosis
• Aortic arch	• Aortic arch obstruction
• Outflow tracts	
• Atrial septum defect patency	• Foramen ovale restriction
• Aortopulmonary or veno-venous collaterals	• Collateral flow >35% of aortic flow
	• Previous catheter-guided interventions

term course and long-term follow-up in SV patients. The findings are frequently addressed preoperatively by catheter-guided intervention.

### 20.4.3 The Borderline Ventricle: Uni- Versus Biventricular Repair

In patients with a borderline left ventricle, usually in the context of a hypoplastic left heart complex (Movie 20.3), or with a borderline right ventricle, such as in unbalanced atrioventricular septal defect, decision for biventricular repair versus univentricular palliation has to be taken during the first

months of life. In these cases, CMR helps to estimate the correct ventricle volume and enable a successful biventricular repair. On the other hand, in patients with hypoplastic left heart complex, late enhancement imaging can demonstrate the presence of endocardial fibroelastosis, which is considered a negative prognostic factor for a biventricular repair [32].

Decision-making for biventricular repair can also be challenging in biventricular hearts with complex cardiac anatomy. Double outlet right ventricle with its almost infinite anatomical variants represents the most frequently discussed lesion [33]. Techniques providing a 3D dataset, specifically 3D SSFP and CEMRA, are very helpful for answering this question. Multiplanar reconstruction and 3D printing are helpful techniques providing unique presurgical information, particularly the position of the ventricular septal defect in relation to the great arteries [34] (Fig. 20.3).

## 20.5 CMR in Relation to Other Non-invasive Modalities

In the modern era, and particularly in congenital cardiology, different imaging modalities should not be considered as competitive techniques, but as diagnostic tools complementing each other. It is therefore the responsibility of every imaging expert to know strengths and weaknesses of every modality and to use and combine them appropriately.

### 20.5.1 Echocardiography

Particularly in newborns and small children with their intact acoustic window echocardiography remains the first line bedside imaging modality. Nevertheless, echocardiography is highly dependent on operator skills, and remote and unusual anatomical structures can be difficult to visualise and understand in their topographic relationship. Thus, in the presence of complex vascular anatomy, a second-line advanced imaging modality is usually required.

The major strength of CMR compared to echocardiography is *quantitative functional assessment*, specifically of ventricular volumes and blood flow. Compared to echocardiography CMR, volume quantification is not based on any geometric model and presents higher reproducibility. In the last few years, 3D echocardiography has evolved into clinical use and has also been validated in children [35]. Both, CMR and 3D echocardiography enable calculation of volumes based on the summation-disc method which reflects the real shape of every ventricle and provides accurate volume measurements; however, 3D echocardiography is still limited by acoustic window and tend to overestimate ventricular volumes. CMR is the only modality able to directly quantify blood flow in each desired vessel; flow sequences have been clinically validated also in children [15, 36].

### 20.5.2 Computed Tomography

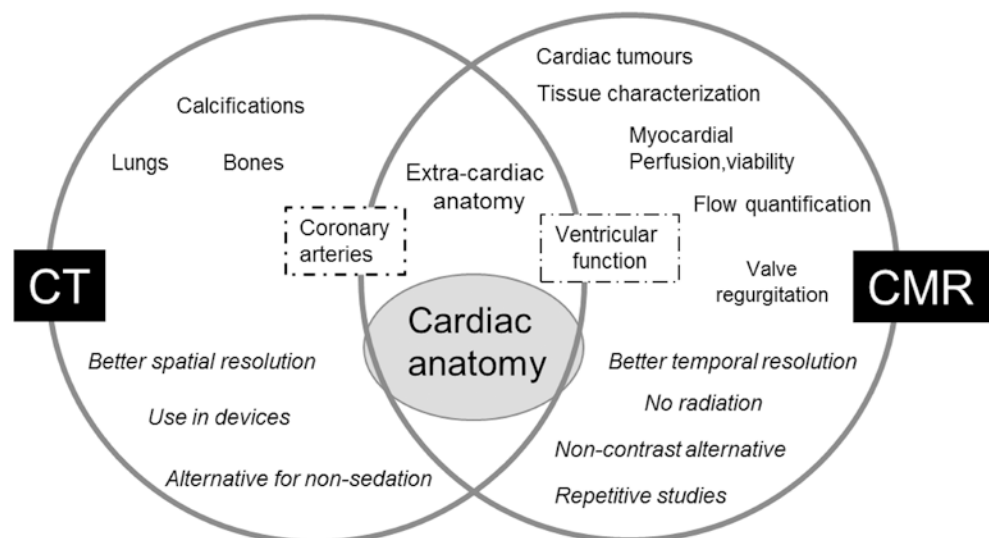
Cardiac computed tomography (CT) shares several advantages with CMR, particularly coverage of a large field of view with outstanding imaging quality and acquisition of 3D data sets. In small children, the superior spatial resolution of CT can be of great advantage for imaging small vascular structures. Newer generation CT scanners enable

rapid image acquisition, submillimetre isotropic spatial resolution, and acceptable temporal resolution as low as 66 ms at lower radiation doses than older technologies. Recently published multi-institutional data reported that CT can be performed in paediatric patients with low diagnostic risk, very short procedural time and a median radiation dose of approximately 1 mSv [37]. For obtaining an outstanding image quality and lowest radiation possible, expertise in paediatric imaging is required and scanning protocols have to be specifically designed for small children. Due to the very short scanning time sedation/anaesthesia can be obviated. Good blood/tissue contrast usually requires contrast agent injection and a correct timing of image acquisition at the best contrast density [38]. CT should be definitely used in the presence of MR incompatible implants and when sedation may be at high risk. Another strength is its ready availability in urgent situations, which makes CT easier to use in critically ill patients or when the clinical status is changing. Regarding the structures to be visualised CT is considered superior to MR to evaluate stent patency after endovascular treatment, for evaluation of the topographic relationship between the airways and the thoracic vessels, and for visualisation of the coronary arteries [38, 39].

In contrast to CMR, functional measurements by CT are limited. Flow visualisation and quantification is an exclusive characteristic of CMR and an important information in most CHD. In cases in which CMR is contraindicated, multiphase functional CT offers reasonable estimation of ventricular function [40]. The common and different features for image acquisition and visualisation in CT and CMR are visualised in Fig. 20.12 (adapted from [1, 41]).

Eventually, due to the radiation burden and the high stochastic effects of exposure to ionizing radiation in young children, we recommend the use of CMR. However, decision

**Fig. 20.12** Overview of strengths of CT and CMR as imaging techniques and regarding the structures to be visualized. (Adapted from [41])



on the best imaging modality depends on the clinical status of the patient, the clinical question as well as the available expertise and technical equipment [41].

### 20.5.3 Cardiac Catheterization

In the last decade, a clear trend toward non-invasive advanced imaging has developed in paediatric cardiology. Therefore, nowadays catheterisation is rarely used for diagnostic purposes, and almost exclusively linked to an intervention. Complications associated with cardiac catheterization in children have been reported in up to 8% of the procedures. The majority of these complications are related to the vascular access, and infants younger than 6 months are at higher risk [42]. With the increasing number of infants with complex CHD who can be treated nowadays, it is crucial to maintain vascular access patent for future therapeutic interventions and to minimise the number of invasive diagnostic procedures.

CEMRA is superior to conventional angiography, as it enables multiplanar and 3D reconstruction of the vascular anatomy. We have previously demonstrated that size measurement taken on CEMRA images in small children are highly comparable to conventional angiography measurements and therefore reliable for surgical planning [5].

CMR is considered superior to cardiac catheterisation for quantitative assessment of most hemodynamic parameters, including ventricular volumes and flow. In contrast, invasive measurements are still needed for determining the pulmonary vascular pressure and resistance.

## 20.6 CMR Limitations and Common Pitfalls

The most important limitation for the use of CMR are costs and need for human and technical resources. This is particularly true for the paediatric population, in which anaesthesia is often required. Anaesthesia in the MR environment requires an infrastructural investment, with purchase of fully equipped CMR-compatible ventilation and monitoring equipment, as well as an interdisciplinary cooperation involving four different teams: cardiac imaging, cardiology, anaesthesiology and imaging technicians.

Moreover, CMR is not a bedside modality and the transport and monitoring of critically ill infants in the CMR unit requires a significant effort from the caring team. Centres not having access to these amenities may use CT as an alternative cross-sectional imaging modality.

**Pitfalls.** During image acquisition, even though arrhythmias are less frequent in children than in adults, inappropriate ECG-gating may deteriorate image quality and affect the

accuracy of functional measurements. The accuracy of flow measurements done by PC cine imaging can be affected by offset errors and in many scanners flow correction with static phantom measurements may be necessary. Each institution needs to be aware of this potential source of error and plan enough time after each examination for performing phantom measurements and calibration if necessary. Off-set errors have also been reported in 4D flow [43]. Some correction tools are integrated in modern postprocessing software, and obviate time-consuming phantom measurements. In children with CHD, the accuracy of flow measurements is crucial, as clinical decision-making is often directly based on the flow information provided by CMR. Therefore, on top of the described technical recommendations, a physiological internal validation should be applied; this can be done by comparing volumetric data from the ventricles with flow data of the great arteries, or by comparing the pulmonary flow measured in the pulmonary side branches with the one measured from all four pulmonary veins. One of the important advantages of 4D flow is the capability to retrospectively measure flow in each required vessel, and therefore performing any required internal flow validation. In small children, accurate measurement of flow requires a minimal cross-sectional area of a vessel; measurements should not be performed in the region of interest containing less than 5 pixels.

During post-processing and reporting, results obtained in a child need to be compared with normal values that (a) have been established for children, and (b) have been acquired with a similar technique [3, 44–46].

Correct reading of CEMRA images requires caution regarding interpretation of narrowing of small vessel. In the presence of an additional flow source, such as a surgical shunt, or aortopulmonary collateral vessels, the concomitant blood flow coming from the shunt, which may not contain contrast medium yet, can impair the visualisation of the vessel and mimic a stenosis. Moreover, artefacts caused by surgical clips or any other metallic implants need to be ruled out, before reporting narrowing of a vessel.

## 20.7 Conclusions

In children with CHD, CMR is the second-line imaging modality after transthoracic echocardiography, and provides almost complete morphological and hemodynamic information before and after surgical or catheter-guided interventions. Neonates and infants are the patients taking the most advantage of CMR, as a radiation-free and non-invasive imaging modality. Performing CMR in a paediatric population requires a specific infrastructure, individual adjustment of the acquisition parameters, a sound expertise in complex CHD, and an excellent interdisciplinary collaboration among

all teams involved. Once these requirements are achieved, CMR can be performed safely and with excellent results.

Continuous improvements in software (sequences) and hardware (gradients, coils) are steadily improving the performance of CMR in small children.

### Practical Pearls

- CMR is nowadays considered a second-line modality after transthoracic echocardiography in diagnosis and follow-up of CHD in children.
- Imaging parameters need to be adapted to the specific paediatric characteristics:
  - Spatial resolution can be improved by using a small field of view, a sufficiently large matrix, and thin slices.
  - Temporal resolution can be optimised by adjusting the number of VPS to heart rate and keeping TR as low as possible.
  - Administration of contrast medium can be avoided by applying the 3D SSFP sequence.
  - 4D flow is easier to acquire than many single flow measurements, and is similarly accurate than 2D Phase-contrast measures.
- Performing paediatric CMR with anaesthesia requires an experienced anaesthesiology team and a close collaboration between the imaging team (paediatric cardiologist and/or paediatric radiologist) and anaesthesiology team. A CMR-compatible ventilatory and hemodynamic monitoring equipment need to be available in the MR unit.
- CMR quantitative data acquired in children need to be compared to normal values established for the paediatric population and obtained with the same technique.

### References

1. Valsangiacomo Buechel ER, et al. Indications for cardiovascular magnetic resonance in children with congenital and acquired heart disease: an expert consensus paper of the Imaging Working Group of the AEPC and the Cardiovascular Magnetic Resonance Section of the EACVI. *Eur Heart J Cardiovasc Imaging*. 2015;16(3):281–97.
2. Kellenberger CJ, Yoo S-J, Büchel ERV. Cardiovascular MR imaging in neonates and infants with congenital heart disease. *Radiographics*. 2007;27(1):5–18.
3. van der Ven JPG, et al. Multicentre reference values for cardiac magnetic resonance imaging derived ventricular size and function for children aged 0-18 years. *Eur Heart J Cardiovasc Imaging*. 2020;21(1):102–13.
4. Bailliard F, Hughes ML, Taylor AM. Introduction to cardiac imaging in infants and children: techniques, potential, and role in the imaging work-up of various cardiac malformations and other pediatric heart conditions. *Eur J Radiol*. 2008;68(2):191–8.
5. Valsangiacomo Büchel ER, et al. Contrast-enhanced magnetic resonance angiography of the great arteries in patients with congenital heart disease: an accurate tool for planning catheter-guided interventions. *Int J Cardiovasc Imaging*. 2005;21(2):313–22.
6. Chung T. Magnetic resonance angiography of the body in pediatric patients: experience with a contrast-enhanced time-resolved technique. *Pediatr Radiol*. 2005;35(1):3–10.
7. Mendichovszky IA, et al. Gadolinium and nephrogenic systemic fibrosis: time to tighten practice. *Pediatr Radiol*. 2008;38(5):489–96; quiz 602–3.
8. Seeger A, et al. Three-dimensional cine MRI in free-breathing infants and children with congenital heart disease. *Pediatr Radiol*. 2009;39(12):1333–42.
9. Moghari MH, et al. Free-breathing whole-heart 3D cine magnetic resonance imaging with prospective respiratory motion compensation. *Magn Reson Med*. 2018;80(1):181–9.
10. Krishnamurthy R, et al. Clinical validation of free breathing respiratory triggered retrospectively cardiac gated cine balanced steady-state free precession cardiovascular magnetic resonance in sedated children. *J Cardiovasc Magn Reson*. 2015;17(1):1.
11. Steeden JA, et al. Real-time assessment of right and left ventricular volumes and function in children using high spatiotemporal resolution spiral bSSFP with compressed sensing. *J Cardiovasc Magn Reson*. 2018;20(1):79.
12. Moghari MH, et al. Accelerated whole-heart MR angiography using a variable-density poisson-disc undersampling pattern and compressed sensing reconstruction. *Magn Reson Med*. 2018;79(2):761–9.
13. Kocaoglu M, et al. Breath-hold and free-breathing quantitative assessment of biventricular volume and function using compressed SENSE: a clinical validation in children and young adults. *J Cardiovasc Magn Reson*. 2020;22(1):54.
14. Dyverfeldt P, et al. 4D flow cardiovascular magnetic resonance consensus statement. *J Cardiovasc Magn Reson*. 2015;17(1):72.
15. Geiger J, et al. Additional value and new insights by four-dimensional flow magnetic resonance imaging in congenital heart disease: application in neonates and young children. *Pediatr Radiol*. 2021;51(8):1503–17.
16. Tariq U, et al. Venous and arterial flow quantification are equally accurate and precise with parallel imaging compressed sensing 4D phase contrast MRI. *J Magn Reson Imaging*. 2013;37(6):1419–26.
17. Gabbour M, et al. 4-D flow magnetic resonance imaging: blood flow quantification compared to 2-D phase-contrast magnetic resonance imaging and Doppler echocardiography. *Pediatr Radiol*. 2015;45(6):804–13.
18. Odegard KC, et al. Anaesthesia considerations for cardiac MRI in infants and small children. *Pediatr Anesth*. 2004;14(6):471–6.
19. Committee on Drugs. Guidelines for monitoring and management of pediatric patients during and after sedation for diagnostic and therapeutic procedures. *Pediatrics*. 1992;89(6):1110–5.
20. Sarikouch S, et al. Cardiovascular magnetic resonance imaging for intensive care infants: safe and effective? *Pediatr Cardiol*. 2009;30(2):146–52.
21. Dorfman AL, et al. Risk factors for adverse events during cardiovascular magnetic resonance in congenital heart disease. *J Cardiovasc Magn Reson*. 2007;9(5):793–8.
22. Windram J, et al. Cardiovascular MRI without sedation or general anesthesia using a feed-and-sleep technique in neonates and infants. *Pediatr Radiol*. 2012;42(2):183–7.
23. Shariat M, et al. Utility of feed-and-sleep cardiovascular magnetic resonance in young infants with complex cardiovascular disease. *Pediatr Cardiol*. 2015;36(4):809–12.
24. Krishnamurthy R, Lee EY. Congenital cardiovascular malformations: noninvasive imaging by MRI in neonates. *Magn Reson Imaging Clin N Am*. 2011;19(4):813–22; viii.
25. Yim D, et al. Disharmonious patterns of heterotaxy and isomerism: how often are the classic patterns breached? *Circ Cardiovasc Imaging*. 2018;11(2):e006917.
26. Geva T, et al. Role of spin echo and cine magnetic resonance imaging in presurgical planning of heterotaxy syndrome. *Comparison*



- with echocardiography and catheterization. *Circulation*. 1994;90(1):348–56.
27. Valsangiacomo ER, et al. Contrast-enhanced MR angiography of pulmonary venous abnormalities in children. *Pediatr Radiol*. 2003;33(2):92–8.
  28. Brown DW, et al. Cardiac magnetic resonance versus routine cardiac catheterization before bidirectional Glenn anastomosis in infants with functional single ventricle: a prospective randomized trial. *Circulation*. 2007;116(23):2718–25.
  29. Banka P, et al. What is the clinical utility of routine cardiac catheterization before a Fontan operation? *Pediatr Cardiol*. 2010;31(7):977–85.
  30. Brown DW, et al. Cardiac magnetic resonance versus routine cardiac catheterization before bidirectional Glenn anastomosis: long-term follow-up of a prospective randomized trial. *J Thorac Cardiovasc Surg*. 2013;146(5):1172–8.
  31. Gartenberg AJ, et al. Variation in advanced diagnostic imaging practice patterns and associated risks prior to superior cavopulmonary connection: a multicenter analysis. *Pediatr Cardiol*. 2021;43:497.
  32. Grosse-Wortmann L, et al. Borderline hypoplasia of the left ventricle in neonates: insights for decision-making from functional assessment with magnetic resonance imaging. *J Thorac Cardiovasc Surg*. 2008;136(6):1429–36.
  33. Bhatla P, et al. Utility and scope of rapid prototyping in patients with complex muscular ventricular septal defects or double-outlet right ventricle: does it alter management decisions? *Pediatr Cardiol*. 2017;38(1):103–14.
  34. Valverde I, et al. Three-dimensional printed models for surgical planning of complex congenital heart defects: an international multicentre study. *Eur J Cardiothorac Surg*. 2017;52(6):1139–48.
  35. Soriano BD, et al. Matrix-array 3-dimensional echocardiographic assessment of volumes, mass, and ejection fraction in young pediatric patients with a functional single ventricle: a comparison study with cardiac magnetic resonance. *Circulation*. 2008;117(14):1842–8.
  36. Powell AJ, et al. Phase-velocity cine magnetic resonance imaging measurement of pulsatile blood flow in children and young adults: in vitro and in vivo validation. *Pediatr Cardiol*. 2000;21(2):104–10.
  37. De Oliveira Nunes M, et al. Multi-institution assessment of the use and risk of cardiovascular computed tomography in pediatric patients with congenital heart disease. *J Cardiovasc Comput Tomogr*. 2021;15(5):441–8.
  38. Raimondi F, Warin-Fresse K. Computed tomography imaging in children with congenital heart disease: indications and radiation dose optimization. *Arch Cardiovasc Dis*. 2016;109(2):150–7.
  39. Han BK, et al. Computed tomography imaging in patients with congenital heart disease part I: rationale and utility. an expert consensus document of the Society of Cardiovascular Computed Tomography (SCCT): Endorsed by the Society of Pediatric Radiology (SPR) and the North American Society of Cardiac Imaging (NASCI). *J Cardiovasc Comput Tomogr*. 2015;9(6):475–92.
  40. Han BK, et al. Multi-institutional evaluation of the indications and radiation dose of functional cardiovascular computed tomography (CCT) imaging in congenital heart disease. *Int J Cardiovasc Imaging*. 2016;32(2):339–46.
  41. Ramirez-Suarez KI, et al. Optimizing neonatal cardiac imaging (magnetic resonance/computed tomography). *Pediatr Radiol*. 2022;52:661.
  42. Mehta R, et al. Complications of pediatric cardiac catheterization: a review in the current era. *Catheter Cardiovasc Interv*. 2008;72(2):278–85.
  43. Callaghan FM, et al. Flow quantification dependency on background phase correction techniques in 4D-flow MRI. *Magn Reson Med*. 2020;83(6):2264–75.
  44. Valsangiacomo Buechel ER. Normal right- and left ventricular volumes and myocardial mass in children measured by steady state free precession cardiovascular magnetic resonance. *J Cardiovasc Magn Reson*. 2009;11:19.
  45. Kaiser T, Kellenberger C, Albisetti M, Bergsträsser E, Valsangiacomo Buechel E. Normal values for aortic diameters in children and adolescents - assessment in vivo by contrast enhanced MR-angiography. *J Cardiovasc Magn Reson*. 2008;10(1):56.
  46. Valsangiacomo Buechel ER, Kaiser T, Jackson C, Schmitz A, Kellenberger CJ. Normal right- and left ventricular volumes and myocardial mass in children measured by steady state free precession cardiovascular magnetic resonance. *J Cardiovasc Magn Reson*. 2009;11:19.



# Fetal Cardiovascular Magnetic Resonance

# 21

Adrienn Szabo, Liqun Sun, and Mike Seed

## 21.1 Introduction

The prenatal diagnosis of fetal cardiovascular disease provides opportunities to improve perinatal outcomes and counsel families about prognosis. In the setting of more severe congenital cardiac malformations, which may be seen in the setting of genetic syndromes and birth defects affecting other organ systems, prenatal diagnosis provides the option of elective termination of pregnancy. With the advent of fetal therapy for cardiac conditions, prenatal imaging can also be used to guide percutaneous interventions and monitor the response to therapy. While ultrasound is a versatile and widely available technique for imaging the fetus, magnetic resonance imaging (MRI) is increasingly used as an adjunct to ultrasound to enhance fetal diagnosis. Fetal cardiovascular magnetic resonance (CMR) has historically been hampered by technical challenges imposed by the small size of the structures of interest, fetal motion, and high fetal heart rates. However, following more than a decade of technical development, approaches to acquiring high-quality fetal CMR

have been achieved. In tandem with the creation of robust CMR sequences and postprocessing methods, the modality has been used to investigate fetal circulatory physiology in health and disease. MRI has revealed relationships between abnormal cardiovascular physiology and disordered fetal development, leading to the investigation of new therapeutic approaches to improving perinatal outcomes. These human studies have been complemented by the application of fetal CMR to study fetal physiology and interventions in large animal models. The added diagnostic value of fetal CMR has been evaluated in cohorts of patients with congenital heart disease (CHD). Similarly, the potential role of fetal CMR techniques in other fetal diseases impacting the fetal cardiovascular physiology including placental insufficiency and fetal anemia has been investigated. In this chapter, we will outline the key methods used in fetal CMR, discuss some of the important principles of fetal cardiovascular physiology that inform the interpretation of fetal CMR studies, and review current and potential future clinical application of fetal CMR (Fig. 21.1).

---

A. Szabo · L. Sun (✉)  
Division of Pediatric Cardiology, Department of Pediatrics, The  
Hospital for Sick Children, University of Toronto,  
Toronto, ON, Canada  
e-mail: [adrienn.szabo@sickkids.ca](mailto:adrienn.szabo@sickkids.ca); [liqun.sun@sickkids.ca](mailto:liqun.sun@sickkids.ca)

M. Seed (✉)  
Division of Pediatric Cardiology, Department of Pediatrics, The  
Hospital for Sick Children, University of Toronto,  
Toronto, ON, Canada

Department of Diagnostic Imaging, The Hospital for Sick  
Children, University of Toronto, Toronto, ON, Canada  
e-mail: [mike.seed@sickkids.ca](mailto:mike.seed@sickkids.ca)

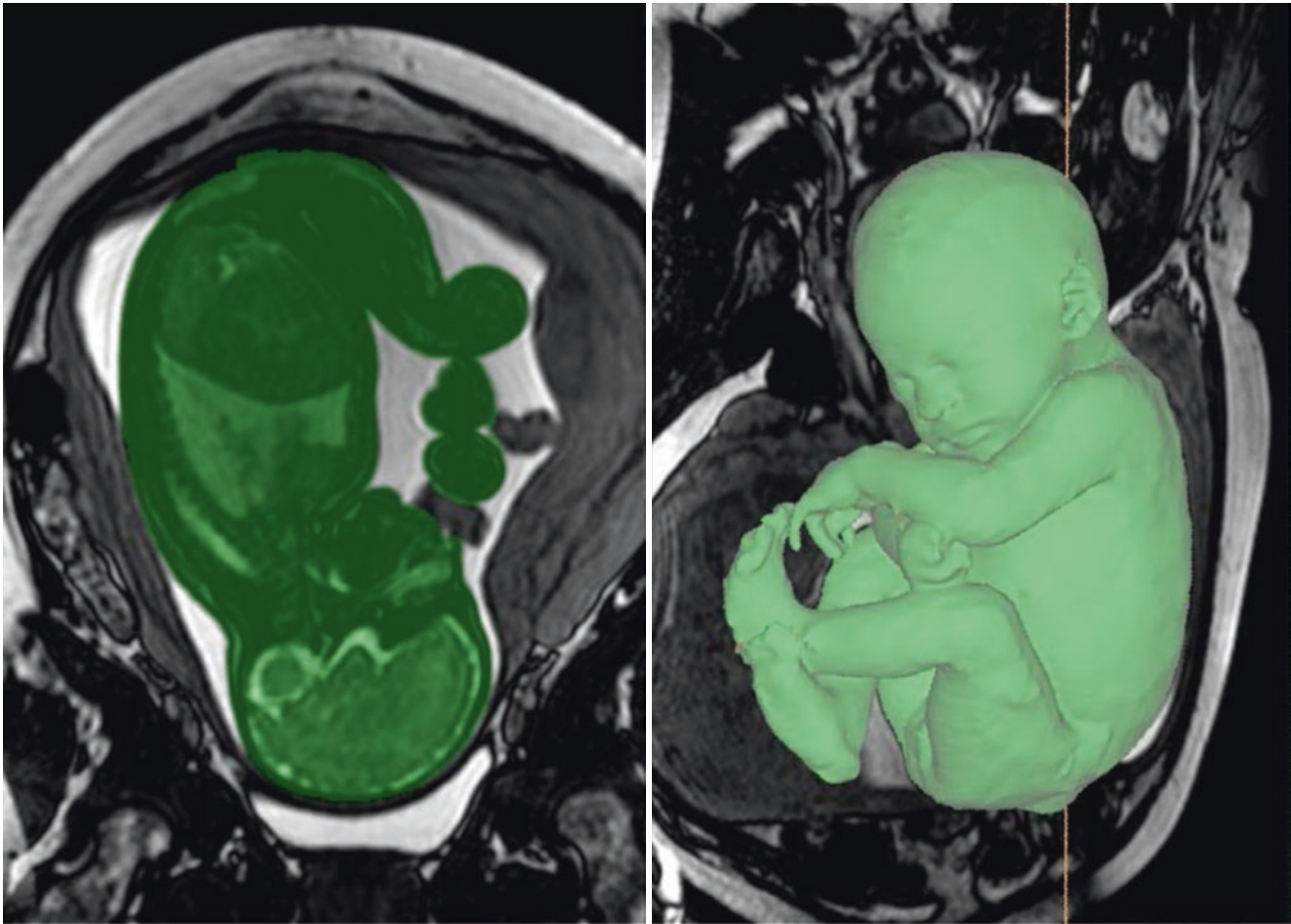


**Fig. 21.1** Sagittal view and 3D reconstruction image of a fetus at 36 weeks gestation by magnetic resonance imaging

## 21.2 Physics and Techniques

### 21.2.1 Challenges of Fetal CMR

Unlike in postnatal cardiac MRI, which utilizes the electrocardiographic (ECG) signal to synchronize the collection of data across the cardiac cycle, the fetal ECG signal is not readily available in an MRI environment; so fetal CMR requires alternative approaches to ECG gating. In addition, standard postnatal CMR approaches depend on a lack of body movement, while fetal imaging is challenged by unpredictable and frequent fetal movements, as well as maternal respiratory variation. Hence, the development of fetal CMR has required the development of novel approaches to cardiac triggering and the incorporation of approaches to motion correction and accelerated image acquisition [1, 2]. This combination has been particularly effective for imaging the late-gestation fetus, which is larger and relatively restricted in terms of fetal body motion. The inherent trade-off between achieving adequate signal-to-noise ratio and spatial resolution while limiting artifact arising from more vigorous fetal

motion continues to pose a challenge to high-quality fetal CMR earlier in pregnancy, when decision-making about whether to continue a pregnancy usually takes place. Fetal CMR also remains significantly more time-consuming and expensive than ultrasound. However, in late gestation, fetal echocardiography can be hampered by acoustic shadowing from the bony thorax, as well as an adverse fetal lie or oligo-hydramnios. Thus, the two imaging modalities may evolve towards playing complementary roles in optimizing image quality across gestation.

### 21.2.2 An Approach to Imaging the Fetal Cardiovascular System

Several different approaches to imaging the fetal heart with MRI now have been described. The exam should be tailored to the main goal of the study, prioritizing those acquisitions crucial to the specific objective. Despite technological advances, gross fetal movements can still pose a challenge, and these are unpredictable. One approach is to start with a

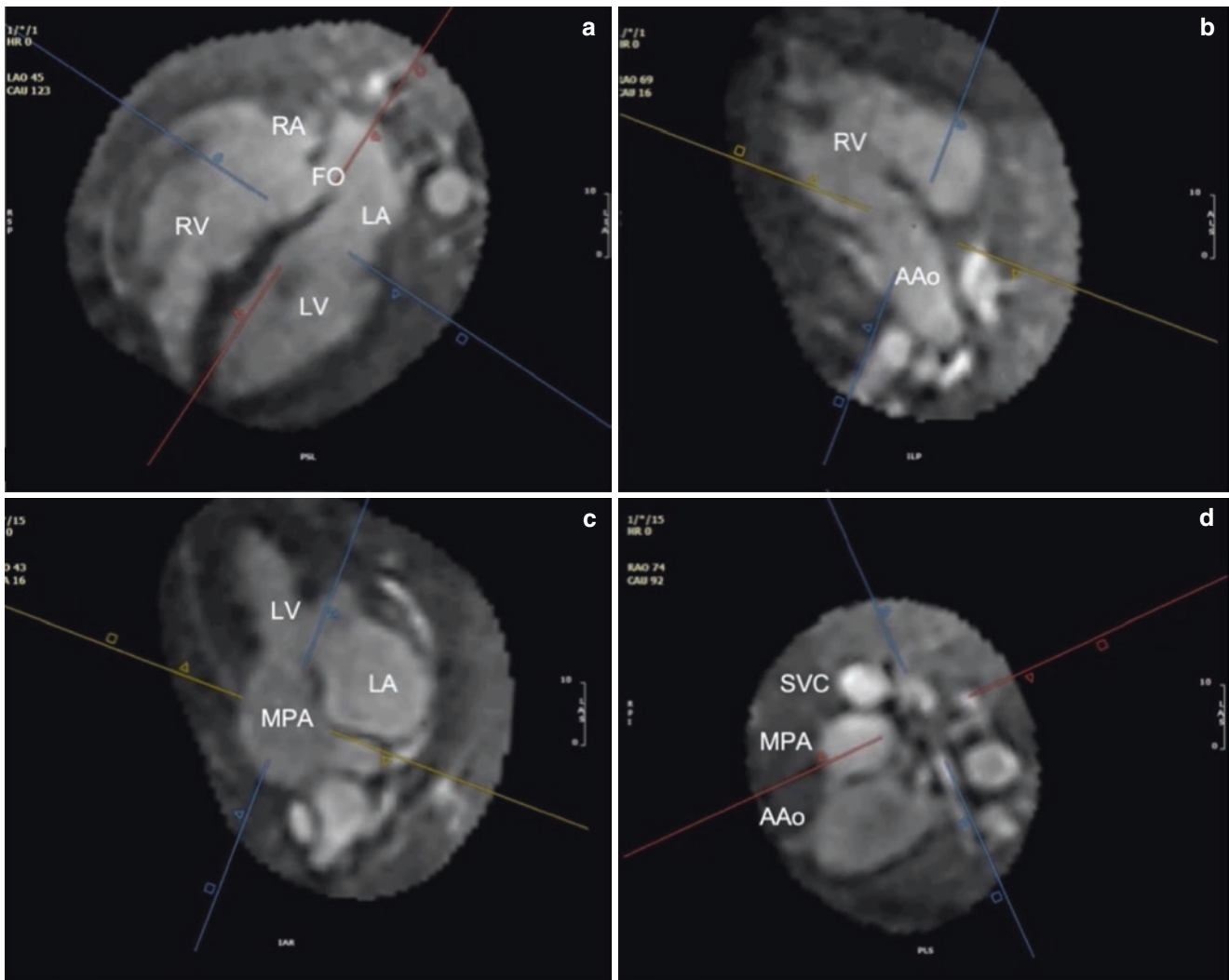


**Fig. 21.2** Cine Stack imaging of a fetus with transposition of great arteries at 36 weeks gestation. (a) typical four-chamber view; (b) right ventricular outflow tract giving rise to the aorta; (c) left ventricular outflow tract with the pulmonary trunk; (d) three vessel view showing the

apparently normal relationship of the great vessels in this rare example of “posterior transposition”. *LA* left atrium, *RA* right atrium, *LV* left ventricle, *RV* right ventricle, *AAo* ascending aorta, *MPA* main pulmonary artery, *SVC* superior vena cava

stack of parallel static steady-state free precession (SSFP) images of the fetal thorax in the three standard orthogonal planes. These can then be used to prescribe the cine phase contrast and oximetry acquisitions if a hemodynamic assessment is required. Segmentation of a 3D-SSFP acquisition covering the entire fetal body allows for the quantification of fetal volume and individual organ volumes. Fetal volume and brain size can be compared with reference data from pre-term and autopsy studies following conversion to fetal and fetal brain weights using previously described conversion factors [3, 4]. If the fetal CMR study has been requested to visualize cardiac anatomy, cine SSFP imaging is likely to be helpful. Motion-compensated cine SSFP of the fetal heart has the advantage of providing excellent images of both intra- and extra-cardiac vascular anatomy and provides an assessment of ventricular function. Using a slice-to-volume

registration algorithm, it is possible to combine stacks of cine SSFP imaging acquired in different planes to provide “four-dimensional” cine imaging that can be reconstructed in any imaging orientation (Fig. 21.2) [5].

### 21.2.3 Triggered Cine Imaging of the Fetal Heart

An artificial cardiac triggering system called **metric-optimized gating (MOG)** was initially proposed in 2010 [6]. MOG involves the acquisition *k*-space data using a synthetic trigger with a longer R-R interval. Hypothetic trigger locations are then retrospectively applied to the data, until an image metric identifies the correct average fetal heart rate that was present during the acquisition by selecting the



reconstruction with the fewest artifacts in the resulting images. The implementation of MOG has allowed cine SSFP imaging of the beating fetal heart and cine phase contrast MRI in fetal vessels [1, 2, 7, 8]. The MOG reconstruction algorithm is available as open-source software for use with one of the commercial vendor MRI systems [9] and its accuracy and reproducibility have also recently been validated by an independent group [10]. The application of compressed sensing to fetal cine imaging results in a dramatic reduction in scan time, providing excellent agreement between the fully sampled and retrospectively undersampled reconstructions of Cartesian data with acceleration factors of up to four [11]. The use of a golden-angle radial acquisition combined with compressed sensing yields acceleration factors up to 16 [11–14]. Fetal data can be acquired using a continuous golden angle radial trajectory with preliminary time-averaged reconstructions for each slice applied to confirm slice prescription and provide an initial assessment of gross fetal movement [11]. Following the MRI examination, offline real-time reconstruction of the data enables assessment and correction of translational in-plane motion and rejection of through-plane motion and calculation of the fetal heart rate using MOG [6, 9, 11, 15]. The motion and gating information are then used to reconstruct high-resolution cine imaging [11]. Real-time and cine reconstructions of the data rely on compressed sensing to suppress streaking artifacts from radial undersampling and provide acceleration factors of up to 27 and 16, respectively [1, 11]. This approach to accelerated motion-corrected imaging has recently been used to implement cine phase contrast fetal vessel blood flow quantification [16]. The application of compressed sensing to fetal cine imaging results in a dramatic reduction in scan time, providing excellent agreement between the fully sampled and retrospectively undersampled reconstructions of Cartesian data with acceleration factors of up to four [11]. The use of a golden-angle radial acquisition combined with compressed sensing yields acceleration factors up to 16 [11–14]. Fetal data can be acquired using a continuous golden angle radial trajectory with preliminary time-averaged reconstructions for each slice applied to confirm slice prescription and provide an initial assessment of gross fetal movement [11]. Following the MRI examination, offline real-time reconstruction of the data enables assessment and correction of translational in-plane motion and rejection of through-plane motion and calculation of the fetal heart rate using MOG [6, 9, 11, 15]. The motion and gating information are then used to reconstruct high-resolution cine imaging [11]. Real-time and cine reconstructions of the data rely on compressed sensing to suppress streaking artifacts from radial undersampling and provide acceleration factors of up to 27 and 16, respectively [1, 11]. This approach to accelerated motion-corrected imaging has recently been used to implement cine phase contrast fetal vessel blood flow quan-

tification [16]. Using this novel phase contrast MR acquisition scheme with golden-angle radial sampling while continuously updating the velocity encoding, a pipeline similar to the one described above has achieved the first motion-corrected multidimensional flow measurement in the fetus [16]. The integration of data from a stack of multidirectional cine phase contrast acquisitions has also allowed for volumetric flow visualization using particle tracking approaches like those obtained using conventional 4D-flow acquisitions to visualize complex human fetal intracardiac flow dynamics, including fetal streaming [17, 18], shown in Fig. 21.3.

#### 21.2.4 Ultrasound-Triggered Fetal Cardiac MRI

Based on the cardiotocographic monitoring commonly used by obstetricians in clinical practice, an alternative technology for obtaining triggered fetal CMR acquisitions involves measurement of the fetal cardiac cycle using Doppler ultrasound via an MR-compatible transducer placed over the maternal abdomen [20]. This portable Doppler Ultrasound Gating (DUS) device has proven to be safe, MRI-compatible, and reliable for different field strengths when applied in human fetuses [21, 22]. The device monitors physiologic motion associated with the fetal cardiac cycle, such as blood flow and cardiac contraction, based on a Doppler waveform. Triggers derived from this waveform are supplied to the MRI scanner to synchronize data acquisition. A practical benefit of this approach is the ability to use established cardiovascular protocols for fetal imaging, which provide immediate in-line image reconstructions to support clinical work. Such devices may also facilitate studies that require prospective triggering, for example, in applications such as triggered T1 or T2 mapping [1]. Dynamic fetal cardiac MRI using cardiotocographic gating allows evaluation of cardiac anatomy in fetuses with CHD, yielding good agreement with fetal echocardiography in terms of the dimensions of structures and cardiac diagnosis [23].

#### 21.2.5 Magnetic Resonance Oximetry

The sensitivity of the MRI signal to the oxygenation of blood underpins one of the unique facets of fetal CMR. Magnetic resonance oximetry relies on the magnetic susceptibility of hemoglobin varying depending on its oxygenation state. T1 and T2 relaxation times of blood are a function of both its hemoglobin concentration (hematocrit) and the fraction of hemoglobin binding sites that are oxygenated. The T2 of blood is primarily determined by its oxygen saturation, although this relationship is dependent also on magnetic field strength and hemoglobin concentration, with increases in hematocrit resulting in a T2 shortening effect [24, 25]. By

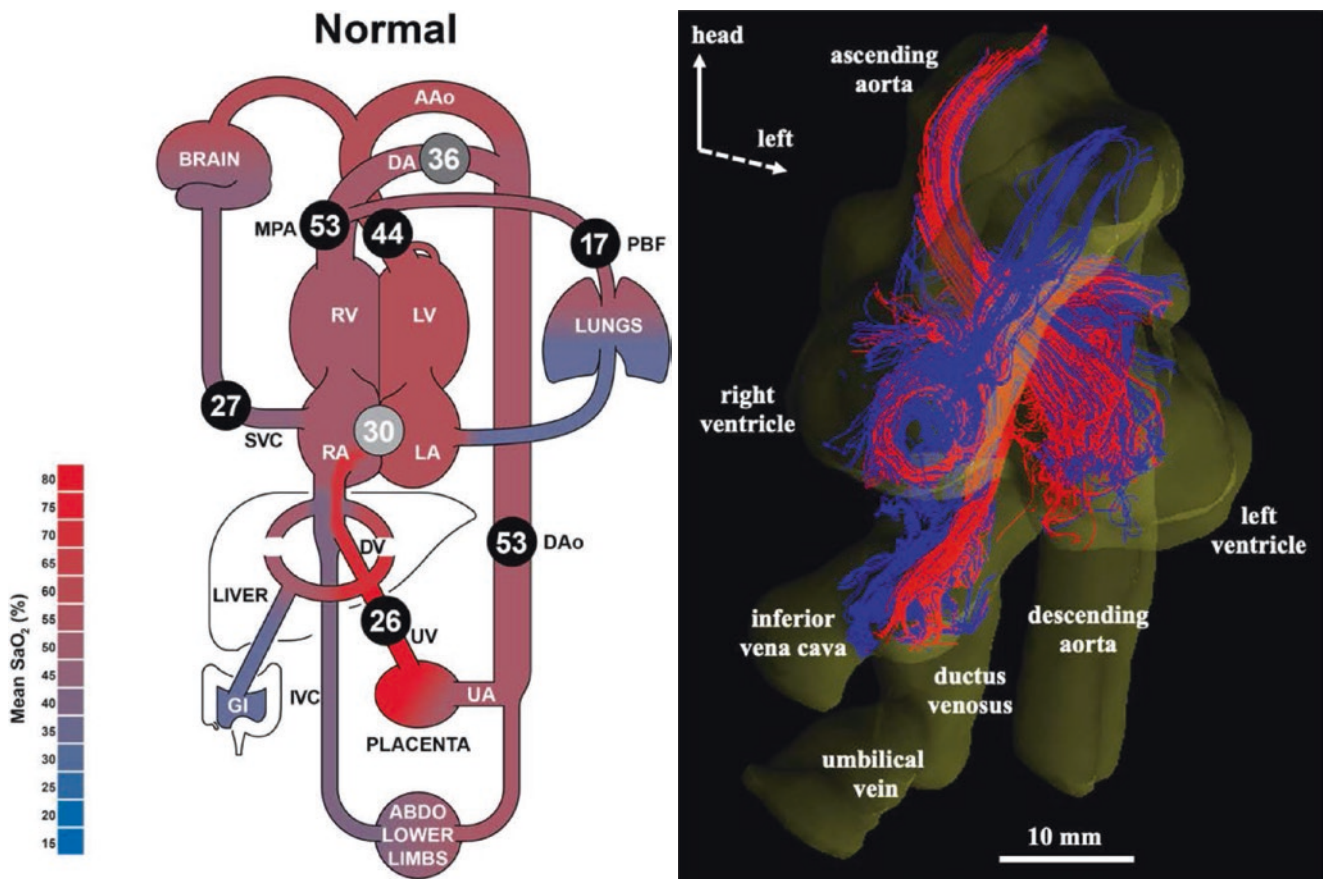


**Fig. 21.3** LEFT: Oxygen transport in the normal human fetus based on Phase Contrast MR and MRI Oximetry model [19]. Blood distribution percentages are indicated by the circled numbers, while oxygen saturations are by color coding, confirming higher oxygen saturations in the left heart than in the right. (Figure with permission from John Wiley & Sons). RIGHT: 4D flow acquisition of fetal streaming in a human fetal heart [18], CC by 4.0. The streaming of well-oxygenated blood (color-

coded as red) from the ductus venosus across the foramen ovale is responsible for higher oxygen saturations in the left heart compared to the right. *UV* umbilical vein, *DV* ductus venosus, *IVC* inferior vena cava, *SVC* superior vena cava, *RA* right atrium, *LA* left atrium, *RV* right ventricle, *LV* left ventricle, *MPA* main pulmonary artery, *DA* ductus arteriosus, *AAo* ascending aorta, *DAo* descending aorta, *PBF* pulmonary blood flow

contrast, the T1 of blood is more strongly related to hematocrit, with higher hematocrit associated with a shortening of T1, although this relationship is also influenced by oxygen saturation. Using cubic polynomial equations, the non-invasive calculation of both oxygen saturation and hematocrit of blood within a specific vessel is possible if the T1 and T2 values are known [25]. T1 and T2 mapping sequences like those used for myocardial T1 and T2 quantification can be used to measure the T1 and T2 of blood in fetal vessels. T1 mapping is based on a standard MOLLI sequence while T2 mapping uses a T2 preparation acquisition. The imaging can be triggered using an artificial gating signal programmed into the scanner with an R-R interval corresponding to the estimated fetal heart rate. Given the relatively long T2 of well-oxygenated blood, the T2 quantification of flowing blood is optimized when an appropriately long echo time (~200 ms) is used for the final T2 preparation acquisition. A short refocusing interval for the T2 preparation helps to minimize artifacts arising from dephasing resulting from turbulent flow [25].

Established criteria regarding the use of MR oximetry in small vessels define the requisite spatial resolution and slice thickness in relation to vessel size and limit the application of this approach to the larger fetal vessels [26]. Open-source software can be used to measure vessels T1 and T2 and convert them into hematocrits and oxygen saturations [27, 28]. The combination of fetal vessel MR oximetry and flow quantification provides a unique non-invasive approach to assessing the hemodynamics of the placental and fetal circulations, an example of which is shown in Fig. 21.4. The Fick principle states that the total uptake of a substance by the tissues is equal to the product of the blood flow to the tissues and the arterio-venous difference in the concentration of the substance. The Fick principle is generally applied to oxygen consumption, whereby blood oxygen content (CaO<sub>2</sub>) is the product of oxygen saturation (SaO<sub>2</sub>) and hemoglobin (Hb) concentration:

$$\text{CaO}_2 = \text{SaO}_2 \times \text{Hb} \times 1.36$$

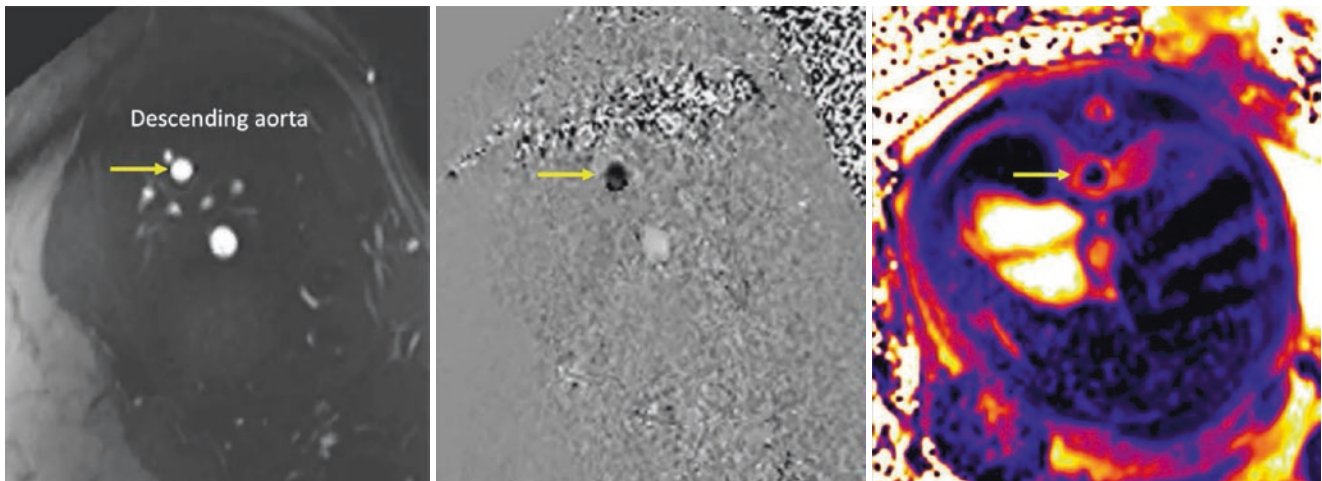


**Fig. 21.4** Descending aortic flow on cine phase contrast MRI and T2 mapping in the descending aorta of a late gestation sheep fetus

where 1.36 is the number of milliliters of oxygen bound to 1 g of hemoglobin at 1 atmosphere [14, 15]. This calculation ignores the contribution to oxygen content of oxygen dissolved in plasma, which is negligible in the fetus [29]. The combination of MRI oximetry with PC-MRI flow quantification allows for the assessment of oxygen transport across the

fetal circulation. Using the Fick principle, oxygen content in the umbilical vein and descending aorta and umbilical vein flow can be used to calculate fetal oxygen delivery ( $DO_2$ ) and consumption ( $VO_2$ ) as follows:

$$\text{Fetal } DO_2 = \text{UV flow} \times \text{UV SaO}_2 \times 1.36 \times \text{Hb} / 100$$

---


$$\text{Fetal } VO_2 = \text{UV flow} \times (\text{UV SaO}_2 - \text{DAO SaO}_2) \times 1.36 \times \text{Hb} / 100$$


---

Assuming the major contribution to blood flow in the superior vena cava is venous return from the cerebral circulation, this approach also allows for an approximation of fetal cerebral flow. Therefore, the product of the blood flow to the brain and the oxygen content of the blood in the aortic arch reflects brain oxygen delivery ( $cDO_2$ ), while the product of

cerebral blood flow and the difference in oxygen content between the aortic arch and superior vena cava provides an estimation of cerebral oxygen consumption ( $cVO_2$ ):

$$cDO_2 = \text{SVC flow} \times \text{AAO SaO}_2 \times 1.36 \times \text{Hb} / 100$$

---


$$cVO_2 = \text{SVC flow} \times (\text{AAO SaO}_2 - \text{SVC SaO}_2) \times 1.36 \times \text{Hb} / 100$$


---

### 21.3 The Normal Fetal Circulation

Our modern understanding of fetal circulatory physiology is largely based on experiments performed in fetal sheep more than 50 years ago. Adopting techniques pioneered by Sir Joseph Barcroft and Sir Geoffrey Dawes, Abraham Rudolph, and his team defined the distribution of blood flow across the fetal sheep circulation by injecting microspheres labeled with various radioactive tracers into different venous compartments of an exteriorized fetal lamb and then measuring

the activity of each tracer in the end-organs supplied by the different arterial branches of the fetal circulation. Rudolph combined these results with sheep catheter and oximetry and pressure measurements made across the fetal circulation to provide a comprehensive picture of fetal hemodynamics and subsequently estimated the distribution of the fetal circulation in humans based on fetal ultrasound data. The fetal circulation differs from the postnatal circulation in relying on the placenta rather than the lungs for gas exchange. Shunts at the ductus venosus (DV), foramen ovale, and ductus arterio-



sus allow blood returning from the placenta to bypass the liver and lungs, providing a pathway for well-oxygenated blood to reach the most metabolically active organs in the developing fetus: the heart and brain. Meanwhile, more deoxygenated blood returning from the lower body and superior vena cava is streamed towards the right ventricle, which directs it to lungs, lower body, and placenta. Thus, the fetal circulation operates in parallel with the right ventricle providing a greater contribution to the combined ventricular output (CVO) than the left, with shunts at the DV, foramen ovale, and ductus arteriosus allowing the umbilical venous return to bypass the liver and lungs resulting in diminished pulmonary blood flow and providing a pathway for the streaming of oxygenated blood towards the ascending aorta (AAo).

Fetal CMR has been applied in the normal late gestation to reveal the cardiovascular physiology of the human fetal circulation is similar to that demonstrated in fetal sheep using invasive techniques [2, 30]. Using cine phase contrast acquisitions in the major vessels of a group of normal control human pregnancies, it has been shown that the right ventricle provides the greater contribution to the CVO, although the difference between the outputs of the ventricles is more modest than in sheep, whereas pulmonary blood flow is higher in the human [17]. By contrast, umbilical flow is significantly lower in the human fetus, presumably reflecting the higher hemoglobin concentration present in the human fetus, which provides comparable fetal oxygen delivery for less flow. Streaming is also present in the human fetal circulation, resulting in oxygen saturations almost 20% higher in the AAo than the main pulmonary artery (MPA) [17, 18].

---

## 21.4 Fetal Circulation in the Context of Congenital Heart Disease

Fetal CMR has provided an opportunity to investigate many of the predictions that have been made based on what was already known from animal models about the effects of CHD on circulatory physiology [31]. For example, fetal CMR has confirmed that obstructions to right or left ventricular inflow or outflow flow are associated with dramatic redistribution of the fetal circulation. Unless there is a ventricular septal defect or atrioventricular valve regurgitation, the reductions in flow seen across the obstructed side of the heart in these malformations are then typically associated with underdevelopment of the ventricular structures and vessels on that side. In addition, fetal CMR studies have demonstrated the expected fetal circulatory adaptations to obstructed flow that allow perfusion of the upper extremities and brain via retrograde flow in the aortic arch in the setting of left heart obstruction, and retrograde ductus arteriosus flow to supply the lungs in fetuses

with right heart obstruction. These findings are in keeping with prior human ultrasound data indicating that the CVO of hearts with single ventricle physiology is reduced. Reductions in CVO are associated with reductions in the perfusion of the various organs supplied by the fetal heart. Seemingly, the first organ to be affected is the placenta, which receives 7% less flow in fetuses with hypoplastic left heart, 33% less flow in fetuses with Ebstein anomaly (EA), and 42% less flow in fetuses with tricuspid atresia. It is interesting to consider whether the underdeveloped villous vasculature reported in fetuses with hypoplastic left heart could be the result of umbilical under-perfusion secondary to impaired CVO [32]. With more severe reductions in CVO, we have observed reductions in systemic and pulmonary blood flow. Cerebral blood flow seems to be preserved at the cost of other organ systems in the setting of single ventricle CHD. However, in those fetuses with the most profound reductions in CVO, even cerebral blood flow is diminished. In our experience, the only fetuses to be affected in this way are those with severe forms of EA, in which we have observed an average reduction in cerebral blood flow of 34%. Interestingly, although those fetuses with EA with circular shunts resulting from pulmonary and tricuspid regurgitation and retrograde flow in the ductus arteriosus demonstrate a CVO approaching normal, these fetuses exhibit more severely compromised systemic blood flow than any other type of congenital cardiac malformation, with reductions in cerebral blood flow of approximately 50%. This failure of fetal cerebral autoregulation presumably reflects a combination of low systemic blood flow with hypotension and elevated central venous pressure relating to this highly inefficient circulation characterized by complete failure of the right ventricle. Reductions in cerebral blood flow may account for the dramatic decrements in brain size that we have observed in fetuses with EA, which are typically one standard deviation below the mean in fetuses with EA without circular shunting and more than two standard deviations below the mean in fetuses with circular shunting [33, 34]. The reductions in pulmonary blood flow (and lung volume) seen in fetuses with EA may also account for the poor pulmonary artery development that is typical of these newborns. Hypoplasia of the pulmonary arteries and elevated pulmonary vascular resistance complicate the management of newborns with EA, in whom the primary aim of management is to reduce right ventricular afterload to help establish normal saturations and a biventricular circulation. The profound hemodynamic compromise and evidence of its impact on end-organ development in fetuses with severe forms of EA support further investigation of fetal pharmacologic interventions aimed at stabilizing the fetal circulation such as the administration of maternal non-steroidal inflammatory drugs to effect ductus arteriosus constriction, thus limiting circular shunting [33].



## 21.5 Fetal Streaming in the Context of Congenital Heart Disease

The impact of many congenital cardiac malformations on fetal streaming has been the subject of considerable interest [7, 31, 35]. Fetal CMR has provided a unique opportunity to study this fascinating mechanism, whereby blood rich in oxygen and nutrients returning from the placenta via the umbilical vein is preferentially directed towards the coronary and cerebral circulations via the DV and foramen ovale [36–38]. Magnetic resonance oximetry also provides us with a unique opportunity to study the impact of the disruption of fetal streaming resulting from the abnormal anatomical connections and obstructions of blood flow that are present in many forms of CHD on fetal oxygen transport. As predicted, the interruption of fetal streaming results in reductions in the oxygen saturations of the blood supplied to the AAO. Figure 21.5 shows the different hemodynamic mechanisms leading to this desaturation of the blood provided to the developing brain and heart compared with normal controls. In transposition of the great arteries (TGA), fetal streaming results in well-oxygenated reaching the left atrium in the normal way. However, because of the discordant ventriculoarterial connections, this blood is now supplied to the pulmonary circulation and descending aorta, while the more deoxygenated blood (which is also likely to be depleted of other metabolic substrates including glucose) that passes into the right ventricle is directed to the brain and heart. In TGA we therefore observe a reversal of the normal gradient in  $\text{SaO}_2$  between the AAO and MPA, with MPA  $\text{SaO}_2$  an average 6% higher than AAO  $\text{SaO}_2$ , associated with AAO  $\text{SaO}_2$ s that are 15% lower than they are in normal controls. It is interesting to note that amongst newborns with CHD studied at a population level, TGA was the only

form of heart disease that was associated with a reduced head circumference in the setting of normal birthweight, in keeping with the abnormal streaming physiology that has been observed by MRI [19, 39].

Fetal streaming is also profoundly altered in fetuses with single ventricle physiology; indeed, streaming is essentially abolished in any form of congenital cardiac malformation in which there is effectively a single outlet of the heart. This is because the venous return is completely mixed in the heart, thus diluting the well-oxygenated blood from the placenta that is preferentially directed to the AAO when the cardiac anatomy is normal. Failure of streaming is therefore present in all forms of cyanotic CHD, resulting in reductions in AAO  $\text{SaO}_2$ . However, the typical reductions in AAO  $\text{SaO}_2$  seen in fetal CHD are more severe than might be expected based on the disruption of streaming alone. This is because diminished umbilical blood flow and impaired placental gas exchange further contribute to the desaturation resulting from failure of streaming. It has been suggested that the interruption of fetal streaming resulting from congenital cardiac malformations might result in increased pulmonary blood flow in some situations [31]. However, MRI measurements of pulmonary blood flow in fetuses with CHD do not confirm this hypothesis. This may be because any pulmonary vasodilatory effect anticipated as a result of more oxygen reaching the pulmonary arteries due to the failure of streaming is usually offset by reductions in fetal oxygen saturations resulting from placental dysfunction and diminished umbilical blood flow. Indeed, magnetic resonance oximetry made in fetuses with CHD has revealed that MPA  $\text{SaO}_2$  is lower than in control fetuses except in fetuses with TGA, in which MPA  $\text{SaO}_2$  is slightly higher than normal, accounting for a 15% increase in pulmonary blood flow compared with controls.

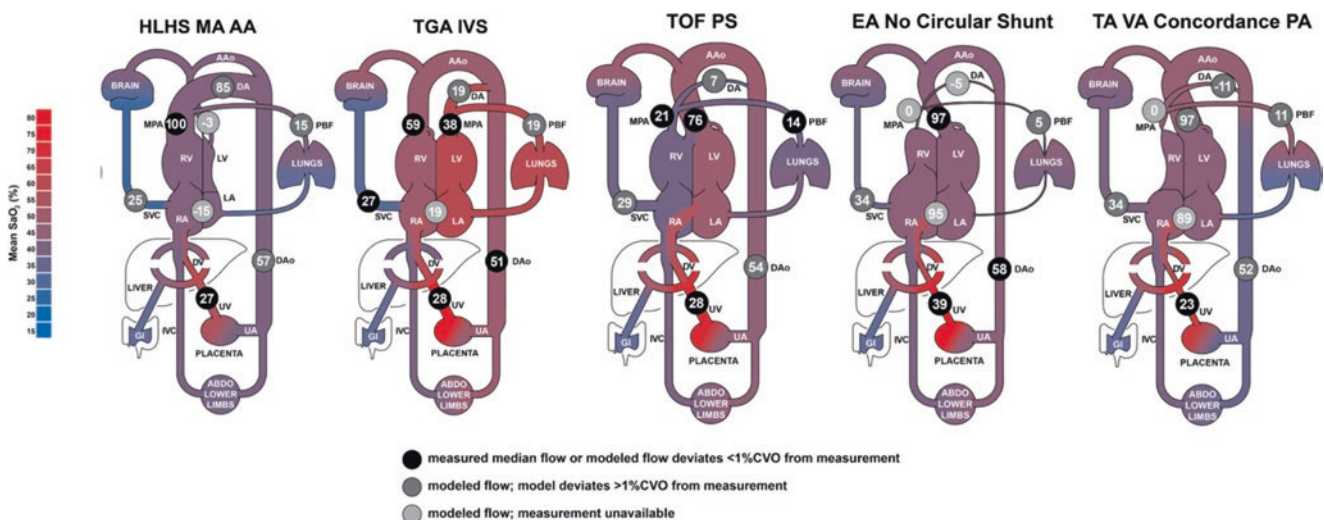


**Fig. 21.5** Fetal blood flow distribution and oxygen saturations in complex congenital heart diseases [19]. Numbers in circles represent flows as percentages of the combined ventricular output, oximetry is indicated by color coding. (Figure with permission from John Wiley & Sons)

## 21.6 Fetal Cerebrovascular Physiology and Neurodevelopment in CHD

Experiments performed in animal models have revealed that exposure to acute hypoxemia induces a robust cerebral vasodilatory response that protects the brain's supply of oxygen [40]. This adaptation is achieved through cerebral arterial smooth muscle relaxation that is mediated by the action of adenosine produced in the cerebral parenchyma, as well as by other local pathways. The fetal cerebral vasodilatory response to hypoxia has been identified in human fetuses with placental insufficiency and is commonly referred to as "brain-sparing physiology" [41]. The detection of reductions in middle cerebral artery pulsatility in fetuses with CHD is in keeping with a similar brain-sparing effect [42]. In fetal CMR studies, measurements of superior vena caval flow are increased in fetuses with TGA compared with normal controls and other CHD fetuses. We have suggested that superior vena caval flow measured by phase contrast MRI in the late gestation fetus may represent a reasonable surrogate for cerebral blood flow [19], based on prior estimates that cerebral blood flow comprises the majority of superior vena caval flow in infants [43]. Fetal CMR has revealed dramatic increases in superior vena caval flow in hypoxemic fetuses with placental insufficiency [44]. It is possible that the increases in cerebral blood

flow that might be anticipated in other forms of CHD in which there is cerebral hypoxemia may be dampened by reductions in CVO. Furthermore, it is interesting to note that the profound cerebral vasodilatation that results in acute "brain-sparing physiology" appears to recede in the setting of chronic fetal hypoxemia, whereby the longer-term impact of cerebral adenosine production is the downregulation of cerebral metabolism. A large body of *in vitro* work implicates the role of hypoxia-inducible factor (HIF) in regulating protein synthesis and cell cycling in response to reductions in the cellular supply of oxygen, while fetal mice engineered to overexpress HIF exhibit Wnt signaling mediated hypomyelination that is typical of newborns with CHD [45, 46]. Similarly, a swine model of perinatal hypoxia exhibits diminished populations of neural stem cells and simplified cortical folding that are also present in newborns with CHD [47].

The demonstration of reductions in fetal brain oxygenation and associated impairment of prenatal brain growth in fetuses with CHD by MRI supports the concept that fetal circulatory disturbances resulting from the heart disease may have a role in the adverse neurodevelopmental outcomes experienced by children with CHD [7]. In fetuses with EA, fetal MRI has revealed how the severity of the impairment of prenatal brain growth is closely linked with the severity of the heart disease (Fig. 21.6), and is associated with neurode-

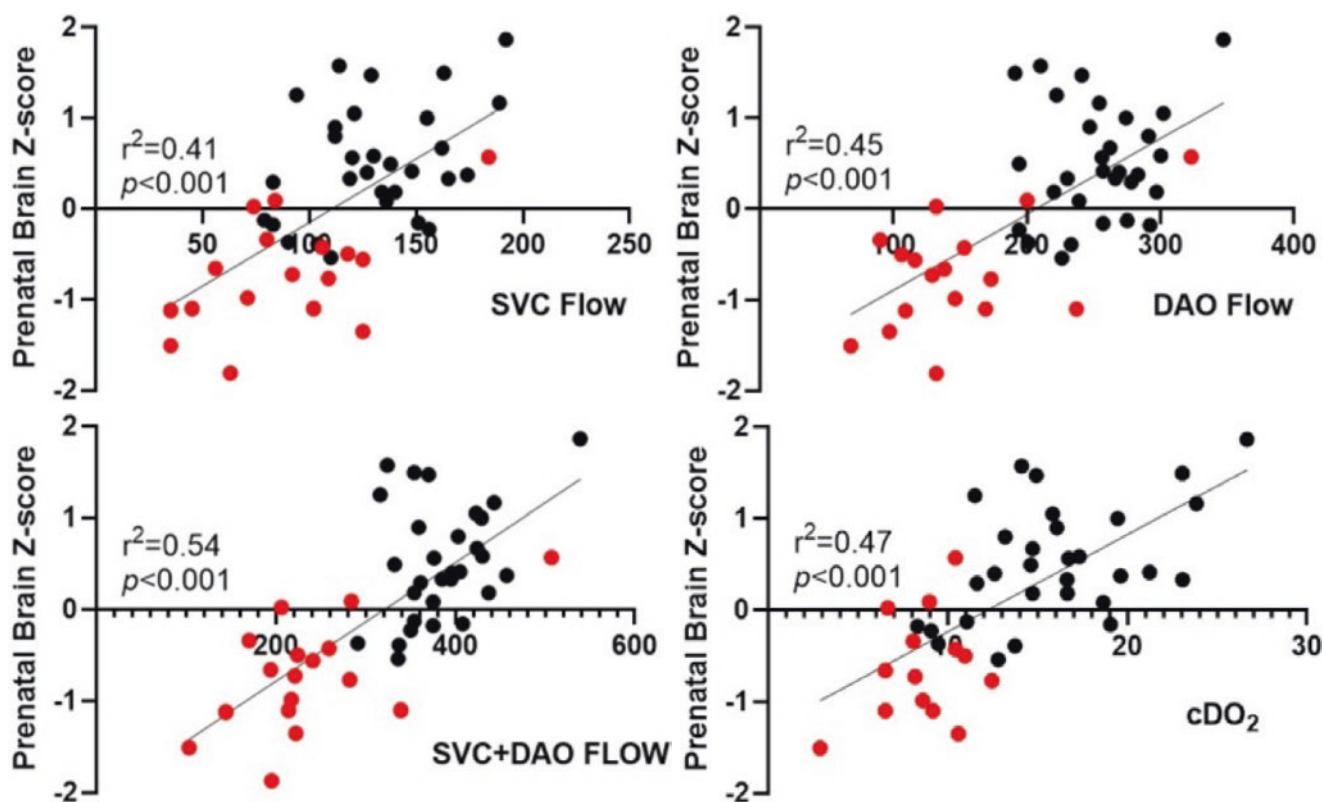


**Fig. 21.6** Correlations between prenatal brain weight z-score and superior vena cava flow, descending aorta flow, cerebral oxygen delivery, and peripheral perfusion in normal fetuses (black) vs. in fetuses with Ebstein anomaly/tricuspid valve dysplasia (red) [34]. With permis-

sion from Cambridge University Press. *SVC* superior vena cava, *DAO* descending aorta, *SVC + DAO* peripheral perfusion, *cDO<sub>2</sub>* cerebral oxygen delivery

velopmental outcomes at 18 months [34]. Thus, fetal interventions that improve cerebral perfusion and oxygenation have the potential to improve neurodevelopmental outcomes in the setting of CHD. However, it has been suggested that impaired cerebral glucose delivery resulting from the same disruption of normal fetal circulatory physiology that results in cerebral hypoxemia may be more significant than any reduction in the oxygen content of the blood supplied to the fetal brain [48]. Ultimately, realistic animal models of CHD are likely to be crucially important in the elucidation of the mechanisms leading to the reduced brain size and immature grey and white matter maturation that is a feature of newborns with cyanotic CHD [49, 50]. A mouse model of hypoplastic left heart syndrome induced by *in utero* embolization of the left atrium represents one promising avenue of investigation in this respect [51].

## 21.7 Diagnosis and Prognosis in CHD

The potential of fetal CMR to enhance the accuracy of prenatal diagnosis in the setting of CHD has been explored by several groups. Lloyd et al. revealed valuable additional

diagnostic information using a novel three-dimensional motion-corrected slice-to-volume black blood CMR technique in 10% of 101 pregnancies affected by fetal CHD [52]. The same group assessed three-dimensional fetal vascular morphology and perfusion using a combination of anatomical and cine phase contrast MRI to investigate the utility of fetal CMR to identify fetuses at risk of aortic coarctation [53], as shown in Fig. 21.6. In this study, the fetal CMR performed well for this difficult prenatal diagnosis, with a multivariate logistic regression model including ascending aortic flow and isthmal displacement explaining 78% of the variation in outcome and correctly predicting the need for intervention in 93% of cases (Fig. 21.7). In a study of 31 fetuses with CHD referred for fetal CMR in the setting of inconclusive fetal echocardiography Salehi et al. reported that fetal CMR contributed to patient management and/or parental counseling in 84% of cases [54]. Sun et al. described how fetal CMR was helpful in informing the perinatal management of a patient with tetralogy of Fallot with pulmonary atresia and suspected major aortopulmonary collaterals in the setting of a large congenital diaphragmatic hernia in whom the prenatal ultrasound imaging was very challenging [55].

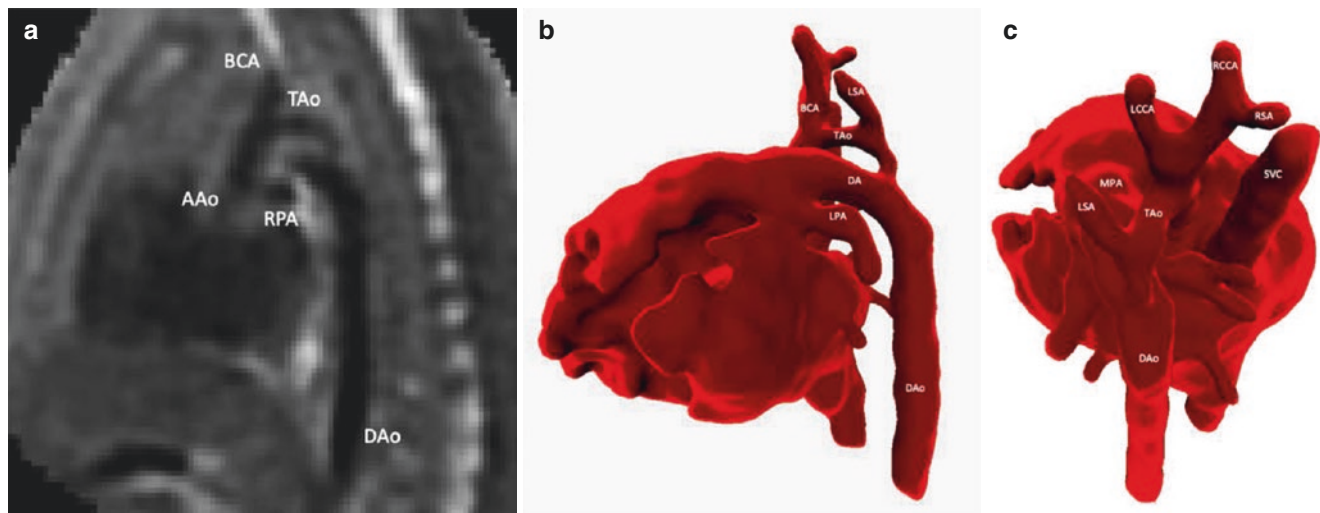


**Fig. 21.7** Fetal CMR imaging with 3D reconstruction in a case of coarctation of the aorta. Fetal heart imaged from a sagittal view (**a**, **b**); and from a posterior-superior position (**c**). *AAo* ascending aorta, *DAo* Descending aorta, *TAo* distal transverse aortic arch, *BCA* brachiocephalic artery, *LCCA* left common carotid artery, *RCCA* right common

carotid artery, *RSA* right subclavian artery, *LSA* left subclavian artery, *DA* ductus arteriosus, *MPA* main pulmonary artery, *LPA* left pulmonary artery, *RPA* right pulmonary artery, *SVC* superior vena cava. (Images are courtesy of Dr. David Lloyd and Dr. Milou van Poppel)



## 21.8 Other Utilities of Fetal CMR

### 21.8.1 The Assessment of Placental Function

Techniques developed for assessing the distribution of blood flow and oxygen transport across the fetal circulation have been applied to the assessment of placental function. MRI measurements of blood flow, hematocrit, and oxygen saturation in the uterine, umbilical arteries, and veins provide an “input and output” model of placental oxygen transfer that constitutes a novel “placental function test” [56]. In addition to the quantification of fetal oxygen delivery and consump-

tion, this approach quantifies uterine blood flow and has provided the first in vivo measurements of human placental oxygen consumption. In a comparison of late gestation human and sheep pregnancies, most of the uterine venous return was observed to pass through the ovarian veins, while human uterine blood flow and oxygen delivery decreased with advancing gestation. Increases in fetal oxygen extraction resulted in preservation of oxygen consumption, as illustrated in Fig. 21.8. This approach requires flow and oxygen content measurements in both uterine and ovarian arteries and veins and in the descending aorta and umbilical vein, as shown in Fig. 21.9.

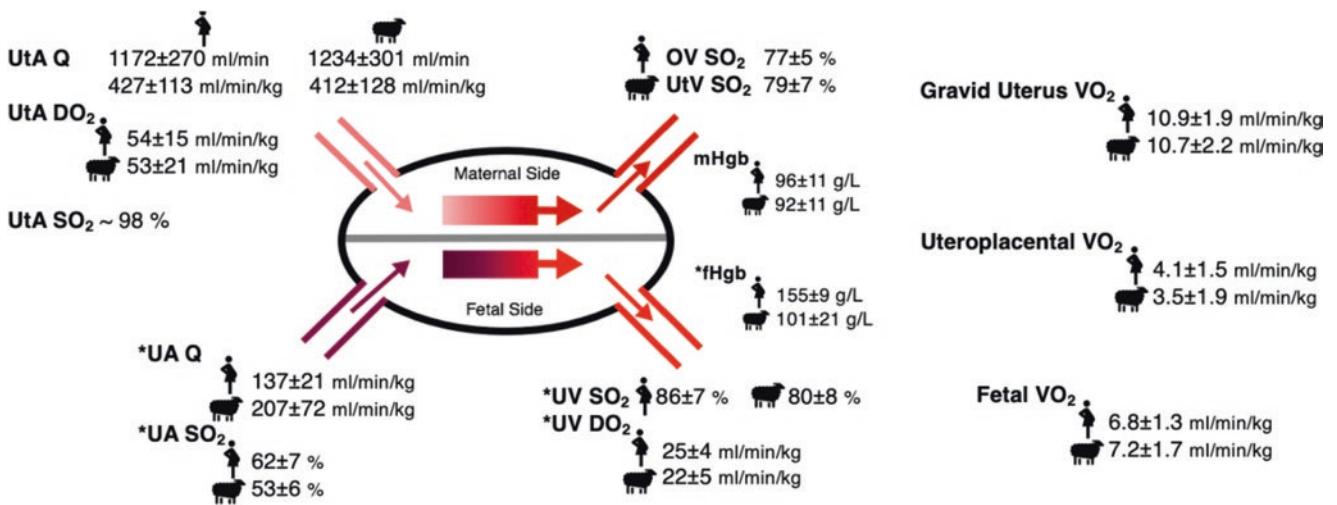


**Fig. 21.8** Placental hemodynamics and oxygen transport and consumption in healthy normal human and sheep pregnant subjects in late gestation [57]. Figure adapted with permission from John Wiley & Sons. *Q* blood flow, *DO<sub>2</sub>* oxygen delivery, *SO<sub>2</sub>* oxygen saturation, *VO<sub>2</sub>*

oxygen consumption, *UtA* uterine artery, *UtV* uterine vein, *OV* ovarian vein, *UA* umbilical artery, *UV* umbilical vein, *Hgb* [hemoglobin], *m* maternal, *f* fetal

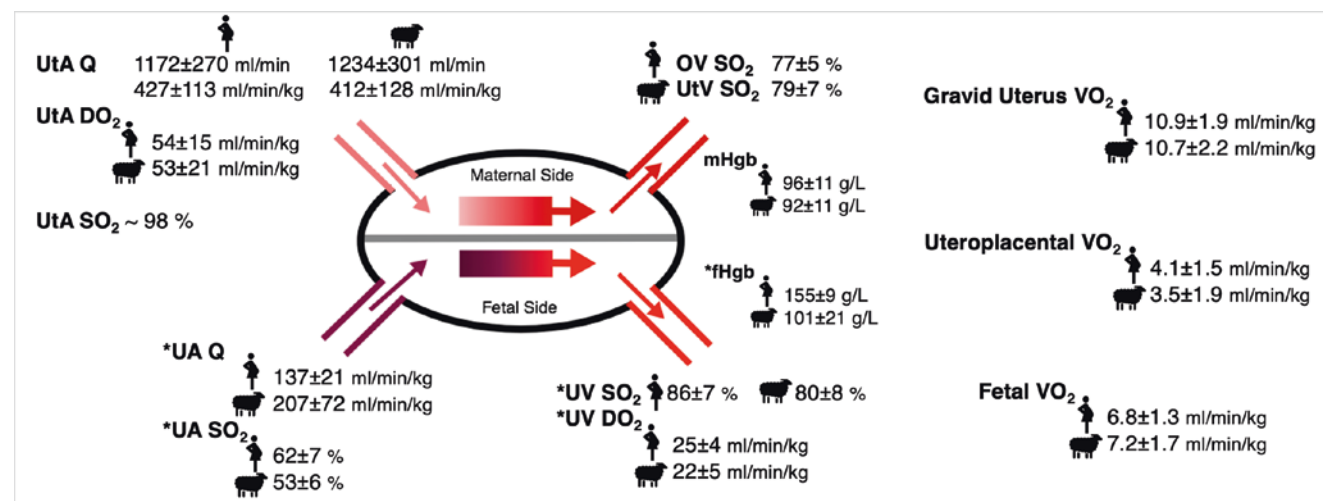


**Fig. 21.9** T2 relaxometry in major fetal and maternal vessel connections to the placenta with T2 recovery curves. *UV* umbilical vein, *LOV* left ovarian vein, *ROV* right ovarian vein, *fDAo* fetal descending aorta, *mDAo* maternal descending aorta



Blood oxygen level-dependent (BOLD) imaging of the placenta represents a somewhat simplified approach to detecting doxyhemoglobin as a biomarker of placental insufficiency and fetal growth restriction, while dynamic contrast-enhanced MRI has been used to quantify placental perfusion in animal models [58], BOLD imaging of the placenta represents a somewhat simplified approach to detecting doxyhemoglobin as a biomarker of placental insufficiency and fetal growth restriction, while dynamic contrast-enhanced MRI has been used to quantify placental perfusion in animal models [59]. Placental BOLD and magnetic resonance spectroscopy have also been used to explore placental function [58–61].

### 21.8.2 Combining Fetal and Placental CMR with Maternal CMR

In a preliminary exploration of the relationships between fetal and placental circulatory physiology and maternal cardiac function and hemodynamics, Ducas et al. performed CMR assessments of the maternal, placental, and fetal circulations in a group of women with pre-existing heart disease in late gestation and at post-pregnancy follow-up (Fig. 21.10). Contrary to our expectations, women with moderate-to-severe valve or myocardial disease generally adapted successfully to the demands of pregnancy, showing a greater increase in cardiac index than their normal counterparts. Placental perfusion and fetal oxygen delivery and growth were normal, even in the setting of Fontan physiology. However, a subset of women with heart disease exhibited a more limited cardiovascular response to pregnancy and were at risk of maternal cardiac complications including heart failure, arrhythmia, hypertension, and preterm birth. It is interesting to consider whether pregnancy may represent a physiologic challenge that may reveal an increased risk of future complications in women with cardiac disease, as it does in pregnant women with normal hearts.

### 21.8.3 Fetal Growth Restriction

Fetal CMR has been used to investigate the hemodynamics of the fetal circulation in the setting of late-onset placental insufficiency [44]. Fetuses exposed to chronic hypoxemia exhibit redistribution of the fetal circulation with diminished umbilical and pulmonary blood flow and increased cerebral blood flow. The results indicate that fetal circulatory “brain-sparing” adaptations tend to preserve cerebral oxygen delivery in the setting of placental insufficiency despite dramatic reductions in overall fetal oxygen delivery, although a subset of growth-restricted fetuses exhibited normally distributed blood flow in keeping with the dampening of brain-sparing physiology in the setting of chronic fetal hypoxia. These fetuses nevertheless exhibited an elevated brain-to-body volume ratio, indicating asymmetrical growth restriction. Despite the presence of asymmetric growth and circulatory adaptations to placental insufficiency, growth-restricted fetuses exhibited smaller brains at birth, which may account for the adverse neurodevelopmental outcomes previously reported following fetal growth restriction.

BOLD imaging of the placenta represents a somewhat simplified approach to detecting doxyhemoglobin as a biomarker of placental insufficiency and fetal growth restriction, while dynamic contrast-enhanced MRI has been used to quantify placental perfusion in animal models [58], BOLD imaging of the placenta represents a somewhat simplified approach to detecting doxyhemoglobin as a biomarker of placental insufficiency and fetal growth restriction, while dynamic contrast-enhanced MRI has been used to quantify placental perfusion in animal models [59]. Placental BOLD and magnetic resonance spectroscopy have also been used to explore placental function 58–61.

### 21.8.4 Placental Function in CHD

The heart and placenta share key developmental pathways and the role of interactions between these two critical organ

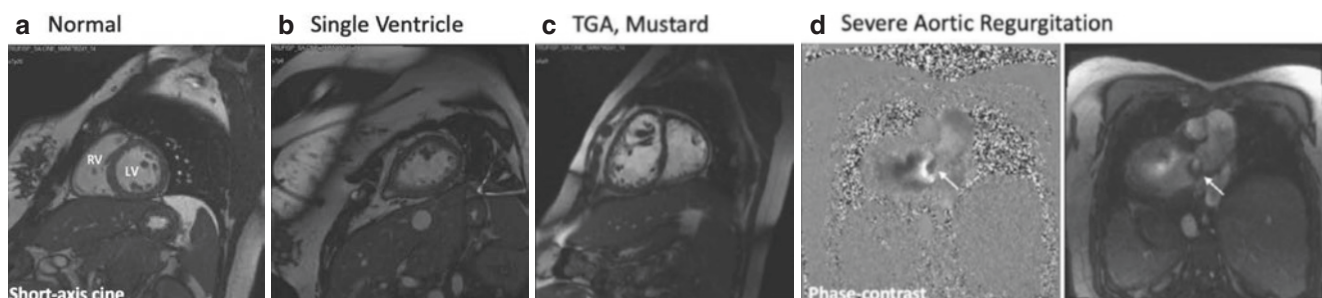


**Fig. 21.10** Maternal cardiac quantitative assessment in the setting of maternal heart disease in late gestation, using cardiovascular MRI. Figure adapted with permission from Elsevier Inc. **(a)** Normal maternal ventricular function. **(b)** Functional assessment of the LV in a pregnant mother with a univentricular heart (tricuspid atresia; Fontan

palliation). **(c)** Bi-ventricular functional assessment in a mother with TGA after Mustard operation with a systemic RV. **(d)** Severe aortic regurgitation measured using a combination of 2D cine phase-contrast and short-axis cine SSFP MRI in a case of maternal bicuspid aortic valve

systems for early human development remains an active field of research [62, 63]. In a cohort of 924,442 liveborn infants including 7569 with CHD, the placentas of newborns with CHD were smaller than controls, with pregnancies affected by fetal tetralogy of Fallot, double outlet right ventricle and major ventricular septal defects the most severely affected [39]. In this study using Danish national registry data, reductions in placental weight were associated with lower birthweight and reductions in neonatal head circumference. Other studies have revealed lower placenta-to-body weight ratios and abnormalities of placental vascular structure including reduced density and maturity of terminal villi, chorangiomas, thrombosis, and infarction in pregnancies affected by fetal CHD [32, 64, 65]. Fetal CMR has revealed reductions in umbilical vein oxygen saturations in pregnancies complicated by a range of fetal cardiac malformations including tetralogy of Fallot and hypoplastic left heart in keeping with subtle placental dysfunction [19].

While the etiology of placental disease in patients with CHD is not yet fully understood, it would now appear to be clear that placental disease plays a role in the fetal growth restriction that is present in all major forms of cyanotic CHD. However, there is likely to be a subtle interplay between fetal cardiovascular function and placental function in the setting of CHD. For example, the diminished umbilical blood flow we found in fetuses with single ventricle physiology associated with reduced CVO further contributed to a reduction in fetal oxygen delivery and therefore fetal oxygen saturations. Thus, the combination of placental and heart disease in the fetus may have an adverse impact on fetal development. For example, moderate-to-severe brain injuries occurred in 55% of CHD pregnancies with abnormal placental histology compared with 11% of those with a normal placenta [64].

### 21.8.5 Percutaneous Fetal Cardiac Interventions

Fetal MRI has an emerging role in the setting of fetal cardiac interventions (FCI). An important example is in the setting of hypoplastic left heart syndrome (HLHS), in which the presence of a severely restrictive or intact interatrial septum confers a significantly more complex clinical course and adverse outcomes [66]. The restrictive atrial communication results in left atrial hypertension, with associated muscularization of the pulmonary veins, hypoplasia of the small pulmonary arteries, and pulmonary lymphangiectasia. In utero decompression of the left atrium by radio-frequency perforation and balloon dilation, with or without stenting, results in more stable hemodynamics in the neonatal period and improved long-term survival [67–

69]. Fetal MRI provides an additional tool for assessing the severity of fetal pulmonary venous obstruction through the identification of pulmonary lymphangiectasia [67, 70]. In pulmonary lymphangiectasia, dilated high-signal lymphatics in the interlobular septa and peri-bronchovascular interstitium result in heterogeneous signal intensity of the fetal lungs on single-shot T2-weighted fast spin echo [71]. These findings may be accompanied by pleural effusions (chylothoraces) and have been referred to as “nutmeg lung” [72]. Fetal CMR measurements made before and after *in utero* atrial septostomy ± atrial stenting reveal improvements in the low pulmonary blood flow that is characteristic of obstructed pulmonary venous drainage. Follow-up fetal MRI after atrial septostomy also reveals an improvement in the appearance of the lung parenchyma, as shown in Fig. 21.11. T2 weighted fast spin echo detects changes suggestive of pulmonary lymphangiectasia as early as 26 weeks gestation, and the findings are consistent with postnatal lung biopsy, which is the gold-standard approach to diagnosing pulmonary lymphangiectasia [67, 70, 73]. While relief of pulmonary venous hypertension during fetal life results in improved hemodynamics in the neonatal period, we have experienced ongoing problems with the pulmonary circulation following initial surgery, including pulmonary vein stenosis and underdevelopment of the pulmonary arteries [74–76].

Fetal CMR has also been used to aid decision-making in the setting of TGA with intact intraventricular septum with a highly restrictive or intact atrial septum. Although atrial septal restriction is a rare complication of fetal transposition, these patients are at high risk of profound cyanosis at birth,

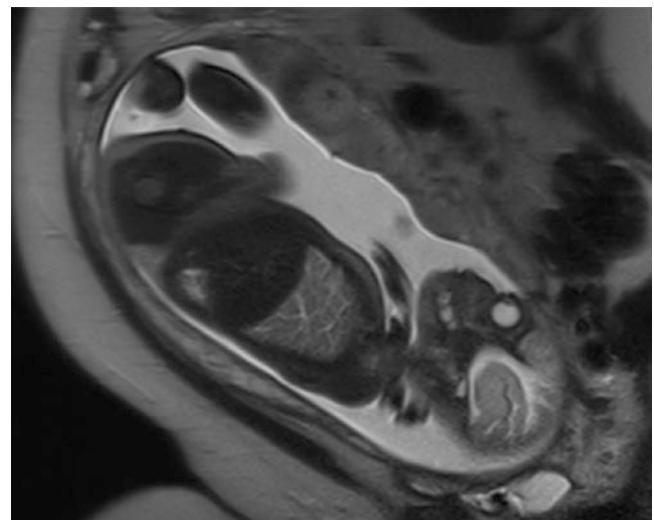


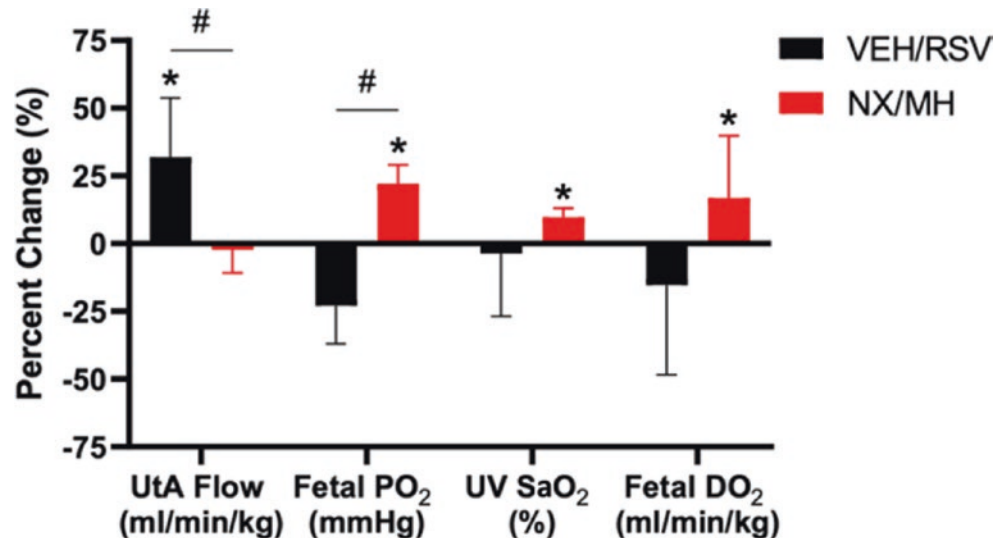
**Fig. 21.11** Fetus with HLHS and highly restrictive atrial septum at 26 weeks gestation. Severe lung lymphangiectasia with markedly heterogeneous lung signal with high signal tubular structures in the lungs on T2 weighted fast spin echo

which may result in hypoxic-ischemic brain injury, or even neonatal death if a balloon atrial septostomy cannot be undertaken in a timely manner [77]. In one case of transposition with a restrictive atrial septum cared for at the Hospital for Sick Children, *in utero* balloon atrial septostomy was performed at 36 weeks gestation [78]. In a second case, fetal CMR confirmed an improvement in atrial level shunting following atrial septostomy. While the pre-procedural oximetry indicated an unusual situation in which oxygen saturations were higher in the right heart than the left, following the septostomy this gradient resolved [55].

### 21.8.6 NSAID Therapy in the Management of a Circular Shunt

In the most profound forms of tricuspid valve dysplasia or EA, the severity of tricuspid regurgitation renders the right ventricle incapable of generating adequate pressure to open the pulmonary valve and produce forward flow into the MPA and the ductus arteriosus. This results in retrograde filling of the pulmonary arteries from the aorta via the ductus arteriosus. In fetuses that also develop pulmonary regurgitation a circular shunt is set up whereby retrograde ductal flow steals blood from the aorta, passing backwards through the right ventricle and tricuspid valve and ultimately flowing back across the foramen ovale and into the left heart and systemic circulation. This results in a life-threatening hemodynamic situation with decreased systemic blood supply and cerebral perfusion [79, 80]. The maternal administration of non-steroidal anti-inflammatory drugs (NSAIDs) has a constricting effect on the ductus arteriosus and stabilizes the circulation in the setting of a circular shunt. Fetal CMR has revealed that while circular shunting has a profound impact on systemic perfusion in fetuses with EA or tricuspid valve dysplasia, this is improved following the administration of NSAIDs [33].

**Fig. 21.12** Percentage changes in UtA flow, UV  $SO_2$ , and fetal  $DO_2$  following the administration of the uterine vasodilator resveratrol and maternal hyperoxygenation. *VEH* vehicle oxygen, *RSV* resveratrol, *NX* normoxic, *MH* maternal hyperoxygenation, *UtA* uterine artery,  $PO_2$  partial pressure of oxygen,  $SaO_2$  oxygen saturation,  $DO_2$  oxygen delivery



### 21.8.7 Fetal Anemia

Fetal anemia resulting from alloimmunization, inherited hemoglobinopathies or parvovirus infection is a critical condition leading to tissue hypoxia, hydrops fetalis, and even fetal death if left untreated [81–83]. Anemia results in a hyperdynamic fetal circulation and the Doppler detection of an elevated peak systolic velocity in the middle cerebral artery is a highly sensitive marker of an initial presentation of fetal anemia [84, 85]. However, middle cerebral artery peak systolic velocity becomes less specific with repeated transfusions, exposing patients to the potential of unnecessary and risky interventions and may be falsely reassuring in approximately 5% of alpha-thalassemia patients with moderate-to-severe anemia [86]. Based on a comparison of hematocrit measured by MRI with direct blood sampling and middle cerebral artery peak systolic velocity, Xu et al. reported that the application of fetal CMR could improve clinical care by limiting unnecessary invasive umbilical cord blood samples in fetuses with abnormal Dopplers [87].

### 21.8.8 Maternal Hyperoxygenation

The maternal administration of supplemental inhaled oxygen results in an increase in fetal  $PaO_2$  and has been explored as a diagnostic challenge to assess fetal pulmonary vascular resistance and as a treatment in the setting of fetal growth restriction and CHD. Porayette et al. confirmed the expected increases in umbilical vein T2 in response to acute maternal hyperoxygenation in human pregnancies with normal hearts and in fetuses with CHD [88]. An episode of acute maternal hyperoxygenation resulted in an increase in umbilical vein  $SO_2$  ( $80.4 \pm 6.9$  vs.  $87.8 \pm 7.3\%$ ,  $P = 0.0004$ ), fetal  $DO_2$  ( $26.4 \pm 7.6$  vs.  $30.6 \pm 5.2$  ml/min/kg,  $P = 0.03$ ) and increases in fetal cerebral oxygen delivery in excess of 20% in late gestation fetal sheep (Fig. 21.12). By

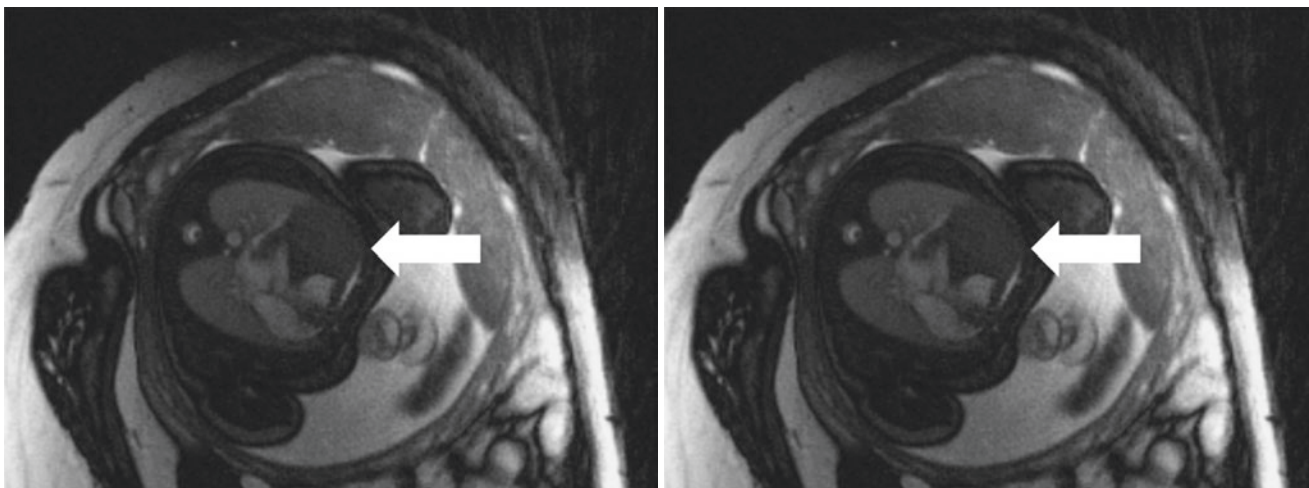


**Fig. 21.13** Magnetic resonance imaging of a large single apical cardiac tumor of a fetus at 35 weeks gestation, compressing on both left and right ventricles (white arrow)

contrast, we observed no increase in fetal oxygenation in response to uterine artery vasodilation with resveratrol (RSV).

### 21.8.9 Fetal Cardiac Tumors

Tumors of the fetal heart rarely reach a size warranting fetal intervention. However, the role of fetal MRI has been explored in the setting of fetal cardiac tumors, as shown in Fig. 21.13. Cerebral T2 weighted fast spin echo may confirm the presence of subependymal nodules and cortical tubers to provide a definitive diagnosis of tuberous sclerosis in the setting of cardiac rhabdomyomas [89]. Giant cardiac tumors may result in impairment of fetal cardiac filling or cause significant outflow tract obstruction. One case report describes the use of cine cardiac SFFP imaging in a fetus presenting with a massive rhabdomyoma at 31 weeks gestation. The imaging clearly demonstrated the extremely large mass involving the free wall of the left ventricle and the interventricular septum and confirmed patency of the left ventricular outflow tract, which had been obscured by the mass on fetal echocardiography [90]. Transplacental treatment was initiated with sirolimus which resulted in significant reduction of the size of the mass and improved biventricular systolic function on MRI.

### 21.8.10 Exploring Fetal Physiology and New Interventions Through Animal Models

DV is an important fetal structure which plays an important role in determining the distribution of oxygen and nutrition-rich blood returning from the placenta via the umbilical vein.

The dynamic tone of the DV is responsive to the oxygenation of the fetus [91–94]. Acute fetal hypoxemia affects dilation of the DV, allowing more oxygenated blood to bypass the portal vein and liver. This phenomenon has also been noted in growth-restricted fetuses, who have been reported to exhibit an increase in the ratio of DV to umbilical blood flow [95–97]. Evidence that endogenous prostaglandins regulate DV tone has been provided by animal studies [98, 99]. Darby et al. used 4D flow and T2 oximetry to examine the fetal circulatory impact of an infusion of PGI<sub>2</sub> delivered to the umbilical vein, as illustrated in Fig. 21.14 [100]. The results confirmed that PGI<sub>2</sub> resulted in a greater proportion of the oxygen-rich blood in the umbilical vein passing through the DV. A positive relationship was observed between the magnitude of DV shunting and the cross-sectional area of the vessel, confirming that dilation of the DV results in increased blood flow through it. However, prostaglandin-induced DV shunting was not associated with any increase in cerebral oxygen delivery, which was attributed to the pulmonary vasodilatory effect of the prostaglandin, which resulted in diminished foramen ovale shunting. The findings of this study emphasize the importance of evaluating the whole fetal circulation in studies investigating the impact of vasoactive drugs.

### 21.8.11 Uterine Artery Vasodilators

In another study conducted by the Early Origins of Adult Health Research Group at the University of South Australia, the effect of subcutaneous RSV was investigated in pregnant sheep [101]. RSV is a uterine artery vasodilator and the study employed MRI to quantify uterine artery blood flow, as well as fetal blood sampling for blood gases and RSV titers and a



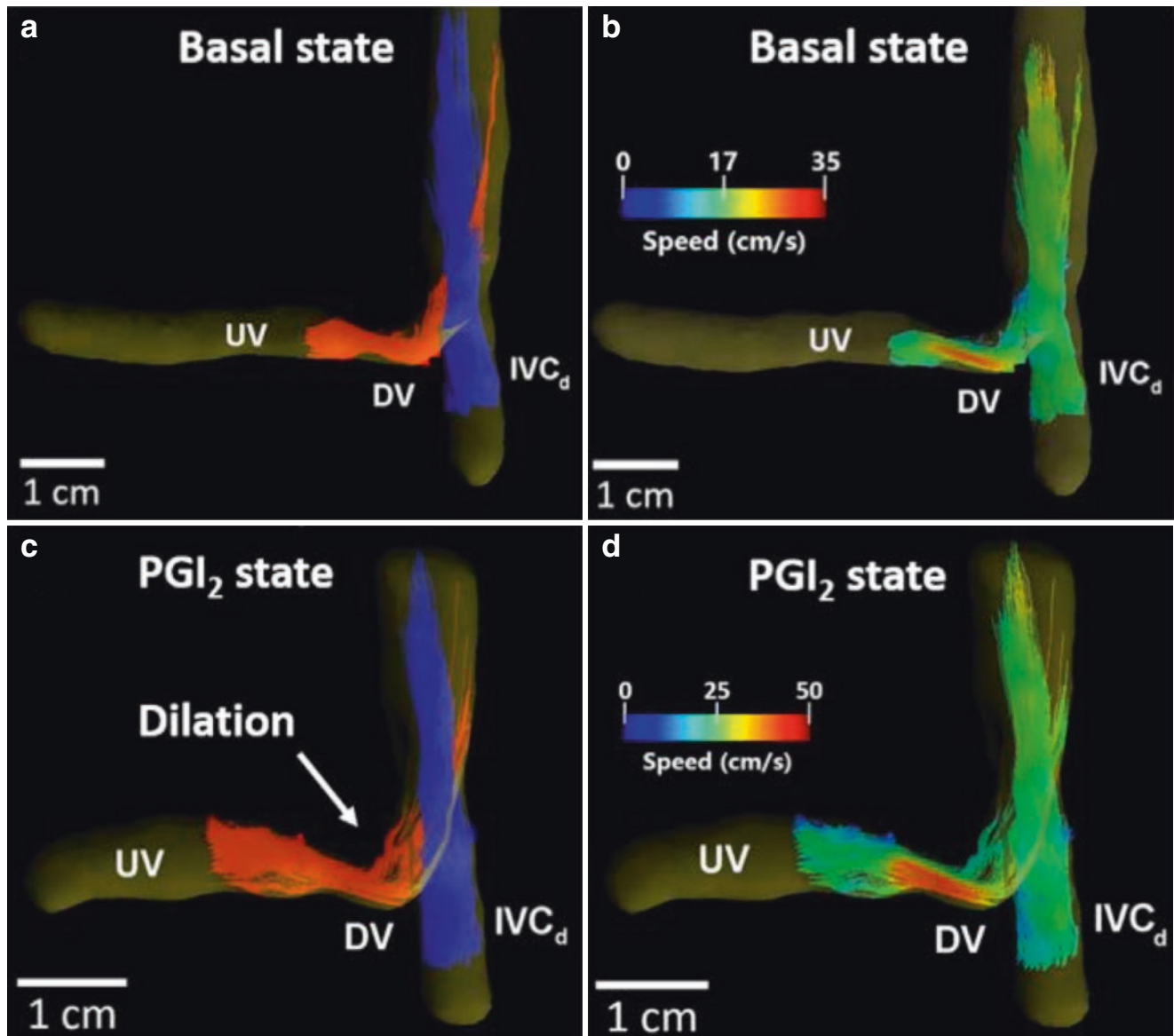


**Fig. 21.14** Blood flow particle trace visualization of UV flow through the DV into the IVC, color-coded based on origin and speed. (a, b) basal state; (c, d) during PGI<sub>2</sub> infusion [100]. Red color on (a) and (c) represents oxygen and nutrition-rich blood from the UV, with blue

representing deoxygenated blood from the distal IVC. Color coding on (b) and (d) represents speed of blood flow across the DV. (With permission from John Wiley & Sons)

range of molecular analyses of fetal tissues. The results revealed an increase in uterine artery blood flow in the RSV treatment group which was associated with an increase in fetal weight. Of note, no RSV was detected in fetal circulation, suggesting that in contrast to several other species, the sheep placenta is impervious to RSV. There remains interest in the potential of RSV as a therapy for fetal growth restriction.

### 21.8.12 Detection of Fetal Myocardial Ischemia

Cardiovascular disease is the leading cause of death in developed countries [102]. As the adult myocardium has a

very limited capacity for regeneration following injury, the focus of attention has been on primary and secondary prevention. In contrast with human adult patients, hypoxic events have revealed remarkable cardiac regenerative properties in a range of animal models (adult zebrafish, newborn mouse, neonatal pig, and fetal sheep) [103–106]. The ability of the myocardium to proliferate rather than scar in response to injury is mostly related the stage of heart development and relation to birth. Lock et al. examined cardiac regeneration in fetal and adolescent sheep using a coronary artery ligation myocardial infarction model. CMR was employed to confirm and measure the extent of myocardial injury on late gadolinium enhancement in fetal and adolescent subjects, revealing remarkable differences between the

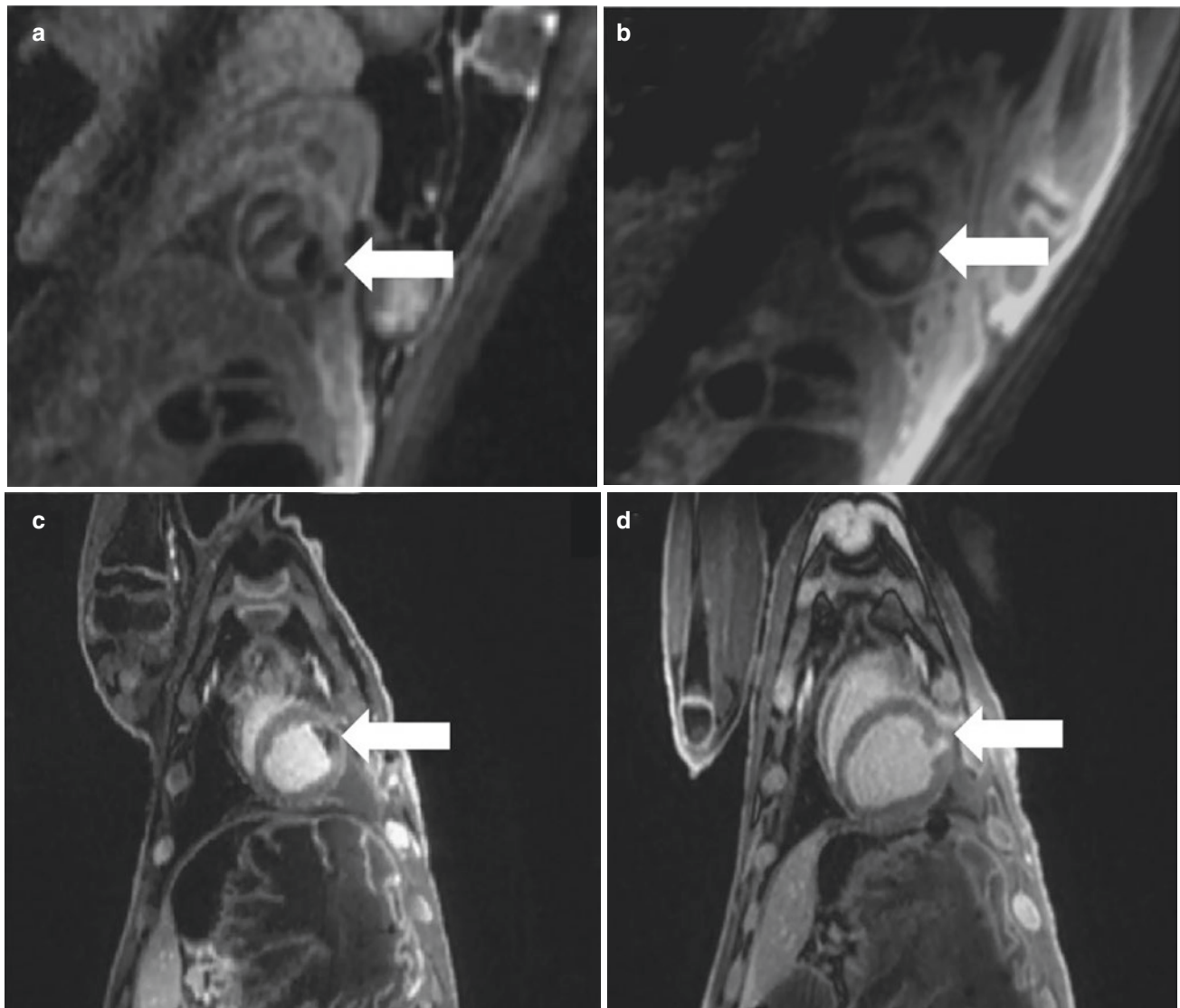


**Fig. 21.15** 3D inversion recovery FLASH (IR-FLASH) gadolinium imaging in fetal (a, b) and adolescent (c, d) sheep model of myocardial infarction (MI) by coronary ligation. Early gadolinium IR-FLASH imaging employed immediately after MI surgery confirmed the extent of myocardial ischemia in the anterior and anterolateral myocardium

(a, c). Late gadolinium IR-FLASH imaging performed 6 days after MI in the fetus (b) and 15 days after MI in the lamb (d) confirmed the extent of myocardial scarring/damage; resolution of  $0.6 \times 0.6 \times 0.6$ – $0.9$  mm (white arrow)

two age groups with obvious myocardial regeneration observed in fetal myocardium [107]. Cho et al. recently explored the use of a 3D inversion recovery FLASH (IR-FLASH) sequence in fetal and adolescent sheep model of myocardial infarction to confirm and measure extent of myocardial ischemia and injury using early and late gad, respectively at various stages of injury, shown in Fig. 21.15 (unpublished data).

### 21.8.13 Fetal Ventricular Volumetry

Ventricular volumetry remains a challenge for fetal CMR. However, under the controlled conditions possible in

a fetal sheep model, ventricular volumetry is feasible [108], as shown in Fig. 21.16. Cho et al. confirmed the accuracy of cine SSFP measurements of stroke volume through comparison with ventricular outputs measured by cine phase contrast MRI. The inclusion of the papillary muscles in the blood pool resulted in small differences in myocardial mass compared to post-mortem pathology. Fetal CMR confirmed the greater contribution to CVO provided by the right ventricle, with larger right ventricular end-diastolic volumes and stroke volumes compared with the left. One interesting observation was the lack of difference between left and right ventricular ejection fractions, which may be explained by the different loading conditions present in the fetal circulation. Ongoing advances in fetal CMR technology are

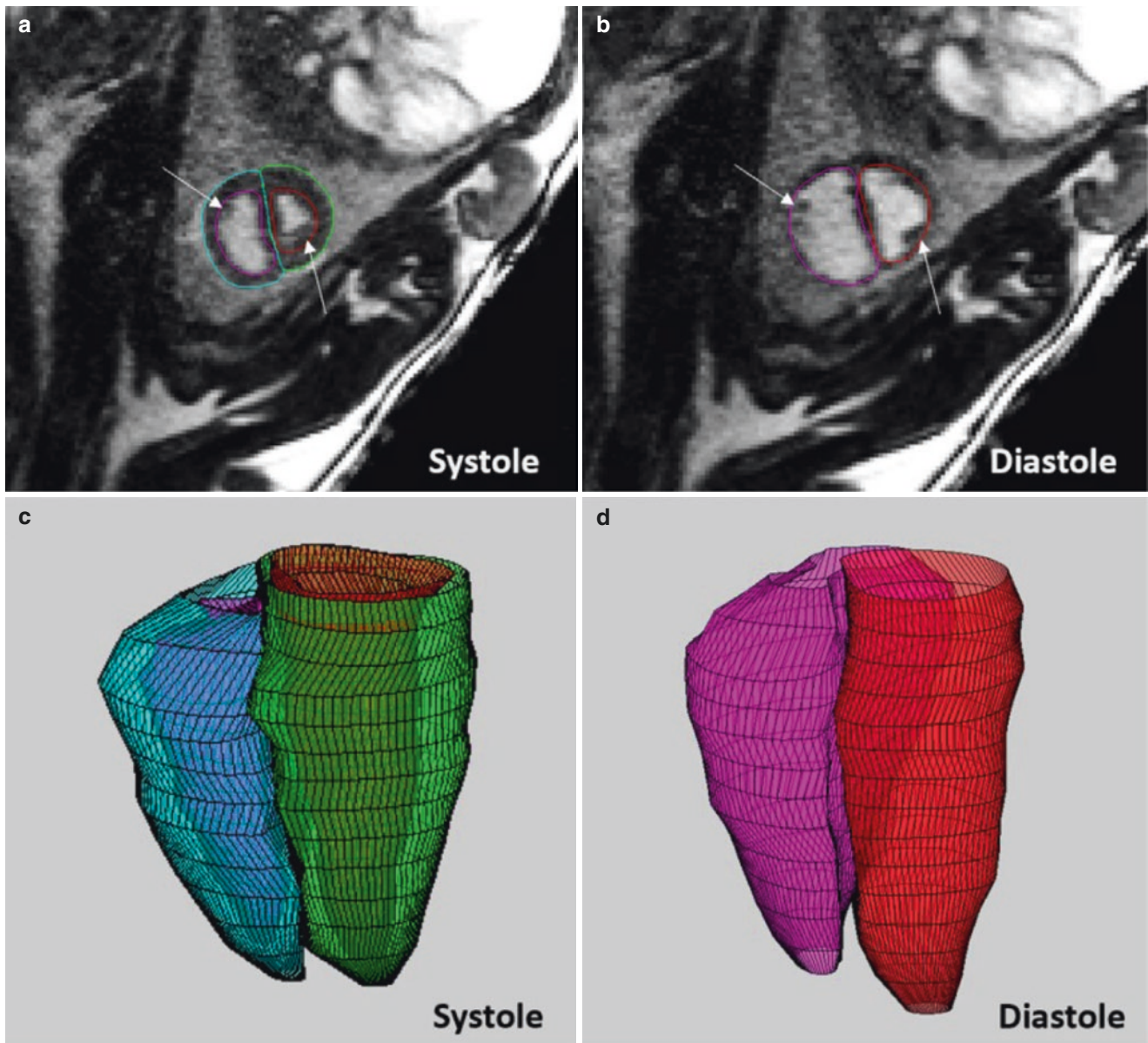


**Fig. 21.16** Ventricular volumetry by post-processing of a short-axis cine fetal CMR in fetal sheep [108]. Contoured 2D cine images of the fetal heart (a, b), reconstructed into ventricular volumes (c, d). (With permission from John Wiley & Sons)

expected to result in the feasibility of human fetal ventricular volumetry by CMR, which would potentially be of interest in a range of settings.

#### 21.8.14 Pathophysiological Impact of Maternal Late Gestation Undernutrition

Fetal CMR has also been used to investigate fetal pulmonary vascular physiology in the setting of a sheep model of maternal undernutrition [109]. Healthy fetal lung development and

surfactant maturation are highly dependent on certain substrates. The supply of these elements is dependent on placental function and/or maternal nutritional status, and the consequences are dependent on the severity and duration of the insult and the timing of gestation. Fetal CMR has been used to characterize fetal pulmonary hemodynamics and oxygenation to examine relationships between maternal undernutrition, fetal surfactant maturation, pulmonary blood flow, and oxygen delivery. Of note, pulmonary surfactant protein gene expression was inversely related to pulmonary oxygenation, raising the possibility that pulmonary vasodilators might have an adverse impact on fetal lung development.



**Acknowledgment** The authors would like to thank Prof. Christopher K. Macgowan and Prof. Janna L. Morrison for their collaborative work. The authors would also like to thank Dr. Brahmdeep S. Saini, Steven K.S. Cho, Tanroop Aujla and Fu-Tsuen Lee for their support with the figures.

## References

- Roy C, Marini D, Lloyd DF, Mawad W, Yoo S, Schrauben E, Jaeggi E, Seed M, Macgowan C. Preliminary experience using motion compensated CINE magnetic resonance imaging to visualise fetal congenital heart disease. *Circ Cardiovasc Imaging*. 2018;11(12):e007745. <https://doi.org/10.1161/CIRCIMAGING.118.007745>.
- Seed M, Van Amerom JF, Yoo S, Al Nafisi B, Grosse-Wortmann L, Jaeggi E, Jansz M, MacGowan C. Feasibility of quantification of the distribution of blood flow in the normal human fetal circulation using CMR: a cross-sectional study. *J Cardiovasc Magn Reson*. 2012;14(1):1. <https://doi.org/10.1186/1532-429X-14-79>.
- Roelfsema NM, Hop WCJ, Boito SME, Wladimiroff JW. Three-dimensional sonographic measurement of normal fetal brain volume during the second half of pregnancy. *Am J Obstet Gynecol*. 2004;190(1):275–80. [https://doi.org/10.1016/S0002-9378\(03\)00911-6](https://doi.org/10.1016/S0002-9378(03)00911-6).
- Baker PN, Johnson IR, Gowland PA, Hykin J, Harvey PR, Freeman A, Adams V, Mansfield P, Worthington BS. Fetal weight estimation by echo-planar magnetic resonance imaging. *Lancet*. 1994;343(8898):644–5. [https://doi.org/10.1016/S0140-6736\(94\)92638-7](https://doi.org/10.1016/S0140-6736(94)92638-7).
- Roberts TA, van Amerom JFP, Uus A, Lloyd DFA, van Poppel MPM, Price AN, Tournier JD, Mohanadass CA, Jackson LH, Malik SJ, Pushparajah K, Rutherford MA, Rezavi R, Deprez M, Hajnal JV. Fetal whole heart blood flow imaging using 4D cine MRI. *Nat Commun*. 2020;11(1):1–13. <https://doi.org/10.1038/s41467-020-18790-1>.
- Jansz MS, Seed M, Van Amerom JFP, Wong D, Grosse-Wortmann L, Yoo SJ, MacGowan CK. Metric optimized gating for fetal cardiac MRI. *Magn Reson Med*. 2010;64(5):1304–14. <https://doi.org/10.1002/mrm.22542>.
- Sun L, Macgowan CK, Sled JG, Yoo SJ, Manthot C, Porayette P, Grosse-Wortmann L, Jaeggi E, McCrindle BW, Kingdom J, Hickey E, Miller S, Seed M. Reduced fetal cerebral oxygen consumption is associated with smaller brain size in fetuses with congenital heart disease. *Circulation*. 2015;131(15):1313–23. <https://doi.org/10.1161/CIRCULATIONAHA.114.013051>.
- Tsai-Goodman B, Zhu MY, Al-Rujaib M, Seed M, Macgowan CK. Foetal blood flow measured using phase contrast cardiovascular magnetic resonance - preliminary data comparing 1.5 T with 3.0 T. *J Cardiovasc Magn Reson*. 2015;17(1):4–9. <https://doi.org/10.1186/s12968-015-0132-2>.
- Roy CW, Seed M, van Amerom JFP, Al Nafisi, Grosse-Wortmann L, Yoo SJ, Macgowan CK. Dynamic imaging of the fetal heart using metric optimized gating. 2013; 70(6):1598-607. <https://doi.org/10.1002/mrm.24614>.
- Bidhult S, Töger J, Heiberg E, Carlsson M, Arheden H, Aletras AH, Hedström E. Independent validation of metric optimized gating for fetal cardiovascular phase-contrast flow imaging. *Magn Reson Med*. 2019;81(1):495–503. <https://doi.org/10.1002/mrm.27392>.
- Roy CW, Seed M, Kingdom JC, Macgowan CK. Motion compensated cine CMR of the fetal heart using radial undersampling and compressed sensing. *J Cardiovasc Magn Reson*. 2017;19(1):29. <https://doi.org/10.1186/s12968-017-0346-6>.
- van Amerom JFP, Lloyd DFA, Price AN, Kuklisova Murgasova M, Aljabar P, Malik SJ, Lohezic M, Rutherford MA, Pushparajah K, Razavi R, Hajnal JV. Fetal cardiac cine imaging using highly accelerated dynamic MRI with retrospective motion correction and outlier rejection. *Magn Reson Med*. 2018;79(1):327–38. <https://doi.org/10.1002/mrm.26686>.
- Chaptinel J, Yerly J, Mivelaz Y, Prsa M, Alamo L, Vial Y, Berchier G, Rohner C, Gudinchet F, Stuber M. Fetal cardiac cine magnetic resonance imaging in utero. *Sci Rep*. 2017;7:15540. <https://doi.org/10.1038/s41598-017-15701-1>.
- Haris K, Hedström E, Bidhult S, Testud F, Maglaveras N, Heiberg E, Hansson SR, Arheden H, Aletras AH. Self-gated fetal cardiac MRI with tiny golden angle iGRASP: a feasibility study. *J Magn Reson Imaging*. 2017;46(1):207–17. <https://doi.org/10.1002/jmri.25599>.
- Kellman P, Hansen MS, Nielles-Vallespin S, Nickander J, Themudo R, Ugander M, Xue H. Myocardial perfusion cardiovascular magnetic resonance: optimized dual sequence and reconstruction for quantification. *J Cardiovasc Magn Reson*. 2017;19(1):1–14. <https://doi.org/10.1186/s12968-017-0355-5>.
- Goolaub DS, Roy CW, Schrauben E, Sussman D, Marini D, Seed M, Macgowan CK. Multidimensional fetal flow imaging with cardiovascular magnetic resonance: a feasibility study. *J Cardiovasc Magn Reson*. 2018;20(1):77. <https://doi.org/10.1186/s12968-018-0498-z>.
- Saini BS, Darby JRT, Portnoy S, Sun L, van Amerom J, Lock MC, Soo JY, Holman SL, Perumal SR, Kingdom JC, Sled JG, Macgowan CK, Morrison JL, Seed M. Normal human and sheep fetal vessel oxygen saturations by T2 magnetic resonance imaging. *J Physiol*. 2020;598(15):3259–81. <https://doi.org/10.1113/JP279725>.
- Goolaub D, Xu J, Schrauben E, Marini D, Seed M, Macgowan C. Volumetric fetal flow imaging with rapid multislice multidimensional radial phase contrast MRI. *IEEE Trans Med Imaging*. 2021;41:2941. <https://doi.org/10.36227/techrxiv.15112944.v1>.
- Sun L, van Amerom JF, Marini D, Portnoy S, Lee FT, Saini BS, Lim JM, Aguet J, Jaeggi E, Kingdom JC, Macgowan CK, Miller SP, Huang G, Seed M. MRI characterization of hemodynamic patterns of human fetuses with cyanotic congenital heart disease. *Ultrasound Obstet Gynecol*. 2021;58(6):824–36. <https://doi.org/10.1002/uog.23707>.
- Yamamura J, Kopp I, Frisch M, Fischer R, Valett K, Hecher K, Adam G, Wedegärtner U. Cardiac MRI of the fetal heart using a novel triggering method: initial results in an animal model. *J Magn Reson Imaging*. 2012;35(5):1071. <https://doi.org/10.1002/jmri.23541>.
- Kording F, Schoennagel BP, de Sousa MT, Fehrs K, Adam G, Yamamura J, Ruprecht C. Evaluation of a portable doppler ultrasound gating device for fetal cardiac MR imaging: initial results at 1.5T and 3T. *Magn Reson Med Sci*. 2018;17(4):308–17. <https://doi.org/10.2463/mrms.mp.2017-0100>.
- Kording F, Yamamura J, De Sousa MT, Ruprecht C, Hedström E, Aletras AH, Ellen Grant P, Powell AJ, Fehrs K, Adam G, Kooijman H, Schoennagel BP. Dynamic fetal cardiovascular magnetic resonance imaging using Doppler ultrasound gating. *J Cardiovasc Magn Reson*. 2018;20(1):17. <https://doi.org/10.1186/s12968-018-0440-4>.
- Tavares de Sousa M, Hecher K, Yamamura J, Kording F, Ruprecht C, Fehrs K, Behzadi C, Adam G, Schoennagel BP. Dynamic fetal cardiac magnetic resonance imaging in four-chamber view using Doppler ultrasound gating in normal fetal heart and in congenital heart disease: comparison with fetal echocardiogra-



- phy. *Ultrasound Obstet Gynecol.* 2019;53(5):669–75. <https://doi.org/10.1002/uog.20167>.
24. Wright GA, Hu BS, Macovski A. Estimating oxygen saturation of blood in vivo with MR imaging at 1.5 T. *J Magn Reson Imaging.* 1991;1(3):275–83. <https://doi.org/10.1002/jmri.1880010303>.
  25. Portnoy S, Seed M, Sled JG, Macgowan CK. Non-invasive evaluation of blood oxygen saturation and hematocrit from T1 and T2 relaxation times: in-vitro validation in fetal blood. *Magn Reson Med.* 2017;78(6):2352–9. <https://doi.org/10.1002/mrm.26599>.
  26. Stainsby JA, Wright GA. Partial volume effects on vascular T2 measurements. *Magn Reson Med.* 1998;40(3):494–9. <https://doi.org/10.1002/mrm.1910400322>.
  27. Portnoy S. Oximetry\_Calculator. 2016. [https://github.com/shportnoy/oximetry\\_calculator](https://github.com/shportnoy/oximetry_calculator)
  28. Portnoy S. MR oximetry. 2016. [https://github.com/shportnoy/blood\\_roi\\_tool](https://github.com/shportnoy/blood_roi_tool).
  29. Hansen MS. Retrospective reconstruction of high temporal resolution cine images from real-time MRI using iterative motion correction. *Magn Reson Med.* 2012;68(3):741–50. <https://doi.org/10.1002/mrm.23284>.
  30. Prsa M, Sun L, Van Amerom J, Yoo SJ, Grosse-Wortmann L, Jaeggi E, MacGowan C, Seed M. Reference ranges of blood flow in the major vessels of the normal human fetal circulation at term by phase-contrast magnetic resonance imaging. *Circ Cardiovasc Imaging.* 2014;7(4):663–70. <https://doi.org/10.1161/CIRCIMAGING.113.001859>.
  31. Rudolph AM. Congenital cardiovascular malformations and the fetal circulation. *Arch Dis Child Fetal Neonatal Ed.* 2010;95(2):F132. <https://doi.org/10.1136/adc.2007.128777>.
  32. Jones B, Muscara F, Lloyd O, McKinlay L, Justo R. Neurodevelopmental outcome following open heart surgery in infancy: 6-year follow-up. *Cardiol Young.* 2015;25(5):903–10. <https://doi.org/10.1017/S1047951114001140>.
  33. Torigoe T, Mawad W, Seed M, Ryan G, Marini D, Golding F, Mieghem VAN, T., & Jaeggi, E. Treatment of fetal circular shunt with non-steroidal anti-inflammatory drugs. *Ultrasound Obstet Gynecol.* 2019;53(6):841–6. <https://doi.org/10.1002/uog.20169>.
  34. Bao M, Jaeggi E, Sun L, Lee F-T, Sananes R, Chau V, Macgowan CK, Miller SP, Seed M, Marini D. Impact of fetal haemodynamics on surgical and neurodevelopmental outcomes in patients with Ebstein anomaly and tricuspid valve dysplasia. *Cardiol Young.* 2022;32:1768. <https://doi.org/10.1017/S1047951121004935>.
  35. Allen DR, Schieken RM, Donofrio MT. Hoarseness as the initial clinical presentation of anomalous left coronary artery from the pulmonary artery. *Pediatr Cardiol.* 2005;26(5):668–71. <https://doi.org/10.1007/s00246-004-0846-7>.
  36. Barcroft J. Phases in foetal life. *Glasgow Med J.* 1943;139(1):1–13.
  37. Dawes G. The physiological control of the fetal circulation. *Obstet Gynecol Surv.* 1961;16(1):20–5. <https://doi.org/10.1097/00006254-196102000-00002>.
  38. Rudolph AM. The circulation of the fetus in utero. *Circ Res.* 1967;21(2):163–84. <https://doi.org/10.1161/01.res.21.2.163>.
  39. Matthiesen NB, Henriksen TB, Gaynor JW, Agergaard P, Bach CC, Hjordtal VE, Østergaard JR. Congenital heart defects and indices of fetal cerebral growth in a Nationwide Cohort of 924 422 liveborn infants. *Circulation.* 2016;133(6):566–75. <https://doi.org/10.1161/CIRCULATIONAHA.115.019089>.
  40. Pearce W. Hypoxic regulation of the fetal cerebral circulation. *J Appl Physiol.* 2006;100(2):731–8. <https://doi.org/10.1152/jappphysiol.00990.2005>.
  41. Wladimiroff JW, Tonge HM, Stewart PA. Doppler ultrasound assessment of cerebral blood flow in the human fetus. *BJOG.* 1986;93(5):471–5. <https://doi.org/10.1111/j.1471-0528.1986.tb08656.x>.
  42. Donofrio MT, Bremer YA, Schieken RM, Gennings C, Morton LD, Eidem BW, Cetta F, Falkensammer CB, Huhta JC, Kleinman CS. Autoregulation of cerebral blood flow in fetuses with congenital heart disease: the brain sparing effect. *Pediatr Cardiol.* 2003;24(5):436–43. <https://doi.org/10.1007/s00246-002-0404-0>.
  43. Shariat M, Mertens L, Seed M, Grosse-Wortmann L, Golding F, Mercer-Rosa L, Harris M, Whitehead KK, Li C, Fogel MA, Yoo SJ. Utility of feed-and-sleep cardiovascular magnetic resonance in young infants with complex cardiovascular disease. *Pediatr Cardiol.* 2015;36(4):809–12. <https://doi.org/10.1007/s00246-014-1084-2>.
  44. Zhu M, Milligan N, Keating S, Windrim R, Keunen J, Thakur V, Ohman A, Portnoy S, Sled J, Kelly E, Yoo S, Gross-Wortmann L, Jaeggi E, MacGowan C, Kingdom J, Seed M. The hemodynamics of late-onset intrauterine growth restriction by MRI. *Am J Obstet Gynecol.* 2016;214(3):367.e1–367.e17. <https://doi.org/10.1016/j.ajog.2015.10.004>.
  45. Wheaton WW, Chandel NS. Hypoxia. 2. Hypoxia regulates cellular metabolism. *Am J Physiol Cell Physiol.* 2011;300(3):C385. <https://doi.org/10.1152/ajpcell.00485.2010>.
  46. Yuen TJ, Silbereis JC, Griveau A, Chang SM, Daneman R, Fancy SPJ, Zahed H, Maltepe E, Rowitch DH. Oligodendrocyte-encoded HIF function couples postnatal myelination and white matter angiogenesis. *Cell.* 2014;158(2):383–96. <https://doi.org/10.1016/j.cell.2014.04.052>.
  47. Andela N, Morton DC, Giglio L, Chen Y, Van Der Werf GR, Kasibhatla PS, DeFries RS, Collatz GJ, Hantson S, Kloster S, Bachelet D, Forrest M, Lasslop G, Li F, Mangeon S, Melton JR, Yue C, Randerson JT. A human-driven decline in global burned area. *Science.* 2017;356(6345):1356–62. <https://doi.org/10.1126/science.aal4108>.
  48. Rudolph AM. Impaired cerebral development in fetuses with congenital cardiovascular malformations: is it the result of inadequate glucose supply? *Pediatr Res.* 2016;80(2):172–7. <https://doi.org/10.1038/pr.2016.65>.
  49. Miller SP. Abnormal brain development in newborns with congenital heart disease. *N Engl J Med.* 2007;357(19):1928–38. <https://doi.org/10.1097/01.sa.0000307878.52543.ba>.
  50. Kelly CJ, Christiaens D, Batalle D, Makropoulos A, Cordero-Grande L, Steinweg JK, O’Muircheartaigh J, Khan H, Lee G, Victor S, Alexander DC, Zhang H, Simpson J, Hajnal JV, Edwards AD, Rutherford MA, Counsell SJ. Abnormal microstructural development of the cerebral cortex in neonates with congenital heart disease is associated with impaired cerebral oxygen delivery. *J Am Heart Assoc.* 2019;8(5):e009893. <https://doi.org/10.1161/JAHA.118.009893>.
  51. Rahman A. A mouse model of hypoplastic left heart syndrome demonstrating left heart hypoplasia and retrograde aortic arch flow. *Dis Model Mech.* 2021;14(11):dmm049077.
  52. Lloyd DFA, Pushparajah K, Simpson JM, van Amerom JFP, van Poppel MPM, Schulz A, Kainz B, Deprez M, Lohezic M, Allsop J, Mathur S, Bellsham-Revell H, Vigneswaran T, Charakida M, Miller O, Zidere V, Sharland G, Rutherford M, Hajnal JV, Razavi R. Three-dimensional visualisation of the fetal heart using prenatal MRI with motion-corrected slice-volume registration: a prospective, single-centre cohort study. *Lancet.* 2019;393:1619. [https://doi.org/10.1016/S0140-6736\(18\)32490-5](https://doi.org/10.1016/S0140-6736(18)32490-5).
  53. Lloyd DFA, van Poppel MPM, Pushparajah K, Vigneswaran TV, Zidere V, Steinweg J, van Amerom JFP, Roberts TA, Schulz A, Charakida M, Miller O, Sharland G, Rutherford M, Hajnal JV, Simpson JM, Razavi R. Analysis of 3-dimensional arch anatomy, vascular flow, and postnatal outcome in cases of suspected coarctation of the aorta using fetal cardiac magnetic resonance imaging. *Circ Cardiovasc Imaging.* 2021;14:e012411. <https://doi.org/10.1161/CIRCIMAGING.121.012411>.
  54. Salehi D, Fricke K, Bhat M, Arheden H, Liuba P, Hedström E. Utility of fetal cardiovascular magnetic resonance for

- prenatal diagnosis of complex congenital heart defects. *JAMA Netw Open*. 2021;4(3):1–11. <https://doi.org/10.1001/jamanetworkopen.2021.3538>.
55. Sun L, Lee F-T, van Amerom JFP, Freud L, Jaeggi E, Macgowan CK, Seed M. Update on fetal cardiovascular magnetic resonance and utility in congenital heart disease. *J Congenit Cardiol*. 2021;5(1):1–13. <https://doi.org/10.1186/s40949-021-00059-x>.
  56. Saini BS, Darby JRT, Marini D, Portnoy S, Lock MC, Yin Soo J, Holman SL, Perumal SR, Wald RM, Windrim R, Macgowan CK, Kingdom JC, Morrison JL, Seed M. An MRI approach to assess placental function in healthy humans and sheep. *J Physiol*. 2021;599(10):2573–602. <https://doi.org/10.1113/JP281002>.
  57. Saini BS, Darby JR, Marini D, Portnoy S, Lock M, Yin Soo J, Holman S, Perumal S, Wald R, Windrim R, Macgowan C, Kingdom J, Morrison J, Seed M. An MRI approach to assess placental function in healthy humans and sheep. *J Physiol*. 2021;599(10):2573–602. <https://doi.org/10.1113/JP281002>.
  58. Sørensen A, Hutter J, Seed M, Grant PE, Gowland P. T2\*-weighted placental MRI: basic research tool or emerging clinical test for placental dysfunction? *Ultrasound Obstet Gynecol*. 2020;55(3):293–302. <https://doi.org/10.1002/uog.20855>.
  59. Siauve N, Chalouhi GE, Deloison B, Alison M. Functional imaging of the human placenta with. *Am J Obstet Gynecol*. 2015;213(4):S103–14. <https://doi.org/10.1016/j.ajog.2015.06.045>.
  60. Sørensen A, Peters D, Simonsen C, Pedersen M, Stausbøl-grøn B, Christiansen OB, Lingman G, Uldbjerg N. Changes in human fetal oxygenation during maternal hyperoxia as estimated by BOLD MRI. *Prenat Diagn*. 2012;33:141. <https://doi.org/10.1002/pd.4025>.
  61. McKelvey SS, Kay HH. Magnetic resonance spectroscopy of the placenta. *Placenta*. 2007;28(5–6):369–77. <https://doi.org/10.1016/j.placenta.2006.05.008>.
  62. Linask KK. The heart-placenta axis in the first month of pregnancy: induction and prevention of cardiovascular birth defects. *J Pregnancy*. 2013;2013:320413. <https://doi.org/10.1155/2013/320413>.
  63. Burton GJ, Jauniaux E. Development of the human placenta and fetal heart: synergic or independent? *Front Physiol*. 2018;9(APR):1–10. <https://doi.org/10.3389/fphys.2018.00373>.
  64. Schlatterer SD, Murnick J, Jacobs M, White L, Donofrio MT, Limperopoulos C. Placental pathology and neuroimaging correlates in neonates with congenital heart disease. *Sci Rep*. 2019;9(1):1–11. <https://doi.org/10.1038/s41598-019-40894-y>.
  65. Rychik J, Goff D, McKay E, Mott A, Tian Z, Licht D, Gaynor JW. Characterization of the placenta in the newborn with congenital heart disease: distinctions based on type of cardiac malformation. *Pediatr Cardiol*. 2018;39(6):1165–71. <https://doi.org/10.1007/s00246-018-1876-x>.
  66. Lowenthal A. Prenatal diagnosis of atrial restriction in hypoplastic left heart syndrome is associated with decreased 2-year survival. *Prenat Diagn*. 2012;32(5):485–90. <https://doi.org/10.1002/pd.3850.Prenatal>.
  67. Chaturvedi RR, Ryan G, Seed M, Van Arsdell G, Jaeggi ET. Fetal stenting of the atrial septum: technique and initial results in cardiac lesions with left atrial hypertension. *Int J Cardiol*. 2013;168(3):2029–36. <https://doi.org/10.1016/j.ijcard.2013.01.173>.
  68. Jantzen DW, Moon-Grady AJ, Morris SA, Armstrong AK, Berg C, Dangel J, Fifer CG, Frommelt M, Gembruch U, Herberg U, Jaeggi E, Kontopoulos EV, Marshall AC, Miller O, Oberhoffer R, Oepkes D, Pedra CA, Pedra SR, Peralta F, et al. Hypoplastic left heart syndrome with intact or restrictive atrial septum: a report from the international fetal cardiac intervention registry. *Circulation*. 2017;136(14):1346–9. <https://doi.org/10.1161/CIRCULATIONAHA.116.025873>.
  69. Marshall AC, Van Der Velde ME, Tworetzky W, Gomez CA, Wilkins-Haug L, Benson CB, Jennings RW, Lock JE. Creation of an atrial septal defect in utero for fetuses with hypoplastic left heart syndrome and intact or highly restrictive atrial septum. *Circulation*. 2004;110(3):253–8. <https://doi.org/10.1161/01.CIR.0000135471.17922.17>.
  70. Seed M, Bradley T, Bourgeois J, Jaeggi E, Yoo S. Antenatal MR imaging of pulmonary lymphangiectasia secondary to hypoplastic left heart syndrome. *Pediatr Radiol*. 2009;39(7):747–9. <https://doi.org/10.1007/s00247-009-1223-8>.
  71. Saul D, Degenhardt K, Iyob SD, Surrey LF, Johnson AM, Johnson MP, Rychik J, Victoria T. Hypoplastic left heart syndrome and the nutmeg lung pattern in utero: a cause and effect relationship or prognostic indicator? *Pediatr Radiol*. 2016;46(4):483–9. <https://doi.org/10.1007/s00247-015-3514-6>.
  72. Victoria T, Andronikou S. The fetal MR appearance of ‘nutmeg lung’: findings in 8 cases linked to pulmonary lymphangiectasia. *Pediatr Radiol*. 2014;44(10):1237–42. <https://doi.org/10.1007/s00247-014-2994-0>.
  73. Al Nafisi B, Van Amerom JF, Forsey J, Jaeggi E, Grosse-Wortmann L, Yoo SJ, Macgowan CK, Seed M. Fetal circulation in left-sided congenital heart disease measured by cardiovascular magnetic resonance: a case-control study. *J Cardiovasc Magn Reson*. 2013;15(1):65. <https://doi.org/10.1186/1532-429X-15-65>.
  74. Luciani GB, Pessotto R, Mombello A, Mazzucco A. Hypoplastic left heart syndrome with restrictive atrial septal defect and congenital pulmonary lymphangiectasis. *Cardiovasc Pathol*. 1999;8(1):49–51. [https://doi.org/10.1016/S1054-8807\(98\)00012-X](https://doi.org/10.1016/S1054-8807(98)00012-X).
  75. Rychik J, Rome JJ, Collins MH, Decampoli WM, Spray TL. The hypoplastic left heart syndrome with intact atrial septum: atrial morphology, pulmonary vascular histopathology and outcome. *J Am Coll Cardiol*. 1999;34(2):554–60. [https://doi.org/10.1016/S0735-1097\(99\)00225-9](https://doi.org/10.1016/S0735-1097(99)00225-9).
  76. Maeno YV, Kamenir SA, Sinclair B, Van Der Velde ME, Smallhorn JF, Hornberger LK. Prenatal features of ductus arteriosus constriction and restrictive foramen ovale in d-transposition of the great arteries. *Circulation*. 1999;99(9):1209–14. <https://doi.org/10.1161/01.CIR.99.9.1209>.
  77. Jouannic JM, Gavard L, Fermont L, Le Bidois J, Parat S, Vouhé PR, Dumez Y, Sidi D, Bonnet D. Sensitivity and specificity of prenatal features of physiological shunts to predict neonatal clinical status in transposition of the great arteries. *Circulation*. 2004;110(13):1743–6. <https://doi.org/10.1161/01.CIR.0000144141.18560.CF>.
  78. Mawad W, Chaturvedi RR, Ryan G, Jaeggi E. Percutaneous fetal atrial balloon septoplasty for simple transposition of the great arteries with an intact atrial septum. *Can J Cardiol*. 2018;34(3):342.e9–342.e11. <https://doi.org/10.1016/j.cjca.2017.12.010>.
  79. Freud LR, Escobar-Diaz MC, Kalish BT, Komarlu R, Puchalski MD, Jaeggi ET, Szwast AL, Freire G, Levasseur SM, Kavanaugh-Mchugh A, Michelfelder EC, Moon-Grady AJ, Donofrio MT, Howley LW, Tierney ESS, Cuneo BF, Morris SA, Pruetz JD, Van Der Velde ME, et al. Outcomes and predictors of perinatal mortality in fetuses with Ebstein anomaly or tricuspid valve dysplasia in the current era: a multicenter study. *Circulation*. 2015;132(6):481–9. <https://doi.org/10.1161/CIRCULATIONAHA.115.015839>.
  80. Wertaschnigg D, Manlhiot C, Jaeggi M, Seed M, Dragulescu A, Schwartz SM, van Arsdell G, Jaeggi ET. Contemporary outcomes and factors associated with mortality after a fetal or neonatal diagnosis of Ebstein anomaly and tricuspid valve disease. *Can J Cardiol*. 2016;32(12):1500–6. <https://doi.org/10.1016/j.cjca.2016.03.008>.

81. Papantoniou N, Sifakis S, Antsaklis A. Therapeutic management of fetal anemia: review of standard practice and alternative treatment options. *J Perinat Med*. 2013;41(1):71–82. <https://doi.org/10.1515/jpm-2012-0093>.
82. Abbasi N, Johnson JA, Ryan G. Fetal anemia. *Ultrasound Obstet Gynecol*. 2017;50(2):145–53. <https://doi.org/10.1002/uog.17555>.
83. Zwiers C, van Kamp I, Oepkes D, Lopriore E. Intrauterine transfusion and non-invasive treatment options for hemolytic disease of the fetus and newborn—review on current management and outcome. *Expert Rev Hematol*. 2017;10(4):337–44. <https://doi.org/10.1080/17474086.2017.1305265>.
84. Mari G. Noninvasive diagnosis by Doppler ultrasonography of fetal anemia due to maternal red-cell alloimmunization. *Obstet Gynecol Surv*. 2000;55(6):341–2. <https://doi.org/10.1097/00006254-200006000-00005>.
85. Gagnon R, Van den Hof M. The use of fetal Doppler in obstetrics. *J Obstet Gynaecol Can*. 2003;25(7):601. [https://doi.org/10.1016/s1701-2163\(16\)31020-9](https://doi.org/10.1016/s1701-2163(16)31020-9).
86. Srisupundit K, Piyamongkol W, Tongsong T. Identification of fetuses with hemoglobin Bart's disease using middle cerebral artery peak systolic velocity. *Ultrasound Obstet Gynecol*. 2009;33(6):694–7. <https://doi.org/10.1002/uog.6342>.
87. Xu J, Duan AQ, Marini D, Lim JM, Keunen J, Portnoy S, Sled JG, McCrindle BW, Kingdom J, Macgowan CK, Seed M. The utility of MRI for measuring hematocrit in fetal anemia. *Am J Obstet Gynecol*. 2020;222:81.e1. <https://doi.org/10.1016/j.ajog.2019.07.016>.
88. Porayette P, Madathil S, Sun L, Jaeggi E, Grosse-Wortmann L, Yoo SJ, Hickey E, Miller SP, Macgowan CK, Seed M. MRI reveals hemodynamic changes with acute maternal hyperoxygenation in human fetuses with and without congenital heart disease. *Prenat Diagn*. 2016;36(3):274–81. <https://doi.org/10.1002/pd.4762>.
89. Mühlner MR, Rake A, Schwabe M, Schmidt S, Kivelitz D, Chaoui R, Hamm B. Value of fetal cerebral MRI in sonographically proven cardiac rhabdomyoma. *Pediatr Radiol*. 2007;37(5):467. <https://doi.org/10.1007/s00247-007-0436-y>.
90. Roy CW, Macgowan CK. Dynamic MRI of a large fetal cardiac mass. *Radiology*. 2019;290(2):288. <https://doi.org/10.1148/radiol.2018182025>.
91. Behrman R, Lees M, Peterson E, De Lannoy C, Seeds A. Distribution of the circulation in the normal and asphyxiated fetal primate. *Am J Obstet Gynecol*. 1970;108(6):956–69.
92. Reuss ML, Rudolph AM. Effects of ductus venosus obstruction on liver and regional blood flows in the fetal lamb. *J Dev Physiol*. 1980;2(1–2):71–84.
93. Paulick R, Meyers R, Rudolph C, AM, R. Venous responses to hypoxemia in the fetal lamb. *J Dev Physiol*. 1990;14(2):81–8.
94. Kiserud T. Fetal venous circulation. *Fetal Matern Med Rev*. 2003;14(1):57–95. <https://doi.org/10.1017/S0965539503001037>.
95. Tchirikov M, Rybakowski C, Hüneke B, Schröder H. Blood flow through the ductus venosus in singleton and multiple pregnancies and in fetuses with intrauterine growth retardation. *Am J Obstet Gynecol*. 1998;178(5):943–9.
96. Bellotti M, Pennati G, Pardi G, Fumero R. Dilatation of the ductus venosus in human fetuses: ultrasonographic evidence and mathematical modeling. *Am J Physiol Heart Circ Physiol*. 1998;275(5):44–5. <https://doi.org/10.1152/ajpheart.1998.275.5.h1759>.
97. Bellotti M, Pennati G, Gasperi C, Bozzo M, Battaglia F, Ferrazzi E. Simultaneous measurements of umbilical venous, fetal hepatic, and ductus venosus blood flow in growth-restricted human fetuses. *Am J Obstet Gynecol*. 2004;190(5):1347–58.
98. Adeagbo ASO, Coceani F, Olley PM. The response of the lamb ductus venosus to prostaglandins and inhibitors of prostaglandin and thromboxane synthesis. *Circ Res*. 1982;51(5):580–6. <https://doi.org/10.1161/01.RES.51.5.580>.
99. Adeagbo ASO, Bishai I, Lees J, Olley PM, Coceani F. Evidence for a role of prostaglandin I2 and thromboxane A2 in the ductus venosus of the lamb. *Can J Physiol Pharmacol*. 1985;63(9):1101–5. <https://doi.org/10.1139/y85-181>.
100. Darby JR, Schrauben EM, Saini BS, Holman SL, Perumal SR, Seed M, Macgowan CK, Morrison JL. Umbilical vein infusion of prostaglandin I2 increases ductus venosus shunting of oxygen-rich blood but does not increase cerebral oxygen delivery in the fetal sheep. *J Physiol*. 2020;598(21):4957–67. <https://doi.org/10.1113/JP280019>.
101. Darby JRT, Saini BS, Soo JY, Lock MC, Holman SL, Bradshaw EL, McInnes SJP, Voelcker NH, Macgowan CK, Seed M, Wiese MD, Morrison JL. Subcutaneous maternal resveratrol treatment increases uterine artery blood flow in the pregnant ewe and increases fetal but not cardiac growth. *J Physiol*. 2019;597(20):5063–77. <https://doi.org/10.1113/JP278110>.
102. WHO. World Health Statistics 2017: monitoring health for the SDGs, sustainable development goals. Geneva: WHO; 2017.
103. Herdrich BJ, Danzer E, Davey MG, Allukian M, Englefield V, Gorman JH, Gorman RC, Liechty KW. Regenerative healing following foetal myocardial infarction. *Eur J Cardiothorac Surg*. 2010;38(6):691–8. <https://doi.org/10.1016/j.ejcts.2010.03.049>.
104. Chris J, Eduard S, Marina R, Mercè M, Angel R, Jopling C, Sleep E, Raya M, Martí M, Raya A, Belmonte JCI. Zebrafish heart regeneration occurs by cardiomyocyte dedifferentiation and proliferation. *Nature*. 2017;176(12):139–48. <https://doi.org/10.1038/nature08899.Zebrafish>.
105. Porrello ER, Mahmoud AI, Simpson E, Hill JA, Richardson JA, Olson EN, Sadek HA. Transient regenerative potential of the neonatal mouse heart. *Science*. 2011;331(6020):1078–80. <https://doi.org/10.1126/science.1200708>.
106. Zhu W, Zhang E, Zhao M, Chong Z, Fan C, Tang Y, Hunter JD, Borovjagin AV, Walcott GP, Chen JY, Qin G, Zhang J. Regenerative potential of neonatal porcine hearts. *Circulation*. 2018;138(24):2809–16. <https://doi.org/10.1161/CIRCULATIONAHA.118.034886>.
107. Duan AQ, Lock MC, Perumal SR, Darby JR, Soo JY, Selvanayagam JB, Macgowan CK, Seed M, Morrison JL. Feasibility of detecting myocardial infarction in the sheep fetus using late gadolinium enhancement CMR imaging. *J Cardiovasc Magn Reson*. 2017;19(1):1–11. <https://doi.org/10.1186/s12968-017-0383-1>.
108. Cho SKS, Darby JRT, Saini BS, Lock MC, Holman SL, Lim JM, Perumal SR, Macgowan CK, Morrison JL, Seed M. Feasibility of ventricular volumetry by cardiovascular MRI to assess cardiac function in the fetal sheep. *J Physiol*. 2020;598(13):2557–73. <https://doi.org/10.1113/JP279054>.
109. Ren J, Darby JRT, Lock MC, Holman SL, Saini BS, Bradshaw EL, Orgeig S, Perumal SR, Wiese MD, Macgowan CK, Seed M, Morrison JL. Impact of maternal late gestation undernutrition on surfactant maturation, pulmonary blood flow and oxygen delivery measured by magnetic resonance imaging in the sheep fetus. *J Physiol*. 2021;599(20):4705–24. <https://doi.org/10.1113/JP281292>.



# Interventional Cardiovascular Magnetic Resonance

# 22

Vivek Muthurangu, Oliver Richard Tann,  
and Andrew M. Taylor

## 22.1 Introduction

Cardiac magnetic resonance (CMR) has increasingly replaced diagnostic cardiac catheterization as a method of assessing cardiac anatomy, measuring blood flow, and quantifying ventricular function. Nevertheless, interventional cardiac catheterization is a growth area for providing treatments for congenital heart disease. Furthermore, diagnostic cardiac catheterization is still necessary when intra-cardiac or intra-vascular pressure measurements are required. Currently, X-ray fluoroscopy is the imaging modality of choice for guiding cardiac catheterization with some interventions also utilizing echocardiography. However, there are problems with this approach and the use of CMR during catheterization may be able to solve them. In this chapter, the role of CMR in the catheterization laboratory, both for guidance and cardiac assessment, will be reviewed. By the end of this chapter, the reader should have a greater understanding of the current state and future possibilities of interventional CMR.

**Supplementary Information** The online version contains supplementary material available at [https://doi.org/10.1007/978-3-031-29235-4\\_22](https://doi.org/10.1007/978-3-031-29235-4_22).

V. Muthurangu  
UCL Institute of Cardiovascular Science, University College  
London, London, UK  
e-mail: [v.muthurangu@ucl.ac.uk](mailto:v.muthurangu@ucl.ac.uk)

O. R. Tann  
Great Ormond Street Hospital for Children, London, UK  
e-mail: [Oliver.Tann@gosh.nhs.uk](mailto:Oliver.Tann@gosh.nhs.uk)

A. M. Taylor (✉)  
UCL Institute of Cardiovascular Science and Great Ormond Street  
Hospital for Children, London, UK  
e-mail: [a.taylor76@ucl.ac.uk](mailto:a.taylor76@ucl.ac.uk)

## 22.2 Rationale for Magnetic Resonance (MR)-Guided Cardiac Catheterization

### 22.2.1 Reduced X-Ray Exposure

Medical exposure to ionizing radiation is increasingly being recognized as a significant health risk for both patients and health care professionals [1, 2]. Although the number of cardiac catheterizations is relatively low when compared to chest X-rays, the exposure levels are much greater. In adults, the UK National Radiation Protection Board has calculated, the mean risk of developing a solid tumor after single cardiac catheterization procedure is approximately 1 in 2500. Unfortunately, in patients with congenital heart disease the risk may be greater for the following reasons.

- Many patients with congenital heart disease are children or young adults and they have a greater risk of malignancy after radiation exposure. For instance, if exposure occurs at 5 years of age, the risk of malignancy is increased to approximately 1 in 1000.
- Interventions in congenital heart disease often take longer than in adult ischemic disease. This is due to both the greater complexity of the actual interventions and the more difficult anatomy of the patients. Unfortunately, this problem is likely to be exacerbated by the increasing complexity of congenital interventions.



- Finally, patients with congenital heart disease are likely to have several catheterizations throughout their lives multiplying the risk of developing radiation exposure-related health problems.

Thus, there is a need to reduce exposure to ionizing radiation during congenital cardiac catheterization. The development of real-time CMR offers the possibility of catheter guidance without exposure to X-ray radiation. Reduction and eventual elimination of the ionizing radiation exposure during cardiac catheterization is one of the main driving forces in the development of interventional CMR.

### 22.2.2 Increased Anatomical Information

Fluoroscopy provides excellent visualization of catheters, guide wires, devices, and bony structures. However, it performs less well in delineating soft tissue structures in the heart and vessels. Furthermore, it only provides 2D projection images, making depth perception more difficult. Invasive angiography can provide lumenographic views of the anatomy, which when combined with the operator's knowledge of the anatomy can provide sufficient information for many interventions. However, in congenital heart disease, there are several problems with this traditional approach to catheterization. Firstly, it is highly dependent on the operators 'mental image' of the anatomy. This may be sufficient in patients with near-normal anatomy, but in more complex cases the lack of true anatomical information makes the intervention more difficult. This not only prolongs the procedure, but also increases the small risk of perforating the heart or great vessels or other complications. Furthermore, as interventions become more ambitious, the need for accurate delineation of cardiac anatomy becomes more pressing. In fact, some novel interventions may not be clinically possible without better imaging. In many centers, CMR has become the optimum way to assess cardiac anatomy due to excellent visualization of soft tissue structures, unrestricted 2D imaging, and true 3D imaging capabilities. These properties of CMR make it particularly interesting as a possible additional or replacement imaging modality for cardiac catheterization.

### 22.2.3 Increased Functional Information

Cardiac catheterization is important in the assessment of ventricular and vascular hemodynamics. For instance, invasive pressures and blood flow measurements allow calculation of pulmonary vascular resistance (PVR), which is a vital part of the diagnostic work-up in patients with pulmonary hypertension. Unfortunately, the currently used invasive methods of flow quantification are associated with signifi-

cant inaccuracies. For instance, the Fick method requires multiple measurements to be taken which multiplies inaccuracy. Other methods of invasive flow quantification (e.g., indicator dilution and thermodilution techniques) also suffer from unreliability, particularly in the presence of valvular regurgitation and shunts. Velocity-encoded phase contrast MR is a very accurate method of measuring flow and has the benefit of being reliable in the presence of regurgitation and shunts. Thus, CMR opens the possibility of more accurate quantification of PVR. CMR-guided cardiac catheterization also allows other physiological parameters to be assessed including the construction of pressure volume (P-V) loops through simultaneous measurement of ventricular volumes and pressures. It has been shown that CMR is the most accurate and reproducible method of quantifying ventricular volumes and thus P-V loops constructed using this technique should be able to accurately gauge abnormal ventricular hemodynamics in disease.

## 22.3 Requirements for Interventional CMR

### 22.3.1 Interventional MR Suite

There are many specialist pieces of equipment required for interventional CMR. However, it can be argued that the most important is the interventional CMR suite. This is because safe procedures are very dependent on the environment in which they are performed. Though interventional CMR can be performed in isolation, most are performed in an environment where it is possible to revert to traditional X-ray fluoroscopy.

There are two common designs for interventional CMR suites. The simplest solution is to include the X-ray equipment in the radiofrequency (RF)-shielded CMR scanner room (Fig. 22.1), with the patient being transferred between the two imaging modalities by some form of moveable tabletop [3]. This requires the scanner room to be enlarged so that the X-ray equipment can be placed safely outside the 5 Gauss line. The enlarged room also enables ferromagnetic materials to be used in the 'X-ray side' of the room without risk of attraction by the static magnetic field. For this solution to work the X-ray intensifier must be shielded to prevent magnetic distortion, while all X-ray equipment must be shut down during CMR scanning to prevent RF interference. The main problems with this solution are that:

1. Bringing ferromagnetic equipment into the scanner room increases the risk of accidental transfer to the 'MR side' of the room, and
2. The enlarged RF-shielded room is significantly more expensive than a normal CMR scanner suite.

**Fig. 22.1** Photograph of an interventional CMR suite in a single-room RF-shielded room. (Courtesy of Reza Razavi, Kings' College London)



**Fig. 22.2** Photograph of an interventional CMR suite consisting of a separate catheterization laboratory and MRI scanner. The two rooms are separated by RF-shielded doors.



The second solution is to have separate MR scanners and cardiac catheterization suites separated by RF-shielded doors (Fig. 22.2) [4]. This solution has the benefit of being able to run both facilities independently, with the only separation

being the RF-shielded doors. However, there are disadvantages including: Further transfer distance for patients, requirement for two anesthetic machines, and the larger total floor space required.



Both solutions have been installed in various centers and the choice is mainly dependent on the requirements of the institution. Irrespective of the solution chosen, it is important that a suitable CMR scanner is used. Most importantly, the configuration of the scanner must allow sufficient access to the patient to perform catheter manipulation.

Over the last 5 years, there has been an increased use of CMR scanners in isolation without the immediate availability of X-ray fluoroscopy (Fig. 22.3). The safety of this approach has been demonstrated in a single-room CMR/X-ray environment (X-ray backup), to successfully perform X-ray free right-heart CMR-guided catheterization in patients with congenital heart disease, using only the CMR component of the suite [5]. Studies using CMR setups in isolation have confirmed the safety and applicability of this approach in both children with CHD [6] and adults undergoing PVR assessment [7].

It should be noted that vertical bore ‘open’ scanners are currently marketed for the interventional MR. However, in most there is still considerable distance between the operator

and the patient, making it difficult to manipulate catheters. Wide short horizontal bore scanners may be a better solution as the operator has better access to the patient’s groin. Of course, it is also important that the CMR scanner produces high-grade cardiac images and the earliest examples of short-bore scanners neither had good enough gradients nor magnetic field homogeneity to provide this. Nevertheless, new scanners have bored lengths of about 120 cm and diameters of about 70 cm, while producing excellent imaging. These new scanners offer a good compromise for interventional CMR. Another vital consideration is the need for in-room controls. Most CMR scanners are controlled from a control room outside the RF cage. However, in interventional MR the operator must be able to view real-time MR images and easily instruct changes in scanning to follow the catheter. Thus, interventional CMR scanners must have some form of in-room control and display that allows complete control of the MR scanner.

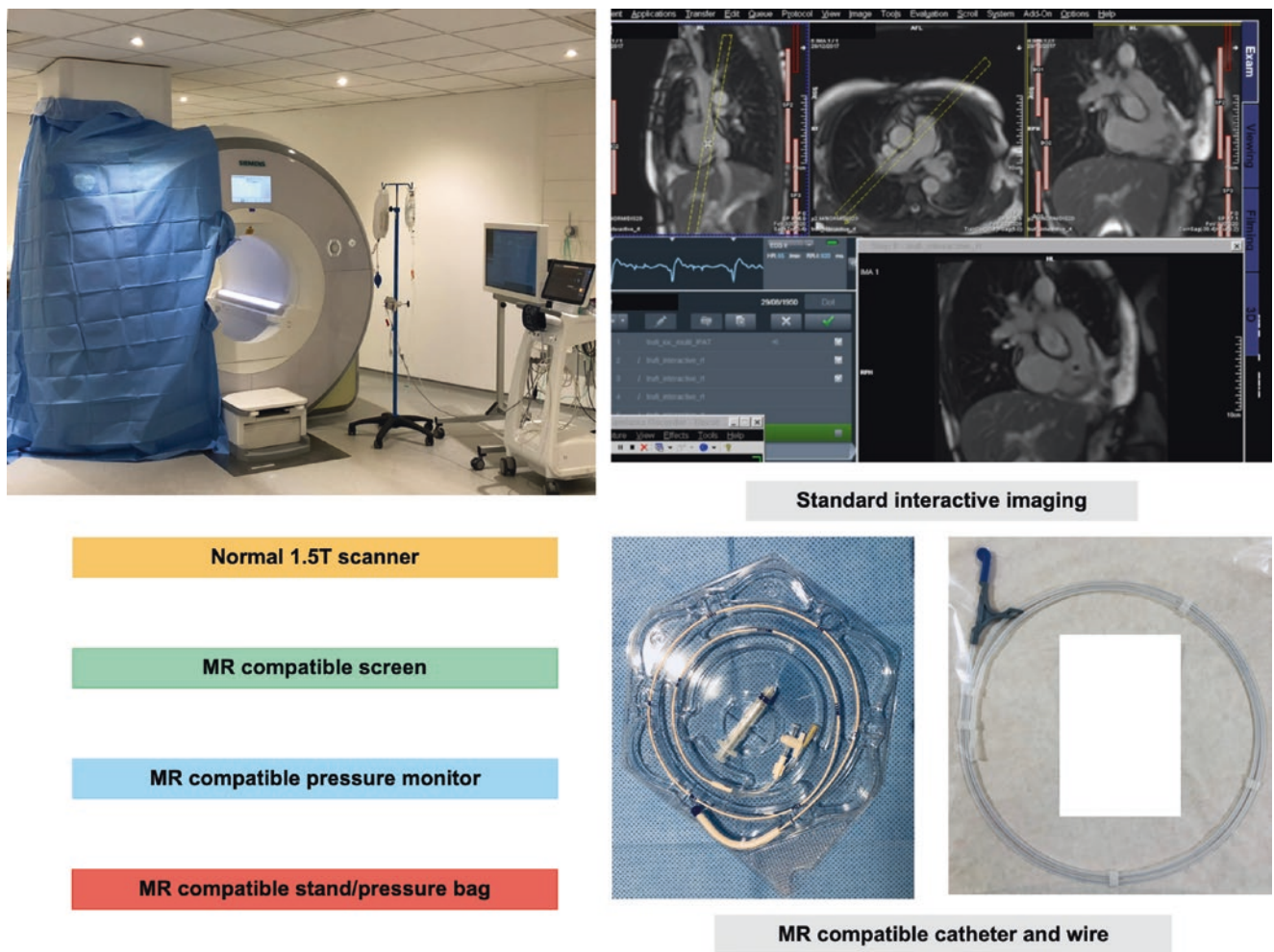


**Fig. 22.3** Setup for using interventional CMR in isolation

### 22.3.2 Real-Time Imaging

Real-time imaging is a prerequisite for CMR-guided interventions. Gradient echo sequences are generally used in real-time imaging due to their short acquisition times. Balanced steady-state free precession (b-SSFP) sequences have become the mainstay of CMR, offering excellent blood pool myocardial delineation and high SNR. In addition, real-time b-SSFP techniques have been used to assess cardiac function and dynamic anatomy. The majority of studies for CMR-guided cardiac catheterization use real-time b-SSFP sequences for catheter and anatomical visualization [8, 9]. In normal cardiac imaging, b-SSFP is performed using cardiac gating. However, for real-time imaging data must be acquired continuously with each  $k$ -space frame being filled in a sequential manner. The temporal resolution is therefore dependent on the time taken to fill a single  $k$ -space frame, which is in turn dependent on repeat time (TR) and the number of phase encoding steps. In b-SSFP imaging, TR is already short and therefore increased temporal resolution requires a reduction in the number of phase-encode steps. This can be accomplished by choosing a lower imaging matrix (i.e.,  $128 \times 128$ ), utilizing a rectangular field of view (FOV) (i.e., 60% of FOV), and using the partial Fourier technique. Utilizing the techniques described above a temporal resolution of 100ms can be achieved translating into a frame rate of 10 per second [10]. This temporal resolution is sufficient for simple interventions (Fig. 22.4) but is probably not sufficient for more complex interventions in congenital heart disease. Another method of increasing temporal resolution is to undersample  $k$ -space and use information from multiple coils or temporal correlations to remove aliasing (i.e., SENSE or kt-BLAST). However, in interventional CMR, real-time acquisition must be coupled with real-time reconstruction. Most modern scanners are able to perform real-time reconstructions of non-undersampled data. Unfortunately, for techniques like SENSE and kt-SENSE, reconstruction is computationally more intensive and real-time image display is difficult. Thankfully the advent of parallel computing, particularly on graphical processing units, does open the possibility of real-time reconstruction of heavily undersampled data [11]. Thus, real-time techniques with a similar spatial and temporal resolution to traditional gated CMR could be used for interventions.

In addition to real-time acquisition, a further requirement of interventional CMR is the ability to interactively change the imaging plane to follow the catheter. This can be accomplished either automatically or manually depending on the mechanism of catheter tracking. Several groups are actively developing methodologies to improve the ability to visualize and track catheters within the heart. These include tracking multiple points on the catheter on an overlaid 3D MR angio-

gram and real-time acquisition of multiple perpendicular planes through the thorax. It is the development of these real-time acquisition and visualization techniques that have made MR-guided cardiac catheterization a possibility.

### 22.3.3 Catheter Visualization

Catheters can be visualized within the cardiovascular system using either active or passive methods. Passive catheter visualization relies on inherent properties of the catheter to provide either local signal enhancement or loss. In b-SSFP sequences the blood is bright and therefore techniques that rely on signal loss/voids are more useful in the cardiovascular system. Several methods have been proposed including the use of dysprosium rings placed on conventional catheters, and the use of standard balloon catheters filled with CO<sub>2</sub>. The signal void produced by dysprosium is due to its inherent lack of signal and magnetic susceptibility artifact [12]. Thus, the signal void produced by a dysprosium ring is larger than the ring itself, which is good as it increases the prominence of the marker. Furthermore, dysprosium rings can provide visualization of the whole length of the catheter. Unfortunately, currently no such catheters are available for human use. The signal void produced by CO<sub>2</sub> is also due to inherent lack of signal. Magnetic susceptibility is less important in this technique and the signal void produced by a balloon filled with CO<sub>2</sub> is approximately the same size as the balloon itself. The benefit of this approach is that it uses standard catheter laboratory equipment and thus, poses no greater safety risk to the patient [7, 10]. More recently, studies have used catheter balloons filled with gadolinium contrast agent [5, 9], providing positive contrast, which may prove more useful for automated catheter-tip tracking in the future.

The other approach is to use active catheter visualization and tracking techniques (Fig. 22.5). Active devices are connected to the scanner and comprise of micro-coils or loopless antennae, which can be used for signal reception. Automatic tracking of micro-coil tips is possible using three 1D projections. Projection imaging can be interleaved with b-SSFP imaging for superimposition of tracking data onto real-time anatomy. As loopless antennae receive signal from the surrounding protons during conventional 2D imaging, they can be visualized along their length and superimposed onto the image from the surface coil [13, 14]. Thus, these active techniques have significant advantages over passive catheter visualization. Unfortunately, the fundamental problem with active devices is their susceptibility to heating with the MR environment. Several techniques are under development to solve this problem, but currently, they have not been utilized in patients with congenital heart disease.



### 22.3.4 Devices and Delivery Systems

Almost all interventional devices (i.e., stents and ASD devices) are MR compatible after insertion. In fact, several groups have performed CMR immediately after device implantation with no adverse effect on device function [3, 4]. However, this is not the case for most delivery systems, as they require guide wires. Guide wires enable proper positioning and delivery of almost all interventional cardiac devices. They are traditionally metallic as this gives them the right combination of stiffness, flexibility, and strength.

Unfortunately, long guide wires are known to heat up during MR scanning. Thus, they are not suitable for interventional CMR. Currently, this is the biggest impediment to the development of interventional cardiac MR. Several solutions have been tried and tested over the last decade [6, 15], including active detuning and decoupling during scanning, integration of serial transformers into the guide wire [16], and the use of novel non-conductive material such as fiberglass. These MR-compatible guide wires are currently in various stages of regulatory approval. Though they may well revolutionize interventional CMR, they are not routinely used at present.

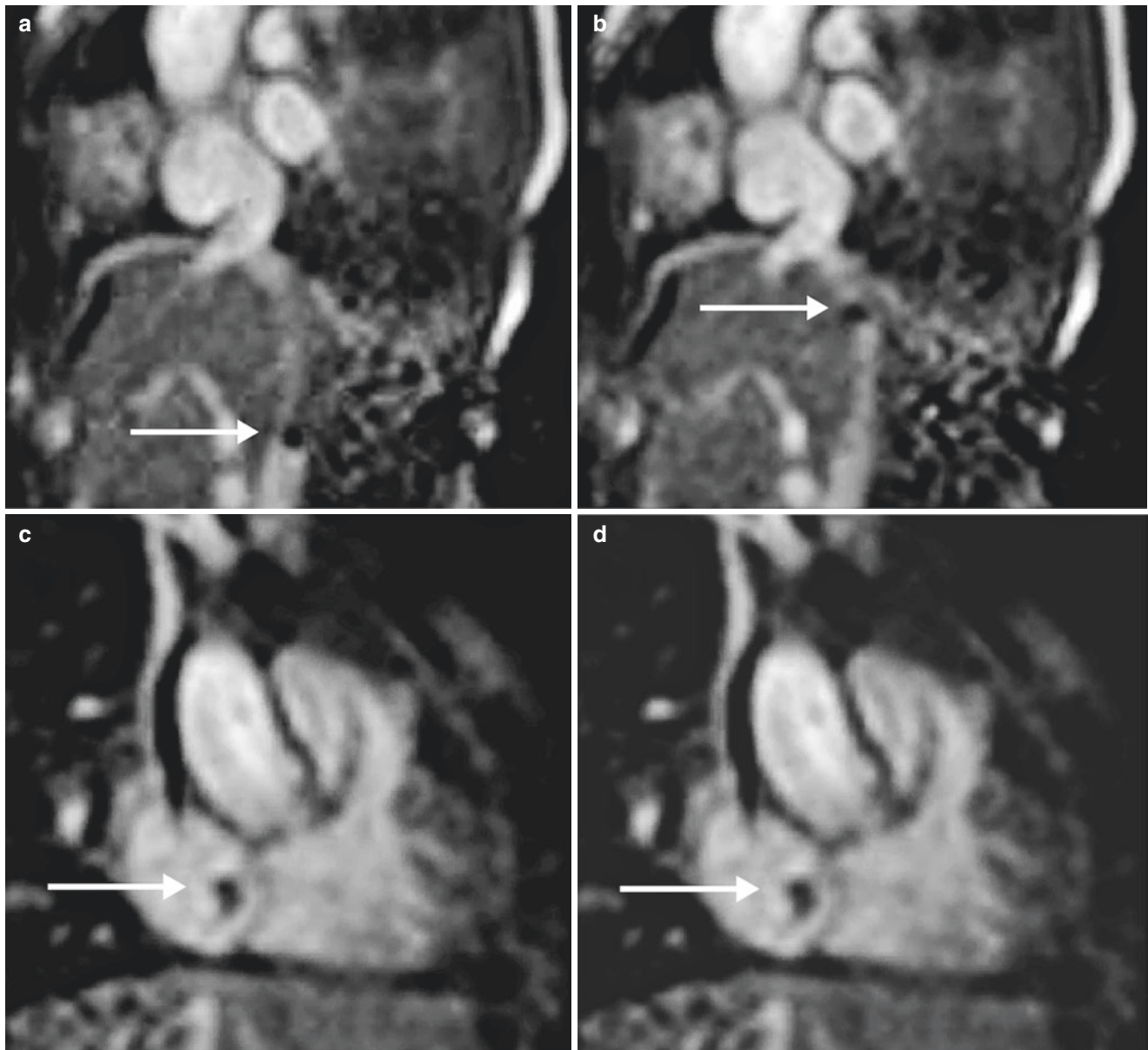


**Fig. 22.4** Frames of CMR guided cardiac catheterization. Imaging sequence: real time b-SSFP. White arrows point to the signal void produced by the CO<sub>2</sub>-filled balloon tip. (a) Catheter in inferior vena cava. (b) Catheter at inferior vena cava right atrial junction. (c) Catheter in

right atrium. (d) Catheter being advanced into right ventricle. (e) Catheter in right ventricular outflow tract. (f) Catheter in right pulmonary artery. (Courtesy of Reza Razavi, Kings' College London)

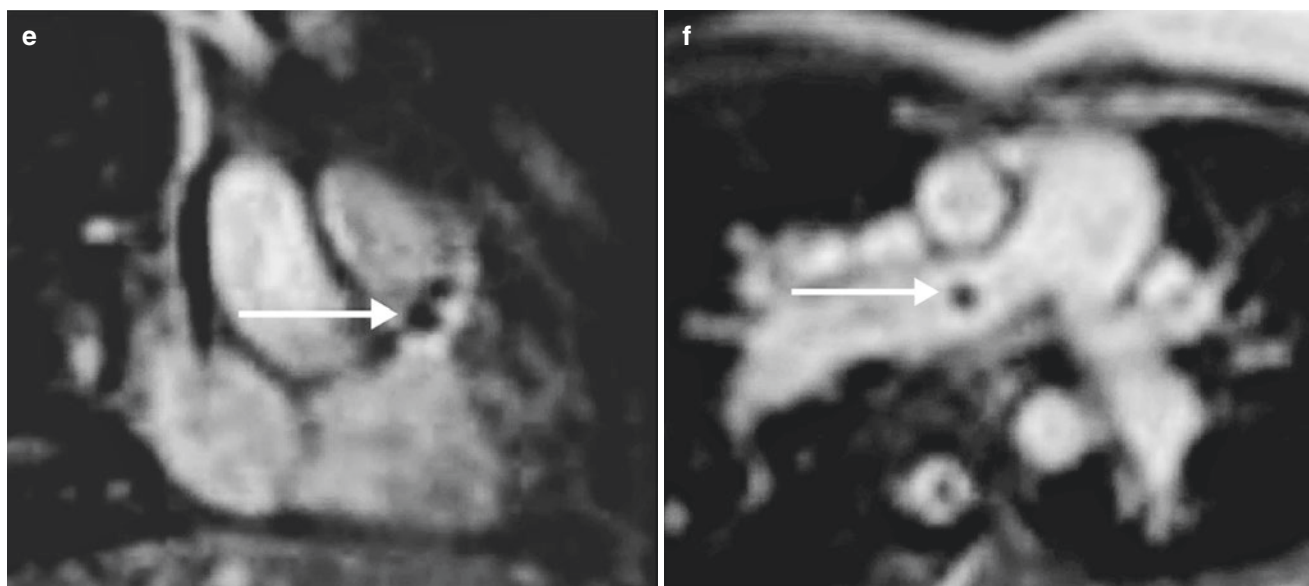


**Fig. 22.4** (continued)

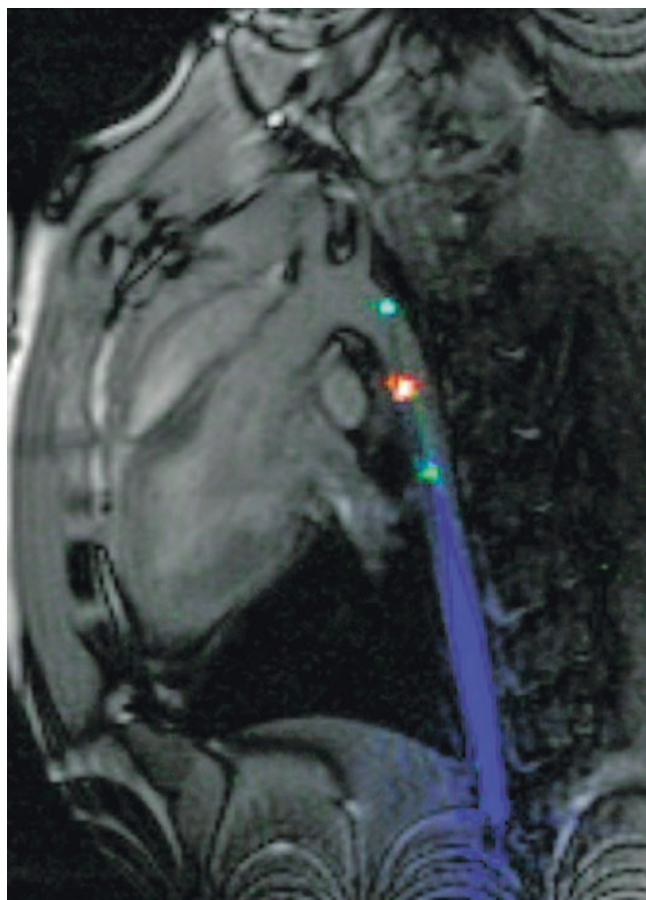


**Fig. 22.5** b-SSFP images of an active catheter inserted percutaneously from the femoral artery, through the aorta, and towards the left subclavian artery. Device-related signal is evident with independent catheter receiver channels allowing colorized reconstruction of the catheter (first and third coil, *green*; middle coil, *red*; catheter shaft, *blue*). (Courtesy Ozgur Kocaturk, NHLBI, NIH)

### 22.3.5 X-Ray/MR Fusion Technology

As previously stated, the lack of MR-compatible delivery systems makes true interventional CMR difficult in humans. Thus, there is a need for an interim solution that uses the power of CMR to improve cardiac catheterization procedures. This can be achieved by X-ray/MR fusion, which uses CMR data to provide anatomical roadmap during fluoroscopy-guided procedures [17, 18] (Videos 22.1 and 22.2, Fig. 22.6). The benefit of this fusion approach is that 3D CMR information can be used to improve visualization during 2D projection fluoroscopic imaging. A necessity for this approach is accurate registration of CMR and X-ray space to prevent misalignment of CMR overlays during catheterization. It is also important that these overlays automatically respond to positioning of the X-ray fluoroscopy C-arms. This can be achieved by using MR and X-ray visible fiducial markers and real-time display of various 3D CMR data depending on the position of the patient and the C-arms. Several centers have demonstrated the use of fusion technology to aid congenital interventions as well as electrophysiological studies.

### 22.3.6 Safety Procedures for Interventional MR

There is a great deal of literature on MR hazards and safety issues and a comprehensive review and discussion of the subject is outside the scope of this chapter (see Chap. 2). However, this area is probably one of the most important in interventional CMR. Traditional catheterization utilizes many ferromagnetic objects, from scissors to introducer needles. In the interven-



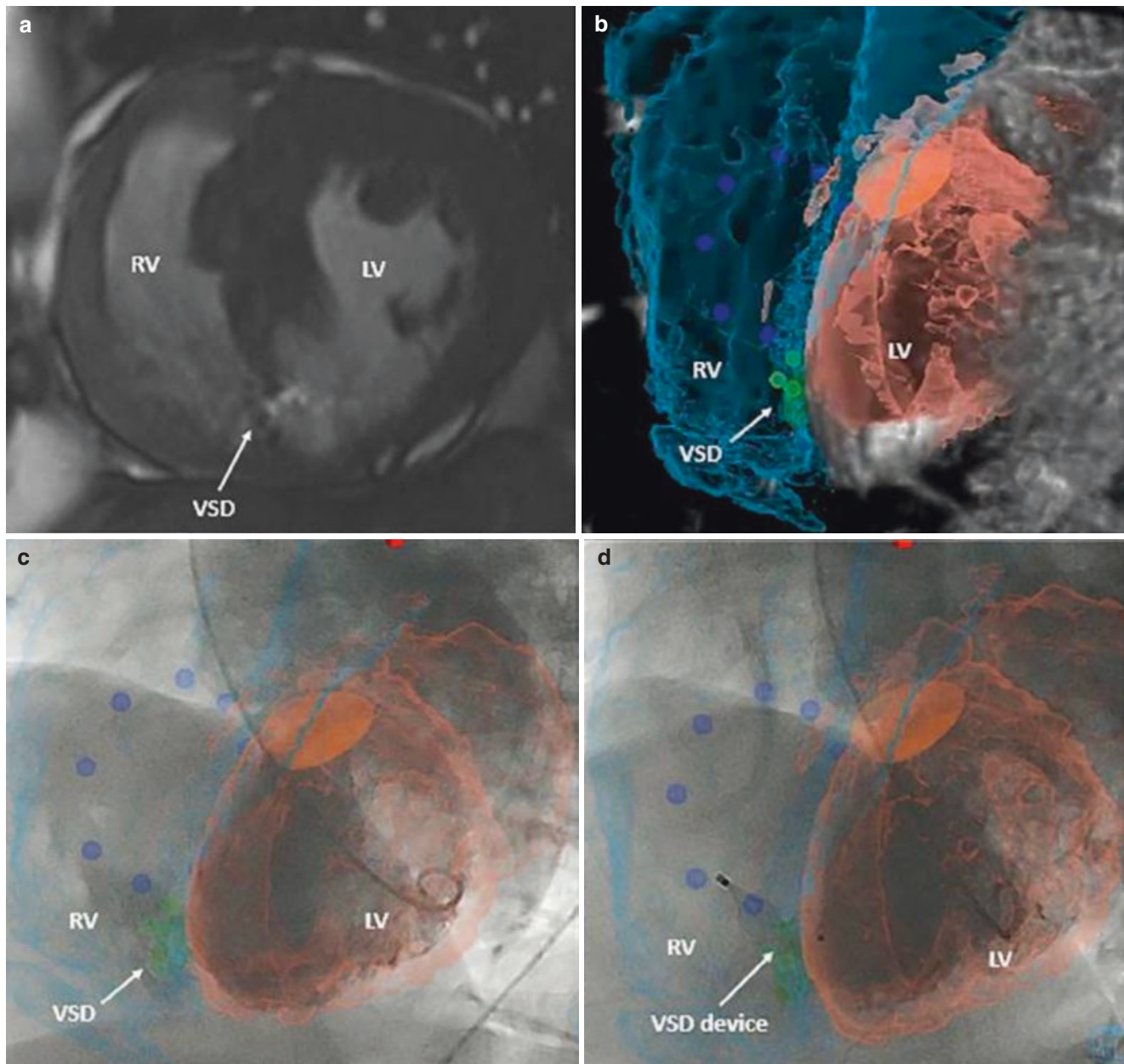


**Fig. 22.6** XFM-guided ventricular septal defect (VSD) device closure. XFM-guided VSD closure in an adult patient. (a) VSD identification by CMR; (b) CMR segmentation of the right ventricle (turquoise), left ventricle (peach), aortic outflow (orange), tricuspid valve markers (dark blue), and VSD (green) demonstrating the ideal camera gantry angle for

intervention; (c) left ventriculogram in the LAO 57/CRAN 15 projections with peak contrast opacification of VSD demonstrating difficulty in angiographic delineation of the shunt; and (d) post device closure of VSD with the device position corresponding to the XFM VSD marker. (With permission from Grant EK, Kanter JP, Olivieri LJ, et al. [18])

tional CMR environment, these would be attracted to the magnet leading to possible projectile injuries. Of course, it is not feasible to replace all the ferromagnetic objects used during cardiac catheterization. Thus, most human interventional CMR relies on using these objects outside the 5 Gauss line of the scanner. In units with interventional CMR suites, this entails performing the initial part of the procedure (i.e., intravascular sheath insertion) in the ‘X-ray side’ of the room before transfer

to the ‘MR side’ of the room. Prior to transfer, mechanisms must be in place to ensure that no ferromagnetic equipment is transferred over with the patient. Other safety features include:

- Compulsory MR safety training for all staff involved in interventional MR procedures.
- Clear demarcation of the ferromagnetic safe and unsafe areas by different color floor covering.

- Restricted entrance to the facility during an interventional MR procedure. This may include prior agreement on which staff members should cross into the MR side of the room.
- Tethering of all Ferromagnetic equipment to the walls. All ferromagnetic equipment should be outside the 5 G line, tethering prevents accidental placement within the magnetic field.
- A safety officer present in the interventional suite throughout the procedure to ensure the safety protocols are adhered to, especially at the time of patient transfer.

The interventional CMR environment is an intrinsically dangerous environment. However, when the correct safety procedures are instigated catheterization can be performed in a safe and reliable manner.

## 22.4 Applications of Interventional CMR

### 22.4.1 Experimental Animal Studies

There have been a number of studies performed that demonstrate the possibility of CMR-guided cardiac catheterization in animal models. Simultaneous measurement of invasive pressure and MR flow has been demonstrated in a porcine model of atrial septal defect (ASD) [8]. In this study, active catheter techniques were used to manipulate the catheter into the right heart from the inferior vena cava. Postmortem analysis revealed no cardiac damage associated with catheterization. The majority of other studies have centered on CMR-guided cardiac interventions. These include placement of ASD/VSD occluders, valve stents in the aortic and pulmonary position, and intra-myocardial injection of stem cells. These studies demonstrate that interventional device placement under passive and active MR guidance is feasible in animal models, showing the benefits of greater anatomical information. In addition, they demonstrate the benefit of physiological monitoring with CMR prior to and after the intervention (i.e., the measurement of valvular regurgitation in valve stent placement). Unfortunately, as previously noted, most of the delivery systems used in these studies are not currently suitable for human use due to safety issues with heating. Until CMR-compatible guide wires and delivery systems are available solely CMR-guided placement of devices in humans is difficult. However, the availability of the real-time techniques described above coupled with passive catheter visualization and PC-MR do make MR-guided diagnostic catheterization in humans a possibility.

### 22.4.2 Diagnostic MR-Guided Cardiac Catheterization

#### 22.4.2.1 Assessment of Pulmonary Vascular Resistance

There have been a number of studies performed demonstrating the feasibility of diagnostic CMR-guided cardiac catheterization. Most of these studies have revolved around PVR assessment of patients with pulmonary hypertension [7, 19, 20]. Currently, PVR is calculated using invasive pressure and flow measurements. However, as previously pointed out invasive flow techniques like thermodilution and the Fick method are prone to inaccuracy. Of course, during CMR-guided cardiac catheterization it is possible to measure pulmonary artery flow using velocity-encoded phase contrast MR. This technique is known to be accurate and may represent the in-vivo gold standard for assessment of flow. Thus, by combining this data with invasive pressure measurements, MR-guided cardiac catheterization can provide a better way to assess PVR. In the first demonstration of this technology, standard balloon wedge catheters were used during MR-guided cardiac catheterization [19]. The benefit of these catheters is that they contain no metal so there is no risk of RF heating. Furthermore, the balloon tip can be filled with CO<sub>2</sub> (or gadolinium contrast) enabling visualization of the catheter tip. Visualization of the catheter is achieved using real-time b-SSFP imaging with manual tracking of the catheter using in-room controls. The catheter is navigated into the pulmonary artery to measure invasive pulmonary artery pressure (Fig. 22.7). Once the catheter is in place, pulmonary artery flow can be measured and combined with invasive pressure measurement to calculate PVR. This study showed

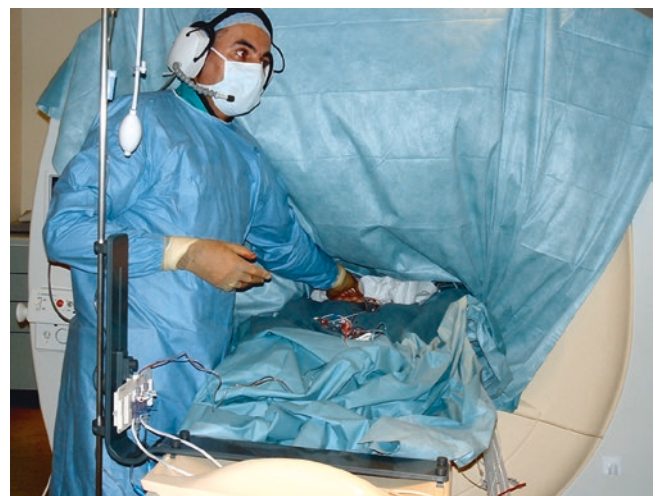


**Fig. 22.7** MR guided cardiac catheterization. (Courtesy of Reza Razavi, Kings' College London)



a significant discrepancy between PVR calculated using Fick-derived flow and MR-derived flow, particularly in the presence of oxygen. This appeared secondary to inaccuracies in the Fick method and suggests that MR may be superior to the traditional Fick method. Further work has demonstrated the utility of this MR technique in a homogeneous population of patients with moderate/severe pulmonary hypertension [21]. The study, and others, also demonstrated the improved precision of phase contrast MR over thermodilution methods [22, 23]. Several groups are now routinely performing all clinical PVR studies using a combination of MR and invasive pressure measurements. Another benefit of using MR to assess physiological parameters during diagnostic catheterization is that it allows other more sophisticated measurements to be made. These include measures like pulmonary arterial compliance, which has been measured during MR-guided cardiac catheterization, and may provide added information about PVR [22].

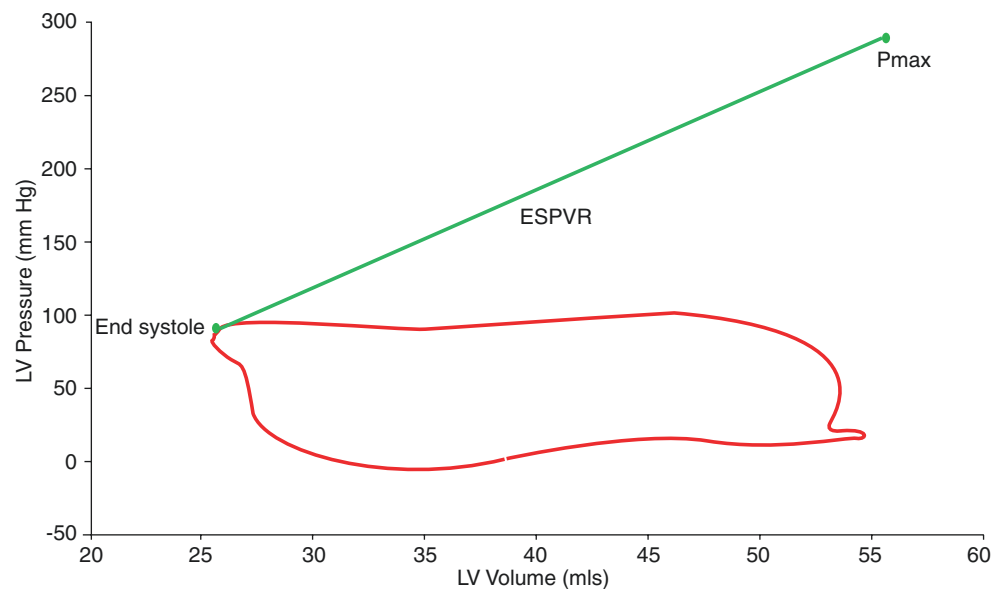
Another example is construction of P-V loops through simultaneous measurement of ventricular volumes and pressures [24, 25] (Fig. 22.8). It has been shown that CMR is the most accurate and reproducible method of quantifying ventricular volumes and thus P-V loops constructed using this technique are able to accurately gauge abnormal ventricular and vascular hemodynamics in pulmonary hypertension. However, measuring these more sophisticated parameters using CMR does raise some problems. This is because only fluid-filled catheters can be used in the MR environment. Unfortunately, fluid-filled catheters have well-known problems with dampening and resonance, which can affect the

shape of the pressure curve. This does not have a major effect on mean pressure but may be problematic when constructing P-V loops. Thus, to really make this technology clinically usable MR-compatible micromanometers must be developed. Several groups are developing such devices based on fiber-optic transmission and these should be available in the near future. Furthermore, more work is required on the best way to combine real-time pressure data with gated flow and cine data acquired over several cardiac cycles. It should be noted that MR guidance is not necessary to harness the power of MR for physiological assessment. Some groups with interventional CMR suites would catheterize under X-ray guidance (which is currently quicker than MR guidance) and then transfer to CMR for flow or volume assessment. This is particularly true in unstable patients with PH in whom procedure time must be limited. Nevertheless, both MR-guided and MR-augmented diagnostic cardiac catheterization have the potential to significantly change practice.

#### 22.4.2.2 Assessment of Congenital Heart Disease

The assessment of congenital heart disease patients with CMR has been demonstrated over the last 20 years [3, 5, 26]. However, the use of this technology has not become widespread, in part as the diagnostic capabilities of CMR have increased and the need for diagnostic cardiac catheterization, except in the setting of PVR assessment, has declined. Despite this, the increasing experience of CMR-guided PVR studies may lead to increasing confidence in the use of interventional CMR for complex cases.

**Fig. 22.8** Example of pressure volume constructed using simultaneously acquired pressure and MR volumetric data. Maximum pressure is calculated using the single beat method which allows calculation load independent contractility



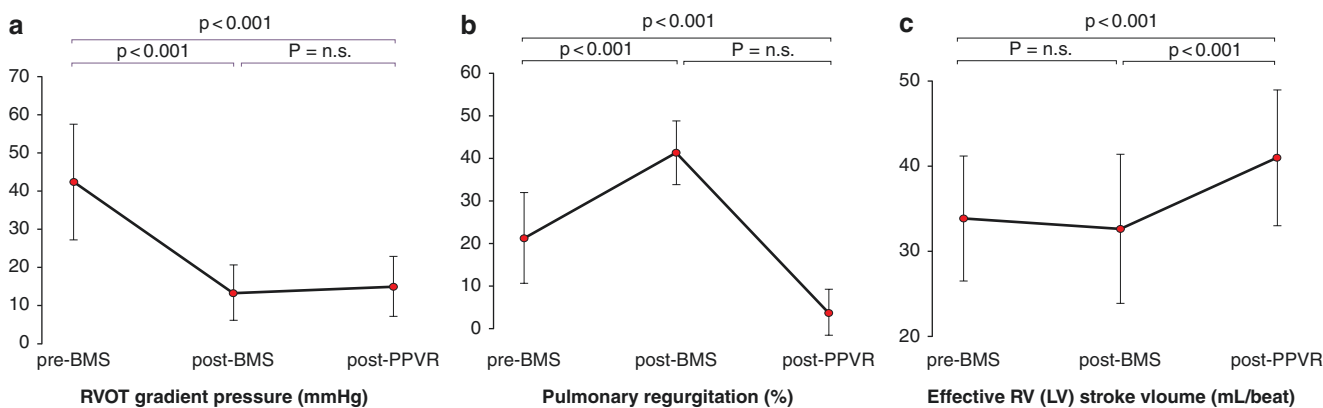


**Fig. 22.9** Acute comparison between bare metal stenting (BMS) and percutaneous pulmonary valve replacement (PPVR). (a) Changes in right ventricular outflow tract (RVOT) gradient—measured during cardiac catheterization—show a significant decrease after BMS, which is maintained after PPVR. (b) Changes in pulmonary regurgitation—measure during CMR—show the creation of free, severe pulmonary regur-

gitation following BMS, with restoration of pulmonary competence after PPVR. (c) Changes in measured effective right ventricular (RV) and left ventricular (LV) stroke volumes—also measured during CMR—show improved cardiac function following PPVR compared to BMS

### 22.4.2.3 Electrophysiology Assessment

Interventional CMR may be useful to guide navigation through the complex anatomy of repaired congenital heart disease for electrophysiology studies, but only limited human studies have been performed to date [27–29], to treat atrial lesions. The majority of studies utilizing CMR continue to use pre-catheter CMR to guide procedures [30] or to provide immediate post-procedural CMR assessment [31]. Despite the lack of the wider utilization of interventional CMR for delivering electrophysiological studies, there remains a keen interest in the potential role of this technology, with the increasing clinician experience of interventional CMR for simple atrial ablations, leading to the development of interventional CMR suites for electrophysiology studies [32].

### 22.4.2.4 CMR/Cardiac Catheterization Physiological Assessment

One interesting use of CMR in combination with cardiac catheterization is to utilize both methods to assess the immediate physiological response of an intervention. In one study, a comparison between the physiological response to bare metal stenting of pulmonary conduit stenosis to that of percutaneous pulmonary valve replacement (PPVR) [4]. In this setting, the ventricular volumes and pulmonary and aortic flow were assessed in the CMR side of an interventional CMR suite. The patient was then slid into the cardiac catheterization side of the suite and pressures in the right ventricle and pulmonary artery measures prior to and after bare metal stenting of the pulmonary conduit stenosis—removes stenosis but creates free pulmonary regurgitation. The patient was then slid back into the CMR scanner to assess the changes in volumes and flow. The patient was then slid back into the

catheterization side of the suite, a PPVR is implanted—maintains stenosis reduction and creates pulmonary valve competence—pressures measured, and then slid back into the CMR scanner for final assessment of cardiac volumes and flow (Fig. 22.9). This demonstrated superior acute cardiac physiology from PPVR compared to bare metal stenting for conduit stenosis.

## 22.5 Conclusion

The feasibility of using CMR-guided cardiac catheterization in humans has been demonstrated. However, a number of issues remain that need to be addressed before CMR-guided cardiac interventions enter widespread clinical use. Further developments by catheter manufacturing companies are needed in order to provide specific products for MR interventions. Currently, catheters are designed for use in the X-ray environment and, consequently, many contain ferromagnetic components (e.g., braiding in catheters) or long conducting materials (e.g., guide wires) that are potentially hazardous in the MR environment. Non-braided balloon catheters can be used in the MR environment; however, they often lack the desired torque and steerability. In addition, catheter visualization and tracking must be improved so that the whole length of the catheter can be automatically tracked. Once these issues have been resolved interventional cardiac MR will be possible in all patients. This should bring the benefits of elimination of exposure to X-ray radiation, better anatomical visualization, and increased physiological information. One area that may support the development of safe catheters and guide wires is the use of low-field CMR, which should reduce the potential hazards. In a recent published

experience at 0.55T, 7 of the 83 studies performed were CMR-guided right heart catheterization using commercial metallic guide wires [33]. Increasing clinical experience with CMR-guided PVR studies and atrial ablations should provide the necessary clinical skills to continue to drive interventional CMR over the next decade and increase its wider clinical adoption.

## References

- Ait-Ali L, Andreassi M, Foffa I, Spadoni I, Vano E, Picano E. Cumulative patient effective dose and acute radiation-induced chromosomal DNA damage in children with congenital heart disease. *Heart*. 2010;96:269–e274.
- Little MP, Azizova TV, Bazyka D, et al. Systematic review and meta-analysis of circulatory disease from exposure to low-level ionizing radiation and estimates of potential population mortality risks. *Environ Health Perspect*. 2012;120(11):1503–11. <https://doi.org/10.1289/ehp.1204982>.
- Razavi R, Hill DL, Keevil SF, et al. Cardiac catheterisation guided by MRI in children and adults with congenital heart disease. *Lancet*. 2003;362(9399):1877–82.
- Lurz P, Nordmeyer J, Muthurangu V, et al. Comparison of bare metal stenting and percutaneous pulmonary valve implantation for treatment of right ventricular outflow tract obstruction: use of an x-ray/magnetic resonance hybrid laboratory for acute physiological assessment. *Circulation*. 2009;119(23):2995–3001.
- Ratnayaka K, Kanter JP, Faranesh AZ, et al. Radiation-free CMR diagnostic heart catheterization in children. *J Cardiovasc Magn Reson*. 2017;19:65. <https://doi.org/10.1186/s12968-017-0374-2>.
- Veeram Reddy SR, Arar Y, Zahr RA, et al. Invasive cardiovascular magnetic resonance (iCMR) for diagnostic right and left heart catheterization using an MR-conditional guidewire and passive visualization in congenital heart disease. *J Cardiovasc Magn Reson*. 2020;22:20. <https://doi.org/10.1186/s12968-020-0605-9>.
- Knight DS, Kotecha T, Martinez-Naharro A, et al. Cardiovascular magnetic resonance-guided right heart catheterization in a conventional CMR environment - predictors of procedure success and duration in pulmonary artery hypertension. *J Cardiovasc Magn Reson*. 2019;21(1):57. <https://doi.org/10.1186/s12968-019-0569-9>.
- Schalla S, Saeed M, Higgins CB, Martin A, Weber O, Moore P. Magnetic resonance – guided cardiac catheterization in a swine model of atrial septal defect. *Circulation*. 2003;108(15):1865–70.
- Velasco Forte MN, Pushparajah K, Schaeffter T, et al. Improved passive catheter tracking with positive contrast for CMR-guided cardiac catheterization using partial saturation (pSAT). *J Cardiovasc Magn Reson*. 2017;19(1):60. <https://doi.org/10.1186/s12968-017-0368-0>.
- Miquel ME, Hegde S, Muthurangu V, et al. Visualization and tracking of an inflatable balloon catheter using SSFP in a flow phantom and in the heart and great vessels of patients. *Magn Reson Med*. 2004;51(5):988–95.
- Sorensen TS, Atkinson D, Schaeffter T, Hansen MS. Real-time reconstruction of sensitivity encoded radial magnetic resonance imaging using a graphics processing unit. *IEEE Trans Med Imaging*. 2009;28(12):1974–85.
- Bakker CJ, Hoogeveen RM, Hurtak WF, van Vaals JJ, Viergever MA, Mali WP. MR-guided endovascular interventions: susceptibility-based catheter and near-real-time imaging technique. *Radiology*. 1997;202(1):273–6.
- Dick AJ, Guttman MA, Raman VK, et al. Magnetic resonance fluoroscopy allows targeted delivery of mesenchymal stem cells to infarct borders in Swine. *Circulation*. 2003;108:2899–904. <https://doi.org/10.1161/01.CIR.0000095790.28368.F9>.
- Lederman RJ. Cardiovascular interventional magnetic resonance imaging. *Circulation*. 2005;112(19):3009–17.
- Yildirim KD, Basar B, Campbell-Washburn AE, et al. A cardiovascular magnetic resonance (CMR) safe metal braided catheter design for interventional CMR at 1.5 T: freedom from radiofrequency induced heating and preserved mechanical performance. *J Cardiovasc Magn Reson*. 2019;21:16. <https://doi.org/10.1186/s12968-019-0526-7>.
- Weiss S, Wirtz D, David B, et al. In vivo evaluation and proof of radiofrequency safety of a novel diagnostic MR-electrophysiology catheter. *Magn Reson Med*. 2011;65(3):770–7.
- Rhode KS, Hill DL, Edwards PJ, et al. Registration and tracking to integrate X-ray and MR images in an XMR facility. *IEEE Trans Med Imaging*. 2003;22(11):1369–78.
- Grant EK, Kanter JP, Olivieri LJ, et al. X-ray fused with MRI guidance of pre-selected transcatheter congenital heart disease interventions. *Catheter Cardiovasc Interv*. 2019;94(3):399–408. <https://doi.org/10.1002/ccd.28324>.
- Muthurangu V, Taylor A, Andriantsimiavona R, et al. Novel method of quantifying pulmonary vascular resistance by use of simultaneous invasive pressure monitoring and phase-contrast magnetic resonance flow. *Circulation*. 2004;110(7):826–34.
- Rogers T, Ratnayaka K, Khan JM, et al. CMR fluoroscopy right heart catheterization for cardiac output and pulmonary vascular resistance: results in 102 patients. *J Cardiovasc Magn Reson*. 2017;19(1):54. <https://doi.org/10.1186/s12968-017-0366-2>.
- Kuehne T, Yilmaz S, Schulze-Neick I, et al. Magnetic resonance imaging guided catheterisation for assessment of pulmonary vascular resistance: in vivo validation and clinical application in patients with pulmonary hypertension. *Heart*. 2005;91(8):1064–9.
- Muthurangu V, Atkinson D, Sermesant M, et al. Measurement of total pulmonary arterial compliance using invasive pressure monitoring and MR flow quantification during MR guided cardiac catheterization. *Am J Physiol Heart Circ Physiol*. 2005;289(3):H1301–6.
- Arar Y, Hussain T, Zahr RA, et al. Fick versus flow: a real-time invasive cardiovascular magnetic resonance (iCMR) reproducibility study. *J Cardiovasc Magn Reson*. 2021;23:95. <https://doi.org/10.1186/s12968-021-00784-7>.
- Kuehne T, Yilmaz S, Steendijk P, et al. Magnetic resonance imaging analysis of right ventricular pressure-volume loops: in vivo validation and clinical application in patients with pulmonary hypertension. *Circulation*. 2004;110(14):2010–6.
- Brener MI, Masoumi A, Ng VG, et al. Invasive right ventricular pressure-volume analysis: basic principles, clinical applications, and practical recommendations. *Circ Heart Fail*. 2022;15(1):e009101. <https://doi.org/10.1161/CIRCHEARTFAILURE.121.009101>.
- Velasco Forte MN, Roujol S, Ruijsink B, et al. MRI for guided right and left heart cardiac catheterization: a prospective study in congenital heart disease. *J Magn Reson Imaging*. 2021;53(5):1446–57. <https://doi.org/10.1002/jmri.27426>.
- Sommer P, Grothoff M, Eitel C, et al. Feasibility of real-time magnetic resonance imaging- guided electrophysiology studies in humans. *Europace*. 2013;15:101–8. <https://doi.org/10.1093/europace/eus230>.
- Hilbert S, Sommer P, Gutberlet M, et al. Real-time magnetic resonance-guided ablation of typical right atrial flutter using a combination of active catheter tracking and passive catheter visualization in man: initial results from a consecutive patient series. *Europace*. 2016;18(4):572–7. <https://doi.org/10.1093/europace/euv249>.

29. Chubb H, Harrison JL, Weiss S, et al. Development, preclinical validation, and clinical translation of a cardiac magnetic resonance - electrophysiology system with active catheter tracking for ablation of cardiac arrhythmia. *JACC Clin Electrophysiol.* 2017;3(2):89–103. <https://doi.org/10.1016/j.jacep.2016.07.005>.
30. Mukherjee RK, Whitaker J, Williams SE, et al. Magnetic resonance imaging guidance for the optimization of ventricular tachycardia ablation. *Eurospace.* 2018;20:1721–32. <https://doi.org/10.1093/europace/euy040>.
31. Grant EK, Berul CI, Cross RR, et al. Acute cardiac MRI assessment of radiofrequency ablation lesions for pediatric ventricular arrhythmia: feasibility and clinical correlation. *J Cardiovasc Electrophysiol.* 2017;28:517–22. <https://doi.org/10.1111/jce.13197>.
32. Bijvoet GP, Holtackers RJ, Smink J, et al. Transforming a pre-existing MRI environment into an interventional cardiac MRI suite. *J Cardiovasc Electrophysiol.* 2021;32(8):2090–6. <https://doi.org/10.1111/jce.15128>.
33. Campbell-Washburn AE, Ramasawmy R, Restivo MC, et al. Opportunities in interventional and diagnostic imaging by using high-performance low-field-strength MRI. *Radiology.* 2019;293:384–93. <https://doi.org/10.1148/radiol.2019190452>.





# Emerging Roles for Cardiovascular Magnetic Resonance in Adult Congenital Heart Disease Electrophysiology

Sophie A. Jenkins, Jennifer Keegan, Sabine Ernst, and Sonya V. Babu-Narayan

## 23.1 Introduction

The population of adults with congenital heart disease is growing. Most children with congenital heart disease now survive into adulthood thanks to innovations in cardiac surgery that allow repair or palliation of many anatomical defects. However, arrhythmia and sudden death remain important causes of late morbidity and mortality. As the population of adult congenital heart disease (ACHD) ages there is an increasing burden of arrhythmia requiring specialist care. Rhythm disturbances may be the first presenting symptom and herald a need for surgical or transcatheter intervention in which case treatment should be directed at the underlying cardiovascular haemodynamics. In this case, electrophysiological (EP) intervention is a secondary concern. Arrhythmia and sudden cardiac death (SCD) may, alternatively occur in the absence of a target haemodynamic lesion. Arrhythmia mechanisms vary according to the exact underlying anatomic congenital defect and method and timing of surgical repair. Whilst the arrhythmia can relate to underlying structural heart disease, such as Wolff-Parkinson-White syndrome associated with Ebstein's anomaly, it often relates to surgically acquired scars combined with chamber enlargement as a consequence of abnormal pressure and volume loads. In congenital heart disease, atrial arrhythmias frequently emanate from the right atrium or right ventricle (RV) and are not

generally confined to the left atrium as with atrial fibrillation triggered by pulmonary vein muscle bundles. ACHD patients with atrial arrhythmia are at particular risk of tachy-myopathy and existing haemodynamic lesions such as valvular regurgitation may be exacerbated by arrhythmia. There is also overlap in clinical presentations, such that ACHD patients presenting with atrial arrhythmia are at higher risk of ventricular arrhythmia [1]. Atrial arrhythmia is well recognised as an important indicator of ventricular dysfunction in congenital heart disease [2]. Adults with congenital heart disease are at risk of SCD and may be referred for diagnostic EP ventricular stimulation study to aid risk stratification [1, 3, 4]. Both atrial and ventricular stimulation at EP study may therefore be indicated for the same patient.

## 23.2 Challenges in EP Procedures for Patients with Congenital Heart Disease

Patients with congenital heart disease are arguably the most challenging patient cohort amongst arrhythmia patients presenting for catheter ablation procedures. Arrhythmia in ACHD is especially difficult to target and treat with EP interventions not least due to the multitude of potential tachycardia substrates that may need to be understood in the presence of complex anatomy and limited accessibility of cardiac structures. Prerequisites for successful treatment include clear and detailed understanding of the clinically relevant tachycardia, the underlying congenital anatomy including rare variants, dimensions of target chambers, previous surgical and transcatheter interventions, and venous and arterial access required. Surgical variations may include differing

S. A. Jenkins · S. Ernst · S. V. Babu-Narayan (✉)  
Royal Brompton Hospital, Part of Guy's and St Thomas' NHS  
Foundation Trust, London, UK

National Heart and Lung Institute, Imperial College, London, UK  
e-mail: [s.babu-narayan@imperial.ac.uk](mailto:s.babu-narayan@imperial.ac.uk)

J. Keegan  
National Heart and Lung Institute, Imperial College, London, UK  
e-mail: [j.keegan@imperial.ac.uk](mailto:j.keegan@imperial.ac.uk)

suture line location, closure of the left atrial appendage, and variation in which side of surgical baffles the coronary sinus or atrioventricular node may be situated postoperatively. Cardiac surgical procedures might also include intraoperative ablation by radiofrequency current or cryoenergy. These can serve as iatrogenic sources of scars that present as the underlying substrate causing re-entrant tachycardia. Operative notes, therefore, warrant meticulous study. Access to the target chamber(s) might be limited following previous surgery to redirect blood flow, for example such as in atrial redirection surgery for transposition of the great arteries (TGA) or total cavopulmonary connection. Conventional, frequently used vascular access routes may be impossible. Three-dimensional guidance during the ablation procedure itself may facilitate the EP procedure. EP studies in ACHD patients, therefore, specifically merit forethought and individualised approaches.

## 23.3 CMR for EP Procedure Planning

### 23.3.1 Haemodynamic Assessment, Appropriateness, and Safety to Proceed

All adult congenital patients merit a full cardiovascular magnetic resonance (CMR) haemodynamic assessment. If there is a target haemodynamic lesion that needs addressing, EP intervention may not be indicated, at least not immediately. Alternatively, EP study may be contraindicated, for example, due to intracardiac thrombus, which can easily be diagnosed with CMR (Fig. 23.1). Once these are excluded CMR imaging can be focused towards the needs of the electrophysiologist.

### 23.3.2 Planning of Venous and Arterial Access Routes

Planning the necessary vascular access steps to reach all relevant heart chambers is required. Less usual venous and arterial access strategies may be required.

Femoral vessels may be blocked due to previous interventional catheterisation, previous surgical femoral access for cardiopulmonary bypass, or longstanding venous and arterial lines required for intensive care in infancy. Arterial vessels may be hypoplastic in patients with aortic coarctation. Venous anomalies, such as left superior vena cava to coronary sinus or interrupted inferior vena cava with azygos continuation, are easily documented by CMR.

All venous and arterial vascular access routes and options need to be determined pre-procedure to allow appropriate equipment to be identified and made available. If intrahepatic venous approach or transbaffle puncture is necessary, the patient should be adequately counselled of the consequent risk–benefit ratio. Non-conventional EP strategies may warrant consideration. For example, the use of remote magnetic navigation for EP catheter guidance may avoid transhepatic cannulation or baffle puncture [5].

### 23.3.3 Useful Intracardiac Shunts

CMR may identify “useful” intracardiac shunts, or useful residual or postoperative anomalous connections that will allow increased options for the electrophysiologist. For example, the presence of an atrial septal defect, patent foramen ovale, patent fenestration, baffle leak, or ventricular septal defect may allow more choice of access routes to the chamber of interest (Figs. 23.2 and 23.3).

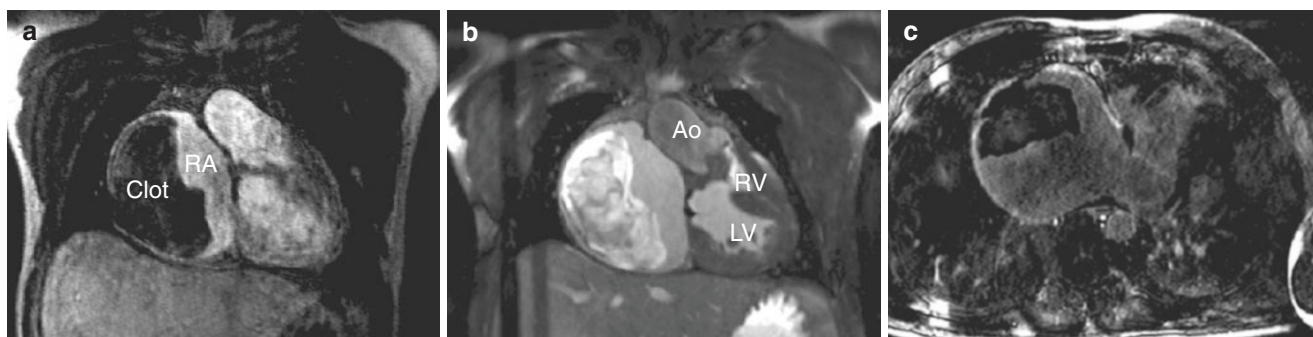


**Fig. 23.1** Large clot in right atrium post-atrio-pulmonary Fontan with consequent decision not to proceed to EP study. This 26-year-old man presented with persistent atrial tachycardia status post-Fontan operation for double inlet left ventricle, transposed great arteries, left-sided anterior subaortic rudimentary RV, and ventricular septal defect. The patient was studied in the rate-controlled atrial tachycardia. (a) CE-MRA

showing large clot in dilated right atrium. (b) 3D bSSFP image showing large clot in dilated right atrium with varying signal intensity suggestive that the inner core is more longstanding than the more recently laid down outer regions. This was timed in systole. (c) 3D LGE CMR showing large clot in the dilated right atrium. The right atrial walls appear thickened and enhanced

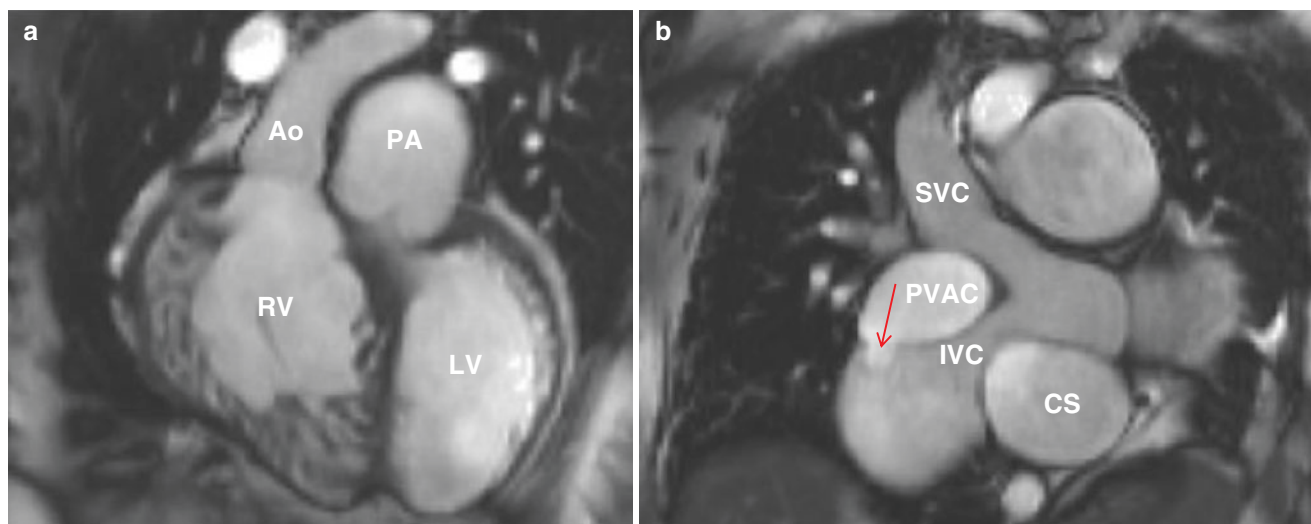


**Fig. 23.2** Useful intracardiac shunt for EP procedure; baffle leak post-Mustard operation for transposition of the great arteries. This 35-year-old woman status post-Mustard operation for transposition of the great arteries presented with atrial tachycardia. This was clinically likely to emanate from the pulmonary venous compartment. (a) The transposed great vessels with parallel orientation are noted. The RV is hypertro-

phied as expected. The pulmonary artery is dilated. (b) A baffle leak was seen (red arrow) from the pulmonary to the inferior systemic venous compartment. The procedure access routes include retrograde access to the pulmonary venous compartment from the aorta but also venous puncture-only, with access to the pulmonary venous compartment from the systemic venous compartment through the baffle leak

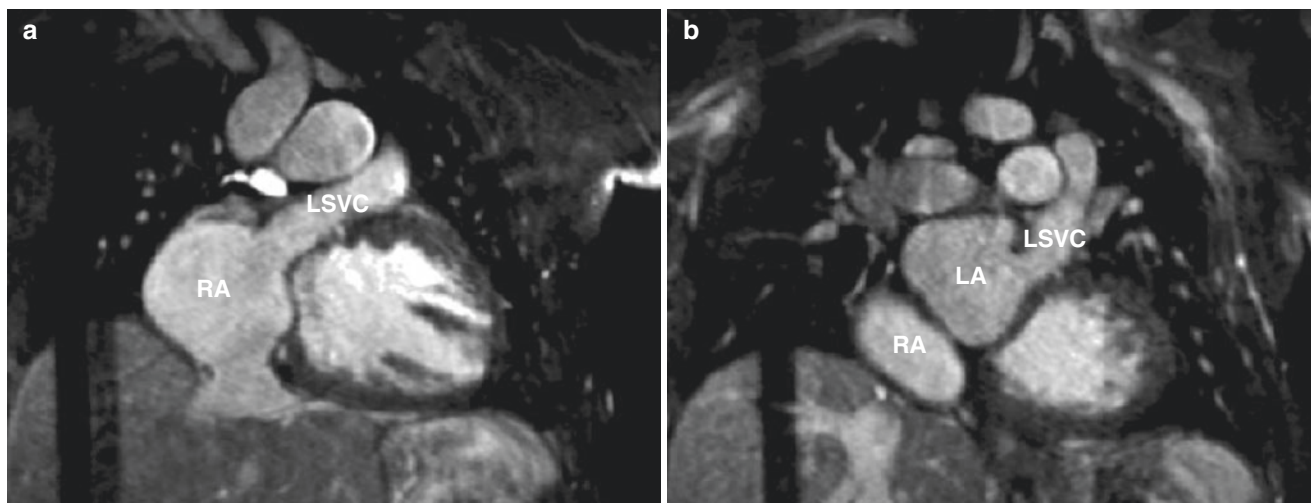


**Fig. 23.3** Venous connection to both atria allowing avoidance of arterial puncture. This 19-year-old man had complex congenital heart disease including left atrial isomerism for which he underwent intra-atrial baffling of his systemic venous return and subsequent balloon dilatation of the inter-atrial baffled superior vena caval pathway. The expected findings were that his left-sided SVC would be baffled to the right atrium with or without narrowing at the entrance to the right atrium. (a)

The connection between the left SVC and the right atrium was easily demonstrated with 3D bSSFP as was hepatic venous return to the right atrium. (b) An unexpected connection between the left SVC and the left atrium was also demonstrated. There was hemiazygos return to the left SVC. EP access options included either hemiazygos or left SVC venous access to the right atrium and the left atrium in addition to arterial retrograde access if needed

### 23.4 CMR to Provide 3D Roadmaps for EP Procedures

3D imaging to provide an anatomical roadmap during EP procedures is invaluable, particularly in congenital heart disease. Normal cardiac anatomy differs substantially from patient to patient but these individual differences are rela-

tively easily predictable from positions of catheters and the operator can mentally visualise the individual cardiac structures in standard fluoroscopy projections. However, in ACHD the orientation and spatial relationships may be challenging to understand, particularly after intra-atrial baffle procedures. There may be distortion and cardiac dilatation. Progressive myocardial fibrosis can result from growth and



advancing age. Scoliosis which is common in congenital heart disease patients may itself radically alter the relevant positions or shapes of even normally connected heart chambers, making conventional fluoroscopic approaches more challenging (Fig. 23.4).

3D anatomical images can be generated using CMR which can be segmented and merged with X-ray fluoroscopy and electroanatomic maps during EP procedures [6–8]. Image integration using CMR may also lead to reduction in fluoroscopy time. Though computed tomography (CT) data can also be used for image integration, this has the drawback of radiation exposure which is a relevant concern as ACHD patients are subject to multiple procedures and diagnostic tests from a young age and over a lifetime [9]. Reducing the lifetime risk of ionising radiation-induced malignancy is important [9] in congenital heart disease patients who may have already undergone multiple serial investigations involving radiation over their lifetime particularly from CT and cardiac catheterisation. It is therefore desirable not to outweigh the value of 3D image integration resulting in reduced fluoroscopy time [5] through additional pre-procedure ionising radiation from CT.

CMR 3D imaging can be performed either using first-pass contrast angiography during a breath-hold acquisition or using a balanced steady-state free precession (bSSFP) sequence during free-breathing with some form of respiratory gating. In neither does visualisation subsequently allow

for heart motion or intracardiac chamber volume changes during the subsequent procedure.

### 23.4.1 First-Pass Contrast Angiography

First-pass contrast angiography is frequently used in clinical practice to obtain 3D images. The precise timing of the acquisition following bolus administration is determined from a pre-scan where a small bolus is injected, followed by continuous 2D imaging of the chamber of specific interest to determine its time of arrival and hence plan the contrast scan. Subtraction of a pre-contrast scan will eliminate the background. The acquisition is rapid and does not significantly prolong clinical scan time (Fig. 23.12b).

First-pass contrast angiography has been used extensively to evaluate the pulmonary veins prior to ablation for atrial fibrillation [10–13] with good reliability [14], though pulmonary vein size is often over-estimated [15]. However, in congenital heart disease, this approach is complicated by unusual flow patterns and shunts. There is therefore a greater chance that acquisitions are mis-timed. It can also prove difficult to appropriately time filling for later segmentation of more than one heart chamber of clinical interest. In ACHD EP, 3D imaging may need to allow segmentation of several or all heart chambers, if both atrial and ventricular studies are planned. Whereas imaging prior to atrial fibrillation ablation

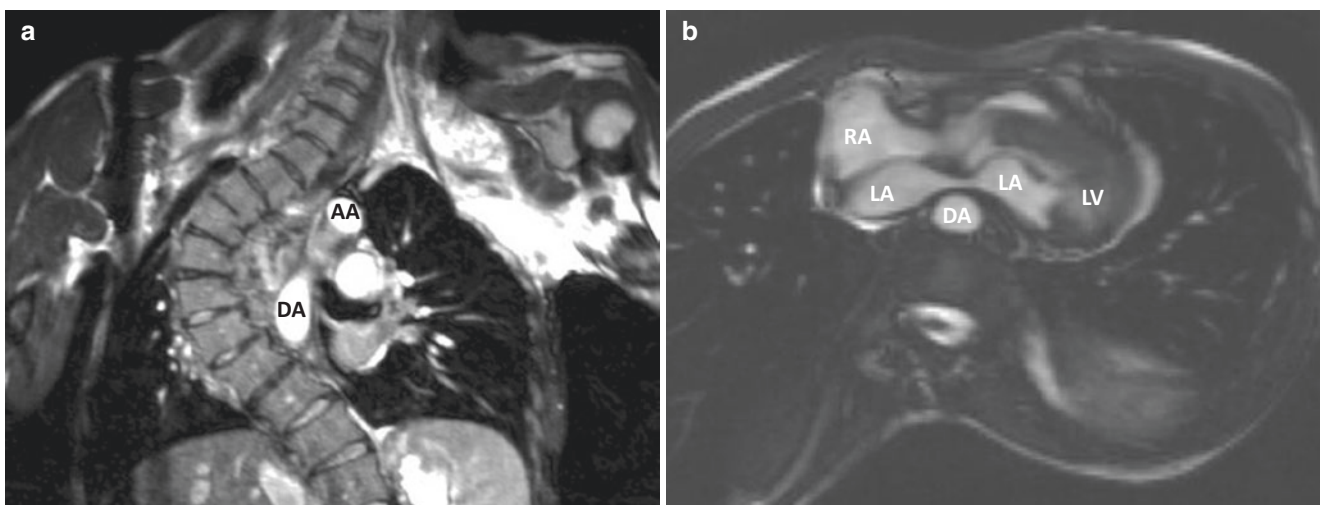


**Fig. 23.4** Atypical shape and position of heart chambers. This patient had severe kyphoscoliosis and Noonan's syndrome. He has no significant target haemodynamic lesion. He presented with symptomatic, recurrent right atrial tachycardia. (a) The severity of the scoliosis can be noted together with the resultant displacement of cardiovascular structures. Fluoroscopy and experience alone would be challenging given the sites of structures will not be in expected locations. (b) Of note, the

right atrium is more dilated than the left atrium. If pulmonary vein isolation were performed for atrial fibrillation this would be difficult. First, the risks associated with atrial septal perforation would be greater given the left atrial deformity. The mid part of the left atrium is squashed flat in the anteroposterior direction between the sternum, ascending and descending aorta, and spinal column. Second, the mechanical deformity of the left atrium might result in multiple triggers for atrial fibrillation



in the structurally normal heart can be directed at the left atrium and pulmonary veins only.

A further drawback is that to acquire the images with good spatial resolution, the acquisition is non-ECG-gated. The resulting images are therefore a composite of the entire cardiac cycle which may result in image blurring. This may contribute to mis-registration in the EP laboratory. Typical acquisition parameters are 96 slices at  $1.1 \text{ mm} \times 0.9 \text{ mm} \times 1.3 \text{ mm}$  acquired with parallel imaging (acceleration factor of 2) and partial Fourier over a 19 cardiac cycle breath-hold. A “dynamic” multi-phase time-resolved approach may instead be chosen in complex congenital heart disease in order to avoid mistiming and to image several chambers of interest but the disadvantages of the lack of ECG gating remain.

Gadolinium contrast agent cannot be used in patients with significantly impaired renal function, particularly group 1 and III agents (see chapter “Gadolinium-Based Contrast Agents”) or in those with inadequate venous access.

### 23.4.2 3D Balanced Steady-State Free Precession

bSSFP produces images with high signal-to-noise ratio (SNR) and good contrast without the need for contrast administration [16]. When directly compared to first-pass contrast angiography for pulmonary vein imaging prior to radiofrequency ablation, it has been shown that 3D bSSFP imaging results in similar conspicuity and fewer motion artefacts [17]. A relative disadvantage of 3D bSSFP is image degradation due to metallic implants. For most congenital heart disease patients, devices such as modern Amplatzer closure devices, stents and stented biological valves do not cause problematic artefacts. Coils used to block veno-venous collaterals after Fontan or to embolise major aortopulmonary collateral arteries (MAPCAs) may, however, cause artefact too difficult to overcome.

3D whole heart data sets can be obtained with high spatial resolution in either the systolic or diastolic cardiac rest periods, when used with diaphragmatic navigators to respiratory gate the acquisition. The duration and exact timing of these rest periods is highly subject-specific [18] and may be determined from observation of a 4-chamber view cine acquisition [19]. The rest period duration determines how much data may be acquired within each cardiac cycle without motion blurring and therefore directly impacts on the acquisition duration. Other factors include the spatial resolution and number of slices required, SNR ratio, respiratory efficiency, and heart rate. Typical acquisition parameters include 96 slices at  $1 \text{ mm} \times 1 \text{ mm} \times 3 \text{ mm}$  (before zero-filling) with

parallel imaging (acceleration factor 2) and partial Fourier with acquisition durations of 5–8 min being typical.

For 3D bSSFP roadmaps, it is important to reduce the sequence echo time (TE) as much as possible so as to minimise artefacts due to flow [20] which result in regions of signal reduction or, in the case of jets, signal void. Such regions may adversely affect the segmentation process which is particularly important if the primary factor guiding it is intensity. Using a sequence with a short TE also reduces problems due to off resonance which result in characteristic dark band artefacts [15]. Signal drop out may be particularly apparent around right inferior pulmonary veins where the frequency of blood flowing from the lungs is close to 100 Hz off resonance [21]. The use of a non-selective radiofrequency pulse enables the TE to be reduced to as low as 1 ms [22] and reduces problems with off-resonance sensitivity, although this requires imaging to be performed in the coronal, rather than the more usual transverse, plane. Using this technique, bSSFP imaging is suggested to outperform contrast enhanced angiography for visualisation of the cardiac chambers, proximal coronary arteries, pulmonary trunk, and aortic root [22].

As noted above, imaging may be performed in either the systolic or diastolic rest period. The end diastolic pause is generally longer than that at end systole ( $152 \pm 67 \text{ ms}$  vs.  $98 \pm 26 \text{ ms}$ ) and would therefore allow the scan to be completed more quickly [23]. However, for subjects with an irregular heart rate, systole is more consistent and imaging in the systolic rest period may be preferred. We have also found systolic imaging helpful at faster heart rates including for studies when patients are in the index atrial tachycardia at CMR attendance awaiting ablation (Figs. 23.5 and 23.6).

When considering the timing of the acquisition, consideration should also be given to flow-inducing artefacts. For pulmonary vein imaging for example, mid-diastolic imaging when pulmonary vein flow is high results in signal voids in the left atrium which may be reduced by imaging in late diastole [20]. In congenital heart disease there are likely to be other sources of turbulent flow from valvular regurgitation or flow accelerations in partially obstructed pathways and timing of the acquisition needs to account for these effects. Where several flow effects may be seen, the flow effects which summate to the least negative impact on the clear delineation of the chamber(s) of interest for the planned EP procedure should be chosen.

Diaphragmatic navigators allow the acquisition to be respiratory-gated so that only data acquired when the diaphragm position is within a narrow window centred on the end-expiratory pause position are accepted [24]. These techniques are inherently inefficient, with the data acceptance rate (or respiratory efficiency) typically being around 40% for a 5 mm acceptance window. Furthermore, in cases where

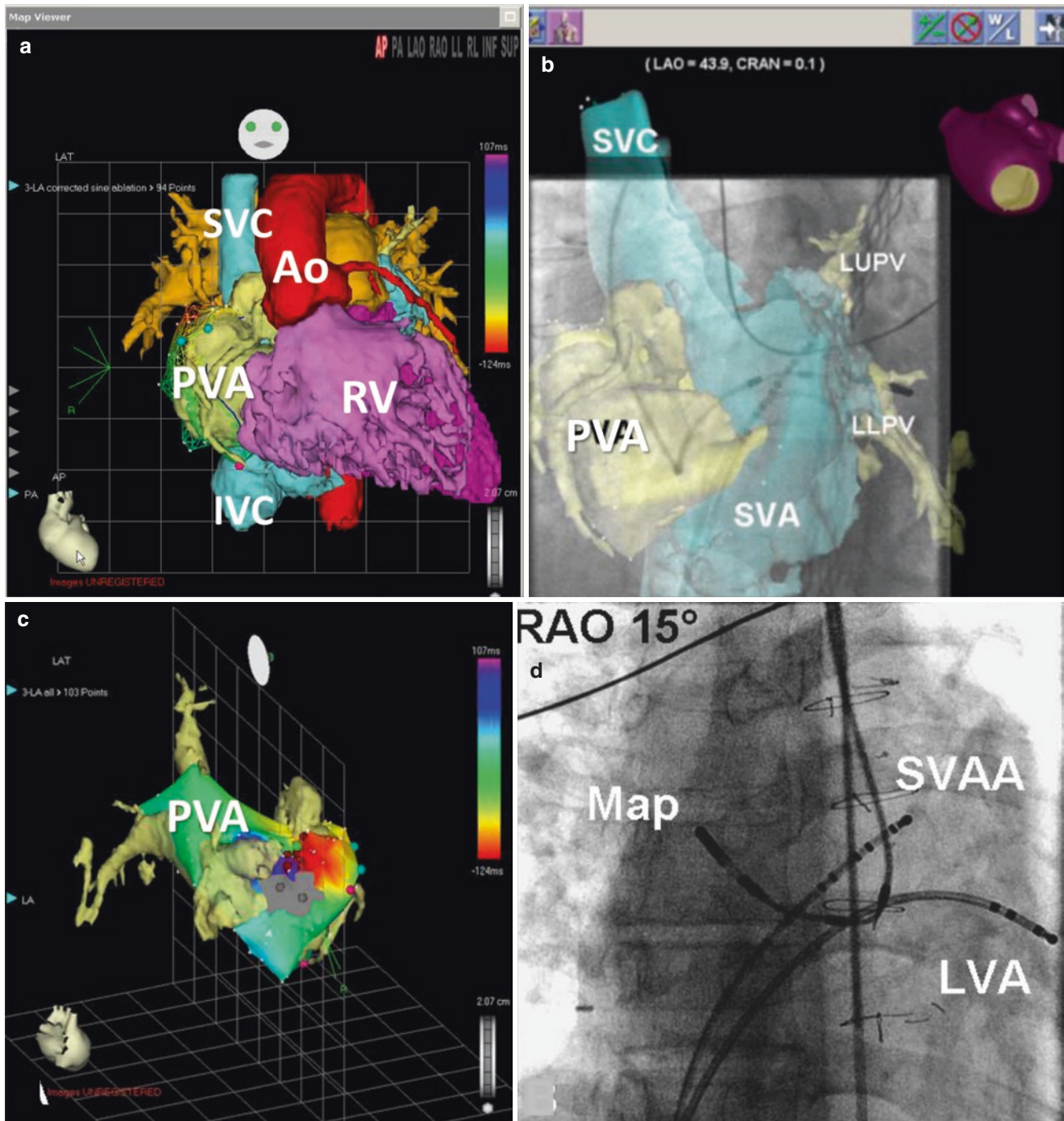


**Fig. 23.5** 3D bSSFP for 3D volume reconstruction and image integration with 3D EP mapping systems to facilitate retrograde approach and avoid puncture of baffled atrial pathways after Mustard operation for transposition of the great arteries. This patient followed up after Mustard operation for transposition of the great arteries and presented with atrial tachycardia requiring cardioversion. His CMR study was performed in sinus rhythm and 3D bSSFP was timed in systole. (a) 3D bSSFP imaging was performed and subsequently segmented with CARTO. The subaortic (red) heavily trabeculated RV (purple) is shown. The pulmonary arteries are coloured orange and the subpulmonary LV brighter purple. The systemic venous baffled atrial compartment (turquoise) and pulmonary venous compartment (yellow) were separately segmented. A rotating movie can be seen (Movie 5.1). (b) 3D CMR reconstructions of the systemic venous compartment (SVA) and pulmo-

nary venous atrial compartment (PVA) were displayed and merged to the local activation time map. The CMR roadmap of all the heart chambers was merged with the EP maps and displayed superimposed on fluoroscopy. (c) Low voltage (grey) scar was found in the pulmonary venous compartment. The dark red tags depict the ablation sites. (d) This site in the left inferior pulmonary vein was reached using retrograde access from the femoral artery and avoiding puncture of the surgical baffle. Retrograde manipulation was made possible by the combination of CMR image integration and remote navigation EP using magnetic navigation allowing several S bends of the catheter. The “MAP” catheter is shown and the retrograde path to reach the site of ablation can be appreciated on the fluoroscopy image. The other two catheters are in the LV apex (LVA) and systemic venous atrial appendage (SVAA) respectively

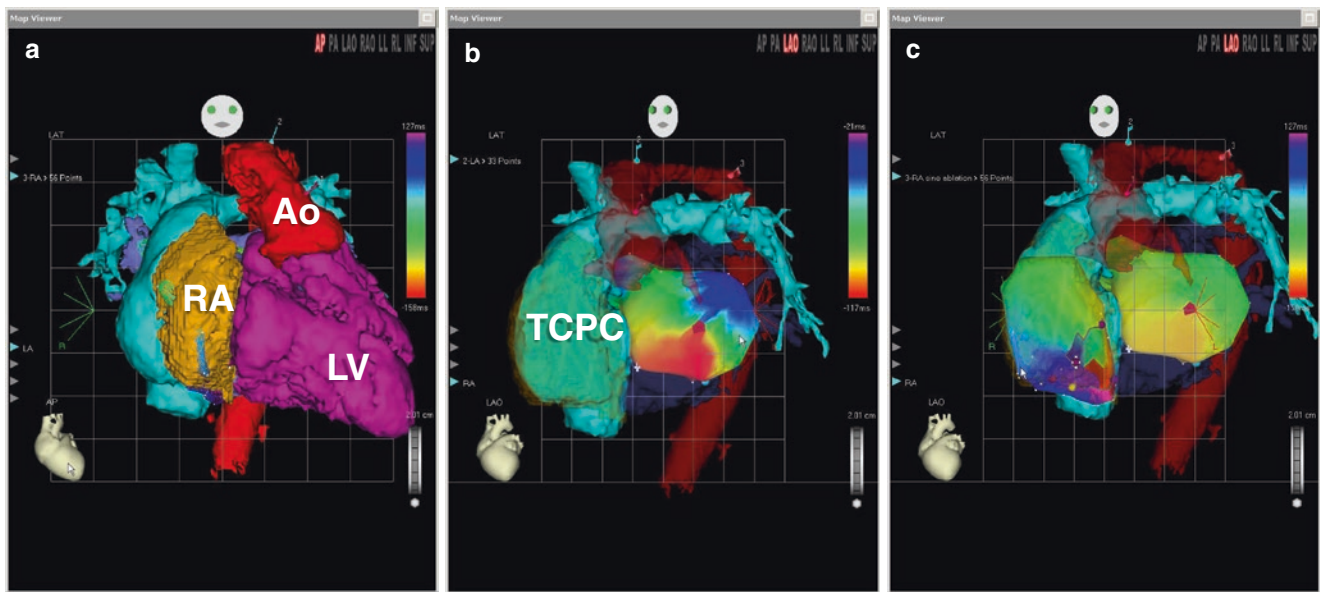


**Fig. 23.6** 3D bSSFP for 3D volume reconstruction and image integration with 3D EP mapping systems to facilitate retrograde approach and avoid puncture of lateral tunnel total cavopulmonary connection and integrated EP activation map. A patient with single ventricle physiology presented clinically with recurrent atrial tachycardia status post-lateral tunnel total cavopulmonary connection (TCPC, blue). The TCPC was performed for situs solitus, discordant atrioventricular connections, double inlet left ventricle, transposed great arteries, and pulmonary stenosis. The CMR was performed in established atrial arrhythmia and 3D

bSSFP was timed in systole. (a) 3D reconstruction of 3D bSSFP CMR imaging showing the lateral tunnel total cavopulmonary connection (turquoise) and the remaining native RA (yellow). The underlying anatomy was double inlet LV (purple). A rotating whole heart structure can be seen in the attached movie (Movie 6.1) whereby the aorta is red and left atrium dark blue. (b) In this image, the ventricular mass has been masked. Re-entrant tachycardia was mapped in the residual RA with counterclockwise activation around the tricuspid annulus. (c) There is bystander activation of the left atrium

the respiratory pattern is irregular or unstable, the respiratory efficiency may drop so low that the acquisition must be abandoned. Improved respiratory gating techniques, such as those implementing real-time motion correction with subject-specific motion models [25], potentially improve the respiratory efficiency and reduce acquisition duration. These models are derived from a short pre-scan and have also been used to generate dynamic roadmaps that vary with respiration [26]. Another option for increasing the respiratory efficiency of an acquisition is to use a real-time and fully automatic algorithm to determine the optimal placement of the navigator acceptance window so as to maximise efficiency (CLAWS [27]).

## 23.5 A Role for Ventricular and Atrial Scar Imaging in ACHD EP

Intravenous gadolinium contrast lingers in scarred regions of the heart. CMR imaging can then be used to visualise scarred myocardial regions enhanced with gadolinium that appear different from neighbouring normal myocardium. Late gadolinium enhancement (LGE) CMR is the gold standard imaging method for non-invasive measurement of myocardial infarction and fibrosis [28]. LGE CMR evidence of fibrosis has been documented in varying extents and patterns in a

number of heart diseases. It predicts outcomes in coronary artery disease [29, 30], dilated cardiomyopathy [31], and hypertrophic cardiomyopathy [32]. Whether these findings can be extrapolated to patients with different congenital heart disease lesions is the subject of ongoing study.

### 23.5.1 2D Late Gadolinium Enhancement Imaging Methods

LGE imaging is usually performed as a 2D stack of breath-hold inversion-prepared segmented gradient-echo acquisitions [33] with inversion time (TI) adjustment to compensate for gadolinium wash-out throughout the study. Imaging is generally performed with alternate R-wave gating which allows for almost complete recovery of the longitudinal magnetisation between sequence repeats and improves contrast between normal and abnormal tissue and reduces the effects of cardiac arrhythmia [34]. In patients with faster or irregular heart rates, gating on every third or even fourth R wave may improve image quality. In-plane resolution is typically 1.2–1.8 mm × 1.2–1.8 mm, with a slice thickness of 6–8 mm in a breath-hold of ~12 s. The inversion time varies from patient to patient and depends on the dose of gadolinium and the time after administration [35]. For experienced operators, this individualised approach with meticulous



inversion time adjustment remains the best [33]. The inversion time can be estimated by visual inspection of an inversion recovery cine scout acquisition [36] and then shifted upwards as the study progresses to account for gadolinium wash-out. Alternatively, phase-sensitive reconstruction of data acquired with a nominal TI eliminates the need for precise setting [37] and has demonstrated better contrast between viable and non-viable myocardium at sub-optimal TI [38, 39]. It also eliminates the ‘dark rim’ artefact apparent in magnitude reconstructed images [40] when the TI is too short, which may aid the depiction of thin-walled structures such as the RV [41] or the atria. Imaging is performed in diastole, when the heart is relatively still, and the number of lines of data acquired per cardiac cycle is reduced in tachycardic patients as the length of this quiescent period is shortened. Recent studies have shown that imaging at higher field strength improves both the SNR and, because of the field dependency of longitudinal relaxation times, the contrast-to-noise ratio (CNR) [38, 42, 43]. BSSFP is an alternative to segmented gradient-echo and has a shorter TE and TR, enabling more lines to be acquired in the cardiac rest period and consequently, a reduced imaging time. However, the contrast achieved between viable and non-viable myocardium may be different, as may the artefacts have generated. Its use for LGE imaging has generally been limited to single-shot acquisitions in patients with frequent arrhythmias or in those who cannot hold their breath [44], but generally, these studies have compromised spatial resolution and much-increased acquisition windows [38, 45, 46]. More recently, parallel imaging has been used to reduce the long acquisition windows with rigid [47] and non-rigid [48] image registration of multiple free-breathing images being performed to improve SNR.

### 23.5.2 3D Late Gadolinium Enhancement Methods

With conventional 2D LGE imaging, the spatial resolution is limited by the need to acquire the complete data set within the duration of a comfortable breath-hold period. For high spatial resolution, respiratory-gated 3D acquisitions may be performed during free-breathing [49, 50]. Registering the LGE images with 3D electrical maps and fluoroscopic images within a catheter navigation environment may guide ablation studies [51–53], potentially increasing procedural success and reducing radiation exposure to patients. High-resolution imaging may also facilitate atrial fibrillation ablation procedures by improving planning and assessing the adequacy of ablation. Atrial fibrosis has been demonstrated in several studies [54–61], with the spatial distribution and extent appears related to the likelihood of arrhythmia recurrence [62–66]. Such imaging could help predict recurrent

arrhythmia in future and help guide ablation procedures in patients with recurrent atrial or ventricular arrhythmia (Fig. 23.7).

For 3D imaging, typical parameters include spatial resolution of 1.25–1.5 mm × 1.25–1.5 mm × 4 mm (before zero-filling) with 32 slices covering the atrial chambers, more being required if whole heart imaging is required. Acquisition duration is reduced by using parallel imaging with a ×2 acceleration factor, the resulting SNR decrease being mitigated by the thick slab excitation. For segmented gradient echo imaging at 1.5 Tesla, selecting a TE of 2.4 ms ensures that fat and water are out of phase at the time of echo formation which reduces partial volume effects around the thin-walled atria and RV. In addition, fat saturation is used to suppress the fat signal. Acquisitions are typically performed within a window of approximately 120 ms in diastole, the exact timing being determined from atrial cine acquisitions. Using alternate R-wave gating, as for 2D imaging, would result in the acquisition duration being prolonged unacceptably. As well as being difficult for the patient, the gadolinium wash-out during this period would result in poor nulling of the normal myocardium and any scarring would be seen with reduced contrast. Consequently, 3D acquisitions are performed with single R-wave gating with the TI used being reduced to compensate. However, although this is necessary to reduce the acquisition duration, incomplete magnetisation recovery between sequence repeats on every heartbeat results in the sequence being very susceptible to changes in the RR interval, resulting in ghosting and poor nulling of the normal myocardium. In the atrial fibrillation population, for example, image quality can be poor [56], with up to 40% of studies being unsuitable for further analysis [59]. The most common cause of a failed acquisition is poor rate control in patients presenting with atrial fibrillation during the scan [65]. Typical acquisition durations are 4–8 min, depending on volume coverage, spatial resolution and respiration, and heart rate. Endo and epicardial atrial borders may be segmented and the extent of atrial scar determined using a threshold-based algorithm [59, 60]. The amount of left atrial scar calculated in this way has been used to stage atrial fibrillation and to allow a more tailored approach to management [61, 67].

As for the roadmap studies discussed above, respiratory gating is generally performed using navigators. These navigators consist of ‘pencil-beam’ or ‘crossed-pair’ excitations which create an inflow artefact in the right pulmonary veins and atrial wall which may obscure detail. This has recently been reduced by using a large slab right hemidiaphragm navigator [68]. In congenital heart disease patients, effort must be taken to place the navigators carefully. The navigators and their localised artefact should not be placed such that they impair imaging of enlarged heart chambers. In some cases, such as dextrocardia the left hemidiaphragm needs to be chosen.



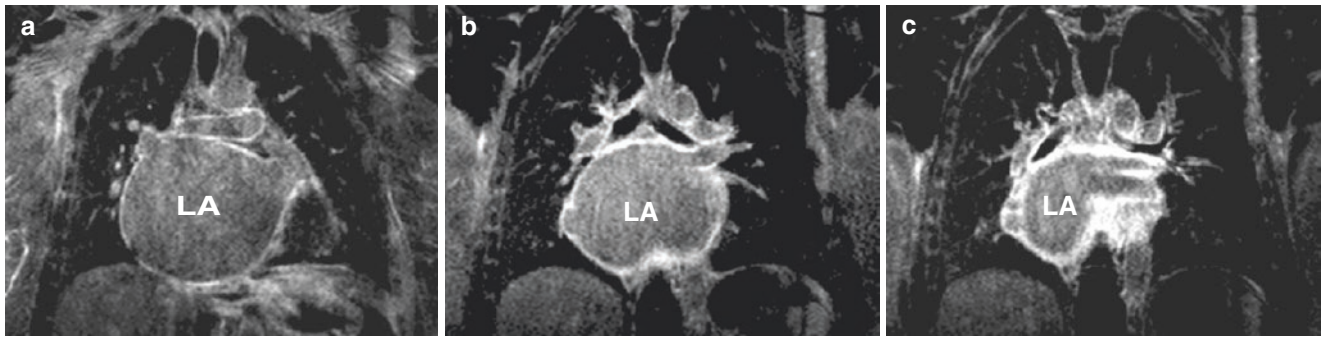


**Fig. 23.7** 3D LGE images in atrial fibrillation and dilated left atrium due to congenital mitral valve disease (a–c). This young woman had mitral valve replacement for congenital mitral regurgitation. The left atrium is markedly dilated and measures  $92 \times 88$  mm in the left-hand image. The giant nature of the left atrium in relation to the chest cavity can also be noted. Of note, the pulmonary veins are not severely dilated.

In this case, there is striking diffuse late gadolinium enhancement and thickening of the atrium in a global distribution. Even if the patient underwent pulmonary vein isolation there may be multiple triggers outside the pulmonary veins and sufficient left atrial body fibrosis for atrial fibrillation maintenance

### 23.5.3 Clinical Application of LGE CMR in Congenital Heart Disease Risk Stratification

#### 23.5.3.1 Transposition of the Great Arteries Following Atrial Redirection Surgery

In patients with TGA, which has been palliated with atrial redirection surgery (Mustard or Senning surgery), the RV supports the systemic circulation. Whilst this has been largely superseded by the neonatal arterial switch procedure, a large cohort of adults with previous atrial redirection surgery remain under follow-up. The RV is poorly adapted to support the high-pressured systemic circulation and long-term complications include progressive systemic RV dysfunction, reduced exercise capacity, arrhythmia, and SCD [69].

A systematic study of LGE in the systemic RV after Mustard operation for TGA demonstrated the presence of LGE. Systemic RV LGE was associated with older patients with later repair, longer follow-up, and adverse clinical risk markers such as right ventricular dysfunction, incidence of atrial arrhythmia, and also prolonged QRS duration and QT dispersion which are markers for SCD in this population [2, 70, 71].

In a larger prospective study of patients with TGA and atrial redirection surgery, RV LGE was present in 56% and predicted a composite outcome of adverse clinical events including new onset sustained arrhythmia, heart failure admission, transplantation, and mortality (Fig. 23.8) [72]. The presence and location of RV LGE agreed with histological fibrosis in an explanted heart from a patient who underwent transplant. The composite endpoint of adverse cardiovascular events was driven by first onset sustained atrial tachyarrhythmia, but this often precedes RV failure [70] and ventricular arrhythmia [2, 73] and is in itself a risk factor for mortality in this patient population. Several uni-

variate predictors for events were identified including maximal right atrial area and reduced RV ejection fraction but only peak oxygen consumption and the presence of RV LGE were independently significant [72]. These can be used together to predict 5-year risk of events in individuals.

#### 23.5.3.2 Repaired Tetralogy of Fallot

RV dysfunction, arrhythmia, and SCD complicate the follow-up for patients with repaired tetralogy of Fallot (ToF) [1, 74]. Despite decades of research, precise risk stratification for ventricular arrhythmia remains challenging. Whilst progress has been made to define timing of pulmonary valve replacement for pulmonary regurgitation to prevent premature heart failure and reduce SCD, myocardial fibrosis remains as an arrhythmic substrate for macro re-entrant ventricular tachycardia (VT) [75, 76].

LGE is seen in the RV and left ventricle (LV) in repaired ToF including in surgical sites (Figs. 23.9 and 23.10). More extensive RV LGE (excluding ubiquitous RV-LV insertion point enhancement) has been associated with RV dysfunction, reduced exercise capacity, increased B-type natriuretic peptide (BNP) level, and sustained arrhythmia in patients with repaired ToF in cross-sectional analysis [77]. Association with restrictive RV physiology and fractionated QRS has also been reported [78, 79].

In a recent prospective study of 550 patients (mean follow-up  $6.4 \pm 5.8$ ; total 3512 years) with repaired ToF, RV LGE independently predicted all-cause mortality and a secondary endpoint of ventricular arrhythmia (a composite of life-threatening sustained VT/resuscitated ventricular fibrillation/SCD but not simply appropriate implantable cardioverter defibrillator (ICD) shock) (Figs. 23.9 and 23.11) [80]. Moreover, a weighted risk score incorporating clinical, LGE CMR, cardiopulmonary exercise, and BNP data was shown to identify patients with repaired ToF at high risk of death.

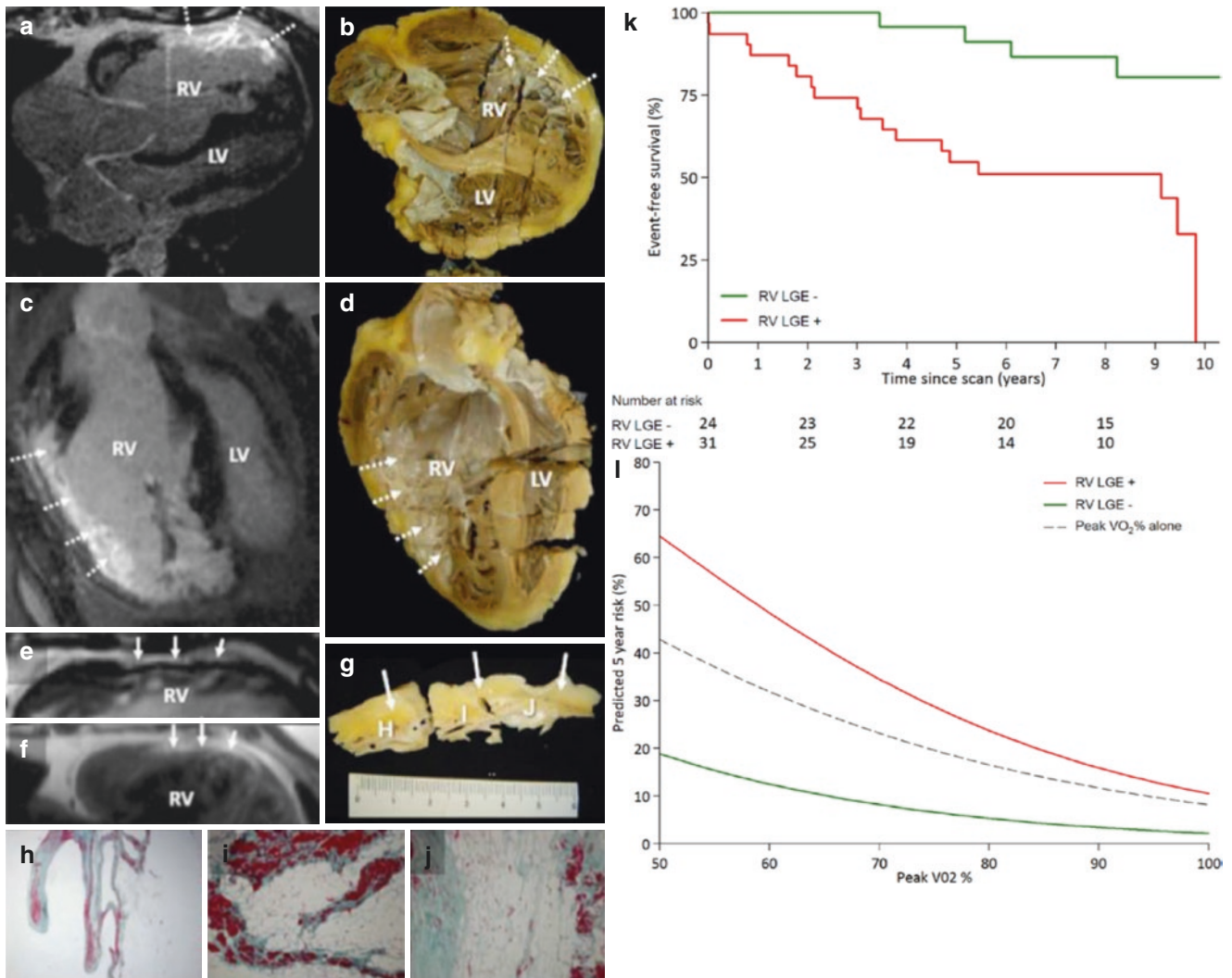


**Fig. 23.8** RV LGE in the systemic RV in patients with transposition of the great arteries post-atrial redirection surgery. Macroscopic fibrosis and correlation with in vivo late gadolinium enhancement (LGE) cardiovascular magnetic resonance (CMR) in heart explanted during follow-up. LGE CMR (**a** and **c**) and corresponding photographs of macroscopic sections (**b** and **d**) showing excellent correlation of CMR LGE with visually fibrotic areas (arrows). The increased signal on balanced steady-state free precession (**e**) and turbo spin echo (**f**; continuous arrows) is compatible with fat. In (**g**), the corresponding macroscopic specimen shows epicardial fatty infiltration (continuous arrows) but also right ventricular (RV) endocardial fibrosis. Corresponding histology is shown after staining with Masson's Trichrome; region (**h**) shows extensive replacement of the compact myocardium by fatty tissue, whereas the trabeculations lining the cavity contain myocardium (red

and extensive fibrous tissue (green,  $\times 16$ ). Regions (**i**) and (**j**) show extensive fatty and fibrous replacement ( $\times 100$ ). (**k**) Kaplan-Meier event-free survival curve for reaching the composite clinical end point of new-onset sustained tachyarrhythmia (atrial and/or ventricular), decompensated heart failure admission, transplantation, or death. Fibrosis-patients without LGE, Fibrosis+ with LGE. Logrank  $P = 0.001$ . (**l**) Five-year risk prediction curve by percent of predicted peak  $VO_2$  and fibrosis status for the composite clinical end point. (With kind permission from Rydman et al, Systemic Right Ventricular Fibrosis Detected by Cardiovascular Magnetic Resonance is Associated with Clinical Outcome, Mainly New-Onset Atrial Arrhythmia, in Patients After Atrial Redirection Surgery for Transposition of the Great Arteries. *Circ Cardiovasc Imaging*, 2015 [72])

This is the first time LGE has been shown to predict mortality in congenital heart disease. Additionally, we have separately demonstrated that RV scar burden identified by 3D LGE segmentation in repaired ToF independently predicts inducible VT during invasive programmed electrical stimulation (Fig. 23.12) [81]. More data are needed to know how right atrial LGE could be relevant to the more prevalent right atrial tachycardias patients with ToF experience.

### 23.5.3.3 Other Congenital Heart Conditions

An association between myocardial LGE and arrhythmia has been reported for other congenital heart disease lesions. Ventricular LGE has been detected in 28% of patients with Fontan palliation, with the presence and extent of ventricular LGE correlating with increased ventricular size, impaired ejection fraction, and prevalence of non-sustained VT [82]. In patients with Ebstein anomaly of the tricuspid

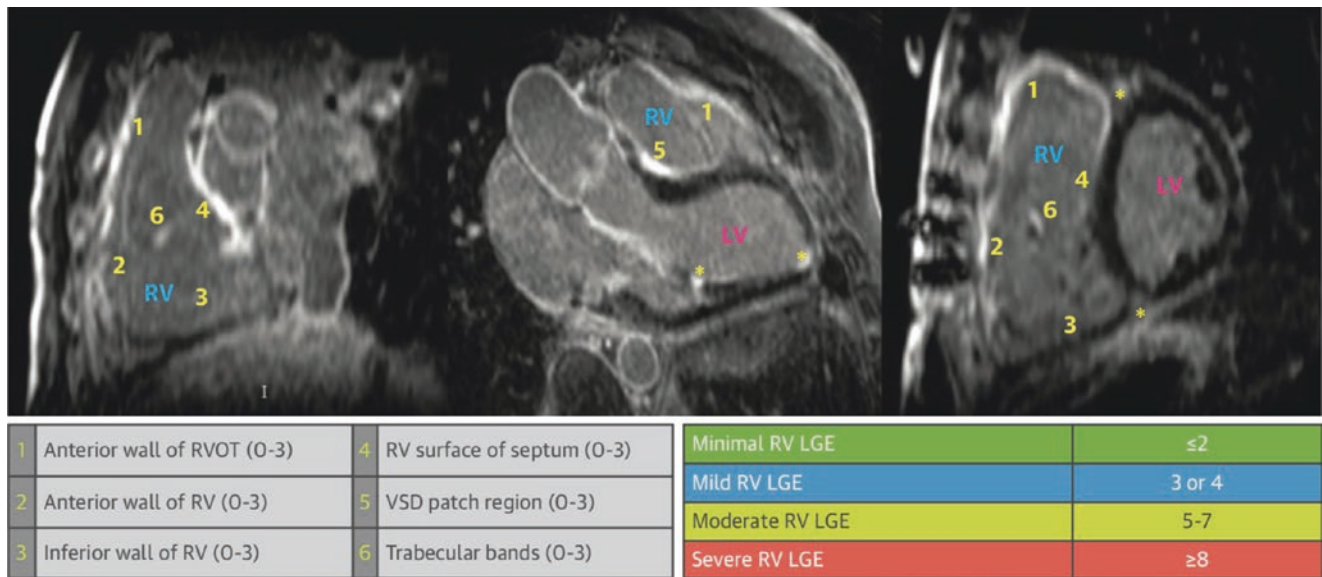


**Fig. 23.9** RV LGE segmental scoring in repaired tetralogy of Fallot. Patients with a total RV LGE score  $\geq 8$  were in the top quartile for RV LGE burden and were graded as severe extent. Patients with a total RV LGE score 5–7 were graded as moderate extent where a score of 5 was the median. A total RV LGE score  $< 5$  was deemed as minimal or mild. The segmental system used for scoring RV LGE has been previously published. The RV is divided into six segments (yellow numbers 1–6). Regions of RV LGE were scored according to linear extent (0 1/4 no enhancement, 1 1/4 up to 2 cm, 2 1/4 up to 3 cm, 3 1/4 3 or more cm in length) and number of trabeculations enhanced including the moderator

band (0 1/4 no enhancement, 1 1/4 1 trabeculation, 2 1/4 2–4). Scoring of LVLGE was performed using the universally accepted 17-segment LV model [77]. Points were attributed to the proportion of LGE present in each myocardial segment, as visually judged: 0 1/4 no LGE, 1 1/4 up to 25%, 2 1/4 up to 50%, 3 1/4 up to 75%, and 4 1/4 up to and including 100% of the myocardium enhanced. LGE 1/4 late gadolinium enhancement; LV 1/4 left ventricle; RV 1/4 right ventricle. (With kind permission from Ghonim et al, Predicting Survival in Repaired Tetralogy of Fallot. JACC Cardiovasc Imaging, 2022 [80])

valve, LGE of the right atrium and ventricle is associated with history of supraventricular arrhythmia [83]. In unrepaired secundum atrial septal defect, atrial arrhythmia documentation was cross-sectionally associated with more extensive right atrial LGE though the independence of this finding compared with right atrial size was not demonstrated [84].

LGE CMR has potential to be a useful tool to refine arrhythmia risk stratification in patients with a variety of congenital heart defects. Moreover, LGE CMR may allow non-invasive imaging of the arrhythmic substrate for re-entrant tachycardias. This could improve patient selection for invasive VT stimulation and primary prevention implantable cardioverter defibrillator. Machine learning and quantification of diffuse ventricular fibrosis using T1 mapping could provide additional insights [85, 86].

#### 23.5.4 Ventricular and Atrial Scar Segmentation and Image Integration in ACHD EP

CMR of scars has been used in invasive arrhythmia diagnostic and therapeutic procedures in ischaemic heart disease and cardiomyopathy patients [52, 87, 88]. 3D LGE CMR at

1.5 Tesla has been correlated with electroanatomical mapping and the use of high-resolution 3D LGE CMR is reported at 3 Tesla [87, 89].

We have applied remote magnetic navigation EP to congenital heart disease patients in our centre [5]. Conventional 3D EP mapping of ventricles by point-by-point voltage amplitude maps to identify the underlying arrhythmia substrate has limitations. First, poor contact for mapping can lead to overestimation of the area of scar (low voltage areas). Remote navigation, however, uses soft catheters that are guided to the region of interest by external magnets overcoming problems relating to anatomic obstacles. Such catheters also have minimal risk of causing perforation of heart chambers compared with conventional catheters. This gives the potential to give adequate “read” by improving catheter tissue contact. Therefore, particularly if the chamber size is provided by CMR, the problem of over-estimating the area of scar (using low voltage mapping) through lack of contact can be overcome. This is especially relevant in congenital heart disease patients where the right atrial and ventricular chambers can be massively enlarged.

Second, conventional mapping of ventricles frequently mechanically induces VT or ventricular fibrillation leading to haemodynamic compromise and possible repetitive DC cardioversion. If the latter causes patient movement on the



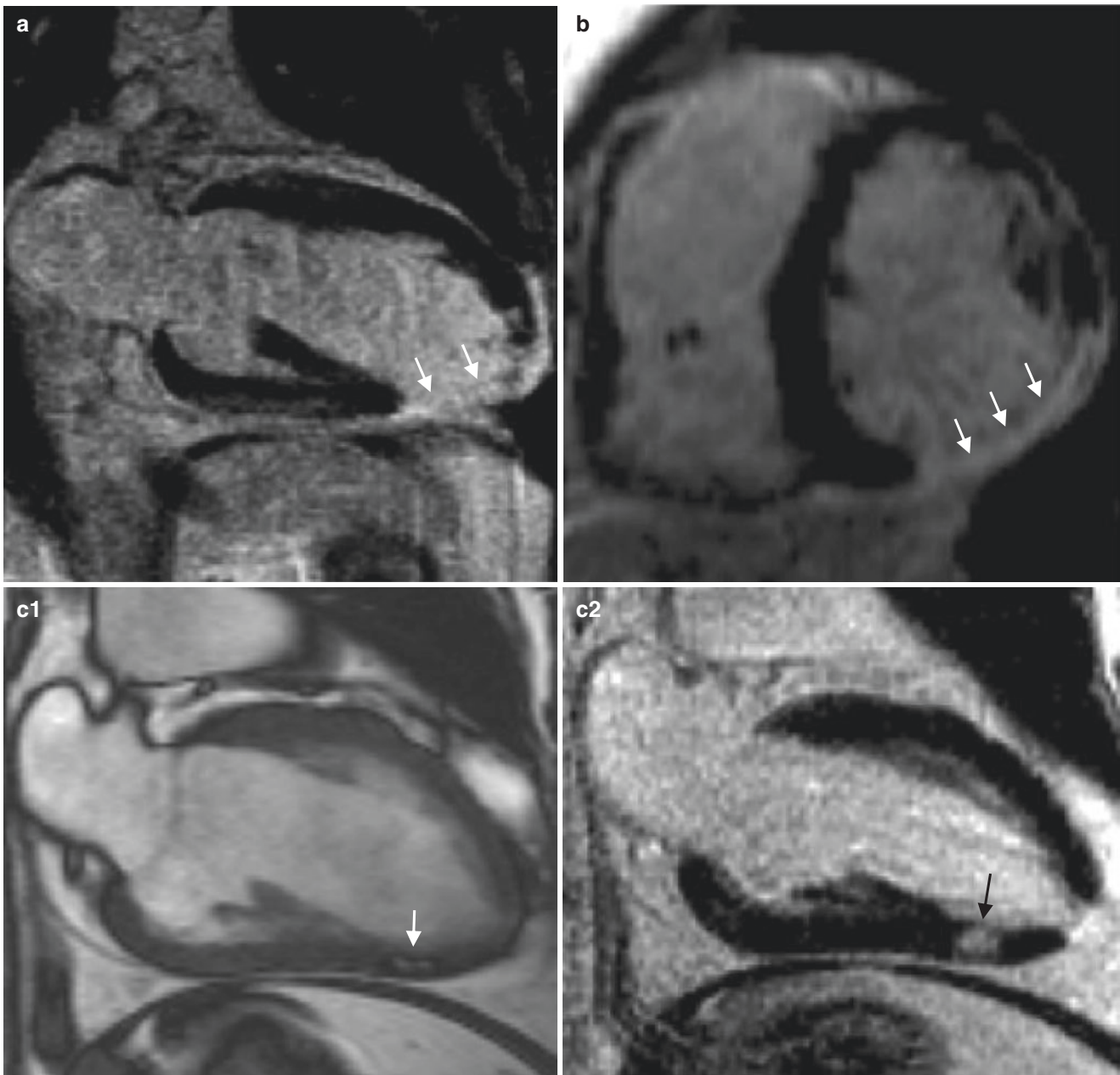


**Fig. 23.10** Examples of LV LGE late after tetralogy of Fallot repair. Images illustrating unexpected LV infarction (arrowed) in two different patients (**a** and **b**) A further example of localised LV LGE in another patient is shown. The cine frame in **C1** and corresponding LGE image in **C2** suggest fibro-fatty change in this region. (With kind permission

from Babu-Narayan et al., Ventricular fibrosis suggested by cardiovascular magnetic resonance in adults with repaired tetralogy of Fallot and its relationship to adverse markers of clinical outcome. *Circulation*, 2006 [77])

EP table, accurate registration of mapping data is more challenging. CMR image resolution and multimodality image registration may provide different potential errors. Congenital heart disease patients are frequently considered to have complex scar substrates and the risk of arrhythmia recurrence following conventional ablation is

higher [90]. Haemodynamic instability may be a reason that the treatment needs to be anatomically “substrate” based. If CMR segmentation and post-processing can be used to demonstrate both heart chambers and complex scars, this will aid an anatomical “substrate” based EP approach (Figs. 23.13 and 23.14). In future, CMR-defined



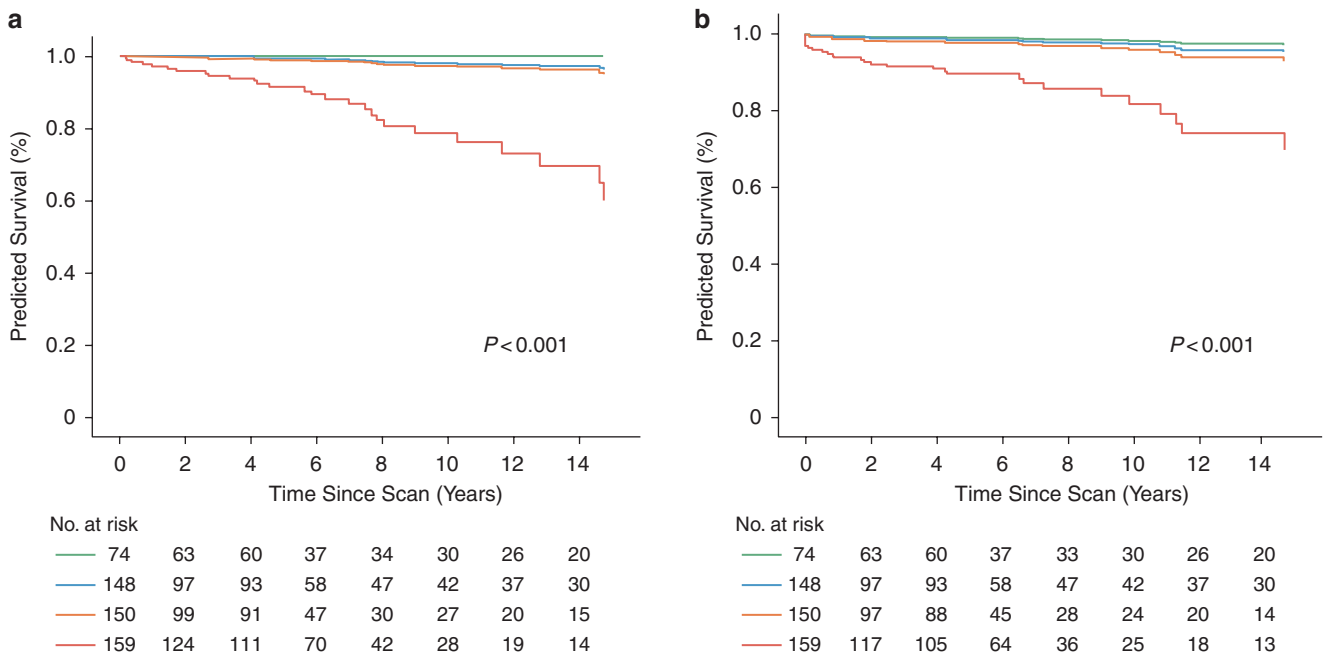


**Fig. 23.11** RV LGE segmental score quartiles predict ventricular arrhythmia and all-cause mortality in repaired tetralogy of Fallot. Cox proportional hazard survival plots for patients with repaired tetralogy of Fallot stratified by RV LGE quartiles to predict (a) ventricular arrhythmia

and (b) all-cause mortality. See Fig. 23.9 for the RV LGE segmental score. (With kind permission from Ghonim et al., Predicting Survival in Repaired Tetralogy of Fallot. JACC Cardiovasc Imaging, 2022 [80])

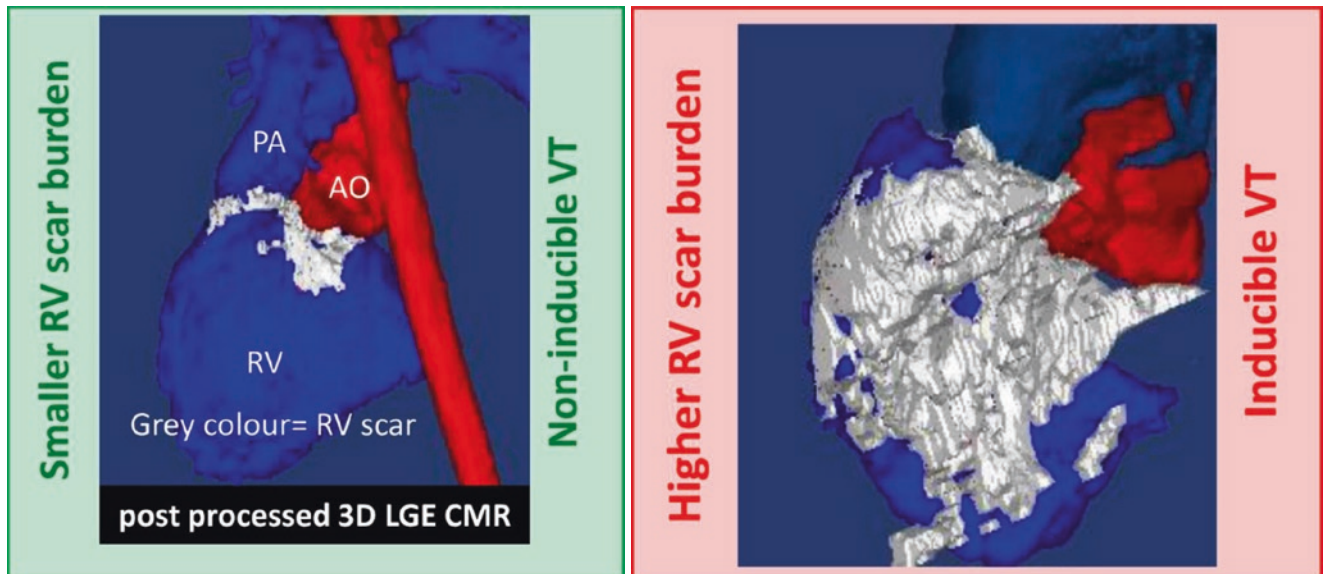


**Fig. 23.12** RV scar burden detected by 3D LGE CMR predicts VT inducibility in repaired tetralogy of Fallot. 3D LGE CMR defined RV scar segmentation for two patients with repaired tetralogy of Fallot. Grey colour = RV scar. Blue colour = healthy tissue. Higher RV scar burden was associated with inducibility of VT for patients undergoing

invasive programmed VT stimulation. (With kind permission from Ghonim et al, Three-Dimensional Late Gadolinium Enhancement Cardiovascular Magnetic Resonance Predict Inducibility of Ventricular Tachycardia in Adults with Repaired Tetralogy of Fallot. Circulation: Arrhythmia and Electrophysiology, 2020 [81])

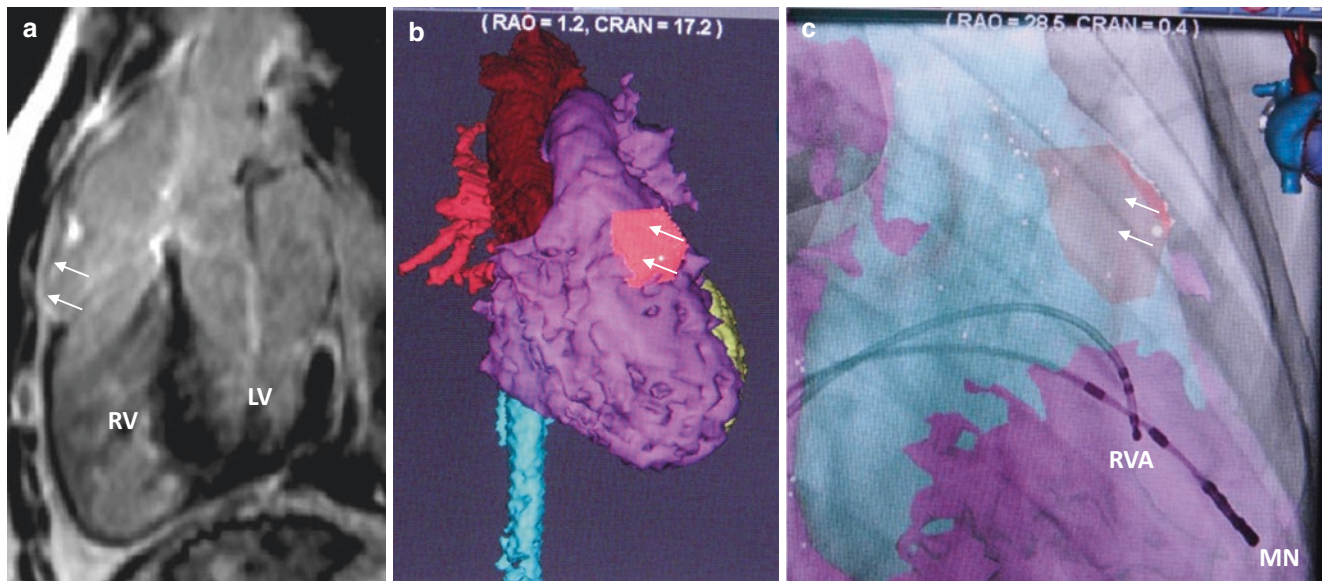


**Fig. 23.13** CE-CMRA for 3D volume reconstruction and image integration with 3D EP mapping systems in repaired tetralogy of Fallot and RV outflow tract ventricular tachycardia. (a) RV LGE in the RV outflow tract after repair of tetralogy of Fallot (arrowed). (b) CE-MRA was performed and segmented with CARTO software to provide an anatomical roadmap of the right ventricle and pulmonary artery (purple). The red patch was segmented from 3D LGE study (arrowed) and reflects CMR

documented anatomical scar. (c) The CMR images were integrated with fluoroscopy. Here there is a catheter in the RV apex (RVA) and the magnetic catheter is also labelled (MN). Ventricular tachycardia was induced at EP study with associated haemodynamic instability and ablation next to the scar defined by LGE CMR terminated the tachycardia. Subsequently, the patient was no longer inducible for ventricular tachycardia

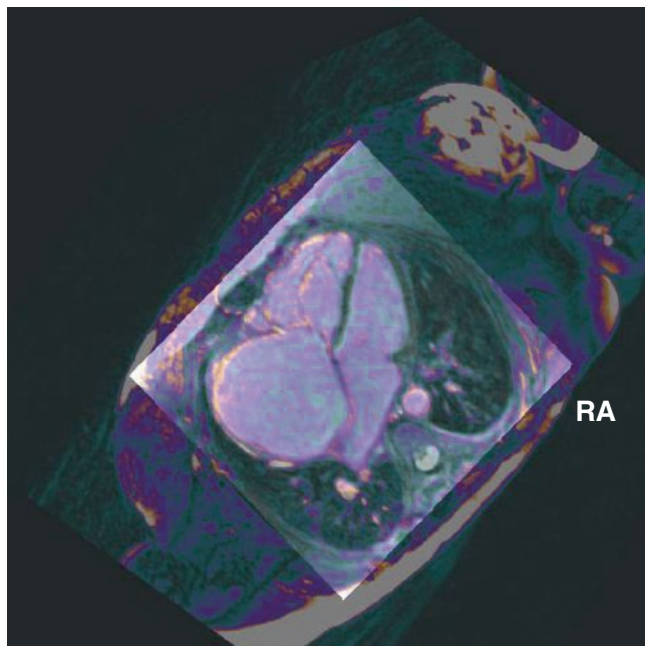


**Fig. 23.14** RA tachycardia with giant RA and both RA and RV LGE. This patient in her fifties had repaired tetralogy of Fallot with pulmonary atresia. She re-presented to follow up with established atrial tachycardia and massively dilated right atrium. The image shown follows Syngofusion™ of 3D bSSFP and 3D LGE CMR sequences. The bright areas show extensive LGE in the right atrium and in the right ventricle

scar images merged with EP data could be used intra-procedure to attempt to image the anatomy including scar and direct the diagnostic elements of the procedure towards the potentially multiple and complex regions of interest, making it more timely and improve outcomes of ablation in ACHD patients.

### 23.6 Real-Time MR Image-Guided Ablation

Over the last few years, there has been progress in animal models and clinical studies to develop real-time CMR-guided electrophysiology workflows [91, 92]. Potential advantages include improved procedural guidance with visualisation of cardiovascular anatomy, improved guidance of catheters to target regions of interest, and real-time evaluation of the arrhythmic substrate and transmuralty of ablation lesions. Moreover, procedural time and radiation exposure could be reduced [93]. CMR has the potential to visualise lesion formation during radiofrequency ablation delivery. T2-weighted imaging allows assessment of acute myocardial oedema. This immediate lesion assessment might enable a deeper ablation without significantly increasing the risk of perforation. LGE can identify ablation lesion necrosis and longer-term scar substrate for prediction of recurrence.

Feasibility of real-time CMR-guided systems to perform electroanatomic mapping and ablation has been demonstrated in porcine ischemia-reperfusion models of VT and in patients with typical atrial flutter [92, 94]. Such systems could potentially help improve arrhythmic substrate assessment in ACHD patients undergoing ablation of complex scar-related tachycardias.

### 23.7 Micro-Structural Myocardial Fibre Architecture

Diffusion tensor cardiac magnetic resonance (DT-CMR) is a novel imaging technique, which allows non-invasive assessment of the myocardial fibre architecture at the micro-structural level. Whilst DT-CMR was previously limited to *ex vivo* studies, advances in sequences have allowed *in vivo* imaging to be acquired. The technique has been applied to assess myocardial fibre orientation and sheetlet function in various cardiac pathologies, primarily in animal models of cardiac disease, but also in hypertrophic cardiomyopathy and ventricular remodelling post-infarction in humans [95]. For example, myocardial disarray identified by DT-CMR *in vivo* has been associated with ventricular arrhythmias in patients with hypertrophic cardiomyopathy [96]. In congenital heart disease, *ex vivo* DT-CMR of pathology specimens has shown myocardial fibre organisation differs between ToF, TGA, CcTGA, systemic RV, and situs inversus [97].

Whilst currently limited to a small number of research centres, DT-CMR has the potential to increase understanding of the myocardial micro-structure in patients with ACHD. This could help identify patients at increased risk of arrhythmia and SCD. In addition, visualisation of surviving myocardial fibre tracts within scarred myocardium could potentially identify the ‘critical isthmus’ for re-entrant tachycardias, thereby increasing the targets for catheter ablation.

### 23.8 Personalised Virtual Heart Computational Modelling

Recent advances in image-based computational modelling have enabled patient-specific virtual hearts to be created. Personalised models are constructed from 3D LGE CMR images, incorporating patient-specific data (chamber geometry and fibrotic remodelling), estimates of myocardial fibre orientation, and EP properties, to reproduce the arrhythmogenic substrate *in silico*. Simulations of electrophysiology testing and catheter ablation can then be applied to predict arrhythmia inducibility and ablation targets [98].

This approach has been applied as proof-of-concept to predict ventricular arrhythmia post-infarction [99], in paediatric

myocarditis [100], and in patients with repaired ToF [101]. Computational modelling has also been used to identify targets for ablation of persistent atrial fibrillation [102] and predict arrhythmia recurrence following pulmonary vein isolation [103]. Translation of personalised computational modelling to patients with ACHD has potential to improve arrhythmia prediction and ablation outcomes.

### 23.9 Conclusion

Imaging the functional details of the cardiovascular system is a forte of CMR. This detailed information is even more important in ACHD when it comes to planning and execution of EP procedures. The true incremental value of LGE CMR applied to adults with congenital heart disease above other, perhaps easier and more widely available markers of risk, remains to be proven in longitudinal, prospective studies. It seems likely that LGE CMR has value in predicting risk of arrhythmia in repaired ToF and systemic RV patients and can lead to better identification of patients at most risk of premature deaths. This will allow referral for surgical, transcatheter, or EP intervention including implantation of an automated internal cardiac defibrillator to be expedited where appropriate and avoidance of the risks, significant morbidity, and costs related to these procedures in patients who do not need these interventions. Visualization of 3D geometry but also fibrosis/scar that serves as the underlying substrate for arrhythmia could result in shorter procedures with better outcome and reduction in radiation exposure.

**Conflicts of Interest** SE is a consultant for Stereotaxis, Inc. and Biosense Webster.

SVBN is supported by the British Heart Foundation.

### References

1. Gatzoulis MA, Balaji S, Webber SA, Siu SC, Hokanson JS, Poile C, et al. Risk factors for arrhythmia and sudden cardiac death late after repair of tetralogy of Fallot: a multicentre study. *Lancet*. 2000;356(9234):975–81.
2. Kammeraad JAE, van Deurzen CHM, Sreeram N, Bink-Boelkens MTE, Ottenkamp J, Helbing WA, et al. Predictors of sudden cardiac death after mustard or Senning repair for transposition of the great arteries. *J Am Coll Cardiol*. 2004;44(5):1095–102.
3. Khairy P, Harris L, Landzberg MJ, Viswanathan S, Barlow A, Gatzoulis MA, et al. Implantable cardioverter-defibrillators in tetralogy of Fallot. *Circulation*. 2008;117(3):363–70.
4. Khairy P, Landzberg MJ, Gatzoulis MA, Lucron H, Lambert J, Marçon F, et al. Value of programmed ventricular stimulation after tetralogy of Fallot repair: a multicenter study. *Circulation*. 2004;109(16):1994–2000.
5. Ernst S, Babu-Narayan SV, Keegan J, Horduna I, Lyne J, Till J, et al. Remote-controlled magnetic navigation and ablation with 3D image integration as an alternative approach in patients



- with intra-atrial baffle anatomy. *Circ Arrhythm Electrophysiol.* 2012;5(1):131–9.
6. Reddy VY, Malchano ZJ, Holmvang G, Schmidt EJ, d'Avila A, Houghtaling C, et al. Integration of cardiac magnetic resonance imaging with three-dimensional electroanatomic mapping to guide left ventricular catheter manipulation. *J Am Coll Cardiol.* 2004;44(11):2202–13.
  7. Dong J, Dickfeld T, Dalal D, Cheema A, Vasamreddy CR, Henrikson CA, et al. Initial experience in the use of integrated electroanatomic mapping with three-dimensional MR/CT images to guide catheter ablation of atrial fibrillation. *J Cardiovasc Electrophysiol.* 2006;17(5):459–66.
  8. Koldaivelu A, Lardo AC, Halperin HR. Cardiovascular magnetic resonance guided electrophysiology studies. *J Cardiovasc Magn Reson.* 2009;11(1):21.
  9. Hoffmann A, Engelfriet P, Mulder B. Radiation exposure during follow-up of adults with congenital heart disease. *Int J Cardiol.* 2007;118(2):151–3.
  10. Ahmed J, Sohail S, Malchano ZJ, Holmvang G, Ruskin JN, Reddy VY. Three-dimensional analysis of pulmonary venous ostial and antral anatomy: implications for balloon catheter-based pulmonary vein isolation. *J Cardiovasc Electrophysiol.* 2006;17(3):251–5.
  11. Mansour M, Holmvang G, Sosnovik D, Migrino R, Abbara S, Ruskin J, et al. Assessment of pulmonary vein anatomic variability by magnetic resonance imaging: implications for catheter ablation techniques for atrial fibrillation. *J Cardiovasc Electrophysiol.* 2004;15(4):387–93.
  12. van der Voort PH, van den Bosch H, Post JC, Meijer A. Determination of the spatial orientation and shape of pulmonary vein ostia by contrast-enhanced magnetic resonance angiography. *Eurospace.* 2006;8(1):1–6.
  13. Wittkamp FHM, Vonken EJ, Derksen R, Loh P, Velthuis B, Wever EFD, et al. Pulmonary vein ostium geometry: analysis by magnetic resonance angiography. *Circulation.* 2003;107(1):21–3.
  14. Greil GF, Powell AJ, Gildein HP, Geva T. Gadolinium-enhanced three-dimensional magnetic resonance angiography of pulmonary and systemic venous anomalies. *J Am Coll Cardiol.* 2002;39(2):335–41.
  15. Hauser TH, Yeon SB, Kissinger KV, Josephson ME, Manning WJ. Variation in pulmonary vein size during the cardiac cycle: Implications for non-electrocardiogram-gated imaging. *Am Heart J.* 2006;152(5):974.e1–6.
  16. Scheffler K, Lehnhardt S. Principles and applications of balanced SSFP techniques. *Eur Radiol.* 2003;13(11):2409–18.
  17. Krishnam MS, Tomasian A, Malik S, Singhal A, Sassani A, Laub G, et al. Three-dimensional imaging of pulmonary veins by a novel steady-state free-precession magnetic resonance angiography technique without the use of intravenous contrast agent: initial experience. *Invest Radiol.* 2009;44(8):447–53.
  18. Wang Y, Vidan E, Bergman GW. Cardiac motion of coronary arteries: variability in the rest period and implications for coronary MR angiography. *Radiology.* 1999;213(3):751–8.
  19. Plein S, Jones TR, Ridgway JP, Sivanathan MU. Three-dimensional coronary MR angiography performed with subject-specific cardiac acquisition windows and motion-adapted respiratory gating. *Am J Roentgenol.* 2003;180(2):505–12.
  20. Markl M, Pelc NJ. On flow effects in balanced steady-state free precession imaging: pictorial description, parameter dependence, and clinical implications. *J Magn Reson Imaging.* 2004;20(4):697–705.
  21. Hu P, Stoeck CT, Smink J, Peters DC, Ngo L, Goddu B, et al. Noncontrast SSFP pulmonary vein magnetic resonance angiography: impact of off-resonance and flow. *J Magn Reson Imaging.* 2010;32(5):1255–61.
  22. Krishnam MS, Tomasian A, Deshpande V, Tran L, Laub G, Finn JP, et al. Noncontrast 3D steady-state free-precession magnetic resonance angiography of the whole chest using nonselective radiofrequency excitation over a large field of view: comparison with single-phase 3D contrast-enhanced magnetic resonance angiography. *Invest Radiol.* 2008;43(6):411–20.
  23. Sakuma H, Ichikawa Y, Chino S, Hirano T, Makino K, Takeda K. Detection of coronary artery stenosis with whole-heart coronary magnetic resonance angiography. *J Am Coll Cardiol.* 2006;48(10):1946–50.
  24. Sachs TS, Meyer CH, Hu BS, Kohli J, Nishimura DG, Macovski A. Real-time motion detection in spiral MRI using navigators. *Magn Reson Med.* 1994;32(5):639–45.
  25. Nehrke K, Börner P. Prospective correction of affine motion for arbitrary MR sequences on a clinical scanner. *Magn Reson Med.* 2005;54(5):1130–8.
  26. King AP, Boubertakh R, Rhode KS, Ma YL, Chinchapatnam P, Gao G, et al. A subject-specific technique for respiratory motion correction in image-guided cardiac catheterisation procedures. *Med Image Anal.* 2009;13(3):419–31.
  27. Jhooti P, Keegan J, Firmin DN. A fully automatic and highly efficient navigator gating technique for high-resolution free-breathing acquisitions: continuously adaptive windowing strategy. *Magn Reson Med.* 2010;64(4):1015–26.
  28. Kwong RY, Korlakunta H. Diagnostic and prognostic value of cardiac magnetic resonance imaging in assessing myocardial viability. *Top Magn Reson Imaging.* 2008;19(1):15–24.
  29. Kim RJ, Wu E, Rafael A, Chen EL, Parker MA, Simonetti O, et al. The use of contrast-enhanced magnetic resonance imaging to identify reversible myocardial dysfunction. *N Engl J Med.* 2000;343(20):1445–53.
  30. Scott PA, Morgan JM, Carroll N, Murday DC, Roberts PR, Peebles CR, et al. The extent of left ventricular scar quantified by late gadolinium enhancement MRI is associated with spontaneous ventricular arrhythmias in patients with coronary artery disease and implantable cardioverter-defibrillators. *Circ Arrhythm Electrophysiol.* 2011;4(3):324–30.
  31. Leyva F, Zegard A, Okafor O, Foley P, Umar F, Taylor RJ, et al. Myocardial fibrosis predicts ventricular arrhythmias and sudden death after cardiac electronic device implantation. *J Am Coll Cardiol.* 2022;79(7):665–78.
  32. O'Hanlon R, Grasso A, Roughton M, Moon JC, Clark S, Wage R, et al. Prognostic significance of myocardial fibrosis in hypertrophic cardiomyopathy. *J Am Coll Cardiol.* 2010;56(11):867–74.
  33. Kim RJ, Shah DJ, Judd RM. How we perform delayed enhancement imaging. *J Cardiovasc Magn Reson.* 2003;5(3):505–14.
  34. Simonetti OP, Kim RJ, Fieno DS, Hillenbrand HB, Wu E, Bundy JM, et al. An improved mr imaging technique for the visualization of myocardial infarction. *Radiology.* 2001;218(1):215–23.
  35. Moran GR, Thornhill RE, Sykes J, Prato FS. Myocardial viability imaging using Gd-DTPA: physiological modeling of infarcted myocardium, and impact on injection strategy and imaging time. *Magn Reson Med.* 2002;48(5):791–800.
  36. Gupta A, Lee VS, Chung YC, Babb JS, Simonetti OP. Myocardial infarction: optimization of inversion times at delayed contrast-enhanced MR imaging. *Radiology.* 2004;233(3):921–6.
  37. Kellman P, Arai AE, McVeigh ER, Aletras AH. Phase-sensitive inversion recovery for detecting myocardial infarction using gadolinium-delayed hyperenhancement. *Magn Reson Med.* 2002;47(2):372–83.
  38. Huber AM, Schoenberg SO, Hayes C, Spannagl B, Engelmann MG, Franz WM, et al. Phase-sensitive inversion-recovery MR imaging in the detection of myocardial infarction. *Radiology.* 2005;237(3):854–60.
  39. Setser RM, Chung YC, Weaver JA, Stillman AE, Simonetti OP, White RD. Effect of inversion time on delayed-enhancement magnetic resonance imaging with and without phase-sensitive reconstruction. *J Magn Reson Imaging.* 2005;21(5):650–5.



40. Droege RT, Adamczak SM. Boundary artifact in inversion-recovery images. *Magn Reson Med*. 1986;3(1):126–31.
41. Grosse-Wortmann L, Macgowan CK, Vidarsson L, Yoo SJ. Late gadolinium enhancement of the right ventricular myocardium: is it really different from the left? *J Cardiovasc Magn Reson*. 2008;10(1):20.
42. Bauner KU, Muehling O, Wintersperger BJ, Winnik E, Reiser MF, Huber A. Inversion recovery single-shot TurboFLASH for assessment of myocardial infarction at 3 Tesla. *Invest Radiol*. 2007;42(6):361–71.
43. Cochet A, Lalande A, Walker PM, Boichot C, Ciappuccini R, Cottin Y, et al. Comparison of the extent of delayed-enhancement cardiac magnetic resonance imaging with and without phase-sensitive reconstruction at 3.0 T. *Invest Radiol*. 2007;42(6):372–6.
44. Sievers B, Rehwald WG, Albert TSE, Patel MR, Parker MA, Kim RJ, et al. Respiratory motion and cardiac arrhythmia effects on diagnostic accuracy of myocardial delayed-enhanced MR imaging in canines. *Radiology*. 2008;247(1):106–14.
45. Sievers B, Elliott MD, Hurwitz LM, Albert TSE, Klem I, Rehwald WG, et al. Rapid detection of myocardial infarction by subsecond, free-breathing delayed contrast-enhancement cardiovascular magnetic resonance. *Circulation*. 2007;115(2):236–44.
46. Huber A, Schoenberg SO, Spannagl B, Rieber J, Erhard I, Klaus V, et al. Single-shot inversion recovery TrueFISP for assessment of myocardial infarction. *Am J Roentgenol*. 2006;186(3):627–33.
47. Kellman P, Larson AC, Hsu LY, Chung YC, Simonetti OP, McVeigh ER, et al. Motion-corrected free-breathing delayed enhancement imaging of myocardial infarction. *Magn Reson Med*. 2005;53(1):194–200.
48. Ledesma-Carbayo MJ, Kellman P, Arai AE, McVeigh ER. Motion corrected free-breathing delayed-enhancement imaging of myocardial infarction using nonrigid registration. *J Magn Reson Imaging*. 2007;26(1):184–90.
49. van den Bosch HCM, Westenberg JJM, Post JC, Yo G, Verwoerd J, Kroft LJM, et al. Free-breathing MRI for the assessment of myocardial infarction: clinical validation. *Am J Roentgenol*. 2009;192(6):W277–81.
50. Nguyen TD, Spincemaille P, Weinsaft JW, Ho BY, Cham MD, Prince MR, et al. A fast navigator-gated 3D sequence for delayed enhancement MRI of the myocardium: comparison with breath-hold 2D imaging. *J Magn Reson Imaging*. 2008;27(4):802–8.
51. Dickfeld T, Kato R, Zviman M, Lai S, Meininger G, Lardo AC, et al. Characterization of radiofrequency ablation lesions with gadolinium-enhanced cardiovascular magnetic resonance imaging. *J Am Coll Cardiol*. 2006;47(2):370–8.
52. Bogun FM, Desjardins B, Good E, Gupta S, Crawford T, Oral H, et al. Delayed-enhanced magnetic resonance imaging in nonischemic cardiomyopathy. *J Am Coll Cardiol*. 2009;53(13):1138–45.
53. Kadish AH, Rubenstein JC. Connecting the dots. *J Am Coll Cardiol*. 2009;53(13):1146–7.
54. Peters DC, Wylie JV, Hauser TH, Kissinger KV, Botnar RM, Essebag V, et al. Detection of pulmonary vein and left atrial scar after catheter ablation with three-dimensional navigator-gated delayed enhancement MR imaging: initial experience. *Radiology*. 2007;243(3):690–5.
55. Wylie JV, Peters DC, Essebag V, Manning WJ, Josephson ME, Hauser TH. Left atrial function and scar after catheter ablation of atrial fibrillation. *Heart Rhythm*. 2008;5(5):656–62.
56. Taclas JE, Nezafat R, Wylie JV, Josephson ME, Hsing J, Manning WJ, et al. Relationship between intended sites of RF ablation and post-procedural scar in AF patients, using late gadolinium enhancement cardiovascular magnetic resonance. *Heart Rhythm*. 2010;7(4):489–96.
57. Badger TJ, Oakes RS, Daccarett M, Burgon NS, Akoum N, Fish EN, et al. Temporal left atrial lesion formation after ablation of atrial fibrillation. *Heart Rhythm*. 2009;6(2):161–8.
58. Knowles BR, Caulfield D, Cooklin M, Rinaldi CA, Gill J, Bostock J, et al. 3-D visualization of acute RF ablation lesions using MRI for the simultaneous determination of the patterns of necrosis and edema. *IEEE Trans Biomed Eng*. 2010;57(6):1467–75.
59. Oakes RS, Badger TJ, Kholmovski EG, Akoum N, Burgon NS, Fish EN, et al. Detection and quantification of left atrial structural remodeling with delayed-enhancement magnetic resonance imaging in patients with atrial fibrillation. *Circulation*. 2009;119(13):1758–67.
60. Benito EM, Carlosena-Remirez A, Guasch E, Prat-González S, Perea RJ, Figueras R, et al. Left atrial fibrosis quantification by late gadolinium-enhanced magnetic resonance: a new method to standardize the thresholds for reproducibility. *Eurospace*. 2017;19(8):1272–9.
61. Marrouche NF, Wilber D, Hindricks G, Jais P, Akoum N, Marchlinski F, et al. Association of atrial tissue fibrosis identified by delayed enhancement MRI and atrial fibrillation catheter ablation: the DECAAF study. *JAMA*. 2014;311(5):498–506.
62. McGann CJ, Kholmovski EG, Oakes RS, Blauer JJE, Daccarett M, Segerson N, et al. New magnetic resonance imaging-based method for defining the extent of left atrial wall injury after the ablation of atrial fibrillation. *J Am Coll Cardiol*. 2008;52(15):1263–71.
63. Peters DC, Wylie JV, Hauser TH, Nezafat R, Han Y, Woo JJ, et al. Recurrence of atrial fibrillation correlates with the extent of post-procedural late gadolinium enhancement. *JACC Cardiovasc Imaging*. 2009;2(3):308–16.
64. Badger TJ, Daccarett M, Akoum NW, Adjei-Poku YA, Burgon NS, Haslam TS, et al. Evaluation of left atrial lesions after initial and repeat atrial fibrillation ablation: lessons learned from delayed-enhancement MRI in repeat ablation procedures. *Circ Arrhythm Electrophysiol*. 2010;3(3):249–59.
65. Daccarett M, McGann CJ, Akoum NW, MacLeod RS, Marrouche NF. MRI of the left atrium: predicting clinical outcomes in patients with atrial fibrillation. *Expert Rev Cardiovasc Ther*. 2011;9(1):105–11.
66. Chelu MG, King JB, Kholmovski EG, Ma J, Gal P, Marashly Q, et al. Atrial fibrosis by late gadolinium enhancement magnetic resonance imaging and catheter ablation of atrial fibrillation: 5-year follow-up data. *J Am Heart Assoc*. 2018;7(23):e006313.
67. Vergara GR, Marrouche NF. Tailored management of atrial fibrillation using a LGE-MRI based model: from the clinic to the electrophysiology laboratory. *J Cardiovasc Electrophysiol*. 2011;22(4):481–7.
68. Moghari MH, Peters DC, Smink J, Goepfert L, Kissinger KV, Goddu B, et al. Pulmonary vein inflow artifact reduction for free-breathing left atrium late gadolinium enhancement: projection navigator for pulmonary vein MRA. *Magn Reson Med*. 2011;66(1):180–6.
69. Davlouros PA. The right ventricle in congenital heart disease. *Heart*. 2006;92(Suppl\_1):i27–38.
70. Gatzoulis MA. Late arrhythmia in adults with the Mustard procedure for transposition of great arteries: a surrogate marker for right ventricular dysfunction? *Heart*. 2000;84(4):409–15.
71. Hong SZ, Happonen JM, Bennhagen R, Sairanen H, Pesonen E, Toivonen L, et al. Increased QT dispersion and loss of sinus rhythm as risk factors for late sudden death after Mustard or Senning procedures for transposition of the great arteries. *Am J Cardiol*. 2004;94(1):138–41.
72. Rydman R, Gatzoulis MA, Ho SY, Ernst S, Swan L, Li W, et al. Systemic right ventricular fibrosis detected by cardiovascular magnetic resonance is associated with clinical outcome, mainly new-onset atrial arrhythmia, in patients after atrial redirection surgery for transposition of the great arteries. *Circ Cardiovasc Imaging*. 2015;8(5):e002628.
73. Gewillig M, Cullen S, Mertens B, Lesaffre E, Deanfield J. Risk factors for arrhythmia and death after Mustard operation for

- simple transposition of the great arteries. *Circulation*. 1991;84(5 Suppl):III187–92.
74. Nollert G, Fischlein T, Bouterwek S, Böhmer C, Klinner W, Reichart B. Long-term survival in patients with repair of tetralogy of Fallot: 36-year follow-up of 490 survivors of the first year after surgical repair. *J Am Coll Cardiol*. 1997;30(5):1374–83.
  75. Geva T, Mulder B, Gauvreau K, Babu-Narayan SV, Wald RM, Hickey K, et al. Preoperative predictors of death and sustained ventricular tachycardia after pulmonary valve replacement in patients with repaired tetralogy of Fallot enrolled in the INDICATOR Cohort. *Circulation*. 2018;138(19):2106–15.
  76. Bokma JP, Geva T, Sleeper LA, Babu Narayan SV, Wald R, Hickey K, et al. A propensity score-adjusted analysis of clinical outcomes after pulmonary valve replacement in tetralogy of Fallot. *Heart*. 2018;104(9):738–44.
  77. Babu-Narayan SV, Kilner PJ, Li W, Moon JC, Goktekin O, Davlouros PA, et al. Ventricular fibrosis suggested by cardiovascular magnetic resonance in adults with repaired tetralogy of Fallot and its relationship to adverse markers of clinical outcome. *Circulation*. 2006;113(3):405–13.
  78. Munkhammar P, Carlsson M, Arheden H, Pesonen E. Restrictive right ventricular physiology after tetralogy of Fallot repair is associated with fibrosis of the right ventricular outflow tract visualized on cardiac magnetic resonance imaging. *Eur Heart J Cardiovasc Imaging*. 2013;14(10):978–85.
  79. Park SJ, On YK, Kim JS, Park SW, Yang JH, Jun TG, et al. Relation of fragmented QRS complex to right ventricular fibrosis detected by late gadolinium enhancement cardiac magnetic resonance in adults with repaired tetralogy of Fallot. *Am J Cardiol*. 2012;109(1):110–5.
  80. Ghonim S, Gatzoulis MA, Ernst S, Li W, Moon JC, Smith GC, et al. Predicting survival in repaired tetralogy of Fallot. *JACC Cardiovasc Imaging*. 2022;15(2):257–68.
  81. Ghonim S, Ernst S, Keegan J, Giannakidis A, Spadotto V, Voges I, et al. Three-dimensional late gadolinium enhancement cardiovascular magnetic resonance predicts inducibility of ventricular tachycardia in adults with repaired tetralogy of Fallot. *Circ Arrhythm Electrophysiol*. 2020;13(11):e008321.
  82. Rathod RH, Prakash A, Powell AJ, Geva T. Myocardial fibrosis identified by cardiac magnetic resonance late gadolinium enhancement is associated with adverse ventricular mechanics and ventricular tachycardia late after Fontan operation. *J Am Coll Cardiol*. 2010;55(16):1721–8.
  83. Cieplucha A, Trojnarowska O, Kociemba A, Łanocha M, Barczynski M, Rozmiarek S, et al. Clinical aspects of myocardial fibrosis in adults with Ebstein's anomaly. *Heart Vessels*. 2018;33(9):1076–85.
  84. O'Neill L, Sim I, O'Hare D, Whitaker J, Mukherjee RK, Razeghi O, et al. CARDiac MagnEtic resonance assessment of bi-atrial fibrosis in secundum atrial septal defects patients: CAMERA-ASD study. *Eur Heart J Cardiovasc Imaging*. 2022;23:1231.
  85. Nagarajan VD, Lee SL, Robertus JL, Nienaber CA, Trayanova NA, Ernst S. Artificial intelligence in the diagnosis and management of arrhythmias. *Eur Heart J*. 2021;42(38):3904–16.
  86. Cochet H, Iriart X, Allain-Nicolaï A, Camaioni C, Sridi S, Nivet H, et al. Focal scar and diffuse myocardial fibrosis are independent imaging markers in repaired tetralogy of Fallot. *Eur Heart J Cardiovasc Imaging*. 2019;20(9):990–1003.
  87. Perez-David E, Arenal Á, Rubio-Guivernau JL, del Castillo R, Atea L, Arbelo E, et al. Noninvasive identification of ventricular tachycardia-related conducting channels using contrast-enhanced magnetic resonance imaging in patients with chronic myocardial infarction. *J Am Coll Cardiol*. 2011;57(2):184–94.
  88. Wijnmaalen AP, van der Geest RJ, van Huls van Taxis CFB, HMJ S, LJM K, Bax JJ, et al. Head-to-head comparison of contrast-enhanced magnetic resonance imaging and electroanatomical voltage mapping to assess post-infarct scar characteristics in patients with ventricular tachycardias: real-time image integration and reversed registration. *Eur Heart J*. 2011;32(1):104–14.
  89. White JA, Fine N, Gula LJ, Yee R, Al-Admawi M, Zhang Q, et al. Fused whole-heart coronary and myocardial scar imaging using 3-T CMR. *JACC Cardiovasc Imaging*. 2010;3(9):921–30.
  90. Walsh EP. Interventional electrophysiology in patients with congenital heart disease. *Circulation*. 2007;115(25):3224–34.
  91. Chubb H, Harrison JL, Weiss S, Krueger S, Koken P, Bloch LØ, et al. Development, preclinical validation, and clinical translation of a cardiac magnetic resonance - electrophysiology system with active catheter tracking for ablation of cardiac arrhythmia. *JACC Clin Electrophysiol*. 2017;3(2):89–103.
  92. Hilbert S, Sommer P, Gutberlet M, Gaspar T, Foldyna B, Piorkowski C, et al. Real-time magnetic resonance-guided ablation of typical right atrial flutter using a combination of active catheter tracking and passive catheter visualization in man: initial results from a consecutive patient series. *Europace*. 2016;18(4):572–7.
  93. Mukherjee RK, Chubb H, Roujol S, Razavi R, O'Neill MD. Advances in real-time MRI-guided electrophysiology. *Curr Cardiovasc Imaging Rep*. 2019;12(2):6.
  94. Mukherjee RK, Roujol S, Chubb H, Harrison J, Williams S, Whitaker J, et al. Epicardial electroanatomical mapping, radio-frequency ablation, and lesion imaging in the porcine left ventricle under real-time magnetic resonance imaging guidance—an in vivo feasibility study. *Eurospace*. 2018;20(FI2):f254–62.
  95. Khalique Z, Ferreira PF, Scott AD, Nielles-Vallespin S, Firmin DN, Pennell DJ. Diffusion tensor cardiovascular magnetic resonance imaging. *JACC Cardiovasc Imaging*. 2020;13(5):1235–55.
  96. Ariga R, Tunnicliffe EM, Manohar SG, Mahmood M, Raman B, Piechnik SK, et al. Identification of myocardial disarray in patients with hypertrophic cardiomyopathy and ventricular arrhythmias. *J Am Coll Cardiol*. 2019;73(20):2493–502.
  97. Tous C, Gentles TL, Young AA, Pontré BP. Ex vivo cardiovascular magnetic resonance diffusion weighted imaging in congenital heart disease, an insight into the microstructures of tetralogy of Fallot, biventricular and univentricular systemic right ventricle. *J Cardiovasc Magn Reson*. 2020;22(1):69.
  98. Niederer SA, Lumens J, Trayanova NA. Computational models in cardiology. *Nat Rev Cardiol*. 2019;16(2):100–11.
  99. Arevalo HJ, Vadakkumpadan F, Guallar E, Jebb A, Malamas P, Wu KC, et al. Arrhythmia risk stratification of patients after myocardial infarction using personalized heart models. *Nat Commun*. 2016;7(1):11437.
  100. Cartoski MJ, Nikolov PP, Prakosa A, Boyle PM, Spevak PJ, Trayanova NA. Computational identification of ventricular arrhythmia risk in pediatric myocarditis. *Pediatr Cardiol*. 2019;40(4):857–64.
  101. Shade JK, Cartoski MJ, Nikolov P, Prakosa A, Doshi A, Binka E, et al. Ventricular arrhythmia risk prediction in repaired tetralogy of Fallot using personalized computational cardiac models. *Heart Rhythm*. 2020;17(3):408–14.
  102. Boyle PM, Zghaib T, Zahid S, Ali RL, Deng D, Franceschi WH, et al. Computationally guided personalized targeted ablation of persistent atrial fibrillation. *Nat Biomed Eng*. 2019;3(11):870–9.
  103. Shade JK, Ali RL, Basile D, Popescu D, Akhtar T, Marine JE, et al. Preprocedure application of machine learning and mechanistic simulations predicts likelihood of paroxysmal atrial fibrillation recurrence following pulmonary vein isolation. *Circ Arrhythm Electrophysiol*. 2020;13(7):e008213.



Michael D. Seckeler, Claudia E. Guerrero,  
and Andrew W. Hoyer

### 24.1 Introduction

Stereolithography, or as it is more commonly known, 3D printing, was first performed by Charles Hull in 1983 when he used the technique to produce a small plastic cup [1], and his first patent was issued in 1986 [2]. Since that time, there has been a rapid expansion of the use of 3D printing, initially in the fields of engineering and manufacturing, but more recently, in medicine. One field in which 3D printing has been embraced is congenital heart disease (CHD). Given the complex and variable nature of CHD, the ability to visualize and hold these hearts in your hand has been a game changer. In this chapter, we will explore some of the technical aspects of 3D printing, image acquisition in CHD, applications and limitations of 3D printing, and future uses of the technology.

### 24.2 The Process of 3D Printing

3D printing, or additive manufacturing, is the process of successive layering of a material to generate a structure with length, width, and height. The steps of digital model development and preparation are illustrated in Fig. 24.1. The first step is to acquire a digital 3D dataset, and for CHD, this is typically from computed tomography (CT) or magnetic resonance imaging (MRI). Once the dataset is acquired, the areas of interest for printing must then be identified and highlighted, a process called segmentation (Fig. 24.1), and usually converted to stereolithographic (STL) file formatting, the same that Charles Hull developed. The segmented data-

set is then sliced, or converted into a stack of cross sections, which will become the printed layers (Fig. 24.1). The sliced file also has instructions for the 3D printer to physically print the object. The process of segmentation and slicing can take minutes to hours, and the print time can be as long as 24 h, depending on the size and complexity of the structure to be printed.

The most common 3D printing technologies in use today are fused deposition modeling (FDM), selective laser sintering (SLS), stereolithography (SLA), PolyJet, and digital light processing (DLP). Each has its own advantages and disadvantages, and a full analysis is beyond the scope of this chapter, but some examples of the printing process and final products from FDM and DLP printers are shown in Fig. 24.2.

Some of the earliest descriptions of 3D printing in CHD came in 2006 when several groups reported printing models of various defects, including direct comparisons between the printed model, standard angiography, and direct visual inspection at the time of surgery [3, 4]. 3D datasets that have typically been used for CHD are CT or MRI, but they need to be high quality for accurate model generation. There is also a need for expertise in software and hardware manipulation [5, 6]. Several groups have quantitatively compared 3D-printed models to the original CT datasets and found high fidelity in the reproductions [7, 8].

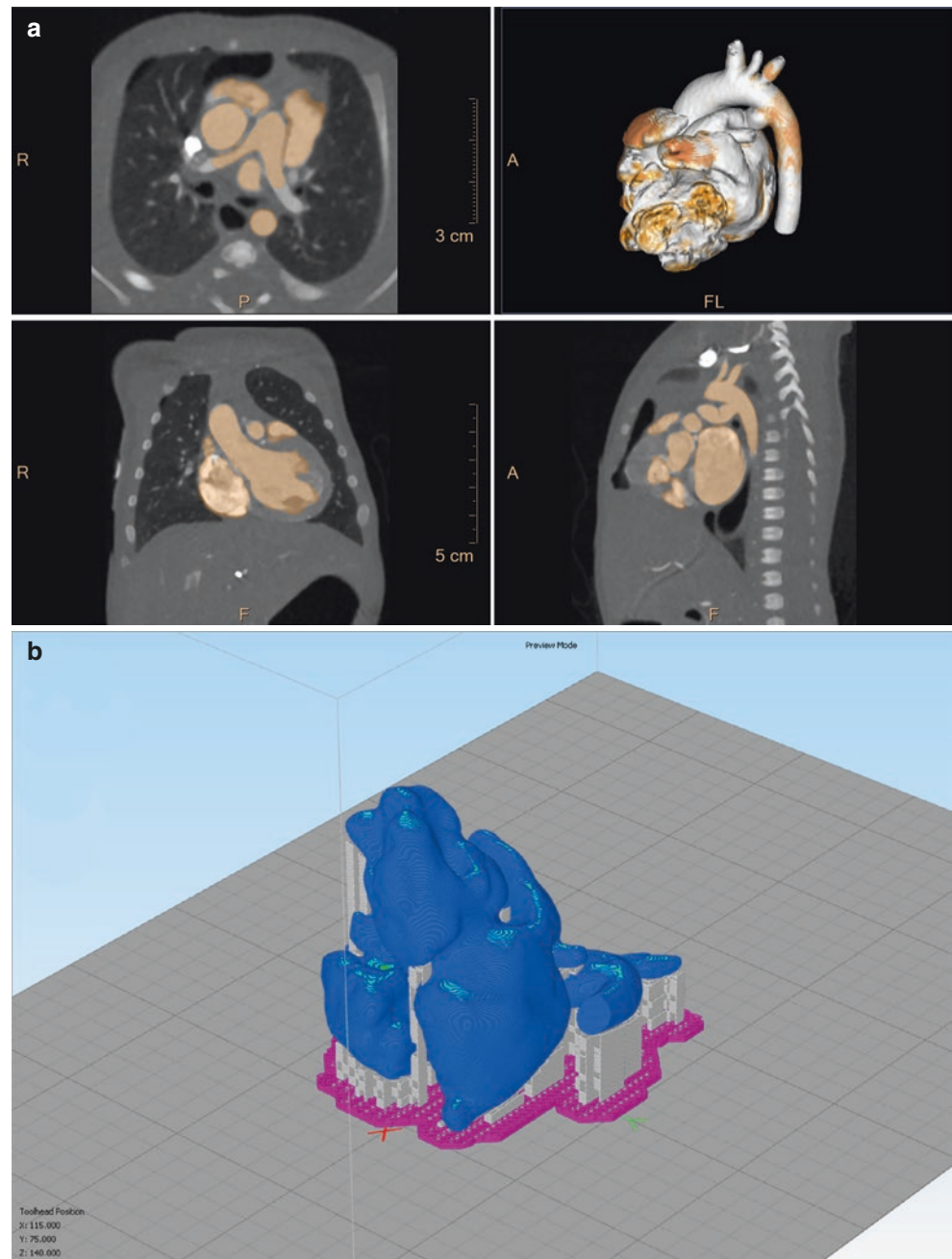
While it is ideal to minimize exposure to ionizing radiation in patients with CHD, many have metallic implants (stents, occluder devices, and coils) which, even if safe for MR imaging, could cause enough image distortion to render MRI useless. In addition, image acquisition time is still longer for MRI such that infants need to be anesthetized to obtain diagnostic images. In response, cardiac CT scans with dose-reduction techniques have been used for infants with a variety of CHD and were found to generate excellent-quality images [9]. There have also been improvements in MR post-processing techniques so 3D modeling from MRI may become more commonplace [10]. While CT typically provides higher resolution imaging for 3D model generation,

The original version of the chapter has been revised. A correction to this chapter can be found at [https://doi.org/10.1007/978-3-031-29235-4\\_25](https://doi.org/10.1007/978-3-031-29235-4_25)

M. D. Seckeler (✉) · C. E. Guerrero · A. W. Hoyer  
Department of Pediatrics (Cardiology), University of Arizona/  
Banner University Medical Center – Tucson, Tucson, AZ, USA  
e-mail: [mseckeler@peds.arizona.edu](mailto:mseckeler@peds.arizona.edu);  
[Claudia.Guerrero@bannerhealth.com](mailto:Claudia.Guerrero@bannerhealth.com); [ahoyer@arizona.edu](mailto:ahoyer@arizona.edu)



**Fig. 24.1** Process of 3D model generation for a neonate with pulmonary atresia, intact ventricular septum, and a tortuous patent ductus arteriosus. **(a)** Once a 3D dataset is obtained (typically from CT or MR imaging), the structures of interest are highlighted, a process known as segmentation. This shows axial, coronal, and sagittal projections with the segmented structures highlighted in orange and the 3D reconstruction in the upper right box. **(b)** Once the model has been cleaned and checked for errors, it is imported into slicing software which will generate support structures (gray) which are needed during the printing process and provide instructions for the movements for the specific 3D printed to be used



our group has been able to successfully use MRI to generate 3D models on newborn infants weighing less than 3 kg (Fig. 24.3).

Newer imaging modalities have allowed for acquisition of 3D datasets at the same time as other clinically indicated procedures. 3D rotational angiography (3DRA), which is increasingly performed as part of routine cardiac catheteriza-

tions, can produce printable 3D datasets [11, 12]. Due to the concern for increased radiation doses with 3DRA, Fetterly performed simulated radiation dose reductions for 3DRA imaging and found that even after reducing the radiation dose by 72%, there were no significant differences in the quality of the imaging or measurements of the structures of interest [13].



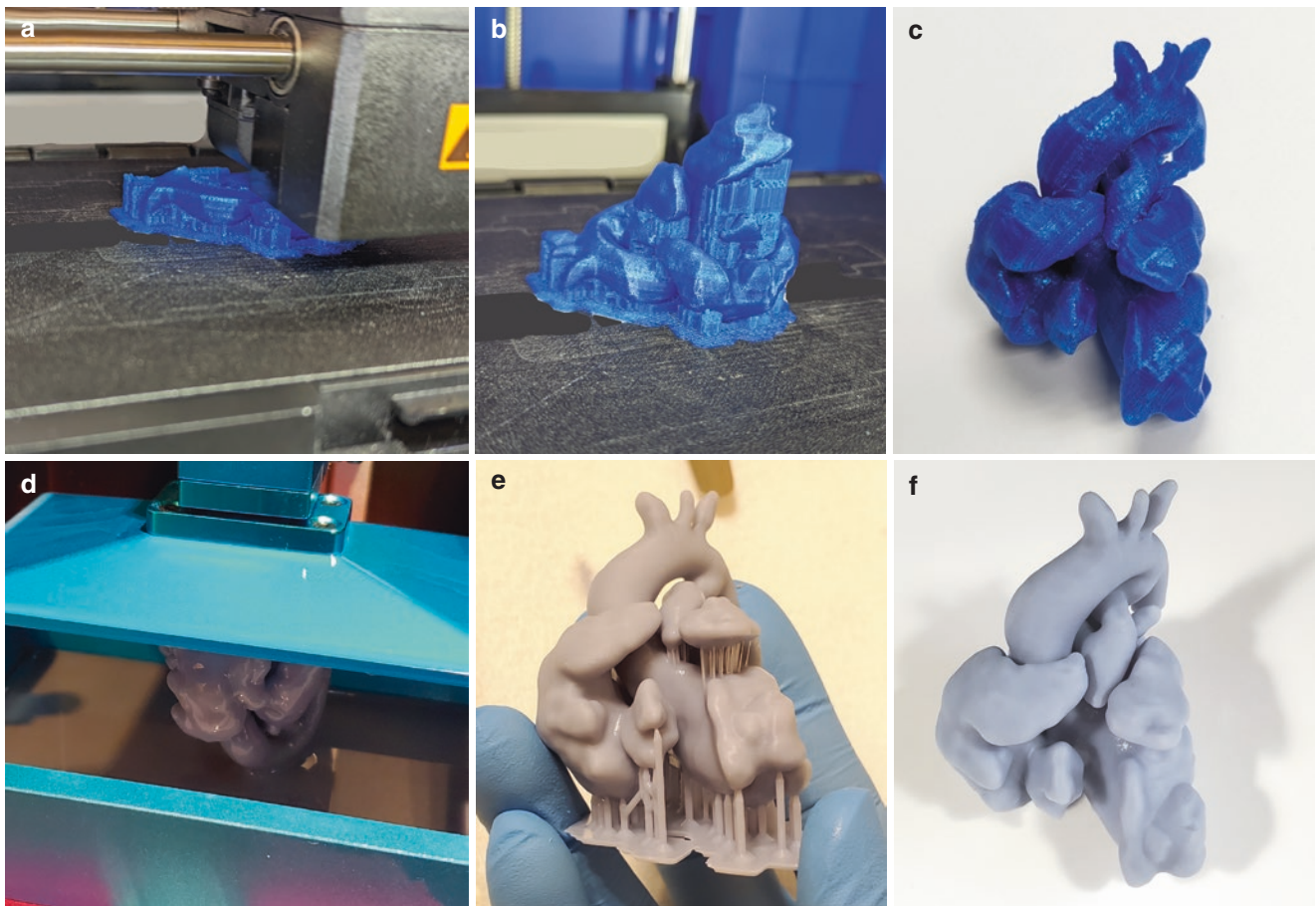


**Fig. 24.2** The process of 3D model printing for a neonate with pulmonary atresia, intact ventricular septum, and a tortuous patent ductus arteriosus. (a–c) An example of fused deposition modelling (FDM) printing which heats and extrudes filament and draws the layers to create a 3D model. Once the model is complete, there are support structures which are needed during the print but are removed afterwards to

produce the final model. (d–f) An example of digital light processing (DLP) printing which uses a light source to photocure resin material to generate the layers and create a 3D model. Once the model is complete, there are support structures which are needed during the print but are removed afterwards to produce the final model. Photos for (d–f) provided by Jason Pedersen

An exciting new development is the use of echocardiographic datasets to generate 3D-printed models without the use of any ionizing radiation. As detailed as CT and MRI are, thin structures, such as the atrioventricular valves, can be difficult to visualize, particularly in smaller patients. Several groups have utilized 3D datasets from either transthoracic or transesophageal echocardiograms to successfully print 3D models [14–17]. Additionally, others have been able to 3D print models of complex CHD with data obtained from fetal

echocardiograms which have been particularly useful for prenatal counseling [18, 19].

Finally, combining all these modalities into hybrid model generation has allowed teams to use the best aspects of each technique to generate accurate 3D-printed models and optimize the clinical data obtained from the models. These models can be used for surgical planning, hemodynamic simulation, or education [14–16].

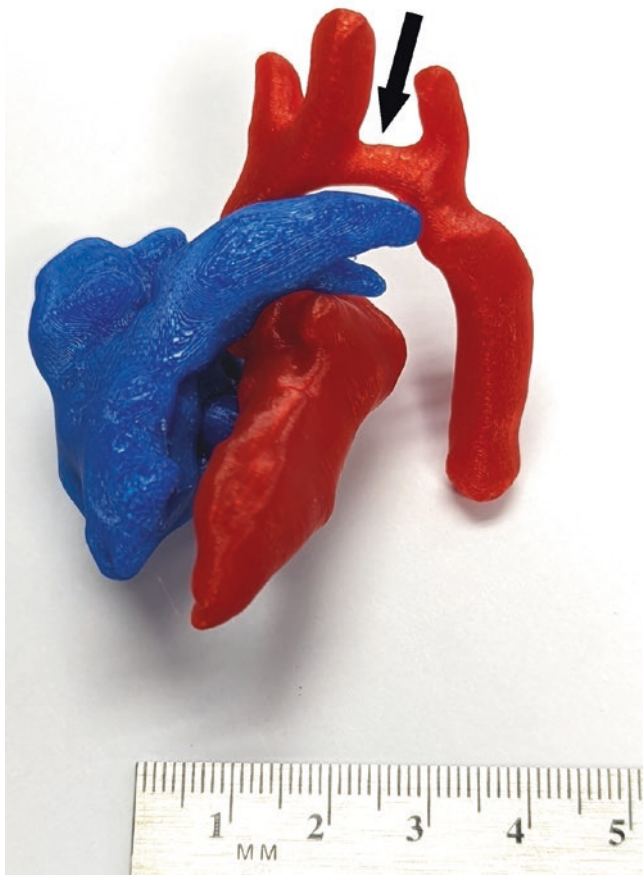


**Fig. 24.3** Printed 3D model of a 2.7 kg neonatal with a hypoplastic transverse aortic arch (arrow) created from a cardiac MRI obtained on a 1.5 T scanner

## 24.3 Current Applications of 3D Printing for Congenital Heart Disease

The use of 3D-printed models in CHD is relatively new [3, 4], but there has been rapid adoption within the field for multiple uses, including procedural planning (surgical and transcatheter), hemodynamic simulations, and education [20]. To support these uses, several studies have demonstrated the accuracy of 3D-printed models within 1 mm of standard clinical imaging [21, 22].

### 24.3.1 Surgical Planning for Complex CHD Repair

Two of the most challenging forms of CHD to repair surgically are double outlet right ventricle (DORV) and complete atrioventricular septal defects (AVSD) as the complex intracardiac relationships can be quite challenging to visualize by standard transthoracic echo alone and the interventional decisions made can greatly alter the long term outcomes for these patients.

For DORV, the location of the aorta relative to the ventricular septal defect (VSD) determines whether a surgeon can create an intracardiac baffle from the left ventricle, through the VSD and out the aorta to establish biventricular circulation (Fig. 24.4). 3D-printed models have been used to guide the critical decision of either initiating single ventricle palliation and potentially later converting to biventricular circulation [23] or performing biventricular repair as the initial intervention in patients where standard imaging supported single ventricle palliation [24–29]. To further understand the potential clinical benefits of a pre-operative 3D-printed model, one team compared outcomes for patients with DORV between those with and those without 3D-printed models. Encouragingly, post-operative ventilator time and ICU stays were significantly shorter in the 3D model group [30].

For patients with an AVSD, particularly in the setting of heterotaxy syndrome, it can be difficult to determine patient suitability for single versus biventricular intracardiac repair. A review of the management of AVSD highlighted the beneficial addition of 3D echocardiography and 3D-printed models in helping to determine adequacy of biventricular repairs in borderline cases [31]. A series of patients with complex AVSD achieved conversion to biventricular circulation with the aid of 3D-printed models as part of the standard pre-operative evaluation [32].

In addition to DORV and AVSD, researchers have utilized 3D-printed models for a variety of complex CHD cases, including variants of tetralogy of Fallot [33, 34], transposition of the great arteries [35], anomalous pulmonary venous connection [36], pulmonary artery pseudoaneurysm resection [37] and rerouting of a Fontan pathway [38]. It is felt that 3D-printed models used for surgical planning can reduce the exploration and surgical times, which in turn can improve clinical outcomes. The 3D model can also help in the understanding of complex patient anatomy and can help improve pre-operative communication between the surgeon and the patient and family [37] (Fig. 24.5).

Overall, 3D printing can be very useful in planning surgical techniques and in choosing between single ventricle, one and a half ventricle, and biventricular repair [39]. It can also improve multidisciplinary team decision-making, patient and family understanding, and education of medical professionals [39, 40].

### 24.3.2 Mechanical Cardiac Support and Heart Transplantation

It is inevitable that some patients with CHD will develop heart failure and require mechanical cardiac support and possible heart transplantation. Many of these patients will have unusual intracardiac and intrathoracic post-operative anat-



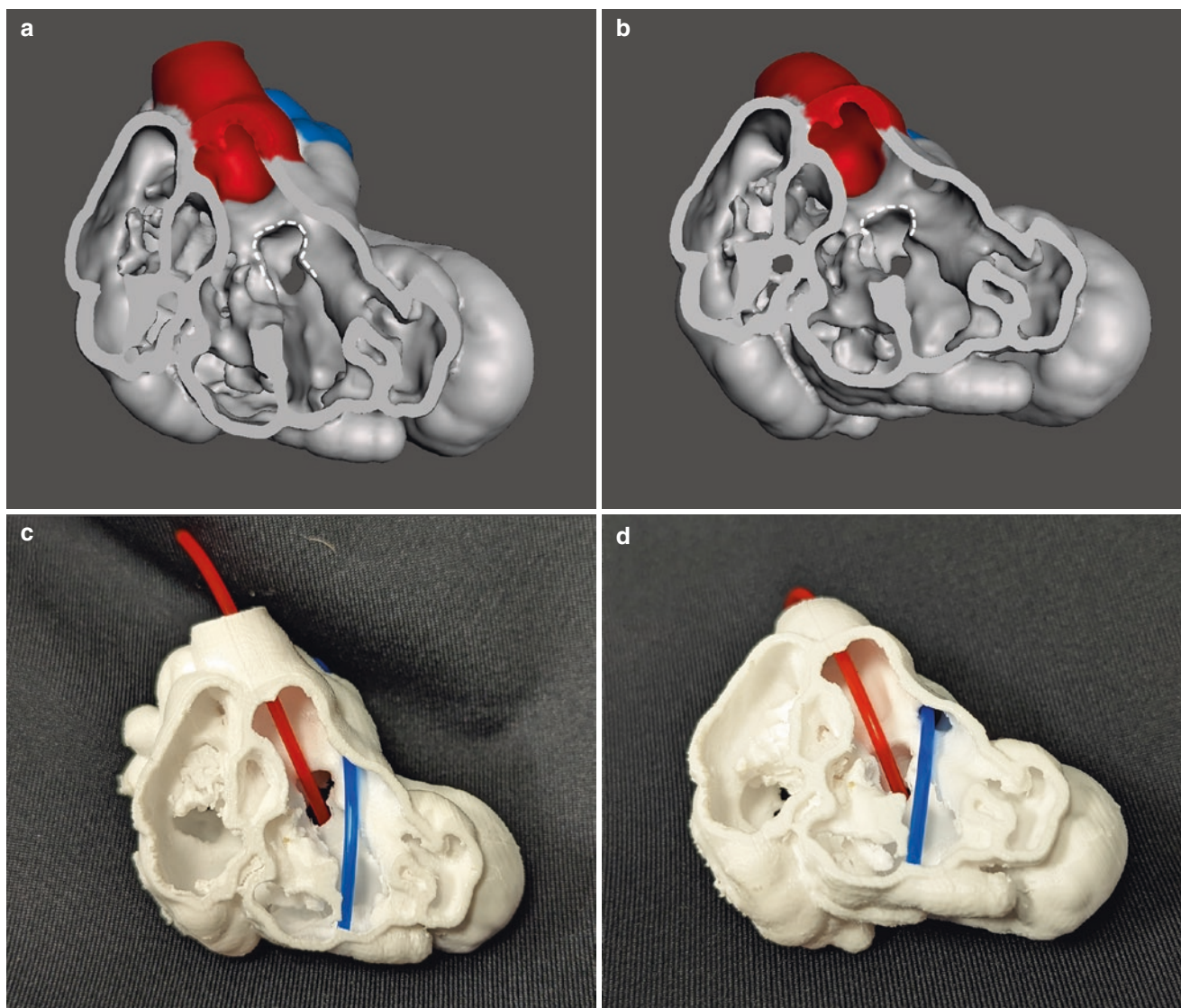


**Fig. 24.4** Utility of 3D models for surgical repair of double outlet right ventricle (DORV). (a, b) Two views of a virtual 3D reconstruction of an infant with DORV (right ventricular free wall removed) with the aorta highlighted in red, the pulmonary artery highlighted in blue, and the ventricular septal defect (VSD) outlined with the dashed line. (c, d)

Two views of a 3D-printed model of the same patient with the red line representing the direction of flow from the left ventricle, through the VSD and out the aorta and the blue line representing flow from the right ventricle through the right ventricular outflow tract and out the pulmonary artery

omy, and 3D-printed models can be used to plan for ventricular assist device (VAD) implantation [41]. This can be particularly important for adults with CHD as the multiple prior surgeries can make re-intervention more challenging and higher risk. And while these patients could benefit from mechanical cardiac support, their anatomy and risk factors may preclude it. 3D-printed models can help identify the best approach for placing mechanical support devices, increasing surgeon confidence to undertake the procedure, and may lead to shorter procedure times as well [42].

For those who go on to heart transplantation, 3D-printed models can help surgeons anticipate and plan for problems that may arise during dissection or implantation of the donor

heart. Models can be particularly useful in determining any special dimensions and requirements of the donor heart, such as extra donor venous tissue to “undo” Fontan procedures [43–45]. Better pre-operative planning can also reduce cross-clamp and total operative time, further reducing patient morbidity [44].

### 24.3.3 Cardiac Catheterization

The field of interventional congenital cardiology has always pushed the envelope to develop minimally-invasive approaches to minimize morbidities for this fragile popula-

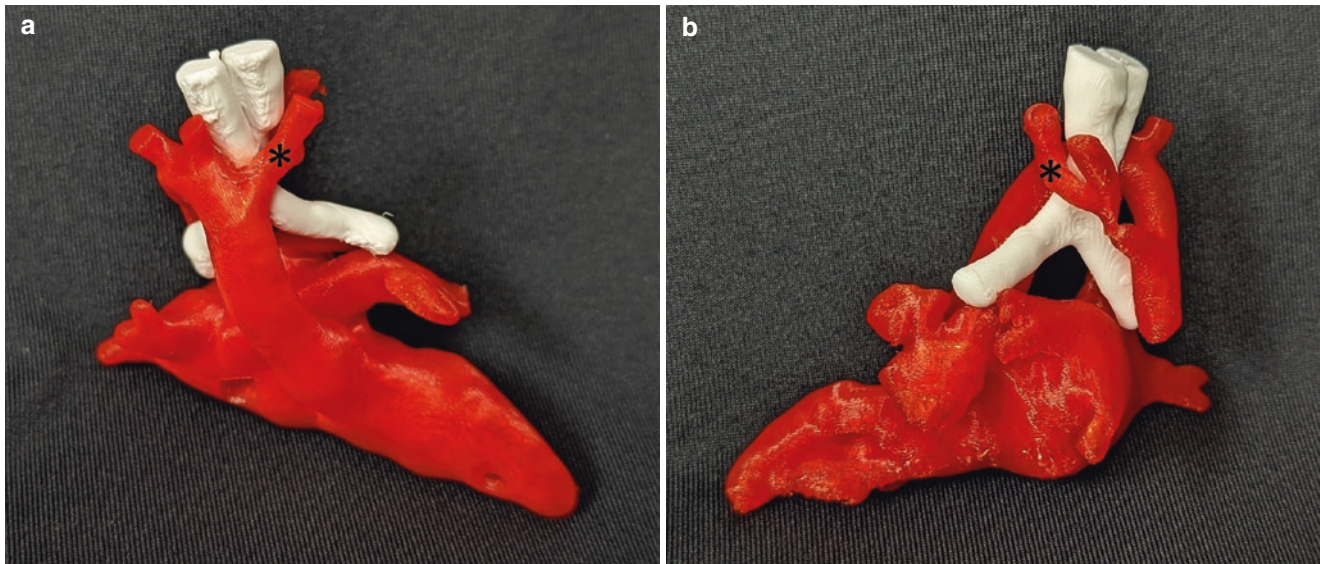


**Fig. 24.5** 3D-printed model of a neonate with double aortic arch from anterior (a) and posterior (b) views. The double aortic arch (red) with a hypoplastic left segment (\*) enwraps the trachea and esophagus (white).

These models can help families to understand the anatomy of their child's congenital heart defect and need for surgical intervention

tion. The complex anatomy can be challenging to understand with angiography alone, so 3D-printed models have been embraced by the interventional community to optimize the planning and safety of interventional catheterizations. There are almost as many uses of 3D-printed models to guide transcatheter interventions as there are CHDs. 3D-printed models have been used for coronary artery fistula closure [46, 47], ductus arteriosus stenting to maintain pulmonary blood flow [48], closure of an atrial baffle leak in a patient with a crisscross heart [49], device closure of a right ventricular outflow tract pseudoaneurysm [50], device closure of a ruptured sinus of Valsalva aneurysm [51], transcatheter Fontan completion [52], closure of an unroofed coronary sinus [53], recanalization of a chronically occluded branch pulmonary artery [54] and percutaneous edge-to-edge repair of systemic atrioventricular valve regurgitation [55]. For each of these reports, the ability to simulate and practice intervention, as well as improved communication with the care team and patients, were noted benefits of the 3D-printed models.

The first reported use of a 3D-printed model to guide a catheterization was in 2014 when Olivieri and colleagues printed a 3D model of the heart of a patient with pulmonary venous baffle obstruction after a Mustard procedure to aid in planning successful transcatheter stent placement [56]. This was followed by reports of 3D-printed models to guide catheter-based interventions on complex aortic coarctation and arch hypoplasia [57, 58].

Device closure of atrial septal defects (ASDs) is one of the earliest transcatheter interventions, but the septal geometry can be complex and hard to assess by standard imaging techniques, such as echocardiography, such that some

patients who could benefit from device closure instead undergo surgical closure. In particular, some patients appear to have insufficient tissue rims around the ASD on echocardiogram to allow for safe placement of standard occluder devices. Several groups have found that 3D-printed models can allow for more accurate visualization and assessment of the tissue rims [59] and for in vitro test closure of complex ASDs with standard and off-label closure devices [60, 61].

An exciting extension of 3D printing in planning transcatheter interventions is the treatment of superior sinus venous ASDs and partial anomalous pulmonary venous return, which have historically required surgical closure. However, using 3D-printed models and bench simulations of covered stent placement has allowed planning to create the “missing” wall between the superior vena cava and the pulmonary veins (Fig. 24.6). The team at Evelina London Children's Hospital in the United Kingdom has pioneered this technique with good medium-term outcomes [62–64]. 3D model planning allows for selection of candidates with anatomy favorable for the transcatheter approach, and the procedure has successfully been replicated at other centers around the world [65].

3D-printed models have been used in electrophysiology catheter interventions as well. A number of adults with CHD will develop conduction abnormalities related to the underlying CHD or as a consequence of their prior interventions. Atypical anatomy is the norm for these patients and unusual approaches may be needed to successfully perform ablation procedures or place transvenous pacemaker leads (Fig. 24.7). Many patients with ventricular looping abnormalities can have unusual coronary sinus anatomy, [66] and it may even be absent [67], making pacemaker lead placement challeng-



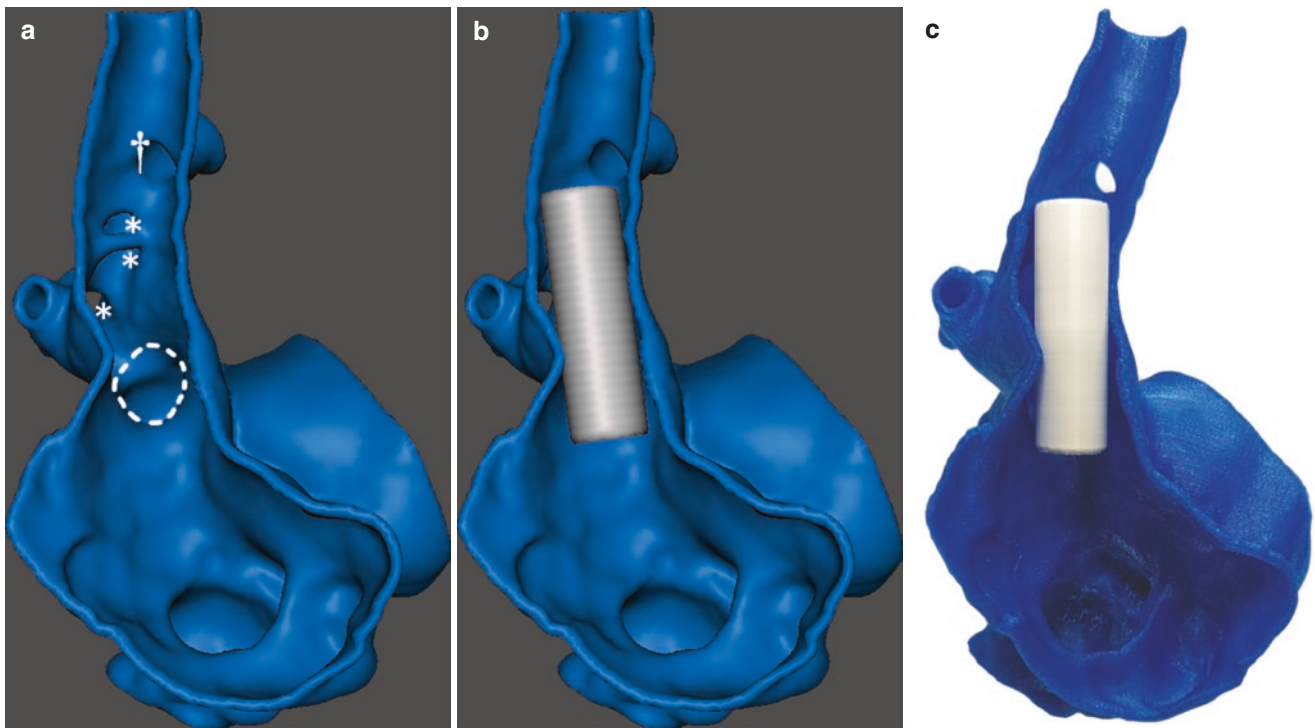


**Fig. 24.6** Planning for transcatheter correction of anomalous right-sided pulmonary venous return and a superior sinus venosus atrial septal defect. (a) 3D virtual model (anterior right atrial wall cut away) demonstrating the anomalous right-sided pulmonary veins entering the superior vena cava (\*), the superior sinus venosus atrial septal defect (dotted line), and the normal entry of the azygous vein (†). (b) Virtual

implantation of a covered stent (white) to recreate the back wall of the superior vena cava, rerouting the anomalous pulmonary venous drainage and closing the atrial septal defect. (c) 3D-printed model for pre-procedure simulation. Note that the azygous vein is not obstructed by the covered stent

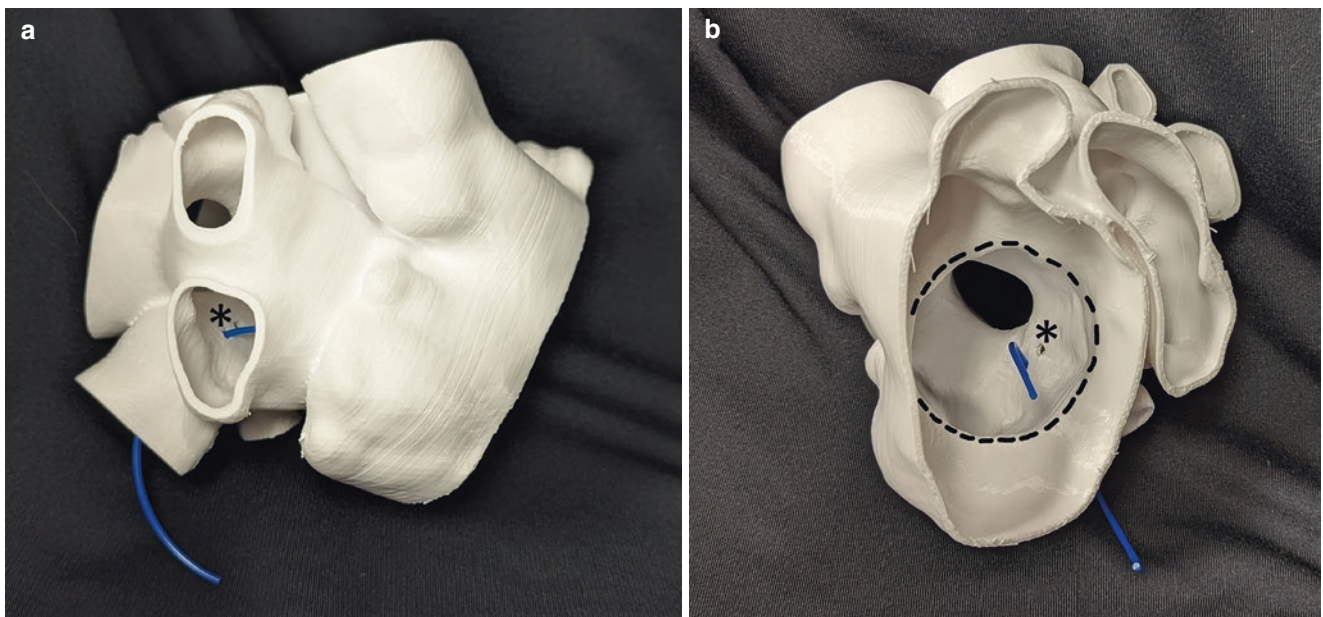


**Fig. 24.7** 3D-printed model of a patient with transposition of the great arteries who has undergone a Mustard procedure and required transcatheter ablation for atrial flutter with a tricuspid annular focus from lateral (a) and anterior (b) views. Because of the complex surgical intra-atrial venous rerouting, the inferior vena cava no longer communicated

with the tricuspid valve annulus (dotted line) and transbaffle puncture was needed to perform the intervention. The 3D-printed model was used to plan the two puncture sites (\*) needed to position the interventional catheters (represented by the blue line)

ing, but 3D-printed models have been used in such cases to plan and guide an alternative approach for successful lead placement.

#### 24.3.4 Simulation

Aside from procedural planning, groups have also been exploring the utility of 3D-printed models for various simulations. The most common use has been simulated surgical intervention [20]. Trainees and junior surgeons can learn complex congenital surgical interventions on life-size 3D-printed models made from thin, flexible materials, such as polyurethane resin, before sewing a stitch in a human [68, 69]. Several authors have published small series and proof-of-concept papers, but these works have lacked objective data to prove the utility of the models in improving surgical outcomes [70], aside from one objective assessment of successful simulated arterial switch procedures, to be able to better understand the utility of surgical simulation in improving outcomes [71]. Groups have also utilized 3D-printed models for simulated transcatheter interventions, such as intracardiac shunt occlusion [69] and interventions for pulmonary artery stenosis [72], but more assessment tools will need to be developed for other lesions to understand the potential benefit of 3D-printed models for clinical care.

Another innovative use of 3D-printed models is to simulate post-intervention physiology. One team 3D printed a series of different-sized simulated ASDs to allow for deployment of a transcatheter ASD occluder to better define and understand the deployed dimensions of different device sizes in different-sized defects [73]. Another group used 3D-printed models to predict adverse outcomes after surgical intervention on coronary arteries both for arterial switch procedures [74] and for repair of anomalous coronary artery origins [75]. 3D-printed models of right ventricular outflow anatomy (normal and tetralogy of Fallot after transannular patch repair) were used in hemodynamic simulators and 4D MRI modeling of flow to assess factors that can affect the longevity of implanted bioprosthetic valves [76]. Another group used 3D-printed mitral valves in hemodynamic simulators to predict hemodynamic changes after transcatheter edge-to-edge valve repair [77], a technique that could potentially be used in single-ventricle patients. Another team compared 3D-printed models of Fontan conduits using SLA, SLS, and FDM printers and assessed flow dynamics with hemodynamic simulators. Overall, each made a reasonable representation, but the internal support structures required in FDM models produced less accurate flow modeling [78]. The

attractive low-cost FDM models will need to be balanced against the anatomic and physiologic accuracy of the model.

#### 24.3.5 Education

Just as surgeons can learn to perform an arterial switch operation on a 3D model, students can learn anatomy of CHD lesions using models. An open-access library of 3D models of CHD that would be freely available for downloading and printing has been proposed [79]. Others have used cardiac CT of fetal hearts [80] and digital manipulation of cardiac CT scans of normal hearts [81] to create libraries of CHD for education.

There have been numerous studies that assess the subjective and objective benefits of incorporating 3D-printed models of CHD into didactic sessions. These have included multiple levels of learners (medical students, nursing staff, cardiology fellows, attending cardiologists and surgeons) and covered a variety of CHD, such as VSDs and tetralogy of Fallot [82–90], extracardiac vascular defects [84, 85, 88–91], crisscross hearts [92], and complex single ventricle lesions [85, 93]. These studies have shown subjective improvements in learner understanding, but the objective improvements have been less consistent. One innovation that improves understanding is the use of different colored materials to distinguish anatomic structures [85]. There is also probably more benefit for higher complexity lesions (tetralogy of Fallot versus an isolated VSD) [87] and for more junior learners [89, 92].

3D-printed models of CHD have also been used for hands-on surgical training which can allow for practice on pathological hearts without patient risk or having to follow the traditional training model of waiting for potential opportunities to present themselves [68, 94–98]. Hearts can be 3D printed with flexible, tissue-like material to allow for cutting and suturing and have been used for transposition of the great arteries, tetralogy of Fallot, and hypoplastic left heart syndrome, among other defects. Earlier studies found the material to be too different from human myocardium to be useful [94], but there have been advances in material development [68]. Cardiac valves were poorly recreated in the earlier models [94], but a newer technique for valve simulation using 3D echocardiographic imaging to print negative molds and then cast silicone valves has created more tissue-like valves for surgical practice [96]. Hussein and colleagues have shown a reduction in simulated operative time for the arterial switch procedure with repeated practice using 3D-printed models [97]. The same group has also created an objective assessment tool to define successful simulated arterial switch procedures to better understand the utility of surgical simulation in improving clinical outcomes beyond just

shorter operative time [71]. Scientific proof of the utility of 3D-printed models for surgical education is challenging due to many confounders that affect outcome [99], and more tools will need to be developed for other CHD to truly understand the potential benefit of 3D-printed models for clinical care.

Besides medical professionals, 3D models can educate patients and their families about their cardiac defect. Children with CHD will require lifelong cardiology care, and a good understanding of the pathologic disease process is likely helpful in improving medical compliance. This can start as early as the initial diagnosis with fetal echocardiograms being used to 3D print models [18, 19]. Pre-operative 3D-printed models can also help families understand the indications for surgery and aid in operative consent [39, 100]. 3D-printed models have also been shown to help reduce patient and family anxiety before cardiac catheterizations [101]. Stressing the importance of lifelong cardiology follow-up, Liddle used virtual 3D models to teach adolescents with CHD about their disease and found improved understanding after the teaching sessions [102]. A meta-analysis found a small number of reports which suggest that 3D models are accurate and help with communication, but consistent with other studies, objective clinical utility has yet to be demonstrated [103].

---

## 24.4 Future of 3D Printing for Congenital Heart Disease

### 24.4.1 Machine Learning

There are several barriers to widespread adoption of 3D printing in CHD, and one of the most important is fast, accurate segmentation from the initial 3D dataset. This is currently mostly a manual, time-consuming process, and any inaccuracies that occur during segmentation will carry through the entire 3D printing process, which can lead to inappropriate clinical interpretations or plans [104]. There are only limited options for semi-automated segmentation of scans [105] and still no consistent method for model creation and printing across centers [106]. Machine learning has been proposed as a solution for improved automated segmentation [107]. The striking variation in CHD anatomy that occurs in a relatively small population of patients limits the datasets available for machine learning [107]. However, progress has been made with development of a machine learning technique to autosegment the left atrium and anomalous pulmonary veins for pre-operative planning in patients with total anomalous pulmonary venous return [108]. The authors report that using their method would decrease the radiologist's workload from several hours per scan to only 400 ms. Expansion of this tech-

nique to other CHD will be critical to widespread and clinically useful adoption of 3D modeling and printing.

### 24.4.2 Bioprinting

An exciting area of future development for 3D printing in CHD is bioprinting of customized implants [109]. Work has been done to create cardiac valve replacements [110], bio-printed scaffolds seeded with a patient's stem cells to create vascular grafts that can be used to replace stenotic or hypoplastic vessels [111], or implanted as Fontan conduits [112] that can grow with the patients. While tissue engineering has existed for some time, 3D printing can aid in more lifelike and anatomically accurate scaffold creation [113]. Another step toward growing implants is 4D bioprinting of materials that are designed to respond to specific stimuli, such as heat, to alter their shape which could allow for growth of implanted structures, such as intravascular stents [114]. In addition, implants printed from biodegradable material could grow with the patients, who would not need chronic anti-coagulation typically used after implantation of metallic devices [115].

Currently, there is no ideal printer available, but industry has taken notice and is working to develop printers that can provide optimal resolution and speed with low costs and high viability of the printed cells [113].

---

## 24.5 Limitations of 3D Printing for Congenital Heart Disease

As exciting as 3D-printed models are for CHD, there are still several limitations that hinder widespread adoption. The first was discussed earlier and relates to the time-consuming nature of the process of model generation and the steep learning curve [104, 106, 116]. There have already been steps made at reducing segmentation time by utilizing machine learning [108] and these will only continue to improve as larger datasets of CHD anatomy are created. There is still a lack of consistency in methods for segmentation and model generation [105, 106], but future work will continue to refine the techniques to aid in universal adoption.

The costs of 3D printing cannot be ignored, and are often cited as a reason to reject adoption [37]. However, several studies have looked at this issue and found that highly accurate and clinically useful models can be printed using free and open source software and commercially available FDM desktop printers, often for average costs of less than €100 per model [117, 118].

Another limitation is the difficulty in quantifying the clinical benefits of 3D-printed models of CHD. There are several



reports of subjective improvements in procedural planning, but objective measures are still lacking [6, 119]. Work that has already been undertaken to develop objective outcome measures for CHD surgery [97] will continue to provide data to “prove” the utility of 3D-printed models in improving care for patients with CHD.

## 24.6 Conclusions

Incorporation of 3D printing into clinical care for patients with CHD has rapidly evolved in the past two decades and has helped increase understanding of the anatomy and physiology and allowed for the development of novel treatment approaches. As technology continues to improve and adoption becomes more widespread, there will be further optimization of the outcomes for this complex patient population.

## References

- Hull CW. The birth of 3D printing. *Res Technol Manag.* 2015;58(6):25–30.
- Hull CWA, inventor; UVP, Inc. (San Gabriel, CA), assignee. Apparatus for production of three-dimensional objects by stereolithography. United States patent 4575330; 1986.
- Ngan EM, Rebeyka IM, Ross DB, Hirji M, Wolfaardt JF, Seelaus R, et al. The rapid prototyping of anatomic models in pulmonary atresia. *J Thorac Cardiovasc Surg.* 2006;132(2):264–9.
- Noecker AM, Chen JF, Zhou Q, White RD, Kopcak MW, Arruda MJ, et al. Development of patient-specific three-dimensional pediatric cardiac models. *ASAIO J.* 2006;52(3):349–53.
- Parthasarathy J, Krishnamurthy R, Ostendorf A, Shinoka T. 3D printing with MRI in pediatric applications. *J Magn Reson Imaging.* 2020;51(6):1641–58.
- Celi S, Gasparotti E, Capellini K, Vignali E, Fanni BM, Ali LA, et al. 3D printing in modern cardiology. *Curr Pharm Des.* 2021;27(16):1918–30.
- Hadeed K, Guitarte A, Briot J, Dulac Y, Alacoque X, Acar P, et al. Feasibility and accuracy of printed models of complex cardiac defects in small infants from cardiac computed tomography. *Pediatr Radiol.* 2021;51(11):1983–90.
- Lee S, Squelch A, Sun Z. Quantitative assessment of 3D printed model accuracy in delineating congenital heart disease. *Biomolecules.* 2021;11(2):270.
- Dodge-Khatami J, Adebo DA. Evaluation of complex congenital heart disease in infants using low dose cardiac computed tomography. *Int J Cardiovasc Imaging.* 2021;37(4):1455–60.
- Talanki VR, Peng Q, Shamir SB, Baete SH, Duong TQ, Wake N. Three-dimensional printed anatomic models derived from magnetic resonance imaging data: current state and image acquisition recommendations for appropriate clinical scenarios. *J Magn Reson Imaging.* 2022;55:1060.
- Parimi M, Buelter J, Thanugundla V, Condoor S, Parkar N, Danon S, et al. Feasibility and validity of printing 3D heart models from rotational angiography. *Pediatr Cardiol.* 2018;39(4):653–8.
- Seckeler MD, Boe BA, Barber BJ, Berman DP, Armstrong AK. Use of rotational angiography in congenital cardiac catheterisations to generate three-dimensional-printed models. *Cardiol Young.* 2021;31(9):1407–11.
- Fetterly KA, Ferrero A, Lewis BR, Anderson JH, Hagler DJ, Taggart NW. Radiation dose reduction for 3D angiography images in pediatric and congenital cardiology. *Catheter Cardiovasc Interv.* 2021;97(4):E502–e9.
- Kurup HK, Samuel BP, Vettukattil JJ. Hybrid 3D printing: a game-changer in personalized cardiac medicine? *Expert Rev Cardiovasc Ther.* 2015;13(12):1281–4.
- Gosnell J, Pietila T, Samuel BP, Kurup HK, Haw MP, Vettukattil JJ. Integration of computed tomography and three-dimensional echocardiography for hybrid three-dimensional printing in congenital heart disease. *J Digit Imaging.* 2016;29(6):665–9.
- Gomez A, Gomez G, Simpson J, Valverde I. 3D hybrid printed models in complex congenital heart disease: 3D echocardiography and cardiovascular magnetic resonance imaging fusion. *Eur Heart J.* 2020;41(43):4214.
- Mowers KL, Fullerton JB, Hicks D, Singh GK, Johnson MC, Anwar S. 3D echocardiography provides highly accurate 3D printed models in congenital heart disease. *Pediatr Cardiol.* 2021;42(1):131–41.
- Huang J, Shi H, Chen Q, Hu J, Zhang Y, Song H, et al. Three-dimensional printed model fabrication and effectiveness evaluation in fetuses with congenital heart disease or with a normal heart. *J Ultrasound Med.* 2021;40(1):15–28.
- Veronese P, Bertelli F, Cattapan C, Andolfatto M, Gervasi MT, Vida VL. Three-dimensional printing of fetal heart with d-transposition of the great arteries from ultrasound imaging data. *World J Pediatr Congenit Heart Surg.* 2021;12(2):291–2.
- Illmann CF, Ghadiry-Tavi R, Hosking M, Harris KC. Utility of 3D printed cardiac models in congenital heart disease: a scoping review. *Heart.* 2020;106(21):1631–7.
- Valverde I, Gomez G, Gonzalez A, Suarez-Mejias C, Adsuar A, Coserria JF, et al. Three-dimensional patient-specific cardiac model for surgical planning in Nikaidoh procedure. *Cardiol Young.* 2015;25(4):698–704.
- Valverde I, Gomez-Ciriza G, Hussain T, Suarez-Mejias C, Velasco-Forte MN, Byrne N, et al. Three-dimensional printed models for surgical planning of complex congenital heart defects: an international multicentre study. *Eur J Cardiothorac Surg.* 2017;52(6):1139–48.
- Farooqi KM, Gonzalez-Lengua C, Shenoy R, Sanz J, Nguyen K. Use of a three dimensional printed cardiac model to assess suitability for biventricular repair. *World J Pediatr Congenit Heart Surg.* 2016;7(3):414–6.
- Garekar S, Bharati A, Chokhandre M, Mali S, Trivedi B, Changela VP, et al. Clinical application and multidisciplinary assessment of three dimensional printing in double outlet right ventricle with remote ventricular septal defect. *World J Pediatr Congenit Heart Surg.* 2016;7(3):344–50.
- Bhatla P, Tretter JT, Chikkabyrappa S, Chakravarti S, Mosca RS. Surgical planning for a complex double-outlet right ventricle using 3D printing. *Echocardiography.* 2017;34(5):802–4.
- Bhatla P, Tretter JT, Ludomirsky A, Argilla M, Latson LA Jr, Chakravarti S, et al. Utility and scope of rapid prototyping in patients with complex muscular ventricular septal defects or double-outlet right ventricle: does it alter management decisions? *Pediatr Cardiol.* 2017;38(1):103–14.
- Tiwari N, Ramamurthy HR, Kumar V, Kumar A, Dhanalakshmi B, Kumar G. The role of three-dimensional printed cardiac models in the management of complex congenital heart diseases. *Med J Armed Forces India.* 2021;77(3):322–30.
- Yang DH, Park SH, Kim N, Choi ES, Kwon BS, Park CS, et al. Incremental value of 3D printing in the preoperative planning of complex congenital heart disease surgery. *JACC Cardiovasc Imaging.* 2021;14(6):1265–70.
- Yıldız O, Köse B, Tamdır IC, Pekkan K, Güzeltaş A, Haydin S. Single-center experience with routine clinical use of 3D tech-



- nologies in surgical planning for pediatric patients with complex congenital heart disease. *Diagn Interv Radiol*. 2021;27(4):488–96.
30. Zhao L, Zhou S, Fan T, Li B, Liang W, Dong H. Three-dimensional printing enhances preparation for repair of double outlet right ventricular surgery. *J Card Surg*. 2018;33(1):24–7.
  31. Taqatqa AS, Vettukattil JJ. Atrioventricular septal defects: pathology, imaging, and treatment options. *Curr Cardiol Rep*. 2021;23(8):93.
  32. Najm HK, Karamlou T, Ahmad M, Hassan S, Yaman M, Stewart R, et al. Biventricular conversion in unseptatable hearts: “ventricular switch”. *Semin Thorac Cardiovasc Surg*. 2021;33(1):172–80.
  33. Elmaghrawy A, Ghareep AN, Alkuwari M, Hijazi ZM, Salustri A. Patient-specific 3-dimensional printing of tetralogy of fallot with major aortopulmonary collaterals. *JACC Case Rep*. 2019;1(4):535–7.
  34. Averkin II, Grehov EV, Pervunina TM, Komlichenko EV, Vasichkina ES, Zaverza VM, et al. 3D-printing in preoperative planning in neonates with complex congenital heart defects. *J Matern Fetal Neonatal Med*. 2022;35:2020.
  35. Yokoyama S, Fukuba R, Mitani K, Uemura H. Preoperative simulation for complex transposition of great arteries using a three-dimensional model. *Cardiol Young*. 2020;30(2):278–80.
  36. Xu J, Tian Y, Yin J, Wang J, Xu W, Shi Z, et al. Utility of three-dimensional printing in preoperative planning for children with anomalous pulmonary venous connection: a single center experience. *Quant Imaging Med Surg*. 2019;9(11):1804–14.
  37. Zhu Y, Zhang XE, Li Q, Yao H. Three-dimensional printing in a patient with pulmonary artery pseudoaneurysm and complex congenital heart disease—a case report. *Clin Case Rep*. 2020;8:2107–10.
  38. Carberry T, Murthy R, Hsiao A, Petko C, Moore J, Lamberti J, et al. Fontan revision: presurgical planning using four-dimensional (4D) flow and three-dimensional (3D) printing. *World J Pediatr Congenit Heart Surg*. 2019;10(2):245–9.
  39. Vettukattil JJ, Mohammad Nijres B, Gosnell JM, Samuel BP, Haw MP. Three-dimensional printing for surgical planning in complex congenital heart disease. *J Card Surg*. 2019;34(11):1363–9.
  40. Kappanayil M, Koneti NR, Kannan RR, Kottayil BP, Kumar K. Three-dimensional-printed cardiac prototypes aid surgical decision-making and preoperative planning in selected cases of complex congenital heart diseases: early experience and proof of concept in a resource-limited environment. *Ann Pediatr Cardiol*. 2017;10(2):117–25.
  41. Miller JR, Singh GK, Woodard PK, Eghtesady P, Anwar S. 3D printing for preoperative planning and surgical simulation of ventricular assist device implantation in a failing systemic right ventricle. *J Cardiovasc Comput Tomogr*. 2020;14:e172.
  42. Farooqi KM, Saeed O, Zaidi A, Sanz J, Nielsen JC, Hsu DT, et al. 3D printing to guide ventricular assist device placement in adults with congenital heart disease and heart failure. *JACC Heart Fail*. 2016;4(4):301–11.
  43. Sodian R, Weber S, Markert M, Loeff M, Lueth T, Weis FC, et al. Pediatric cardiac transplantation: three-dimensional printing of anatomic models for surgical planning of heart transplantation in patients with univentricular heart. *J Thorac Cardiovasc Surg*. 2008;136(4):1098–9.
  44. Smith ML, McGuinness J, O’Reilly MK, Nolke L, Murray JG, Jones JFX. The role of 3D printing in preoperative planning for heart transplantation in complex congenital heart disease. *Ir J Med Sci*. 2017;186(3):753–6.
  45. Blitzer D, Nguyen S, Farooqi KM, Takeda K. Orthotopic heart transplantation and concomitant aortic arch replacement in an adult Fontan patient with hypoplastic left heart syndrome. *Interact Cardiovasc Thorac Surg*. 2021;32(2):325–7.
  46. Aroney N, Putrino A, Scalia G, Walters D. 3D printed cardiac fistula: guiding percutaneous structural intervention. *Catheter Cardiovasc Interv*. 2018;92(7):E478–e80.
  47. Aroney N, Markham R, Putrino A, Crowhurst J, Wall D, Scalia G, et al. Three-dimensional printed cardiac fistulae: a case series. *Eur Heart J Case Rep*. 2019;3(2):ytz060.
  48. Chamberlain RC, Ezekian JE, Sturgeon GM, Barker PCA, Hill KD, Fleming GA. Preprocedural three-dimensional planning aids in transcatheter ductal stent placement: a single-center experience. *Catheter Cardiovasc Interv*. 2020;95(6):1141–8.
  49. Hassler KR, Stephens EH, Miranda WR, Foley TA, Dearani JA. Intra-atrial pulmonary venous conduit leak in criss-cross heart: role of three-dimensional modeling. *World J Pediatr Congenit Heart Surg*. 2022;13:113.
  50. Jivanji SGM, Qureshi SA, Rosenthal E. Novel use of a 3D printed heart model to guide simultaneous percutaneous repair of severe pulmonary regurgitation and right ventricular outflow tract aneurysm. *Cardiol Young*. 2019;29(4):534–7.
  51. Kern MC, Janardhanan R, Kelly T, Fox KA, Klewer SE, Seckeler MD. Multimodality imaging for diagnosis and procedural planning for a ruptured sinus of Valsalva aneurysm. *J Cardiovasc Comput Tomogr*. 2020;14(6):e139–e42.
  52. Aregullin EO, Mohammad Nijres B, Al-Khatib Y, Vettukattil J. Transcatheter Fontan completion using novel balloon and stent system. *Catheter Cardiovasc Interv*. 2021;97(4):679–84.
  53. Lee DT, Venkatesh P, Bravo-Jaimes K, Lluri G, Yang EH, Tan W, et al. Using a 3-dimensional printed model to plan percutaneous closure of an unroofed coronary sinus. *Circ Cardiovasc Imaging*. 2021;14:e013018.
  54. Seckeler MD, Pineda J, Lotun K. Successful transcatheter recanalization of a chronically occluded left pulmonary artery due to fibrosing mediastinitis. *JACC Cardiovasc Interv*. 2021;14(16):e215–e6.
  55. Alshawabkeh L, Mahmud E, Reeves R. Percutaneous mitral valve repair in adults with congenital heart disease: report of the first case-series. *Catheter Cardiovasc Interv*. 2021;97(3):542–8.
  56. Olivieri L, Krieger A, Chen MY, Kim P, Kanter JP. 3D heart model guides complex stent angioplasty of pulmonary venous baffle obstruction in a Mustard repair of D-TGA. *Int J Cardiol*. 2014;172(2):e297–8.
  57. Valverde I, Gomez G, Coserria JF, Suarez-Mejias C, Uribe S, Sotelo J, et al. 3D printed models for planning endovascular stenting in transverse aortic arch hypoplasia. *Catheter Cardiovasc Interv*. 2015;85(6):1006–12.
  58. Pluchinotta FR, Giugno L, Carminati M. Stenting complex aortic coarctation: simulation in a 3D printed model. *EuroIntervention*. 2017;13(4):490.
  59. Yan C, Wang C, Pan X, Li S, Song H, Liu Q, et al. Three-dimensional printing assisted transcatheter closure of atrial septal defect with deficient posterior-inferior rim. *Catheter Cardiovasc Interv*. 2018;92(7):1309–14.
  60. He L, Cheng GS, Du YJ, Zhang YS. Feasibility of device closure for multiple atrial septal defects with an inferior sinus venosus defect: procedural planning using three-dimensional printed models. *Heart Lung Circ*. 2020;29:914.
  61. Yan C, Li S, Song H, Jin J, Zheng H, Wang C, et al. Off-label use of duct occluder in transcatheter closure of secundum atrial septal defect with no rim to right pulmonary vein. *J Thorac Cardiovasc Surg*. 2019;157(4):1603–8.
  62. Riahi M, Velasco Forte MN, Byrne N, Hermuzi A, Jones M, Baruteau AE, et al. Early experience of transcatheter correction of superior sinus venosus atrial septal defect with partial anomalous pulmonary venous drainage. *EuroIntervention*. 2018;14(8):868–76.
  63. Velasco Forte MN, Byrne N, Valverde I, Gomez Ciriza G, Hermuzi A, Prachasilchai P, et al. Interventional correction of sinus venosus atrial septal defect and partial anomalous pulmonary venous drainage: procedural planning using 3D printed models. *JACC Cardiovasc Imaging*. 2018;11(2 Pt 1):275–8.

64. Hansen JH, Duong P, Jivanji SGM, Jones M, Kabir S, Butera G, et al. Transcatheter correction of superior sinus venosus atrial septal defects as an alternative to surgical treatment. *J Am Coll Cardiol.* 2020;75(11):1266–78.
65. Batteux C, Azarine A, Karsenty C, Petit J, Ciobotaru V, Brenot P, et al. Sinus venosus ASDs: imaging and percutaneous closure. *Curr Cardiol Rep.* 2021;23(10):138.
66. Kanawati J, Kanawati AJ, Rowe MK, Khan H, Chan WK, Yee R. Utility of 3-D printing for cardiac resynchronization device implantation in congenital heart disease. *HeartRhythm Case Rep.* 2020;6:754–6.
67. Seckeler MD, White SC, Klewer SE, Ott P. Transjugular transseptal approach for left ventricular pacing lead in an adult with criss-cross heart. *JACC Clin Electrophysiol.* 2019;5(8):998–9.
68. Hoashi T, Ichikawa H, Nakata T, Shimada M, Ozawa H, Higashida A, et al. Utility of a super-flexible three-dimensional printed heart model in congenital heart surgery. *Interact Cardiovasc Thorac Surg.* 2018;27(5):749–55.
69. Pushparajah K. Non-invasive imaging in the evaluation of cardiac shunts for interventional closure. *Front Cardiovasc Med.* 2021;8:651726.
70. Hussein N, Honjo O, Haller C, Hickey E, Coles JG, Williams WG, et al. Hands-on surgical simulation in congenital heart surgery: literature review and future perspective. *Semin Thorac Cardiovasc Surg.* 2020;32(1):98–105.
71. Hussein N, Lim A, Honjo O, Haller C, Coles JG, Van Arsdell G, et al. Development and validation of a procedure-specific assessment tool for hands-on surgical training in congenital heart surgery. *J Thorac Cardiovasc Surg.* 2020;160(1):229–40.e1.
72. Tomov ML, Cetnar A, Do K, Bauser-Heaton H, Serpooshan V. Patient-specific 3-dimensional-bioprinted model for in vitro analysis and treatment planning of pulmonary artery atresia in tetralogy of fallot and major aortopulmonary collateral arteries. *J Am Heart Assoc.* 2019;8(24):e014490.
73. O'Halloran CP, Qadir A, Ramlogan SR, Nugent AW, Tannous P. Deployed dimensions of the GORE® CARDIOFORM ASD occluder as function of defect size. *Pediatr Cardiol.* 2021;42(5):1209–15.
74. Batteux C, Abakka S, Gaudin R, Vouhé P, Raisy O, Bonnet D. Three-dimensional geometry of coronary arteries after arterial switch operation for transposition of the great arteries and late coronary events. *J Thorac Cardiovasc Surg.* 2021;161(4):1396–404.
75. Parthasarathy J, Hatoum H, Flemister DC, Krull CM, Walter BA, Zhang W, et al. Assessment of transfer of morphological characteristics of anomalous aortic origin of a coronary artery from imaging to patient specific 3D Printed models: a feasibility study. *Comput Methods Programs Biomed.* 2021;201:105947.
76. Schiavone NK, Elkins CJ, McElhinney DB, Eaton JK, Marsden AL. In vitro assessment of right ventricular outflow tract anatomy and valve orientation effects on bioprosthetic pulmonary valve hemodynamics. *Cardiovasc Eng Technol.* 2021;12(2):215–31.
77. Mashari A, Knio Z, Jeganathan J, Montealegre-Gallegos M, Yeh L, Amador Y, et al. Hemodynamic testing of patient-specific mitral valves using a pulse duplicator: a clinical application of three-dimensional printing. *J Cardiothorac Vasc Anesth.* 2016;30(5):1278–85.
78. Medero R, Garcia-Rodriguez S, Francois CJ, Roldan-Alzate A. Patient-specific in vitro models for hemodynamic analysis of congenital heart disease - additive manufacturing approach. *J Biomech.* 2017;54:111–6.
79. Bramlet M, Olivieri L, Farooqi K, Ripley B, Coakley M. Impact of three-dimensional printing on the study and treatment of congenital heart disease. *Circ Res.* 2017;120(6):904–7.
80. Sandrini C, Lombardi C, Shearn AIU, Ordonez MV, Caputo M, Presti F, et al. Three-dimensional printing of fetal models of congenital heart disease derived from microfocus computed tomography: a case series. *Front Pediatr.* 2019;7:567.
81. Hopfner C, Jakob A, Tengler A, Grab M, Thierfelder N, Brunner B, et al. Design and 3D printing of variant pediatric heart models for training based on a single patient scan. *3D Print Med.* 2021;7(1):25.
82. Costello JP, Olivieri LJ, Krieger A, Thabit O, Marshall MB, Yoo SJ, et al. Utilizing three-dimensional printing technology to assess the feasibility of high-fidelity synthetic ventricular septal defect models for simulation in medical education. *World J Pediatr Congenit Heart Surg.* 2014;5(3):421–6.
83. Costello JP, Olivieri LJ, Su L, Krieger A, Alfares F, Thabit O, et al. Incorporating three-dimensional printing into a simulation-based congenital heart disease and critical care training curriculum for resident physicians. *Congenit Heart Dis.* 2015;10(2):185–90.
84. Anwar S, Singh GK, Varughese J, Nguyen H, Billadello JJ, Sheybani EF, et al. 3D printing in complex congenital heart disease: across a spectrum of age, pathology, and imaging techniques. *JACC Cardiovasc Imaging.* 2017;10(8):953–6.
85. Biglino G, Capelli C, Koniordou D, Robertshaw D, Leaver LK, Schievano S, et al. Use of 3D models of congenital heart disease as an education tool for cardiac nurses. *Congenit Heart Dis.* 2017;12(1):113–8.
86. Loke YH, Harahsheh AS, Krieger A, Olivieri LJ. Usage of 3D models of tetralogy of Fallot for medical education: impact on learning congenital heart disease. *BMC Med Educ.* 2017;17(1):54.
87. White SC, Sedler J, Jones TW, Seckeler M. Utility of three-dimensional models in resident education on simple and complex intracardiac congenital heart defects. *Congenit Heart Dis.* 2018;13(6):1045–9.
88. Awori J, Friedman SD, Chan T, Howard C, Seslar S, Soriano BD, et al. 3D models improve understanding of congenital heart disease. *3D Print Med.* 2021;7(1):26.
89. Hon NWL, Hussein N, Honjo O, Yoo SJ. Evaluating the impact of medical student inclusion into hands-on surgical simulation in congenital heart surgery. *J Surg Educ.* 2021;78(1):207–13.
90. Karsenty C, Guitarte A, Dulac Y, Briot J, Hascoet S, Vincent R, et al. The usefulness of 3D printed heart models for medical student education in congenital heart disease. *BMC Med Educ.* 2021;21(1):480.
91. Jones TW, Seckeler MD. Use of 3D models of vascular rings and slings to improve resident education. *Congenit Heart Dis.* 2017;12(5):578–82.
92. Valverde I, Gomez G, Byrne N, Anwar S, Silva MA, Martin Talavera M, et al. Criss-cross heart three-dimensional printed models in medical education: a multi-center study on their value as a supporting tool to conventional imaging. *Anat Sci Educ.* 2022;15:719.
93. Lee C, Lee JY. Utility of three-dimensional printed heart models for education on complex congenital heart diseases. *Cardiol Young.* 2020;30(11):1637–42.
94. Yoo SJ, Spray T, Austin EH III, Yun TJ, van Arsdell GS. Hands-on surgical training of congenital heart surgery using 3-dimensional print models. *J Thorac Cardiovasc Surg.* 2017;153(6):1530–40.
95. Chen SA, Ong CS, Malguria N, Vricella LA, Garcia JR, Hibino N. Digital design and 3D printing of aortic arch reconstruction in HLHS for surgical simulation and training. *World J Pediatr Congenit Heart Surg.* 2018;9(4):454–8.
96. Scanlan AB, Nguyen AV, Ilina A, Lasso A, Cripe L, Jegatheeswaran A, et al. Comparison of 3D echocardiogram-derived 3d printed valve models to molded models for simulated repair of pediatric atrioventricular valves. *Pediatr Cardiol.* 2018;39(3):538–47.
97. Hussein N, Honjo O, Haller C, Coles JG, Hua Z, Van Arsdell G, et al. Quantitative assessment of technical performance during

- hands-on surgical training of the arterial switch operation using 3-dimensional printed heart models. *J Thorac Cardiovasc Surg.* 2020;160(4):1035–42.
98. Nam JG, Lee W, Jeong B, Park EA, Lim JY, Kwak Y, et al. Three-dimensional printing of congenital heart disease models for cardiac surgery simulation: evaluation of surgical skill improvement among inexperienced cardiothoracic surgeons. *Korean J Radiol.* 2021;22(5):706–13.
99. Yoo SJ, Hussein N, Peel B, Coles J, van Arsdell GS, Honjo O, et al. 3D modeling and printing in congenital heart surgery: entering the stage of maturation. *Front Pediatr.* 2021;9:621672.
100. Deng X, He S, Huang P, Luo J, Yang G, Zhou B, et al. A three-dimensional printed model in preoperative consent for ventricular septal defect repair. *J Cardiothorac Surg.* 2021;16(1):229.
101. Boyer PJ, Yell JA, Andrews JG, Seckeler MD. Anxiety reduction after pre-procedure meetings in patients with CHD. *Cardiol Young.* 2020;30:991.
102. Liddle D, Balsara S, Hamann K, Christopher A, Olivieri L, Loke YH. Combining patient-specific, digital 3D models with tele-education for adolescents with CHD. *Cardiol Young.* 2022;32:912.
103. Lau IWW, Sun Z. Dimensional accuracy and clinical value of 3D printed models in congenital heart disease: a systematic review and meta-analysis. *J Clin Med.* 2019;8(9):1483.
104. Meier LM, Meineri M, Qua Hiansen J, Horlick EM. Structural and congenital heart disease interventions: the role of three-dimensional printing. *Neth Heart J.* 2017;25(2):65–75.
105. Byrne N, Velasco Forte M, Tandon A, Valverde I, Hussain T. A systematic review of image segmentation methodology, used in the additive manufacture of patient-specific 3D printed models of the cardiovascular system. *JRSM Cardiovasc Dis.* 2016;5:2048004016645467.
106. Cantinotti M, Valverde I, Kutty S. Three-dimensional printed models in congenital heart disease. *Int J Cardiovasc Imaging.* 2017;33(1):137–44.
107. Huff TJ, Ludwig PE, Zuniga JM. The potential for machine learning algorithms to improve and reduce the cost of 3-dimensional printing for surgical planning. *Expert Rev Med Devices.* 2018;15(5):349–56.
108. Li J, Chen H, Zhu F, Wen C, Wang L. Automatic pulmonary vein and left atrium segmentation for TAPVC preoperative evaluation using V-net with grouped attention. *Annu Int Conf IEEE Eng Med Biol Soc.* 2020;2020:1207–10.
109. Kiraly L, Vijayavenkataraman S. Biofabrication in congenital cardiac surgery: a plea from the operating theatre, promise from science. *Micromachines (Basel).* 2021;12(3):332.
110. Kehl D, Weber B, Hoerstrup SP. Bioengineered living cardiac and venous valve replacements: current status and future prospects. *Cardiovasc Pathol.* 2016;25(4):300–5.
111. Fukunishi T, Best CA, Sugiura T, Opfermann J, Ong CS, Shinoka T, et al. Preclinical study of patient-specific cell-free nanofiber tissue-engineered vascular grafts using 3-dimensional printing in a sheep model. *J Thorac Cardiovasc Surg.* 2017;153(4):924–32.
112. Best C, Strouse R, Hor K, Pepper V, Tipton A, Kelly J, et al. Toward a patient-specific tissue engineered vascular graft. *J Tissue Eng.* 2018;9:2041731418764709.
113. Derakhshanfar S, Mbeleck R, Xu K, Zhang X, Zhong W, Xing M. 3D bioprinting for biomedical devices and tissue engineering: a review of recent trends and advances. *Bioact Mater.* 2018;3(2):144–56.
114. Kwok JKS, Lau RWH, Zhao ZR, Yu PSY, Ho JYK, Chow SCY, et al. Multi-dimensional printing in thoracic surgery: current and future applications. *J Thorac Dis.* 2018;10(Suppl 6):S756–S63.
115. Hadeed K, Acar P, Dulac Y, Cuttone F, Alacoque X, Karsenty C. Cardiac 3D printing for better understanding of congenital heart disease. *Arch Cardiovasc Dis.* 2018;111(1):1–4.
116. Pluchinotta FR, Sturla F, Caimi A, Giugno L, Chessa M, Giamberti A, et al. 3-Dimensional personalized planning for transcatheter pulmonary valve implantation in a dysfunctional right ventricular outflow tract. *Int J Cardiol.* 2020;309:33–9.
117. Perens G, Chyu J, McHenry K, Yoshida T, Finn JP. Three-dimensional congenital heart models created with free software and a desktop printer: assessment of accuracy, technical aspects, and clinical use. *World J Pediatr Congenit Heart Surg.* 2020;11(6):797–801.
118. Gómez-Ciriza G, Gómez-Cía T, Rivas-González JA, Velasco Forte MN, Valverde I. Affordable three-dimensional printed heart models. *Front Cardiovasc Med.* 2021;8:642011.
119. Han F, Co-Vu J, Lopez-Colon D, Forder J, Bleiweis M, Reyes K, et al. Impact of 3D printouts in optimizing surgical results for complex congenital heart disease. *World J Pediatr Congenit Heart Surg.* 2019;10(5):533–8.



---

## Correction to: 3D Printing in Congenital Heart Disease

Michael D. Seckeler, Claudia E. Guerrero,  
and Andrew W. Hoyer

---

**Correction to:**  
**Chapter 24 in: M. A. Syed, R. H. Mohiaddin (eds.), *Magnetic Resonance Imaging of Congenital Heart Disease*, [https://doi.org/10.1007/978-3-031-29235-4\\_24](https://doi.org/10.1007/978-3-031-29235-4_24)**

The original version of this chapter was inadvertently published with a spelling error in the second author's name. The correct name should read as 'Claudia E. Guerrero'. The chapter has been updated with this correction.

---

The updated version of this chapter can be found at [https://doi.org/10.1007/978-3-031-29235-4\\_24](https://doi.org/10.1007/978-3-031-29235-4_24)



# Index

- A**  
Acute kidney injury (AKI), 46, 53  
Adenosine stress, 259, 334  
Aneurysm clip, 39, 40, 42, 44, 164  
Anomalous pulmonary venous, 91, 106, 113, 418, 420, 421, 423  
Anomalous pulmonary venous connection, 64, 65, 79–87, 92, 97, 180, 181, 354–356, 418  
Aortic root, 112, 120, 155, 157, 161, 190, 192, 195, 215, 218, 220, 222, 227, 229, 232, 234, 237–240, 274, 277, 284, 297, 299, 401  
Aortic valve, 11, 24, 26–28, 70–72, 75, 109, 112, 116, 117, 133, 147, 149, 168, 173, 179, 188–190, 192–196, 207, 214, 216, 221, 223, 224, 229, 231, 232, 234, 237–240, 242, 275, 310, 322, 372  
Arrhythmogenic cardiomyopathy, 262, 263  
Atrial septal defect (ASD), 22, 24, 67–69, 72, 81, 83–85, 90, 103–105, 122, 148, 168, 169, 175, 176, 180, 184, 187, 201, 238, 305, 391, 398, 407, 420, 421  
Atrioventricular valve (AVV), 22, 27, 70, 104, 108, 118, 119, 122, 123, 128, 187, 195, 200, 215, 217–220, 222–224, 227, 367, 417, 420
- C**  
Cardiac catheterization, 34, 35, 60, 76, 95, 97, 121, 125, 127, 130, 164, 210, 311, 327, 335, 336, 358, 383–385, 387–393, 416, 419, 420, 423  
Cardiac computed tomography (CT), 142, 180, 219, 285, 357  
Cardiac magnetic resonance (CMR) imaging, 1–5, 8, 10, 11, 13–19, 21, 22, 24–35, 51, 59, 79, 83–85, 87, 89, 97, 100, 168, 169, 179, 207, 209, 213, 251, 303  
Cardiac mass, 53, 315, 319, 321, 326–328  
Cardiac tumor, 34, 35, 315, 316, 318–328, 375  
Cardiovascular anatomy, 14, 22, 52, 59, 410  
Cardiovascular magnetic resonance (CMR) imaging, 1, 103, 115, 137, 139, 147, 204, 229, 283–284, 312, 315, 331, 333–341, 361–378, 383–389, 391–394, 397–411  
Complex congenital heart disease, 118, 119, 234, 238, 244, 347, 368, 399, 401  
Congenital heart disease (CHD), 14–16, 18–35, 55, 59, 60, 62, 63, 65, 66, 68, 69, 72, 73, 75, 76, 79, 99, 105, 109, 115, 118, 151, 226, 305, 383, 384, 386, 387, 392, 393, 397, 399–401, 403–407, 411, 415, 418, 423–424  
Constrictive pericarditis, 305, 308, 309, 312  
Contrast agent, 1, 16, 39, 44, 45, 47, 48, 51–56, 142, 230, 251, 321, 326, 327  
Contrast medium, 349, 358, 359  
Coronary artery abnormalities, 126, 240, 332, 336
- D**  
Dilated cardiomyopathy, 184, 260–262, 268, 403  
Dobutamine stress, 46, 154, 227, 292, 332–335, 337–341
- E**  
Exercise stress MRI, 219, 336, 338
- F**  
Fetal, 103, 126, 168, 169, 244, 361, 362, 364–378  
Fontan, 5, 7, 10, 16, 27, 126, 176, 333, 336–338, 341, 372, 398, 401, 406, 418, 420, 422, 423  
Fontan circulation, 71, 138, 200, 201, 203, 204, 206, 333, 337–341  
Fontan patient, 203–206, 208–211, 337–341  
Fontan procedure, 97, 99, 176, 199, 202, 204, 206, 208, 209, 355, 419  
Fontan surgery, 60, 69, 176, 200, 203–205  
4D flow, 110, 111, 142–143, 162, 163, 205, 336, 337, 350, 351, 354, 355, 358, 359, 364, 365, 375
- G**  
Gadolinium, 8, 16, 20, 21, 23, 26, 28–33, 35, 45–47, 52–54, 92  
Gadolinium-based contrast agents (GBCA), 39, 44, 45, 47, 51–56, 151, 251, 311, 319, 349  
Guide wires, 388, 391
- H**  
Hemodynamics, 121, 128, 203, 218, 331, 365, 366, 371–373, 378, 384, 392  
Heterotaxy syndrome, 60–62, 95, 203, 353–356, 418  
Hypertrophic cardiomyopathy, 31, 188, 253, 255, 275, 331, 411
- I**  
Infants, 17, 30, 75, 85, 86, 100, 120, 121, 184, 218, 335, 347, 349–353, 358, 369, 373, 415, 416  
Inherited cardiomyopathy, 251  
Iron overload related cardiomyopathy, 268
- K**  
Kawasaki's disease, 6, 34, 275
- L**  
Late gadolinium enhancement (LGE), 53, 109, 112, 141, 150, 153, 175, 180, 185, 208, 219, 223, 253–256, 292, 305, 320, 321, 323, 325, 326, 328, 334, 376, 403–404, 406, 407, 409  
Late gadolinium enhancement imaging, 52, 170, 175, 328, 403, 404  
Left ventricular outflow tract, 18, 23, 24, 33, 72, 89, 123, 179, 182, 188, 189, 193, 194, 196, 217, 224, 225, 231, 234, 239, 240, 363, 375

**M**

Magnetic resonance angiography (MRA), 28–31, 83, 88, 89, 92, 107, 120, 142, 173–175, 219, 231, 233, 321  
 Magnetic resonance imaging (MRI), 1, 39, 51, 52, 319–321, 341, 361, 362, 375  
 Main pulmonary artery (MPA), 14, 18, 20, 23, 27, 96, 112, 120, 143, 163, 170, 173, 174, 180, 181, 184, 186, 188, 190, 195, 214–222, 225, 238, 240, 241, 244–246, 296, 304, 351, 353, 363, 365, 367, 368, 370, 374  
 Mitral regurgitation, 182, 184–188, 193–195, 208, 238, 405  
 Mitral valve, 66–68, 72, 75, 104, 106, 107, 112, 168, 170, 179–188, 194, 195, 214, 216, 219, 220, 223, 234, 237, 238, 254, 305, 320, 322, 324, 405, 422  
 Muscular dystrophies (MD), 267–268

**N**

Neonates, 17, 30, 31, 55, 103, 121, 122, 126, 169, 189, 347, 349, 350, 352, 353  
 Nephrogenic systemic fibrosis (NSF), 28, 39, 44–45, 51, 53–54, 79, 349  
 Normal myocardium, 31–34, 52, 117, 219, 320, 325, 404

**O**

Oximetry, 46, 47, 352, 363–366, 368, 374, 375

**P**

Patent ductus arteriosus (PDA), 20, 72, 75, 121, 148, 168, 184, 194, 214, 217, 230, 240, 242, 244, 305, 348, 355, 416, 417  
 Pericardial disease, 303, 304, 311, 312  
 Pericardial effusion, 32, 176, 306–309, 311–313, 316, 319, 324, 327, 328  
 Pharmacological stress MRI, 34, 154, 332, 333  
 Pulmonary arterial hypertension (PAH), 115, 118, 119, 130, 137, 138, 140, 187, 338  
 Pulmonary arterial pressure, 137, 138, 142  
 Pulmonary artery flow, 23, 27, 111, 120, 204, 208, 337, 391  
 Pulmonary hypertension, 79, 80, 87, 89, 100, 107, 120, 130, 131, 137–143, 169, 183, 184, 187, 218, 240, 242–245, 352, 384, 391, 392  
 Pulmonary valve, 23, 27, 71, 72, 110, 111, 120, 121, 123, 125, 126, 139, 147–149, 152, 154–159, 161, 162, 187, 219, 242, 277, 292, 296, 322, 338, 374, 393, 405  
 Pulmonary vascular resistance (PVR), 107, 130–131, 137, 138, 199, 201, 205, 206, 367, 374, 384, 386, 391–392  
 Pulmonary veins, 19, 27, 29, 62, 64, 65, 79–93, 97, 99, 100, 104, 106, 107, 112, 116, 121, 129, 152, 180, 181, 195, 203, 206, 207, 208, 215, 226, 316, 324, 350, 353–356, 358, 373, 397, 400–402, 404, 405, 411, 420, 421, 423

**R**

Regadenoson, 46, 223, 292, 332, 333, 335  
 Right ventricle, 10, 12, 14, 29, 31, 35, 61, 62, 66, 67, 69–72, 79–81, 84, 87–89, 91, 92, 95, 99, 100, 105, 115, 118–126, 131, 132, 137, 149, 156, 158, 167–170, 172, 175–177, 181–183,

185–189, 193, 200, 203, 206, 208, 213–219, 221, 223, 225, 226, 240, 262, 263, 308, 309, 317, 320, 323, 325, 328, 333–339, 341, 350, 351, 353, 355, 356, 363, 365, 367, 368, 373–375, 377, 388, 390, 393, 397, 404, 405, 407, 410, 418, 419

Right ventricular, 9, 35, 85, 87, 89, 100, 115–134, 147, 159, 168–170, 175, 176, 181, 184, 194, 227, 242, 243, 254, 318, 422

Right ventricular function, 137, 213, 218, 226, 227

Right ventricular outflow tract (RVOT), 14, 20, 115, 120, 126, 148, 158, 161, 169, 170, 173, 176, 193, 220, 221, 225, 239, 318, 319, 363, 388, 393, 419, 420

**S**

Sedation, 16–18, 79, 112, 204, 230, 351–353, 357  
 Septal defect, 22, 24, 27, 67–69, 71, 72, 75, 81, 83, 84, 87, 90, 95, 99, 103–105, 107–112, 119–121, 125, 127, 147–149, 168–170, 172, 173, 175–177, 188, 193, 194, 200, 214, 217, 219, 356  
 Shunt, 19, 22, 23, 27, 30, 43, 53, 62, 68, 69, 80, 83, 84, 92, 95, 103, 104, 107, 110–113, 118, 122, 127, 138, 139, 142, 148, 151, 152, 155, 156, 169, 173, 175, 180, 181, 187, 195, 200, 204, 207, 209, 211, 213, 214, 242, 244, 245, 281, 297, 349, 350, 358, 366, 367, 374, 384, 398, 400  
 Specific absorption rate (SAR), 41  
 Stress cardiovascular magnetic resonance imaging, 333–341

**T**

Tetralogy of Fallot (TOF), 13, 14, 26, 27, 30, 31, 68, 81, 95, 99, 108, 119, 120, 124–126, 147–149, 151, 154–159, 161, 163, 164, 213, 217, 218, 242, 245, 274, 293, 305, 333, 335, 336, 338, 339, 341, 370, 373, 405, 407–410, 418, 422  
 3D printing, 107, 356, 415–424  
 Transposition of the great arteries (TGA), 22, 23, 27, 31, 34, 61, 62, 71, 72, 85, 120, 121, 168, 175, 176, 188, 213–217, 220, 221, 223–225, 234, 238, 245, 274, 332–334, 338, 341, 368, 369, 373, 398, 399, 402, 405, 406, 418, 421, 422  
 Tricuspid regurgitation, 118, 138, 149, 167–170, 172, 175–177, 185, 219, 367, 374  
 Tricuspid valve, 66–68, 70, 72, 105, 106, 116, 120–122, 126, 127, 129, 130, 132, 148, 149, 152, 167–170, 172, 173, 175–177, 183, 185, 187, 188, 206, 214, 218, 219, 221, 223, 305, 322, 369, 374, 390, 406–407, 421

**V**

Velocity mapping, 7, 11, 14, 15, 21, 23, 25–29, 35, 117, 118, 121, 122, 124, 125, 127–129, 131–133, 153, 155, 156, 162, 181, 184, 188, 190, 204, 233  
 Vena cava, 18, 24, 29, 43, 60–63, 127, 128, 148, 170, 200, 202, 216, 218, 220, 224, 227, 308, 309, 316, 321, 354, 363, 365–367, 369, 370, 388, 391, 398, 399, 420, 421  
 Ventricular septal defect (VSD), 67–69, 71, 72, 75, 87, 99, 103, 105–108, 110, 120–121, 125, 147, 168, 169, 173, 175, 184, 186, 200, 204, 210, 214, 217, 221, 224, 225, 234, 237, 238, 240–242, 244, 245, 348, 350, 356, 367, 373, 390, 398, 418, 419